pe
Publicaciones Geológicas Especiales

The Geology of Colombia book provides an updated background of the geological knowledge of Colombia by integrating the most up–to–date research covering paleontology, biostratigraphy, sedimentary basin analysis, sedimentology, sequence stratigraphy, stratigraphy, geophysics, geochronology, geochemistry, thermochronology, tectonics, structure, volcanology, petrology, environmental science, climate change, and space geodesy.

Each chapter has a complete framework of a major branch of geology providing an invaluable resource for geologists interested in the geological history of Colombia.

The second volume has fourteen chapters presenting the geological history of Permian – Triassic magmatic rocks of the northern Andes, Late Triassic – Jurassic magmatism, Jurassic magmatic arcs in northwestern Gondwana, the petrological nature of the Dunita de Medellín, oceanic tectonostratigraphic terranes in Colombia, evolution of the tropical biome, the Cretaceous back–arc basin, Barremian marine strata, plesiosaurs and palaeoenvironments of the Paja Formation Lagerstätte, and Cretaceous subduction events in the Central Cordillera.

Other volumes in *The Geology of Colombia* book
Volume 1: Proterozoic – Paleozoic
Volume 3: Paleogene – Neogene
Volume 4: Quaternary

SERVICIO GEOLÓGICO COLOMBIANO

El futuro es de todos | Minenergía

ISBN: 978-958-52959-3-3

Jorge GÓMEZ TAPIAS
Ana Oliva PINILLA–PACHON
Editors

THE GEOLOGY OF COLOMBIA
VOLUME 2 • MESOZOIC

pe
36

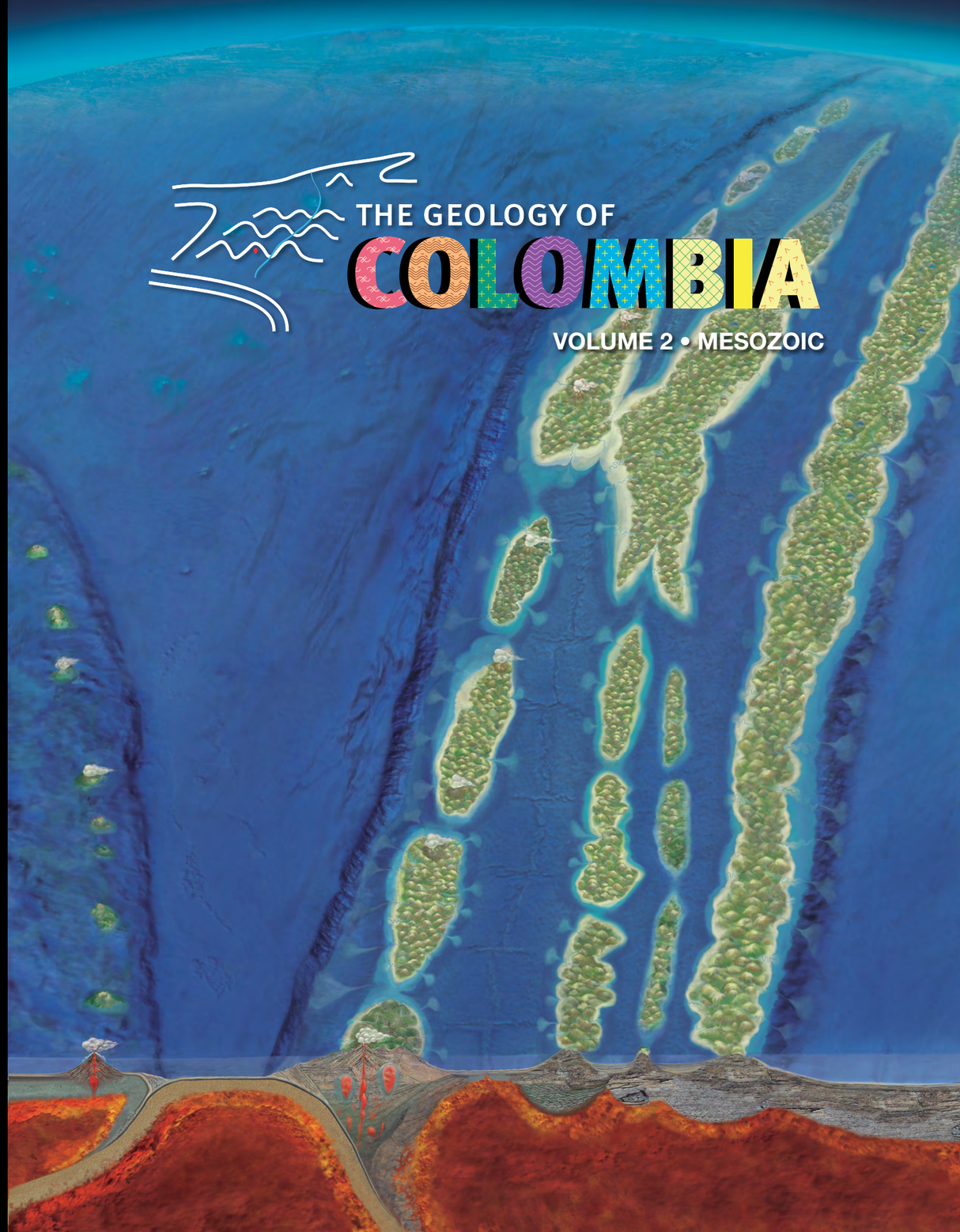

Publicaciones Geológicas Especiales

THE GEOLOGY OF COLOMBIA

Jorge GÓMEZ TAPIAS and Ana PINILLA–PACHON
Servicio Geológico Colombiano
Editors

SERVICIO GEOLÓGICO COLOMBIANO

El futuro es de todos | Minenergía

ISBN impreso obra completa: 978-958-52959-1-9
ISBN digital obra completa: 978-958-52959-6-4

ISBN impreso Vol. 2: 978-958-52959-3-3
ISBN digital Vol. 2: 978-958-52959-8-8

Jorge GÓMEZ TAPIAS
Daniela MATEUS–ZABALA
Ana PINILLA–PACHON
Editores

Miguel Gerardo RAMÍREZ–LEAL
Diseñador

Imprenta Nacional de Colombia
Impresión

Bogotá D. C., Colombia
2020

Cover

Illustration showing the geological framework for Cretaceous—ca. 110 Ma—with two subduction zones. From left to right the Colombian Caribbean Oceanic Plateau (CCOP) created by a hypothetical subduction zone located eastward, the Farallón Plate, the Quebradagrande Volcanic Arc with its linked back–arc basin, the Abejorral Basin, and San Luis Basin.

Scientific illustration made by Marie Joëlle GIRAUD, a geologist. The illustration is based on 3D representation of Google Earth.

Suggested citation for Volume 2

Gómez, J. & Pinilla–Pachon, A.O., editors. 2020. The Geology of Colombia, Volume 2 Mesozoic. Servicio Geológico Colombiano, Publicaciones Geológicas Especiales 36, 498 p. Bogotá. https://doi.org/10.32685/pub.esp.36.2019

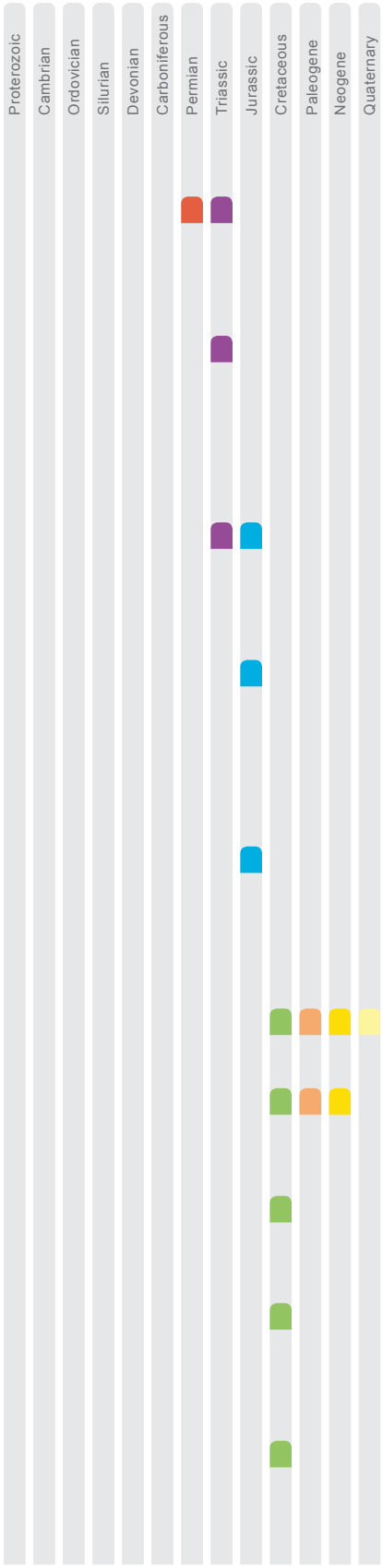

Content

Volume 2

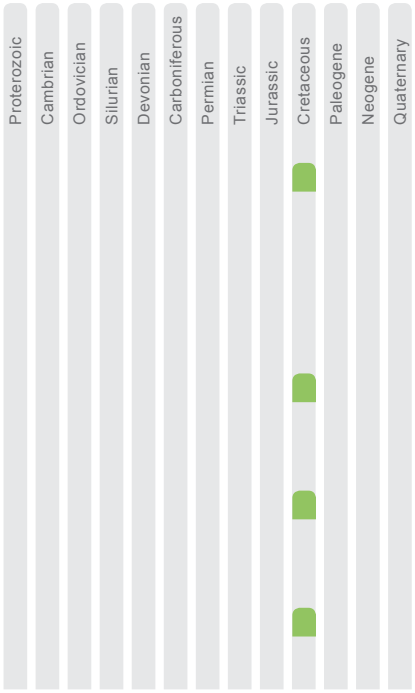

Contributing authors

María Isabel ARANGO–MEJÍA
Juan Camilo ARENAS
Germán BAYONA
José Gilberto BERMÚDEZ
Idael Francisco BLANCO–QUINTERO
Andres BUSTAMANTE
Camilo BUSTAMANTE
Lidia BUTJOSA
William G. CARANTON–MATEUS
Agustín CARDONA
Alejandro CORRALES–GARCÍA
Ana María CORREA–MARTÍNEZ
Antonio GARCIA–CASCO
Marcela GÓMEZ–PÉREZ
Javier GUERRERO
Carlos JARAMILLO
Juan S. JARAMILLO
Santiago LEÓN
Julián Andrés LÓPEZ–ISAZA
Dany MEJÍA
Alejandra MEJÍA–MOLINA
Leslie F. NOÈ
Giovanny NOVA
Gloria OBANDO–ERAZO
José OSORNO
Andrés PARDO–TRUJILLO
Pedro PATARROYO
Andre PAUL
Joaquín Antonio PROENZA
Jorge Julián RESTREPO
José Vicente RODRÍGUEZ
Gabriel RODRÍGUEZ–GARCÍA
Ana Milena SALAZAR–FRANCO
Axel K. SCHMITT
Richard SPIKINGS
Jean–François TOUSSAINT
Victor A. VALENCIA
Marion WEBER
Sebastian ZAPATA
Gilberto ZAPATA–GARCÍA
Juan Pablo ZAPATA–VILLADA
Carlos Augusto ZULUAGA

Volume 2

Chapter 1

The Permian – Triassic History of Magmatic Rocks of the Northern Andes (Colombia and Ecuador): Supercontinent Assembly and Disassembly

https://doi.org/10.32685/pub.esp.36.2019.01
Published online 23 October 2019

Richard SPIKINGS[1]* and Andre PAUL[2]

1 richard.spikings@unige.ch
University of Geneva
Department of Earth Sciences and the Environment
Rue des Maraichers 13, Geneva 1205
Switzerland

2 andre.paul@unige.ch
University of Geneva
Department of Earth Sciences and the Environment
Rue des Maraichers 13, Geneva 1205
Switzerland

* Corresponding author

Abstract Northwestern South America and its conjugate margins record the Permian assembly of Pangaea, its Triassic fragmentation and opening of the proto–Caribbean ocean, and the onset of the Andean cycle at ca. 209 Ma. We review Permian and Triassic magmatic rocks exposed in the cordilleras and dispersed inliers in Colombia and Ecuador, and present a large geochronological, geochemical, isotopic, and thermochronological database. These data are used to develop a model for the evolution of rocks within Colombia and Ecuador during the formation and destruction of Pangaea. Similar data has been assembled from studies of the southern North American and western Caribbean plates, as well as Venezuela and further south within South America, and a large–scale reconstruction for western Pangaea is provided. Permian magmatic rocks in Colombia and Ecuador (288–253 Ma) formed within a continental arc system which extended from at least southern North America to southern Perú. The Permian arc within northwestern South America was dismembered during Cenozoic interactions with the Caribbean Plate, causing some blocks to be transferred eastwards. Compression and regional metamorphism at ca. 250 Ma is best recorded in the Sierra Nevada de Santa Marta, and represents the final stages of amalgamation and thickening of western Pangaea. Continental rifting prevailed within southern North America and the entire western margin of South America during 245–216 Ma. Significant back–arc extension in northwestern South America leads to a rift–to–drift transition in Colombia and Ecuador, forming oceanic lithosphere of the proto–Caribbean. Rifting failed south of the Huancabamba Deflection, and is preserved as Triassic basins in Perú, western Argentina, and Chile. Triassic rifting represents the early fragmentation of western Pangaea, and the attenuation of its margin may be a prelude to complete separation by enhancing mantle upwelling, inducing a Large Igneous Province and weakening the crust within a tensile regime.

Keywords: *Permian – Triassic, Pangaea, supercontinent, continental rift, anatexis.*

Resumen El noroccidente de Suramérica y sus márgenes conjugados registran la formación de Pangea durante el Pérmico, su fragmentación durante el Triásico y la apertura del océano proto–Caribe, así como el comienzo del ciclo andino hace ca. 209 Ma. En este capítulo presentamos una revisión de las rocas magmáticas del Pérmico y Triá-

Citation: Spikings, R. & Paul, A. 2019. The Permian – Triassic history of magmatic rocks of the northern Andes (Colombia and Ecuador): Supercontinent assembly and disassembly. In: Gómez, J. & Pinilla–Pachon, A.O. (editors), The Geology of Colombia, Volume 2 Mesozoic. Servicio Geológico Colombiano, Publicaciones Geológicas Especiales 36, p. 1–43. Bogotá. https://doi.org/10.32685/pub.esp.36.2019.01

sico que afloran como fragmentos dispersos en las cordilleras de Colombia y Ecuador; además, presentamos una amplia base de datos geocronológica, geoquímica, isotópica y termocronológica. Estos datos se utilizan para desarrollar un modelo de la evolución de las rocas en Colombia y Ecuador durante la formación y la separación de Pangea. Otros estudios en el sur de la Placa de Norteamérica y en el occidente de la Placa del Caribe, así como en Venezuela y más al sur dentro de Suramérica, han sido también tenidos en cuenta para este análisis. Adicionalmente, se preparó una reconstrucción a gran escala del occidente de Pangea. Las rocas magmáticas del Pérmico de Colombia y Ecuador (288–253 Ma) se formaron en un ambiente de arco continental que se extendió al menos desde el sur de Norteamérica hasta el sur de Perú. En el noroccidente de Suramérica, este arco pérmico se separó durante las interacciones con la Placa del Caribe en el Cenozoico, de forma que algunos bloques fueron transferidos hacia el oriente. La compresión y el metamorfismo regional que ocurrieron hace ca. 250 Ma se observan claramente en la Sierra Nevada de Santa Marta y representan los estados finales de la amalgamación y engrosamiento del occidente de Pangea. El *rift* continental continuó en el sur de Norteamérica y todo el margen occidental de Suramérica durante 245–216 Ma. La extensión en el retroarco en Suramérica fue muy importante y llevó a una transición *rift–drift* en Colombia y Ecuador, lo que causó la formación de la litósfera oceánica del proto–Caribe. El *rift* fue abortado al sur de la deflexión de Huancabamba, pero se preservó como cuencas triásicas en Perú, el occidente de Argentina y Chile. Este *rift* triásico representa una separación temprana del occidente de Pangea y la atenuación de su margen podría ser el preludio de la separación completa de los continentes, ya que potencia el ascenso del manto y esto induce a la formación de una Gran Provincia Ígnea, debilitando la corteza en un régimen de extensión.

Palabras clave: *Pérmico–Triásico, Pangea, supercontinente, rift continental, anatexis.*

1. Introduction

The northwestern South American Plate hosts a Rodinia–aged (ca. 1 Ga) and Ordovician basement, which was modified during the amalgamation and disassembly of Pangaea. Subsequent active margin magmatism (209–115 Ma) within the proto–Caribbean and Pacific Wilson cycle occurred during a prolonged period of extension (Cochrane et al., 2014a; Spikings et al., 2015), which was interrupted by compression at ca. 115 Ma (Spikings et al., 2015) and the collision of the voluminous Caribbean Large Igneous Province at ca. 75 Ma (Vallejo et al., 2006), which added new crust to South America. This chapter is a review of crystalline and some sedimentary rocks exposed in Colombia and Ecuador that formed during the Permian and Triassic. These rocks record the period between the final assembly of Pangaea in the early Permian, and its early disassembly during the Triassic. Colombia and Ecuador are considered together because their Permian and Triassic rock records are extremely similar and complementary, and thus studying both countries increases our chances of observing poorly exposed sequences and obtaining an accurate geological model, and provides a means to identify plate margin trends. The studied units are mainly exposed in the Central Cordillera, Sierra Nevada de Santa Marta, and Santander Massif of Colombia, and the Cordillera Real and Amotape Complex of Ecuador. We will also consider Permian and Triassic crystalline rocks exposed in Perú and other regions of South America, as well as the southernmost North American and western Caribbean plates, which were coeval with and probably formed in the same general tectonic setting as crystalline rocks in northwestern South America, facilitating reconstructions of western Pangaea.

The amalgamation of Pangaea in the Permian coincided with a drastic reduction in plate velocities and an almost complete pause in continental drift during the late Permian – Early Jurassic (Vilas & Valencio, 1978). This relatively stationary period was characterised by heat accumulation, the production of large volumes of magmas (e.g., Kay et al., 1989), and geographically extensive extension along western South America (e.g., Charrier et al., 2007; Spikings et al., 2015, 2016). Increased plate velocities in the earliest Jurassic (e.g., Ramos, 1988) were coeval with the disassembly of Pangaea, although the relationship between Triassic extension and the rapid disassembly of Pangaea in the Early Jurassic is unclear.

This review presents geochronological (U–Pb zircon), geochemical, isotopic (Hf, Pb, Sr, Nd, O), and thermochronological (U–Pb and $^{40}Ar/^{39}Ar$) data from the Permian and Triassic magmatic rocks of the Central Cordillera of Colombia, and coeval magmatic and metasedimentary units of the Sierra Nevada de Santa Marta. The same techniques have been applied to the Tres Lagunas Granite, Sabanilla Migmatite (Cordillera Real, Ecua-

dor), and the Moromoro Granite (Amotape Complex, Ecuador), along with Triassic mafic units in both countries. These data are used to develop a temporally constrained tectonic framework for the Permian – Triassic, culminating with rifting along western Pangaea (proto–Caribbean; Jaillard et al., 1990, 1995; Pindell, 1985), and to investigate the relationship between initial Triassic rifting and the final disassembly of Pangaea.

2. Geological Framework and Previous Work

Phanerozoic rocks in the northern Andes (north of the Huancabamba Deflection; at 5° S; Figure 1) can be separated into a relatively undifferentiated oceanic Upper Cretaceous sequence, which is faulted against older, differentiated continental crust. The Upper Cretaceous oceanic rocks form the basement to the Western Cordillera and the forearcs of Colombia (Calima and Chocó–Panamá Terranes; Figure 1; e.g., Kerr et al., 1997, 2002) and Ecuador (Pallatanga–Piñon Terrane; e.g., Vallejo et al., 2009). Geochemical, isotopic, and geochronological data suggests these laterally accreted ultramafic and mafic rocks formed in an oceanic hot–spot setting during 99–87 Ma (e.g., Kerr et al., 1997; Vallejo et al., 2006; Villagómez et al., 2011), and that they are equivalent to the oceanic plateau rocks that form the Caribbean Plate (e.g., Sinton et al., 1998; van der Lelij et al., 2010). Field relationships and U–Pb zircon dates show that the oceanic plateau was intruded by an east–facing intra–oceanic arc prior to their collision with South America in the Campanian (e.g., Spikings et al., 2010; Vallejo et al., 2006, 2009), although this is not consistent with the plate reconstructions of Pindell & Kennan (2009), who suggest that arcs at this time were west–facing and were intruding the continental margin of South America. The accretion of allochthons of the Caribbean Large Igneous Province added at least $5 \times 10^6 - 1 \times 10^7$ km^3 of new crust to the South American Plate (Cochrane et al., 2014a). These terranes are bound to the east by the Cauca–Almaguer Fault (Colombia; Figure 1), and the buried Ingapirca Fault (Ecuador).

The Early Cretaceous continental margin hosts linear belts that are exposed within the Central Cordillera and Sierra Nevada de Santa Marta of Colombia, and the Cordillera Real and Amotape Complex of Ecuador (Figure 1). These belts mainly strike to the north, although they have been partially segmented and rotated, resulting in a NE (Sierra Nevada de Santa Marta, Colombia; Bayona et al., 2010) and E–W (Amotape Complex, Ecuador; Mitouard et al., 1990) strike. Traversing eastwards from the Campanian suture, these are M–HP/LT complexes of amphibolites, blueschists, and eclogites (e.g., Arquía and Barragán Complexes, Colombia; Raspas Complex, Ecuador; e.g., Bustamante et al., 2012; John et al., 2010; Spikings et al., 2015), Cretaceous arc rocks of the Quebradagrande (Colombia; Nivia et al., 2006) and Alao sequences (Ecuador; Cochrane et al., 2014a; Spikings et al., 2015), poorly differentiated Paleozoic rocks that contain isolated exposures of Ordovician gneisses (e.g., Martens et al., 2014; Villagómez et al., 2011; Vinasco et al., 2006), minor Permian intrusions and extensive Triassic anatectites (Cochrane et al., 2014a; Paul et al., 2018; Spikings et al., 2015), foliated Jurassic arc rocks that are best exposed in Ecuador, and large unfoliated Jurassic batholiths along the eastern flank of the Central Cordillera in Colombia, and Cordillera Real in Ecuador (Figure 1). McCourt et al. (1984), Aspden & McCourt (1986), Aspden & Litherland (1992), and Litherland et al. (1994) suggest that these belts are in tectonic contact, and the Triassic and younger belts were juxtaposed during compression at 140–120 Ma. Alternatively, Pratt et al. (2005) suggest that the contacts are intrusive, and the rock units within Ecuador are autochthonous, which is similar to the model proposed by Villagómez & Spikings (2013), Cochrane et al. (2014a), and Spikings et al. (2015) for Colombia and Ecuador. The Permian and Triassic rocks form the focus of this review.

Traversing further eastwards, the Eastern Cordillera of Colombia has no equivalent topographic feature in Ecuador, and it includes the high plains of the Santander Massif in the north (Figure 1). The Santander Massif has an extensive metamorphic basement that is dominated by amphibolite grade Ordovician gneisses of the Bucaramanga Gneiss and Berlin Orthogneiss (van der Lelij et al., 2016). In contrast to the rocks exposed in the Central Cordillera, a significant magmatic hiatus exists between the Ordovician basement (500–415 Ma; van der Lelij et al., 2016), and intruding late Triassic (209 Ma; van der Lelij et al., 2016) and younger continental arc rocks of the Santander Plutonic Group. Triassic anatexis, which is extensively preserved in the cordilleras, did not affect the Ordovician basement exposed in the Santander Massif, and the Permian is only recorded by a single rhyolite (251 ± 4 Ma; van der Lelij et al., 2016) along the western margin of the massif. The Permian Diamante, Tiburón, and the fossiliferous Bocas sedimentary Formations are sporadically exposed across the Santander Massif, although the tectonic environment in which they were deposited is undetermined. Coeval Permian sedimentary successions in the juxtaposed Mérida Andes of Venezuela (Palmarito Formation; Figure 1) are interpreted to have deposited in a foreland basin (Laya & Tucker, 2012), which may have formed during the final stages of the Alleghanian Orogeny, culminating with the amalgamation of Pangaea by the early Permian (Hatcher, 2002).

The Sierra Nevada de Santa Marta resides within a triangular faulted block in northern Colombia (Figure 1). The northern margin of the Sierra Nevada de Santa Marta Block is truncated by the right–lateral Oca Fault, which is displacing Cretaceous and older continental crust of the Guajira Peninsula to the east (Figure 1). The western margin of the triangular block is defined by the Santa Marta–Bucaramanga Fault (Figure 1), which separates crystalline rocks in the east from the Oligocene – Miocene Plato–San Jorge Basin to the west, which is floored by Triassic rocks similar to those exposed in the Sierra Nevada

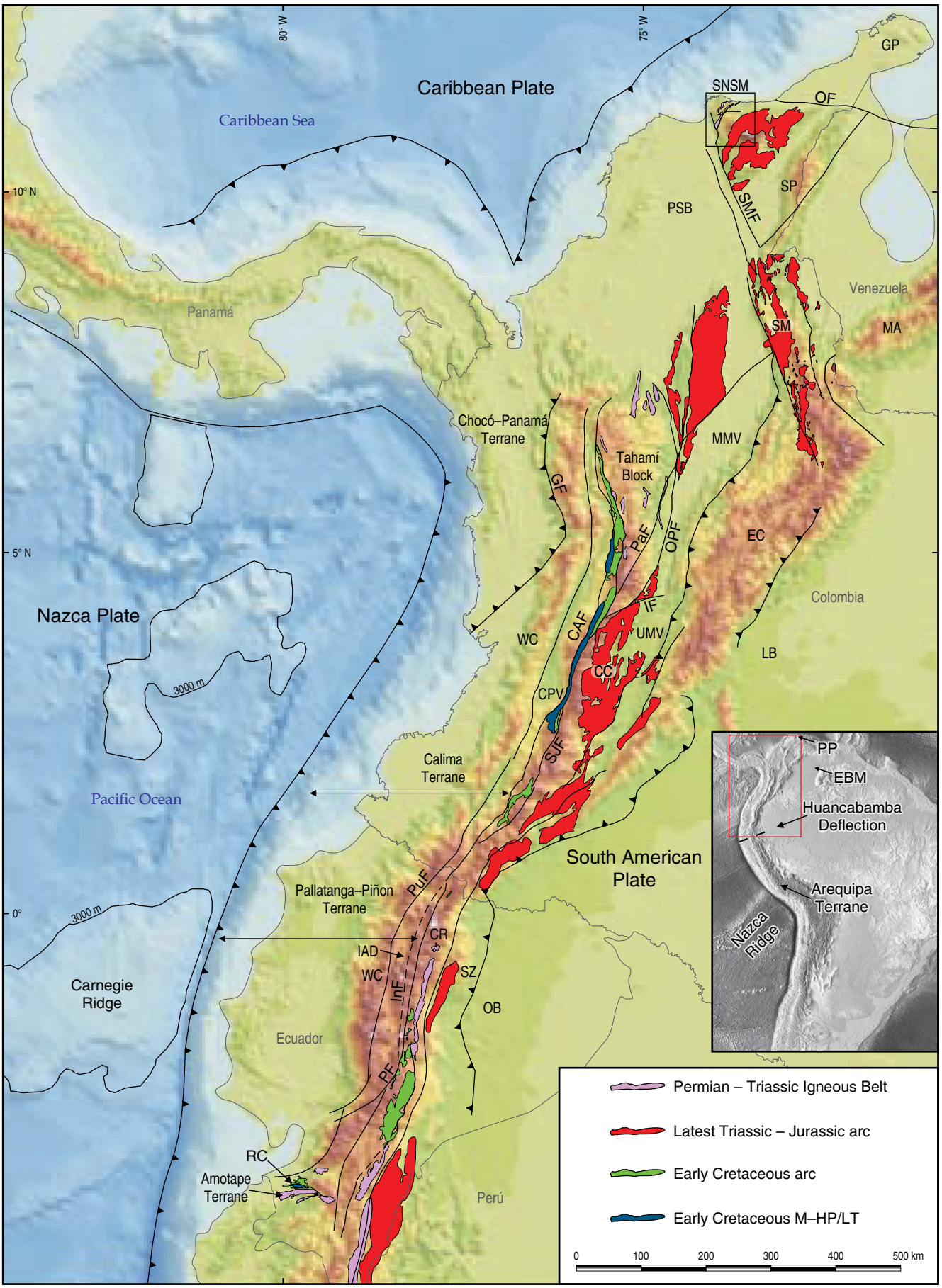
Caribbean Plate
Caribbean Sea
Panamá
Nazca Plate
Pacific Ocean
South American Plate
Carnegie Ridge
Ecuador
Perú
Colombia
Venezuela
80° W
75° W
10° N
5° N
0°
3000 m
GP
SNSM
OF
SP
SMF
PSB
SM
MA
MMV
Chocó–Panamá Terrane
Tahamí Block
GF
PaF
OPF
EC
IF
CAF
WC
UMV
CC
CPV
SUF
LB
Calima Terrane
Pallatanga–Piñon Terrane
PuF
CR
IAD
WC
InF
SZ
OB
PF
RC
Amotape Terrane
PP
EBM
Huancabamba Deflection
Arequipa Terrane
Nazca Ridge
Permian – Triassic Igneous Belt
Latest Triassic – Jurassic arc
Early Cretaceous arc
Early Cretaceous M–HP/LT
0
100
200
300
400
500 km

de Santa Marta (Montes et al., 2010). The Santa Marta–Bucaramanga Fault extends towards the SSE where it defines the western margin of the Santander Massif within the Colombian Eastern Cordillera (Figure 1). The present study follows the geological subdivisions of the Sierra Nevada de Santa Marta proposed by Tschanz et al. (1974), which were structurally revised by Colmenares et al. (2007a, 2007b) and better temporally constrained by Cardona et al. (2010a, 2010b) and Piraquive (2017). The Inner Santa Marta Metamorphic Belt of the Sierra Nevada de Santa Marta consists of Paleozoic orthogneisses and schists, which were intruded by Permian – Triassic syntectonic granitoids (Piraquive, 2017) that are studied in this review. Palaeomagnetic studies (Bayona et al., 2006, 2010) suggest that Jurassic rocks exposed along the southern border of the Sierra Nevada de Santa Marta rotated clockwise (17 ± 13°) between the Middle – Late Jurassic and Early Cretaceous, and thus it is likely that there is a genetic link between Permian – Triassic magmatic rocks exposed in the Central Cordillera and the Sierra Nevada de Santa Marta. Similarly, Pindell et al. (1998) used palinspastic reconstructions to reach the same conclusion.

3. Historical Perspective and Occurrence of Permian – Triassic Igneous Rocks

Widely dispersed and variably deformed Permian and Triassic meta–granitoids, ultra–mafic – mafic rocks, and metasedimentary rocks occur within the northern Central Cordillera of Colombia (Figure 2). These rocks were initially described by Hall et al. (1972), Feininger et al. (1972), and González (1980), who considered them to be Permian – Triassic on the basis of K/Ar dates. Restrepo & Toussaint (1988) suggested the Permian – Triassic rocks defined the basement of the fault–bounded Tahamí Terrane, and placed them within the Central Cordillera Polymetamorphic Complex (Restrepo & Toussaint, 1982). The Tahamí Terrane of Restrepo & Toussaint (1988) is bound by the Otú–Pericos Fault to the east, which separates it from Grenvillian aged metamorphic basement of the postulated Chibcha Terrane (e.g., Ordóñez–Carmona et al., 2006), and the San Jerónimo Fault to the west, which separates it from the Cretaceous Quebradagrande Arc (Figure 1). Maya & González (1995) and Villagómez et al. (2011) group the Triassic metamorphosed igneous and sedimentary rocks into the Cajamarca Complex, which will be adopted in this manuscript. The geological map of Colombia (Gómez et al., 2007) reveals a paucity of Triassic lithologies within the Central Cordillera south of the Ibagué Fault (Figure 2). Vinasco et al. (2006), Correa–Martínez (2007), Cardona et al. (2010a), Montes et al. (2010), Weber et al. (2010), Restrepo et al. (2011), Villagómez et al. (2011), Cochrane et al. (2014b), Martens et al. (2014), Spikings et al. (2015), Bustamante et al. (2017), and Paul et al. (2018) present a large quantity of geochemical data and concordant zircon U–Pb dates (Figure 2; Table 1) from the Cajamarca unit, confirming the Permian – Triassic crystallisation gneisses of the Central Cordillera, which are faulted against Paleozoic (mainly Ordovician) metamorphic rocks such as La Miel unit (e.g., Martens et al., 2014; Restrepo et al., 1991; Villagómez et al., 2011). In contrast, anatexis of undifferentiated Upper Devonian – Carboniferous metasedimentary rocks forming the Triassic Sabanilla Migmatite can be observed in the Cordillera Real. Correa–Martínez (2007) reports a series of metagabbros and amphibolites in the northern Central Cordillera, which she attributes to a Triassic ophiolitic sequence, referred to as the Aburrá Ophiolite (Figure 2). Permian and/or Triassic igneous and metamorphic rocks have also been recognised in the Guajira Peninsula, Sierra Nevada de Santa Marta (Figure 3), and at the base of boreholes drilled though the Plato–San Jorge Basin located north of the Central Cordillera (Figure 1; Cardona et al., 2010b; Montes et al., 2010; Piraquive, 2017; Weber et al., 2010). Granites from the basement of the Plato–San Jorge Basin are mildly deformed, while the intrusions from the Sierra Nevada de Santa Marta are mylonitised.

Triassic rocks within the Cordillera Real and Amotape Terrane of Ecuador include granitoids of the Tres Lagunas and Moromoro units, migmatites of the Sabanilla unit, geographically scattered amphibolitic dykes and sills (Piedras and Monte Olivo units), and sedimentary rocks of the Piuntza unit (Figure 2). The granites were first described by Colony & Sinclair (1932). Mapping by the British Geological Survey during 1986–1993 linked these occurrences into a semi–continuous belt, and they were grouped into the Loja Terrane (Litherland et al., 1994) along with undifferentiated Paleozoic metamorphic rocks of the Chiguinda and Agoyán units. The Loja Terrane of Litherland et al. (1994) is bound to the

Triassic
Permian

Figure 1. Digital elevation model for northwestern South America showing the cordilleras, terranes, main faults, and the exposure of Permian – Cretaceous magmatic rocks in Ecuador and Colombia. Small black box indicates the location of Figure 3. Inset shows the location of the Arequipa Terrane in southern Perú. Faults: (CAF) Cauca–Almaguer Fault; (GF) Garrapatas Fault; (IF) Ibagué Fault; (InF) Ingapirca Fault; (OF) Oca Fault; (OPF) Otú–Pericos Fault; (PaF) Palestina Fault; (PF) Peltetec Fault; (PuF) Pujili Fault; (SJF) San Jerónimo Fault; (SMF) Santa Marta–Bucaramanga Fault. Other abbreviations: (CC) Central Cordillera; (EC) Eastern Cordillera; (CPV) Cauca–Patía valley; (CR) Cordillera Real; (EBM) El Baúl Massif; (GP) Guajira Peninsula; (IAD) Interandean Depression; (LB) Llanos Basin; (MA) Mérida Andes; (MMV) Middle Magdalena Valley Basin; (OB) Oriente Basin; (PP) Paraguaná Peninsula; (PSB) Plato–San Jorge Basin; (RC) Raspas Complex; (SM) Santander Massif; (SNSM) Sierra Nevada de Santa Marta; (SP) serranía de Perijá; (SZ) Sub–Andean Zone; (UMV) Upper Magdalena Valley Basin; (WC) Western Cordillera. Geology from Litherland et al. (1994) and Gómez et al. (2007).

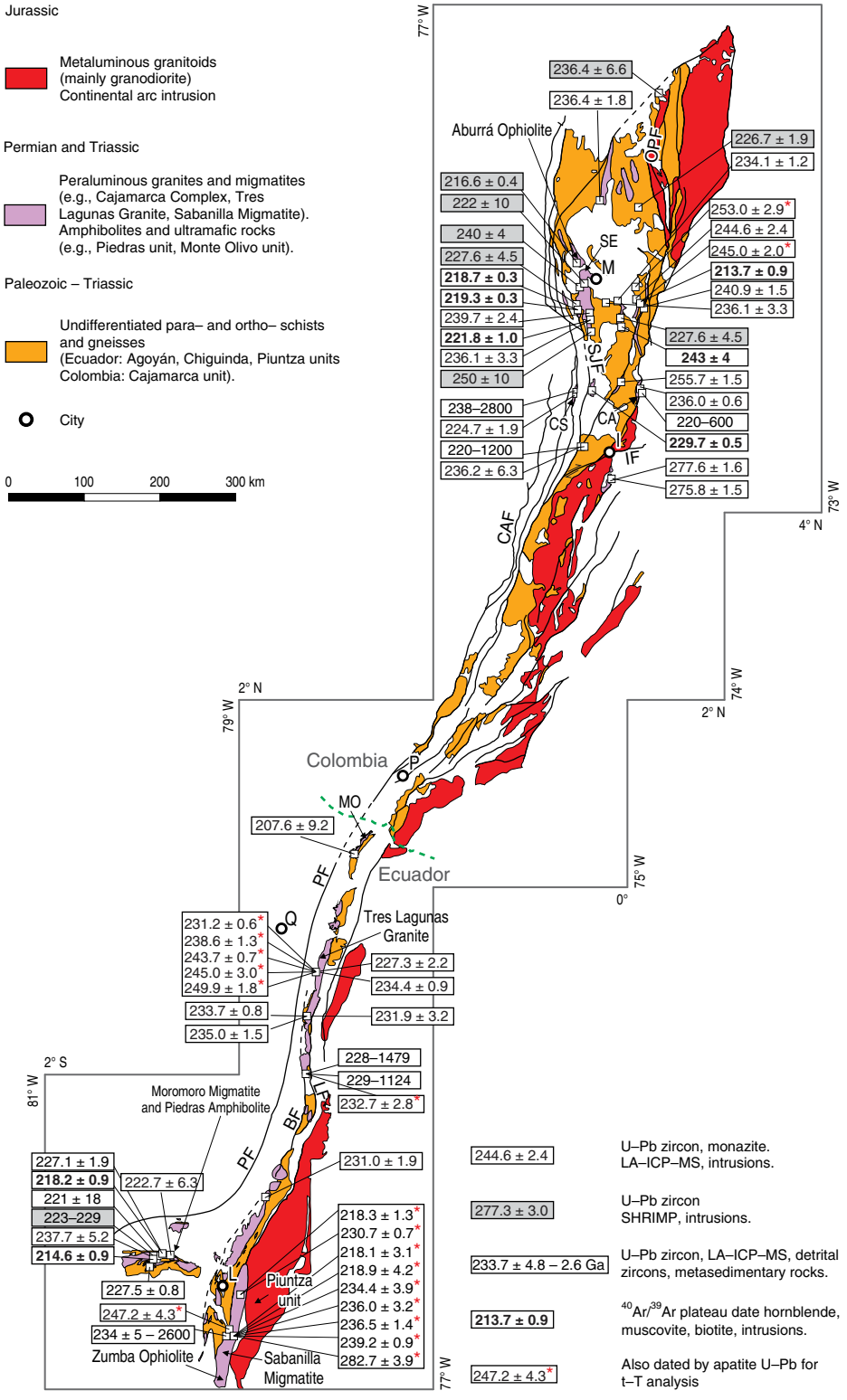

Figure 2. Geology of the Central Cordillera of Colombia and the Cordillera Real and Amotape Complex of Ecuador, showing the distribution of Paleozoic, Permian – Triassic rocks. The Jurassic continental arc is also shown for reference. Concordant Permian and Triassic zircon U–Pb and plateau $^{40}Ar/^{39}Ar$ dates and their uncertainties (±2σ) obtained by various analytical methods (see Table 1) are shown (see references in Table 1). Cities: (I) Ibagué; (L) Loja; (M) Medellín; (P) Pasto; (Q) Quito. Faults: (BF) Baños Fault; (CAF) Cauca–Almaguer Fault; (SJF) San Jerónimo Fault; (IF) Ibagué Fault; (LF) Llanganates Fault; (OPF) Otú–Pericos Fault; (PF) Peltetec Fault. Map compiled from Litherland et al. (1994) and Gómez et al. (2007). Amphibolite occurrences: (CA) Cajamarca Amphibolites; (CS) Chinchina Stock; (MO) Monte Olivo; (SE) Santa Elena Amphibolites.

Table 1. Summary of data collected from Permian – Triassic rocks of Ecuador and Colombia.

Sample	Unit	Lithology	Latitude d° m' s''	Longitude W d° m' s''	Zircon $^{206}Pb/^{238}U$ age (Ma) ± 2σ	MSWD	Apatite^{V} $^{206}Pb/^{238}U$ ages (Ma)	$^{40}Ar/^{39}Ar$ age (Ma) ± 2σ	εHf$_t$ zircon ± 2σ	εNd$_t$ w.r ± 2σ	$(^{87}Sr/^{86}Sr)i$ wr ± 2σ	$(^{206}Pb/^{204}Pb)i$ fs ± 2σ	$(^{207}Pb/^{204}Pb)i$ fs ± 2σ	$\delta^{18}O$ (‰) ± 2σ	Th/U zircon ± 2σ	A/CNK wr	(La/Yb) n wr	Publication
Granitoids and migmatitic leucosomes																		
Ecuador																		
Cordillera Real																		
09RC25	Tr. Lagunas	metagranite	1° 23' 51" S	78° 21' 15"	233.7 ± 0.8	1.1			10.5 to –3.2					15.3 ± 0.2	0.26 ± 0.1	1.99	13.24	Cochrane et al. (2014b)
09RC31	Tr. Lagunas	metagranite	0° 22' 33" S	78° 08' 32"	234.4 ± 0.9	0.8			–11.0 to +3.2					15.1 ± 0.2	0.04 ± 0.1	1.40	16.16	Cochrane et al. (2014b)
09RC42	Sabanilla	metagranite	4° 27' 43" S	79° 08' 52"	247.2 ± 4.3	3.0	138–82		–5.3 to –0.5			18.58 ± 0.190	15.64 ± 0.080	16.8 ± 0.2	0.69 ± 0.5	1.23	13.86	Cochrane et al. (2014b)
09RC53	Tr. Lagunas	metagranite	3° 09' 24" S	78° 48' 45"	231.0 ± 1.9	2.1			–2.63 ± 0.43						0.24 ± 0.1	1.19	12.91	Cochrane et al. (2014b)
09RC44	Sabanilla	paragneiss	4° 29' 02" S	79° 08' 55"												1.37	15.47	Cochrane et al. (2014b)
09RC45	Sabanilla	paragneiss	3° 58' 41" S	79° 01' 15"														Cochrane et al. (2014b)
09RC56	Tr. Lagunas	metagranite	1° 23' 57" S	78° 22' 08"	235.0 ± 1.5	3.0			–6.0 to +1.7					12.1 ± 0.2	0.14 ± 0.1	2.24		Cochrane et al. (2014b)
11RC03	Agoyan Fm.	metagranite	0° 23' 24" N	77° 51' 44"	207.6 ± 9.2	1.9			–16.3 to –9.0					15.1 ± 0.2	0.01 ± 0.0			Cochrane et al. (2014b)
13AP07	Tr. Lagunas	metagranite	1° 23' 55'' S	78° 21' 39''	232.7 ± 2.8		227–68					18.62 ± 0.001	15.67 ± 0.001		0.35	1.68	13.26	Paul et al. (2018)
13AP20	Tr. Lagunas	metagranite	0° 22' 18'' S	78° 06' 50''	231.2 ± 0.6		210–207					18.75 ± 0.005	15.67 ± 0.005		0.21 ± 0.15	1.05	11.47	Paul et al. (2018)
13AP22	Tr. Lagunas	metagranite	0° 23' 30'' S	78° 03' 31''	238.6 ± 1.3		149–143					18.59 ± 0.006	15.65 ± 0.005		0.14 ± 0.08	1.25	20.91	Paul et al. (2018)
13AP23	Tr. Lagunas	metagranite	0° 22' 55'' S	78° 04' 07''	249.9 ± 1.8		195–171					18.87 ± 0.014	15.65 ± 0.012		0.68 ± 0.25	1.51	13.41	Paul et al. (2018)
13AP24	Tr. Lagunas	metagranite	0° 22' 54'' S	78° 07' 51	243.7 ± 0.7		208–158	164.8 ± 0.9[m]				18.85 ± 0.015	15.74 ± 0.016		0.74 ± 0.56	1.11	17.45	Paul et al. (2018)
13AP25	Tr. Lagunas	metagranite	0° 22' 44'' S	78° 08' 09''	245.0 ± 3.0							18.63 ± 0.005	15.63 ± 0.004		0.65 ± 0.17	1.09	8.03	Paul et al. (2018)
13AP35	Sabanilla	leucosome	4° 32' 36'' S	79° 07' 55''	236.0 ± 3.2		93–85					18.40 ± 0.101	15.53 ± 0.067		1.22 ± 1.38	1.26	12.9	Paul et al. (2018)
13AP36	Sabanilla	leucosome	4° 32' 36'' S	79° 07' 55''	234.4 ± 3.9		114–69	70.7 ± 0.4[m]				18.84 ± 0.001	15.67 ± 0.001		0.24 ± 0.19	1.09	4.4	Paul et al. (2018)
13AP37	Sabanilla	leucosome	4° 32' 36'' S	79° 07' 55''	234.4 ± 3.9		101–76	70.7 ± 0.4[m]				18.55 ± 0.001	15.67 ± 0.001		0.24 ± 0.19	1.12	4.06	Paul et al. (2018)
13AP38	Sabanilla	leucosome	4°35'08'' S	79° 07' 51''	282.7 ± 3.9		99–98					18.56 ± 0.001	15.61 ± 0.001		0.9	1.35	16.19	Paul et al. (2018)
13AP42	Sabanilla	leucosome	4° 34' 19'' S	79° 08' 16''	239.2 ± 0.9		76–75					18.63 ± 0.004	15.63 ± 0.004		0.61 ± 0.12	1.22	11.26	Paul et al. (2018)
13AP43	Sabanilla	leucosome	4° 34' 19'' S	79° 08' 16''	218.1 ± 3.1		106–42	75.3 ± 1.3[m]							0.04	1.64	6.12	Paul et al. (2018)
13AP46	Sabanilla	leucosome	4° 31' 26'' S	79° 07' 50''	236.5 ± 1.4		80–74								0.02 ± 0.01	1.37		Paul et al. (2018)
13AP47	Sabanilla	leucosome	4° 27' 43'' S	79° 08' 52''	218.9 ± 4.2		96–81					18.58 ± 0.004	15.64 ± 0.004		0.03 ± 0.03	1.71	11.84	Paul et al. (2018)
13AP51	Sabanilla	leucosome	4° 02' 34'' S	78° 59' 40''	218.3 ± 1.3		129–74					18.53 ± 0.001	15.64 ± 0.001		0.006 ± 0.003	1.33	3.64	Paul et al. (2018)
13AP52	Sabanilla	leucosome	4° 00' 41'' S	79° 01' 17''	230.7 ± 0.7		91–71	72.0 ± 0.6[m]				18.53 ± 0.001	15.64 ± 0.001		0.23 ± 0.04	1.08	32.12	Paul et al. (2018)
Tr. Lagunas	Tr. Lagunas	granite			227.3 ± 2.2													Litherland et al. (1994)
Amotape Complex																		
09RC40	Moromoro	migmatite	3° 42' 16" S	79° 51' 07"	237.7 ± 5.2	4.6		214.6 ± 0.9[m]	–7.5 to +0.8						0.42 ± 0.5	2.38	11.36	Cochrane. (2013)
VI–08–12	La Bocana	migmatite			226.0 ± 1.3*													Riel et al. (2013)
PU–08–10	La Bocana	migmatite	3° 42' 58" S	80° 03' 18"	223.2 ± 2.2*											1.85		Riel et al. (2013)
AV–08–31	La Bocana	migmatite			229.3 ± 2.4										0.13			Riel et al. (2013)
AV–08–28d	La Bocana	migmatite	3° 40' 41" S	79° 54' 14"	225.7 ± 6.5										0.10	1.50		Riel et al. (2013)
13AP30	Moromoro	granite	3° 39' 53'' S	79° 45' 28''	227.1 ± 1.9			218.2 ± 0.9[m]										Paul et al. (2018)
Moromoro	Moromoro	granite			227.5 ± 0.8*													Aspden et al. (1995)

Permian Triassic

Table 1. Summary of data collected from Permian – Triassic rocks of Ecuador and Colombia (*continued*).

Sample	Unit	Lithology	Latitude d° m' s''	Longitude W d° m' s''	Zircon $^{206}Pb/^{238}U$ age (Ma) ± 2σ	MSWD	Apatite[y] $^{206}Pb/^{238}U$ ages (Ma)	$^{40}Ar/^{39}Ar$ age (Ma) ± 2σ	εHf_i zircon ± 2σ	eNd_i w.r ± 2σ	$(^{87}Sr/^{86}Sr)i$ wr ± 2σ	$(^{206}Pb/^{204}Pb)i$ fs ± 2σ	$(^{207}Pb/^{204}Pb)i$ fs ± 2σ	$\delta^{18}O$ (‰) ± 2σ	Th/U zircon ± 2σ	A/CNK wr	(La/Yb) n wr	Publication
Colombia																		
Central Cordillera																		
10RC04	Rovira	metagranite	4° 19' 24'' N	75° 12' 07''	277.6 ± 1.6	1.2			1.96 ± 0.31					13.6 ± 0.2	1.27 ± 0.6	1.18	16.23	Cochrane et al. (2014b)
10RC40	Cajamarca	metagranite	5° 53' 13'' N	75° 25' 28''	236.1 ± 3.3	3.7		221.8 ± 1.0[m]	−6.57 ± 0.66					17.4 ± 0.2	0.08 ± 0.1	1.73	8.19	Cochrane et al. (2014b)
10RC41	Cajamarca	metagranite	6° 01' 08'' N	75° 07' 28''	234.1 ± 1.2	1.2			−9.5 to −0.2					13.1 ± 0.2	0.23 ± 0.1	1.27	11.49	Cochrane et al. (2014b)
10RC42	Cajamarca	metagranite	5° 59' 17'' N	74° 55' 37''	244.6 ± 2.4	2.3			−8.2 to +1.4					13.1 ± 0.2	0.35 ± 0.1	1.33	12.00	Cochrane et al. (2014b)
10RC43	Cajamarca	metagranite	5° 58' 34'' N	74° 54' 02''	245.0 ± 2.0	0.6	232–231	213.7 ± 0.9[m]	−11.7 to −3.1						0.42 ± 0.4	1.36	15.70	Cochrane et al. (2014b)
10RC53	Cajamarca	metagranite	7° 00' 56'' N	75° 22' 28''	236.4 ± 1.8	3.0			−5.9 to +3.1					15.9 ± 0.2	0.30 ± 0.2	1.56	14.27	Cochrane et al. (2014b)
10RC66	Cajamarca	qtz–schist	5° 08' 20'' N	75° 09' 47''												1.84	12.63	Cochrane et al. (2014b)
10RC69	Rovira	metagranite	5° 09' 27'' N	75° 07' 57''	255.7 ± 1.5	1.2			−3.16 ± 0.7					15.6 ± 0.2	1.10 ± 0.2	1.70	12.81	Cochrane et al. (2014b)
10RC71	Cajamarca	pegmatite	5° 07' 34'' N	74° 54' 38''	236.0 ± 0.6	0.9			−6.0 to +0.4						0.31 ± 0.1			Cochrane et al. (2014b)
DV65	Cajamarca	metagranite	5° 59' 16'' N	74° 55' 34''	240.9 ± 1.5	0.6			−5.9 to +0.7						0.26 ± 0.2			Cochrane et al. (2014b)
DV82	Rovira	metagranite	4° 17' 16'' N	75° 13' 59''	275.8 ± 1.5	3.0			−3.7 to +0.3						0.66 ± 0.1			Cochrane et al. (2014b)
DV02	Cajamarca	paragneiss	4° 46' 42'' N	74° 57' 54''	238–582													Villagómez et al. (2011)
DV18	Cajamarca	gneiss	4° 28' 19'' N	75° 33' 18''	236.2 ± 6.3	0.6												Villagómez et al. (2011)
DV19	Cajamarca	quartzite	4° 28' 19'' N	75° 33' 18''	231–1163													Villagómez et al. (2011)
I4AP14	Rovira	metagranite	6° 01' 08'' N	75° 07' 28''	253.0 ± 2.9		200–198					18.66 ± 0.003	15.67 ± 0.003		0.52 ± 0.62			Paul et al. (2018)
Abejorral	Abejorral	gneiss			250 ± 10[#]										0.82			Vinasco et al. (2006)
Palmitas	Palmitas	gneiss			240 ± 4[#]										0.25			Vinasco et al. (2006)
Amaga	Amaga	granite			227.6 ± 4.5	1.4									0.30			Vinasco et al. (2006)
La Honda	La Honda	granite						218.7 ± 0.3[b]										Vinasco et al. (2006)
El Buey	El Buey	granite						219.3 ± 0.3[m]										Vinasco et al. (2006)
Manizales	Manizales	granite						229.7 ± 0.5[b]										Vinasco et al. (2006)
GSI1	Santa Isabel	gneiss	6° 57' 34'' N	74° 45' 13''	226.7 ± 1.6	1.2									0.19			Restrepo et al. (2011)
GN1	Nechi	gneiss	8° 10' 13'' N	74° 46' 55''	236.4 ± 6.6	2.1									0.23			Restrepo et al. (2011)
PALM–1	Palmas	migmatite	6° 09' 14'' N	75° 32' 36''	222 ± 10[#]										0.24			Restrepo et al. (2011)
P21	Las Palmas	paragneiss			237 ± 2										0.005			Martens et al. (2014)
P22	Las Palmas	gneiss			244 ± 2													Martens et al. (2014)
GCC8	Tierradentro	orthogneiss			244.3 ± 4.8	2.8												Bustamante et al. (2017)
CI12	Tierradentro	orthogneiss			271.3 ± 1.3	1.4				−0.1 to −2.5					0.47–1.04			Bustamante et al. (2017)
Sierra Nevada de Santa Marta																		
A14	S.M. mylonite	granite			288.1 ± 4.5	1.0									0.73			Cardona et al. (2010a)
A48	S.M. mylonite	granite			276.5 ± 5.1	1.8									0.57			Cardona et al. (2010a)
EAM–12–05	S.M. mylonite	granite			264.9 ± 4.0	0.0												Cardona et al. (2010a)
MPR–33A	El Encanto	orthogneiss	11°04'23'' N	74° 04' 26''	274.8 ± 2.1	0.1									0.80	0.66	23.09	Piraquive (2017)
GLV–11	Gaira Schists	gnt–schist	11°01'18'' N	74° 10' 15''	283.7 ± 6.1										0.84			Piraquive (2017)
MG–063	Gaira Schists	schist	11°14'50'' N	73° 44' 33''	261.4 ± 2.6										0.75			Piraquive (2017)

Table 1. Summary of data collected from Permian – Triassic rocks of Ecuador and Colombia (*continued*).

Sample	Unit	Lithology	Latitude d° m' s''	Longitude W d° m' s''	Zircon $^{206}Pb/^{238}U$ age (Ma) ± 2σ	MSWD	Apatite[¥] $^{206}Pb/^{238}U$ ages (Ma)	$^{40}Ar/^{39}Ar$ age (Ma) ± 2σ	εHf$_t$ zircon ± 2σ	εNd$_t$ w.r ± 2σ	$(^{87}Sr/^{86}Sr)i$ wr ± 2σ	$(^{206}Pb/^{204}Pb)i$ fs ± 2σ	$(^{207}Pb/^{204}Pb)i$ fs ± 2σ	$\delta^{18}O$ (‰) ± 2σ	Th/U zircon ± 2σ	A/CNK wr	(La/Yb) n wr	Publication
Sierra Nevada de Santa Marta																		
CVI13108	La Secreta	meta–tuff	10°56'04" N	74° 08' 14"	224.6 ± 2.6										0.17	1.12	9.62	Piraquive (2017)
LRW–21	La Secreta	gabbro	10°54'46" N	74° 08' 40"	237.4 ± 1.1	3.5									0.21	1.08	10.80	Piraquive (2017)
Plato–San Jorge Basin																		
Cicuco–2a	unknown	granite	9° 16' 25" N	74° 38' 53"	241.6 ± 3.9	3.9												Montes et al. (2010)
Cicuco–3	unknown	granite	9° 17' 39" N	74° 38' 52"	241.6 ± 3.9	6.0												Montes et al. (2010)
Lobita 1	unknown	granite	9° 18' 30" N	74° 41' 31"	239.6 ± 2.9	0.6												Montes et al. (2010)
Guajira Peninsula																		
AVO–03	Uray Gneiss	gneiss			247.6 ± 4.1	0.5									0.20			Weber et al. (2010)
AVO–06	Uray Gneiss	gneiss			245.6 ± 3.9	0.5									0.59			Weber et al. (2010)
Amphibolites																		
Ecuador																		
10RC28	Chinchina	amphibolite	5° 03' 05" N	75° 34' 25"	224.7 ± 1.9	0.8			13.31 ± 0.25	9.83	0.70354	17.52	15.40		0.20 ± 0.1	0.66	1.41	Cochrane et al. (2014b)
11RC04	Monte Olivo	amphibolite	0° 23' 24" N	77° 51' 44"												0.61	2.59	Cochrane et al. (2014b)
11RC10	Monte Olivo	amphibolite	1° 23' 56" S	78° 22' 52"	231.9 ± 3.2	1.6			–6.3 to +11.2	5.03	0.71470	18.71	15.68		0.19 ± 0.1	0.63	1.71	Cochrane et al. (2014b)
11RC14	Piedras	amphibolite	3° 39' 9" S	79° 50' 35"	222.7 ± 6.3	1.9			15.00 ± 0.29	9.79	0.70271	17.75	15.48		0.32 ± 0.2	0.61	0.81	Cochrane et al. (2014b)
JR148	Piedras	amphibolite			221 ± 17.0											0.52		Noble et al. (1997)
Colombia																		
10RC39	Santa Elena	amphibolite	5° 54' 06" N	75° 24' 31"						8.98	0.70430	18.12	15.61			0.82	2.34	Cochrane et al. (2014b)
10RC39A	Santa Elena	amphibolite	5° 53' 52" N	75° 24' 37"	239.7 ± 2.4	1.9			–4.8 to +10.0	4.13	0.70535	18.30	15.64			0.62	2.02	Cochrane et al. (2014b)
10RC50	Tr. Intrusive	amphibolite	6° 09' 26" N	75° 44' 31"						10.18	0.70243	16.61	15.53			0.50	0.49	Cochrane et al. (2014b)
AC32B	El Picacho	plagiogranite			216.6 ± 0.4	0.7				3.4	0.70448					0.97	8.00	Correa–Martínez (2007)
CMK040A	El Picacho	metagabbro								8.4						0.61	0.64	Correa–Martínez (2007)
Padua	Padua	amphibolite						243 ± 4[b]										Vinasco et al. (2006)
CAT1A	Tierradentro	amphibolite			234.1 ± 5.3	7.1			+9.2 to +10.9						0.12–0.25			Bustamante et al. (2017)

Abbreviations: (b) biotite; (h) hornblende; (m) muscovite; (fs) feldspar; (wr) whole–rock; A/CNK (Molecular $Al_2O_3/CaO + Na_2O + K_20$); (La/Yb)n (normalized to N–MORB).

$^{87}Sr/^{86}Sr$ 2s.d. (ext. reproducibility) = 0.0007%; $^{143}Nd/^{144}Nd$ = <0.0005 %; $^{206}Pb/^{204}Pb$ = 0.12 %.

The zircon $^{238}U/^{206}Pb$ ages are weighted mean ages of concordant analyses.

*Monazite date.

[#]Date obtained from the youngest zircon when a large spread of zircon ages were obtained due to xenocrystic contamination.

Dates acquired by LA–ICP–MS (Cochrane et al., 2014b; Cardona et al., 2010a; Martens et al., 2014; Montes et al., 2010; Paul et al., 2018; Piraquive, 2017; Villagómez et al., 2011; Weber et al., 2010).

Dates acquired by TIMS (Aspden et al., 1995; Litherland et al., 1994).

Dates acquired by SHRIMP (Restrepo et al., 2011; Vinasco et al., 2006).

[¥]Dates are from a range of apatite grain sizes, and are shown as largest grain–smallest grain. Grain radii are typically 100 mm and 50 mm. 2σ uncertainties are <5 % (Paul, 2017).

All $^{40}Ar/^{39}Ar$ dates are plateau dates.

Permian Triassic

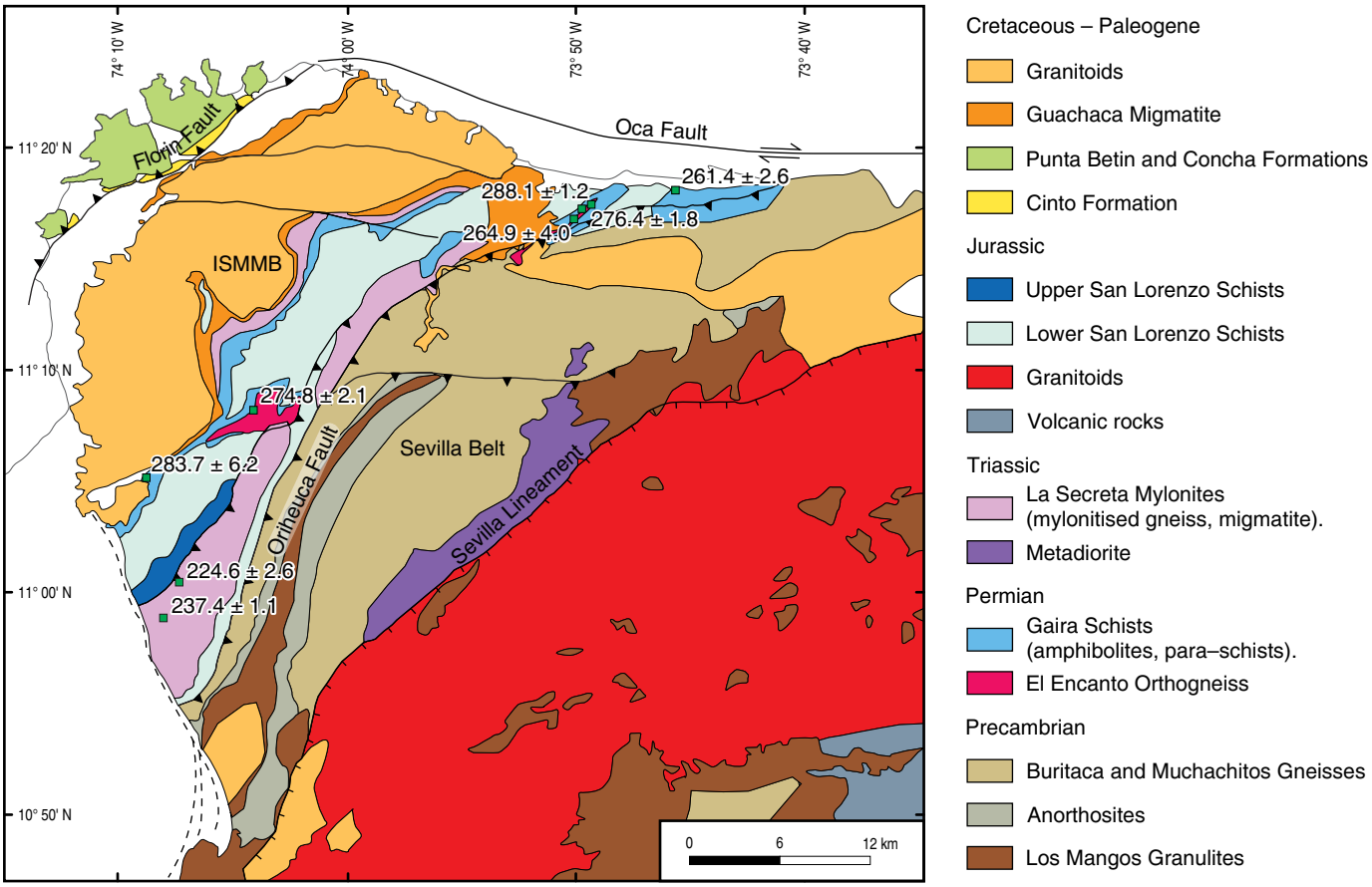

Figure 3. Geological map of the northwestern corner of the Sierra Nevada de Santa Marta after Tschanz et al. (1974), Colmenares et al. (2007a, 2007b), and Piraquive (2017), showing the main structural belts of the Sierra Nevada, Sevilla, and Santa Marta provinces. Concordant zircon U–Pb dates of Permian and Triassic rocks (Table 1) are shown (Cardona et al., 2010a; Piraquive, 2017). ISMMB: Inner Santa Marta Metamorphic Belt (after Piraquive, 2017).

east by the Llanganates Fault and to the west by the Baños Fault (Figure 2). Triassic igneous and metamorphic lithologies are dominated by cordierite and garnet bearing monzogranites and granodiorites (Tres Lagunas unit), and medium– to high–grade, sillimanite and kyanite bearing orthogneisses and migmatites (Sabanilla unit). Litherland et al. (1994), Noble et al. (1997), Riel et al. (2013), Cochrane et al. (2014b), Spikings et al. (2015), and Paul et al. (2018) present a large quantity of geochronological and geochemical data from the igneous and metamorphic rocks in Ecuador (Table 1). The Piuntza unit consists of metamorphosed and skarnified siliciclastic rocks, tuffs, and limestones that host Triassic bivalves (Litherland et al., 1994). The unit is exposed beyond the structural limits of the Loja Terrane of Litherland et al. (1994) along the eastern flank of the southern Cordillera Real (Figure 2), where it is surrounded by the Jurassic Zamora Batholith although the nature of the contact is either unknown or unreported.

4. Geochronology of Permian and Triassic Magmatic Rocks

Early attempts to date the Permian – Triassic crystalline rocks utilised the K/Ar and Rb/Sr methods (e.g., Feininger et al., 1972; Hall et al., 1972; Litherland et al., 1994; McCourt et al., 1984; Ordóñez–Carmona & Pimentel, 2002; Restrepo et al., 1991), resulting in a large scatter of ages spanning between the Permian – Tertiary due to variable degrees of daughter isotope loss. This review of geochronological work is restricted to more accurate measurements of the crystallisation ages of granitoids and mafic intrusions, which have been provided by numerous concordant zircon and few monazite U–Pb dates (Table 1), obtained using TIMS, SHRIMP, and LA–ICP–MS. Unless otherwise stated, the LA–ICP–MS and SHRIMP dates that are reported here were obtained from the rims of zircons, and are considered to date either the most recent phase of magmatic crystallisation or the

most recent metamorphic event that crystallised zircon. Most of these dates have been peer reviewed, with the exception of several data points from PhD theses (e.g., Piraquive, 2017).

4.1. Permian

Permian magmatic rocks in the cordilleras of the northern Andes are sparse compared to the exposure of Triassic rocks. Six granitoids in the central and northern Central Cordillera yield dates spanning between 278 and 253 Ma (Figures 2, 4; Table 1; Bustamante et al., 2017; Cochrane et al., 2014b; Paul et al., 2018; Vinasco et al., 2006). These Permian intrusions are tentatively assigned the name *Rovira Complex*, referring to the locality (close to the town of Ibagué) where Cochrane et al. (2014b) sampled and dated two Permian granites (Table 1). El Encanto Orthogneiss forms the crystalline basement of the Inner Santa Marta Metamorphic Belt of the Sierra Nevada de Santa Marta, and yields a zircon U–Pb age of 274.8 ± 2.1 Ma (Figure 3), which is considered to be the time of initial magmatic crystallisation (Piraquive, 2017). These are overlain by paraschists of the 2000 m thick Gaira Amphibolite sequence, which yields a large range of concordant zircon U–Pb dates (2235–261 Ma), reflecting their sedimentary protoliths. Two schists yield youngest concordant age clusters with U–Pb ages of 283.7 ± 6.2 Ma and 261.5 ± 2.6 Ma (Piraquive, 2017) from laser spots within zircons, constraining their maximum stratigraphic ages. Cardona et al. (2010a) obtained zircon U–Pb concordia ages ranging between 288–265 Ma from mylonitised gneisses within the northern Inner Santa Marta Metamorphic Belt (Figure 3). A migmatite exposed in the southern Cordillera Real is the only Permian magmatic rock identified in Ecuador, and yields a zircon U–Pb age of 282.7 ± 3.9 Ma (Figure 2; Table 1; Paul et al., 2018). The Permian leucosome (rock 13AP38) was previously mapped as part of the Sabanilla Migmatite unit (Litherland et al., 1994). The Sabanilla Migmatite is defined on geochemical and geochronological grounds as Triassic (Spikings et al., 2015), and thus we tentatively assign the Permian leucosome to the newly named *Malacatos Complex*, referring to the nearest town to the sampled location.

4.2. Triassic

Triassic felsic magmatic rocks are abundant in Colombia and Ecuador, and this review includes new data obtained from Paul et al. (2018), and the recent PhD study of Piraquive (2017). Twenty five gneissic granites and pegmatites exposed in the Central Cordillera, the basement of the Plato–San Jorge Basin, the Sierra Nevada de Santa Marta, and the Guajira Peninsula yield zircon U–Pb concordia ages ranging between 247.6 ± 4.1 Ma and 222 ± 10 Ma (Figures 2, 4; Table 1; Bustamante et al., 2017; Cardona et al., 2010a; Cochrane et al., 2014b; Martens et al., 2014; Montes et al., 2010; Piraquive, 2017; Villagómez et al., 2011; Vinasco et al., 2006; Restrepo et al., 2011; Weber et al., 2010). La Secreta Mylonites form part of the Inner Santa Marta Metamorphic Belt within the Sierra Nevada de Santa Marta, and overthrust the Permian El Encanto Orthogneiss and Gaira Schists (Figure 3; Piraquive, 2017). A peraluminous gabbro from the mylonitic sequence yields a zircon U–Pb date of 237.4 ± 1.1 Ma (Piraquive, 2017), while a mylonite hosts detrital zircons that yield concordant U–Pb dates from cores and rims spanning between 1300–224 Ma, and yields a concordant youngest age cluster of 224.6 ± 2.6 Ma, overlapping with dates from Triassic intrusions (Piraquive, 2017). These dates from Colombian rocks overlap with concordant zircon and monazite U–Pb ages from twenty nine granites and leucosomes of the Tres Lagunas Granite and Sabanilla Migmatite (Cordillera Real), and the Moromoro Granite (Amotape Complex), which range between 249.9 ± 1.8 Ma and 207.6 ± 9.2 Ma (Figure 4; Table 1; Aspden et al., 1995; Chew et al., 2008; Cochrane et al., 2014b; Litherland et al., 1994; Paul et al., 2018; Riel et al., 2013; Spikings et al., 2015).

Multi–phase, plateau $^{40}Ar/^{39}Ar$ dates (Table 1) from Triassic granites and migmatites in Colombia and Ecuador (Cochrane et al., 2014b; Paul et al., 2018; Spikings et al., 2001; Vinasco et al., 2006) are younger than the U–Pb dates obtained from the same rocks, reflecting various degrees of Ar loss. Triassic dates span between 243 ± 4 Ma and 213.7 ± 0.9 Ma and are restricted to the northern Central Cordillera (Table 1). However, Triassic magmatic rocks from the Cordillera Real yield younger plateau muscovite $^{40}Ar/^{39}Ar$ dates that span between 164.8 ± 0.9 Ma and 70.7 ± 0.4 Ma (Table 1; Paul et al., 2018). These reflect the time of cooling of each rock through ~450–400 ºC (Harrison et al., 2009) subsequent to crystallisation and metamorphic retrogression, and the difference in dates between northern (Colombia) and southern (Ecuador) latitudes reveals trench–parallel differences in their thermal histories (see section 7).

A majority of U–Pb dates of zircons extracted from granites and migmatites in Colombia and Ecuador range between 240–230 Ma (Figure 4a), and a comparison with latitude (Figure 4d) does not reveal any trench–parallel trends in Triassic crystallisation. Permian ages are mainly found in Colombia, and are restricted to exposures in the Inner Santa Marta Metamorphic Belt of the Sierra Nevada de Santa Marta, and faulted blocks in the region of the Ibagué Fault (Figures 2, 3). This may reflect exposure, the approximate primary distribution of Permian magmatic intrusions, or the extent of reworking during Triassic anatexis.

Concordant zircon U–Pb dates of amphibolites and a plagiogranite from the Cordilleras Central (Colombia) and Real (Ecuador) range between 243 ± 4 Ma and 216.6 ± 0.4 Ma (Figure 2; Bustamante et al., 2017; Cochrane et al., 2014b; Correa–Martínez, 2007; Noble et al., 1997; Spikings et al., 2015; Vinasco et al., 2006). Within Ecuador, these are exposed as dykes and sills (e.g., the Piedras and Monte Olivo units; see Figure 2), whereas they are more massive in the northern Central Cordillera. The youngest of these ages was obtained from a

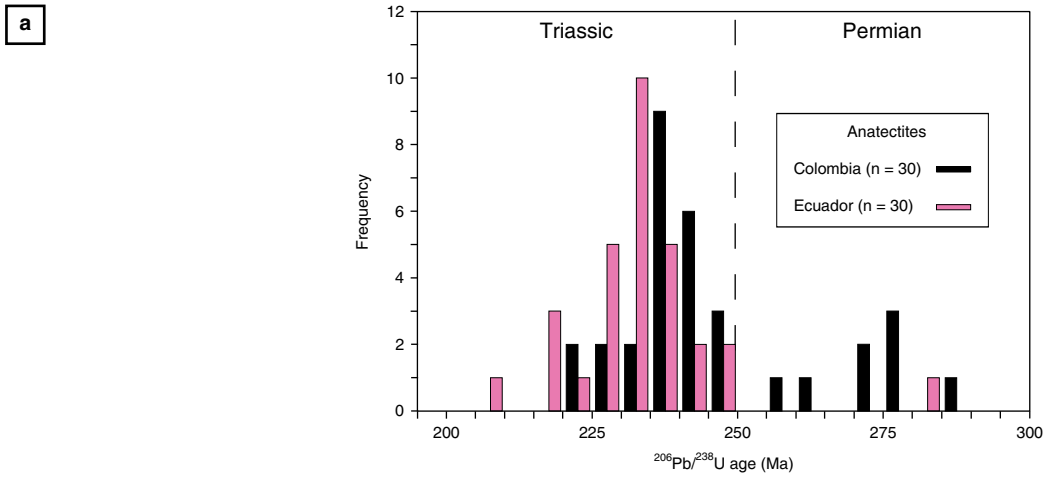
a
Triassic
Permian
Anatectites
Colombia (n = 30)
Ecuador (n = 30)
Frequency
$^{206}Pb/^{238}U$ age (Ma)

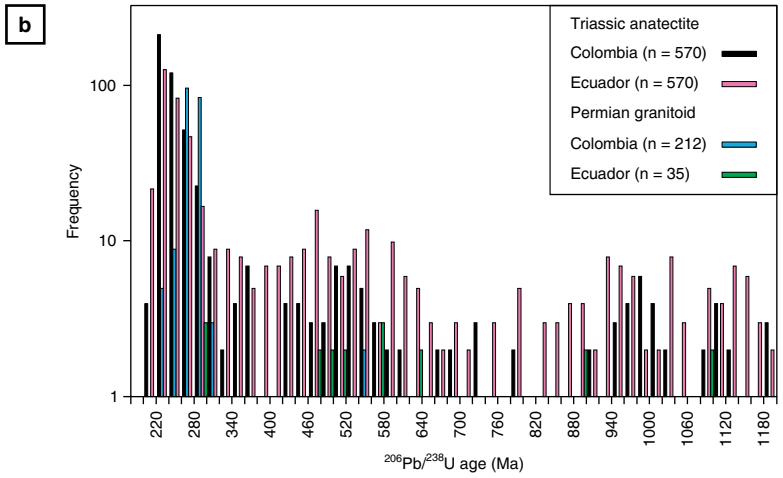
b
Triassic anatectite
Colombia (n = 570)
Ecuador (n = 570)
Permian granitoid
Colombia (n = 212)
Ecuador (n = 35)
Frequency
$^{206}Pb/^{238}U$ age (Ma)

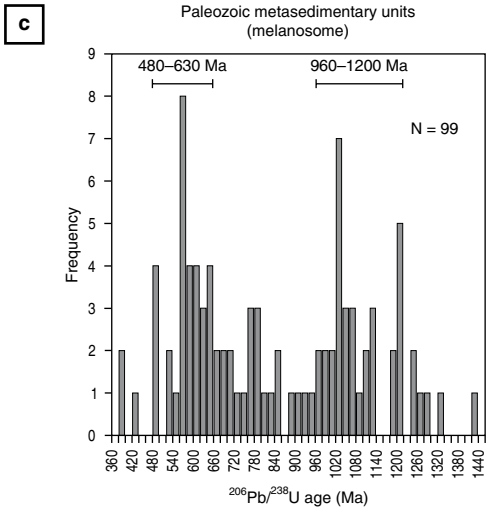
c
Paleozoic metasedimentary units
(melanosome)
480–630 Ma
960–1200 Ma
N = 99
Frequency
$^{206}Pb/^{238}U$ age (Ma)

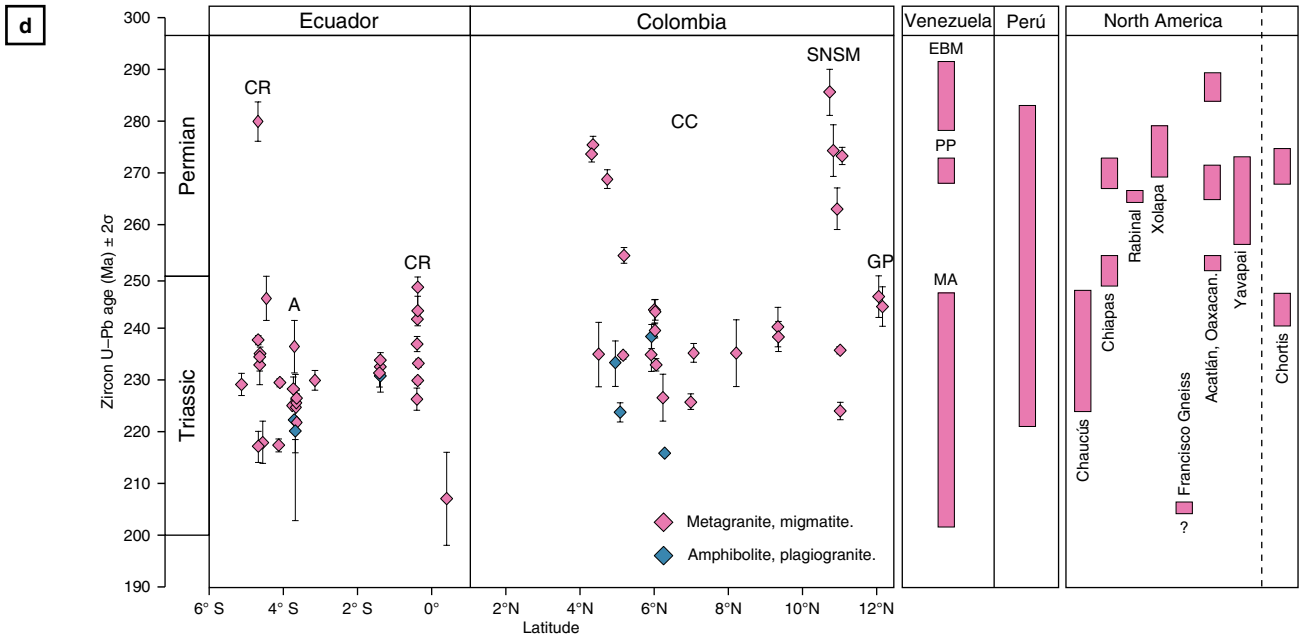
d
Ecuador
Colombia
Venezuela
Perú
North America
Permian
Triassic
Zircon U–Pb age (Ma) ± 2σ
CR
A
CR
CC
SNSM
GP
EBM
PP
MA
Chaucús
Chiapas
Rabinal
Xolapa
Francisco Gneiss
Acatlán, Oaxacan.
Yavapai
Chortis
Metagranite, migmatite.
Amphibolite, plagiogranite.
Latitude

plagiogranite that formed by magmatic fractionation within the Aburrá Ophiolite in northern Colombia, and thus is a minimum age for the ophiolite (Correa–Martínez, 2007).

4.3. Zircons Inherited by Permian and Triassic Magmas

Many concordant zircon U/Pb dates determined by in–situ methods were obtained from the cores of zircon grains that were identified using cathodoluminescence. A frequency analysis of the distribution of these older concordant laser–spot dates from the granitoids and migmatitic leucosomes in Colombia and Ecuador yields broad $^{206}Pb/^{238}U$ age peaks at 580–420 Ma and 1200–950 Ma (Figure 4b), which are the ages of protolith rocks and inherited grains. These age peaks are typical of the distribution of dates obtained from detrital zircons from most Paleozoic rocks distributed along western South America (e.g., Chew et al., 2007). The younger age group broadly corresponds with the age of the Famatinian arc, the Brasiliano Orogeny, and the timing of rifting during the fragmentation of Rodinia and the opening of the Iapetus Ocean. The Famatinian arc (ca. 510–415 Ma; see zircon U–Pb ages presented in Bahlburg et al., 2009; Cardona et al., 2007; Chew et al., 2007; Mišković et al., 2009; Pankhurst et al., 2000; Spikings et al., 2016; Villagómez et al., 2011; van der Lelij et al., 2016) formed during the subduction of Iapetus lithosphere beneath western South America subsequent to the fragmentation of Rodinia, and has been recorded in Venezuela, Colombia, Perú, and Argentina (see previous citations). Inherited zircons with U–Pb dates spanning 650–450 Ma also occur in Cretaceous and Tertiary sedimentary rocks of the Oriente (Amazon retro–foreland; see Figure 1) Basin in Ecuador (Martin–Gombojav & Winkler, 2008). Similarly, Horton et al. (2010) present a large database of U–Pb dates obtained from detrital zircons in the Eastern Cordillera and the western margin of the Llanos Basin in Colombia, which reveal a peak at 520–420 Ma. No Ordovician intrusions of the Famatinian arc have been recorded in Ecuador. However, within Colombia they are recorded within the northern Central Cordillera (470–440 Ma; La Miel Orthogneiss; Martens et al., 2014; Villagómez et al., 2011), Quetame and Floresta Massifs (Horton et al., 2010), and a majority of the exposed crystalline basement of the Santander Massif (Figure 1; van der Lelij et al., 2016) yields Ordovician dates ranging between 500 and 415 Ma.

Triassic field relationships are clearly exposed in Ecuador (e.g., Litherland et al., 1994), and indicate that the protoliths of the Triassic migmatites and S–type granites within Ecuador were sedimentary rocks of the Paleozoic, fossil bearing Chiguinda and Isimanchi units that are exposed in the Cordillera Real (Figure 2). These sparsely studied sequences yield a detrital zircon U–Pb age spectrum that has the same age peaks as the Triassic anatectites (Figure 4c; Chew et al., 2008), although the tectonic setting within which these potentially Devonian (minimum zircon U–Pb date of 360 ± 2 Ma; Chew et al., 2007) sequences were deposited is undetermined.

The Brasiliano metamorphic belts (Cordani et al., 2003) formed during the late Neoproterozoic amalgamation of Gondwana, and may have supplied some detritus to western South America. However, these belts are located in eastern South America, and a lack of evidence for detritus being sourced from the intervening Amazonia Craton suggests the Brasiliano Orogenic belts were not a major source region (Chew et al., 2008). Finally, most magmatism associated with Neoproterozoic extension is mafic (e.g., the Puncoviscana fold belt in northwestern Argentina; Omarini et al., 1999), which led Chew et al. (2008) to suggest that it is unlikely that these rocks were a major contributor of zircons to Paleozoic sequences along western South America. However, Neoproterozoic rift related dacites occur along the margin of the central Andes (Ramos, 2009), and may have supplied sedimentary detritus towards the west.

4.4. Comparison with the Ages of Permian and Triassic Rocks in Venezuela, Perú, Northern Chile, and Argentina

Rhyolites and granites of El Baúl Massif in Venezuela yield zircon U–Pb dates that span between 291.1 ± 3.1 Ma and 283.3

Figure 4. (a) Histogram of zircon $^{206}Pb/^{238}U$ concordia (crystallisation) ages for Permian and Triassic magmatism and metamorphic zircon growth for variably foliated granites and migmatites (leucosomes) in Ecuador and Colombia (see Table 1 for references). **(b)** $^{206}Pb/^{238}U$ (concordant) age histogram for Permian and Triassic granites and migmatites (leucosomes) from Colombia and Ecuador. Ages are single spot zircon ages determined using LA–ICP–MS and SIMS. **(c)** $^{206}Pb/^{238}U$ age histogram for detrital zircons from the Paleozoic Chiguinda and Isimanchi metasedimentary units of the Cordillera Real of Ecuador (Chew et al., 2008). **(d)** A comparison of Permian and Triassic concordant zircon and monazite U–Pb dates with latitude along the Central Cordillera, Guajira Peninsula, and the Sierra Nevada de Santa Marta of Colombia, and the Cordillera Real and Amotape Complex of Ecuador. The ranges of concordant zircon U–Pb dates obtained from granitoid intrusions and volcano–sedimentary rocks from Venezuela (van der Lelij et al., 2016), the Eastern Cordillera of Perú (Mišković et al., 2009; Spikings et al., 2016), and various regions of the southern North American and western Caribbean Plate (Ducea et al., 2004; Elías–Herrera & Ortega–Gutiérrez, 2002; Helbig et al., 2012; Keppie et al., 2004, 2006; Kirsch et al., 2012; Ortega–Obregón et al., 2014; Ratschbacher et al., 2009; Solari et al., 2001, 2011; Weber et al., 2005, 2007; Yañez et al., 1991) are shown for comparison. Data and citations are presented in Table 1. Abbreviations: (A) Amotape Complex; (CC) Central Cordillera; (CR) Cordillera Real; (EBM) El Baúl Massif; (GP) Guajira Peninsula; (MA) Mérida Andes; (PP) Paraguaná Peninsula; (SNSM) Sierra Nevada de Santa Marta.

± 2.5 Ma (Viscarret et al., 2009), and a zircon U–Pb age of 272.2 ± 2.6 Ma was obtained from a granitic intrusion in the Paraguaná Peninsula (van der Lelij et al., 2016). van der Lelij et al. (2016) report concordant zircon U–Pb dates (LA–ICP–MS) from four granitoid intrusions and a dacitic lava from the Mérida Andes of Venezuela (Figure 1). These dates range between 202.0 ± 1.8 Ma (La Quinta Formation) and 243.5 ± 3.4 Ma, and overlap with dates obtained from Colombia and Ecuador (Figure 4d). No Permian concordant zircon U–Pb dates have been reported from the Mérida Andes.

Voluminous, partly migmatised middle Permian – Triassic magmatic intrusions are exposed throughout the southern and central Eastern Cordillera of Perú (Mišković et al., 2009; Spikings et al., 2016). Zircon U–Pb dates range between 293–223 Ma (Figures 4d, 5; Mišković et al., 2009; Reitsma, 2012; Spikings et al., 2016), with a peak at 245–225 Ma. The crystallisation ages show a southward younging trend, and the oldest plutons south of 13° S are younger than ca. 245 Ma (Spikings et al., 2016). The Mitu Group of the central and southern Eastern Cordillera of Perú hosts abundant Triassic sedimentary and volcanic sequences. Volcanic tuffs and lavas of the Mitu Group yield concordant zircon U–Pb (LA–ICP–MS) dates ranging between 238.7 ± 1.8 Ma and 219.7 ± 1.8 Ma (Chew et al., 2008; Mišković et al., 2009; Spikings et al., 2016). Detrital zircons extracted from oxidised terrigenous sedimentary rocks of the Mitu Group yield minimum dates ranging between 255.4 ± 3.2 Ma and 223.5 ± 7.5 Ma, which constrain their maximum stratigraphic ages (Spikings et al., 2016). Several authors propose that the Mitu Group was deposited within a rift (Laubacher, 1978; Mégard, 1978; Reitsma, 2012; Spikings et al., 2016), which was active during 245–220 Ma (Spikings et al., 2016). This time period precisely overlaps with the majority of Triassic intrusions in Colombia and Ecuador (Figure 5a). Romero et al. (2013) recently published a concordant zircon U–Pb age of 243 ± 0.1 Ma from a basalt exposed in Macabí Island offshore northern Perú (~8° S), although these zircons are probably xenocrystic.

Further south, a series of Middle – Late Triassic rift systems and sinistral pull–apart basins with a NNW–SSE trend in northern and central Chile and Argentina propagated along the hanging wall of previous sutures that separate Paleozoic terranes (e.g., Ramos, 1994; Ramos & Kay, 1991). U–Pb dates of tuffs from the Cuyo Basin span between 246–230 Ma (Potrerillos Formation; Barredo et al., 2012; Spalletti et al., 2008), and a tuff from the rift–related Ischigualasto Formation (Ischigualasto–Villa Unión Basin) yields a sanidine $^{40}Ar/^{39}Ar$ date of 231.4 ± 0.3 Ma (Martínez et al., 2011; recalibration of the 227.8 ± 0.3 Ma age of Rogers et al., 1993). Similarly, ignimbrites within the Los Menucos depocenter yield zircon U–Pb ages of 257–248 Ma (Luppo et al., 2018). Maksaev et al. (2014) compile and present new zircon U–Pb dates from volcanic rocks in northern Chile, which reveals a peak in activity between 240–210 Ma, temporally overlapping with the peak in magmatic activity in Colombia, Ecuador, and Perú.

4.5. Comparison with the Ages of Permian and Triassic Magmatic Rocks in the Southernmost North American and Western Caribbean Plates

Permian – Triassic intrusive rocks occur along most of the length of México and Central America (e.g., Ortega–Obregón et al., 2014; Weber et al., 2007), and Centeno–García & Keppie (1999), Torres et al. (1999), and Dickinson & Lawton (2001) suggested they are a continuation of exposures in northwestern South America. A plethora of K–Ar dates range between 287–232 Ma (see the review of Torres et al., 1999, and references therein) although interpreting these are crystallisation ages is problematic due to the propensity for Ar loss. Yañez et al. (1991), Solari et al. (2001), Elías–Herrera & Ortega–Gutiérrez (2002), and Ducea et al. (2004) present concordant zircon U–Pb dates from acidic intrusions in southern México (Oaxacan, Xolapa, and Acatlán Complexes; Figures 4d, 5b) ranging between 287–272 Ma. Keppie et al. (2004), Kirsch et al. (2012), and Ortega–Obregón et al. (2014) report Permian concordant zircon U–Pb dates (ID–TIMS) of 298–255 Ma from acidic plutons and dykes within the Acatlán and Oaxacan Complexes, all of which are interpreted as crystallisation ages. Ratschbacher et al. (2009) obtained a concordant U–Pb date of 268.0 ± 0.6 Ma from rounded zircon cores extracted from a migmatitic gneiss of the Rabinal Complex (Maya Block, southern Guatemala). Orthogneisses within the Chiapas Massif of the Maya Block, yield zircon U–Pb discordia intercepts at ca. 251 Ma (Weber et al., 2005), while in–situ dates reveal a Permian U–Pb date of 272 ± 3 Ma from magmatic zones, with metamorphic zircon overgrowths at 254 ± 2 Ma (Weber et al., 2007), which precisely overlaps with anatexis of sedimentary rocks in the same region at 254 ± 2 Ma (Weber et al., 2007). Arvizu et al. (2009) present zircon U–Pb ages (LA–MC–ICP–MS) from monzogranites, granites, and granodiorites ranging between 275–258 Ma from northern México, which intrude crust of the Yavapai Province. Summarising, Permian magmatism intruded large regions of the far southern Northern American Plate, and is also preserved in the Chortis Block (Caribbean Plate). Most zircons formed within magmatic intrusions, although zircon growth and recrystallisation during the latest Permian was associated with metamorphic processes.

Triassic magmatism is scarce in southern North America, and reliable, concordant Triassic zircon U–Pb dates of igneous rocks are mainly exposed in the Chaucús Metamorphic Complex (Guatemala; Maya Block), where they range between 249–226 Ma (Figures 4d, 5b; Solari et al., 2011) and are interpreted as the crystallisation ages of intrusions with a peak at ca. 226 Ma. Ratschbacher et al. (2009) report a single Triassic rim (215.9 ± 0.2 Ma) surrounding a Permian zircon core in the Rabinal Complex (Maya Block). Helbig et al. (2012) obtained a

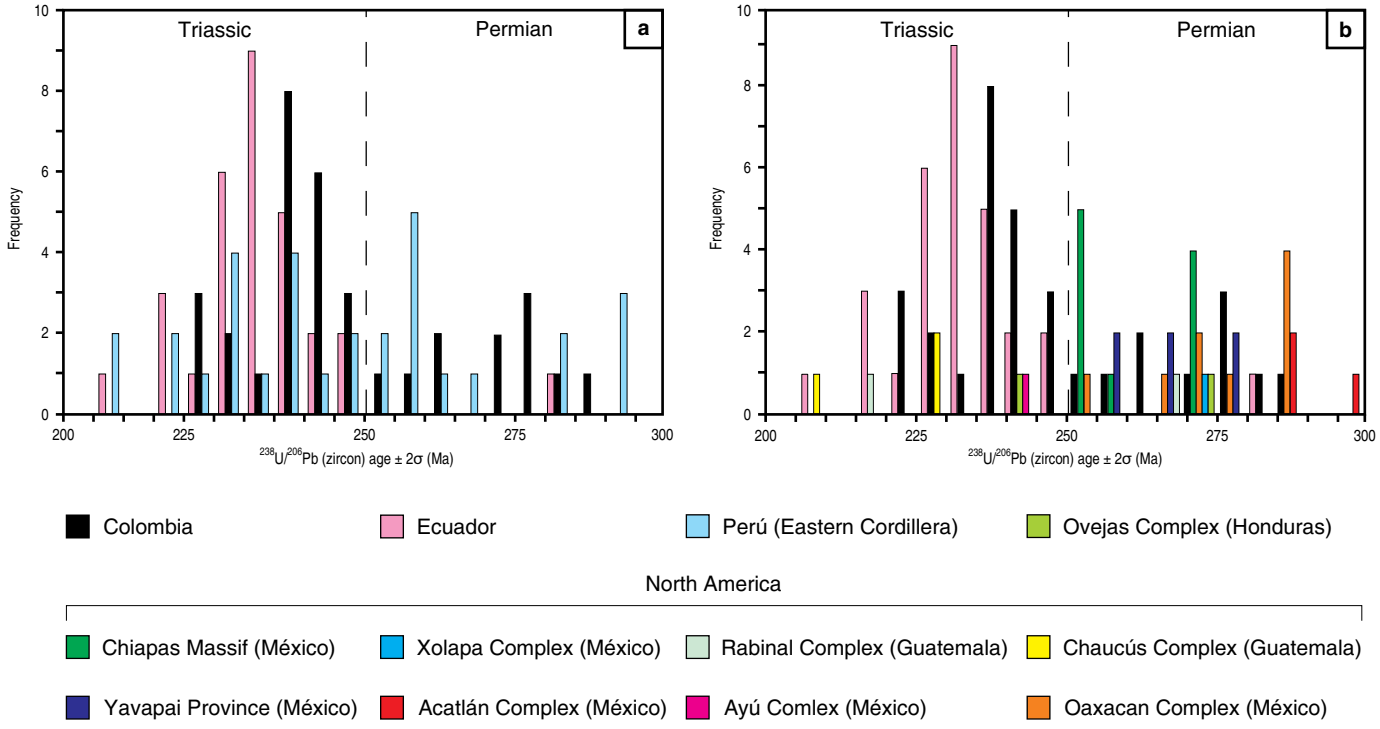

Figure 5. Weighted mean zircon $^{206}Pb/^{238}U$ (concordant) age histogram for Permian and Triassic magmatism and metamorphic zircon growth for variably foliated granites and migmatites (leucosomes) in **(a)** the Eastern Cordillera of Perú (Mišković et al., 2009; Spikings et al., 2016), and **(b)** various regions of the southern North American and western Caribbean Plate (references in caption for Figure 4). Concordant $^{206}Pb/^{238}U$ zircon dates are also shown for Colombia and Ecuador.

concordant zircon U–Pb age of 244 ± 4 Ma from a granitic dyke within the Ayú Complex, and inherited zircons that yield dates between 242–209 Ma. A migmatite from the Ayú Complex yields inherited zircons with U–Pb dates of 239–225 Ma (Helbig et al., 2012). These overlap with Triassic ages for migmatites and plutons in northwestern South America (Figures 4, 5b). Keppie et al. (2006) present discordant zircon U–Pb dates from migmatitic gneisses of the Francisco Gneiss (Guerrero composite terrane) that span between 216 and 197 Ma. These are not reliable estimates of the timing of crystallisation, although Keppie et al. (2006) suggest they record crystallisation at ca. 206 Ma. If accurate, these would be younger than the timing of anatexis in northwestern South America.

The Chortis Block currently forms part of the western Caribbean Plate, and several Permian and Triassic zircon U–Pb dates have been obtained from intrusions that must be accounted for when reconstructing western Pangaea. Ratschbacher et al. (2009) report U–Pb dates of 272.8 ± 2.8 Ma and 244.8 ± 2.3 Ma from zircon cores in Eocene granitic gneisses of Las Ovejas Complex (northwestern Honduras; Figures 4d, 5b). The Permian cores yield magmatic Th/U ratios (~0.7), while the Triassic group yields Th/U ratios of ~0.04, which is typical of metamorphic, sub–solidus growth.

5. Geochemistry

5.1. Granites and Migmatites: Central Cordillera of Colombia and the Cordillera Real of Ecuador

Major oxide, trace element, and rare earth element (REE) abundances and oxygen isotope compositions (Table 1) have been obtained from Permian and Triassic granites and migmatitic leucosomes from Colombia (Cardona et al., 2010a; Correa–Martínez, 2007; Piraquive, 2017; Spikings et al., 2015; Vinasco et al., 2006) and Ecuador (Cochrane et al., 2014b; Litherland et al., 1994; Paul et al., 2018; Spikings et al., 2015). Both Permian and Triassic granodiorites, monzogranites, and syenogranites (Figure 6a) span the boundaries of calcic to alkali–calcic differentiation trends on the modified alkali–lime index of Peacock (1931) (Figure 6b), with a compositional range of 77–59 (Permian) and 78–65 wt % SiO_2 (Triassic). The Triassic acidic rocks plot within the high–K calc–alkaline and calc–alkaline fields when comparing SiO_2 with K_2O (Figure 7a).

The Triassic anatectites have strongly peraluminous aluminium saturation indices (ASI 1.05–2.38; calculated using Maniar

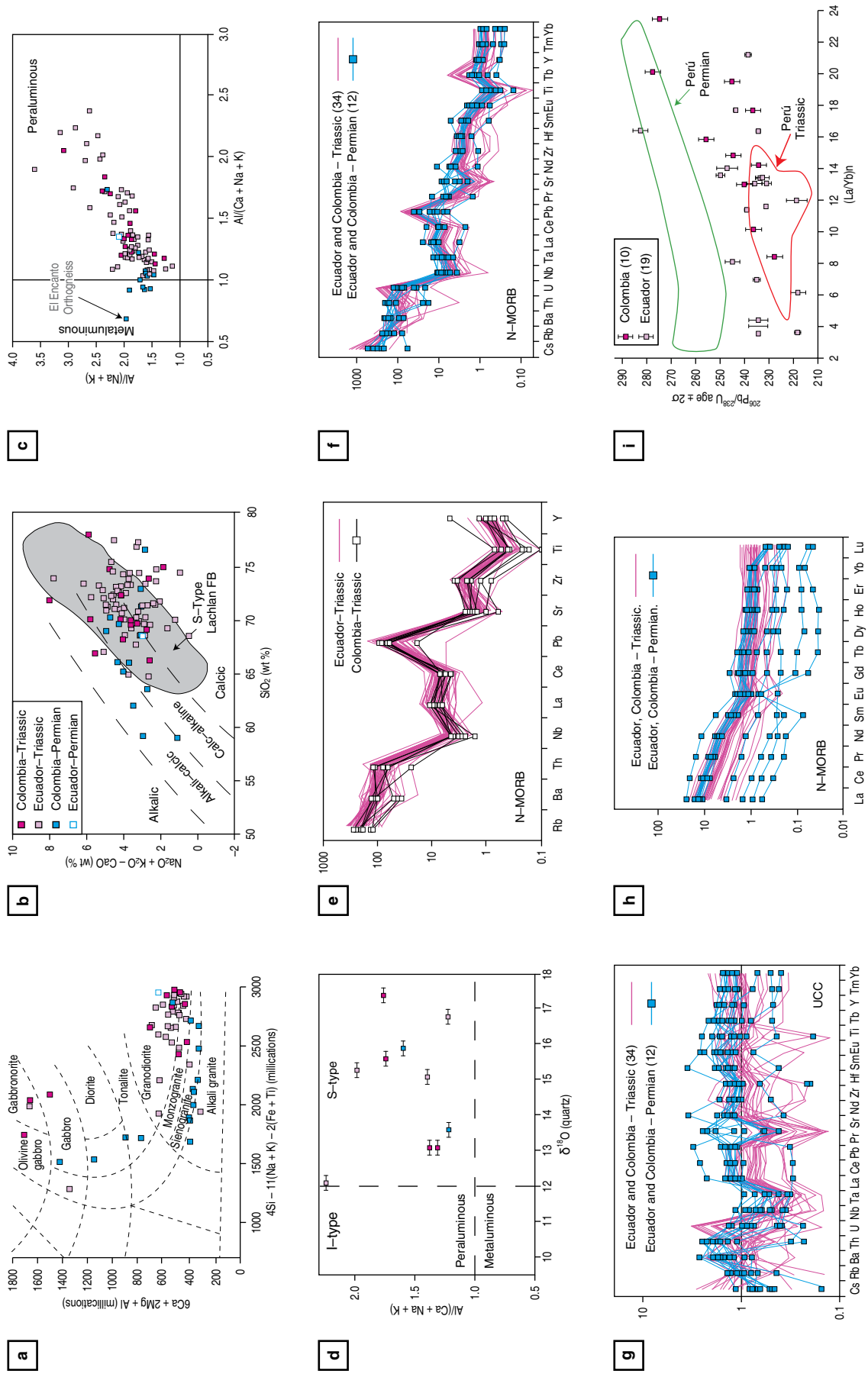

Figure 6. Geochemical data from Permian and Triassic granites and migmatitic leucosomes from the Central Cordillera (Cajamarca and Rovira Complexes) and Inner Santa Marta Metamorphic Belt (El Encanto Orthogneiss and La Secreta Orthogneiss) of Colombia, and the Cordillera Real (Sabanilla and Tres Lagunas units) and Amotape Complex (Moromoro unit) of Ecuador. Lithological discriminatory fields shown in **(a)** are from Batchelor & Bowden (1985), while the fields in **(b)**, **(c)**, and **(d)** are from Peacock (1931), Maniar & Piccoli (1989), and Harris et al. (1997), respectively. Fields for Peruvian rocks in **(i)** are from Mišković et al. (2009) and Spikings et al. (2016). Multi–element plots are normalised to N–MORB (Sun & McDonough, 1989) and upper continental crust (UCC) (Taylor & McLennan, 1995). Data from Colombia: Vinasco et al. (2006), Correa–Martínez (2007), Cardona et al. (2010a), Cochrane et al. (2014b), Piraquive (2017). Data from Ecuador: Litherland et al. (1994), Cochrane et al. (2014b), Paul et al. (2018).

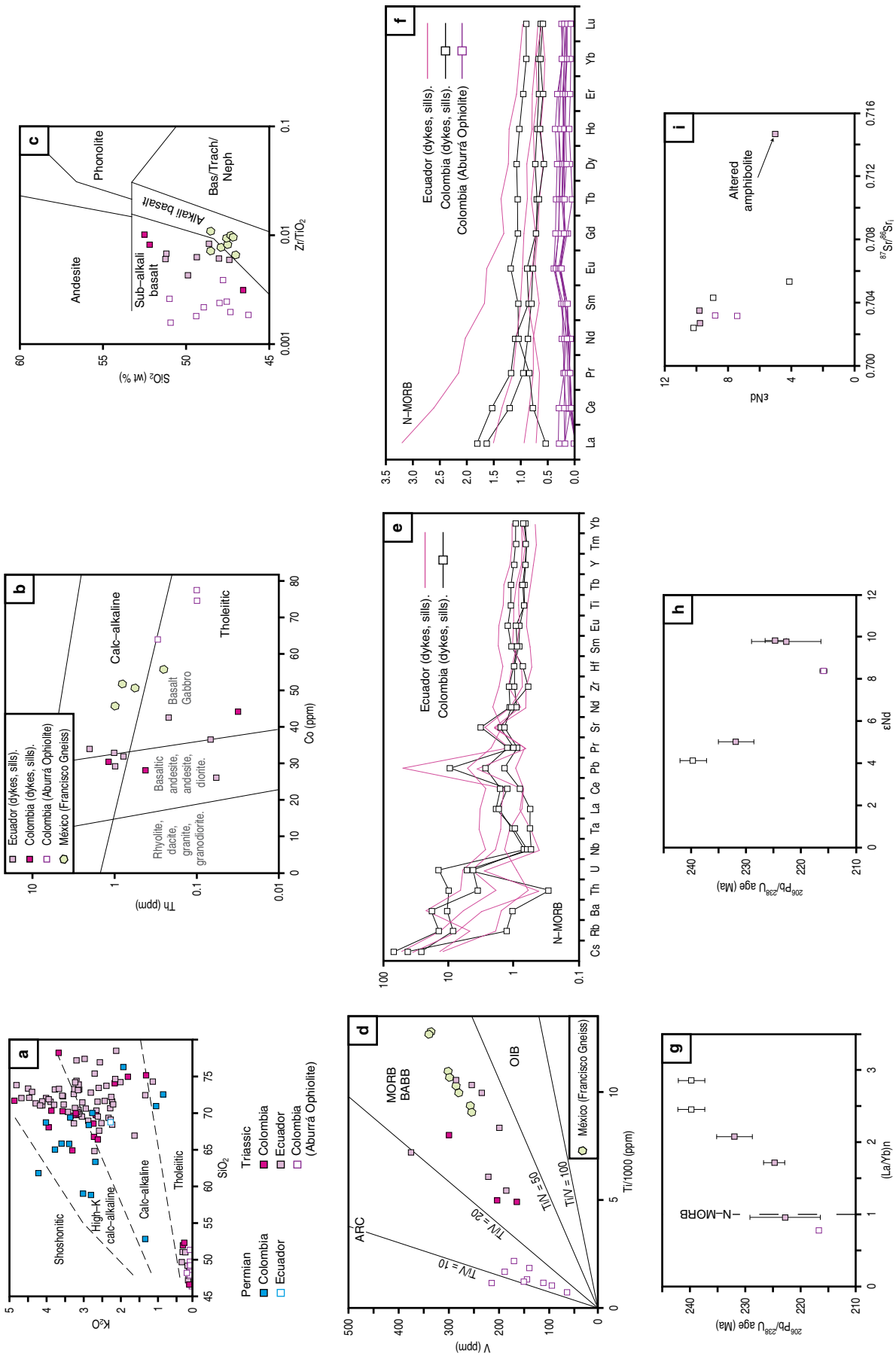

Figure 7. Geochemical data from Triassic amphibolitic dykes and metagabbros of the Central Cordillera (Chinchina and Santa Elena Amphibolites, and the Aburrá Ophiolite), and Cordillera Real (Monte Olivo unit) and Amotape Complex (Piedras unit). Multi–element plots are normalised to N–MORB (Sun & McDonough, 1989). Data is also shown for the Triassic? Francisco Gneiss (México; Keppie et al., 2006). Data from Colombia: Correa–Martínez (2007), Cochrane et al. (2014b). Data from Ecuador: Litherland et al. (1994), Cochrane et al. (2014b). Discriminatory fields in **(a)** are from Peccerillo & Taylor (1976), **(b)** are from Hastie et al. (2007), **(c)** are from Winchester & Floyd (1977), and **(d)** are from Shervais (1982).

& Piccoli, 1989; Figure 6c), while the Permian granitoids tend to cluster at slightly lower peraluminous and mildly metaluminous values (ASI 0.92–1.73, with a majority <1.1). The Triassic anatectites yield elevated $\delta^{18}O$ quartz (Figure 6d), which along with their high ASI places these granites and leucosomes within the "S–type granite" field of Chappell & White (1974) and Harris et al. (1997). Normal mid–ocean ridge basalts (N–MORB) normalized trace element abundances of Triassic granitoids from Ecuador and Colombia are identical (Figure 6e), suggesting there are no significant along–strike changes in the fractionation and assimilation history of these high–SiO_2 melts. Trace elements in both the Permian and Triassic granitoids are enriched in light–ion lithophile elements (LILE), and negative Nb, Ta, and Ti anomalies are present (Figure 6f), suggesting that a subduction–derived component was incorporated into these rocks and it is likely that they formed within a continental arc. The Triassic granitoids yield slight negative N–MORB normalized Ba, Eu, Sr, and Ti anomalies, which suggests that plagioclase and Fe–Ti oxides have fractionated, and a positive Pb anomaly that may be derived from a protolith within the continental crust. In contrast, most of the Permian granites do not yield Ba, Eu, and Sr anomalies, although they do have negative Ti anomalies, and positive Pb anomalies are less pronounced, suggesting they evolved via a different fractionation scheme.

Trace element concentrations of Triassic rocks normalized to the composition of average upper continental crust (Taylor & McLennan, 1995) plot close to unity, corroborating the S–type character of these rocks (Figure 6g), whereas a majority of Permian rocks plot slightly above unity. REE abundances in the Triassic granites and leucosomes normalized to N–MORB reveal light–REE enrichment (Figure 6h) with (La/Yb)n ranging between 2.3–19.8 (Figure 6i), with a mildly positive correlation with ^{206}Pb–^{238}U crystallisation age. (La/Yb)n ratios from Permian granites yield values of 23.09–16.1, and the REE concentrations have a larger range to lower values relative to N–MORB, compared to the Triassic rocks (Figure 6h).

5.2. Amphibolites: Central Cordillera of Colombia and the Cordillera Real of Ecuador

A comparison of the abundance of K_2O and SiO_2 (Figure 7a) in all of the Triassic magmatic rocks reveals the bimodal nature of Triassic magmatism within northwestern South America as part of Pangaea between 243 ± 4 Ma and 216.6 ± 0.4 Ma (Table 1). In contrast, Permian intrusions reveal a more continuous spread in SiO_2 abundance (Figure 6a, 6b), and a bimodal character is not evident. Here we review the geochemical characteristics of the mafic intrusions in Colombia and Ecuador, all of which are Triassic.

Amphibolitic dykes and massive metagabbros from the Central Cordillera of Colombia (Chinchina, Santa Elena, Padua, and Aburrá; Figure 2), and the Cordillera Real and Amotape Complex of Ecuador (Monte Olivo and Piedras units) yield low K_2O (<0.5 wt %) relative to SiO_2 (46–55 wt %), placing them within the tholeiitic field of Peccerillo & Taylor (1976) (Figure 7a). However, a comparison of the immobile elements Th and Co (Figure 7b) suggests that amphibolitic dykes straddle the tholeiite and calc–alkaline fields, while the massive metagabbros of the Aburrá Ophiolite plot in the tholeiite field. These discrepancies suggest the amphibolitic dykes may be partially altered. The amphibolites and metagabbros have Zr/TiO_2 that are lower than 0.01 (Figure 7c), placing them within the sub–alkaline basalt field, implying that the tholeiitic nature is primary. The amphibolitic dykes are enriched in Ti relative to V (Figure 7d), and plot in the MORB or back–arc basin basalt (BABB) field of Shervais (1982). The massive metagabbros of the Aburrá Ophiolite (El Picacho Metagabbros) that yield very low K_2O abundances of 0.02–0.12 wt % (Figure 7a), plot closer to the arc field. LILE abundances within the amphibolitic dykes from Colombia and Ecuador (Figure 7e) are enriched (up to ~100 times) relative to N–MORB and lack significant Nb and Ta anomalies. The high field strength elements (HFSE) plot close to parity with N–MORB, which is consistent with the tectonic discrimination plots. Similarly, N–MORB normalised REE plots (Figure 7f) for the amphibolitic dykes plot close to MORB compositions, although the LREE are slightly enriched with (La/Yb)n ratios varying between 3.16–0.59, while the massive metagabbros of the Aburrá Ophiolite yield approximately flat REE patterns that are slightly depleted relative to N–MORB. N–MORB normalised La/Yb ratios from all of these rock sequences show a progressive reduction with crystallisation age from 243 ± 4 Ma to 216.6 ± 0.4 Ma (Figure 7g). Finally, whole–rock εNd_i values for the amphibolitic dykes and the metagabbros range between 10.18 and 3.40, and become more juvenile with younger crystallisation ages (Figure 7h). The most juvenile rocks are characteristic of MORB and back–arc basin basalts (BABB) isotopic compositions.

A single amphibolite from the Monte Olivo unit in the Cordillera Real of Ecuador yields a whole–rock $^{87}Sr/^{86}Sr_i$ of 0.7147 (Figure 7i), which is extremely high relative to its $^{143}Nd/^{144}Nd_i$ of 0.5126 and low La/Yb ratio of 1.71 (Cochrane et al., 2014b). This is consistent with low temperature alteration, which has preferentially mobilized the LILE but had a minimal effect on the REE.

5.3. Comparison with Permian and Triassic Rocks in Perú

Permian granitoids within the Eastern Cordillera of Perú that crystallised during 293–254 Ma are alkali–calcic to calc–alkaline high–SiO_2 monzo–, syeno–, and alkali granites (Figure 8a, 8b), which are mildly metaluminous to peraluminous (ASI 1.0–1.1; Figure 8c) and yield K_2O/Na_2O ratios that mainly range between 0.8 and 1.2 (Mišković et al., 2009). N–MORB

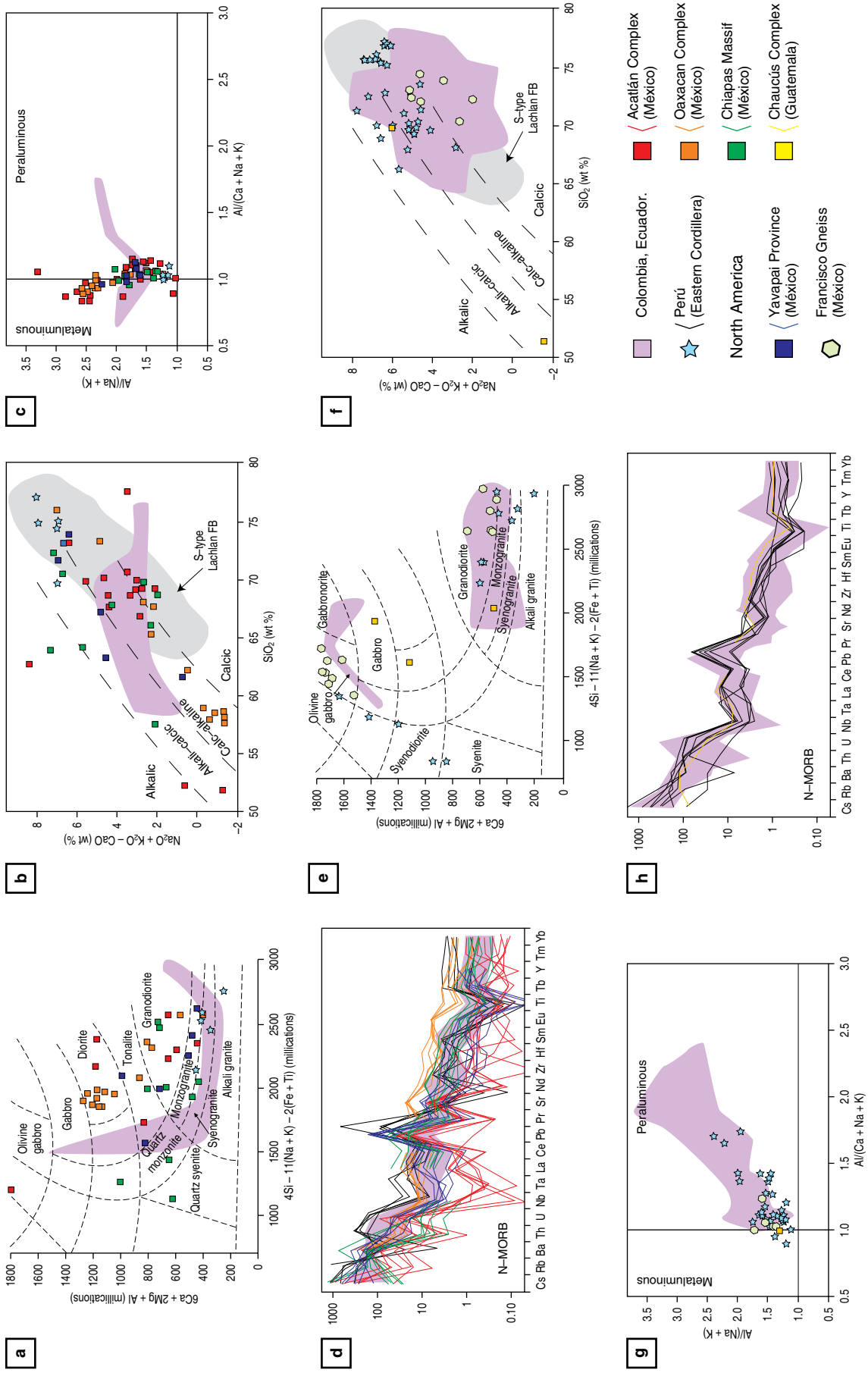

Figure 8. Geochemical data from **(a–d)** Permian and **(e–h)** Triassic granites and migmatitic leucosomes from the Eastern Cordillera of Perú, and various regions in the southern North American and western Caribbean plates. Pink shading shows the data fields obtained from Colombia and Ecuador. Data from Perú published in Mišković et al. (2009) and Spikings et al. (2016). Other data are from Solari et al. (2001; Oaxacan Complex), Keppie et al. (2006; Francisco Gneiss), Weber et al. (2005; Chiapas Massif), Arvizu et al. (2009; Yavapai Province), Solari et al. (2011; Chaucús Complex), Kirsch et al. (2012; Acatlán Complex). Lithological discriminatory fields shown in **(a)** and **(e)** are from Batchelor & Bowden (1985).

normalized multi–element plots reveal negative Nb, Ta, and Ti anomalies (Figure 8d), and resemble the composition of Permian intrusions from Colombia and Ecuador. The Permian intrusions in Perú have high SiO_2 (>69 wt %) and do not reveal a bimodal composition (Figure 8a), which is also the case in Colombia and Ecuador. Mišković et al. (2009) combined major element characteristics with iron oxide number, SiO_2 (e.g., Frost et al., 2001), and trace element abundances, to classify the Permian plutons of the Eastern Cordillera of Perú as late– to post–orogenic.

Triassic intrusions are mainly located in the southern Eastern Cordillera of Perú (Cordillera de Carabaya), and similar to the case of Colombia and Ecuador, they are geochemically distinct from the Permian intrusions (e.g., Mišković et al., 2009; Spikings et al., 2016). Triassic alkali–calcic to calc–alkaline granodiorites, monzo–, syeno–, and alkali granites in Perú (Figure 8e, 8f) are strongly peraluminous (ASI 0.98–1.42; Figure 8g), and yield anomalously high whole–rock K_2O/Na_2O ratios (0.55–2.22, with a majority >1.20; Mišković et al., 2009). N–MORB normalized multi–element plots (Figure 8h) reveal negative Nb, Ta, and Ti anomalies, and a positive Pb anomaly, suggesting the anatectites derived from source rocks with a subduction signature. Geochemically, the Triassic migmatites and granites of the Cordillera Real of Ecuador and the Central Cordillera of Colombia (K_2O/Na_2O 0.77–2.93; ASI 0.92–2.38) resemble the Triassic granites of the Eastern Cordillera of Perú. The Triassic anatectites in Perú were coeval with alkali olivine gabbro to syenitic lavas (Figure 8e) that intercalate oxidised terrigenous sedimentary rocks. Collectively these are referred to as the Mitu Group, which was deposited in a continental rift during 245–220 Ma (Spikings et al., 2016).

5.4. Comparison with Permian and Triassic Rocks in the Southernmost North American Plate

Permian intrusions in the Acatlán Complex, Oaxacan Complex, Chiapas Massif, and Yavapai Province of México are dominated by tonalites, diorites, and granodiorites (Figure 8a) with calcic to alkali–calcic differentiation trends (Figure 8b), while some upper Permian quartz monzogranites and quartz syenites are exposed in the Chiapas Massif. All of these rocks are mildy peraluminous to metaluminous (ASI 0.83–1.14; Figure 8c). All Permian rocks yield N–MORB normalized trace element plots (Figure 8d) with enriched LILE, and negative Nb, Ta, and Ti anomalies, although diorites and tonalites of the Oaxacan Complex are more enriched, while granodiorites of the Aca-tlán Complex are the most depleted. These characteristics generally resemble the Permian intrusions of Colombia, Ecuador, and Perú, suggesting they may have all formed within different regions of the same east–dipping subduction zone along the western margin of Pangaea (e.g., Dickinson & Lawton, 2001; Kirsch et al., 2012; Ortega–Obregón et al., 2014; Solari et al., 2001; Torres et al., 1999).

Triassic intrusions in México and Central America are sparse (see section 4.5) and thus comparisons with regions within South America are not statistically robust. Nevertheless, orthogneisses in the Chaucús Metamorphic Complex of Guatemala are alkali–calcic, gabbros to monzogranites with mildly peraluminous compositions, and yield N–MORB normalized trace element compositions (Figure 8e–h; Solari et al., 2011) that are very similar to coeval Triassic rocks exposed in Colombia, Ecuador, and Perú. Solari et al. (2011) tentatively suggest these formed in an arc formed by east–dipping subduction of the Pacific lithosphere, and are a temporal extension of the Permian arc rocks found elsewhere in México. Keppie et al. (2006) suggest the Francisco Gneiss, which is exposed within the core of a Tertiary core complex in the Guerrero composite arc terrane is Late Triassic. The magmatic assemblage is bimodal (Figure 8e), and the acidic end–member is moderately peraluminous and calc alkaline rhyolites (Figure 8f, 8g). The mafic end member amphibolites are alkali to sub–alkali basalts with within–plate characteristics (Figure 7b–d) that intruded continental crust. These characteristics closely resemble the Triassic igneous assemblage in Colombia and Ecuador although the accuracy of their crystallisation ages is questionable (see section 4.5).

6. Isotope Geochemistry

Cochrane et al. (2014b) and Paul et al. (2018) report Hf (zircon) and Pb (feldspars) isotopic compositions from thirty seven Triassic migmatitic leucosomes, massive granitoids, and amphibolitic dykes exposed throughout the Central Cordillera of Colombia and the Cordillera Real and Amotape Complex of Ecuador (Table 1). The zircons, which have been dated by LA–ICP–MS (U–Pb), yield a large range of weighted mean (average of several zircon grains) εHf_i values of +15 and –20 (Figure 9; Table 1), which is consistent with the Pb isotopes (Figure 10; Table 1), and suggests that isotopically juvenile material was added to the continental crust during the Triassic, which also introduced heat and recycled continental crust via anatexis, generating the acidic end–member (Cochrane et al., 2014b; Collins et al., 2011; Spikings et al., 2015).

6.1. Zircon Hf: Granites and Migmatitic Leucosomes

Single Triassic leucosomes of migmatites and peraluminous granites generally yield high, intra–sample variations (e.g., εHf_i +3 to –11; Figure 9a) within coeval magmatic rims that surround variably aged xenocrystic cores (Cochrane et al., 2014b), and within samples that lack older cores. These varia-

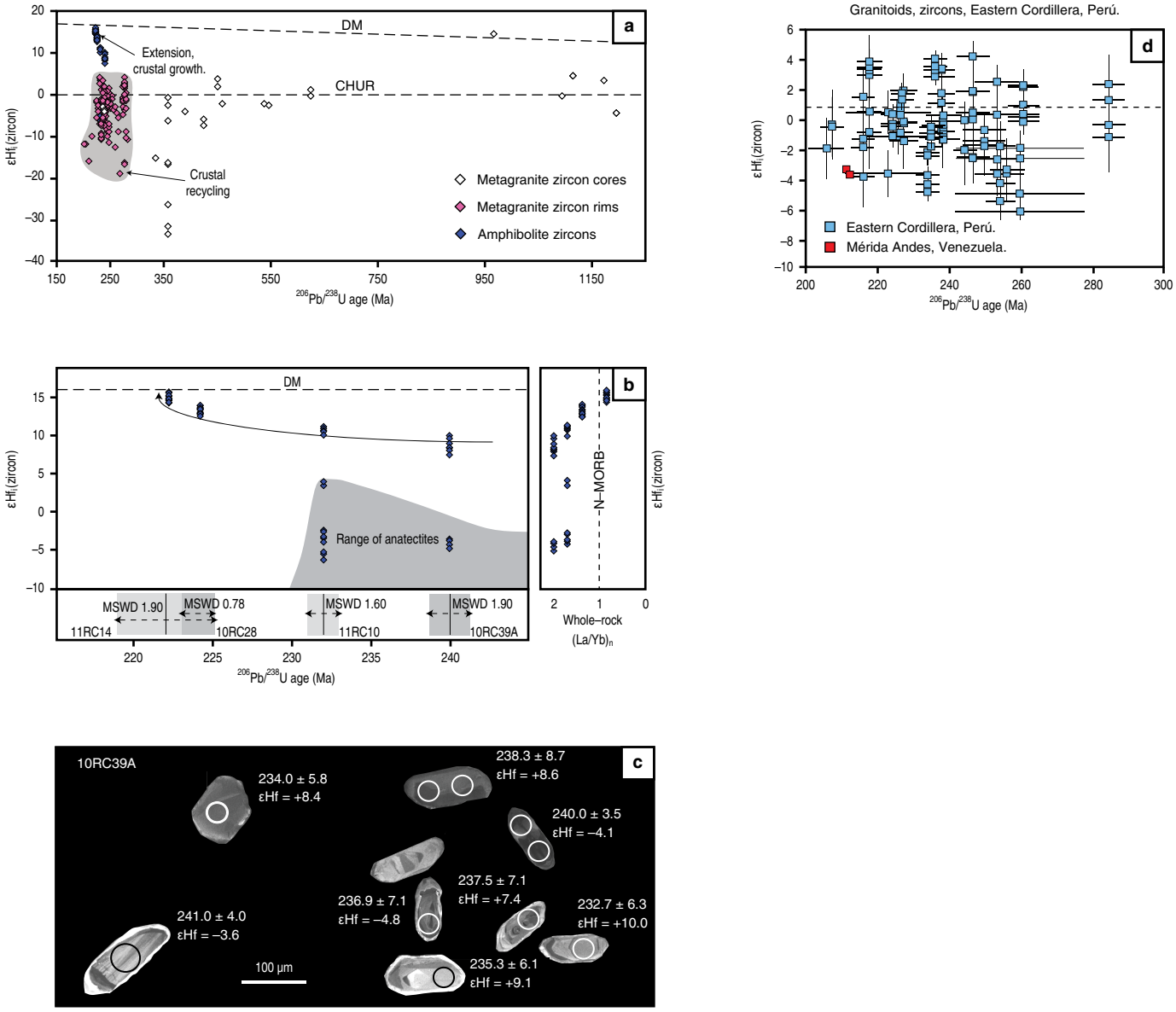

Figure 9. (a) Hf (zircon) isotope data (Cochrane et al., 2014b) acquired from rims and xenocrystic cores (single spots) of Permian and Triassic peraluminous granitoids, migmatitic leucosomes, and amphibolitic dykes and sills of the Central Cordillera, Cordillera Real, and the Amotape Complex. εHf_i was determined using zircon crystallisation dates found using LA–ICP–MS, and the CHUR composition ($^{176}Lu/^{177}Hf$ = 0.0336, $^{176}Hf/^{177}Hf$ = 0.282785; Bouvier et al., 2008). **(b)** Variation in εHf_i (zircon) of the amphibolites with zircon crystallisation date and whole–rock (La/Yb)n (N–MORB), showing a trend towards depleted mantle isotopic and geochemical signatures, with time. **(c)** Representative cathodoluminescence images for amphibolite 10RC39A (Central Cordillera; Table 1) show that juvenile εHf_i values (7.4 to 10) are yielded by patchy or unzoned zircons, whereas less juvenile values (–3.6 to –4.8) are obtained from oscillatory zoned zircons. **(d)** εHf_i (zircon) data from Permian – Triassic granitoids of the Eastern Cordillera of Perú (rims and cores; Mišković et al., 2009; Spikings et al., 2016), and the Mérida Andes (mean values; van der Lelij et al., 2016).

tions are too large for magmatic zircons that crystallised from a single, well–mixed source (e.g., Gerdes et al., 2002), and Cochrane et al. (2014b) conclude that they are mainly derived from multiple crustal sources. A small proportion of granites yield εHf_i (zircon) values that statistically define a single population, suggesting that they were derived from a distinct, homogeneous source. No correlation is found between the εHf_i values obtained from the rims of xenocryst bearing and xenocryst free zircons, and crystallisation age, which is not surprising given the heterogeneous nature of the source rocks within the crust. εHf_i values obtained from xenocrystic zircon cores (Figure 9a) span a large range and are representative of

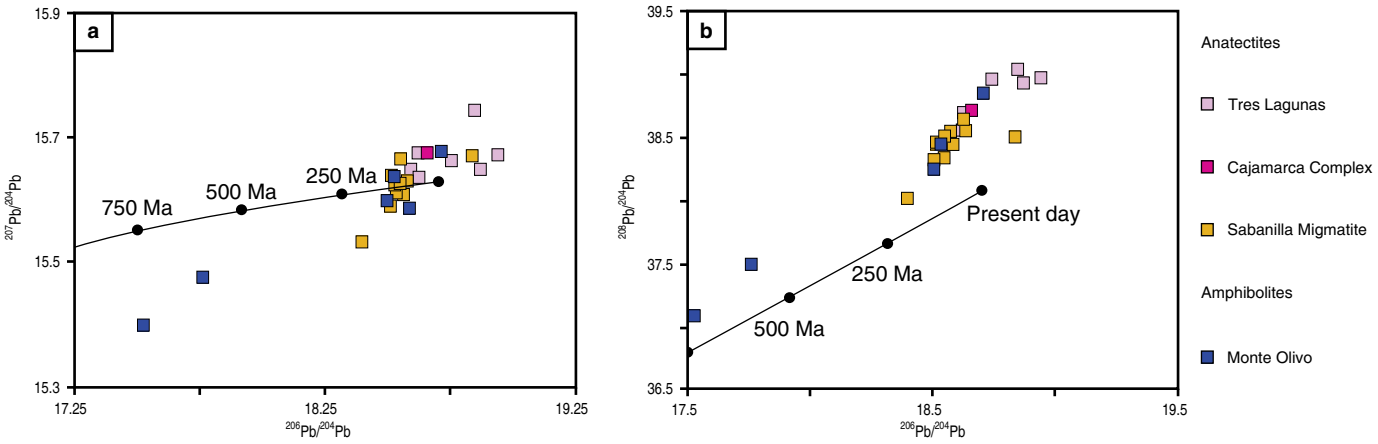

Figure 10. (a) and **(b)** $^{206}Pb/^{204}Pb$, $^{207}Pb/^{204}Pb$ and $^{208}Pb/^{204}Pb$ compositions of feldspar (mixed plagioclase and K–feldspar) extracted from granites and leucosomes of the Cajamarca Complex, Tres Lagunas Granite, and the Sabanilla Migmatite. Data from the Monte Olivo Amphibolites (Figure 2) is also shown. The Stacey & Kramers (1975) two–stage crustal evolution line is drawn as a reference. The data reveal mixing between a mafic end–member defined by amphibolites of the Monte Olivo unit, and the most radiogenic, highly peraluminous melts represented by the Tres Lagunas Granite.

the sedimentary protoliths that melted to form the anatectites. The large heterogeneity in εHf_i corroborates the large range in $^{238}U/^{206}Pb$ dates of the protoliths.

6.2. Zircon Hf: Amphibolites

Cochrane et al. (2014b) report εHf_i (zircon) values from four amphibolites which show a negative correlation with crystallisation age (Figure 9b). The two older amphibolitic dykes (240–232 Ma) yield a large range in εHf_i, with juvenile values (7.4 to 10) obtained from patchy or unzoned (cathodoluminescence) zircons, and crustal compositions (–3.6 to –4.8) from zircons that exhibit oscillatory zoning, similar to the zircons extracted from the anatectites (Figure 9c). The two youngest amphibolites (225–223 Ma) define single populations of εHf_i (13.3–15.0) from unzoned zircons, which approach the depleted mantle array. Crustal contamination of the mafic melts during emplacement was an important process in the petrogenesis of the older amphibolites prior to ca. 225 Ma. However, there is no evidence for the assimilation of significant continental crust after ca. 225 Ma. This interpretation is supported by a negative correlation between (i) εHf_i (zircon) and (La/Yb)n, (Figure 9b), and (ii) crystallisation age and eNd (whole–rock; Figure 7h; Table 1), suggesting that the mafic dykes trend towards MORB compositions with a depleted mantle source, during 240–223 Ma.

6.3. Feldspar Pb: Granites and Migmatitic Leucosomes

Cochrane et al. (2014c) and Paul et al. (2018) present Pb isotopic compositions (measured by ID–TIMS) of a combination of calcic and potassium feldspars (Figure 10; Table 1) extracted from Triassic leucosomes and anatectites of the Cordilleras Central and Real. These data show that the Triassic monzogranites of the Cajamarca Complex (Colombia) and Tres Lagunas Granite (Ecuador) are the most radiogenic suite amongst the Triassic igneous units in the northern Andes (e.g., $^{206}Pb/^{204}Pb$ 18.94–18.59), while the Triassic amphibolitized mafic intrusions yield the least radiogenic compositions ($^{206}Pb/^{204}Pb$ 18.53–18.51) and reveal progressive mixing and contamination with continental crust. Leucosomes of the Sabanilla Migmatite (Ecuador) are slightly less radiogenic than the Tres Lagunas Granite with respect to Pb, and plot between the fields defined by the juvenile mafic intrusions and the Tres Lagunas Granite (Figure 10). This trend corroborates the εHf_i (zircon) values of the amphibolites (Cochrane et al., 2014b) that define a mixing array between the Tres Lagunas Granite end member and depleted mantle during 239.7 ± 2.4 Ma and 216.6 ± 0.4 Ma. These mixing trends are interpreted to reflect progressive contamination of continental crust with juvenile magmas that were emplaced during extensional decompression. Leucosomes of the Sabanilla Migmatite represent incipient melting and moderate crustal contamination of juvenile magmas. Plutons of the Tres Lagunas Granite and Cajamarca Complex are interpreted to be the product of accumulation of leucosomal melts.

6.4. Comparison with Zircon Hf Isotope Compositions in Perú

Hf isotopic compositions obtained from Permian and Triassic peraluminous granitoids of the Eastern Cordillera of Perú yield no clear trends with time, and εHf_t values range between +6 and –8 (Figure 9d; Mišković & Schaltegger, 2009; Spikings et al., 2016). This range overlaps with that obtained from Triassic

granitoids of Ecuador and Colombia, and individual, intra–grain spot analyses show a large spread, reflecting the heterogeneity of the source rocks. Mean zircon εHf_i values from the Early and Late Triassic of 0.02 ± 1.56 and –1.96 ± 1.56 suggest that this period was characterised by the addition of isotopically juvenile, mantle derived magmas, which were underplating previously attenuated continental crust (Mišković & Schaltegger, 2009; Spikings et al., 2016).

7. Thermochronology

Numerous K/Ar dates have been obtained from Paleozoic and Triassic magmatic rocks in the Central Cordillera of Colombia (Aspden et al., 1987; Feininger et al., 1972; Hall et al., 1972; McCourt et al., 1984) and the Cordillera Real of Ecuador (Litherland et al., 1994). Within Ecuador, muscovite, biotite, and whole–rock K/Ar dates of the Tres Lagunas Granite and Sabanilla unit (migmatites) range between 100–50 Ma (Litherland et al., 1994), revealing a clear disturbance to the isotopic system. Unfortunately, we cannot extract useful time–Temperature (t–T) information from these data because the degree of daughter isotope loss cannot be quantified. Nevertheless, McCourt et al. (1984) and Litherland et al. (1994) interpret these data to reflect continental collision at ca. 120 and 65–55 Ma.

Spikings et al. (2000, 2001, 2010) and Villagómez & Spikings (2013) present $^{40}Ar/^{39}Ar$ (white mica, biotite, alkali feldspar) and fission track (zircon, apatite) data from Triassic magmatic rocks in Colombia and Ecuador, which were used to construct time(t)–Temperature(T) paths. However, the collision of the Caribbean Large Igneous Province with South America at ca. 75 Ma drove more than 350 ºC of cooling via exhumation (Spikings et al., 2010), and Triassic thermal histories are not preserved in the isotopic systems.

Recently, Cochrane et al. (2014c) and Paul et al. (2018) published apatite U–Pb data from the Triassic Cajamarca Complex, Sabanilla Migmatite, and Tres Lagunas Granite (Figure 11; Table 1). The authors demonstrate that Pb was lost from the apatite grains by thermally activated diffusion, and thus the dates can be combined with grain sizes and the diffusion properties of Pb in apatite to generate a series of plausible t–T paths at temperatures >380 ºC (Figure 11) using a computed Monte Carlo algorithm. Apatite $^{238}U–^{206}Pb$ dates from the Cajamarca Complex in the northern Central Cordillera are 10–20 my younger than their zircon U–Pb dates (Figure 11a), reflecting rapid cooling through 550–380 °C in the latest Triassic (Figure 11b), and no subsequent re–heating to temperatures >380 °C. In contrast, a majority of $^{238}U–^{206}Pb$ dates from Triassic anatectites in the southern Cordillera Real are younger than 100 Ma (Figure 11a). Numerical modelling suggests these rocks also cooled rapidly through 550–380 °C in the latest Triassic, although the rocks were re–heated to >380 °C in the Cretaceous (Figure 11c). $^{40}Ar/^{39}Ar$ muscovite plateau dates and low temperature thermochronometers (Spikings et al., 2010) support the accuracy of the t–T paths (Table 1).

Rapid cooling from anatectic temperatures to less than ~380 °C during the Triassic is probably mainly a consequence of thermal relaxation subsequent to the removal of the heat source at a local geographic scale. Some component of cooling may also be a consequence of exhumation during Triassic extension (see section 8.2).

8. Interpretation

8.1. Permian: Arc Magmatism and Metamorphism along Western Pangaea

8.1.1. Arc Magmatism

The exposure of Permian granitoids within the northern Andes (Figure 2) is restricted to the Sierra Nevada de Santa Marta (ca. 288–264 Ma), the central Central Cordillera (ca. 278–253 Ma), and a single rock located in the far southern Cordillera Real (ca. 283 Ma), close to the Peruvian border. Mylonitic granites and orthogneisses from the Sierra Nevada de Santa Marta yield dates spanning between ca. 288–264 Ma, while detrital zircons in metasedimentary rocks have maximum depositional ages of ca. 284–261 Ma. The aluminium saturation index of the Permian alkali–calcic to calcic granites straddles the peraluminous and metaluminous fields, while the $\delta^{18}O$ values (quartz) of 14–17 ‰ suggests that some of these syenogranites formed by partial melting of sedimentary rocks. Zircons yield magmatic Th/U ratios of 0.26–1.27 suggesting that they crystallised from magmas, and have not undergone sub–solidus metamorphic recrystallisation (Figures 12a, 13; Table 1). This is consistent with a high Y content (550–7750 ppm) and negative Eu anomalies in zircons of El Encanto Orthogneiss (Sierra Nevada de Santa Marta; Piraquive, 2017), which is corresponds to with a magmatic origin. The whole–rock trace element abundances are characteristic of subduction related magmatism. Magmatism during this period was not bimodal and thus not accompanied by a mafic end–member, and all rocks yield >58 wt % SiO_2 (Figure 6a, 6b). The Permian granites within the Sierra Nevada de Santa Marta (Cardona et al., 2010a; Piraquive, 2017) and the Central Cordillera of Colombia (Cochrane et al., 2014b; Villagómez et al., 2011) are interpreted to have formed within a continental arc above an east dipping Pacific subduction zone beneath western Pangaea during 288–255 Ma (Figures 13, 14). U–Pb dates of detrital zircons from two metasedimentary schists of the Gaira Schists (Sierra Nevada de Santa Marta) yield maximum depositional ages of ca. 284 and ca. 261 Ma (Piraquive, 2017), and thus these sedimentary rocks were coeval with and probably sourced from the continental arc.

Inherited early Neoproterozoic and Ordovician zircon cores are common in Permian intrusions in Colombia and

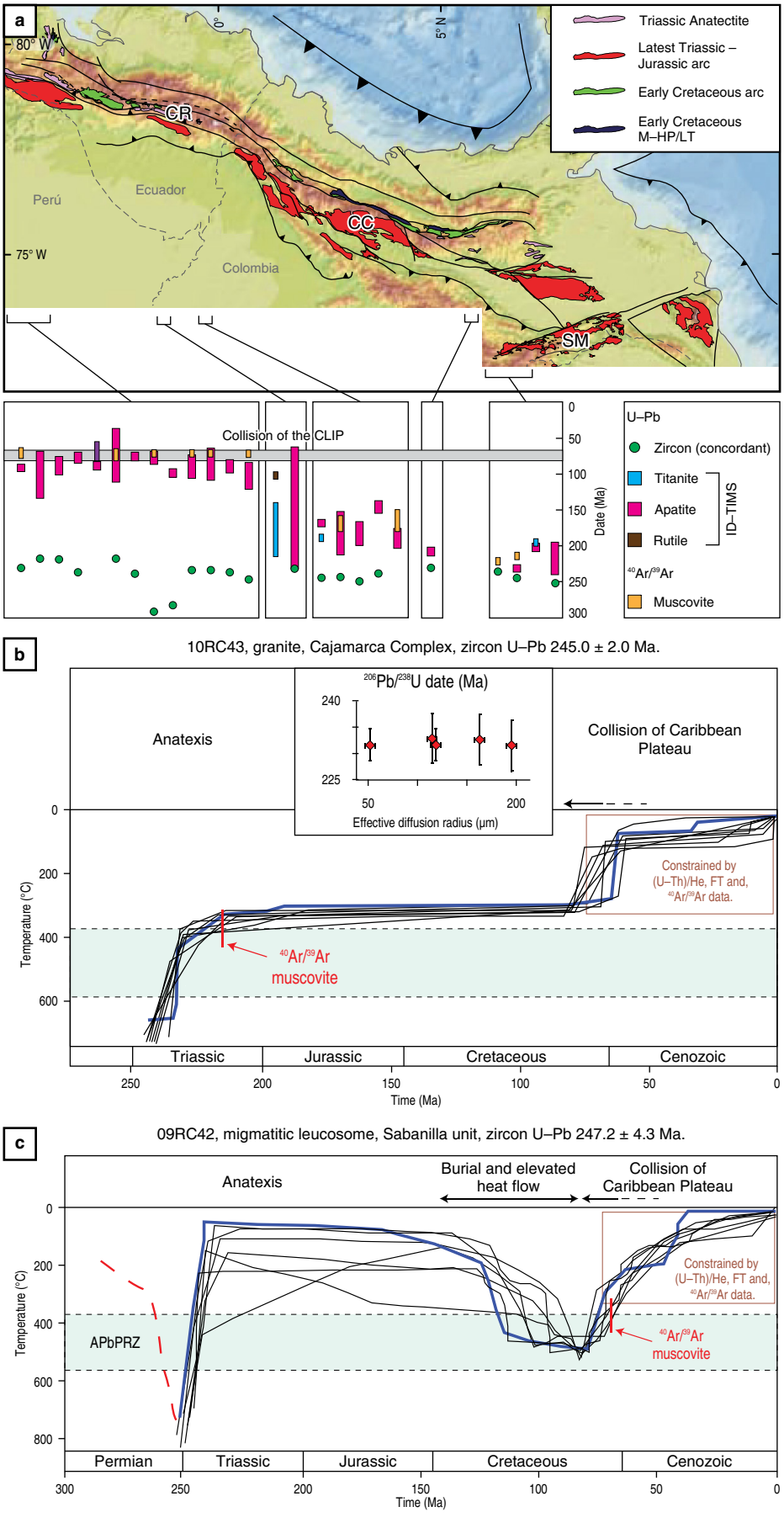
a
80° W
0°
5° N
75° W
CR
CC
SM
Perú
Ecuador
Colombia
Triassic Anatectite
Latest Triassic – Jurassic arc
Early Cretaceous arc
Early Cretaceous M–HP/LT
Collision of the CLIP
0
50
100
150
200
250
300
Date (Ma)
U–Pb
Zircon (concordant)
Titanite
Apatite
Rutile
ID–TIMS
40Ar/39Ar
Muscovite
b
10RC43, granite, Cajamarca Complex, zircon U–Pb 245.0 ± 2.0 Ma.
206Pb/238U date (Ma)
240
225
50
200
Effective diffusion radius (μm)
Anatexis
Collision of Caribbean Plateau
Constrained by (U–Th)/He, FT and, 40Ar/39Ar data.
40Ar/39Ar muscovite
Temperature (°C)
0
200
400
600
Triassic
Jurassic
Cretaceous
Cenozoic
250
200
150
100
50
0
Time (Ma)
c
09RC42, migmatitic leucosome, Sabanilla unit, zircon U–Pb 247.2 ± 4.3 Ma.
Anatexis
Burial and elevated heat flow
Collision of Caribbean Plateau
Constrained by (U–Th)/He, FT and, 40Ar/39Ar data.
40Ar/39Ar muscovite
APbPRZ
Temperature (°C)
0
200
400
600
800
Permian
Triassic
Jurassic
Cretaceous
Cenozoic
300
250
200
150
100
50
0
Time (Ma)

Ecuador, and thus the Permian continental arc recycled Sunsas and Famatinian–aged crust (see section 4.3), which is consistent with the mildly peraluminous and calc–alkaline compositions. Cathodoluminescence images show that many detrital zircons from the Gaira Schists (Sierra Nevada de Santa Marta) consist of Ordovician cores (Piraquive, 2017) with Permian rims, which suggests that anatexis of the crust accompanied arc magmatism during the middle part of the Permian. This is consistent with the high $\delta^{18}O$ values (quartz), and thus could be described as a high–temperature metamorphic event at some time between 288 and 264 Ma (Figure 13). Vinasco et al. (2006), suggest that zircon U–Pb (SHRIMP) dates of ca. 275 Ma obtained from the Abejorral granitic gneiss record a metamorphic event, although no evidence is presented for the metamorphic nature of the zircons. Similarly, Piraquive (2017) refers to anatexis at ca. 278 Ma in the Sierra Nevada de Santa Marta as a regional metamorphic event, although evidence for Barrovian metamorphism at that time is lacking, and the Th/U values of zircons is ~1 (Figure 12), suggesting they crystallised in a magmatic environment.

Remnants of Permian magmatism have also been found within the serranía de Perijá (Figure 1; Dasch, 1982), Paraguaná Peninsula (272.2 ± 2.6 Ma; van der Lelij et al., 2016), and El Baúl Massif (294.1 ± 3.1 – 283.3 ± 2.5 Ma) in Venezuela (Figure 4d; Viscarret et al., 2009). The geochemical composition of these rocks is also typical of a calc–alkaline continental arc (e.g., van der Lelij et al., 2016). These dates and geochemical characteristics overlap with Permian intrusions in the Central Cordillera, and the Sierra Nevada de Santa Marta, and thus it is not unrealistic to suggest they all formed within the same subduction zone. However, these Permian intrusions are currently located up to ~500 km to the east of the Sierra Nevada de Santa Marta and the Central Cordillera (Figure 1), whereas there is a magmatic gap between 415–209 Ma in the Santander Massif (van der Lelij et al., 2016), which is only located 200–150 km east of the Central Cordillera (Figure 1). El Baúl Massif may have been closer to the continental margin before north–eastward movement of the Maracaibo Block during the Cenozoic (Figure 14; Pindell & Dewey, 1982). These translations would place the rocks of El Baúl Massif in a similar palinspastic position as the Permian rocks of the Sierra Nevada de Santa Marta. We suggest that the basement of the Santander Massif was located east of the Permian arc axis (Figure 14), and the poorly studied sedimentary rocks of the Tiburón and Bocas Formations, which overly its basement, may host detritus shed from the arc into its back–arc.

Permian granitoids in Colombia, Ecuador, and Venezuela that intruded during 294–255 Ma, were coeval and share the same geochemical characteristics to those found in the southern North American and western Caribbean plates. Permian intrusive magmatism in the Chiapas Massif, the Xolapa, Acatlán, and Oaxacan Complexes, and the Yavapai Province was not bimodal, alkali–calcic to calcic, mildly metaluminous to peraluminous, magmatic (zircon Th/U > 0.1; Figure 12) and includes components derived from subducted oceanic lithosphere (Figure 8). Hf (zircon) isotopic compositions of Permian intrusions in the Acatlán and Oaxacan Complexes suggest that arc magmatism recycled continental crust (Ortega–Obregón et al., 2014). These observations are consistent with previous suggestions that the Permian intrusions in Laurentia and Gondwana formed within a continental arc above the same east–dipping subduction zone along the western margin of Pangaea (Figure 14; e.g., Centeno–García & Keppie, 1999; Dickinson & Lawton, 2001; Kirsch et al., 2012; Ortega–Obregón et al., 2014; Torres et al., 1999; Ratschbacher et al., 2009; Solari et al., 2001).

Using the same logic, the close geochemical similarities between Permian arc intrusions in southern North America, Colombia, Ecuador, and Venezuela with calc–alkaline Permian intrusions in the Eastern Cordillera of Perú (Figure 8; e.g., Mišković et al., 2009) that are older than ca. 260 Ma suggests

Figure 11. (a) Along strike variations of $^{238}U/^{206}Pb$ dates (apatite, titanite, and rutile; ID–TIMS) and plateau $^{40}Ar/^{39}Ar$ dates (biotite and muscovite) from Triassic lithologies (Cajamarca Complex, Tres Lagunas Granite, Sabanilla Migmatite, and various amphibolites). Bars indicate the range of $^{238}U/^{206}Pb$ dates obtained from grains with radii of ~50 (youngest date) and 100 mm (oldest date). The larger grains yield older dates than the smaller grains supporting the premise that Pb has been lost by thermally activated volume diffusion, and thus the data can be used to extract time(t)–Temperature(T) paths. The grey bar represents the timing of the collision and accretion of the Caribbean Large Igneous Province (CLIP), determined using various low–T thermochronometers, sedimentological and palaeomagnetic evidence (Luzieux et al., 2006; Spikings et al., 2001, 2010; Vallejo et al., 2006). $^{238}U/^{206}Pb$ and $^{40}Ar/^{39}Ar$ dates clearly younger towards the south, with the oldest dates in northern Colombia. Time (t)–Temperature (T) solutions to the apatite $^{238}U/^{206}Pb$ data are shown for **(b)** a Triassic granite of the Cajamarca Complex (10RC43), and **(c)** a Triassic leucosome of the Sabanilla Migmatite (09RC42) of the southern Cordillera Real, and the northern Central Cordillera, respectively (locations shown in Figure 2). Data and t–T models are obtained from Cochrane et al. (2014c) and Spikings et al. (2015). $^{40}Ar/^{39}Ar$ muscovite plateau dates are also shown, with the closure temperature range determined from the diffusion parameters presented in Harrison et al. (2009). The t–T paths are determined using a computed Monte Carlo algorithm constrained by the diffusivity and activation energy of diffusion of Pb in apatite (Cherniak et al., 1991), apatite grain size and $^{238}U/^{206}Pb$ date (data shown in (b). Models are only constrained using low–T thermochronological data (Spikings et al., 2010). The thick blue line yields the best fit between measured and predicted data. The red dashed line has not been computed, and only serves to illustrate heating of a Paleozoic sedimentary protolith during anatexis. APbPRZ: Apatite Lead Partial Retention Zone.

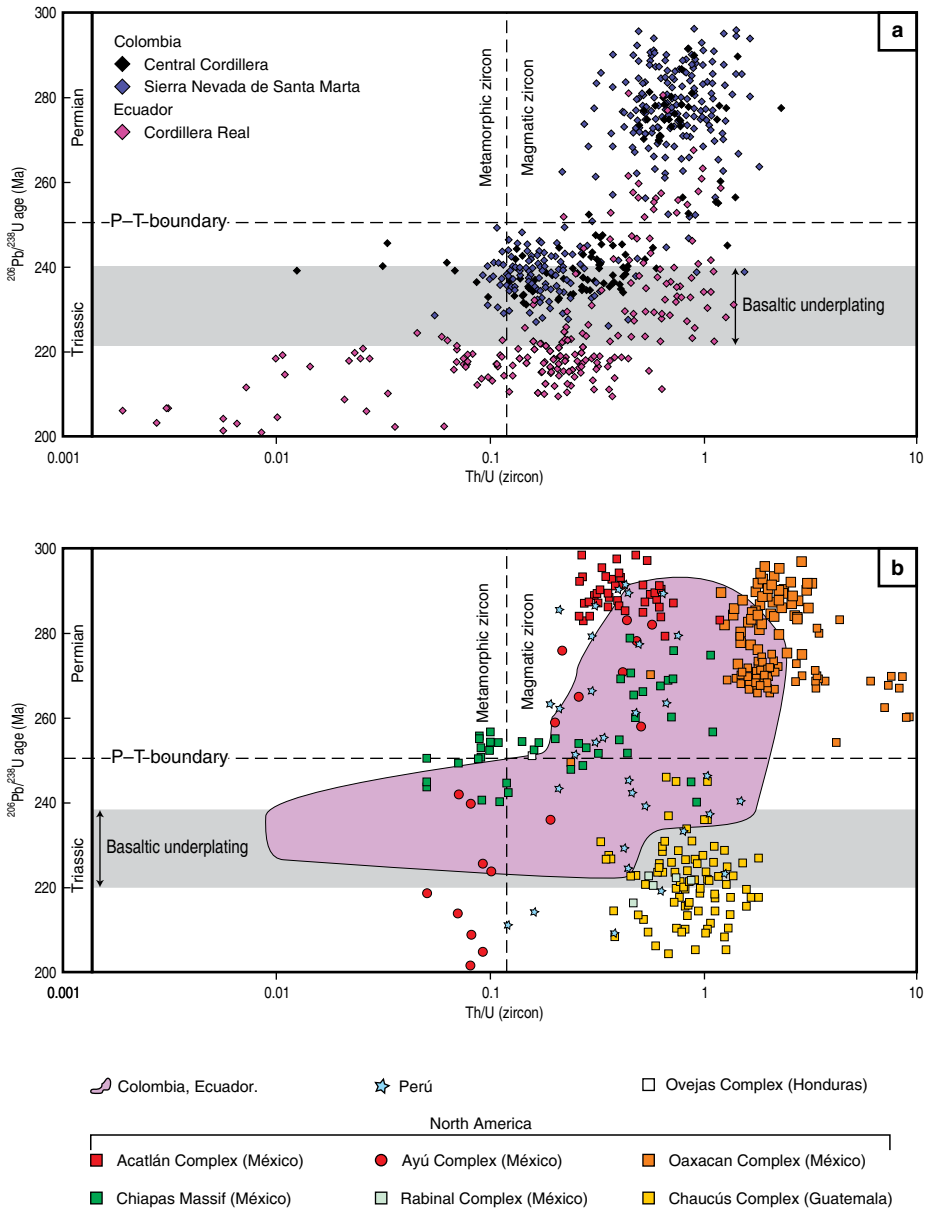

Figure 12. Variations in Th/U ratios with $^{206}Pb/^{238}U$ crystallization age of individual zircons extracted from Permian and Triassic granites and migmatitic leucosomes from **(a)** the Sierra Nevada de Santa Marta, Central Cordillera, and Cordillera Real of Colombia and Ecuador, and **(b)** various regions in the southern North American and western Caribbean plates. The zircon Th/U ratios show a significant reduction in some zircons at ca. 250 Ma in Colombia, Ecuador, the Chiapas Massif (southern Maya Block), the juxtaposing Acatlán and Ayú Complexes (Mixteca Terrane), and the Ovejas Complex (Chortis Block). These are attributed to (i) metamorphic zircon growth during regional metamorphism and crustal thickening (e.g., Weber et al., 2007), and (ii) metamorphic zircon growth, which accompanied anatexis during increased fluid expulsion and geothermal gradients during basaltic underplating (240–223 Ma). Metamorphic and magmatic zircon fields after Hartmann & Santos (2004). Uncertainties of the $^{206}Pb/^{238}U$ ages are ±1 – 2%. Data from Colombia: Cardona et al. (2010a); Cochrane et al. (2014c); Piraquive (2017). Data from Ecuador: Cochrane et al. (2014b), Paul et al. (2018). Other data: Weber et al. (2007; Chiapas Massif), Ratschbacher et al. (2009; Ovejas Complex, Rabinal Complex), Solari et al. (2001, 2011; Chaucús Complex and Oaxacan Complex), Kirsch et al. (2012; Acatlán Complex), Helbig et al. (2012; Ayú Complex), Ortega–Obregón et al. (2014; Oaxacan Complex), Mišković et al. (2009; Perú, Eastern Cordillera).

the arc was geographically extensive and Pacific subduction beneath Pangaea continued towards southern Perú. The shift from a well characterised, calc–alkaline Carboniferous arc in Perú to Permian post–tectonic alkali granites (Mišković et al., 2009) and ultimately Triassic alkaline bimodal intrusions (see below) and volcanic rocks of the Mitu Group is characteristic of lithospheric thinning (e.g., Spikings et al., 2016; Xu et al., 2007). Mišković et al. (2009) suggest that the Permian granitoids of southern

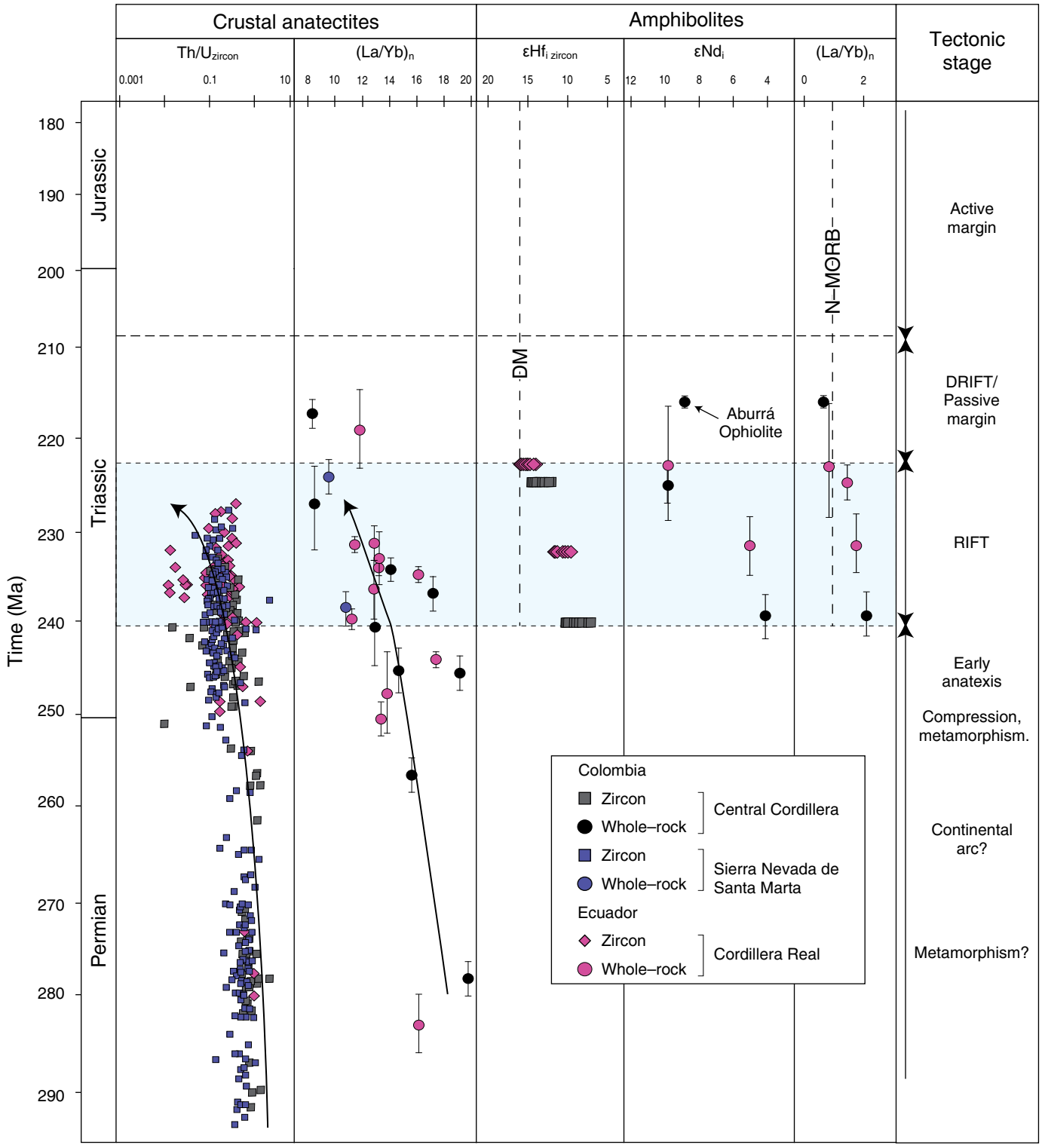

Figure 13. Geochronological and geochemical summary of data from Permian and Triassic granites and leucosomes, tholeiitic basaltic sills and dykes, and the Aburrá Ophiolite. These data define (i) Permian continental arc magmatism, (ii) bimodal magmatism during lithospheric thinning and continental rifting (240–223 Ma), and (iii) a passive margin stage during which oceanic lithosphere was forming (223–209 Ma). Active margin magmatism commences in the Santander Massif at ca. 209 Ma (Spikings et al., 2015; van der Lelij et al., 2016). Regional metamorphism is shown at ca. 275 Ma although this is poorly defined (see 2: 1: 8.1.1). Metamorphism at ca. 250 Ma is obtained from Weber et al. (2007) and Piraquive (2017; see section 8.1.2). Data are from Vinasco et al. (2006), Cochrane et al. (2014b), and Piraquive (2017).

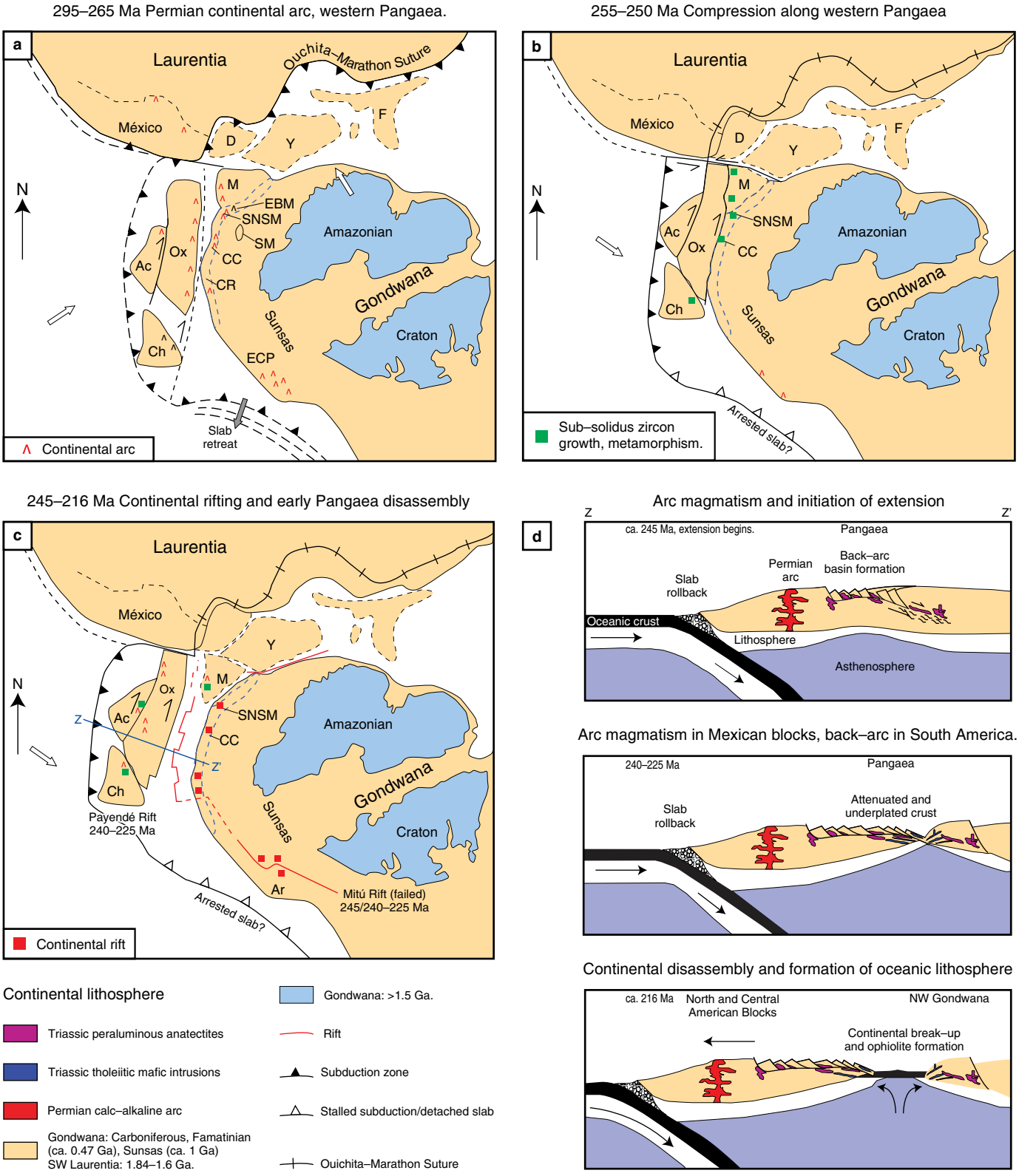

Figure 14. (a–c) Tectonic reconstructions for the Permian and Triassic, modified after Dickinson & Lawton (2001), Elías–Herrera & Ortega–Gutiérrez (2002), and Weber et al. (2007). Africa is not shown. **(d)** Schematic cross sections showing the Triassic rift to drift transition (Payandé Rift), failed rift (Mitu Rift), and early disassembly of Pangaea. Abbreviations: (F) Florida; (D) Delicias; (Y) Yucatán; (M) Maya Block; (EBM) El Baúl Massif; (SNSM) Sierra Nevada de Santa Marta; (SM) Santander Massif; (Ox) Oaxaquia; (CC) Central Cordillera; (Ac) Acatlán Block; (CR) Cordillera Real; (Ch) Chortis Block; (ECP) Eastern Cordillera of Perú.

Perú formed within an extensional regime during extensive slab retreat, which thermally weakened the subducted slab, leading to slab–break–off by ca. 270–260 Ma (Figure 14). Alternatively, orogenic collapse could also be responsible for the switch from a normal magmatic arc to generalised extension, e.g., collapse of the late Paleozoic arc in Chile and Argentina (e.g., Hervé et al., 2014). Rocks of the southern Eastern Cordillera of Perú were deformed by the poorly temporally constrained middle Permian Tardihercynian deformation phase, giving rise to folding and an angular unconformity between Permian – Carboniferous rocks and the overlying Triassic Mitu Group (Laubacher, 1978; Rosas et al., 2007; Spikings et al., 2016).

Any model which includes a Permian arc spanning from North to South America must account for the relatively low volume of Permian arc rocks in Colombia and only a single exposed location in Ecuador, compared to substantial volumes preserved in México and Perú. Most reconstructions (e.g., Dickinson & Lawton, 2001; Elías–Herrera & Ortega–Gutiérrez, 2002) place various Mexican and Central American crustal blocks (Maya, Acatlán–Mixteca, Oaxaquia, Chortis; Figure 14) outboard of the northwestern corner of South America within Pangaea, and therefore it is likely that with the exception of the Inner Santa Marta Metamorphic Belt (Figure 3), a majority of Colombia and Ecuador existed in the Permian back–arc, and most of the Permian arc was displaced northwards during the fragmentation of Pangaea in the Triassic (Spikings et al., 2015). Other blocks, for example the Paraguana Peninsula, El Baúl Massif, and perhaps the Inner Santa Marta Metamorphic Belt were displaced eastwards during the Cenozoic (Pindell & Dewey, 1982).

8.1.2. Latest Permian – Early Triassic Metamorphism

Garnet amphibolites of La Secreta Mylonites of the Inner Santa Marta Metamorphic Belt record prograde metamorphism with peak metamorphic conditions of ~770–830 °C and ~11.5–14 kb (hbl–grt; hbl–plag–qtz), followed by retrogression to 530 °C and 5.5 kb (Piraquive, 2017). Piraquive (2017) identifies sub–solidus metamorphic zircon cores that were coeval with garnet growth at ca. 250 Ma and suggests these date peak metamorphism (Figure 13), while retrogression continued through the Triassic (Spikings et al., 2015). Cardona et al. (2010a) describe kinked plagioclase in mylonitic Permian intrusions (288–264 Ma) of the Sierra Nevada de Santa Marta, which they interpret as a high temperature (>450 °C) deformational event. The same authors interpret amphibole K–Ar dates of ca. 250 Ma (MacDonald & Hurley, 1969) obtained from a gneissic clast located proximal to the mylonites to be the result of a thermal disturbance at ca. 250 Ma, and further suggest that the same thermal event may be responsible for the high–temperature deformation and mylonitisation of the Permian intrusions. The Th/U content of zircons at ca. 250 Ma approaches 0.1 (Figure 12a), corroborating sub–solidus zircon growth and a metamorphic event at that time (Figure 13).

Weber et al. (2007) report concordant zircon U–Pb dates from migmatites of the Chiapas Massif of 254.0 ± 2.3 Ma – 251.8 ± 3.8 (Figures 4d, 5b). These dates are derived from the rims of zircons which yield Th/U ratios <0.1 (Figure 12b), and they are interpreted to be a result of medium pressure–high temperature (MP–HT) metamorphism during compression, and stacking within an orogenic wedge. Similarly, Ratschbacher et al. (2009) also report zircon rims in Permian intrusions at ca. 250–245 Ma from the Chortis Block of Central America, which yield metamorphic Th/U ratios of ~0.04 (Figure 12b). These dates overlap with, and perhaps add credence to suggestions for latest Permian – earliest metamorphism in Colombia (Figure 13). However, quantitative evidence for the precise timing of a high–temperature metamorphic event in Colombia at ca. 250 Ma is weak, and there is a requirement for further studies to directly date deformation and metamorphism during the Permian and earliest Triassic. Weber et al. (2007) attribute metamorphism in the Chiapas Massif to compression that closed marginal basins, previously formed during extension that accompanied Permian arc magmatism (Figures 13, 14). The cause of compression has been attributed to either terrane accretion, subduction of thickened, topographically prominent and buoyant oceanic lithosphere (e.g., Weber et al., 2007), or increased plate coupling during the waning stages of the amalgamation of Pangaea (Cardona et al., 2010a). The collision event post–dates the early amalgamation of Pangaea by ca. 50 Ma, which is recorded along the diachronous Ouachita–Marathon Suture (Figure 14) that had formed by the early Permian.

Geochemical and isotopic evidence from Permian – Triassic intrusions in Perú provides no clear evidence for compression at ca. 250 Ma (Figure 12; Mišković et al., 2009; U/Th zircons > 0.1). However, rocks of the southern Eastern Cordillera of Perú were deformed by the poorly temporally constrained middle Permian Tardihercynian deformation phase, giving rise to folding and an angular unconformity between Permian – Carboniferous rocks and the overlying Triassic Mitu Group (Laubacher, 1978; Rosas et al., 2007; Spikings et al., 2016). Therefore, it is likely that compression may have also affected the Peruvian margin, although this is not clearly expressed in the composition of magmatic rocks, suggesting that compression may have been less intense to the south of Colombia and Ecuador. A southward waning of compression during the Permian would spatially correlate with the location of continental lithosphere outboard of the Triassic margins of Colombian and Ecuadorian crust within South America, and was perhaps lacking outboard of Perú (Figure 14). This supports a hypothesis that compression at ca. 250 Ma was a consequence of the collision of terranes that now form the basement of México and Central

America. Alternatively, varying stress regimes may be a consequence of varied displacement at the ocean–continent plate interface to the north and south of the Huancabamba Deflection.

8.2. Triassic: Rift to Drift Transition and the Early Disassembly of Pangaea

8.2.1. The Magmatic Record

The Triassic crustal anatectites of the Sierra Nevada de Santa Marta and Central Cordillera of Colombia, and the Amotape Complex and Cordillera Real of Ecuador that formed during 240–225 Ma yield lower whole–rock (La/Yb)n, lower zircon Th/U (Figures 12a, 13), and are significantly more peraluminous than the Permian granitoids in Colombia and Ecuador (Figure 6c), the Eastern Cordillera of Perú (Mišković et al., 2009), and the southwestern North American Plate (Figure 8). These corroborate upper continental crust normalised trace element concentrations close to unity (Figure 6g), and are indicative of increased partial melting of pelitic rocks after ca. 240 Ma, forming metamorphic zircon within the anatectites, and perhaps an overall greater volume of magmatism compared to the Permian, which is reflected by a peak in the quantity of dated samples during 240–225 Ma (Figure 4a). This period was characterised by bimodal magmatism (Figures 7a, 8e), and Cochrane et al. (2014a) suggest that mafic underplating elevated the geothermal gradient, driving fluid expulsion from the pelitic protoliths and lowering their solidus.

The trace element content of the Triassic amphibolitised tholeiitic dykes is characteristic of a back–arc basin or MORB setting (Figure 7d), and the progressive trend in isotopic compositions towards the depleted mantle (Figure 13), combined with progressive depletions in incompatible elements during 240–225 Ma (Figure 7g) suggests they were emplaced within a lithosphere that was thinning. Hafnium isotopic compositions in zircons show that mantle derived tholeiites emplaced during 240–232 Ma assimilated isotopically evolved continental crust (Figure 9), whereas there is little evidence of the assimilation of significant crust after 225 Ma, when εHf_i approaches depleted mantle compositions. Pb isotopes in feldspars (Figure 10) also reveal mixing between a highly radiogenic component that is compatible with upper continental crust, with a juvenile source that approaches the depleted mantle and is represented by the mafic end member rocks.

The geographically widespread occurrence of coeval, Triassic tholeiitic, amphibolitised dykes and crustal anatectites within Colombia and Ecuador (Figure 4a) supports an extensional setting, which probably formed within a region of increased heat flow that is characteristic of an attenuated back–arc basin (e.g., Collins & Richards, 2008). Cochrane et al. (2014b), and Spikings et al. (2015, 2016) suggest that the period between 240–225 Ma was dominated by progressive thinning of the continental lithosphere during rifting and the disassembly of western Pangaea (Figure 14c). Mafic underplating and anatexis occurred because of doming and decompression of the asthenosphere during extension (Figure 14d), and heat convection during the intrusion of mafic magmas into the crust. Within Colombia, this interpretation is supported by the identification of rapid extension and subsidence located between the present Central and Eastern Cordilleras, resulting in the deposition of red beds of the Luisa and Payandé Formations, and the Chicalá Member of the Saldaña Formation during the Middle – Late Triassic (Mojica & Kammer, 1995; Mojica & Prinz–Grimm, 2000; Senff, 1995). Within Ecuador, Triassic rifting is supported by (i) the tentatively mapped Triassic Zumba Ophiolite in the southernmost Cordillera Real of Ecuador, although its Triassic age is assumed based on its structural position (Figure 2; Litherland et al., 1994), and (ii) late Middle to Upper Triassic continental and marine volcano–sedimentary rocks of the Piuntza unit (southern Cordillera Real) that were deposited in rift grabens (Figure 2; Litherland et al., 1994). Spikings et al. (2016) refer to this rift as the Payandé Rift (w), which was also used by Senff (1995) to describe the tectonic setting of Triassic, red siliciclastic rocks of the Payandé Formation in northern Colombia.

A majority of crustal anatectites are older than 225 Ma, and the basaltic amphibolites that formed during and after 225 Ma yield N–MORB isotopic and geochemical signatures (Figure 13). Cochrane et al. (2014a) suggest that the continental crust was either extremely thin or absent after 225 Ma (Figure 14d). Correa–Martínez (2007) documents a series of metagabbros, amphibolites, and plagiogranites from the northern Central Cordillera, and utilizes petrological observations, isotopic and geochemical analyses, and field mapping to conclude that they are part of an ophiolitic sequence (the Aburrá Ophiolite; Figure 2) that formed within a back–arc basin. U–Pb dating of magmatic zircons from the plagiogranite yields an age of ca. 216 Ma (Table 1) suggesting that seafloor spreading started between ca. 225 and ca. 216 Ma. The youngest plateau $^{40}Ar/^{39}Ar$ date of 213.7 ± 0.9 Ma (muscovite; Figure 2; Table 1) obtained from an anatectite in Colombia, combined with apatite U–Pb dates of 232–198 Ma (Figure 11) records cooling below ~380 °C as the margin drifted further from the source of elevated heat flow, and possibly exhumation during continued extension. Some regions of the continental margin remained at temperatures that were sufficiently high to form metamorphic zircon rims until ca. 207 Ma (Figures 4d, 12a; Table 1; Cochrane et al., 2014b). The rift and transition to drift occurred over a period of ca. 20–25 my (Figures 13, 14), which is comparable with the duration of other examples of rifting and the transition to a drift phase, including the Lau–Havre–Taupo system (south Pacific; Parson & Wright, 1996), and the west Iberian – Newfoundland conjugate margins (Russell & Whitmarsh, 2003).

Rifting starting at ca. 240 Ma is consistent with the geochronology and geochemistry of bimodal, highly peraluminous granites, alkaline intra–plate basalts, and volcanic tuffs in the central and southern Eastern Cordillera of Perú. Mišković et al. (2009) suggest that decompression melting generated basaltic magmas at the base of the lower crust, resulting in crustal melting during 260–200 Ma, ultimately giving rise to the bimodal Mitu Group within a continental rift. The age of the Mitu Group (245–240 to 220 Ma; Spikings et al., 2016) closely overlaps with the timing of rifting within Colombia and Ecuador. However, unlike the case of Colombia and Ecuador, Spikings et al. (2016) demonstrate that the rift formed in the absence of subduction, either above an arrested slab or a slab that was detached (e.g., Franzese & Spalletti, 2001; Kay, 1993). Alternatively, Noble et al. (1978) and Reitsma (2012) suggested that extension occurred in a back–arc setting, and the Triassic arc was obliterated by Cenozoic tectonic erosion (e.g., Clift & Hartley, 2007). There is no evidence for the formation of Triassic oceanic lithosphere within the Eastern Cordillera of Perú, and the rift foundered during ca. 220–190 Ma, resulting in the deposition of limestones of the Pucará Group during thermal sag (Rosas et al., 2007). Extensive tracts of continental Precambrian – Triassic continental crust, including the Arequipa Terrane (Figure 1), lie outboard of the Mitu Group, and it is likely that the rift failed to advance to a drift phase (Figure 14c). In contrast, no Triassic continental crust is found outboard of the Triassic anatectites within Colombia and Ecuador (Figure 2), and this region advanced to the drift phase. The recent discovery of Triassic xenocrystic zircons in basalt offshore northern Perú (8° S; Romero et al., 2013) suggests this may also be a product of extension of the continental crust. These rocks are exposed along the Outer Shelf High (Romero et al., 2013), and no continental crust has been found to the west, suggesting the Mexican and Central American conjugate margin may have extended into Perú, within Pangaea.

Triassic U–Pb dates obtained from the amphibolites and crustal anatectites from northern Colombia to southernmost Ecuador reveal no trend with latitude (Figure 4d), suggesting that extension and rifting was not diachronous within the northern Andes. Similarly, Spikings et al. (2016) compare U–Pb dates of detrital zircons within the Mitu Group along the strike of the Eastern Cordillera in central and southern Perú, and conclude that the basal strata were coeval everywhere, although Triassic plutons young from central towards southern Perú (Mišković et al., 2009). Rifting along western Pangaea commenced at ca. 240 Ma and affected >2500 km of the Gondwanan margin. Furthermore, Middle to Late Triassic extensional basins are dispersed throughout central and southern Chile, western Argentina (Franzese & Spalletti, 2001), and southern Brazil (Zerfass et al., 2004), suggesting that western Gondwana was placed under tension (e.g., Ramos, 2009) at ca. 240 Ma, culminating in the fragmentation of western Pangaea by ca. 195–180 Ma.

The Pacific margin of northwestern Gondwana remained passive until ca. 209 Ma, after which a prolonged period of latest Triassic – Early Cretaceous magmatism modified the margin of Colombia and Ecuador, and southernmost Perú (Figure 13; Spikings et al., 2015).

8.2.2. Conjugate Margins to Gondwana

Triassic rifting within Colombia and Ecuador is considered to have occurred within a back–arc (Cochrane et al., 2014b; Spikings et al., 2015, 2016). Reconstructions of Pangaea based on Atlantic seafloor magnetic anomalies show that northwestern South America lay close to Laurentia during the Permian and Triassic, and overlapped half of present day México (Dickinson & Lawton, 2001; Pindell & Barrett, 1990). Consequently, it is logical that the rifted margins currently form part of Central America, southern North America, and perhaps parts of the Caribbean Plate. Several lines of evidence suggest that the basement to Mexican and Central American terranes, including the Mixteca Terrane (e.g., the Acatlán and Ayú Complexes), Oaxaquia (including the Oaxacan Complex), the Maya Block (including the Chiapas Massif and Rabinal Complex), and, controversially, the Chortis Block (including the Ovejas Complex) may have been part of Gondwana and were the rifted Triassic conjugate margin to northwestern Gondwana (Figure 14). Other evidence includes (i) Grenville–aged granulite belts with similar Pb isotope signatures (Restrepo–Pace et al., 1997; Ruiz et al., 1999; Weber & Köhler, 1999), (ii) anorthosite complexes (Restrepo–Pace & Cediel, 2010), and (iii) similar Cambrian fauna (Cocks & Torsvik, 2002; Restrepo–Pace & Cediel, 2010).

Triassic igneous rocks are sporadically exposed in (i) the Chaucús Complex (intrusions), (ii) the Chortis Block (Ovejas Complex, zircon inheritance in Eocene intrusions; Figures 5b, 8d), (iii) the Rabinal Complex (intrusions; Maya Block), and (iv) the Ayú Complex (granitic dykes; currently part of the Mixteca Terrane and juxtaposed against the Acatlán Complex). Concordant zircon U–Pb dates from these primary and inherited zircons span between 245–215 Ma, overlapping with the timing of rifting in Colombia and Ecuador. Keppie et al. (2006) present discordant zircon U–Pb dates from migmatitic gneisses of the Francisco Gneiss (northern Guerrero composite terrane, northern México) that span between 216 and 197 Ma, although they interpret these are recording crystallisation at ca. 206 Ma. Their coeval association with mafic amphibolites, combined with intra–plate geochemical characteristics led Keppie et al. (2006) to propose that they formed in a rift located in a continental back–arc. Zircon Th/U values from Triassic zircons in the Chaucús Metamorphic Complex and the Rabinal Complex support an igneous origin (Figure 12b), although zircon Th/U values <0.01 from inherited zircons in the Chortis Block (Ovejas Complex) suggest these may have formed in a sub–solidus,

metamorphic environment (Ratschbacher et al., 2009). Similarly, Th/U (zircon) ratios in the Acatlán Complex and juxtaposed Ayú Complex show a gradual reduction from the Permian to the end of the Triassic (Figure 12). Robust geochemical and isotopic analyses of the Triassic igneous rocks are lacking (e.g., Figure 8), and it is possible that some Triassic rocks formed along an arc axis, whereas others may have formed in the back–arc and resemble the Triassic monzogranites of Colombia and Ecuador. Poorly dated Late Triassic (216–197 Ma) rhyolites and tholeiitic basalts in the Guerrero composite terrane of México are interpreted to have formed in a continental rift (Keppie et al., 2006), and the same authors attribute Upper Triassic rocks of the Oaxaquia Terrane to a back–arc setting. Similarly, Helbig et al. (2012) suggest that Upper Triassic volcanic rocks with E–MORB to MORB characteristics within the Acatlán Complex (Ayú Complex; Figure 5b) formed within a back–arc.

Triassic roll–back of the east–dipping Pacific slab drove widespread extension along most of western Gondwana, resulting in complete rifting of continental crust in the region of northwestern South America. Further south, tensile forces failed to form oceanic lithosphere in Perú (Mitu Rift; Figure 14), western Argentina, and Chile (Cuyo and Ischigualasto–Villa Unión Basins; Spikings et al., 2016), and these regions remain as failed rifts. Perhaps the orthogonal component of roll–back was less severe in these regions, or the continental crust was stronger. The Middle – Late Triassic rifts in Chile and western Argentina, and associated magmatic units are collectively considered to have formed subsequent to slab–detachment, giving rise to intense crustal melting under extensional tectonic conditions during a period of arrested subduction (e.g., Kay et al., 1989; Parada et al., 2007; Spalletti et al., 2008). Consequently, the origin of extension may differ compared to the case of Colombia and Ecuador, where subduction is thought to have continued throughout the Triassic.

9. The Triassic – Jurassic Transition, and the Separation of Pangaea

The magmatic and sedimentary rocks associated with Triassic (240–225 Ma) rifting in Colombia and Ecuador (e.g., Sabanilla Migmatite, Tres Lagunas Granite, and the Cajamarca Complex) are mainly in faulted contact with the younger Late Triassic – Jurassic continental arc, which commenced at ca. 209 Ma in the Santander Massif (Figure 13; Spikings et al., 2015; van der Lelij et al., 2016), and had migrated westwards to the region of the Cordilleras Central and Real by ca. 189 Ma (Spikings et al., 2015). Jurassic extension north of the Huancabamba Deflection (Figure 1) had multiple effects, including (i) trenchward migration of the Jurassic arc (189–145 Ma; Cochrane et al., 2014a; Spikings et al., 2015), (ii) graben formation (e.g., Uribante and Espina grabens; Bartok, 1993), (iii) carbonate (Jaillard et al., 1990; Toussaint & Restrepo, 1994) and red–bed deposition (e.g., La Quinta Formation; van der Lelij et al., 2016), (iv) the extrusion of the Central Atlantic Magmatic Province during 202–201 Ma (e.g., Davies et al., 2017), and (v) the separation of North America, Yucatán and South America at 195 Ma (e.g., Beutel, 2009; Pindell & Kennan, 2009), forming the proto–Caribbean seaway and the central Atlantic Ocean.

The relationship between the driving forces of Triassic extension in northwestern South America, and Jurassic extension which lead to the fragmentation of western Pangaea is unclear because the rift–related Triassic units are persistently faulted against the Jurassic rocks (Figure 2). Rifting commenced in south–eastern North America at ca. 230 Ma (Schlische, 2002), and possibly also within far southern North America (e.g., northern Florida; Beutel, 2009). Magmatic injection in the form of giant dyke swarms (Central Atlantic Magmatic Province) accompanied rifting within North America at 200 ± 2 Ma (Beutel, 2009 and references therein), and South America at 201.6–201.3 Ma (Davies et al., 2017), which coincides with 202 ± 1.8 Ma tuffs at the base of the rift–related, la Quinta Formation of the Mérida Andes, Venezuela (Figure 1; van der Lelij et al., 2016), and oceanic crust started forming between North and South America at ca. 180 Ma. This sequence of events opens the possibility that plate tectonic forces initiated the early break–up of western Pangaea by attenuating its margins and enhancing mantle upwelling (Figure 14d). Prolonged extension may have propagated along pre–existing weak zones that extended into the continental interior (e.g., the South America–Yucatán–North America–Central African Sutures). These zones captured melts derived from the upwelled mantle (e.g., Buiter & Torsvik, 2014) forming a Large Igneous Province, became hot and eventually lead to the formation of a juvenile ocean.

10. The Suspect Tahamí Terrane

The Tahamí Block (Antioquia Terrane sensu Pindell & Kennan, 2009) of northern Colombia (Restrepo & Toussaint, 1982) is fault bounded by the Otú–Pericos and Palestina Faults to the east, the San Jerónimo Fault to the west, and the Ibagué Fault in the south (Figure 1). It is considered by some authors to be a distinct terrane because (i) it is separated from Rodinia–aged (ca. 1 Ga) crust to the east, (ii) it does not expose Jurassic arc rocks, unlike the region to the east, and (iii) Martens et al. (2014) suggest that the Tahamí Terrane is restricted to Triassic ortho– and paragneiss, and that juxtaposed Ordovician rocks (e.g., La Miel Gneiss; Villagómez et al., 2011) define the separate suspect Anacona Terrane. Thus, the basement rocks in this suspect terrane only yield Triassic (Cajamarca Complex; e.g., Cochrane et al., 2014b; Martens et al., 2014) U–Pb dates, which are intruded by the ca. 90 Ma Antioquia Batholith. We suggest these criteria are insufficient to assign a terrane status to the Triassic rocks of the Tahamí

Block, and it is not proven that they are derived from several hundred km to the south, as is advocated in some models (e.g., Kennan & Pindell, 2009). First, Ordovician basement is widespread in the Mérida Andes, Santander Massif, and the Quetame Massif, and Ordovician zircon cores are abundant in Triassic anatectites of the Cajamarca unit. Ordovician crystalline rocks of the Mérida Andes and Santander Massif yield Pb isotopic compositions that are Gondwanan (van der Lelij, 2013), and thus we propose that the Ordovician basement is autochthonous to South America, and extends to the San Jerónimo Fault. Evidence includes the presence of abundant Ordovician zircon cores in zircons extracted from gneisses of the Triassic Cajamarca Complex (Figure 4). Field relationships in the Cordillera Real of Ecuador reveal in–situ anatexis of undifferentiated Devonian metasedimentary rocks, forming the Triassic Sabanilla Migmatite. We interpret the currently faulted juxtaposition of Ordovician and Triassic gneisses in northern Colombia (e.g., Martens et al., 2014) to be a consequence of exhumation of the Ordovician basement during Jurassic – Early Cretaceous extension. The simplest explanation of rock relationships in a W–E traverse across the Central Cordillera and Cordillera Real (juxtaposition of high–pressure/low–temperature (HP/LT) metamorphic rocks, a Cretaceous arc, Paleozoic and Triassic basement, latest Jurassic arc, and Jurassic – Early Triassic arc), is a consequence of Jurassic – Early Cretaceous attenuation of the margin, followed by a switch to compression starting at ca. 120–115 Ma (Spikings et al., 2015). Jurassic intrusive rocks are not found in the Tahamí Block because the Triassic rocks exposed there did not overlie the arc axis at that time (Spikings et al., 2015). Finally, models which place the Jurassic subduction zone outboard of a hypothetical Tahamí Terrane (e.g., Pindell & Kennan, 2009), create a distance between the trench and the Jurassic arc in South America that is too large (Spikings et al., 2015). Consequently, we do not include these rocks as terranes in our reconstruction (Figure 14). Rather, they are considered to be an attenuated part of autochthonous South America.

11. Conclusions

- Variably foliated Permian granites, granodiorites tonalites, and gabbros of the Rovira Complex (Central Cordillera), El Encanto Gneiss (Sierra Nevada de Santa Marta), and the Malacatos Complex (Cordillera Real) are calc–alkaline to calcic, metaluminous to mildly peraluminous continental arc intrusions. Concordant U–Pb dates of magmatic zircons constrain Permian arc magmatism to 288–253 Ma. The arc reworked and assimilated Sunsas (ca. 1 Ga) and Famatinian (Ordovician) continental crust, and is partly composed of S–type granites. The geochemical compositions and crystallisation ages of Permian intrusions in Colombia and Ecuador are extremely similar to (i) intrusions and volcanic rocks in the far southern North American and western Caribbean plates (298–255 Ma), (ii) intrusions in the serranía de Perijá, Paraguaná Peninsula, and El Baúl Massif (Venezuela; 294–272 Ma), and (iii) intrusions and volcanic rocks in the southern Eastern Cordillera of Perú (293–252 Ma). Collectively these are considered to have formed within the same east–dipping subduction system, which consumed oceanic lithosphere of the Pacific Ocean beneath western Pangaea. A majority of the arc is preserved in far northern Colombia (Sierra Nevada de Santa Marta) and conjugate margin blocks that are currently preserved in México and Central America. A majority of Ordovician and older basement in Colombia and Ecuador is interpreted to have resided in the Permian back–arc, while rocks of the Santander Massif were located further east, beyond the magmatic reach of the arc.
- Vinasco et al. (2006) and Piraquive (2017) suggest that a regional metamorphic event affected the Permian intrusions in the Central Cordillera and Sierra Nevada de Santa Marta, respectively, at ca. 278 Ma. We find that this is extremely tentative because evidence for a widespread metamorphic event at that time is lacking, and a majority of zircon growth at ca. 278 Ma occurred in a magmatic environment. Further studies are required to identify a metamorphic event in South American lithosphere, which may have formed in response to the early collisional events that lead to the formation of Pangaea in the earliest Permian.
- The margin of western Pangaea was compressed at ca. 250 Ma, driving regional metamorphism with peak conditions of 770–830 °C and 11.5–14 kb in the Sierra Nevada de Santa Marta of northern Colombia. Metamorphism at ca. 250 Ma has also been observed in the western Maya Block and the Chortis Block (México and Honduras, respectively), where it induced anatexis and perhaps sub–solidus zircon recrystallisation. Compression drove deformation in Perú prior to the onset of rifting at 245–240 Ma, although there is no evidence for regional metamorphism. Compressive forces may have been weaker south of the Huancabamba Deflection, revealing large–scale trench–parallel differences in the prevailing stress regime. Stronger compression and Barrovian metamorphism towards the north may be due to either terrane accretion (e.g., the Chortis Block; Figure 14), or the subduction of thickened and relatively buoyant continental lithosphere. The lack of metamorphism in southern Perú coincides with reconstructions that do not place Mexican and Central American terranes outboard of Perú, supporting a model whereby compression towards the north was driven by terrane accretion.
- Magmatic underplating and anatexis of continental crust throughout 245/240–225 Ma occurred during progressive

thinning of the continental lithosphere over rifting along western Pangaea. Rifting advanced to complete separation of continental crust by ca. 216 Ma, and the formation of oceanic lithosphere between the conjugate margins of northwestern South America and basement terranes of México and Central America. The rifting event is recorded by amphibolitised tholeiitic basaltic dykes and extensive tracts of migmatites and S–type granites within the conjugate margins. These are the Cajamarca Complex and La Secreta Mylonites (Colombia), and the Tres Lagunas Granite, Sabanilla Migmatite, and Moromoro Granite (Ecuador) in northwestern South America. Various Triassic units in the Chaucús Complex, Chortis Block, Maya Block, the Mixteca Terrane (México and Central America), and perhaps in the lower plate of Tertiary metamorphic core complexes in the Guerrero composite terrane formed within the Triassic arc and back–arc. Rifting north of the Huancabamba Deflection was accompanied by subduction, and occurred within a backarc. The rift axis propagated southwards, and extension is recorded along western Perú (the Mitu Aulacogen), western Argentina, Chile, and southern Brazil. Rifting along northwestern South America started as a back–arc basin to a Permian arc, and represents the early break–up of western Pangaea, leading to the separation of North and South America by ca. 180 Ma.

The relationship between Triassic plate margin extension and the final fragmentation of Pangaea is unclear. However, the sequence of events: Plate margin rifting during ca. 245–220 Ma, the extrusion of a Large Igneous Province at ca. 201 Ma, and the opening of the proto–Caribbean seaway and central Atlantic at ca. 195 Ma opens the possibility that plate tectonic forces initiated the early break–up of Pangaea by attenuating its margins and enhancing mantle upwelling. Prolonged extension may have propagated along pre–existing weak zones that extended into the continental interior (e.g., the South America–Yucatán–North America–Central African Sutures). These zones captured melts derived from the upwelled mantle (e.g., Buiter & Torsvik, 2014) forming the Central Atlantic Magmatic Province, became hot and weak and eventually lead to the formation of a juvenile ocean.

We suggest that there is very little evidence for the existence of the allochthonous continental Tahamí Terrane, which is considered by some authors to have been outboard of northwestern South America during the Jurassic – Early Cretaceous. Triassic zircon rims around Ordovician zircon cores, combined with field relationships that reveal melting of Paleozoic basement rocks, forming the Triassic anatectites are evidence that Triassic rocks of the Tahamí Block are melts of Ordovician basement. Ordovician basement can be traced eastwards to the Santander Massif and Mérida Andes, where it yields Pb isotope signatures that are Gondwanan. We conclude that the rocks of the Tahamí Block are autochthonous.

Acknowledgments

We thank Ecopetrol S.A., Andrés MORA, Andreas KAMMER, Luis Carlos MANTILLA, Agustín CARDONA, Jaime CORREDOR, Jaime CASTELLANOS, Wilson CASALLAS, Luis QUIROZ, and Alejandro BELTRÁN for their assistance during field work in Colombia. Cristian VALLEJO, Bernardo BEATE, Arturo EGÜEZ, Etienne JAILLARD, Alfredo BUITRON, Byron PELICITA, and Luis LOPEZ are thanked for their assistance in the field in the cordilleras of Ecuador. The manuscript benefited from detailed discussions with Alejandro PIRAQUIVE about the Sierra Nevada de Santa Marta. We thank Victor RAMOS and Bodo WEBER for helpful and thorough reviews, which improved the manuscript.

References

Arvizu, H.E., Iriondo, A., Izaguirre, A., Chávez–Cabello, G., Kamenov, G.D., Solís–Pichardo, G., Foster, D.A. & Lozano–Santa Cruz, R. 2009. Rocas graníticas pérmicas en la Sierra Pinta, NW de Sonora, México: Magmatismo de subducción asociado al inicio del margen continental activo del SW de Norteamérica. Revista Mexicana de Ciencias Geológicas, 26(3): 709–728.

Aspden, J.A. & Litherland, M. 1992. The geology and Mesozoic collisional history of the Cordillera Real, Ecuador. Tectonophysics, 205(1–3): 187–204. https://doi.org/10.1016/0040-1951(92)90426-7

Aspden, J.A. & McCourt, W.J. 1986. Mesozoic oceanic terrane in the central Andes of Colombia. Geology, 14(5): 415–418. https://doi.org/10.1130/0091-7613(1986)14<415:MOTITC>2.0.CO;2

Aspden, J.A., McCourt, W.J. & Brook, M. 1987. Geometrical control of subduction–related magmatism: The Mesozoic and Cenozoic plutonic history of western Colombia. Journal of the Geological Society, 144(6): 893–905. https://doi.org/10.1144/gsjgs.144.6.0893

Aspden, J.A., Bonilla, W. & Duque, P. 1995. The El Oro Metamorphic Complex, Ecuador: Geology and economic mineral deposits. British Geological Survey, Overseas Geology and Mineral Resources 67, 63 p. Nottingham, United Kingdom.

Bahlburg, H., Vervoort, J.D., Du Frane, S.A., Bock, B., Augustsson, C. & Reimann, C. 2009. Timing of crust formation and recycling in accretionary orogens: Insights learned from the western margin of South America. Earth–Science Reviews, 97(1–4): 215–241. https://doi.org/10.1016/j.earscirev.2009.10.006

Barredo, S., Chemale, F., Marsicano, C., Ávila, J.N., Ottone, E.G. & Ramos, V.A. 2012. Tectono–sequence stratigraphy and U–Pb zircon ages of the Rincón Blanco depocenter, northern Cuyo

Rift, Argentina. Gondwana Research, 21(2–3): 624–636. https://doi.org/10.1016/j.gr.2011.05.016

Bartok, P. 1993. Prebreakup geology of the Gulf of Mexico–Caribbean: Its relation to Triassic and Jurassic rift systems of the region. Tectonics, 12(2): 441–459. https://doi.org/10.1029/92TC01002

Batchelor, R.A. & Bowden, P. 1985. Petrogenetic interpretation of granitoid rock series using multicationic parameters. Chemical Geology, 48(1–4): 43–55. https://doi.org/10.1016/0009-2541(85)90034-8

Bayona, G., Rapalini, A. & Costanzo–Álvarez, V. 2006. Paleomagnetism in Mesozoic rocks of the northern Andes and its implications in Mesozoic tectonics of northwestern South America. Earth, Planets and Space, 58(10): 1255–1272. https://doi.org/10.1186/BF03352621

Bayona, G., Jiménez, G., Silva, C., Cardona, A., Montes, C., Roncancio, J. & Cordani, U. 2010. Paleomagnetic data and K–Ar ages from Mesozoic units of the Santa Marta Massif: A preliminary interpretation for block rotation and translations. Journal of South American Earth Sciences, 29(4): 817–831. https://doi.org/10.1016/j.jsames.2009.10.005

Beutel, E.K. 2009. Magmatic rifting of Pangaea linked to onset of South American Plate motion. Tectonophysics, 468(1–4): 149–157. https://doi.org/10.1016/j.tecto.2008.06.019

Bouvier, A., Vervoort, J.D. & Patchett, P.J. 2008. The Lu–Hf and Sm–Nd isotopic composition of CHUR: Constraints from unequilibrated chondrites and implications for the bulk composition of terrestrial planets. Earth and Planetary Science Letters, 273(1–2): 48–57. https://doi.org/10.1016/j.epsl.2008.06.010

Buiter, S.J.H. & Torsvik, T.H. 2014. A review of Wilson cycle plate margins: A role for mantle plumes in continental break–up along sutures? Gondwana Research, 26(2): 627–653. https://doi.org/10.1016/j.gr.2014.02.007

Bustamante, A., Juliani, C., Essene, E.J., Hall, C.M. & Hyppolito, T. 2012. Geochemical constraints on blueschist– and amphibolite–facies rocks of the Central Cordillera of Colombia: The Andean Barragán region. International Geology Review, 54(9): 1013–1030. https://doi.org/10.1080/00206814.2011.594226

Bustamante, C., Archanjo, C.J., Cardona, A., Bustamante, A. & Valencia, V.A. 2017. U–Pb ages and Hf isotopes in zircons from parautochthonous Mesozoic terranes in the western margin of Pangea: Implications for the terrane configurations in the northern Andes. The Journal of Geology, 125(5): 487–500. https://doi.org/10.1086/693014

Cardona, A., Cordani, U. & Sánchez, A. 2007. Metamorphic, geochronological and geochemical constraints from the pre–Permian basement of the eastern Peruvian Andes (10° S): A Paleozoic extensional–accretionary orogen? 20th Colloquium on Latin American Earth Sciences, p. 29–30. Kiel, Germany.

Cardona, A., Valencia, V., Garzón, A., Montes, C., Ojeda, G., Ruiz, J. & Weber, M. 2010a. Permian to Triassic I to S–type magmatic switch in the northeast Sierra Nevada de Santa Marta and adjacent regions, Colombian Caribbean: Tectonic setting and implications within Pangea paleogeography. Journal of South American Earth Sciences, 29(4): 772–783. https://doi.org/10.1016/j.jsames.2009.12.005

Cardona, A., Valencia, V., Bustamante, C., García–Casco, A., Ojeda, G., Ruiz, J., Saldarriaga, M. & Weber, M. 2010b. Tectonomagmatic setting and provenance of the Santa Marta Schists, northern Colombia: Insights on the growth and approach of Cretaceous Caribbean oceanic terranes to the South American continent. Journal of South American Earth Sciences, 29(4): 784–804. https://doi.org/10.1016/j.jsames.2009.08.012

Centeno–García, E. & Keppie, J.D. 1999. Latest Paleozoic – early Mesozoic structures in the central Oaxaca Terrane of southern Mexico: Deformation near a triple junction. Tectonophysics, 301(3–4): 231–242. https://doi.org/10.1016/S0040-1951(98)00213-3

Chappell, B.W. & White, A.J.R. 1974. Two contrasting granite types. Pacific Geology, 8: 173–174.

Charrier, R., Pinto, L. & Rodríguez, M.P. 2007. Tectonostratigraphic evolution of the Andean Orogen in Chile. In: Moreno, T. & Gibbons, W. (editors), The geology of Chile. The Geological Society, p. 21–114. London. https://doi.org/10.1144/GOCH.3

Cherniak, D.J., Lanford, W.A. & Ryerson, F.J. 1991. Lead diffusion in apatite and zircon using ion implantation and Rutherford backscattering techniques. Geochimica et Cosmochimica Acta, 55(6): 1663–1673. https://doi.org/10.1016/0016-7037(91)90137-T

Chew, D.M., Schaltegger, U., Košler, J., Whitehouse, M.J., Gutjahr, M., Spikings, R. & Mišković, A. 2007. U–Pb geochronologic evidence for the evolution of the Gondwanan margin of north–central Andes. Geological Society of America Bulletin, 119(5–6): 697–711. https://doi.org/10.1130/B26080.1

Chew, D.M., Magna, T., Kirkland, C.L., Mišković, A., Cardona, A., Spikings, R. & Schaltegger, U. 2008. Detrital zircon fingerprint of the proto–Andes: Evidence for a Neoproterozoic active margin? Precambrian Research, 167(1–2): 186–200. https://doi.org/10.1016/j.precamres.2008.08.002

Clift, P.D. & Hartley, A.J. 2007. Slow rates of subduction erosion and coastal underplating along the Andean margin of Chile and Peru. Geology, 35(6): 503–506. https://doi.org/10.1130/G23584A.1

Cochrane, R. 2013. U–Pb thermochronology, geochronology and geochemistry of NW South America: Rift to drift transition, active margin dynamics and implications for the volume balance of continents. Doctoral thesis, University of Geneva, 191 p. Geneva, Switzerland. https://doi.org/10.13097/archive-ouverte/unige:30029

Cochrane, R., Spikings, R., Gerdes, A., Winkler, W., Ulianov, A., Mora, A. & Chiaradia, M. 2014a. Distinguishing between in–situ and accretionary growth of continents along active margins. Lithos, 202–203: 382–394. https://doi.org/10.1016/j.lithos.2014.05.031

Cochrane, R., Spikings, R., Gerdes, A., Ulianov, A., Mora, A., Villagómez, D., Putlitz, B. & Chiaradia, M. 2014b. Permo–Triassic anatexis, continental rifting and the disassembly of western Pangaea. Lithos, 190–191: 383–402. https://doi.org/10.1016/j.lithos.2013.12.020

Cochrane, R., Spikings, R., Chew, D., Wotzlaw, J.F., Chiaradia, M., Tyrrell, S., Schaltegger, U. & van der Lelij, R. 2014c. High temperature (>350 °C) thermochronology and mechanisms of Pb loss in apatite. Geochimica et Cosmochimica Acta, 127: 39–56. https://doi.org/10.1016/j.gca.2013.11.028

Cocks, L.R.M. & Torsvik, T.H. 2002. Earth geography from 500 to 400 million years ago: A faunal and palaeomagnetic review. Journal of the Geological Society, 159(6): 631–644. https://doi.org/10.1144/0016-764901-118

Collins, W.J. & Richards, S.W. 2008. Geodynamic significance of S–type granites in circum–Pacific orogens. Geology, 36(7): 559–562. https://doi.org/10.1130/G24658A.1

Collins, W.J., Belousova, E.A., Kemp, A.I.S. & Murphy, J.B. 2011. Two contrasting Phanerozoic orogenic systems revealed by hafnium isotope data. Nature Geoscience, 4: 333–337. https://doi.org/10.1038/NGEO1127

Colmenares, F.H., Mesa, A.M., Roncancio, J.H., Arciniegas, E.G., Silva, C.A., Romero, A.J., Pedraza, P.E., Alvarado, S.I., Romero, O.A., Vargas, A.F., Santamaría, J.C. & Cardona, A. 2007a. Geologic map of the Sierra Nevada de Santa Marta. Scale 1:200 000. Ingeominas–Invemar–Ecopetrol–ICP–Geosearch Ltda. Bogotá.

Colmenares, F.H., Mesa, A.M., Roncancio, J.H., Arciniegas, E.G., Pedraza, P.E., Cardona, A., Romero, A.J., Silva, C.A., Alvarado, S.I., Romero, O.A. & Vargas, A.F. 2007b. Geología de las planchas 11, 12, 13, 14, 18, 19, 20, 21, 25, 26, 27, 33, 34 y 40. Proyecto: Evolución geohistórica de la Sierra Nevada de Santa Marta. Invemar–Ingeominas–ICP–Ecopetrol–Geosearch Ltda., 401 p. Bogotá.

Colony, R.J. & Sinclair, J.H. 1932. Metamorphic and igneous rocks of eastern Ecuador. Annals of the New York Academy of Sciences, 34(1): 1–53. https://doi.org/10.1111/j.1749-6632.1932.tb56973.x

Cordani, U.G., Brito–Neves, B.B. & D'Agrella, M.S. 2003. From Rodinia to Gondwana: A review of the available evidence from South America. Gondwana Research, 6(2): 275–283. https://doi.org/10.1016/S1342-937X(05)70976-X

Correa–Martínez, A.M. 2007. Petrogênese e evolução do Ofiolito de Aburrá, Cordilhera Central dos Andes colombianos. Doctoral thesis, Universidade de Brasília, 204 p. Brasilia.

Dasch, L.E. 1982. U–Pb geochronology of the Sierra de Perijá, Venezuela. Master thesis, Case Western Reserve University, 183 p. Cleveland, USA.

Davies, J.H.F.L., Marzoli, A., Bertrand, H., Youbi, N., Ernesto, M. & Schaltegger, U. 2017. End–Triassic mass extinction started by intrusive CAMP activity. Nature Communications, 8(15996): 1–8. https://doi.org/10.1038/ncomms15596

Dickinson, W.R. & Lawton, T.F. 2001. Carboniferous to Cretaceous assembly and fragmentation of Mexico. Geological Society of America Bulletin, 113(9): 1142–1160. https://doi.org/10.1130/0016-7606(2001)113<1142:CTCAAF>2.0.CO;2

Ducea, M.N., Gehrels, G.E., Shoemaker, S., Ruiz, J. & Valencia, V.A. 2004. Geologic evolution of the Xolapa Complex, southern Mexico: Evidence from U–Pb zircon geochronology. Geological Society of America Bulletin, 116(7–8): 1016–1025. https://doi.org/10.1130/B25467.1

Elías–Herrera, M. & Ortega–Gutiérrez, F. 2002. Caltepec Fault zone: An early Permian dextral transpressional boundary between the Proterozoic Oaxacan and Paleozoic Acatlán Complexes, southern Mexico, and regional tectonic implications. Tectonics, 21(3): 4-1–4-18. https://doi.org/10.1029/2000TC001278

Feininger, T., Barrero, D. & Castro, N. 1972. Geología de parte de los departamentos de Antioquia y Caldas (sub–zona II–B). Boletín Geológico, 20(2): 1–173.

Franzese, J.R. & Spalletti, L.A. 2001. Late Triassic – Early Jurassic continental extension in southwestern Gondwana: Tectonic segmentation and pre–break–up rifting. Journal of South American Earth Sciences, 14(3): 257–270. https://doi.org/10.1016/S0895-9811(01)00029-3

Frost, B.R., Barnes, C.G., Collins, W.J., Arculus, R.J., Ellis, D.J. & Frost, C.D. 2001. A geochemical classification for granitic rocks. Journal of Petrology, 42(11): 2033–2048. https://doi.org/10.1093/petrology/42.11.2033

Gerdes, A.G., Montero, P.M., Bea, F.B., Fershater, G.F., Borodina, N.B., Osipova, T.O. & Shardakova, G.S. 2002. Peraluminous granites frequently with mantle–like isotope compositions: The continental–type Murzinka and Dzhabyk Batholiths of the eastern Urals. International Journal of Earth Sciences, 91(1): 3–19. https://doi.org/10.1007/s005310100195

Gómez, J., Nivia, Á., Montes, N.E., Jiménez, D.M., Tejada, M.L., Sepúlveda, M.J., Osorio, J.A., Gaona, T., Diederix, H., Uribe, H. & Mora, M., compilers. 2007. Geological Map of Colombia 2007. Scale 1:1 000 000. Ingeominas, 2 sheets. Bogotá.

González, H. 1980. Geología de las planchas 167 Sonsón y 187 Salamina. Scale 1:100 000. Ingeominas, Internal report 1760, 262 p. Medellín.

Hall, R.B., Álvarez, J. & Rico, H. 1972. Geología de parte de los departamentos de Antioquia y Caldas (sub–zona II–A). Boletín Geológico, 20(1): 1–85.

Harris, C., Faure, K., Diamond, R.E. & Scheepers, R. 1997. Oxygen and hydrogen isotope geochemistry of S– and I–type granitoids: The Cape Granite Suite, South Africa. Chemical Geology, 143(1–2): 95–114. https://doi.org/10.1016/S0009-2541(97)00103-4

Harrison, T.M., Célérier, J., Aikman, A.B., Hermann, J. & Heizler, M.T. 2009. Diffusion of ^{40}Ar in muscovite. Geochimica et Cosmochimica Acta, 73(4): 1039–1051. https://doi.org/10.1016/j.gca.2008.09.038

Hartmann, L.A. & Santos, J.O.S. 2004. Predominance of high Th/U, magmatic zircon in Brazilian Shield sandstones. Geology, 32(1): 73–76. https://doi.org/10.1130/G20007.1

Hastie, A.R., Kerr, A.C., Pearce, J.A. & Mitchell, S.F. 2007. Classification of altered volcanic island arc rocks using immobile trace elements: Development of the Th–Co discrimination diagram. Journal of Petrology, 48(12): 2341–2357. https://doi.org/10.1093/petrology/egm062

Hatcher, R.D. 2002. Alleghanian (Appalachian) Orogeny, a product of zipper tectonics: Rotational transpressive continent–continent collision and closing of ancient oceans along irregular margins. In: Martínez, J.R., Hatcher, R.D., Arenas, R. & Díaz–García, F. (editors), Variscan–Appalachian dynamics: The building of the late Paleozoic basement. Geological Society of America, Special Paper 364, p. 199–208. https://doi.org/10.1130/0-8137-2364-7.199

Helbig, M., Keppie, J.D., Murphy, J.B. & Solari, L.A. 2012. U–Pb geochronological constraints on the Triassic – Jurassic Ayú Complex, southern Mexico: Derivation from the western margin of Pangea–A. Gondwana Research, 22(3–4): 910–927. https://doi.org/10.1016/j.gr.2012.03.004

Hervé, F., Fanning, C.M., Calderón, M. & Mpodozis, C. 2014. Early Permian to Late Triassic batholiths of the Chilean Frontal Cordillera (28°–31° S): SHRIMP U–Pb zircon ages and Lu–Hf and O isotope systematics. Lithos, 184–187: 436–446. https://doi.org/10.1016/j.lithos.2013.10.018

Horton, B.K., Saylor, J.E., Nie, J., Mora, A., Parra, M., Reyes–Harker, A. & Stockli, D.F. 2010. Linking sedimentation in the northern Andes to basement configuration, Mesozoic extension, and Cenozoic shortening: Evidence from detrital zircon U–Pb ages, Eastern Cordillera, Colombia. Geological Society of America Bulletin, 122(9–10): 1423–1442. https://doi.org/10.1130/B30118.1

Jaillard, E., Soler, P., Carlier, G. & Mourier, T. 1990. Geodynamic evolution of the northern and central Andes during early to middle Mesozoic times: A Tethyan model. Journal of the Geological Society, 147(6): 1009–1022. https://doi.org/10.1144/gsjgs.147.6.1009

Jaillard, E., Sempere, T., Soler, P., Carlier, G. & Marocco, R. 1995. The role of Tethys in the evolution of the northern Andes between late Permian and late Eocene times. In: Nairn, A.E.M., Ricou, L.E., Vrielynck, B., Dercourt, J., (editors), The ocean basins and margins: The Tethys Ocean. Springer Science+Business Media, p. 463–492. New York. https://doi.org/10.1007/978-1-4899-1558-0_15

John, T., Scherer, E.E., Schenk, V., Herms, P., Halama, R. & Garbe–Schönberg, D. 2010. Subducted seamounts in an eclogite–facies ophiolite sequence: The Andean Raspas Complex, SW Ecuador. Contributions to Mineralogy and Petrology, 159(2): 265–284. https://doi.org/10.1007/s00410-009-0427-0

Kay, S.M. 1993. Late Paleozoic tectonics in southern South America: A global perspective. Douzième Congrés International de la Stratigraphie et Géologie du Carbonifére et Permien. Comptes Rendus, I, p. 109–122.

Kay, S.M., Ramos, V.A., Mpodozis, C. & Sruoga, P. 1989. Late Paleozoic to Jurassic silicic magmatism at the Gondwana margin: Analogy to the middle Proterozoic in North America? Geology, 17(4): 324–328. https://doi.org/10.1130/0091-7613(1989)017<0324:LPTJSM>2.3.CO;2

Kennan, L. & Pindell, J.L. 2009. Dextral shear, terrane accretion and basin formation in the northern Andes: Best explained by interaction with a Pacific–derived Caribbean Plate? In: James, K.H., Lorente, M.A. & Pindell, J.L. (editors), The origin and evolution of the Caribbean Plate. Geological Society of London, Special Publication 328, p. 487–531. https://doi.org/10.1144/SP328.20

Keppie, J.D., Sandberg, C.A., Miller, B.V., Sánchez–Zavala, J.L., Nance, R.D. & Poole, F.G. 2004. Implications of latest Pennsylvanian to middle Permian paleontological and U–Pb SHRIMP data from the Tecomate Formation to re–dating tectonothermal events in the Acatlán Complex, southern Mexico. International Geology Review, 46(8): 745–753. https://doi.org/10.2747/0020-6814.46.8.745

Keppie, J.D., Dostal, J., Miller, B.V., Ortega–Rivera, A., Roldán–Quintana, J. & Lee, J.W.K. 2006. Geochronology and geochemistry of the Francisco Gneiss: Triassic continental rift tholeiites on the Mexican margin of Pangea metamorphosed and exhumed in a Tertiary core complex. International Geology Reviews, 48(1): 1–16. https://doi.org/10.2747/0020-6814.48.1.1

Kerr, A.C., Marriner, G.F., Tarney, J., Nivia, Á., Saunders, A.D., Thirlwall, M.F. & Sinton, C.W. 1997. Cretaceous basaltic terranes in western Colombia: Elemental, chronological and Sr–Nd isotopic constraints on petrogenesis. Journal of Petrology, 38(6): 677–702. https://doi.org/10.1093/petrology/38.6.677

Kerr, A.C., Aspden, J.A., Tarney, J. & Pilatasig, L.F. 2002. The nature and provenance of accreted oceanic terranes in western Ecuador: Geochemical and tectonic constraints. Journal of the Geological Society, 159(5): 577–594. https://doi.org/10.1144/0016-764901-151

Kirsch, M., Keppie, J.D., Murphy, J.B. & Solari, L.A. 2012. Permian – Carboniferous arc magmatism and basin evolution along the western margin of Pangea: Geochemical and geochronological evidence from the eastern Acatlán Complex, southern Mexico. Geological Society of America Bulletin, 124(9–10): 1607–1628. https://doi.org/10.1130/B30649.1

Laubacher, G. 1978. Géologie des Andes Péruviennes. Géologie de la Cordillère Orientale et de l'Altiplano au nord et nord–ouest du lac Titicaca, Pérou. ORSTOM, 217 p. Paris.

Laya, J.C. & Tucker, M.E. 2012. Facies analysis and depositional environments of Permian carbonates of the Venezuelan Andes: Palaeogeographic implications for northern Gondwana. Palaeogeography, Palaeoclimatology, Palaeoecology, 331–332: 1–26. https://doi.org/10.1016/j.palaeo.2012.02.011

Litherland, M., Aspden, J.A. & Jemielita, R.A. 1994. The metamorphic belts of Ecuador. Overseas Memoir of the British Geological Survey 11, 147 p. Nottingham, England.

Luppo, T., López de Luchi, M.G., Rapalini, A.E., Martínez–Dopico, C.I. & Fanning, C.M. 2018. Geochronologic evidence of a large magmatic province in northern Patagonia encompassing the Permian – Triassic boundary. Journal of South American Earth Sciences, 82: 346–355. https://doi.org/10.1016/j.jsames.2018.01.003

Luzieux, L.D.A., Heller, F., Spikings, R., Vallejo, C.F. & Winkler, W. 2006. Origin and Cretaceous tectonic history of the coastal Ecuadorian forearc between 1° N and 3° S: Paleomagnetic, radiometric and fossil evidence. Earth and Planetary Science Letters, 249(3–4): 400–414. https://doi.org/10.1016/j.epsl.2006.07.008

MacDonald, W.D. & Hurley, P.M. 1969. Precambrian gneisses from northern Colombia, South America. Geological Society of America Bulletin, 80(9): 1867–1872. https://doi.org/10.1130/0016-7606(1969)80[1867:PGFNCS]2.0.CO;2

Maksaev, V., Munizaga, F. & Tassinari, C. 2014. Timing of magmatism of the paleo–Pacific border of Gondwana: U–Pb geochronology of late Paleozoic to early Mesozoic igneous rocks of the north Chilean Andes between 20° and 31° S. Andean Geology, 41(3): 447–506. https://doi.org/10.5027/andgeoV41n3-a01

Maniar, P.D. & Piccoli, P.M. 1989. Tectonic discrimination of granitoids. Geological Society of America Bulletin, 101(5): 635–643. https://doi.org/10.1130/0016-7606(1989)101<0635:TDOG>2.3.CO;2

Martens, U., Restrepo, J.J., Ordóñez–Carmona, O. & Correa–Martínez, A.M. 2014. The Tahamí and Anacona Terranes of the Colombian Andes: Missing links between South American and Mexican Gondwana margins. The Journal of Geology, 122(5): 507–530. https://doi.org/10.1086/677177

Martínez, R.N., Sereno, P.C., Alcober, O.A., Colombi, C.E., Renne, P.R., Montañez, I.P. & Currie, B.S. 2011. A basal dinosaur from the dawn of the dinosaur era in southwestern Pangaea. Science, 331(6014): 206–210. https://doi.org/10.1126/science.1198467

Martin–Gombojav, N. & Winkler, W. 2008. Recycling of Proterozoic crust in the Andean Amazon foreland of Ecuador: Implications for orogenic development of the northern Andes. Terra Nova, 20(1): 22–31. https://doi.org/10.1111/j.1365-3121.2007.00782.x

Maya, M. & González, H. 1995. Unidades litodémicas en la cordillera Central de Colombia. Boletín Geológico, 35(2–3): 43–57.

McCourt, W.J., Aspden, J.A. & Brook, M. 1984. New geological and geochronological data from the Colombian Andes: Continental growth by multiple accretion. Journal of the Geological Society, 141(5): 831–845. https://doi.org/10.1144/gsjgs.141.5.0831

Mégard, F. 1978. Etude géologique des Andes du Pérou central. ORSTOM, 310 p. Paris.

Mišković, A. & Schaltegger, U. 2009. Crustal growth along a non–collisional cratonic margin: A Lu–Hf isotopic survey of the eastern cordilleran granitoids of Peru. Earth and Planetary Science Letters, 279(3–4): 303–315. https://doi.org/10.1016/j.epsl.2009.01.002

Mišković, A., Spikings, R.A., Chew, D.M., Košler, J., Ulianov, A. & Schaltegger, U. 2009. Tectonomagmatic evolution of western Amazonia: Geochemical characterization and zircon U–Pb geochronologic constraints from the Peruvian eastern cordilleran granitoids. Geological Society of America Bulletin, 121(9–10): 1298–1324. https://doi.org/10.1130/B26488.1

Mitouard, P., Kissel, C. & Laj, C. 1990. Post–Oligocene rotations in southern Ecuador and northern Peru and the formation of the Huancabamba Deflection in the Andean Cordillera. Earth and Planetary Science Letters, 98(3–4): 329–339. https://doi.org/10.1016/0012-821X(90)90035-V

Mojica, J. & Kammer, A. 1995. Eventos jurásicos en Colombia. Geología Colombiana, 19: 165–172.

Mojica, J. & Prinz–Grimm, P. 2000. La fauna de amonitas del Triásico Tardío en el Miembro Chicalá (parte baja de la Formación Saldaña) en Payandé, Tolima, Colombia. Geología Colombiana, 25: 13–23.

Montes, C., Guzman, G., Bayona, G., Cardona, A., Valencia, V. & Jaramillo, C. 2010. Clockwise rotation of the Santa Marta Massif and simultaneous Paleogene to Neogene deformation of the Plato–San Jorge and Cesar–Ranchería Basins. Journal of South American Earth Sciences, 29(4): 832–848. https://doi.org/10.1016/j.jsames.2009.07.010

Nivia, Á., Marriner, G.F., Kerr, A.C. & Tarney, J. 2006. The Quebradagrande Complex: A Lower Cretaceous ensialic marginal basin in the Central Cordillera of the Colombian Andes. Journal of South American Earth Sciences, 21(4): 423–436. https://doi.org/10.1016/j.jsames.2006.07.002

Noble, D.C., Silberman, M.L., Megard, F. & Bowman, H.R. 1978. Comendite (peralkaline rhyolite) and basalt in the Mitu Group, Peru: Evidence of Permian – Triassic lithospheric extension in the central Andes. U.S. Geological Survey Journal of Research, 6(4): 453–457.

Noble, S.R., Aspden, J.A. & Jemielita, R. 1997. Northern Andean crustal evolution: New U–Pb geochronological constraints from Ecuador. Geological Society of America Bulletin, 109(7): 789–798. https://doi.org/10.1130/0016-7606(1997)109<0789:NACENU>2.3.CO;2

Omarini, R.H., Sureda, R.J., Götze, H.J., Seilacher, A. & Pflüger, F. 1999. Puncoviscana folded belt in northwestern Argentina: Testimony of late Proterozoic Rodinia fragmentation and pre–Gondwana collisional episodes. International Journal of Earth Sciences, 88(1): 76–97. https://doi.org/10.1007/s005310050247

Ordóñez–Carmona, O. & Pimentel, M.M. 2002. Rb–Sr and Sm–Nd isotopic study of the Puquí Complex, Colombian Andes. Journal of South American Earth Sciences, 15(2): 173–182. https://doi.org/10.1016/S0895-9811(02)00017-2

Ordóñez–Carmona, O., Restrepo, J.J. & Pimentel, M.M. 2006. Geochronological and isotopical review of pre–Devonian crustal

basement of the Colombian Andes. Journal of South American Earth Sciences, 21(4): 372–382. https://doi.org/10.1016/j.jsames.2006.07.005

Ortega–Obregón, C., Solari, L., Gómez–Tuena, A., Elías–Herrera, M., Ortega–Gutiérrez, F. & Macías–Romo, C. 2014. Permian – Carboniferous arc magmatism in southern Mexico: U–Pb dating, trace element and Hf isotopic evidence on zircons of earliest subduction beneath the western margin of Gondwana. International Journal of Earth Sciences, 103(5): 1287–1300. https://doi.org/10.1007/s00531-013-0933-1

Pankhurst, R.J., Rapela, C.W. & Fanning, C.M. 2000. Age and origin of coeval TTG, I– and S–type granites in the Famatinian belt of NW Argentina. Transactions of the Royal Society of Edinburgh: Earth and Environmental Sciences, 91(1–2): 151–168. https://doi.org/10.1017/S0263593300007343

Parada, M.A., López–Escobar, L., Oliveros, V., Fuentes, F., Morata, D., Calderón, M., Aguirre, L., Féraud, G., Espinoza, F., Moreno, H., Figueroa, O., Muñoz–Bravo, J., Troncoso–Vásquez, R. & Stern, C.R. 2007. Andean magmatism. In: Moreno, T. & Gibbons, W. (editors), The geology of Chile. The Geological Society, p. 115–146. London. https://doi.org/10.1144/GOCH.4

Parson, L.M. & Wright, I.C. 1996. The Lau–Havre–Taupo back–arc basin: A southward–propagating, multi–stage evolution from rifting to spreading. Tectonophysics, 263(1–4): 1–22. https://doi.org/10.1016/S0040-1951(96)00029-7

Paul, A. 2017. Advancing U–Pb high–temperature thermochronology by combining single grain and intra–grain dating. Doctoral thesis, University of Geneva. Geneva, 201 p., Switzerland. https://doi.org/10.13097/archive-ouverte/unige:102601

Paul, A., Spikings, R., Ulianov, A. & Ovtcharova, M. 2018. High temperature (>350 °C) thermal histories of the long lived (>500 Ma) active margin of Ecuador and Colombia: Apatite, titanite and rutile U–Pb thermochronology. Geochimica et Cosmochimica Acta, 228: 275–300. https://doi.org/10.1016/j.gca.2018.02.033

Peacock, M.A. 1931. Classification of igneous rock series. The Journal of Geology, 39(1): 54–67.

Peccerillo, A. & Taylor, S.R. 1976. Geochemistry of Eocene calc–alkaline volcanic rocks from the Kastamonu area, northern Turkey. Contributions to Mineralogy and Petrology, 58(1): 63–81. https://doi.org/10.1007/BF00384745

Pindell, J.L. 1985. Alleghenian reconstruction and subsequent evolution of the Gulf of Mexico, Bahamas, and proto–Caribbean. Tectonics, 4(1): 1–39. https://doi.org/10.1029/TC004i001p00001

Pindell, J. & Barrett, S.F. 1990. Geological evolution of the Caribbean region; a plate–tectonic perspective. In: Dengo, G. & Case, J.E. (editors), The Caribbean region. Geological Society of America, p. 405–432. https://doi.org/10.1130/DNAGGNA-H.405

Pindell, J. & Dewey, J.F. 1982. Permo–Triassic reconstruction of western Pangaea and the evolution of the Gulf of Mexico/Caribbean region. Tectonics, 1(2): 179–211. https://doi.org/10.1029/TC001i002p00179

Pindell, J.L. & Kennan, L. 2009. Tectonic evolution of the Gulf of Mexico, Caribbean and northern South America in the mantle reference frame: An update. In: James, K.H., Lorente, M.A. & Pindell, J.L. (editors), The origin and evolution of the Caribbean Plate. Geological Society of London, Special Publication 328, p. 1–55. https://doi.org/10.1144/SP328.1

Pindell, J.L., Higgs, R. & Dewey, J.F. 1998. Cenozoic palinspastic reconstruction, paleogeographic evolution and hydrocarbon setting of the northern margin of South America. In: Pindell, J.L. & Drake, C. (editors), Paleogeographic evolution and non–glacial eustasy, northern South America. Society for Sedimentary Geology, Special Publication 58, p. 45–85. https://doi.org/10.2110/pec.98.58.0045

Piraquive, A. 2017. Structural framework, deformation and exhumation of the Santa Marta Schists: Accretion and deformational history of a Caribbean Terrane at the north of the Sierra Nevada de Santa Marta. Doctoral thesis, Université Grenoble Alpes and Universidad Nacional de Colombia, 393 p. Grenoble–Bogotá.

Pratt, W.T., Duque, P. & Ponce, M. 2005. An autochthonous geological model for the eastern Andes of Ecuador. Tectonophysics, 399(1–4): 251–278. https://doi.org/10.1016/j.tecto.2004.12.025

Ramos, V.A. 1988. The tectonics of the central Andes; 30° to 33° S latitude. In: Clark Jr., S.P., Burchfiel, B.C. & Suppe, J. (editors), Processes in continental lithospheric deformation. Geological Society of America, Special Paper 218, p. 31–54. https://doi.org/10.1130/SPE218-p31

Ramos, V.A. 1994. Terranes of southern Gondwanaland and their control in the Andean structure (30°–33° S latitude). In: Reutter, K.J., Scheuber, E. & Wigger, P.J. (editors), Tectonics of the southern central Andes. Springer–Verlag, p. 249–261. Heidelberg. https://doi.org/10.1007/978-3-642-77353-2_18

Ramos, V.A. 2009. Anatomy and global context of the Andes: Main geologic features and the Andean orogenic cycle. In: Kay, S.M., Ramos, V.A. & Dickinson, W.R. (editors), Backbone of the Americas: Shallow subduction, plateau uplift, and ridge and terrane collision. Geological Society of America, Memoirs 204, p. 31–65. https://doi.org/10.1130/2009.1204(02)

Ramos, V.A. & Kay, S.M. 1991. Triassic rifting and associated basalts in the Cuyo Basin, central Argentina. In: Harmon, R. & Rapela, C. (editors), Andean magmatism and its tectonic setting. Geological Society of America, Special Paper 265, p. 79–92. https://doi.org/10.1130/SPE265-p79

Ratschbacher, L., Franz, L., Min, M., Bachmann, R., Martens, U., Stanek, K., Stübner, K., Nelson, B.K., Herrmann, U., Weber, B., López–Martínez, M., Jonckheere, R., Sperner, B., Tichomirowa, M., Mcwilliams, M.O., Gordon, M., Meschede, M. & Bock, P. 2009. The North American–Caribbean Plate boundary in Mexico–Guatemala–Honduras. In: James, K.H.,

Lorente, M.A. & Pindell, J.L. (editors), The origin and evolution of the Caribbean Plate. Geological Society of London, Special Publication 328, p. 219–293. https://doi.org/10.1144/SP328.11

Reitsma, M.J. 2012. Reconstructing the late Paleozoic: Early Mesozoic plutonic and sedimentary record of south–east Peru: Orphaned back–arcs along the western margin of Gondwana. Doctoral thesis, University of Geneva, 226 p. Geneva. https://doi.org/10.13097/archive-ouverte/unige:23095

Restrepo, J.J. & Toussaint, J.F. 1982. Metamorfismos superpuestos en la cordillera Central de Colombia. V Congreso Latinoamericano de Geología, p. 505–512. Buenos Aires, Argentina.

Restrepo, J.J. & Toussaint, J.F. 1988. Terranes and continental accretion in the Colombian Andes. Episodes, 11(3): 189–193. https://doi.org/10.18814/epiiugs/1988/v11i3/006

Restrepo, J.J., Toussaint, J.F., González, H., Cordani, U., Kawashita, K., Linares, E. & Parica, C. 1991. Precisiones geocronológicas sobre el occidente colombiano. Simposio sobre magmatismo andino y su marco tectónico. Memoirs, I, p. 1–22. Manizales.

Restrepo, J.J., Ordóñez–Carmona, O., Armstrong, R. & Pimentel, M.M. 2011. Triassic metamorphism in the northern part of the Tahamí Terrane of the Central Cordillera of Colombia. Journal of South American Earth Sciences, 32(4): 497–507. https://doi.org/10.1016/j.jsames.2011.04.009

Restrepo–Pace, P.A. & Cediel, F. 2010. Northern South America basement tectonics and implications for paleocontinental reconstructions of the Americas. Journal of South American Earth Sciences, 29(4): 764–771. https://doi.org/10.1016/j.jsames.2010.06.002

Restrepo–Pace, P.A., Ruiz, J., Gehrels, G. & Cosca, M. 1997. Geochronology and Nd isotopic data of Grenville–age rocks in the Colombian Andes: New constraints for late Proterozoic – early Paleozoic paleocontinental reconstructions of the Americas. Earth and Planetary Science Letters, 150(3–4): 427–441. https://doi.org/10.1016/S0012-821X(97)00091-5

Riel, N., Guillot, S., Jaillard, E., Martelat, J.E., Paquette, J.L., Schwartz, S., Goncalves, P., Duclaux, G., Thebaud, N., Lanari, P., Janots, E. & Yuquilema, J. 2013. Metamorphic and geochronological study of the Triassic El Oro Metamorphic Complex, Ecuador: Implications for high–temperature metamorphism in a forearc zone. Lithos, 156–159: 41–68. https://doi.org/10.1016/j.lithos.2012.10.005

Rogers, R.R., Swisher, C.C., Sereno, P.C., Monetta, A.M., Forster, C.A. & Martínez, R.N. 1993. The Ischigualasto tetrapod assemblage (Late Triassic, Argentina) and $^{40}Ar/^{39}Ar$ dating of dinosaur origins. Science, 260(5109): 794–797. https://doi.org/10.1126/science.260.5109.794

Romero, D., Valencia, K., Alarcón, P., Peña, D. & Ramos, V.A. 2013. The offshore basement of Perú: Evidence for different igneous and metamorphic domains in the forearc. Journal of South American Earth Sciences, 42: 47–60. https://doi.org/10.1016/j.jsames.2012.11.003

Rosas, S., Fontboté, L. & Tankard, A. 2007. Tectonic evolution and paleogeography of the Mesozoic Pucará Basin, central Peru. Journal of South American Earth Sciences, 24(1): 1–24. https://doi.org/10.1016/j.jsames.2007.03.002

Ruiz, J., Tosdal, R.M., Restrepo, P.A. & Murillo–Muñetón, G. 1999. Pb isotope evidence for Colombia–southern México connections in the Proterozoic. In: Ramos, V.A. & Keppie, J.D. (editors), Laurentia–Gondwana connections before Pangea. Geological Society of America, Special Paper 336, p. 183–197. https://doi.org/10.1130/0-8137-2336-1.183

Russell, S.M. & Whitmarsh, R.B. 2003. Magmatism at the west Iberia non–volcanic rifted continental margin: Evidence from analyses of magnetic anomalies. Geophysical Journal International, 154(3): 706–730. https://doi.org/10.1046/j.1365-246X.2003.01999.x

Schlische, R.W. 2002. Progress in understanding the structural geology, basin evolution, and tectonic history of the eastern North American rift system. In: LeTourneau, P.M. & Olsen, P.E. (editors), The Great Rift valleys of Pangaea in eastern North America, 1. Columbia University Press, p. 21–64. New York. https://doi.org/10.7312/leto11162-003

Senff, M. 1995. Sedimentologie, fauna und fazies des präkretazischen Mesozoikum im Oberen Magdalenatal von zentralkolumbien unter besonderer berüecksichtigung der obertriassischen Payande Formation. Doctoral thesis, Univeristät Giessen, 114 p. Germany.

Shervais, J.W. 1982. Ti–V plots and the petrogenesis of modern and ophiolitic lavas. Earth and Planetary Science Letters, 59(1): 101–118. https://doi.org/10.1016/0012-821X(82)90120-0

Sinton, C.W., Duncan, R.A., Storey, M., Lewis, J. & Estrada, J.J. 1998. An oceanic flood basalt province within the Caribbean Plate. Earth and Planetary Science Letters, 155(3–4): 221–235. https://doi.org/10.1016/S0012-821X(97)00214-8

Solari, L.A., Dostal, J., Ortega–Gutiérrez, F. & Keppie, J.D. 2001. The 275 Ma arc–related La Carbonera stock in the northern Oaxacan Complex of southern Mexico: U–Pb geochronology and geochemistry. Revista Mexicana de Ciencias Geológicas, 18(2): 149–161.

Solari, L., Gómez–Tuena, A., Ortega–Gutiérrez, F. & Ortega–Obregón, C. 2011. The Chuacús Metamorphic Complex, central Guatemala: Geochronological and geochemical constraints on its Paleozoic – Mesozoic evolution. Geologica Acta, 9(3–4): 329–350. https://doi.org/10.1344/105.000001695

Spalletti, L.A., Fanning, C.M. & Rapela, C.W. 2008. Dating the Triassic continental rift in the southern Andes: The Potrerillos Formation, Cuyo Basin, Argentina. Geologica Acta, 6(3): 267–283. https://doi.org/10.1344/105.000000256

Spikings, R., Seward, D., Winkler, W. & Ruiz, G.M. 2000. Low–temperature thermochronology of the northern Cordillera Real, Ecuador: Tectonic insights from zircon and apatite fission track analysis. Tectonics, 19(4): 649–668. https://doi.org/10.1029/2000TC900010

Spikings, R., Winkler, W., Seward, D. & Handler, R. 2001. Along–strike variations in the thermal and tectonic response of the continental Ecuadorian Andes to the collision with heterogeneous oceanic crust. Earth and Planetary Science Letters, 186(1): 57–73. https://doi.org/10.1016/S0012-821X(01)00225-4

Spikings, R., Crowhurst, P.V., Winkler, W. & Villagómez, D. 2010. Syn– and post–accretionary cooling history of the Ecuadorian Andes constrained by their in–situ and detrital thermochronometric record. Journal of South American Earth Sciences, 30(3–4): 121–133. https://doi.org/10.1016/j.jsames.2010.04.002

Spikings, R., Cochrane, R., Villagómez, D., van der Lelij, R., Vallejo, C., Winkler, W. & Beate, B. 2015. The geological history of northwestern South America: From Pangaea to the early collision of the Caribbean Large Igneous Province (290–75 Ma). Gondwana Research, 27(1): 95–139. https://doi.org/10.1016/j.gr.2014.06.004

Spikings, R., Reitsma, M.J., Boekhout, F., Mišković, A., Ulianov, A., Chiaradia, M., Gerdes, A. & Schaltegger, U. 2016. Characterization of Triassic rifting in Peru and implications for the early disassembly of western Pangaea. Gondwana Research, 35: 124–143. https://doi.org/10.1016/j.gr.2016.02.008

Stacey, J.S. & Kramers, J.D. 1975. Approximation of terrestrial lead isotope evolution by a two–stage model. Earth and Planetary Science Letters, 26(2): 207–221. https://doi.org/10.1016/0012-821X(75)90088-6

Sun, S.S. & McDonough, W.F. 1989. Chemical and isotopic systematics of oceanic basalts: Implications for mantle composition and processes. In: Saunders, A.D. & Norry, M.J. (editors), Magmatism in the ocean basins. Geological Society of London, Special Publication 42, p. 313–345. https://doi.org/10.1144/GSL.SP.1989.042.01.19

Taylor, S.R. & McLennan, S.M. 1995. The geochemical evolution of the continental crust. Reviews of Geophysics, 33(2): 241–265. https://doi.org/10.1029/95RG00262

Torres, R., Ruiz, J., Patchett, P.J. & Grajales–Nishimura, J.M. 1999. Permo–Triassic continental arc in eastern Mexico: Tectonic implications for reconstructions of southern North America. In: Bartolini, C., Wilson, J.L. & Lawton, T.F. (editors), Mesozoic sedimentary and tectonic history of north–central Mexico. Geological Society of America, Special Paper 340, p. 191–196. https://doi.org/10.1130/0-8137-2340-X.191

Toussaint, J.F. & Restrepo, J.J. 1994. The Colombian Andes during Cretaceous times. In: Salfity, J.A. (editor), Cretaceous tectonics of the Andes. Earth Evolution Sciences. Vieweg + Teubner Verlag, p. 61–100. Wiesbaden, Germany. https://doi.org/10.1007/978-3-322-85472-8_2

Tschanz, C.M., Marvin, R.F., Cruz, J., Mehnert, H.H. & Cebula, G.T. 1974. Geologic evolution of the Sierra Nevada de Santa Marta, northeastern Colombia. Geological Society of America Bulletin, 85(2): 273–284. https://doi.org/10.1130/0016-7606(1974)85<273:GEOTSN>2.0.CO;2

Vallejo, C., Spikings, R., Luzieux, L., Winkler, W., Chew, D. & Page, L. 2006. The early interaction between the Caribbean Plateau and the NW South American Plate. Terra Nova, 18(4): 264–269. https://doi.org/10.1111/j.1365-3121.2006.00688.x

Vallejo, C., Winkler, W., Spikings, R.A., Luzieux, L., Heller, F. & Bussy, F. 2009. Mode and timing of terrane accretion in the forearc of the Andes in Ecuador. In: Kay, S.M., Ramos, V.A. & Dickinson, W.R. (editors), Backbone of the Americas: Shallow subduction, plateau uplift, and ridge and terrane collision. Geological Society of America, Memoirs 204, p. 197–216. https://doi.org/10.1130/2009.1204(09)

van der Lelij, R. 2013. Reconstructing north–western Gondwana with implications for the evolution of the Iapetus and Rheic Oceans: A geochronological, thermochronological and geochemical study. Doctoral thesis, University of Geneva, 248 p. Geneva. https://doi.org/10.13097/archive-ouverte/unige:31653

van der Lelij, R., Spikings, R., Kerr, A.C., Kounov, A., Cosca, M., Chew, D. & Villagómez, D. 2010. Thermochronology and tectonics of the Leeward Antilles: Evolution of the southern Caribbean Plate boundary zone. Tectonics, 29(6): 1–30. https://doi.org/10.1029/2009TC002654

van der Lelij, R., Spikings, R., Ulianov, A., Chiaradia, M. & Mora, A. 2016. Palaeozoic to Early Jurassic history of the northwestern corner of Gondwana, and implications for the evolution of the Iapetus, Rheic and Pacific Oceans. Gondwana Research, 31: 271–294. https://doi.org/10.1016/j.gr.2015.01.011

Vilas, J.F. & Valencio, D.A. 1978. Palaeomagnetism and K–Ar age of the Upper Ordovician Alcaparrosa Formation, Argentina. Geophysical Journal International, 55(1): 143–154. https://doi.org/10.1111/j.1365-246X.1978.tb04753.x

Villagómez, D. & Spikings, R. 2013. Thermochronology and tectonics of the Central and Western Cordilleras of Colombia: Early Cretaceous – Tertiary evolution of the northern Andes. Lithos, 160–161: 228–249. https://doi.org/10.1016/j.lithos.2012.12.008

Villagómez, D., Spikings, R., Magna, T., Kammer, A., Winkler, W. & Beltrán, A. 2011. Geochronology, geochemistry and tectonic evolution of the Western and Central Cordilleras of Colombia. Lithos, 125(3–4): 875–896. https://doi.org/10.1016/j.lithos.2011.05.003

Vinasco, C.J., Cordani, U.G., González, H., Weber, M. & Peláez, C. 2006. Geochronological, isotopic, and geochemical data from Permo–Triassic granitic gneisses and granitoids of the Colombian central Andes. Journal of South American Earth Sciences, 21(4): 355–371. https://doi.org/10.1016/j.jsames.2006.07.007

Viscarret, P., Wright, J. & Urbani, F. 2009. New U–Pb zircon ages of El Baúl Massif, Cojedes state, Venezuela. Revista Técnica de la Facultad de Ingeniería, Universidad del Zulia, 32(3): 210–221.

Weber, B. & Köhler, H. 1999. Sm–Nd, Rb–Sr and U–Pb geochronology of a Grenville Terrane in southern Mexico: Origin and geologic history of the Guichicovi Complex. Precambrian

Research, 96(3–4): 245–262. https://doi.org/10.1016/S0301-9268(99)00012-1

Weber, B., Cameron, K.L., Osorio, M. & Schaaf, P. 2005. A late Permian tectonothermal event in Grenville crust of the southern Maya Terrane: U–Pb zircon ages from the Chiapas Massif, southeastern Mexico. International Geology Review, 47(5): 509–529. https://doi.org/10.2747/0020-6814.47.5.509

Weber, B., Iriondo, A., Premo, W.R., Hecht, L. & Schaaf, P. 2007. New insights into the history and origin of the southern Maya Block, SE México: U–Pb–SHRIMP zircon geochronology from metamorphic rocks of the Chiapas Massif. International Journal of Earth Sciences, 96(2): 253–269. https://doi.org/10.1007/s00531-006-0093-7

Weber, M., Cardona, A., Valencia, V., García–Casco, A., Tobón, M. & Zapata, S. 2010. U/Pb detrital zircon provenance from Late Cretaceous metamorphic units of the Guajira Peninsula, Colombia: Tectonic implications on the collision between the Caribbean Arc and the South American margin. Journal of South American Earth Sciences, 29(4): 805–816. https://doi.org/10.1016/j.jsames.2009.10.004

Winchester, J.A. & Floyd, P.A. 1977. Geochemical discrimination of different magma series and their differentiation products using immobile elements. Chemical Geology, 20: 325–343. https://doi.org/10.1016/0009-2541(77)90057-2

Xu, H., Ma, C. & Ye, K. 2007. Early Cretaceous granitoids and their implications for the collapse of the Dabie Orogen, eastern China: SHRIMP zircon U–Pb dating and geochemistry. Chemical Geology, 240(3–4): 238–259. https://doi.org/10.1016/j.chemgeo.2007.02.018

Yañez, P., Ruiz, J., Patchett, P.J., Ortega–Gutiérrez, F. & Gehrels, G.E. 1991. Isotopic studies of the Acatlan Complex, southern Mexico: Implications for Paleozoic North American tectonics. Geological Society of America Bulletin, 103(6): 817–828. https://doi.org/10.1130/0016-7606(1991)103<0817:ISOTAC>2.3.CO;2

Zerfass, H., Chemale, F., Schultz, C.L. & Lavina, E. 2004. Tectonics and sedimentation in southern South America during Triassic. Sedimentary Geology, 166(3–4): 265–292. https://doi.org/10.1016/j.sedgeo.2003.12.008

Explanation of Acronyms, Abbreviations, and Symbols:

BABB	Back–arc basin basalt
CHUR	Chondritic uniform reservoir
E–MORB	Enriched mid–ocean ridge basalt
HFSE	High field strength elements
HP/LT	High–pressure/low–temperature
ID–TIMS	Isotope dilution thermal ionization mass spectrometry
ISMMB	Inner Santa Marta Metamorphic Belt
LA–ICP–MS	Laser ablation inductively coupled plasma mass spectrometry
LA–MC–ICP–MS	Laser ablation multi–collector inductively coupled plasma mass spectrometry
LILE	Light–ion lithophile element
LREE	Light rare earth element
MORB	Mid–ocean ridge basalt
MP–HT	Medium pressure–high temperature
N–MORB	Normal mid–ocean ridge basalt
REE	Rare earth element
SHRIMP	Sensitive high–resolution ion microprobe
SIMS	Secondary ion mass spectrometry

Authors' Biographical Notes

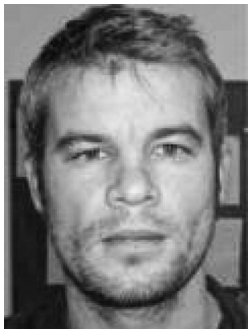

Richard SPIKINGS graduated in geochemistry at the University of St. Andrews in 1993. His research in thermochronology earned a PhD in geology in 1998 from La Trobe University, Melbourne. Since 1998, he has worked as a postdoctoral fellow at the ETH–Zurich, and as tenured research staff at the University of Geneva where he currently manages the $^{40}Ar/^{39}Ar$ laboratory. His research has focussed on thermochronology and geochronology of the Andean cordilleras in Ecuador, Colombia, Venezuela, Perú, and Chile. More recently, Richard has focussed his research efforts on bulk and in–situ U–Pb thermochronology of accessory phases.

Andre Navin PAUL obtained a BSc in geoscience in 2010 and a MS in geoscience in 2012 at the University of Hamburg, Germany. He then completed his PhD at the University of Geneva, Switzerland in 2017, where he studied U–Pb thermochronology. Since then Andre has been investigating Boron isotope systematics in the earth's mantle as a post–doctoral research assistant at the University of Edinburgh, in collaboration with the University of Bristol and University of Leeds, United Kingdom. His research is focused on the use of radiogenic and stable isotope systematics, with high spatial resolution and high precision analyses.

Volume 2

Chapter 2

https://doi.org/10.32685/pub.esp.36.2019.02
Published online 24 April 2020

The Petrologic Nature of the "Medellín Dunite" Revisited: An Algebraic Approach and Proposal of a New Definition of the Geological Body

Antonio GARCIA–CASCO[1]*, Jorge Julián RESTREPO[2], Ana María CORREA–MARTÍNEZ[3], Idael Francisco BLANCO–QUINTERO[4], Joaquín Antonio PROENZA[5], Marion WEBER[6], and Lidia BUTJOSA[7]

Abstract The "Medellín Dunite", the main ultramafic body of the Central Cordillera of Colombia, constitutes a fragment of oceanic lithospheric mantle formed at a back–arc basin/incipient arc scenario emplaced onto the western continental margin of Pangaea during Triassic time. This body has been classically, and is still considered, mainly of dunite composition. However, in spite of two subsequent metamorphic imprints that obscure the primary mantle mineralogical composition, there is petrographic and geochemical evidence that points to a harzburgitic nature of the unit. In order to overcome the petrographic effects of medium–T metamorphism, metasomatism, and serpentinization, we analyzed published and new major–element geochemical data by means of algebraic methods to approximate the mantle mineralogical composition of ultramafic rocks. The restored mantle mineralogy clearly indicates that the body is mainly of harzburgitic composition, and therefore we propose that the term "Medellín Dunite" should no longer be applied to avoid terminological confusion. Furthermore, a phase–relation approach in simple systems for the metamorphic evolution allows identifying the main reason for the contradictory terminology used so far: olivine is paragenetic (stable) with tremolite and talc during medium–T (ca. 600 °C) metamorphic imprint undergone by the body. During this initial metamorphic event, characterized by full hydration (as opposed to the late–stage serpentinization), mantle pyroxenes reacted out and medium–T olivine formed while high–T olivine persisted metastably as a likely consequence of moderate temperature and sluggish diffusion kinetics. On the other hand, we analyze two likely geodynamic scenarios to provide a common context of metamorphism for the ultramafic body and associated metabasites (Aburrá Ophiolite): (i) ocean–floor metamorphism and (ii) intra–backarc subduction–initiation metamorphism. The latter allows a new tectonic view of the Aburrá Ophiolite, formed by tectonic units from the upper and down going plates on a nascent active plate margin. For all these reasons, we propose the new term "Medellín Metaharzburgitic Unit" in order to combine in a single term the original high–T mantle composition, its subsequent metamorphic transformation and the independent tectonic character of the ultramafic body.

Keywords: *Medellín Dunite, Medellín Metaharzburgitic Unit, metaharzburgite, phase relations, ophiolite.*

1 agcasco@ugr.es
Universidad de Granada
Departamento de Mineralogía y Petrología
Avenida Fuente Nueva s/n, 18079
Granada, España
Instituto Andaluz de Ciencias de la Tierra, CSIC–UGR
Avenida de las Palmeras, 4, 18100 Armilla
Granada, España

2 jjrestrepoa@gmail.com
Universidad Nacional de Colombia
Sede Medellín
GEMMA Research Group
Medellín, Colombiaa

3 amcorream@yahoo.com
Universidade de Brasília
Instituto de Geociências
Servicio Geológico Colombiano
Dirección de Geociencias Básicas
Grupo de Estudios Geológicos Especiales
Calle 75 n.° 79A–51
Medellín, Colombia

4 if.blanco@ua.es
if.blanco@uniandes.edu.co
Universidad de Alicante
Departamento Ciencias de la Tierra y del Medio Ambiente
San Vicente del Raspeig, Alicante, España
Universidad de los Andes
Departamento de Geociencias
Carrera 1 n.° 18A–70
Bogotá D. C., Colombia

5 japroenza@ub.edu
University of Barcelona
Department of Mineralogy, Petrology, and Applied Geology
Calle Martí i Franquès s/n, 08028
Barcelona, España

6 mweber@unal.edu.co
Universidad Nacional de Colombia
Sede Medellín
Departamento de Geociencias y Medio Ambiente
Carrera 80 n.° 65–223
Medellín, Colombia

7 lbutjosa@ub.edu
University of Barcelona
Department of Mineralogy, Petrology, and Applied Geology
Calle Martí i Franquès s/n, 08028
Barcelona, España

* Corresponding author

Citation: Garcia–Casco, A., Restrepo, J.J., Correa–Martínez, A.M., Blanco–Quintero, I.F., Proenza, J.A., Weber, M. & Butjosa, L. 2020. The petrologic nature of the "Medellín Dunite" revisited: An algebraic approach and proposal of a new definition of the geological body. In: Gómez, J. & Pinilla–Pachon, A.O. (editors), The Geology of Colombia, Volume 2 Mesozoic. Servicio Geológico Colombiano, Publicaciones Geológicas Especiales 36, p. 45–75. Bogotá. https://doi.org/10.32685/pub.esp.36.2019.02

Resumen La "Dunita de Medellín", principal cuerpo ultramáfico de la cordillera Central de Colombia, constituye un fragmento de manto litosférico oceánico formado en un ambiente de cuenca de retroarco/arco incipiente emplazado sobre el margen continental occidental de Pangea durante el periodo Triásico. Este cuerpo es y ha sido clásicamente considerado de composición esencialmente dunítica. Sin embargo, y a pesar de dos eventos metamórficos subsecuentes sufridos que han enmascarado su composición mineralógica mantélica primaria, existe evidencia petrográfica y geoquímica que indica una naturaleza harzburgítica generalizada de la unidad. Para evitar los efectos petrográficos del metamorfismo de T–media, metasomatismo y serpentinización, analizamos datos geoquímicos publicados y nuevos de rocas ultramáficas mediante métodos algebraicos para deducir su composición mineralógica mantélica primaria. La mineralogía mantélica reconstruida claramente indica que el cuerpo es principalmente de composición harzburgítica y, por tanto, proponemos que el término "Dunita de Medellín" no debe aplicarse en el futuro para evitar confusiones terminológicas. Aún más, un análisis de las relaciones de fases en sistemas simples durante la evolución metamórfica sufrida permite identificar la razón principal por la cual se ha llegado a esta terminología contradictoria: el olivino es paragenético (estable) con tremolita y talco durante el evento metamórfico generalizado de T–media (ca. 600 °C) sufrido por el cuerpo. Durante este evento metamórfico inicial, caracterizado por hidratación completa (a diferencia de la serpentinización tardía), se consumieron los piroxenos primarios mantélicos y se formó olivino, en tanto que el olivino de T–alta persistió de forma metaestable probablemente como consecuencia de una cinética de difusión lenta a temperatura moderada. Por otro lado, analizamos dos posibles ambientes geodinámicos para ofrecer un contexto común para el metamorfismo del cuerpo ultramáfico y las rocas básicas asociadas (Ofiolita de Aburrá): (i) metamorfismo de fondo oceánico y (ii) metamorfismo de inicio de subducción intra cuenca de retroarco. Este último modelo permite una nueva conceptualización tectónica de la Ofiolita de Aburrá, conformada por unidades tectónicas pertenecientes al techo y muro del incipiente margen de placa activo. Por todo ello, proponemos el nuevo término "Unidad Metaharzburgítica de Medellín" para unir en una sola expresión la composición mantélica original de T–alta, la subsiguiente transformación metamórfica y la naturaleza tectónica independiente del cuerpo ultramáfico.

Palabras clave: *Dunita de Medellín, Unidad Metaharzburgítica de Medellín, metaharzburgita, relaciones de fases, ofiolita.*

1. The Origin and Evolution of the Concept "Medellín Dunite" and Its Metamorphic Imprint

Ultramafic bodies with variable extent of metamorphic imprint and serpentinization are found in the Central Cordillera of Colombia. The largest of these bodies, and probably the largest one in the entire Andes, crops out to the east and north of the Aburrá valley and Medellín. This body, generally termed as the "Medellín Dunite", is composed of three outcrops separated by the Santa Elena Creek and the Medellín River (Figure 1). The whole body trends N–NW and is 35 km long and 5 km wide, with a total area of about 71 km^2. In the first modern geological study of the region (Botero, 1963), the ultramafic rocks were termed "Medellín Serpentinites", made of serpentinites containing 15–35 % of olivine. Botero (1963) considered these rocks to have formed as an almost crystalline ultramafic magma "intrusion" into the surrounding metamorphic rocks, in particular amphibolites that developed a strong foliation/lineation of hornblende and plagioclase upon the proposed intrusion. With the advent of plate–tectonics theory, the emplacement of the ultramafic rocks was attributed to a probable Cretaceous obduction of oceanic mantle over Paleozoic metamorphic rocks (mostly amphibolites) (Restrepo, 1986; Restrepo & Toussaint, 1973, 1974).

As new petrographic studies became available, it was apparent that the amount of olivine in the ultramafic rocks was higher than reported by Botero (1963) and that the rock ensemble should not be termed "Medellín Serpentinites". Álvarez (1982, 1987) considered that the body represents the solid residue of partial melting of the mantle in the transition zone of an oceanic lithosphere and ascribed the strong banding of the rocks and oriented olivine fabrics to ductile mantle deformation. This led

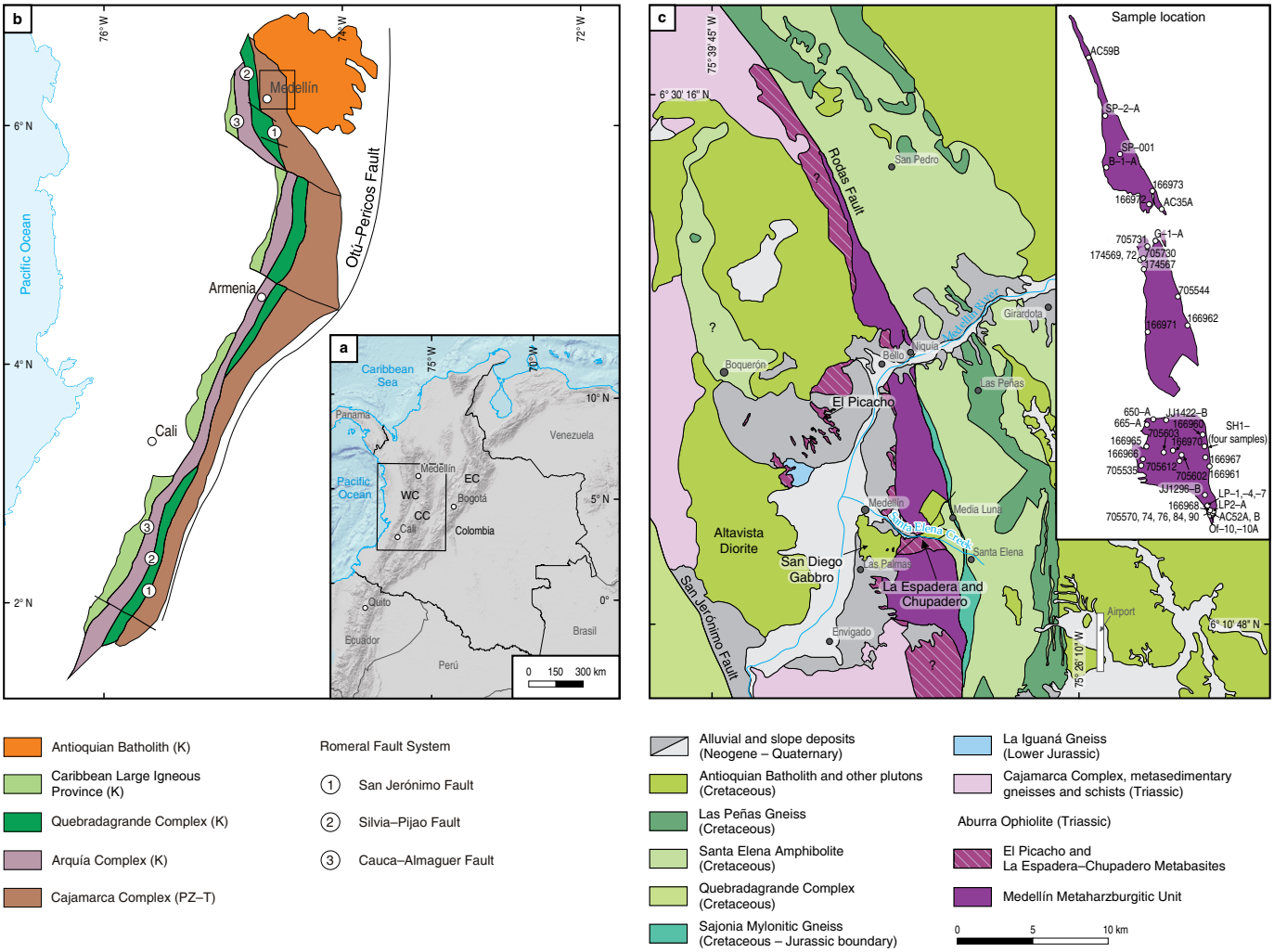

Figure 1. (a) Topography of northwestern South America (National Geographic MapMaker Interactive, http://mapmaker.nationalgeographic.org/) with indication of Eastern, Central, and Western Cordilleras (EC, CC, and WC, respectively) and the area shown in Figure 1b. **(b)** Geological sketch map of the Central Cordillera of Colombia (adapted from Nivia et al., 2016) with indication of map in Figure 1c. **(c)** Simplified geological map of the Medellín region compiled after Botero (1963), Rendón (1999), Correa–Martínez & Martens (2000), Rodríguez et al. (2005), Restrepo et al. (2012), and Rodríguez & Correa–Martínez (2015). The question marks indicate possible extension of the La Espadera–Chupadero and Santa Elena Amphibolites. The location of samples studied in this paper (Table 1) is indicated. Pg—Paleogene; K—Cretaceous; PZ—Paleozoic; T—Triassic.

this author to name the body "Medellín Dunite Tectonite". Metamorphic minerals such as tremolite, chlorite, talc, and serpentine were related to a late low–temperature alteration event which included metasomatic formation of Al–rich minerals (essentially, chlorite). Restrepo & Toussaint (1984) followed Álvarez (1982) and formally used the term "Medellín Dunite", though these authors emphasized that, even if pyroxenes were not generally present, tremolite and chlorite aggregates replace probable former pyroxene(s) and, consequently, indicated that at least some rocks may not have a dunitic composition. Notably, these authors considered tremolite and chlorite the result of a regional metamorphic event affecting the unit. Álvarez (1987) presented 14 whole–rock chemical analyses of the ultramafic rocks and used Coleman's (1977) SiO_2 versus FeO*/(FeO* + MgO) diagram to show that the samples plot between the fields of dunite and harzburgite. He emphasized that the bulk composition of the dunite tectonite is relatively restricted and that it compares well, except for Al_2O_3 contents, with ophiolitic dunites reported by Coleman (1977). The observations of Álvarez (1982, 1987) and Restrepo & Toussaint (1984) influenced other workers to name the body as "dunite" almost ever since their work.

Thus, González (2001), in the memoir of the Mapa geológico del departamento de Antioquia, used the term "Medellín Dunite" and emphasized the olivine–rich primary composition (with relicts of Cr–spinel) transformed to variable extent to serpentine group minerals, tremolite, chlorite, talc, magnetite, and carbonates. Similarly, Rodríguez et al. (2005), in the memoir of the Geological Map of East Medellín (sheet 147; 1:100 000), introduce the term "Medellín Serpentinized Dunite" to emphasize the variable extent of serpentinization. These authors

recognized the relict high–T banding as a preferential orientation for serpentinization and formation of tremolite and talc. In their modal analyses of 45 samples (800 points per thin section) Rodríguez et al. (2005) identified olivine (up to 76 mode %), chromian–spinel, tremolite, talc, chrysotile, antigorite, carbonates, chlorite, and magnetite, but no pyroxene. These authors presented whole–rock major elements analyses of 12 samples and follow Álvarez's (1987) conclusion that the composition of the body is similar to dunitic rocks of ophiolitic complexes as defined by Coleman (1977). Because these authors considered that the composition of the ultramafic rocks is dunitic, i.e., poor in SiO_2, Al_2O_3, and CaO, the formation of secondary minerals such as talc, chlorite, and amphibole was associated with metasomatic transformations triggered by addition of these elements from external sources. They also indicate that MgO–loss likely took place during serpentinization.

Correa–Martínez & Nilson (2003) and Correa–Martínez (2007) reported very local occurrences of unaltered and altered harzburgite and wehrlite and considered that the unit forms part of the Aburrá Ophiolite of Correa–Martínez & Martens (2000; see section 2 for details). However, these authors report that most of the body corresponds to massive dunites, with only minor harzburgitic rocks classified as I– and II–type harzburgites with preserved and altered orthopyroxene, respectively. These rocks present variable amounts of serpentine, tremolite, talc, and carbonates that are considered secondary minerals formed after primary mantle minerals. Correa–Martínez & Nilson (2003), Correa–Martínez et al. (2004), Proenza et al. (2004), and Correa–Martínez (2007) concluded that the body formed in a suprasubduction environment (back–arc basin). Correa–Martínez & Nilson (2003) and Proenza et al. (2004) still retained the term "Medellín Dunite", but Correa–Martínez (2007) dropped this term and proposed "Medellín Ultramafic Massif" to emphasize that, in spite of a predominance of dunitic composition, the unit contains minor amounts of harzburgite, ultramafic dikes, and wehrlite (in addition to chromitite). Though the last author did not present major–element bulk–rock chemical analyses of the ultramafic rocks, four unpublished analyses obtained during her PhD thesis are presented in this paper (see below).

Pereira et al. (2006) and Restrepo (2008) published bulk–rock major–element analyses of 2 and 6 samples, respectively. Even if small in number, they show a relatively large chemical spread that suggests varied lithology. Restrepo (2008) analyzed samples from the main body and from other smaller bodies, some of which may not be related to the former. Both Pereira et al. (2006) and Restrepo (2008) use the term "Medellín Dunite". Interestingly, however, Restrepo (2008) highlights the (very) local presence of fresh and tremolite + talc–altered orthopyroxene in samples from Chupadero Creek, San Pedro, and the southern part of the body and suggested that, if ubiquitous tremolite formed at the expense of clinopyroxene the body may correspond to the mantle section of a lherzolite–harzburgite ophiolite type (following the nomenclature of Nicolas & Boudier, 2003). Moreover, Restrepo (2008) emphasized that because the body suffered medium grade metamorphism (tremolite + chlorite ± talc ± anthophyllite–bearing assemblages) the correct definition of the body should be "Medellín Metadunite".

Hernández–González (2014) presented 4 chemical analyses of serpentinized samples and recognized the presence of dunite, harzburgite, and lherzolite, the latter based on one chemical analysis of Restrepo (2008) that is probably carbonated (as discussed below). This author used the term "Medellín Metaperidotite", but did not offer a comprehensive treatment of metamorphism. A suprasubduction environment of formation is proposed, probably a back–arc basin. Recently, González–Ospina (2016) published chemical analyses of 9 samples. This author indicated that the geochemical characteristics of most samples conform to an island arc environment of formation, assigned a (serpentinized) dunitic composition based on petrographic analyses, and retained the term "Medellín Dunite". However, the calculated CIPW norm of the samples clearly points to harzburgitic composition (the abundance of normative hypersthene ranges from 42 to 24%; see Table 6.5 in González–Ospina, 2016).

In summary, the term "Medellín Dunite" is strongly rooted in the Colombian geological literature and is still used in spite of petrographic (i.e., presence of tremolite) and geochemical (i.e., large variability in major element composition) indications that the unit does not comprise mainly dunite. Except Correa–Martínez & Nilson (2003), Correa–Martínez (2007), and Restrepo (2008), previous authors have not addressed this fundamental contradiction. Also, except Restrepo (2008), the evaluation and terminological significance of the metamorphic imprint of the "Medellín Dunite" has not been discussed. However, it is of paramount importance to give its proper name to each rock (paraphrasing the influential paper by Streckeisen, 1976).

In this paper, we address the terminological issue of the "Medellín Dunite". In the first part of the paper, we use published and new chemical analyses to show the petrological nature of the body. In the second part, we will focus on the origin of the most important and paradoxical characteristic of these ultramafic rocks: why olivine has generally resisted metamorphic overprinting. We show that the body originally was harzburgitic and should no longer be termed "Medellín Dunite" in order to avoid terminological confusion. Furthermore, since metamorphic conditions attained by these rocks are the reason for the presence of olivine, we propose the term "Medellín Metaharzburgitic Unit", which will be used henceforth in this paper.

2. Geologic Setting

The bedrock geology of the Central Cordillera of Colombia is essentially made of low–, medium–, and high–grade metasedimentary and metaigneous rocks and post–metamorphic igneous intrusions and volcanic and sedimentary sequences of mainly

Permian – Triassic to Late Cretaceous age (Rodríguez et al., 2005, and references therein). To the west, the lithological ensemble is cut by a number of strike–slip faults grouped in the Romeral–Cauca Fault System, including the San Jerónimo and Cauca–Almaguer Faults that separate these complexes from the Western Cordillera (Cretaceous Oceanic Colombian–Caribbean Plateau Basalt Province). To the east, the Otú–Pericos Fault separates the ensemble from the Chibcha Terrane, located in the eastern flank of the Central Cordillera, and the Eastern Cordillera (Mesozoic continental passive margin) (Maya & González, 1995). Roughly, metamorphic ages in the Central Cordillera follow an east–west younging trend, including the Grenvillian Chibcha Terrane, the Permian – Triassic Tahamí Terrane, the small Devonian Anacona Terrane, the volcanic–sedimentary slightly metamorphic to non–metamorphic Cretaceous Quebradagrande Complex, and the Cretaceous Arquía Complex, while plutonic intrusions are of Triassic, Jurassic, and, mainly, mid–late Cretaceous age (Cochrane et al., 2014; Jaramillo et al., 2017; Martens et al., 2014; Maya & González, 1995; Ordóñez–Carmona, 2001; Restrepo et al., 1991; Spikings et al., 2015; Toussaint & Restrepo, 1989; Villagómez et al., 2011; Vinasco et al., 2006). Recently, an eastern fragment of the Tahamí Terrane has been dated Jurassic, emphasizing the need of further geochronologic work to better define terranes and terrane boundaries (Blanco–Quintero et al., 2014). In this work we follow Restrepo (2008) and consider that the Medellín Metaharzburgitic Unit forms part of the Tahamí Terrane. This terrane is roughly equivalent to the "Polymetamorphic Complex of the Central Cordillera" of Restrepo & Toussaint (1984) and the "Cajamarca Complex" of Maya & González (1995).

The metamorphic rocks in the Medellín region (Aburrá valley) are mostly metabasite and, to a lesser extent, low–, medium–, and high–grade metasedimentary and metagranitic rocks, including muscovite–quartz schist, migmatite, and biotite gneiss (e.g., Figure 1; Restrepo, 2008; Restrepo & Toussaint, 1984; Rodríguez et al., 2005) that were grouped initially in the "Ayurá–Montebello Group" by Botero (1963) and more commonly in the "Cajamarca Complex" after Maya & González (1995). Metamorphic ages are essentially Permian – Triassic (Bustamante et al., 1999; Cochrane et al., 2014; Martens et al., 2014; Ordóñez–Carmona, 2001; Restrepo et al., 1991, 2011; Vinasco et al., 2006). Since Restrepo & Toussaint (1984) defined the term Medellín Amphibolite to name the amphibolitic body of the basal part of Ayurá–Montebello Group/Cajamarca Complex in the region, different metabasite units have been separated from this geologic unit, making the term Medellín Amphibolite no longer valid. Correa–Martínez & Martens (2000) and Correa–Martínez et al. (2005) defined four units, the Medellín, El Retiro, and Boquerón Amphibolites and the El Picacho Metagabbros, the latter including plagiogranite bodies. Restrepo (2008) defined two main units: the Santa Elena Amphibolites, which bear intercalations of Las Peñas Paragneiss, and the La Espadera–Chupadero Amphibolites, the latter grouped with the Picacho Metagabbros as the Picacho Metabasites. For the El Retiro Amphibolites, Restrepo (2008) suggested that they could constitute the southern extension of the Santa Elena Amphibolites, but recent U–Pb zircon ages provided by Cochrane et al. (2014) and Restrepo et al. (2012) indicate that there is no relation. Amphibolites are (almost) totally recrystallized, while igneous relict textures are present in metagabbros, in particular in banded varieties (El Picacho). Metamorphic recrystallization yielded relatively homogeneous amphibole + plagioclase ± clinopyroxene–bearing assemblages denoting medium grade, conditions. Garnet is locally present in the Santa Elena Amphibolites. Correa–Martínez (2007) calculated 6.5–9 kbar for the garnet–bearing samples, and ca. 5 kbar for other samples of the Santa Elena Amphibolites. The pressure calculation of other metabasite units has not been addressed. However, Correa–Martínez (2007) indicates that metamorphic pressure in the El Picacho and Boquerón Metagabbros is <2 kbar. Since these rocks are probably related to the La Espadera–Chupadero Amphibolites (see below), similar pressures could be anticipated.

The contacts between units are generally obscured by strike–slip faults, such as the Rodas Fault that separates the Medellín Metaharzburgitic Unit from the Santa Elena Amphibolites (Figure 1). Restrepo & Toussaint (1974) and Restrepo (2008) claimed that the Medellín Metaharzburgitic Unit overrides the La Espadera–Chupadero Amphibolites (Figure 2a), which in turn would override the Santa Elena Amphibolites. Restrepo (2008) suggested that the La Espadera–Chupadero Amphibolites formed the metamorphic sole of the ophiolite. The structural position of other metabasite units is uncertain. The fabric of the Santa Elena Amphibolites is complex, with development of at least two syn–metamorphic foliations and associated folding (Martens, 2003; Rodríguez et al., 2005). In all other metabasite units the fabric is simpler, with development of a single foliation, often mylonitic (Correa–Martínez, 2007). In this regard, mid–Cretaceous U–Pb zircon ages from the Santa Elena Amphibolites and related rocks (Restrepo et al., 2012), similar to metamorphic ages of the Arquía Complex, challenge the present view of the structural architecture and tectonics of the region. On the other hand, if La Espadera–Chupadero Amphibolites forms the metamorphic sole of the ophiolite, the proposal of a "normal" (i.e., Penrose–type) ophiolitic sequence would be defeated (see section 8).

All metabasite rocks are of oceanic origin and likely formed in a back–arc basin (Correa–Martínez, 2007; Correa–Martínez & Martens, 2000; Correa–Martínez et al., 2005). Correa–Martínez & Martens (2000) proposed that, in addition to the "Medellín Dunite", at least the El Picacho Metagabbros forms part of an ophiolitic complex, termed the Aburrá Ophiolite. Correa–Martínez (2007) expanded the concept to all other metabasite units in the region, including the Santa Elena Amphibolites and the El Picacho and Boquerón Metagabbros, which were consid-


a
Medellín Metaharzburgitic Unit
La Espadera–Chupadero Amphibolite


b


c


d


e


f


g

Figure 2. (a) Panoramic view of the Medellín Metaharzburgitic Unit on top of the La Espadera–Chupadero Amphibolites at Chupadero Creek. **(b)** Typical outcrop aspect of ultramafic rocks showing massive structure. **(c)** Detail of massive ultramafic rock showing foliated structure on weathered surface. **(d)** Foliated ultramafic rock showing probable altered orthopyroxene porphyroclasts. **(e)** Banded structure with variable amount of probable pyroxene. **(f)** Detail of foliated ultramafic rock with orthopyroxene porphyroclasts. **(g)** Magnesite veins in altered ultramafic rocks.

ered to form part of the volcanic and plutonic crustal sections, respectively, of the Aburrá Ophiolite. U–Pb zircon data from a plagiogranite sample and a margarite–bearing metagabbro–pegmatite yielded concordant 216.6 ± 0.4 Ma and 228 ± 0.92 Ma ages, respectively (Correa–Martínez, 2007; Restrepo et al., 2007). The 216.6 ± 0.4 Ma age is considered by Correa–Martínez (2007) as the timing of syn–oceanic shearing, metamorphism, and partial melting of the El Picacho Metagabbros and, hence, the minimum age of ophiolite formation. Restrepo et al. (2007) indicate that 228 ± 0.92 Ma is the timing of the late stages of magmatism or, more unlikely, of a metasomatic overprinting.

However, Restrepo (2008) established geochemical contrasts between the Santa Elena (MORB–like) and other metabasite units (IAT–like), and considered the former as older than, and not–related to, the Aburrá Ophiolite. Following this author, the Santa Elena Amphibolites are related to the medium– to high–grade metasedimentary rocks of the Tahamí Terrane that form the basement overridden by the Medellín Metaharzburgitic Unit. Only the La Espadera–Chupadero Amphibolites and the El Picacho Metagabbros were considered as the basaltic and plutonic parts of the ophiolitic sequence by Restrepo (2008). This is in agreement with the mid–Cretaceous age (Restrepo et al., 2012), the more complex deformation and the higher metamorphic pressure of the Santa Elena Amphibolites.

The Medellín Metaharzburgitic Unit and other minor bodies occur to the east of the Medellín (Figure 1). As described above, the body is apparently made mainly of "dunite", with minor harzburgite, wehrlite, and ultramafic dykes (Correa–Martínez, 2007). Ductile deformation is generally weak, showing metamorphic massive non–oriented to oriented fabrics that overprint previous high–temperature mantle foliation, local banding, and porphyroclastic fabrics (Figure 2b–f). This metamorphic event is characterized by the generalized development of Tr + Tlc + Chl ± recrystallized olivine and will be termed in this paper as Tr + Tlc + Ol event (in this paper, mineral abbreviations are from Whitney & Evans, 2010). Previous high–temperature deformation is more common and intense towards the base of the main body in contact with country–rock amphibolites, where the extent of serpentinization is lower (Correa–Martínez, 2007). However, strong deformation in this part of the body is indicated by strongly oriented chlorite–actinolite schists formed at intermediate temperature after metasomatic transformation of ultramafic rocks (Correa–Martínez, 2007; Restrepo, 2008; Rodríguez et al., 2005). It hence seems that, at least more intensely at the base of the unit, the Tr + Tlc + Ol event is related to strong deformation. This event is overprinted by late serpentinization, carbonation (Figure 2g), and talc–forming episodes. The unit contains podiform chromite deposits. The composition and texture of the original chromite and olivine are strongly affected by the Tr + Tlc + Ol metamorphic event and late serpentinization. However, relict compositions point to formation in a back–arc basin (Correa–Martínez, 2007; Hernández–González, 2014; Proenza et al., 2004).

3. Mineral Assemblages and Textures

Most rocks of the Medellín Metaharzburgitic Unit lack pyroxenes and preserve only primary olivine with a variable extent of replacement by serpentine–group minerals and iddingsite (a very fine–grained mixture of chlorite group and smectite group minerals and iron oxi–hydroxides). They also contain chromian–spinel with moderate to strong transformation to ferrian–chromite and replacement by magnetite and chlorite. The primary fabric is defined by orientation of medium– to coarse–grained olivine and medium– to fine–grained spinel parallel to mineralogical banding and extent of serpentinization/weathering. Olivine is granular to elongated, and shows evidence of ductile/cataclastic mylonitic deformation, with undulose extinction and development of subgrains and recrystallization (Álvarez, 1982, 1987; Correa–Martínez, 2007; Restrepo, 2008; Rodríguez et al., 2005). Correa–Martínez (2007) indicates that mylonitic deformation is more intense towards the base, near the contact with amphibolites. Accessory chromian–spinel is equant to holly–leaf textured.

The rocks contain secondary minerals, which include tremolite, talc, chlorite, serpentine group minerals, magnetite, iddingsite and, locally, carbonates, that formed at various stages during the thermal evolution of the body. Serpentinization follows and crosscuts the primary foliation. Olivine is commonly replaced by lizardite–like serpentine (mesh texture) and masses of variably intersected sheet crystals of antigorite (Figure 3a), indicating mild deformation during serpentinization. Chrysotile and asbestoid aggregates occur in fractures, which also host garnierite (Restrepo, 2008). Serpentine group minerals occur associated with fine–grained magnetite and, locally, talc and carbonates, the latter more common in discordant veinlets that may contain serpentine and magnetite (Figure 3b). Chlorite is present as alteration haloes around chromian spinel altered to ferrian chromite/magnetite and as isolated grains/aggregates in the matrix associated with tremolite, talc, and serpentine.

Tremolite is fine–to–coarse grained. It is generally decussate (Figure 3a, 3c) but is locally oriented following post–high–

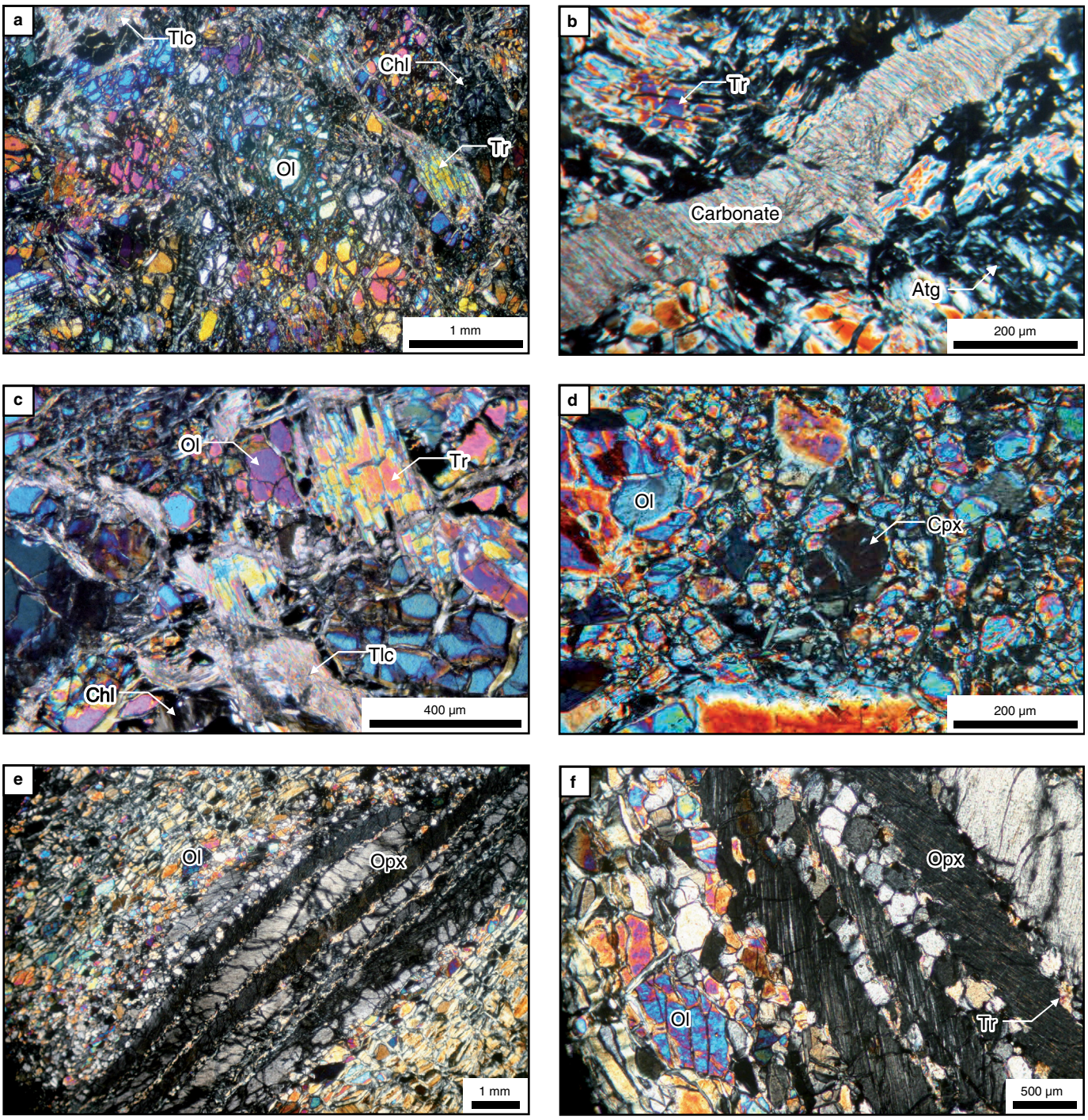

Figure 3. Optical images (cross–polarized light) of metaharzburgitic rocks. **(a)** Large mantle olivine grains (partly affected by late serpentinization) and tremolite. **(b)** Fine carbonate (magnesite?) vein in strongly serpentinized sample. **(c)** Tremolite + talc + olivine + chlorite in close association. **(d)** Relict(?) grain of clinopyroxene (refractive indexes oriented almost parallel to the polarizers in order to better see the exfoliation planes) in a matrix of olivine from a sample taken close to the base of the unit. **(e)** Large orthopyroxene porphyroclast showing kink bands and recrystalized grains in a matrix of deformed recrystallized olivine. **(f)** Detail of (e) showing clinopyroxene exsolutions (lamellae) within orthopyroxene and newly formed tremolite.

temperature fabrics. It locally occurs in aggregates (Figure 3a, 3c) and it forms intergrowths with neoformed olivine (Restrepo, 2008). A similar textural scenario applies to talc, which commonly occurs associated with tremolite (Figure 3c). However, replacement of tremolite by talc is not uncommon and late talc locally crosscuts serpentine, suggesting that talc formed at various stages along the metamorphic evolution.

Clinopyroxene is extremely rare. It occurs as distinct fine–grained crystals in the matrix (Figure 3d). González–Ospina (2016) indicated up to 4 mode % in samples B–1–A and LP–1

at vereda Chachafruto (Bello) and Medellín–Las Palmas road (Las Palmas), respectively. In all cases the identification has been made by means of optical microscopy, and chemical analyses are needed to allow classification, as far as subcalcic ("augitic") compositions are typical of primary mantle mineralogy while diopside would indicate metamorphic growth at low temperature. The clinopyroxene–bearing samples are moderately to highly serpentinized and show similar textures and all common minerals of "dunites", including olivine, chromian spinel, tremolite, talc, chlorite, and serpentine. This suggests that clinopyroxene may have formed part of the primary mantle assemblage, an inference anticipated by Restrepo (2008) based on the generalized presence of tremolite in "dunites".

To date, fresh orthopyroxene has been reported only in the Chupadero Creek locality (Restrepo, 2008). It amounts 10–15 modal % (Restrepo, 2008); similar amount is reported by Correa–Martínez (2007) and occurs as porphyroclasts up to 12 mm long that show exsolution lamellae of clinopyroxene and intense ductile and cataclastic deformation parallel to the main foliation with development of undulose extinction, kink bands, subgrains and grain recovery (Figure 3e, 3f). The groundmass is made of fine– to medium–grained recrystallized olivine indicating similar intense deformation and recrystallization. The extent of medium temperature metamorphic imprint is mild but, importantly, tremolite grains formed at the rims of orthopyroxene and within deformed crystals with clinopyroxene exsolution lamellae (Figure 3f; Correa–Martínez, 2007). This is interpreted as a result of very limited fluid infiltration during tremolite growth after exsolution of clinopyroxene (see below), but it nonetheless indicates stability of the assemblage Ol–Opx–Tr at high temperature. In this regard, the widespread presence of tremolite in "dunites" can be explained, at least in part, if high–Ca orthopyroxene formed part of the rocks in significant amount, pointing to generalized non–dunitic composition of the body. If this holds true, the former presence of clinopyroxene can be anticipated, for high–Ca orthopyroxene is only possible if subcalcic augitic clinopyroxene forms part of the primary mineral assemblage (e.g., Lindsley, 1983). In fact, distinct fine– to medium–grained talc + tremolite aggregates and bastite (a very fine–grained mixture of, mostly, serpentine group minerals) occur in some rare samples where the former presence of orthopyroxene porphyroblast/clast is inferred, located in Chupadero Creek, San Pedro, and the southern part of the body (Figure 2d–f; Correa–Martínez, 2007; Restrepo, 2008). Except for the Tlc + Tr and bastite pseudomorphs, all other mineralogical and textural relations described above for "dunites" are observed in these samples, strengthening the view that "dunites" contained orthopyroxene previous to the Tr + Tlc + Ol metamorphic event. It follows that temperature (and fluid flow) was intense enough as to assure element mobility and widespread metamorphic recrystallization during the Tr + Tlc + Ol event in order to completely erase orthopyroxene porphyroclast–replacement textures in common "dunites".

Nevertheless, dunite bands several centimetres in thickness are locally present (Correa–Martínez, 2007). This type of rock is clearly distinct from common "dunites". In addition to trace amounts of spinel, tremolite, talc, and sulfides, it is made almost exclusively of variably serpentinized coarse–grained flattened olivine (98–99 mode %) that shows significant recovery with common triple junctions (Correa–Martínez, 2007).

The varied mineralogical nature of blastesis and replacement events mentioned above indicates contrasted P–T–hydration/carbonation conditions. Our observations suggest the following general textural sequence of metamorphic imprint (with or without associated deformation) Ol + Opx + Tr (only locally preserved) > Ol + Tr + Tlc + Chl > Tlc + Atg/Lz + Chl > Atg/Lz + Chl > Tlc/carbonates (though carbonates may have formed during much of the metamorphic/metasomatic imprint), implying cooling from high–T mantle conditions. This sequence can be simplified in two distinct thermal + hydration events, one characterized by generalized Tr + Tlc + Ol (containing newly formed olivine) at medium to high temperature, as indicated by the widespread occurrence of this assemblage in the body, followed by generalized partial serpentinization to variable extent (except in some serpentinites sensu stricto lacking olivine) which locally includes talc–forming events. These observations agree with descriptions and interpretations by Restrepo (2008). This author concurs with the idea that at least part of olivine recrystallized during amphibolite–facies metamorphic imprint at temperature likely higher than 670 ºC. Restrepo (2008) included tremolite and anthophyllite in his argument. However, even if the anthophyllite–bearing Media Luna metaultramafic rocks forms a distinct body, the high temperature of the Tr + Tlc + Ol event is warranted, as will be discussed below (see section 7.1).

4. Geochemical and Algebraic Methods

We will follow here a bulk–rock major element geochemical approach. Whole–rock composition are taken from the literature (Figure 1; Table 1; Álvarez, 1987; Botero, 1963; González–Ospina, 2016; Hernández–González, 2014; Pereira et al., 2006; Restrepo, 2008; Rodríguez et al., 2005). Of the 6 analyses presented by Restrepo (2008) we have considered only samples JJ1296–B (Las Palmas) and JJ1422–B (Chupadero Creek, with relict orthopyroxene) and have excluded other samples because they were taken from bodies that may not form part of the main Medellín body (e.g., Media Luna; Figure 1). For the same reason, we have excluded sample 724A of Botero (1963). In addition, we also use unpublished data of Ana María CORREA–MARTÍNEZ obtained during her PhD thesis and published here for the first time (Figure 1; Table 1). These samples were analyzed at the ACME Laboratory, Canada by means of inductively coupled plasma optical emission spectrometry

Table 1. Whole–rock composition of samples from the Medellín Metaharzburgitic Unit.

Sample	SiO_2	TiO_2	Al_2O_3	Cr_2O_3	FeO*	MnO	MgO	CaO	Na_2O	K_2O	P_2O_5	LOI**	Total	Publication
AC52A	39.40	0.00	0.91	0.09	6.87	0.10	42.75	0.70	0.03	0.00	0.00	7.70	98.55	This study
AC52B	33.54	0.00	0.53	0.12	7.46	0.10	43.99	0.05	0.01	0.00	0.00	12.40	98.20	This study
AC59B	39.44	0.00	0.80	0.09	7.01	0.11	37.80	0.69	0.02	0.00	0.00	12.70	98.66	This study
AC35A	40.00	0.02	1.29	0.08	7.16	0.11	42.50	1.13	0.02	0.00	0.00	6.10	98.41	This study
650–A	38.56	0.01	2.81		6.61	0.03	40.97	0.61	0.47	0.01		8.76	98.84	Botero (1963)
665–A	45.14	0.01	8.90		6.91	0.02	30.61	1.75	0.41	0.01		9.01	102.77	Botero (1963)
166960	39.82	0.00	0.76	0.21	8.14	0.13	42.75	1.13	0.02	0.00		4.91	97.87	Álvarez (1987)
166961	38.05	0.00	0.76	0.26	7.37	0.10	39.30	1.69	0.01	0.00		10.51	98.05	Álvarez (1987)
166962	39.74	0.00	0.81	0.27	7.91	0.10	39.71	1.69	0.03	0.00		8.26	98.52	Álvarez (1987)
166965	36.26	0.00	0.64	0.10	9.54	0.14	42.55	1.69	0.02	0.00		7.07	98.01	Álvarez (1987)
166966	38.60	0.00	0.64	0.34	7.63	0.10	38.09	2.25	0.04	0.00		10.63	98.32	Álvarez (1987)
166967	34.62	0.00	1.19	0.12	8.59	0.13	42.14	1.13	0.01	0.00		10.39	98.32	Álvarez (1987)
166968	35.30	0.00	0.21	0.07	8.70	0.12	45.18	0.56	0.01	0.00		7.60	97.76	Álvarez (1987)
166970	35.90	0.00	0.53	0.17	7.22	0.13	42.35	0.84	0.01	0.00		10.78	97.93	Álvarez (1987)
166971	38.54	0.00	1.30	0.26	7.30	0.10	41.53	0.84	0.01	0.00		8.71	98.59	Álvarez (1987)
166972	38.46	0.00	0.32	0.16	7.90	0.10	38.50	1.13	0.02	0.00		11.36	97.94	Álvarez (1987)
166973	37.32	0.00	0.10	0.26	7.12	0.10	40.12	1.69	0.04	0.00		11.28	98.02	Álvarez (1987)
174567	30.12	0.00	9.25	0.19	13.47	0.13	30.00	4.90	0.35	0.02		7.00	95.43	Álvarez (1987)
174569	31.06	0.00	4.06	0.29	10.17	0.09	43.74	0.08	0.01	0.01		9.36	98.87	Álvarez (1987)
174572	32.82	0.00	7.31	0.45	9.98	0.10	38.61	0.01	0.01	0.01		8.93	98.23	Álvarez (1987)
705612	35.60	0.02	0.29	0.28	7.77	0.12	45.27	0.11	0.26	0.03		9.68	99.43	Rodríguez et al. (2005)
705731	40.70	0.03	0.62	0.32	7.88	0.12	42.40	0.56	0.20	0.02		6.37	99.21	Rodríguez et al. (2005)
705535	40.40	0.01	0.60	0.13	7.66	0.12	42.48	0.71	0.08	0.02		6.71	98.93	Rodríguez et al. (2005)
705544	40.20	0.03	1.25	0.36	7.53	0.09	38.51	0.04	0.09	0.02		11.13	99.25	Rodríguez et al. (2005)
705730	40.30	0.02	0.74	0.26	8.08	0.10	39.65	0.04	0.03	0.01		9.74	98.98	Rodríguez et al. (2005)
705570	36.10	0.02	0.04	0.09	8.32	0.12	43.92	0.36	0.08	0.02		9.28	98.35	Rodríguez et al. (2005)
705574	38.80	0.02	0.75	0.17	7.23	0.11	42.53	0.77	0.11	0.01		8.56	99.06	Rodríguez et al. (2005)
705576	39.10	0.03	0.71	0.17	7.77	0.11	43.49	0.83	0.09	0.01		6.46	98.78	Rodríguez et al. (2005)
705584	40.70	0.02	1.48	0.23	7.46	0.11	39.15	2.94	0.17	0.02		7.36	99.64	Rodríguez et al. (2005)
705590	37.70	0.04	0.94	0.23	7.60	0.15	41.48	0.57	0.06	0.01		10.55	99.32	Rodríguez et al. (2005)
705602	38.80	0.02	0.49	0.15	6.87	0.10	44.02	0.40	0.06	0.01		7.96	98.88	Rodríguez et al. (2005)
705603	38.50	0.02	0.60	0.18	7.71	0.11	42.02	0.77	0.06	0.01		9.26	99.24	Rodríguez et al. (2005)
Of–10	34.96	0.08	2.24	0.34	9.29	0.15	42.23	0.08	0.20	0.03		9.92	99.52	Pereira et al. (2006)
Of–10A	36.91	0.04	0.79	0.11	9.03	0.13	43.26	0.32	0.20	0.03		8.60	99.42	Pereira et al. (2006)
JJ1296–B	40.91	0.02	1.20	0.35	6.57	0.11	38.95	2.21	0.14	0.07		9.24	99.77	Restrepo (2008)
JJ1422–B	38.85	0.02	1.06	0.29	7.31	0.11	40.13	0.95	0.07	0.02		11.20	100.01	Restrepo (2008)
SP–001	38.93	0.04	0.77	0.23	6.82	0.12	39.92	0.53				11.29	98.64	Hernández–González (2014)
LP–7	31.18	0.30	5.27	0.22	9.72	0.12	37.20	0.07				9.79	93.86	Hernández–González (2014)
LP–4	40.60	0.06	0.96	1.87	7.22	0.12	40.36	0.74				8.63	100.55	Hernández–González (2014)
LP–1	39.59	0.02	0.84	0.33	7.75	0.13	41.20	0.57				8.17	98.59	Hernández–González (2014)
B–1–A	42.86		1.17	0.29	10.82	0.14	33.65	1.03	0.04			8.77	98.78	González–Ospina (2016)
G–1–A	43.11		0.42	0.38	6.87	0.14	39.97	0.34				7.96	99.20	González–Ospina (2016)
G–1–C	42.48		0.98	0.43	7.24	0.12	43.34	1.44				3.10	99.14	González–Ospina (2016)
LP2–A	41.75		0.66	0.36	11.61	0.13	40.67	0.42				3.06	98.66	González–Ospina (2016)
SH–1–(A)–A	42.10		1.15	0.41	6.96	0.13	42.45	1.50				4.50	99.19	González–Ospina (2016)
SH–1–(A)–B	42.36	0.02	0.96	0.47	7.74	0.14	43.34	0.31				3.79	99.13	González–Ospina (2016)
SH–1–(B)–B	43.04	0.04	1.41	0.47	7.22	0.12	41.07	0.71				5.14	99.22	González–Ospina (2016)
SH–1–(B)–C	42.13		0.92	0.43	7.43	0.14	42.96	1.66	0.02			3.43	99.13	González–Ospina (2016)
SP–2–A	42.62	0.02	1.17	0.36	12.81	0.14	40.55	0.57				2.03	100.28	González–Ospina (2016)

Source: Samples labels and analyses of Álvarez (1987) were taken from Rodríguez et al. (2005).

* Total Fe expressed as FeO.

** LOI—Loss on ignition.

(ICP–OES) using a Jarrel Ash Atomcomp model 975. Because of the lack of chemical analyses, other types of rock, such as wehrlite and ultramafic dikes described by Correa–Martínez (2007), are not considered. The total number of analyzed samples considered here is 49. In all cases, iron is treated as Fe^{2+}_{total}. Mass loss on ignition (LOI) is treated as H_2O, though, as described in the original papers and discussed below, part of the measurements should be considered CO_2 since carbonates are present in (at least some of) the analyzed samples. The amount of analyzed H_2O/LOI ranges between 2.03 and 12.70 wt %. Taking into account that a fully serpentinized peridotite yields ca. 12–13 wt % H_2O, these values indicate variable extent of serpentinization (± carbonation).

In order to give each sample its proper name following the IUGS classification scheme, petrographic amounts of high T mantle minerals must be measured (e.g., Le Bas & Streckeisen, 1991; Le Maitre, 2002). However, because metamorphism and serpentinization (± carbonation) have commonly replaced pyroxene(s) and only olivine is generally present, the application of this petrographic scheme leads to the conclusion that the rocks are dunitic. But the metamorphic mineralogy of the samples indicates that, by no means, all samples are dunitic, for talc and tremolite cannot form in a dunite in such a high amount (up to 20 modal % summing–up both phases) as recorded in many samples. A similar conclusion was reached by Correa–Martínez (2007) after recognizing the presence of bastite (alteration of orthopyroxene).

However, it is important to quantitatively assess the high–T mantle mineralogy of the geological body in order to show whether it is dunitic or not. A geochemical method that allows applying such a classification scheme to altered samples, and that offers insight into the nature of alteration, involves algebraic mapping of the bulk rock compositions in transformed n–dimensional composition spaces defined ad hoc for the problem under consideration (see, for example, Spear et al., 1982; Thompson, 1982; Torres–Roldán et al., 2000). In this task, components are generally expressed in molar units, for wt % units depend on the molar weight of components rather than on true atomic/molecular abundance. However, oxy–equivalent (gram–oxygen) units are in particular convenient for reconstructing mineralogical composition, since this measure of component abundance has the advantage of being an estimate of the volume of solids in which oxygen is the only major anion (Brady & Stout, 1980; Thompson, 1982). The general composition space considered here is 9–dimensional, as defined by the chemical components SiO_2–TiO_2–Al_2O_3–Cr_2O_3–FeO–MnO–MgO–CaO–H_2O (Na_2O, K_2O, and P_2O_5 are neglected due to their low amounts in the samples considered; note, also, that because independent Fe_2O_3 and FeO estimates are known for only a few samples, they are not considered as independent components and total iron is expressed as FeO). The definition of the new set of 9 chemical species is flexible, but we will concentrate on new system components that allow obtaining meaningful graphical representations. These are obtained after projection onto selected (hyper–) planes of the 9–dimensional composition space from particular phases (minerals and fluids) and along mathematical operators (simple and coupled exchange vectors) that allow condensation of the composition space. This is convenient for visualization of the whole 9–dimensional chemical system in appropriate diagrams, though the information contained in the new components that are affected by the exchange vectors is complex and, in cases, not straight forward (see below for clarification).

The procedure followed here makes use of barycentric, rather than Cartesian, coordinates, because the focus is put in component/mineral proportions rather than absolute abundances. The projected barycentric diagrams have the advantage of considering all 9 variables at a time. In this regard, this method supersedes binary Cartesian diagrams relating the absolute amount of components (e.g., the Harker diagrams of Figure 4) or component ratios (e.g., the MgO/SiO_2 – Al_2O_3/SiO_2 diagram of Figure 5) where only 2 or 4 chemical components, respectively, are considered while all other components are neglected. We have performed the corresponding calculations and 3D and 2D projections using software CSpace (Torres–Roldán et al., 2000), that makes use of the singular value decomposition technique for solving linear equations (Fisher, 1989, 1993).

Appropriate diagrams for describing ultramafic compositions correspond to the 3D CaO–MgO–Al_2O_3–SiO_2 (CMAS) and 2D CaO–MgO–SiO_2 (CMS) molar plots and the 3D Ol–Opx–Cpx–Spl and 2D Ol–Opx–Cpx oxy–equivalent plots, all projected from the phases and exchange vectors indicated in Figures 6–12. Figure 10 (Ol–Opx–Cpx oxy–equivalent plot, projected from spinel) shows the reconstructed high–T mantle mineral composition of the studied samples in the petrographic classification scheme of ultramafic rocks by Le Maitre (2002). Figure 12 (Ol–Opx–Cpx oxy–equivalent plot, projected from chlorite) shows the phase relations appropriate for the Tr + Tlc + Ol metamorphic event.

In restoring of the mineralogy of metamorphic/serpentinized ultramafic rocks at high–T mantle conditions, H_2O component can be dropped from consideration in the manipulation of the composition space, as long as H_2O content at high–T subsolidus conditions adjacent to the site of generation of oceanic lithospheric mantle can be effectively considered 0. However, this does not hold true during cooling at mantle conditions in the oceanic realm, when H_2O infiltrates the rocks and causes growth of hydrated minerals. For this reason, and in order to evaluate the effects of metamorphism/alteration, component H_2O is considered and hydrated minerals such as tremolite, talc, anthophyllite, antigorite/lizardite, brucite, and clinohumite are projected in the molar and oxy–equivalent diagrams. On the other hand, because of the lack of CO_2 estima-

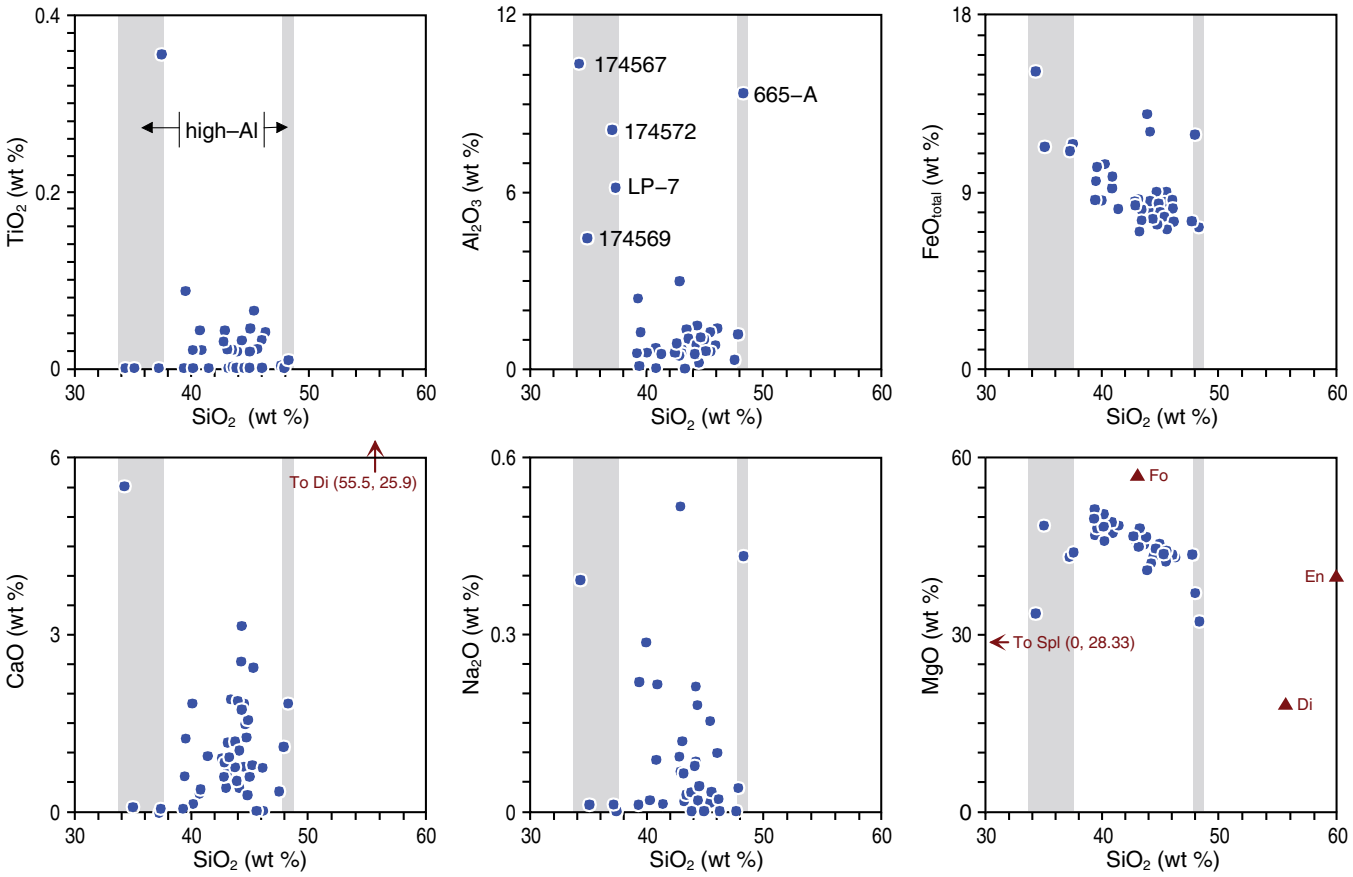

Figure 4. Harker diagrams for the Medellín Metaharzburgitic Unit (anhydrous basis). Samples with high Al_2O_3 are labeled in the SiO_2 versus Al_2O_3 diagram and indicated with grey bands in the rest of the diagrams for reference. Also for reference, the projection of forsterite, enstatite, diopside, and spinel is indicated.

tions in the studied samples, carbonates cannot be projected. However, they are plotted as if they were CO_2–free chemical species (for this reason the labels appear within brackets). In spite of this deficiency, the consideration of these species in the diagrams is valuable because it allows evaluation of the effects of carbonation.

Further details of the procedure followed for each diagram are described below when required.

5. General Geochemical Features of the Medellín Metaharzburgitic Unit

On anhydrous basis (Figure 4), the compositional range of the Medellín Metaharzburgitic Unit is 34.13–48.14 wt % SiO_2, 0.00–0.36 wt % TiO_2, 0.05–10.48 wt % Al_2O_3, 7.28–15.26 wt % $FeO_{(total)}$, 0.02–0.17 wt % MnO, 32.65–51.34 wt % MgO, 0.01–5.55 wt % CaO, 0.01–0.52 wt % Na_2O, 0.00–0.08 wt % K_2O, 0.00 wt % P_2O_5. The amount of Cr ranges between 500 and 12 770 ppm and Mg# (molar MgO/(MgO + FeO)) ranges between 0.80 and 0.92. It is obvious that some samples are problematic in terms of comparison with "normal" peridotite composition, particularly in terms of Al_2O_3 contents above 4 wt % (Figure 4).

Five samples are clear outliers: samples 174569, 174572, and 174567 from Álvarez (1987) yielded 4.55, 8.23, and 10.48 wt % Al_2O_3, respectively, sample LP–7 from Hernández–González (2014) yielded 6.28, and sample 665–A from Botero (1963) yielded 9.49 wt % Al_2O_3. Sample LP–7, taken from the Medellín–airport road (Las Palmas region) is rich in olivine and relatively rich in chromian spinel (>5%, totally altered to ferrian–chromite/magnetite and chlorite) and in Fe–Ni–Cu–sulfides and Ni–Fe arsenides and sulfoarsenides (Hernández–González, 2014). This author classifies the rock as a dunite. Álvarez (1987) identified the high–Al contents of some of his samples and considered it the result of metasomatism, but did not go further in the problem. Botero (1963) does not comment on the issue. Nevertheless, even if all these samples clearly are not of peridotite composition, they will be considered below.

On the other hand, samples with relatively high MgO and low SiO_2 within the group of seemingly normal peridotitic composition compare with dunitic (sensu lato) compositions, but samples with relatively high SiO_2, Al_2O_3, and CaO, and relatively low MgO, suggest instead non–dunitic compositions (Figure 4).

A complementary geochemical view of the samples can be gained by means of inspecting chemical ratios rather than abso-

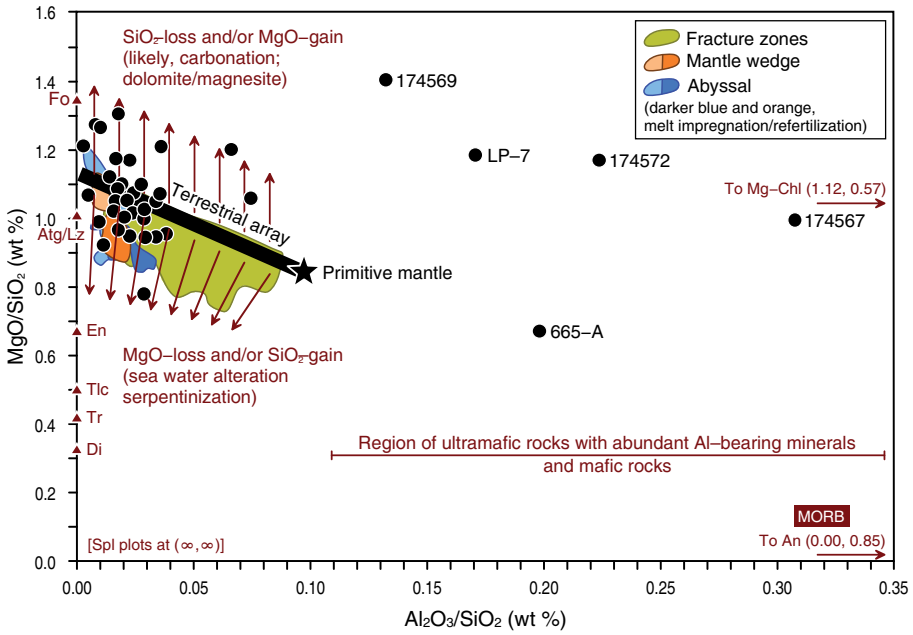

Figure 5. MgO/SiO_2 (wt %) versus Al_2O_3/SiO_2 (wt %) diagram for the Medellín Metaharzburgitic Unit. The samples indicated with labels correspond to Al–rich non–peridotite compositions of Botero (1963), Álvarez (1987), and Hernández–González (2014) indicated in Figure 4. The terrestrial array of mantle peridotites is after Jagoutz et al. (1979) and Hart & Zindler (1986) and primitive mantle (PM) is from McDonough & Sun (1995). Samples of serpentinite/hydrated peridotite derived from harzburgite from abyssal (Paulick et al., 2006), mantle wedge (Kodolányi et al., 2012; Pearce et al., 2000), and oceanic fracture zone (Chen et al., 2015; Niu, 2004; Pearce et al., 2000) settings are plotted for comparison. Mg–end members of phases of interest, anorthite, and the region of MORB are also indicated (note that spinel plots at infinity).

lute component concentrations. In terms of major element composition, perhaps the most widely used and informative plot is the MgO/SiO_2 (wt %) versus Al_2O_3/SiO_2 (wt %) diagram of Figure 5. In this diagram many samples plot close to the so–called "terrestrial array", defined by the composition of unaltered mantle peridotites with $Al_2O_3/SiO_2 < 0.1$ (Hart & Zindler, 1986; Jagoutz et al., 1979). These samples should be considered essentially unaltered peridotites that are strongly depleted relative to the composition of the primitive mantle, suggesting one or more partial melting and melt extraction events (Restrepo, 2008). To be noted is that, in terms of major elements, these samples are similar in composition to both drilled/dredged samples of mantle wedge and abyssal harzburgites worldwide (Figure 5).

However, the scattering of "normal" peridotitic samples with $Al_2O_3/SiO_2 < 0.1$ in terms of MgO/SiO_2 is noticeable, suggesting that metasomatic processes related to magmatic percolation/impregnation/refertilization and/or seawater alteration/serpentinization and/or carbonation have largely transformed the original mantle bulk compositions. Among this group of samples, those with lower MgO/SiO_2 were most likely affected by seawater alteration/serpentinization, which typically involves MgO–loss (by dissolution of brucite as a result of low–temperature alteration/weathering; e.g., Boschi et al., 2017; Milliken et al., 1996; Niu, 2004; Snow & Dick, 1995; and references therein) and/or SiO_2–gain (due reaction with fluids containing aqueous silica during serpentinization at high fluid/rock ratios; e.g., Bonnemains et al., 2017; Malvoisin, 2015; and references therein). However, pre–alteration magmatic impregnation/refertilization cannot be ruled out (Figure 5; Kodolányi et al., 2012; Paulick et al., 2006; Pearce et al., 2000).

On the other hand, the samples within this group of $Al_2O_3/SiO_2 < 0.1$ that plot above the terrestrial array indicate SiO_2–loss and/or MgO–gain, which can hardly be related to early magmatic impregnation and late serpentinization processes. Carbonation, however, can potentially explain these geochemical characteristics, as long as precipitation of magnesite and/or dolomite (and/or hydrous Mg–carbonates) increases the MgO/SiO_2 ratio and does not affect Al_2O_3/SiO_2. The presence of carbonates is generally indicated in papers dealing with the Medellín Metaharzburgitic Unit though, to our knowledge, its nature (calcite and/or dolomite and/or magnesite and/or hydrous carbonates) has not being reported except for microscopic to macroscopic veins of calcite reported by Rodríguez et al. (2005) and small magnesite stockworks in Niquía mentioned by Correa–Martínez (2007). However, one of us (Jorge Julián RESTREPO) has collected altered samples with typical clayey magnesite. Therefore, it appears that, at least magnesite, is present in the unit, as otherwise would be expected in serpentinized and metamorphic metaultramafic rocks (e.g., Evans, 1977; O'Hanley, 1996; Trommsdorff & Connolly, 1990). In order to assess the original geochemical composition

of carbonate–bearing samples, the bulk compositions should be restored substracting the amount of CaO and MgO "stored" in dolomite/calcite and magnesite/dolomite, respectively (± hydrous carbonates). However, because CO_2 has not been analyzed and the nature of the carbonates present has not been identified in the studied samples, the restoration of bulk compositions of the potentially carbonated samples with high MgO/SiO_2 cannot be carried out.

Finally, the MgO/SiO_2 (wt %) versus Al_2O_3/SiO_2 (wt %) diagram of Figure 5 shows that some samples of Botero (1963), Álvarez (1987), and Hernández–González (2014) have non–peridotitic compositions ($Al_2O_3/SiO_2 > 0.1$) that can hardly be interpreted as a result of metasomatism/alteration during serpentinization/sea water alteration or carbonation. Their large amount in Al_2O_3 (Figure 4) points to either a non–peridotitic sensu stricto composition likely rich in spinel (e.g., LP–7 from Hernández–González, 2014) and/or the presence of plagioclase.

In spite of metasomatic alterations and (local) presence of non–peridotitic compositions, such a varied geochemistry illustrated in Figures 4, 5 points to a varied mineralogy of the high–T mantle protoliths, rather than to a simple dunitic composition of the Medellín Metaharzburgitic Unit. An attempt to "restore" the high–T mantle mineralogy of the Medellín Metaharzburgitic Unit is presented below.

6. The Restored High–T Mantle Mineralogy of the Medellín Metaharzburgitic Unit

6.1. The CMAS Diagram

The bulk rock compositions are first mapped in the 9–dimensional composition space defined by the new components SiO_2, Al_2O_3, MgO, CaO, $TiO_2MgO(Al_2O_3)_{-1}$, $Cr_2O_3(Al_2O_3)_{-1}$, $FeO(MgO)_{-1}$, $MnO(MgO)_{-1}$, and pure H_2O–fluid expressed in molar units. This procedure allows projection onto the SiO_2, Al_2O_3, MgO, and CaO tetrahedron along simple and coupled exchange vectors, resulting in *condensation* of the composition space. Note that the information contained in the new components CaO, MgO, Al_2O_3, and SiO_2 that are affected by the exchange vectors do not correspond to that of the original components. For this reason, the new components are termed C, M, A, and S, and the resulting diagram is termed CMAS. Also note that in this particular case CaO and SiO_2 are not affected by the projection (i.e., exchange vectors do not add extra components to these components), but M and A represent in fact new complex components, i.e., MgO + MnO + FeO–TiO_2 and Al_2O_3 + Cr_2O_3 + TiO_2 (old variables), respectively. This procedure is justified because Mg–Mn–Fe and Al–Cr are exchanged in all mineral structures considered (i.e., Cpx, Opx, Tr, Ol, Tlc, etc.), following the indicated simple exchange vectors, while Ti + Mg exchanges with 2Al (coupled exchange vector) in the structure of spinel. Note that not only Al and Mg are involved in the latter exchange, but also Cr, Fe, and Mn as long as the vectors $Cr_2O_3(Al_2O_3)_{-1}$, $FeO(MgO)_{-1}$, and $MnO(MgO)_{-1}$ are considered. For this reason, the Ti–spinel exchange vector ($TiO_2MgO(Al_2O_3)_{-1}$) accounts, in fact, for a complex exchange vector ($TiO_2(Fe,Mn,Mg)O((Al,Cr)_2O_3)_{-1}$) that includes all significant potential compositional variations of Fe^{3+}–free spinel. This implies that projected spinel corresponds to a mixture of Cr–, Mg–, Fe–, Mn– and Ti–spinel end–members, including, ulvospinel, and chromite. The same concept applies to other phases, namely olivine (forsterite–fayalite), orthopyroxene (enstatite–ferrosilite and Al–Cr–Ti–end–members), and all other phases projected except quartz and anorthite.

The resulting tetrahedral CMAS diagram is presented in Figure 6. The space defined by the Ol–Opx–Cpx–Spl tie–tetrahedron (in white) marks the locus of Spl–bearing anhydrous ultramafic rocks. The high–A samples (labeled in Figure 6) correspond to the samples with Al–rich non–peridotitic composition indicated in Figure 5. A group of low–A samples plots within the Ol–Opx–Cpx–Spl tie–tetrahedron comparable to "normal" peridotitic compositions. However, another group plots outside it, away from the Opx apex, which is obviously not permitted in pristine Spl–bearing anhydrous peridotitic compositions. This latter group of samples (labeled in Figure 6) roughly corresponds to samples with MgO/SiO_2 higher than the terrestrial array in Figure 5.

6.2. The CMS Diagram Projected from Spinel

Details in a 3D diagram are not easily appreciated. For this reason, it is convenient to reduce the dimension of the diagram in order to generate a 2D triangular representation. This can be accomplished projecting form a given phase, in this case spinel, onto the CMS plane. This is done in Figure 7 and implies recasting sample compositions in a 9–dimensional new set of components including spinel ($MgAl_2O_4$) instead of Al_2O_3 (all other components used above to generate the CMAS diagram are retained). Note that the use of exchange vectors applies as above, so that the new components M and A do not represent exclusively old components MgO and Al_2O_3 and projection phase spinel and projected phases correspond to a mixture of Cr–, Mg–, Fe–, Mn–, and Ti end–members.

Projection from spinel implicitly requires that the rock samples plotted in the diagram contain this phase. If this is not so, the conclusions reached are flawed. This may (or may not) apply to the Al–rich samples of the data base. All other samples, however, are expected to be Spl–bearing at high–T mantle conditions, as recorded by relict spinel and newly formed ferrian–chromite and magnetite (e.g., Correa–Martínez, 2007; Hernández–González, 2014; Proenza et al., 2004). Hence, the space defined by the Ol–Opx–Cpx tie–triangle (white in Figure 7) marks the locus

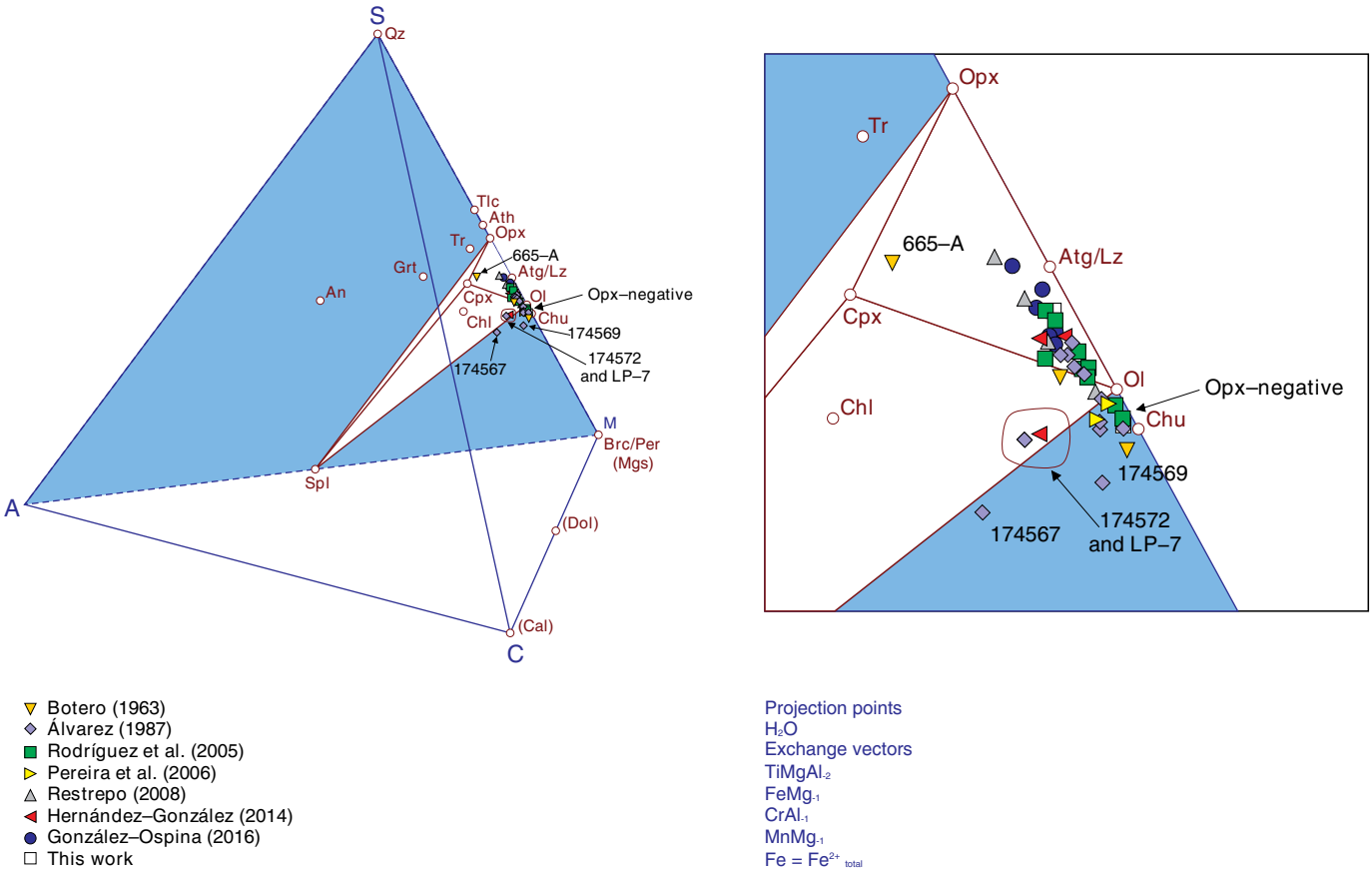

Figure 6. Samples of the Medellín Metaharzburgitic Unit plotted in the CMAS diagram. Note that projection from H_2O is not needed to illustrate the phase relations at high mantle temperature (Ol–Opx–Cpx–Spl tetrahedron), but it has been done so for convenience in order to represent the locus of hydrated phases produced during the Tr + Tlc + Ol metamorphic and late serpentinization events. Also, carbonates are indicated between brackets as far as CO_2 contents are not available for the studied samples and, hence, this component is not considered in the transformation of coordinates. The labeled samples correspond to the non–peridotite compositions indicated in Figures 4, 5. See text for further explanation.

of Spl–bearing anhydrous ultramafic rocks. This diagram more clearly depicts the distribution of rocks. Samples rich in Al (labeled) are no longer commented, for they are not of normal peridotitic composition. The rest of samples distribute across the Ol–Cpx tie–line, indicating that some samples bear "negative" calculated orthopyroxene (see below and Figures 8–10). Clearly, these samples are affected by SiO_2–loss and/or MgO–(± FeO ± MnO)–gain. Lines are drawn that describe the expected chemical behavior in case of addition of carbonates. The results point to addition of magnesite rather than dolomite or calcite. Only Al–rich non–peridotitic sample 174567 may have been affected by dolomite addition, though this conclusion is uncertain as far as it relies in the unknown presence of spinel in this sample.

6.3. The Ol–Opx–Cpx–Spl Diagram and Ol–Opx–Cpx Diagram Projected from Spinel

The bulk compositions of the samples can be recasted to directly reflect their high–T mantle mineralogy. This is done defining four new components, Fo, En, Di, Spl that, together with the exchange vectors used for the construction of the CMAS and CMS diagrams, represent in fact Ol, Opx, Cpx, and Spl solid solutions. However, instead of following the common practice of defining these components with molecular formulas based on 4, 3 (or 6), 6, and 4 oxygens, respectively (e.g., Putirka et al., 2011), it is more convenient to define all four chemical species as having the same number of oxygens (no matter what the number). As justified above (see section 4), this allows a better approximation of calculated mineral abundance to real mineral volume proportions. For this particular case, the calculated molar and oxy–equivalent contents of Ol, Opx, Cpx, and Spl are similar, for they have similar oxygen content in their molecular formulas. However, this is not the case if species with contrasted oxygen contents are used (e.g., amounts of SiO_2–quartz– versus $KAlSi_3O_8$ –orthoclase– in granites). This and the use of an appropriate set of projection phases and exchange vectors are important issues that should be seriously considered in classifying altered

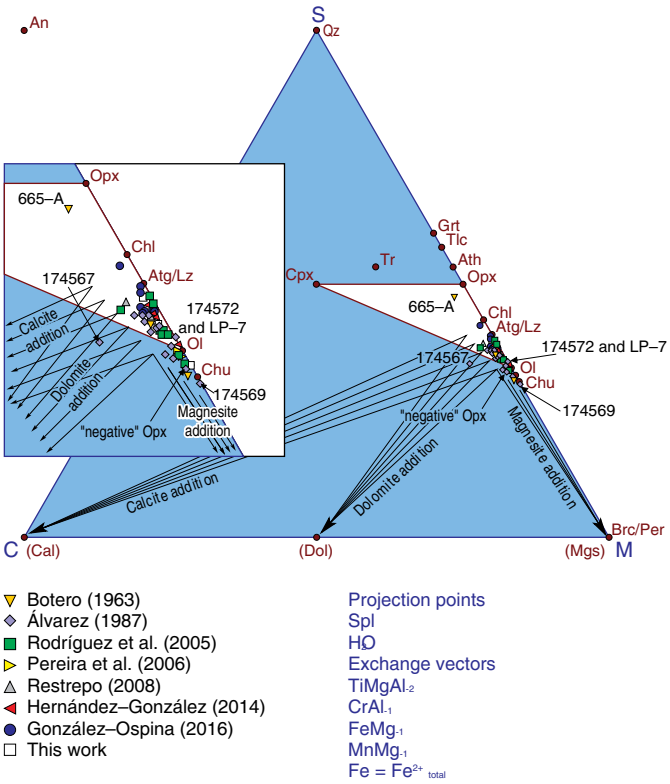

Figure 7. Samples of the Medellín Metaharzburgitic Unit plotted in the CMS diagram projected from spinel. Arrows indicate the expected geochemical behavior upon carbonation. See Figure 6 and text for further explanation.

rocks using modal–abundance diagrams (e.g., Streckeisen diagrams). Thus, while this procedure using oxy–equivalent units was followed by Cárdenas–Párraga et al. (2017) for serpentinites of Cuba, Blanco–Quintero et al. (2011), Putirka et al. (2011), and Hernández–González (2014) used molar rather than oxy–equivalent units of Ol, Opx, Cpx, and Spl.

The result of the described procedure in oxy–equivalent units is represented in the Ol–Opx–Cpx–Spl and Ol–Opx–Cpx diagrams of Figures 8–10, the latter two projected from spinel. All issues considered so far can be more clearly appreciated in these diagrams, including the outlier nature of Al–rich rocks, the projection of low–Al samples of non–normal peridotite composition outside the Ol–Opx–Cpx–Spl tie–tetrahedron and Ol–Opx–Cpx tie–triangle and the potential carbonation of these samples by means of addition of magnesite. However, two additional aspects illustrated in these figures are of interest. First, some of the samples within the group of normal peridotite composition are likely carbonated by means of addition of dolomite and/or calcite. This is indicated by the displacements towards the Ol–Cpx tie–line, which is more clearly appreciated in Figure 10 containing the modal classification scheme of Le Maitre (2002). In this classification scheme, potentially carbonated samples plot rather away from the harzburgite field and classify as lherzolite, an unlikely picture given the residual nature of the Medellín Metaharzburgitic Unit (Figure 5; Correa–Martínez, 2007).

A second point of major interest is that most samples of normal peridotite composition plot within the field of harzburgite, not dunite. Moreover, even if the lack of CO_2 analysis prevents the restoration of the composition of carbonated samples, it can be deduced that the samples that bear negative Opx (most likely affected by magnesite carbonation) and the samples that plot within the lherzolite field (potentially dolomite/calcite–carbonated) should probably have harzburgitic composition previous to carbonate alteration. Furthermore, at least some of the samples that properly plot within the harzburgite and dunite fields of Figure 10 are also likely affected by subtle carbonation. This implies that the original composition of these samples should plot displaced towards the Opx apex, and that samples that plot within the dunite field would, in fact, be of harzburgite composition. On the other hand, the bulk composition of the Cpx–bearing sample B–1–A of González–Ospina (2016) lies close to the harzburgite–lherzolite boundary, suggesting that clinopyroxene is a relict high–T phase (though metamorphic recrystallization/growth is also possible; see below). This suggests that many other samples may have contained clinopyroxene previous to metamorphism/serpentinization.

Another issue is that of samples plotting below the terrestrial array of mantle peridotites and that likely have undergone SiO_2–gain and/or MgO–loss during serpentinization (Figure 5). These samples correspond to those that plot closer to the Opx apex in Figures 8–10 within the harzburgite field. After eventual restoration of their composition previous to SiO_2–gain and/or MgO–loss these samples would plot closer to the olivine apex.

Therefore, if our inferences hold true, the pre–serpentinization and pre–carbonation scatter of samples would contract significantly within the Ol–Opx–Cpx diagram, and we speculate that most samples of the Medellín Metaharzburgitic Unit had a relatively restricted composition within the field of harzburgite, as indicated in Figure 10. This picture of the Medellín Metaharzburgitic Unit as being essentially composed of relatively restricted harzburgite composition is not to say, of course, that dunite and, eventually, lherzolite do not exist in the body. Though scarce, dunite is present as thin bands within harzburgite and as envelopes around chromitite bodies (Correa–Martínez, 2007; Hernández–González, 2014) and some samples may indeed contain enough clinopyroxene as to be termed lherzolite. But the amount of these rocks in the unit seems small. We consequently propose that the "Medellín Dunite" should no longer be termed "dunite", for it introduces major confusion in the description of this geologic body. The "Medellín Ultramafic Massif", as proposed by Correa–Martínez (2007), would more closely correspond to the presented evidence.

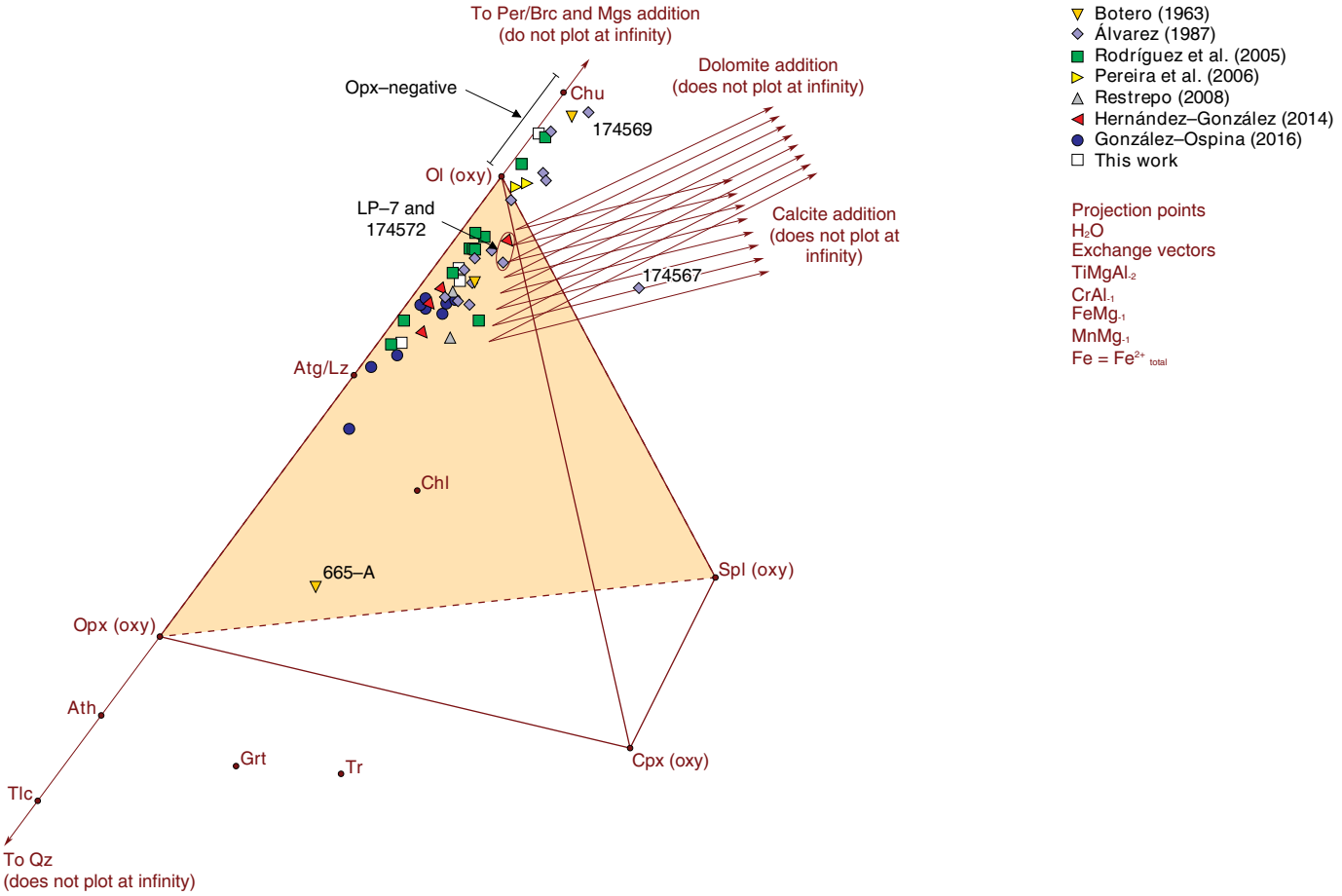

Figure 8. Samples of the Medellín Metaharzburgitic Unit plotted in the Ol–Opx–Cpx–Spl diagram in oxy–equivalent units. Arrows indicate the projection of quartz and brucite/periclase and the effects of carbonation. See Figure 6 and text for further explanation.

7. Altered or Metamorphosed Mantle? Another Key Terminological Issue

7.1. The Mineralogy of the Medellín Metaharzburgitic Unit during Medium–T Metamorphic Conditions

Dragged/drilled samples of present–day abyssal and forearc/backarc lithospheric sections show that shallow oceanic mantle undergoes cooling and hydration upon drift from spreading centers (e.g., Bach et al., 2006; Kimball et al., 1985). A variety of new hydrated minerals are hence developed during eventual influx of seawater along fractures. The most common transformation is serpentinization, which takes place at temperature lower than ca. 500 ºC down to ambient surface temperature. Full serpentinization of a harzburgitic composition made of Mg_2SiO_4 (Ol) and $MgSiO_3$ (Opx) in equimolar amounts needs up to 13 wt % H_2O, which translates into 28.6 mole % abundance (Figure 11a). Somewhat higher amounts of H_2O are needed if the molar olivine/orthopyroxene ratio is greater than 1, because brucite ($Mg(OH)_2$) is formed in addition to serpentine ($Mg_3Si_2O_5(OH)_4$), reaching up to 16.1 wt % H_2O for 100% Mg_2SiO_4 dunitic composition (which translates into 33.3 mole % H_2O; Figure 11a). Such a flux of external H_2O is not readily available to relatively large sections of the oceanic mantle, and full hydration is only generally reached at location of intense deformation, such as along transform faults/fracture zones, oceanic core–complex fault systems, and lithosphere bending–related faulting at subduction zones (Guillot et al., 2015 and references therein). Hence, most mantle sections are only partly serpentinized and, for this reason, such rocks are generally considered "serpentinized peridotite" or "hydrated peridotite", not serpentinites sensu stricto, in an attempt to emphasize the variable extent of alteration and, importantly, that the event has not fully transformed the protholith into a new rock.

It is to be noted that full serpentinization of peridotite allows H_2O to coexist with solid phases after consumption of high–T mantle minerals (e.g., Atg/Lz–Tlc–H_2O and Atg–Brc–H_2O assemblages colored in blue in Figure 11a), while partial serpentinization does not. In this case, reactions triggered by fluid infiltration consume all H_2O and produce stable assemblages

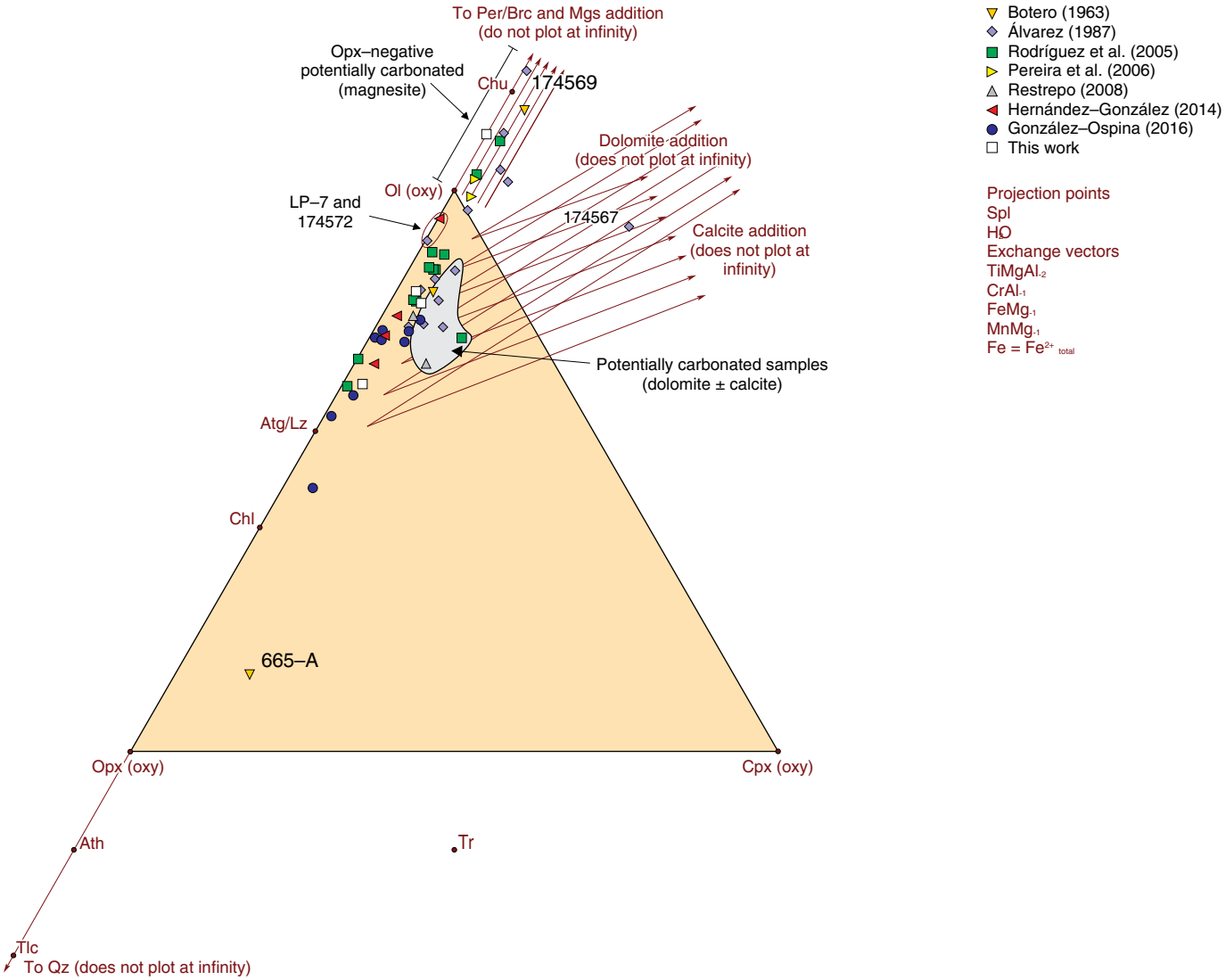

Figure 9. Samples of the Medellín Metaharzburgitic Unit plotted in the Ol–Opx–Cpx projected from spinel in oxy–equivalent units. Note the area of potentially carbonated (dolomite and/or calcite addition) samples within the group of samples of normal peridotite composition. See Figures 6, 8, and text for further explanation.

made only of solids including those stable at high temperature (e.g., Atg/Lz–Brc–Ol, Atg/Lz–Tlc–Ol, and Tlc–Ol–Opx in the orange region of Figure 11a). In complex natural chemical systems, however, the equilibrium composition of these minerals differs at high– and low–T conditions, but the chemical differences can be subtle (e.g., Mg/(Mg + Fe) and Ni contents in olivine, Ca contents in orthopyroxene) or large (e.g., Al content in orthopyroxene, Al, Ca, and Na content in clinopyroxene). Coupled with the low temperature of transformation, that hampers reaction kinetics and intra–crystalline diffusion, this fact explains the relict presence of high–T mantle mineral composition in partially serpentinized rocks.

A quite different scenario occurs when the temperature of shallow oceanic mantle is higher than 500 ºC, above the stability field of antigorite. At these conditions, hydration reactions trigger the formation of other minerals, such as tremolite and talc, which bear much less H_2O (ca. 2 and ca. 4.5 wt %, respectively) than serpentine–group minerals and brucite. The lack of the latter minerals in peridotitic compositions at intermediate temperature conditions allows topological relations that make the maximum hydration of peridotite to involve less than 10 mole % H_2O (i.e., less than 1/3 of the amount needed for full serpentinization). Typically, the amount of H_2O needed for saturation (full hydration) in the simple $MgO–SiO_2–H_2O$ system is less than 5 and close to 0 mole % in harzburgitic and dunitic compositions, respectively (Figure 11b). Hence, during cooling and hydration of shallow oceanic mantle at temperature higher than the stability field of antigorite, the amount of H_2O needed to fully saturate a peridotite rock and to transform it into a new fully hydrated metamorphic rock is much less than the amount needed at conditions of serpentinization. In short, a new fully hydrated rock is more easily formed at intermediate (and high)

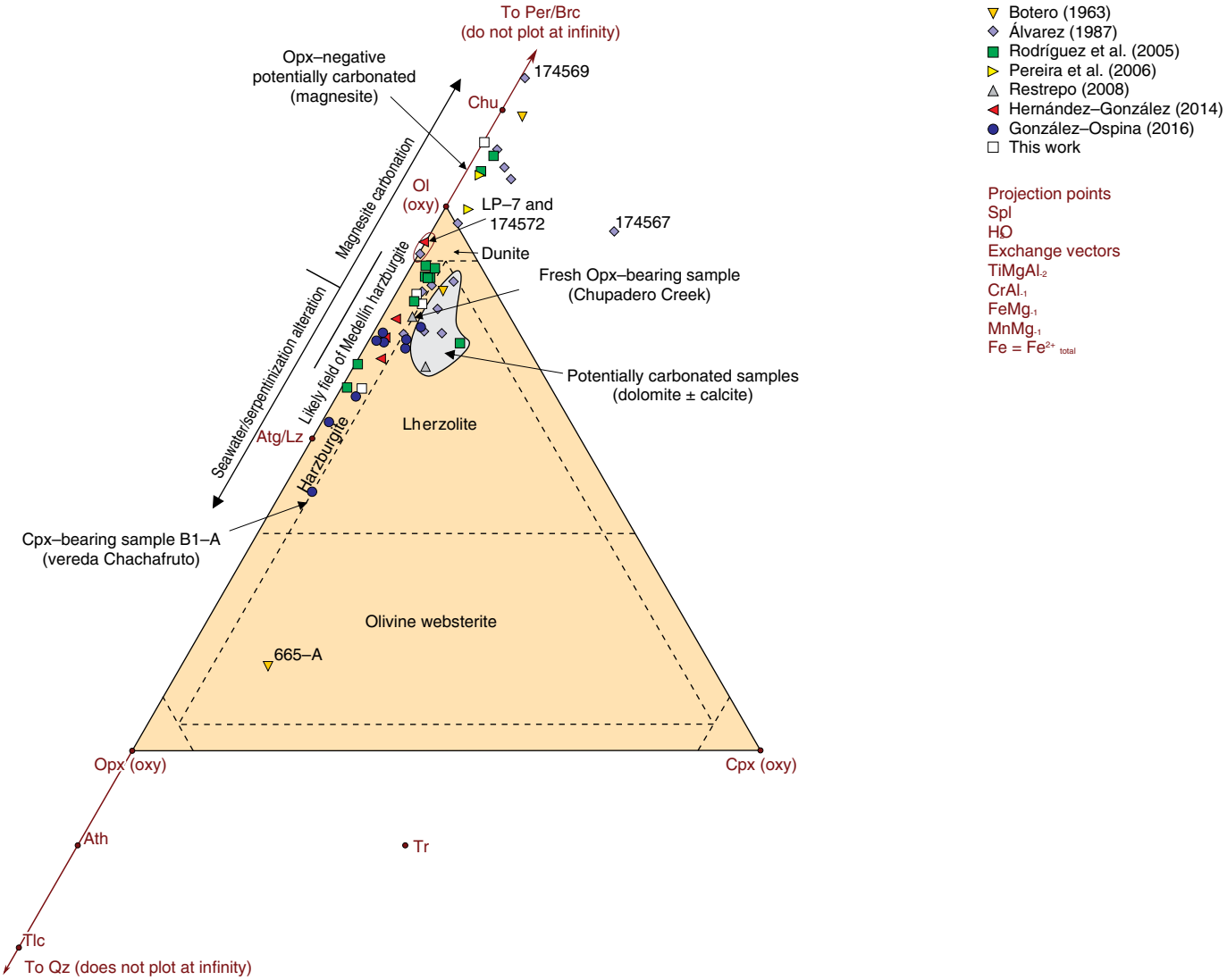

Figure 10. Samples of the Medellín Metaharzburgitic Unit plotted in the Ol–Opx–Cpx projected from spinel in oxy–equivalent units. The fields of ultramafic rocks of Le Maitre (2002) are indicated. Note that most samples of normal peridotite composition are harzburgite. See Figures 6, 8, 9, and text for further explanation.

temperature than at low temperature upon fluid infiltration (see, for example, Schmädicke, 2000, for moderate– to high–T metamorphic ultramafic rocks).

As for serpentinization, it should be no surprise that high–T mantle minerals coexist metastably with newly formed hydrated minerals at intermediate temperature conditions. At the condition of full hydration, H_2O coexist with solid phases but reactions triggered upon infiltration do not consume all mantle minerals. This is illustrated for the simple MgO–SiO_2–H_2O (MSH) system by the blue Tlc–Ol–H_2O assemblage of Figure 11b. The extreme case is dunite made of 100% olivine in this system, that does not react upon fluid infiltration and no hydrated phase is formed, allowing the stable coexistence of olivine and fluid (i.e., Ol–H_2O tie–line of Figure 11b). Hence, as opposed to serpentinization, olivine in this type of rock is a stable metamorphic mineral and not the result of limited availability of external H_2O. Moreover, during partial hydration due to limited availability of external H_2O, reactions completely consume H_2O and produce stable assemblages made of solids only, including those stable at high temperature (illustrated by the assemblage Tlc–Ol–Opx in the orange region of Figure 11b, MSH system). Partial replacement due to limited availability of H_2O is, likely, the most feasible interpretation for (i) the presence of olivine, orthopyroxene, tremolite, and talc in samples of the San Pedro locality, where the amount of orthopyroxene is small (ca. 2%), and (ii) the rather small amount of tremolite in the fresh orthopyroxene–bearing sample of Chupadero Creek, where talc is not present (Figure 3f). Hence, at least part of the typical high–T mantle mineralogy of ultramafic rocks characterizes intermediate temperature conditions, though the corresponding equilibrium compositions of the minerals are different. As indicated above for serpentinization, the chem-

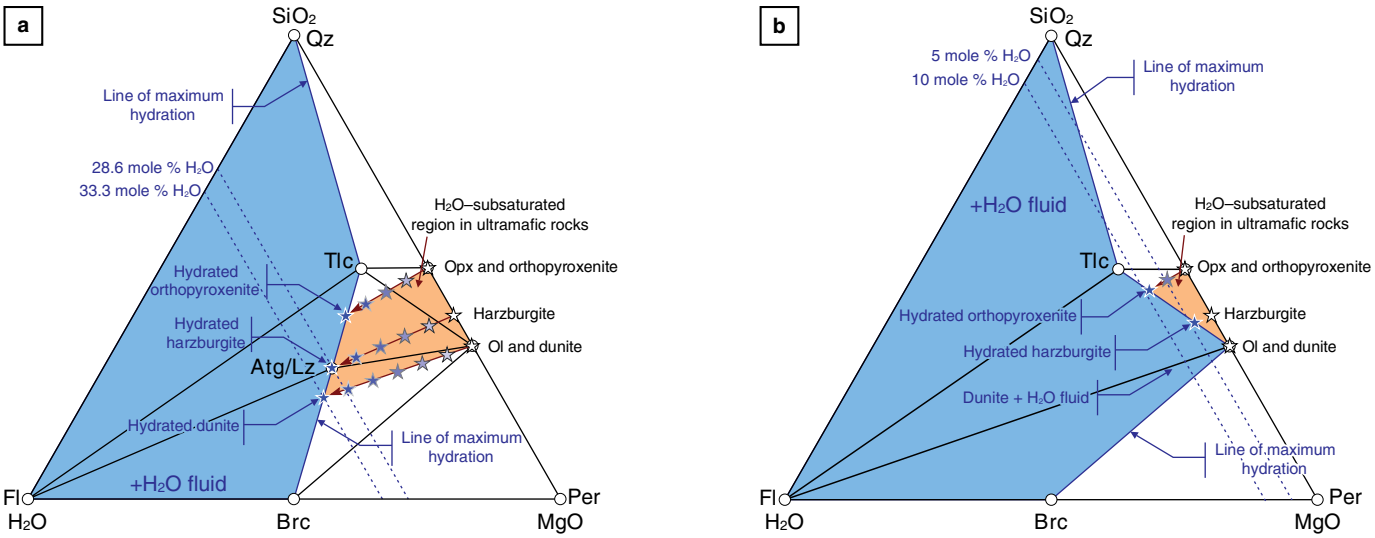

Figure 11. Hydration in the MgO–SiO_2–H_2O system. Phase relations appropriate for **(a)** serpentinization upon fluid infiltration at low–temperature and **(b)** talc formation at intermediate temperature compatible with the stability of Tr + Tlc + Ol of Figures 12, 13. Upon fluid infiltration, the bulk compositions (dunite, harzburgite, and orthopyroxenite) are displaced towards H_2O–fluid (Fl) until the line of maximum hydration is reached if enough H_2O is available from external sources; otherwise the bulk composition is displaced to an intermediate composition that lacks a fluid phase. Tie–lines and tie–triangles denote stable assemblages. Note that olivine is stable at intermediate temperature in fully hydrated rocks and that orthopyroxene is stable in partly hydrated rocks at low and intermediate temperature (i.e., the orange fields of the fluid–absent assemblage Ol + Opx + Tlc where ultramafic rocks totally consume infiltrated H_2O at these conditions). At intermediate temperature, brucite is not stable in peridotitic compositions.

ical differences can be small or large, depending of the solid solution involved but, because temperature is closer to the original mantle temperature, the chemical gap is narrower. This, together with sluggish kinetic factors at moderate temperature, explains the metastable persistence of high–T olivine in fully and partly hydrated metaultramafic rocks.

In conclusion, the name applied to a fully–hydrated intermediate–temperature ultramafic rock should not be biased by the fact that its mineral assemblage contains minerals that characterize its high–T mantle mineralogy, even if the compositions of these minerals have been partly preserved due to sluggish kinetic factors (this concept also applies to any rock formed at high temperature). In our case, the presence of ubiquitous olivine in the Medellín Metaharzburgitic Unit is the consequence of the metamorphic conditions attained (see below) and not necessarily of limited supply of fluid (full hydration was likely attained at intermediate temperature), rendering the term "dunite" incorrect.

During the Tr + Tlc + Ol metamorphic event of the Medellín Metaharzburgitic Unit, compatible with Tlc–Ol–H_2O assemblage of Figure 11b, the equilibrium assemblage in fully hydrated (i.e., maximum hydration) harzburgitic compositions is Tr + Tlc + Ol + Chl + H_2O. This assemblage is shown in the Ol–Opx–Cpx phase diagram projected from chlorite of Figure 12. In the simple CaO–MgO–SiO_2–H_2O system, the corresponding assemblage under the condition of maximum hydration is Tr + Tlc + Ol + H_2O, which is stable at temperature higher than 500 ºC and below 650 ºC at the moderate to low pressures expected for a shallow suboceanic mantle (Figure 13; Spear, 1995). The presence of widespread chlorite, particularly as concordant deformed bands of tremolite + chlorite schists at the base of the unit in contact with the La Espadera–Chupadero amphibolitic sole, is consistent with this temperature interval, suggesting roughly co–facial assemblages of ultramafic and metabasite rocks at intermediate temperature conditions.

To be noted is that all assemblages indicated in Figure 12 contain chlorite and H_2O (projection points), and that chlorite, instead of spinel, is used as a projection point due to the instability of this phase at temperature lower than ca. 800 ºC (Figure 13). This has the effect of modifying the projection of bulk compositions compared to previous diagrams projected from spinel. While most samples undergo subtle displacements because of their low–Al content, the Al–rich samples of non–peridotitic composition are strongly modified. Even if subtle, this effect invalidates the application of the classification scheme of Le Maitre (2002), but it has been retained in Figure 12 for reference. Also, note that at these conditions serpentine–group minerals and orthopyroxene are not stable under the condition of maximum hydration, though Ol and Cpx are (depending on bulk composition). The topology shown (colored tie–triangles) defines all the stable assemblages at these conditions. In addition to the predicted Tr + Tlc + Ol assemblage that characterize almost all rocks of the Medellín Metaharzburgitic Unit, the topology indicates that Ol + Tr + Cpx may characterize some of the analyzed samples. The common lack of Cpx points, in fact, to calcite/dolomite carbonation. In this regard, the bulk

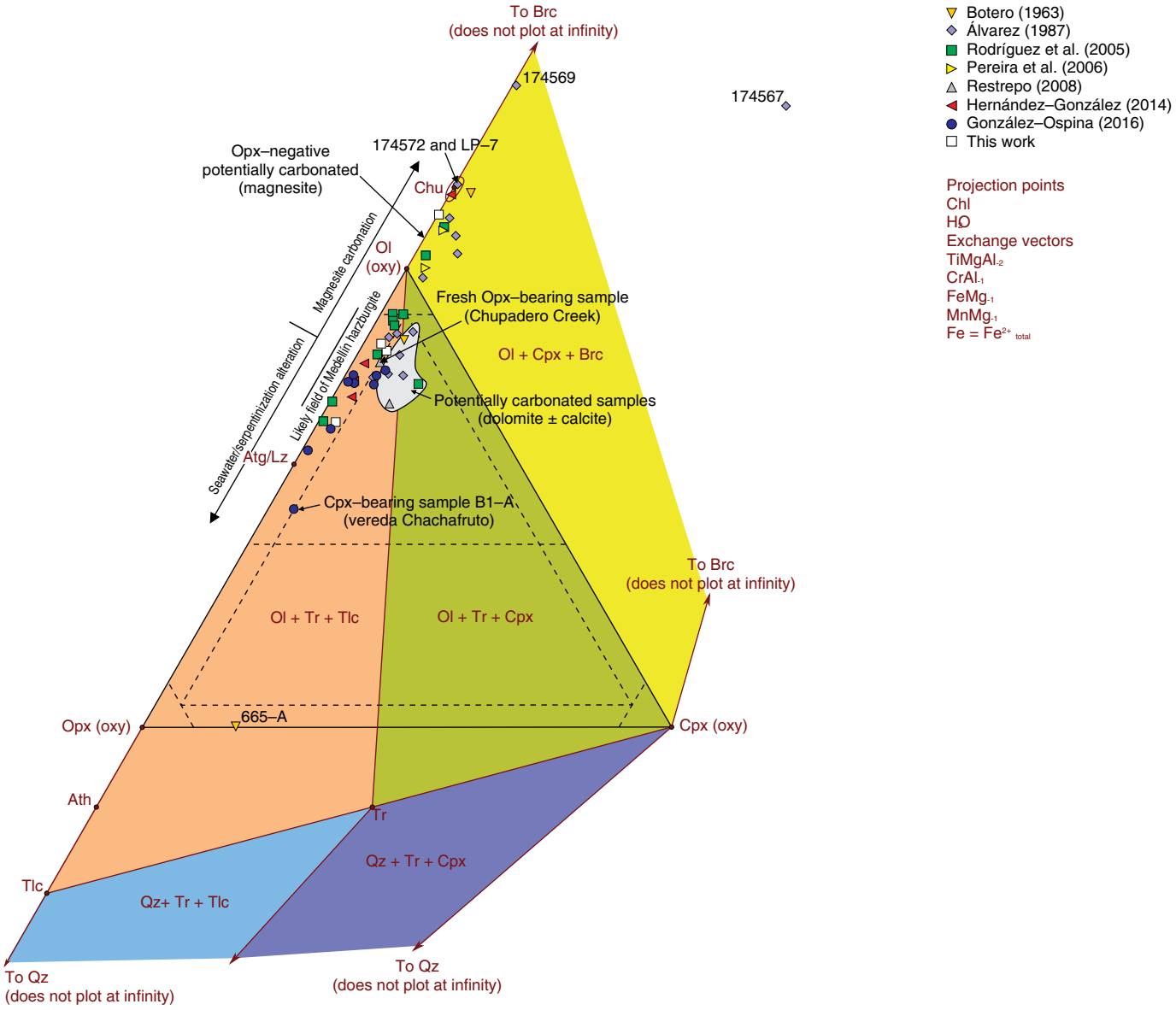

Figure 12. Samples of the Medellín Metaharzburgitic Unit plotted in the Ol–Opx–Cpx projected from chlorite in oxy–equivalent units. Projection from chlorite prevents using the classification scheme of Le Maitre (2002), which is indicated only for reference. Most samples should have developed the Ol + Tr + Tlc assemblage during the Tr + Tlc + Ol metamorphic event, including the carbonated samples (+ magnesite ± dolomite/calcite) some of which plot in the Ol + Cpx + Brc and Ol + Tr + Cpx fields (see text for further explanation). Anthophyllite and antigorite/lizardite are not stable at these conditions.

composition of the Cpx–bearing sample of González–Ospina (2016) is harzburgitic and not compatible with metamorphic clinopyroxene at these conditions (Figure 12), pointing to a relict high–T mantle nature of this phase in this sample.

No matter whether the metasomatic transformation of samples affected by SiO_2–gain and/or MgO–loss (Figure 5; samples with higher calculated Opx in Figures 8–10) took place during the Tr + Tlc + Ol metamorphic event or during late serpentinization, these samples should have developed the same Tr + Tlc + Ol assemblage of non–altered harzburgite at medium temperature conditions, as predicted in the phase diagram of Figure 12 (note vector "seawater/serpentinization alteration" pointing away from brucite in this figure). On the other hand, the case of the samples affected by SiO_2–loss and/or MgO–gain (Figure 5; samples with negative calculated Opx in Figures 8–10) is more complex. If this alteration is due to true SiO_2–loss and/or MgO–gain involving no carbonation, these samples should contain brucite, i.e., Ol + Cpx + Brc if developed during the Tr + Tlc + Ol event (Figures 12, 13) or Brc + Atg + Cpx if developed during the late serpentinization event (Figure 13). But, if this alteration is apparent and simply due to the effect of magnesite carbonation with little or no true SiO_2–loss and/or MgO–gain (note vector "magnesite carbonation" towards brucite in Figure 12), the corresponding samples would not have developed the

predicted Ol + Cpx + Brc assemblage, but Tr + Tlc + Ol, as other samples discussed above. The fact that the assemblage Ol + Cpx + Brc has not been described in the unit and that Tr + Tlc + Ol–bearing samples contain carbonate strengthens magnesite carbonation as a main process underwent by rocks in the unit. Similarly, the samples that have undergone potential dolomite/calcite carbonation (Figure 9) would have developed Ol + Tr + Cpx (Figure 12), which is not generally described in the unit. In other words, the silicate mineralogy of carbonated samples during the Tr + Tlc + Ol event would have consisted of this assemblage, which explains the widespread development of this silicate assemblage and the lack of brucite– and clinopyroxene–bearing assemblages in the Medellín Metaharzburgitic Unit, even if the composition of many samples project erroneously (as a result of not considering component CO_2 and CO_2–bearing phases) in fields appropriate for their development (note the "likely field of Medellín harzburgite" in Figures 10, 12).

It is apparent that most samples of the Medellín Metaharzburgitic Unit should have developed Tr + Tlc + Ol at intermediate–T metamorphic conditions. Besides the presence of fine–grained recrystallized olivine in many samples, a major point of concern here is that the textural relations of olivine do not generally indicate metamorphic growth and, instead, resembles relict mantle olivine. In order to solve this problem, it should be noted that the influx of external H_2O would have fully consumed Opx (and Cpx, if present) under the condition of maximum hydration, but only a small part of olivine would have been involved in recrystallization as long as this mineral is stable at intermediate–T conditions. As indicated above, it is certainly true that the composition of mantle olivine (in terms of Mg#) should have been readjusted, either by intracrystalline volume–diffusion and/or dissolution–precipitation processes. However, a broad formation of new composition of olivine should not be expected, as the difference in composition of high–T and medium–T olivine is small (basically, a slight change in molar MgO/(MgO + FeO)) and intracrystalline volume diffusion in large relict olivine grains is a sluggish process at medium temperature conditions (Chakraborty, 1997, 2010, and references therein), preventing widespread compositional re–homogenization in larger grains and allowing high–T mantle olivine to persist metastably (see discussion above). Even if detailed petrological work is needed to demonstrate this scenario, we speculate that a significant amount of olivine with slight different compositions developed during the Tr + Tlc + Ol metamorphic event. In this regard, the rock should be termed Tlc + Tr + Ol metaharzburgite, raising the question of the use of metamorphic versus common igneous terminology.

7.2. A Note on IUGS Rules

The recommendations of the IUGS Subcommission on the Systematics of Metamorphic Rocks (Schmid et al., 2007) indicate that only metamorphic ultramafic rocks containing olivine, and/or pyroxene and/or hornblende such as peridotite, harzburgite, lherzolite, wehrlite, websterite, pyroxenite, and hornblendite should be termed on the basis of mineral content as given by Le Maitre (2002). However, this rule does not apply for other types of rock containing lower temperature minerals, and terms like metaharzburgite, metaperidotite, or metadunite are permitted, implying that the protolith was a harzburgite, peridotite, or dunite and having no implications about the mineral content or structure of the rock, which may or may not have been substantially changed from that of the protolith. In this regard, terms like Tr + Tlc + Ol metaharzburgite are not only permitted, but desirable. Furthermore, the IUGS rules also indicate that the prefix meta "should, of course, only be applied to a protolith name when the protolith can be fully identified by some means". In this respect, our harzburgite compositions deduced by algebraic means perfectly fit the rules.

The IUGS rules recall that the term "ultramafic" refers to the predominance of mafic minerals in a rock and that this adjectival term may be used to name a rock, such as ultramafic Tr + Tlc + Ol granofels, which can also be used to term the studied rocks. However, we prefer to use this adjectival term to describe the geologic unit, not to name rocks. In this regard, our term Medellín Metaharzburgitic Unit, predominantly consisting of harzburgitic granofels and, to a lesser extent of dunitic granofels, does not violate the rules.

7.3. Late Serpentinization

Eventual late hydration during cooling after the Tr + Tlc +Ol metamorphic event allowed serpentinization (Figure 13). Provided that external H_2O is available for full saturation of the rocks at all stages during cooling, the expected sequence of mineral assemblage development is illustrated in Figure 13 as colored tie–triangles. At temperature lower than the Tr + Tlc + Ol event Tr + Tlc is not stable and, for the common harzburgitic composition of the Medellín Metaharzburgitic Unit, talc should have been consumed upon reaction with olivine and initial growth of antigorite. The same applies to Tr + Ol at still lower temperature, and tremolite should have been totally consumed upon reaction with olivine and growth of diopside and additional antigorite. Since tremolite and talc persist, it must be concluded that H_2O availability for full saturation of the rocks during the serpentinization event was limited (Figure 11a). Interestingly, the topology at lower temperature predicts the generalized presence of brucite together with antigorite/lizardite, even though brucite has not been reported in the Medellín Metaharzburgitic Unit. This is also a likely consequence of limited availability of fluid (see the orange field within the Tlc–Opx–Ol tie–triangle of Figure 11a; see also, for example, Fyfe et al., 1978, their Figure 7.4). However, perhaps a detailed study focused on the metamorphic evolution of the unit would

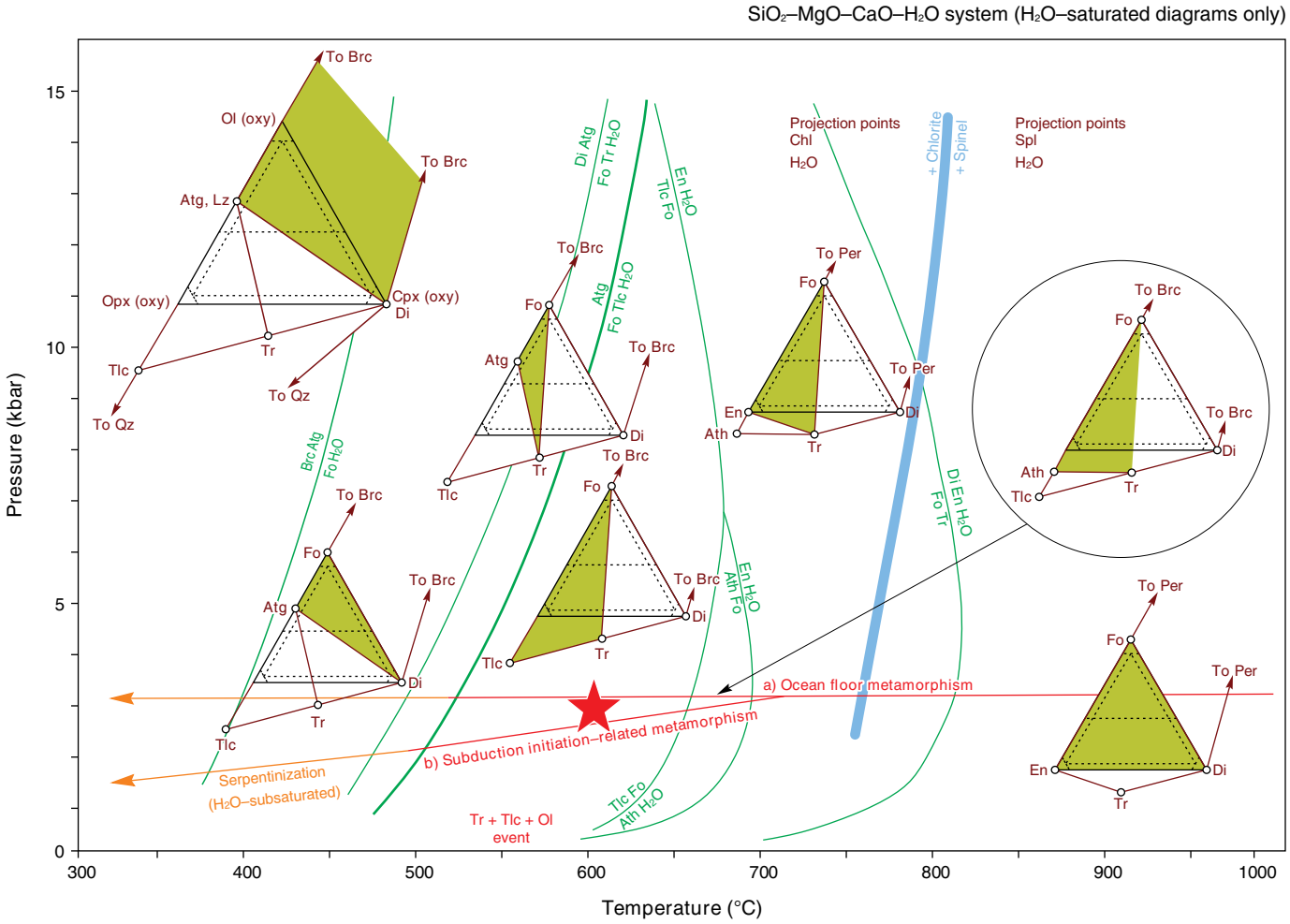

Figure 13. P–T diagram showing relevant reactions (after Spear, 1995) in the CaO–MgO–SiO_2–H_2O system and associated phase diagrams in oxy–equivalent units projected from spinel and chlorite to the right and left of the maximum stability limit of chlorite (light blue curve, schematic), respectively. Note that the phase diagrams do not represent H_2O–subsaturated assemblages. The classification scheme of Le Maitre (2002) is indicated in the diagrams for reference. The assemblages expected for the common harzburgitic composition of the Medellín Metaharzburgitic Unit are indicated (mustard color). Most samples should have developed the sequence of assemblages Ol + En + Tr (partly hydrated sample in Figure 3f) > Tr + Tlc + Ol (Tr + Tlc + Ol metamorphic event, red star) > Ol + Tr + Atg > Ol + Atg + Cpx and finally Atg/Lz + Cpx + Brc (late serpentinization event). The lack of late Cpx and Brc suggests H_2O–subsaturated conditions at this stage. Arrows indicate schematic P–T paths expected for a) static hydrothermal (ocean–floor) metamorphism of oceanic mantle that undergoes cooling upon drifting from a mid–ocean ridge and b) dynamic underriding of oceanic lithosphere below upper–plate oceanic mantle that undergoes extension (i.e., decompression) and cooling in a subduction–initiation related setting. See Figure 14 and text for further explanation.

"discover" this predicted mineral in fully serpentinized samples. Similarly, metamorphic clinopyroxene is predicted below ca. 450 ºC. As noted above, the fact that tremolite has been preserved due to limited availability of H_2O for full saturation of the rocks explains this observation, though it should be stressed that the presence of this mineral, together with brucite, is predicted in fully serpentinized samples (Figure 13).

The late talc–forming event recorded in some samples (e.g., Rodríguez et al., 2005) can be explained as a result of the open–system behavior at low temperature. Indeed, talc is expected to form in rocks that underwent intense SiO_2–gain and/or MgO–loss, as can be deduced in the three phase diagrams below the antigorite stability field of Figure 13 (i.e., the Atg/Lz–Tr–Tlc assemblage). Note that this process also helps to explain the lack of brucite and clinopyroxene below 450 ºC.

8. Tectonic Implications of the Tr–Tlc–Ol Event

Mantle sections of onshore ophiolitic tectonic units do not generally show Tr + Tlc + Ol assemblages of regional extent. They generally show low–T serpentine ± talc ± brucite assemblages and only local development of higher–T tremolite. Given the regional extent of the Tr + Tlc +Ol–forming metamorphic im-

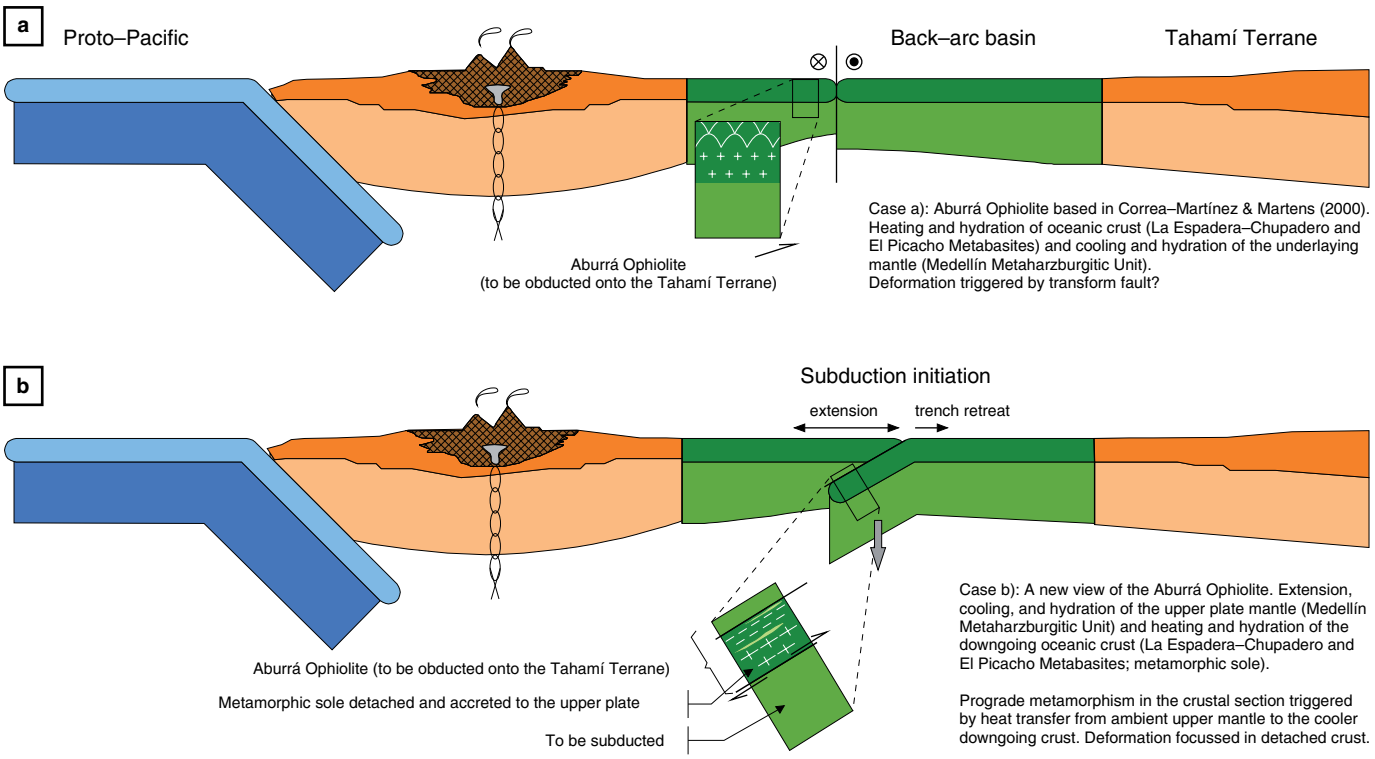

Figure 14. Alternative schematic tectonic interpretations of the Aburrá Ophiolite (general geodynamic setting after Spikings et al., 2015). **(a)** Formation in a back–arc scenario followed by static hydrothermal metamorphism, perhaps in a transform–fault setting, which developed Tr + Tlc + Ol assemblage and late serpentinization (path a in Figure 13). **(b)** Subduction initiation in a back–arc setting, likely at a transform–fault, triggered prograde metamorphism of the underriding oceanic crust (La Espadera–Chupadero and El Picacho Metabasites) and extension (decompression), cooling, and hydration of upper–plate mantle (i.e., the Medellín Metaharzburgitic Unit; path b in Figure 13). In both cases, the "Aburrá Ophiolite" would be eventually emplaced onto the Tahamí Terrane upon closure of the back–arc basin.

print in the whole Medellín Metaharzburgitic Unit, we propose that a distinct medium–temperature hydration event took place in the geologic evolution of the associated mantle lithosphere.

This proposal is not to say that the unit underwent prograde metamorphism. As proved by textural analysis, this distinct medium–T metamorphic imprint took place during cooling. However, such event must have to do with an episode of generalized infiltration of H_2O in a broad region. Two main tectonic scenarios (Figure 14) are envisaged in a back–arc region where the protoliths of the Medellín Metaharzburgitic Unit likely formed (Correa–Martínez, 2007; Correa–Martínez & Nilson, 2003; Correa–Martínez et al., 2004; Proenza et al., 2004) in the context of a Permian – Triassic geodynamic evolution of the northwestern corner of Gondwana characterized by the formation of a continental volcanic arc and late extension and rifting of continental crust while the paleo–Pacific ocean subducted below Gondwana (e.g., Cochrane et al., 2014; Riel et al., 2018; Spikings et al., 2015, and references therein). A first scenario is a fracture zone in the back–arc (Figure 14a), where the corresponding shallow mantle would have been relatively hot because ca. 600 ºC characterizes the Tr–Tlc + Ol event. Hence, the fracture zone should be relatively close to the spreading ridge where the ultramafic rocks formed (i.e., the precise location may have been a transform–fault sensu stricto). It should be noted that a fracture zone is a first–order mechanical discontinuity in the lithosphere that may help the process of closure of a back–arc basin and obduction of oceanic mantle onto continental margins (e.g., Stern, 2004). In this context, obduction of Tr + Tlc + Ol metamorphic rocks over the Tahamí Terrane is a likely hypothesis. However, this setting can hardly explain (i) amphibolite facies metamorphic conditions in the basaltic crustal section of the Aburrá Ophiolite (i.e., La Espadera–Chupadero Amphibolites), (ii) prograde metamorphism and generalized hydration plus coeval intense deformation of this basaltic (and plutonic) section, (iii) the tectonic location of the basaltic section below the associated mantle (i.e., Medellín Metaharzburgitic Unit), and (iv) the fact that the metamorphic assemblages of the mantle and basaltic sections of the Aburrá Ophiolite indicate metamorphism at roughly similar temperature, an unexpected feature for a 5–15 km thick crust + mantle section that experiences cooling upon drifting from the corresponding ridge.

Obduction of the Aburrá Ophiolite was only possible after closure of the back–arc basin, implying subduction of a fragment of the back–arc lithosphere and offering an alternative scenario

for metamorphism, hydration, and deformation of all types of rock. Upon subduction initiation, a first frequent step in the obduction process, relatively cold mafic–sedimentary oceanic crust is dragged down into the mantle, resulting in prograde metamorphism and accretion as a medium– to high–grade metamorphic sole made of metabasic and metasedimentary oceanic rocks that may undergo partial melting during emplacement below the ambient hanging–wall mantle (e.g., Boudier et al., 1988; Lázaro et al., 2013; Robertson, 2004; Stern, 2004; Wakabayashi & Dilek, 2003). During this process, the overriding mantle adjacent to the slab experiences extension (i.e., decompression, as a result of trench retreat, e.g., Stern, 2004), cooling (as a result of heat transfer to the underlying crustal section), and hydration (as a result of slab devolatilization). Intense deformation is expected in the volcanic and, to a lesser extent, plutonic crustal section adjacent to the slab–mantle interface, while the mantle section remains relatively less affected by deformation except at its base close to the accreted crust. This general scenario is consistent with observations in the Aburrá Ophiolite. The La Espadera–Chupadero metamorphic sole (Restrepo, 2008) likely developed upon subduction initiation after heating (prograde metamorphism) of the back–arc crust dragged down below the Medellín Metaharzburgitic Unit, which experienced contemporaneous cooling and uplift (Figure 14b). This scenario explains the observed contrasted thermal evolution of the crustal and mantle sections of the Aburrá Ophiolite (i.e., one is heated while the other cools) and the arrival of both sections to roughly co–facial metamorphic conditions. Similar medium–grade metamorphism of ultramafic bodies and associated metabasites worldwide are also explained in the context of subduction, though much higher pressures are observed if accretion takes place at the mature stages of subduction (e.g., Khedr & Arai, 2010). It should be noted, however, that in this model the ultramafic body and amphibolites form part of the overriding and downgoing plates, respectively (Figure 14b), implying that the obducted "ophiolite" (i.e., the Aburrá Ophiolite) does not represent fragments of a former coherent oceanic lithosphere. In this regard, it should not be considered as characterized by the typical Penrose pseudostratigraphy, though the crustal and mantle sections would certainly be closely and, henceforth, petrogenetically related (Figure 14).

It could be argued that both scenarios discussed above are not contradictory and can be merged into a single model, or that a different scenario is possible. However, given the scarcity of detailed structural and petrological data we cannot go further in the analysis of potential geodynamic scenarios in the present contribution. Future work should concentrate in detailed textural–chemical relations (using, for example, XR and EBSD maps), calculation of P–T conditions, structural relations, and geochronology of the different rock types related to the Aburrá Ophiolite. In any case, we note that the term Medellín Metaharzburgitic Unit is still even more appropriate, for it strengthens the view of a distinct tectonic unit affected by geodynamic processes that distorted the mantle geotherm (onset of subduction?), allowed cooling and hydration at medium temperature, and finally resulted in the tectonic emplacement of the ophiolite in the continental margin of Pangea (Figure 14).

9. Conclusions

The rocks that form the Medellín Metaharzburgitic Unit are mostly metaharzburgite and, to a lesser extent metadunite, bearing relict mantle–derived olivine and spinel–group minerals (plus local orthopyroxene), but much of the mineral assemblage is metamorphic made of olivine, tremolite, chlorite, talc, and spinel–group minerals, in addition to lower grade serpentine–group minerals. These associations are not co–facial. The assemblage chlorite + tremolite + talc + olivine indicates medium–grade conditions (ca. 600 ºC) at indeterminate to low pressure. However, if anthophyllite forms part of the assemblage, relatively low pressure is anticipated (<6 kbar). The widespread presence of tremolite, talc, and chlorite indicates a distinct thermal/hydration event in the metamorphic evolution of the unit. This metamorphic imprint can be the result of cooling and hydration of oceanic mantle in a back–arc setting before the tectonic processes that finally led to the obduction of the metaharzburgitic unit onto the continental margin of western Pangea. Roughly co–facial metamorphism and strong deformation in associated metabasite rocks point, however, to a complex scenario that likely involved subduction initiation.

Acknowledgments

We acknowledge Carlos ZULUAGA and Robert OBERHANSLI for their reviews and editor Jorge GÓMEZ TAPIAS for edition and giving us the opportunity to contribute to this book. This paper is part of Spanish MINECO project CGL2015–65824. The AC–coded chemical analyses in Table 1 were acquired by Ana María CORREA–MARTÍNEZ during her PhD project supported by a grant from the Brazilian National Council for Technological and Scientific Development (CNPq)–process 141622/03–2.

References

Álvarez, A.J. 1982. Tectonitas dunitas de Medellín, departamento de Antioquia, Colombia. Ingeominas, internal report 1896, 73 p. Medellín.

Álvarez, A.J. 1987. Tectonitas dunitas de Medellín, departamento de Antioquia, Colombia. Boletín Geológico, 28(3): 9–44.

Bach, W., Paulick, H., Garrido, C.J., Ildefonse, B., Meurer, W.P. & Humphris, S.E. 2006. Unraveling the sequence of serpentinization reactions: Petrography, mineral chemistry, and petrophysics of serpentinites from MAR 15° N (ODP Leg 209, Site 1274). Geophysical Research Letters, 33(13): 1–4. https://doi.org/10.1029/2006GL025681

Blanco–Quintero, I.F., Proenza–Fernandez, J.A., García–Casco, A., Tauler, E. & Galí–Medina, S. 2011. Serpentinites and serpentinites within a fossil subduction channel: La Corea mélange, eastern Cuba. Geologica Acta, 9(3–4): 389–405. https://doi.org/10.1344/105.000001662

Blanco–Quintero, I.F., García–Casco, A., Toro, L.M., Moreno–Sánchez, M., Ruiz, E.C., Vinasco, C.J., Cardona, A., Lázaro, C. & Morata, D. 2014. Late Jurassic terrane collision in the northwestern margin of Gondwana (Cajamarca Complex, eastern flank of the Central Cordillera, Colombia). International Geology Review, 56(15): 1852–1872. https://doi.org/10.1080/00206814.2014.963710

Bonnemains, D., Escartín, J., Mével, C., Andreani, M. & Verlaguet, A. 2017. Pervasive silicification and hanging wall overplating along the 13° 20' N oceanic detachment fault (Mid–Atlantic Ridge). Geochemistry, Geophysics, Geosystems, 18(6): 2028–2053. https://doi.org/10.1002/2017GC006846

Boschi, C., Dini, A., Baneschi, I., Bedini, F., Perchiazzi, N. & Cavallo, A. 2017. Brucite–driven CO_2 uptake in serpentinized dunites (Ligurian Ophiolites, Montecastelli, Tuscany). Lithos, 288–289: 264–281. https://doi.org/10.1016/j.lithos.2017.07.005

Botero, G. 1963. Contribución al conocimiento de la geología de la zona central de Antioquia. Universidad Nacional de Colombia, Anales de la Facultad de Minas, 57, 101 p. Medellín.

Boudier, F., Ceuleneer, G. & Nicolas, A. 1988. Shear zones, thrusts and related magmatism in the Oman Ophiolite: Initiation of thrusting on an oceanic ridge. Tectonophysics, 151(1–4): 275–296. https://doi.org/10.1016/0040-1951(88)90249-1

Brady, J.B. & Stout, J.H. 1980. Normalizations of thermodynamic properties and some implications for graphical and analytical problems in petrology. American Journal of Science, 280(2): 173–189. https://doi.org/10.2475/ajs.280.2.173

Bustamante, A., Cardona, A. & Durán, C.T. 1999. Estratigrafía y petrogénesis de las sedimentitas paleozoicas en el flanco occidental de la cordillera Central, departamento de Antioquia. Bachelor thesis, Universidad EAFIT, 102 p. Medellín.

Cárdenas–Párraga, J., García–Casco, A., Proenza, J.A., Harlow, G.E., Blanco–Quintero, I.F., Lázaro, C., Villanova–de–Benavent, C. & Núñez–Cambra, K. 2017. Trace–element geochemistry of transform–fault serpentinite in high–pressure subduction mélanges (eastern Cuba): Implications for subduction initiation. International Geology Review, 59(16): 2041–2064. https://doi.org/10.1080/00206814.2017.1308843

Chakraborty, S. 1997. Rates and mechanisms of Fe–Mg interdiffusion in olivine at 980º–1300 ºC. Journal of Geophysical Research: Solid Earth, 102(B6): 12317–12331. https://doi.org/10.1029/97JB00208

Chakraborty, S. 2010. Diffusion coefficients in olivine, wadsleyite and ringwoodite. Reviews in Mineralogy and Geochemistry, 72(1): 603–639. https://doi.org/10.2138/rmg.2010.72.13

Chen, L., Chu, F.Y., Zhu, J.H., Dong, Y.H., Yu, X., Li, Z.G. & Tang, L.M. 2015. Major and trace elements of abyssal peridotites: Evidence for melt refertilization beneath the ultraslow–spreading southwest Indian Ridge (53° E segment). International Geology Review, 57(13): 1715–1734. https://doi.org/10.1080/00206814.2015.1029014

Cochrane, R., Spikings, R., Gerdes, A., Ulianov, A., Mora, A., Villagómez, D., Putlitz, B. & Chiaradia, M. 2014. Permo–Triassic anatexis, continental rifting and the disassembly of western Pangaea. Lithos, 190–191: 383–402. https://doi.org/10.1016/j.lithos.2013.12.020

Coleman, R.G. 1977. Ophiolites: Ancient oceanic lithosphere? Springer–Verlag, 229 p. Berlin–Heildelberg, New York.

Correa–Martínez, A.M. 2007. Petrogênese e evolução do Ofiolito de Aburrá, Cordilheira Central dos Andes Colombianos. Doctoral thesis, Universidade de Brasília, 204 p. Brasilia.

Correa–Martínez, A.M. & Martens, U. 2000. Caracterización geológica de las anfibolitas de los alrededores de Medellín. Bachelor thesis, Universidad Nacional de Colombia, 363 p. Medellín.

Correa–Martínez, A.M. & Nilson, A. 2003. Dunitas de Medellín y Metagabros de El Picacho: Posibles fragmentos de ofiolita subtipo harzburgita, tipo zona de suprasubducción. IX Congreso Colombiano de Geología. Memoirs, p. 46–47. Medellín.

Correa–Martínez, A.M., Nilson, A.A. & Pimentel, M. 2004. The Aburra Ophiolitic Complex, Antioquia–Colombia a fragment of a harzburgite ophiolite–type. 32nd International Geological Congress. Abstracts, 1, p. 374–375. Florence, Italy.

Correa–Martínez, A.M., Martens, U., Restrepo, J.J., Ordóñez–Carmona, O. & Martins, M. 2005. Subdivisión de las metamorfitas básicas de los alrededores de Medellín–cordillera Central de Colombia. Revista de la Academia Colombiana de Ciencias Exactas, Físicas y Naturales, 29(112): 325–344.

Evans, B.W. 1977. Metamorphism of Alpine peridotite and serpentinite. Annual Review of Earth and Planetary Sciences, 5: 397–447. https://doi.org/10.1146/annurev.ea.05.050177.002145

Fisher, G.W. 1989. Matrix analysis of metamorphic mineral assemblages and reactions. Contributions to Mineralogy and Petrology, 102(1): 69–77. https://doi.org/10.1007/BF01160191

Fisher, G.W. 1993. An improved method for algebraic analysis of metamorphic mineral assemblages. American Mineralogist, 78(11–12): 1257–1261.

Fyfe, W.S., Price, N.J. & Thompson, A.B. 1978. Fluids in the Earth's crust. Elsevier, 401 p. Amsterdam.

González, H. 2001. Memoria explicativa: Mapa geológico del departamento de Antioquia. Scale 1:400 000. Ingeominas, 240 p. Medellín.

González–Ospina, L.J. 2016. Petrogénesis de los complejos ultramáficos de Heliconia–Angelópolis y del oriente de Medellín, Antioquia, Colombia. Master thesis, Universidad Nacional de Colombia, 108 p. Bogotá.

Guillot, S., Schwartz, S., Reynard, B., Agard, P. & Prigent, C. 2015. Tectonic significance of serpentinites. Tectonophysics, 646: 1–19. https://doi.org/10.1016/j.tecto.2015.01.020

Hart, S.R. & Zindler, A. 1986. In search of a bulk–Earth composition. Chemical Geology, 57(3–4): 247–267. https://doi.org/10.1016/0009-2541(86)90053-7

Hernández–González, J.S. 2014. Mineralizaciones de Cr y elementos del grupo del platino (EGP) asociadas a las Metaperidotitas de Medellín, Colombia. Master thesis, Universidad de Barcelona and Universidad Autónoma de Barcelona, 21 p. Barcelona.

Jagoutz, E., Palme, H., Baddenhausen, H., Blum, K., Cendales, M., Dreibus, G., Spettel, B., Lorenz, V. & Wänke, H. 1979. The abundances of major, minor and trace elements in the Earth's mantle as derived from primitive ultramafic nodules. 10th Lunar and Planetary Science Conference. Proceedings, p. 2031–2050. Houston, USA.

Jaramillo, J.S., Cardona, A., León, S., Valencia, V. & Vinasco, C. 2017. Geochemistry and geochronology from Cretaceous magmatic and sedimentary rocks at 6° 35' N, western flank of the Central Cordillera (Colombian Andes): Magmatic record of arc growth and collision. Journal of South American Earth Sciences, 76: 460–481. https://doi.org/10.1016/j.jsames.2017.04.012

Khedr, M.Z. & Arai, S. 2010. Hydrous peridotites with Ti–rich chromian spinel as a low–temperature forearc mantle facies: Evidence from the Happo–O'ne Metaperidotites (Japan). Contributions to Mineralogy and Petrology, 159(2): 137–157. https://doi.org/10.1007/s00410-009-0420-7

Kimball, K.L., Spear, F.S. & Dick, H.J.B. 1985. High temperature alteration of abyssal ultramafics from the islas Orcadas fracture zone, South Atlantic. Contributions to Mineralogy and Petrology, 91(4): 307–320. https://doi.org/10.1007/BF00374687

Kodolányi, J., Pettke, T., Spandler, C., Kamber, B.S. & Gméling, K. 2012. Geochemistry of ocean floor and fore–arc serpentinites: Constraints on the ultramafic input to subduction zones. Journal of Petrology, 53(2): 235–270. https://doi.org/10.1093/petrology/egr058

Lázaro, C., Blanco–Quintero, I.F., Rojas–Agramonte, Y., Proenza, J.A., Núñez–Cambra, K. & García–Casco, A. 2013. First description of a metamorphic sole related to ophiolite obduction in the northern Caribbean: Geochemistry and petrology of the Güira de Jauco Amphibolite Complex (eastern Cuba) and tectonic implications. Lithos, 179: 193–210. https://doi.org/10.1016/j.lithos.2013.08.019

Le Bas, M.J. & Streckeisen, A.L. 1991. The IUGS systematics of igneous rocks. Journal of the Geological Society, 148(5): 825–833. https://doi.org/10.1144/gsjgs.148.5.0825

Le Maitre, R.W., editor. 2002. Igneous rocks. A classification and glossary of terms. 2nd edition. Recommendations of the International Union of Geological Sciences Subcommission on the systematics of igneous rocks. Cambridge University Press, 236 p. New York, USA. https://doi.org/10.1017/CBO9780511535581

Lindsley, D.H. 1983. Pyroxene thermometry. American Mineralogist, 68(5–6): 477–493.

Malvoisin, B. 2015. Mass transfer in the oceanic lithosphere: Serpentinization is not isochemical. Earth and Planetary Science Letters, 430: 75–85. https://doi.org/10.1016/j.epsl.2015.07.043

Martens, U. 2003. Crenulación de las Anfibolitas de Medellín y milonitización del Neis Augen de las Palmas: ¿Evidencias de un cabalgamiento post–Cretácico medio de la Dunita de Medellín? IX Congreso Colombiano de Geología. Memoirs, p. 39–40. Medellín.

Martens, U., Restrepo, J.J., Ordóñez–Carmona, O. & Correa–Martínez, A.M. 2014. The Tahamí and Anacona Terranes of the Colombian Andes: Missing links between the South American and Mexican Gondwana margins. The Journal of Geology, 122(5): 507–530. https://doi.org/10.1086/677177

Maya, M. & González, H. 1995. Unidades litodémicas en la cordillera Central de Colombia. Boletín Geológico, 35(2–3): 43–57.

McDonough, W.F. & Sun, S.S. 1995. The composition of the Earth. Chemical Geology, 120(3–4): 223–253. https://doi.org/10.1016/0009-2541(94)00140-4

Milliken, K.L., Lynch, F.L. & Seifert, K.E. 1996. Marine weathering of serpentinites and serpentinite breccias, Sites 897 and 899, Iberia abyssal plain. In: Whitmarsh, R.B., Sawyer, D.S., Klaus, A. & Masson, D.G. (editors), Proceedings of the Ocean Drilling Program, Scientific Results 149, p. 529–540.

Nicolas, A. & Boudier, F. 2003. Where ophiolites come from and what they tell us. In: Dilek, Y. & Newcomb, S. (editors), Ophiolite concept and the evolution of geological thought. Geological Society of America, Special Paper 373, p. 137–152. Boulder, Colorado. https://doi.org/10.1130/0-8137-2373-6.137

Niu, Y. 2004. Bulk–rock major and trace element compositions of abyssal peridotites: Implications for mantle melting, melt extraction and post–melting processes beneath mid–ocean ridges. Journal of Petrology, 45(12): 2423–2458. https://doi.org/10.1093/petrology/egh068

Nivia, A., Marriner, G. F., Kerr, A. C., & Tarney, J. 2006. The Quebradagrande Complex: A Lower Cretaceous ensialic marginal basin in the Central Cordillera of the Colombian Andes: Journal of South American Earth Sciences, 21(4): 423–436. https://doi.org/10.1016/j.jsames.2006.07.002

O'Hanley, D.S. 1996. Serpentinites: Records of tectonic and petrological history. Oxford Monographs on Geology and Geophysics, 34. Oxford University Press, 277 p. Oxford.

Ordóñez–Carmona, O. 2001. Caracterização isotópica Rb–Sr e Sm–Nd dos principais eventos magmáticos nos Andes colombianos. Doctoral thesis, Universidad de Brasilia, 176 p. Brasilia.

Paulick, H., Bach, W., Godard, M., De Hoog, J.C.M., Suhr, G. & Harvey, J. 2006. Geochemistry of abyssal peridotites (Mid–Atlantic Ridge, 15° 20' N, ODP Leg 209): Implications for fluid/rock interaction in slow spreading environments. Chemical Geology, 234(3–4): 179–210. https://doi.org/10.1016/j.chemgeo.2006.04.011

Pearce, J.A., Barker, P.F., Edwards, S.J., Parkinson, I.J. & Leat, P.T. 2000. Geochemistry and tectonic significance of peridotites

from the south Sandwich arc–basin system, South Atlantic. Contributions to Mineralogy and Petrology, 139(1): 36–53. https://doi.org/10.1007/s004100050572

Pereira, E., Ortiz, F. & Prichard, H. 2006. Contribución al conocimiento de las Anfibolitas y Dunitas de Medellín (Complejo Ofiolítico de Aburrá). DYNA, 73(149): 17–30.

Proenza, J.A., Escayola, M., Ortiz, F., Pereira, E. & Correa–Martínez, A.M. 2004. Dunite and associated chromitites from Medellín (Colombia). 32nd International Geological Congress. Memoirs, I, p. 507. Florence, Italy.

Putirka, K., Ryerson, F.J., Perfit, M. & Ridley, W.I. 2011. Mineralogy and composition of the oceanic mantle. Journal of Petrology, 52(2): 279–313. https://doi.org/10.1093/petrology/egq080

Rendón, D.A. 1999. Cartografía y caracterización de las unidades geológicas del área urbana de Medellín. Bachelor thesis, Universidad Nacional de Colombia, 113 p. Medellín.

Restrepo, J.J. 1986. Metamorfismo en el sector norte de la cordillera Central de Colombia. Universidad Nacional de Colombia, Trabajo presentado como requisito parcial para la promoción a Profesor Titular. unpublished report, 276 p. Medellín.

Restrepo, J.J. 2008. Obducción y metamorfismo de ofiolitas triásicas en el flanco occidental del Terreno Tahamí, cordillera Central de Colombia. Boletín de Ciencias de la Tierra, (22): 49–100.

Restrepo, J.J. & Toussaint, J.F. 1973. Obducción cretácea en el occidente colombiano. Publicación Especial de Geología, 3, p. 1–26. Medellín.

Restrepo, J.J. & Toussaint, J.F. 1974. Obducción cretácea en el occidente colombiano. Universidad Nacional de Colombia, Anales de la Facultad de Minas, 58, p. 73–105. Medellín.

Restrepo, J.J. & Toussaint, J.F. 1984. Unidades litológicas de los alrededores de Medellín. Primera conferencia sobre riesgos geológicos del valle de Aburrá. Sociedad Colombiana de Geología. Memoirs, p. 1–26. Medellín.

Restrepo, J.J., Toussaint, J.F., González, H., Cordani, U., Kawashita, K., Linares, E. & Parica, C. 1991. Precisiones geocronológicas sobre el occidente colombiano. Simposio sobre magmatismo andino y su marco tectónico. Memoirs, I, p. 1–22. Manizales.

Restrepo, J.J., Frantz, J.C., Ordóñez–Carmona, O., Correa–Martínez, A.M., Martens, U. & Chemale, F. 2007. Edad triásica de formación de la Ofiolita de Aburrá, flanco occidental de la cordillera Oriental. XI Congreso Colombiano de Geología. Abstracts, p. 49. Bucaramanga.

Restrepo, J.J., Ordóñez–Carmona, O., Armstrong, R. & Pimentel, M.M. 2011. Triassic metamorphism in the northern part of the Tahamí Terrane of the Central Cordillera of Colombia. Journal of South American Earth Sciences, 32(4): 497–507. https://doi.org/10.1016/j.jsames.2011.04.009

Restrepo, J.J., Ibañez–Mejia, M. & García–Casco, A. 2012. U–Pb zircon ages of the Medellín Amphibolites (Central Cordillera of Colombia) reveal mid–Cretaceous tectonic juxtaposition of Triassic and mid–Cretaceous metamorphic complexes. VIII South American Symposium on Isotope Geology. USB memory device, 33 slides. Medellín.

Riel, N., Jaillard, E., Martelat, J.E., Guillot, S. & Braun, J. 2018. Permian – Triassic Tethyan realm reorganization: Implications for the outward Pangea margin. Journal of South American Earth–Sciences, 81: 78–86. https://doi.org/10.1016/j.jsames.2017.11.007

Robertson, A. 2004. Development of concepts concerning the genesis and emplacement of Tethyan ophiolites in the eastern Mediterranean and Oman regions. Earth Science Reviews, 66(3–4): 331–387. https://doi.org/10.1016/j.earscirev.2004.01.005

Rodríguez, G. & Correa–Martínez, A.M. 2015. Edad jurásica del Neis Milonítico de Sajonia y su posible significado en la evolución geotectónica del sector noroccidental de la cordillera Central de Colombia. Simposio: Tectónica jurásica en la parte noroccidental de Sur América y bloques adyacentes. Abstracts, 1 p. Medellín.

Rodríguez, G., González, H. & Zapata, G. 2005. Memoria explicativa: Geología de la plancha 147 Medellín Oriental. Scale: 1:100 000. Ingeominas, 300 p. Bogotá.

Schmädicke, E. 2000. Phase relations in peridotitic and pyroxenitic rocks in the model systems CMASH and NCMASH. Journal of Petrology, 41(1): 69–86. https://doi.org/10.1093/petrology/41.1.69

Schmid, R., Fettes, D., Harte, B., Davis, E. & Desmons, J. 2007. How to name a metamorphic rock. Recommendations by the International Union of Geological Sciences Subcommission on the systematics of metamorphic rocks: Web version 01/02/07. http://www.bgs.ac.uk/SCMR/docs/papers/paper_1.pdf (consulted in December 2011).

Snow, J.E. & Dick, H.J.B. 1995. Pervasive magnesium loss by marine weathering of peridotite. Geochimica et Cosmochimica Acta, 59(20): 4219–4235. https://doi.org/10.1016/0016-7037(95)00239-V

Spear, F.S. 1995. Metamorphic phase equilibria and pressure–temperature–time paths. Mineralogical Society of America Monographs, 1995, 799 p. Washington, D.C.

Spear, F.S., Rumble III, D. & Ferry, J.M. 1982. Linear algebraic manipulation of n–dimensional composition space. In: Ferry, J.M. (editor), Characterization of metamorphism through mineral equilibria. Mineralogical Society of America, Reviews in Mineralogy and Geochemistry 10, p. 53–104.

Spikings, R., Cochrane, R., Villagómez, D., van der Lelij, R., Vallejo, C., Winkler, W. & Beate, B. 2015. The geological history of northwestern South America: From Pangaea to the early collision of the Caribbean Large Igneous Province (290–75 Ma). Gondwana Research, 27(1): 95–139. https://doi.org/10.1016/j.gr.2014.06.004

Stern, R.J. 2004. Subduction initiation: Spontaneous and induced. Earth and Planetary Science Letters, 226(3–4): 275–292. https://doi.org/10.1016/j.epsl.2004.08.007

Streckeisen, A. 1976. To each plutonic rock its proper name. Earth–Science Reviews, 12(1): 1–33. https://doi.org/10.1016/0012-8252(76)90052-0

Thompson, J.B. 1982. Composition space: An algebraic and geometric approach. In: Ferry, J.M. (editor), Characterization of metamorphism through mineral equilibria. Mineralogical Society of America, Reviews in Mineralogy 10, p. 1–31.

Torres–Roldán, R.L., García–Casco, A. & García–Sánchez, P.A. 2000. CSpace: An integrated workplace for the graphical and algebraic analysis of phase assemblages on 32–bit wintel platforms. Computers & Geosciences, 26(7): 779–793. https://doi.org/10.1016/S0098-3004(00)00006-6

Toussaint, J.F. & Restrepo, J.J. 1989. Acreciones sucesivas en Colombia: Un nuevo modelo de evolución geológica. V Congreso Colombiano de Geología. Memoirs, I, p. 127–146. Bucaramanga.

Trommsdorff, V. & Connolly, J.A.D. 1990. Constraints on phase diagram topology for the system CaO–MgO–SiO_2–CO_2–H_2O. Contributions to Mineralogy and Petrology, 104(1): 1–7. https://doi.org/10.1007/BF00310641

Villagómez, D., Spikings, R., Magna, T., Kammer, A., Winkler, W. & Beltrán, A. 2011. Geochronology, geochemistry and tectonic evolution of the Western and Central Cordilleras of Colombia. Lithos, 125(3–4): 875–896. https://doi.org/10.1016/j.lithos.2011.05.003

Vinasco, C.J., Cordani, U.G., González, H., Weber, M. & Peláez, C. 2006. Geochronological, isotopic, and geochemical data from Permo–Triassic granitic gneisses and granitoids of the Colombian central Andes. Journal of South American Earth Sciences, 21(4): 355–371. https://doi.org/10.1016/j.jsames.2006.07.007

Wakabayashi, J. & Dilek, Y. 2003. What constitutes 'emplacement' of an ophiolite?: Mechanisms and relationship to subduction initiation and formation of metamorphic soles. In: Dilek, Y. & Robinson, P.T. (editors), Ophiolites and Earth history. Geological Society of London, Special Publication 218, p. 427–448. https://doi.org/10.1144/GSL.SP.2003.218.01.22

Whitney, D.L. & Evans, B.W. 2010. Abbreviations for names of rock–forming minerals. American Mineralogist, 95(1): 185–187. https://doi.org/10.2138/am.2010.3371

Explanation of Acronyms, Abbreviations, and Symbols:

An	Anorthite
Atg	Antigorite
Ath	Anthophyllite
Brc	Brucite
Cal	Calcite
Chl	Chlorite
Chu	Clinohumite
CIPW	Cross, Iddings, Pierson, and Washington
CMAS	CaO–MgO–Al_2O_3–SiO_2
CMS	CaO–MgO–SiO_2
CNPq	Conselho Nacional de Desenvolvimento Científico e Tecnológico
Cpx	Clinopyroxene
Di	Diopside
Dol	Dolomite
En	Enstatite
Fl	H_2O–fluid
Fo	Forsterite
Grt	Garnet
IAT	Island–arc tholeiite
ICP–OES	Inductively coupled plasma optical emission spectrometry
LOI	Loss on ignition
Lz	Lizardite
Mgs	Magnesite
MORB	Mid–ocean ridge basalt
Ol	Olivine
Opx	Orthopyroxene
P	Pressure
Per	Periclase
Qz	Quartz
Spl	Spinel
Tlc	Talc
T	Temperature
Tr	Tremolite
*	Total Fe expressed as FeO
** LOI	Loss on ignition

Authors' Biographical Notes

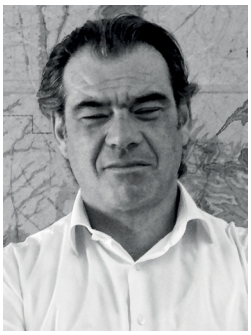

Antonio GARCIA–CASCO is full professor at the Universidad de Granada, España, researcher at the Instituto Andaluz de Ciencias de la Tierra, IACT, UGR–CSIC, España, and associate researcher at the Department of Earth and Planetary Sciences, American Museum of Natural History, NY. His scientific profile is centered in petrology and geochemistry metamorphic and igneous rocks, with emphasis in phase equilibrium, thermodynamics, and geochronology in order to establish P–T–t paths and decipher orogenic evolution of active plate margins. He has leaded and collaborated in national and international research projects with focus in the geodynamic evolution of the Caribbean Plate (e.g., UNESCO–IGCP 546 "Subduction Zones of the Caribbean"; http://www.ugr.es/~agcasco/igcp546/), in particular in Cuba, Dominican Republic, Guatemala, and the Sierra Nevada de Santa Marta and Central Cordillera of Colombia, subduction–related accretionary complexes of Chile and Kirgizia, the Betic–Rif and Variscan belts of Spain and Morocco and Neoproterozic belts in Morocco and Brazil, among others. He has also contributed to archaeometric research in pre–Columbian Greater and Lesser Antilles, Bahamas, Colombia, and Panamá, with special emphasis in jade. For more information http://www.ugr.es/~agcasco/personal/ > CV.

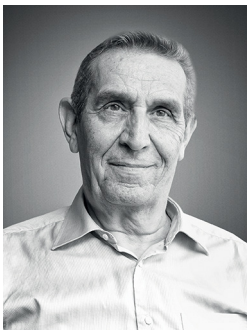

Jorge Julián RESTREPO obtained a degree in mining engineering and metallurgy from the Universidad Nacional de Colombia in 1968 and a MS in geology at the Colorado School of Mines in 1973. He was a faculty member of the Universidad Nacional de Colombia Sede Medellín, for over 40 years and currently holds the title of Professor Emeritus. He taught mineralogy, metamorphic petrology, regional geology, field geology, and geochronology. His research focused on plate tectonics applied to the geology of Colombia, tectonostratigraphic terranes, geochronology and the geologic evolution of metamorphic and mafic/ultramafic complexes of the Central Cordillera.

Ana María CORREA–MARTÍNEZ graduated in geological engineering from the Universidad Nacional de Colombia Sede Medellín and has a PhD in Geology from the Universidade de Brasília (Brasil), where she studied the petrogenesis of the Aburrá Ophiolite in the Colombian Central Cordillera. Between 2008 and 2013, she worked as a gold exploration geologist and chief of mineral exploration projects. She was lecturer at the Universidad Nacional de Colombia (Medellín) in the Departamento de Recursos Minerales. Since 2014, she has worked in the Servicio Geológico Colombiano on geochronology of metamorphic units from the northwestern slope of the Central Cordillera and on the project "Jurassic Magmatism in the Colombian Andes".

Idael Francisco BLANCO–QUINTERO did his undergraduate geological engineering at the Instituto Superior Minero Metalúrgico (ISMM) in Cuba. He obtained the FPU grant from the Spanish Ministry of Education, to support the PhD studies in the Universidad de Granada (España). The PhD studies focused on a subduction system, studying the partial melting of a slab, and the evolution of arc magma in eastern Cuba. During the past 5 years, he was a professor (assistant and associate) at the Universidad de los Andes (Colombia). Currently he is assistant professor at the Universidad de Alicante (España). The research activity are mainly associated with regional metamorphism associate with evolution of convergent margins (subduction) and the pressure–temperature path of the metamorphic rocks. He uses thermobarometric calculations combined with geochemistry and mineralogy studies to determine the evolution of the complexes obtaining regional implications.

Joaquín Antonio PROENZA is an associate professor in the Department of Mineralogy, Petrology, and Applied Geology at the University of Barcelona (España). His research activities are concerned with mineralogy, petrology, geochemistry and metallogenesis of mafic, and ultramafic rocks. His recent projects include metallogenetic processes of supergene Co–Ni enrichment and platinum group elements in Ni–laterite deposits, and the study of ultramafic complexes along the (paleo–) margins of the Caribbean Plate. He is currently investigating the discovery of exotic minerals, normally associated with conditions of ultra–high pressure in highly reducing envi-

ronments and with continental domains, in chromitites and associated peridotites within ophiolite complexes.

Marion WEBER has a PhD in Geochemistry from Leicester University, and is a full professor at the Geosciences and Environmental Department from the Universidad Nacional de Colombia Sede Medellín. Research interests comprise metamorphic petrology and geochemistry applied to understanding the evolution of the Caribbean region. Dr. Weber currently holds the position of Museum Director of the University Geosciences Museum.

Lidia BUTJOSA graduated in geology in 2011 (University of Barcelona) and MS in geology in 2012 (University of Barcelona and Autonomous University of Barcelona). Member of research group "Mineral Resources: Deposits, applications and sustainability" (2014 SGR 1661). Nowadays, she is doing the PhD focused on the petrogenesis of the ophiolitic mélange of central Cuba and their origin and evolution from abyssal to subduction and supra-subduction zone settings. The PhD is part of the Spanish MINECO project of "Complejos ultramáficos oceánicos en márgenes de placa convergentes: un registro petrológico, geoquímico y metalogenético de la tectónica global (región del Caribe)" (CGL2012–36263). Research interest: Igneous and metamorphic petrology, subduction processes, formation of serpentinitic mélanges, thermodynamic modelling and metasomatism in the crust and mantle.

Volume 2

Chapter 3

Late Triassic to Jurassic Magmatism in Colombia: Implications for the Evolution of the Northern Margin of South America

https://doi.org/10.32685/pub.esp.36.2019.03
Published online 16 October 2020

Julián Andrés LÓPEZ–ISAZA[1]* and Carlos Augusto ZULUAGA[2]

1 jlopez@sgc.gov.co, jalopezi@unal.edu.co
Servicio Geológico Colombiano
Diagonal 53 n.° 34–53
Bogotá, Colombia
Universidad Nacional de Colombia
Sede Bogotá
Carrera 30 n.° 45–03
Bogotá, Colombia

2 cazuluagacas@unal.edu.co
Universidad Nacional de Colombia
Sede Bogotá
Carrera 30 n.° 45–03
Bogotá, Colombia

* Corresponding author

Supplementary Information:

S: https://www2.sgc.gov.co/LibroGeologiaColombia/tgc/sgcpubesp36201903s.pdf

Abstract Volcanic and plutonic rocks that compose the Late Triassic to Jurassic magmatic belt in Colombia result from partial melting of lower crustal rocks mixed with mantle melts in a continental margin setting. Lithologies include quartz monzonites, monzogranites, syenogranites (locally leucocratic), granodiorites, tonalites, diorites, gabbros, and volcaniclastic successions intersected by porphyritic hypabyssal rocks of andesitic, dacitic, and latitic compositions. The elongated geometry of plutons suggests that the accommodation spaces of magmatic pulses were related to transtensional environments in a supra–subduction tectonic framework with mantle interaction, melting of slab sediments, and crustal contamination. The nature of magmatism resulted from interactions between crustal and mantle–derived magmas in a continental margin setting that progressively changed from Late Triassic postcollisional extension (associated with orogenic collapse?) to a predominantly Late Jurassic volcanic arc developed in a supra–subduction regime; the evolution of the magmatic belt is marked spatially from east to west and temporally over a time span of approximately 60 my. The sources of the Late Triassic to Jurassic magmatic belt are varied and associated with melting of the supra–subduction mantle wedge and differentiation of tholeiitic or mildly calc–alkaline basalts and intermediate rocks and include partial melting of pelitic rocks, tonalites, granodiorites, tholeiites, and high–aluminum basalts or andesites.

Keywords: *high–potassium calc–alkaline rocks, shoshonitic magmatism, active continental margin, postcollisional magmatism, oblique subduction.*

Resumen Las rocas volcánicas y plutónicas que conforman el cinturón magmático del Triásico Tardío–Jurásico en Colombia son el resultado de la fusión parcial de rocas de la corteza inferior mezcladas con fundidos provenientes del manto en un ambiente de margen continental. Las litologías corresponden a cuarzomonzonitas, monzogranitos, sienogranitos (localmente leucocráticos), granodioritas, tonalitas, dioritas, gabros y sucesiones volcanosedimentarias cortadas por rocas hipoabisales porfídicas de composición andesítica, dacítica y latítica. La geometría alargada de los plutones sugiere que los espacios para la acomodación de los pulsos magmáticos se relacionaron con ambientes estructurales transtensivos en un marco tectónico de suprasubducción con interacción del manto, fusión de los sedimentos de la placa subductante y contaminación cortical. La naturaleza del magmatismo es resultado de interacciones entre magmas derivados de la corteza y magmas derivados del manto en un margen continental

Citation: López–Isaza, J.A. & Zuluaga, C.A. 2020. Late Triassic to Jurassic magmatism in Colombia: Implications for the evolution of the northern margin of South America. In: Gómez, J. & Pinilla–Pachon, A.O. (editors), The Geology of Colombia, Volume 2 Mesozoic. Servicio Geológico Colombiano, Publicaciones Geológicas Especiales 36, p. 77–116. Bogotá. https://doi.org/10.32685/pub.esp.36.2019.03

que cambió progresivamente de extensional poscolisional (¿asociado con colapso orogénico?) durante el Triásico Tardío a un arco volcánico desarrollado en un régimen de suprasubducción durante el Jurásico Tardío predominantemente; la evolución del cinturón magmático se marca espacialmente de este a oeste y temporalmente sobre un lapso de aproximadamente 60 millones de años. Las fuentes del arco magmático del Triásico Tardío–Jurásico son variadas y están asociadas con la fusión de la cuña mantélica de suprasubducción y diferenciación de basaltos y rocas intermedias toleíticas o ligeramente calcoalcalinas e incluye fusión parcial de rocas pelíticas, tonalitas, granodioritas, toleítas y basaltos o andesitas ricas en aluminio.

Palabras clave: *rocas calcoalcalinas con alto potasio, magmatismo shoshonítico, margen continental activa, magmatismo poscolisional, subducción oblicua.*

1. Introduction

Igneous rocks, both volcanic and plutonic, develop in different tectonic settings, all of which are linked to the Wilson cycle and therefore to the supercontinent cycle (see, e.g., Nance et al., 2014; Frost et al., 2016; Chen & Zhao, 2017; and references therein). The Pangaea supercontinent reached its configuration during the Triassic, amalgamating continental blocks and terranes (ribbon continents) of different origins (Pindell, 1985; Jaillard et al., 1990; Stampfli et al., 2013; Scotese, 2014a; Belica et al., 2017; Riel et al., 2018). Paleogeographic reconstructions suggest that during late Paleozoic to early Mesozoic times, the northwestern margin of South America (Gondwana) was dominated by the convergence of the Farallón oceanic plate, also defined as the Panthalassa subduction zone along the western margin of Pangaea (Mišković et al., 2009; Muttoni et al., 2009; Belica et al., 2017; Riel et al., 2018). In this paper, we review the significance of Late Triassic and Jurassic magmatism in Colombia and its implications for the evolution of the northwestern margin of Gondwana.

During the Pangaea supercontinent agglomeration, the Alleghanian orogen recorded the closure of the Rheic Ocean and subsequent collision between Laurasia and Gondwana (Craddock et al., 2017). This tectonic framework allowed dextral transcurrent plate motion and the emplacement of Permian – Triassic syntectonic granitoids (e.g., Vinasco et al., 2006; López et al., 2007; Muttoni et al., 2009; Cardona et al., 2010; Cochrane et al., 2014a). On the other hand, the circum–Pacific orogenic system recorded the subduction of Panthalassa (van der Meer et al., 2012; Ganne et al., 2017; Ganne & Feng, 2018).

Later, during the Jurassic, the Pangaea supercontinent breakup marked the progressive opening of ocean basins and the drifting of Gondwana and Laurasia (Scotese, 2014b; Dera et al., 2015; Matthews et al., 2016; Martini & Ortega–Gutiérrez, 2018). In this context, prior to the Atlantic Ocean opening, the separation between the Yucatán Block and the passive margin of Gondwana to the north (today Venezuela) favored the development of the proto–Caribbean seaway (Pindell & Kennan, 2009; Noguera et al., 2011; Martini & Ortega–Gutiérrez, 2018). The Pacific margin of South America, during Mesozoic times, was also experiencing an extensional tectonic regime associated with block faulting and extension above a retreating slab (Pitcher, 1988, 1997). According to Pitcher (1997), this extensional regime started as early as the Permian – Triassic with the development of a graben in the eastern Andes of Perú and Bolivia, which led to crustal thinning and the formation of fault–bounded marginal basins to the west from mid–Ecuador to Patagonia. The northwestern corner of South America is also characterized by Late Triassic to Jurassic extensional marginal basins infilled with deposits produced from erosion, red beds and volcanic products (Cediel et al., 2003).

The modern Andes form a continuous mountain range along the western margin of South America and include fragments of several orogens that partly represent long–lived subduction. Magmatic arc assemblages were emplaced in a continental margin by persistent convergence and interaction between the "Pacific oceanic crust" and the continental "South American Plate" since the Paleozoic (Kirsch et al., 2016; Paul et al., 2018). In particular, a Late Triassic to Jurassic magmatic belt is recognized along the northern Andes from the Gulf of Guayaquil (southern Ecuador) to northern Colombia and Venezuela (Gansser, 1973; Pennington, 1981; Aggarwal, 1983; Aspden et al., 1992; Litherland et al., 1994; Ramos, 1999, 2009; Cediel et al., 2003; Leal–Mejía, 2011; Maloney et al., 2013; Cochrane et al., 2014a, 2014b; Spikings et al., 2015; van der Lelij et al., 2016). Across the Colombian Andes (Figure 1), the belt intersects crystalline basements composed of schists, amphibolites, gneisses, local granulites, and granitoids, with Proterozoic, Paleozoic, and Triassic ages (Aspden et al., 1987; 1992; Bayona et al., 1994; Litherland et al., 1994; Bustamante et al., 2010; Leal–

→

Figure 1. Distribution of Late Triassic to Jurassic magmatism in Colombia; plutonic, hypabyssal, and volcanic rocks representative of each zone are shown with the U/Pb zircon age ranges. Northern Zone: Guajira and Sierra Nevada de Santa Marta, Eastern Central Zone: Santander Massif, Western Central Zone: serranía de San Lucas and Central Cordillera north of 5° N, and Southern Zone: Upper Magdalena Valley.

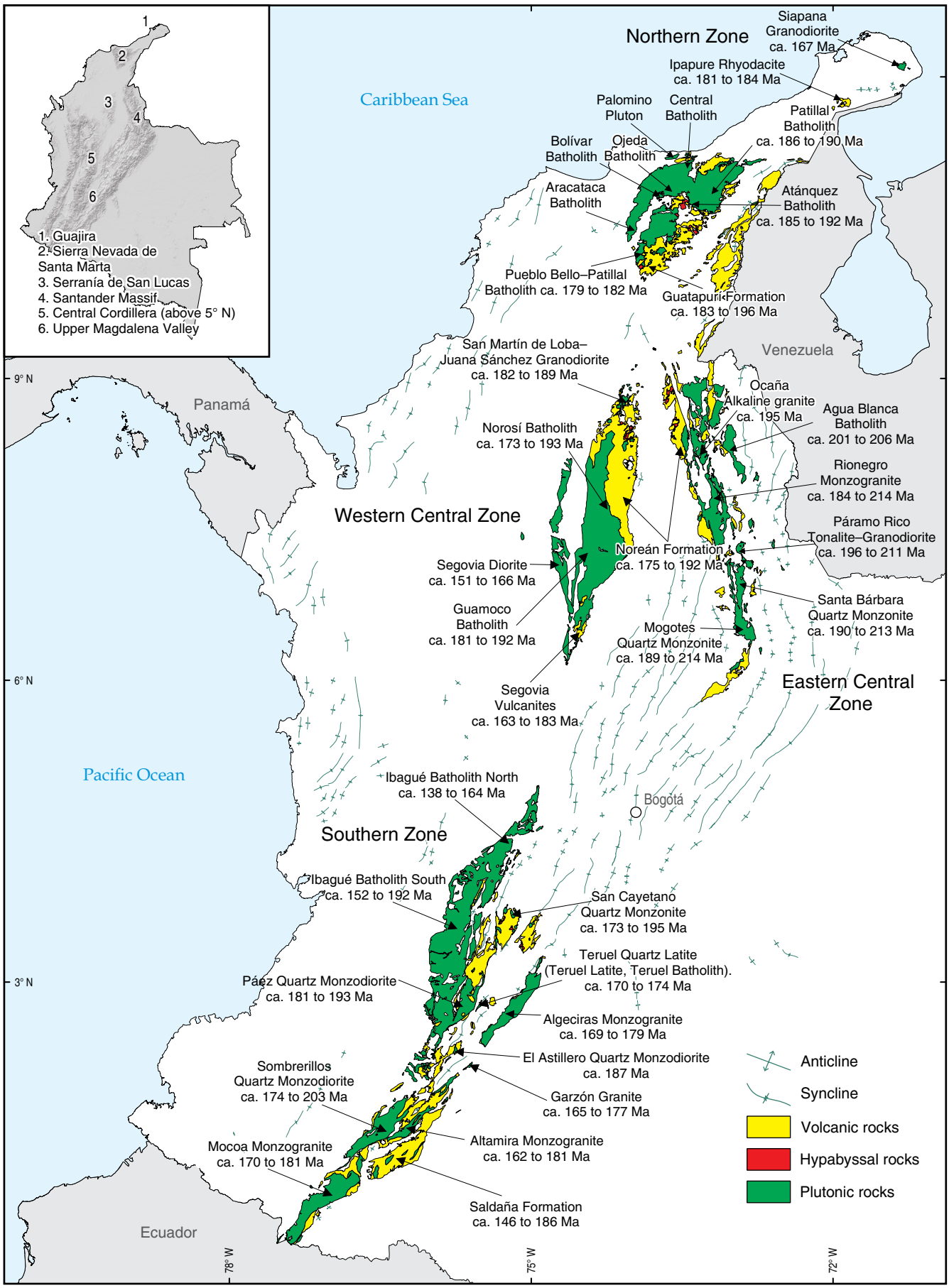
1
2
3
4
5
6
1. Guajira
2. Sierra Nevada de Santa Marta
3. Serranía de San Lucas
4. Santander Massif
5. Central Cordillera (above 5° N)
6. Upper Magdalena Valley
Northern Zone
Siapana Granodiorite ca. 167 Ma
Ipapure Rhyodacite ca. 181 to 184 Ma
Caribbean Sea
Palomino Pluton
Central Batholith
Patillal Batholith ca. 186 to 190 Ma
Bolívar Batholith
Ojeda Batholith
Aracataca Batholith
Atánquez Batholith ca. 185 to 192 Ma
Pueblo Bello–Patillal Batholith ca. 179 to 182 Ma
Guatapurí Formation ca. 183 to 196 Ma
Venezuela
San Martín de Loba–Juana Sánchez Granodiorite ca. 182 to 189 Ma
Ocaña Alkaline granite ca. 195 Ma
Agua Blanca Batholith ca. 201 to 206 Ma
Norosí Batholith ca. 173 to 193 Ma
Rionegro Monzogranite ca. 184 to 214 Ma
Panamá
Western Central Zone
Páramo Rico Tonalite–Granodiorite ca. 196 to 211 Ma
Noreán Formation ca. 175 to 192 Ma
Segovia Diorite ca. 151 to 166 Ma
Santa Bárbara Quartz Monzonite ca. 190 to 213 Ma
Guamoco Batholith ca. 181 to 192 Ma
Mogotes Quartz Monzonite ca. 189 to 214 Ma
Eastern Central Zone
Segovia Vulcanites ca. 163 to 183 Ma
Pacific Ocean
Ibagué Batholith North ca. 138 to 164 Ma
Bogotá
Southern Zone
Ibagué Batholith South ca. 152 to 192 Ma
San Cayetano Quartz Monzonite ca. 173 to 195 Ma
Teruel Quartz Latite (Teruel Latite, Teruel Batholith). ca. 170 to 174 Ma
Páez Quartz Monzodiorite ca. 181 to 193 Ma
Algeciras Monzogranite ca. 169 to 179 Ma
El Astillero Quartz Monzodiorite ca. 187 Ma
Sombrerillos Quartz Monzodiorite ca. 174 to 203 Ma
Garzón Granite ca. 165 to 177 Ma
Mocoa Monzogranite ca. 170 to 181 Ma
Altamira Monzogranite ca. 162 to 181 Ma
Saldaña Formation ca. 146 to 186 Ma
Ecuador
9° N
6° N
3° N
78° W
75° W
72° W
Anticline
Syncline
Volcanic rocks
Hypabyssal rocks
Plutonic rocks

Mejía, 2011; Leal–Mejía et al., 2011; Cochrane et al., 2014a, 2014b; Gómez et al., 2015; Spikings et al., 2015; Zuluaga et al., 2015; van der Lelij et al., 2016).

Models explaining this Late Triassic to Jurassic magmatic belt range from intracontinental extension to continental arc magmatism. Some models suggest the presence of bimodal magmatism that developed during intracontinental extension related to rifting and drifting of the Pangaea supercontinent (Pindell & Dewey, 1982; Clavijo, 1995a; Mojica & Kammer, 1996; Sarmiento–Rojas, 2001; Rolon, 2004; Sarmiento–Rojas et al., 2006; Bayona et al., 2012; Zapata et al., 2012). However, most commonly accepted models involve continental arc magmatism either in a back–arc extension tectonic setting (Leal–Mejía, 2011; Cochrane et al., 2014a, 2014b; Spikings et al., 2015) or along intra–arc extensional basins (Zuluaga et al., 2015). In either case, the geodynamic context is interpreted to have been dominated by subduction–related magmatism followed by the development of transtensional basins from the Late Jurassic to the Early Cretaceous.

The aim of this review is to document the interactions between crustal and mantle–derived magmas in a continental margin that progressively changed from a Late Triassic postcollisional extensional setting (associated with orogenic collapse?) to a predominantly Late Jurassic volcanic arc setting developed in a supra–subduction regime. To support this review, we present an analysis and interpretation of published and unpublished field relations, petrographic descriptions, whole–rock geochemical data, and U/Pb zircon ages. The data set is divided into four zones: (1) Northern Zone (Guajira and Sierra Nevada de Santa Marta); (2) Eastern Central Zone (Santander Massif); (3) Western Central Zone (north of 5° N latitude in the Central Cordillera and serranía de San Lucas); and (4) Southern Zone (Upper Magdalena Valley). This division takes into account both the distribution of igneous rocks along massifs and mountain ranges and the temporality of the magmatism. We argue that the dataset indicates (i) a supra–subduction regime and (ii) a northwestern South America Late Triassic to Jurassic flare–up over a time span of approximately 60 my. This model is supported mostly by an interpretation of variations in magmatic activity based on the relative abundance of known U/Pb zircon ages.

Tectonic interpretations presented here follow the collision concept of Bonin et al. (1998) and Song et al. (2015); e.g., collision is the "welding of at least two terranes into a new continental land", and from this concept, postcollision (or 'late orogenic') is defined as the "episode occurring after the major collision", postorogenic as the "subsequent episodes when the geodynamic context becomes entirely intraplate, with the welded terranes moving according to same pole of rotation", and anorogenic as "later episodes characterized by the presence of alkaline magmatic suites emplaced in intraplate rifts and not associated with local plate convergence". In this context, the magmatic events that accompany the postcollision state are characterized by the presence of peraluminous S–type granite suites and high–K calc–alkaline suites. Pearce et al. (1984) also note that granitic rocks are the most significant magmatic products of collisional belts and can be geochemically discriminated according to the type of collision (continent–continent, continent–arc, arc–arc) and the timing of the main deformation event (syncollisional, postcollisional). Chemically, peraluminous granites are approximately equivalent to S–type granites, and metaluminous granites are approximately equivalent to I–type granites (Chappell & White, 1974; Clarke, 1981; Nédélec & Bouchez, 2015), although I–type granites include Al–poor granites or weakly peraluminous granites (Miller, 1985; Nédélec & Bouchez, 2015). Peraluminous rocks are composed of muscovite, biotite, ilmenite, monazite, aluminosilicates, cordierite, garnet, topaz, tourmaline, spinel, and corundum and are related to continent–continent collision tectonics involving thickened continental crust (Clarke, 1992). Metaluminous rocks consist of biotite, minor muscovite, magnetite, titanite, allanite, orthopyroxene, clinopyroxene, hornblende, and epidote and are associated with subduction–related continental and island arcs (Clarke, 1992). Syncollisional granites are peraluminous S–type granites, and postcollisional granites commonly are calc–alkaline, weakly peraluminous to metaluminous I–type granites, although S– and A–type granites may also be found in this type of environment (Pearce et al., 1984).

The elements Zr, Nb, Y, Yb, La, Ta, Th, Hf, and Co are considered immobile in different geological environments. Therefore, they are used to discriminate tectonic settings and to differentiate magmatic processes and magma sources (Pearce, 1982, 1983; Pearce et al., 1984; Harris et al., 1986; Müller et al., 1992; Thiéblemont & Tégyey, 1994; Gorton & Schandl, 2000; Schandl & Gorton, 2002; Elliott, 2003; Pearce, 2008; Moreno et al., 2014). Additionally, the presence of high–potassium rocks is used to complement interpretations since the K_2O enrichments in granites from the high–potassium calc–alkaline and shoshonitic fields are features that can be generated by different mechanisms, including mantle–derived magma differentiation, reworking of sedimentary materials induced by mantle–derived magmas, or lower continental crust melting (Zhao et al., 2013; Bao et al., 2018).

2. Late Triassic to Jurassic Magmatic Belt in Colombia

The magmatic belt has a longitudinal axis that is parallel to the axes of the mountain ranges and intersects the crystalline cores. In this belt, a magma productivity of ca. 675 000 to 2 362 500 km^3 over a length of ca. 1500 km is estimated by Cochrane et al. (2014b). Most intrusive bodies are nested plutons with mainly sharp faulted contacts and local evidence of injection processes. Common compositional varieties in plutons include quartz monzonites, monzogranites, syenogranites, granodi-

orites, tonalites, diorites, and gabbros (Ordóñez–Carmona et al., 2006; Mantilla–Figueroa et al., 2013; van der Lelij, 2013; Cochrane et al., 2014b; Spikings et al., 2015; van der Lelij et al., 2016). These intrusive rocks usually contain quartz, alkali feldspar, and plagioclase and locally contain pyroxenes, some with muscovite and garnet (typical of S–type peraluminous granitoids) and others with biotite, hornblende, epidote (allanite), and titanite (typical of I–type metaluminous granitoids). In many cases, it is possible to identify intrusive relations with adjacent units due to the development of local injection fabrics and contact zones with hornfels (Figure 2). Plutons commonly have associated aplitic and pegmatitic dikes with compositions ranging from tonalite to gabbro; they are also cut by hypabyssal rhyolite to basalt dikes.

Within the belt, it is common to see volcanic rocks, including tuffs, ignimbrites, lavas, and hypabyssal rocks of different compositions. Volcanic rocks are found in volcanic–sedimentary successions that generally include poorly sorted, matrix–supported to clast–supported coarse tuffaceous deposits. Other commonly observed lithologies include lavas and hypabyssal rocks of dacitic to rhyolitic compositions (Tschanz et al., 1969, 1974; Jaillard et al., 1990; Bayona et al., 1994; Clavijo, 1995a, 1995b; Núñez et al., 1996; Ingeominas & Universidad Industrial de Santander, 2006a, 2006b, 2006c, 2006d; Colmenares et al., 2007; Pinilla–Ocampo, 2013; González et al., 2015a, 2015b, 2015c, 2015d, 2015e, 2015f; Zuluaga et al., 2015; Rodríguez et al., 2016a, 2016b, 2018a, 2018b, 2018c). Lavas are generally porphyritic with phenocrysts of feldspar, quartz, biotite, hornblende, and pyroxenes in a hyalocrystalline to microcrystalline matrix.

The petrographic characteristics for each zone are summarized in the following sections.

2.1. Northern Zone (Guajira and Sierra Nevada de Santa Marta, Table 1)

2.1.1. Guajira

In the Guajira region of Colombia, metaluminous and peraluminous granitoids and volcanic rocks of the high–potassium calc–alkaline series have been related to volcanic arcs that developed in a collisional setting along an active continental margin in the Jurassic (Zuluaga et al., 2015). Plutonic rocks belong to three main large bodies (Ipapure Granodiorite, Siapana Granodiorite, and Cosinas Tonalite) and include granodiorites, monzodiorites, diorites, and tonalites; the estimated ages of these rocks (Rb/Sr whole–rock and U/Pb zircon dating) range from 167 to 184 Ma (MacDonald, 1964; Cardona et al., 2006; Zuluaga et al., 2015; Ríos–Blandón, 2016). The volcanic rocks include andesites, dacites, rhyodacites, and tuffs, which are collectively termed the Ipapure Rhyodacite (Pinilla–Ocampo, 2013; Zuluaga et al., 2015).

2.1.2. Sierra Nevada de Santa Marta

The plutons in Sierra Nevada de Santa Marta consist of diorites, tonalites, granodiorites, and granites of Early Jurassic age that have been grouped into the Socorro Stock, the Nueva Lucha Pluton, and the Central, Bolívar, Ojeda, Aracataca, Atánquez, Pueblo Bello, and Patillal Batholiths (Tschanz et al., 1969, 1974; Colmenares et al., 2007; Quandt, 2013). These rocks have been classified as metaluminous, I–type calc–alkaline rocks of the medium to high–potassium series, considered typical of continental arc settings (Quandt, 2013; López & Zuluaga, 2016; Quandt et al., 2018). Rb/Sr (whole–rock) and K/Ar (hornblende, muscovite, and biotite) ages range from 162 to 181 Ma (Tschanz et al., 1969, 1974), while U/Pb (zircon) crystallization ages range between 176 Ma and 196 Ma (Leal–Mejía, 2011; Quandt et al., 2018). Plutons of the Sierra Nevada de Santa Marta are associated with volcanic rocks, hypabyssal intrusions, and volcaniclastic rocks with andesitic, dacitic, rhyolitic, and basaltic compositions (Tschanz et al., 1969, 1974). Several large ignimbrite bodies are recognized (Los Tábanos, La Piña, Los Clavos, La Paila, and Caja de Ahorros); these rocks were grouped informally with the Golero Rhyolite in the "Jurassic volcaniclastic and volcanic rocks"; however, this grouping did not consider a systematic difference in composition relative to the observed plutonic rocks (see Colmenares et al., 2007 and Quandt et al., 2018).

2.2. Eastern Central Zone (Santander Massif, Table 2)

The Santander Massif is largely composed of several Upper Triassic to Lower Jurassic metaluminous to strongly peraluminous granitoids intruding the Bucaramanga Gneiss and the Silgará Schist metamorphic rocks (Onzaga Granodiorite, Guaca River Diorite, San Martín Tonalite, Suratá Diorite, Tonalite and Granodiorite, Páramo Rico Tonalite and Granodiorite, La Corcova Quartz Monzonite, Pescadero Monzogranite, Santa Bárbara Quartz Monzonite, Mogotes Quartz Monzonite, Ocaña Alkaline Granite, and Rionegro Monzogranite). Compositionally, they are mainly diorite, tonalite, granodiorite, and granite; petrographic and geochemical characteristics and isotopic ages are discussed in several publications including Goldsmith et al. (1971), Ward et al. (1973), Dörr et al. (1995), Restrepo–Pace (1995), Ordóñez–Calderón (2003), Mantilla–Figueroa et al. (2009), Leal–Mejía (2011), Mantilla–Figueroa et al. (2013), van der Lelij (2013), Bissig et al. (2014), Arango et al. (2016), Correa–Martínez et al. (2016, 2018), Rodríguez et al. (2016a, 2017b, 2018c), González et al. (2015g), van der Lelij et al. (2016), Zapata et al. (2016a, 2018), Hernández et al. (2017), López et al. (2017), Rodríguez et al. (2017a), Leal–Mejía et al. (2019), and Zuluaga & López (2019). Geochemical interpretations from these publications agree that the granites have I–

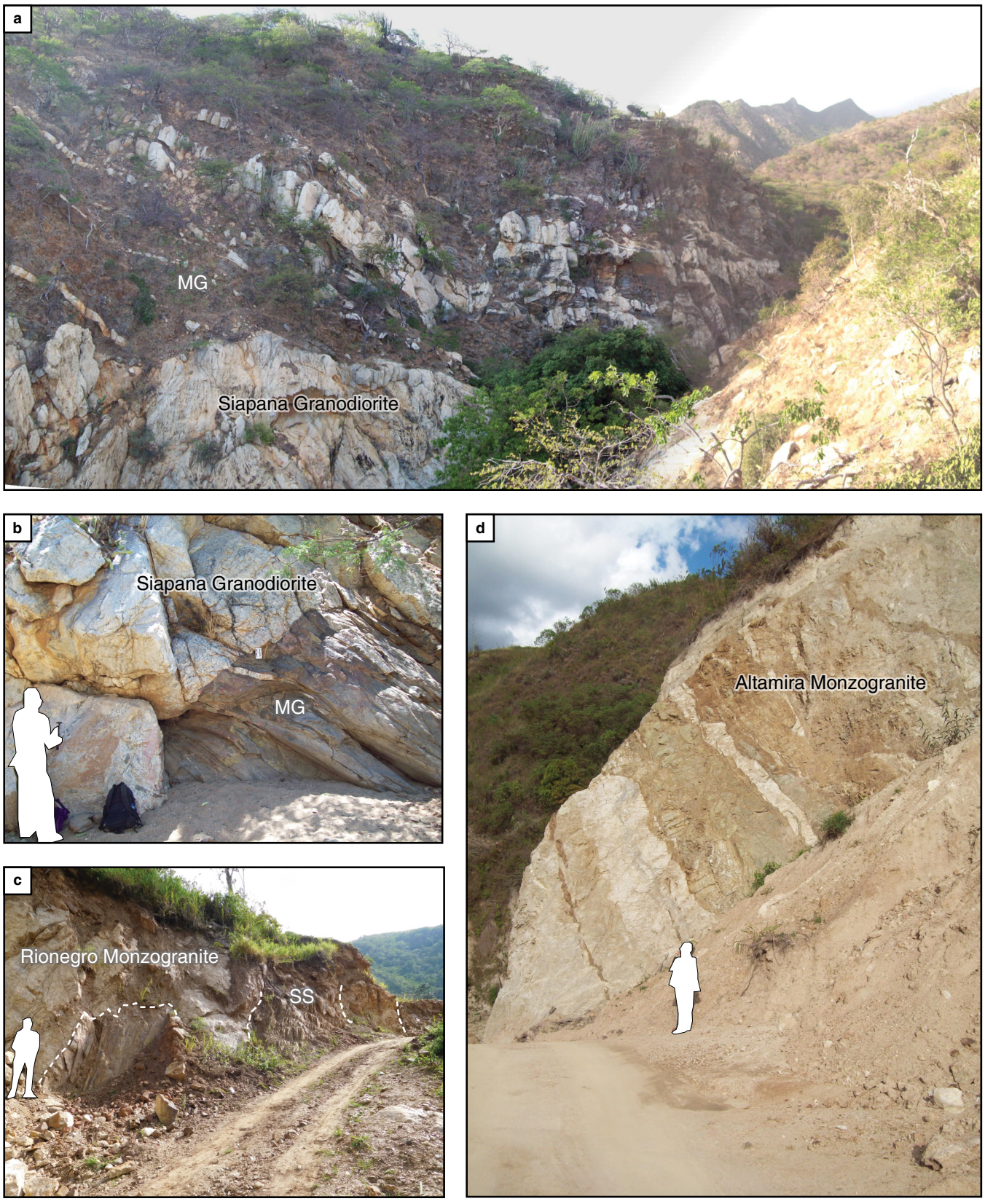

Figure 2. Typical intrusive contacts of plutonic rocks of the Late Triassic to Jurassic magmatic belt in Colombia. **(a)** Border zone of the contact between the Siapana Granodiorite and the Macuira Gneiss (MG), arroyo Guajarima, serranía de Macuira, Northern Zone. **(b)** Sharp contact between the Siapana Granodiorite and the Macuira Gneiss (MG), arroyo Guajarima, serranía de Macuira, Northern Zone. **(c)** Sharp contact between the Rionegro Monzogranite and the Silgará Formation (SS), Santander Massif, Eastern Central Zone. **(d)** Aplitic and mafic dikes intruding the Altamira Monzogranite, Garzón Massif, Eastern Cordillera, Southern Zone.

Table 1. Characteristics of the lithostratigraphic units of the Northern Zone.

Lithostratigraphic unit	Lithology	Contact type/country rock	Age (Ma)	Method	Reference
Guajira Sector					
Siapana Granodiorite	Granodiorite	Intrusive/Permian metamorphic amphibolite facies	167.0 ± 9.4	LA–ICP–MS	Cardona et al. (2006)
Cosinas Tonalite	Tonalite, quartz diorite, quartz monzodiorite.	Faulted/Cenozoic sedimentary rocks			
Ipapure Granodiorite	Tonalite, diorite, granodiorite, monzodiorite, monzogranite.	Intrusive/Jurassic volcanic rocks			
Ipapure Rhyodacite	Andesites, dacites, rhyolite, rhyodacites, tuffs.	Discordant–Intrusive/Jurassic rocks	184.0 ± 0.7 184.0 ± 0.8 181.7 ± 1.0	LA–ICP–MS	Zuluaga et al. (2015)
Sierra Nevada de Santa Marta Sector					
Triassic keratophyric porphyry	Rhyolite, latite, basalt.	Intrusive/Triassic volcanic–sedimentary successions			
Triassic spilites	Basalt, latite.	Triassic volcanic–sedimentary successions			
Pueblo Bello–Patillal Batholith	Quartz monzonite, monzogranite (locally leucocratic), granophyric granite.	Gradational intrusive/Jurassic plutonic and Neoproterozoic metamorphic granulite facies	179.8 ± 3.3 182.2 ± 1.0 179.8 ± 3.3	LA–MC–ICP–MS LA–ICP–MS	Leal–Mejía (2011) Quandt et al. (2018)
Patillal Batholith	Quartz monzonite, monzogranite (locally leucocratic), granophyric granite.	Gradational intrusive/Jurassic plutonic	186.0 ± 0.7 186.4 ± 1.6 189.4 ± 2.0 190.3 ± 1.2	LA–ICP–MS	Quandt et al. (2018)
Central Batholith	Quartz diorite, granodiorite, quartz monzonite.	Intrusive–Faulted/Neoproterozoic metamorphic granulite facies and Jurassic plutonic			
Caja de Ahorros Ignimbrite	Trachytic to andesitic tuffs and ignimbrites.	Discordant–Faulted/Jurassic volcanic–sedimentary successions			
La Paila Ignimbrite	Breccias, ignimbrites and rhyolitic to trachytic tuffs.	Discordant/Jurassic volcanic–sedimentary successions			
Ojeda Batholith	Quartz monzonite, granodiorite, granite.	Intrusive locally gradational			
Atánquez Batholith	Monzogranite, granite, granodiorite, syenite, tonalite.	Gradational intrusive–Faulted/Neoproterozoic metamorphic granulite facies and Jurassic plutonic	192.1 ± 1.7 185.7 ± 1.0	LA–ICP–MS	Quandt et al. (2018)
Aracataca Batholith	Granodiorite, quartz monzonite.	Sharp and gradational intrusive–Faulted/Neoproterozoic metamorphic granulite facies and Jurassic plutonic			
La Piña Ignimbrite	Vitreous–crystalline, trachytic quartz, latitic quartz, and rhyodacitic and lithic tuffs.	Discordant–Faulted/Jurassic volcanic–sedimentary successions			
Los Clavos Ignimbrite	Trachytic to andesitic tuffs and ignimbrites	Discordant/Jurassic plutonic	180.6 ± 1.2 187.2 ± 1.0	LA–ICP–MS	Quandt et al. (2018)
Bolívar Batholith	Tonalite, granodiorite.	Intrusive/Neoproterozoic metamorphic granulite facies and Jurassic plutonic			
Porphyritic granite	Granite	Intrusive			
Nueva Lucha Pluton	Quartz diorite	Intrusive–Faulted/Metamorphic granulite facies and volcanic–sedimentary successions			
Los Tábanos Rhyodacite	Rhyolitic and dacitic tuffs	Discordant/Jurassic volcanic–sedimentary successions	176.0 ± 0.9	LA–ICP–MS	Quandt et al. (2018)
Golero Rhyolite	Rhyolitic and rhyodacitic tuffs, rhyolitic porphyries.	Discordant–Faulted/Jurassic volcanic–sedimentary successions and plutonic rocks			
Socorro Stock	Diorite, granodiorite.	Faulted/Neoproterozoic metamorphic granulite facies			
Guatapurí Formation	Rhyodacite, rhyolite, lithic tuff.	Intrusive–Discordant	196.5 ± 4.9 183.3 ± 3.0 184.5 ± 1.4	LA–MC–ICP–MS LA–ICP–MS	Leal–Mejía (2011) Quandt et al. (2018)

Table 2. Characteristics of the lithostratigraphic units of the Eastern Central Zone.

Lithostratigraphic unit	Lithology	Contact type/country rock	Age (Ma)	Method	Reference
		Santander Sector			
Agua Blanca Batholith	Quartz monzonite, monzogranite, syenogranite, granodiorite, tonalite, gabbro, microgabbro.	Intrusive–Faulted/Ordovician metamorphic granulite – amphibolite – greenschist facies and Triassic – Jurassic volcanic rocks	202.2 ± 1.0 201.4 ± 3.6 204.9 ± 3.6 206 201.0 ± 3.6 204	LA–ICP–MS CA–ID–TIMS	van der Lelij (2013) González et al. (2015g)
Santa Bárbara Quartz Monzonite	Monzonite, monzogranite, granodiorite, syenogranite.	Intrusive–Faulted/Ordovician metamorphic granulite – amphibolite facies and Paleozoic metasedimentary rocks	190.6 ± 1.5 191.9 ± 1.1 195.1 ± 1.9 196.8 ± 2.0 200.7 ± 2.0 201.6 ± 4.0 203.0 ± 2.6 203.8 ± 2.7 213.9 ± 4.3 199.1 ± 5.7 198.0 ± 2.7 202.5 ± 7.8 209.3 ± 7.3 201.6 ± 4.0 203.8 ± 5.8 213.9 ± 4.3 200.7 ± 2.0 203.0 ± 2.6	LA–ICP–MS	Rodríguez et al. (2018b)
Mogotes Quartz Monzonite	Quartz monzonite, monzogranite, syenogranite, granodiorite, quartz monzodiorite, tonalite.	Intrusive/Ordovician metamorphic granulite – amphibolite – greenschist facies and Paleozoic metasedimentary rocks	211.8 ± 3.8 191.0 ± 3.5 198.0 ± 0.8 201.0 ± 0.9 200.4 ± 0.7 202.5 ± 1.3 198.0 ± 0.8 200.4 ± 2.2 195.7 ± 3.9 199.6 ± 1.8 199.6 ± 2.6 189.1 ± 3.6 193.7 ± 1.3 205.4 ± 3.0 202.1 ± 1.8 191.0 ± 3.5 214.0 ± 7.0 199.0 ± 6.0 203.9 ± 3.9 203.8 ± 4.2 197.6 ± 3.8 191.0 ± 6.5 199.0 ± 6.5 199.6 ± 2.6 193.0 ± 5.6 203.0 ± 4.5 201.0 ± 3.7	LA–ICP–MS CA–ID–TIMS	van der Lelij (2013) Correa–Martínez et al. (2016) Zapata et al. (2018)
La Corcova Quartz Monzonite	Monzogranite, granodiorite, syenogranite, alkali feldspar granite, quartz diorite, quartz monzonite, tonalite subordinate near the margin.	Intrusive/Ordovician metamorphic granulite – amphibolite facies	192.5 ± 2.6 198.3 ± 1.8 199.5 ± 4.6 202.7 ± 1.2 204.8 ± 6.1 210.48 ± 0.92 201.8 ± 4.0 199.5 ± 6.3 214.9 ± 7.3 200.0 ± 11.0 192.9 ± 2.7	LA–ICP–MS CA–ID–TIMS	van der Lelij (2013) Rodríguez et al. (2016a)

Table 2. Characteristics of the lithostratigraphic units of the Eastern Central Zone (*continued*).

Lithostratigraphic unit	Lithology	Contact type/country rock	Age (Ma)	Method	Reference
		Santander Sector			
Páramo Rico Tonalite–Granodiorite	Granodiorite, tonalite, monzogranite (locally) leucocratic.	Intrusive/Ordovician metamorphic granulite – amphibolite – greenschist facies and Upper Triassic plutonic rocks	208.9 211.1 205+5/–9 205–210 210.6 ± 3.5 204.3+2.7/–3.3 202.2+5.3/–3.3 199.1+2.5/–2.6 199.2+2.8/–2.7 199.0+2.5/–2.6 198.4+2.5/–2.6 198.7–2.6/–2.9 196.7+2.9/–2.8 199.8 ± 1.2 208.8 ± 4.1	LA–ICP–MS LA–MC–ICP–MS TIMS CA–ID–TIMS Total dilution	Dörr et al. (1995) Leal–Mejía (2011) Mantilla–Figueroa et al. (2009, 2013) van der Lelij (2013) Bissig et al. (2014)
Rionegro Monzogranite	Quartz monzonite, monzogranite, syenogranite, quartz diorite, quartz syenite, granodiorite, tonalite, diorite, gabbro, gabbronorite, subordinate charnockite.	Intrusive/Ordovician metamorphic granulite – amphibolite – greenschist facies	196.0 ± 1.1 184.1 ± 2.3 186.7 ± 1.9 194.5 ± 1.2 195.5 ± 3.5 196.6 ± 2.1 197.2 ± 1.5 200.8 ± 1.9 214.5 ± 2.7 189.9 ± 1.6 191.2 ± 9.7 186.4 ± 3.6 184.3 ± 6.6 213.6 ± 3.2 193.0 ± 16.0 207.3 ± 1.6 196.6 ± 2.1 195.9 ± 1.6	LA–ICP–MS CA–ID–TIMS	van der Lelij (2013) Arango et al. (2016)
Pescadero Monzogranite	Monzogranite with biotite and muscovite, syenogranite, local granodiorite.	Intrusive/Ordovician metamorphic granulite – amphibolite – greenschist facies	194.8 ± 3.2 197.3 ± 2.4 199.1 ± 1.3 198.1 ± 8.2 196.0 ± 15.0	LA–ICP–MS CA–ID–TIMS	van der Lelij (2013) Zapata et al. (2016a)
Ocaña Alkaline Granite	Quartz monzonite and monzogranite with biotite and muscovite, in complex relationships with rhyolite.	Intrusive/Ordovician metamorphic granulite – amphibolite facies	195.8 ± 1.8 195.9 ± 1.6	CA–ID–TIMS	van der Lelij (2013) Arango et al. (2016)
Onzaga Granodiorite	Granodiorite, quartz monzonite, monzonite.	Intrusive/Ordovician metamorphic granulite – amphibolite facies	200.4 ± 0.7 201.0 ± 0.9	CA–ID–TIMS	van der Lelij (2013)
Suratá Diorite, Tonalite and Granodiorite	Diorite, granodiorite, tonalite with biotite and hornblende.	Intrusive/Ordovician metamorphic granulite – amphibolite – greenschist facies	201.1 ± 1.4 200.0 ± 1.5	CA–ID–TIMS	van der Lelij (2013)
Guaca River Diorite	Diorite	Intrusive/Ordovician metamorphic granulite – amphibolite facies			
San Martín Tonalite	Monzogranite, granodiorite, tonalite, quartz diorite, quartz monzonite, quartz monzodiorite.	Intrusive/Ordovician metamorphic granulite – amphibolite facies	198.9 ± 1.8 198.0 ± 2.8 187.3 ± 7.2 196.6 ± 2.5 197.8 ± 7.0 195.0+6.0–7.7 191.0 ± 5.0	LA–ICP–MS	Rodríguez et al. (2017b)
El Uvo Rhyolites	Rhyolite	Intrusive/Upper Triassic plutonic rocks	197.5 ± 1.5	LA–ICP–MS	Zapata et al. (2018)
San Joaquín Rhyolite	Rhyolite, pheno dacite, pheno–andesite.	Intrusive–Faulted/Paleozoic metasedimentary and Upper Triassic plutonic rocks	201.0 ± 2.1	LA–ICP–MS	Rodríguez et al. (2018c)

Table 2. Characteristics of the lithostratigraphic units of the Eastern Central Zone (*continued*).

Lithostratigraphic unit	Lithology	Contact type/country rock	Age (Ma)	Method	Reference
		Santander Sector			
Alto Los Cacaos Rhyolite	Rhyolite, quartz trachyte, pheno–andesite.	Intrusive–Faulted/Ordovician metamorphic granulite – amphibolite – greenschist facies and Upper Triassic plutonic rocks	205.2 ± 2.6	LA–ICP–MS	Correa–Martínez et al. (2018)
Noreán Formation (Noreán Volcanic Complex)	Lapilli and ash crystal lithic tuffs of dacitic to rhyolitic compositions, lithic agglomerates, polymictic igneous breccias of andesitic and dacitic compositions, and rhyodacitic lavas in addition to basalts, trachytes and andesites. Hypabyssal rocks of andesitic composition.	Discordant–Intrusive/Jurassic rocks	192.4 ± 2.2 184.9 ± 2.0 175.9 ± 1.1	LA–ICP–MS	Correa–Martínez et al. (2019)

and S–type high–potassium calc–alkaline and shoshonitic series signatures and that they were likely emplaced in a continental margin arc setting. Rb/Sr (whole–rock) and U/Pb (zircon) ages range from 210 to 111 Ma. K/Ar (biotite) and Ar/Ar (biotite–hornblende) plutonic and host metamorphic rock cooling ages range between ca. 208 and 172 Ma. Cooling ages in the metamorphic host rocks suggest that the calc–alkaline magmatic event was an important regional thermal disturbance; e.g., a large volume of magma was emplaced during crustal thinning coeval with the disaggregation of the Pangaea supercontinent. The magmatic pulses also produced significant amounts of volcanic rocks, hypabyssal intrusions, and volcaniclastic rocks with andesitic, dacitic, rhyolitic, and rhyodacitic compositions (Norean Formation; Clavijo, 1995a; Rodríguez et al., 2017b, 2018c; Correa–Martínez et al., 2018; Zapata et al., 2018).

2.3. Western Central Zone (Serranía de San Lucas and Central Cordillera, Table 3)

2.3.1. Serranía de San Lucas

Plutons in the serranía de San Lucas include the San Lucas Granitoids, Norosí and Guamoco Batholiths, San Martín de Loba–Juana Sánchez Granodiorites, and Papayal Monzonite; these are Jurassic granodioritic to dioritic I–type calc–alkaline medium– to high–potassium series granites emplaced in a continental arc setting (see Mantilla–Figueroa et al., 2007; Leal–Mejía, 2011; González et al., 2015a, 2015b, 2015c, 2015d, 2015e). Rb/Sr (whole–rock), K/Ar (hornblende, muscovite, and biotite), and U/Pb (zircon) ages range from 201 to 135 Ma (Ingeominas & Universidad Industrial de Santander, 2006a, 2006b, 2006c, 2006d; Leal–Mejía, 2011; González et al., 2015a, 2015b, 2015c, 2015d, 2015e). Associated volcanic rocks include andesite to rhyodacite hypabyssal intrusions and volcaniclastic rocks. Volcanic and volcaniclastic rocks, mostly dacitic crystalline tuffs, andesitic–dacitic breccias, and basaltic flows, are grouped as the Noreán Formation or the Noreán Volcanic Complex (Clavijo et al., 1992; Clavijo, 1995a, 1995b; Ingeominas & Universidad Industrial de Santander, 2006a, 2006b, 2006c, 2006d; González et al., 2015a, 2015b, 2015c, 2015d, 2015e).

2.3.2. Central Cordillera (North of 5° N)

In the northern part of the Central Cordillera (north of 5° N), Upper Jurassic quartz diorite to tonalite calc–alkaline plutonic rocks (Segovia Diorite) and dacite to latite calc–alkaline volcanic rocks (Segovia Vulcanites and La Malena Volcanic Asssemblage) have been related to volcanic arcs in subduction settings (González & Londoño, 2002; Leal–Mejía, 2011; Universidad Pedagógica y Tecnológica de Colombia & Ingeominas, 2011; Zapata et al., 2013; González et al., 2015f). Lu/Hf and U/Pb (zircon) ages range from 158 to 183 Ma (Leal–Mejía, 2011; Zapata et al., 2013; González et al., 2015f).

2.4. Southern Zone (Upper Magdalena Valley, Table 4)

Jurassic dioritic to tonalitic stocks and batholiths, hypabyssal intrusions and dacitic crystalline tuffs, andesitic–dacitic breccias and basaltic flows in the Upper Magdalena Valley are distributed in three geographical provinces: (i) Eastern slope of the Central Cordillera, (ii) Magdalena Valley, and (iii) Eastern Cordillera. The petrological characteristics and ages of these plutons and volcanics are presented and discussed in Álvarez (1983), Jaillard et al. (1990), Bayona et al. (1994), Núñez et al. (1996), Gómez (2002), González & Núñez (2002), Núñez (2002), Leal–Mejía (2011), Villagómez et al. (2011), Álvarez (2013), Cochrane et al. (2014b), Arango et al. (2015a, 2015b, 2015c), Rodríguez et al. (2015a, 2015b, 2015c, 2015d, 2016a,

Table 3. Characteristics of the lithostratigraphic units of the Western Central Zone.

Lithostratigraphic unit	Lithology	Contact type/country rock	Age (Ma)	Method	Reference
Serranía de San Lucas Sector					
Noreán Formation (Noreán Volcanic Complex)	Lapilli and ash crystal lithic tuffs of dacitic to rhyolitic compositions, lithic agglomerates, polymictic igneous breccias of andesitic and dacitic compositions, and rhyodacitic lavas in addition to basalts, trachytes and andesites. Hypabyssal rocks of andesitic composition.	Discordant–Intrusive/Jurassic plutonic rocks	196.1 ± 4.4 190.1 ± 3.2 189.0 ± 3.3 190.0 ± 2.2 194.0 ± 2.3 201.6 ± 3.6 189.0 ± 3.0 187.0 ± 0.96 178.1 ± 5.6 201.6 ± 3.6 174.3 ± 2.7 192.0 ± 3.2 189.6 ± 1.7 187.44 ± 0.96 189.0 ± 3.0 187.0 ± 0.96	LA–ICP–MS LA–MC–ICP–MS	Leal–Mejía (2011) González et al. (2015a, 2015b, 2015e)
Norosí Granite (Norosí Batholith)	Monzogranite, syenogranite, tonalite, granodiorite, monzodiorite, microdiorite, subordinate gabbronorite, with pyroxene (clino– and orthopyroxene).	Intrusive/Jurassic volcanic–sedimentary successions	184.6 ± 3.6 193.4 ± 5.8 189.0 ± 2.8 187.2 ± 2.8 180 178.2 ± 4.3 181.8 ± 3.2 173 184 193.0 ± 3.3 189.0 ± 2.8	LA–MC–ICP–MS	Ordóñez–Carmona et al. (2009) Leal–Mejía (2011) Cuadros (2012) Cuadros et al. (2013) González et al. (2015b)
Guamoco Granodiorite (Guamoco Batholith)	Granodiorite, tonalite, monzogranite, quartz monzodiorite, quartz diorite, syenogranite, granites.	Intrusive–Faulted/Mesoproteroizoic metamorphic granulite – amphibolite facies, Paleozoic metasedimentary rocks and Triassic – Jurassic volcanic–sedimentary successions	186.8 ± 2.9 190.3 ± 3.1 190.3 ± 1.6 186.0 ± 2.5 183.3 ± 4.4 183.0 ± 2.5 184.0 ± 3.5 183.2 ± 2.8 185.4 ± 3.4 189.6 ± 2.8 189.4 ± 1.3 187.2 ± 2.9 186.6 ± 1.6 188.8 ± 2.6 185.3 ± 2.6 182.1 ± 3.0 181.9 ± 2.7 185.7 ± 2.6 188.8 ± 1.3 185.4 ± 2.1 185.3 ± 1.4 185.7 ± 2.6 192.0 ± 3.2	LA–MC–ICP–MS	Leal–Mejía (2011) González et al. (2015e)
San Martín de Loba–Juana Sánchez Granodiorites	Granodiorite, with pyroxene (clino– and orthopyroxene).	Intrusive/Jurassic volcanic–sedimentary successions	182.0 ± 3.0 186.3 ± 5.2 189.0 ± 4.0 184.6 ± 4.8	SHRIMP LA–MC–ICP–MS	Leal–Mejía (2011)
Papayal Monzonite	Monzonite	Intrusive/Jurassic volcanic–sedimentary successions	193.6 ± 5.4	LA–MC–ICP–MS	Leal–Mejía (2011)

Table 3. Characteristics of the lithostratigraphic units of the Western Central Zone (*continued*).

Lithostratigraphic unit	Lithology	Contact type/country rock	Age (Ma)	Method	Reference
Central Cordillera (north of 5° N) Sector					
Segovia Vulcanites	Dacites, andesites, latites, subordinate tuffs.	Intrusive–Faulted/Paleozoic? metamorphic amphibolite facies and Jurassic plutonic rocks	165.5 ± 2.1	LA–MC–ICP–MS	González et al. (2015f)
La Malena Volcanic Assemblage	Dacitic, latitic, trachytic, basaltic, rhyolitic and rhyodacitic volcanic flows, volcanic breccias, lamprophyres, crystalline, crystal–vitreous and lithic ash tuffs, and andesitic and trachytic porphyries.	Discordant–Faulted–Intrusive/ Metasedimentary and plutonic rocks	183.2 ± 3.0 163.1 ± 2.18 163.51 ± 0.95	LA–ICP–MS	González et al. (2015e)
Segovia Diorite	Granodiorite, tonalite, diorite, quartz diorite, gabbro, quartz monzonite, monzogranite, syenogranite, subordinate alkali feldspar granite.	Intrusive–Faulted/Paleozoic? metamorphic amphibolite facies and Jurassic volcanic–sedimentary rocks	166.5+2.3/2.5 164.6 ± 2.4 158.7 ± 2.0 160.7+2.4/–2.3 159.0 ± 2.4 162.7 ± 2.6 163.1 ± 2.8 160.0 ± 2.4 158.0 ± 2.4 158.0 ± 0.87 155.37 ± 0.81 162.0 ± 2.5 157.0 ± 7.2 158.0 ± 0.87 154.0 ± 1.6 151.1 ± 7.2 161.0 ± 2.7	LA–MC–ICP–MS	Frantz et al. (2007) Leal–Mejía (2011) González et al. (2015b, 2015f)

2016b, 2018a), Spikings et al. (2015), Bustamante et al. (2016), van der Lelij et al. (2016), Zapata et al. (2016b), García–Chinchilla (2018), and Rodríguez (2018). The main named bodies include Las Minas Monzonite, Garzón Granite, Altamira, Algeciras, and Mocoa Monzogranites, San Cayetano, Anchique, Dolores, Sombrerillos, and Los Naranjos Quartz Monzonites, El Astillero Quartz Monzodiorite, Teruel Quartz Latite, Del Páez Quartz Monzodiorite, Ibagué Batholith, and the Saldaña Formation. These rocks have been classified as I–type granites (Cordilleran or Andean) of the calc–alkaline and high–K calc–alkaline series related to magmatic arc settings on continental margins. U/Pb (zircon) ages allow the identification of two groups likely related to magmatic pulses: (i) a pulse that produced most plutonic rocks with ages ranging from 203 to 162 Ma (including an age group at the southern end of the Ibagué Batholith of 192 to 152 Ma) and (ii) a pulse that produced acidic volcanic rocks (Saldaña Formation) with ages ranging from 200 to 146 Ma and probably the northern sector of the Ibagué Batholith with ages ranging from 164 to 138 Ma. The remnants of the calc–alkaline magmatic belt in the Upper Magdalena Valley intrude the metamorphic basement of the Garzón Massif and the eastern flank of the Central Cordillera (Bayona et al., 1994; Altenberger & Concha, 2005; Bustamante et al., 2010, 2016; Leal–Mejía, 2011; Villagómez et al., 2011; Cochrane et al., 2014b; García–Chinchilla, 2018).

3. Age Data Compilation

Three hundred ten U/Pb crystallization ages for intrusive and effusive igneous rocks were compiled from Dörr et al. (1995), Bustamante et al. (2010, 2016), Leal–Mejía (2011), Mantilla–Figueroa et al. (2013), Cochrane (2013), Salazar–Torres et al. (2013), van der Lelij (2013), Bissig et al. (2014), Cochrane et al. (2014a, 2014b), Arango et al. (2015a, 2015b, 2015c, 2015d, 2015e, 2016), Gómez et al. (2015), González et al. (2015a, 2015b, 2015c, 2015d, 2015e, 2015f, 2015g), Rodríguez et al. (2015a, 2015b, 2015c, 2015d, 2016a, 2016b, 2017a, 2017b, 2018a, 2018b, 2018c), Bustamante (2016), Correa–Martínez et al. (2016, 2018), Quiceno–Colorado et al. (2016), van der Lelij et al. (2016), Zapata et al. (2016a, 2016b, 2018), García–Chinchilla (2018), Quandt et al. (2018), and Leal–Mejía et al. (2019). Age compilation combines data obtained by laser ablation inductively coupled plasma mass spectrometer (LA–ICP–MS), laser ablation multi–collector inductively coupled plasma mass spectrometer (LA–MC–ICP–MS), sensitive high–resolution ion microprobe (SHRIMP), and chemical decomposition (dilution) of zircons.

Table 4. Characteristics of the lithostratigraphic units of the Southern Zone.

Lithostratigraphic unit	Lithology	Contact type/country rock	Age (Ma)	Method	Reference
		Central Cordillera Sector			
Ibagué Batholith	North: Tonalite, granodiorite, diorite, granite (ca. 154 Ma). South: Quartz monzodiorite, diorite, quartz diorite, granodiorite, quartz monzonite, monzonite, monzodiorite (ca. 182 Ma).	Intrusive–Faulted/Neoproterozoic? metamorphic amphibolite – granulite facies, Paleozoic metamorphic greenschist – amphibolite facies and Triassic calcareous rocks.	138.7 ± 1.0 145.56 ± 0.92 149.3 ± 2.8 152.9 ± 3.1 153.9 ± 1.1 155.4 ± 2.2 156.5 ± 1.1 164.4 ± 1.1 186.8 ± 2.8 182.7 ± 2.7 188.4+2.8/–2.7 186.0 ± 3.1 188.5 ± 3.3 192.3 ± 3.1 166.0 ± 10.0 159.6 ± 2.4 175.0 ± 2.0 173.6 ± 1.5 164.4 ± 1.1 168.8 ± 0.7 156.5 ± 1.1 155.7 ± 2.2 188.9 ± 2.0 169.6 ± 2.4 180.4 ± 1.6 180.5 ± 2.7 185.9 ± 1.4 186.0 ± 2.6 141.9+1.1–0.8 158.2+1.2–0.4 152.61+1.82–0.74	LA–MC–ICP–MS LA–ICP–MS	Bustamante et al. (2010) Leal–Mejía (2011) Villagómez et al. (2011) Cochrane et al. (2014b) Bustamante et al. (2016) Zapata et al. (2016b) Rodríguez et al. (2018a)
Payandé Stock	Granodiorite	Intrusive/Triassic calcareous rocks and Permian? plutonic rocks	164.07 +2.11/–0.96 164.59 +1.05/–2.76	LA–ICP–MS	Bustamante (2016)
Del Páez Quartz Monzodiorite	Quartz monzodiorite, monzodiorite, gabbro, diorite, monzogranite, tonalite, granodiorite, with pyroxene (clino– and orthopyroxene).	Intrusive–Faulted/Neoproterozoic? metamorphic amphibolite – granulite facies; Jurassic volcanic–sedimentary successions and Cretaceous sedimentary rocks.	181.7 ± 3.8 193.13 ± 1.4	LA–MC–ICP–MS LA–ICP–MS	Rodríguez et al. (2018a)
Anchique Quartz Monzonite	Quartz monzonite, monzonite, granite, with pyroxene (clinopyroxene).	Intrusive/Jurassic volcanic–sedimentary successions	183.5 ± 3.0 186.4 ± 1.4	LA–MC–ICP–MS LA–ICP–MS	Arango et al. (2015c) Rodríguez et al. (2018a)
El Astillero Quartz Monzodiorite	Quartz monzodiorite, monzodiorite, quartz diorite, quartz monzonite, with pyroxene (clino– and orthopyroxene).	Intrusive/Jurassic volcanic–sedimentary successions	187.0 ± 3.3	LA–MC–ICP–MS LA–ICP–MS	Rodríguez et al. (2015c) Rodríguez et al. (2018a)
Sombrerillos Quartz Monzonite (Quartz Monzodiorite)	Granodiorite, syenogranite, tonalite, quartz monzonite, and quartz monzodiorite, with pyroxene (clino– and orthopyroxene).	Intrusive–Faulted/Paleozoic sedimentary rocks and Jurassic volcanic–sedimentary successions	189.0 ± 7.0 187.0 ± 1.0 187.0 ± 2.0 203.9 ± 2.3 180.3 ± 2.9 174.0 ± 1.5	LA–MC–ICP–MS LA–ICP–MS	García–Chinchilla (2018) Rodríguez et al. (2018a)

Table 4. Characteristics of the lithostratigraphic units of the Southern Zone (*continued*).

Lithostratigraphic unit	Lithology	Contact type/country rock	Age (Ma)	Method	Reference
Magdalena Valley Sector					
San Cayetano Quartz Monzonite	Quartz monzonitie and quartz monzodioritie, with pyroxene (clino– and orthopyroxene).	Intrusive/Jurassic volcanic–sedimentary successions	195.8 ± 1.5 173.3 ± 1.3	LA–MC–ICP–MS LA–ICP–MS	Rodríguez et al. (2018a)
Los Naranjos Quartz Monzonite	Quartz monzonite, monzonite and granite, with pyroxene (clinopyroxene).	Intrusive/Jurassic volcanic–sedimentary successions	187.9 ± 1.3	LA–MC–ICP–MS LA–ICP–MS	Rodríguez et al. (2015b) Rodríguez et al. (2018a)
Teruel Quartz Latite (Teruel Latite, Teruel Batholith)	Quartz latite, rhyolite, dacite, with pyroxene (clinopyroxene).	Intrusive–Faulted/Jurassic volcanic–sedimentary successions and Cretaceous sedimentary rocks	174.1 ± 2.0 170.5 ± 1.1	LA–MC–ICP–MS LA–ICP–MS	Arango et al. (2015b) Rodríguez et al. (2018a)
Eastern Cordillera Sector					
Dolores Quartz Monzonite (Dolores Stock)	Quartz monzonite, quartz syenite.	Faulted/Cretaceous sedimentary rocks			
Algeciras Monzogranite	Monzogranite, granodiorite, with pyroxene (clinopyroxene).	Intrusive–Faulted/Paleozoic sedimentary rocks, Jurassic volcanic–sedimentary successions and Paleogene – Neogene sedimentary rocks	176.0 ± 2.0 179.0 ± 1.9 169.6 ± 1.2	LA–MC–ICP–MS LA–ICP–MS	Rodríguez et al. (2015d) García–Chinchilla (2018) Rodríguez et al. (2018a)
Garzón Granite	Granodiorite, monzodiorite, quartz monzodiorite, with pyroxene (clinopyroxene).	Faulted/Cenozoic sedimentary rocks	177.8 ± 4.2 165.3 ± 4.0 170.8 ± 2.4	LA–MC–ICP–MS LA–ICP–MS	Bustamante et al. (2010) Rodríguez et al. (2015a) Rodríguez et al. (2018a)
Altamira Monzogranite	Monzogranite, quartz monzonite, syenogranite.	Intrusive–Faulted/Jurassic volcanic–sedimentary successions and Cenozoic sedimentary rocks	181.6 ± 1.3 181.7 ± 6.3 162.0 ± 3.0 178.97 ± 0.4 169.4 ± 3.2	LA–MC–ICP–MS LA–ICP–MS	Bustamante et al. (2010) Arango et al. (2015d) García–Chinchilla (2018) Rodríguez et al. (2018a)
Mocoa Monzogranite	Monzogranite, granodiorite, syenogranite, tonalite, quartz diorite, quartz monzonite, quartz monzodiorite.	Intrusive/Jurassic volcanic–sedimentary successions	170.2 ± 2.7 180.4 ± 1.6 181.8 ± 1.3 170.7 ± 2.1	LA–MC–ICP–MS LA–ICP–MS	Leal–Mejía (2011) Arango et al. (2015e) Zapata et al. (2016b) Rodríguez et al. (2018a)
Serranía de Las Minas (transition between the Upper Magdalena Valley and the Central Cordillera) Sector					
Las Minas Monzonite	Quartz monzodiorite, diorite–monzodiorite, dioritic, with pyroxene (clino– and orthopyroxene).	Intrusive/Jurassic volcanic–sedimentary successions, Neoproterozoic? metamorphic amphibolite – granulite facies and Paleozoic sedimentary rocks.	193.4 ± 1.0 197.6 ± 1.9 187.4 ± 2.3 181.6 ± 3.4	LA–MC–ICP–MS LA–ICP–MS	Arango et al. (2015a) Bustamante et al. (2010) Rodríguez et al. (2018a)
Andesitic–dacitic porphyry	Andesite, dacite.	Intrusive/Jurassic volcanic–sedimentary successions			
Hypabyssal porphyries	Rhyolite, dacite.	Intrusive/Jurassic plutonic rocks	172.0 ± 1.0 175.0 ± 3.0 167.0 ± 2.0	LA–MC–ICP–MS LA–ICP–MS	García–Chinchilla (2018)
Saldaña Formation	Glassy, lithic and crystal tuffs, lavas of andesitic, dacitic, trachyandesitic, quartz latitic, and rhyolitic compositions, and hypabyssal andesitic and dacitic rocks.	Discordant–Intrusive	185.9 ± 1.4 186.0 ± 2.6 179.0 ± 2.0 181.5 ± 1.6 158.5 ± 1.0 146.8 ± 1.5	LA–ICP–MS	Cochrane et al. (2014b) Rodríguez et al. (2016b) Zapata et al. (2016b)

The following list gives the geochronological data distribution: (i) 19 U/Pb ages for the Northern Zone, (ii) 86 U/Pb ages for the Southern Zone, (iii) 132 U/Pb ages for the Eastern Central Zone, and (iv) 73 U/Pb ages for the Western Central Zone.

U/Pb (zircon) geochronological data were plotted in histograms with a 2 my bin width overlain by the kernel density estimates (KDEs; Vermeesch, 2012). The histograms were constructed using a constant bin size for visually evaluating the numbers of samples forming age peaks between the geochronological U/Pb (zircon) data, allowing comparisons between the age populations in the four zones. We adopted the KDE calculation, which visually has an appearance similar to that of probability density plots (PDPs), in which the bandwidth is varied according to the local density (Vermeesch, 2012). KDE calculation was accomplished using an open–source Java application developed by Vermeesch (2012) that enables the visualization of U/Pb age data (Density Plotter – a Java application for kernel density estimation, downloaded from https://www.ucl.ac.uk/~ucfbpve/densityplotter/). For the spatiotemporal distribution and the representation of magmatic activity in terms of the episodic pattern behavior (magmatic tempo) of arc magmatism, we use the terms flare–up (periods with high magma addition rates or waxing magmatism) and lulls (periods with low magma addition rates or reduced magmatism) in the sense of De Silva et al. (2015), Ducea et al. (2015), Paterson & Ducea (2015), and Kirsch et al. (2016).

4. Geochemical Data Compilation

This review is based on a compilation of published and unpublished whole–rock geochemical data for Colombia and contains major (1059) and trace (1006) element analyses at different locations along the Late Triassic to Jurassic magmatic belt. The published geochemical data set was compiled using information from Dörr et al. (1995), Bustamante et al. (2010; 2016), Mantilla–Figueroa et al. (2013), Cochrane (2013), Salazar–Torres et al. (2013), van der Lelij (2013), Bissig et al. (2014), Cochrane et al. (2014b), Arango et al. (2015a, 2015b, 2015c, 2015d, 2016), González et al. (2015a, 2015b, 2015c, 2015d, 2015e, 2015f, 2015g), Rodríguez et al. (2015a, 2015b, 2015c, 2015d, 2016a, 2016b, 2017a, 2017b, 2018a, 2018b, 2018c), Correa–Martínez et al. (2016, 2018), Quiceno–Colorado et al. (2016), van der Lelij et al. (2016), Zapata et al. (2016a, 2016b, 2018), García–Chinchilla (2018), Quandt et al. (2018), Leal–Mejía et al. (2019), and Zuluaga & López (2019). New whole–rock geochemical data for the San Cayetano Stock and the Saldaña Formation complement the compilation presented here (see Table 1 of the Supplementary Information). The compilation includes 713 samples of plutonic rocks, 51 samples of hypabyssal rocks, and 224 samples of volcanic rocks, all distributed along the four zones: (i) 193 analyses for the Northern Zone, (ii) 235 analyses for the Southern Zone, (iii) 275 analyses for the Eastern Central Zone, and (iv) 285 analyses for the Western Central Zone. The dataset was filtered in order to exclude geochemical analyses with loss on ignition (LOI) greater than 2.5% (71 analyses). During processing, the results obtained with major elements were contrasted with results obtained from trace elements to ensure consistency. All graphics were obtained using the open–source (freeware) R language package called Geochemical Data Toolkit (GCDkit), which provides a flexible and comprehensive environment for efficient data processing and visualization (Janoušek et al., 2004).

5. Spatiotemporal Distribution of Upper Triassic to Jurassic Igneous Rocks in Colombia

In the current tectonic configuration of northwestern South America, the Upper Triassic to Jurassic plutonic suites are spatially located in the mountain ridges and piedmonts (Central and Eastern Cordilleras, Sierra Nevada de Santa Marta, and serranía de Perijá), whereas Jurassic volcaniclastic successions are mainly distributed towards the margins of intramontane valleys (Magdalena and Cesar Rivers); these magmatic suites are distributed across a total area of approximately 50 500 km^2. U/Pb (zircon) ages from the Late Triassic to Jurassic magmatic belt show several peaks interpreted as results of periods of increase and decrease in magmatic activity (Figure 3). A peak of approximately 200 Ma characterizes the Eastern Central Zone, and this peak represents the oldest pulse in the belt (Figure 3a). Magmatic activity is null in this zone from ca. 184 Ma; this magmatic quiescence contrasts with the presence of peaks of high magmatic activity in the Southern, Western Central, and Northern zones at ca. 186 Ma (Figure 3b–d) and suggests a migration of the magmatic front towards the west. In the Southern Zone, an important peak is observed at ca. 170 Ma (Figure 3b), whereas in the Western Central and Northern zones, there is a lull during this time (Figure 3c, 3d). The final magmatic episode is registered in the Southern and Western Central zones with a peak at ca. 158 Ma (Figure 3b, 3c). Overall, the magmatic activity in the northwestern margin of South America spanned a time of approximately 60 my. This activity had lull periods during the Late Triassic and Early Jurassic – Early Cretaceous (Figure 3e). The described pattern for the Late Triassic to Jurassic magmatic belt is a probable record of a magmatic flare–up with magmatic tempos between 10 and 20 my (cf., Paterson & Ducea, 2015; Kirsch et al., 2016).

6. Geochemical Characteristics of the Late Triassic to Jurassic Magmatic Belt in Colombia

Harker diagrams show that most major element concentrations ($Fe_2O_{3(T)}$, TiO_2, MgO, CaO, Al_2O_3, and P_2O_5) decrease with in-

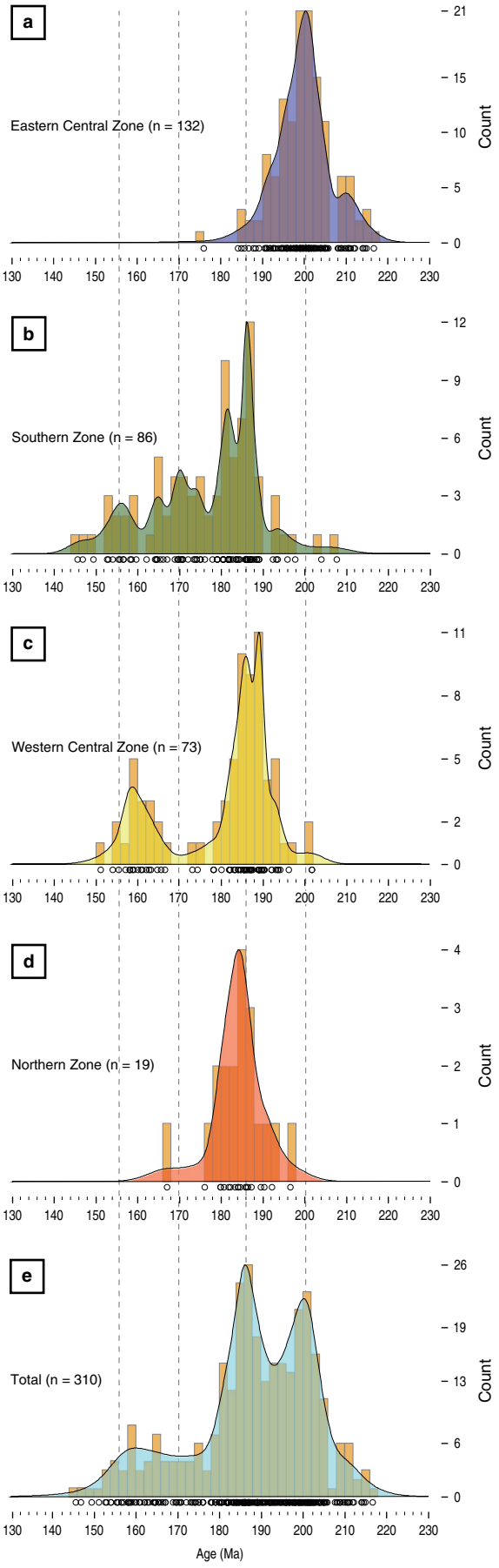

Figure 3. Igneous U/Pb zircon age spectra providing a temporal record of arc magmatism between 230 and 130 Ma. **(a)** Eastern Central Zone. **(b)** Southern Zone. **(c)** Western Central Zone. **(d)** Northern Zone. **(e)** Total U/Pb ages. Individual diagrams include LA–ICP–MS, LA–MC–ICP–MS, and SHRIMP age data presented as histograms with a 2 my bin width and adaptive Kernel density estimation (KDE) functions (see text). The number of analyses (n) given in each plot represents the number of crystallization ages.

creasing SiO_2. In contrast, K_2O shows random variations within very narrow ranges of SiO_2 concentrations (but with an overall increasing trend), and there are slight increases in Na_2O with increasing SiO_2. Trace elements show marked negative trends for Sr and slight negative trends for Y in all regions. Zr tends to have negative trends in the Central Eastern and Northern zones and random trends in the Central Western and Southern zones as well as low average values in the Central Western Zone. Ba has random trends, albeit with slight negative trends in the Central Eastern and Central Western zones.

6.1. Volcanic Rocks

The major element contents generally range from 45.62 to 82.6% SiO_2, 0.01 to 9.93% K_2O, 0.04 to 8.1% Na_2O, and 0.02 to 15.15% CaO. Trace element concentrations range from 4.0 to 351 ppm Rb, 12 to 8220 ppm Sr, 19 to 3523.74 ppm Ba, 1.3 to 736.81 ppm Cr, 0.025 to 533.1 ppm Ni, 0.5 to 173.61 ppm La, 0.23 to 62.66 ppm Eu, 1.8 to 351.26 ppm Y, and 1.2 to 503.41 ppm Zr. In the SiO_2 vs. Zr/TiO_2 diagram (Winchester & Floyd, 1977), they plot within the andesitic basalt, andesite, dacite, rhyodacite, and rhyolite fields following a subalkaline trend and within the transitional and calc–alkaline fields based on the Th/Yb vs. Zr/Y diagram (cf., Ross & Bédard, 2009). On the ternary La/10–Y/15–Nb/8 diagram, rocks plot mainly in the calc–alkaline orogenic to postorogenic fields (Figure 4a), suggesting an association of marginal arcs and crustal intracontinental domains (Figure 4b).

6.2. Plutonic Rocks–Granitoids

In plutonic rocks, major element concentrations range from 50.3 to 82.47% SiO_2, 0.04 to 8.83% K_2O, 0.03 to 8.42% Na_2O, and 0.02 to 16% CaO. Their $(La/Yb)_N$ ratios range from 0.64 to 263.33, and the Eu/Eu* ratios range from 0.06 to 3.27. Trace element concentrations range from 1.5 to 385 ppm Rb, 5 to 7430 ppm Sr, 8.5 to 3451.3 ppm Ba, 0.25 to 217 ppm Cr, 0.05 to 525.2 ppm Ni, 1.3 to 130.3 ppm La, 0.01 to 4.8 ppm Eu, 0.32 to 130.5 ppm Y, and 0.53 to 1895.47 ppm Zr. Plutons are mostly normal (SiO_2 < 70%) and silica–rich (SiO_2 > 70%) granitoids with ASI > 1.5 (peraluminous leucogranites), calcic to calc–alkalic magnesian and ferrous, and calc–alkalic and alkali–calcic granite signatures (Frost et al., 2016).

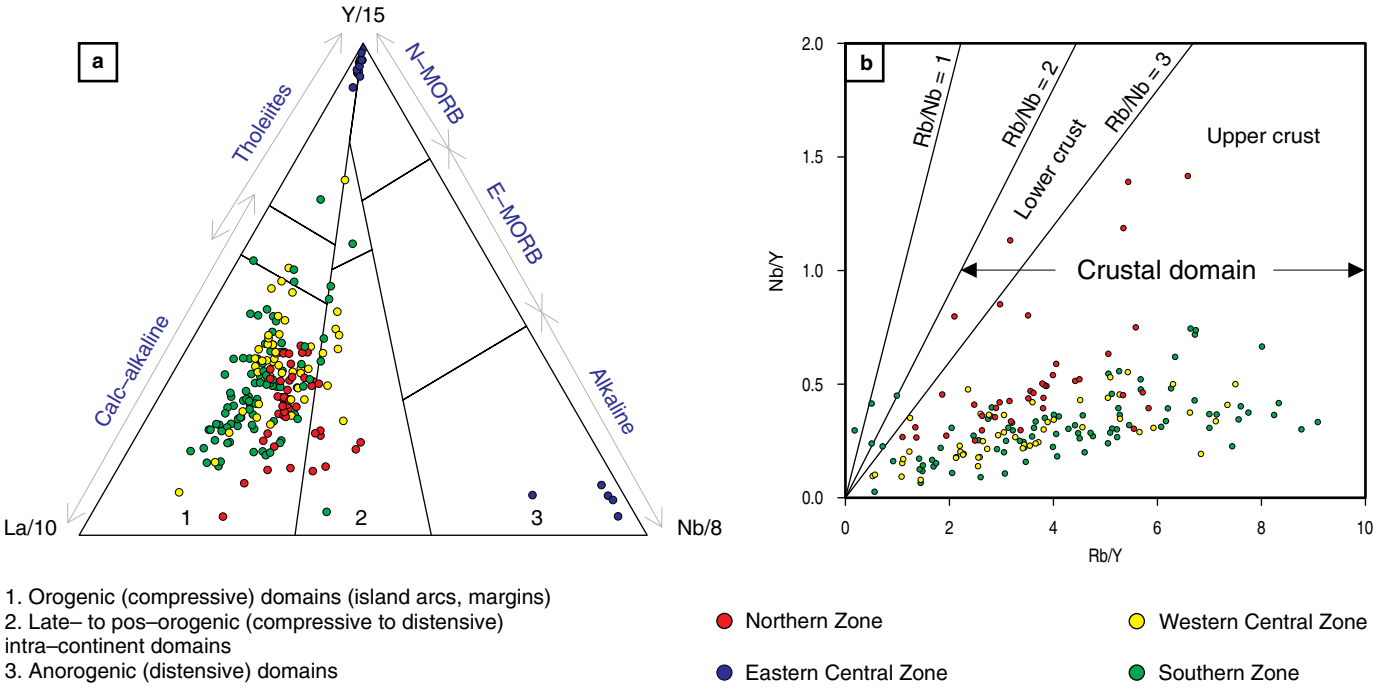

Figure 4. Discrimination diagrams for volcanic rocks. (**a**) Ternary La/10–Y/15–Nb/8 diagram (Cabanis & Lecolle, 1989) for the discrimination of tectonic regimes. Note that the rocks are grouped in the calc–alkaline orogenic domain. **(b)** Nb/Y vs. Rb/Y diagram (Chazot & Bertrand, 1995) showing the distribution of the samples associated with a crustal domain.

In Figure 5, several discrimination diagrams support a calc–alkaline, transitional, and tholeiitic magma series affinity interpretation (Figure 5a); some diagrams also indicate a high–potassium calc–alkaline and shoshonitic character (Figure 5b, 5c). The A/CNK Shand indexes range from 0.53 to 11.8 and indicate peraluminous to metaluminous characters consistent with the results from the multicationic B–A diagram (Figure 5d) of Debon & Le Fort (1983). Rocks also have agpaitic indexes ranging from 0.044 to 0.965, which confirms the absence of peralkaline associations.

Chemical analyses plotted in the S–I–A–M classification diagrams (Figure 6) show that most plutons are primarily classified as I–type. A few samples have A–type signatures (mostly A2 – postcollisional field in Figure 6a, 6b), and some others, primarily those in the Eastern Central Zone, have diffuse S–type trends (Figure 6c). Although the differentiation of granitoids into the S–I–A–M types is considered highly ambiguous (cf., Chappell, 1984; Chappell & White, 1974, 1992, 2001; Whalen et al., 1987; Eby, 1990, 1992; Castro, 2004; Castro et al., 1991a, 1991b; Chappell et al., 2012), results from these diagrams are consistent with other geochemical parameters from the dataset.

Differentiation trends as seen in the Ba–Rb–Sr diagram show that (Figure 7a) (i) the Eastern Central Zone primarily contains anomalous, normal, and strongly differentiated granites with diorites, quartz diorites, and subordinate granodiorites; (ii) the Northern Zone contains anomalous granites to normal granites, quartz diorites, and subordinate granodiorites; (iii) the Southern Zone shows an increasing trend from the quartz diorite and granodiorite fields to that of the anomalous granites with strongly differentiated normal granites and subordinate diorites; and (iv) the Western Central Zone shows an increasing trend from the diorite field to those of quartz diorites and granodiorites with anomalous and strongly differentiated subordinate granites. Note that rocks from the Eastern Central Zone tend to be the most differentiated, whereas those of the Western Central Zone tend to be the least differentiated. The low Ba–Sr granites from the Eastern Central Zone with an increasing Rb trend (and decreasing Ba) could be associated with a source likely related to volcanic or syncollisional arc settings, whereas the high Ba–Sr granites of the Northern, Southern, and Western Central zones may be connected to mixing with mantle components (Figure 7b). The presence of both strongly fractionated and unfractionated granitic rocks is also evident in Figure 7c, where rocks range from unevolved to strongly evolved and fractionated.

Petrographic (modal) and total rock geochemical (Q–P) classification diagrams show the wide lithological range of the assemblages: granites (syenogranites and monzogranites), quartz monzodiorites, granodiorites, tonalites, gabbros, monzogabbros, quartz diorites, quartz monzonites, monzonites, and subordinate syenites. All of these rocks likely originated

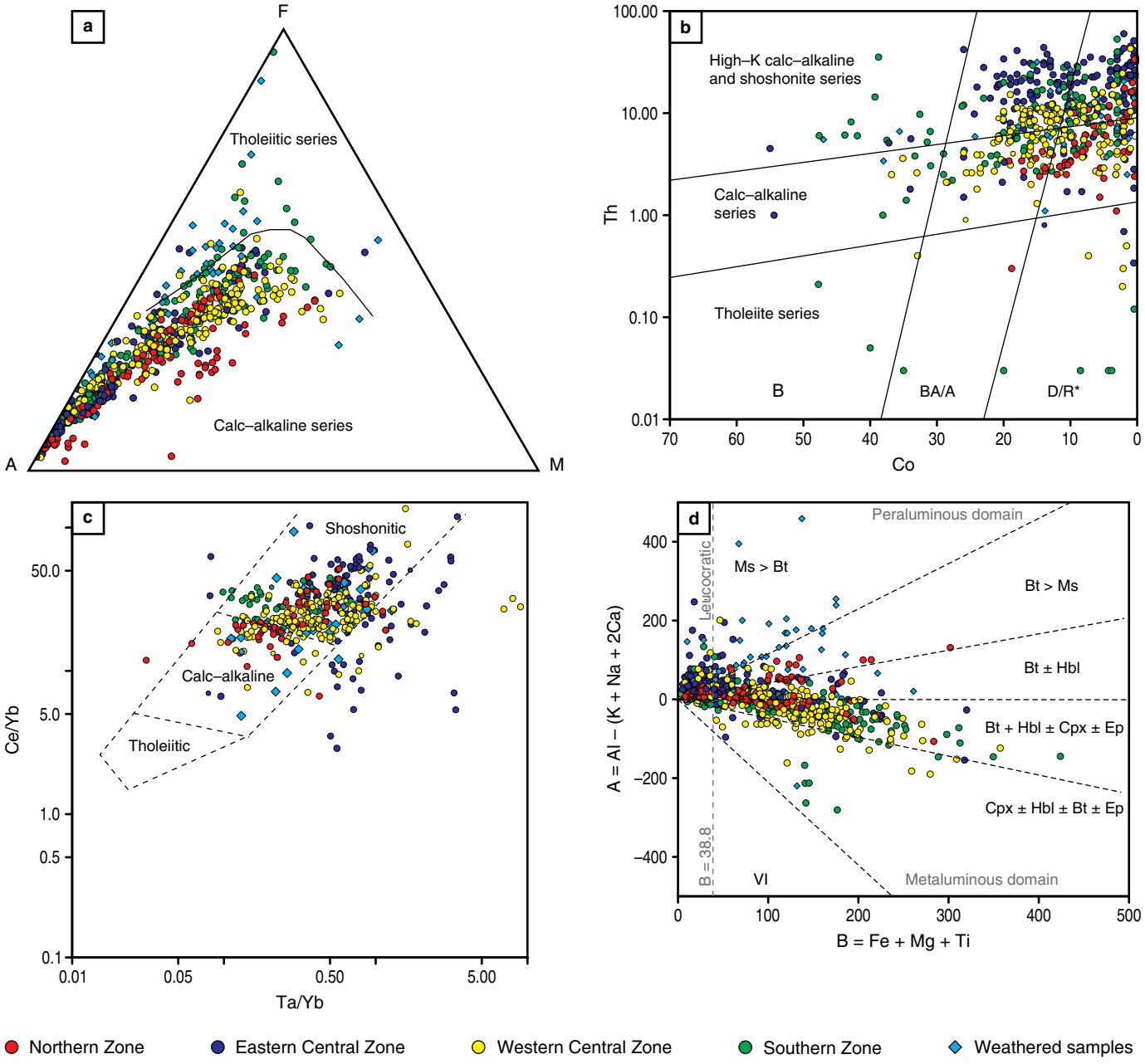

Figure 5. Discrimination of magmatic series. **(a)** Alkali–FeO–MgO (AFM) diagram (Irvine & Baragar, 1971) showing a calc–alkaline trend in the Late Triassic to Jurassic magmatic belt. **(b)** Th (ppm) vs. Co (ppm) diagram (Hastie et al., 2007) grouping rocks of the Late Triassic to Jurassic magmatic belt into the fields for the calc–alkaline, high–potassium/calc–alkaline and shoshonitic series. **(c)** Ce/Yb vs. Ta/Yb diagram (Müller et al., 1992) grouping the units primarily into the shoshonitic and calc–alkaline fields. **(d)** B–A multicationic diagram (Debon & Le Fort, 1983) showing that the plutonic rocks vary between the peraluminous and metaluminous domains.

in a typical arc, as indicated by the diagram in Figure 8a and by the already mentioned geochemical characteristics. The ample chemical variations allow the suite to have associations from leucocratic (Central Eastern Zone) to sodic and mesocratic (Northern, Central Western, and Southern zones; Figure 8b). The suite also has a wide distribution between ferrous and magnesian varieties (Figure 8c), but it is mostly constrained to alkali–calcic and calc–alkaline characters (Figure 8d).

7. Discussion

7.1. Tectonic Environment and Petrogenesis

Late Triassic – Jurassic magmatism in Colombia is of subalkaline affinity (primarily of the calc–alkaline and shoshonitic series), suggesting the presence of subduction fluids in the magma source (cf., Bustamante et al., 2010; Leal–Mejía,

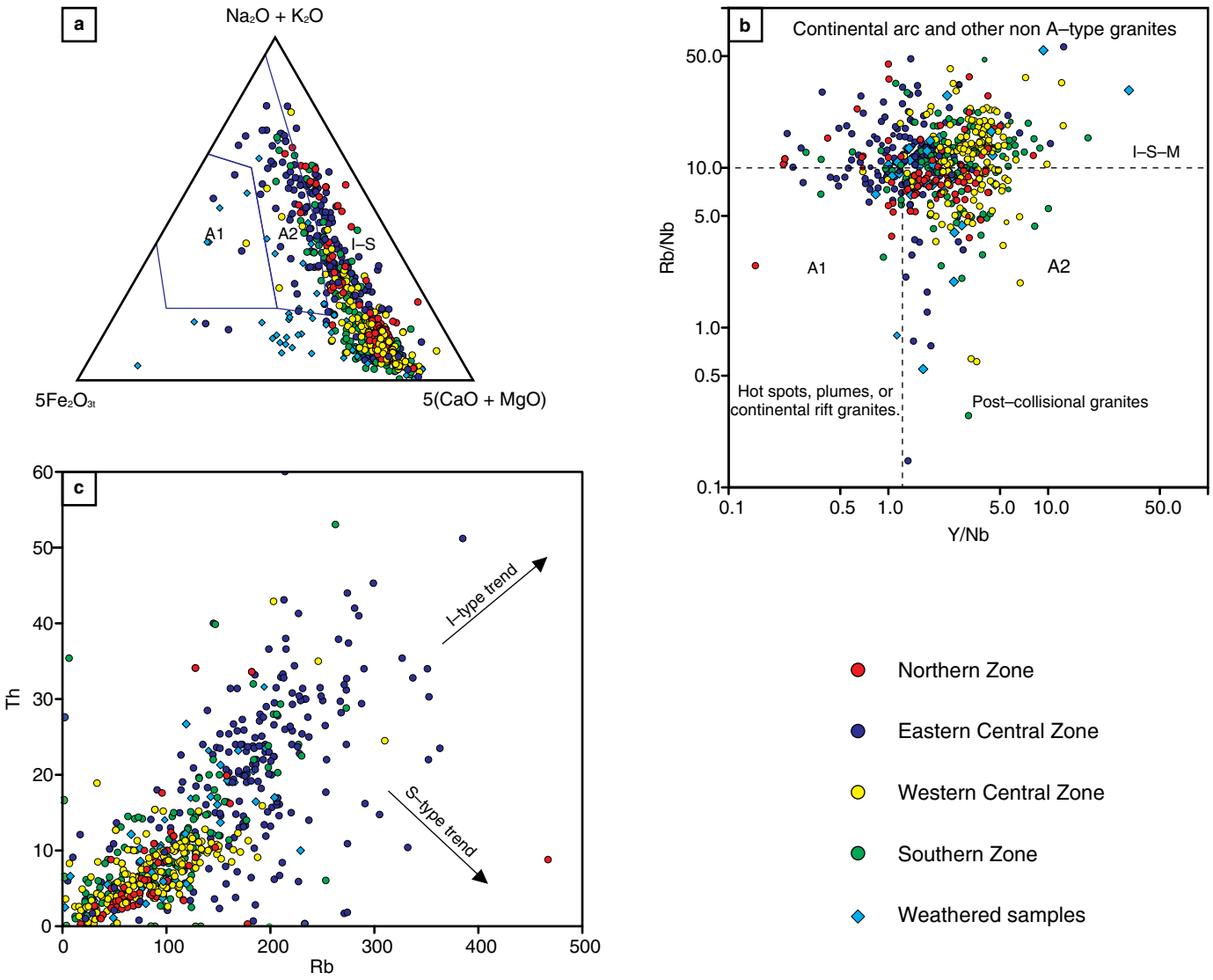

Figure 6. Discrimination among I–, S–, and A–type granites. **(a)** $5Fe_2O_{3t} - Na_2O + K_2O - 5(CaO + MgO)$ diagram (Grebennikov, 2014) discriminating A–type granites from I– and S–type granites. **(b)** Y/Nb vs. Rb/Nb discrimination diagram (Bahajroy & Taki, 2014) classifying the granites as postcollisional (A2), continental arc and other non A–type granites (I–S–M) subordinately associated with hotspots, mantle plumes, or continental rifts (A1). **(c)** Rb (ppm) vs. Th (ppm) diagram (Chappell, 1999). Note the distribution of samples following an I–type trend.

2011; Cochrane, 2013; Cochrane et al., 2014a, 2014b; Spikings et al., 2015; Zuluaga et al., 2015; van der Lelij et al., 2016; García–Chinchilla, 2018; Quandt et al., 2018; Rodríguez et al., 2018a). The magmatism ranges from metaluminous to strongly peraluminous and contains no rocks with peralkaline affinity, which precludes the presence of anorogenic magmatism typical of an intracontinental rift (see, e.g., Bowden et al., 1984; Brown et al., 1984; Pearce et al., 1984; Whalen et al., 1987; Maniar & Piccoli, 1989; Barbarin, 1990, 1999; Bonin, 1990, 1998, 2007; Bonin et al., 1998; Eby, 1990; Frost et al., 2001; Nédélec & Bouchez, 2015).

Volcanic rocks vary compositionally between andesitic basalts and rhyolites, which are typical arc rocks (cf., Figure 4), whereas the granitic rocks include (i) peraluminous granitoids with muscovite; (ii) high–potassium calc–alkaline to shoshonitic granitoids; (iii) calc–alkaline metaluminous granitoids with amphibole, biotite, and pyroxene; and (iv) granitoids discriminated as I–, S–, and A–type. Note that the compositional groups suggest the contribution of crustal melts and mixing with slab– (and mantle–?) derived components in an active continental margin setting (cf., Barbarin, 1999; Castro, 2014; Zhao et al., 2019).

In addition to the plots presented in the previous sections, the convergent geodynamic setting is supported by other discrimination diagrams that suggest an active continental margin regime in an orogenic domain with a syncollisional to post-

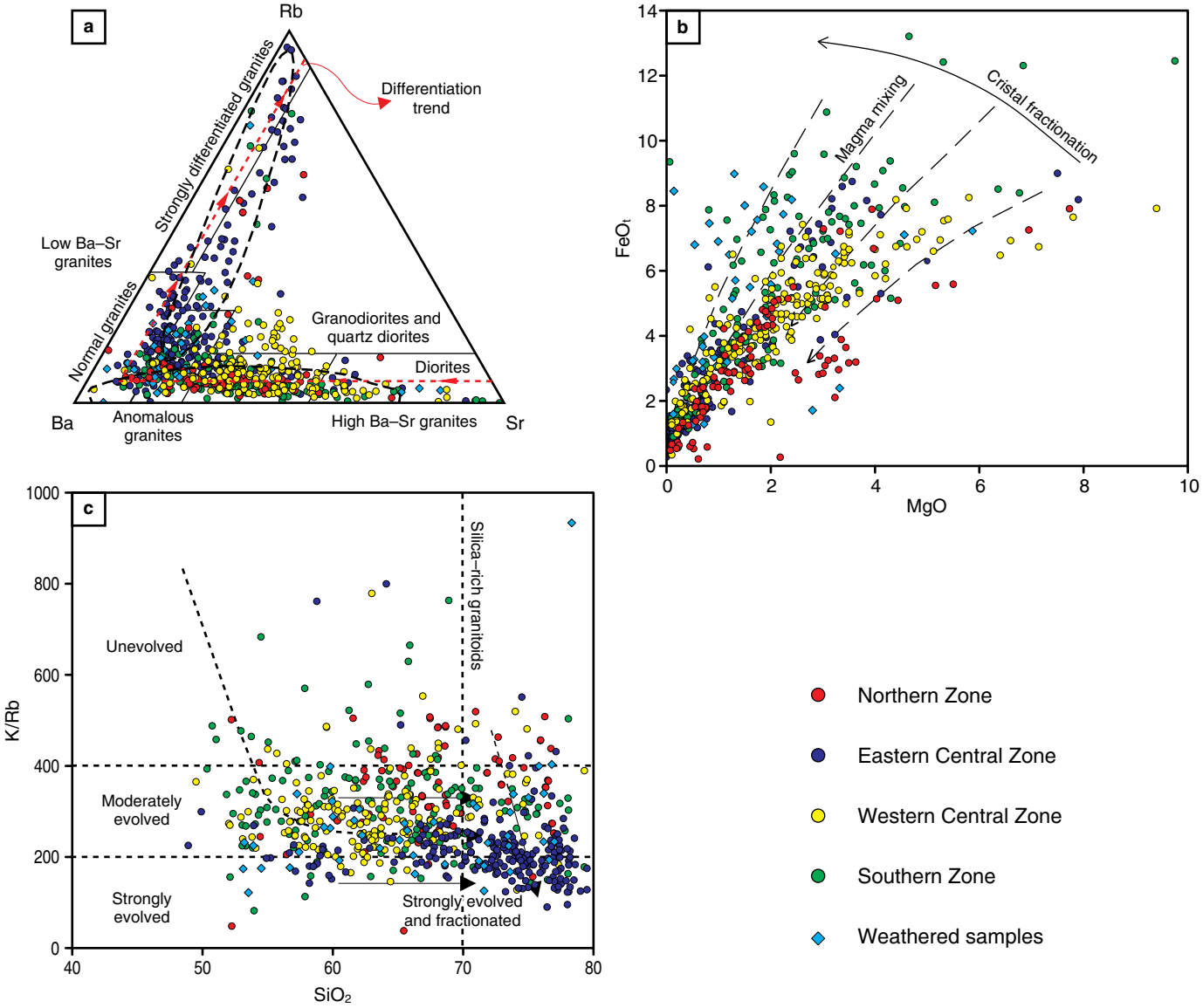

Figure 7. Fractionation grades of granitic rocks. **(a)** Ba–Rb–Sr diagram (El Bouseily & El Sokkary, 1975) showing that rocks in the Eastern Central Zone are the most differentiated, whereas rocks in the Western Central Zone are the least differentiated. High– and low–Ba–Sr granite fields complemented by Tarney & Jones (1994). **(b)** MgO vs. FeO_t diagram (Zorpi et al., 1989; Goswami & Bhattacharyya, 2014) showing that magma mixing processes were important mechanisms in the formation of the Late Triassic to Jurassic magmatic belt. **(c)** SiO_2 vs. K/Rb discrimination diagram (Blevin, 2004) classifying the rocks as a function of the evolution and fractionation of melts.

collisional (syn–subduction) regime and with a predominant calc–alkaline volcanic arc signature (Figure 9a–d).

The mineralogy of plutonic and volcanic rocks indicates associations of metaluminous and peraluminous magmas, which suggests one or more of the following processes: assimilation of country rock, incorporation of mantle–derived melts, contamination of magmas with melts from slab sediments, and magma mingling and mixing. Geochemical characteristics extracted from the dataset help to discriminate among the variety of sources and mechanisms pointing to (i) peraluminous leucogranites resulting from partial melting of pelitic rocks; (ii) calc–alkaline ferrous rocks from the partial melting of tonalites and granodiorites; (iii) alkali–calcic ferrous rocks from melting and/or differentiation of tholeiites, and (iv) magnesian rocks from the differentiation of high–aluminum basalts or andesites (see, e.g., Frost et al., 2016). However, magma mixing processes likely played a key role in the formation of the Late Triassic – Jurassic magmatic belt, as suggested by MgO–FeOt trends and a lack of correlation between Zr and Y (Goswami & Bhattacharyya, 2014). This point is significant because FeOt–MgO trends can be affected by other mechanisms, such as the variable onset of crystallization of iron oxides in magmas with distinct oxygen fugacities and/or water contents (cf., Figure 7b).

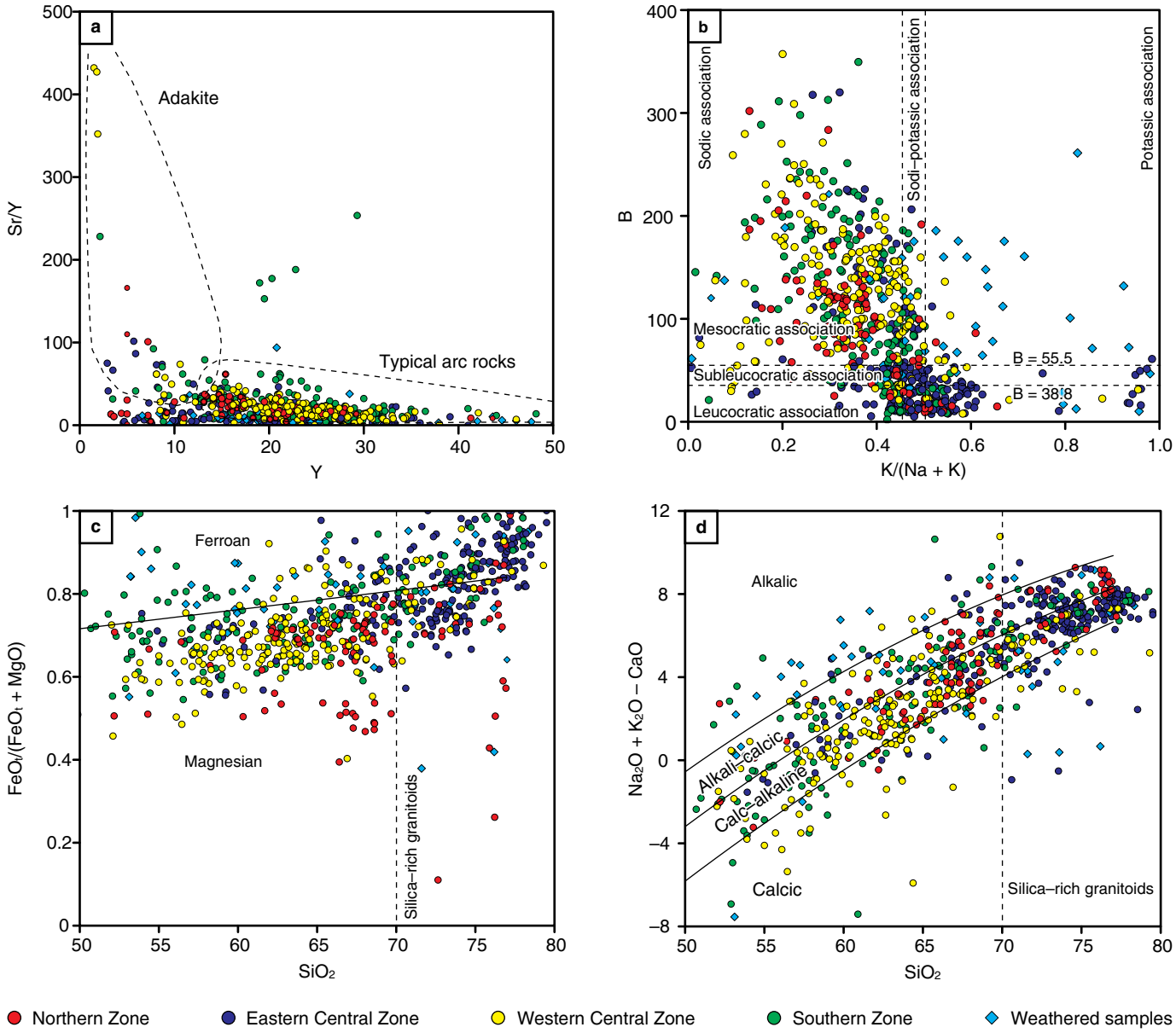

Figure 8. Discrimination diagrams for plutonic rocks. **(a)** Y (ppm) vs. Sr/Y diagram (Drummond & Defant, 1990) grouping the rocks within the fields of typical arc rocks and adakitic rocks. **(b)** K/(Na + K) vs. B diagram (Debon & Le Fort, 1983, 1988) relating the color index (B) to the alkali ratio (K/(Na + K)). **(c)** Modified SiO_2 vs. modified alkali–lime index (MALI) diagram (Frost & Frost, 2008; Frost et al., 2001, 2016). **(d)** SiO_2 vs. $Na_2O + K_2O$ – CaO diagram (Frost & Frost, 2008; Frost et al., 2001, 2016).

The suite has mostly rocks with moderate potassium concentrations suggesting potassium–depleted sources, but there are also high–potassium rocks that could have been generated by partial melting of potassium–enriched mantle sources (Bao et al., 2018), which further supports the interpretation of different sources for magmatism. Potassic rocks are assemblages that include the specimens richest in potassium on the calc–alkaline spectrum and are geochemically different from other geochemical varieties (Müller et al., 1992). To obtain better control on the interpretation of this group and following Müller et al. (1992), rocks were hierarchically discriminated first based on the La–TiO_2/100–10Hf diagram (Figure 10a) and then on the 50Nb–3Zr–Ce/P_2O_5 diagram (Figure 10b). Most of the rocks plot in the continental arc potassic (CAP) field, which suggests the recycling of oceanic crust in a subduction environment. In the diagram of Figure 10a, some rocks associated with oceanic potassic arcs (especially from the Western Central Zone) plot in the IOP–LOP field, suggesting ambiguity regarding the element concentrations considered, which is probably related to mixing and metasomatic enrichment by fluids derived from the underlying mantle wedge (Müller et al., 1992).

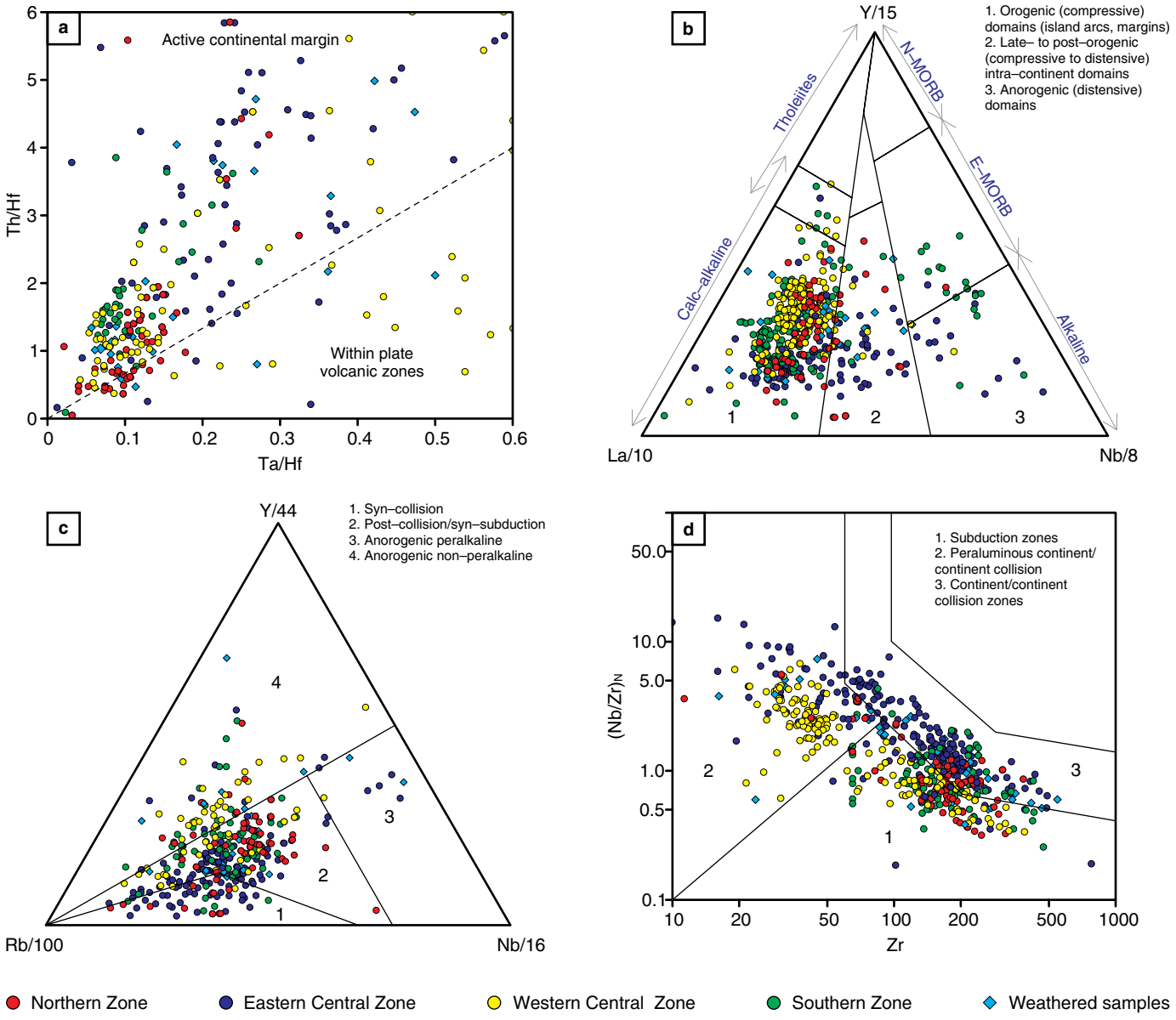

Figure 9. Tectonic discrimination diagrams. **(a)** Ta/Hf vs. Th/Hf discrimination diagram (Schandl & Gorton, 2002) suggests an active continental margin regime. **(b)** La/10–Y/15–Nb/8 plot (Cabanis & Lecolle, 1989) shows an orogenic domain for the granitic rocks. **(c)** Rb/100–Y/44–Nb/16 discrimination diagram (Thiéblemont & Cabanis, 1990) shows a syncollisional to postcollisional (syn–subduction) tectonic regime. **(d)** Zr (ppm) vs. $(Nb/Zr)_N$ diagram (Thiéblemont & Tégyey, 1994) showing a transition between the fields of continent–continent collision (fields 2 and 3) and subduction zones (field 1).

The Zr saturation temperatures tend to be higher than 600 °C and reach approximately 1000 °C (Figure 10c), which suggests the presence of high– and low–temperature granites (Watson & Harrison, 1983; Miller et al., 2003). High–temperature granites have Zr saturation temperatures higher than 750 °C and generally contain no zircon xenocrysts inherited from the regions of the magma source, which is consistent with the fractionation of mantle–derived magmas (Miller et al., 2003). Note that there is a negative correlation between Zr saturation temperatures and SiO_2 in samples from the Eastern Central Zone, suggesting that zircon saturation in these samples occurred early in the fractionation process (Janoušek et al., 2004; Figure 10d). Therefore, Zr saturation temperatures indicate the liquidus temperature of the granitic melt (Watson & Harrison, 1983). In some cases, the Zr concentrations confirm the tholeiitic affinities shown by some lithological assemblages (for example, the Central Western Zone), which suggests very little contamination of the parental magma by continental crust and is cor-

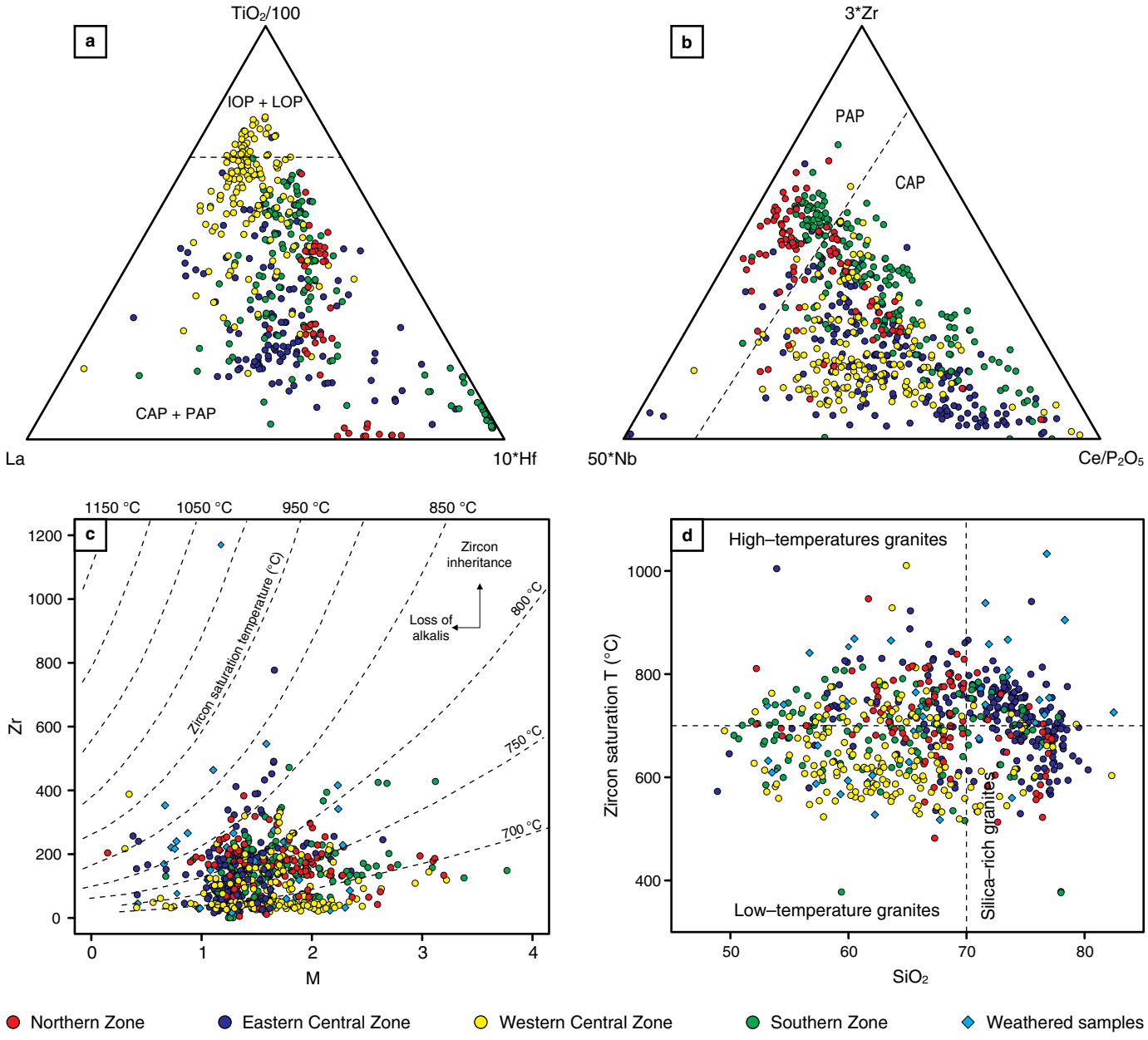

Figure 10. Discrimination diagrams for potassic rocks and zirconium saturation temperature. **(a)** La (ppm) –TiO_2/100–10*Hf discrimination diagrams differentiating continental and postcollisional (CAP + PAP) arc potassic rocks from initial and late oceanic (IOP + LOP) arc potassic rocks. **(b)** 50*Nb–3*Zr–Ce/P_2O_5 discrimination diagrams plotting the rocks in the fields of continental arc potassic (CAP) rocks. **(c)** M vs. Zr (ppm) diagram (Janoušek et al., 2004). Note that the Zr saturation temperatures tend to be higher than 600 °C and reach approximately 1000 °C. **(d)** SiO_2 vs. Zr saturation diagram. Note the distribution of lithological units into high– and low–temperature granite fields.

roborated by the concentrations of Y. Additionally, the Nb/Yb and Th/Yb ratios suggest contributions from subduction–related fluids and magma evolution by either fractional crystallization with assimilation or a process related to the melting–assimilation–storage–homogenization (MASH) zone in a volcanic arc setting with interaction between the enriched mantle and the crust (Pearce, 2008).

Chondrite–normalized spider diagrams show the presence of negative Nb, Ta, and Ti anomalies (Figure 11a), consistent with retention of oxide phases during partial melting in subduction zones (see Pearce, 1982; Pearce et al., 1984, 1990; Müller et al., 1992; Pe–Piper et al., 2009; Goswami & Bhattacharyya, 2014; Moreno et al., 2014). Negative Eu anomalies (Figure 11b) are observed in the chondrite C1–normalized diagrams of the Eastern Central and Western zones, suggesting fractional crystallization of plagioclase and alkali feldspar, whereas the Eu anomalies of the Northern and Southern zones tend to be flat to positive, which suggests the likely

accumulation of plagioclase in the source (Hess, 1989; Keshavarzi et al., 2014). Overall, REE patterns show steep slopes for LREE, suggesting melting of a substantial proportion of clinopyroxene or melting of enriched amphibolite metabasalt (Pe–Piper et al., 2009), and flat curves for HREE, suggesting the addition of a small proportion of partial melts of garnet (Pe–Piper et al., 2009). Several processes from trace element ratio diagrams (Figure 11c–d) can be highlighted: variable differentiation grades, residual garnet (Eastern Central Zone), mixing of components from different sources including a subduction component, crustal contamination, and crystallization of accessory phases (Kay et al., 2013).

Note that there is an apparent contradiction between the $(Y/Nb)_N$ and $(Ce/Pb)_N$ ratios since observed $(Y/Nb)_N$ ratios <1 suggest that mantle sources were not involved in the genesis of the magmas or that this ratio decreased during the evolution of the continental margin magma, while $(Ce/Pb)_N$ ratios > 1 suggest that the crust is not a key factor in the genesis of the magmas (Figure 11e, 11f). Here, it is important to remember that we discard intracontinental rift magmatism based on the absence of peralkaline rocks and the postorogenic tectonic affinity. The apparent contradiction is resolved by considering the mixing of melts from different sources (crustal and mantle melts). Magma mixing is also indicated by high $(Th/Nb)_N$ and $(Th/Ta)_N$ ratios (higher than those observed in island arc magmas and higher than the crustal trend).

To evaluate the geochemical links between granitic melts and their sources, we use the methodology of Moyen et al. (2017). In the diagrams of Figure 12 (projected from biotite + quartz + H_2O), all liquids from the same source should plot along a tight array, pointing to the Na + K + Al apex (the granite minimum) and have a slope that depends solely on the nature of the source (Moyen et al., 2017). In this diagram, two lines are important: (i) the line connecting the feldspars and representing peraluminous rocks (horizontal in the figure, corresponding to A/CNK = 1) and (ii) the line connecting the 3Al + 2(Na + K) and the (Ca + Al) apices. This line separates mafic from felsic sources. Some samples from the Northern and Western Central zones can be interpreted as crystallized melts that originated with some influence from felsic sources. Samples from the Northern, Western Central, and Southern zones plot in a nearly horizontal trend along the line A/CNK = 1, suggesting melting of the supra–subduction mantle wedge. Samples from the Eastern Central Zone plot above the A/CNK = 1 line towards the 3Al + 2(Na + K) apex, which suggests a felsic crustal aluminous source (metasediments or metaigneous) and peraluminous affinity.

7.2. Evolution of the Magmatic Belt in Colombia

The age distribution within the belt allows the identification of several patterns: (i) the oldest magmas occur in the Eastern Central Zone with ages ranging from 216 to 186 Ma and a magmatic peak at ca. 200 Ma (see Figure 3); (ii) in the Northern, Western Central, and Southern zones, uninterrupted magmatic activity began at approximately 196 Ma, with a peak of magmatic activity at ca. 186 Ma; magmatic activity was interrupted in the Northern Zone at ca. 174 Ma; (iii) the youngest peaks of magmatic activity are observed in the Western Central and Southern zones (ca. 156 and 158 Ma); and (iv) magmatic activity between 165 and 175 Ma seems to have been concentrated in the Southern Zone. Note that the youngest magmatism has the most basic compositions (quartz diorites, tonalites, diorites, and granodiorites), whereas the oldest magmatism has more felsic compositions (monzogranites and subordinate syenogranites). Figure 13 illustrates how the magmatism varied spatially and temporally during the evolution of the belt. Plutons from the Eastern Central Zone are mostly peraluminous, while there is a slight tendency towards a metaluminous character in the plutons from the Southern, Western Central, and Northern zones.

In the diagrams of Figure 14, it is evident that plutonic rocks from the Eastern Central Zone, which record the oldest magmatism, cluster around the syncollisional field (Figure 14a). Plutonic rocks from the Southern, Western Central, and Northern zones have a wider distribution with compositions that vary progressively from subduction to late–orogenic regimes (Figure 14b–d), which reflects general and consistent increases in K and Na (Batchelor & Bowden, 1985). The previous discriminations suggest that a subduction regime prevailed with the development of active continental margin magmatism (see also Figure 9); this interpretation is also consistent with what is observed in $(Th/Ta)_N$ vs. $(Y/Nb)_N$ and $(Ce/Pb)_N$ vs. $(Y/Nb)_N$ diagrams (Figure 11e, 11f).

Note that published Pb, Nd, and Sr isotope compositions reveal an increased juvenile magmatic component in progressively younger rocks, which is consistent with Hf isotope data, and demonstrate an increased proportion of juvenile mass within the crystallizing magma (Leal–Mejía, 2011; Bissig et al., 2014; Cochrane et al., 2014b; Bustamante et al., 2016). This interpretation is also supported by trends in εNd_i and εHf_i from negative values in Early Jurassic time to positive values in Early Cretaceous time (Ordóñez–Calderón, 2003; Ordóñez–Carmona et al., 2006; Cochrane et al., 2014b; Spikings et al., 2015; Bustamante et al., 2016). Negative εNd_i and εHf_i values in the oldest samples of the suite suggest an important crustal component in the parental magma (Figure 14e), which is coherent with the observed high $^{87}Sr/^{86}Sr$ ratios (>0.705). Spatially, a greater contribution of lithospheric mantle and crustal assimilation in the arc magmas towards the east has also been suggested (Ordóñez–Calderón, 2003; Quandt et al., 2018). Pb isotope data further indicate a mostly "orogenic" or arc–type juvenile crust source (Figure 14f), with a more radiogenic lead contribution from the upper continental crust (Leal–Mejía, 2011; Quandt et al., 2018). Hf isotope data point

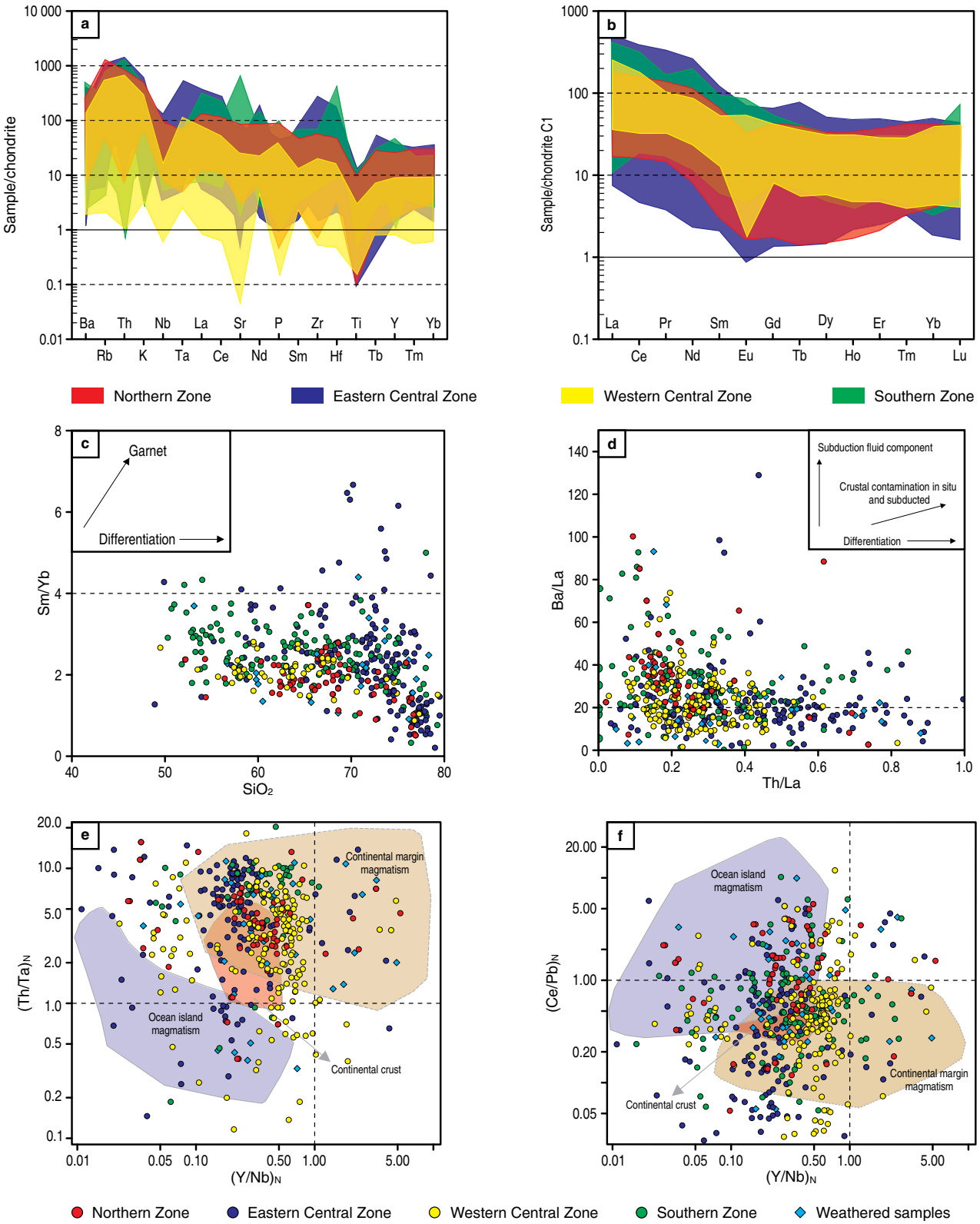

Figure 11. Geochemical REE patterns for the different regions of the Late Triassic to Jurassic magmatic belt in Colombia. **(a)** Chondrite–normalized (Thompson, 1982) spider diagrams show the presence of negative Nb, Ta, and Ti anomalies. **(b)** Chondrite C1–normalized (McDonough & Sun, 1995) diagrams show sloping patterns for LREE and flat patterns for HREE. **(c)** SiO_2 vs. Sm/Yb ratio (Kay et al., 2013); the Sm/Yb ratio greater than ca. 4 suggests Yb retention in residual garnet formed at high pressure. **(d)** Th/La vs. Ba/La ratios (Kay et al., 2013). Note the relevance of the subduction fluid component in relation to the crustal contamination. **(e, f)** $(Th/Ta)_N$ vs. $(Y/Nb)_N$ and $(Ce/Pb)_N$ vs. $(Y/Nb)_N$ discrimination diagrams (Moreno et al., 2014) showing that the evolution of magmatism is mainly consistent with an active continental margin environment. Note the high values of the $(Ce/Pb)_N$ ratios, which suggest a contribution from mantle melts.

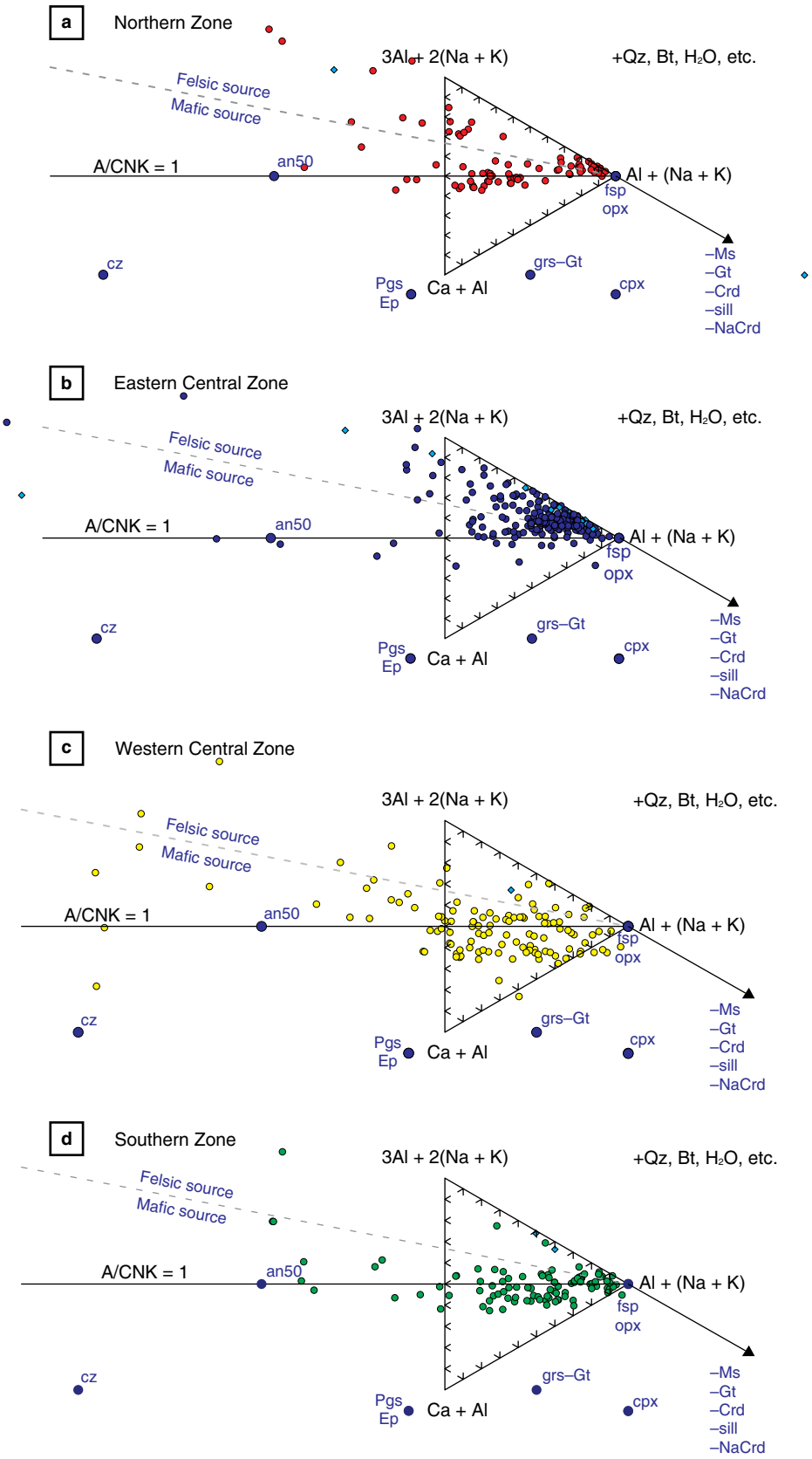

Figure 12. Ca + Al – Al + (Na + K) – 3Al + 2(Na + K) diagram (Moyen et al., 2017) for the sources of granitic rocks. **(a)** Northern Zone. **(b)** Eastern Central Zone. **(c)** Western Central Zone. **(d)** Southern Zone.

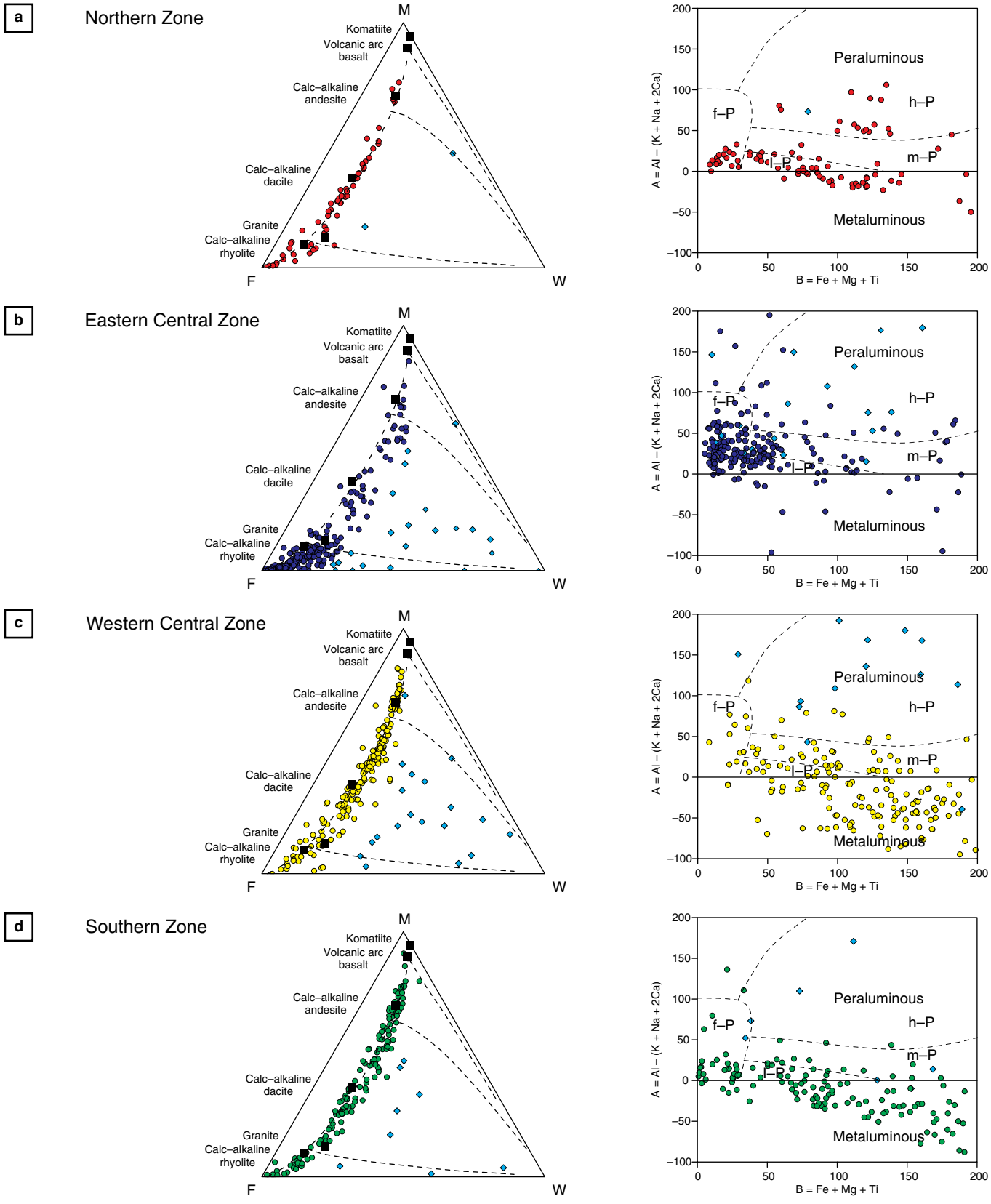

Figure 13. M–F–W diagrams (Ohta & Arai, 2007) showing the effects of differentiation and alteration on igneous rocks by combining several indicators, in which M corresponds to mafic rocks, F to felsic rocks, and W to weathered compositions (left) and a B–A multicationic diagram (Villaseca et al., 1998) showing that the plutonic rocks vary between the peraluminous and metaluminous domains (right). **(a)** Northern Zone. **(b)** Eastern Central Zone. **(c)** Western Central Zone. **(d)** Southern Zone. The blue diamonds represent weathered samples.

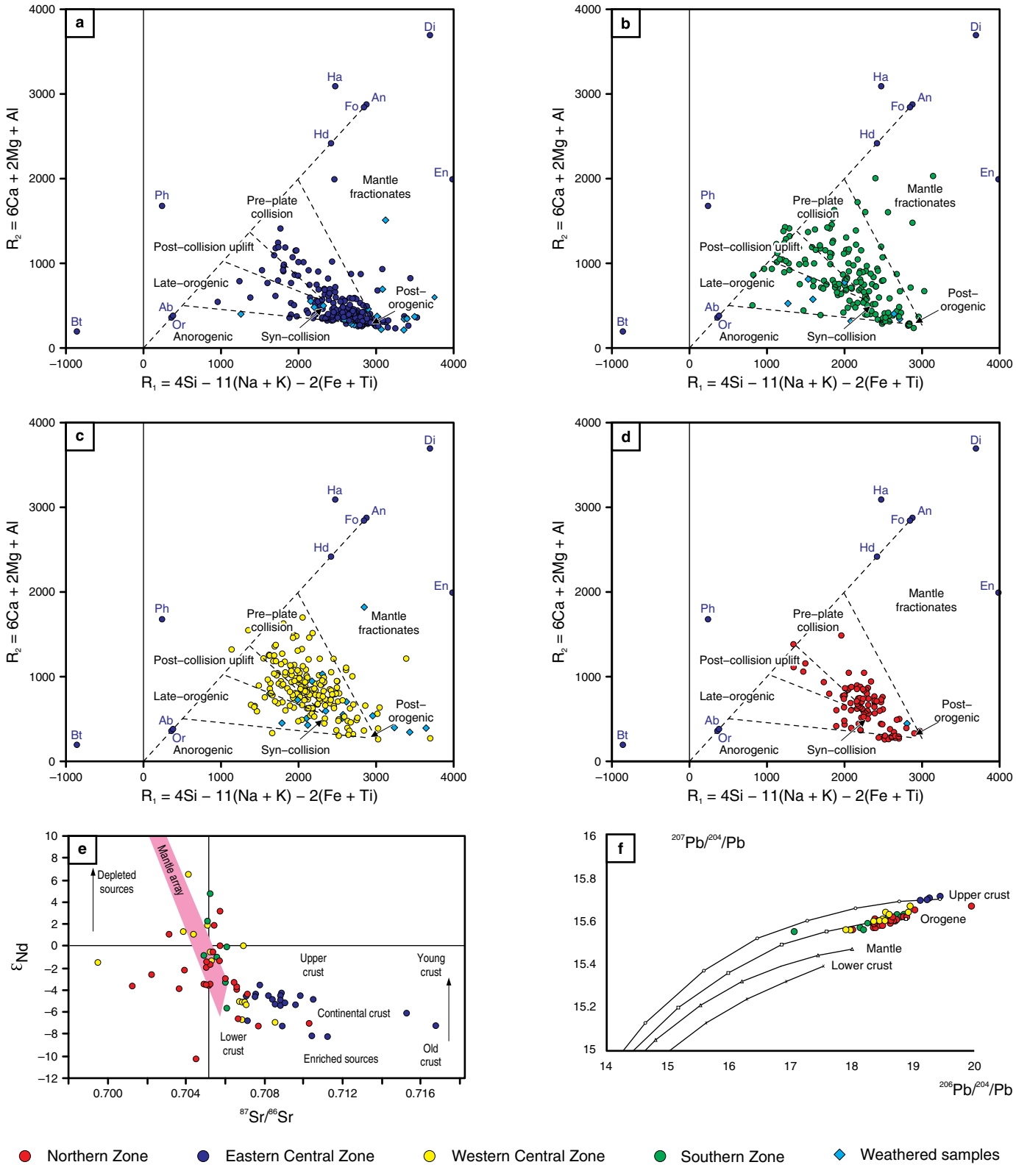

Figure 14. Discrimination diagrams of the tectonic settings of granitic rocks from the R1–R2 cationic values (Batchelor & Bowden, 1985). (**a)** Northern Zone. **(b)** Eastern Central Zone. **(c)** Western Central Zone. **(d)** Southern Zone. **(e)** $^{86}Sr/^{87}Sr$ vs. ε_{Nd} plot for the Late Triassic to Jurassic magmatic belt. **(f)** Lead isotope compositions of the Late Triassic to Jurassic magmatic belt. Lead isotope evolution curves after the Plumbotectonics model of Zartman & Doe (1981) are shown for comparison.

to an increasing proportion of juvenile input in the magmas from Early Jurassic to Early Cretaceous times (20% to 80%); this feature is also observed spatially along an oceanward trend (Cochrane et al., 2014b).

8. Conclusions

The elongated shapes of the Late Triassic to Jurassic magmatic belt and individual plutons (cf., Figure 1) suggest that the generation of spaces to accommodate the magmatic pulses was related to transtensional environments, which in turn were related to crustal evolution in a tectonic framework dominated by oblique subduction. This interpretation is consistent with an extensional environment in the northern corner of South America during the Late Triassic to Jurassic, which has been reported by several authors (Mojica et al., 1996; Cediel et al., 2003; Pindell & Kennan, 2009; van der Lelij, 2013; van der Lelij et al., 2016), but the triggering mechanism has not been provided. In turn, extensional environments promote crustal thinning and favor a high–temperature thermal regime in the continental crust, which can trigger partial melting at the base of the crust or the decompression of intermediate to mafic rocks as an alternative mechanism for the occurrence of high–potassium granites. The interpretation of a thermal anomaly at the base of the crust due to the action of the enriched mantle (mantle wedge), in a tectonic setting of oblique subduction, is supported by the high–potassium calc–alkaline to shoshonitic affinities, magma mixing, and negative Nb, Ta, and Ti anomalies typical of subduction. High Ce and Pb concentrations and positive Pb, Rb, K, and Ba anomalies are attributed to metasomatism of the mantle wedge by fluids derived by melting during slab subduction and/or contamination by the continental crust (see, for example, Keshavarzi et al., 2014). This interpretation is also supported by the presence of S–, I–, and A–type granitic rocks recording high and low temperatures; these rocks range from strongly peraluminous to metaluminous and have geochemical signatures suggesting crustal contamination, as interpreted here and previously by other authors (e.g., van der Lelij et al., 2016), and different sources of melts.

Plutonic, hypabyssal, and volcanic successions are distributed in four zones: Northern, Eastern Central, Western Central, and Southern, covering a total area of approximately 50 500 km^2. The effusive volcanism and subvolcanic plutons indicate the presence of magmatic arcs along belts from south to north in Colombia (cf., Figure 1), through the Northern Andean Block, and from the Ecuadorian Andes to the Venezuelan Andes. The presence of abundant associations of S–type granites followed by associations of slightly peraluminous to metaluminous I–type granites and subordinate associations of A–type granites combined with a clear evolutionary trend towards I–type granites suggests the occurrence of processes that greatly modified the magma composition.

Magmatism on the continental margin varied spatially and temporally from a postcollisional extensional setting (associated with orogenic collapse?) to a volcanic arc setting in an active continental margin dominated by subduction over a time span of approximately 60 my. The S–, I–, and A–type granites of high–potassium calc–alkaline to shoshonitic affinity with strong peraluminous to metaluminous characters in the belt are key features to develop interpretations about the origin and evolution of these magmas and to understand the tectonics of the northwestern margin of Gondwana between the Late Triassic and the Jurassic. The age distribution and geochemistry indicate a trend where the youngest and most metaluminous mafic compositions of the tholeiitic to calc–alkaline series are located in the west, while the oldest and most alkaline compositions of the high–potassium calc–alkaline and peraluminous series are located in the eastern part of the belt. The youngest magmatism is typical of environments related to subduction associated with active continental margins, whereas the oldest magmatism is characteristic of syncollisional to postcollisional (postorogenic) settings. The magmatic age distribution is also characterized by several peaks and lulls interpreted as records of magmatic flare–ups with magmatic tempos between 10 and 20 Ma (Figure 3); however, it is likely that at least some of the age distribution was controlled by exhumation and erosional processes, as well as the preservation bias inherent in the geological record. The most noticeable gap in the age distribution that may indicate an important interruption (a lull) in magmatic activity is observed between 165 and 175 Ma in all but the Southern Zone.

Figure 15 shows the spatiotemporal distribution of plutons in the magmatic belt; this figure also portrays the interpreted spatial location of the transition from the postcollisional stage to the arc stage and the location of the subduction zone. The oldest magmas from the postcollisional stage are interpreted as a result of melting of the lower crust due to a thermal anomaly (possibly associated with the mantle wedge, slab breakoff, or slab tearing of the subducting plate along a transform fault) during oblique subduction. Magmas from the arc stage are mostly "orogenic" or arc–type juvenile crust, with contributions from the lithospheric mantle and crustal assimilation in a supra–subduction regime; these magmas show an increasing proportion of juvenile mass within the crystallizing magma in progressively younger rocks. Note that this framework interpretation is consistent with those observed in many cordilleran–type magmatic belts containing multiple intrusions with variable composition and arranged as nested complexes in linear arrays (Cobbing & Pitcher, 1972; Pitcher, 1997; Winter, 2014). The most basic compositions of tholeiitic to potassium–depleted calc–alkaline affinity are located near

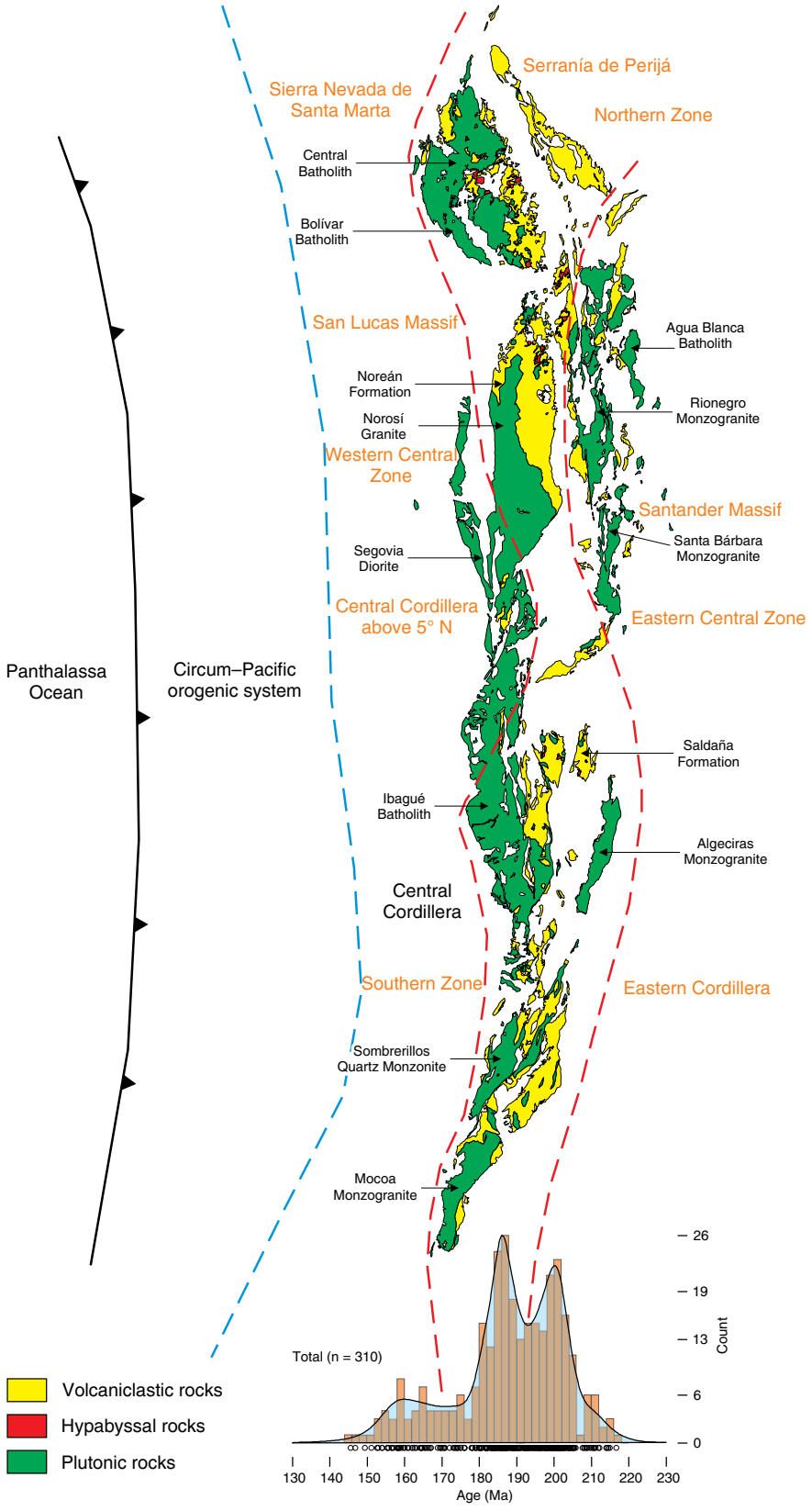

Figure 15. Schematic diagram showing the spatial and temporal variations in the Late Triassic to Jurassic magmatic belt along the continental margin in a supra–subduction tectonic regime. The oldest magmatism has more felsic compositions (monzogranites and subordinate syenogranites) and is typical of syncollisional to postcollisional (postorogenic) settings. The youngest magmatism has the most basic compositions (quartz diorites, tonalites, diorites, and granodiorites), which are typical of subduction–related environments associated with active continental margins.

the trench, whereas the most evolved, potassium–rich calc–alkaline affinities are found towards the back–arc region and ultimately change to the shoshonitic or trans–alkaline series (Brown, 1981; Lameyre, 1988; Winter, 2014).

Acknowledgments

The authors are grateful to the Universidad Nacional de Colombia and the Servicio Geológico Colombiano and the support of these two institutions through several projects from the outcomes of this research. Special thanks to Jorge GÓMEZ TAPIAS for fostering the publication of this study. We appreciate helpful and constructive reviews from David BUCHS and Yamirka ROJAS AGRAMONTE. We also recognize that this work would not have been possible without all the contributions made by different authors concerning the characterization of the Triassic to Jurassic magmatic belt in Colombia; to all of them, thank you for your valuable work.

References

Aggarwal, Y.P. 1983. Seismic slip rates and earthquakes ruptures zones in the southern Caribbean: Implications for plate motions and earthquake hazard in this region. 10th Caribbean Geological Conference. Memoirs, p. 157. Cartagena.

Altenberger, U. & Concha, A. 2005. Late Lower to early Middle Jurassic arc magmatism in the northern Ibagué–Batholith, Colombia. Geología Colombiana, 30: 87–97.

Álvarez, A.J. 1983. Geología de la cordillera Central y el occidente colombiano y petroquímica de los intrusivos granitoides meso–cenozoicos. Boletín Geológico, 26(2): 1–175.

Álvarez, M.J. 2013. Petrologia, geoquímica isotópica e metalogenia dos depósitos de ouro El Silencio e La Gran Colômbia, Distrito Mineiro Segovia–Remedios, Colômbia. Master thesis, Universidade de Brasilia, 178 p. Brasilia.

Arango, M.I., Rodríguez, G., Bermúdez, J.G. & Zapata, G. 2015a. Catálogo de unidades litoestratigráficas de Colombia: Cuarzomonzodiorita de Las Minas, cordillera Central. Servicio Geológico Colombiano, 26 p. Bogotá.

Arango, M.I., Rodríguez, G., Zapata, G. & Bermúdez, J.G. 2015b. Catálogo de unidades litoestratigráficas de Colombia: Cuarzolatita de Teruel, cordillera Central. Servicio Geológico Colombiano, 25 p. Bogotá.

Arango, M.I., Rodríguez, G., Bermúdez, J.G. & Zapata, G. 2015c. Catálogo de unidades litoestratigráficas de Colombia: Cuarzomonzonita de Anchique, cordillera Central. Servicio Geológico Colombiano, 26 p. Bogotá.

Arango, M.I., Rodríguez, G., Zapata, G. & Bermúdez, J.G. 2015d. Catálogo de unidades litoestratigráficas de Colombia: Monzogranito de Altamira, cordilleras Oriental y Central. Servicio Geológico Colombiano, 31 p. Bogotá.

Arango, M.I., Rodríguez, G., Zapata, G. & Bermúdez, J.G. 2015e. Catálogo de unidades litoestratigráficas de Colombia: Monzogranito de Mocoa, cordillera Oriental. Servicio Geológico Colombiano, 41 p. Bogotá.

Arango, M.I., Rodríguez, G., Zapata, G. & Correa–Martínez, A.M. 2016. Catálogo de unidades litoestratigráficas de Colombia: Monzogranito de Rionegro, cordillera Oriental. Servicio Geológico Colombiano, 128 p. Bogotá.

Aspden, J.A., McCourt, W.J. & Brook, M. 1987. Geometrical control of subduction–related magmatism: The Mesozoic and Cenozoic plutonic history of western Colombia. Journal of the Geological Society, 144(6): 893–905. https://doi.org/10.1144/gsjgs.144.6.0893

Aspden, J.A., Harrison, S.H. & Rundle, C.C. 1992. New geochronological control for the tectono–magmatic evolution of the metamorphic basement, Cordillera Real and El Oro Province of Ecuador. Journal of South American Earth Sciences, 6(1–2): 77–96. https://doi.org/10.1016/0895-9811(92)90019-U

Bahajroy, M. & Taki, S. 2014. Study of the mineralization potential of the intrusives around Valis (Tarom–Iran). Earth Sciences Research Journal, 18(2): 123–129. https://doi.org/10.15446/esrj.v18n2.44799

Bao, Z., Cai, K., Sun, M., Xiao, W., Wan, B., Wang, Y., Wang, X. & Xia, X. 2018. Continental crust melting induced by subduction initiation of the south Tianshan Ocean: Insight from the latest Devonian granitic magmatism in the southern Yili Block, NW China. Journal of Asian Earth Sciences, 153: 100–117. https://doi.org/10.1016/j.jseaes.2017.04.026

Barbarin, B. 1990. Plagioclase xenocrysts and mafic magmatic enclaves in some granites of the Sierra Nevada Batholith, California. Journal of Geophysical Research: Solid Earth, 95(B11): 17747–17756. https://doi.org/10.1029/JB095iB11p17747

Barbarin, B. 1999. A review of the relationships between granitoid types, their origins and their geodynamic environments. Lithos, 46(3): 605–626. https://doi.org/10.1016/S0024-4937(98)00085-1

Batchelor, R.A. & Bowden, P. 1985. Petrogenetic interpretation of granitoid rock series using multicationic parameters. Chemical Geology, 48(1–4): 43–55. https://doi.org/10.1016/0009-2541(85)90034-8

Bayona, G., García, D.F. & Mora, G. 1994. La Formación Saldaña: Producto de la actividad de estratovolcanes continentales en un dominio de retroarco. En: Etayo–Serna, F. (editor), Estudios Geológicos del Valle Superior del Magdalena, Universidad Nacional de Colombia. Capítulo 1, 21 p. Bogotá.

Bayona, G., Cardona, A., Vásquez, M. & Montes, C. 2012. Subduction to rift–related evolution of Triassic and Jurassic rocks in the northern Andes. 108th Annual Meeting, Geological Society of America, Cordilleran Section, Abstracts with Programs, 44(3), p. 23. Queretaro. https://gsa.confex.com/gsa/2012CD/webprogram/Paper201809.html

Belica, M.E., Tohver, E., Pisarevsky, S.A., Jourdan, F., Denyszyn, S. & George, A.D. 2017. Middle Permian paleomagnetism of the Sydney Basin, eastern Gondwana: Testing Pangaea models and the timing of the end of the Kiaman Reverse Superchron. Tectonophysics, 699: 178–198. https://doi.org/10.1016/j.tecto.2016.12.029

Bissig, T., Mantilla–Figueroa, L.C. & Hart, C.J.R. 2014. Petrochemistry of igneous rocks of the California–Vetas mining district, Santander, Colombia: Implications for northern Andean tectonics and porphyry Cu (–Mo, Au) metallogeny. Lithos, 200–201: 355–367. https://doi.org/10.1016/j.lithos.2014.05.003

Blevin, P. 2004. Metallogeny of granitic rocks. The Ishihara Symposium: Granites and associated metallogenesis. Geoscience Australia, 37 p. Canberra.

Bonin, B. 1990. From orogenic to anorogenic settings: Evolution of granitoid suites after a major orogenesis. Geological Journal, 25(3–4): 261–270. https://doi.org/10.1002/gj.3350250309

Bonin, B. 1998. Alkaline rocks and geodynamics. Turkish Journal of Earth Sciences, 7: 105–118.

Bonin, B. 2007. A–type granites and related rocks: Evolution of a concept, problems and prospects. Lithos, 97(1–2): 1–29. https://doi.org/10.1016/j.lithos.2006.12.007

Bonin, B., Azzouni–Sekkal, A., Bussy, F. & Ferrag, S. 1998. Alkali–calcic and alkaline post–orogenic (PO) granite magmatism: Petrologic constraints and geodynamic settings. Lithos, 45(1–4): 45–70. https://doi.org/10.1016/S0024-4937(98)00025-5

Bowden, P., Batchelor, R.A., Chappell, B.W., Didier, J. & Lameyre, J. 1984. Petrological, geochemical and source criteria for the classification of granitic rocks: A discussion. Physics of the Earth and Planetary Interiors, 35(1–3): 1–11. https://doi.org/10.1016/0031-9201(84)90029-3

Brown, G.C. 1981. Space and time in granite plutonism. Philosophical Transactions of the Royal Society A, 301(1461): 321–336. https://doi.org/10.1098/rsta.1981.0114

Brown, G.C., Thorpe, R.S. & Webb, P.C. 1984. The geochemical characteristics of granitoids in contrasting arcs and comments on magma sources. Journal of the Geological Society, 141(3): 413–426. https://doi.org/10.1144/gsjgs.141.3.0413

Bustamante, C. 2016. Geoquímica e geocronologia do plutonismo de arco Meso–Cenozoico na Cordilheira Central da Colômbia e os processos de acresção crustal nos Andes do Norte. Doctoral thesis, Universidade de São Paulo, 130 p. São Paulo.

Bustamante, C., Cardona, A., Bayona, G., Mora, A., Valencia, V., Gehrels, G. & Vervoort, J. 2010. U–Pb LA–ICP–MS geochronology and tectonic correlation of Middle Jurassic intrusive rocks from the Garzón Massif, Upper Magdalena Valley and the Central Cordillera, southern Colombia. Boletín de Geología, 32(2): 93–109.

Bustamante, C., Archanjo, C., Cardona, A. & Vervoort, J. 2016. Late Jurassic to Early Cretaceous plutonism in the Colombian Andes: A record of long–term arc maturity. Geological Society of America Bulletin, 128(11–12): 1762–1779. https://doi.org/10.1130/B31307.1

Cabanis, B. & Lecolle, M. 1989. Le diagramme La/10–Y/15–Nb/8: Un outil pour la discrimination des series volcaniques et la mise en evidence des processus de mélange et/ou de contamination crustale. Comptes Rendus l'Académie des Sciences, Série 2, Mécanique, Physique, Chimie, Sciences de l'univers, Sciences de la Terre, 309: 2023–2029. Paris.

Cardona, A., Cordani, U. & MacDonald, W.D. 2006. Tectonic correlations of pre–Mesozoic crust from the northern termination of the Colombian Andes, Caribbean region. Journal of South American Earth Sciences, 21(4): 337–354. https://doi.org/10.1016/j.jsames.2006.07.009

Cardona, A., Valencia, V., Garzón, A., Montes, C., Ojeda, G., Ruiz, J. & Weber, M. 2010. Permian to Triassic I to S–type magmatic switch in the northeast Sierra Nevada de Santa Marta and adjacent regions, Colombian Caribbean: Tectonic setting and implications within Pangea paleogeography. Journal of South American Earth Sciences, 29(4): 772–783. https://doi.org/10.1016/j.jsames.2009.12.005

Castro, A. 2004. The source of granites: Inferences from the Lewisian Complex. Scottish Journal of Geology, 40(1): 49–65. https://doi.org/10.1144/sjg40010049

Castro, A. 2014. The off–crust origin of granite batholiths. Geoscience Frontiers, 5(1): 63–75. https://doi.org/10.1016/j.gsf.2013.06.006

Castro, A., Moreno–Ventas, I. & De La Rosa, J.D. 1991a. H–type (hybrid) granitoids: A proposed revision of the granite–type classification and nomenclature. Earth–Science Reviews, 31(3–4): 237–253. https://doi.org/10.1016/0012-8252(91)90020-G

Castro, A., Moreno–Ventas, I. & De La Rosa, J.D. 1991b. Multistage crystallization of tonalitic enclaves in granitoid rocks (Hercynian belt, Spain): Implications for magma mixing. Geologische Rundschau, 80(1): 109–120. https://doi.org/10.1007/BF01828770

Cediel, F., Shaw, R.P. & Cáceres, C. 2003. Tectonic assembly of the northern Andean Block. In: Bartolini, C., Buffler, R.T. & Blickwede, J. (editors), The circum–Gulf of Mexico and the Caribbean: Hydrocarbon habitats, basin formation, and plate tectonics. American Association of Petroleum Geologists, Memoir 79, p. 815–848. Tulsa, USA.

Chappell, B.W. 1984. Source rocks of I– and S–type granites in the Lachlan fold belt, southeastern Australia. Philosophical Transactions of the Royal Society A, 310(1514): 693–706. https://doi.org/10.1098/rsta.1984.0015

Chappell, B.W. 1999. Aluminium saturation in I– and S–type granites and the characterization of fractionated haplogranites. Lithos, 46(3): 535–551. https://doi.org/10.1016/S0024-4937(98)00086-3

Chappell, B.W. & White, A.J.R. 1974. Two contrasting granite types. Pacific Geology, 8: 173–174.

Chappell, B.W. & White, A.J.R. 1992. I– and S–type granites in the Lachlan fold belt. In: Brown, P.E. & Chappell, B.W. (editors), The Second Hutton Symposium on the Origin of Granites and Related Rocks. Geological Society of America, Special Paper 272, p. 1–26. https://doi.org/10.1130/SPE272-p1

Chappell, B.W. & White, A.J.R. 2001. Two contrasting granite types: 25 years later. Australian Journal of Earth Sciences, 48(4): 489–499. https://doi.org/10.1046/j.1440-0952.2001.00882.x

Chappell, B.W., Bryant, C.J. & Wyborn, D. 2012. Peraluminous I–type granites. Lithos, 153: 142–153. https://doi.org/10.1016/j.lithos.2012.07.008

Chazot, G. & Bertrand. H. 1995. Genesis of silicic magmas during Tertiary continental rifting in Yemen. Lithos, 36(2): 69–83. https://doi.org/10.1016/0024-4937(95)00012-5

Chen, L. & Zhao, Z.F. 2017. Origin of continental arc andesites: The composition of source rocks is the key. Journal of Asian Earth Sciences, 145(part A): 217–232. https://doi.org/10.1016/j.jseaes.2017.04.012

Clarke, D.B. 1981. The mineralogy of peraluminous granites: A review. Canadian Mineralogist, 19(1): 3–17.

Clarke, D.B. 1992. Granitoid rocks. Springer Science & Business Media, 284 p. London.

Clavijo, J. 1995a. La Formación Noreán: Nueva evidencia de volcanismo explosivo en la paleocuenca del Magdalena (Colombia) y su relación con otras unidades del Jurásico norandino. IX Congreso Latinoamericano de Geología. Memoirs, 10 p. Caracas, Venezuela.

Clavijo, J. 1995b. Memoria explicativa: Mapa geológico de la plancha 75 Aguachica. Scale 1:100 000. Ingeominas, 48 p. Bucaramanga.

Clavijo, J., Barbosa, G., Camacho, J.A., Bernal, L.E., Royero, J.M. & Castro, G.E. 1992. Geología de la plancha 75 Aguachica. Scale 1:100 000. Ingeominas. Bogotá.

Cobbing, E.J. & Pitcher, W.S. 1972. The Coastal Batholith of central Peru. Journal of the Geological Society, 128(5): 421–451. https://doi.org/10.1144/gsjgs.128.5.0421

Cochrane, R.S. 2013. U–Pb thermochronology, geochronology and geochemistry of NW South America: Rift to drift transition, active margin dynamics and implications for the volume balance of continents. Doctoral thesis, University of Geneva, 118 p. Geneva, Switzerland. https://doi.org/10.13097/archive-ouverte/unige:30029

Cochrane, R., Spikings, R., Gerdes, A., Ulianov, A., Mora, A., Villagómez, D., Putlitz, B. & Chiaradia, M. 2014a. Permo–Triassic anatexis, continental rifting and the disassembly of western Pangaea. Lithos, 190–191: 383–402. https://doi.org/10.1016/j.lithos.2013.12.020

Cochrane, R., Spikings, R., Gerdes, A., Winkler, W., Ulianov, A., Mora, A. & Chiaradia, M. 2014b. Distinguishing between in–situ and accretionary growth of continents along active margins. Lithos, 202–203: 382–394. https://doi.org/10.1016/j.lithos.2014.05.031

Colmenares, F.H., Mesa, A.M., Roncancio, J.H., Arciniegas, E.G., Pedraza, P.E., Cardona, A., Romero, A.J., Silva, C.A., Alvarado, S.I., Romero, O.A. & Vargas, A.F. 2007. Geología de las planchas 11, 12, 13, 14, 18, 19, 20, 21, 25, 26, 27, 33, 34 y 40. Proyecto: Evolución geohistórica de la Sierra Nevada de Santa Marta. Invemar–Ingeominas–ICP–Ecopetrol–Geosearch Ltda., 401 p. Bogotá.

Correa–Martínez, A.M., Rodríguez, G., Arango, M.I., Zapata, G. & Bermúdez, J.G. 2016. Catálogo de unidades litoestratigráficas de Colombia: Batolito de Mogotes, cordillera Oriental. Servicio Geológico Colombiano, 112 p. Medellín.

Correa–Martínez, A.M., Rodríguez, G., Bermúdez, J.G., Arango, M.I. & Zapata, G. 2018. Catálogo de unidades litoestratigráficas de Colombia: Riolitas del Alto Los Cacaos, cordillera Oriental. Servicio Geológico Colombiano, 47 p. Medellín.

Correa–Martínez, A.M., Rodríguez, G., Arango, M.I. & Zapata–García, G. 2019. Petrografía, geoquímica y geocronología U–Pb de las rocas volcánicas y piroclásticas de la Formación Noreán al NW del Macizo de Santander, Colombia. Boletín de Geología, 41(1): 29–54. http://dx.doi.org/10.18273/revbol.v41n1-2019002

Craddock, J.P., Malone, D.H., Porter, R., Compton, J., Luczaj, J., Konstantinou, A., Day, J.E. & Johnston, S.T. 2017. Paleozoic reactivation structures in the Appalachian–Ouachita–Marathon foreland: Far–field deformation across Pangea. Earth–Science Reviews, 169: 1–34. https://doi.org/10.1016/j.earscirev.2017.04.002

Cuadros, F.A. 2012. Caracterização geoquímica e geocronológica do embasamento mesoproterozóico da parte norte da serranía de San Lucas (Colômbia). Master thesis, Universidade de Brasilia, 113 p. Brasilia.

Cuadros, F.A., Botelho, N.F., Ordoñez–Carmona, O. & Matteini, M. 2013. Edades U–Pb en zircón por LA–MC–ICP–MS del Gneis de San Lucas y el Batolito de Norosí en la parte septentrional de la serranía de San Lucas. XIV Congreso Colombiano de Geología y Primer Simposio de Exploradores. Memoirs, p. 193–194. Bogotá.

Debon, F. & Le Fort, P. 1983. A chemical–mineralogical classification of common plutonic rocks and associations. Earth and Environmental Science Transactions of the Royal Society of Edinburgh, 73(3): 135–149. https://doi.org/10.1017/S0263593300010117

Debon, F. & Le Fort, P. 1988. A cationic classification of common plutonic rocks and their magmatic associations: Principles, method, applications. Bulletin de Minéralogie, 111: 493–510. https://doi.org/10.3406/bulmi.1988.8096

Dera, G., Prunier, J., Smith, P.L., Haggart, J.W., Popov, E., Guzhov, A., Rogov, M., Delsate, D., Thies, D., Cuny, G., Pucéat, E., Charbonnier, G. & Bayon, G. 2015. Nd isotope constraints on ocean circulation, paleoclimate, and continental drainage during the Jurassic breakup of Pangea. Gondwana Research, 27(4): 1599–1615. https://doi.org/10.1016/j.gr.2014.02.006

De Silva, S.L., Riggs, N.R. & Barth, A.P. 2015. Quickening the pulse: Fractal tempos in continental arc magmatism. Elements, 11(2): 113–118. https://doi.org/10.2113/gselements.11.2.113

Dörr, W., Grösser, J.R., Rodríguez, G.I. & Kramm, U. 1995. Zircon U–Pb age of the Paramo Rico tonalite–granodiorite, Santander Massif (cordillera Oriental, Colombia) and its geotectonic significance. Journal of South American Earth Sciences, 8(2): 187–194. https://doi.org/10.1016/0895-9811(95)00004-Y

Drummond, M.S. & Defant, M.J. 1990. A model for trondhjemite–tonalite–dacite genesis and crustal growth via slab melting: Archean to modern comparisons. Journal of Geophysical Research: Solid Earth, 95(B13): 21503–21521. https://doi.org/10.1029/JB095iB13p21503

Ducea, M.N., Paterson, S.R. & DeCelles, P.G. 2015. High–volume magmatic events in subduction systems. Elements, 11(2): 99–104. https://doi.org/10.2113/gselements.11.2.99

Eby, G.N. 1990. The A–type granitoids: A review of their occurrence and chemical characteristics and speculations on their petrogenesis. Lithos, 26(1–2): 115–134. https://doi.org/10.1016/0024-4937(90)90043-Z

Eby, G.N. 1992. Chemical subdivision of the A–type granitoids: Petrogenetic and tectonic implications. Geology, 20(7): 641–644. https://doi.org/10.1130/0091-7613(1992)020<0641:CSOTAT>2.3.CO;2

El Bouseily, A.M. & El Sokkary, A.A. 1975. The relation between Rb, Ba and Sr in granitic rocks. Chemical Geology, 16(3): 207–219. https://doi.org/10.1016/0009-2541(75)90029-7

Elliott, T. 2003. Tracers of the slab. In: Eiler, J. (editor), Inside the subduction factory. Geophysical Monograph Series 138, p. 23–45.

Frantz, J.C., Ordoñez, O. & Chemale, F. 2007. Caracterización de ambientes geológicos con mineralizaciones de oro en los Andes colombianos. VIII Congreso Colombiano de Minería. Memoirs, CD. Medellín.

Frost, B.R. & Frost, C.D. 2008. A geochemical classification for feldspathic igneous rocks. Journal of Petrology, 49(11): 1955–1969. https://doi.org/10.1093/petrology/egn054

Frost, B.R., Barnes, C.G., Collins, W.J., Arculus, R.J., Ellis, D.J. & Frost, C.D. 2001. A geochemical classification of granitic rocks. Journal of Petrology, 42(11): 2033–2048. https://doi.org/10.1093/petrology/42.11.2033

Frost, C.D., Frost, B.R. & Beard, J.S. 2016. On silica–rich granitoids and their eruptive equivalents. American Mineralogist, 101(6): 1268–1284. https://doi.org/10.2138/am-2016-5307

Ganne, J. & Feng, X. 2018. Magmatism: A crustal and geodynamic perspective. Journal of Structural Geology, 114: 329–335. https://doi.org/10.1016/j.jsg.2018.02.002

Ganne, J., Schellart, W.P., Rosenbaum, G., Feng, X. & De Andrade, V. 2017. Probing crustal thickness evolution and geodynamic processes in the past from magma records: An integrated approach. In: Bianchini, G., Bodinier, J.L., Braga, R. & Wilson, M. (editors), The crust–mantle and lithosphere–asthenosphere boundaries: Insights from xenoliths, orogenic deep sections, and geophysical studies. Geological Society of America, Special Paper 526, 25 p. https://doi.org/10.1130/2017.2526(01)

Gansser, A. 1973. Facts and theories on the Andes. Journal of the Geological Society of London, 129(2): 93–131. https://doi.org/10.1144/gsjgs.129.2.0093

García–Chinchilla, D.A. 2018. Petrogênese e evolução tectônica de rochas graníticas da região de Garzón, Cordilheira Oriental da Colômbia. Doctoral thesis, Universidade de São Paulo, 214 p. São Paulo. https://doi.org/10.11606/T.44.2018.tde-10072018-150324

Goldsmith, R., Marvin, R.F. & Mehnert, H.H. 1971. Radiometric ages in the Santander Massif, Eastern Cordillera, Colombian Andes. United States Geological Survey, Professional Paper 750, p. D41–D49.

Gómez, J. 2002. Catálogo de unidades litoestratigráficas de Colombia: Cuarzomonzonita de Dolores, cordillera Oriental. Ingeominas, 15 p. Bogotá.

Gómez, J., Montes, N.E., Alcárcel, F.A. & Ceballos, J.A. 2015. Catálogo de dataciones radiométricas de Colombia en ArcGIS y Google Earth. In: Gómez, J. & Almanza, M.F. (editors), Compilando la geología de Colombia: Una visión a 2015. Servicio Geológico Colombiano, Publicaciones Geológicas Especiales 33, p. 63–419. Bogotá.

González, H. & Londoño, A.C. 2002. Catálogo de las unidades litoestratigráficas de Colombia: Diorita de Segovia, cordillera Central. Ingeominas, 17 p. Bogotá.

González, H. & Núñez, A. 2002. Catálogo de las unidades litoestratigráficas de Colombia: Monzogranito de Mocoa. Ingeominas, unpublished report, 30 p. Bogotá.

González, H., Maya, M., Camacho, J., Cardona, O.D. & Vélez, W. 2015a. Memoria explicativa: Plancha 74 Guaranda. Scale 1:100 000. Servicio Geológico Colombiano, 184 p. Medellín.

González, H., Maya, M., García, J.F., Gómez, J.P., Palacio, A.F. & Vélez, W. 2015b. Memoria explicativa: Plancha 84 Los Canelos. Scale 1:100 000. Servicio Geológico Colombiano, 147 p. Medellín.

González, H., Maya, M., García, J.F., Gómez, J.P., Palacio, A.F. & Vélez, W. 2015c. Memoria explicativa: Plancha 95 Buenavista. Scale 1:100 000. Servicio Geológico Colombiano. 128 p. Medellín.

González, H., Maya, M., Tabares, L.F., Palacio, A.F., Gómez, J.P., Montoya, A. & Vélez, W. 2015d. Memoria explicativa: Plancha 107 Cerro Azul. Scale 1:100 000. Servicio Geológico Colombiano, 167 p. Medellín.

González, H., Maya, M., Tabares, L.F., Montoya, A., Palacio, A.F., Sánchez, C., Barajas, A. & Vélez, W. 2015e. Memoria explicativa: Plancha 118 San Francisco. Scale 1:100 000. Servicio Geológico Colombiano, 220 p. Medellín.

González, H., Maya, M., García, J.F., Camacho, J.A., Gómez, J.P., Cardona, O.D., Palacio, A.F. & Vélez, W. 2015f. Memoria explicativa: Plancha 94 El Bagre. Scale 1:100 000. Servicio Geológico Colombiano, 196 p. Medellín.

González, H., Salinas, R., Cárdenas, J.I., Muñoz, C.M. Dávila, G.C. & Vélez, W. 2015g. Memoria explicativa: Plancha 77 Campo Dos. Scale 1:100 000. Servicio Geológico Colombiano, 234 p. Medellín.

Gorton, M.P. & Schandl, E.S. 2000. From continents to island arcs: A geochemical index of tectonic setting for arc–related and within–plate felsic to intermediate volcanic rocks. The Canadian Mineralogist, 38(5): 1065–1073. https://doi.org/10.2113/gscanmin.38.5.1065

Goswami, B. & Bhattacharyya, C. 2014. Petrogenesis of shoshonitic granitoids, eastern India: Implications for the late Grenvillian post–collisional magmatism. Geoscience Frontiers, 5(6): 821–843. https://doi.org/10.1016/j.gsf.2013.09.003

Grebennikov, A.V. 2014. A–type granites and related rocks: Petrogenesis and classification. Russian Geology and Geophysics, 55(11): 1354–1366. https://doi.org/10.1016/j.rgg.2014.10.011

Harris, N.B.W., Pearce, J.A. & Tindle, A.G. 1986. Geochemical characteristics of collision–zone magmatism. In: Coward, M.P. & Ries, A.C. (editors), Collision tectonics. Geological Society of London, Special Publication 19, p. 67–81. https://doi.org/10.1144/GSL.SP.1986.019.01.04

Hastie, A.R., Kerr, A.C., Pearce, J.A. & Mitchell, S.F. 2007. Classification of altered volcanic island arc rocks using immobile trace elements: Development of the Th–Co discrimination diagram. Journal of Petrology, 48(12): 2341–2357. https://doi.org/10.1093/petrology/egm062

Hernández, S.A., López, J.A. & Zuluaga, C.A. 2017. Petrografía y geoquímica del Batolito de Rionegro al sur del municipio de Cáchira, Macizo de Santander, Colombia. XVI Congreso Colombiano de Geología. Memoirs, p. 1294–1301. Santa Marta.

Hess, P.C. 1989. Origins of igneous rocks. Harvard University Press, 336 p. Cambridge, USA.

Ingeominas & Universidad Industrial de Santander. 2006a. Memoria explicativa: Cartografía geológica de la plancha 55 El Banco. Scale 1:100 000. Ingeominas, 192 p. Bogotá.

Ingeominas & Universidad Industrial de Santander. 2006b. Memoria explicativa: Cartografía geológica de la plancha 64 Barranco de Loba. Scale 1:100 000. Ingeominas, 201 p. Bogotá.

Ingeominas & Universidad Industrial de Santander. 2006c. Memoria explicativa: Cartografía geológica de la plancha 85 Simití. Scale 1:100 000. Ingeominas, 140 p. Bogotá.

Ingeominas & Universidad Industrial de Santander. 2006d. Memoria explicativa: Cartografía geológica de la plancha 96 Bocas del Rosario. Scale 1:100 000. Ingeominas, 126 p. Bogotá.

Irvine, T.N. & Baragar, W.R.A. 1971. A guide to the chemical classification of the common volcanic rocks. Canadian Journal of Earth Sciences, 8(5): 523–548. https://doi.org/10.1139/e71-055

Jaillard, E., Soler, P., Carlier, G. & Mourier, T. 1990. Geodynamic evolution of the northern and central Andes during early to middle Mesozoic times: A Tethyan model. Journal of the Geological Society, 147(6): 1009–1022. https://doi.org/10.1144/gsjgs.147.6.1009

Janoušek, V., Finger, F., Roberts, M., Frýda, J., Pin, C. & Dolejš, D. 2004. Deciphering the petrogenesis of deeply buried granites: Whole–rock geochemical constraints on the origin of largely undepleted felsic granulites from the Moldanubian Zone of the Bohemian Massif. Earth and Environmental Science Transactions of the Royal Society of Edinburgh, 95(1–2): 141–159. https://doi.org/10.1017/S0263593300000985

Kay, S.M., Mpodozis, C. & Gardeweg, M. 2013. Magma sources and tectonic setting of Central Andean andesites (25.5–28° S) related to crustal thickening, forearc subduction erosion and delamination. In: Gómez–Tuena, A., Straub, S. M. & Zellmer, G. F. (editors). Orogenic andesites and crustal growth. Geological Society, London, Special Publication 385: 303–334.

Keshavarzi, R., Esmaili, D., Kahkhaei, M.R., Mokhtari, M.A.A. & Jabari, R. 2014. Petrology, geochemistry and tectonomagmatic setting of Neshveh Intrusion (NW Saveh). Open Journal of Geology, 4(5): 177–189. https://doi.org/10.4236/ojg.2014.45013

Kirsch, M., Paterson, S.R., Wobbe, F., Martínez–Ardila., A.M., Clausen, B.L. & Alasino, P.H. 2016. Temporal histories of cordilleran continental arcs: Testing models for magmatic episodicity. American Mineralogist, 101(10): 2133–2154. https://doi.org/10.2138/am-2016-5718

Lameyre, J. 1988. Granite settings and tectonics. Rendiconti della Società Italiana di Mineralogia e Petrologia, 43(2): 215–236.

Leal–Mejía, H. 2011. Phanerozoic gold metallogeny in the Colombian Andes: A tectono–magmatic approach. Doctoral thesis, Universitat de Barcelona, 989 p. Barcelona.

Leal–Mejía, H., Melgarejo, C. & Shaw, R. 2011. Phanerozoic gold metallogeny in the Colombian Andes. In: Proceedings Let´s talk ore deposits. Society for Geology Applied to Mineral Deposits, SGA Biennial Meeting. Extended abstracts, p. 209–211. Antofagasta, Chile.

Leal–Mejía, H., Shaw, R.P. & Melgarejo i Draper, J.C. 2019. Spatial–temporal migration of granitoid magmatism and the Phanerozoic tectono–magmatic evolution of the Colombian Andes. In: Cediel, F. & Shaw, R.P. (editors), Geology and tectonics of northwestern South America: The Pacific–Caribbean–Andean junction. Frontiers in Earth Sciences. Springer, p. 253–410. Cham, Germany. https://doi.org/10.1007/978-3-319-76132-9_5

Litherland, M., Aspden, J.A. & Jemielita, R.A. 1994. The metamorphic belts of Ecuador. Overseas Memoir of the British Geological Survey 11, 147 p. Nottingham, England.

López, J.A. & Zuluaga, C.A. 2016. Geoquímica de roca total y ambiente geodinámico del magmatismo calcoalcalino de edad Triásico–Jurásico de la Sierra Nevada de Santa Marta y Alta Guajira. The Colombian and Venezuelan Caribbean–Geology Workshop. Abstracts, 2 p. Bogotá.

López, J.A., Cuellar, M.A., Aguirre, R., Valencia, M. & Sánchez, C.A. 2007. Evidencias petrográficas y de campo de una intrusión sintectónica en la cordillera Central de Colombia: El caso de la Milonita Granítica del Guacaica. XI Congreso Colombiano de Geología. Memoirs, p. 17. Bucaramanga.

López, J.A., Zuluaga, C.A. & Tassinari, C.C.G. 2017. Geoquímica de roca total de la Cuarzomonzonita de Santa Bárbara, Macizo de Santander. XVI Congreso Colombiano de Geología. Memoirs, p. 1326–1332. Santa Marta.

MacDonald, W.D. 1964. Geology of the serranía de Macuira area, Guajira Peninsula, Colombia. Doctoral thesis, Princeton University, 237 p. Princeton, USA.

Maloney, K.T., Clarke, G.L., Klepeis, K.A. & Quevedo, L. 2013. The Late Jurassic to present evolution of the Andean margin: Drivers and the geological record. Tectonics, 32(5): 1049–1065. https://doi.org/10.1002/tect.20067

Maniar, P.D. & Piccoli, P.M. 1989. Tectonic discrimination of granitoids. Geological Society of America Bulletin, 101(5): 635–643. https://doi.org/10.1130/0016-7606(1989)101<0635:TDOG>2.3.CO;2

Mantilla–Figueroa, L.C., Bernal, L.E., Clavijo, J., Pinto, J.E., Osorio, J., Ibáñez, D., Castro, E., López, E., Duarte, R., Celada, C.M., Gómez, E., Quintero, I., Pérez, A., Páez, L.A., García, C., Colegial, J.D., Correa, K., Serrano, J., Gaviria, J., Casas, R., Lasso, S., Niz, L., García, M., Nava, G., Martínez, A.M., Silva, A., Prada, D., Calderón, H., Jiménez, G., Cuellar, M., Franco, R. & Caballero, V. 2007. Generalidades sobre la geología de la serranía de San Lucas: Planchas 55, 64, 85 y 96. XI Congreso Colombiano de Geología. Memoirs, p. 14–17. Bucaramanga.

Mantilla–Figueroa, L.C., Valencia, V.A., Barra, F., Pinto, J. & Colegial, J. 2009. Geocronología U–Pb del distrito aurífero de Vetas–California (departamento de Santander, Colombia). Boletín de Geología, 31(1): 31–43.

Mantilla–Figueroa, L.C., Bissig, T., Valencia, V. & Hart, C.J.R. 2013. The magmatic history of the Vetas–California mining district, Santander Massif, Eastern Cordillera, Colombia. Journal of South American Earth Sciences, 45: 235–249. https://doi.org/10.1016/j.jsames.2013.03.006

Martini, M. & Ortega–Gutiérrez, F. 2018. Tectono–stratigraphic evolution of eastern Mexico during the break–up of Pangea: A review. Earth–Science Reviews, 183: 38–55. https://doi.org/10.1016/j.earscirev.2016.06.013

Matthews, K.J., Maloney, K.T., Zahirovic, S., Williams, S.E., Seton, M. & Müller, R.D. 2016. Global plate boundary evolution and kinematics since the late Paleozoic. Global and Planetary Change, 146: 226–250. https://doi.org/10.1016/j.gloplacha.2016.10.002

McDonough, W.F. & Sun, S.S. 1995. The composition of the Earth. Chemical Geology, 120(3–4): 223–253. https://doi.org/10.1016/0009-2541(94)00140-4

Miller, C.F. 1985. Are strongly peraluminous magmas derived from pelitic sedimentary sources? The Journal of Geology, 93(6): 673–689. https://doi.org/10.1086/628995

Miller, C.F., McDowell, S.M. & Mapes, R.W. 2003. Hot and cold granites? Implications of zircon saturation temperatures and preservation of inheritance. Geology, 31(6): 529–532. https://doi.org/10.1130/0091-7613(2003)031<0529:HACGIO>2.0.CO;2

Mišković, A., Spikings, R.A., Chew, D.M., Košler, J., Ulianov, A. & Schaltegger, U. 2009. Tectonomagmatic evolution of western Amazonia: Geochemical characterization and zircon U–Pb geochronologic constraints from the Peruvian Eastern Cordilleran granitoids. Geological Society of America Bulletin, 121(9–10): 1298–1324. https://doi.org/10.1130/B26488.1

Mojica, J. & Kammer, A. 1996. Resumen del Jurásico en Colombia. Contribution International Geological Correlation Programme (IGCP) 322: Jurassic events in South America. Geología Colombiana, 20: 160–162.

Mojica, J., Kammer, A. & Ujueta, G. 1996. El Jurásico del sector noroccidental de Suramérica y guía de la excursión al Valle Superior del Magdalena (Nov. 1–4/95), regiones de Payandé y Prado, departamento del Tolima, Colombia. Geología Colombiana, 21: 3–40.

Moreno, J.A., Molina, J.F., Montero, P., Abu–Anbar, M., Scarrow, J.H., Cambeses, A. & Bea, F. 2014. Unraveling sources of A–type magmas in juvenile continental crust: Constraints from compositionally diverse Ediacaran post–collisional granitoids in the Katerina Ring Complex, southern Sinai, Egypt. Lithos, 192–195: 56–85. https://doi.org/10.1016/j.lithos.2014.01.010

Moyen, J.F., Laurent, O., Chelle–Michou, C., Couzinié, S., Vanderhaeghe, O., Zeh, A., Villaros, A. & Gardien, V. 2017. Collision vs. subduction–related magmatism: Two contrasting ways of granite formation and implications for crustal growth. Lithos, 277: 154–177. https://doi.org/10.1016/j.lithos.2016.09.018

Müller, D., Rock, N.M.S. & Groves, D.I. 1992. Geochemical discrimination between shoshonitic and potassic volcanic rocks in different tectonic settings: A pilot study. Mineralogy and Petrology, 46: 259–289. https://doi.org/10.1007/BF01173568

Muttoni, G., Gaetani, M., Kent, D.V., Sciunnach, D., Angiolini, L., Berra, F., Garzanti, E., Mattei, M. & Zanchi, A. 2009. Opening of the Neo–Tethys Ocean and the Pangea B to Pangea A transformation during the Permian. GeoArabia, 14(4): 17–48.

Nance, R.D., Murphy, J.B. & Santosh, M. 2014. The supercontinent cycle: A retrospective essay. Gondwana Research, 25: 4–29. https://doi.org/10.1016/j.gr.2012.12.026

Nédélec, A. & Bouchez, J.L. 2015. Granites: Petrology, structure, geological setting, and metallogeny. Oxford University Press, 335 p. Oxford. https://doi.org/10.1093/acprof:oso/9780198705611.001.0001

Noguera, M.I., Wright, J.E., Urbani, F. & Pindell, J. 2011. U–Pb geochronology of detrital zircons from the Venezuelan passive margin: Implications for an Early Cretaceous proto–Orinoco river system and proto–Caribbean ocean basin paleogeography. Geologica Acta, 9(3–4): 265–272. https://doi.org/10.1344/105.000001698

Núñez, A. 2002. Catálogo de unidades litoestratigráficas de Colombia: Batolito de Ibagué, cordillera Central. Ingeominas, 26 p. Bogotá.

Núñez, A., Bocanegra, A. & Gómez, J. 1996. Los plutones jurásicos del Valle Superior del Magdalena (Colombia). VII Con-

greso Colombiano de Geología. Memoirs, II, p. 226–239. Bogotá.

Ohta, T. & Arai, H. 2007. Statistical empirical index of chemical weathering in igneous rocks: A new tool for evaluating the degree of weathering. Chemical Geology, 240(3–4): 280–297. https://doi.org/10.1016/j.chemgeo.2007.02.017

Ordóñez–Calderón, J.C. 2003. Petrology of the granitoid rocks in the Santander Massif, northeast Colombia. Master thesis. Shimane University, 122 p. Shimane, Japan.

Ordóñez–Carmona, O., Restrepo, J.J. & Pimentel, M.M. 2006. Geochronological and isotopical review of pre–Devonian crustal basement of the Colombian Andes. Journal of South American Earth Sciences, 21(4): 372–382. https://doi.org/10.1016/j.jsames.2006.07.005

Ordóñez–Carmona, O., Frantz, J.C., Chemale, F. & Londoño, C. 2009. Serranía de San Lucas: Mineralizaciones auríferas, intrusiones de 1500 Ma, metamorfismo Grenville y magmatismo jurásico. XII Congreso Colombiano de Geología. Memoirs in CD ROM, T003–R117, 1 p. Paipa, Boyacá.

Paterson, S.R. & Ducea, M.N. 2015. Arc magmatic tempos: Gathering the evidence. Elements, 11(2): 91–98. https://doi.org/10.2113/gselements.11.2.91

Paul, A.N., Spikings, R.A., Ulianov, A. & Ovtcharova, M. 2018. High temperature (>350 ºC) thermal histories of the long lived (>500 Ma) active margin of Ecuador and Colombia: Apatite, titanite and rutile U–Pb thermochronology. Geochimica et Cosmochimica Acta, 228: 275–300. https://doi.org/10.1016/j.gca.2018.02.033

Pearce, J.A. 1982. Trace element characteristics of lavas from destructive plate boundaries. In: Thorpe, R.S. (editor), Andesites. John Wiley & Sons, p. 525–548. New York.

Pearce, J.A. 1983. Role of sub–continental lithosphere in magma genesis at active continental margins. In: Hawkesworth, C.J. & Nurry, M.J. (editors), Continental basalts and mantle xenoliths. Shiva Publications, p. 230–249. Nantwich, UK.

Pearce, J.A. 2008. Geochemical fingerprinting of oceanic basalts with applications to ophiolite classification and the search for Archean oceanic crust. Lithos, 100(1–4): 14–48. https://doi.org/10.1016/j.lithos.2007.06.016

Pearce, J.A., Harris, N.B.W. & Tindle, A.G. 1984. Trace elements discrimination diagrams for the tectonic interpretation of granitic rocks. Journal of Petrology, 25(4): 956–983. https://doi.org/10.1093/petrology/25.4.956

Pearce, J.A., Bender, J.F., De Long, S.E., Kidd, W.S.F., Low, P.J., Guner, Y., Saroglu, F., Yilmaz, Y., Moorbath, S. & Mitchell, J.G. 1990. Genesis of collision volcanism in eastern Anatolia, Turkey. Journal of Volcanology and Geothermal Research, 44(1–2): 189–229. https://doi.org/10.1016/0377-0273(90)90018-B

Pennington, W.D. 1981. Subduction of eastern Panama Basin and seismotectonics of northwestern South America. Journal of Geophysical Research: Solid Earth, 86(B11): 10753–10770. https://doi.org/10.1029/JB086iB11p10753

Pe–Piper, G., Piper, D.J.W., Koukouvelas, I., Dolansky, L.M. & Kokkalas, S. 2009. Postorogenic shoshonitic rocks and their origin by melting underplated basalts: The Miocene of Limnos, Greece. Geological Society of America Bulletin, 121(1–2): 39–54. https://doi.org/10.1130/B26317.1

Pindell, J.L. 1985. Alleghenian reconstruction and subsequent evolution of the Gulf of Mexico, Bahamas, and proto–Caribbean. Tectonics, 4(1): 1–39. https://doi.org/10.1029/TC004i001p00001

Pindell, J.L. & Dewey, J.F. 1982. Permo–Triassic reconstruction of western Pangea and the evolution of the Gulf of Mexico/Caribbean region. Tectonics, 1(2): 179–211. https://doi.org/10.1029/TC001i002p00179

Pindell, J.L. & Kennan, L. 2009. Tectonic evolution of the Gulf of Mexico, Caribbean and northern South America in the mantle reference frame: An update. In: James, K.H., Lorente, M.A. & Pindell, J.L. (editors), The origin and evolution of the Caribbean Plate. Geological Society of London, Special Publication 328, p. 1–55. https://doi.org/10.1144/SP328.1

Pinilla–Ocampo, A. 2013. Modelo del ambiente tectónico a partir de estudios petrográficos y geoquímicos de la Riodacita de Ipapure–Cerro La Teta. Master thesis, Universidad Nacional de Colombia, 157 p. Bogotá.

Pitcher, W.S. 1988. Andean batholiths and marginal basins. Rendiconti della Società Italiana di Mineralogia e Petrologia, 43(2): 275–280.

Pitcher, W.S. 1997. The nature and origin of granite. Chapman & Hall, 387 p. https://doi.org/10.1007/978-94-011-5832-9

Quandt, D. 2013. The magmatic evolution of the Sierra Nevada de Santa Marta during the Jurassic. Master thesis, University of Postdam, 190 p. Berlin, Germany.

Quandt, D., Trumbull., R.B., Altenberger, U., Cardona, A., Romer, R.L., Bayona, G., Ducea, M., Valencia, V., Vásquez, M., Cortés, E. & Guzman, G. 2018. The geochemistry and geochronology of Early Jurassic igneous rocks from the Sierra Nevada de Santa Marta, NW Colombia, and tectono–magmatic implications. Journal of South American Earth Sciences, 86: 216–230. https://doi.org/10.1016/j.jsames.2018.06.019

Quiceno–Colorado, J., Osorio–Ocampo, S., Vallejo–Hincapié, F., Salazar–Ríos, A., Ossa–Meza, C.A., Giraldo–Alzate, L. & Romero–Arboleda, L. 2016. Petrografía y geoquímica del Stock de Payandé y su posible relación con el magmatismo Jurásico al sur de Colombia. Boletín de Geología, 38(2): 39–53.

Ramos, V.A. 1999. Plate tectonic setting of the Andean Cordillera. Episodes, 22(3): 183–190.

Ramos, V.A. 2009. Anatomy and global context of the Andes: Main geologic features and the Andean orogenic cycle. In: Kay, S.M., Ramos, V.A. & Dickinson, W.R. (editors), Backbone of the Americas: Shallow subduction, plateau uplift, and ridge and terrane collision. Geological Society of America, Memoirs 204, p. 31–65. https://doi.org/10.1130/2009.1204(02)

Restrepo–Pace, P. 1995. Late Precambrian to early Mesozoic tectonic evolution of the Colombian Andes based on new geochronological, geochemical and isotopic date. Doctoral thesis, University of Arizona, 189 p. Tucson.

Riel, N., Jaillard, E., Martelat, J.E., Guillot, S. & Braun, J. 2018. Permian – Triassic Tethyan realm reorganization: Implications for the outward Pangea margin. Journal of South American Earth Sciences, 81: 78–86. https://doi.org/10.1016/j.jsames.2017.11.007

Ríos–Blandón, P.A. 2016. Petrografía y geoquímica de la Granodiorita de Ipapure y su relación con las rocas encajantes en la Alta Guajira–Colombia. Master thesis, Universidad Nacional de Colombia, 103 p. Bogotá.

Rodríguez, G. 2018. Caracterización petrográfica, química y edad Ar–Ar de cuerpos porfídicos intrusivos en la Formación Saldaña. Boletín Geológico, 44: 5–23. https://doi.org/10.32685/0120-1425/boletingeo.44.2018.5

Rodríguez, G., Arango, M.I., Bermúdez, J.G. & Zapata, G. 2015a. Catálogo de unidades litoestratigráficas de Colombia: Granito de Garzón, cordillera Oriental. Servicio Geológico Colombiano, 23 p. Medellín.

Rodríguez, G., Arango, M.I., Bermúdez, J.G. & Zapata, G. 2015b. Catálogo de unidades litoestratigráficas de Colombia: Cuarzomonzonita de Los Naranjos, cordillera Central. Servicio Geológico Colombiano, 28 p. Medellín.

Rodríguez, G., Arango, M.I., Zapata, G. & Bermúdez, J.G. 2015c. Catálogo de unidades litoestratigráficas de Colombia: Cuarzomonzodiorita de El Astillero, serranía de Las Minas. Servicio Geológico Colombiano, 27 p. Medellín.

Rodríguez, G., Zapata, G., Arango, M.I. & Bermúdez, J.G. 2015d. Catálogo de unidades litoestratigráficas de Colombia: Monzogranito de Algeciras, cordillera Oriental. Servicio Geológico Colombiano, 36 p. Medellín.

Rodríguez, G., Correa, A.M., Zapata, G. & Arango, M.I. 2016a. Catálogo de unidades litoestratigráficas de Colombia: Monzogranito de La Corcova, cordillera Oriental. Servicio Geológico Colombiano, 106 p. Medellín.

Rodríguez, G., Arango, M.I., Zapata, G. & Bermúdez, J.G. 2016b. Catálogo de unidades litoestratigráficas de Colombia: Formación Saldaña, cordilleras Central y Oriental. Servicio Geológico Colombiano, 92 p. Medellín.

Rodríguez, G., Zapata, G., Correa–Martínez, A.M. & Arango, M.I. 2017a. Caracterización petrográfica, química y geocronológica del magmatismo triásico–jurásico del Macizo de Santander, Colombia. XVI Congreso Colombiano de Geología y III Simposio de Exploradores. Memoirs, p. 1430–1433. Santa Marta.

Rodríguez, G., Arango, M.I., Zapata, G. & Correa–Martínez, A.M. 2017b. Catálogo de unidades litoestratigráficas de Colombia: Tonalita de San Martín, cordillera Oriental. Servicio Geológico Colombiano, 56 p. Medellín.

Rodríguez, G., Arango, M.I., Zapata, G. & Bermúdez, J.G. 2018a. Petrotectonic characteristics, geochemistry, and U–Pb geochronology of Jurassic plutons in the Upper Magdalena Valley, Colombia: Implications on the evolution of magmatic arcs in the NW Andes. Journal of South American Earth Sciences, 81: 10–30. https://doi.org/10.1016/j.jsames.2017.10.012

Rodríguez, G., Zapata, G., Arango, M.I. & Correa, A.M. 2018b. Catálogo de unidades litoestratigráficas de Colombia: Monzogranito de Santa Bárbara, cordillera Oriental. Servicio Geológico Colombiano, 96 p. Medellín.

Rodríguez, G., Arango, M.I., Correa, A.M. & Zapata, G. 2018c. Catálogo de unidades litoestratigráficas de Colombia: Riolita de San Joaquín, cordillera Oriental. Servicio Geológico Colombiano, 46 p. Medellín.

Rolon, L.F. 2004. Structural geometry of the jura–Cretaceous rift of the Middle Magdalena Valley Basin–Colombia. Master thesis, West Virginia University, 63 p. Morgantown, USA.

Ross, P.S. & Bédard, J.H. 2009. Magmatic affinity of modern and ancient subalkaline volcanic rocks determined from trace–element discriminant diagrams. Canadian Journal of Earth Sciences, 46(11): 823–839. https://doi.org/10.1139/E09-054

Salazar–Torres, J.C., Agudelo, W.J., Toro–Toro, L.M., Moreno–Sánchez, M. & Gómez–Cruz, A.J. 2013. Petrografía y geoquímica de las rocas volcánicas del cerro La Teta y el arroyo Jurarein, Alta Guajira colombiana. Boletín de Geología, 35(2): 53–63.

Sarmiento–Rojas, L.F. 2001. Mesozoic rifting and Cenozoic Basin inversion history of the Eastern Cordillera, Colombian Andes: Inferences from tectonic models. Doctoral thesis, Vrije Universiteit, 295 p. Amsterdam, the Netherlands.

Sarmiento–Rojas, L.F., van Wess, J.D. & Cloetingh, S. 2006. Mesozoic transtensional basin history of the Eastern Cordillera, Colombian Andes: Inferences from tectonic models. Journal of South American Earth Sciences, 21(4): 383–411. https://doi.org/10.1016/j.jsames.2006.07.003

Schandl, E.S. & Gorton, M.P. 2002. Application of high field strength elements to discriminate tectonic settings in VMS environments. Economic Geology, 97(3): 629–642. https://doi.org/10.2113/gsecongeo.97.3.629

Scotese, C.R. 2014a. Atlas of permo–Triassic paleogeographic maps (Mollweide Projection). Maps 43–52, volumes 3 & 4 of the PALEOMAP Atlas for ArcGIS. PALEOMAP Project. Evanston, USA. https://doi.org/10.13140/2.1.2609.9209

Scotese, C.R. 2014b. Atlas of Jurassic paleogeographic maps (Mollweide Projection). Maps 32–42, volume 3 of the PALEOMAP Atlas for ArcGIS. PALEOMAP Project. Evanston, USA. https://doi.org/10.13140/2.1.4850.4321

Song, S.G., Wang, M.J., Wang, C. & Niu, Y.L. 2015. Magmatism during continental collision, subduction, exhumation and mountain collapse in collisional orogenic belts and continental net growth: A perspective. Science China, Earth Sciences, 58(8):1284–1304. https://doi.org/10.1007/s11430-015-5102-x

Spikings, R., Cochrane, R., Villagómez, D., van der Lelij, R., Vallejo, C., Winkler, W. & Beate, B. 2015. The geological history of northwestern South America: From Pangaea to the early col-

lision of the Caribbean Large Igneous Province (290–75 Ma). Gondwana Research, 27(1): 95–139. https://doi.org/10.1016/j.gr.2014.06.004

Stampfli, G.M., Hochard, C., Vérard, C., Wilhem, C. & von Raurmer, J. 2013. The formation of Pangea. Tectonophysics, 593: 1–19. https://doi.org/10.1016/j.tecto.2013.02.037

Tarney, J. & Jones, C.E. 1994. Trace element geochemistry of orogenic igneous rocks and crustal growth models. Journal of the Geological Society, 151(5): 855–868. https://doi.org/10.1144/gsjgs.151.5.0855

Thiéblemont, D. & Cabanis, B. 1990. Utilisation d'un diagramme (Rb/100)–Tb–Ta pour la discrimination géochimique et l'etude pétrogénétique des roches magmatiques acides. Bulletin de la Société Géologique de France, 8–6(1): 23–35. https://doi.org/10.2113/gssgfbull.VI.1.23

Thiéblemont, D. & Tégyey, M. 1994. Une discrimination géochimique des roches différenciés témoin de la diversité d'origine et de situation tectonique des magmas calco–alcalins. Comptes Rendus Académie des Sciences, 319 (série II): 87–94. Paris.

Thompson, R.N. 1982. Magmatism of the British Tertiary Volcanic Province. Scottish Journal of Geology, 18(1): 49–107. https://doi.org/10.1144/sjg18010049

Tschanz, C.M., Jimeno, A. & Cruz, J. 1969. Geology of the Sierra Nevada de Santa Marta area (Colombia): Preliminary report. Ingeominas, 288 p. Bogotá.

Tschanz, C.M., Marvin, R.F., Cruz, J., Mehnert, H.H. & Cebula, G.T. 1974. Geologic evolution of the Sierra Nevada de Santa Marta, northeastern Colombia. Geological Society of America Bulletin, 85(2): 273–284. https://doi.org/10.1130/0016-7606(1974)85<273:GEOTSN>2.0.CO;2

Universidad Pedagógica y Tecnológica de Colombia & Ingeominas. 2011. Memoria explicativa: Cartografía geológica de la plancha 133 Puerto Berrío. Scale 1:100 000. Ingeominas, 145 p. Sogamoso.

van der Lelij, R. 2013. Reconstructing north–western Gondwana with implications for the evolution of the Iapetus and Rheic Oceans: A geochronological, thermochronological and geochemical study. Doctoral thesis, University of Geneva, 248 p. Geneva. https://doi.org/10.13097/archive-ouverte/unige:31653

van der Lelij, R., Spikings, R., Ulianov, A., Chiaradia, M. & Mora, A. 2016. Palaeozoic to Early Jurassic history of the northwestern corner of Gondwana, and implications for the evolution of the Iapetus, Rheic and Pacific Oceans. Gondwana Research, 31: 271–294. https://doi.org/10.1016/j.gr.2015.01.011

van der Meer, D.G., Torsvik, T.H., Spakman, W., van Hinsbergen, D.J.J. & Amaru, M.L. 2012. Intra–Panthalassa Ocean subduction zones revealed by fossil arcs and mantle structure. Nature Geoscience, 5: 215–219. https://doi.org/10.1038/ngeo1401

Vermeesch, P. 2012. On the visualisation of detrital age distributions. Chemical Geology, 312–313: 190–194. https://doi.org/10.1016/j.chemgeo.2012.04.021

Villagómez, D., Spikings, R., Magna, T., Kammer, A., Winkler, W. & Beltrán, A. 2011. Geochronology, geochemistry and tectonic evolution of the Western and Central Cordilleras of Colombia. Lithos, 125(3–4): 875–896. https://doi.org/10.1016/j.lithos.2011.05.003

Villaseca, C., Barbero, L. & Herreros, V. 1998. A re–examination of the typology of peraluminous granite types in intracontinental orogenic belts. Earth and Environmental Science Transactions of the Royal Society of Edinburgh, 89(2): 113–119. https://doi.org/10.1017/S0263593300007045

Vinasco, C.J., Cordani, U.G., González, H., Weber, M. & Peláez, C. 2006. Geochronological, isotopic, and geochemical data from Permo–Triassic granitic gneises and granitoids of the Colombian Central Andes. Journal of South American Earth Sciences, 21(4): 355–371. https://doi.org/10.1016/j.jsames.2006.07.007

Ward, D.E., Goldsmith, R., Cruz, J. & Restrepo, H. 1973. Geología de los cuadrángulos H–12 Bucaramanga y H–13 Pamplona, departamento de Santander. Boletín Geológico, 21(1–3): 132 p.

Watson, E.B. & Harrison, T.M. 1983. Zircon saturation revisited: Temperature and composition effects in a variety of crustal magma types. Earth and Planetary Science Letters, 64(2): 295–304. https://doi.org/10.1016/0012-821X(83)90211-X

Whalen, J.B., Currie, K.L. & Chappell, B.W. 1987. A–type granites: Geochemical characteristics, discrimination and petrogenesis. Contributions to Mineralogy and Petrology, 95(4): 407–419. https://doi.org/10.1007/BF00402202

Winchester, J.A. & Floyd, P.A. 1977. Geochemical discrimination of different magma series and their differentiation products using immobile elements. Chemical Geology, 20: 325–343. https://doi.org/10.1016/0009-2541(77)90057-2

Winter, J. 2014. An introduction to igneous and metamorphic petrology. Prentice Hall Inc., 697 p. Upper Saddle River, USA.

Zapata, S., Cardona, A., Bayona, G., Bustamante, C., Mora, A., Silva–Tamayo, J.C. & Valencia, V. 2012. Tracing major changes in middle Mesozoic plate convergence in the northern Andes: Insights from the Jurassic magmatic record of southern Colombia. 108th Annual Meeting, Geological Society of America, Cordilleran Section, Abstracts with programs, 44(3), p. 24. Queretaro. https://gsa.confex.com/gsa/2012CD/webprogram/Paper201832.html

Zapata, G., Bermúdez, J.G., Rodríguez, G. & Arango, M.I. 2013. Memoria explicativa: Cartografía geológica de la plancha 83 Nechí. Scale 1:100 000. Servicio Geológico Colombiano, 93 p. Medellín.

Zapata, G., Correa, A.M., Rodríguez, G. & Arango, M.I. 2016a. Catálogo de unidades litoestratigráficas de Colombia: Granito de Pescadero, cordillera Oriental. Servicio Geológico Colombiano, 54 p. Medellín.

Zapata, S., Cardona, A., Jaramillo, C., Valencia, V. & Vervoort, J. 2016b. U–Pb LA–ICP–MS geochronology and geochemistry of Jurassic volcanic and plutonic rocks from the Putumayo region (southern Colombia): Tectonic setting and regional

correlations. Boletín de Geología, 38(2): 1–38. https://doi.org/10.18273/revbol.v38n2-2016001

Zapata, G., Arango, M.I., Rodríguez, G. & Correa–Martínez, A.M. 2018. Catálogo de unidades litoestratigráficas de Colombia: Riolitas El Uvo, cordillera Oriental. Servicio Geológico Colombiano, 39 p. Medellín.

Zartman, R.E. & Doe, B.R. 1981. Plumbotectonics–the model. Tectonophysics, 75(1–2): 135–162. https://doi.org/10.1016/0040-1951(81)90213-4

Zhao, Z.F., Dai, L.Q. & Zheng, Y.F. 2013. Postcollisional mafic igneous rocks record crust–mantle interaction during continental deep subduction. Scientific Reports, 3(3413): 1–6. https://doi.org/10.1038/srep03413

Zhao, S.W., Lai, S.C., Pei, X.Z., Qin, J.F., Zhu, R.Z., Tao, N. & Gao, L. 2019. Compositional variations of granitic rocks in continental margin arc: Constraints from the petrogenesis of Eocene granitic rocks in the Tengchong Block, SW China. Lithos, 326–327: 125–143. https://doi.org/10.1016/j.lithos.2018.12.026

Zorpi, M.J., Coulon, C., Orsini, J.B. & Cocirta, C. 1989. Magma mingling, zoning and emplacement in calc–alkaline granitoid plutons. Tectonophysics, 157(4): 315–329. https://doi.org/10.1016/0040-1951(89)90147-9

Zuluaga, C.A. & López, J.A. 2019. Ordovician orogeny and Jurassic low–lying orogen in the Santander Massif, northern Andes (Colombia). In: Cediel, F. & Shaw, R.P. (editors), Geology and tectonics of northwestern South America: The Pacific–Caribbean–Andean junction. Frontiers in Earth Sciences. Springer Nature Switzerland, p. 195–250. https://doi.org/10.1007/978-3-319-76132-9_4

Zuluaga, C.A., Pinilla, A. & Mann, P. 2015. Jurassic silicic volcanism and associated continental–arc basin in northwestern Colombia (southern boundary of the Caribbean Plate). In: Bartolini, C. & Mann, P. (editors), Petroleum geology and potential of the Colombian Caribbean margin. American Association of Petroleum Geologists, Memoir 108, p. 137–160. https://doi.org/10.1306/13531934M1083640

Explanation of Acronyms, Abbreviations, and Symbols:

ASI	Aluminum saturation index
ca.	Circa, about
CA–ID–TIMS	Chemical abrasion isotope dilution thermal ionization mass spectrometry
CAP	Continental arc potassic
cf.	Confer, compare
GCDkit	Geochemical Data Toolkit
HREE	Heavy rare earth element
IOP	Initial oceanic arc potassic rocks
KDE	Kernel density estimates
LA–ICP–MS	Laser ablation inductively coupled plasma mass spectrometer
LA–MC–ICP–MS	Laser ablation multi–collector inductively coupled plasma mass spectrometer
LOI	Loss on ignition
LOP	Late oceanic arc potassic rocks
LREE	Light rare earth element
MALI	Modified alkali–lime index
MASH	Melting–assimilation–storage–homogenization
PAP	Postcollisional arc potassic
PDPs	Probability density plots
REE	Rare earth element
SHRIMP	Sensitive high–resolution ion

Authors' Biographical Notes

Julián Andrés LÓPEZ–ISAZA is a researcher at the Servicio Geológico Colombiano. He was a professor of petrology and structural geology at the Universidad Industrial de Santander. His work is concentrated in the northern Andes and applies to tectonic evolution and metallogenesis.

Carlos Augusto ZULUAGA is a full professor and researcher at the Departamento de Geociencias of the Universidad Nacional de Colombia. He works on petrology applied to crustal evolution, thermodynamic modeling, and the tectonic evolution of the northern Andes.

Volume 2

Chapter 4

Diverse Jurassic Magmatic Arcs of the Colombian Andes: Constraints from Petrography, Geochronology, and Geochemistry

https://doi.org/10.32685/pub.esp.36.2019.04
Published online 12 May 2020

Gabriel RODRÍGUEZ–GARCÍA[1]*, Ana María CORREA–MARTÍNEZ[2], Gilberto ZAPATA–GARCÍA[3], María Isabel ARANGO–MEJÍA[4], Gloria OBANDO–ERAZO[5], Juan Pablo ZAPATA–VILLADA[6], and José Gilberto BERMÚDEZ[7]

Abstract New field, petrographic, whole–rock geochemical, and U–Pb zircon geochronological data obtained from Jurassic plutonic rocks of the Santander Massif, plutonic and volcanic rocks in the Upper Magdalena Valley, and plutonic rocks in the northern block of the Ibagué Batholith provide evidence that the Jurassic igneous activity that is recorded in several blocks of the Colombian Andes began in the Late Triassic and ended in the Early Cretaceous. This magmatism developed in at least three different magmatic arcs, during clearly defined time periods, over basements with different characteristics. The first stationary continental margin arc was active between the Late Triassic (ca. 214 Ma) and the Early Jurassic (ca. 184 Ma). It is located in the Santander Massif and is primarily represented by monzogranitic, peraluminous plutons generated by multiple magmatic pulses that involved varying degrees of crustal melting. This study proposes, for the first time, that most of the arc was emplaced into primarily Ordovician basement and that a small part was emplaced into early Neoproterozoic basement. The second arc, which is located in the Upper Magdalena Valley, developed between the Early Jurassic (ca. 197 Ma) and the Middle Jurassic (ca. 167 Ma) during at least three magmatic pulses related to arc migration, which is evidenced by compositional and temporal variations in which the plutons evolved from metaluminous monzodiorites to peraluminous granites, and the volcanic rocks evolved from andesites to rhyolites. This second arc was emplaced into Neoproterozoic metamorphic basement, Paleozoic sedimentary rocks, Permian igneous rocks, and Triassic sedimentary rocks. The third continental margin arc, which is located in the northern block of the Ibagué Batholith, formed from the Late Jurassic (ca. 158 Ma) to the Early Cretaceous (ca. 138 Ma). It is characterized by at least two pulses that are represented by a western syntectonic pluton and an eastern post–tectonic pluton, both of which have calc–alkaline metaluminous tonalitic compositions, that are separated by a band of metamorphic basement rocks of Late Jurassic age, not Neoproterozoic or Permian – Triassic as was previously thought.

Keywords: *continental arc magmatism, U–Pb zircon geochronology, metamorphic basement, peraluminous magmatism, metaluminous magmatism.*

1 grodriguez@sgc.gov.co
Servicio Geológico Colombiano
Dirección de Geociencias Básicas
Grupo de Estudios Geológicos Especiales
Calle 75 n.° 79A–51
Medellín, Colombia

2 amcorrea@sgc.gov.co
Servicio Geológico Colombiano
Dirección de Geociencias Básicas
Grupo de Estudios Geológicos Especiales
Calle 75 n.° 79A–51
Medellín, Colombia

3 gilbertozapatag@yahoo.com
Servicio Geológico Colombiano
Calle 24A n.° 50A–31 Ap. 901
Edificio Santa Clara
Bello, Colombia

4 isabelara84@hotmail.com
Carrera 14 n.° 22–18
Cartago, Valle del Cauca, Colombia

5 gbando@sgc.gov.co
Servicio Geológico Colombiano
Dirección de Geociencias Básicas
Grupo de Estudios Geológicos Especiales
Calle 75 n.° 79A–51
Medellín, Colombia

6 jpzapata@sgc.gov.co
Servicio Geológico Colombiano
Dirección de Geociencias Básicas
Grupo de Estudios Geológicos Especiales
Calle 75 n.° 79A–51
Medellín, Colombia

7 jbermudez@sgc.gov.co
Servicio Geológico Colombiano
Dirección de Geociencias Básicas
Grupo de Estudios Geológicos Especiales
Calle 75 n.° 79A–51
Medellín, Colombia

* Corresponding author

Supplementary Information:

S: https://www.sgc.gov.co/LibroGeologiaColombia/tgc/sgcpubesp36201904s.pdf

Citation: Rodríguez–García, G., Correa–Martínez, A.M., Zapata–García, G., Arango–Mejía, M.I., Obando–Erazo, G., Zapata–Villada, J.P. & Bermúdez, J.G. 2020. Diverse Jurassic magmatic arcs of the Colombian Andes: Constraints from petrography, geochronology, and geochemistry. In: Gómez, J. & Pinilla–Pachon, A.O. (editors), The Geology of Colombia, Volume 2 Mesozoic. Servicio Geológico Colombiano, Publicaciones Geológicas Especiales 36, p. 117–170. Bogotá. https://doi.org/10.32685/pub.esp.36.2019.04

Resumen Nuevos datos de campo, petrografía, litogeoquímica y geocronología U–Pb en circón de plutones jurásicos del Macizo de Santander, plutones y volcanitas del Valle Superior del Magdalena y plutones del bloque norte del Batolito de Ibagué demuestran que la actividad ígnea jurásica registrada en varios bloques de los Andes colombianos comenzó en el Triásico Tardío y finalizó en el Cretácico Temprano. Este magmatismo se desarrolló en por lo menos tres arcos magmáticos diferentes, durante intervalos de tiempo claramente definidos y sobre basamentos con distintas características. El primer arco de margen continental estacionario estuvo activo entre el Triásico Tardío (ca. 214 Ma) y el Jurásico Temprano (ca. 184 Ma). El registro de este arco se encuentra en el Macizo de Santander y está representado por plutones principalmente monzograníticos, peraluminosos, generados por múltiples pulsos magmáticos que involucraron diversos grados de fusión cortical. En este estudio se propone, por primera vez, que la mayor parte del arco se emplazó en basamento principalmente ordovícico y otra menor en basamento neoproterozoico temprano. El segundo arco se localiza en el Valle Superior del Magdalena y se desarrolló entre el Jurásico Temprano (ca. 197 Ma) y el Jurásico Medio (ca. 167 Ma) durante al menos tres pulsos magmáticos relacionados con la migración del arco. Esto se evidencia por las variaciones composicionales y temporales en las cuales los plutones evolucionaron de monzodioritas metaluminosas a granitos peraluminosos y las rocas volcánicas, de andesitas a riolitas. El segundo arco se emplazó en basamento metamórfico neoproterozoico, sedimentario paleozoico, ígneo pérmico y sedimentario triásico. El tercer arco de margen continental se encuentra localizado en el bloque norte del Batolito de Ibagué y se formó durante el Jurásico Tardío (ca. 158 Ma) al Cretácico Temprano (ca. 138 Ma). Se caracteriza por al menos dos pulsos representados en un plutón sintectónico occidental y un plutón postectónico oriental, ambos compuestos por tonalitas metaluminosas calcoalcalinas separadas por una franja de rocas metamórficas del basamento de edad jurásica temprana y no del Neoproterozoico ni del Pérmico–Triásico como se consideraba anteriormente.

Palabras clave: *magmatismo de arco continental, geocronología U–Pb en circón, basamento metamórfico, magmatismo peraluminoso, magmatismo metaluminoso.*

1. Introduction

The Upper Triassic – Jurassic igneous rocks of the Colombian Andes are plutonic and volcanic rocks with ages between ca. 214 Ma to ca. 145 Ma that are distributed in tectonic blocks located on the eastern margin of the Central Cordillera, Magdalena River Valley, Eastern Cordillera, Sierra Nevada de Santa Marta, and Upper Guajira (Figure 1a). These units have been studied by several authors (Álvarez, 1983; Aspden et al., 1987; Bustamante et al., 2010; Gendall et al., 2000; Goldsmith et al., 1971; Leal–Mejía, 2011; Mantilla–Figueroa et al., 2013; Noble et al., 1997; Rodríguez et al., 2018a; van der Lelij, 2013; van der Lelij et al., 2016; Villagómez et al., 2011; Ward et al., 1973).

Previous tectonic models of the Jurassic magmatism in the northern Andes have been based on two hypotheses: 1) the development of an intracontinental rift related to the breakup of Pangaea (Cediel et al., 2003; Cochrane et al., 2014; Mojica et al., 1996; Pindell & Dewey, 1982; Ross & Scotese, 1988) and 2) the establishment of continental arc magmatism (Bustamante et al., 2010, 2016; Leal–Mejía, 2011; McCourt et al., 1984; Meschede & Frisch, 1998; Rodríguez et al., 2015a; Spikings et al., 2015; Toussaint, 1995; van der Lelij et al., 2016; Villagómez et al., 2015; Zapata et al., 2016a). The latter is the consensus model; however, different authors have presented several variations. Spikings et al. (2015) suggest that an arc formed by a single subduction zone located west of the South American margin was active between 209 and 114 Ma, whereas Bustamante et al. (2016) proposed that a stationary continental margin arc was active for at least 40 Ma due to oblique convergence between the Farallón Plate and the northwestern margin of South America. Bayona et al. (2010) and Villagómez et al. (2015) proposed that a continental arc, encompassing the blocks of Jurassic rocks in the Upper Magdalena, Central Cordillera, serranía de San Lucas, and Sierra Nevada de Santa Marta, moved from a southern

Figure 1. (a) Occurrences of Jurassic igneous rocks in the Colombian Andes. Retrieved and modified from Gómez et al. (2015a). Data source: U–Pb ages from several authors compiled by Gómez et al. (2015b). **(b)** Proposed distribution of metamorphic basement in the regions related to Jurassic magmatism and volcanism.

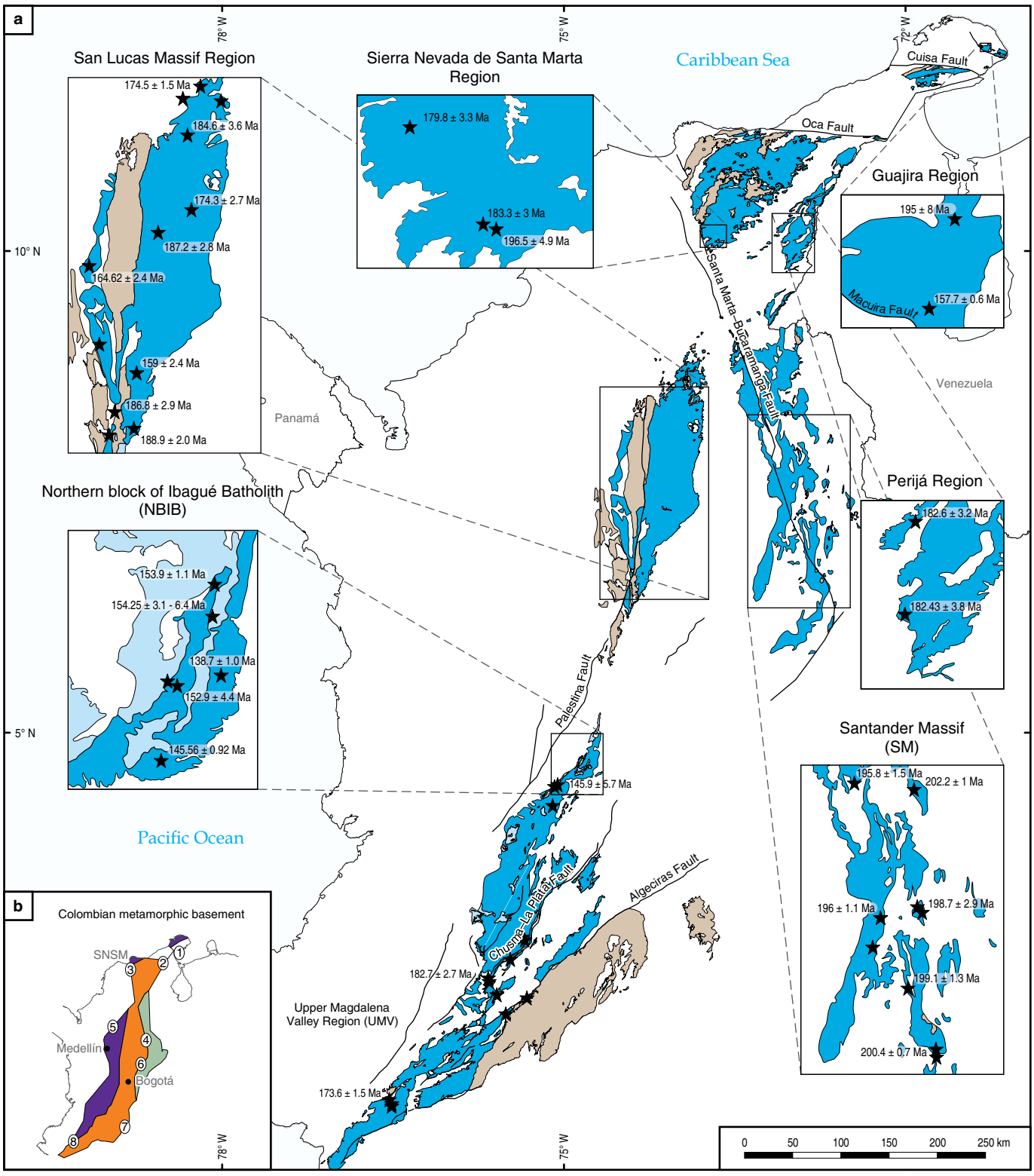
a
San Lucas Massif Region
174.5 ± 1.5 Ma
184.6 ± 3.6 Ma
174.3 ± 2.7 Ma
187.2 ± 2.8 Ma
164.62 ± 2.4 Ma
159 ± 2.4 Ma
186.8 ± 2.9 Ma
188.9 ± 2.0 Ma
Sierra Nevada de Santa Marta Region
179.8 ± 3.3 Ma
183.3 ± 3 Ma
196.5 ± 4.9 Ma
Caribbean Sea
Cuisa Fault
Oca Fault
Guajira Region
195 ± 8 Ma
157.7 ± 0.6 Ma
Macuira Fault
Santa Marta–Bucaramanga Fault
Venezuela
Panamá
Perijá Region
182.6 ± 3.2 Ma
182.43 ± 3.8 Ma
Northern block of Ibagué Batholith (NBIB)
153.9 ± 1.1 Ma
154.25 ± 3.1 - 6.4 Ma
138.7 ± 1.0 Ma
152.9 ± 4.4 Ma
145.56 ± 0.92 Ma
Palestina Fault
145.9 ± 5.7 Ma
Santander Massif (SM)
195.8 ± 1.5 Ma
202.2 ± 1 Ma
196 ± 1.1 Ma
198.7 ± 2.9 Ma
199.1 ± 1.3 Ma
200.4 ± 0.7 Ma
Pacific Ocean
Chusma–La Plata Fault
Algeciras Fault
182.7 ± 2.7 Ma
Upper Magdalena Valley Region (UMV)
173.6 ± 1.5 Ma
10° N
5° N
78° W
75° W
72° W
0 50 100 150 200 250 km
b
Colombian metamorphic basement
SNSM
Medellín
Bogotá
1
2
3
4
5
6
7
8
Jurassic units (plutons and volcanic units)
Jurassic basement
Precambrian basement
Triassic – Jurassic Central Cordillera basement
Paleozoic metamorphic basement
Neoproterozoic basement
U–Pb
1 Cuisa Fault
2 Oca Fault
3 Santa Marta Fault
4 Bucaramanga Fault
5 Espíritu Santo Fault
6 Altamira Fault
7 Algeciras Fault
8 Suaza Fault

location northward (Bayona et al., 2006, 2010), which masked the original tectonic relationships between the units (Bayona et al., 2010; Villagómez et al., 2015; Zapata et al., 2016a; Zuluaga et al., 2017).

We present new petrographic, whole–rock geochemical, and LA–ICP–MS U–Pb zircon geochronological data and compile published data from three Colombian blocks: the Santander Massif (SM), Upper Magdalena Valley (UMV), and northern block of the Ibagué Batholith (NBIB), to understand the Jurassic geological evolution of the northern Andes as well as the distribution of blocks and metamorphic terranes associated with the Jurassic plutonism and volcanism in Colombia. The compositional and geochronological differences between the metamorphic basement units and Jurassic rocks of the three blocks are discussed. A redefinition of the northern section of the Ibagué Batholith is also proposed based on geological data that indicate that it is not homogeneous.

2. Geologic Framework

The geologic configuration of Colombia is the result of the interactions between the Caribbean, South American, North American, and Pacific Plates, which throughout geologic history have formed the Andean province on the northwestern margin of South America (Mantilla–Figueroa et al., 2013; van der Lelij et al., 2016; Zuluaga et al., 2017). This province is composed of accreted and diverse continental and oceanic terranes that amalgamated during multiple subduction and orogenic events from Proterozoic to Cenozoic times (Cediel et al., 2003; Etayo–Serna et al., 1983; Kennan & Pindell, 2009; Restrepo & Toussaint, 1988, 1989). Their boundaries remain unclear; however, the province is separated from the crystalline basement of the Amazonian Craton by the Borde Llanero Fault (Forero–Suárez, 1990).

This Andean province includes the SM, the UMV, and the NBIB, which are the focus of this study (Figure 1a).

2.1. Santander Massif (SM)

The SM is located in the Colombian Eastern Cordillera and is part of a triangular regional block that is delimited by the Santa Marta–Bucaramanga Fault on the west, the Oca Fault on the north, and the Boconó Fault on the east (Cediel et al., 2003; Mantilla–Figueroa et al., 2013; van der Lelij et al., 2016).

The metamorphic basement of the SM includes the Bucaramanga Gneiss, the Silgará Formation, and granitic orthogneisses (Ward et al., 1973). The Bucaramanga Gneiss consists of sillimanite–cordierite gneisses with garnet, amphibolic gneisses, quartz feldspar granofels, and amphibolites with migmatitic structures (Ward et al., 1973), and it is traditionally considered to have a Proterozoic age and to be related to the Grenville Orogeny (Cordani et al., 2005; García & Ríos, 1999; Goldsmith et al., 1971; Ordóñez–Carmona et al., 2006; Restrepo–Pace et al., 1997; Ward et al., 1973). However, recent studies report metamorphic ages of approximately 477 Ma (van der Lelij, 2013; van der Lelij et al., 2016) that are associated with the Caparonensis Orogeny, which is also known as the Famatinian Orogeny (van der Lelij, 2013; van der Lelij et al., 2016; Zuluaga et al., 2017). Overlying the Bucaramanga Gneiss, the Silgará Formation (Ward et al., 1973), which is also called the Silgará Schists by Mantilla–Figueroa et al. (2016), consists of Paleozoic schists, phyllites, metamudstones, metasandstones, and marbles (Clavijo et al., 2008; Mantilla–Figueroa et al., 2012; Ordóñez–Carmona et al., 2006; Ríos et al., 2003; van der Lelij et al., 2016; Zuluaga et al., 2017). These rocks are possibly related to the main Famatinian orogenic event (Mantilla–Figueroa et al., 2016; Restrepo–Pace, 1995; Restrepo–Pace & Cediel, 2010). Deformed Ordovician granitoids ("Orthogneiss Unit" of Ward et al., 1973) intrude the Bucaramanga Gneiss and the Silgará Formation. These three units record a common Ordovician metamorphic event (Mantilla–Figueroa et al., 2012, 2013; Restrepo–Pace et al., 1997) that affected the entire SM basement (van der Lelij et al., 2016; Zuluaga et al., 2017).

Paleozoic magmatism is represented by orthogneisses and plutonic and volcanic rocks that originated during magmatic events before and after the Famatinian Orogeny, most of which developed in a continental arc environment. The igneous plutons are Ordovician, Silurian, Lower Devonian, and Carboniferous (Leal–Mejía, 2011; Mantilla–Figueroa et al., 2012; Restrepo–Pace, 1995; Rodríguez et al., 2017a; Ulloa & Rodríguez, 1982; van der Lelij, 2013; van der Lelij et al., 2016). Mesozoic magmatism occurred mainly during the Late Triassic to Late Jurassic and is represented by batholiths and subordinate stocks in the core and along the western edge of the SM (Figure 2). These include the Mogotes Batholith (Correa–Martínez et al., 2016; Ward et al., 1973), Pescadero Granite (Ward et al., 1973; Zapata et al., 2016b), Santa Bárbara Monzogranite (Rodríguez et al., 2017b; Ward et al., 1973, 1977a); La Corcova Monzogranite (Goldsmith et al., 1971; Rodríguez et al., 2017c; Ward et al., 1973), Páramo Rico Pluton (Dörr et al., 1995; Royero & Clavijo, 2001; Ward et al., 1973), San Martín Tonalite (Arias–Tauta & Vargas–Higuera, 1978; Rodríguez et al., 2017d), Rionegro Monzogranite (Arango et al., 2016; Arias–Tauta & Vargas–Higuera, 1978; Daconte & Salinas, 1980a; Ward et al., 1973), and three porphyritic bodies: the Alto de Los Cacaos Rhyolite, San Joaquín Rhyolite, and El Uvo Rhyolite (Correa–Martínez et al., 2018; Rodríguez et al.,

Figure 2. Distribution and U–Pb zircon ages of Late Triassic – Early Jurassic plutons in the Santander Massif. Modified from Ward et al. (1973, 1977a, 1977b, 1977c, 1977d, 1977e, 1977f); Daconte & Salinas (1980b, 1980c); Vargas & Arias (1981a, 1981b); Vargas et al. (1984); Clavijo (1994); Royero & Clavijo (2001); and Arias & Morales (2003).

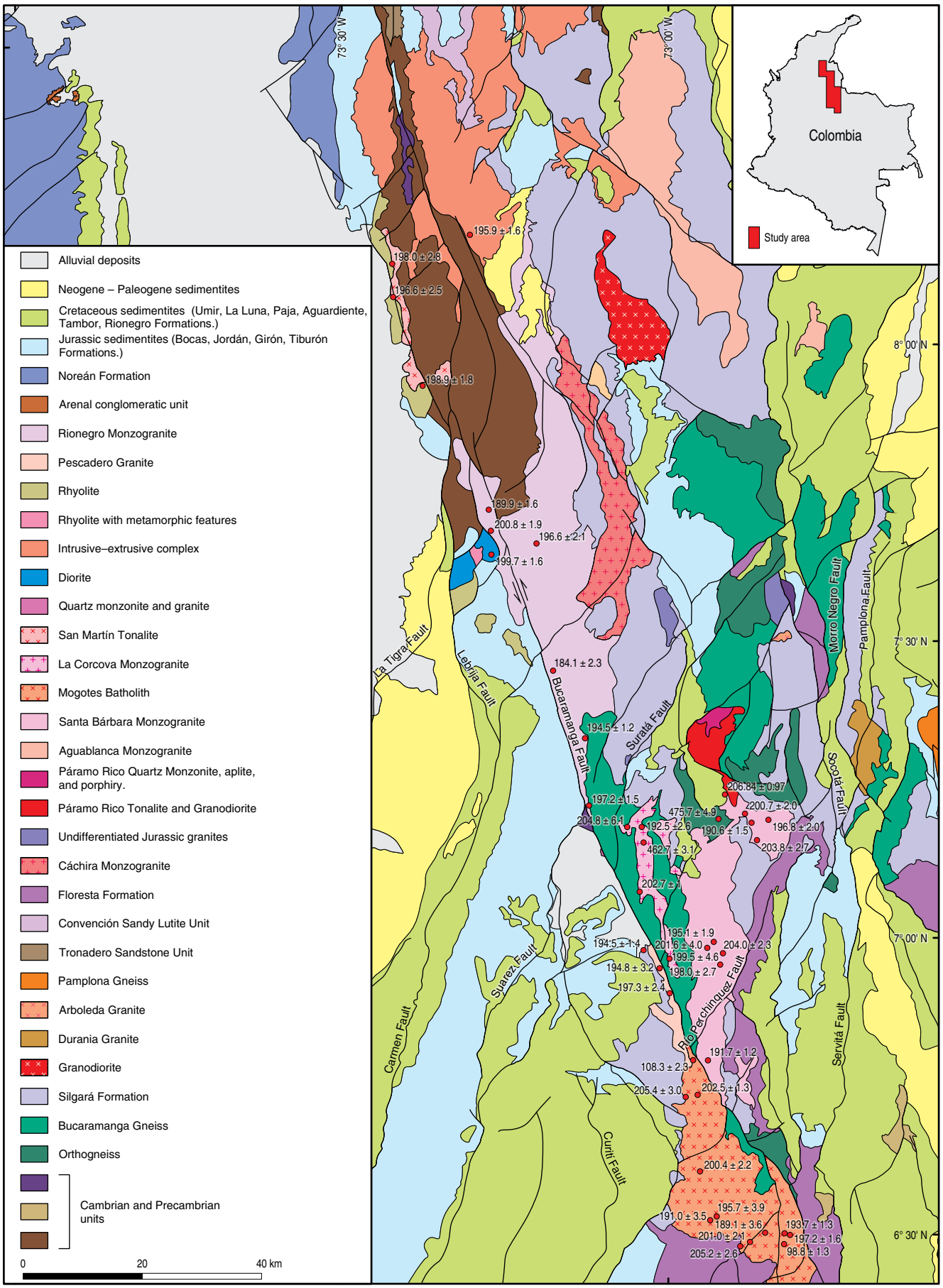
Colombia
Study area
Alluvial deposits
Neogene – Paleogene sedimentites
Cretaceous sedimentites (Umir, La Luna, Paja, Aguardiente, Tambor, Rionegro Formations.)
Jurassic sedimentites (Bocas, Jordán, Girón, Tiburón Formations.)
Noreán Formation
Arenal conglomeratic unit
Rionegro Monzogranite
Pescadero Granite
Rhyolite
Rhyolite with metamorphic features
Intrusive–extrusive complex
Diorite
Quartz monzonite and granite
San Martín Tonalite
La Corcova Monzogranite
Mogotes Batholith
Santa Bárbara Monzogranite
Aguablanca Monzogranite
Páramo Rico Quartz Monzonite, aplite, and porphiry.
Páramo Rico Tonalite and Granodiorite
Undifferentiated Jurassic granites
Cáchira Monzogranite
Floresta Formation
Convención Sandy Lutite Unit
Tronadero Sandstone Unit
Pamplona Gneiss
Arboleda Granite
Durania Granite
Granodiorite
Silgará Formation
Bucaramanga Gneiss
Orthogneiss
Cambrian and Precambrian units
0
20
40 km
73° 30' W
73° 00' W
8° 00' N
7° 30' N
7° 00' N
6° 30' N
La Tigra Fault
Lebrija Fault
Bucaramanga Fault
Suratá Fault
Morro Negro Fault
Pamplona Fault
Soapta Fault
Suarez Fault
Carmen Fault
Río Perchinquez Fault
Servitá Fault
Curití Fault
195.9 ± 1.6
198.0 ± 2.8
196.6 ± 2.5
198.9 ± 1.8
189.9 ± 1.6
200.8 ± 1.9
196.6 ± 2.1
199.7 ± 1.6
184.1 ± 2.3
194.5 ± 1.2
197.2 ± 1.5
204.8 ± 6.1
206.84 ± 0.97
200.7 ± 2.0
475.7 ± 4.9
192.5 ± 2.6
190.6 ± 1.5
196.8 ± 2.0
203.8 ± 2.7
462.7 ± 3.1
202.7 ± 1
195.1 ± 1.9
194.5 ± 1.4
201.6 ± 4.0
204.0 ± 2.3
199.5 ± 4.6
194.8 ± 3.2
198.0 ± 2.7
197.3 ± 2.4
191.7 ± 1.2
108.3 ± 2.3
205.4 ± 3.0
202.5 ± 1.3
200.4 ± 2.2
195.7 ± 3.9
191.0 ± 3.5
189.1 ± 3.6
193.7 ± 1.3
201.0 ± 2.1
197.2 ± 1.6
205.2 ± 2.6
98.8 ± 1.3

2018b; Zapata et al., 2018). Few small microtonalite dikes of Albian – Cenomanian age also intrude the Triassic – Jurassic granitoids (Correa–Martínez et al., 2016).

Cretaceous marine sedimentary successions discordantly overlie the Paleozoic and/or Jurassic rocks (Mojica & Villarroel, 1984; Ward et al., 1973). Porphyritic bodies with Miocene gold mineralization exist locally (Leal–Mejía, 2011; Mantilla–Figueroa et al., 2013).

2.2. Upper Magdalena Valley (UMV)

The UMV is located between the Colombian Central and Eastern Cordilleras in the southern sections of the Magdalena River Valley.

The metamorphic basement of the UMV includes migmatites, granofels, granulites, anatectic granites, and gneisses of granulite to high amphibolite facies that form the Garzón Group, the Guapotón and Mancagua Gneisses, Las Minas Migmatites, and El Recreo Granite of Neoproterozoic age (Ibañez–Mejia et al., 2011; Jiménez–Mejía et al., 2006; Kroonenberg & Diederix, 1982; Rodríguez, 1995a, 1995b; Rodríguez et al., 2003; Velandia et al., 2001a, 2001b). Paleozoic sedimentary rocks, such as the Mudstones and Granadillo Limestones, La Jagua Paleozoic, El Hígado Formation, and La Batalla Limestones and Sandstones, discordantly overlie the Precambrian crystalline basement (Mojica et al., 1988; Velandia et al., 2000, 2001b; Villarroel & Mojica, 1988; Stibane & Forero, 1969). The Permian units are represented by La Plata Granite continental margin arc granitoids that intrude the basement rocks (Leal–Mejía, 2011; Rodríguez, 1995a; Rodríguez et al., 1998, 2017a; Velandia et al., 2001b).

The Neoproterozoic basement, Paleozoic sedimentary formations, Permian arc granitoids, and Triassic limestones are intruded by Jurassic plutons and covered by Jurassic volcanic rocks (Rodríguez et al., 2018a) and continental and marine sedimentary successions of late Mesozoic and Cenozoic age. These rocks are faulted and uplifted in blocks bounded by strike–slip and thrust faults, such as the Algeciras Fault (Velandia et al., 2005), the Betania–El Agrado Fault, and La Plata–Chusma Fault, which expose the Jurassic rocks and basement to varying degrees. None of these faults correspond to the boundary of the Neoproterozoic metamorphic basement, which appears to be fragmented. Similar blocks with Jurassic rocks border the western margin of the South American Plate, such as the serranía de San Lucas, Sierra Nevada de Santa Marta, and Upper Guajira, where the Neoproterozoic basement crops out near fragments of Permian granitoids and Jurassic arc rocks (Rodríguez et al., 2018a).

The assemblage described above is separated by the Avirama Fault from the Tahamí Terrane (Restrepo & Tousssaint, 1989) or the Cajamarca Complex (Maya & González, 1995). These metamorphic terranes consist of schists, quartzites, gneisses, granofels, and amphibolites (Feininger et al., 1972; González, 1980; Hall et al., 1972; Maya & González, 1995; Restrepo & Toussaint, 1988; Rodríguez et al., 2005) that are separated into blocks that have yielded Triassic (Martens et al., 2014; Restrepo et al., 2009; Vinasco et al., 2006), Jurassic (Blanco–Quintero et al., 2014), and Cretaceous ages (Restrepo et al., 2012; Rodríguez et al., 2016a).

2.3. Northern Block of the Ibagué Batholith (NBIB)

The Ibagué Batholith is exposed along the eastern slope of the Central Cordillera from Armero, in the Tolima Department, to La Plata, in the Huila Department (Nelson, 1957, 1962). It is considered to be the largest Jurassic pluton in Colombia, and it covers approximately 11 000 km^2 (Bustamante et al., 2016; Gómez et al., 2015a; Nelson, 1957, 1962; Núñez, 2001, 2002; Rodríguez & Núñez, 1999; Velandia et al., 2001b). A summary of the geochronological data from other studies is presented in Table 1.

Based on whole–rock geochemical data, Álvarez (1983) noted the absence of a genetic relationship between the Ibagué Batholith and several intrusives that outcrop to the south (e.g., the Páez River Pluton, the San Agustín and Gallego granitoids, and the Suaza Pluton). He suggested that these plutons likely corresponded to previous magmatic pulses. More recent U–Pb zircon geochronology and whole–rock geochemistry studies have enabled researchers to divide and separate large blocks, such as the Páez Quartz Monzodiorite (Álvarez, 1983; Rodríguez et al., 2018a; Zapata et al., 2015) and La Plata Granite (Rodríguez, 1995b, 2018a; Velandia et al., 2001b), and show that the so–called Ibagué Batholith is composed of different plutons that were generated in a continental arc environment in the Permian and Jurassic. These plutons were emplaced into different metamorphic basement rocks in different geotectonic positions (Rodríguez et al., 2018a). The results from the "Jurassic Magmatism of Colombia" project also show that the northern part of the Ibagué Batholith, north of the Ibagué Fault, is not a homogeneous unit, and the geological division of this block, called the northern block of the Ibagué Batholith (NBIB), is presented in this study.

The metamorphic basement of the NBIB consists of gneisses, amphibolites, quartzites, sericitic quartz–schist, greenschist, and graphitic schists known as the Tierradentro Gneisses and Amphibolites, which are likely Precambrian (Barrero & Vesga, 1976; Núñez, 2001). Bustamante et al. (2017) found Permian and Triassic crystallization ages in the orthogneisses and amphibolites of the Tierradentro protolithic unit, respectively, and interpreted that the granodioritic magma of the Ibagué Batholith intruded into Permian – Triassic basement. Farther south, Zapata et al. (2016a) concluded that this metamorphic basement, which is represented by La Cocha–Río Téllez Migmatitic Com-

Table 1. K/Ar, Ar–Ar, and LA–ICP–MS U–Pb zircon ages in the NBIB from other authors.

Sample	Latitude N	Longitude W	Classification	Unit	Age (Ma)	Method	Source
GCC6	4° 47' 44.27''	75° 2' 5.75''		Anzoátegui Metatonalite	158.17 +1.17/–0.35	U–Pb	Bustamante et al. (2016)
Cl11	4° 38' 47.63''	75° 2' 15.17''		Anzoátegui Metatonalite	152.61 +1.82/–0.74	U–Pb	Bustamante et al. (2016)
IGM–69974	4° 39' 35.99''	74° 57' 0.06''	Quartz diorite	Ibagué Tonalite	142 ± 9	K/Ar–Hbl	Vesga & Barrero (1978)
Cl 9B	4° 44' 40.13''	74° 57' 35.90''		Ibagué Tonalite	142.07 +1.08/–0.86	U–Pb	Bustamante et al. (2016)
Cl2	4° 39' 36.47''	74° 57' 54.76''		Ibagué Tonalite	143.52 +1.38/–0.64	U–Pb	Bustamante et al. (2016)
Cl15	4° 51' 53.58''	74° 56' 19.71''		Ibagué Tonalite	145.71 +0.72/–1.42	U–Pb	Bustamante et al. (2016)
	4° 39' 36.02''	75° 0' 0.05''		Tierradentro Gneisses and Amphibolites	146 ± 3	K–Ar–RT	McCourt et al. (1984)
DV04	4° 47' 0.19''	74° 58' 31.44''	Diorite	Tierradentro Gneisses and Amphibolites	159.2 ± 5.2	Ar–Ar–Hbl	Villagómez et al. (2011)

plex, may correspond to a Jurassic terrane that is correlated with the Jurassic metamorphic assemblage southwest of the NBIB that was studied by Blanco–Quintero et al. (2014).

3. Materials and Methods

To analyze the Jurassic magmatism in the SM, UMV, and NBIB, regional mapping studies and published articles were compiled. Field and sampling campaigns and petrography, geochemistry, and geochronology analyses were performed. Finally, the results were analyzed and interpreted separately for each block.

3.1. Petrography

The petrographic analyses included descriptions of thin sections from new samples and the reanalysis of samples from previous projects of the Servicio Geológico Colombiano (SGC). The plutonic igneous rocks were classified according to Streckeisen (1974), and the volcanic rocks were classified according to Streckeisen (1979) based on the recommendations for the classification and nomenclature of igneous rocks provided by Le Maitre et al. (2002). The mineral abbreviations in the rock descriptions are based on Siivola & Schmid (2007).

3.2. Whole–Rock Geochemical Analyses

Whole–rock analyses were performed in the laboratory of the SGC in Bogotá. Major oxides were determined using the X–ray fluorescence (XRF) method, including trace elements such as V, Mo, Nb, Ta, W, Zr, and Hf, in an Axios–Mineral PANalytical XRF spectrometer. Major oxides were quantified in melted samples with lithium metaborate and tetraborate, and minor elements were quantified in pressed samples. MRC–GSP–2 was used as a reference, and it produced a difference of <5% between the certified and measured values. Major oxides were recalculated on an anhydrous basis before interpretation. Trace elements were measured by inductively coupled plasma mass spectrometry (ICP–MS) in a PerkinElmer NEXION ICP mass spectrometer. The rock samples were dissolved by multi–acid digestion with strong inorganic acids (HF, HNO_3, $HClO_4$, and HCl). The process was conducted in an open system using different temperature ramps and heating times. The AGV–2 (andesite) USGS references were used with most of the trace elements and produced a difference of <10% between the certified and measured values. The elements Eu, Gd, and Tb produced higher values than the certified reference.

The rock samples for the geochemical analyses were selected based on: 1) no evidence of high–grade mineral alteration under microscopic inspection and 2) Loss on ignition (LOI) values lower than 2%.

3.3. U–Pb Zircon Geochronology

The U–Pb zircon dating was performed at the Isotopic Studies Laboratory (LEI) at the Centro de Geociencias of the Universidad Autónoma de México (UNAM) and the Laser Ablation Laboratory of the SGC.

The concentration of zircon crystals was obtained by panning and using a Frantz isodynamic magnetic separator. Zircon grains from each sample were selected under an Olympus binocular microscope and subsequently embedded in epoxy resin (Struers EpoFix).

Cathodoluminescence (CL) images of the zircons were acquired using an ELM–3R Luminoscope (Marshall, 1988) at LEI, UNAM. The U–Pb zircon isotopic analyses were performed using the laser ablation method (LA–ICP–MS) with a Resolution M50 "Resonetics" consisting of an LPX 220 193 nm wavelength excimer laser coupled to a Thermo Scientific X–Series quadrupole plasma mass spectrometer (ICP–MS). The diameter of the laser beam was 23 μm. The analyses included measurements of the concentrations of Th, Si, P, Ti, Y, Zr, Nb, Hf, and rare earth elements (REE) in the zircon crystals, which

were used as petrogenetic tracers. The methodological details are available in Solari et al. (2010). A glass standard (NIST 610) and two natural zircon standards, including one primary (91500; Wiedenbeck et al., 1995) and one secondary (Plešovice; Slama et al., 2008), were intercalated in the analytical sequences for quality control.

Prior to the isotopic analyses at the Laser Ablation Laboratory, SGC, cathodoluminescence images of the zircons were acquired. Some samples were photographed at the Lithological Characterization Laboratory (LCL) of the Universidad Nacional de Colombia, Red Nacional de Laboratorios de Geociencias, using a CITL CL8200 MK–5 Optical Cathodoluminescence System adapted to a Leica DM 2500 P versatile modular polarization microscope at 220 μA and a 15 kV current. Cathodoluminescence, secondary, and backscattered images of other samples were acquired using a JEOL scanning electron microscope, model JSM IT–300LV, operating at high and low vacuum conditions. It was equipped with a tungsten filament that works at accelerating voltages of electrons from 300 V to 30 kV and was equipped with four detectors: secondary (SE) and backscattered (BED) electron and Energy–Dispersive X–ray Spectroscopy (EDS, OXFORD 51–XMX 1181) and cathodoluminescence (CL; Gatan miniCL EGA 0028). Isotopic analyses were performed at the Laser Ablation Laboratory, SGC, using the LA–ICP–MS method in an Element 2 ICP–MS coupled to a Photon Machines laser ablation system with a 193 nm Excite laser. The ablation points were 30 micrometers in diameter. The Plešovice, 91500, and M. Dromedary crystals were used as reference standards. The Iolite IGOR-Pro software was used for data reduction. Integration times of 0 s to 38 s were used for the baseline, whereas integration times of 32.5 s to 8 s were used for the samples and reference standards. The final results correspond to mean data assessed after discriminating at 2 standard deviations. The data were processed using the routines of the Isoplot V3.5 software, and the correction of common lead was calculated according to the evolution model of Stacey & Kramers (1975). The geochronological data were plotted using Isoplot (Ludwig, 2012).

4. Results

4.1. Santander Massif

This study presents the results from the following plutons: the Mogotes Batholith, Pescadero Granite, Santa Bárbara Monzogranite, La Corcova Monzogranite, Páramo Rico Pluton, San Martín Tonalite, Rionegro Monzogranite, and three porphyritic bodies, including the Alto de Los Cacaos Rhyolite, San Joaquín Rhyolite, and El Uvo Rhyolite (Figure 2).

Most of the plutons intrude metasedimentary rocks of the Bucaramanga Gneiss and the Silgará Formation and metaigneous felsic rocks of the granitic orthogneiss. Additionally, the Rionegro Monzogranite intrudes the Cáchira Monzogranite in the east and a unit of amphibolites and migmatites that have been traditionally included as a part of the Bucaramanga Gneiss in the west. The San Martín Tonalite is in faulted contact with the Rionegro Monzogranite along the Bucaramanga Fault and is apparently in both intrusive and faulted contact with the overlying amphibolites and migmatites.

4.1.1. Petrography

The Late Triassic – Early Jurassic plutons of the SM consist of monzogranites, granodiorites, syenogranites, and tonalites (Figures 3, 4b, 4d) with no notable changes in their interior. Subvolcanic rocks of rhyolitic and dacitic compositions are also present (Figures 3, 4c). All of these rocks are white mottled with pink and black, gray mottled with black, and pink mottled with white spots. They are equigranular to inequigranular, fine to medium–grained, and some are bimodal. Graphic, perthitic, and symplectitic textures are locally developed. The rocks contain pink and white potassium feldspar, plagioclase, and quartz, and the most common mafic mineral is biotite, although rocks with hornblende and marginal rocks with clinopyroxene occur locally. The accessory minerals include apatite, magnetite, ilmenite, pyrite, titanite, allanite, and very rare garnet and muscovite. Chlorite, sericite, epidote, and clay aggregates are common alteration minerals. Enclaves of microdiorites, andesites, and dacites are present and may contain xenoliths of the Bucaramanga Gneiss, orthogneisses, and the Silgará Formation (Figure 4e, 4f).

The plutons are intersected by dikes and veins of syenogranites and aplitic saccharoidal and granophyric monzogranites, which have been described as alaskites (Mantilla–Figueroa et al., 2013). Dikes of micro quartz diorites, microdiorites, andesites, quartz latites, and rhyolites are also present.

4.1.2. Geochemistry

The Triassic – Jurassic granitoids of the SM have SiO_2 contents ranging from 65% to 79% in most rocks, K_2O ranging from 3% to 5.4%, and TiO_2 <1%. TiO_2, Al_2O_3, MgO, CaO, P_2O_5, and FeO decrease and K_2O increases with increasing SiO_2 concentration. The chemical classification of the rocks is highly consistent with the petrographic classification, with a predominance of granitic rocks and subordinate granodiorites, quartz monzonites, and quartz monzodiorites. The Mogotes Batholith and the Rionegro Monzogranite have the greatest lithological variations, as shown in the TAS diagram of Middlemost (1985) (Figure 5a; see Table 1, Supplementary Information).

The rocks that plot in the field of the high–K calc–alkaline series (Figure 5b, 5c) are mostly peraluminous (Figure 5d) and felsic with A/CNK ratios ranging from 1 to 1.4 and A/NK ratios ranging from 1 to 2. This indicates a contribution of crustal material to the parental magma as well as high magmatic

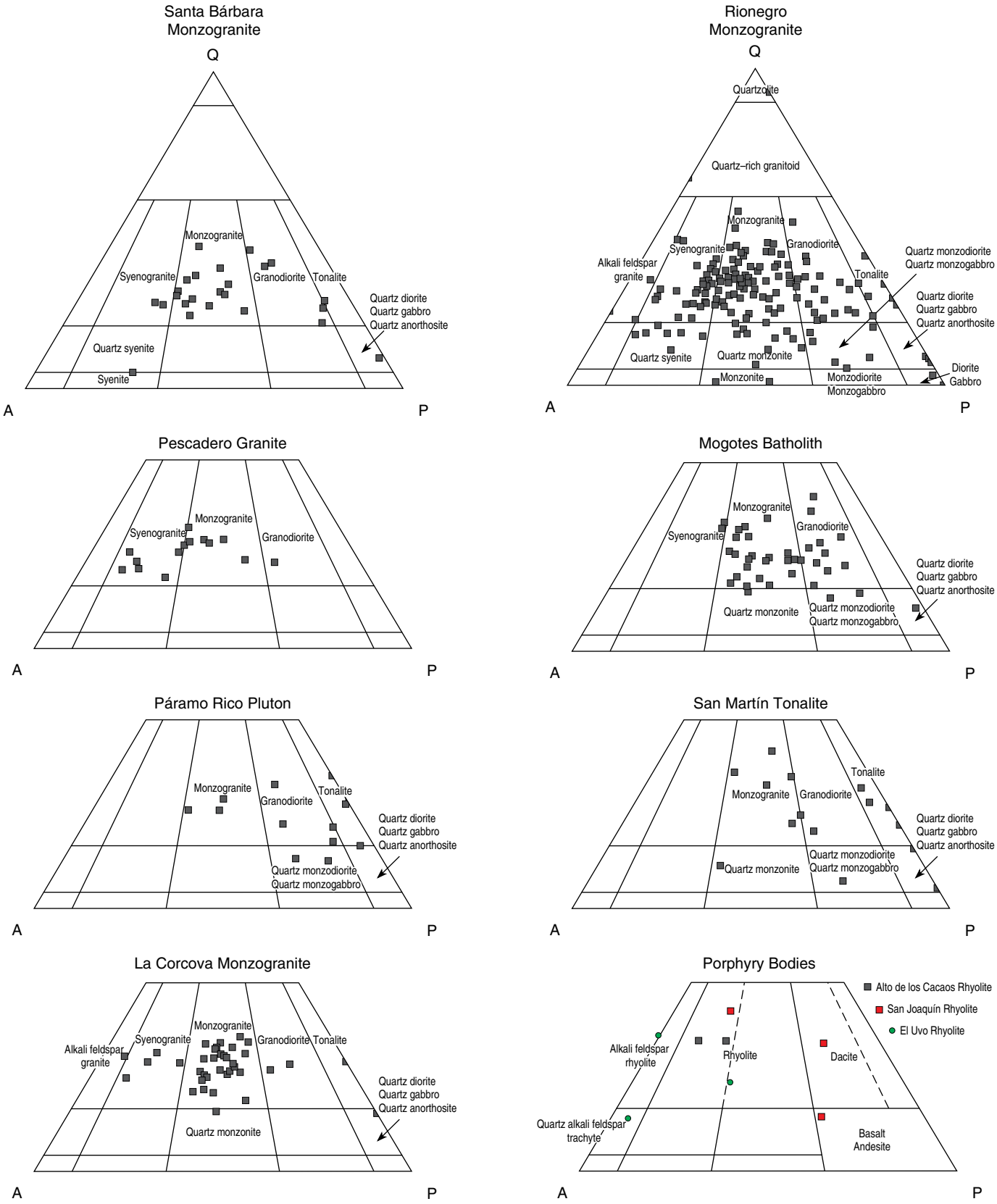

Figure 3. Modal compositions of Triassic – Jurassic granitoids from the Santander Massif in Quartz, Alkali feldspar, Plagioclase, Feldspathoid (QAPF) diagrams of Streckeisen (1974, 1979). Data sources: Arango et al. (2016); Correa–Martínez et al. (2018); Rodríguez et al. (2017c, 2017d, 2018c); Zapata et al. (2016b, 2017b).

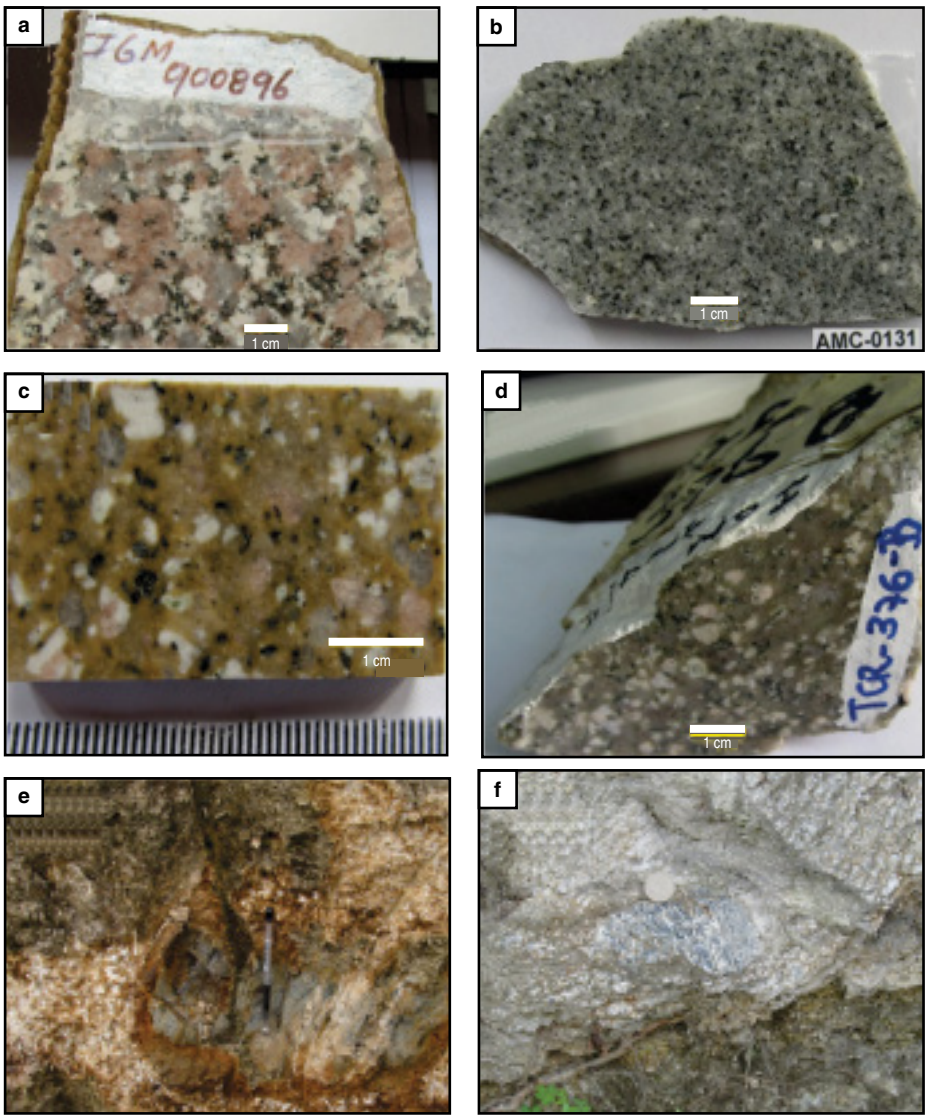

Figure 4. Macroscopic view of igneous rocks in the SM: **(a)** Santa Bárbara Monzogranite, **(b)** La Corcova Monzogranite, **(c)** San Joaquín Rhyolite, **(d)** Mogotes Batholith, **(e)** schist xenolith in La Corcova Monzogranite, **(f)** gneiss xenolith in La Corcova Monzogranite.

differentiation. Most are I–type plutons (Figure 5e), although some rocks in the same pluton plot in the fields of both I–type and S–type granites (Figure 5e). This phenomenon may be due to the variable extent of crustal melting in the different pulses that generated the plutons.

The granitoids of the SM have markedly negative Nb, Ti, and P anomalies as well as positive anomalies and high values of Cs, Ba, Th, Sr, K, Pb, and Rb, which are typical of continental margin magmatic arc environments (Figure 5f; Pearce, 1996, 2008), and gradual depletion from large ion lithophile elements (LILE) to high field strength elements (HFSE) (Figure 6).

The rare earth element (REE) patterns differ between rocks of similar compositions within each pluton (Figure 7), suggesting multiple magmatic pulses during their formation. The patterns resemble those of rocks generated in subduction environments above the subducted plate, with enrichment in light rare earth elements (LREE), depletion in heavy rare earth elements (HREE), and negative Eu anomalies (Eu/Eu* < 1) in most samples (Table 2). In rocks with higher SiO_2 contents, Eu/Eu* ratios <1 are more prominent.

The $(La/Yb)_n$ ratios are greater than 2 in all samples and vary markedly in the same intrusive body from one REE pattern to another compared to chondrites. The sums of the rare earth element contents (∑ REE = sum of the rare earth element values before normalization) range from 63.97 to 586.13. The rocks of the Rionegro Monzogranite have the lowest values, and those of the Mogotes Batholith have the highest values (Table 2).

4.1.3. Geochronology

Forty–one samples of the rocks and saprolites of the main granitoids in the SM and a few small dikes and minor intrusives of

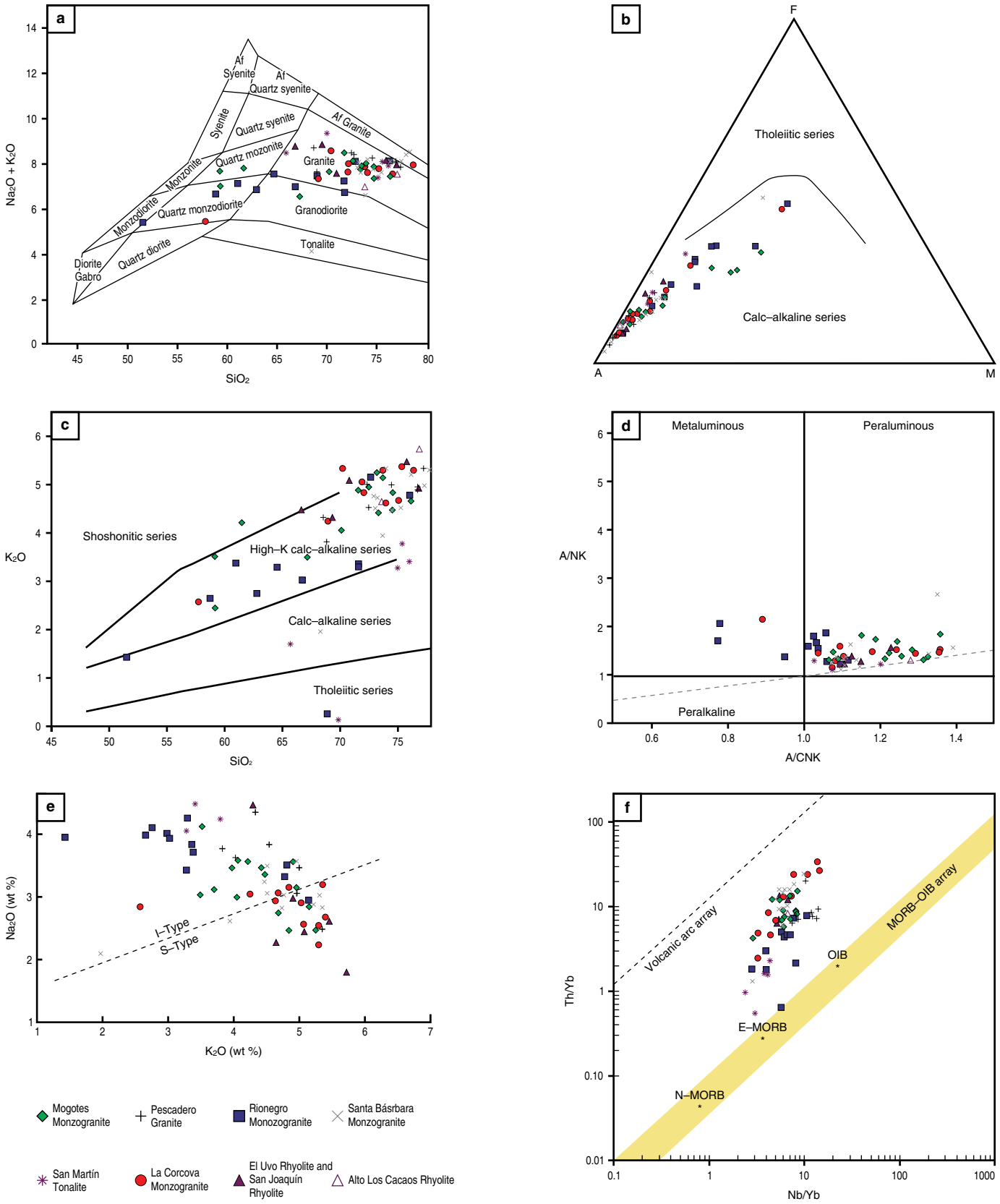

Figure 5. Classification and discrimination diagrams for Triassic – Jurassic granitoids in the SM: **(a)** TAS diagram of Middlemost (1985), **(b)** AFM diagram (Irvine & Baragar, 1971), **(c)** alkalinity index diagram of Peccerillo & Taylor (1976), **(d)** alumina saturation index diagram of Shand (1943); **(e)** K_2O vs. Na_2O diagram of Chappell & White (1974) discriminating between I–type and S–type granites, **(f)** Nb/Yb vs. Th/Yb diagram of Pearce (2008).

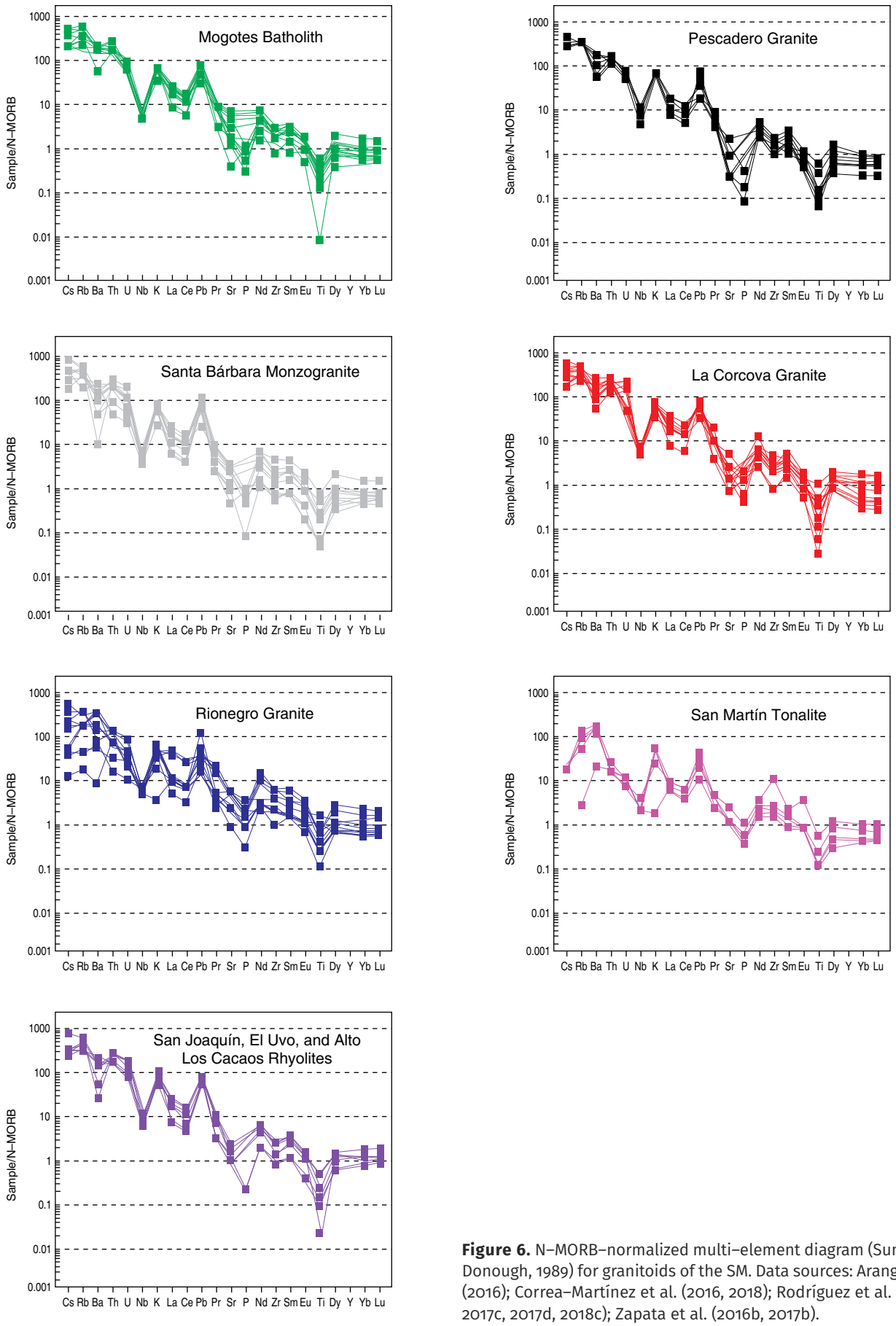

Figure 6. N–MORB–normalized multi–element diagram (Sun & McDonough, 1989) for granitoids of the SM. Data sources: Arango et al. (2016); Correa–Martínez et al. (2016, 2018); Rodríguez et al. (2017b, 2017c, 2017d, 2018c); Zapata et al. (2016b, 2017b).

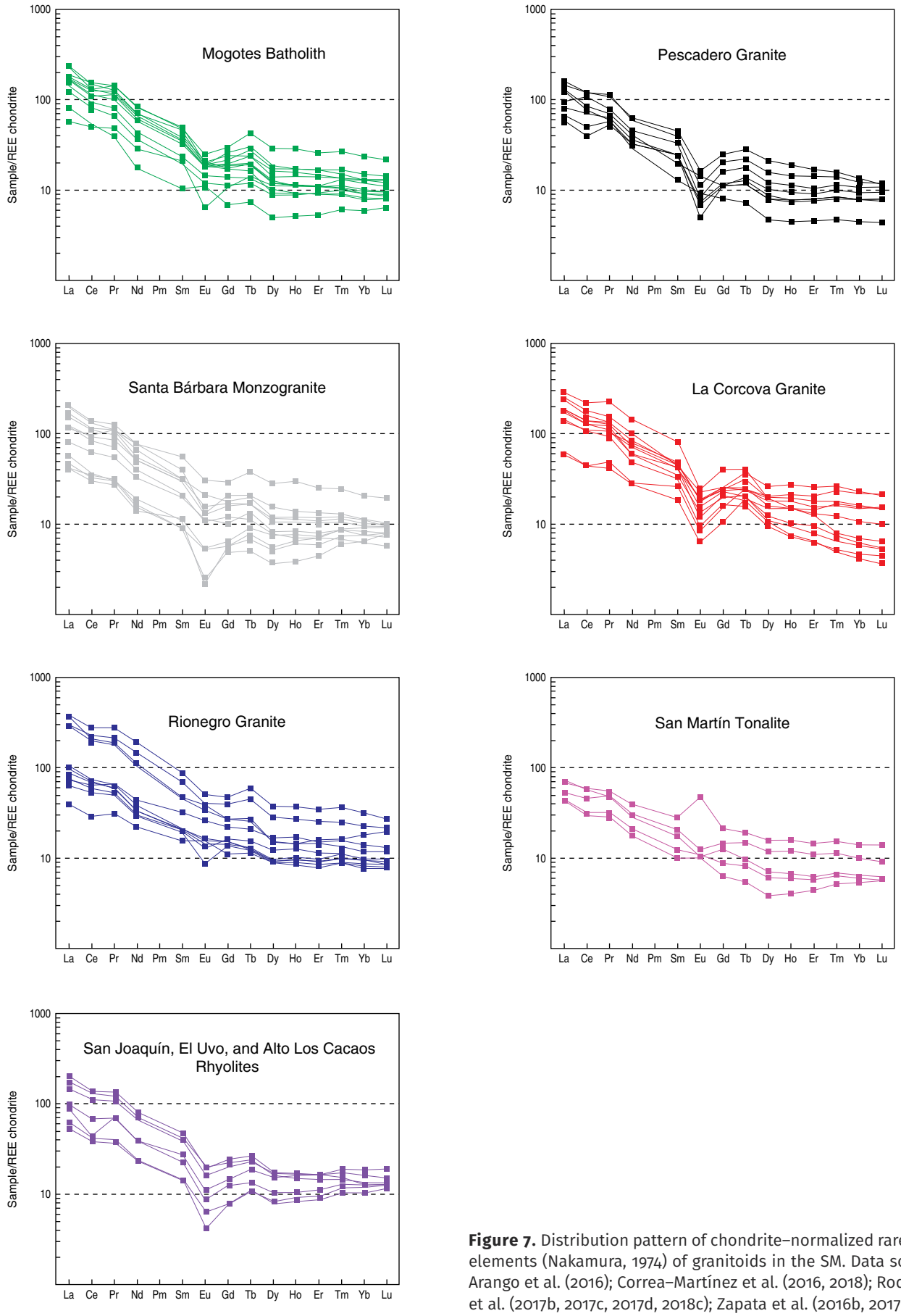

Figure 7. Distribution pattern of chondrite–normalized rare earth elements (Nakamura, 1974) of granitoids in the SM. Data sources: Arango et al. (2016); Correa–Martínez et al. (2016, 2018); Rodríguez et al. (2017b, 2017c, 2017d, 2018c); Zapata et al. (2016b, 2017b).

Table 2. Chondrite–normalized rare earth element diagram (Nakamura, 1974) for SM granitoids.

Sample	Unit	Eu/Eu*	$(La/Yb)_n$	$(La/Sm)_n$	$(Ce/Yb)_n$	$(Ce/Sm)_n$	$(Eu/Yb)_n$	∑REE
900910	Santa Bárbara Monzogranite	0.76	5.55	2.06	4.6	1.71	1.48	226.12
900941	Santa Bárbara Monzogranite	0.91	20.56	6.31	13.77	4.22	2.25	254.88
900857	Santa Bárbara Monzogranite	0.47	18.25	5.17	12.14	3.44	1.2	277.55
900920	Santa Bárbara Monzogranite	0.68	16.68	5.28	11.36	3.59	1.58	222.02
900882	Santa Bárbara Monzogranite	0.62	12.06	4.02	9.09	3.03	1.3	182.25
900870	Santa Bárbara Monzogranite	0.67	19.32	5.57	13.51	3.89	1.73	159.87
900896	Santa Bárbara Monzogranite	0.59	13.57	5.2	9.93	3.8	1.15	211.01
900933	Santa Bárbara Monzogranite	0.8	10.77	4.06	8.45	3.18	1.52	123.24
900908	Santa Bárbara Monzogranite	0.73	7.91	6.45	4.97	4.06	0.71	73.01
900911	Santa Bárbara Monzogranite	0.63	5.09	3.7	3.64	2.65	0.65	63.97
900881	Santa Bárbara Monzogranite	0.37	7.06	5.19	4.95	3.63	0.37	65.17
900935	Santa Bárbara Monzogranite	0.29	4.48	3.79	3.75	3.18	0.24	69.75
900862	La Corcova Monzogranite	0.4	45.44	4.5	33.62	3.33	2.86	264.4
900861	La Corcova Monzogranite	0.5	40.78	5.8	29.62	4.21	2.55	350.7
900863	La Corcova Monzogranite	0.42	30.69	4.59	22.79	3.41	2.05	201.05
900929	La Corcova Monzogranite	0.52	30.73	5.09	22.21	3.68	2.35	241.55
900921	La Corcova Monzogranite	0.43	40.84	3.56	31.2	2.72	3.48	445.1
10DVL05	La Corcova Monzogranite	0.67	15.88	5.28	10.66	3.54	1.52	319.9
900930	La Corcova Monzogranite	0.59	15.78	3.96	12.24	3.07	1.74	250.83
900937	La Corcova Monzogranite	0.53	11.79	3.87	8.8	2.89	1.15	284.63
900931	La Corcova Monzogranite	0.45	3.77	3.13	2.88	2.39	0.4	102.71
900909	La Corcova Monzogranite	0.43	2.88	2.45	1.99	1.69	0.39	113.15
900936	La Corcova Monzogranite	0.55	5.89	2.97	4.7	2.37	0.8	241
900997	Rionegro Monzogranite	0.98	5.16	2.27	4.51	1.99	1.84	144.42
900999	Rionegro Monzogranite	1.17	5.1	2.5	3.74	1.83	2.02	71.39
900954	Rionegro Monzogranite	1.09	20.17	7.75	11.45	4.4	2.14	428.36
900949	Rionegro Monzogranite	0.78	12.1	4.34	8.65	3.1	1.59	586.13
900952	Rionegro Monzogranite	0.77	13.07	4.31	10.12	3.34	1.77	468.08
900950	Rionegro Monzogranite	0.96	24.87	6.42	16.92	4.37	2.86	388.6
900985	Rionegro Monzogranite	0.73	7.94	3.94	6.18	3.07	1.36	121.45
900973	Rionegro Monzogranite	0.87	11.11	5.01	7.87	3.55	1.63	150.28
900990	Rionegro Monzogranite	0.97	11.85	4.8	8.62	3.49	2.06	138.65
900971	Rionegro Monzogranite	0.84	8.79	4.25	6.82	3.3	1.43	134.5
900974	Rionegro Monzogranite	0.52	7.37	3.08	6.16	2.57	1.01	108.8
901002	San Martín Tonalite	1.04	7.45	3.56	5.39	2.58	1.82	71.26
901003	San Martín Tonalite	0.72	5.35	2.59	4.61	2.23	1.25	102.47
901004	San Martín Tonalite	1.26	8.2	4.35	5.53	2.93	1.87	63.85
901032	San Martín Tonalite	1.93	4.88	2.42	4.18	2.07	3.39	135.25
901033	San Martín Tonalite	0.71	11.24	4.17	8.86	3.29	1.62	111.65
900864	Pescadero Granite	0.43	8.63	2.77	6.4	2.05	0.93	108.96
900871	Pescadero Granite	0.3	10.22	3.48	8.83	3.01	0.62	132.52
900872	Pescadero Granite	0.4	12.75	4.06	9.62	3.06	0.91	233.56
900873	Pescadero Granite	0.49	10.64	3.2	8.8	2.65	1.21	236.52
900897	Pescadero Granite	0.42	6.17	2.4	4.25	1.65	0.73	98.21

Table 2. Chondrite–normalized rare earth element diagram (Nakamura, 1974) for SM granitoids *(continued)*.

Sample	Unit	Eu/Eu*	$(La/Yb)_n$	$(La/Sm)_n$	$(Ce/Yb)_n$	$(Ce/Sm)_n$	$(Eu/Yb)_n$	∑REE
900898	Pescadero Granite	0.36	8.85	2.91	10	3.29	0.76	184.71
900867	Pescadero Granite	0.89	28.59	9.83	17.47	6.01	2.04	144.13
900899	Pescadero Granite	0.94	16.54	6.56	10.79	4.28	1.79	164.94
900944	Mogotes Batholith	0.68	11.72	4.57	7.01	2.74	1.3	235.48
900887	Mogotes Batholith	0.43	4.52	2.78	3.91	2.4	0.5	104.36
900927	Mogotes Batholith	1.31	13.85	7.91	9	5.14	1.87	98.55
900965	Mogotes Batholith	0.53	18.57	5.16	11.63	3.23	1.43	298.16
900869	Mogotes Batholith	0.8	12.7	6.31	8.6	4.27	1.24	158.31
900943	Mogotes Batholith	0.66	9.74	4.87	5.48	2.74	1.04	302.12
900966	Mogotes Batholith	0.71	13.33	5.1	8.42	3.22	1.38	232.43
900874	Mogotes Batholith	0.79	17.41	6.02	11.45	3.96	1.75	183.7
900962	Mogotes Batholith	0.89	17.88	5.58	11.33	3.54	2.08	227.96
900917	Mogotes Batholith	0.79	23.14	5.76	16.61	4.13	2.35	240.22
900900	Mogotes Batholith	0.7	18.33	4.63	13.48	3.41	2	245
900903	Mogotes Batholith	0.61	15.9	3.93	12.91	3.19	1.76	295.37
900902	Mogotes Batholith	0.76	18.67	4.78	13.61	3.49	2.14	242.71
900945	El Uvo Rhyolite	0.6	5.78	4.24	3.94	2.89	0.6	91.99
900946	El Uvo Rhyolite	0.39	4.35	3.64	3.18	2.66	0.35	86.3
900890	San Joaquin Rhyolite	0.58	8.93	3.77	6.83	2.89	0.99	232.69
900891	San Joaquin Rhyolite	0.58	15.71	4.24	10.86	2.93	1.55	291.01
900892	San Joaquin Rhyolite	0.66	12.89	4.14	9.64	3.1	1.5	264.35
900876	Alto de Los Cacaos Rhyolite	0.52	7.68	4.32	5.39	3.03	0.68	144.54
900916	Alto de Los Cacaos Rhyolite	0.56	4.75	3.25	2.34	1.61	0.59	126.22

Source: Data from Arango et al. (2016); Correa–Martínez et al. (2016, 2018); Rodríguez et al. (2017b, 2017c, 2017d, 2018c); Zapata et al. (2016b, 2017b); sample 10DVL05 from van der Lelij (2013).

aplitic monzogranites (corresponding to the Mogotes Batholith, the Pescadero Granite, the Santa Bárbara Monzogranite, La Corcova Monzogranite, the Páramo Rico Pluton, the San Martín Tonalite, the Rionegro Monzogranite, and three porphyritic bodies called the Alto de Los Cacaos Rhyolite, San Joaquín Rhyolite, and El Uvo Rhyolite) were dated using U–Pb zircon LA–ICPMS (data sources: Arango et al., 2016; Correa–Martínez et al., 2016, 2018; Rodríguez et al., 2017b, 2017c, 2017d, 2018c; Zapata et al., 2016b, 2018). The zircons of the granitoids from the SM are predominantly short prisms and elongated subordinates with concentric zoning, which are typical of igneous zircons. Inherited cores are identified in multiple crystals. The ages of the different samples analyzed are shown in Figure 2 and are presented in Table 3.

4.1.4. Igneous Ages

Most of the ages obtained from the granitoids from the SM (Table 3) are between 205 to 188 Ma. The exceptions include samples MIA–648B and MIA–650B, which yielded weighted mean ages of 214.5 ± 2.7 and 184.1 ± 2.3 Ma, respectively (Arango et al., 2016), that may correspond to the initiation and the final stage of the arc, respectively. The main set of ages represents the peak magmatic activity. The geochronological results from each granitoid show different ages for rocks with similar compositions (monzogranites); however, the ages are related to nonparallel REE trends, suggesting that they correspond to plutons that resulted from multiple magmatic pulses that occurred over 17 Ma and that the arc had very little compositional variation during its activity, in which the magmatic pulses involved variable crustal melting with variable $(La/Yb)_n$ ratios.

The ages of the dikes and minor intrusive bodies have an age distribution coeval to the crystallization time of the main mass of the granitoids. These rocks are predominantly monzogranitic, suggesting that younger pulses intruded previous assemblages of crystallized monzogranites within an arc system characterized by multiple magmatic pulses.

Table 3. LA–ICP–MS U–Pb zircon ages of granitoid bodies from the SM.

Sample	Latitude N	Longitude W	Classification	Unit	Age (Ma)	Inherited ages (Ma)
AMC–0162	6° 27' 41.16''	72° 49' 52.55''	Deformed monzogranite	Mogotes Batholith	189.1 ± 3.6	224–222, n=2; 234–231, n=4; 252–248, n=2; 298–270, n=5; 386–376, n=5; 420–395, n=5; ; 445–437, n=5; 459–451, n=5 513, n=1; 360–338, n=6; 585, n=2; 680–650, n=2; 800–735, n=3; 970, n=2; 1290–115, n=4;
GZ–6831	6° 27' 39.59''	72° 48' 31.34''	Deformed quartz monzodiorite	Mogotes Batholith	193.7 ± 1.3	268.3 ± 7.6, n=1; 287.7 ± 8.8, n=1; 905 ± 25, n=1;
LMC–075	6° 28' 35.52''	72° 53' 34.39''	Monzogranite	Mogotes Batholith	195.7 ± 3.9	248.5 ± 10, n=1; 1040-1020 ± 34, n=2; 1230 ± 43, n=1
MIA–638	6° 33' 30.57''	72° 56' 16.58''	Monzogranite	Mogotes Batholith	200.4 ± 2.2	234.4 ± 7.1, n=1; 316.9 ± 6.8, n=1; 1120 ± 79, n=1; 1627 ± 77, n=1
TCR–376	6° 41' 6.91''	72° 57' 13.31''	Monzogranite	Mogotes Batholith	202.5 ± 1.3	880 ± 15, n=1
MIA–636	6° 41' 0.05''	72° 57' 59.68''	Micrographic monzogranite	Mogotes Batholith	205.4 ± 3.0	571.7 ± 6, n=1; 1316 ± 76, n=1
AMC–0144	6° 25' 27.04''	72° 50' 23.16''	Aplitic Syenogranite (dike)	Mogotes Batholith	202.1 ± 1.8	435 ± 6.7, n=1
TCR380	6° 28' 21.43''	72° 54' 17.89''	Quartz monzonite (dike)	Mogotes Batholith	191.0 ± 3.5	330–302, n=3; 267, n=1; 215, n=1; 399–391, n=2; 448–432, n=4; 923–851, n=4
AMC–136A	6° 45' 20.98''	72° 57' 21.48''	Microdiorite (dike)	Mogotes Batholith	108.3 ± 2.3	221 ± 8, n=1; 250 ± 10, n=1; 1154 ± 35, n=1; 1335 ± 40, n=1;
GZ–6829B	6° 26' 33.53''	72° 48' 33.94''	Syenogranite (dike)	Mogotes Batholith	98.8 ± 1.3	199 ± 6, n=2; 214 ± 7; 207 ± 7
TCR–389	7° 37' 59.55''	73° 16' 55.66''	Diorite	Minor Body	199.7 ± 1.6	
GZ–6823	6° 55' 14.09''	73° 0' 59.90''	Monzogranite	Pescadero Granite	194.8 ± 3.2	451 ± 18, n=10; 995 ± 20, n=2
GZ–6824	6° 53' 22.17''	72° 59' 48.41''	Monzogranite	Pescadero Granite	197.3 ± 2.4	324.18 ± 18, n=1; 432.5 ± 25, n=1; 754.1 ± 45, n=1; 959 ± 31, n=3; 1047.8 ± 64, n=1; 1873.1 ± 105
AMC–0131	7° 9' 47.68''	73° 2' 22.93''	Syenogranite	La Corcova Monzogranite	192.5 ± 2.6	338.8 ± 10, n=1; 408.5 ± 7.3,n=3
JGB–456B	6° 57' 2.43''	72° 56' 13.82''	Quartz diorite	La Corcova Monzogranite	201.6 ± 4.0	304.6 ± 15
MIA–630B	7° 2' 12.10''	73° 2' 42.78''	Quartz diorite	La Corcova Monzogranite	202.7 ± 1	
LMC–077	7° 9' 39.68''	73° 3' 40.44''	Monzogranite	La Corcova Monzogranite	204.8 ± 6.1	230, n=1; 262 ± 13, n=2; 289 ± 8, n=1; 362 ± 15, n=2; 390–415, n=2; 435–457, n=3; 463.8 ± 7.3, n=3; 490 ± 20, n=3; 618 ± 30 , n=1; 911 ± 40, n=1; 1091 ± 39, n=1; 1426 ± 38, n=1
AMC–128A	7° 8' 12.44''	73° 2' 17.93''	Meta-syenogranite Xenolith	La Corcova Monzogranite	462.7 ± 3.1	525 ± 7.8, n=1; 533.8 ± 7, n=1; 1099 ± 74, n=1
MIA–627A	6° 55' 24.42''	72° 59' 51.19''	Monzogranite-(dike)	La Corcova Monzogranite	199.5 ± 4.6	281.2 ± 5.6, n=1; 419.4 ± 7, n=1; 430.5 ± 4.7, n=1; 457.1 ± 5.0, n=11; 482.1 ± 3.1, n=3; 1498–1418, n=3
MIA–650B	7° 25' 42.08''	73° 10' 50.27''	Syenogranite	Rionegro Monzogranite	184.1 ± 2.3	928 ± 55, n=2; 1005, n=1; 1485, n=1
LMC–082	7° 42' 2.95''	73° 16' 53.05''	Diorite	Rionegro Monzogranite	189.9 ± 1.6	
GR–6743	8° 11' 22.47''	73° 19' 0.48''	Granodiorite-Monzogranite	Rionegro Monzogranite	195.9 ± 1.6	230.9 ± 7.9, n=1
GZ–6848A	7° 38' 55.80''	73° 13' 16.64''	Granodiorite	Rionegro Monzogranite	196.6 ± 2.1	451, n=1; 877.9, n=1; 93,40, n=1; 1035.2, n=1; 1143.33, n=1
MIA-648A	7° 19' 10.76''	73° 7' 40.63''	Porphyritic rhyolite (dike)	Rionegro Monzogranite	194.5 ± 1.2	1021.6, n=1
JGB-462	7° 11' 26.11''	73° 7' 26.48''	Quartz monzonite (dike)	Rionegro Monzogranite	197.2 ± 1.5	
LMC–084	7° 39' 53.04''	73° 16' 34.56''	Granodiorite with hornblende	Rionegro Monzogranite	200.8 ± 1.9	230.8 ± 5, n=2
MIA–648B	7° 19' 10.73''	73° 7' 40.61''	Granodiorite	Rionegro Monzogranite -Minor Body	214.5 ± 2.7	244.3 ± 4.0, n=6; 288–267, n=2; 320 ± 15, n=1
AMC–0137	6° 45' 18.64''	72° 55' 57.78''	Monzogranite	Santa Bárbara Monzogranite	191.7 ± 1.2	201.4–200.8, n=3; 1122 and 1158, n=2 unconformable
JGB–457A	6° 57' 32.95''	72° 55' 44.00''	Monzogranite	Santa Bárbara Monzogranite	195.1 ± 1.9	392, n=1
GR–6719	7° 10' 32.46''	72° 49' 32.68''	Monzogranite	Santa Bárbara Monzogranite	196.8 ± 2.0	224–221, n=2 unconformable; 474, n=1 unconformable
GZ–6821	6° 55' 14.09''	72° 54' 19.44''	Monzogranite	Santa Bárbara Monzogranite	198.0 ± 2.7	238.4–213.3, n=4; 395.6–380.8, n=3; 427.9–417.8, n=3; 470–447.4, n=3
GR–6718	7° 7' 53.82''	72° 51' 2.68''	Monzogranite	Santa Bárbara Monzogranite	203.8 ± 2.7	
GR–6717	7° 10' 7.27''	72° 51' 46.08''	Monzogranite (minor body)	Santa Bárbara Monzogranite	190.6 ± 1.5	425.2, n=1 unconformable; 208–202.9; n=3
LMC–059A	7° 10' 44.67''	72° 52' 12.58''	Syenogranite (dike)	Santa Bárbara Monzogranite	200.7 ± 2.0	628 ± 26, n=1
AMC–0127	6° 56' 10.40''	72° 54' 6.56''	Pheno-dacite (dike)	Santa Bárbara Monzogranite	204.0 ± 2.3	267, n=1

Table 3. LA–ICP–MS U–Pb zircon ages of granitoid bodies from the SM *(continued).*

Sample	Latitude N	Longitude W	Classification	Unit	Age (Ma)	Inherited ages (Ma)
AMC–0145	6° 26' 4.14''	72° 52' 37.30''	Quartz-trachyte of Kfs (dike)	Alto de Los Cacaos Rhyolite	205.2 ± 2.6	279 ± 2.8, n=1; 410 ± 4.4, n=1; 429 ± 8.3, n=1; 454 ± 7.5, n=1; 464 ± 4.2, n=1;1681 ± 67, n=1
GR–6729	6° 26' 37.39''	72° 51' 22.91''	Pheno dacite	San Joaquín Rhyolite	201.0 ± 2.1	390 ± 20, n=1; 446 ± 8, n=1; 1630 ± 170, n=1 unconformable
MIA–641	6° 27' 33.24''	72° 48' 4.01''	Porphyritic rhyolite (dike)	El Uvo Rhyolite	197.2 ± 1.6	218.2 ± 4.0, n=2; 1168 ± 25, n=1
LMC–088	8° 8' 36.39''	73° 26' 32.93''	Granodiorite	San Martín Tonalite	198.0 ± 2.8	
TCR–395A	7° 55' 41.64''	73° 23' 44.50''	Metatonalite	San Martín Tonalite	198.9 ± 1.8	
LMC–090B	8°5′3.51''	73° 26' 26.86''	Phenodacite (dike)	San Martín Tonalite	196.6 ± 2.5	999 ± 26, n=1
TCR–363	7° 12' 51.61''	72° 53' 55.78''	Granodiorite	Páramo Rico Tonalite	206.84 ± 0.98	

Source: Data from Arango et al. (2016); Correa–Martínez et al. (2016, 2018); Rodríguez et al. (2017b, 2017c, 2017d, 2018c); Zapata et al. (2016b, 2017b).

4.1.5. Inherited Ages

The inherited zircon cores of the granitoids from the SM yield ages ranging from 1873.1 ± 105 (Mesoproterozoic) to approximately 220 Ma (Early Triassic) (Figure 8; Table 3).

Inherited ages of approximately 1800 and 1600 Ma are found in zircon cores of the Mogotes Batholith, Pescadero Granite, and El Uvo and San Joaquín Rhyolites. Rare inherited cores with ages ranging from 850 to 635 Ma (Cryogenian) and from 635 to 542 Ma (Ediacaran) are found in the Mogotes Batholith, Pescadero Granite, and Santa Bárbara Monzogranite. A set of Early, Middle, and Late Ordovician ages is found in the Mogotes Batholith; La Corcova, Santa Bárbara, and Rionegro Monzogranites; and the San Joaquín Rhyolite (Figure 8).

Permian ages ranging from 290 to 262 Ma, as well as Triassic to Carnian ages, occur in inherited zircon cores from the Mogotes Batholith and La Corcova, Santa Bárbara, and Rionegro Monzogranites.

4.1.6. Age of the Basement in the NW zone

A U–Pb zircon age from an amphibolite of the amphibolite and migmatite unit in the northwest part of the SM yielded a metamorphic age of ca. 897 ± 28 Ma, a Th/U ratio <0.2, and inherited ages of 1120 ± 58 Ma (n = 4) and 1421 ± 40 Ma (n = 16) (Figure 9).

4.2. Upper Magdalena Valley

The Jurassic magmatism in the UMV is represented by batholiths, stocks, and volcano–sedimentary units that are distributed on the eastern edge of the Central Cordillera and on the western edge of the Eastern Cordillera of Colombia. All of the units were grouped according to their current spatial positions, compositions, and ages into the western and eastern plutons (Rodríguez et al., 2015a, 2018a).

The western plutons are located between the western Avirama and the eastern Betania–El Agrado Faults. They are composed of the Anchique Quartz Monzonite (Arango et al., 2015a; Cossio et al., 1994), San Cayetano Quartz Monzonite (Bermúdez et al., 2015; Carvajal et al., 1983, 1993), Los Naranjos Quartz Monzonite (Rodríguez & Fuquen, 1989; Rodríguez et al., 2015b; Velandia et al., 2001b), Páez Quartz Monzodiorite (Zapata et al., 2015), El Astillero Quartz Monzodiorite (Rodríguez et al., 2015c; Velandia et al., 2001b), and Las Minas Monzonite (Arango et al., 2015b; Velandia et al., 2001b) (Figure 10).

The eastern plutons are located between the Betania–El Agrado and Algeciras Faults. This group is represented by the Algeciras Monzogranite (Ferreira et al., 1998, 2002; Rodríguez et al., 2015d), Teruel Quartz Latite (Arango et al., 2015c), Garzón Granite (Rodríguez et al., 2015e; Velandia et al., 2001b), Altamira Monzogranite (Arango et al., 2015d), Sombrerillo Quartz Monzonite (Rodríguez et al., 2018a), and Mocoa Monzogranite (Arango et al., 2015e) (Figure 10).

4.2.1. Petrography

The western plutons consist of quartz monzonites, quartz monzodiorites, quartz diorites, and some monzogranites (Figure 11). They range from quartz monzonites in the north to quartz monzodiorites in the south and consist of Pl + Kfs + Qtz (<20%) ± Hbl ± Bt ± Cpx ± Opx with opaques, apatite, zircon, and titanite as accessory minerals. The eastern plutons include monzogranite rocks with slight lithological variations between syenogranites and granodiorites (Figure 11), which consist of Kfs + Pl + Qtz (>20%) + Bt ± Hbl ± Cpx with opaques, apatite, zircon, titanite ± allanite as accessory minerals.

The modal quartz contents differ markedly between the two groups. The quartz contents of the western plutons are generally lower than 20%, whereas the eastern plutons of the UMV contain rocks with quartz contents higher than 20%. Mafic minerals are commonly found in higher modal quantities in the western plutons, particularly hornblende, biotite, clinopyroxene, and subordinate orthopyroxene. Mafic minerals occur in lower ratios in the eastern plutons and include biotite and hornblende with or without clinopyroxene and completely lacking orthopyroxene.

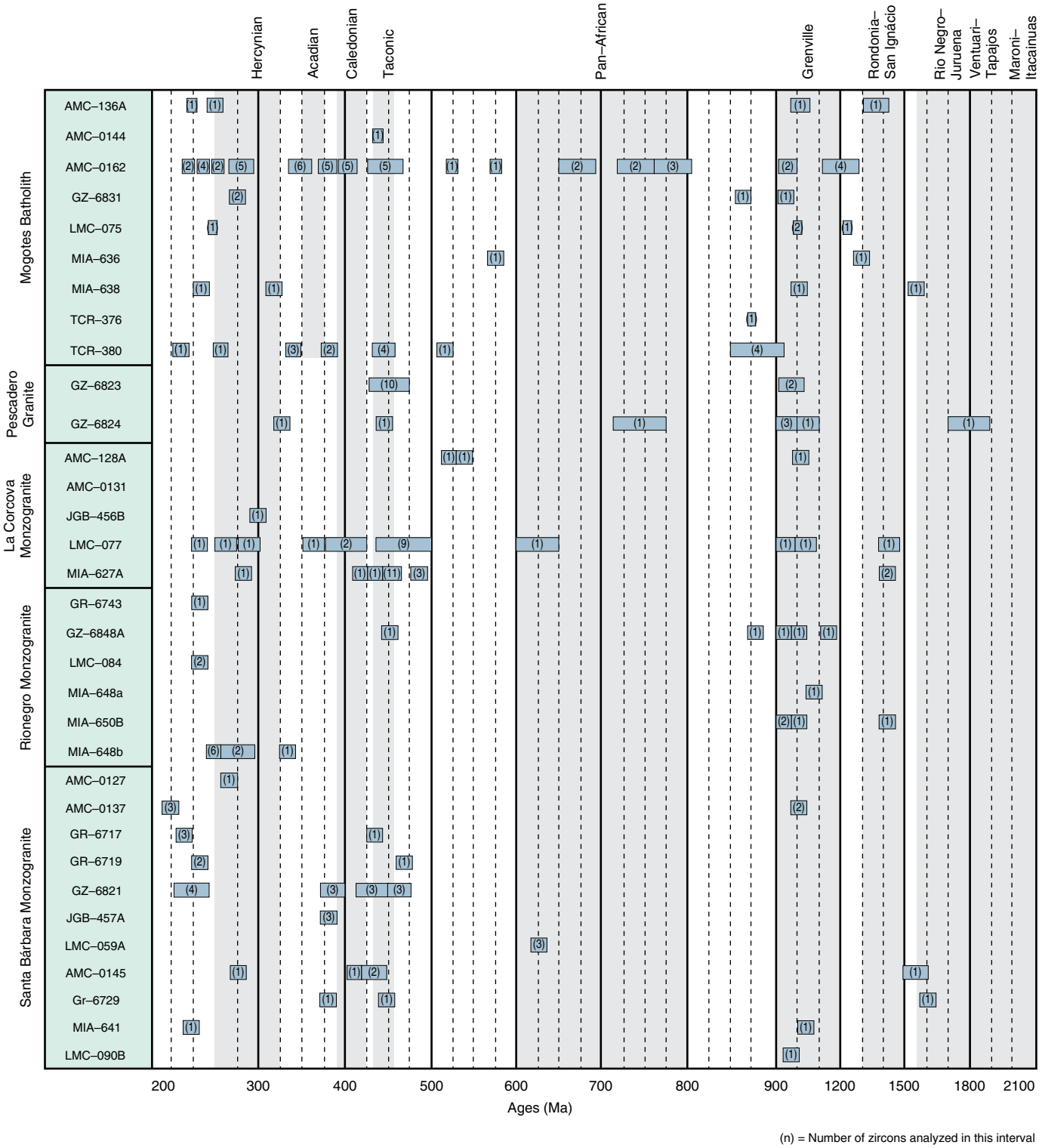

Figure 8. Ages of inherited zircons in samples of granitoids from the SM (data sources: Arango et al., 2016; Correa–Martínez et al., 2016, 2018; Rodríguez et al., 2017b, 2017c, 2017d, 2018c; Zapata et al., 2016b, 2017b).

Both groups of plutons are intruded by dikes of basic to intermediate compositions, including andesites, microdiorites, and basalts, as well as acidic dikes such as rhyolites, dacites, and aplitic monzogranites.

Texturally, the western plutons range from equigranular to inequigranular and commonly show micrographic intergrowths. The eastern plutons are inequigranular with bimodal crystals of alkaline feldspar.

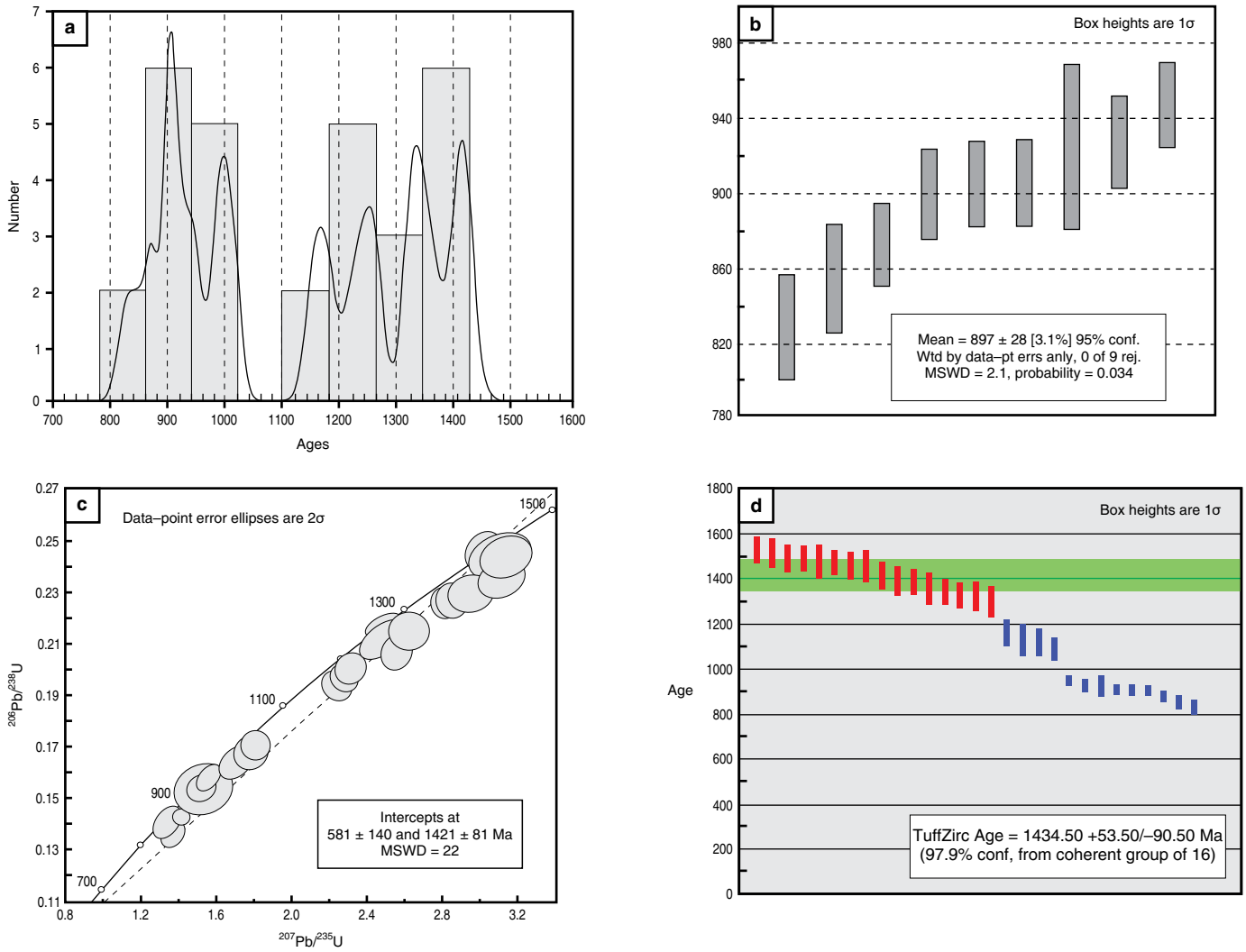

Figure 9. Age and inheritance of amphibolite sample MIA-661 from the Aguachica–Ocaña road. **(a)** Probability density diagram; **(b)** weighted average age diagram; **(c)** concord diagram; **(d)** tuffzirc age diagram.

The volcanic units include the Saldaña Formation and the Pitalito Vulcanites (Rodríguez et al., 2016b, 2018a). The former is located in the Central Cordillera and the serranía de Las Minas near the western plutons. The latter is located near the western edge of the Eastern Cordillera near the eastern plutons (Figure 10). They consist of andesitic to rhyolitic lava flows, tuffs, and agglomerates.

4.2.2. Geochemistry

Whole–rock geochemical analyses were performed on 72 samples from the eastern and western plutons (Rodríguez et al., 2018a). Data sources include Arango et al. (2015a, 2015b, 2015c, 2015d, 2015e); Bermúdez et al. (2015); Bustamante et al. (2010); Rodríguez et al. (2015a, 2015b, 2015c, 2015d, 2015e, 2016b); and Zapata et al. (2015) (see Table 1, Supplementary Information).

The eastern plutons are grouped in the TAS diagram (Figure 12a) in the field of granites, although a few rocks from the Algeciras and Altamira Monzogranites are alkali feldspar granites. The western plutons tend to have more basic compositions, varying between quartz diorites and quartz monzodiorites. Some rocks from the Páez Quartz Monzodiorite reach the granite field, which is consistent with the petrographic data (Figures 11, 12a).

The Jurassic granitoids of the UMV show decreases in TiO_2, Al_2O_3, MgO, CaO, and P_2O_5 and increases in K_2O and Na_2O with increasing SiO_2. The rocks in the A (Al_2O_3), F (FeO), M (MgO) (AFM) diagram range from tholeiitic to more differentiated calc–alkaline rocks (Figure 12b) and mostly plot within the field of the high–K, calc–alkaline series (Figure 12c). These rocks transition from metaluminous in the western granitoids to peraluminous in the eastern granitoids (Figure 12d), with A/CNK ratios ranging from 0.5 to 1.2 and A/NK ratios ranging from 1 to 2.8, suggesting magmatic differentiation.

The eastern granitoids are high–K calc–alkaline, and some rocks are shoshonitic (Figure 12c), with SiO_2 contents ranging

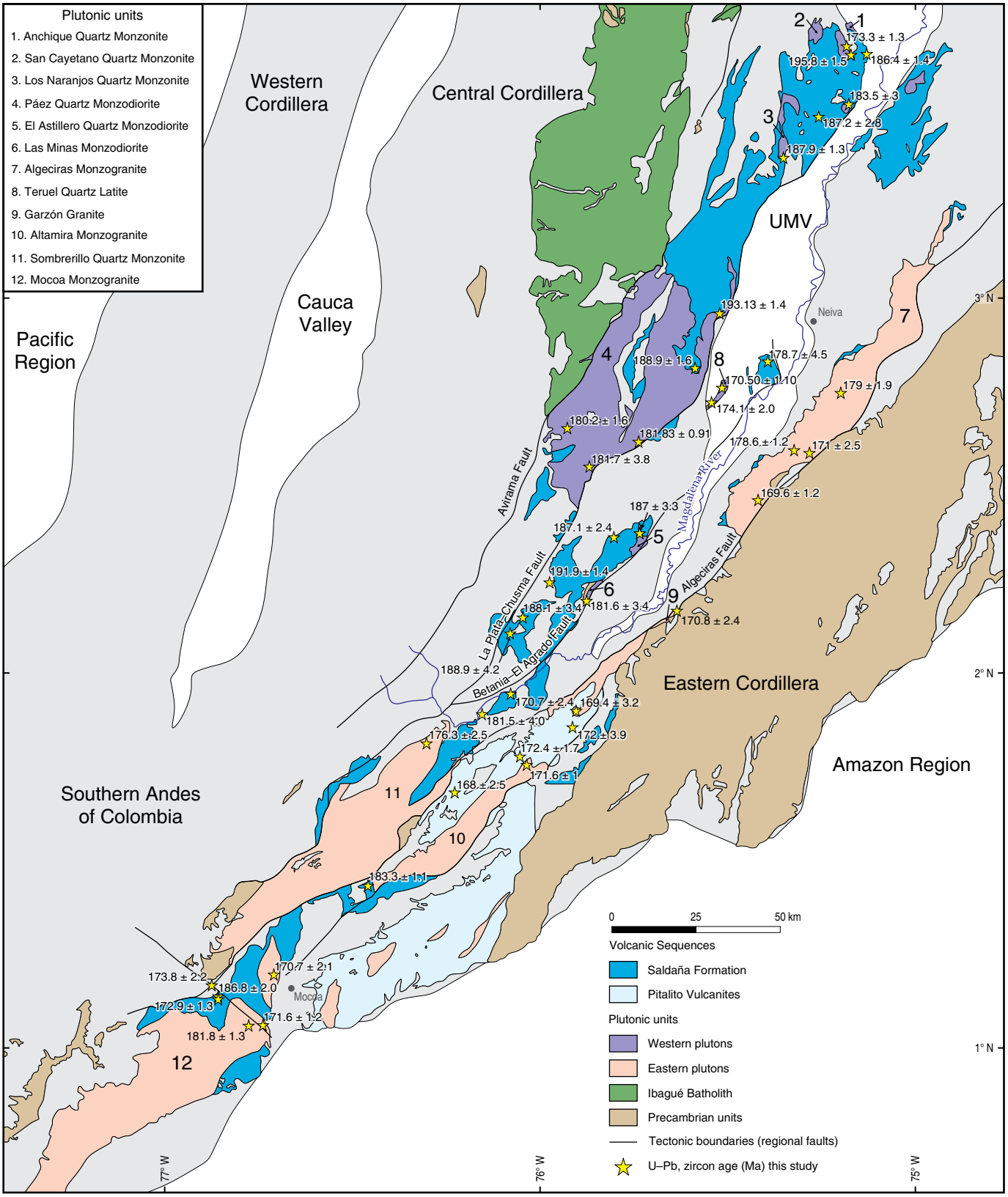

Figure 10. Locations and U–Pb ages of Jurassic plutons and volcanic rocks associated with the UMV (taken from Rodríguez et al., 2018a).

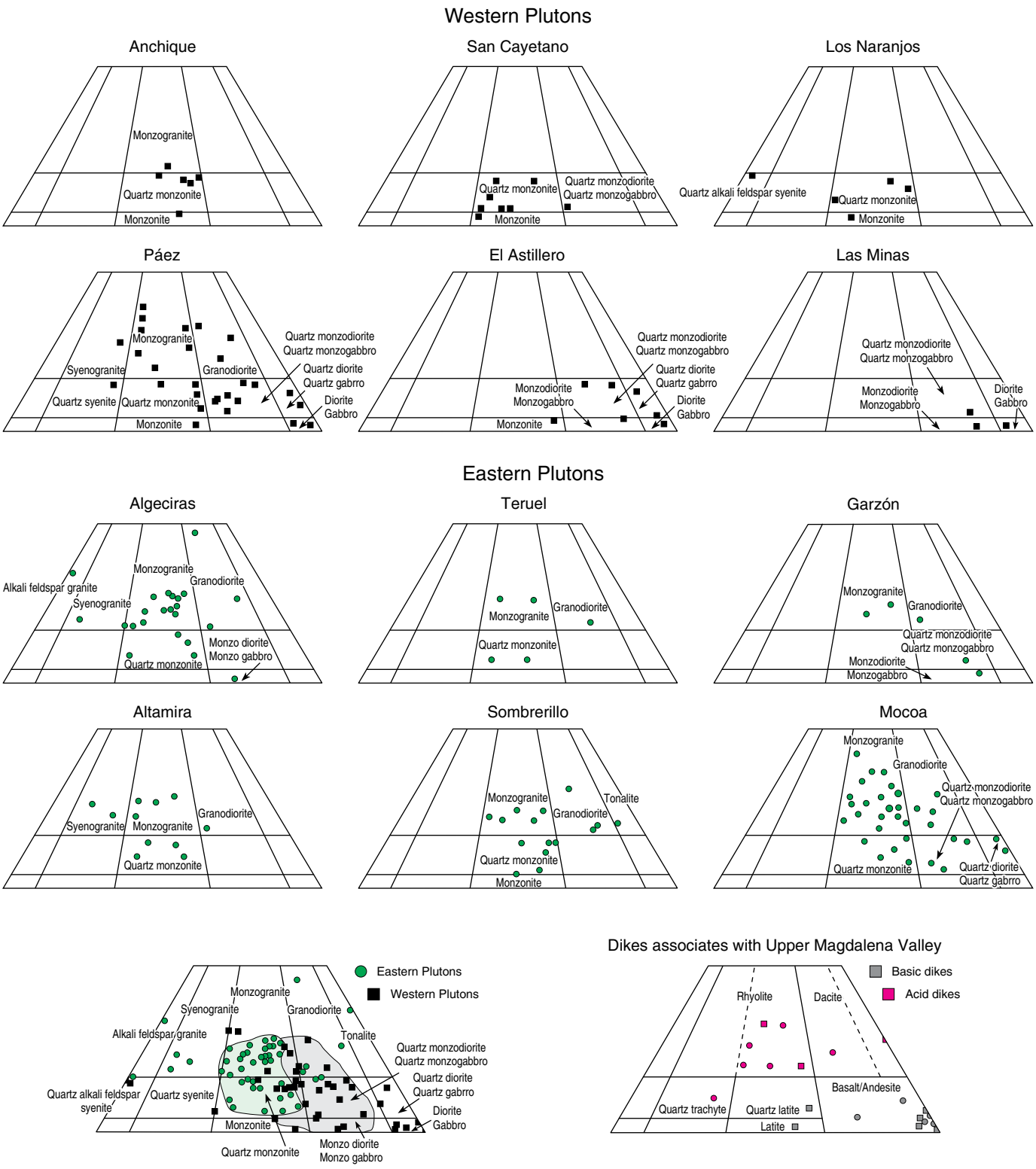

Figure 11. Modal compositions of Jurassic granitoids from the Upper Magdalena Valley (UMV) of Streckeisen (1974). Western plutons are shown in black, and eastern plutons are shown in green. Data sources: Arango et al. (2015a, 2015b, 2015c, 2015d, 2015e); Bermúdez et al. (2015); Rodríguez et al. (2015a, 2015b, 2015c, 2015d, 2015e, 2018a); Zapata et al. (2015).

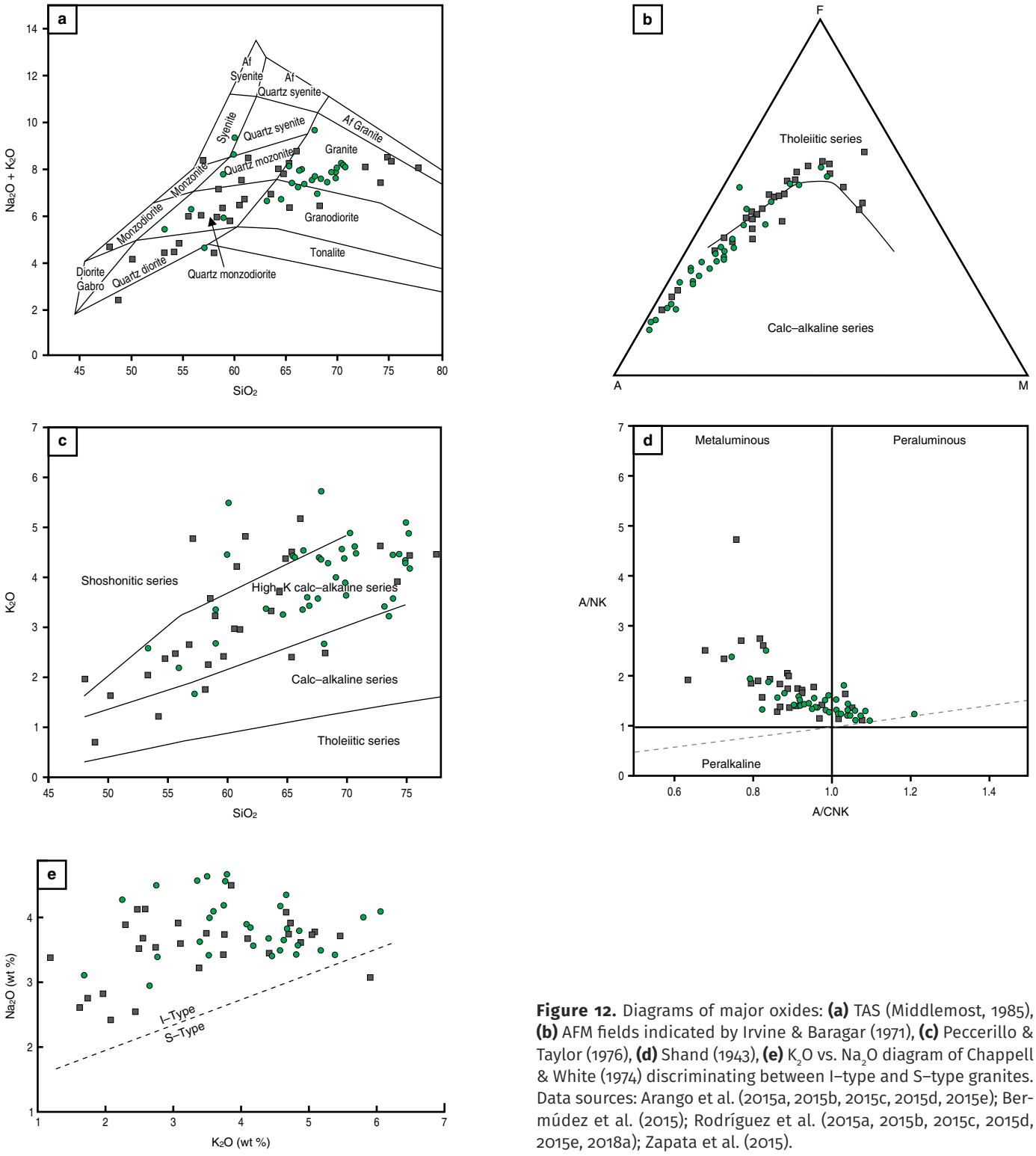

Figure 12. Diagrams of major oxides: **(a)** TAS (Middlemost, 1985), **(b)** AFM fields indicated by Irvine & Baragar (1971), **(c)** Peccerillo & Taylor (1976), **(d)** Shand (1943), **(e)** K_2O vs. Na_2O diagram of Chappell & White (1974) discriminating between I–type and S–type granites. Data sources: Arango et al. (2015a, 2015b, 2015c, 2015d, 2015e); Bermúdez et al. (2015); Rodríguez et al. (2015a, 2015b, 2015c, 2015d, 2015e, 2018a); Zapata et al. (2015).

from 53% to 78%, Na_2O contents ranging from 2.8% to 4.7%, and K_2O contents ranging from 2.1% to 5% (Figure 12e). They have low Fe_2O_3 contents ranging from 0.5% to 10.4% and MgO contents ranging from 0.18 to 6.4%. The western plutons vary between tholeiitic to calc–alkaline in the AFM diagram (Figure 12b) and are calc–alkaline (Figure 12c), with low SiO_2 contents ranging from 47.6% to 74.8% (average of 61%), low Na_2O contents ranging from 2.4% to 4.2%, with most values near 3.30%, and higher Fe_2O_3 (6.21%) and MgO (3.39%) contents. The TiO_2 content is usually less than 1%.

The western plutons have a predominantly metaluminous character (Figure 12d), with mean Al_2O_3 contents of 15.5% wt

and lower ($CaO + Na_2O + K_2O$) contents of 11.7% wt. Some silica–enriched rocks reach the peraluminous series. The western plutons range from metaluminous, with Al_2O_3 contents of 15.34% wt and ($CaO + Na_2O + K_2O$) contents of 10.86% wt, to peraluminous in the rocks from the Garzón Granite and in most samples from the Altamira Monzogranite, with A/NK (1.74) > A/CNK (1.46).

Both groups of plutons of the UMV have markedly negative Nb, Ti, and P anomalies and positive anomalies and high values of Cs, Ba, Th, Sr, K, Pb, and Rb. These characteristics are typical of magmas that are generated in continental margin arc environments (Pearce et al., 1984; Pearce, 1996) with gradual depletion from LILE to HFSE (Figure 13).

The K_2O versus CaO ratios allow the differentiation between the high–K calc–alkaline granitoids (KCG) of the eastern plutons and the arc calc–alkaline granitoids (ACG) of the western plutons, according to the classification of Barbarin (1999). This suggests a mixed component (mantle and crust contributions) in the origin of these groups of granitoids. KCG are associated with crustal melting with a minor mantle contribution, whereas the mantle fraction prevails over the crustal component in ACG.

The (Ba/Sr) and (K/Rb) ratios are higher in the eastern bodies, with values of 3.29 and 34.92, respectively, that are associated with plagioclase crystallization (Green, 1980) and the ease of Ba replacement by K, indicating higher alkali enrichment. In contrast, the western plutons have values of 1.93 and 31.42, respectively.

The patterns of the chondrite–normalized rare earth elements (REE) (McDonough & Sun, 1995) of most of the samples are subparallel in both groups of plutons, with negative slopes and patterns similar to those of rocks generated in subduction environments above the subducted plate, including enrichment in light rare earth elements (LREE) and depletion in heavy rare earth elements (HREE) (Figure 14). Most samples have slightly positive Eu anomalies, with mean ratios of Eu/Eu* = 1.22 in the western plutons and Eu/Eu* = 1.14 in the eastern plutons; some of the samples had ratios of Eu/Eu* < 1 (Table 4).

The $(La/Yb)_n$ ratios range from 10 to 26 in the eastern plutons, with most values between 10 and 15, except in the Sombrerillo Quartz Monzonite, where they range from 4.8 to 7.3. In the western plutons, $(La/Yb)_n < 10$ in most samples, and a few rocks have values between 10 and 20 (e.g., 900642, 900643, 900752, 900673). These values are consistent and lower than those of the eastern plutons, suggesting decreased magmatic differentiation and decreased crustal contribution. The sums of the contents of the rare earth elements (∑ REE) range from 62.3 to 338 in the eastern plutons and from 36.7 to 252 in the western plutons (Table 4).

Both groups of plutons show characteristics of continental arc (Figure 15a, 15b), I–type (cordilleran) (Figure 15c), magnesian (oxidizing magmas) (Figure 15d) granites with greater enrichments in SiO_2 in the eastern plutons.

4.2.3. Geochronology

Forty samples of rocks and saprolites of granitoids and volcanic rocks from the UMV were dated using the U–Pb zircon LA–ICP–MS method. The samples correspond to the Anchique Quartz Monzonite, San Cayetano Quartz Monzonite, Los Naranjos Quartz Monzonite, Páez Quartz Monzodiorite, El Astillero Quartz Monzodiorite, Las Minas Monzonite, Algeciras Monzogranite, Teruel Quartz Latite, Garzón Granite, Altamira Monzogranite, Sombrerillo Quartz Monzonite, Mocoa Monzogranite, Saldaña Formation, and Pitalito Vulcanites (data sources: Arango et al., 2015a, 2015b, 2015c, 2015d, 2015e; Bermúdez et al., 2015; Rodríguez et al., 2015a, 2015b, 2015c, 2015d, 2015e, 2018a; Zapata et al., 2015). The locations of the samples are shown in Figure 10, and the ages are presented in Table 5.

The ages reported for the eastern and western plutons show clustering according to the spatial position of the bodies in the UMV, and the different age groups identify at least three magmatic pulses. The western plutons record a main magmatic pulse between 193 and 186 Ma with some ages between 182 and 178 Ma. The eastern plutons indicate narrow crystallization ages ranging from 173 to 169 Ma with some inherited and crystallization ages ranging from 182 to 179 Ma. The latter age range suggests an intermediate magmatic event that is present both in the western and eastern plutons, which likely occurred during the migration of magmatism within the arc (Rodríguez et al., 2018a).

The ages of the volcanic units in the UMV match the spatial distribution of the ages of both the western and eastern plutons. The Saldaña Formation is exposed near the western plutons and has crystallization ages ranging from 188.9 ± 4.2 to 186 ± 2.0 Ma with some intermediate ages of approximately 183 Ma, which is similar to those obtained in the western plutons (Rodríguez et al., 2016b). The Pitalito Vulcanites are located near the eastern plutons and have ages ranging from 172.4 ± 1.7 to 168 ± 2.5 Ma with intermediate ages of approximately 183–178 Ma, similar to those obtained in the eastern plutons (Table 5).

Zircons from Jurassic granitoids and volcanic rock samples from the UMV have rare inherited cores (Table 5), which suggest that they are derived from the Neoproterozoic basement that outcrops in the UMV, including the Garzón Group, the Mancagua and Guapotón Gneisses, and Las Minas Metamorphites. The metamorphic and inherited ages are similar to those found in zircon cores of the Jurassic granitoids and volcanic rocks (MIA–538, GZ–6774, GR–6611B, GR–6636, and JGB–355; data sources: Arango et al., 2015a, 2015b, 2015c, 2015d, 2015e; Bermúdez et al., 2015; Rodríguez et al., 2015a, 2015b, 2015c, 2015d, 2015e, 2018a; Zapata et al., 2015). These zircons may have been inherited from the Paleozoic sedimentary rocks that overlie the Precambrian crystalline basement. A second group of inherited ages of 183–181 Ma is interpreted to repre-

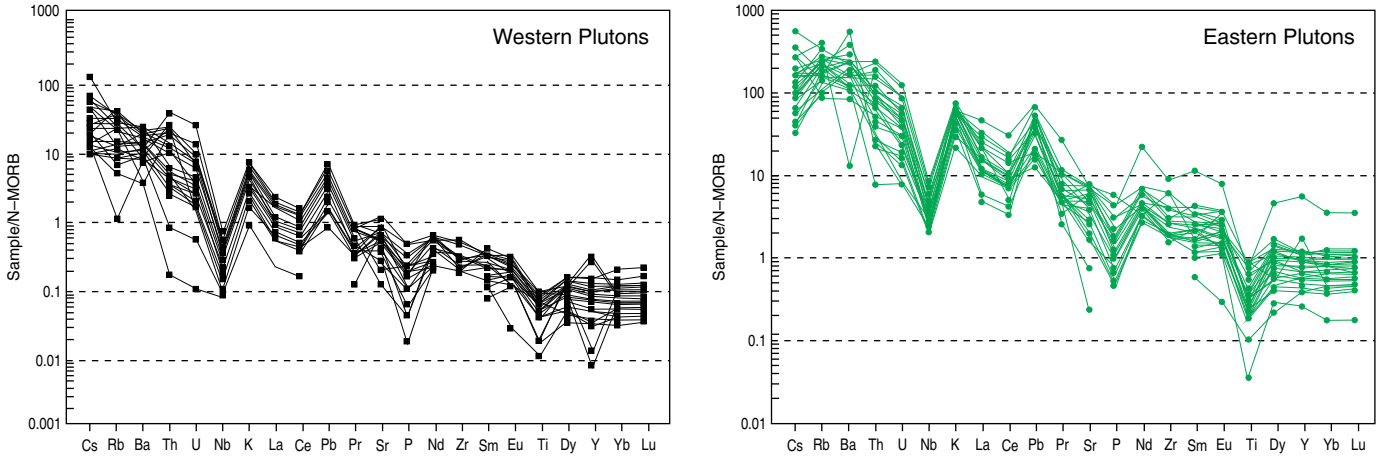

Figure 13. N–MORB–normalized trace element diagrams (Sun & McDonough, 1989) for both groups of plutons from the Upper Magdalena Valley (UMV). Data sources: Arango et al. (2015a, 2015b, 2015c, 2015d, 2015e); Bermúdez et al. (2015); Rodríguez et al. (2015a, 2015b, 2015c, 2015d, 2015e, 2018a); Zapata et al. (2015). Gray shading indicates the general pattern of trace elements of the arc.

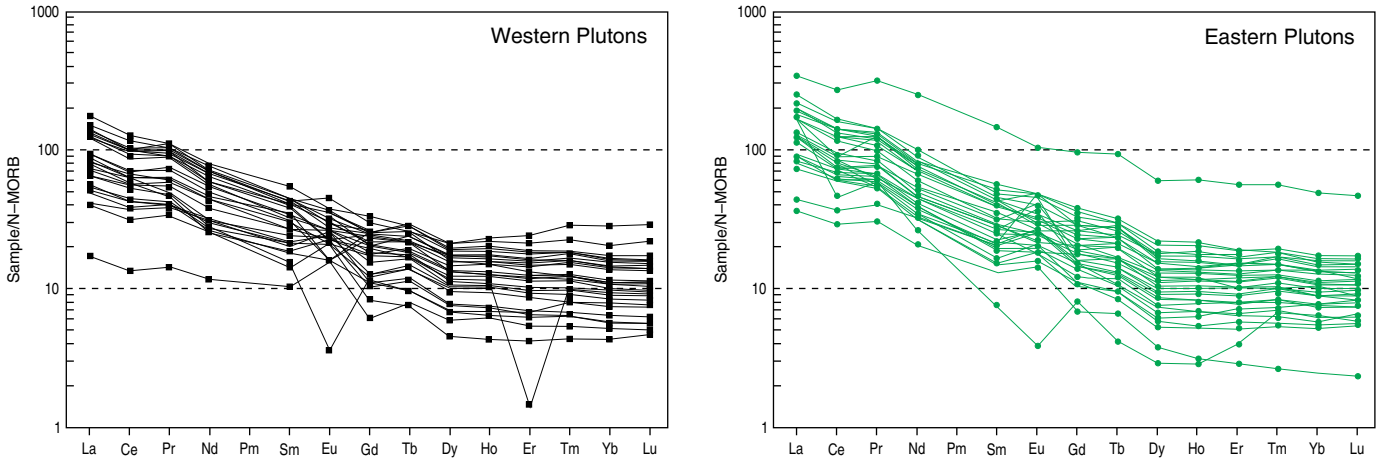

Figure 14. Chondrite–normalized rare earth element diagram (Nakamura, 1974) for both groups of plutons from the Upper Magdalena Valley (UMV). Data sources: Arango et al. (2015a, 2015b, 2015c, 2015d, 2015e); Bermúdez et al. (2015); Rodríguez et al. (2015a, 2015b, 2015c, 2015d, 2015e; 2018a); Zapata et al. (2015).

sent zircons or zircon cores that were inherited from previous pulses of magmatism in the same arc, which were assimilated or reincorporated in subsequent pulses in the magmatic chamber.

4.3. Northern Block of the Ibagué Batholith (NBIB)

The northern section of the Ibagué Batholith is called the "northern block of the Ibagué Batholith (NBIB)" in this paper. This block is bounded by the Ibagué Fault to the south and by the Otú–Pericos Fault to the east, and it is located southwest of the town of Armero to the Ibagué Fault line on the eastern flank of the Central Cordillera of Colombia (Figures 1, 16). Two intrusives, the Anzoátegui Metatonalite to the west and the Ibagué Tonalite to the east, have been identified in this block. They are separated by a block of metamorphic rocks that consists of schists, gneisses, quartzites, and amphibolites (Tierradentro Gneisses and Amphibolites sensu Barrero & Vesga, 1976).

The Anzoátegui Metatonalite has an irregular elongated shape that is approximately 55 km long and 27 km wide (Figure 16). It is in intrusive and locally faulted contact on the east and west with the Tierradentro Gneisses and Amphibolites. The granitoid shows mineral orientation and local development of gneissic structures (Figure 17a). The Ibagué Tonalite is elongated in the N–S direction and is approximately 78 km long and 19 km wide. It is covered by alluvial deposits and alluvial fans to the east and intrudes the metamorphic strip of Tierradentro Gneisses and Amphibolites to the west (Figure 16). It has a granular texture and an isotropic (Figure 17b) to locally oriented structure near the contact with the metamorphic block (Figures 16, 17). Both plutons are intruded by andesitic and dacitic dikes.

Table 4. Chondrite–normalized rare earth element diagram (Nakamura, 1974) for granitoids from the UMV.

IGM	UNIT	Eu/Eu*	(La/Yb)n	(La/Sm)n	(Ce/Yb)n	(Ce/Sm)n	(Eu/Yb)n	∑REE
			Western Plutons					
CB0007A*	Las Minas Monzodiorite	0.9	6.92	2.92	5.53	2.33	1.77	116.6
900752	Las Minas Monzodiorite	1.26	11.23	2.84	9.12	2.31	4.14	219.53
900643	Anchique Quartz Monzonite	1.08	15.05	4.29	11.23	3.2	2.83	204.95
900642	Anchique Quartz Monzonite	1.02	15.99	4.29	11.65	3.13	2.77	252.38
900647	Los Naranjos Quartz Monzonite	1.21	5.04	2.1	4.35	1.81	2.24	145.26
900651	Los Naranjos Quartz Monzonite	0.93	5.71	2.72	4.65	2.22	1.49	145.53
900650	Los Naranjos Quartz Monzonite	0.95	8.16	2.94	6.34	2.28	2.03	217.48
900641	Los Naranjos Quartz Monzonite	0.89	6.54	2.99	4.86	2.22	1.46	224.33
900649	Los Naranjos Quartz Monzonite	0.82	9.15	3.51	7.03	2.69	1.65	240.88
900823	San Cayetano Quartz Monzonite	1.07	9.11	3.04	6.27	2.09	2.57	197.82
900827	San Cayetano Quartz Monzonite	0.72	9.17	3.52	6.36	2.44	1.52	201.28
900825	San Cayetano Quartz Monzonite	0.69	8.04	3.08	6.06	2.32	1.43	201.81
900826	San Cayetano Quartz Monzonite	0.51	4.95	3.88	3.69	2.89	0.55	222.14
900824	San Cayetano Quartz Monzonite	0.89	8.52	2.57	6.22	1.88	2.3	237.3
900719	El Astillero Quartz Monzodiorite	1.1	6.2	2.62	4.88	2.07	2.25	132.55
900721	El Astillero Quartz Monzodiorite	1.11	7.57	2.95	5.73	2.23	2.43	142.48
900720	El Astillero Quartz Monzodiorite	0.94	6.58	2.72	4.92	2.04	1.89	163.41
900678	Páez Quartz Monzodiorite	1.97	3.33	1.7	2.63	1.34	3.01	36.68
900683	Páez Quartz Monzodiorite	1.63	7.06	2.16	5.55	1.7	3.96	74.86
900725	Páez Quartz Monzodiorite	1.13	9.79	3.12	7.28	2.32	2.77	89.79
900738	Páez Quartz Monzodiorite	1.14	4.06	1.68	3.71	1.54	2.32	91.87
900658	Páez Quartz Monzodiorite	1.46	6.61	2.25	5.15	1.75	3.28	92.17
900679	Páez Quartz Monzodiorite	1.27	5.72	2.4	4.71	1.98	2.29	94.39
900665	Páez Quartz Monzodiorite	1.28	6.05	2.53	5.07	2.12	2.32	98.43
900664	Páez Quartz Monzodiorite	1.73	10.36	3.28	8.26	2.62	4.04	108.23
900673	Páez Quartz Monzodiorite	1.96	18.86	5.8	13.14	4.04	4.87	108.29
900737	Páez Quartz Monzodiorite	0.27	11.35	5.72	8.05	4.06	0.47	119.76
900681	Páez Quartz Monzodiorite	1.28	7.68	2.41	6.62	2.08	3.07	120.75
900722	Páez Quartz Monzodiorite	0.97	8.07	2.89	6.52	2.33	2.28	138.87
900730	Páez Quartz Monzodiorite	0.6	5.71	2.97	4.4	2.29	1	161.17
900667	Páez Quartz Monzodiorite	1.1	8.05	3.12	6.2	2.4	2.12	228.64
			Eastern Plutons					
900718	Altamira Monzogranite	0.89	12.49	5.52	7.03	3.11	1.74	165.9
900734	Altamira Monzogranite	0.83	12.29	4	6.56	2.14	2.1	226
900745	Altamira Monzogranite	0.51	26.95	23.21	7.1	6.12	0.61	127.1
900749	Altamira Monzogranite	0.68	10.37	4.38	7.33	3.09	1.38	186.4
CB0005*	Altamira Monzogranite	1.49	14.81	2.73	11.77	2.17	5.82	62.28
900691	Altamira Monzogranite	1.2	17.65	7.28	10.92	4.51	2.35	166.6
900692	Altamira Monzogranite	1.03	13.09	4.13	10.17	3.21	2.54	250.2
900694	Altamira Monzogranite	1.54	20.56	6.69	14.41	4.69	3.81	147.1
900697	Altamira Monzogranite	1.13	14.75	4.49	10.71	3.26	3.03	331.7
900699	Altamira Monzogranite	1.1	16.77	5.43	11.25	3.65	2.68	338
900703	Altamira Monzogranite	1.44	14.9	7.54	9.13	4.62	2.35	139.1

Table 4. Chondrite–normalized rare earth element diagram (Nakamura, 1974) for granitoids from the UMV *(continued).*

IGM	UNIT	Eu/Eu*	(La/Yb)n	(La/Sm)n	(Ce/Yb)n	(Ce/Sm)n	(Eu/Yb)n	∑REE
900704	Altamira Monzogranite	1.15	15.28	5.13	10.6	3.56	2.74	230.4
900706	Altamira Monzogranite	1.04	15.95	5.22	10.36	3.39	2.45	269.3
900708	Altamira Monzogranite	1.03	14.89	5.03	10.34	3.49	2.38	283.1
900709	Altamira Monzogranite	1.03	12.93	4.37	9.4	3.18	2.34	287.8
900711	Altamira Monzogranite	1.24	17.54	6	11.57	3.96	3.11	119.6
900715	Garzón Granite	1.17	14.9	4.74	10.51	3.35	3.11	134.5
900716	Garzón Granite	1.43	11.14	3.77	8.01	2.71	3.25	182.7
900698	Teruel Quarz Latite	1.83	13.54	4.88	9.09	3.27	3.97	177.5
900712	Teruel Quarz Latite	1.7	12.13	4.38	8.41	3.04	3.65	196.4
900713	Teruel Quarz Latite	2.67	21.89	5.99	13.81	3.78	8.35	159.9
900781	Mocoa Monzogranite	1.05	10.35	2.9	7.88	2.21	3.09	272.2
900782	Mocoa Monzogranite	1.1	9.28	3.11	7	2.34	2.72	267.5
900784	Mocoa Monzogranite	1.02	11.28	4.67	8.17	3.39	2.04	188.2
900785	Mocoa Monzogranite	1.14	11.83	4.71	7.92	3.15	2.41	176.5
900813	Mocoa Monzogranite	1.06	11.88	5.35	7.9	3.56	1.99	162.1
900815	Mocoa Monzogranite	0.86	10.75	4.9	7.29	3.32	1.59	172
900816	Mocoa Monzogranite	1.4	12.38	4.14	8.5	2.84	3.46	137.3
900818	Mocoa Monzogranite	1.52	10.99	3.82	8.53	2.97	3.67	127.4
900819	Mocoa Monzogranite	1.36	12.72	4.97	8.46	3.31	2.95	155.3
900820	Mocoa Monzogranite	1.46	9.78	4.27	6.8	2.97	2.83	126.8
900821	Mocoa Monzogranite	1.18	9.65	4.44	6.53	3	2.17	158.9
900822	Mocoa Monzogranite	0.83	11.39	4.18	8.97	3.29	1.92	285.8
900764	Sombrerillo Quartz Monzonite	1.35	4.84	1.89	4.1	1.6	2.94	93.44
900765	Sombrerillo Quartz Monzonite	0.86	5.5	2.55	4.45	2.06	1.57	170
900766	Sombrerillo Quartz Monzonite	1.01	6.37	2.54	5.23	2.08	2.13	137.4
900768	Sombrerillo Quartz Monzonite	1.4	7.28	2.57	5.98	2.11	3.27	202.1
900768	Sombrerillo Quartz Monzonite	1.15	6.54	2.49	5.47	2.08	2.4	165.3
900768	Sombrerillo Quartz Monzonite	0.89	6.25	2.94	5.16	2.43	1.62	149
900808	Sombrerillo Quartz Monzonite	0.92	5.57	2.79	4.64	2.33	1.54	147.8
900810	Sombrerillo Quartz Monzonite	0.88	7.07	2.38	5.54	1.86	2.11	664.9

Source: Data from Arango et al. (2015a, 2015b, 2015c, 2015d, 2015e); Bermúdez et al. (2015); Rodríguez et al. (2015a, 2015b, 2015c, 2015d, 2015e, 2018a); Zapata et al. (2015).
n—normalized to chondrite values of Nakamura (1974).

4.3.1. Petrography

The Anzoátegui Metatonalite consists of metatonalites and metagranodiorites (Figure 18; Table 6) with polycrystalline quartz in polygonal to sutured mosaics (Figure 17c, 17d), which resulted from metamorphic recrystallization. The rocks are equigranular to inequigranular, medium–grained, white or gray with black spots, and have mineral orientation in most outcrops. Locally, the rocks lack mineral orientation and are isotropic. Plagioclase is zoned from oligoclase to sodic andesine (An28 to An34) based on the symmetrical zone albite twin method of Michel–Lévy. Orthoclase is rare and varies to interstitial microcline. The rocks contain mafic minerals such as biotite, which is usually altered to slightly oriented chlorite, and hornblende with clinopyroxene cores. Opaque minerals, apatite, zircon, and titanite are accessory minerals.

The Ibagué Tonalite consists of tonalites, subordinate quartz diorites and granodiorites (Figure 18; Table 7). It is white or gray with black spots and has an equigranular texture. The rocks are composed of anhedral quartz, oligoclase to sodic andesine plagioclase, and occasional interstitial orthoclase. It contains mafic minerals such as hornblende and biotite that are partly altered to chlorite, and it contains accessory minerals such as zircon, apatite, titanite, and opaque minerals (Figure 17e, 17f).

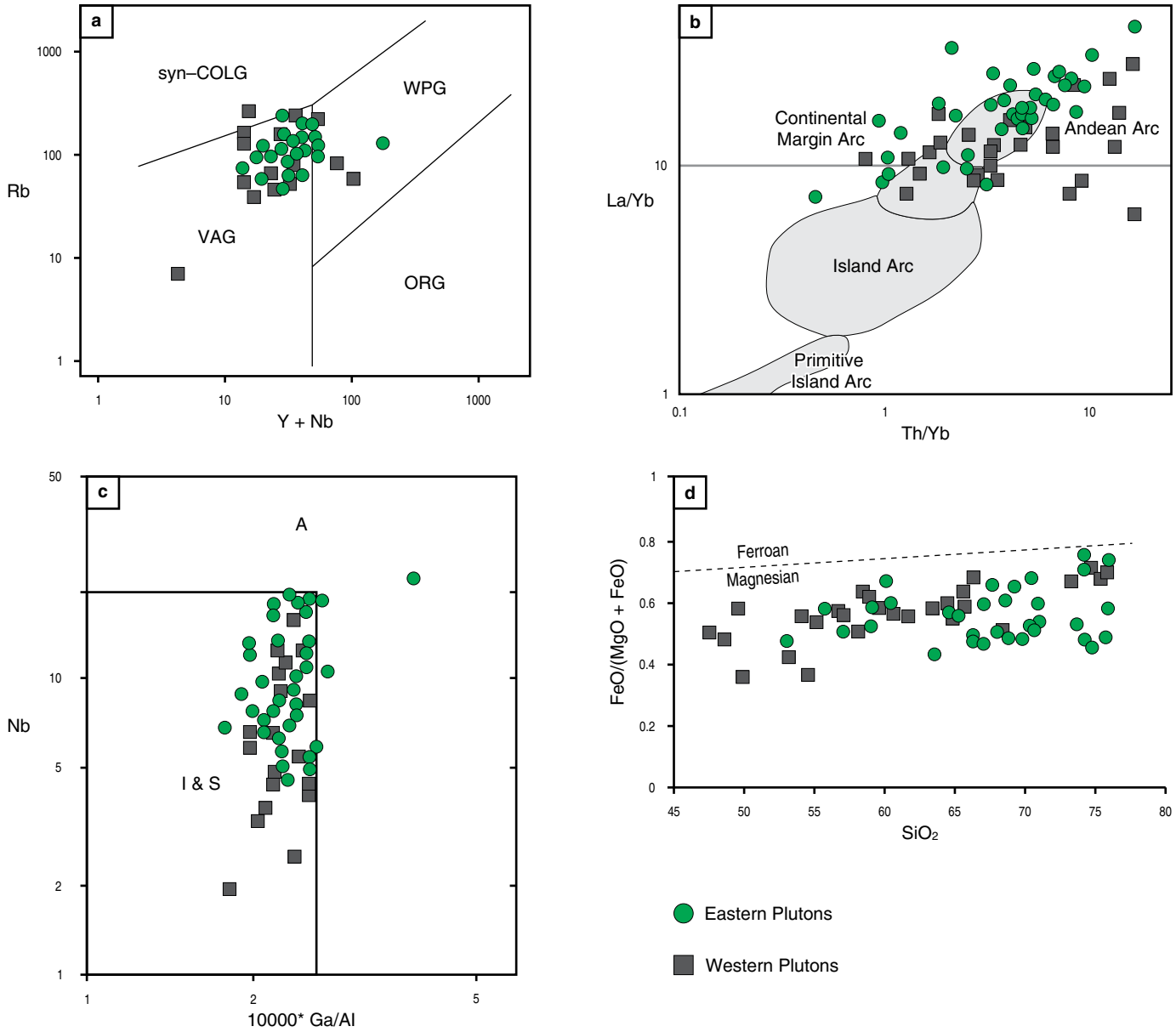

Figure 15. Geotectonic discrimination diagrams: **(a)** Y+Nb vs. Rb diagram of Pearce et al. (1984), **(b)** La/Yb vs. Th/Yb diagram of Condie (1989), **(c)** (Ga/al*10,000) vs. Nb diagram of Whalen et al. (1987), **(d)** FeO/(FeO + MgO) vs. SiO_2 diagram of Frost et al. (2001). Data sources: Arango et al. (2015a, 2015b, 2015c, 2015d, 2015e); Bermúdez et al. (2015); Rodríguez et al. (2015a, 2015b, 2015c, 2015d, 2015e, 2018a); Zapata et al. (2015).

4.3.2. Geochemistry

Whole–rock chemical analyses were performed on 3 rocks from the Anzoátegui Metatonalite and 4 rocks from the Ibagué Tonalite (Table 8). In addition, 8 sets of data from Bustamante et al. (2016) were compiled (see Table 1, Supplementary Information). The samples from both plutons have SiO_2 contents ranging from 50.3% to 67.8%. The K_2O contents range from 0.84% to 3.3% with values from 1% to 2% in most samples. CaO ranges from 3.35% to 9.8%, and TiO_2 is <1% except in sample JGB–492 (1.4% TiO_2). The plutons cluster in the field of tonalites and granodiorites in the TAS diagram, with some reaching the field of quartz diorites and quartz monzodiorites (Figure 19a), which is consistent with the petrographic data. The samples show decreases in TiO_2, MgO, and CaO and an increase in K_2O with increasing SiO_2.

The rocks plot in the field of the calc–alkaline series (Figure 19b, 19c). These rocks are mostly metaluminous (Figure 19d) with A/CNK ratios ranging from 0.7 to 1.05 and A/NK ratios ranging from 1.4 to 3, which indicates a low contribution of crustal material to the magma during the formation of the plutons.

Table 5. LA–ICP–MS U–Pb zircon ages of granitoid bodies and volcanic rocks from the UMV.

Sample	Latitude N	Longitude W	Classification	Unit	Age (Ma)	Inherited ages (Ma)
Western Plutons						
MIA–438	3° 33' 46.184"	75° 08' 26.761"	Monzonite	Anchique Quartz Monzonite	183.5 ± 3	
MIA–440	3° 39' 47.772"	75° 06' 20.693"	Monzonite	Anchique Quartz Monzonite	186.4 ± 1.4	
JGB–357	3° 41' 17.677"	75° 10' 51.437"	Quartz monzonite with px	San Cayetano Quartz Monzonite	173.3 ± 1.3	
JGB–356	3° 39' 52.894"	75° 10' 16.665"	Quartz monzonite with px	San Cayetano Quartz Monzonite	195.8 ± 1.5	
JGB–345	3° 21' 58.505"	75° 20' 38.041"	Monzodiorite	Los Naranjos Quartz Monzonite	187.9 ± 1.3	
GR–6634	2° 39' 57.305"	75° 55' 35.226"	Granodiorite	Páez Quartz Monzodiorite	180.2 ± 1.6	
GR–6639	2° 37' 45.611"	75° 44' 07.812"	Tonalite	Páez Quartz Monzodiorite	181.83 ± 0.91	
GR–6645	2° 15' 07.848"	75° 58' 19.470"	Granite	Páez Quartz Monzodiorite	191.9 ± 1.4	
MIA–454	2° 56' 37.242"	75° 30' 41.603"	Monzodiorite	Páez Quartz Monzodiorite	193.13 ± 1.4	
MIA–499	2° 32' 51.609"	75° 49' 56.785"	Quartz monzodiorite	Páez Quartz Monzodiorite	181.7 ± 3.8	
GR–6625	2° 20' 19.440"	75° 44' 44.618"	Monzodiorite	El Astillero Quartz Monzodiorite	187 ± 3.3	
MIA–482	2° 11' 43.395"	75° 51' 27.021"	Quartz monzodiorite	Las Minas Monzodiorite	181.6 ± 3.4	
Eastern Plutons						
GR–6585	2° 36' 17.331"	75° 19' 09.103"	Aplite in granodiorite	Algeciras Monzogranite	178.6 ± 1.2	
GR–6586	2° 35' 59.239"	75° 16' 49.980"	Granodiorite	Algeciras Monzogranite	171 ± 2.5	
GR–6589	2° 28' 22.946"	75° 24' 58.344"	Granite	Algeciras Monzogranite	169.6 ± 1.2	
GZ–6750	2° 45' 36.701"	75° 11' 48.824"	Quartz monzonite	Algeciras Monzogranite	179 ± 1.9	
MIA–458	2° 46' 25.626"	75° 30' 46.993"	Quartz monzonite	Teruel Quartz Latite	170.50 ± 1.10	181.1 ± 1.70
MIA–460	2° 44' 08.778"	75° 32' 25.933"	Quartz monzonite	Teruel Quartz Latite	174.1 ± 2.0	
GR–6619	2° 10' 01.284"	75° 36' 36.632"	Granite	Garzón Granite	170.8 ± 2.4	
GR–6652	1° 44' 56.859"	76° 01' 25.944"	Granite	Altamira Monzogranite	171.6 ± 1	
JGB–390	1° 50' 36.121"	75° 54' 31.726"	Granite	Altamira Monzogranite	172 ± 3.9	
MIA–478	1° 53' 05.855"	75° 53' 44.793"	Monzogranite	Altamira Monzogranite	169.4 ± 3.2	
GZ–6780	1° 10' 04.832"	76° 51' 39.289"	Quartz monzodiorite	Sombrerillo Quartz Monzonite	173.8 ± 2.2	
MIA–512	1° 48' 42.758"	76° 17' 34.195"	Granodiorite	Sombrerillo Quartz Monzonite	176.3 ± 2.5	
MIA–525	1° 54' 17.460"	76° 08' 48.014"	Monzogranite Saprolite	Sombrerillo Quartz Monzonite	181.5 ± 4.0	
GR–6672	1° 04' 17.186"	76° 44' 12.719"	Quartz monzodiorite	Mocoa Monzogranite	171.6 ± 1.2	
MIA–538	1° 04' 08.328"	76° 46' 16.618"	Granitic saprolite	Mocoa Monzogranite	181.8 ± 1.3	939 ± 40
MIA–543	1° 12' 06.116"	76° 40' 54.752"	Granitic saprolite	Mocoa Monzogranite	170.7 ± 2.1	
Volcanic Rocks						
GR–6611B	2° 48' 40.70"	75° 35' 22.34"	Phenotrachyte	Saldaña Formation	188.9 ± 1.6	923 ± 24, n=1
GR–6636	2° 19' 46.38"	75° 48' 47.34"	Andesite	Saldaña Formation	187.1 ± 2.4	510, n=1; 1960, n=1
GR–6664	1° 26' 0.53"	76° 26' 47.05"	Andesite	Saldaña Formation	183.3 ± 1.1	
MIA–504	2° 7' 48.30"	76° 4' 7.02"	Andesite	Saldaña Formation	188.9 ± 4.2	
MIA–519	2° 9' 24.95"	76° 0' 59.55"	Andesite	Saldaña Formation	188.1 ± 3.4	
GR–6579	3° 28' 55.25"	75° 14' 42.79"	Lithic tuff	Saldaña Formation	187.2 ± 2.8	
GZ–6775	1° 6' 43.10"	76° 50' 5.32"	Crystal tuff	Saldaña Formation	186.8 ± 2.0	
GZ–6774	1° 5' 35.28"	76° 50' 20.90"	Crystal tuff	Saldaña Formation	172.9 ± 1.3	223.48 ± 9.5, n=1 and 906.3 ± 21.1, n=1
JGB–355	2° 48' 59.55"	75° 21' 46.52"	Tuff	Pitalito Vulcanites	178.7 ± 4.5	980–1060, n=4; 1460, n=1; 1570, n=1; 1630, n=1; 2770, n=1
GR–6649	1° 45' 42.92"	76° 2' 25.09"	Phenocryst andesite	Pitalito Vulcanites	172.4 ± 1.7	183.30 +0.30/-3.30, n=20

Table 5. LA–ICP–MS U–Pb zircon ages of granitoid bodies and volcanic rocks from the UMV *(continued)*.

Sample	Latitude N	Longitude W	Classification	Unit	Age (Ma)	Inherited ages (Ma)
GZ–6766	1° 57' 1.26"	76° 3' 20.24"	Dacite	Pitalito Vulcanites	170.7 ± 2.4	
GZ–6769	1° 40' 54.67"	76° 13' 7.69"	Rhyolite	Pitalito Vulcanites	168 ± 2.5	

Source: Data from Arango et al. (2015a, 2015b, 2015c, 2015d, 2015e); Bermúdez et al. (2015); Rodríguez et al. (2015a, 2015b, 2015c, 2015d, 2015e, 2018); Zapata et al. (2015).

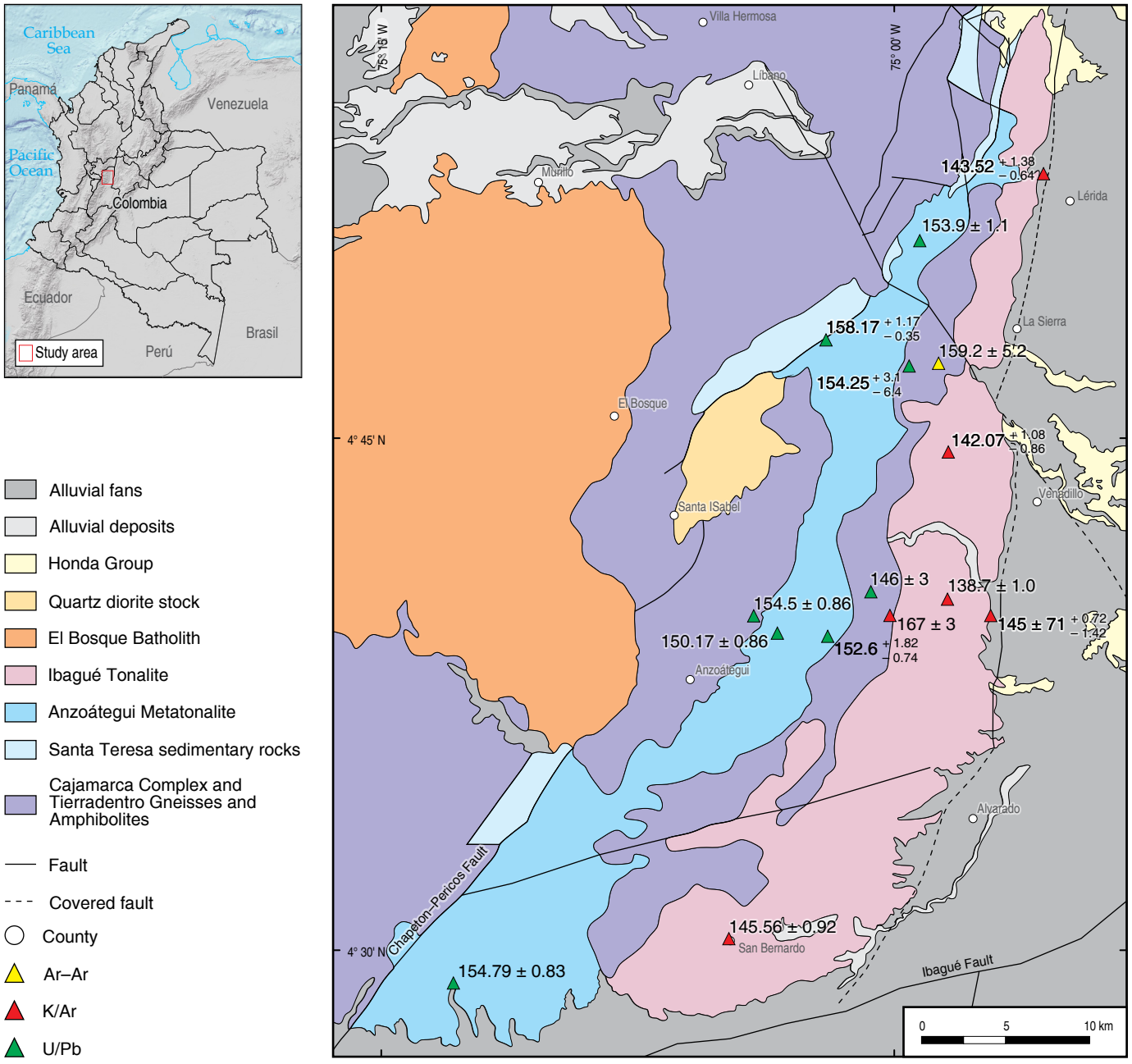

Figure 16. Geological map and U–Pb zircon ages of the Anzoátegui Metatonalite and Ibagué Tonalite. The K–Ar data are from Vesga & Barrero (1978) and McCourt et al. (1984), the Ar–Ar data are from Villagómez et al. (2011), and the U–Pb data are from Bustamante et al. (2016) and this study.

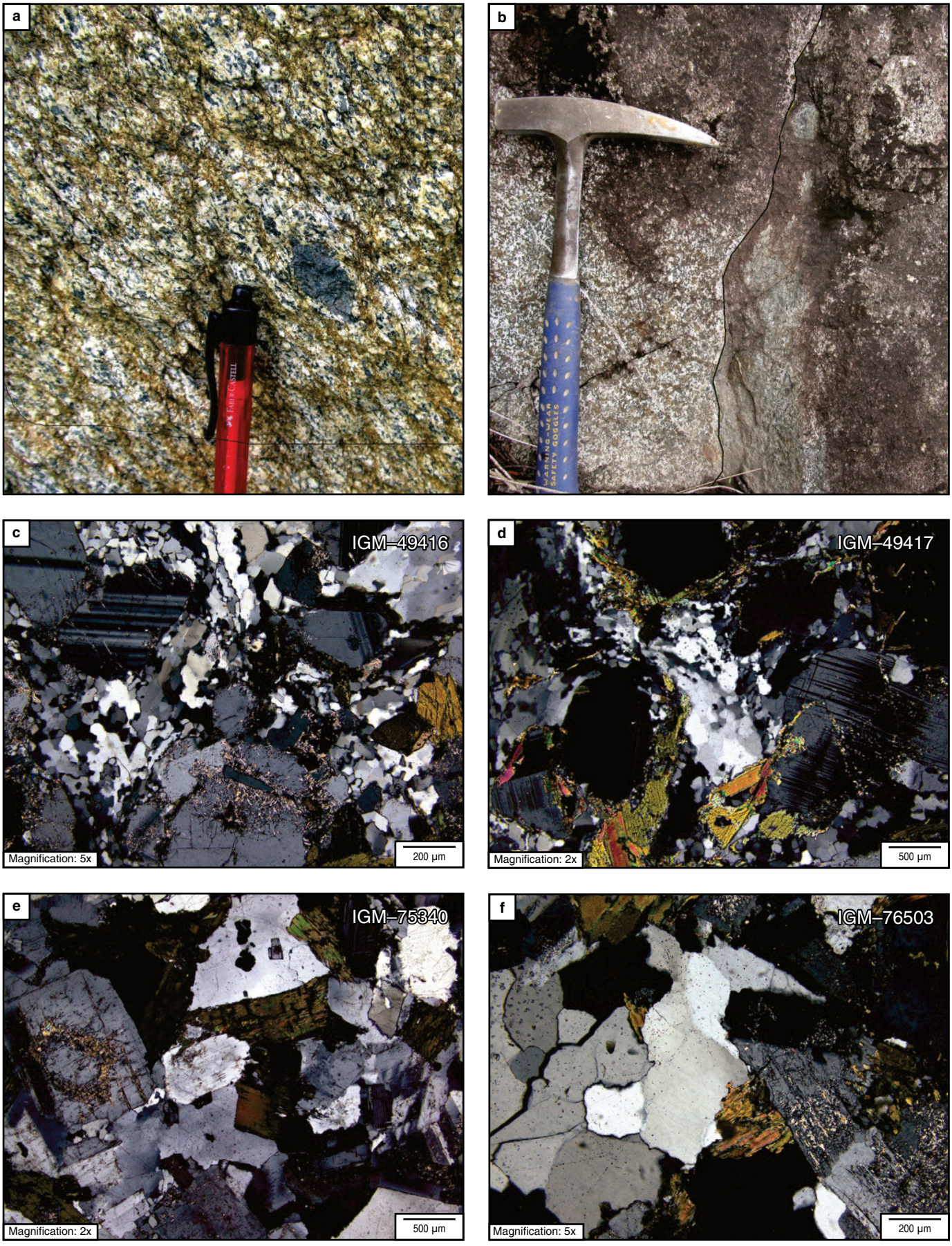
a
b
c
IGM–49416
Magnification: 5x
200 µm
d
IGM–49417
Magnification: 2x
500 µm
e
IGM–75340
Magnification: 2x
500 µm
f
IGM–76503
Magnification: 5x
200 µm

Figure 17. (a) Macroscopic view of the Anzoátegui Metatonalite (IGM–49416, IGM–49417) with mineral orientation and enclaves. **(b)** Ibagué Tonalite with schist xenolith and granular texture. **(c), (d)** microscopic views of the Anzoátegui Metatonalite (IGM–49416, IGM–49417). **(e), (f)** microscopic views of the Ibagué Tonalite (IGM–75340, IGM–76503).

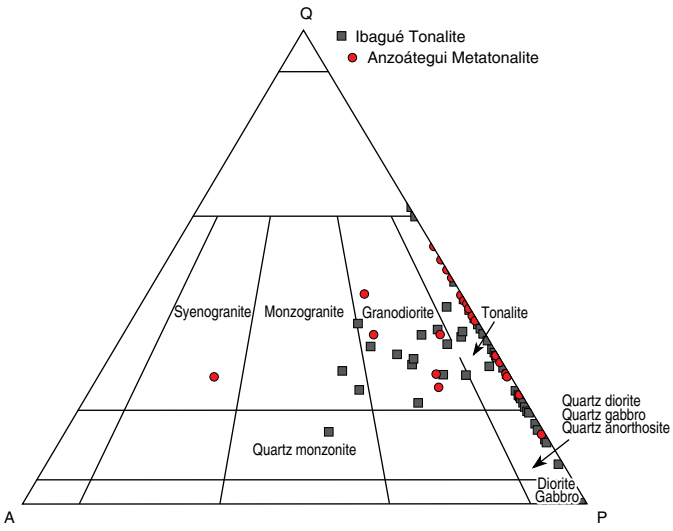

Figure 18. Modal compositions of the Anzoátegui Metatonalite and Ibagué Tonalite in the NBIB. Quartz, Alkali feldspar, Plagioclase, Feldspathoid (QAPF) diagrams of Streckeisen (1974).

Both tonalitic plutons show markedly negative Nb, Ti, Ce, and P anomalies and positive anomalies and high values of Cs, Ba, Th, Sr, K, Pb, and Rb, similar to the patterns of continental margin magmatic arcs (Pearce, 1996) with gradual depletion from LILE to HFSE (Figure 19e).

Based on the values of Nakamura (1974), the patterns of the chondrite–normalized REE for both plutons are subparallel with negative slopes and are similar to patterns for rocks that are generated in subduction environments above the subducted plate, with enrichment in LREE and depletion in HREE (Figure 19f). These results are consistent with those of Bustamante et al. (2016). They have negative Eu anomalies with Eu/Eu* ratios ranging from 0.52 to 0.93, indicating plagioclase fractionation at the source (Table 9). The $(La/Yb)_n$ ratios range from 3.9 to 10.9 with no major differences in the $(La/Sm)_n$, $(Ce/Yb)_n$, $(Ce/Sm)_n$, and $(Eu/Yb)_n$ ratios between the two plutons (Table 9).

In the tectonic environment discrimination diagrams, the samples from both intrusives plot within continental margin arcs of calc–alkaline affinity (Figure 20a) and within I–type granites (Figure 20b).

4.3.3. Geochronology

Eight rocks from the NBIB were dated, including three samples from the Anzoátegui Metatonalite, two from the Ibagué Tonalite, and three from the Tierradentro Gneisses and Amphibolites (Table 10).

4.3.3.1. Igneous Ages

The following samples from the Anzoátegui Metatonalite were dated: one tonalite (GOE–1088) with a weighted mean age of 154.79 ± 0.83 Ma (n = 91, MSWD = 3.1, and Th/U ratios ranging from 0.3 to 1.3); one metatonalite (LMC–104) with a U–Pb weighted mean age of 153.9 ± 1.1 Ma (n = 39, MSWD = 2.5, and Th/U ratios ranging from 0.43 to 0.9); and one metagranodiorite (AMC–0153) with a U–Pb zircon weighted mean age of 159.91 ± 0.69 Ma (n = 67, MSWD = 1.4, and Th/U ratios ranging from 0.31 to 1.24) (Figure 21). These ages represent magmatic crystallization ages based on the concentric structures of the zircons in CL images and the Th/U ratios.

Two samples from the Ibagué Tonalite were dated, including a granodiorite (MIG–076) with a U–Pb weighted mean age of 145.52 ± 0.82 (n = 67, MSWD = 4.5, and Th/U ratios ranging from 0.34 to 1.1; Figure 21) and a tonalite (JPZ–001A) with a U–Pb zircon weighted mean age of 138.48 ± 0.95 Ma (n = 53, MSWD = 2.2, and Th/U ratios ranging from 0.45 to 0.88). These ages represent magmatic crystallization ages based on the concentric structures of the zircons in CL images and the Th/U ratios.

4.3.3.2. Basement Ages

Three samples from the Tierradentro Gneisses and Amphibolites unit were dated, including two amphibolites from the metamorphic strip that separates the two intrusive bodies (AMC–0171 and MIG–074) and one sample from a metamorphic strip west of the Anzoátegui Metatonalite (AMC–0152). The results are shown in Figure 22. AMC–0171 corresponds to an amphibolite with a weighted mean age from zircon edges of 167.3 ± 3.0 Ma (n = 11, MSWD = 3.2, and Th/U ratios ranging from 0.012 to 0.048), in which the individual ages range from 174.6 Ma to 161.3 Ma. These are interpreted as metamorphic ages. AMC–0171 shows inheritances from the Mesoproterozoic (n = 1), Neoproterozoic (1141 to 728 Ma; n = 9), Cambrian (n = 5), Devonian (n = 4), Permian (264.7 Ma; n = 1), Triassic (223 Ma to 240 Ma; n = 3), and Early Jurassic (187.1 ± 3.8 Ma; n = 9). The structures of the zircons are complex and are characterized by abundant inherited cores and metamorphic overgrowths. MIG–074 also corresponds to an amphibolite, and the analyzed zircons were concentrated from a saprolite. Thirty–two consistent analyses indicate a median age of 154.5 +3.1/–6.4 Ma, which is interpreted as a magmatic crystallization age based on the concentric, zoned structures of the zircons in the CL images and the Th/U ratios ranging from 0.25 to 3.9. This sample yielded the following ages from inherit-

Table 6. Modal compositions of rocks from the Anzoátegui Metatonalite.

Anzoátegui Metatonalite															
IGM	**Sample**	**Longitude W**	**Latitude N**	**Qtz**	**Pl**	**Kfs**	**Cpx**	**Hbl**	**Bt**	**Op**	**Ap**	**Zrn**	**Ttn**	**Ep**	**Classification**
49277	GB–1422	74° 58' 14.24''	4° 51' 11.38''	7	41	Tr	Tr	33	19		Tr	Tr	Tr	Tr	Quartz diorite
901079	LMC–104	74° 59' 3.23''	4° 50' 36.88''	18	45	10		15	12	Tr	Tr	Tr		Tr	Granodiorite
77804	PM–8221	75° 9' 13.61''	4° 33' 21.50''	26.3	57.7	12.4	Tr	2.1	1.5	Tr	Tr	Tr	Tr		Metagranodiorite
49668	DMT–5474	75° 2' 54.50''	4° 38' 5.88''	25.4	31.7	14.3	1.6	7.9	12.7	Tr			4.8		Metagranodiorite
77805	PM–8224	75° 9' 27.27''	4° 33' 46.22''	31	49.6	7	Tr	3.1	9.3	Tr	Tr	Tr	Tr		Metagranodiorite
49444	VW–4539	75° 1' 35.44''	4° 43' 20.10''	17.5	13	34.8	Tr	18.8	Tr				5.8	Tr	Metagranodiorite
49644	IB–167	75° 2' 12.49''	4° 40' 10.28''	25.3	22.3	10	Tr	38.7	Tr						Metagranodiorite
48469	GB–1104	74° 57' 0.70''	4° 52' 41.64''	21.8	51.5	Tr	Tr	16.5	8	1.5	0.25	0.25	0.25	Tr	Metatonalite
48473	GB–1114	74° 56' 13.30''	4° 52' 29.66''	22.5	33.3	Tr	Tr	24.3	5	1.4		3.6	6.8		Metatonalite
49304	HP–3214	75° 0' 8.98''	4° 45' 24.89''	21	33	Tr	Tr	15	5		Tr		Tr	7	Metatonalite
49243	PM–6028	75° 0' 24.49''	4° 48' 37.56''	19	51	Tr	Tr	0	13		Tr	Tr	Tr	4	Metatonalite
49416	PM–6388	75° 2' 21.72''	4° 41' 58.99''	24	53	Tr	Tr	10	8		Tr	Tr	3	Tr	Metatonalite
49417	PM–6391	75° 2' 32.10''	4° 41' 56.37''	35	39	Tr	Tr	9	16		Tr	Tr	1	Tr	Metatonalite
48470	GB–1105	74° 56' 55.50''	4° 52' 40.02''	31.5	50.5	Tr	Tr	12.5	4	0.75	0.35	0.2	0.2	Tr	Metatonalite
48471	GB–1109	74° 56' 30.51''	4° 52' 37.12''	33.5	47	Tr	Tr	8	10.5	0.6	0.3		0.1	Tr	Metatonalite
68436	PM–7124	75° 3' 20.60''	4° 35' 58.24''	27.3	26.1	Tr	Tr	33	10.2	Tr		3.4			Metatonalite
49673	DMT–5519	75° 3' 41.81''	4° 37' 33.26''	26.7	28	Tr	Tr	22.7	6.7	Tr	0		2.7	4	Metatonalite
901072	JPZ–004	75° 2' 40.24''	4° 39' 4.03''	29.2	37.5			25	2.8	1.4	2.8		1.4		Metatonalite
49425	VW–4349	75° 2' 57.19''	4° 47' 7.19''	39	33.7				26	Tr			1.3		Metatonalite
49298	HP–3169	74° 59' 17.87''	4° 49' 27.62''	18	61	Tr	Tr	14	5		Tr	Tr	0	Tr	Tonalite
49301	HP–3195	74° 58' 47.30''	4° 50' 41.88''	16	44	Tr	Tr	25	15		Tr	Tr		Tr	Tonalite
49643	IB–643	75° 3' 13.15''	4° 40' 6.29''	20	44.1	Tr	Tr	22	10.2		1.7		1.7		Tonalite
49647	IB–187	75° 4' 10.95''	4° 36' 49.60''	26.5	42.2	Tr	4.8	21.7	0	Tr			2.4	2.4	Tonalite
49646	IB–180	75° 4' 58.59''	4° 36' 15.03''	22.9	31.3	Tr	Tr	31.3	0	1	2		7.3	4.2	Tonalite

Tr—Traces of accessory mineral.

ed cores: a crystal with Neoproterozoic ages of 1084.6 Ma (n = 1) and 987.9 Ma (n = 1), a concordant age of 207.6 Ma (n = 1), and a discordant age of 187 Ma (n = 1). Sample AMC–0152, which was collected from an amphibolite, yielded a weighted mean age of 154.5 ± 3.6 Ma (n = 13, MSWD = 6.3, and Th/U ratio <0.2). The zircons are homogeneous, and some have luminescent borders and rounded ends (Figure 22). They are interpreted as metamorphic zircons.

5. Discussion

5.1. SM, UMV, and NBIB Basements

Our interpretation of the distribution of metamorphic basement related to the Jurassic magmatism in Colombia is shown in Figure 1b, which shows three basement units. These include an Early Neoproterozoic basement, which corresponds to the Andaquí Terrane and most of the Chibcha Terrane based on Restrepo & Toussaint (1989); a Paleozoic basement, which corresponds to most of the Norte de Santander, Santander, Floresta, and Quetame Terranes, according to Etayo–Serna et al. (1983); and an Ordovician and Mesozoic basement, which includes most of the Tahamí Terrane as described by Restrepo & Toussaint (1989), the Tierradentro Gneisses and Amphibolites (previously included in the Chibcha Terrane by Restrepo & Toussaint, 1989), and the Anacona Terrane (Martens et al., 2014; Restrepo et al., 2009).

In the SM, Late Triassic – Early Jurassic arc magmatic rocks were emplaced in a variable metamorphic basement. In the extreme northern part of the SM, the basement is represented by Neoproterozoic migmatitic amphibolites (dated at approximately 945 ± 40 Ma K–Ar by Goldsmith et al. (1971) and at approximately 897 ± 28 Ma U–Pb in this study; coordinates 8° 17' 21" N, 73° 24' 56" W). The Neoproterozoic data are correlated with those reported by Ibañez–Mejia et al. (2011) in units of the Putumayo Orogen (Garzón Massif, Las Minas Migmatites,

Table 7. Modal compositions of rocks from the Ibagué Tonalite.

Ibagué Tonalite																
IGM	Sample	Longitude N	Latitude W	Qtz	Pl	Kfs	Cpx	Hbl	Bt	Chl	Op	Ap	Zrn	Ttn	Ep	Classification
49280	GB–1462	4° 45' 14.72"	74° 56' 59.48"	15	57	Tr	Tr	12	16	Tr				Tr	Tr	Quartz diorite
49290	GB–1517	4° 38' 58.92"	74° 59' 2.94"	19	65	Tr	Tr	5	11	Tr		Tr	Tr			Quartz diorite
76501	HC–748	4° 34' 42.36"	74° 59' 46.41"	15.6	64.35	Tr	Tr	11.9	7.92	Tr	Tr				Tr	Quartz diorite
77741	HC–946	4° 30' 37.55"	75° 4' 17.57"	17.5	42.97	4.94	Tr	19.4	15.2	Tr	Tr	Tr	Tr	Tr	Tr	Quartz diorite
49291	HP–3140	4° 47' 52.18"	74° 58' 1.65"	14	60	Tr	Tr	17	9	Tr			Tr		Tr	Quartz diorite
49295	HP–3159	4° 48' 46.26"	74° 57' 27.98"	16	57	Tr	Tr	6	14	Tr					7	Quartz diorite
49241	PM–6021	4° 47' 27.57"	74° 56' 25.25"	12	65	Tr	Tr	5	12	Tr	4	Tr		Tr		Quartz diorite
49242	PM–6034	4° 46' 59.54"	74° 56' 55.39"	15	63	Tr	Tr	8	14	Tr		Tr	Tr	Tr	Tr	Quartz diorite
49246	PM–6050	4° 44' 13.20"	74° 56' 51.29"	10	68	Tr	Tr	13	9	Tr	Tr	Tr	Tr	Tr	Tr	Quartz diorite
49256	PM–6105	4° 40' 47.73"	74° 57' 48.46"	13	65	Tr	Tr	17	5	Tr		Tr			Tr	Quartz diorite
49248	PM–6260	4° 44' 6.24"	74° 58' 28.29"	14	53	Tr	7	17	9	Tr	Tr	Tr	Tr		Tr	Quartz diorite
49258	PM–C15	4° 40' 50.92"	74° 58' 46.21"	15	59	Tr	1Tr	15	1	Tr		Tr		Tr	Tr	Quartz diorite
75339	VW–4851	4° 28' 54.65"	75° 6' 44.52"	10	64	Tr	Tr	18.5	7	Tr	0.5	Tr	Tr	Tr	Tr	Quartz diorite
76502	HC–760	4° 33' 47.05"	74° 59' 24.93"	5.6	61.7			17	8.1	Tr	Tr	Tr			1.5	Quartz diorite
49274	GB–1401	4° 50' 16.20"	74° 56' 13.78"	19	54	17	Tr	0	9	Tr	1		Tr		Tr	Quartz monzodiorite
49310	HP–3273	4°45´42.29"	74° 58' 15.60"	0	75	Tr	Tr	25	Tr	Tr		Tr	Tr		Tr	Diorite
49492	JV–4342	4° 54' 40.83"	74° 56' 18.33"	15	40	Tr	Tr	44	Tr	Tr	1				Tr	Diorite
49281	GB–1471	4° 45' 8.12"	74° 58' 8.26"	26	50	Tr	Tr	12	12	Tr		Tr	Tr	Tr	Tr	Granodiorite
76503	HC–779	4° 33' 34.02"	74° 59' 31.07"	13	39.9	32.5	Tr	Tr	11.4	Tr	Tr	Tr		0.2		Granodiorite
77765	HC–980	4° 32' 8.59"	75° 9' 11.56"	33.5	36.6	19.5	Tr	Tr	9.3	Tr	0.5	Tr	Tr	0.6	Tr	Granodiorite
48533	IV–3656	4° 55' 16.63"	74° 56' 24.38"	30.4	53.8	6.9	Tr	Tr	7.9		0.5	Tr	0.5	0	Tr	Granodiorite
77793	PM–8167	4° 28' 20.30"	75° 6' 47.55"	29.5	44.5	9.43	Tr	8.68	6.32	Tr	0.8	Tr	0	0.75	Tr	Granodiorite
901080	LMC–105	4° 50' 42.37"	74° 56' 42.27"	26	47	13			12	Tr	2	Tr	0		Tr	Granodiorite
48534	IV–3656–A	4° 55' 16.63"	74° 56' 24.38"	22.7	37.1	12.8	Tr	19.8	0	Tr	2.1	1.5	1.3	2.7	Tr	Granodiorite
68438	PM–7131–A	4° 35' 49.90"	75° 1' 53.65"	14.3	27	7.9	Tr	25.4	11.1	Tr	1.6	3.2		9.5	Tr	Granodiorite
76499	HC–728	4° 35' 42.32"	74° 58' 56.85"	22.4	50.9	9.69	Tr	10.6	5.73	Tr	0.4		Tr	0.2	Tr	MetaGranodiorite
68440	DMT–6059	4° 35' 55.79"	75° 1' 26.41"	26.1	36.2	17.4	Tr	5.8	8.7	Tr	1.4	Tr		4.3	Tr	MetaGranodiorite
77795	PM–8174	4° 29' 26.88"	75° 4' 40.51"	28.6	45.2	Tr	Tr	9.5	14.3		2.4	Tr		0	Tr	MetaTonalite
48537	JV–3660	4° 54' 54.04"	74° 56' 0.99"	24.8	52.2	Tr	Tr	15.7	3.6	TR	1.22	1.5	Tr	1		MetaTonalite
901098	MIG–076	4° 30' 9.62"	75° 4' 37.45"	17.5	62.7			7.2	11.4		1.2	Tr	Tr	0	Tr	MetaTonalite
49303	HP–3207	4° 45' 44.21"	74° 58' 41.07"	30	44	Tr	Tr	5	10	Tr		Tr	Tr	3	8	MetaTonalite
49305	HP–3220	4° 45' 21.53"	74° 59' 23.71"	29	18	Tr	Tr	7	9	Tr		Tr		2	Tr	MetaTonalite
76493	PM–7977	4° 34' 40.07"	74° 59' 54.19"	17	59	Tr	Tr	9	15	Tr	Tr	Tr	Tr	0	Tr	MetaTonalite
77794	PM–8171	4° 29' 1.41"	75° 5' 36.26"	48.6	32.4	Tr	Tr	8.2	2.7		2.7			5.4		MetaTonalite
49275	GB–1405	4° 50' 8.67"	74° 56' 47.52"	22	44	26	Tr	Tr	8	Tr					Tr	Monzogranite
49294	HP–3152	4° 48' 52.68"	74° 56' 30.87"	22	34	23	Tr	7	11	Tr		Tr			3	Monzogranite
48474	GB–1118	4° 52' 23.18"	74° 55' 51.87"	17.1	43.8	Tr	Tr	22.9	0	5.2	2.9		2.4	1	Tr	Tonalite
49276	GB–1409	4° 50' 9.27"	74°57' 28.08"	30	58	Tr	Tr	0	12	Tr	Tr	Tr	Tr		Tr	Tonalite
49288	GB–1502	4° 39' 1.00"	74° 57' 21.08"	22	50	Tr	Tr	11	17	Tr		Tr				Tonalite
49289	GB–1507	4° 38' 38.81"	74° 58' 4.52"	16	55	Tr	Tr	10	19			Tr		Tr	Tr	Tonalite
48507	HP–2761	4° 53' 10.38"	74° 55' 45.93"	29.5	49.5	3	Tr	11.5	4.5	Tr	1	0.25	0.25	0.5	Tr	Tonalite
49293	HP–3149	4° 48' 49.44"	74° 56' 24.06"	18	33	Tr	Tr	39	10	Tr		Tr	Tr		Tr	Tonalite
49302	HP–3200	4° 46' 7.90"	74° 57' 31.02"	25	56	Tr	Tr	10	9	Tr		Tr	Tr	Tr	Tr	Tonalite
49306	HP–3225	4° 42' 0.21"	74° 59' 16.31"	22	55	Tr	Tr	9	17	Tr		Tr	Tr		Tr	Tonalite
48536	IV–3659	4° 55' 0.71"	74° 56' 5.22"	24.8	38.1	5.4	Tr	14.9	3.5	6.9	1		1			Tonalite
49322	JV–4075	4° 54' 21.80"	74° 56' 9.71"	19	52	Tr	Tr	21	8	Tr		Tr	Tr	Tr	Tr	Tonalite
49244	PM–6047	4° 44' 10.30"	74° 56' 32.47"	15.9	40.7	Tr	Tr	23.4	0	7.5	3.3		1.9		2.8	Tonalite
49257	PM–6110	4° 40' 49.33"	74° 58' 14.42"	22	56	Tr	Tr	13	9	Tr		Tr	Tr		Tr	Tonalite
49259	PM–6122	4° 40' 16.37"	74° 59' 15.53"	27	45	Tr	Tr	15	13	Tr		Tr	Tr	Tr	Tr	Tonalite
49452	VW–4620	4° 54' 23.89"	74° 56' 31.94"	23	50	Tr	Tr	27	0		Tr	Tr				Tonalite
75338	VW–4850	4° 28' 54.65"	75° 6' 44.52"	20	64.6	Tr	Tr	1.4	13	Tr	1	Tr	Tr	Tr	Tr	Tonalite
75340	VW–4852	4° 28' 54.65"	75° 6' 44.52"	25	60	2	Tr	2.5	9	Tr	1.5	Tr	Tr	Tr	Tr	Tonalite

Table 7. Modal compositions of rocks from the Ibagué Tonalite *(continued).*

Ibagué Tonalite																
IGM	**Sample**	**Longitude N**	**Latitude W**	**Qtz**	**Pl**	**Kfs**	**Cpx**	**Hbl**	**Bt**	**Chl**	**Op**	**Ap**	**Zrn**	**Ttn**	**Ep**	**Classification**
49287	GB–1501	4° 38' 57.11''	74° 57' 8.42''	18	67			9	6			Tr				Tonalite
49267	PM–6145	4° 46' 20.78''	74° 57' 8.00''	20	54			15	11	Tr	Tr	Tr	Tr		Tr	Tonalite
49498	JV–4375	4° 55' 40.46''	74° 55' 31.35''	26.7	36	Tr	Tr	25.3	Tr		Tr				Tr	Tonalite
48535	IV–3658	4° 55' 6.40''	74° 56' 8.63''	33.7	45.2	3.1	Tr	3.8	12.7	Tr	1	0.5	Tr			Tonalite
49230	PM–5977	4° 51' 34.68''	74° 55' 51.00''	27.3	47.7	Tr	Tr	15.9	6.8	Tr	2.3		Tr		Tr	Tonalite
49635	PM–6551	4° 36' 17.29''	75° 1' 18.65''	25.7	30	Tr	Tr	30	8.6	Tr					Tr	Tonalite
901070	JPZ–001–A	4° 40' 11.16''	74° 58' 26.37''	23.1	44.6			24.6	6.2		Tr		Tr	1.5		Tonalite
48529	IV–3643	4° 56' 4.78''	74° 56' 47.49''	25.3	44.2	3.2	Tr	21.4	0	Tr	1.1	0.7			Tr	Tonalite

Tr—Traces of accessory mineral.

Los Mangos Granulite–Dibulla Gneiss) and correspond to the Andaquí Terrane and to the eastern edge of the Chibcha Terrane according to Restrepo & Toussaint (1989). Toward the SM core, the metamorphic basement consists of schists and gneisses with Early Ordovician metamorphic ages (Bucaramanga Gneiss, Silgará Schists, orthogneiss bodies) (Rodríguez et al., 2017b; van der Lelij, 2013; van der Lelij et al., 2016; Zuluaga et al., 2017) and pre–kinematic and post–kinematic Paleozoic plutons, which together form a terrain that has been related to the Famatinian Orogeny (Mantilla–Figueroa et al., 2016; van der Lelij, 2013; van der Lelij et al., 2016; Zuluaga et al., 2017) that has been identified along the western continental margin of South America from Chile to Venezuela. The boundary between the Neoproterozoic basement terrane and the terrane that forms the Santander Famatinian Orogen likely corresponds to a branch of the Bucaramanga Fault (Figure 2), although this is not well established due to mapping problems. The relationships between the Jurassic plutons and volcanic rocks and the basement remain unclear. Apparently, the compositions and ages of the plutons vary from the Neoproterozoic basement to the Ordovician basement, although further studies are necessary to document these characteristics in detail.

The Jurassic igneous rocks of the UMV block have a Neoproterozoic metamorphic basement (Garzón Group, Mancagua and Guapotón Gneisses, Las Minas Metamorphites), which is similar to the rocks of similar ages at serranía de San Lucas (San Lucas Gneiss) and Sierra Nevada de Santa Marta (Los Mangos Granulite) as well as those outcropping at serranía de Cocinas in Upper Guajira (Jojoncito Gneiss) and in the NW part of the SM (migmatitic amphibolites). Paleozoic sedimentary rocks (Mudstones and Granadillo Limestones, La Jagua Paleozoic, El Hígado Formation, and La Batalla Limestones and Sandstones at the UMV), blocks of Permian granitoids that formed in a continental margin arc environment (La Plata Granite at the UMV, Nechí Gneiss at serranía de San Lucas, and mylonitic granitoids in the Sierra Nevada de Santa Marta), and Upper Triassic limestones (Payandé Formation at the UMV) have been identified over the metamorphic basement.

The results of this study show that the metamorphic basement of the NBIB corresponds to the Tierradentro Gneisses and Amphibolites unit, which as U–Pb metamorphic ages of 167–154 Ma (Middle to Late Jurassic). This unit was interpreted by Bustamante et al. (2017) as Permian – Triassic. Our new U–Pb data indicate that the Tierradentro Gneisses and Amphibolites are geochronologically correlated with the metamorphic rocks of the Cajamarca Complex, in which Blanco–Quintero et al. (2014) found Jurassic metamorphic ages. Thus, the basement corresponds to a Jurassic metamorphic block that likely developed during its accretion to the continental margin and whose boundaries with adjacent terranes have not been established.

Based on current geological knowledge (Rodríguez–García et al., 2019), we propose that to the south, the Ibagué Fault borders the Jurassic orogen and the Chibcha Terrane (or Putumayo Orogen), which is composed of Permian granitoids, Triassic limestones (Payandé Formation), and Middle Jurassic plutons with no metamorphic involvement. To the east, the suture with the Chibcha Terrane is covered by alluvial fans; to the west, the tectonic boundary with the Tahamí Terrane is unknown; and to the north, its limit is unknown because its length within the Central Cordillera of Colombia has not yet been determined. The terrane that constitutes the Jurassic orogen likely represents a collision between the Chibcha and Tahamí Terranes between 166 and 154 Ma. Furthermore, La Cocha–Río Téllez Complex (described by Zapata et al., 2017a) is part of this terrane.

5.2. Characteristics of Jurassic Magmatism in the SM, UMV, and NBIB

5.2.1. Magmatism

The fact that the magmatism in the three blocks (SM, UMV, and NBIB) is of Jurassic age does not imply that they developed from a single arc and that the basement units were amalgamated and in similar geotectonic positions throughout Jurassic time. The differences in the composition, crystallization age,

Table 8. Major and trace elements of the Anzoátegui Metatonalite and Ibagué Tonalite in the NBIB.

Sample	JGB–492	JPZ–004	LMC–104	*CI11A	GOE–1001	JPZ–001–A	LMC–105	MIG–076	*CI2	*CI9B	*CI13	*CI15	*CI5B	*CI7	*CI10
wt%															
SiO2	50.3	61.1	59	61.2	65.6	58	64.6	61.3	67.8	57.8	61.7	58.9	64.3	63.7	57.2
Al2O3	16.7	15.4	15.6	16.1	15.7	17.4	15.4	17.2	15.6	17.9	16.4	16.8	15.8	17.9	17.2
Fe2O3	9.8	6.1	6.8	6.3	4.5	6.5	4.3	5.6	3.6	6.9	5.5	6	4.8	4.6	6.7
MgO	6.3	4	3.5	3.6	2.2	3.8	1.8	2.8	1.4	3.9	3	3.7	2.1	1.8	4.2
MnO	0.2	0.1	0.1	0.1	0.1	0.1	0.1	0.1	0	0.1	0.1	0.1	0.1	0.1	0.1
CaO	9.8	5	4.2	6.1	4.9	6.3	3.3	5.2	3.4	7.2	5.4	6.7	4	5.9	5.3
K2O	1.2	2.2	3.3	2	1.7	1.6	1.2	1.8	2.3	0.8	1.8	1.4	1.9	1.3	1.1
Na2O	2.8	3.6	2.6	3.9	3.4	3.5	5.4	3.4	4.1	4	3.8	3.6	4.7	3.7	4.3
P2O5	0.2	0.2	0.2	0.2	0.2	0.2	0.1	0.2	0.1	0.2	0.1	0.2	0.1	0.1	0.2
TiO2	1.4	0.7	0.8	0.7	0.5	0.8	0.6	0.7	0.5	0.8	0.7	0.7	0.6	0.5	0.9
LOI	1.2	1.5	3.7	0.6	1.2	1.8	3.1	1.6	1.5	0.8	1.3	0.8	2.2	0.6	2.2
SUM	99.9	99.8	99.6	100.7	99.9	99.9	99.9	99.9	98.8	100.4	99.8	98.1	98.3	99.7	97.1
ppm															
Ba	308.5	741.6	1254.5	804	499.4	441.3	185.3	638.3	488.5	318	475	292.2	525.8	674.2	285.5
Ce	36.9	44	49.3	49.8	45.5	29.9	42.8	48.9	47.3	27.4	44.9	33.6	36.1	25.2	39.2
Ga	26.7	23	22.2	17.8	21.5	25.5	21.4	24.3	17.4	17.9	16.6	18.9	16.8	18.8	17.7
La	16.7	23.6	26	23.5	26.2	15	22.3	27.4	24.4	12.8	18.8	13.4	19	12.7	16
Nb	6.3	5.3	7.3	5.9	5.4	4.7	7.4	4.8	7.6	6	8	7.3	8.6	4.9	7.6
Nd	26.7	27.5	25.8	21.7	22.1	17.5	23.6	25.2	21.9	13.8	26.1	16.7	19.6	9.9	21.9
Rb	39.1	68.2	111.7	43.7	37.9	50.7	50.3	38.4	45.3	12.2	41	36	43.6	52.3	21.7
Sr	629.2	680.5	362.7	704	747.1	595.3	441.5	826	305.6	503.6	458	402.4	514.4	420.5	438.8
Th	0.8	6.5	5.7	3.3	7.5	2.9	8.1	5.5	6.5	1.3	8.3	5.1	8.8	4.5	3.2
U	0.3	1.3	1.6	0.9	1.7	0.9	1.9	1	3	0.3	5	1.4	2.7	0	0
V	290.9	135.4	144.2	172	84.1	141.3	78.9	105.3	75.7	172	138	166.5	101.4	63.6	178.3
Y	29.3	17.3	21	18.6	17.4	21.3	23.7	19.4	18.8	17.3	31.3	24.2	23.5	12.2	29.5
Zr	94.1	151.6	194.1	182.1	113.5	104.4	185	136.1	166.9	112.5	151	130.6	202	134	182
Cu	11.8	49.6	23.7	63.9	7.8	28.7	14.4	6.9	5.9	23.9	52.6	27.3	3.3	6.6	36.6
Ni	1.6	2.1	1.7	10.3	1.9	1.8	1.9	1.7	2.2	10.1	7.3	13.5	7.1	4.3	11.5
Pb	3.1	3.8	7.5	1.3	4.2	5.2	<2.0	3.1	4.2	0.4	2.3	6.7	2.5	5.9	4.6
Zn	125	87.9	76.9	37	60.1	94.4	59.4	77.6	17.2	22	32	72.6	37	71.3	79.4

* Data from Bustamante et al. (2016)

LOI: loss on ignition

and evolutionary development of the arcs suggest independent and non–correlative magmatic events.

The lithological compositions of the SM plutons are primarily monzogranitic to syenogranitic without key compositional variations or spatial migration throughout the period of arc activity (25 to 30 Ma) (Figure 23a, 23d). The Jurassic magmatism in the UMV was quartz monzodioritic–quartz monzonitic in its initial stages and changed to monzogranitic after 20 to 27 Ma of arc evolution. Its spatial migration is reflected in the ages and positions of the plutons and volcanic products in the UMV (Figure 23b, 23e). The compositions of the Jurassic magmatic rocks of the NBIB indicate no changes in the compositions of the plutons, which are predominantly tonalitic with minor variations to quartz dioritic and granodioritic (Figure 23c, 23f) and show a migration of the magmatism from west to east over a time period of 15 to 20 Ma.

The Jurassic magmatic rocks in the three blocks (SM, UMV, NBIB) are sub–alkaline. In the SM, the plutonic rocks are more differentiated and are characterized by minor lithological variations (Figure 23g). They have higher Al_2O_3 and SiO_2 contents and belong to the high–K calc–alkaline series of peraluminous affinity (Figure 23j). In the UMV, the arc development had greater magmatic differentiation, which is clearly observed in the AFM diagram (Figure 23h). It began with rocks that were

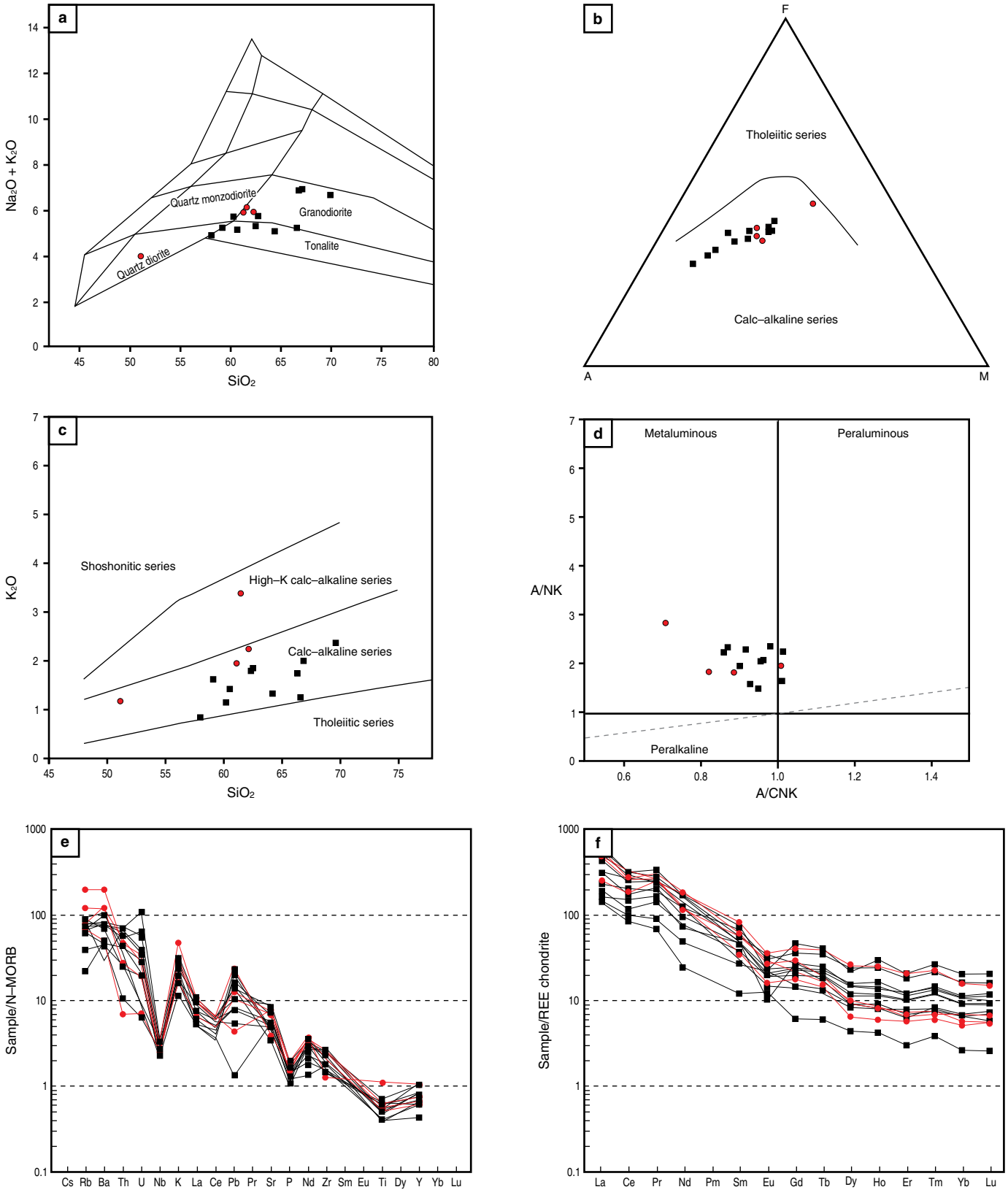

Figure 19. Diagrams of major oxides and multi–element diagrams. **(a)** TAS (Middlemost, 1985). **(b)** AFM fields indicated by Irvine & Baragar (1971). **(c)** diagram of Peccerillo & Taylor (1976). **(d)** diagram of Shand (1943). **(e)** N–MORB–normalized multi–element diagram (Sun & McDonough, 1989). **(f)** chondrite–normalized rare earth elements (Nakamura, 1974) diagram. The Ibagué Tonalite is shown in black, and the Anzoátegui Metatonalite is shown in red.

Table 9. Chondrite–normalized rare earth element diagram (Nakamura, 1974) for the Anzoátegui Metatonalite and Ibagué Tonalite.

Sample	Unit	Eu/Eu*	$(La/Yb)_n$	$(La/Sm)_n$	$(Ce/Yb)_n$	$(Ce/Sm)_n$	$(Eu/Yb)_n$
JGB–492	Anzoátegui Metatonalite	0.78	3.97	1.76	3.35	1.48	1.48
JPZ–004	Anzoátegui Metatonalite	0.8	9.41	2.87	6.7	2.04	2.18
LMC–104	Anzoátegui Metatonalite	0.93	8.21	3.31	5.94	2.39	1.93
GOE–1001	Ibagué Tonalite	0.8	10.97	4.14	7.27	2.74	1.78
JPZ–001–A	Ibagué Tonalite	0.84	4.78	2.32	3.63	1.76	1.46
LMC–105	Ibagué Tonalite	0.52	6.52	3.02	4.78	2.22	0.97
MIG–076	Ibagué Tonalite	0.82	10.24	3.74	6.96	2.54	1.89

n: normalized to chondrite values of Nakamura (1974).

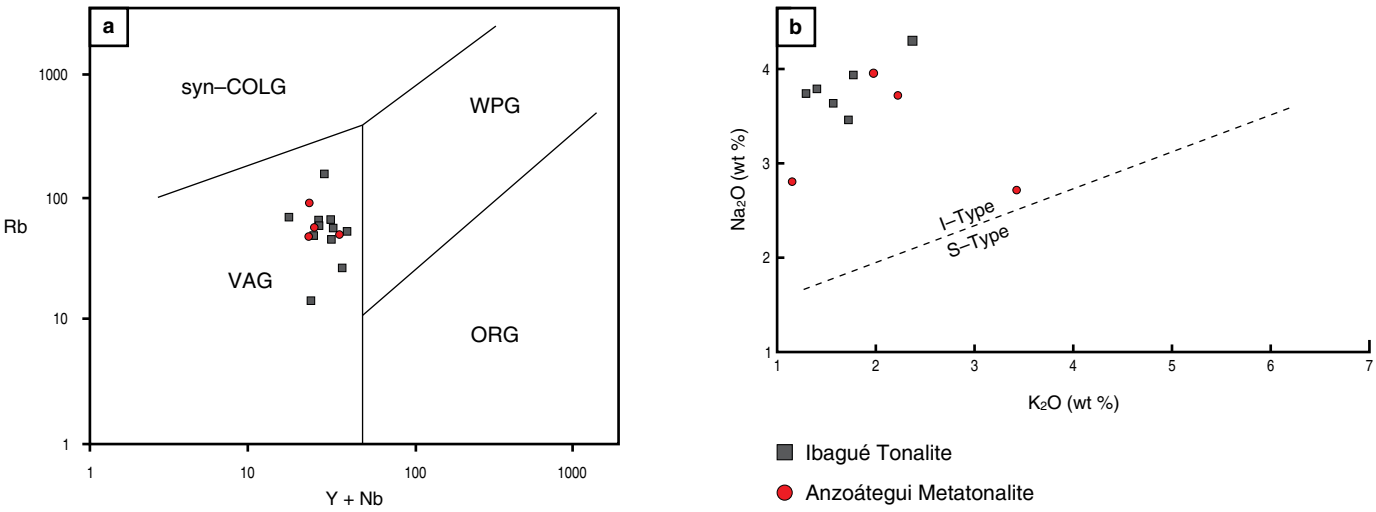

Figure 20. Geotectonic discrimination diagrams: **(a)** Pearce et al. (1984), **(b)** K_2O vs. Na_2O diagram of Chappell & White (1974) discriminating between I–type and S–type granites.

Table 10. LA–ICP–MS U–Pb zircon ages in the NBIB.

Sample	Longitude W	Latitude N	Classification	Unit	Age (Ma)
GOE–1088	75° 12' 47,8''	4° 29' 5.46''	Tonalite	Anzoátegui Metatonalite	154.79 ± 0.83
AMC–0153	75° 2' 56.93''	4°38´56.20¨	Metagranodiorite	Anzoátegui Metatonalite	150.17 ± 0.86
LMC–104	74° 59' 3.23''	4° 50' 36.88''	Metatonalite	Anzoátegui Metatonalite	153.9 ± 1.1
JPZ–001A	74° 58' 26.37''	4° 40' 11.16''	Tonalite	Ibagué Tonalite	138.7 ± 1.0
MIG–076	75° 4' 37.45''	4° 30' 9.62''	Granodiorite	Ibagué Tonalite	145.56 ± 0.92
MIG–O74	74° 59' 21.96''	4° 46' 58.24''	Amphibolite	Tierradentro Gneisses and Amphibolite	154.25 +3.1/-6.4
AMC–0152	75° 3' 54.37''	4° 39' 29.16''	Amphibolite	Tierradentro Gneisses and Amphibolite	154.5 ± 3.6
AMC–0171	75° 0' 41.5''	4° 40' 29.5''	Amphibolite	Tierradentro Gneisses and Amphibolite	167.0 ± 3.0

poor in quartz (<20%) and had a higher content of ferromagnesian minerals, which is reflected in the high content of total FeO and MgO. The arc gradually became enriched in quartz–rich rocks (>20%) of the high–K calc–alkaline series and subordinate shoshonitic series throughout its evolution, starting with metaluminous rocks and changing to granitic peraluminous rocks as its composition varied over time (Figure 23k). This was accompanied by a decrease in the A/NK ratios and an increase in the A/CNK ratios. In the NBIB, the rocks have lower alkali ($Na_2O + K_2O$) values, and the differentiation within the

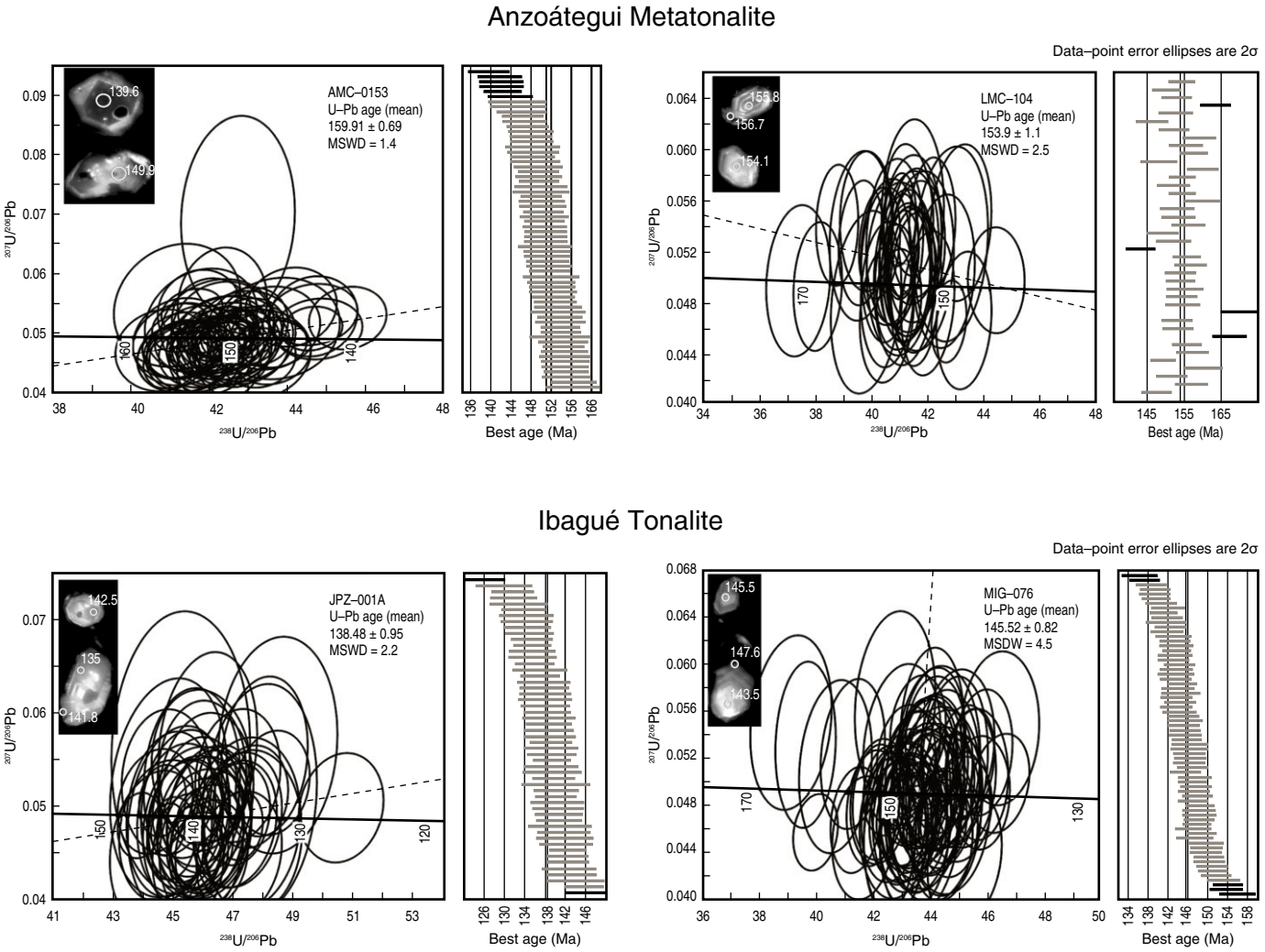

Figure 21. Geochronological results of the Anzoátegui Metatonalite (AMC–0153, LMC–104) and the Ibagué Tonalite (JPZ–001A, MIG–076). CL images of zircons representative of each sample.

arc is lower than in the UMV and SM (Figure 23i) with intermediate SiO_2 values, quartz contents >20% in most rocks, and lower total FeO and MgO contents than rocks with similar SiO_2 contents in the SM and UMV. They correspond to the normal calc–alkaline series and are metaluminous with higher A/NK ratios than those in the SM and UMV (Figure 23j, 23k, 23l).

A comparison of the patterns of N–MORB–normalized trace elements (Figure 24; Sun & McDonough, 1989) and chondrite–normalized rare earth elements (based on the values in Nakamura, 1974) of Triassic and Jurassic plutons from the SM, UMV, and NBIB shows that they are similar to rocks generated in continental margin arcs (Figure 24). However, the data from different arcs have different trace element distribution patterns and negative Nb, Ti, and P anomalies. The high anomalous values of Rb, Ba, Th, and Pb, albeit nonparallel, suggest that they correspond to different magmatic arc events or to different arcs. The magmatic arc of the SM is characterized by nonparallel REE patterns compared to rocks with similar SiO_2 contents. The data have different intersecting patterns in the same pluton, different HREE enrichments, minor or major LREE enrichments, and negative or no Eu anomalies (Figure 7). There are also different U–Pb zircon ages for each pattern and different $(La/Yb)_n$ values, suggesting multi–pulse plutons with different crustal contributions. This characteristic is not observed in the Jurassic arc rocks of the UMV and NBIB, where the rocks in each of these areas have similar compositions and ages. The REE and trace element patterns are parallel with LREE enrichments in the eastern plutons of the UMV, which are related to greater K contents and major rock differentiation (Figure 14).

The lack of analytical results of Ta and Y (see Table 1, Supplementary Information) limits the interpretation of the tectonic

Figure 22. Geochronological results of the Tierradentro Gneisses and Amphibolites; photomicrographs showing microscopic views and CL images of representative zircons.

Tierradentro Gneisses and Amphibolites

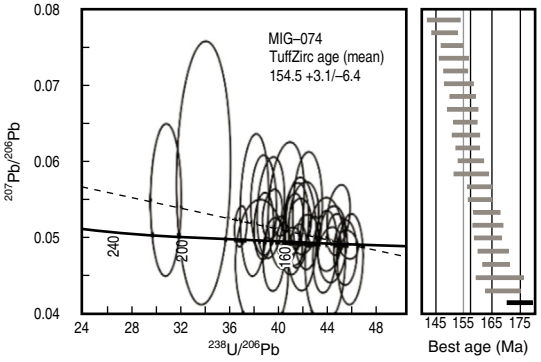

Data–point error ellipse are 2σ

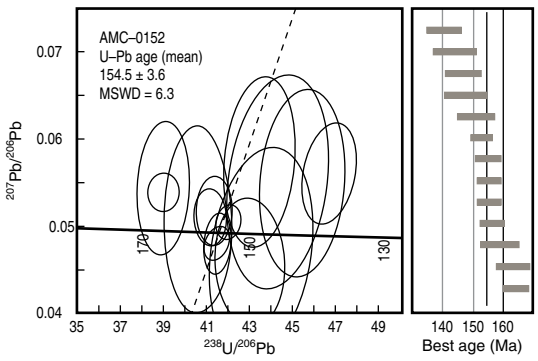

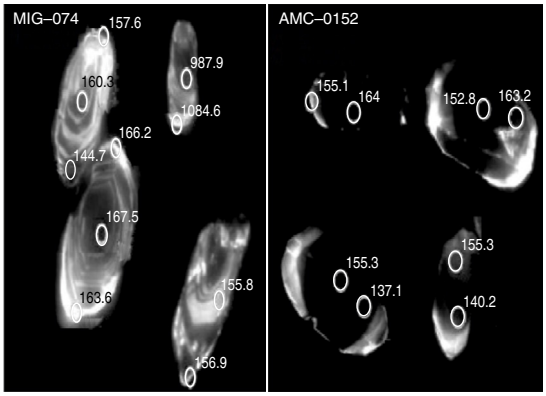

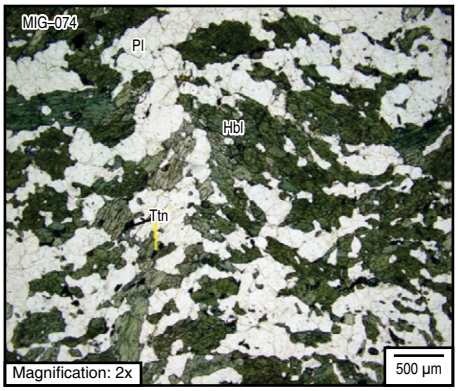

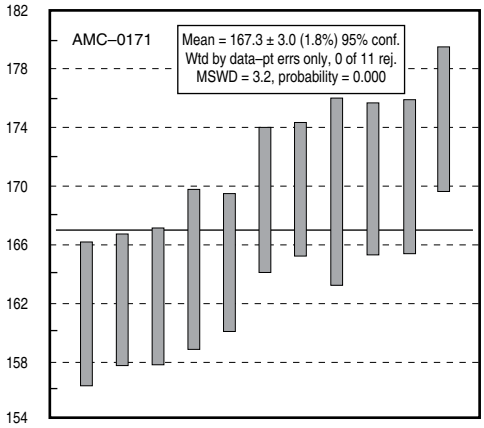

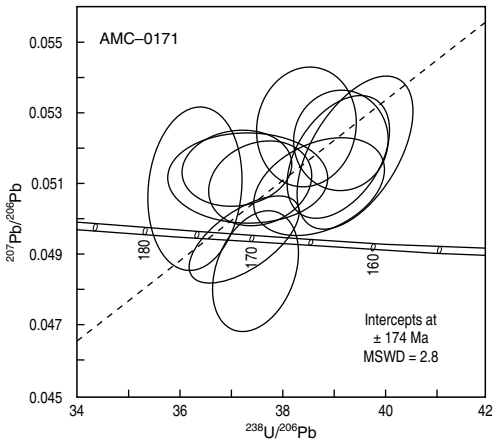

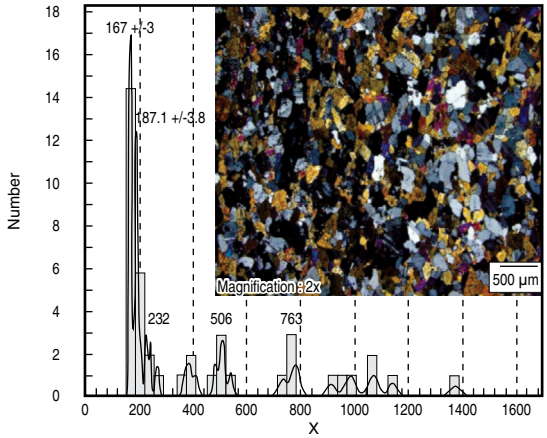

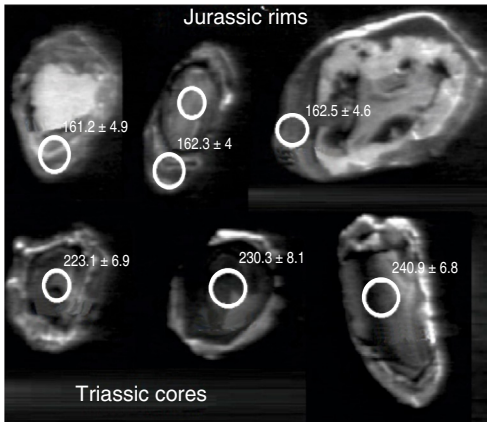

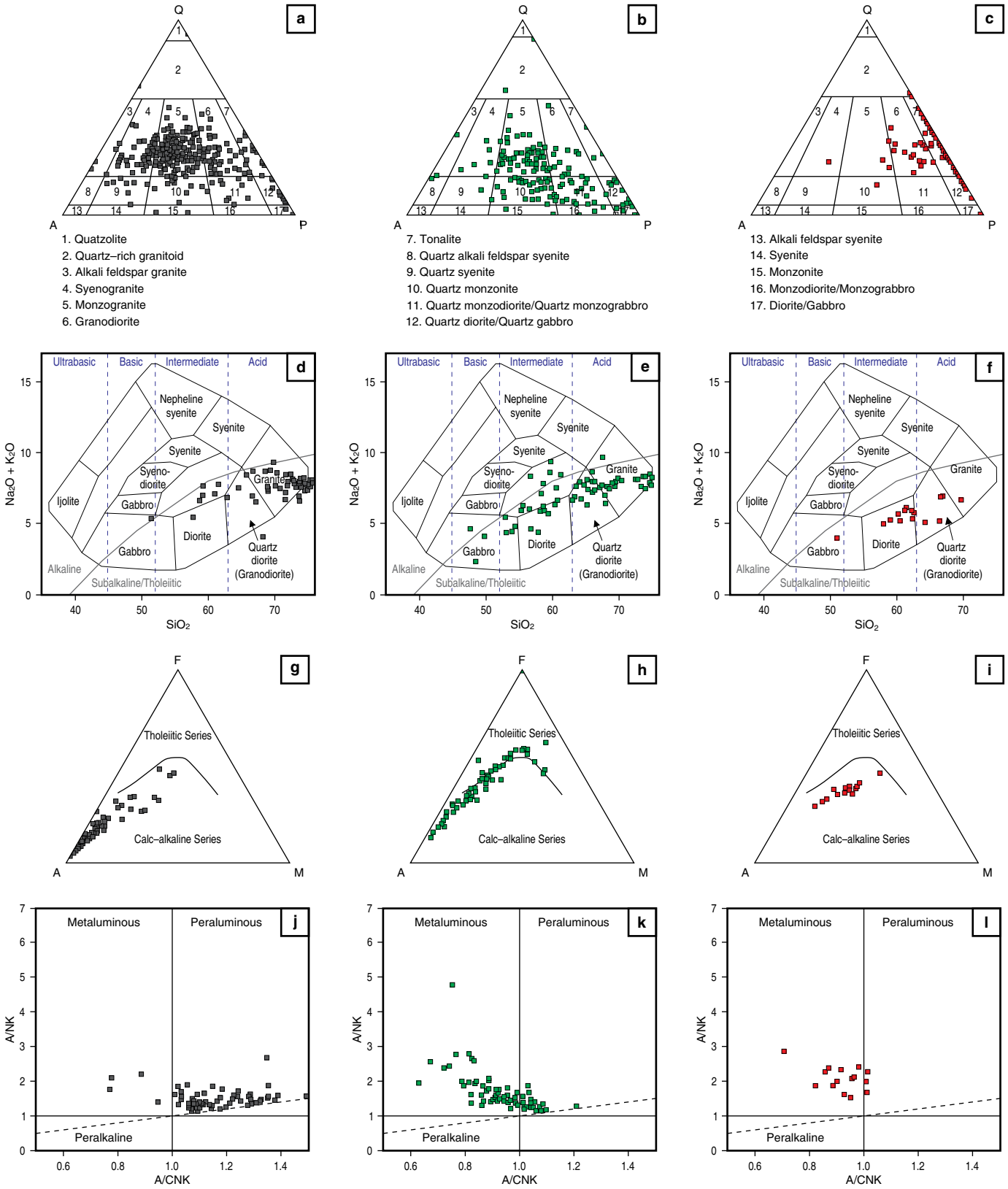

Figure 23. Compositional and geochemical characteristics of the Jurassic arc plutons. SM (black) period of arc activity (25 to 30 Ma); UMV (green) period of arc activity (20 to 27 Ma), and NBIB (red) period of arc activity (15 to 20 Ma). **(a)**, **(b)**, **(c)** Streckeisen diagrams (1979) for the rocks of the SM, UMV, and NBIB, respectively. **(d)**, **(e)**, **(f)** TAS diagrams (Cox et al., 1979) for the rocks of the SM, UMV, and NBIB, respectively. **(g)**, **(h)**, **(i)** AFM diagrams (Irvine & Baragar, 1971) for the rocks of the SM, UMV, and NBIB, respectively. **(j)**, **(k)**, **(l)** Alumina saturation index diagrams (Shand, 1943) for the rocks of the SM, UMV, and NBIB, respectively.

environment and the discrimination between volcanic arc granites and post–collisional granites. According to the diagrams of Pearce (1982) and Pearce et al. (1984), the samples plot within the field of volcanic arc granites (Figures 24, 25a). The UMV and SM plutons have slightly higher Rb values than those of the NBIB within the field of volcanic arcs. The samples of van der Lelij (2013) in the SM and Bustamante et al. (2016) in the NBIB plot within the volcanic arcs field in the discrimination diagram of Harris et al. (1986) (Figure 25b).

Magmatic activity occurred during different time intervals in each block. In the SM, the arc initiated at approximately 214 Ma, and most magmatic activity occurred from 203 to 197 Ma. It lasted for approximately 30 Ma and continued until 184 Ma (Figure 26). In the UMV, the magmatic arc activity started at approximately 195 Ma and included three periods of formation of plutons and volcanic rocks at 187, 182, and 172 Ma. These are reflected in the ages of the western and eastern plutons and the associated volcanic rocks and in the spatial migration of the arc. The magmatism lasted for approximately 27 Ma and ended at approximately 168 Ma (Figure 26). In the NBIB, we interpret that the arc had two periods of magmatic activity. The first period occurred from 158 to 152 Ma, and it generated the Anzoátegui Metatonalite, which was syntectonically emplaced during metamorphism of the Tierradentro Gneisses and Amphibolites and the Cajamarca Complex. The second period occurred from 145 to 138 Ma, when the Ibagué Tonalite intruded after the metamorphic event.

5.2.2. Inheritances

Inherited zircon cores in plutonic and volcanic rocks provide valuable information about the relationship between crustal basement and arc magmatism. The highest numbers of inheritances were found in granitoids of the SM, whereas inheritances are rare in the UMV and NBIB granitoids.

The xenocrysts and inherited zircon cores in the Late Triassic – Early Jurassic plutons in the SM show several inherited populations. These include a minor Paleoproterozoic to Neoproterozoic population, a major Ordovician to Devonian population, and a moderate Permian – Triassic population (Figure 27).

Inherited Paleoproterozoic ages have also been found in basement units such as the Bucaramanga Gneiss, the Silgará Schists, the Chicamocha Schists, and the San Pedro Phyllites. Cordani et al. (2005) and Mantilla–Figueroa et al. (2016) suggest that these zircons were possibly derived from the Rio Negro Juruena, Rondonian, and Sunsás units in the Amazonian Craton. A second group of inherited zircon cores in the Triassic – Jurassic granitoids yielded ages ranging from 1200 to 1000 Ma. These ages have also been reported in the Chicamocha Schists, San Pedro Phyllites, and Silgará Schists (Cardona et al., 2016; Mantilla–Figueroa et al., 2016) and could be related to both the Amazonian Craton (Cordani et al., 2005; Mantilla–Figueroa et al., 2016) and to the pericratonic magmatic arc of the Colombo Oaxaquian Terrane (Ibañez–Mejia et al., 2011). Inherited ages ranging from 1000 to 850 Ma have been identified in inherited cores in the Silgará Schists (Cardona et al., 2016; Mantilla–Figueroa et al., 2016) and in the Santa Rosita Monzogranite (Zapata et al., 2017b) and could be related to the Grenville Orogeny (Cordani et al., 2005) or to the Putumayo Orogeny (Ibañez–Mejia et al., 2011). Finally, Mantilla–Figueroa et al. (2016) related the zircons inherited from the Proterozoic, which have ages ranging from 850 to 540 Ma, to the Brasiliano/Pan–African Orogeny. They are present in units that are currently buried under the basin and in some intrusive bodies, such as the Ediacaran San José del Guaviare Nepheline Syenite (Arango et al., 2012), which are the possible source of these inherited cores.

Ordovician inherited zircon cores have been found in several Late Triassic – Jurassic granitoids. This group of zircons likely represents the crystallization age of the Ordovician pre–, syn–, and post–tectonic plutons associated with the Famatinian Orogeny in the Santander Massif (Mantilla–Figueroa et al., 2012; Restrepo–Pace & Cediel, 2010) and Floresta Massif (Horton et al., 2010) and the metamorphic age of the Bucaramanga Gneiss related to the Famatinian Orogeny. Silurian inherited zircon cores may be derived from plutons related to continental arc magmatism that developed on the western margin of Gondwana during this time period (van der Lelij et al., 2016). The Devonian and Carboniferous inherited zircon cores may also be related to magmatic bodies of the SM.

Middle and Lower Triassic and Permian ages ranging from 262 to 290 Ma have been reported for small intrusive bodies in the SM, serranía de Perijá, and Mérida Andes (van der Lelij, 2013; van der Lelij et al., 2016). They occur in inherited zircon cores in the Mogotes Batholith and La Corcova, Santa Bárbara, and Rionegro Monzogranites. These ages are common in the metamorphic basement of the Central Cordillera associated with the Tahamí Terrane (Restrepo et al., 2011; Rodríguez et al., 2016a; Spikings et al., 2015; Villagómez et al., 2011; Vinasco et al., 2006), in the Permian arc that developed on the western margin of the Chibcha Terrane (Cardona et al., 2010; Rodríguez et al., 2017a) in the Central Cordillera, and in the serranía de San Lucas and Sierra Nevada de Santa Marta. They also occur in small intrusive bodies east of Pamplona, where a U–Pb age of 265.2 ± 4.5 Ma was determined in granodiorite intruding metamorphic rocks that are similar to the Bucaramanga Gneiss, which were mapped and identified as granodiorites and granites (Ward et al., 1973).

In summary, the Late Triassic – Early Jurassic plutons of the SM contain abundant inherited zircons of crustal origin that are correlated with the ages of inherited and primary zircons of metasedimentary, metaigneous, and igneous units that form the SM basement, such as the Bucaramanga Gneiss, Silgará Schists,

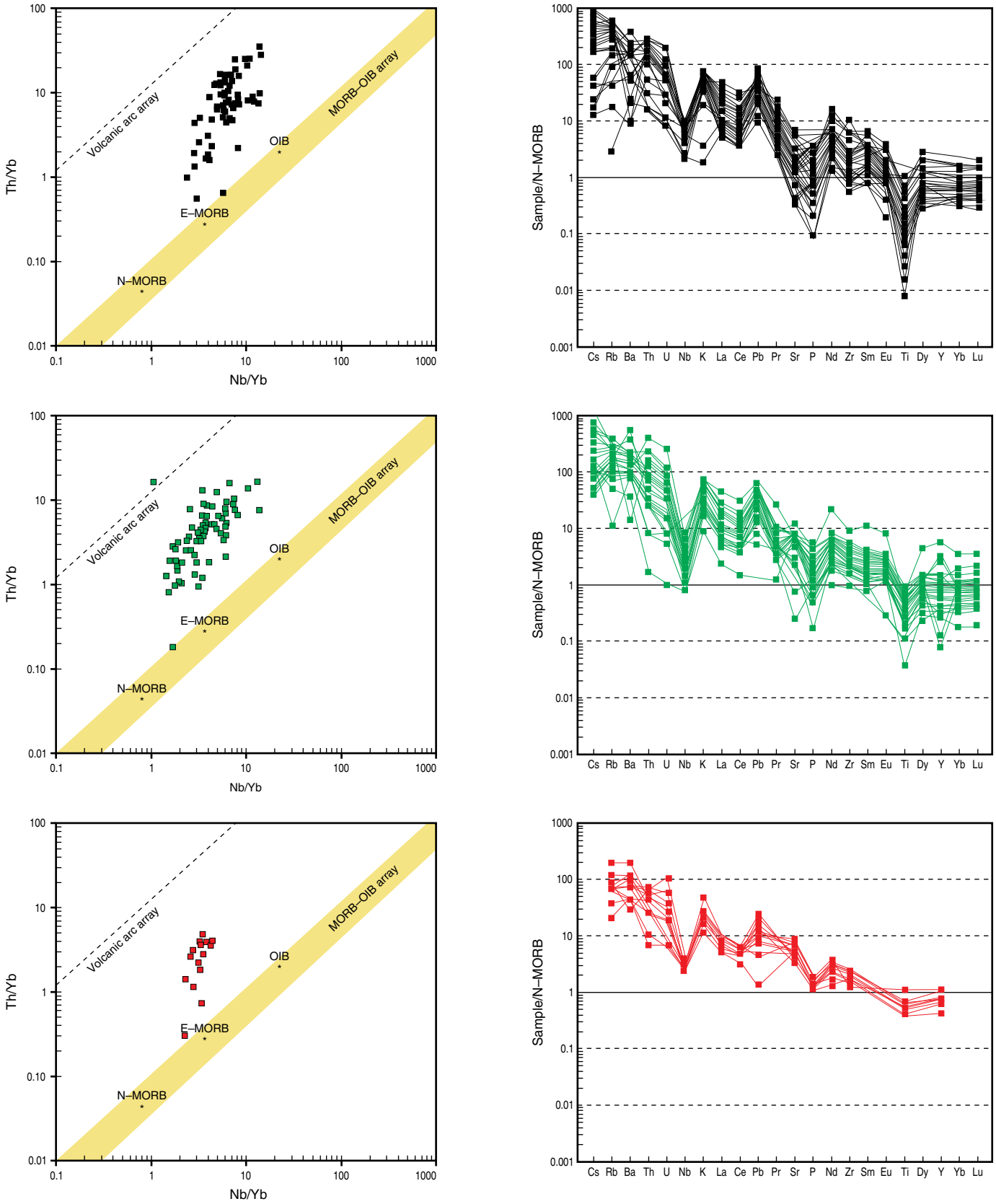

Figure 24. Multi–element diagrams and tectonic discrimination diagrams (Pearce, 1982) for plutonic bodies from the SM, UMV, and NBIB blocks. Samples from the SM are shown in black, samples from the UMV are shown in green, and samples from the NBIB are shown in red.

and Paleozoic pre– and post–kinematic orthogneissic and plutonic bodies, among others. The probability density diagram of the inherited ages (Figure 27) of the granitoids is similar to the results of inherited zircons from the Silgará Formations reported by Cardona et al. (2016) and Mantilla–Figueroa et al. (2016), which range from the Mesoproterozoic to the Devonian.

The geochemical characteristics and the quantity of inherited zircons suggest different degrees of crustal melting, which implies a high heat gradient in the arc that melted the continental basement rocks and incorporated them into the magma (Figure 27). In line with the crustal melting phenomenon and advanced magmatic differentiation in the SM, the plutons have a peraluminous affinity and dual classification as I– and S–type granites, which could result from the melting of basement metasedimentites in some pulses but not in others.

In the UMV, inheritance is limited to a few inherited zircon cores with Mesoproterozoic to Neoproterozoic and Jurassic ages. The former ages suggest a contribution of the Amazonian Craton to the oldest cores and of metamorphic basement of the Chibcha Terrane (Putumayo Orogen), whereas the Jurassic inheritances are related to previous periods of magmatic activity within the same arc.

No record of inheritance was found in the Anzoátegui Metatonalite and in the Ibagué Tonalite of the NBIB.

5.3. Evolutionary Model

The Triassic – Jurassic magmatic histories of the SM, UMV, and NBIB blocks are represented by different lithological, geochemical, and geochronological data that differentiate them. Furthermore, these rocks were emplaced in metamorphic basement units of different ages. Therefore, the correlations between Jurassic magmatic events and the regional models from a single arc model described previously are less valid (Bustamante et al., 2010, 2016; Leal–Mejía, 2011; Spikings et al., 2015; Villagómez et al., 2015; Zapata et al., 2016a). We propose a model involving several arcs that developed in different geotectonic positions that were emplaced in different metamorphic terranes with unique compositional, geochronological, and evolutionary characteristics without any similarity that would allow their correlation.

Figure 28 shows the evolutionary model proposed to explain the genesis of the Late Triassic – Early Cretaceous igneous activity in Colombia.

5.3.1. ca. 214 to 195 Ma

During this time period, we propose that an active subduction zone was located along the NW edge of Gondwana that generated a magmatic arc that is current recorded in the Santander Massif. This arc mainly intrudes the Famatinian Orogen (Bucaramanga Gneiss, Silgará Formation, orthogneisses, and post–tectonic granites) and, to a lesser extent, part of the Neoproterozoic basement that outcrops NW of the Santander Massif. Between ca. 194 to 189 Ma, the arc axis migrated toward the ocean (Spikings et al., 2015), and a possible clockwise rotation of the continental plate occurred.

5.3.2. ca. 195 to 168 Ma

Extension of the continental margin began during this period, causing the formation of back–arc basins, similar to the interpretation of Toussaint (1995). Arc volcanism, plutonism, and sedimentation occurred concurrently. Volcano–sedimentary sequences formed, including the Saldaña Formation and Pitalito Vulcanites in the UMV, the Noreán Formation in the Middle Magdalena Valley and on the eastern flank of serranía de San Lucas, La Quinta Formation in serranía de Perijá, La Caja de Ahorros Ignimbrite and Los Clavos Ignimbrite in the Sierra Nevada de Santa Marta, and sedimentary rocks such as the Jordán and Girón Formations in the SM. Plutonism generated, in approximately chronological order, the western plutons in the UMV and the Norosí Batholith in serranía de San Lucas, the plutons in the SNSM, the intermediate plutons between the western and eastern plutons in the UMV, the eastern plutons of the UMV, and plutons of the same age in the Sierra Nevada de Santa Marta.

5.3.3. ca. 167 to ca. 138 Ma

This interval is divided into three time periods. The first event was the collision of allochthonous terranes with the continental margin between ca. 167 and ca. 154 Ma with consequent metamorphism that formed the metamorphic assemblage of Tierradentro Gneisses and Amphibolites (this study) in the NBIB (167–154 Ma), the SW section of the Cajamarca Complex (158 and 147 Ma; Blanco–Quintero et al., 2014), and La Cocha–Río Téllez Complex (163 Ma; Zapata et al., 2017a). The second event, which lasted from ca. 158 to 150 Ma, included syntectonic arc magmatism that produced the Anzoátegui Metatonalite in the NBIB. The third event, which lasted from ca. 145 to ca. 138 Ma, was the post–tectonic magmatism that generated the Ibagué Tonalite in the NBIB.

Alternative hypotheses to explain the arc magmatism during this period include: (1) Genesis of the arc at another paleolatitude and transport to the current position along regional faults, and (2) the creation of different volcanic fronts in a supra–subduction system. However, in the latter, the spatial position with respect to the trench and the westward migration coeval with terrane accretion on the western margin of the Neoproterozoic basement appear to be problematic.

Due to the lack of geological data about the central section of the batholith, its corresponding model is unknown. The geochronological data available in the literature for the southern section (Páez Quartz Monzodiorite) (Leal–Mejía, 2011; Zapata

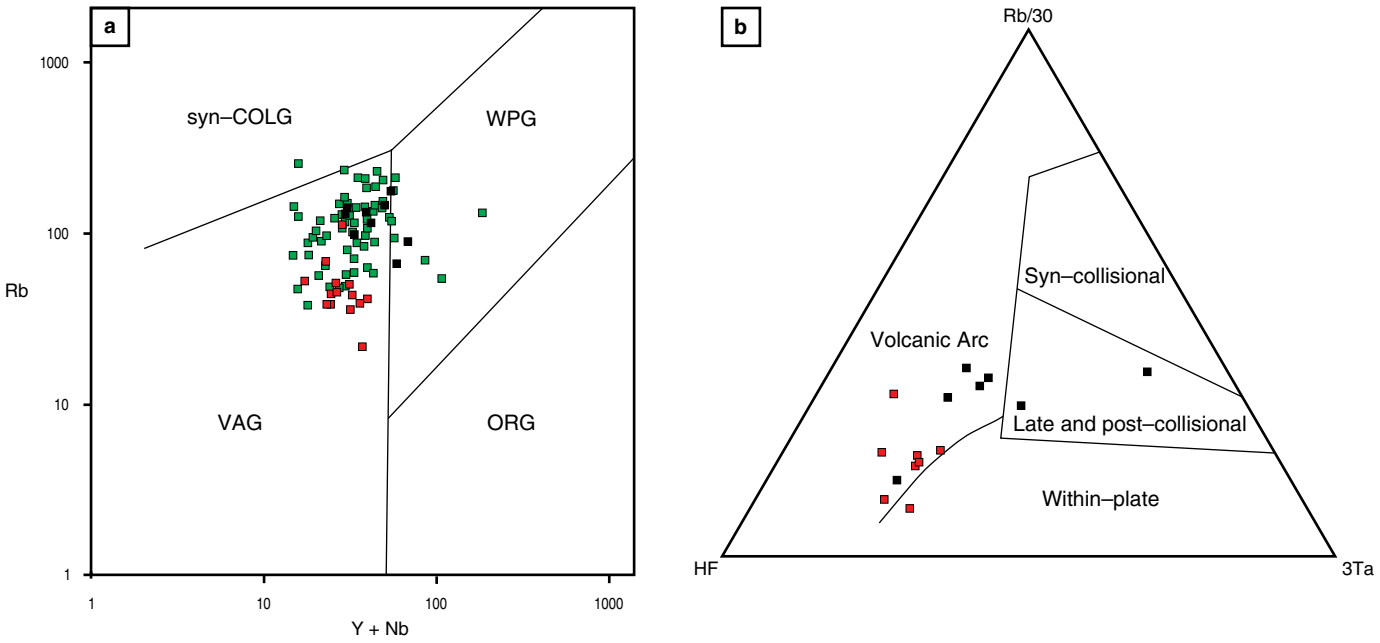

Figure 25. Tectonic discrimination diagrams: **(a)** Pearce et al. (1984), **(b)** Harris et al. (1986). Diagrams for plutonic bodies from the SM, UMV, and NBIB blocks. Samples from the SM are shown in black, samples from the UMV are shown in green, and samples from the NBIB are shown in red.

et al., 2015) suggest a correlation with the western plutons of the UMV (Zapata et al., 2015). Conversely, some data from the central section of the Ibagué Batholith indicate its heterogeneity and inclusion of Permian (Villagómez et al., 2011; preliminary results from the "Jurassic Magmatism of Colombia" project of the SGC) and Jurassic bodies ranging from 170 to 150 Ma (Villagómez et al., 2011; Leal–Mejía, 2011). Future studies will make it possible to understand this section of the batholith and correlate it with the other Jurassic units.

6. Conclusions

The compositional characteristics and crystallization ages of the Late Triassic and Jurassic igneous units in the Santander Massif, Upper Magdalena Valley, and northern block of the Ibagué Batholith have no common features that make it possible to correlate the magmatism associated with each block.

The Triassic and Jurassic magmatic rocks in Colombia were emplaced during different orogens. The Late Triassic – Jurassic plutons of the Santander Massif were emplaced into metamorphic and igneous units related to the Famatinian or Quetame–Caparonensis Orogeny, which occurred in the Early Ordovician (480–465 Ma). North of the massif, several plutons (Rionegro Monzogranite and San Martín Tonalite) were emplaced into Neoproterozoic basement, which is associated with the Chibcha Terrane or Putumayo Orogen (approximately 990 Ma), although the boundary between the orogens in the northern SM remains unclear. The Early Jurassic – Middle Jurassic plutons and volcanic rocks in the Upper Magdalena Valley were emplaced into basement consisting of Neoproterozoic metamorphic rocks, Paleozoic sedimentary rocks and Permian arc rocks related to the Chibcha Terrane or Putumayo Orogen. The Jurassic magmatic rocks associated with the northern block of the Ibagué Batholith were emplaced syn–tectonically and post–tectonically into metamorphic rocks related to a Late Jurassic orogen that includes units such as the Tierradentro Gneisses and Amphibolites, part of the Cajamarca Complex, and La Cocha–Río Téllez Complex. We suggest that this orogen should be called the Tierradentro Terrane, which borders the Chibcha Terrane to the east and the Tahamí Terrane to the west, although the tectonic borders between these three terranes are unknown.

Late Triassic – Jurassic magmatism occurred in several subduction zones that were active at different times, likely through the westward migration of the subduction zone. This generated different continental margin arcs that evolved independently in the three tectonic blocks (Santander Massif, Upper Magdalena Valley, and northern block of the Ibagué Batholith).

In the Santander Massif, arc magmatism lasted for approximately 30 Ma (from 214 to 184 Ma) and included multiple pulses of different–aged monzogranitic magmatism that generated batholitic bodies and stocks. The magmatism involved major crustal melting, represented by I– and S–type peraluminous granitoids. In the Upper Magdalena Valley, arc magmatism lasted for approximately 30 Ma (197 to 167 Ma) and included three large magmatic pulses (187, 182, and 172 Ma), starting with the formation of metaluminous monzodioritic stocks and batholiths

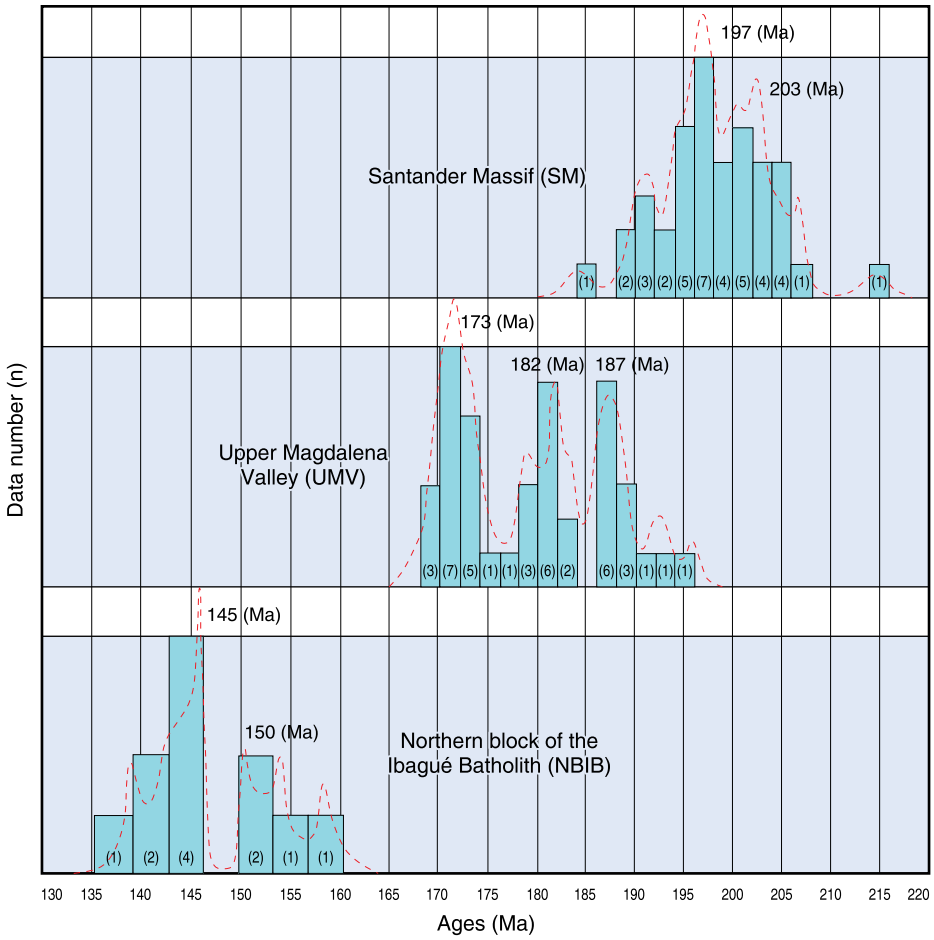

Figure 26. Frequency diagrams of U–Pb zircon ages for Triassic – Jurassic magmatic bodies of the SM, UMV, and NBIB.

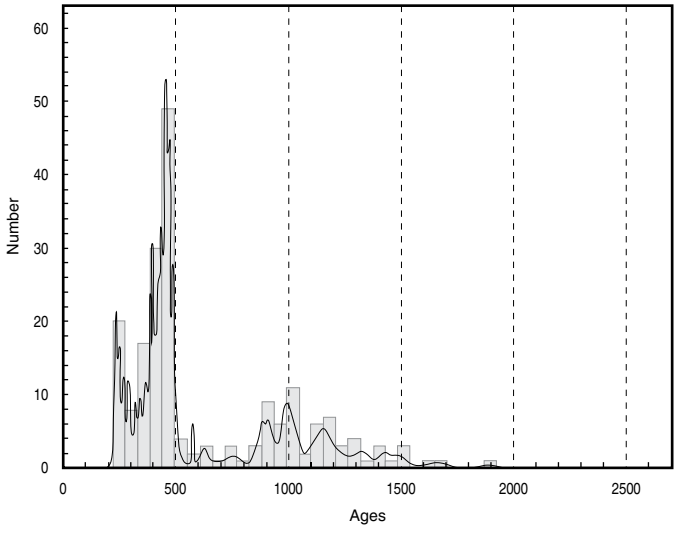

Figure 27. Probability density diagram of 200 xenocrysts and inherited zircon cores related to 41 U–Pb ages of SM plutons.

and ending with the emplacement of I–type metaluminous and peraluminous batholiths and monzogranitic stocks. The spatial migration of the arc is recorded in the composition of the igneous rocks. In the northern block of the Ibagué Batholith, the arc lasted for 20 Ma (from 158 to 138 Ma) and contained at least two magmatic pulses (154 and 144 Ma) that formed I–type metaluminous plutons with tonalitic compositions. The arc migrated from west to east without a record of compositional changes during arc activity. The first pulse (Anzoátegui Metatonalite), which occurred from 158 to 151 Ma, is interpreted as syntectonic with the metamorphism based on the similarity of the ages of the metamorphic rocks and the development of metamorphic structures. The second pulse (Ibagué Tonalite), which occurred from 145 to 138 Ma, is interpreted as post–tectonic based on the isotropic structure of the rocks.

The large number of inheritances found in the Triassic – Jurassic granitoids of the SM, which have Mesoproterozoic, Neoproterozoic, Cambrian, Ordovician, Silurian, Devonian, Carboniferous, Permian, and Upper and Lower Triassic ages,

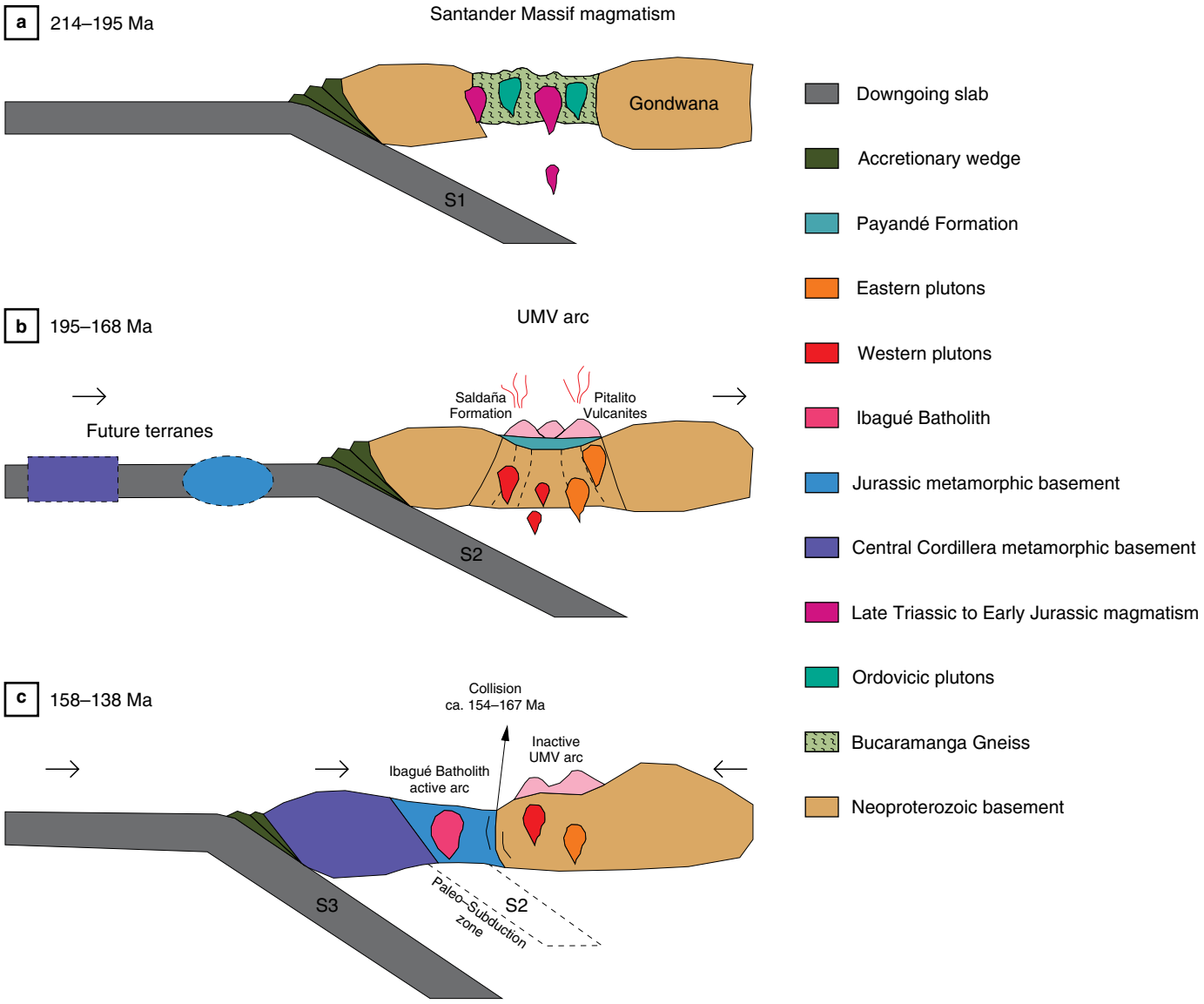

Figure 28. Geologic model of the evolution of the Santander Massif (SM), Upper Magdalena Valley (UMV), and northern block of the Ibagué Batholith (NBIB) during the Late Triassic – Early Cretaceous at: **(a)** 214–195 Ma, **(b)** 195–168 Ma, **(c)** 158–138 Ma.

suggests magmatism that assimilated crustal material from the basement and included most of the units preceding the magmatic event of the Triassic – Jurassic arc.

Acknowledgments

The authors acknowledge the Servicio Geológico Colombiano for the support in developing the "Magmatismo Jurásico en Colombia" project as well as geologists Tomás CORREA, Lina María CETINA, Milton OBANDO, Ángela RINCÓN, and María Isabel GIRALDO, who helped with the sampling. We thank Diego RAMÍREZ for editing the text. Special thanks are given to the staff of the Laser Ablation Geochronology Laboratory, SGC, for conducting the U–Pb zircon dating of the samples reported in this study.

References

Álvarez, A.J. 1983. Geología de la cordillera Central y el occidente colombiano y petroquímica de los intrusivos granitoides mesocenozoicos. Boletín Geológico, 26(2): 1–175. Bogotá.

Arango, M.I., Zapata, G. & Martens, U. 2012. Caracterización petrográfica, geoquímica y edad de la Sienita Nefelínica de San José del Guaviare. Boletín de Geología, 34(1): 15–26.

Arango, M.I., Rodríguez, G., Bermúdez, J.G. & Zapata, G. 2015a. Cuarzomonzonita de Anchique. Catálogo de unidades li-

toestratigráficas de Colombia. Servicio Geológico Colombiano, 26 p. Medellín.

Arango, M.I., Rodríguez, G., Bermúdez, J.G. & Zapata, G. 2015b. Monzodiorita de Las Minas. Catálogo de unidades litoestratigráficas de Colombia. Servicio Geológico Colombiano, 26 p. Medellín.

Arango, M.I., Rodríguez, G., Zapata, G. & Bermúdez, J.G. 2015c. Cuarzolatita de Teruel. Catálogo de unidades litoestratigráficas de Colombia. Servicio Geológico Colombiano, 25 p. Medellín.

Arango, M.I., Rodríguez, G., Zapata, G. & Bermúdez, J.G. 2015d. Monzogranito de Altamira. Catálogo de unidades litoestratigráficas de Colombia. Servicio Geológico Colombiano, 31 p. Medellín.

Arango, M.I., Rodríguez, G., Zapata, G. & Bermúdez, J.G. 2015e. Monzogranito de Mocoa. Catálogo de unidades litoestratigráficas de Colombia. Servicio Geológico Colombiano, 41 p. Bogotá.

Arango, M.I., Rodríguez, G., Zapata, G. & Correa, A.M. 2016. Monzogranito de Rionegro. Catálogo de unidades litoestratigráficas de Colombia. Servicio Geológico Colombiano, 128 p. Medellín.

Arias, A. & Morales, C.J. 2003. Memoria explicativa: Mapa geológico generalizado del departamento del Cesar. Scale 1:250 000. Ingeominas, 93 p. Bogotá.

Arias–Tauta, A. & Vargas–Higuera, R. 1978. Memoria explicativa: Geología de las planchas 86 Ábrego y 97 Cáchira. Scale 1:100 000. Boletín Geológico, 23(2): 3–38. Bogotá.

Aspden, J.A., McCourt, W.J. & Brook, M. 1987. Geometrical control of subduction–related magmatism: The Mesozoic and Cenozoic plutonic history of western Colombia. Journal of the Geological Society, 144(6): 893–905. https://doi.org/10.1144/gsjgs.144.6.0893

Barbarin, B. 1999. A review of the relationships between granitoid types, their origins and their geodynamic environments. Lithos, 46(3): 605–626. https://doi.org/10.1016/S0024-4937(98)00085-1

Barrero, D. & Vesga, C.J. 1976. Mapa geológico del cuadrángulo K–9 Armero y mitad sur del J–9 La Dorada. Scale 1:100 000. Ingeominas. Bogotá.

Bayona, G., Rapalini, A. & Costanzo–Álvarez, V. 2006. Paleomagnetism in Mesozoic rocks of the northern Andes and its implications in Mesozoic tectonics of northwestern South America. Earth, Planets and Space, 58(10): 1255–1272. https://doi.org/10.1186/BF03352621

Bayona, G., Jiménez, G., Silva, C., Cardona, A., Montes, C., Roncancio, J. & Cordani, U. 2010. Paleomagnetic data and K–Ar ages from Mesozoic units of the Santa Marta Massif: A preliminary interpretation for block rotation and translations. Journal of South American Earth Sciences, 29(4): 817–831. https://doi.org/10.1016/j.jsames.2009.10.005

Bermúdez, J.G., Arango, M.I., Rodríguez–García, G. & Zapata–García, G. 2015. Cuarzomonzonita de San Cayetano. Catálogo de unidades litoestratigráficas de Colombia. Servicio Geológico Colombiano, 37 p. Medellín.

Blanco–Quintero, I.F., García–Casco, A., Toro, L.M., Moreno, M., Ruiz, E.C., Vinasco, C.J., Cardona, A., Lázaro, C. & Morata, D. 2014. Late Jurassic terrane collision in the northwestern margin of Gondwana (Cajamarca Complex, eastern flank of the Central Cordillera, Colombia). International Geology Review, 56(15): 1852–1872. https://doi.org/10.1080/00206814.2014.963710

Bustamante, C., Cardona, A., Bayona, G., Mora, A., Valencia, V., Gehrels, G. & Vervoort, J. 2010. U–Pb LA–ICP–MS geochronology and regional correlation of Middle Jurassic intrusive rocks from the Garzón Massif, Upper Magdalena Valley and Central Cordillera, southern Colombia. Boletín de Geología, 32(2): 93–109.

Bustamante, C., Archanjo, C.J., Cardona, A. & Vervoort, J.D. 2016. Late Jurassic to early Cretaceous plutonism in the Colombian Andes: A record of long–term arc maturity. Geological Society of America Bulletin, 128(11–12): 1762–1779. https://doi.org/10.1130/B31307.1

Bustamante, C., Archanjo, C.J., Cardona, A., Bustamante, A. & Valencia, V.A. 2017. U–Pb ages and Hf isotopes in zircons from parautochthonous Mesozoic terranes in the western margin of Pangea: Implications for the terrane configurations in the northern Andes. The Journal of Geology, 125(5): 487–500. https://doi.org/10.1086/693014

Cardona, A., Valencia, V., Garzón, A., Montes, C., Ojeda, G., Ruiz, J. & Weber, M. 2010. Permian to Triassic I to S–type magmatic switch in the northeast Sierra Nevada de Santa Marta and adjacent regions, Colombian Caribbean: Tectonic setting and implications within Pangea paleogeography. Journal of South American Earth Sciences, 29(4): 772–783. https://doi.org/10.1016/j.jsames.2009.12.005

Cardona, A., Valencia, V.A., Lotero, A., Villafañez, Y. & Bayona, G. 2016. Provenance of middle to late Palaeozoic sediments in the northeastern Colombian Andes: Implications for Pangea reconstruction. International Geology Review, 58(15): 1914–1939. https://doi.org/10.1080/00206814.2016.1190948

Carvajal, C.A., Fuquen, J.A., Gómez, L.A. & Núñez, A. 1983. Memoria explicativa: Cartografía geológica y prospección geoquímica regional de la plancha 282 Chaparral. Ingeominas, 88 p. Bogotá.

Carvajal, C.A., Fuquen, J.A. & Gómez, L.A. 1993. Geología de la plancha 282 Chaparral. Scale 1:100 000. Ingeominas. Bogotá.

Cediel, F., Shaw, R.P. & Cáceres, C. 2003. Tectonic assembly of the northern Andean Block. In: Bartolini, C., Buffler, R.T. & Blickwede, J. (editors), The circum–Gulf of Mexico and the Caribbean: Hydrocarbon habitats, basin formation, and plate tectonics. American Association of Petroleum Geologists, Memoir 79, p. 815–848. Tulsa, USA.

Chappell, B.W. & White, A.J.R. 1974. Two contrasting granite types. Pacific Geology, 8: 173–174.

Clavijo, J. 1994. Memoria explicativa: Mapa geológico generalizado del departamento de Norte de Santander. Scale 1:250 000. Ingeominas, Internal report 2182, 47 p. Bucaramanga.

Clavijo, J., Mantilla, L., Pinto, J., Bernal, L. & Pérez, A. 2008. Evolución geológica de la serranía de San Lucas, norte del Valle Medio del Magdalena y noroeste de la cordillera Oriental. Boletín de Geología, 30(1): 45–62.

Cochrane, R., Spikings, R., Gerdes, A., Winkler, W., Ulianov, A., Mora, A. & Chiaradia, M. 2014. Distinguishing between in–situ and accretionary growth of continents along active margins. Lithos, 202–203: 382–394. https://doi.org/10.1016/j.lithos.2014.05.031

Condie, K.C. 1989. Plate tectonics and crustal evolution. Third edition, Pergamon Press, 476 p. Oxford.

Cordani, U.G., Cardona, A., Jiménez, D., Liu, D. & Nutman, A.P. 2005. Geochronology of Proterozoic basement inliers in the Colombian Andes: Tectonic history of remnants of a fragmented Grenville belt. In: Vaughan, A.P.M., Leat, P.T. & Pankhurst, R.J. (editors), Terrane processes at the margins of Gondwana. Geological Society of London, Special Publication 246, p. 329–346. https://doi.org/10.1144/GSL.SP.2005.246.01.13

Correa–Martínez, A.M., Rodríguez, G., Arango, M.I., Zapata, G. & Bermúdez, J.G. 2016. Batolito de Mogotes. Catálogo de unidades litoestratigráficas de Colombia. Servicio Geológico Colombiano, 110 p. Medellín.

Correa–Martínez, A.M., Rodríguez, G., Bermúdez, J.G., Arango, M.I. & Zapata, G. 2018. Riolitas del Alto Los Cacaos. Catálogo de unidades litoestratigráficas de Colombia. Servicio Geológico Colombiano, 54 p. Medellín.

Cossio, U., Rodríguez, G. & Rodríguez, M.A. 1994. Memoria explicativa: Geología de la plancha 283 Purificación, departamento del Tolima. Scale 1:100 000. Ingeominas, 108 p. Bogotá.

Cox, K.G., Bell, J.D. & Pankhurst, R.J. 1979. The interpretation of igneous rocks. George Allen & Unwin, 464 p. London.

Daconte, R. & Salinas, R. 1980a. Memoria explicativa: Geología de las planchas 66 Miraflores y 76 Ocaña. Scale 1:100 000. Ingeominas, 105 p. Bucaramanga.

Daconte, R. & Salinas, R. 1980b. Geología de la plancha 66 Miraflores. Scale 1:100 000. Ingeominas. Bucaramanga.

Daconte, R. & Salinas, R. 1980c. Geología de la plancha 76 Ocaña. Scale 1:100 000. Ingeominas. Bucaramanga.

Dörr, W., Grösser, J.R., Rodríguez, G.I. & Kramm, U. 1995. Zircon U–Pb age of the Paramo Rico tonalite–granodiorite, Santander Massif (Cordillera Oriental, Colombia) and its geotectonic significance. Journal of South American Earth Sciences, 8(2): 187–194. https://doi.org/10.1016/0895-9811(95)00004-Y

Etayo–Serna, F., Barrero, D., Lozano, H., Espinosa, A., González, H., Orrego, A., Ballesteros, I., Forero, H., Ramírez, C., Zambrano–Ortiz, F., Duque–Caro, H., Vargas, R., Núñez, A., Álvarez, J., Ropaín, C., Cardozo, E., Galvis, N., Sarmiento, L., Alberts, J.P., Case, J.E., Singer, D.A., Bowen, R.W., Berger, B.R., Cox, D.P. & Hodges, C.A. 1983. Mapa de terrenos geológicos de Colombia. Publicaciones Geológicas Especiales del Ingeominas 14(1), p. 1–235. Bogotá.

Feininger, T., Barrero, D. & Castro, N. 1972. Geología de parte de los departamentos de Antioquia y Caldas–subzona II–B. Boletín Geológico, 20(2): 1–173.

Ferreira, P., Núñez, A. & Rodríguez, M.A. 1998. Geología de la plancha 323 Neiva. Scale 1:100 000. Ingeominas. Bogotá.

Ferreira, P., Núñez, A. & Rodríguez, M.A. 2002. Memoria explicativa: Levantamiento geológico de la plancha 323 Neiva. Scale 1:100 000. Ingeominas. 100 p. Bogotá.

Forero–Suárez, A. 1990. The basement of the Eastern Cordillera, Colombia: An allochthonous terrane in northwestern South America. Journal of South American Earth Sciences, 3(2–3): 141–151. https://doi.org/10.1016/0895-9811(90)90026-W

Frost, B.R., Barnes, C.G., Collins, W.J., Arculus, R.J., Ellis, D.J. & Frost, C.D. 2001. A geochemical classification for granitic rocks. Journal of Petrology, 42(11): 2033–2048. https://doi.org/10.1093/petrology/42.11.2033

García, C.A. & Ríos, C.A. 1999. Metamorfismo y metalogenia asociada del Macizo de Santander, cordillera Oriental, Colombia. Proyecto de investigación 1102–05–083–95, Informe final, unpublished. Universidad Industrial de Santander. 191 p. Bucaramanga.

Gendall, I.R., Quevedo, L.A., Sillitoe, R.H., Spencer, R.M., Puente, C.O., León, J.P. & Povedo, R.R. 2000. Discovery of a Jurassic porphyry copper belt, Pangui area, southern Ecuador. SEG Newsletter, 43(1): 8–15.

Goldsmith, R., Marvin, R.F. & Mehnert, H.H. 1971. Radiometric ages in the Santander Massif, Eastern Cordillera, Colombian Andes. United States Geological Survey, Professional Paper, 750–D: D41–D49.

Gómez, J., Montes, N., Nivia, Á. & Diederix, H., compiladores. 2015a. Geological Map of Colombia 2015. Scale 1:1 000 000. Servicio Geológico Colombiano, 2 sheets. Bogotá.

Gómez, J., Montes, N.E., Alcárcel, F.A. & Ceballos, J.A. 2015b. Catálogo de dataciones radiométricas de Colombia en ArcGIS y Google Earth. In: Gómez, J. & Almanza, M.F. (editors), Compilando la geología de Colombia: Una visión a 2015. Servicio Geológico Colombiano, Publicaciones Geológicas Especiales 33, p. 63–419. Bogotá.

González, H. 1980. Geología de las planchas 167 Sonsón y 187 Salamina. Scale 1:100 000. Boletín Geológico, 23(1): 1–174.

Green, T.H. 1980. Island arc and continent–building magmatism: A review of petrogenetic models based on experimental petrology and geochemistry. Tectonophysics, 63(1–4): 367–385. https://doi.org/10.1016/0040-1951(80)90121-3

Hall, R.B., Álvarez, J. & Rico, H. 1972. Geología de parte de los departamentos de Antioquia y Caldas (Sub–Zona II–A). Boletín Geológico, 20(1): p. 1–85.

Harris, N.B.W., Pearce, J.A. & Tindle, A.G. 1986. Geochemical characteristics of collision–zone magmatism. In: Coward, M.P. & Ries, A.C. (editors), Collision tectonics. Geological Soci-

ety of London, Special Publication 19, p. 67–81. https://doi.org/10.1144/GSL.SP.1986.019.01.04

Horton, B.K., Saylor, J.E., Nie, J., Mora, A., Parra, M., Reyes–Harker, A. & Stockli, D.F. 2010. Linking sedimentation in the northern Andes to basement configuration, Mesozoic extension, and Cenozoic shortening: Evidence from detrital zircon U–Pb ages, Eastern Cordillera, Colombia. Geological Society of America Bulletin, 122(9–10): 1423–1442. https://doi.org/10.1130/B30118.1

Ibañez–Mejia, M., Ruiz, J., Valencia, V., Cardona, A., Gehrels, G.E. & Mora, A. 2011. The Putumayo Orogen of Amazonia and its implications for Rodinia reconstructions: New U–Pb geochronological insights into the Proterozoic tectonic evolution of northwestern South America. Precambrian Research, 191(1–2): 58–77. https://doi.org/10.1016/j.precamres.2011.09.005

Irvine, T.N. & Baragar, W.R.A. 1971. A guide to the chemical classification of the common volcanic rocks. Canadian Journal of Earth Sciences, 8(5): 523–548. https://doi.org/10.1139/e71-055

Jiménez–Mejía, D.M., Juliani, C. & Cordani, U.G. 2006. P–*T*–*t* conditions of high–grade metamorphic rocks of the Garzón Massif, Andean basement, SE Colombia. Journal of South American Earth Sciences, 21(4): 322–336. https://doi.org/10.1016/j.jsames.2006.07.001

Kennan, L. & Pindell, J.L. 2009. Dextral shear, terrane accretion and basin formation in the northern Andes: Best explained by interaction with a Pacific–derived Caribbean Plate? In: James, K.H., Lorente, M.A. & Pindell, J.L. (editors), The origin and evolution of the Caribbean Plate. Geological Society of London, Special Publication 328, p. 487–531. https://doi.org/10.1144/SP328.20

Kroonenberg, S.B. & Diederix, H. 1982. Geology of south–central Huila, uppermost Magdalena Valley, Colombia. A preliminary note. Guide Book 21 Annual Field Trip. Colombian Society Petroleum Geologists and Geophysicists, 39 p. Bogotá.

Le Maitre, R.W., Streckeisen, A., Zanettin, B., Le Bas, M.J., Bonin, B., Bateman, P., Bellieni, G., Dudek, A., Efremova, S., Keller, J., Lameyre, J., Sabine, P.A., Schmid, R., Sørensen, H. & Woolley, A.R., editors. 2002. Igneous rocks: A classification and glossary of terms. Recommendations of the International Union of Geological Sciences Subcommission on the systematics of igneous rocks. Cambridge University Press, 236 p. Cambridge, UK. https://doi.org/10.1017/CBO9780511535581

Leal–Mejía, H. 2011. Phanerozoic gold metallogeny in the Colombian Andes: A tectono–magmatic approach. Doctoral thesis, Universitat de Barcelona, 989 p. Barcelona.

Ludwig, K.R. 2012. User´s manual for Isoplot 3.75. A geochronological toolkit for Microsoft Excel. Berkeley Geochronology Center Special Publication 5, 75 p. Berkeley, USA.

Mantilla–Figueroa, L.C., Bissig, T., Cottle, J.M. & Hart, C.J.R. 2012. Remains of early Ordovician mantle–derived magmatism in the Santander Massif (Colombian Eastern Cordillera). Journal of South American Earth Sciences, 38: 1–12. https://doi.org/10.1016/j.jsames.2012.03.001

Mantilla–Figueroa, L.C., Bissig, T., Valencia, V. & Hart, C.J.R. 2013. The magmatic history of the Vetas–California mining district, Santander Massif, Eastern Cordillera, Colombia. Journal of South American Earth Sciences, 45: 235–249. https://doi.org/10.1016/j.jsames.2013.03.006

Mantilla–Figueroa, L.C., García–Ramírez, C.A., Valencia, V.A. 2016. Propuesta de escisión de la denominada 'Formación Silgará' (Macizo de Santander, Colombia), a partir de edades U–Pb en zircones detríticos. Boletín de Geología, 38(1): 33–50. https://doi.org/10.18273/revbol.v38n1-2016002

Marshall, J.D. 1988. Cathodoluminescence of geological materials. Unwin Hyman, 146 p. Boston.

Martens, U., Restrepo, J.J., Ordoñez–Carmona, O. & Correa–Martínez, A.M. 2014. The Tahamí and Anacona Terranes of the Colombian Andes: Missing links between South American and Mexican Gondwana margins. The Journal of Geology, 122(5): 507–530. https://doi.org/10.1086/677177

Maya, M. & González, H. 1995. Unidades litodémicas en la cordillera Central de Colombia. Boletín Geológico, 35(2–3): 43–57.

McCourt, W.J., Aspden, J.A. & Brook, M. 1984. New geological and geochronological data from the Colombian Andes: Continental growth by multiple accretion. Journal of the Geological Society, 141(5): 831–845. https://doi.org/10.1144/gsjgs.141.5.0831

McDonough, W.F. & Sun, S.S. 1995. The composition of the Earth. Chemical Geology, 120(3–4): 223–253. https://doi.org/10.1016/0009-2541(94)00140-4

Meschede, M. & Frisch, W. 1998. A plate–tectonic model for the Mesozoic and early Cenozoic history of the Caribbean Plate. Tectonophysics, 296(3–4): 269–291. https://doi.org/10.1016/S0040-1951(98)00157-7

Middlemost, E.A.K. 1985. Magmas and magmatic rocks: An introduction to igneous petrology. Addison–Wesley Longman Ltd., 266 p. London & New York.

Mojica, J. & Villarroel, C. 1984. Contribución al conocimiento de las unidades paleozoicas del área de Floresta (cordillera Oriental colombiana; departamento de Boyacá) y en especial al de la Formación Cuche. Geología Colombiana, (13): 55–79.

Mojica, J., Villarroel, C., Cuerda, A. & Alfaro, M. 1988. La fauna de graptolites de la Formación El Hígado (Llanvirniano?–Llandeiliano). Serranía de Las Minas, Valle Superior del Magdalena, Colombia. V Congreso Geológico Chileno. Memoirs, II, p. 189–202. Santiago de Chile.

Mojica, J., Kammer, A. & Ujueta, G. 1996. El Jurásico del sector noroccidental de Suramérica y guía de la excursión al Valle Superior del Magdalena (Nov. 1–4/95), regiones de Payandé y Prado, departamento del Tolima, Colombia. Geología Colombiana, (21): 3–40.

Nakamura, N. 1974. Determination of REE, Ba, Fe, Mg, Na and K in carbonaceous and ordinary chondrites. Geochimica et Cosmochimica Acta, 38(5): 757–775. https://doi.org/10.1016/0016-7037(74)90149-5

Nelson, H.W. 1957. Contribution to the geology of the Central and Western Cordillera of Colombia in the sector between Ibagué and Cali. Leidse Geologische Meaedelingen, 22, 75 p. Leiden, the Netherlands.

Nelson, W.H. 1962. Contribución al conocimiento de la cordillera Central de Colombia sección entre Ibagué y Armenia. Boletín Geológico, 10(1–3): 161–202.

Noble, S.R., Aspden, J.A. & Jemielita, R. 1997. Northern Andean crustal evolution: New U–Pb geochronological constraints from Ecuador. Geological Society of America Bulletin, 109(7): 789–798. https://doi.org/10.1130/0016-7606(1997)109<0789:NACENU>2.3.CO;2

Núñez, A. 2001. Memoria explicativa: Mapa geológico del departamento del Tolima: Geología, recursos geológicos y amenazas geológicas. Scale 1:250 000. Ingeominas, 100 p. Bogotá.

Núñez, A. 2002. Batolito de Ibagué. Catálogo de unidades litoestratigráficas de Colombia. Ingeominas, 26 p. Bogotá.

Ordóñez–Carmona, O., Restrepo, J.J. & Pimentel, M.M. 2006. Geochronological and isotopical review of pre–Devonian crustal basement of the Colombian Andes. Journal of South American Earth Sciences, 21(4): 372–382. https://doi.org/10.1016/j.jsames.2006.07.005

Pearce, J. 1982. Trace element characteristics of lavas from destructive plate boundaries. In: Thorpe, R.S. (editor), Andesites: Orogenic andesites and related rocks. John Wiley and Sons, p. 525–548.

Pearce, J.A. 1996. A user's guide to basalt discrimination diagrams. In: Wyman, D.A. (editor), Trace element geochemistry of volcanic rocks: Applications for massive sulphide exploration. Geological Association of Canada, Short Course Notes 12, p. 79–113. Winnipeg, Canada.

Pearce, J.A. 2008. Geochemical fingerprinting of oceanic basalts with applications to ophiolite classification and the search for Archean oceanic crust. Lithos, 100(1–4): 14–48. https://doi.org/10.1016/j.lithos.2007.06.016

Pearce, J.A., Harris, N.B.W. & Tindle, A.G. 1984. Trace element discrimination diagrams for the tectonic interpretation of granitic rocks. Journal of Petrology, 25(4): 956–983. https://doi.org/10.1093/petrology/25.4.956

Peccerillo, A. & Taylor, S.R. 1976. Geochemistry of Eocene calc–alkaline volcanic rocks from the Kastamonu area, northern Turkey. Contributions to Mineralogy and Petrology, 58(1): 63–81. https://doi.org/10.1007/BF00384745

Pindell, J. & Dewey, J.F. 1982. Permo–Triassic reconstruction of western Pangea and the evolution of the Gulf of Mexico and south Caribbean region. Tectonics, 1(2): 179–211. https://doi.org/10.1029/TC001i002p00179

Restrepo, J.J. & Toussaint, J.F. 1988. Terranes and continental accretion in the Colombian Andes. Episodes, 11(3): 189–193. https://doi.org/10.18814/epiiugs/1988/v11i3/006

Restrepo, J.J. & Toussaint, J.F. 1989. Terrenos alóctonos en los Andes colombianos: Explicación de algunas paradojas geológicas. V Congreso Colombiano de Geología. Memoirs, I, p. 92–107. Bucaramanga.

Restrepo, J.J., Ordóñez–Carmona, O., Martens, U. & Correa, A.M. 2009. Terrenos, complejos y provincias en la cordillera Central colombiana. Ingeniería, Investigación y Desarrollo, 9(2): 49–56.

Restrepo, J.J., Ordóñez–Carmona, O., Armstrong, R. & Pimentel, M.M. 2011. Triassic metamorphism in the northern part of the Tahamí Terrane of the Central Cordillera of Colombia. Journal of South American Earth Sciences, 32(4): 497–507. https://doi.org/10.1016/j.jsames.2011.04.009

Restrepo, J.J., Ibañez–Mejia, M. & García–Casco, A. 2012. U–Pb zircon ages of the Medellín Amphibolites (Central Cordillera of Colombia) reveal mid–Cretaceous tectonic juxtaposition of Triassic and mid–Cretaceous metamorphic complexes. VIII South American Symposium on Isotope Geology. USB memory device, 33 slides. Medellín.

Restrepo–Pace, P. 1995. Late Precambrian to early Mesozoic tectonic evolution of the Colombian Andes based on new geocronological, geochemical and isotopic data. Doctoral thesis, University of Arizona, 195 p. Arizona.

Restrepo–Pace, P.A. & Cediel, F. 2010. Northern South America basement tectonics and implications for paleocontinental reconstructions of the Americas. Journal of South American Earth Sciences, 29(4): 764–771. https://doi.org/10.1016/j.jsames.2010.06.002

Restrepo–Pace, P.A., Ruiz, J., Gehrels, G. & Cosca, M. 1997. Geochronology and Nd isotopic data of Grenville–age rocks in the Colombian Andes: New constraints for late Proterozoic–early Paleozoic paleocontinental reconstructions of the Americas. Earth and Planetary Science Letters, 150(3–4): 427–441. https://doi.org/10.1016/S0012-821X(97)00091-5

Ríos, C., García, C. & Takusa, A. 2003. Tectono–metamorphic evolution of the Silgará Formation metamorphic rocks in the southwestern Santander Massif, Colombian Andes. Journal of South American Earth Sciences, 16(2): 133–154. https://doi.org/10.1016/S0895-9811(03)00025-7

Rodríguez, G. 1995a. Petrografía y microtexturas del Grupo Garzón y el Granito de anatexis de El Recreo, Macizo de Garzón, cordillera Oriental–Colombia. Revista Ingeominas, (5): 17–36.

Rodríguez, G. 1995b. Petrografía del Macizo de La Plata, departamento del Huila. Revista Ingeominas, (5): 5–16.

Rodríguez, G. & Fuquen, J.A. 1989. Geología y prospección geoquímica de la plancha 302 Aipe (Huila). Ingeominas, internal report 2103, 152 p. Ibagué.

Rodríguez, G. & Núñez, A. 1999. Geología del departamento del Tolima. Scale 1:300 000. Ingeominas. Bogotá.

Rodríguez, G., Ferreira, P., Velandia, F. & Núñez, A. 1998. Geología de la plancha 366 Garzón. Scale 1:100 000. Ingeominas. Bogotá.

Rodríguez, G., Zapata, G., Velásquez, M.E., Cossio, U. & Londoño, A.C. 2003. Memoria explicativa: Geología de las planchas 367

Gigante, 368 San Vicente del Caguán, 389 Timaná, 390 Puerto Rico, 391 Lusitania (parte noroccidental) y 414 El Doncello. Scale 1:100 000. Ingeominas, 166 p. Bogotá.

Rodríguez, G., González, H. & Zapata, G. 2005. Memoria explicativa: Geología de la plancha 147 Medellín oriental. Scale: 1:100 000. Ingeominas, 300 p. Medellín.

Rodríguez, G., Arango, M.I., Zapata, G. & Bermúdez, J.G. 2015a. Características petrográficas, geoquímicas y edad U–Pb de los plutones jurásicos del Valle Superior del Magdalena. XV Congreso Colombiano de Geología. Poster. Bucaramanga.

Rodríguez, G., Arango, M.I., Bermúdez, J.G. & Zapata, G. 2015b. Cuarzomonzonita de Los Naranjos. Catálogo de unidades litoestratigráficas de Colombia. Servicio Geológico Colombiano, 28 p. Medellín.

Rodríguez, G., Arango, M.I., Zapata, G. & Bermúdez, J.G. 2015c. Cuarzomonzodiorita de El Astillero. Catálogo de unidades litoestratigráficas de Colombia. Servicio Geológico Colombiano, 27 p. Medellín.

Rodríguez, G., Zapata, G., Arango, M.I. & Bermúdez, J.G. 2015d. Monzogranito de Algeciras. Catálogo de unidades litoestratigraficas de Colombia. Servicio Geológico Colombiano, 36 p. Medellín.

Rodríguez, G., Arango, M.I., Bermúdez, J.G. & Zapata, G. 2015e. Granito de Garzón. Catálogo de unidades litoestratigráficas de Colombia. Servicio Geológico Colombiano, 23 p. Medellín.

Rodríguez, G., González, H., Zapata, G., Cossio, U. & Correa–Martínez. A.M. 2016a. Geología de la plancha 147 Medellín Oriental. Scale 1:50 000. Servicio Geológico Colombiano, 464 p. Bogotá.

Rodríguez, G., Arango, M.I., Zapata, G. & Bermúdez, J.G. 2016b. Formación Saldaña. Catálogo de las unidades litoestratigráficas de Colombia. Servicio Geológico Colombiano, 90 p. Medellín.

Rodríguez, G., Zapata, G., Arango, M.I. & Bermúdez, J.G. 2017a. Caracterización petrográfica, geoquímica y geocronología de rocas granitoides pérmicas al occidente de La Plata y Pacarní, Huila, Valle Superior del Magdalena, Colombia. Boletín de Geología, 39(1): 41–68. https://doi.org/10.18273/revbol.v39n1-2017002

Rodríguez, G., Zapata, G., Correa–Martínez, A.M. & Arango, M.I. 2017b. Caracterización petrográfica, química y geocronológica del magmatismo Triásico–Jurásico del Macizo de Santander, Colombia. XVI Congreso Colombiano de Geología y III Simposio de Exploradores. Memoirs, p. 1430–1433. Santa Marta.

Rodríguez, G., Correa, A.M., Zapata, G. & Arango, M.I. 2017c. Monzogranito de La Corcova. Catálogo de unidades litoestratigráficas de Colombia. Servicio Geológico Colombiano, 105 p. Medellín.

Rodríguez, G., Arango, M.I., Zapata, G. & Correa–Martínez, A.M. 2017d. Tonalita de San Martín. Catálogo de las unidades litoestratigráficas de Colombia. Servicio Geológico Colombiano, 55 p. Medellín.

Rodríguez, G., Arango, M.I., Zapata, G. & Bermúdez, J.G. 2018a. Petrotectonic characteristics, geochemistry, and U–Pb geochronology of Jurassic plutons in the Upper Magdalena Valley–Colombia: Implications on the evolution of magmatic arcs in the NW Andes. Journal of South American Earth Sciences, 81: 10–30. https://doi.org/10.1016/j.jsames.2017.10.012

Rodríguez, G., Arango, M.I., Correa, A.M. & Zapata, G. 2018b. Riolita de San Joaquín. Catálogo de unidades litoestratigráficas de Colombia. Servicio Geológico Colombiano, 46 p. Medellín.

Rodríguez, G., Zapata, G., Arango, M.I. & Correa, A.M. 2018c. Monzogranito de Santa Bárbara. Catálogo de unidades litoestratigráficas de Colombia. Servicio Geológico Colombiano, 95 p. Medellín.

Rodríguez–García, G., Correa–Martínez, A.M., Zapata–Villada, J.P. & Obando–Erazo, G. 2019. Fragments of a Permian arc on the western margin of the Neoproterozoic basement of Colombia. In: Gómez, J. & Mateus–Zabala, D. (editors), The Geology of Colombia, Volume 1 Proterozoic – Paleozoic. Servicio Geológico Colombiano, Publicaciones Geológicas Especiales 35, p. 205–239. Bogotá. https://doi.org/10.32685/pub.esp.35.2019.10

Ross, M.I. & Scotese, C.R. 1988. A hierarchical tectonic model of the Gulf of Mexico and Caribbean region. Tectonophysics, 155(1–4): 139–168. https://doi.org/10.1016/0040-1951(88)90263-6

Royero, J.M. & Clavijo, J. 2001. Memoria explicativa: Mapa geológico generalizado, departamento de Santander. Scale 1:400 000. Ingeominas, 91 p. Bogotá.

Shand, S.J. 1943. Eruptive rocks. Their genesis, composition, classification and their relation to ore deposits, with a chapter on meteorites. Wiley & Sons, 488 p. New York.

Siivola, J. & Schmid, R. 2007. List of mineral abbreviations. In: Fettes, D. & Desmons, J. (editors), Metamorphic Rocks: A Classification and Glossary of Terms. Recommendations of the International Union of Geological Sciences Subcommission on the Systematics of Metamorphic Rocks. Cambridge University Press, p. 93–110. Cambridge, UK

Slama, J., Kosler, J., Condon, D.J., Crowley, J.L., Gerdes, A., Hanchar, J.M., Horstwood, M.S.A., Morris, G.A., Nasdala, L., Norberg, N., Schaltegger, U., Schoene, B., Tubrett, M. & Whitehouse, M.J. 2008. Plešovice zircon–A new natural reference material for U–Pb and Hf isotopic microanalysis. Chemical Geology, 249(1–2): 1–35. https://doi.org/10.1016/j.chemgeo.2007.11.005

Solari, L., Gómez–Tuena, A., Bernal, J.P., Pérez–Arvizu, O. & Tanner, M. 2010. U–Pb zircon geochronology with an integrated LA–ICP–MS microanalytical workstation: Achievements in precision and accuracy. Geostandards and Geoanalytical Research, 34(1): 5–18. https://doi.org/10.1111/j.1751-908X.2009.00027.x

Spikings, R., Cochrane, R., Villagómez, D., van der Lelij, R., Vallejo, C., Winkler, W. & Beate, B. 2015. The geological history of northwestern South America: From Pangaea to the early collision of the Caribbean Large Igneous Province (290–75 Ma). Gondwana Research, 27(1): 95–139. https://doi.org/10.1016/j.gr.2014.06.004

Stacey, J.S. & Kramers, J.D. 1975. Approximation of terrestrial lead isotope evolution by a two–stage model. Earth and Planetary Science Letters, 26(2): 207–221. https://doi.org/10.1016/0012-821X(75)90088-6

Stibane, F. & Forero, A. 1969. Los afloramientos del Paleozoico en la Jagua (Huila) y río Nevado (Santander del sur). Geología Colombiana, (6): 31–66.

Streckeisen, A. 1974. Classification and nomenclature of plutonic rocks recommendations of the IUGS subcommission on the systematics of igneous rocks. Geologische Rundschau., 63(2): 773–786. https://doi.org/10.1007/BF01820841

Streckeisen, A. 1979. Classification and nomenclature of volcanic rocks, lamprophyres, carbonatites, and melilitic rocks: Recommendations and suggestions of the IUGS subcommission on the systematics of igneous rocks. Geology, 7(7): 331–335. https://doi.org/10.1130/0091-7613(1979)7<331:-CANOVR>2.0.CO;2

Sun, S.S. & McDonough, W.F. 1989. Chemical and isotopic systematics of oceanic basalts: Implications for mantle composition and processes. In: Saunders, A.D. & Norry, M.J. (editors), Magmatism in the ocean basins. Geological Society of London, Special Publications 42, p. 313–345. https://doi.org/10.1144/GSL.SP.1989.042.01.19

Toussaint, J.F. 1995. Evolución geológica de Colombia; 2 Triásico–Jurásico. Universidad Nacional de Colombia, 94 p. Medellín.

Ulloa, C. & Rodríguez, G.I. 1982. Intrusiones ácidas ordovícicas y post–devónicas en la Floresta (Boyacá). IV Congreso Colombiano de Geología. Memoirs, p. 23. Cali.

van der Lelij, R. 2013. Reconstructing northwestern Gondwana with implications for the evolution of the Iapetus and Rheic oceans: A geochronological, thermochronological and geochemical study. Doctoral thesis, University of Genève, 248 p. Genève. https://doi.org/10.13097/archive-ouverte/unige:31653

van der Lelij, R., Spikings, R.A. & Mora, A. 2016. Thermochronology and tectonics of the Mérida Andes and the Santander Massif, NW South America. Lithos, 248–251: 220–239. https://doi.org/10.1016/j.lithos.2016.01.006

Vargas, R. & Arias, A. 1981a. Geología de la plancha 86 Ábrego. Scale 1:100 000. Ingeominas. Bogotá.

Vargas, R. & Arias, A. 1981b. Geología de la plancha 97 Cáchira. Scale 1:100 000. Ingeominas. Bogotá.

Vargas, R., Arias, A., Jaramillo, L., & Tellez, N. 1984. Geología de la Plancha 136 Málaga. Scale 1:100 000. Ingeominas. Bogotá.

Velandia, F., Morales, C.J., Caicedo, J.C. & Núñez, A. 2000. Geología de la plancha 345 Campoalegre. Scale 1:100 000. Ingeominas. Bogotá.

Velandia, F., Ferreira, P., Rodríguez, G. & Núñez, A. 2001a. Memoria explicativa: Levantamiento geológico de la plancha 366 Garzón. Ingeominas, 81 p. Bogotá.

Velandia, F., Nuñez, A. & Marquínez, G. 2001b. Memoria explicativa: Mapa geológico del departamento del Huila. Scale 1:300 000. Ingeominas, 151 p. Bogotá.

Velandia, F., Acosta, J., Terraza, R. & Villegas, H. 2005. The current tectonic motion of the northern Andes along the Algeciras Fault System in SW Colombia. Tectonophysics, 399(1–4): 313–329. https://doi.org/10.1016/j.tecto.2004.12.028

Vesga, C.J. & Barrero, D. 1978. Edades K/Ar en rocas ígneas y metamórficas de la cordillera Central de Colombia y su implicación geológica. II Congreso Colombiano de Geología. Abstracts, p. 19. Bogotá.

Villagómez, D., Spikings, R., Magna, T., Kammer, A., Winkler, W. & Beltrán, A. 2011. Geochronology, geochemistry and tectonic evolution of the Western and Central cordilleras of Colombia. Lithos, 125(3–4): 875–896. https://doi.org/10.1016/j.lithos.2011.05.003

Villagómez, D., Martens, U. & Pindell, J. 2015. Are Jurassic and some older blocks in the northern Andes in–situ or far–travelled? Potential correlations and new geochronological data from Colombia and Ecuador. Conference paper. Tectónica jurásica en la parte noroccidental de Sur América y bloques adyacentes. Universidad EAFIT, 1 p. Medellín.

Villarroel, C. & Mojica, J. 1988. El Paleozoico superior (Carbonífero–Pérmico) sedimentario de Colombia: Afloramientos conocidos y características generales. Geología Colombiana, (16): 81–87.

Vinasco, C.J., Cordani, U.G., González, H., Weber, M. & Peláez, C. 2006. Geochronological, isotopic, and geochemical data from Permo–Triassic granitic gneisses and granitoids of the Colombian central Andes. Journal of South American Earth Sciences, 21(4): 355–371. https://doi.org/10.1016/j.jsames.2006.07.007

Ward, D.E., Goldsmith, R., Cruz, J. & Restrepo, H. 1973. Geología de los cuadrángulos H–12 Bucaramanga y H–13 Pamplona, departamento de Santander. Boletín Geológico, 21(1–3): 132 p.

Ward, D.E., Goldsmith, R., Cruz, J., Jaramillo, L. & Vargas, R. 1977a. Geología de la plancha 110 Pamplona. Scale 1:100 000. Ingeominas. Bogotá.

Ward, D.E., Goldsmith, R., Cruz, J., Jaramillo, L. & Vargas, R. 1977b. Mapa geológico del cuadrángulo Pamplona H–13. Scale 1:100 000. Ingeominas. Bogotá.

Ward, D.E., Goldsmith, R., Cruz, J., Téllez, N. & Jaramillo, L. 1977c. Mapa geológico San Gil y Málaga (parte de los cuadrángulos I–12 y I–13), Colombia. Scale 1:100 000. Ingeominas. Bogotá.

Ward, D.E., Goldsmith, R., Jimeno, A., Cruz, J., Restrepo, H. & Gómez, E. 1977d. Geología de la plancha 109 Rionegro. Scale 1:100 000. Ingeominas. Bogotá.

Ward, D.E., Goldsmith, R., Jimeno, A., Cruz, J., Restrepo, H. & Gómez, E. 1977e. Geología de la plancha 120 Bucaramanga. Scale 1:100 000. Ingeominas. Bogotá.

Ward, D.E., Goldsmith, R., Cruz, J., Jaramillo, L. & Vargas, R. 1977f. Geología de la plancha 121 Cerrito. Scale 1:100 000. Ingeominas. Bogotá.

Whalen, J.B., Currie, K.L. & Chappell, B.W. 1987. A–type granites: Geochemical characteristics, discrimination and petrogenesis. Contributions to Mineralogy and Petrology, 95(4): 407–419. https://doi.org/10.1007/BF00402202

Wiedenbeck, M., Allé, P., Corfu, F., Griffin, W.L., Meier, M., Oberli, F., von Quadt, A., Roddick, J.C. & Spiegel, W. 1995. Three natural zircon standards for U–Th–Pb, Lu–Hf, trace element and REE analyses. Geostandards Newsletter, 19(1): 1–23. https://doi.org/10.1111/j.1751-908X.1995.tb00147.x

Zapata, G., Rodríguez, G., Arango, M.I. & Bermúdez, J.G. 2015. Cuarzomonzodiorita de Páez. Catálogo de unidades litoestratigráficas de Colombia. Servicio Geológico Colombiano, 51 p. Medellín.

Zapata, S., Cardona, A., Jaramillo, C., Valencia, V. & Vervoort, J. 2016a. U–Pb LA–ICP–MS geochronology and geochemistry of Jurassic volcanic and plutonic rocks from the Putumayo region (southern Colombia): Tectonic setting and regional correlations. Boletín de Geología, 38(2): 1–38. https://doi.org/10.18273/revbol.v38n2-2016001

Zapata, G., Correa, A.M., Rodríguez, G. & Arango, M.I. 2016b. Granito de Pescadero. Catálogo de unidades litoestratigráficas de Colombia. Servicio Geológico Colombiano, 54 p. Medellín.

Zapata, G., Rodríguez, G. & Arango, M.I. 2017a. Petrografía, geoquímica y geocronología de rocas metamórficas aflorantes en San Francisco Putumayo y la vía Palermo–San Luis asociadas a los complejos La Cocha–Río Téllez y Aleluya. Boletín de Ciencias de la Tierra, (41): 48–65.

Zapata, G., Correa–Martínez, A.M., Rodríguez, G. & Arango, M.I. 2017b. Monzogranito de Santa Rosita. Catálogo de unidades litoestratigráficas de Colombia. Servicio Geológico Colombiano, 57 p. Medellín.

Zapata, G., Arango, M.I., Rodríguez, G. & Correa–Martínez, A.M. 2018. Riolitas El Uvo. Catálogo de unidades litoestratigráficas de Colombia. Servicio Geológico Colombiano, 39 p. Medellín.

Zuluaga, C.A., Amaya, S., Urueña, C. & Bernet, M. 2017. Migmatization and low–pressure overprinting metamorphism as record of two pre–Cretaceous tectonic episodes in the Santander Massif of the Andean basement in northern Colombia (NW South America). Lithos, 274–275: 123–146. https://doi.org/10.1016/j.lithos.2016.12.036

Explanation of Acronyms, Abbreviations, and Symbols:

ACG	Arc calc–alkaline granitoids
CL	Cathodoluminescence
E–MORB	Enriched mid–ocean ridge basalt
HFSE	High field strength element
HREE	Heavy rare earth element
KCG	High–K calc–alkaline granitoids
ICP–MS	Inductively coupled plasma mass spectrometry
LA–ICP–MS	Laser ablation inductively coupled plasma mass spectrometry
LAI	Laboratorio de Estudios Isotópicos
LCL	Lithological Characterization Laboratory
LILE	Large–ion lithophile element
LOI	Loss on ignition
LREE	Light rare earth element
MORB	Mid–ocean ridge basalt
N–MORB	Normal mid–ocean ridge basalt
NBIB	Northern block of Ibagué Batholith
OIB	Ocean island basalt
REE	Rare earth element
SGC	Servicio Geológico Colombiano
SM	Santander Massif
SNSM	Sierra Nevada de Santa Marta
UNAM	Universidad Autónoma de México
UMV	Upper Magdalena Valley
XRF	X–ray fluorescence

Authors' Biographical Notes

Gabriel RODRÍGUEZ–GARCÍA graduated in 1987 with a degree in geological engineering from the Universidad Nacional de Colombia, Sede Medellín. Subsequently, he completed specialization studies at the École Nationale Supérieure des Mines de Paris in 1995, specializing in technical evaluation–economics of mining projects. He has worked for 30 years at the Servicio Geológico Colombiano. He was the head of cartography of the regional headquarters of Ibagué, and acts as coordinator of projects and regional cartography and of work groups for the exploration and evaluation of deposits. He currently coordinates the Medellín headquarters and the Grupo de Estudios Geológicos Especiales of the Servicio Geológico Colombiano. He has previously been a professor of Colombian Geology, Field Geology I, and Physical Geology at Universidad EAFIT and the director of geology of Grupo Argos. He has authored over 100 publications, including geological maps, memoirs, and scientific articles in geology.

Ana María CORREA–MARTÍNEZ graduated in geological engineering from the Universidad Nacional de Colombia, Sede Medellín and has a PhD in geology from the Universidade de Brasília (Brasil), where she studied the petrogenesis of the Aburrá Ophiolite in the Colombian Central Cordillera. Between 2008 and 2013, she worked as a gold exploration geologist and chief of mineral exploration projects. She was lecturer at the Universidad Nacional de Colombia (Medellín) in the Departamento de Recursos Minerales. Since 2014, she has worked in the Servicio Geológico Colombiano on geochronology of metamorphic units from the northwestern slope of the Central Cordillera and on the project "Jurassic Magmatism in the Colombian Andes".

Gilberto ZAPATA–GARCÍA graduated with a degree in mining and geological engineering from the Russian State Geological Prospecting University (Российский государственный геологоразведочный университет) (MGRI–RSGPU) in 1977 and specialized in urban–regional planning at the Universidad Nacional de Colombia, Sede Medellín in 2000. He worked in geological mapping at a scale of 1:100.000, exploration, and petrography at Servicio Geológico Colombiano, from 1978 to 2017. Since 2014, he has been a member of the Proyecto Estudios Geológicos Especiales, participating in studies on Jurassic magmatism in Colombia.

María Isabel ARANGO–MEJÍA is a geologist who graduated from the Universidad de Caldas in 2008 and specialized in Geographic Information Systems (GIS) at the Universidad de San Buenaventura in 2016. She has worked on seismic projects, geological mapping, and geological research in Colombia. She is currently working on environmental projects.

Gloria OBANDO–ERAZO has a BS in geology, Universidad Nacional de Colombia Sede Bogotá, an MS in environmental geology with an emphasis in geophysics, processing and interpretation of aerial gamma ray spectrometry and aerial magnetometry (Universidade de Brasília, 2001), and is a PhD candidate in aerial geophysics (Universidade de Brasilia, 2006). She has worked since 1995 on multiple projects in Colombia using potential fields at the Servicio Geológico Colombiano. Since 2014, she has been working in the Grupo de Estudios Geológicos Especiales of the Servicio Geológico Colombiano on the project "Jurassic Magmatism in the Colombian Andes".

Juan Pablo ZAPATA–VILLADA is a geological engineer and MS in mineral resources of Universidad Nacional de Colombia Sede Medellín. He worked for the Cordilleran project of México (Tectonic Analysis) and has expertise in GIS, U–Pb analysis, and heavy minerals. He works for the Servicio Geológico Colombiano. His job includes GIS and the geochronology, and geochemistry of the Western Cordillera and Jurassic magmatism in Colombia. He has participated as a speaker at the Colombian Geological Congress, winning the Ricardo Lleras Codazzi in the XIV edition.

José Gilberto BERMÚDEZ graduated in 1989 with a degree in geology from the Universidad Pedagógica y Tecnológica de Sogamoso (UPTC), Boyacá, Colombia. He worked as a groundwater, geophysics and geology consultant from 1989 to 2009, was the general manager of Hidrocol Ltda and Gesprocom Ltda, worked as an exploration geologist for Coexminas and currently works as a basic geosciences specialist for the Servicio Geológico Colombiano. He has published more than 15 studies in the field of regional geology.

Volume 2

Chapter 5

https://doi.org/10.32685/pub.esp.36.2019.05
Published online 28 April 2020

Jurassic Evolution of the Northwestern Corner of Gondwana: Present Knowledge and Future Challenges in Studying Colombian Jurassic Rocks

Germán BAYONA[1]*, Camilo BUSTAMANTE[2], Giovanny NOVA[3], and Ana Milena SALAZAR–FRANCO[4]

1 gbayona@cgares.org
Corporación Geológica ARES
Calle 26 n.° 69C–03 Torre C Of. 904
Bogotá, Colombia

2 cbustam3@eafit.edu.co
Universidad EAFIT
Carrera 49 n.° 7 sur–50
Medellín, Colombia

3 gnova@cgares.org
Corporación Geológica ARES
Calle 26 n.° 69C–03 Torre C Of. 904
Bogotá, Colombia

4 asalazar@cgares.org
Corporación Geológica ARES
Calle 26 n.° 69C–03 Torre C Of. 904
Bogotá, Colombia

* Corresponding author

Abstract This chapter summarizes knowledge (published up to February 2019) of metamorphic, plutonic, volcanic, carbonate, and clastic sedimentary Jurassic rocks that are exposed from northern Perú to Venezuela. This compilation allows an evaluation of three tectonic models that have been proposed for the evolution of the northwestern corner of Gondwana: an extensional model, a subduction–dominated model, and the along–marginal migration of blocks model, that last of which considers the interaction of western subduction and the north–south separation of continental blocks. We conclude that (1) the Jurassic evolution of this orthogonal margin cannot be represented in a single paleogeographic map that represents a dominant geodynamic process; (2) future analyses must consider the superposition of both Pacific subduction and proto–Caribbean extensional processes; (3) extensional basins in La Guajira, the serranía de Perijá, and the Mérida Andes include the sedimentary record of predominantly proto–Caribbean extension, whereas western–subduction processes are recorded by a batholith chain that extends from southern Ecuador to the Santa Marta Massif in northern Colombia; and (4) a Middle Jurassic unconformity separates Lower to Middle Jurassic sedimentary and volcanic successions, which are related to subduction magmatism and the separation of the North and South American Plates, from Upper Jurassic continental and marine deposits in extensional basins along the northern margin, which record the opening of the proto–Caribbean Sea. Future geochemical studies in Jurassic intrusive bodies should be able to evaluate the contamination from Triassic versus Grenvillian and older continental crust. Metamorphic studies should concentrate on the petrology and the pressure–temperature–time (P–T–t) paths. The chronostratigraphic framework of sedimentary basins should be improved by resuming paleontological investigations and geochronological analysis at the base and top of volcanoclastic rocks. Sedimentological analysis should focus on establishing the geometry of sedimentary basins, the relationship of basin generation with magmatic centers, and documenting the record of paleo–climate indicators in order to establish possible paleo–latitudinal variations of tectonic blocks. Paleomagnetic studies should be conducted at different localities in Lower – Middle Jurassic rocks to test whether tectonic blocks have been static or record northward translations. The strong decrease in magmatic activity during the Late Jurassic time should be explained within a regional tectono–magmatic framework.

Keywords: *Jurassic, tectonic evolution, Gondwana, orthogonal margins, geodynamics.*

Citation: Bayona, G., Bustamante, C., Nova, G. & Salazar–Franco, A.M. 2020. Jurassic evolution of the northwestern corner of Gondwana: Present knowledge and future challenges in studying Colombian Jurassic rocks. In: Gómez, J. & Pinilla–Pachon, A.O. (editors), The Geology of Colombia, Volume 2 Mesozoic. Servicio Geológico Colombiano, Publicaciones Geológicas Especiales 36, p. 171–207. Bogotá. https://doi.org/10.32685/pub.esp.36.2019.05

Resumen Este capítulo resume el conocimiento (publicado a febrero de 2019) sobre las rocas metamórficas, plutónicas, volcánicas y sedimentarias calcáreas y clásticas de edad jurásica expuestas desde el norte de Perú hasta Venezuela. Esta compilación permite evaluar tres modelos tectónicos propuestos para la evolución de la esquina noroccidental de Gondwana: un modelo de extensión, uno de subducción y uno de movimiento de bloques paralelo a la margen que considera la interacción de la subducción al occidente y la separación norte–sur de bloques continentales. Concluimos que (1) la evolución tectónica del Jurásico en esta margen ortogonal no puede ser representada en un solo mapa paleogeográfico que represente un proceso geodinámico dominante; (2) futuros análisis deben considerar la superposición de la subducción en el Pacífico y los procesos extensionales del proto–Caribe; (3) cuencas extensionales en La Guajira, la serranía de Perijá y los Andes de Mérida contienen el registro sedimentario predominantemente de la extensión proto–Caribe, mientras que los procesos de subducción en la margen occidental están registrados por la cadena de batolitos que se extiende desde el sur de Ecuador hasta el Macizo de Santa Marta en el norte de Colombia; (4) una discordancia del Jurásico Medio separa las sucesiones sedimentarias y volcánicas del Jurásico Inferior a Medio, que están relacionadas con magmatismo de subducción y con la separación de las placas de Norteamérica y de Suramérica, de depósitos continentales y marinos en cuencas extensionales a lo largo del margen norte de edad Jurásico Superior que registran la apertura del mar proto–Caribe. Futuros estudios geoquímicos en rocas plutónicas jurásicas deben evaluar si la contaminación más antigua proviene de corteza continental triásica o grenvilliana, o más vieja. En las rocas metamórficas, los estudios deben enfocarse en análisis petrológicos y trayectorias de presión–temperatura–tiempo (P–T–t). Reanudar los estudios paleontológicos y los análisis geocronológicos en la base y tope de las sucesiones volcanoclásticas mejorará el marco cronoestratigráfico de las cuencas sedimentarias. Los análisis sedimentológicos deben centrarse en establecer la geometría de las cuencas sedimentarias, la relación genética de estas cuencas con los centros magmáticos y la documentación de los marcadores paleoclimáticos que permitan establecer las variaciones paleolatitudinales de bloques tectónicos. Se deben realizar estudios paleomagnéticos en diferentes localidades de rocas del Jurásico Inferior y Medio para probar si los bloques tectónicos han sido estáticos o registran translaciones hacia el norte. La fuerte disminución en la actividad magmática durante el Jurásico Superior debe ser explicada en un contexto de análisis tectonomagmático.

Palabras clave: *Jurásico, evolución tectónica, Gondwana, márgenes ortogonales, geodinámica.*

1. Introduction

Why is studying the Jurassic record in the northern Andes important? After the collision of several blocks to form the western margin of Pangea during the end of the Permian and the beginning of the Triassic (247– 299 Ma) (see summary in Martini & Ortega–Gutiérrez, 2016; Torsvik & Cocks, 2016), the northwestern corner of Gondwana became bounded by two active margins: (1) a western active margin, which experienced the long–lived subduction process of the Oceanic Pacific (Farallón) Plate; and (2) a northern tectonic boundary, which was dominated by the breakup of Pangea, separation of the North and South American Plates, and consequent opening of the proto–Caribbean Sea. Well–exposed Jurassic magmatic, sedimentary and documented metamorphic rocks in the northern Andes (Figure 1) are the key to understanding the evolution of these two active tectonic margins and testing different hypotheses of the westward and northward continental growth of Gondwana.

The interaction of these two margins led to a complex and controversial internal organization of Gondwana and peri–Gondwana blocks in the Middle Triassic to Jurassic (145–247 Ma) (see summary in Martini & Ortega–Gutiérrez, 2016; Spikings et al., 2015). New geochronological data available in the literature, demand a revision of the former identification of tectonic terranes (see discussion in Rodríguez et al., 2018), and paleomagnetic data test the concept that continental crustal blocks to the east of the Romeral Suture Zone (Figure 1) have an autochthonous origin (Bayona et al., 2006, 2010). Therefore, the understanding of the Jurassic tectonic evolution of these two orthogonal margins of Gondwana requires the clear identification of terrane boundaries of continental blocks, its paleogeographic

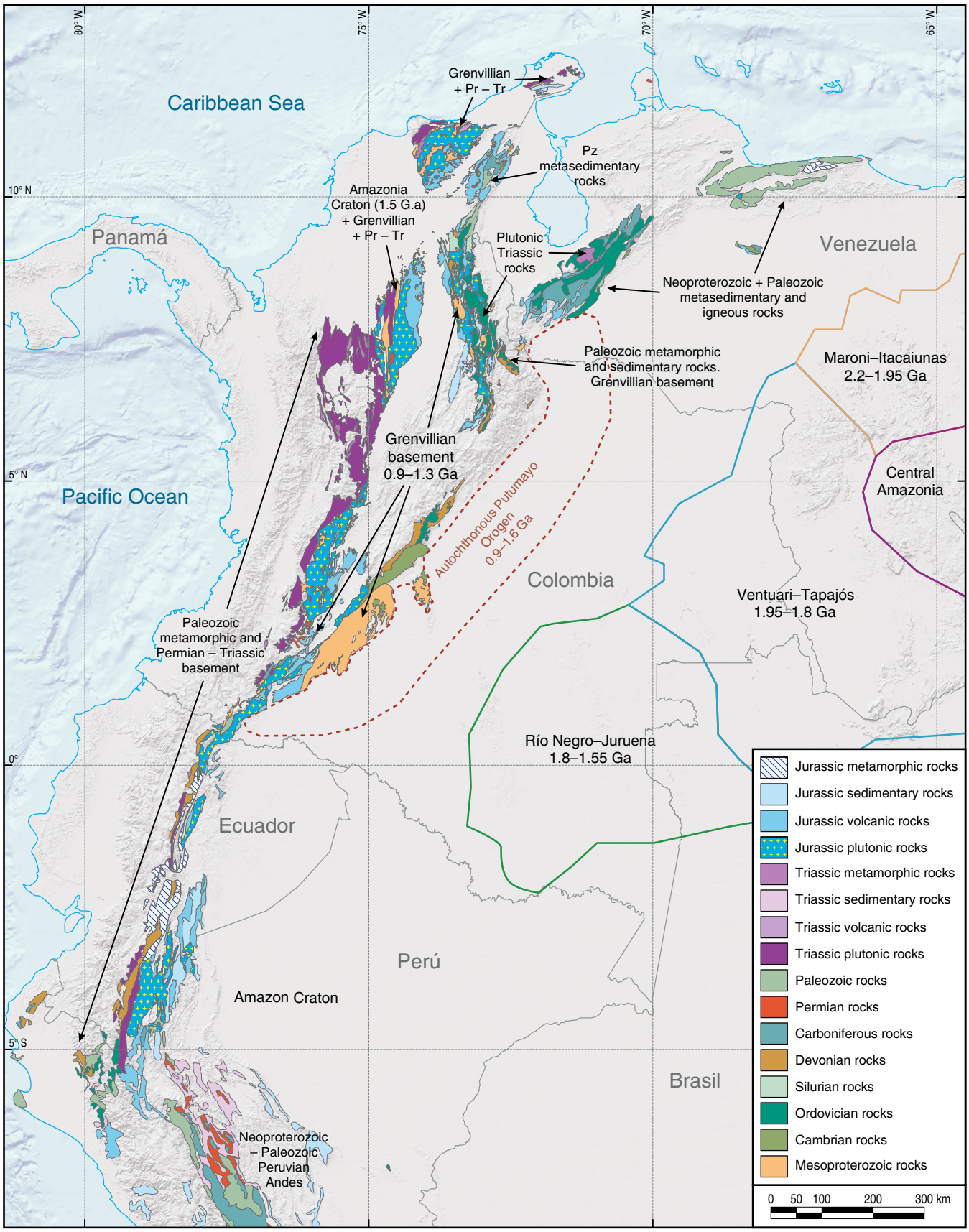

Figure 1. Exposure of Jurassic and pre–Jurassic basement and sedimentary rocks that are in intrusive/faulted/depositional contact in the northern Peruvian to Venezuela Andes. Faults are not shown for simplicity. The basement provinces in the Amazon Craton and Putumayo Orogen are modified from Ibañez–Mejia et al. (2011 and references therein). Simplified and modified from Gómez et al. (2019).

distribution, and how these continental blocks interacted with one or both of these margins.

Although geochronological data has improved the age control of plutonic and volcanic rocks, the age control of sedimentary and volcanoclastic rocks shows little advance since the review presented in Toussaint (1995) and Mojica et al. (1996). Recent papers about Triassic – Jurassic magmatism focus their studies in restricted areas (e.g., van der Lelij et al., 2016, for Santander Massif and Mérida Andes; Cuadros et al., 2014, for serranía de San Lucas; Bustamante et al., 2016, for Ibagué Batholith; Rodríguez et al., 2018, for southern Upper Magdalena batholiths; Quandt et al., 2018, for Santa Marta Massif). Triassic – Jurassic sedimentary record has been used for the analysis of tectonic–basin forming processes (see summary in Kammer & Sánchez, 2006; Sarmiento–Rojas et al., 2006), proposing the generation of narrow extensional basins related to four tectonic events (Sarmiento–Rojas et al., 2006): Triassic, Late Triassic to Middle Jurassic, Middle Jurassic, and latest Jurassic – Cretaceous events. In these studies, there is not an integration of magmatism and basin evolution processes, and it is necessary to incorporate new evidences of Jurassic metamorphism (e.g., Blanco–Quintero et al., 2014; Bustamante et al., 2017; Rodríguez et al., 2018; Zuluaga et al., 2017).

Tectonic models that have been proposed for the Triassic – Jurassic evolution of the NW corner of Gondwana may be grouped into three tectonic settings (Figure 2), keeping in mind that most of these models use the concept of a single tectonic framework for the ca. 100 my of the Triassic and Jurassic (Figure 1). These three models show different options of continental margin growth:

- The static configuration of Jurassic intracontinental rifts that formed at the northwestern margin of Gondwana as the result of extensional tectonism (taphrogenesis; Mojica & Kammer, 1995; see Cediel et al., 2003 for details of the Bolívar Aulacogen). In the Jurassic (Figure 2a), continental growth was supported by plutonic rocks occupying space that was generated by extension.
- The static configuration of the continental margin with the lateral migration of magmatic arcs that resulted from subduction–zone migration. The growth or destruction of the western continental margin occurred if the subduction zone migrated westward (see Cochrane et al., 2014a; Spikings et al., 2015, for details) or eastward (e.g., Rodríguez et al., 2018), respectively (Figure 2b). The tectonic activity of the northward margin was not considered as a relevant factor in terms of modifying the intraplate tectonic settings of Gondwana.
- Changes in the convergence angle between Pacific and western Gondwana Plates, which controlled subduction processes, the generation of magmatic arcs, and the marginal mobilization of para–autochthonous terranes (Bayona et al., 2006, 2010; Toussaint, 1995) or the accretion of marginal magmatic arcs (Rodríguez et al., 2018) (Figure 2c). In this hypothesis, extensional tectonism occurred simultaneously along the northward margin affecting the intraplate internal tectonic configuration of Gondwana (Bayona et al., 2013a, 2013b).

The continental–crust growth mechanism in active continental margins differs among models (see discussion in Cochrane et al., 2014a). Juvenile magmatism is the only mechanism that generates continental crust in the dominant extensional model; volcanism occurs before extension in active rifting settings, whereas volcanism is uncommon and only ever occurs during and/or after rifting in passive rift settings (see discussion in Frizon de Lamotte et al., 2015). In the second model, subduction rollback favors the migration of the magmatic arc (Cochrane et al., 2014a), but subduction may also erode the continental margin if the advancement occurs in the opposite direction, as suggested by Rodríguez et al. (2018). In the third model, plutonism also induces the growth of the continental margin; the northward migration of continental blocks favors the growth of the margin to the north but also the loss of the crustal margin to the south.

This work is a compendium that summarizes advances in different disciplines regarding the evolution of Jurassic rocks in the northwestern corner of Gondwana (presently the northern Andes and northern Peruvian Andes) based on a comprehensive analysis of the Jurassic metamorphism, plutonism, volcanism, and sedimentation that were documented by several authors. This study is not intended to solve all the problems but will provide some insights regarding how to improve our understanding of the geodynamic evolution the complex, tectonically active northwestern corner of Gondwana, which was affected by different tectonic mechanisms. Most of these publications analyzed a specific type of rock in one area. The strength of this work is the integration of these findings to examine the complete rock system; we do not describe details of published data, but we provide some suggestions regarding what discipline must be implemented to gain knowledge and obtain better constraints in the interpretations. This manuscript focuses on understanding what documentation we have, how the new data fit among the above three models (Figure 2), and in which directions we should move to achieve a robust collection of data for future interpretations. Future research in Jurassic rocks must constrain robust models to better define terranes and interpret the pre– and post–Jurassic tectonic evolution.

2. Materials and Methods

A total of nine "continental crustal blocks" were defined according to (1) the presence and dominance of one or two of volcanic, plutonic, metamorphic, or sedimentary rocks and (2) its present geographic position and relationship with major massifs or ranges (Figure 3). These blocks are bounded by Cenozoic structures and Cenozoic – Quaternary sediments may cover im-

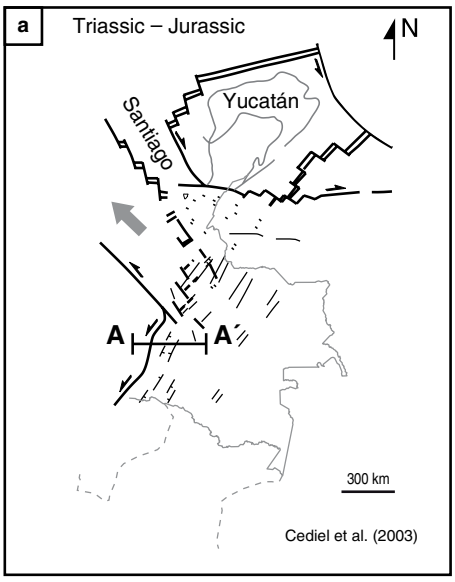

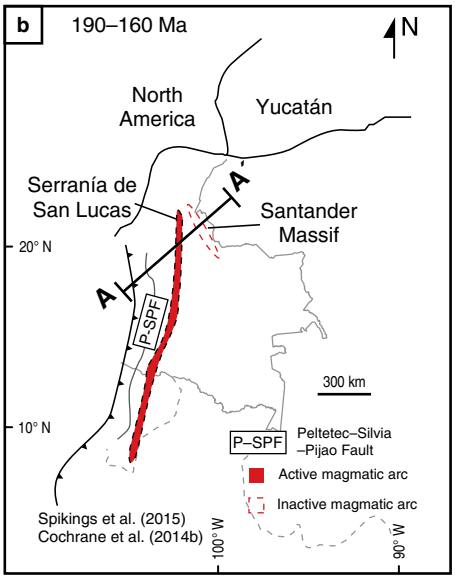

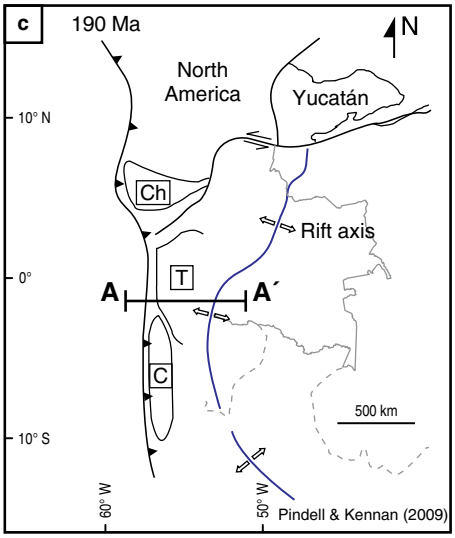

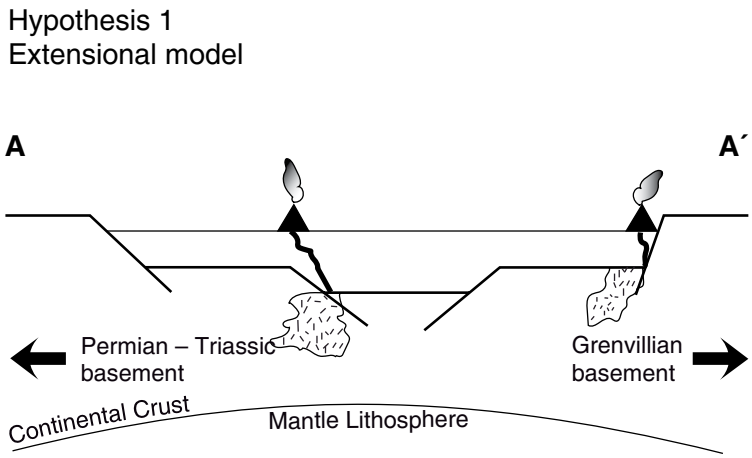

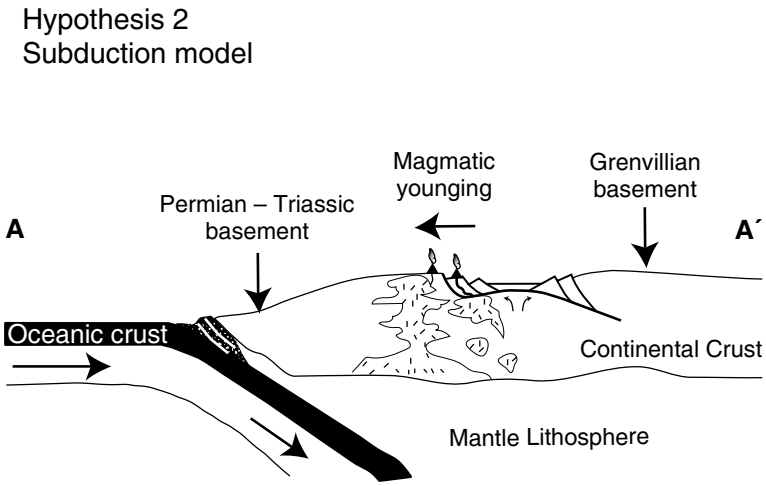

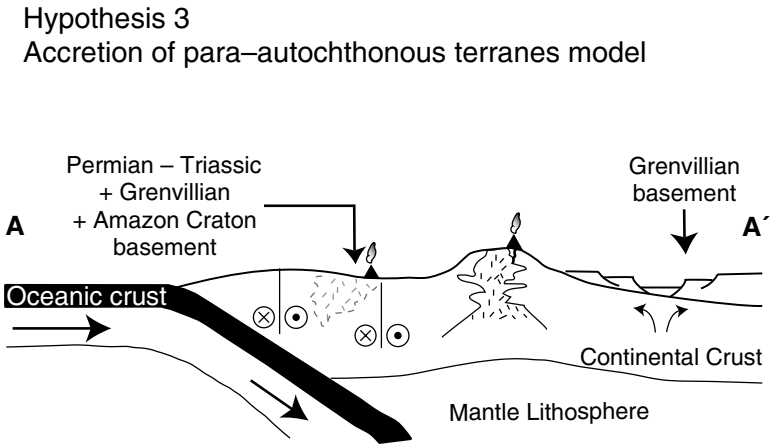

Figure 2. Map view and cross section of the proposed tectonic models for the Jurassic, and the mechanism of continental growth: **(a)** extensional, **(b)** subduction–related, **(c)** along–marginal migration of continental crust models: (Ch) Chortis Terrane, (T) Tahamí Terrane, and (C) Calima Terrane. The cross sections only show the geodynamic processes at the western margin.

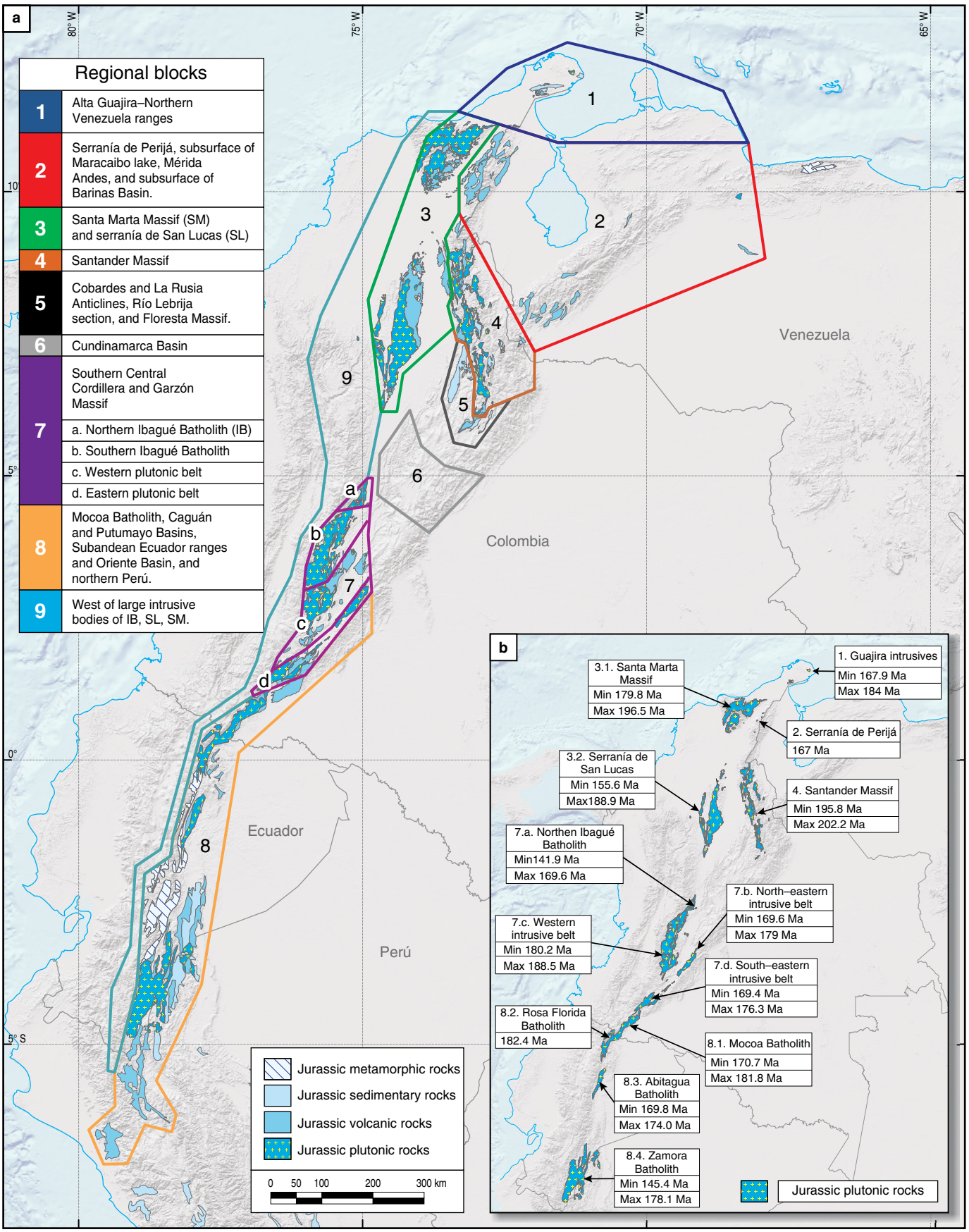
a
80° W
75° W
70° W
65° W
10°
5°
0°
5° S
Regional blocks
1 Alta Guajira–Northern Venezuela ranges
2 Serranía de Perijá, subsurface of Maracaibo lake, Mérida Andes, and subsurface of Barinas Basin.
3 Santa Marta Massif (SM) and serranía de San Lucas (SL)
4 Santander Massif
5 Cobardes and La Rusia Anticlines, Río Lebrija section, and Floresta Massif.
6 Cundinamarca Basin
7 Southern Central Cordillera and Garzón Massif
a. Northern Ibagué Batholith (IB)
b. Southern Ibagué Batholith
c. Western plutonic belt
d. Eastern plutonic belt
8 Mocoa Batholith, Caguán and Putumayo Basins, Subandean Ecuador ranges and Oriente Basin, and northern Perú.
9 West of large intrusive bodies of IB, SL, SM.
Venezuela
Colombia
Ecuador
Perú
Jurassic metamorphic rocks
Jurassic sedimentary rocks
Jurassic volcanic rocks
Jurassic plutonic rocks
0 50 100 200 300 km
b
1. Guajira intrusives
Min 167.9 Ma
Max 184 Ma
3.1. Santa Marta Massif
Min 179.8 Ma
Max 196.5 Ma
2. Serranía de Perijá
167 Ma
3.2. Serranía de San Lucas
Min 155.6 Ma
Max188.9 Ma
4. Santander Massif
Min 195.8 Ma
Max 202.2 Ma
7.a. Northen Ibagué Batholith
Min141.9 Ma
Max 169.6 Ma
7.b. North–eastern intrusive belt
Min 169.6 Ma
Max 179 Ma
7.c. Western intrusive belt
Min 180.2 Ma
Max 188.5 Ma
7.d. South–eastern intrusive belt
Min 169.4 Ma
Max 176.3 Ma
8.2. Rosa Florida Batholith
182.4 Ma
8.1. Mocoa Batholith
Min 170.7 Ma
Max 181.8 Ma
8.3. Abitagua Batholith
Min 169.8 Ma
Max 174.0 Ma
8.4. Zamora Batholith
Min 145.4 Ma
Max 178.1 Ma
Jurassic plutonic rocks

Figure 3. (a) Division of the nine continental crustal blocks that were used to present the Jurassic rock data. **(b)** Age ranges of the uppermost Triassic and Jurassic plutonic rocks from Ecuador to northern Colombia (Rodríguez–García et al., 2020). The ages in the Santander Massif and serranía de San Lucas are younger to the west but older to the north (the plutonic rocks in the Santa Marta Massif are older than those in the serranía de Perijá) and south (the Ibagué Batholith and western belt have older ages than the eastern intrusive belt). See the text for a complete reference of the age control in plutonic and volcanic rocks for each block. Simplified and modified from Gómez et al. (2019).

portant subsurface structures, so we do not provide a specific reference regarding fault limits. Instead, we concentrate on the internal relationships of Jurassic rocks and the contacts with overlying Cretaceous and underlying older rocks to understand the expected boundaries, which are affected by Cretaceous and Cenozoic tectonic activity.

In the next section, we provide a brief description of the present knowledge and summarize the interpretations of each of these blocks. We follow this organization for each block:

- Metamorphism: mineral assemblage, grade of metamorphism, geochronological control, and protolith identification.
- Plutonism: age control (U/Pb), geochemical data (Hf, REE, trace, and other), and inferred tectonic setting (subduction related or rifting). We clearly indicate if another absolute geochronology method is used, but we limit the age reference to U/Pb ages.
- Volcanism: age control (U/Pb), geochemical data (REE, trace, and other), stratigraphic relationships of Jurassic units with underlying (Triassic and older) and overlying (Cretaceous) units, lateral changes in thickness, fault–controlled deposition, inferred tectonic setting (subduction related or rifting), and relationship with plutonism.
- Sedimentation: lithology (siliciclastic, volcanoclastic, carbonate, or mixed); paleontology (macro and micro), stratigraphic relationships of Jurassic units with underlying (Triassic and older) and overlying (Cretaceous) units, lateral changes in thickness, fault–controlled deposition, depositional environments, provenance and detrital geochronology, and tectonic setting.
- Paleomagnetism: results of paleomagnetic directions (declination and inclination), timing of magnetization, and the implications of paleomagnetic directions for vertical–axis rotations and paleolatitudinal location.

For simplicity, references that are related to each stratigraphic section for each block are shown in the respective figure.

3. Jurassic Rocks in Continental Crust Blocks

3.1. Block 1: Alta Guajira and Northern Venezuela Ranges (Figure 4)

3.1.1. Metamorphism

Jurassic rocks in the Cosinas Anticline, Punta Espada, Paraguana Peninsula, and Cordillera de la Costa belt areas show high deformation and strong cleavage fabric but were more likely produced during Cenozoic deformation (Irving, 1972; Zuluaga et al., 2009).

3.1.2. Plutonism

The Ipapure Granodiorite is of Lower Jurassic age (see age control in volcanic units), whereas the Siapana Granodiorite is of Middle Jurassic age (167 ± 9.4 Ma; Cardona et al., 2006). Both bodies show a geochemical signature that is related to subduction–zone magmatism (Zuluaga et al., 2015).

3.1.3. Volcanism

Zuluaga et al. (2015) mapped and dated the Ipapure–Cerro La Teta Rhyodacite, which has a mean age of 183.5 ± 2.9 Ma (N=3 samples), and is genetically related to the Ipapure Granodiorite.

3.1.4. Sedimentation

The La Guajira ranges have the most complete upper Middle to Upper Jurassic succession, which encompasses (1) continental fluvial strata at the base (Rancho Grande and Chertelo Formations), (2) a marine ingression at the Oxfordian (Caju and lower Uitpana Formations) followed by a progradation of marginal environments of the Chinapa and upper Uitpana Formations, and (3) a marine ingression at Kimmeridgian – Tithonian (Nova–Rodríguez et al., 2017; Zuluaga et al., 2009). Lateral changes in the thickness of the upper two units and the up–section dominance of marine strata indicate accumulation in extensional settings (Cuisa Formation). The Rancho Grande Formation rests unconformably upon the Ipapure–Cerro la Teta Rhyodacite, whereas the uppermost marine Jurassic rocks are covered disconformably by Lower Cretaceous rocks. Marine and marginal deposits of Upper Jurassic age are also reported in the northernmost exposures of the Jurassic rocks in the Paraguana Peninsula and Cordillera de la Costa belt of Venezuela. These units rest unconformably upon metamorphic and intrusive rocks of Paleozoic age and are overlain in an unconformable contact with Lower Cretaceous marginal siliciclastic or calcareous marine rocks (Salazar, 2010).

3.1.5. Paleomagnetism

Reported results in Jurassic rocks show eastward declinations with positive inclinations suggesting magnetization events in

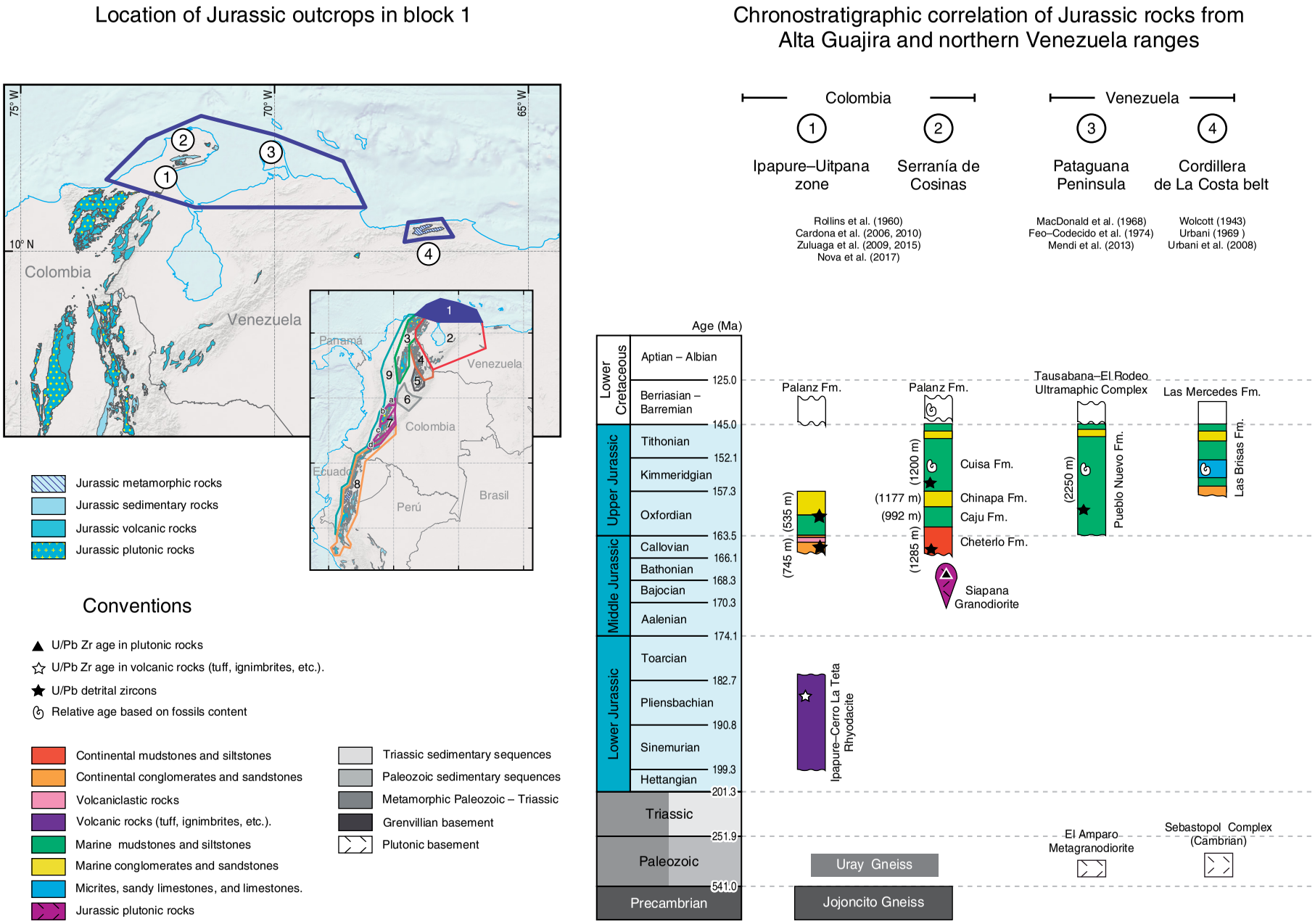

Figure 4. Chronostratigraphic correlation of Jurassic rocks in block 1: Alta Guajira and northern Venezuela ranges.

northern paleolatitudes (Bayona et al., 2016; MacDonald & Opdyke, 1972; Nova–Rodríguez et al., 2017) and ca. 90º of clockwise rotations with respect to the stable South America Plate, which is consistent with the nearly eastward–to–northeastward strike of the Cosinas Anticline.

3.2. Block 2: serranía de Perijá (Machiques Basin), Subsurface of Maracaibo Lake (Uribante Basin), Mérida Andes (Barquisimeto Basin), and Subsurface of the Barinas Basin (El Espino Basin) (Figure 5)

3.2.1. Metamorphism

No evidence of metamorphism or deformation in Jurassic rocks has been reported in this block.

3.2.2. Plutonism

Small intrusive bodies (167 ± 3 Ma) have been documented within the La Quinta Formation (Dasch, 1982) but have not been mapped independently of the La Quinta Formation.

3.2.3. Volcanism

Volcanoclastic rocks are the dominant lithology of La Quinta Formation, with localized interbeds of volcanic rocks at different stratigraphic positions (Forero, 1970; Maze, 1984; Ortega–Montero et al., 2012). The reported ages of these volcanic rocks on the western side of the serranía de Perijá vary from 162 to 183 Ma (Bayona et al., 2012a; Dasch, 1982; González et al., 2015a; Montaño, 2009). The major– and trace–element geochemical signatures show intermediate composition (Maze, 1984). van der Lelij et al. (2016) reported tuffs with a 202 Ma age at the base of La Quinta Formation in the Mérida Andes.

3.2.4. Sedimentation

The Machiques, Uribante, Barquisimeto, and Espino extensional basins have a record of Jurassic rocks with abrupt changes in thickness within the same basin but of different age ranges (Eva et al., 1989; Forero, 1970; Maze, 1984; Ortega–Montero et al., 2012). The oldest record (Triassic? to Lower Jurassic) is reported in the Barquisimeto Basin, which exhibits continental fluvial accumulation with interbeds of volcanoclastic and volcanic deposits. Upper Jurassic sediments consist of continental to marginal (lacustrine) deposits that dominate over the volcanic–related rocks. In contrast, basaltic lavas are reported in Upper Jurassic continental deposits in the El Espino Basin. In this block, Jurassic rocks rest unconformably upon Paleozoic sedimentary strata and are overlain disconformably by Lower Cretaceous continental fluvial deposits of the Río Negro Formation or by marine carbonate rocks of the Cogollo Group (Aptian age).

3.2.5. Paleomagnetism

Reported results in Jurassic rocks from the serranía de Perijá show northeastward declinations with positive inclinations (Gose et al., 2003; Nova–Rodríguez et al., 2012), suggesting magnetization events at northern paleolatitudes and ca. 45º of clockwise rotations with respect to the stable South America Plate, which is consistent with the NE strike of the serranía de Perijá. In the Mérida Andes, reported paleomagnetic data shows northern declinations and shallow positive inclinations (Castillo et al., 1991), suggesting no rotations and magnetization at northern paleolatitudes.

3.3. Block 3: Santa Marta Massif and serranía de San Lucas (Figure 6)

3.3.1. Metamorphism

The Jurassic rocks to the east of the Santa Marta Massif do not show evidence of metamorphism.

3.3.2. Plutonism

Large intrusive bodies of Lower – Middle Jurassic age constitute the Santa Marta and San Lucas Massifs. In the San Lucas Massif, intermediate–composition batholiths have ages ranging from 193 Ma to 162 Ma (Cuadros et al., 2014; González et al., 2015b). In the Santa Marta Massif, the ages range from 192 to 180 Ma (Quandt et al., 2018). Geochemical signatures of those batholiths indicate tectonic settings of magmatic arcs adjacent to subduction zones (Quandt et al., 2018; Vásquez et al., 2006). Jurassic magmatism affected Grenvillian basement rocks in both massifs, but Cuadros et al. (2014) reported older basement rocks (1.5 Ga).

3.3.3. Volcanism

Thick volcanoclastic and volcanic deposits of very variable thickness from the Noreán Formation are exposed in the eastern flank of the San Lucas Massif and western flank of the Santander Massif, and volcanic deposits of poor lateral continuity are exposed in the eastern flank of the Santa Marta Massif. In the Santa Marta Massif, the volcanic rocks have reported ages between 187 and 176 Ma (Quandt et al., 2018). In the San Lucas Massif, two ages of 200 and 163 Ma have been reported in the Noreán Formation and equivalent unit in the subsurface (La Malena volcanic unit) (González et al., 2015b; Horton et al., 2015; Leal–Mejía, 2011). Correa–Martínez et al. (2019) reported two U–Pb ages in andesite lavas (192 and 185 Ma) and

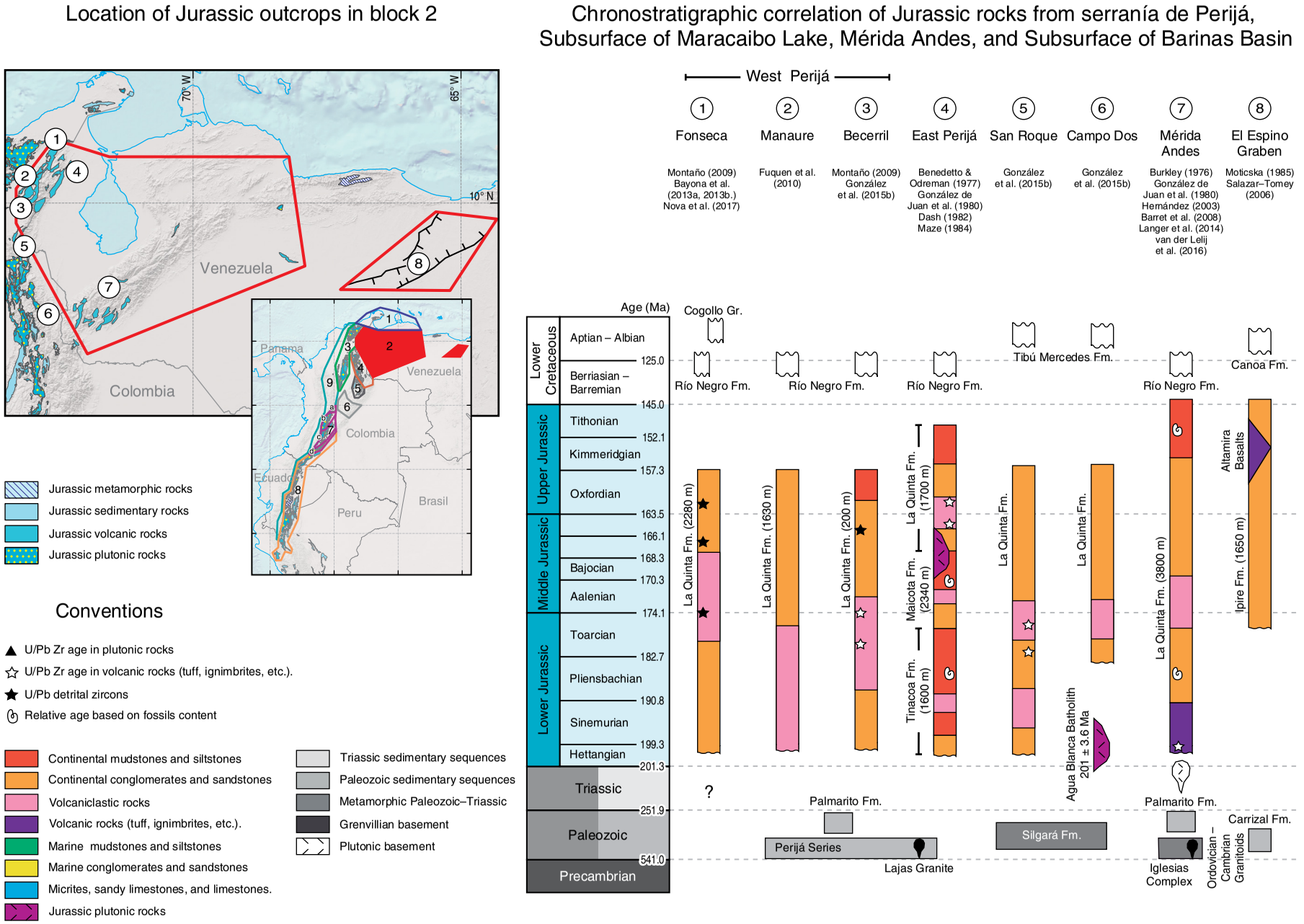

Figure 5. Chronostratigraphic correlation of Jurassic rocks in block 2: serranía de Perijá (Machiques Basin), subsurface of Maracaibo lake (Uribante Basin), Mérida Andes (Barquisimeto Basin), and subsurface of the Barinas Basin (El Espino Basin).

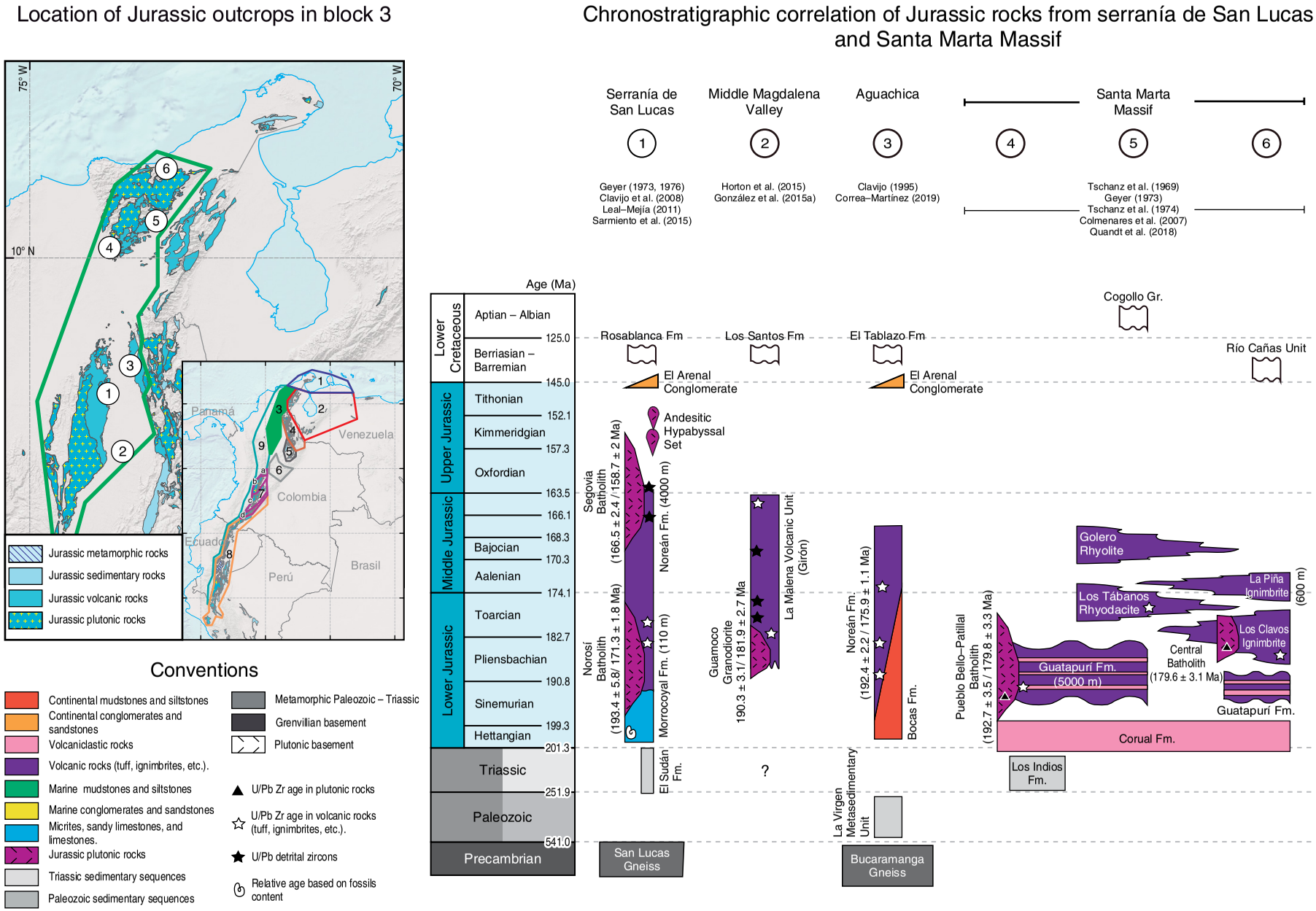

Figure 6. Chronostratigraphic correlation of Jurassic rocks in block 3: Santa Marta Massif and serranía de San Lucas.

another age in a rhyolite lava (176 Ma); all analyzed volcanic rocks show geochemical signatures of continental magmatic arcs.

3.3.4. Sedimentation

Short periods of continental fluvial deposition are recorded in some units from the Guatapurí Formation in the Santa Marta Massif (Tschanz et al., 1974), whereas most of the record in the Noreán Formation may be related to gravity–flow deposits (Clavijo et al., 2008). Volcanic deposits rest disconformably upon marine to marginal deposits of Upper Triassic age in the Santa Marta Massif (Los Indios Formation) or lowermost Jurassic age in the San Lucas Massif (Morrocoyal Formation). The onset of Cretaceous deposition is diachronous in both massifs; the lowermost marginal to marine Cretaceous rocks overlie the San Lucas Massif and northern face of the Santa Marta Massif, whereas accumulation began in the Aptian in most areas with a record of marine deposits of the Cogollo Group or equivalent units.

3.3.5. Paleomagnetism

The reported results in Lower Jurassic volcanic rocks from the Santa Marta Massif indicate an NNE declination and negative inclinations, suggesting moderate clockwise rotations and magnetization at southern paleolatitudes (Bayona et al., 2010). No studies have been conducted in the serranía de San Lucas.

3.4. Block 4: Santander Massif (Figure 7)

3.4.1. Metamorphism

The Bucaramanga Paragneiss reached granulite–facies metamorphism during the Early Ordovician (zircon U–Pb ages from 490 to 450 Ma in van der Lelij et al., 2016), whereas rocks of the Silgará Formation were affected by this Ordovician regional metamorphism and maybe by a younger event in the late Paleozoic (Cardona et al., 2016). These metamorphic rocks are overprinted by a thermal anomaly and low–pressure metamorphism associated to the Late Triassic – Early Jurassic magmatism, as suggested by the growth of cordierite (Cardona et al., 2016; Zuluaga et al., 2017). This metamorphism was related to the subduction of oceanic crust from the proto–Pacific Ocean beneath western Pangea (Zuluaga et al., 2017).

3.4.2. Plutonism

The Santander Massif records the earliest magmatic activity after Pangea's break–up according to the U–Pb in zircon ages, which span from ca. 213 to 196 Ma (Correa–Martínez et al., 2016; Mantilla–Figueroa et al., 2013; van der Lelij et al., 2016). Geochemical data that were reported by Correa–Martínez et al. (2016) and van der Lelij et al. (2016) indicate that the granitoids are mildly peraluminous and have K_2O and Na_2O compositions that are typical of I–type granites. The geochemical data indicate a convergent margin setting because of the similar trends of the trace elements and REE abundances compared to the upper crust. In the same work, the Pb isotopic ratios were interpreted as indicative of crustal sources. These authors interpreted that the voluminous shallow batholiths from the Santander Massif formed in a subduction zone with coeval extension because of a slab rollback process. In the southernmost extension of the Santander Massif, plutonic rocks show similar macroscopic composition (Vargas et al., 1981), but geochemical and geochronological studies are required to test their Triassic – Jurassic age.

3.4.3. Volcanism

The documented volcanic rocks in the Santander Massif have local extension and an inferred Jurassic age. Basalts with porphyritic and amygdalar texture have been formalized as the Nogontova Formation by Moreno–Sánchez et al. (2016). These undated rocks might be of Lower Jurassic age because the composition and texture are similar to the basalts from the Jordán Formation (Ayala–Calvo et al., 2005). In the southernmost extension of the Santander Massif, porphyritic rhyolites have been reported next to plutonic rocks and intruding Paleozoic metasedimentary rocks; the relationship with interpreted Jurassic sedimentary rocks is not clear (Vargas et al., 1981).

3.4.4. Sedimentation

A thin record (a few hundred of meters) of continental fluvial sandstones and conglomerate deposits has been correlated with the Girón Formation, which accumulated to the east of the Bucaramanga Fault. Similarly, the record of lacustrine to marine deposits has been associated with the Bocas Formation, but with no report of clear marine–fossil associations. Some areas have interbeds of volcanoclastic deposits within this unit. A rhyolitic unit that cuts through the Bocas Formation has been dated to 250 Ma (van der Lelij et al., 2016); this relationship should be revised because this age suggests a Paleozoic age for the Bocas Formation. No provenance analyses in the Girón Formation have been conducted in this block. These deposits rest unconformably upon Paleozoic sedimentary and metamorphic rocks and are overlain by either continental Lower Cretaceous continental deposits or by marginal to marine Aptian deposits.

3.4.5. Paleomagnetism

No studies have been conducted in these units.

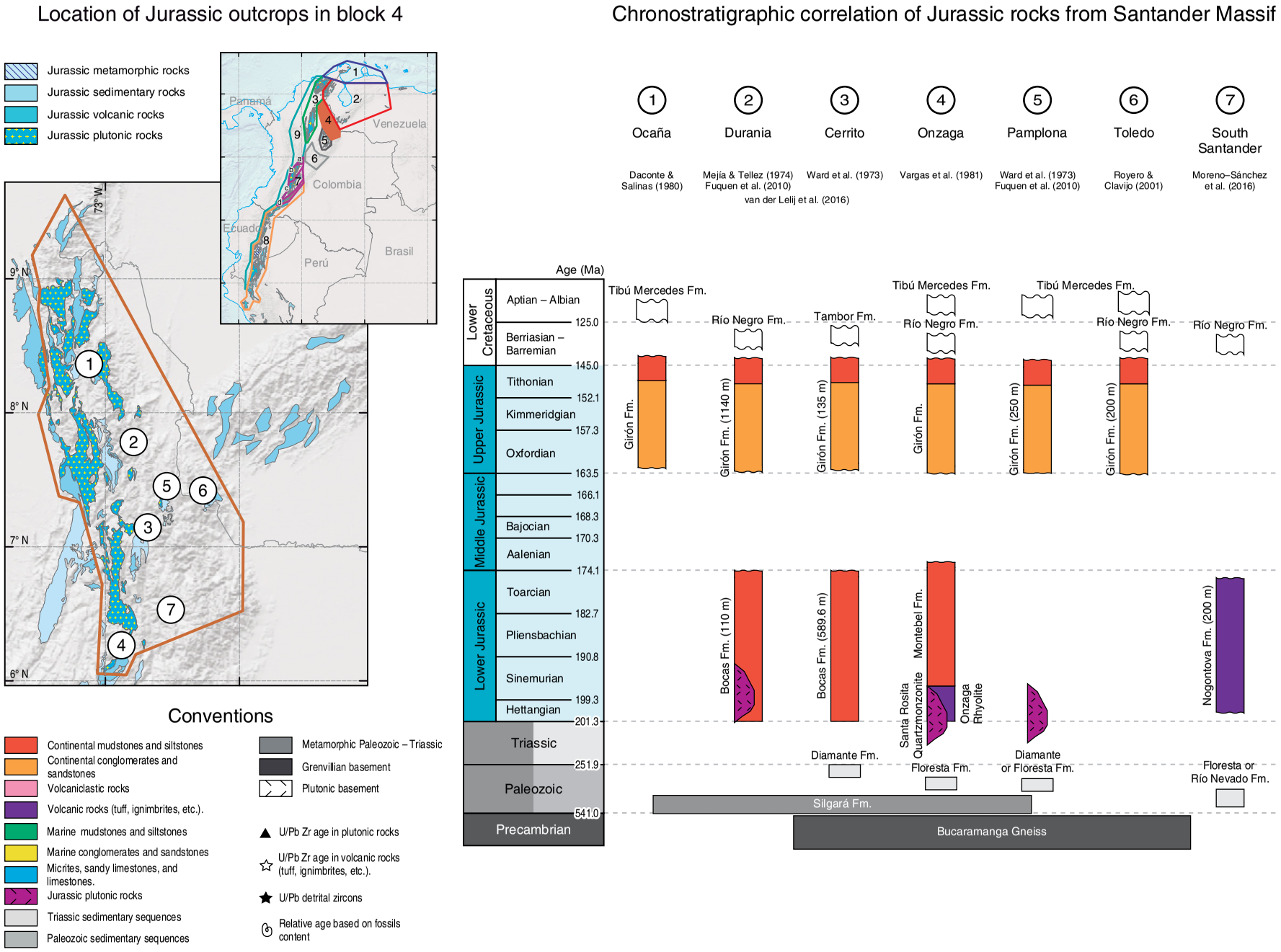

Figure 7. Chronostratigraphic correlation of Jurassic rocks in block 4: Santander Massif.

3.5. Block 5: Los Cobardes and La Rusia Anticlines, Río Lebrija Section, and Floresta Massif (Figure 8)

3.5.1. Metamorphism

No evidence of metamorphism has been reported in this block, but strong cleavage in the La Rusia Anticline records deformation processes that have not been documented in other Cretaceous rocks.

3.5.2. Plutonism

No record of Jurassic plutonic rocks exists in this block.

3.5.3. Volcanism

Jordán and La Rusia Formations show thin interbeds of volcanic and volcanoclastic rocks, which have been identified in previous studies (Cediel, 1968; Suárez & Díaz, 2016). Ayala–Calvo et al. (2005) reported very altered basalts (sericite and chlorite) that were interbedded with red mudstones of the Jordán Formation. Suárez & Díaz (2016) made petrographic and macroscopic identification of those volcanoclastic rocks interbedded with rhyolitic tuffs, feldspar–bearing sandstones and red mudstones and locally cut by mafic dikes. The Jordán Formation accumulated in fluvial–lacustrine systems affected by volcanic activity (Suárez & Díaz, 2016). Field observations of the Jordán and La Rusia units by the main author noted that "red siltstones" may really correspond to "red fine tuff beds". These units are in two localities with the most continuous record of Jurassic deposition in this block.

3.5.4. Sedimentation

The accumulation of siliciclastic rocks dominated in extensional basins. Two major depocenters have the most complete record of Jurassic deposition: the Río Lebrija section and La Rusia Anticline. In these two areas, Lower Jurassic rocks rest unconformably upon sedimentary and metamorphic Paleozoic rocks and consist of fluvial (Palermo–Montebel Formations in La Rusia Anticline) and marginal deposits (Bocas Formation in Río Lebrija). In the La Rusia Anticline, this succession changes up–section to high–energy fluvial and volcanoclastic deposits of the Middle Jurassic La Rusia Formation, whereas that in the Río Lebrija section has low–energy continental and volcanoclastic deposits of the Middle Jurassic Jordán Formation. A short period of deformation (local angular unconformity with range of 10–15º, Ward et al., 1973) separates the accumulation of the Upper Jurassic continental Girón and Arcabuco Formations, both units passing up–section conformably to the marine transgression that was recorded by the lowermost Cretaceous units. In other areas outside of these two depocenters, the Jurassic record is coeval with the accumulation of the Upper Jurassic Girón Formation; however, this accumulation is accompanied by strong changes in stratigraphic thickness from tens of meters in the La Mesa de Los Santos region (Ayala–Calvo et al., 2005) to ca. 4 km of thickness in the Río Lebrija section (Cediel, 1968). Osorio–Afanador (2016) argues that the strong lateral variation in thickness and depositional systems in continental settings makes difficult the correlation of the Upper Jurassic Girón Formation. Provenance analysis (petrography and detrital zircons) shows supply from nearby areas in the Santander and Floresta Massifs.

3.5.5. Paleomagnetism

The reported results in Jurassic rocks from the La Mesa de Los Santos to Lebrija area and in the Floresta Massif show that the northward declinations of Middle Jurassic rocks have negative inclination, whereas Upper Jurassic rocks and Lower Cretaceous rocks show positive inclinations (Bayona et al., 2006). These results, alongside the lack of paleosol development in Middle Jurassic rocks and extensive paleosol development in Upper Jurassic rocks, support the hypothesis of the northward translation of blocks from southern paleolatitudes and dry conditions to northern paleolatitudes and humid conditions (Bayona et al., 2010). Jiménez et al. (2017) documented moderate clockwise rotation and shallow positive inclinations (northward paleolatitudes) for the Girón Formation in Los Cobardes Anticline.

3.6. Block 6: Cundinamarca Basin (sensu Sarmiento–Rojas et al., 2006) (Figure 9)

3.6.1. Metamorphism, Plutonism, and Volcanism

Metamorphic and magmatic events have not been reported in this block.

3.6.2. Sedimentation

Uppermost Jurassic to lowermost Cretaceous marine deposits have been reported in this block, which have variable lithofacies association (Mora et al., 2009). In the eastern margin of the Cretaceous Cundinamarca Basin, gravity–flow deposits of the Brecha Buenavista Formation and carbonate rocks of the Guavio Formation record the irregular onset of accumulation prior to the Cretaceous marine ingression. In the depocenter of the basin, evaporate accumulation may record the onset of accumulation.

3.6.3. Paleomagnetism

No studies have been conducted in Jurassic rocks from this block.

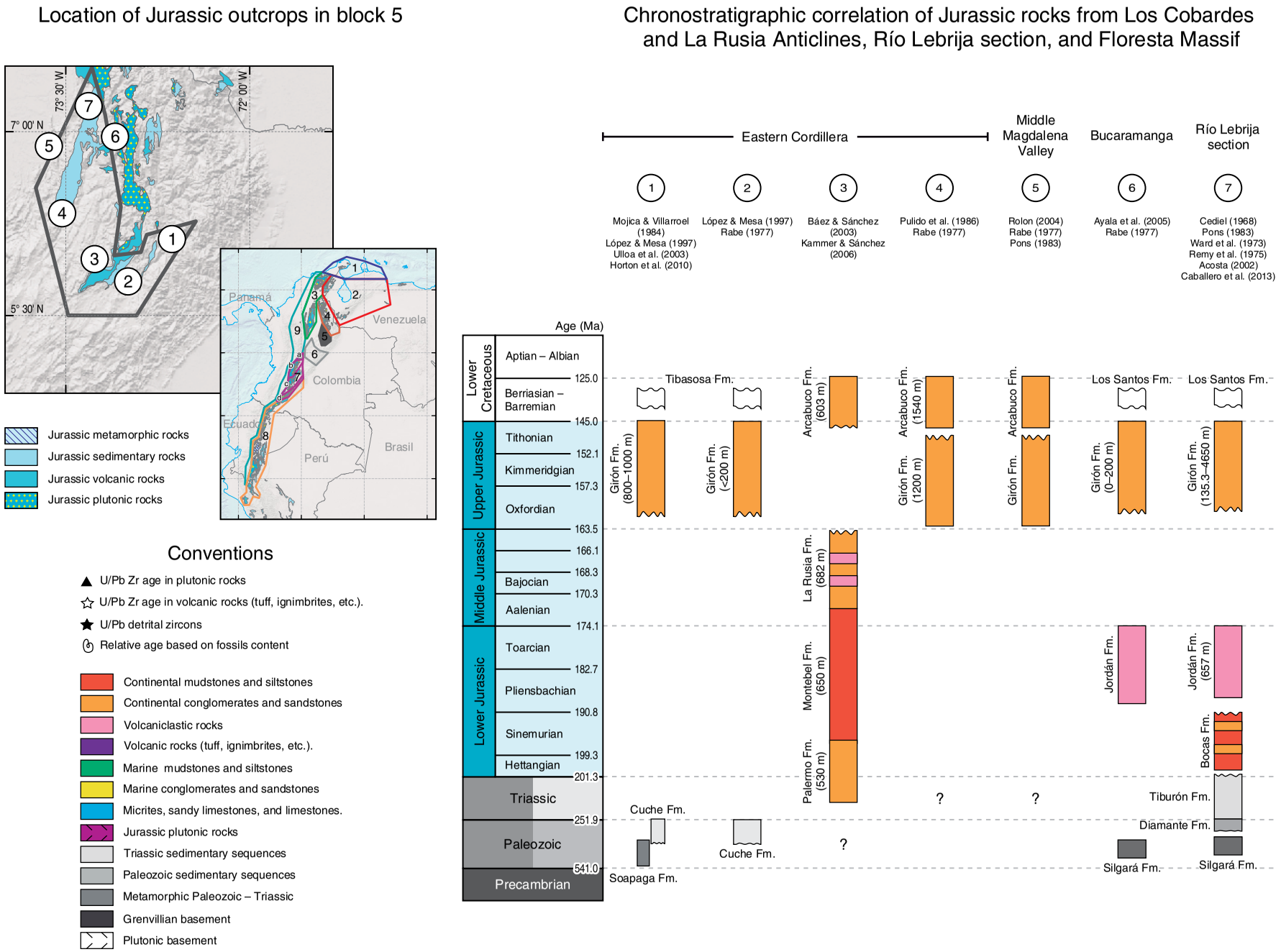

Figure 8. Chronostratigraphic correlation of Jurassic rocks in block 5: Los Cobardes and La Rusia Anticlines, and Floresta Massif.

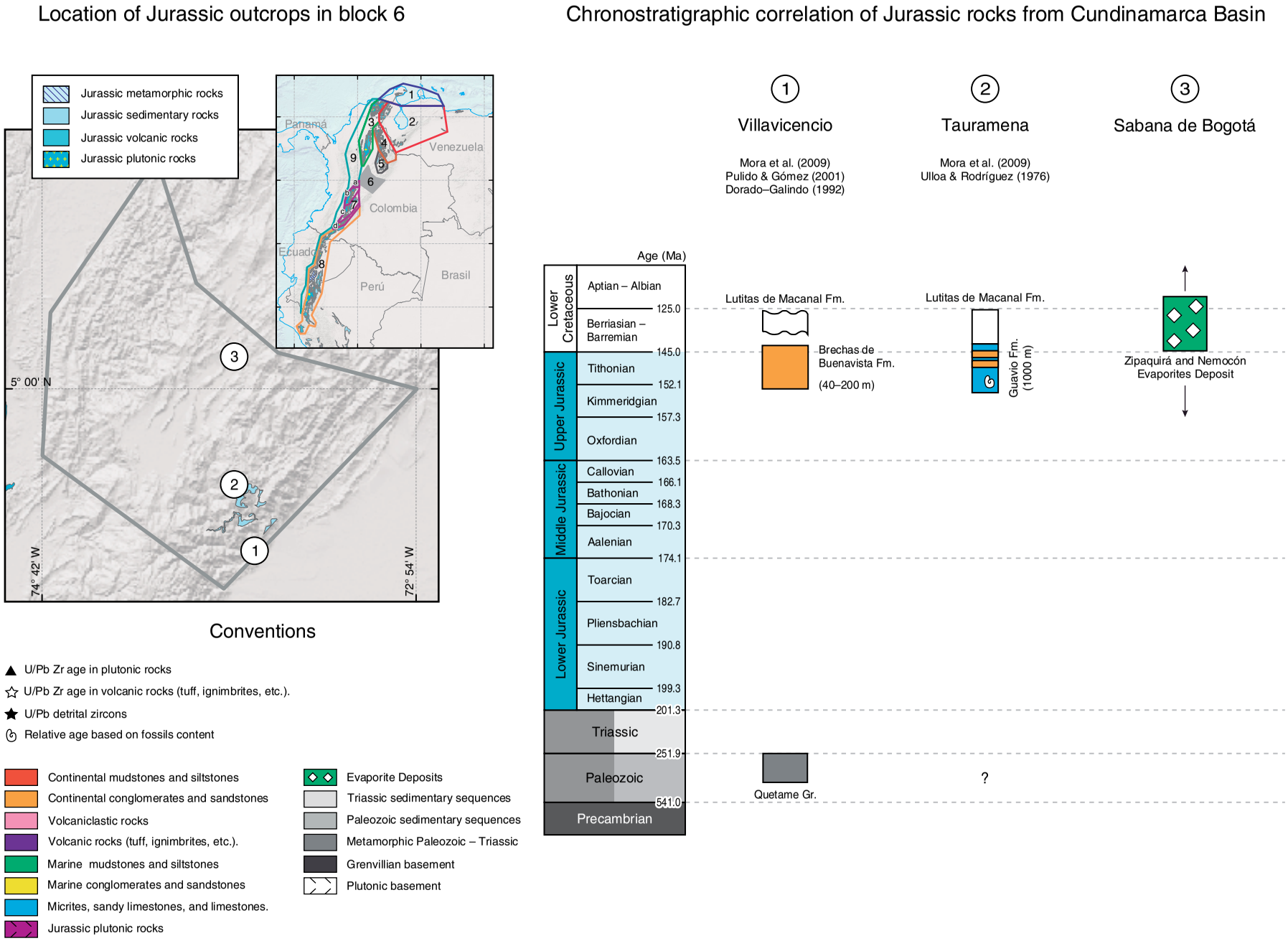

Figure 9. Chronostratigraphic correlation of Jurassic rocks in block 6: Cundinamarca Basin (sensu Sarmiento–Rojas et al., 2006).

3.7. Block 7: Jurassic Rocks between the Southern Central Cordillera and Garzón Massif (Figure 10)

3.7.1. Metamorphism

Rodríguez et al. (2018) reported Jurassic metamorphism (ca. 154 Ma) in the Tierradentro Gneisses and Amphibolites, coeval with the emplacement of a metatonalite between 158 and 150 Ma, which reached the amphibolite facies.

3.7.2. Plutonism

The Ibagué Batholith is the largest plutonic body to the north and west of the Inzá, La Plata, and Chusma Fault System. This plutonic rock formed from successive pulses of magmatism between ca. 189 Ma and 138 Ma (Bustamante et al., 2010, 2016; Cochrane et al., 2014b; Rodríguez et al., 2018). The whole–rock geochemistry that was presented in several works and compiled in Bustamante et al. (2016) shows enrichment in LREE over HREE (chondrite normalized) and pronounced negative Nb and Ti anomalies (primitive mantle normalization). The reported Hf and Nd isotopic compositions in these works also show clear crustal source of the older pulses and an increase in the juvenile component with time, where the youngest pulses record a depleted mantle source (Bustamante et al., 2016; Cochrane et al., 2014b). The whole–rock geochemistry and isotopic data suggest a subduction–related magmatism for the origin of the Ibagué Batholith.

Plutonic rocks to the east and south of the Inzá, La Plata, and Chusma Fault System show petrographic and geochemical signatures of a continental magmatic arc that was related to a subduction zone, with plutons being older (195–186 Ma) and of intermediate composition in the western belt than in the eastern belt, which are younger (173–169 Ma) and granitic in composition (Rodríguez et al., 2018). Rodríguez et al. (2018) argued that the differences in the ages of the plutonic rocks and type of basement rocks to the north and south of the Inzá, La Plata, and Chusma Fault System are evidence to separate these two areas into different magmatic arcs.

3.7.3. Volcanism

The volcanic and volcanoclastic succession of the Saldaña Formation is of intermediate to felsic, calc–alkaline composition based on petrography and major and trace–element analysis (Bayona et al., 1994; Cajas, 2003; Rodríguez–García et al., 2016; Vásquez et al., 2006). The reported U/Pb ages range from 189 to 173 Ma (Rodríguez–García et al., 2016). One Ar–Ar age in a plagioclase mineral from a subvolcanic andesitic rock that intruded the Saldaña Formation yielded an age of 159.3 ± 0.5 Ma (Rodríguez–García, 2018), whereas U–Pb ages of 151 to 155 Ma were reported from volcanic and subvolcanic dykes of rhyolitic to andesitic composition (Hincapié–Gómez, 2018). Any calculation of thickness among areas is relative because of structural complexities and a lack of exposed lower and upper contacts. The Saldaña Formation to the west of Inzá, La Plata and Chusma Fault System rests conformably upon Upper Triassic – Lower Jurassic rocks (see descriptions below), whereas the Saldaña Formation to the east of these faults rests unconformably upon sedimentary Paleozoic or Precambrian units (Rodríguez et al., 2018). Geochemical data indicate a subduction–related tectonic setting (Rodríguez et al., 2018; Vásquez et al., 2006).

3.7.4. Sedimentation

Upper Triassic – Lower Jurassic deposits to the north and west of the Inzá, La Plata, and Chusma Fault System consist of a marine sequence from the Payandé Formation (Norian to Rhaetian, Geyer, 1982) resting unconformably upon the Luisa Formation. Thin interbeds of sedimentary carbonate rocks at the base of the Saldaña Formation (Chicalá and Río Frío units, Mojica & Llinás, 1984; Mojica & Prinz–Grimm, 2000; Rodríguez et al., 1995) that accumulated in shallow–marine environments are considered of Lower Jurassic age. Fluvial and lacustrine deposits within the Saldaña Formation are present but regionally very uncommon (Bayona et al., 1994; Cajas, 2003). Detrital U–Pb geochronological data from clastic and pyroclastic rocks of the Luisa Formation yielded the youngest age population from 270 to 278 Ma suggesting accumulation in mid–Permian (Hincapié–Gómez, 2018); therefore, the Luisa Formation should not be considered as part of the Triassic – Jurassic succession.

3.7.5. Paleomagnetism

Bayona et al. (2005, 2006) reported paleomagnetic directions with northern and negative inclinations (or its reversal) in rocks from the Saldaña Formation at both sides of the Inzá, La Plata, and Chusma Fault System. These directions differ from the northern and positive inclinations in rocks from the Aptian Yaví Formation. These directions allow the interpretation of the northward migration of these blocks during Middle to Late Jurassic.

3.8. Block 8: Mocoa Batholith, Caguán and Putumayo Basins, Subandean Ecuador Ranges and Oriente Basin, and Northern Perú (Figure 11)

3.8.1. Metamorphism

Quartz–feldspar schists from the La Cocha–Río Téllez Complex yielded U–Pb zircons ages of 163.6 ± 4.7 Ma, which were interpreted by Zapata–García et al. (2017) as the metamorphism age of a sequence of pelites that reached the amphibolite facies. According to these authors, these rocks could be correlated with

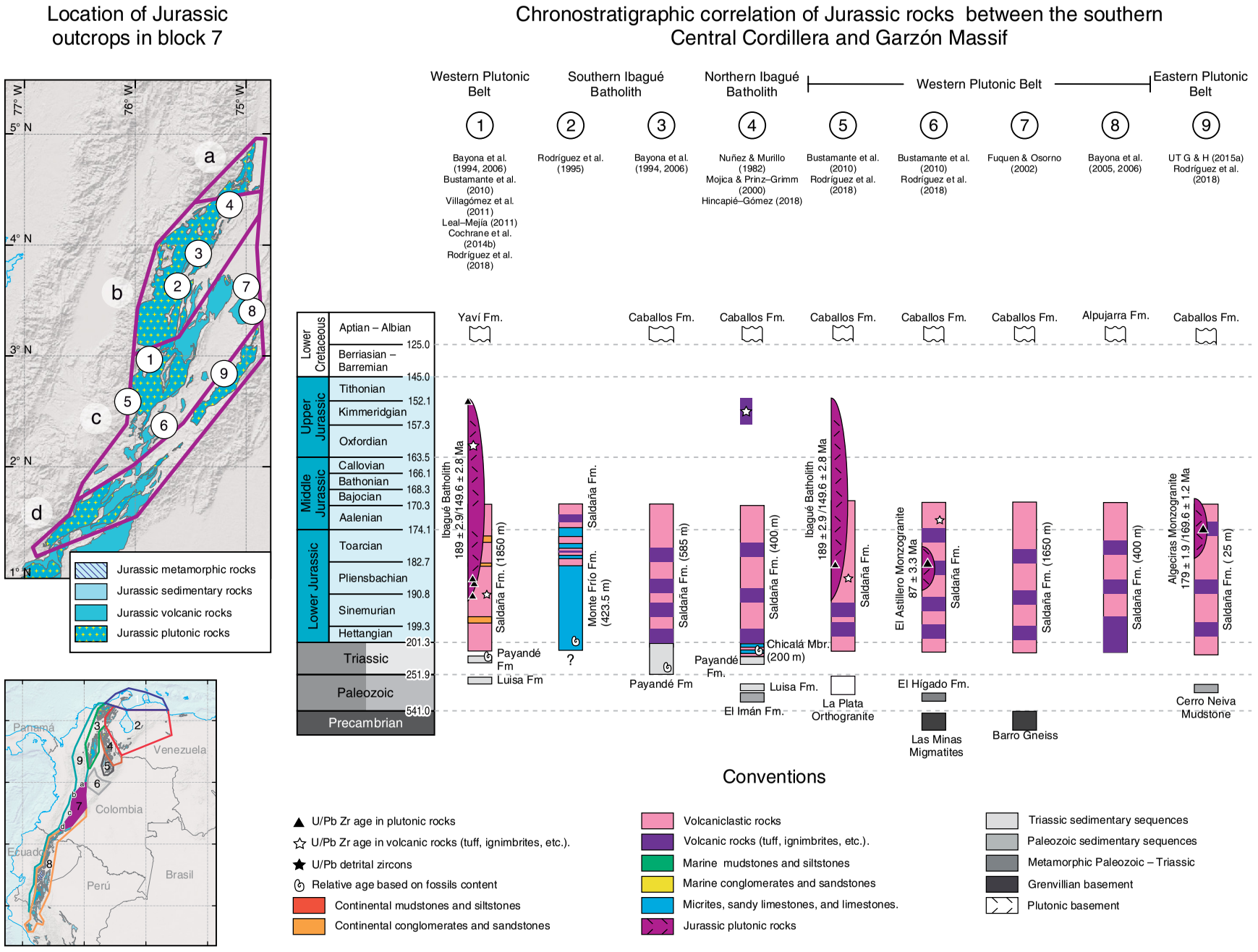

Figure 10. Chronostratigraphic correlation of Jurassic rocks in block 7: Jurassic rocks between the southern Central Cordillera and Garzón Massif.

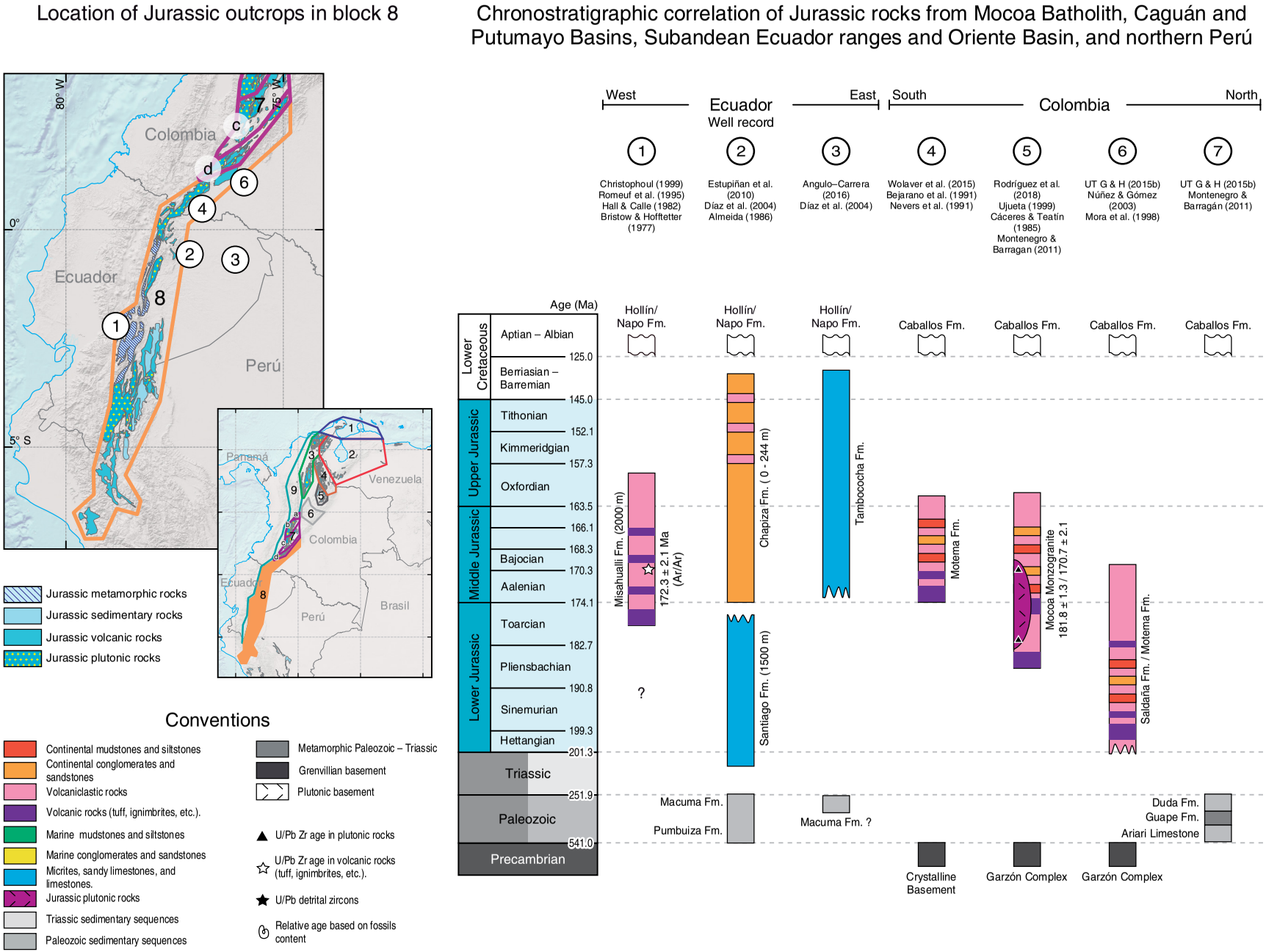

Figure 11. Chronostratigraphic correlation of Jurassic rocks in block 8: Mocoa Batholith, Caguán and Putumayo Basins, Subandean Ecuador ranges and Oriente Basin, and northern Perú.

schists from the Cajamarca Complex, which outcrops to the west of the Ibagué Batholith.

3.8.2. Plutonism

The Mocoa Batholith is a poorly studied plutonic body that outcrops in southern Colombia. Available U–Pb geochronological and whole–rock geochemistry data (Cochrane et al., 2014a; Leal–Mejía, 2011; Rodríguez et al., 2018; Zapata et al., 2016) indicates 181 to 170 Ma U–Pb crystallization ages for a high–K calc–alkaline granitoid with typical Nb and Ti negative anomalies compared to primitive mantle. The latter indicates an arc–related granitoid. The εNd value from Leal–Mejía (2011) in samples of the Mocoa Batholith revealed a crustal source. In Ecuador, the ages become younger southward; the Rosa Florida Batholith has an age of 182 Ma; the ages of the Abitagua Batholith range from 174 to 170 Ma, whereas Jurassic ages of the Zamora Batholith to the south range from 178 to 145 Ma (Spikings et al., 2015). The geochemical signatures are similar to the reported results for the Mocoa Batholith.

3.8.3. Volcanism

Rhyolite–dominated Pitalito volcanic rocks have a similar reported U–Pb age to those of the plutonic rocks (183–168 Ma; Rodríguez et al., 2018). In the Putumayo Basin in Colombia and Ecuador, intermediate and felsic volcanic and volcanoclastic rocks have been grouped as the Motema and Misahualli Formations, the latter with an Ar/Ar age of 172.3 ± 2.1 Ma (Romeuf et al., 1997). In the sub–Andean zone of Ecuador, the Misahualli Formation consists of basaltic andesites to rhyolitic lavas that are interbedded with felsic pyroclastic flows (Romeuf et al., 1997); this unit is covered unconformably by Aptian beds. The southern extension of the Misahualli Formation in Perú is named the Colán Formation (Pardo & Sanz, 1979) or Oyotun Formation (Jaimes et al., 2011), with a similar geochemical composition of volcanic and pyroclastic rocks. However, the Colán Formation rests upon carbonate rocks of the Upper Triassic Pucara Group and is covered by Neocomian quartzites (Mourier et al., 1988).

3.8.4. Sedimentation

In Ecuador, Lower Jurassic shales and carbonate rocks from the Santiago Formation include to the top some volcanic interbeds with tholeiitic affinity, which are related to an extensional event of Triassic to Early Jurassic age. This marginal to marine unit changes northward to continental red beds of the Sacha Formation (Díaz et al., 2004; Gaibor et al., 2008). An angular unconformity separates the Chapiza Formation, which consists of clastic red beds that accumulated in continental dry conditions; to the west, this unit changes to volcanoclastic rocks from the Misahualli Formation (Díaz et al., 2004), which represents the southern continuity of the volcanic rocks in Colombia. To the east, the Tambococha Formation has been interpreted as marine deposits of Middle to Upper Jurassic age (Díaz et al., 2004). The tectonic setting of these units has been related to extension from an active subduction zone to the west (Díaz et al., 2004). In northern Perú, the Upper Triassic to Lower Jurassic Pucara Group includes (1) bituminous and fossiliferous (ammonites and brachiopods) black limestones with thin pyroclastic levels of the La Leche Formation at the base and (2) black shales with thin interbeds of sandstones and limestones with ammonites of the Sávila Formation at the top (Jaimes et al., 2011).

3.8.5. Paleomagnetism

No studies have been conducted in these units. However, clockwise rotation and the northward displacement of southern terranes in Ecuador (Jaillard et al., 1999; Mourier et al., 1988) have been considered to have occurred in the Late Jurassic (Spikings et al., 2015).

3.9. Block 9: West of Large Intrusive Bodies of the Ibagué Batholith, serranía de San Lucas, and Santa Marta Massif (Figure 3)

3.9.1. Metamorphism

A Jurassic metamorphic event was defined by Blanco–Quintero et al. (2014) in metabasites and metapelites from the Cajamarca Complex (Nelson, 1962). Metamorphic cooling ages from Ar–Ar in hornblende ranged from ca. 146.5 ± 1.1 Ma to 157.8 ± 0.6 Ma, and the age in one phengitic mica from a pelitic schist was 157.5 ± 0.4 Ma. The hornblende + plagioclase + epidote + quartz assemblage defines the amphibolite facies of the sequence; according to Blanco–Quintero et al. (2014) and Bustamante et al. (2017), this sequence may constitute a continuous Jurassic metamorphic belt that extends from Ecuador possibly until Santa Marta, always to the west of the Jurassic batholiths. The San Lorenzo Schists on the Santa Marta Massif consist of low– to middle–grade and high–pressure metamorphic bodies, including amphibolites, eclogites, mica schist, and phyllite with zircon ages from 188 to 157 Ma, which are considered either detrital fragments (Cardona et al., 2010) or components of a Jurassic protolith (Piraquive, 2017).

4. Discussion and Consideration of Future Works

4.1. Review of Geologic Data

4.1.1. Metamorphic Rocks

Defined metamorphic sequences require adequate studies on the metamorphic petrology to detail the pressure–temperature–time

(P–T–t) paths. These sequences likely require a compressional setting to produce amphibolite facies metamorphism, which cannot be satisfied with a slab rollback process (Spikings et al., 2015), where extensional forces are dominant. Additionally, researchers must establish these sequences' relationships with the large intrusive bodies and surrounding basement rocks to establish the type of metamorphism (contact versus regional). Determining their correlation with contemporary rocks in similar tectonic positions in Ecuador is critical.

The main problems that must be solved are related to the recent recognition of a Late Jurassic collisional metamorphic event in the Central Cordillera (Blanco–Quintero et al., 2014; Zapata–García et al., 2017). An adequate cartography and microstructural description is lacking, and the limit of this metamorphic belt is not clear, nor is its southern prolongation along the Central Cordillera towards the Cordillera Real in Ecuador. Although Blanco–Quintero et al. (2014) indicated that this belt is in faulted contact with the Ibagué Batholith, Rodríguez et al. (2018) suggested that the Jurassic metamorphic belt is syntectonic with the magmatism based on U–Pb geochronology. However, the latter model did not discuss the presence of Triassic metamorphic roof pendants (Bustamante et al., 2017) in the same tectonic position as the Jurassic metamorphic rocks. One possibility is that the metamorphic event that was recorded by Rodríguez et al. (2018) corresponds to a dynamic event that affected the mafic facies of the Ibagué Batholith.

4.1.2. Plutonic Rocks

U–Pb geochronology and geochemical studies have increased the knowledge of Jurassic magmatism in the northern Andes. Although geochemical data from these studies show a clear evidence of magmatism from subduction processes, and the crustal origin of magmatic material, we must consider the effects of contamination of different types of continental crust and its position relative to extensional geodynamic processes that have occurred in the north since the Early Jurassic.

As examples, Lower and Middle Jurassic granitoids from the Upper Magdalena Valley intrude Grenvillian basement rocks (0.9–1.2 Ga) both to the east and to the west of the valley, but the sedimentary cover differs in both areas. In the western belt of the Upper Magdalena Valley, Lower and Middle Jurassic granitoids affect Triassic sedimentary rocks (Rodríguez et al., 2018) and are in faulted contact with Triassic metamorphic rocks (Figure 1). The northern Ibagué Batholith intruded Jurassic and Triassic metamorphic basement rocks from the Central Cordillera (Blanco–Quintero et al., 2014; Rodríguez et al., 2018). Similarly, Upper Triassic and Lower – Middle Jurassic plutonic rocks from the Garzón Massif, serranía de San Lucas, Santander Massif, and Mérida Andes intruded different sets of Precambrian and Paleozoic rocks, which record different histories of tectonic evolution (Figure 1). The San Lucas Massif has a protolith age from 1.54 to 1.50 Ga, whose basement has been related with the Río Negro Province of the Amazon Craton (Cuadros et al., 2014); this range does not include the thick Paleozoic record that is preserved in the Mérida Andes and Santander Massif (Rodríguez et al., 2017; van der Lelij et al., 2016). The serranía de San Lucas represents one portion of the Amazonia Basement, whereas the Santander and Santa Marta Massifs correspond to peripheral basins, microcontinents or island arcs that were metamorphosed in the Grenvillian event (Cardona et al., 2010). The Mérida Andes corresponds to the northern segment of the Guiana Shield (van der Lelij et al., 2016). Therefore, future geochemical analyses may elucidate whether Jurassic granitoids intruded rocks of the same terrane or different tectonic terranes.

Reported geochronological data show no clear trend of the migration of magmatic activity. Spikings et al. (2015) proposed a westward migration of magmatism by comparing Upper Triassic plutonic rocks from the Santander Massif and Lower–to–Middle Jurassic plutonic rocks from the serranía de San Lucas. However, similar trends cannot be compared along the margin because of a lack of regional Late Triassic magmatism in other ranges (Figure 1). Lower to Middle Jurassic magmatism in the other ranges showed, in present geographic position, either a static behavior (e.g., the Zamora and Ibagué Batholiths) or an eastward migration, as suggested by Rodríguez et al. (2018) for the batholiths in the southern Upper Magdalena Valley. Considering the autochthonous hypothesis, an eastward widening of magmatic activity is documented in the Santa Marta Massif and serranía de Perijá (González et al., 2015a; Quandt et al., 2018) (Figure 2a, 2b).

The abrupt interruption of regional magmatism in the early Late Jurassic should also be investigated. Some authors argued that the peak of magmatism was related to orthogonal plate convergence, whereas a decrease in magmatic activity may have been related to oblique convergence between plates (Bustamante et al., 2016). A similar cessation of volcanic arc magmatism because of the oblique convergence of oceanic plates is recorded between the early and middle Eocene (Bayona et al., 2012b). The strong decrease in magmatic activity in the Late Jurassic should be explained within a regional tectono–magmatic framework by considering the event that caused the Middle Jurassic unconformity and the change in sedimentation patterns in northeastern Colombia and Venezuela.

4.1.3. Volcanic Rocks

Although the amount of geochemical and geochronological data from volcanic rocks has increased, published data did not consider the stratigraphic position of these rocks. Geochronological investigations at different stratigraphic positions of volcanic successions (e.g., the Saldaña and Noreán Formations) should supply value information regarding (1) the duration of

Figure 12. Middle Jurassic unconformity that was identified in three areas: **(a)** serranía de San Lucas foothills, Rosablanca Formation resting upon the deformed Noreán Formation, **(b)** Upper Magdalena Valley, Aptian – Albian strata of the Yaví and Caballos Formations resting upon the Saldaña Formation with a significant angular unconformity, **(c)** La Mesa de Los Santos, where strata of the Girón and Los Santos Formations are nearly horizontal, with a low–angle angular unconformity (10–15º) documented by Ward et al. (1973). Note the large change in thickness of the Girón Formation from 0 to 100 m in La Mesa de Los Santos, increasing northward and westward to hundreds of meters.

the magmatic activity in the area, (2) the documentation of pulses of volcanism, and (3) explanations for composition changes in volcanic rocks (from more felsic to more intermediate or mafic). Hincapié–Gómez (2018) and Rodríguez–García (2018) documented 151 to 159 Ma subvolcanic dykes that intruded the Saldaña Formation, but these subvolcanic rocks originated from a different tectono–magmatic event.

These changes in the composition of the volcanic rocks may also represent supply from different volcanic arcs. Rodríguez et al. (2018) argued that the composition of the western magmatic belt in the southern Upper Magdalena Valley is intermediate, whereas the eastern magmatic belt is more felsic.

Defining the timing and rates of accumulation of volcanic rocks within extensional basins may also supply information regarding the mechanism of extension (tectonic or magmatic). Rift basins may migrate or completely shift laterally. Large magmatic bodies may explain the faster evolution of rift systems, whereas an evolved magmatic stage with lower magma supply may cause cessation (Villamor et al., 2017).

The location of the plutonic belt in relation to the geometry of the accumulation of volcanic and sedimentary rocks, and the position of major faults are elements necessary to identify whether a basin is "intra–arc" or "retroarc" or whether it formed within a complex rift system that was dominated by strike–slip faults, such as in central Perú in the Early Triassic (Rosas et al., 2007). For the serranía de Perijá and the Mérida Andes, the intrusive bodies are very small and more likely components of rift systems. In the Santa Marta Massif and Upper Magdalena Valley, volcanic rocks are surrounded by regional intrusive rocks, which may record changes from continental retro–arc to intra–arc systems (upper plate extension and active volcanism in a subduction zone). In the serranía de San Lucas, the intrusive belt is clearly to the west and volcanic rocks accumulated to the east in a more typical retro–arc system. However, this relationship must be analyzed from a palinspastic position rather than the present geographic position.

4.1.4. Sedimentary Rocks

Detailed sedimentological and paleontological studies of Jurassic rocks in the northern Andes have significantly decreased over the last decade. New efforts should be made to conduct these types of studies in the future to establish the temporal and spatial extension of stratigraphic units, which is currently confusing in the literature, as discussed below.

Detrital zircons geochronology is one of the few tools that shed some light regarding the age of red continental successions, such as the Girón Formation. However, a lack of coeval magmatic activity may cause a misleading interpretation. The erosion of Upper Triassic plutonic rocks supplied the youngest zircon population to the Upper Jurassic Girón Formation in the Santander Massif and Los Cobardes Anticline (Horton et al., 2010; Valencia et al., 2011). Farther to the south in the Floresta Massif, the youngest population corresponds to Ordovician zircons because of the absence of these plutonic rocks in the source area (Saylor et al., 2011). In the La Quinta Formation in the serranía de Perijá and Rancho Grande Formation in the Alta Guajira, the documented coeval magmatism with sedimentation supports the assumption that the youngest age population nearly corresponds to the depositional age. Thin interbeds of volcanic rocks at the top of carbonate units with ammonites (e.g., the base of the Monte Frío and Chicalá Members of the Saldaña Formation) must be used to calibrate ammonite zonation in the Early Jurassic.

The analysis of Jurassic sedimentary successions should be the key to understanding whether terrains have been in the same paleo–latitudinal position since the Mesozoic. The absence or presence of paleosol profiles in continental red beds was an argument that was proposed by Bayona et al. (2006, 2010) as an evidence of latitudinal climate differences as response to northward translation of terranes. If terrains have been in the same paleolatitudinal position since the Triassic, as proposed by the two static models (Figure 2a, 2b), Upper Triassic carbonate rocks must have accumulated in similar tropical conditions as Lower Cretaceous carbonate rocks, and clastic sequences may be able to generate paleosol profiles if humid conditions were constant in the Jurassic.

Based on the comprehensive analysis of magmatic and sedimentary data, we can propose that the Jurassic succession may be divided by a regional unconformity in the Middle Jurassic (Figure 12). Marine and continental accumulation in Lower Jurassic units is rapidly covered by volcanoclastic and volcanic units in most of the basins. A few exceptions occur in the Mérida Andes, Lebrija area, and La Rusia Anticline, where continental deposition was dominant and only few interbeds of volcanic material have been documented (or needed to be documented) or in the La Guajira region, where volcanic activity was dominant. This regional dominance of volcanic deposition is coeval with a regional peak of magmatism in the early Middle Jurassic in all the regional batholiths (Figure 3). In the Late

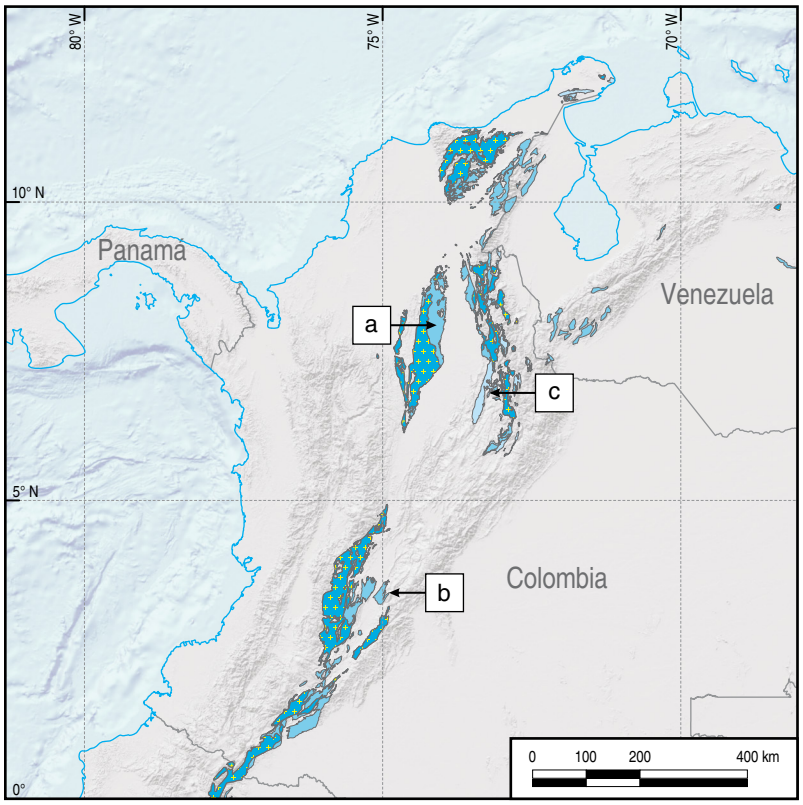

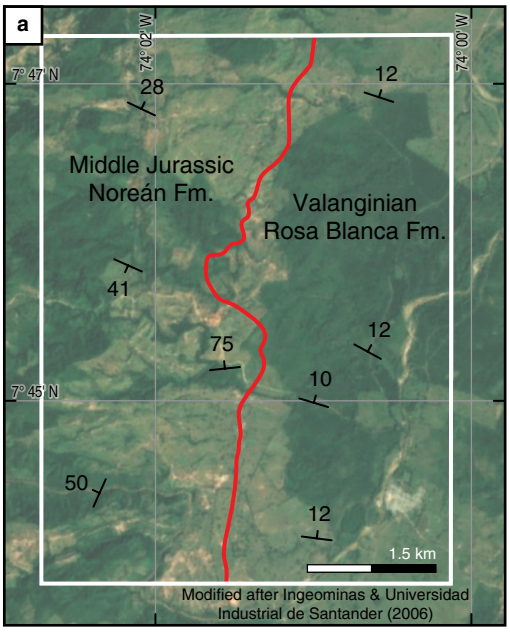

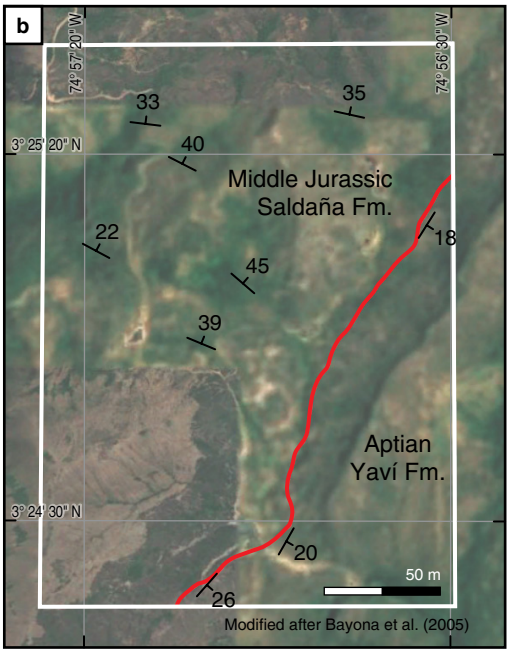

Jurassic metamorphic rocks
Jurassic sedimentary rocks
Jurassic volcanic rocks
Jurassic plutonic rocks

Conventions

Unconformity
Depositional contact
Strike and dip
Horizontal

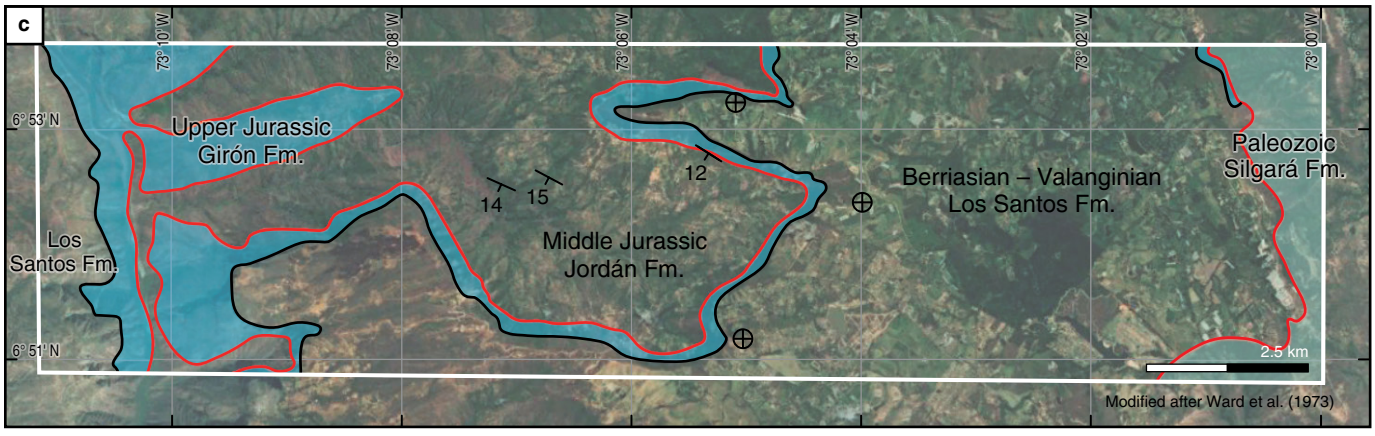

Figure 13. Early Jurassic tectonic evolution according to the **(a)** extensional, **(b)** subduction–related, **(c)** along–marginal migration of continental crust tectonic models. See the text for discussion.

Jurassic, the onset of continental deposition with the absence of coeval volcanic activity occurred in blocks 2, 4, and 5 (Figure 3), recording the Upper Jurassic Girón Formation and equivalent strata in the Mérida Andes (lacustrine beds of the upper La Quinta Formation; Hernández, 2003). Next to the regional batholiths (Mocoa, Upper Magdalena Valley, serranía de San Lucas, and Santa Marta Massif), sedimentation resumed in the Early Cretaceous; therefore, the lacuna of the Middle Jurassic unconformity increased towards these areas. In contrast, the sedimentation processes in the La Guajira and northern Venezuela areas changed from continental to marine in the Late Jurassic (Figure 4).

Deformation occurred in different areas since the end of the Middle Jurassic volcanic activity because different degrees of angular unconformities have been documented between Middle Jurassic rocks and overlying units (Upper Jurassic or Lower Cretaceous) (Figure 12). In the latest Jurassic, in areas where accumulation continued (e.g., Lebrija area), eustatic changes caused the incision and later filling of incised valleys with marginal to marine clastic deposits supplied from cratonic areas (contact of the Girón and Tambor–Los Santos Formations in Los Cobardes Anticline).

Therefore, this study concludes that the simplification of "Triassic – Jurassic rocks in Colombia" is misleading and should be avoided. The lithology (e.g., conglomerates), sandstone/conglomerate composition and reddish color are not enough evidence for a correlation between the La Quinta Formation in the serranía de Perijá and the Girón Formation in the Santander Massif or between the Girón and Noreán Formations in the serranía de San Lucas. As discussed in the next section, the mechanism of basin generation may differ depending upon the assumptions of the different tectonic models.

4.2. Review of Tectonic Models

The change from broad volcanic deposition in the Middle Jurassic to restricted continental accumulation in extensional basins in the Late Jurassic reflects a re–organization of tectonic plates (Figures 13, 14, 15). Collected geological data in northwestern Gondwana (northern Perú to Venezuela) were input into three tectonic models that were proposed by several authors to discuss (1) how each model explains the growth of continental plates and (2) whether each model explains the tectonic–plate reorganization along the northwestern corner of Gondwana. Extensional (e.g., Cediel et al., 2003) and subduction (e.g., Spikings et al., 2015) models with static continental blocks only consider one geodynamic model as the main driver to control the Triassic – Jurassic record. The third model of para–autochthonous terranes along both margins (Bayona et al., 2010; Pindell & Kennan, 2009; Toussaint, 1995) requires the reorganization of major plates because of changes in the Pacific–subduction and proto–Caribbean extensional geodynamic processes, similar to the model that was proposed for southern Mexican terranes (Martini & Ortega–Gutiérrez, 2016). This reconstruction does not emphasize the conjugate margin of peri–Gondwana terranes (see discussion in Spikings et al., 2015).

In the Early Jurassic (Figure 13), the onset of magmatism and coeval sedimentation could be explained by either extensional or subduction tectonic processes, although geochemical data support the latter. The extensional model considers that Early Jurassic magmatism was closely related to the extension and thinning of the continental crust (Cediel et al., 2003) (Figure 13a). In contrast, the second model considers that Late Triassic – Early Jurassic extension was related to the rollback of the subduction zone, producing subduction–related magmas with less contamination of continental crust (Spikings et al., 2015). Widespread extension in western Gondwana caused the separation of peri–Gondwana terrains and intraplate aulacogens, such as the Middle Triassic Mitú Graben in Perú (Figure 13b). In the Mérida Andes, van der Lelij et al. (2016) reported 202–Ma tuffs at the base of the La Quinta Formation, coeval with the separation between North and South America, and the generation of proto–Caribbean oceanic crust at 180 Ma (Spikings et al., 2015). The relationship between this extension and subduction in western Gondwana is unclear (Spikings et al., 2015).

In these two static models, Lower Jurassic marine, continental and volcaniclastic strata accumulated in intraplate extensional basins. Marine strata in the Upper Magdalena Valley and northern serranía de San Lucas are not connected with the Perú–Ecuador marine system (Figure 13a, 13b); instead, they record isolated marine deposition along the margin, and these rocks were covered with volcanoclastic deposits. These two models do not explain the presence of volcanic rocks in northern Perú because no Jurassic batholiths have been documented in northern Perú. Additionally, why some extensional basins only have a record of continental deposits (e.g., Lebrija and La Rusia areas) yet others have volcanic deposits remains unclear.

The third hypothesis, which considers paleomagnetic data and the presence of Amazon cratonic rocks in the serranía de San Lucas (Cuadros et al., 2014), considers that marine strata in the Upper Magdalena Valley and northern serranía de San Lucas are connected with marine to marginal basins that developed in Ecuador and Perú since the Late Triassic (Bayona et al., 2010; Sarmiento–Rojas et al., 2006) (Figure 13c). Rosas et al. (2007) interpreted the accumulation of these marine strata

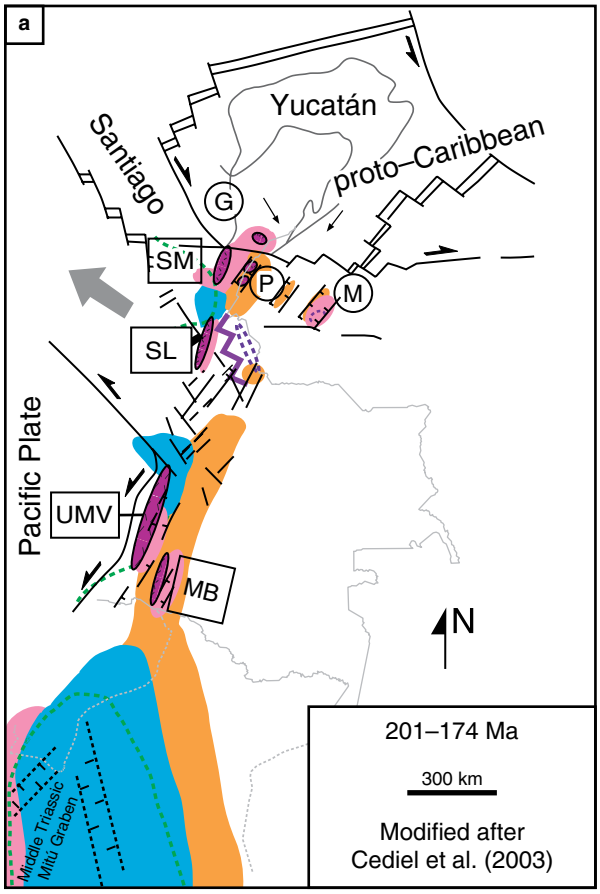
a
Yucatán
Santiago
proto–Caribbean
G
SM
P
M
SL
Pacific Plate
UMV
MB
N
Middle Triassic Mitú Graben
201–174 Ma
300 km
Modified after Cediel et al. (2003)

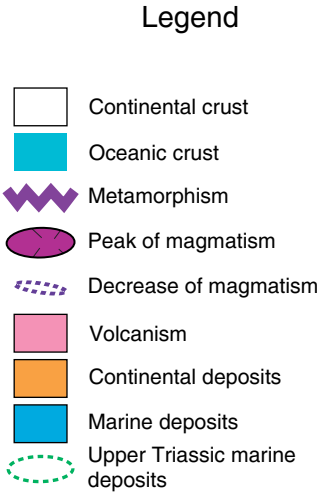
Legend
Continental crust
Oceanic crust
Metamorphism
Peak of magmatism
Decrease of magmatism
Volcanism
Continental deposits
Marine deposits
Upper Triassic marine deposits
SM Santa Marta batholiths
SL San Lucas batholiths
NIB Northern Ibagué Batholith
UMV Upper Magdalena Valley batholiths (e= eastern belt; w= western belt).
GM Garzón Massif batholiths
MB Mocoa Batholith
ZB Zamora Batholith
G La Guajira
P Perijá
NV Northern Venezuela
M Mérida
E El Espino Graben

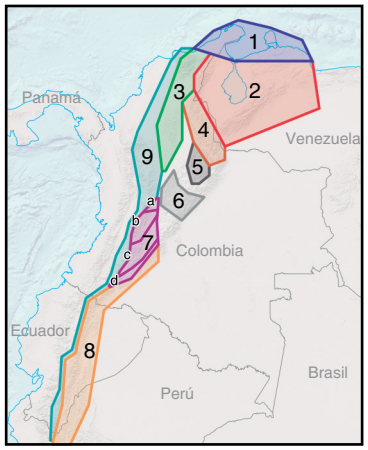
Panamá
Venezuela
Colombia
Ecuador
Perú
Brasil
1
2
3
4
5
6
7
8
9
a
b
c
d

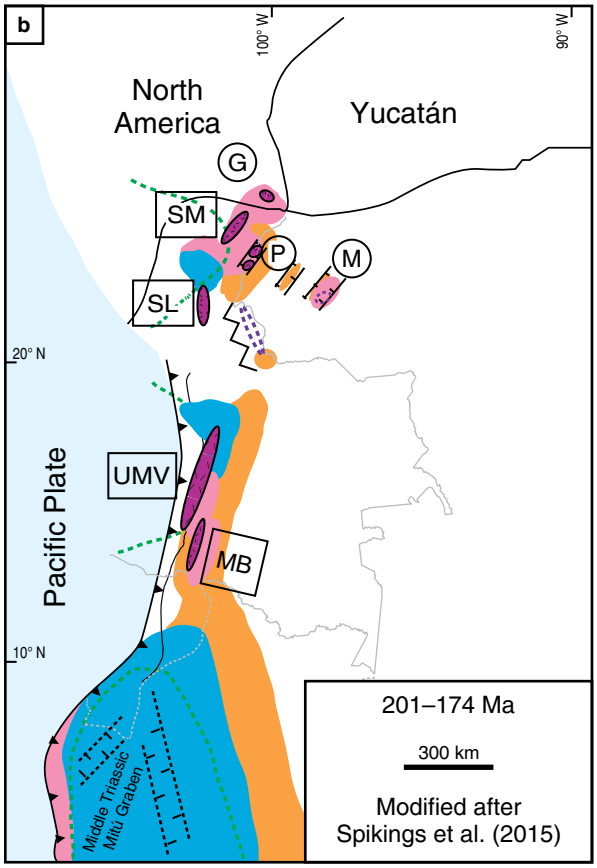
b
100° W
90° W
North America
Yucatán
G
SM
P
M
SL
20° N
Pacific Plate
UMV
MB
10° N
Middle Triassic Mitú Graben
201–174 Ma
300 km
Modified after Spikings et al. (2015)

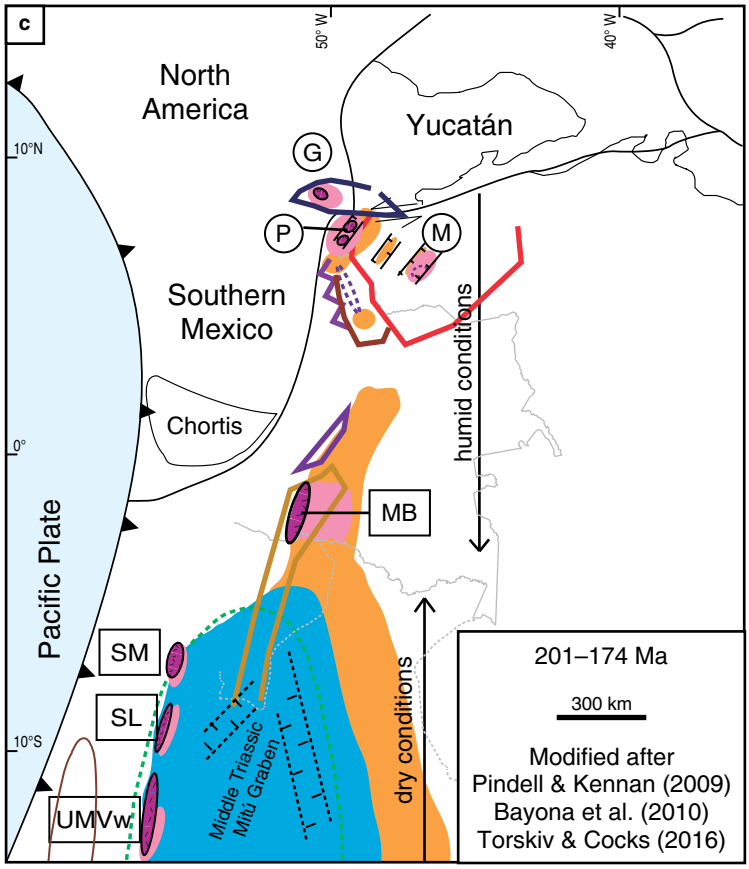
c
50° W
40° W
North America
Yucatán
10°N
G
P
M
Southern Mexico
Chortis
0°
humid conditions
MB
Pacific Plate
SM
SL
10°S
UMVw
Middle Triassic Mitú Graben
dry conditions
201–174 Ma
300 km
Modified after
Pindell & Kennan (2009)
Bayona et al. (2010)
Torskiv & Cocks (2016)

Figure 14. Middle Jurassic tectonic evolution according to the **(a)** extensional, **(b)** subduction–related, **(c)** along–marginal migration of continental crust tectonic models. See the text for discussion.

(limestones, fine–grained organic–rich clastics, and evaporites) as a record of a post–rift regional sag following the Middle Triassic structures of the Mitú extensional system. Interbedded volcanic rocks in northwestern Perú, the western Upper Magdalena Valley and the serranía de San Lucas have a volcanic–arc affinity (Romeuf et al., 1997; Rodríguez et al., 2018; Vásquez et al., 2006), whereas volcanic rocks farther to the southeast in Perú have an intraplate affinity (Rosas et al., 2007). The Lower Jurassic extensional system in northern Gondwana was related to the separation of the North and South American Plates, generating intraplate rift basins (transtensional basins) that were filled with continental to marginal strata and minor interbeds of volcanic rocks; these rocks' geochemistry indicates subduction settings, reflecting the superposition of both Pacific subduction and proto–Caribbean extensional processes, as documented in southern Mexican terranes (Martini & Ortega–Gutiérrez, 2016) (Figure 13c).

One possible peri–Gondwana conjugate margin of these terranes is the Oaxaquia continental block. According to Ramos (2008) and Ramos & Aleman (2000), the trilobite assemblages were similar to those in northern Perú. Graptolite associations in Ordovician rocks that unconformably underlie volcanic rocks from the Saldaña Formation in the Upper Magdalena Valley (Río Venado section) have been associated with Argentine–Bolivian graptolites (Moreno–Sánchez et al., 2008).

In the Middle Jurassic (Figure 14), magmatic activity reached its maximum extension, with the exception of the Santa Martha Massif, where magmatic activity ended in the Early Jurassic. Marine deposition was only restricted to Ecuador within isolated extensional basins (Díaz et al., 2004). In the extensional model, volcanic deposits rapidly filled extensional basins to the south, whereas continental deposition with minor volcanic activity occurred in northern extensional basins (Figure 14a); no explanation is offered for this change in magmatic activity. In the subduction–related model, a marginal volcanic arc formed after the westward rollback of the subduction zone (Spikings et al., 2015) (Figure 14b); however, a gap in the volcanic arc was created between the Upper Magdalena Valley and serranía de San Lucas batholiths. At this time, the magmatism in the Upper Magdalena Valley migrated eastward and became more felsic in composition; therefore, volcanic accumulation occurred in intra–arc volcanic basins (Rodríguez et al., 2018) (Figure 14b). To the north, volcanic rocks in the serranía de San Lucas accumulated in a retro–arc basin, whereas isolated plutons, volcanism and continental deposition in the serranía de Perijá occurred in an intra–plate extensional basin. Neither model explains the isolated magmatic activity and continental deposition in the La Guajira area (block 1). Middle and Late Jurassic metamorphic events are not shown in these two models.

In the third model, the magmatic front that grew in northwestern Perú and Ecuador (acting as the source of volcanic material in northwestern Perú) began to migrate northward (Figure 14c). Both continental (e.g., La Rusia, Jordán, and Chapiza Formations) and volcanic deposition lack evidence of paleosol development, suggesting accumulation at southern paleolatitudes under dry conditions. The northward migration and collision of the arc induced (1) the cessation of magmatism from north to south (Santa Marta Massif, serranía de San Lucas, and eastern belt of the Upper Magdalena batholiths), (2) metamorphic activity adjacent to the Mocoa Batholith and in the northern and western Upper Magdalena Valley, and (3) the deformation of Middle Jurassic continental and volcanic rocks in intraplate extensional basins (Figure 12). Volcanic rocks that were related to the evolution of these magmatic arcs accumulated in retro–arc and intra–arc basins. In contrast, continental extension in the northern region of Gondwana (La Guajira, the serranía de Perijá, and the Mérida Andes) is associated with the onset of the counterclockwise rotation of the Yucatán Block and generation of the proto–Caribbean seafloor. Small intraplate batholiths are documented in the Alta Guajira and serranía de Perijá, and thick continental deposition with thin volcanic interbeds are common in this northern area. This northward migration of terranes along the northwestern margin of Gondwana was first interpreted by Toussaint (1995) by comparing of the Jurassic succession between the block 9 (one portion of his Tahamí Terrane) and the blocks to the east of block 9.

In the Late Jurassic (Figure 15), magmatism ceased to the west as subduction became more oblique, with the exception of the Zamora and Ibagué Batholiths and localized subvolcanic units to the west; in northern basins, only the El Espino Graben has a record of volcanism. Marine deposition is only recorded in La Guajira and northern Venezuela, likely connected with the proto–Caribbean ocean, and in isolated basins in Ecuador (Díaz et al., 2004). For the first two models, the cessation of magmatism must have been related to either the end of extensional tectonism or the end of subduction (Figure 15a, 15b). However, extensional deformation in northern Gondwana resumed according to the broad accumulation of the Girón and upper strata of the La Quinta Formation in the Mérida Andes. The extensional model does not explain the end of extension in the Upper Magdalena Valley and Putumayo regions (Figure 15a). The westward retreat of the subduction zone must have created a new volcanic arc to the west in the basement rocks of the Central Cordillera, but this process does not explain the

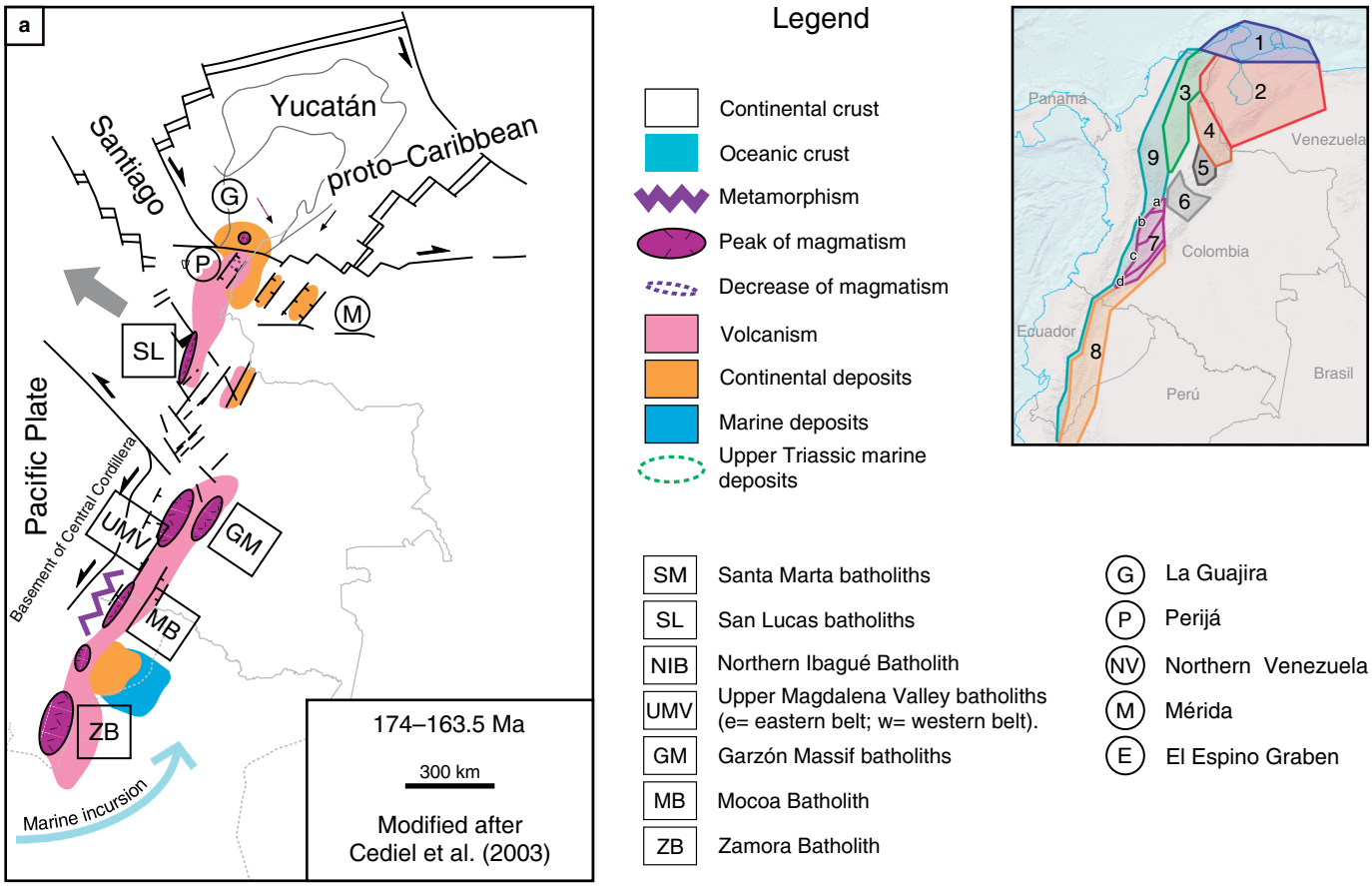
a
Yucatán
Santiago
proto–Caribbean
G
P
M
SL
Pacific Plate
Basement of Central Cordillera
UMV
GM
MB
ZB
Marine incursion
174–163.5 Ma
300 km
Modified after
Cediel et al. (2003)
Legend
Continental crust
Oceanic crust
Metamorphism
Peak of magmatism
Decrease of magmatism
Volcanism
Continental deposits
Marine deposits
Upper Triassic marine deposits
Panamá
Venezuela
Colombia
Ecuador
Perú
Brasil
1
2
3
4
5
6
7
8
9
a
b
c
d
SM Santa Marta batholiths
SL San Lucas batholiths
NIB Northern Ibagué Batholith
UMV Upper Magdalena Valley batholiths (e= eastern belt; w= western belt).
GM Garzón Massif batholiths
MB Mocoa Batholith
ZB Zamora Batholith
G La Guajira
P Perijá
NV Northern Venezuela
M Mérida
E El Espino Graben

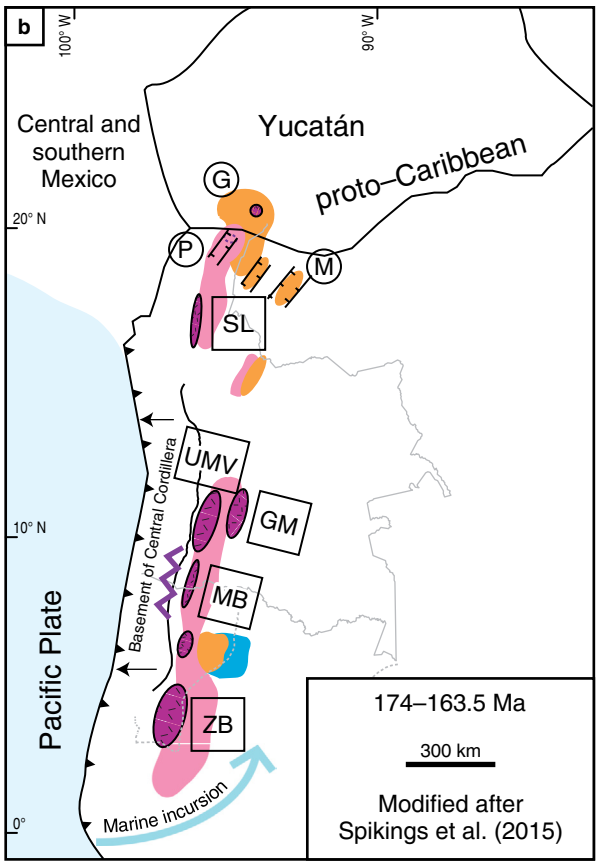
b
100° W
90° W
Central and southern Mexico
Yucatán
proto–Caribbean
20° N
10° N
0°
G
P
M
SL
UMV
GM
MB
ZB
Basement of Central Cordillera
Pacific Plate
Marine incursion
174–163.5 Ma
300 km
Modified after
Spikings et al. (2015)

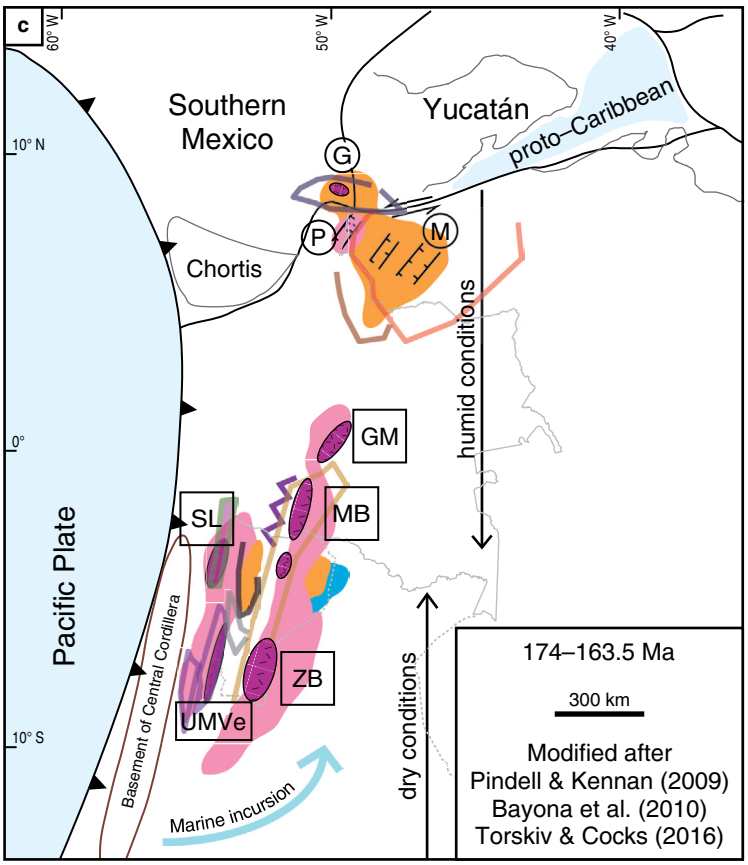
c
60° W
50° W
40° W
10° N
0°
10° S
Southern Mexico
Yucatán
proto–Caribbean
Chortis
G
P
M
humid conditions
GM
SL
MB
ZB
UMVe
Basement of Central Cordillera
Pacific Plate
Marine incursion
dry conditions
174–163.5 Ma
300 km
Modified after
Pindell & Kennan (2009)
Bayona et al. (2010)
Torskiv & Cocks (2016)

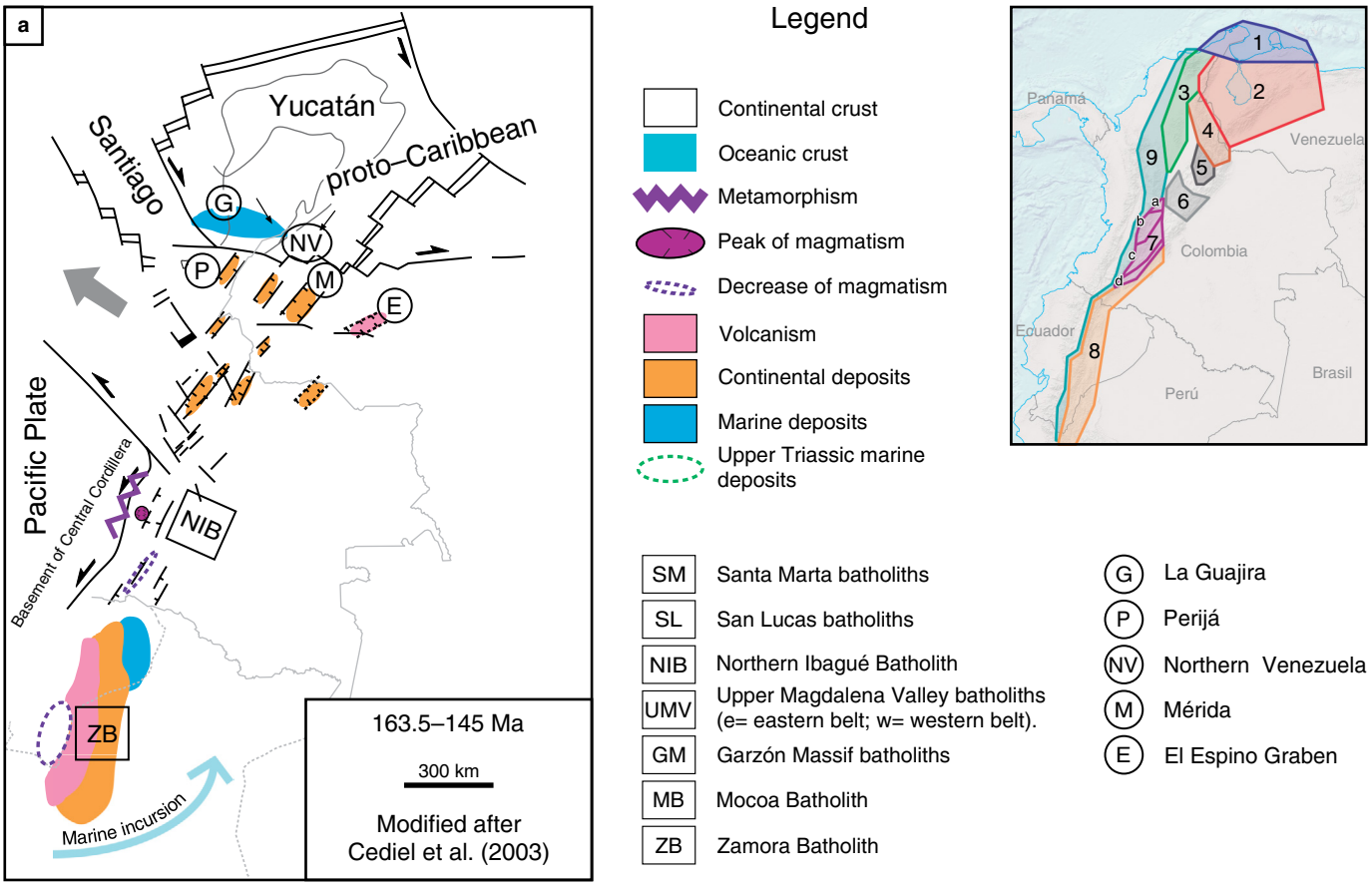
a
Yucatán
Santiago
proto–Caribbean
G
NV
P
M
E
Pacific Plate
Basement of Central Cordillera
NIB
ZB
Marine incursion
163.5–145 Ma
300 km
Modified after
Cediel et al. (2003)
Legend
Continental crust
Oceanic crust
Metamorphism
Peak of magmatism
Decrease of magmatism
Volcanism
Continental deposits
Marine deposits
Upper Triassic marine deposits
Panamá
Venezuela
Colombia
Ecuador
Perú
Brasil
1
2
3
4
5
6
7
8
9
a
b
c
d
SM Santa Marta batholiths
SL San Lucas batholiths
NIB Northern Ibagué Batholith
UMV Upper Magdalena Valley batholiths (e= eastern belt; w= western belt).
GM Garzón Massif batholiths
MB Mocoa Batholith
ZB Zamora Batholith
G La Guajira
P Perijá
NV Northern Venezuela
M Mérida
E El Espino Graben

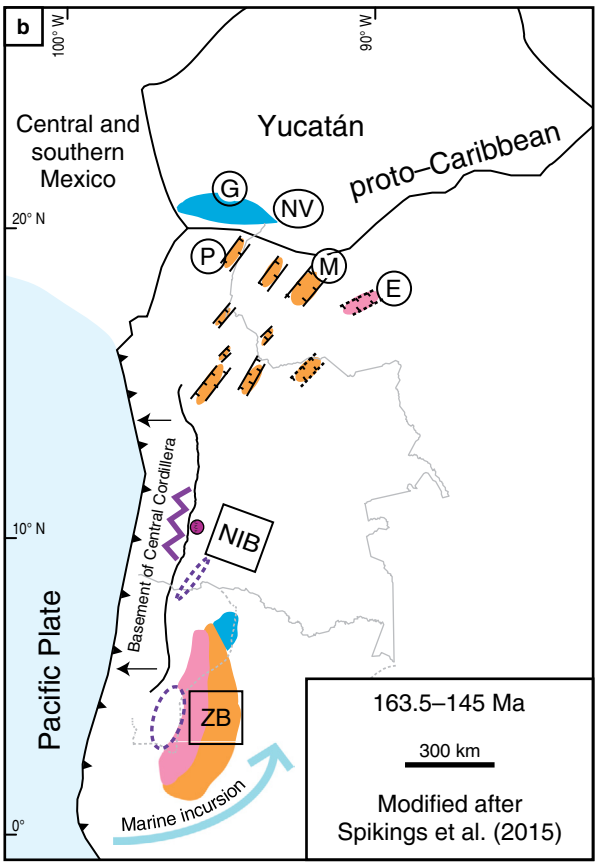
b
100° W
90° W
Central and southern Mexico
Yucatán
proto–Caribbean
20° N
10° N
0°
G
NV
P
M
E
NIB
ZB
Basement of Central Cordillera
Pacific Plate
Marine incursion
163.5–145 Ma
300 km
Modified after
Spikings et al. (2015)

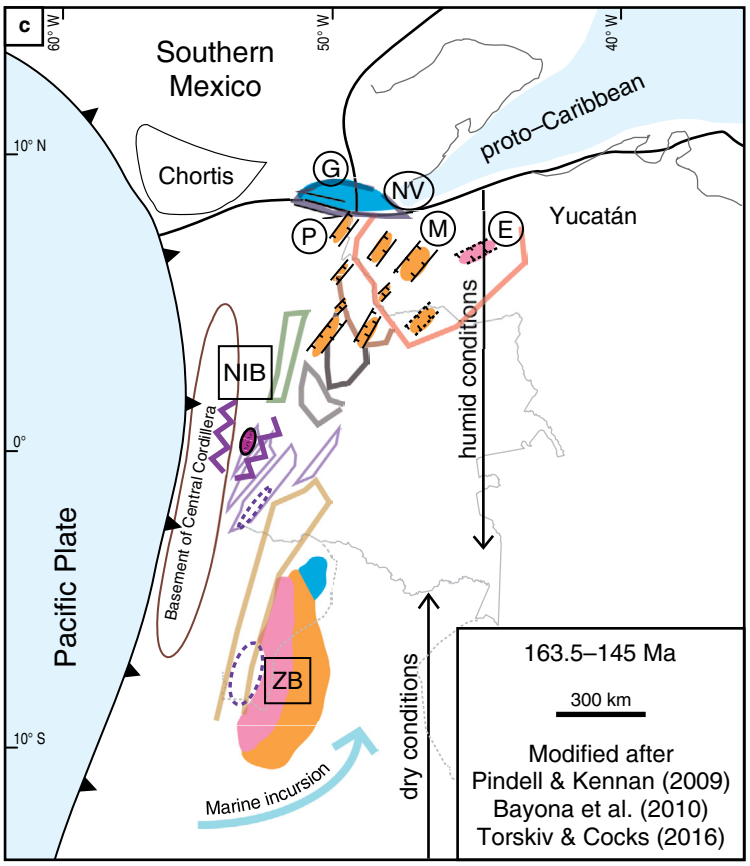
c
60° W
50° W
40° W
Southern Mexico
Chortis
10° N
0°
10° S
proto–Caribbean
Yucatán
G
NV
P
M
E
NIB
ZB
Basement of Central Cordillera
Pacific Plate
humid conditions
dry conditions
Marine incursion
163.5–145 Ma
300 km
Modified after
Pindell & Kennan (2009)
Bayona et al. (2010)
Torskiv & Cocks (2016)

Figure 15. Upper Jurassic tectonic evolution according to the **(a)** extensional, **(b)** subduction–related, **(c)** along–marginal migration of continental crust tectonic models. See the text for discussion.

end of accumulation to the south or the continuous extensional accumulation to northern Gondwana (Figure 15b).

Continuous continental extension in the northward region is related to the counterclockwise rotation of the Yucatán Block and spreading of the proto–Caribbean seafloor (Pindell & Kennan, 2009) (Figure 15c). The final accretion of para–autochthonous terranes from oblique subduction produced the westward migration of the subduction zone and the lack of continental deposition near the collisional margin (e.g., Perijá, San Lucas, Upper Magdalena Valley, and Mocoa Batholith areas). However, other continental crust blocks and oceanic terranes continued accretion in the Cretaceous (Hincapié–Gómez et al., 2018; Spikings et al., 2015) and Cenozoic (Cediel et al., 2003). The development of paleosol profiles to the top of the Girón Formation shows evidence of humid conditions at tropical latitudes (Bayona et al., 2010).

5. Conclusions

The Jurassic record in the northern Andes (northern Perú to Venezuela) is important to analyze the onset of the development of an orthogonal margin in the northwestern corner of Gondwana, where no single geodynamic process may explain the complex configuration and record of metamorphism, magmatism, and sedimentation.

Despite the growing evidence of Lower to Middle Jurassic magmatism that was related to Pacific subduction systems, which created the large intrusive bodies along the western margin of Gondwana (Santa Marta, San Lucas, Upper Magdalena Valley, and Mocoa), extensional tectonism in northern Gondwana (Perijá, La Guajira, northern Venezuela, and the Mérida Andes) was related to the separation of the North and South America Plates, the anticlockwise rotation of the Yucatán Block and seafloor spreading in the proto–Caribbean ocean. Northern Gondwana intraplate transtensional basins were filled with continental to marginal strata and minor interbeds of volcanic rocks. The geochemistry in these intraplate basins indicates subduction settings, reflecting the superposition of both Pacific subduction and proto–Caribbean extensional processes. The Middle Jurassic unconformity at the top of the continental and magmatic successions in this study documents both (1) the cessation of subduction–related magmatism along the western margin as para–autochthonous continental blocks collided and (2) increasing extensional tectonism along the northern margin from the opening of the proto–Caribbean crust.

Future geochemical studies should evaluate the contamination of young (Triassic) versus old (Grenvillian) continental crust, whereas sedimentological analysis should focus on the geometry of sedimentary basins in relation to magmatic depocenters and the record of paleo–climate indicators to document possible paleo–latitudinal variations. Paleomagnetic studies should be conducted at different localities in Lower and Middle Jurassic rocks to test the hypothesis of the along–marginal migration of terranes.

Acknowledgments

German BAYONA acknowledges the invitation of the editorial committee to write this chapter of "The Geology of Colombia Book" and the co–authors to accept this challenge. The figures in this manuscript were prepared by Fernando ALCÁRCEL (Servicio Geológico Colombiano, SGC) and Manuela TABARES (ARES). Project 727771451027 from Colciencias funded Giovanny NOVA, Corporación Geológica ARES funded Ana Milena SALAZAR and Germán BAYONA, and project 828–000061 from Universidad EAFIT funded Camilo BUSTAMANTE. Germán BAYONA acknowledges discussions with Gabriel RODRÍGUEZ (SGC), Agustín CARDONA (Universidad Nacional de Colombia Sede Medellín), Giovanny JIMÉNEZ (Universidad Industrial de Santander), and Camilo MONTES (Universidad del Norte) regarding the Jurassic rocks and their evolution in the Colombian Andes. Comments and suggestions from the reviewers Idael BLANCO and Uwe ALTENBERGER, alongside editorial comments from the editorial board and revision of the American Journal Experts, improved the content of this manuscript.

References

Acosta, J.E. 2002. Structure, tectonics and 3D models of the western foothills of the Eastern Cordillera and Middle Magdalena Valley, Colombia. Doctoral thesis, Imperial College London, 213 p. London.

Almeida, J.P. 1986. Estudio de litofacies y del contacto agua petróleo de la Arenisca T del campo Libertador. Geología de petróleos e Ingeniería de petróleos. Memoirs, III, p. 119–148.

Angulo–Carrera, A.K. 2016. Arquitectura estructural y estratigráfica de la secuencia pre–Aptiense, en la sección norte del corredor Sacha–Shushufindi. Bachelor thesis, Universidad Central de Ecuador, 70 p. Quito.

Ayala–Calvo, R.C., Veloza–Fajardo, G.E., Bayona, G., Gómez–Casallas, M., Rapalini, A.E., Costanzo–Álvarez, V., Aldana, M. & Cortés, M. 2005. Paleomagnetismo y mineralogía magnética en las unidades del Mesozoico de Bucaramanga y macizo de Floresta. Geología Colombiana, (30): 49–66.

Báez, L.A. & Sánchez, C.J. 2003. Un escenario paleoambiental para una tectónica extensional jurásica mediante la caracterización de las formaciones La Rusia y Montebel, al noroccidente de la Falla de Boyacá, en cercanías a los municipios de Paipa, Duitama, Cerinza y Belén. Bachelor thesis, Universidad Nacional de Colombia, 83 p. Bogotá.

Barret, P.M., Butler, R.J, Novas, F.E.., Moore–Fay, S.C., Moody, J.M., Clark, J.M. & Sánchez–Villagra, M.R. 2008. Dinosaur remains from the La Quinta Formation (Lower or Middle Jurassic) of the Venezuelan Andes. Paläontologische Zeitschrift, 82(2): 163–177. https://doi.org/10.1007/BF02988407

Bayona, G., García, D.F. & Mora, G. 1994. La Formación Saldaña: Producto de la actividad de estratovolcanes continentales en un dominio de retroarco. En: Etayo–Serna, F. (editor), Estudios Geológicos del Valle Superior del Magdalena, Universidad Nacional de Colombia–Ecopetrol. p. I–1–1–21. Bogotá.

Bayona, G., Silva, C., Rapalini, A.E., Costanzo–Álvarez, V., Aldana, M. & Roncancio, J. 2005. Paleomagnetismo y mineralogía magnética en rocas de la Formación Saldaña y unidades cretácicas suprayacentes en la parte norte del Valle Superior del Magdalena, Colombia. Boletín de Geología, 27(2): 69–85.

Bayona, G., Rapalini, A. & Costanzo–Álvarez, V. 2006. Paleomagnetism in Mesozoic rocks of the northern Andes and its implications in Mesozoic tectonics of northwestern South America. Earth, Planets and Space, 58(10): 1255–1272. https://doi.org/10.1186/BF03352621

Bayona, G., Jiménez, G., Silva, C., Cardona, A., Montes, C., Roncancio, J. & Cordani, U. 2010. Paleomagnetic data and K–Ar ages from Mesozoic units of the Santa Marta Massif: A preliminary interpretation for block rotation and translations. Journal of South American Earth Sciences, 29(4): 817–831. https://doi.org/10.1016/j.jsames.2009.10.005

Bayona, G., Cardona, A., Jaramillo, C., Montaño, P., Montenegro, C., Mahecha, H., Nova, G., Ortiz, J. & Montes, C. 2012a. Análisis sedimentológico, petrográfico, bioestratigráfico y geocronológico de las unidades perforadas por el pozo WILDSUR. Internal report, 34 p.

Bayona, G., Cardona, A., Jaramillo, C., Mora, A., Montes, C., Valencia, V., Ayala, C., Montenegro, O. & Ibañez–Mejia, M. 2012b. Early Paleogene magmatism in the northern Andes: Insights on the effects of oceanic plateau–continent convergence. Earth and Planetary Science Letters, 331–332: 97–111. https://doi.org/10.1016/j.epsl.2012.03.015

Bayona, G., Cardona, A. & Montes, C. 2013a. The NW margin of South America in Jurassic time: Southern effects of the opening of the Gulf of Mexico and proto–Caribbean tectonics. Poster, Southeastern Section 62nd Annual Meeting, Geological Society of America Abstracts with Programs, 45(2), p. 61. San Juan, Puerto Rico.

Bayona, G., Cardona, A., Nova, G., Montaño, P., Zapata, S., Rapalini, A., Montes, C., Vásquez, M. & Valencia, V. 2013b. Paleomagnetism, geochemistry and geochronology insights of the Jurassic – Lower Cretaceous of NW South America. XIV Congreso Colombiano de Geología. Memoirs, p. 240–241. Bogotá.

Bayona, G., Montes, C., Cardona, A., Niño, H., Ramírez, V., Baquero, M., Nova, G., Montaño, P., Zapata, S. & Rapalini, A. 2016. How isolated blocks formed in the Alta Guajira? Insights for southern Caribbean margin exploration. XII Simposio Bolivariano–Exploración Petrolera en las Cuencas Subandinas. Proceedings, 9 p. Bogotá.

Bejarano, A., Villegas E. & Reyes, R. 1991. Caracterización y evaluación de parámetros de registros de pozos en la Cuenca del Putumayo. 4th Simposio Bolivariano. Exploración–Petrolera en las Cuencas Subandinas. Proceedings, p. 200. Bogotá.

Benedetto, G. & Odreman, O. 1977. Nuevas evidencias paleontológicas en la Formación La Quinta, su edad y correlación con las unidades aflorantes en la Sierra de Perijá y cordillera Oriental de Colombia. V Congreso Geológico de Venezuela. Memoirs, I, p. 87–106.

Blanco–Quintero, I.F., García–Casco, A., Toro, L.M., Moreno–Sánchez, M., Ruiz, E.C., Vinasco, C.J., Cardona, A., Lázaro, C. & Morata, D. 2014. Late Jurassic terrane collision in the northwestern margin of Gondwana (Cajamarca Complex, eastern flank of the Central Cordillera, Colombia). International Geology Review, 56(15): 1852–1872. https://doi.org/10.1080/00206814.2014.963710

Bristow, C.R. & Hoffstetter, R. 1977. Lexique stratigraphique International: Amérique Latine. Ecuador. Centre National de la Recherche Scientifique 5, Fascicule 5a, 410 p. Paris.

Burkley, L.A. 1976. Geochronology of the central Venezuela Andes. Doctoral thesis, Case Western Reserve University, 155 p. Cleveland, USA.

Bustamante, C., Cardona, A., Bayona, G., Mora, A., Valencia, V., Gehrels, G. & Vervoort, J. 2010. U–Pb LA–ICP–MS geochronology and regional correlation of Middle Jurassic intrusive rocks from the Garzón Massif, Upper Magdalena Valley and Central Cordillera, southern Colombia. Boletín de Geología, 32(2): 93–109.

Bustamante, C., Archanjo, C.J., Cardona, A. & Vervoort, J.D. 2016. Late Jurassic to Early Cretaceous plutonism in the Colombian Andes: A record of long–term arc maturity. Geological Society of America Bulletin, 128(11–12): 1762–1779. https://doi.org/10.1130/B31307.1

Bustamante, C., Archanjo, C.J., Cardona, A., Bustamante, A. & Valencia, V.A. 2017. U–Pb ages and Hf isotopes in zircons from parautochthonous Mesozoic terranes in the western margin of Pangea: Implications for the terrane configurations in the northern Andes. The Journal of Geology, 125(5): 487–500. https://doi.org/10.1086/693014

Caballero, V., Parra, M., Mora, A., López, C., Rojas, L.E. & Quintero, I. 2013. Factors controlling selective abandonment and reactivation in thick–skin orogens: A case study in the Magdalena Valley, Colombia. In: Nemčok, M., Mora, A. & Cosgrove, J.W. (editors), Thick–skin–dominated orogens: From initial inversion to full accretion. Geological Society of London,

Special Publication 377, p. 343–367. London. https://doi.org/10.1144/SP377.4

Cáceres, H. & Teatin, P. 1985. Cuenca del Putumayo, provincia petrolera meridional de Colombia. II Simposio Bolivariano–Exploración Petrolera en las Cuencas Subandinas. Memoirs, I, p. 1–80. Bogotá.

Cajas, L. 2003. Estudio petrográfico de la Formación Saldaña entre los municipios de Alpujarra y Natagaima. Bachelor thesis, Universidad Nacional de Colombia, 128 p. Bogotá.

Cardona, A., Cordani, U.G. & MacDonald, W.D. 2006. Tectonic correlations of pre–Mesozoic crust from the northern termination of the Colombian Andes, Caribbean region. Journal of South American Earth Sciences, 21(4): 337–354. https://doi.org/10.1016/j.jsames.2006.07.009

Cardona, A., Chew, D., Valencia, V.A., Bayona, G., Mišković, A. & Ibañez–Mejia, M. 2010. Grenvillian remnants in the northern Andes: Rodinian and Phanerozoic paleogeographic perspectives. Journal of South American Earth Sciences, 29(1): 92–104. https://doi.org/10.1016/j.jsames.2009.07.011

Cardona, A., Valencia, V.A., Lotero, A., Villafañez, Y. & Bayona, G. 2016. Provenance of middle to late Palaeozoic sediments in the northeastern Colombian Andes: Implications for Pangea reconstruction. International Geology Review, 58(15): 1914–1939. https://doi.org/10.1080/00206814.2016.1190948

Castillo, J., Gose, W.A. & Perarnau, A. 1991. Paleomagnetic results from Mesozoic strata in the Mérida Andes, Venezuela. Journal of Geophysical Research: Solid Earth, 96(B4): 6011–6022. https://doi.org/10.1029/90JB02282

Cediel, F. 1968. El Grupo Girón, una molasa mesozoica de la cordillera Oriental. Boletín Geológico, 16(1–3): 5–96.

Cediel, F., Shaw, R.P. & Cáceres, C. 2003. Tectonic assembly of the northern Andean Block. In: Bartolini, C., Buffler, R.T. & Blickwede, J. (editors), The circum–Gulf of Mexico and the Caribbean: Hydrocarbon habitats, basin formation, and plate tectonics. American Association of Petroleum Geologists, Memoir 79, p. 815–848. Tulsa, USA.

Christophoul, F. 1999. Discrimination des influences tectoniques et eustatiques dans les basins liés à des zones de convergence: Exemples du bassin subandin d'Equateur. Doctoral thesis, Université de Toulouse 3, 184 p. Toulouse, France.

Clavijo, J. 1995. Memoria explicativa: Mapa geológico de la plancha 75 Aguachica. Scale 1:100 000. Ingeominas, 48 p. Bucaramanga.

Clavijo, J., Mantilla, L., Pinto, J., Bernal, L. & Pérez, A. 2008. Evolución geológica de la Serranía de San Lucas, norte del Valle Medio del Magdalena y noroeste de la cordillera Oriental. Boletín de Geología, 30(1): 45–62.

Cochrane, R., Spikings, R., Gerdes, A., Winkler, W., Ulianov, A., Mora, A. & Chiaradia, M. 2014a. Distinguishing between in–situ and accretionary growth of continents along active margins. Lithos, 202–203: 382–394. https://doi.org/10.1016/j.lithos.2014.05.031

Cochrane, R., Spikings, R., Gerdes, A., Ulianov, A., Mora, A., Villagómez, D., Putlitz, B. & Chiaradia, M. 2014b. Permo–Triassic anatexis, continental rifting and the disassembly of western Pangaea. Lithos, 190–191: 383–402. https://doi.org/10.1016/j.lithos.2013.12.020

Colmenares, F.H., Mesa, A.M., Roncancio, J.H., Arciniegas, E.G., Pedraza, P.E., Cardona, A., Romero, A.J., Silva, C.A., Alvarado, S.I., Romero, O.A. & Vargas, A.F. 2007. Geología de las planchas 11, 12, 13, 14, 18, 19, 20, 21, 25, 26, 27, 33, 34 y 40. Proyecto: Evolución geohistórica de la Sierra Nevada de Santa Marta. Invemar–Ingeominas–ICP–Ecopetrol–Geosearch Ltda., 401 p. Bogotá.

Correa–Martínez, A.M., Rodríguez, G., Arango, M.I., Zapata, G. & Bermúdez, J.G. 2016. Catálogo de unidades litoestratigráficas de Colombia: Batolito de Mogotes, cordillera Oriental. Servicio Geológico Colombiano. 112 p. Medellín.

Correa–Martínez, A.M., Rodríguez, G., Arango, M.I., & Zapata–García, G. 2019. Petrografía, geoquímica y geocronología U–Pb de las rocas volcánicas y piroclásticas de la Formación Noreán al NW del macizo de Santander, Colombia. Boletín de Geología, 41(1), 29–54. https://doi.org/10.18273/revbol.v41n1-2019002

Cuadros, F.A., Botelho, N.F., Ordóñez–Carmona, O. & Matteini, M. 2014. Mesoproterozoic crust in the San Lucas Range (Colombia): An insight into the crustal evolution of the northern Andes. Precambrian Research, 245: 186–206. https://doi.org/10.1016/j.precamres.2014.02.010

Daconte, R. & Salinas, R. 1980. Memoria Explicativa: Geología de las planchas 66 Miraflores y 76 Ocaña. Scale 1: 100 000. 105 p. Ingeominas. Bucaramanga.

Dasch, L.E. 1982. U–Pb geochronology of the Sierra de Perijá, Venezuela. Master thesis, Case Western Reserve University, 183 p. Cleveland, USA.

Díaz, M., Baby, P., Rivadeneira, M. & Christophoul, F. 2004. El pre–Aptiense en la Cuenca Oriente Ecuatoriana. In: Baby, P., Rivadeneira, M. & Barragán, R. (editors), La Cuenca Oriente: Geología y petróleo. Travaux de L'Institut Francais d'Études Andines l'IFEA, 144, p. 23–44. https://doi.org/10.4000/books.ifea.2971

Dorado–Galindo, J. 1992. Contribución al conocimiento de la estratigrafía de la Formación Brechas de Buenavista (límite Jurásico–Cretácico). Región noroeste de Villavicencio (Meta). Geología Colombiana, 17: 7–39.

Estupiñan, J., Marfil, R., Scherer, M. & Permanyer, A. 2010. Reservoir sandstones of the Cretaceous Napo Formation U and T members in the Oriente Basin, Ecuador: Links between diagenesis and sequence stratigraphy. Journal of Petroleum Geology, 33(3): 221–245. https://doi.org/10.1111/j.1747-5457.2010.00475.x

Eva, A.N., Burke, K., Mann, P. & Wadge, G. 1989. Four–phase tectonostratigraphic development of the southern Caribbean. Marine and Petroleum Geology, 6(1): 9–21. https://doi.org/10.1016/0264-8172(89)90072-X

Feo–Codecido, G., Martin–Bellizzia, C. & Bartok, P. 1974. Excursión geológica a la península de Paraguaná. Asociación Venezolana de Geología, Minería y Petróleo, 23 p. Caracas.

Forero, A. 1970. Estratigrafía del pre–Cretácico en el flanco occidental de la Serranía de Perijá. Geología Colombiana, 7: 7–77.

Frizon de Lamotte, D., Fourdan, B., Leleu, S., Leparmentier, F. & De Clarens, P. 2015. Style of rifting and the stages of Pangea breakup. Tectonics, 34(5): 1009–1029. https://doi.org/10.1002/2014TC003760

Fuquen, J.A. & Osorno, J.F. 2002. Memoria explicativa: Plancha 303 Colombia, departamentos de Huila, Tolima y Meta. Scale 1:100.000. Ingeominas, 88 p. Bogotá.

Fuquen, J.A., Gómez, L.A., Buchely, F., Lancheros, J., Dávila, C., López, C., Romero, O. & González, F. 2010. Cartografía geológica y muestreo geoquímico de la parte norte de la Serranía de Perijá: Planchas 21, 22, 27, 28, 34 y 35. Informe final contrato 369 del 2009. Ingeominas–GRP, 204 p. Bogotá.

Gaibor, J., Hochuli, J.P.A., Winkler, W. & Toro, J. 2008. Hydrocarbon source potential of the Santiago Formation, Oriente Basin, SE of Ecuador. Journal of South American Earth Sciences, 25(2): 145–156. https://doi.org/10.1016/j.jsames.2007.07.002

Geyer, O.F. 1973. Das präkretazische Mesozoikum von Kolumbien. Geologisches Jahrbuch, 5: 1–155.

Geyer, O.F. 1976. La fauna de amonitas del perfil típico de la Formación Morrocoyal. I Congreso Colombiano de Geología. Memoirs, p. 111–134. Bogotá.

Geyer, O.F. 1982. Comparaciones estratigráficas y faciales en el Triásico norandino. Geología Norandina, 5: 27–31.

Gómez, J., Schobbenhaus, C. & Montes, N.E., compilers. 2019. Geological Map of South America 2019. Scale 1:5000000. Commission for the Geological Map of the World (CGMW), Colombian Geological Survey and Geological Survey of Brazil. Paris. https://doi.org/10.32685/10.143.2019.929

González de Juana, C., Iturralde de Arozena, J.M. & Picard–Cadillat, X. 1980. Geología de Venezuela y de sus cuencas petrolíferas. Ediciones Foninves, I–II, 1031 p. Caracas.

González, H., Salinas–Echeverri, R., Cárdenas, J.I., Muñoz, C.M. & Vélez–Giraldo, W. 2015a. Memoria explicativa: Plancha 41 Becerril. Servicio Geológico Colombiano, 160 p. Medellín.

González, H., Maya, M., Tabares, L.F., Montoya, A., Palacio, A.F., Sánchez, C., Barajas A. & Vélez–Giraldo, W. 2015b. Memoria explicativa: Plancha 118 San Francisco. Scale 1:100 000. Servicio Geológico Colombiano, 220 p. Medellín.

Gose, W.A., Perarnau, A. & Castillo, J. 2003. Paleomagnetic results from the Perijá Mountains, Venezuela: An example of vertical axis rotation. In: Bartolini, C., Buffler, R.T. & Blickwede, J. (editors), The circum–Gulf of Mexico and the Caribbean: Hydrocarbon habitats, basin formation, and plate tectonics. American Association of Petroleum Geologists, Memoir 79, p. 969–975. Tulsa, USA.

Hall, M.L. & Calle, J. 1982. Geochronological control for the main tectonic–magmatic events of Ecuador. Earth–Science Reviews, 18(3–4): 215–239. https://doi.org/10.1016/0012-8252(82)90038-1

Hernández, M. 2003. Análisis geológico integrado en la facies no–roja de la Formación La Quinta (sección de carretera Jají–San Juan), Edo. Mérida. Bachelor thesis, Universidad Central de Venezuela, 280 p. Caracas.

Hincapié–Gómez, S. 2018. Paleogeografía jurásica de los Andes colombianos en la región de Payandé–Rovira, Tolima: Evolución de arcos magmáticos en ambientes de convergencia oblicua. Master Thesis, Universidad Nacional de Colombia, 66 p. Medellín.

Hincapié–Gómez, S., Cardona, A., Jiménez, G., Monsalve, G., Ramírez–Hoyos, L. & Bayona, G. 2018. Paleomagnetic and gravimetrical reconnaissance of Cretaceous volcanic rocks from the western Colombian Andes: Paleogeographic connections with the Caribbean Plate. Studia Geophysica et Geodaetica, 62(3): 485–511. https://doi.org/10.1007/s11200-016-0678-y

Horton, B.K., Saylor, J.E., Nie, J., Mora, A., Parra, M., Reyes–Harker, A. & Stockli, D.F. 2010. Linking sedimentation in the northern Andes to basement configuration, Mesozoic extension, and Cenozoic shortening: Evidence from detrital zircon U–Pb ages, Eastern Cordillera, Colombia. Geological Society of America Bulletin, 122(9–10): 1423–1442. https://doi.org/10.1130/B30118.1

Horton, B.K., Anderson, V.J., Caballero, V., Saylor, J.E., Nie, J., Parra, M. & Mora, A. 2015. Application of detrital zircon U–Pb geochronology to surface and subsurface correlations of provenance, paleodrainage and tectonics of the Middle Magdalena Valley Basin of Colombia. Geosphere, 11(6): 1790–1811. https://doi.org/10.1130/GES01251.1

Ibañez–Mejia, M., Ruiz, J., Valencia, V.A., Cardona, A., Gehrels, G.E. & Mora, A. 2011. The Putumayo Orogen of Amazonia and its implications for Rodinia reconstructions: New U–Pb geochronological insights into the Proterozoic tectonic evolution of northwestern South America. Precambrian Research, 191(1–2): 58–77. https://doi.org/10.1016/j.precamres.2011.09.005

Ingeominas & Universidad Industrial de Santander. 2006. Memoria explicativa: Plancha 96 Bocas del Rosario. Scale 1:100 000. Ingeominas, 126 p. Bogotá.

Irving, E.M. 1972. Mapa geológico de la península de la Guajira, Colombia (compilación). Scale 1:100 000. Ingeominas. Bogotá.

Jaillard, E., Laubacher, G., Bengston, P., Dhondt, A.V. & Bulot, L.G. 1999. Stratigraphy and evolution of the Cretaceous forearc Celica–Lancones Basin of southwestern Ecuador. Journal of South American Earth Sciences, 12(1): 51–68. https://doi.org/10.1016/S0895-9811(99)00006-1

Jaimes, F., Navarro, J., Russe, E., Santos, A. & Bellido, F. 2011. Geología del cuadrángulo de Olmos: Hoja 12–d. Scale 1:50 000. Instituto Geológico, Minero y Metalúrgico. Carta Geológica Nacional, Boletín, 140 (Serie A), 76 p. Lima.

Jiménez, G., García, H., Cardona, A. & García, L. 2017. Preliminary results on magnetic properties of the Girón Group Colombia: Implications in stratigraphy and tectonics in the NW margin of South America. Annual Meeting, Geological Society of America Abstracts with Programs, 49(6). Seattle. USA. https://doi.org/10.1130/abs/2017AM-304657

Kammer, A. & Sánchez, J. 2006. Early Jurassic rift structures associated with the Soapaga and Boyacá Faults of the Eastern Cordillera, Colombia: Sedimentological inferences and regional implications. Journal of South American Earth Sciences, 21(4): 412–422. https://doi.org/10.1016/j.jsames.2006.07.006

Langer, M.C., Rincón, A.D., Ramezani, J., Solórzano, A. & Rauhut, O.W.M. 2014. New dinosaur (Theropoda, stem–Averostra) from the earliest Jurassic of the La Quinta Formation, Venezuelan Andes. Open Science, 1(2): 13 p. https://doi.org/10.1098/rsos.140184

Leal–Mejía, H. 2011. Phanerozoic gold metallogeny in the Colombian Andes: A tectono–magmatic approach. Doctoral thesis, Universitat de Barcelona, 989 p. Barcelona.

López, A. & Mesa, J.E. 1997. Estratigrafía y ambientes de depósito de la Formación Girón en el macizo de Floresta, Departamento de Boyacá. Bachelor thesis, Universidad Nacional de Colombia, 104 p. Bogotá.

MacDonald, W.D. & Opdyke, N.D. 1972. Tectonic rotations suggested by paleomagnetic results from northern Colombia, South America. Journal of Geophysical Research, 77(29): 5720–5730. https://doi.org/10.1029/JB077i029p05720

MacDonald, W.D., Álvarez, W. & Lockwood, J.P. 1968. Mesozoic stratigraphy, structure and metamorphism, Guajira Peninsula, Colombia. Geological Society of America, Abstracts for 1968, Special Paper (121), p. 183. Boulder, USA.

Mantilla–Figueroa, L.C., Bissig, T., Valencia, V. & Hart, C.J.R. 2013. The magmatic history of the Vetas–California mining district, Santander Massif, Eastern Cordillera, Colombia. Journal of South American Earth Sciences, 45: 235–249. https://doi.org/10.1016/j.jsames.2013.03.006

Martini, M. & Ortega–Gutiérrez, F. 2016. Tectono–stratigraphic evolution of eastern Mexico during the break–up of Pangea: A review. In: Gómez–Tuena, A. & Ortega–Gutiérrez, F. (editors), Tectonic systema of Mexico: Origin and evolution, Earth–Science Reviews, 183: p. 38–55. https://doi.org/10.1016/j.earscirev.2016.06.013

Maze, W.B. 1984. Jurassic La Quinta Formation in the Sierra de Perijá, northwestern Venezuela: Geology and tectonic environment of red beds and volcanic rocks. In: Bonini, W.E., Hargraves, R.B. & Shagan, R. (editors), The Caribbean–South American Plate boundary and regional tectonics, Geological Society of America, Memoir 162, p. 263–282. https://doi.org/10.1130/MEM162-p263

Mejía, J.L. & Tellez, N. 1974. Prospección geoquímica del Páramo de Cáchira. Ingeominas, 45 p. Bucaramanga.

Mendi, M., Baquero, M., Paiva–Oliveira, E. & Urbani, F. 2013. Petrografía y geocronología U–Pb en zircones de las unidades ígneo–metamórficas en la Mesa de Cocodite, península Paraguaná, Venezuela. GEOS, 45: 99–102.

Mojica, J. & Kammer, A. 1995. Eventos jurásicos en Colombia. Geología Colombiana, 19: 165–172.

Mojica, J. & Llinás, R. 1984. Observaciones recientes sobre las características del basamento económico del Valle Superior del Magdalena en la región de Payandé–Rovira (Tolima, Colombia), y en especial sobre la estratigrafía y petrografía del Miembro Chicalá (=parte baja de la Fm. Saldaña). Geología Colombiana, 13: 81–127.

Mojica, J. & Prinz–Grimm, P. 2000. La fauna de amonitas del Triásico Tardío en el Miembro Chicalá (parte baja de la Formación Saldaña) en Payandé, Tolima, Colombia. Geología Colombiana, 25: 13–23.

Mojica, J. & Villarroel, C. 1984. Contribución al conocimiento de las unidades paleozoicas del área de Floresta (cordillera Oriental colombiana; departamento de Boyacá) y en especial de la Formación Cuche. Geología Colombiana, (13): 55–79.

Mojica, J., Kammer, A. & Ujueta, G. 1996. El Jurásico del sector noroccidental de Suramérica y guía de la excursión al Valle Superior del Magdalena (Nov. 1–4/95), regiones de Payandé y Prado, departamento del Tolima, Colombia. Geología Colombiana, 21: 3–40.

Montaño, P. 2009. Caracterización petrográfica y geocronología detrítica de las rocas aflorantes en el arroyo Alberto (Serranía del Perijá), infrayacentes a la Formación Río Negro. Bachelor thesis, Universidad Nacional de Colombia, 20 p. Bogotá.

Montenegro, G. & Barragán, M. 2011. Caguán and Putumayo Basin. In: Cediel, F. (editor), Petroleum Geology of Colombia 4, Agencia Nacional de Hidrocarburos and Fondo Editorial Universidad EAFIT, 127 p. Medellín.

Mora, A., Venegas, D. & Vergara, L. 1998. Estratigrafía del Cretácico Superior y Terciario inferior en el sector norte de la Cuenca del Putumayo, departamento del Caquetá, Colombia. Geología Colombiana, 23: 31–77.

Mora, A., Gaona, T., Kley, J., Montoya, D., Parra, M., Quiroz, L.I., Reyes, G. & Strecker, M. 2009. The role of inherited extensional fault segmentation and linkage in contractional orogenesis: A reconstruction of Lower Cretaceous inverted rift basins in the Eastern Cordillera of Colombia. Basin Research, 21(1): 111–137. https://doi.org/10.1111/j.1365-2117.2008.00367.x

Moreno–Sánchez, M., Gómez–Cruz, A. J. & Castillo–González, H. 2008. Graptolitos del Ordovícico y geología de los afloramientos del río Venado (norte del departamento del Huila). Boletín de Geología, 30(1): 9–19.

Moreno–Sánchez, M., Toro–Toro, L.M., Gómez–Cruz, A. & Ruiz, E.C. 2016. Formación Nogontova, una nueva unidad litoestratigráfica en la cordillera Oriental de Colombia. Boletín de Geología, 38(2): 55–62. https://doi.org/10.18273/revbol.v38n2-2016003

Moticska, P. 1985. Volcanismo mesozoico en el subsuelo de la faja petrolífera del Orinoco, estado Guárico, Venezuela. In: Ríos, J.H. & Pimentel de Bellizzia, N. (editors), VI Congreso Geológico Venezolano. Memoirs, III, p. 1930–1943. Caracas.

Mourier, T., Laj, C., Mégard, F., Roperch, P., Mitouard, P. & Farfan–Medrano, A. 1988. An accreted continental terrane in northwestern Perú. Earth and Planetary Science Letters, 88(1–2): 182–192. https://doi.org/10.1016/0012-821X(88)90056-8

Nelson, W.H. 1962. Contribución al conocimiento de la cordillera Central de Colombia sección entre Ibagué y Armenia. Servicio Geológico Nacional, Boletín Geológico, 10(1–3): 161–202.

Nevers, G.M., Dorman, J.H., Harrison, P.J. & Rojas, O. 1991. Recent exploration results in northern Putumayo Basin, Colombia. IV Simposio Bolivariano–Exploración Petrolera en las Cuencas Subandinas. Memoirs, I(8), p. 18. Bogotá.

Nova–Rodríguez, G., Montaño, P., Bayona, G., Rapalini, A & Montes, C. 2012. Paleomagnetismo en rocas del Jurásico y Cretácico Inferior en el flanco occidental de la Serranía del Perijá: Contribuciones a la evolución tectónica del NW de Suramérica. Boletín de Geología, 34(2): 117–138.

Nova–Rodríguez, G., Silva–Tamayo, J.C. & Bayona, G. 2017. Stratigraphy and petrography from the Jurassic–Cretaceous transition in the Guajira Peninsula: Understanding the proto–Caribbean margin. XVI Congreso Colombiano de Geología–III Simposio de Exploradores. Memoirs, p. 327–332. Santa Marta.

Núñez, A. & Gómez, J. 2003. Geología de las planchas 411 La Cruz, 412 San Juan de Villalobos, 430 Mocoa, 431 Piamonte, 448 Monopamba, 449 Orito y 465 Churuyaco. Scale 1:200 000. Ingeominas. Bogotá.

Núñez, A. & Murillo, A. 1982. Memoria explicativa: Geología y prospección geoquímica de las planchas 244 Ibagué y 263 Ortega. Ingeominas, Informe 1879, 366 p. Ibagué.

Ortega–Montero, C.R.. Rojas–Martínez, E.E. & Manco–Jaraba, D.C. 2012. Mineralización de cobre en el sector de San Diego, Serranía del Perijá. Geología Colombiana, 37: 51–62.

Osorio–Afanador, D. A., 2016. Estratigrafía y deformación del Grupo Girón en el Anticlinorio de los Yariguíes ("Anticlinal de los Cobardes"), sectores de Zapatoca y río Lebrija. Bachelor thesis, Universidad Industrial de Santander, 173 p. Bucaramanga.

Pardo, A. & Sanz, V. 1979. Estratigrafía del curso medio del río La Leche, departamento de Lambayeque. Boletín Sociedad Geológica del Perú, 60: 251–266.

Pindell, J.L. & Kennan, L. 2009. Tectonic evolution of the Gulf of Mexico, Caribbean and northern South America in the mantle reference frame: An update. In: James, K.H., Lorente, M.A. & Pindell, J.L. (editors), The origin and evolution of the Caribbean Plate. Geological Society of London, Special Publication 328, p. 1–55. https://doi.org/10.1144/SP328.1

Piraquive, A. 2017. Structural framework, deformation and exhumation of the Santa Marta Schists: Accretion and deformational history of a Caribbean Terrane at the north of the Sierra Nevada de Santa Marta. Doctoral thesis, Université Grenoble Alpes & Universidad Nacional de Colombia, 393 p. Grenoble–Bogotá.

Pons, D. 1983. Ëtudes paléobotanique et palynologique de la Formation de Girón (Jurassique moyen–Crétacé Inférieur) dans la région de Lebrija, département de Santander, Colombie. Comptes Rendus, Congrès Sociétés Sevantes, 1(107): 53–78.

Pulido, O. & Gómez, L.S. 2001. Memoria explicativa: Geología de la plancha 266 Villavicencio. Scale 1:100 000. Ingeominas, 52 p. Bogotá.

Pulido, O., Ulloa, C. & Rodríguez, E. 1986. Relaciones estratigráficas entre el Jurásico y el Cretácico de la cordillera de Los Cobardes. Geología Colombiana, 15: 55–64.

Quandt, D., Trumbull, R.B., Altenberger, U., Cardona, A., Romer, R.L., Bayona, G., Ducea, M., Valencia, V., Vásquez, M., Cortés, E. & Guzmán, G. 2018. The geochemistry and geochronology of Early Jurassic igneous rocks from the Sierra Nevada de Santa Marta, NW Colombia, and tectono–magmatic implications. Journal of South American Earth Sciences, 86: 216–230. https://doi.org/10.1016/j.jsames.2018.06.019

Rabe, E. 1977. Zur Stratigraphie des Ostandinen Raumes von Kolumbien I: Die Abfolge Devon bis Perm der Ost–Kordillere Nördlich von Bucaramanga, II: Conodonten des jünqeren Palazoikums der Ost–Kordillere Sierra Nevada de Santa Marta und der Sierra de Perijá. Giessner Geologishe Schriften, 11: 1–95.

Ramos, V.A. 2008. The basement of the central Andes: The Arequipa and related terranes. Annual Review of Earth and Planetary Sciences, 36: 289–324. https://doi.org/10.1146/annurev.earth.36.031207.124304

Ramos, V.A. & Aleman, A. 2000. Tectonic evolution of the Andes. In: Cordani, U.G., Milani, E.J., Thomaz–Filha, A. & Campos, D.A. (editors), Tectonic evolution of South America. 31st International Geological Congress. Proceedings, p. 635–685. Rio de Janeiro, Brazil.

Remy, W., Remy, R., Pfefferkorn, H.W., Volkheimer, W. & Rabe, E. 1975. Neueinstufung der Bocas–Folge (Bucaramanga, Kolumbien) in den unteren Jura anhand einer Phlebopteris–branneri– und Classopollis–Flora. Argumenta Palaeobotanica, (4): 55–77.

Rodríguez–García, G. 2018. Caracterización petrográfica, química y edad Ar–Ar de cuerpos porfídicos intrusivos en la Formación Saldaña. Boletín Geológico, (44): 5–23. https://doi.org/10.32685/0120-1425/boletingeo.44.2018.5

Rodríguez–García, G., Arango, M.I., Zapata, G. & Bermúdez, J.G. 2016. Catálogo de unidades litoestratigráficas de Colombia: Formación Saldaña. Servicio Geológico Colombiano. 91 p. Medellín.

Rodríguez, G., Zapata, G., Correa–Martínez, A.M. & Arango, M.I. 2017. Caracterización petrográfica, química y geocronológica del magmatismo Triásico–Jurásico del macizo de Santander–Colombia. XVI Congreso Colombiano de Geología–III Simposio de Exploradores. Memoirs, p. 1430–1433. Santa Marta.

Rodríguez, G., Arango, M.I., Zapata, G. & Bermúdez, J.G. 2018. Petrotectonic characteristics, geochemistry, and U–Pb geochronology of Jurassic plutons in the Upper Magdalena Valley–Colombia: Implications on the evolution of magmatic arcs in the NW Andes. Journal of South American Earth Sciences, 81: 10–30. https://doi.org/10.1016/j.jsames.2017.10.012

Rodríguez–García, G., Correa–Martínez, A.M., Zapata–García, G., Arango–Mejía, M.I., Obando–Erazo, G., Zapata–Villada, J.P. & Bermúdez, J.G. 2020. Diverse Jurassic magmatic arcs of the Colombian Andes: Constraints from petrography, geochronology, and geochemistry. In: Gómez, J. & Pinilla–Pachon, A.O. (editors), The Geology of Colombia, Volume 2 Mesozoic. Servicio Geológico Colombiano, Publicaciones Geológicas Especiales 36, p. 117–170. Bogotá. https://doi.org/10.32685/pub.esp.36.2019.04

Rodríguez, M.A., Rodríguez–García, G. & Viana, R.L. 1995. Contribución al conocimiento de la estratigrafía de las rocas sedimentarias de Monte Frío (Jurásico Inferior, Valle Superior del Magdalena, Colombia). Geología Colombiana, 19: 45–57.

Rollins, J.F. 1960. Stratigraphy and structure of the Goajira Peninsula: Northwestern Venezuela and northeastern Colombia. Doctoral thesis, University of Nebraska, 102 p. Lincoln, USA.

Rolon, L. 2004. Structural geometry of the Jura–Cretaceus rift of the Middle Magdalena Valley Basin–Colombia. Master thesis, West Virginia University, 63 p. Morgantown, WV, USA.

Romeuf, N., Münch, P., Soler, P., Jaillard, É., Pik, R. & Aguirre, L. 1997. Mise en évidence de deux lignées magmatiques dans le volcanisme du Jurassique inférieur de la zone subandine équatorienne. Comptes–Rendus de l´Académie des Sciences, Série 2a, 324: 361–368.

Rosas, S., Fontboté, L. & Tankard, A. 2007. Tectonic evolution and paleogeography of the Mesozoic Pucará Basin, central Peru. Journal of South American Earth Sciences, 24(1): 1–24. https://doi.org/10.1016/j.jsames.2007.03.002

Royero, J.M. & Clavijo, J. 2001. Memoria explicativa: Mapa geológico generalizado departamento de Santander. Scale 1:400 000. Ingeominas, 91 p. Bogotá.

Salazar, E. 2010. Análisis estratigráfico y determinación de ambientes de depósito para la Formación Palanz: Inicio de la sedimentación cretácica en la Alta Guajira, Colombia. Master thesis, Universidad Nacional de Colombia, 137 p. Bogotá.

Salazar–Tomey, B.A. 2006. Evolución estructural e implicaciones tectónicas del graben de Espino. Master thesis, Universidad Simón Bolívar, 197 p. Caracas.

Sarmiento, G., Puentes, J. & Sierra, C. 2015. Evolución geológica y estratigrafía del sector norte del Valle Medio del Magdalena. Geología Norandina, (12): 51–82.

Sarmiento–Rojas, L.F., van Wess, J.D. & Cloetingh, S. 2006. Mesozoic transtensional basin history of the Eastern Cordillera, Colombian Andes: Inferences from tectonic models. Journal of South American Earth Sciences, 21(4): 383–411. https://doi.org/10.1016/j.jsames.2006.07.003

Saylor, J.E., Horton, B.K., Nie, J., Corredor, J. & Mora, A. 2011. Evaluating foreland basin partitioning in the northern Andes using Cenozoic fill of the Floresta Basin, Eastern Cordillera, Colombia. Basin Research, 23(4): 377–402. https://doi.org/10.1111/j.1365-2117.2010.00493.x

Spikings, R., Cochrane, R., Villagómez, D., van der Lelij, R., Vallejo, C., Winkler, W. & Beate, B. 2015. The geological history of northwestern South America: From Pangaea to the early collision of the Caribbean Large Igneous Province (290–75 Ma). Gondwana Research, 27(1): 95–139. https://doi.org/10.1016/j.gr.2014.06.004

Suárez, C. A & Díaz, A. F., 2016. Estudio petrográfico y estratigráfico de la Formación Jordán en su localidad tipo sobre el escarpe sur de la Mesa de Los Santos y cañón del río Chicamocha, Santander. Bachelor thesis, Universidad Industrial de Santander, 117 p. Bucaramanga.

Torsvik, T.H. & Cocks, L.R.M. 2016. Earth history and palaeogeography. Cambridge University Press, 332 p. Cambridge. https://doi.org/10.1017/9781316225523

Toussaint, J.F. 1995. Evolución geológica de Colombia: 2 Triásico–Jurásico. Universidad Nacional de Colombia, 94 p. Medellín.

Tschanz, C.M., Jimeno, A. & Cruz, J. 1969. Geology of the Sierra Nevada de Santa Marta area (Colombia): Preliminary report. Ingeominas, 288 p. Bogotá.

Tschanz, C.M., Marvin, R.F., Cruz, J., Mehnert, H.H. & Cebula, G.T. 1974. Geologic evolution of the Sierra Nevada de Santa Marta, northeastern Colombia. Geological Society of America Bulletin, 85(2): 273–284. https://doi.org/10.1130/0016-7606(1974)85<273:GEOTSN>2.0.CO;2

Ujueta, G. 1999. La cordillera Oriental colombiana no se desprende de la cordillera Central. Geología Colombiana, 24: 3–28.

Ulloa, C.E. & Rodríguez, E. 1976. Geología del cuadrángulo K–13 Tauramena. Boletín Geológico, 24(2): 3–30.

Ulloa, C., Rodríguez, E. & Rodríguez, G.I. 2003. Memoria explicativa: Geología de la plancha 172 Paz de Río. Scale 1:100 000. Ingeominas, 109 p. Bogotá.

Urbani, F. 1969. Primera localidad fosilífera del Miembro Zenda de la Formación Las Brisas: Cueva El Indio, La Guairita, estado Miranda. Asociación Venezolana de Geología, Minería y Petróleo. Boletín Informativo, 12(12): 447–453.

Urbani, F., Camposano, L.A., Mendi, D.J., Martínez, A. & González, A. 2008. Consideraciones geológicas y geoquímicas de la zona de Yumare, estados Falcón y Yaracuy, Venezuela. Boletín de la Academia de Ciencias Físicas, Matemáticas y Naturales, 68(2): 9–30.

UT G&H. 2015a. Memoria explicativa: Geología de la Plancha 284 Santana. Scale 1:100 000. Ingeominas, 93 p. Bogotá.

UT G&H. 2015b. Memoria explicativa: Geología de la Plancha 413 Florencia. Scale 1:100 000. Ingeominas, 126 p. Bogotá.

Valencia, V.A., Cardona, A., Ibañez–Mejia, M., Bayona, G., Lotero, A. & Villafañez, Y. 2011. Pre–Cretaceous record of the Santander Massif, northeastern Colombian Andes: Insights from

U–Pb zircon LA–ICP–MS. XIV Congreso Latinoamericano de Geología–XIII Congreso Colombiano de Geología. Memoirs, p. 322–323. Medellín.

van der Lelij, R., Spikings, R., Ulianov, A., Chiaradia, M. & Mora, A. 2016. Palaeozoic to Early Jurassic history of the northwestern corner of Gondwana, and implications for the evolution of the Iapetus, Rheic and Pacific Oceans. Gondwana Research, 31: 271–294. https://doi.org/10.1016/j.gr.2015.01.011

Vargas, R., Arias, A., Jaramillo, L. & Téllez, N. 1981. Memoria explicativa: Geología de las planchas 136 Málaga y 152 Soatá, Cuandrángulo I–13. Boletín Geológico, 24(3): 76 p.

Vásquez, M., Bayona, G. & Romer, R.L. 2006. Geochemistry of Jurassic volcanic rocks of the northern Andes: Insights for the Mesozoic evolution of northwestern Gondwana. In: Especiales, A.P. Meetings, G.S. (editors), Backbone of Americas–Patagonia to Alaska, p. 62. Mendoza, Argentina.

Villagómez, D., Spikings, R., Magna, T., Kammer, A., Winkler, W. & Beltrán, A. 2011. Geochronology, geochemistry and tectonic evolution of the Western and Central Cordilleras of Colombia. Lithos, 125(3–4): 875–896. https://doi.org/10.1016/j.lithos.2011.05.003

Villamor, P., Berryman, K.R., Ellis, S.M., Schreurs, G., Wallace, L.M., Leonard, G.S., Langridge, R.M. & Ries, W.F. 2017. Rapid evolution of subduction–related continental intraarc rifts: The Taupo Rift, New Zealand. Tectonics, 36(10): 2250–2272. https://doi.org/10.1002/2017TC004715

Ward, D.E., Goldsmith, R., Cruz, J. & Restrepo, H. 1973. Geología de los cuadrángulos H–12 Bucaramanga y H–13 Pamplona, Departamento de Santander. Boletín Geológico, 21(1–3): 132 p.

Wolaver, B.D., Coogan, J.C., Horton, B.K., Suarez–Bermúdez, L., Sun, A.Y., Wawrzyniec, T.F., Zhang, T., Shanahan, T.M., Dunlap, D.B., Costley, R.A. & de la Rocha, L. 2015. Structural and hydrogeologic evolution of the Putumayo Basin and adjacent fold–thrust belt, Colombia. American Association of Petroleum Geologists Bulletin, 99(10): 1893–1927. https://doi.org/10.1306/05121514186

Wolcott, P.P. 1943. Fossils from metamorphic rocks of Coast Range of Venezuela: Geological notes. American Association of Petroleum Geologists Bulletin, 27(12): p. 1632.

Zapata–García, G., Rodríguez–García, G. & Arango–Mejía, M.I. 2017. Petrografía, geoquímica y geocronología de rocas metamórficas aflorantes en San Francisco Putumayo y la vía Palermo–San Luis asociadas a los complejos La Cocha–río Téllez y Aleluya. Boletín de Ciencias de la Tierra, (41): 48–65.

Zapata, S., Cardona, A., Jaramillo, C., Valencia, V. & Vervoort, J. 2016. U–Pb LA–ICP–MS geochronology and geochemistry of Jurassic volcanic and plutonic rocks from the Putumayo region (southern Colombia): Tectonic setting and regional correlations. Boletín de Geología, 38(2): 21–38. https://doi.org/10.18273/revbol.v38n2-2016001

Zuluaga, C.A., Ochoa–Yarza, A., Muñoz, C.A., Guerrero, N.M., Martínez, A.M., Medina, P.A., Pinilla, A., Ríos, P.A., Rodríguez, B.P., Salazar, E.A. & Zapata, V.L. 2009. Memoria de las planchas 2, 3, 5 y 6 (con parte de las planchas 4, 10 y 10Bis). Proyecto de investigación: Cartografía e historia geológica de la Alta Guajira. Ingeominas, 564 p. Bogotá.

Zuluaga, C.A., Pinilla, A. & Mann, P. 2015. Jurassic silicic volcanism and associated continental–arc basin in northwestern Colombia (southern boundary of the Caribbean Plate). In: Bartolini, C. & Mann, P. (editors), Petroleum geology and potential of the Colombian Caribbean margin. American Association of Petroleum Geologists, Memoir 108, p. 137–159. https://doi.org/10.1306/13531934M1083640

Zuluaga, C.A., Amaya, S., Urueña, C. & Bernet, M. 2017. Migmatization and low–pressure overprinting metamorphism as record of two pre–Cretaceous tectonic episodes in the Santander Massif of the Andean basement in northern Colombia (NW South America). Lithos, 274–275: 123–146. https://doi.org/10.1016/j.lithos.2016.12.036

Explanation of Acronyms, Abbreviations, and Symbols:

HREE	Heavy rare earth element	REE	Rare earth element
LREE	Light rare earth element	SGC	Servicio Geológico Colombiano

Authors' Biographical Notes

Germán BAYONA is a geologist with a BS from the Universidad Nacional de Colombia (1992), MS from New Mexico State University (1998), and PhD from the University of Kentucky (2003). His research interests include understanding the relationship between mountain–building and basin–filling processes in tropical settings; the stratigraphy and petrology of sedimentary and volcanic systems; the influence of basement structures in sedimentary–basin evolution, thrust–belt geometry and kinematics; and paleomagnetism applied to tectonic, structural and stratigraphic analyses.

Camilo BUSTAMANTE obtained his degree in geology in 2007 (Universidad EAFIT) and PhD in mineralogy and petrology in 2016 (Universidade de Sao Paulo). He is currently a professor of igneous petrology at the Universidad EAFIT in Colombia. His main research areas are the tectono–magmatic and metamorphic evolution of the northern Andes.

Giovanny NOVA received his BS degree in geology in 2009 from the Universidad Nacional de Colombia. He earned an MS degree in Earth Sciences in 2016 from the Universidad Nacional Autonoma de Mexico, UNAM. His main research interests include understanding the tectonic evolution of sedimentary basins with analytical techniques such as paleomagnetism, detrital geochronology and sedimentary petrology.

Ana Milena SALAZAR–FRANCO received her BS degree in geology in 2014 from the Universidad de Caldas (Manizales, Colombia). Her main research interests are basin analysis and the sedimentology of carbonate rocks.

Volume 2

Chapter 6

140 Million Years of Tropical Biome Evolution

https://doi.org/10.32685/pub.esp.36.2019.06
Published online 3 October 2019

Carlos JARAMILLO[1]*

1 jaramilloc@si.edu
Smithsonian Tropical Research Institute
Apartado 0843–03092, Balboa, Ancón, Panamá
Panamá

Institut des sciences de l'évolution,
Montpellier, France

* Corresponding author

Abstract The origin and development of Neotropical biomes are central to our understanding of extant ecosystems and our ability to predict their future. During the Cretaceous, biomass of tropical rainforests was mostly dominated by gymnosperms and ferns, forest structure was poorly stratified and the canopy was open and dominated by gymnosperms. Extant tropical rainforests first developed at the onset of the Cenozoic, as a result of the massive extinction of the Cretaceous – Paleocene boundary. Paleocene rainforests were multistratified, with an angiosperm–dominated canopy that had high photosynthetic potential. Tropical climate has followed global patterns of warmings and coolings during the last 60 Ma. Rainforest diversity has increased during the warmings while it has decreased during coolings. Several extant biomes, including páramos, cloud forest, savannas, and dry/xerophytic forest, have increase significantly during the late Neogene at the expense of the reduction of the rainforest. Timing and drivers of these changes are still unknown but seem to be related to the onset of our modern, cool–state climate since the onset of the Pleistocene, 2.6 Ma ago.

Keywords: *Neotropical biomes, tropical rainforest, gymnosperms, angiosperms, evolution.*

Resumen El origen y el desarrollo de los biomas neotropicales son fundamentales para nuestra comprensión de los ecosistemas actuales y nuestra capacidad para predecir su futuro. Durante el Cretácico, la biomasa de los bosques tropicales estaba dominada principalmente por gimnospermas y helechos, la estructura del bosque no poseía una estratificación marcada y el dosel era abierto y dominado por gimnospermas. Los bosques tropicales actuales se desarrollaron por primera vez al inicio del Cenozoico, como resultado de la extinción masiva del límite Cretácico–Paleoceno. Los bosques tropicales del Paleoceno eran multiestratificados, con un dosel dominado por angiospermas con alto potencial fotosintético. El clima tropical ha seguido patrones globales de calentamiento y enfriamiento durante los últimos 60 Ma. La diversidad del bosque tropical ha aumentado durante los calentamientos y disminuido durante los enfriamientos. Varios biomas que hoy existen, incluyendo páramos, bosques nubosos, sabanas y bosques secos/xerofíticos, han crecido significativamente desde el Neógeno tardío en áreas ocupadas previamente por el bosque tropical. Las causas y temporalidad de este cambio masivo en el paisaje aún se desconocen, pero parecen estar relacionadas con el inicio de nuestro clima frío moderno desde el comienzo del Pleistoceno, hace 2,6 Ma.

Palabras clave: *biomas neotropicales, bosque tropical, gimnospermas, angiospermas, evolución.*

Citation: Jaramillo, C. 2019. 140 million years of tropical biome evolution. In: Gómez, J. & Pinilla–Pachon, A.O. (editors), The Geology of Colombia, Volume 2 Mesozoic. Servicio Geológico Colombiano, Publicaciones Geológicas Especiales 36, p. 209–236. Bogotá. https://doi.org/10.32685/pub.esp.36.2019.06

1. Introduction

The biota that occupies tropical landscapes is anything but stable. Over geological time, forests have transformed into deserts and vice versa. Entire mountain chains are created while others are weathered away. What are the main drivers of tropical landscape change? How do geology and climate interact with each other to transform plant and animal communities? And how does the biota, in turn, affect its landscape, the climate, and ultimately our survival?

We are studying a number of dramatic landscape changes that have occurred in the tropics over the past 140 million years and how they have influenced the extinction and origination of tropical biotas: From the extreme effects of global warming during the early Cenozoic 50 million years ago to the global cooling of the Pleistocene 2.6 million years ago; from the lifting of the Andes mountains to the creation of savannas; from periods with low levels of CO_2 to events with extremely high CO_2, similar to the levels that we will reach by the end of the century.

The most extensive biome within the Neotropics is the lowland tropical rainforest. It has the largest number of plant species on Earth, about 90 000, most of them (~96%) angiosperms (Thomas, 1999). Many hypotheses have been proposed to explain why it is so diverse, how it originated, and how its diversity is maintained (Connell, 1971; Fine & Ree, 2006; Gaston, 2000; Gillett, 1962; Hoorn et al., 2010; Jablonski, 1993; Janzen, 1970; Kreft & Jetz, 2007; Leigh et al., 2004; Leighton, 2005; Moritz et al., 2000); these are well summarized by Leigh et al., 2004. There are hypotheses that consider the key factor to be the low rates of extinction and/or high rates of origination in the tropics over millions of years while other consider the high diversity to be developed during the last 2.6 Ma during the Quaternary period driven by habitat fragmentation (Haffer, 1969). The problem to solve is not only how the tropics generate more species than other regions but also how that diversity is maintained (Leigh et al., 2004). Moreover, not only do tropical forests have high diversity, but they also have a unique, multistratified forest structure. When did this structure originate? What were its effects, if any, on the water cycle, nutrients, and carbon at a local, regional, or global level? (Boyce & Lee, 2010; Burnham & Graham, 1999; Burnham & Johnson, 2004). Such questions have puzzled scientists for more than a century but still remain unanswered, yet they are critical to understanding how tropical biomes will respond to our ongoing climate change.

Extant Neotropical rainforests are dominated mostly by angiosperms (flowering plants). A natural starting point to unravel the evolution of extant biomes, therefore, is the time of angiosperm origination, which occurred during the Early Cretaceous, ca. 145 Ma ago (Sun et al., 2002). The history of extant Neotropical biomes comprises a total transformation of how the landscape is occupied, from a forest with no angiosperms at the onset of the Cretaceous to the extant forest fully dominated by them. This change is far more substantial than for temperate forests, many of which are still dominated by gymnosperms as they were at the onset of the Cretaceous.

There always have been forests in tropical latitudes, therefore, it is important to define what I mean by a Neotropical rainforest, as this term has various meanings. Here I follow the definition of Burnham & Johnson (2004) and Jaramillo & Cárdenas (2013), which refers to a forest defined by the combination of four parameters: climate, floristic composition, vegetation structure, and plant physiognomy. Accordingly, a Neotropical rainforest is a lowland forest, with high mean annual precipitation (>1.8 m/y), high mean annual temperature (>18 °C), low temperature seasonality (< 7 °C), and dominance–in diversity and abundance–by 11 families of angiosperms: Leguminosae, Moraceae, Annonaceae, Euphorbiaceae, Lauraceae, Sapotaceae, Myristicaceae, and Palmae represent ~50% of the diversity, whereas Leguminosae, Palmae, Rubiaceae, Violaceae, Euphorbiaceae, Meliaceae, Sapotaceae y Moraceae represent ~57% of all trees and shrubs. The forest is multistratified, with lianas and epiphytes and a closed canopy that is dominated by angiosperms. A high proportion of species have large leaves >4500 mm^2 (mesophylls), entire (smooth) margins, and drip–tips; the density of leaf venation has a bimodal distribution, with low density in the understory and high density in the canopy.

The development of Neotropical terrestrial communities can be divided into two major phases, Cretaceous and Cenozoic. During the Cretaceous, angiosperms originated and had a massive radiation (Crane & Lidgard, 1989; Magallón & Castillo, 2009; Magallón et al., 1999), terrestrial vertebrate communities were dominated by Dinosauria, CO_2 concentrations were high (>1000 ppm) (Royer, 2010; Royer et al., 2012), and by the middle Cretaceous, high mean annual temperatures were ~7 °C above modern values (Jaramillo & Cárdenas, 2013). In contrast, the Cenozoic is characterized by a complete dominance of angiosperms (Graham, 2010, 2011), massive radiations of mammals that expanded into a variety of habitats (Gingerich, 2006; Simpson, 1983), and the transition from a warm–mode climate to the pre–industrial cool–mode climate (Royer, 2016; Royer et al., 2012; Zachos et al., 2001).

2. Cretaceous

The oldest records of angiosperms in both high and low latitudes is Barremian (ca. 130 Ma); the fossil pollen *Clavatipollenites* has a worldwide distribution including Israel, England, equatorial Africa, and Argentina (Archangelsky & Taylor, 1993; Brenner, 1974; Doyle et al., 1977; Gübeli et al., 1984; Kemp, 1968) and *Walkeripollis*, a pollen that belongs to Winteraceae, is found in equatorial Africa (Doyle et al., 1990). The oldest records of megafossils (leaves, flowers, fruits) are *Archeofructus*

and *Leefructus* from the Aptian (ca. 122 Ma) of China (Sun & Dilcher, 2002; Sun et al., 2002, 2011). The first angiosperms were small, with reduced flowers and small seed size; they were opportunistic, early successional colonizers, probably living in aquatic habitats or near water bodies that were often submitted to disturbance (Doyle, 2012; Friis et al., 2015; Sun et al., 2002). A global meta–analysis of the Cretaceous paleobotanical record (Crane & Lidgard, 1989, 1990) showed that angiosperms gradually increased their diversity and abundance throughout the Cretaceous, and by the Maastrichtian, they surpassed other plant groups in diversity, including cycadophytes, pteridophytes (ferns), and Coniferales. This global analysis, however, lacked tropical megafossils and had very few sites with quantitative palynological data (Mejía–Velásquez, 2007). Thus, patterns of dominance, diversification, and distribution of forests within tropical zones during the Cretaceous still remain very unclear.

DNA–based phylogenies show a Jurassic (183 Ma) angiosperm origin (Bell et al., 2010; Wikström et al., 2001), and a rapid radiation of the major angiosperm orders during the Cenomanian (ca. 100–90 Ma) (Moore et al., 2010; Wang et al., 2009). Other genetic studies have shown that by the Cretaceous even many of the extant angiosperm families were already present (Bell et al., 2010; Davis et al., 2005). These phylogenies, however, are in stark contrast with the fossil record, which lacks angiosperms in pre–Cretaceous strata (Herendeen et al., 2017). It has been proposed that the molecular and fossil records can be reconciled if Jurassic angiosperms were restricted to the understory of rainforest habitats and did not radiate until the Cretaceous (Doyle, 2012). In contrast, some have suggested that heterogeneous rates of molecular evolution could push divergence ages in DNA–based analysis to appear much older than they truly are (Beaulieu et al., 2015). There is still a large disparity that needs to be solved, underscoring the importance of plant fossil data from tropical latitudes during the earliest Cretaceous and Jurassic.

The disparity between DNA and fossils also exists in the genesis of the rainforest structure. Molecular studies have suggested that Cenomanian tropical forests were already dominated by angiosperms (Wang et al., 2009) and were similar in structure to extant forests (Davis et al., 2005). However, the fossil record of the Cretaceous suggests otherwise. Multiple lines of evidence indicate that angiosperms did not dominate the biomass of most Cretaceous forests (Wing & Boucher, 1998). Angiosperm fossil wood is scarce compared to gymnosperm wood, indicating that most angiosperms did not occupy the canopy. Most angiosperms seeds were small (Wing & Boucher, 1998), indicating that the canopy was not closed, in contrast to modern multistratified forests where there is a large variance in seed size, a byproduct of the intense competition for light in a closed–canopy environment (Muller–Landau, 2010). Leaf venation density was much lower than in extant forests (Feild et al., 2011a), and even during the Maastrichtian leaf density venation did not follow the pattern found in extant angiosperm–dominated forests (Crifò et al., 2014), suggesting the absence of a multistratified forest with a canopy dominated by angiosperms where the competition for light is intense. The fossil record of lianas, mainly Menispermaceae and Bignoniaceae, is very scarce, whereas it is abundant during the Cenozoic (Burnham, 2009; Doria et al., 2008; Jacques et al., 2011). In summary, angiosperms, although already diverse, did not dominate the forest biomass during the Cretaceous, neither in Neotropical nor in temperate regions.

One of the oldest Cretaceous records in tropical latitudes is the fossil flora of San Felix (Hauterivian, ca. 135 Ma), in Caldas, Colombia (González et al., 1977; Lemoigne, 1984) (Figure 1). Although it contains angiosperms, it has an abundance of Benettitales, ferns, Cycadales, and a few conifers (González et al., 1977; Lemoigne, 1984; Sucerquia & Jaramillo, 2008). Leaf morphology of the San Felix flora differs greatly from extant tropical leaves by having a much smaller leaf area and a lower leaf vein density (Feild et al., 2011a), indicating a lower photosynthetic capacity and therefore lower rates of biomass production. The Barremian – Aptian flora of Villa de Leyva (Figure 1), found in marine deposits, is composed mainly of ferns and cones of Cycadales and conifers (mainly Cupressioidae and Araucariaceae), which probably floated into the epicontinental Cretaceous seas. Many of these taxa are related to southern Gondwana clades (Huertas, 2003; van Waveren et al., 2002). Palynofloras from the Upper Magdalena Basin and the Llanos Foothills during the Albian – Aptian were dominated by pteridophytes and gymnosperms (mainly *Araucariacites*, cycads, and *Classopollis*), while angiosperm diversity was very low, an average of 3.7% per sample in the Aptian and 3.3% in the Albian. Abundance was also low (7.2% for the Aptian, 5.3% for the Albian) (Mejía–Velásquez, 2007; Mejía–Velásquez et al., 2012) (Figure 1). The abundance of humidity indicators was higher than that of aridity indicators (61% versus 10%) (Mejía–Velásquez et al., 2012), suggesting that northwestern Gondwana had humid climates during the Aptian – Albian contrary to the widespread aridity that had been assumed for the tropical belt (Herngreen et al., 1996). Furthermore, there was an inverted latitudinal diversity gradient during the Albian—the tropics had fewer species than the temperate regions even though the rate of floristic turnover was higher (Mejía–Velásquez et al., 2012). Perhaps the modern steep latitudinal diversity gradient is an intrinsic angiosperm property.

During the Cenomanian, the low dominance of angiosperms continued and a group of gymnosperms, Gnetales, significantly increased its diversity and abundance (Herngreen & Dueñas, 1990; Herngreen et al., 1996), although the high abundance and diversity of ferns still continued, suggesting that humid conditions in northwestern Gondwana prevailed, in agreement with some hydrological models (Ufnar et al., 2002, 2004, 2008). Angiosperm pollen morphology became more variable, sim-

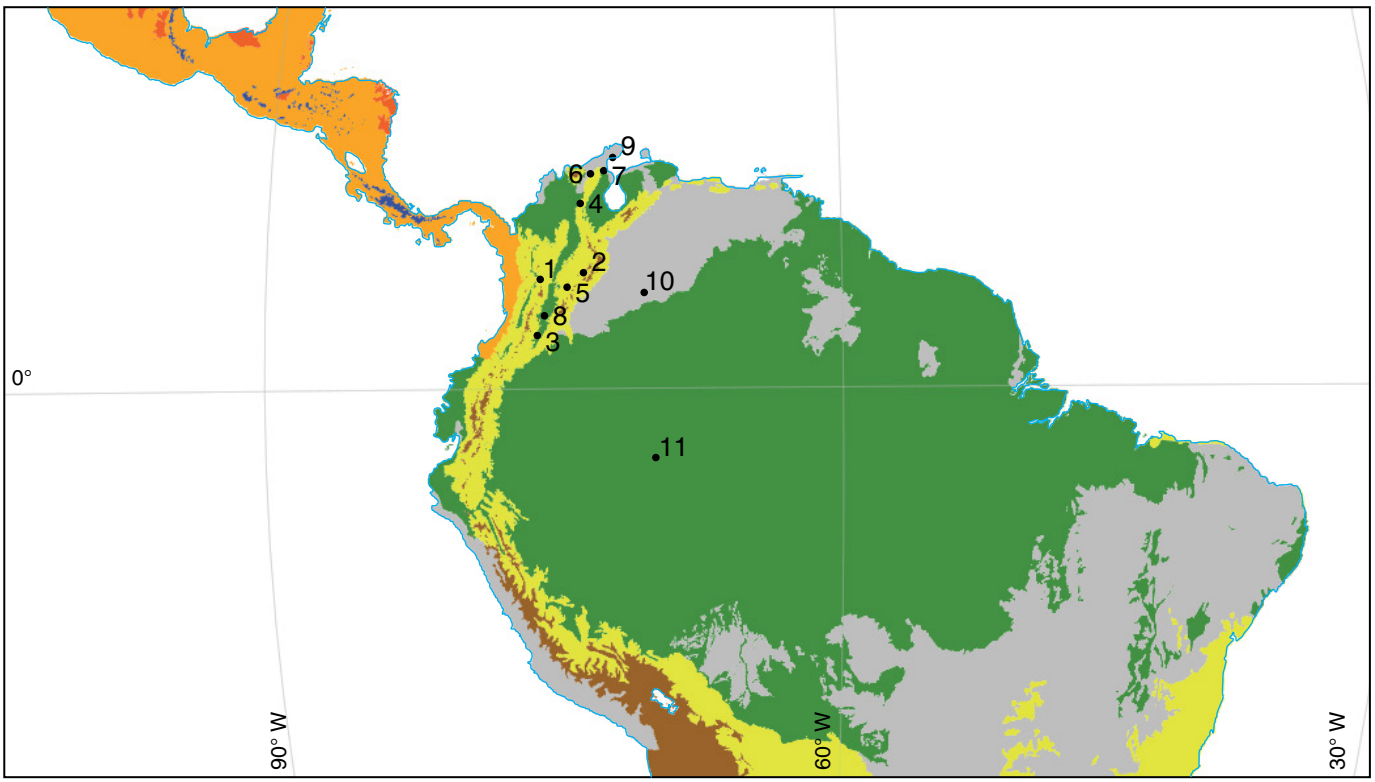

Figure 1. Extant terrestrial biomes of Colombia following the classification given in Figure 2. Biomes distribution was derived from the WWF global ecoregion map (Olson et al., 2001). Sites described in the manuscript include: **(1)** San Felix, **(2)** Villa de Leyva, **(3)** Upper Magdalena Valley (Mejía–Velásquez et al., 2012), **(4)** Cretaceous/Paleocene (De la Parra, 2009), **(5)** Guaduas (Martínez et al., 2015), **(6)** Cerrejón, **(7)** PETM (Jaramillo et al., 2010b), **(8)** Villavieja, **(9)** Ware, **(10)** Llanos, and **(11)** 105–AM (Jaramillo et al., 2017b).

ilar to the pattern seen in North America (Doyle & Hickey, 1976; Lupia et al., 1999), although it still needs to be properly quantified. No Cenomanian tropical macrofloras have been discovered, and they are highly needed as this is a critical time for angiosperm evolution.

Peak temperatures of the last 140 Ma occurred during the Cenomanian – Turonian transition (Bice et al., 2006), when the tropics were 7 °C warmer than modern values (Jaramillo & Cárdenas, 2013) and CO_2 levels were >1000 ppm (Royer, 2006). Eustatic sea level also reached the maximum levels of the past 140 Ma, producing epicontinental seas as extensive continental areas were flooded (Haq et al., 1988; Miller et al., 2005). By the early Turonian, the abundance and diversity of Gnetales in the Neotropics had greatly diminished, but it is still uncertain whether this reduction was gradual or abrupt.

The Late Cretaceous (90–66 Ma) is characterized by a gradual reduction of global temperatures together with a reduction of CO_2 levels, but information about tropical forests during most of this period is scarce. During the Maastrichtian (70–66 Ma), sea level started to drop rapidly and extensive coastal plains covered with forests developed (Nichols & Johnson, 2008). The Maastrichtian paleoflora of the Guaduas (Figure 1) and Umir Formations indicates a co–dominance of angiosperms, cycads, gymnosperms (Araucariaceae), and pteridophytes (ferns). The palynological record indicates that the angiosperms and ferns co–dominated, with angiosperms representing ~50% of assemblages (De la Parra et al., 2008a, 2008b), a pattern that is also seen in the Oleanane/Opane biomarker record (Rangel et al., 2002). Although several angiosperm families had been present here, including Palmae, Annonaceae, Lauraceae, Piperaceas, Rhamnacea, many others had uncertain affinities (Correa et al., 2010; García, 1958; Gutiérrez & Jaramillo, 2007; Martínez et al., 2015; Sarmiento, 1992; Sole de Porta, 1971). Most Maastrichtian fossil seeds are small, and Menispermaceae and Bignoniacea, families with high abundance of lianas, are missing. Overall, Guaduas still does not correspond to a Neotropical forest floristically. Guaduas leaf venation density also does not show the bimodal distribution of extant forests, suggesting that the canopy was not fully closed yet (Crifò et al., 2014), although it had already large leaves with entire margins and drip–tips similar to extant forests (Feild et al., 2011a). Neotropical Maastrichtian forests follow the same pattern as coetaneous forests from Nebraska, where angiosperms were the dominant element in floodplains, similar to the environment of the Guaduas deposits, but gymnosperms and ferns dominated in all other habitats (Wing et al., 1993). Angiosperms were mostly herbaceous and had only a 12% of the dominance overall (Wing et al., 1993).

Both forest composition and structure changed radically following the impact of a meteorite in the Yucatán peninsula and the associated climatic events (Nichols & Johnson, 2008; Schulte et al., 2010). The Colombian palynological record indicates a 75% plant extinction of late Maastrichtian taxa (De la Parra, 2009) (Figure 1), an extinction level higher than in North America, where the palynological extinction levels reached ~30% (Hotton, 2002). By the Paleocene, as we will see next, the flora already resembled that of extant forests.

This floristic change could have had climatic consequences as well. Nowadays, a large component of the precipitation over Amazonia is produced by forest evapotranspiration (Wright et al., 2017), driven by the high photosynthetic capacity of angiosperms, much higher than gymnosperms (Boyce & Lee, 2010). Angiosperm venation density in the Cretaceous is generally low, and not much higher than gymnosperms (Feild et al., 2011a, 2011b), but at the onset of the Cenozoic, leaf vein density increases considerably to levels similar to extant forest (Crifò et al., 2014; Feild et al., 2011a). Experiments of climate sensitivity have shown that replacing an angiosperm forest with a conifer forest in Amazonia generates higher mean annual temperatures (3 °C), a 30% drop in annual precipitation, and an increase in the length of the dry season by two months, changes that are mostly due to the lower venation density of gymnosperms and associated lower photosynthetic and evapotranspiration rates (Boyce & Lee, 2010). This suggests that the change in landscape occupancy at the Cretaceous – Cenozoic transition, from a forest dominated by conifers and ferns to one of angiosperm dominance, transformed the tropical climate to being more humid, less warm, and less seasonal.

Why was angiosperm success and radiation in the Cretaceous so closely associated with disturbed and flooded environments? That is still an unsolved question. One hypothesis suggests that the time needed to generate the pollen tube, a critical step in seed production, is part of the answer. While the pollen tube in gymnosperms takes a long time to be generated, over a year in some cases, angiosperms produce it much faster, even in less than two hours (Williams, 2008). Angiosperms therefore might have been able to produce more seeds at a faster rate than gymnosperms, and this could have been an advantage in flooded and disturbed ecosystems, where the landscape is often changing and plants must grow fast and produce seeds quickly before the next flooding event occurs.

Overall, the fossil record suggests that Neotropical Cretaceous forests lacked multistratification and canopy was open and dominated by gymnosperms. Most angiosperms were shrubs or small plants, ruderals, dominating both floodplains and forest gaps but not most of the landscape. A historical accident, a meteorite collision, permanently changed the structure and composition of the tropical forests, thus delaying the ecological success of the angiosperms following their origination during the Early Cretaceous by 55 my.

3. Paleogene

Neotropical floras of the Paleocene were already dominated by angiosperms (~80% of palynoflora) (De la Parra, 2009; Doubinger, 1973; Jaramillo et al., 2006, 2007; Pardo–Trujillo, 2004; Pardo–Trujillo & Jaramillo, 2002; Pardo–Trujillo et al., 2003; van der Hammen, 1958), as is also indicated by biomarkers (Rangel et al., 2002), a foliar physiognomy typical of tropical forests (entire margins, large leaves, and drip–tips) (Wing et al., 2009), and a floristic composition similar to modern Neotropical forests including Fabaceae, Moraceae, Annonaceae, Euphorbiaceae, Lauraceae, Sapotaceae, Arecaceae, Araceae, Flacourtiaceae, Anacardaceae, Tiliaceae, and Meliaceae (Carvalho et al., 2011; Doria et al., 2008; Gómez–Navarro et al., 2009; Herrera et al., 2008; Jaramillo et al., 2007, 2014a; Pons, 1988; Wing et al., 2009). Forests also have abundant Menispermaceae (Doria et al., 2008), a family rich with lianas; this, together with the bimodal distribution of leaf venation density (Crifò et al., 2014; Feild et al., 2011a) and a high variance in seed size reaching up to 20 cm (Gómez–Navarro et al., 2009; Herrera et al., 2011, 2014b; Stull et al., 2012), indicates that the Paleocene forests were competing for light and the canopy was closed and dominated by angiosperms, characteristics of a multistratified forest. The high abundance of Fabaceae in the Paleocene, the most abundant family of trees/shrubs in all extant tropical forests (Ricklefs & Renner, 2012) but absent from the Cretaceous record, also indicates a profound transformation of the forest across the Cretaceous – Paleocene boundary. There are also aquatic ferns including *Salvinia* (Pérez–Consuegra et al., 2017). This large body of information about Paleocene forests comes mainly from the fossil record of the Cerrejón Formation gathered at the Cerrejón Coal mine (Figure 1), the largest open–pit coal mine in the world, which offers large–scale exposures (Jaramillo et al., 2014a). The fauna indicates a productive ecosystem: freshwater turtles up to 2 m long and related to the charapas of the Orinoco Basin; several species of crocodiles, mostly Dyrosauridae, some reaching 12–15 m; snakes related to boas reaching 13–15 m in length and 1 m in diameter; 2–m–long lungfishes; and several mollusks (Bayona et al., 2011; Cadena & Jaramillo, 2006; Cadena & Schweitzer, 2014; Cadena et al., 2012a, 2012c; Hastings et al., 2010, 2011, 2014; Head et al., 2009a, 2009b). In 16 years of exploration, no mammals have been found, suggesting that they were scarce. The Cerrejón deposits represent the oldest multistratified tropical forest known, similar to extant rainforests but with two marked differences. First, the mean annual temperature was ~1.5–2 °C higher than in extant forests and CO_2 was almost double (~500 ppm) (Royer, 2010). Mean annual temperature in Cerrejón and nearby areas has been estimated at ~29 °C using a variety of techniques including TEX_{86} (Jaramillo et al., 2010b), leaf margin analysis (Peppe et al., 2011; Wing et al., 2009), and snake paleothermometry (Head et al., 2009a, 2009b). The

second difference is a significantly lower plant diversity than in extant forests (Jaramillo et al., 2007; Wing et al., 2009), which is accompanied by a lower abundance of specialized herbivores (Carvalho et al., 2014; Wing et al., 2009). This difference could be explained by soil control, as the water table in Cerrejón probably was very high all year long. However, this low Paleocene diversity is observed in the palynological record throughout Colombia and Venezuela across a wide variety of depositional settings (Jaramillo, 2002; Jaramillo & Dilcher, 2000, 2001; Jaramillo et al., 2006, 2010b). An alternative hypothesis is that recovery following the K–Pg mass extinction was slow and took several million years to reach prior diversity levels, as has been observed in others mass extinctions (Erwin, 2008).

At the onset of the Eocene, a short–lived (ca. 200 ky) warming event known as the PETM (Paleocene Eocene Thermal Maximum) occurred (McInerney & Wing, 2011). Beginning ca. 56.3 Ma, temperature increased globally 5–7 °C over ca. 10 000–50 000 years (Frieling et al., 2017; Kennett & Stott, 1991; Westerhold et al., 2009; Zachos et al., 2003). The rapid and intense warming was produced by the addition to the atmosphere of ~10 000 Pg of carbon during a 50 ky interval, derived from volcanism in the North Sea (Gutjar et al., 2017); this input is roughly equivalent to adding 1300 ppm of CO_2 to a Paleocene atmosphere that had ~500 ppm of CO_2. The PETM is the most rapid addition of CO_2 to the atmosphere over the past 140 million years and produced a greenhouse effect similar to the warming we are currently experiencing but at a rate ten times slower than today (McInerney & Wing, 2011). It is estimated that by the year 2250, we will reach ~2000 ppm of CO_2. In other words, in just 400 years we will have increased CO_2 to the same levels that it took 50 000 years to reach following the onset of the PETM.

The PETM is a good analogue for understanding the consequences of our ongoing warming. The main process that can effectively remove CO_2 from the atmosphere is weathering of carbonates and silicates, but this is a process that operates at geological scales. During the PETM, it took ca. 180 000 years to return to previous levels (Bowen & Zachos, 2010). For our modern climate, and assuming that no more CO_2 is added, it would take geological time—thousands of years—to return to preindustrial values (Archer et al., 2009). After 1000 years, 25 to 60% of the injected CO_2 would still remain in the atmosphere (Archer et al., 2009). Was discovered in the deep ocean by the Ocean Drilling Project (Kennett & Stott, 1991; Westerhold et al., 2009; Zachos et al., 2003). At the Paleocene – Eocene boundary, marine paleontologists had long recognized a stratigraphic interval where all carbonate was dissolved; this interval was also associated with a negative excursion of ~4–5 ‰ in $\delta^{13}C$. The same interval was later recognized in terrestrial sediments worldwide (Wing et al., 2005). Both changes in this interval could only be explained by a massive release of carbon with negative values of $\delta^{13}C$. Several hypotheses have been proposed to explain the source of this carbon and the subject is still controversial (McInerney & Wing, 2011). One proposed source is the release of methane hydrates that are trapped at the bottom of the ocean and contain massive amounts of carbon. About ~2500 to 4500 Gt of highly ^{13}C–depleted marine methane clathrates that rapidly oxidizes to CO_2 (Bralower et al., 1997; Dickens et al., 1995, 1998), increasing CO_2 by ~500 ppm (Gehler et al., 2016). However, the volume of methane trapped in the hydrates is still uncertain. Another explanation, which has recently received large support, is the massive release of CO_2 by North Sea volcanism (Gutjar et al., 2017).

Whatever the source, the PETM produced large changes in the ocean with a massive extinction of benthic foraminifera (Thomas & Shackleton, 1996) and radiations of planktonic foraminifera. On land, changes were even more drastic. Most modern mammal orders originated during the PETM, including artiodactyls (deer), perissodactyls (horses), and primates (excluding plesiadiforms), and these quickly dispersed across Asia, Europe, and North America (Clyde & Gingerich, 1998; Gingerich, 2006). The effect on plants was diverse; for example, in midlatitudes such as Wyoming (midwestern USA), there is rapid immigration by southern angiosperms, which replaced the existing vegetation of conifers and angiosperms (Wing et al., 2005). This PETM vegetation also experienced more intense herbivory than the pre–PETM floras (Currano et al., 2008). Once the event ended, the pre–PETM flora returned to Wyoming and replaced the immigrant vegetation.

In this process, there are very few originations or extinctions and most of the changes are the product of migrations. In the Neotropics the effects of the PETM were different (Figure 1). The fossil record of three sites in northeast Colombia and northwest Venezuela indicated that the mean annual temperature increased ~3.5 °C during the PETM (Jaramillo & Cárdenas, 2013; Jaramillo et al., 2010b), similar to the increase in oceanic temperatures of tropical oceans (Frieling et al., 2017; Zachos et al., 2003). The vegetation rapidly became more diverse, by about 30%, with the addition of a new group of taxa (Jaramillo et al., 2010b), e.g., *Tetracolporopollenites maculosus* (Sapotacea), *Retitrescolpites? irregularis* (Phyllantacea), *Striatopollis catatumbus* (Fabaceae), *Margocolporites vanwijhei* (Fabaceae). Extinction rates did not change while origination rates doubled, with many taxa appearing for the first time all across the Neotropics, suggesting that these new taxa were a product of evolution rather than migration from other latitudes. This radiation can also be seen in DNA–based phylogenies of many tropical clades, including epiphytic ferns, typical of Neotropical forests, orchids, and leaf–cutter ants (Ramírez et al., 2007; Schuettpelz & Pryer, 2009; Schultz & Brady, 2008). There is also no evidence of an increase in aridity, but plant water use became more efficient due to high concentrations of CO_2, as seen in the deuterium isotopic record (Jaramillo et al., 2010b); similar results

have been seen in greenhouse experiments with extant plants (Cernusak et al., 2011, 2013).

These results contradict paleoclimatic global models that predict temperatures >45 °C for most of the Neotropics and a major collapse of Neotropical vegetation due to heat stress (Bowen & Zachos, 2010; Huber, 2008; Huber & Caballero, 2011; Huber & Sloan, 2000). In order to simulate the PETM, climatic models add large volumes of CO_2 to the atmosphere (Huber & Sloan, 1999; Huber et al., 2003; Shellito et al., 2003; Sloan & Barron, 1992; Sloan & Morrill, 1998; Sloan & Rea, 1996; Sloan & Thomas, 1998; Sloan et al., 1995), making the tropical temperature too hot compared to empirical data. There must be a mechanism, still unknown, that is heating poles at a much higher pace than the tropics during periods of global warming.

The rapid ending of the PETM is also an enigma. The PETM ends ten times faster than expected by the standard rates of the weathering process (Bowen & Zachos, 2010). One hypothesis is that both onset and termination of the PETM were facilitated by the collapse of the tropical vegetation (Bowen & Zachos, 2010; Huber, 2008). However, the empirical record demonstrates that tropical vegetation did not collapse during the PETM and that plant water use efficiency (WUE) increased (Jaramillo et al., 2010b). The WUE is the proportion of water that the plant uses for photosynthesis and to produce biomass versus the proportion of water that is lost by transpiration. An increase in WUE at the continental scale could indirectly promoted capture of atmospheric CO_2 in two ways: first, it could have increased biomass production (this effect is seen in diversity, as there is strong correlation between biomass and diversity). Second, it could decrease the water that the plant transpires, this "excess" water not used by the plant could therefore reach the water–table and the drainage systems, raising the weathering potential and thus increasing the trapping of atmospheric CO_2 (De Boer et al., 2011; Lammertsma et al., 2011). In summary, tropical forests could have facilitated the termination of the PETM by increasing biomass production and accelerating weathering, both of which quickly trapped atmospheric CO_2.

From the Eocene (56 Ma) to the early Miocene (ca. 16 Ma), global temperature varied greatly, with a gradual increase during the early Eocene until it peaked during the Early Eocene Thermal Maximum (ETM), which began at the end of the early Eocene and lasted until the start of the middle Eocene. Following the ETM, there is a long and slow drop in temperature during the middle and late Eocene. At the Eocene – Oligocene transition, ca. 34 my ago, there is sharp cooling that is coetaneous with the earliest glacial development in Antarctica (Anderson et al., 2011; Liu et al., 2009; Zachos et al., 2001). First glaciations in Antarctica appear to be correlated with the onset of South America's separation from Antarctica, which made possible a circumpolar current and thus the cooling of Antarctica. However, some models have not been able to reproduce a massive glacial buildup in Antarctica without a sharp drop in CO_2 below a threshold value of ~450 ppm (Lefebvre et al., 2012), values that are not reached until the Pliocene. It seems then, that the extensive modern Antarctic glacial cover is a recent phenomenon, probably occurring within the last 5 my (Anderson et al., 2011). As further evidence, the evolution of antifreeze glycoproteins in Antarctic notothenioid fishes, which are uniquely adapted to freezing waters, occurs only during the late Neogene (Near et al., 2012), and the distribution of the limpet *Nacella* was also recently established (González–Wevar et al., 2016).

During the Oligocene, global temperatures remained largely stable, with a small warming at the end of the Oligocene that was followed by another cooling at the onset of the Miocene (Zachos et al., 2001). The overall trend in the diversity of the Neotropical forest follows the same variations as the global temperature, increasing during warming periods and dropping during cooling intervals (Jaramillo & Cárdenas, 2013; Jaramillo et al., 2006). This relation could reflect the positive effect of temperature increases on rates of molecular mutations (Wright et al., 2006) and on biotic interactions, including herbivory, due to higher energy in the system (Jaramillo & Cárdenas, 2013). Some authors have proposed that Neotropical forests expanded during global warmings, thus increasing diversity by the area–diversity effect (larger area leads to more species) (Fine & Ree, 2006; Fine et al., 2008; Rosenzweig, 1995). However, the empirical paleobotanical record of South America shows that Neotropical forests do not expand beyond the tropical latitudes during warmings, especially the early Eocene warming (Jaramillo & Cárdenas, 2013) (Figure 2b). Instead, a non–analogue biome, the "mixed forest," occupied most of the temperate regions during warming events. This biome does not exist nowadays, as temperate regions are much cooler today than in the early Eocene (Hinojosa & Villagrán, 2005).

Several authors have predicted that tropical terrestrial ecosystems will collapse as a consequence of the ongoing climate warming, under the assumption that the extant tropical vegetation lives close to its climatic optimum (Huber, 2008; Stoskopf, 1981; Tewksbury et al., 2008). Several deleterious effects in plants are observed when temperature rises, including an increase in respiration that decreases net production, a decrease in photosynthesis, and increases in photoinjuries, leaf stress, and the emission of isoprenes (Bassow et al., 1994; Cernusak et al., 2013; Huber, 2008, 2009; Lerdau & Throop, 1999; Lewis et al., 2004; Stoskopf, 1981; Tewksbury et al., 2008), although recent studies have shown that the upper thermal stress of canopy leaves is ~50–53 °C (Krause et al., 2010) and tropical trees can acclimate very fast (Slot & Winter, 2017). How to explain that tropical plants did not collapse during past global warmings but rather increased in diversity and biomass? Leaf temperature, a critical factor for plants, mainly depends on three factors: air temperature, levels of atmospheric CO_2, and soil moisture. The combination of all three factors deter-

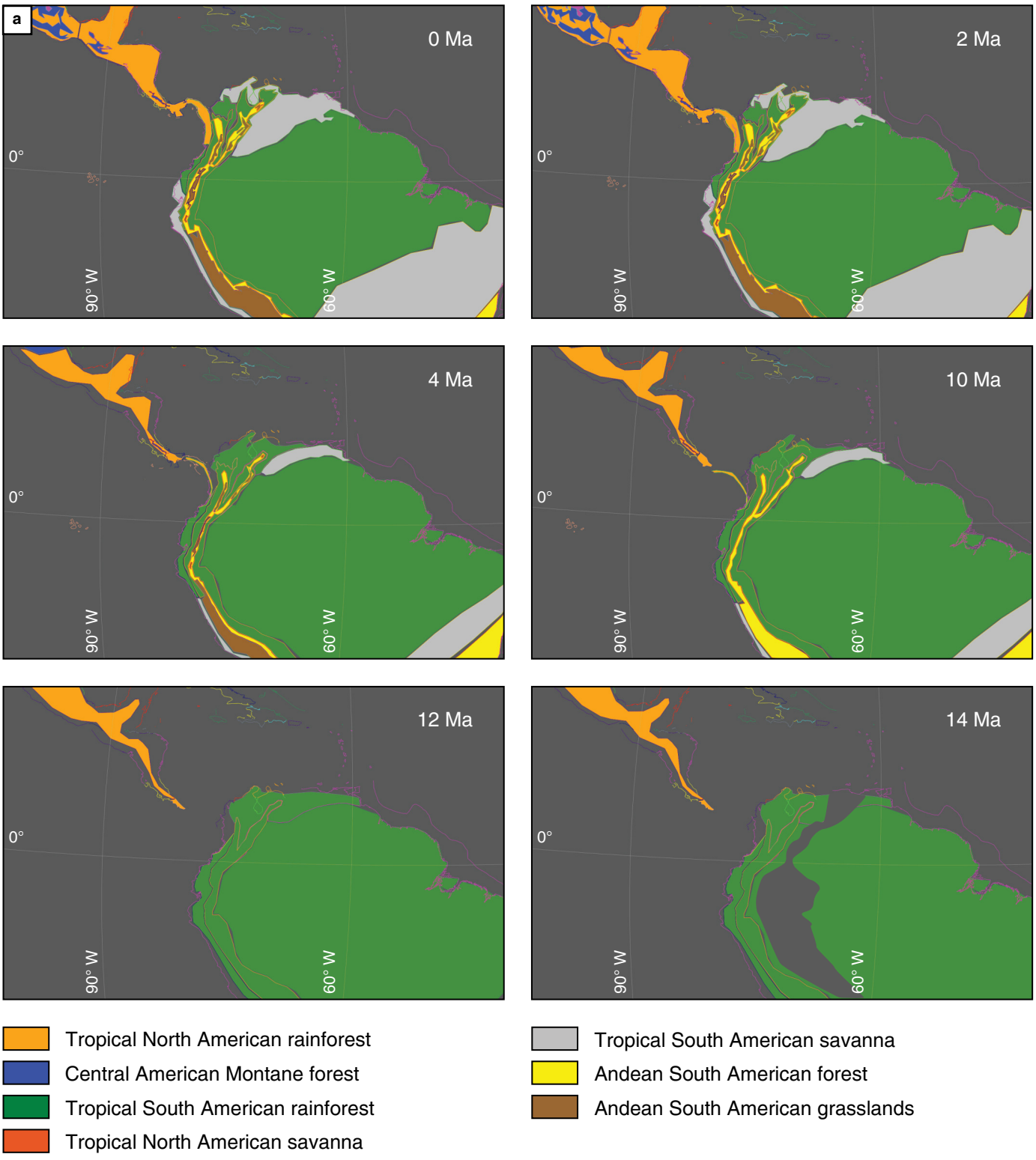

Figure 2. Terrestrial biome reconstruction for the past 55 my of the Neotropics. **(a)** Reconstruction from 0 to 14 Ma. **(b)** Reconstruction from 15.5 to 55 Ma. The reconstruction is an orthographic projection based on the plate tectonic model of GPlates 1.5.0, using the plate reconstruction of Seton (Seton et al., 2012). Terrestrial biomes include the tropical rainforest, which was divided into South America and North American (Central American) rainforests; the montane forest (forest > 2000 m of elevation), which is divided into the Andean South American forest and the Central American Montane forest; the Andean South American grasslands (or páramos, grasslands above the tree line in the Andes of South America); and the tropical South and North American savannas, which includes the xerophytic forests. Terrestrial biomes adapted from Jaramillo & Cárdenas (2013) and Jaramillo (2018). The exhumation evolution of the Isthmus of Panamá from the Montes models (Farris et al., 2011; Montes et al., 2012a, 2012b, 2015).

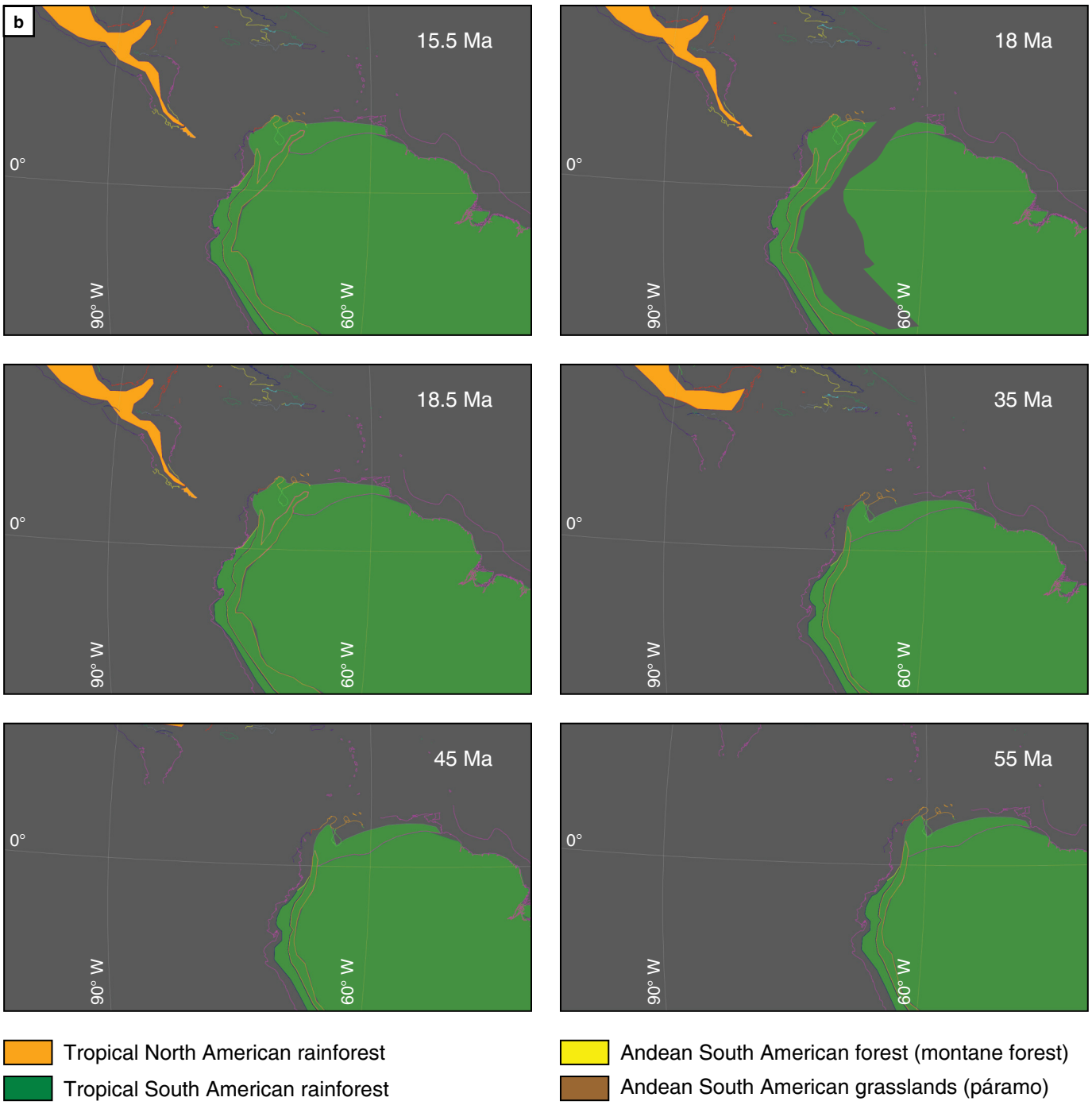

Figure 2. Terrestrial biome reconstruction for the past 55 my of the Neotropics. **(a)** Reconstruction from 0 to 14 Ma. **(b)** Reconstruction from 15.5 to 55 Ma. The reconstruction is an orthographic projection based on the plate tectonic model of GPlates 1.5.0, using the plate reconstruction of Seton (Seton et al., 2012). Terrestrial biomes include the tropical rainforest, which was divided into South America and North American (Central American) rainforests; the montane forest (forest > 2000 m of elevation), which is divided into the Andean South American forest and the Central American Montane forest; the Andean South American grasslands (or páramos, grasslands above the tree line in the Andes of South America); and the tropical South and North American savannas, which includes the xerophytic forests. Terrestrial biomes adapted from Jaramillo & Cárdenas (2013) and Jaramillo (2018). The exhumation evolution of the Isthmus of Panamá from the Montes models (Farris et al., 2011; Montes et al., 2012a, 2012b, 2015) *(continued)*.

mines a plant's response to ambient temperature. Warming events during the Cretaceous and Paleogene are characterized by elevated levels of CO_2 together with high precipitation (Jaramillo et al., 2010b; Royer, 2010; Ufnar et al., 2002, 2004, 2008; Wing et al., 2009) and short dry seasons (Jaramillo et al., 2010b). Physiological studies indicate that plants are more

efficient at photosynthesis at higher temperatures (up to 10 °C) provided that levels of both CO_2 and soil moisture are high (Aber et al., 2001; Berry & Björkman, 1980; Lloyd & Farquhar, 2008; Niu et al., 2008). Furthermore, WUE increases when levels of CO_2 increase (Cernusak et al., 2011). The genes that regulate photosynthesis are deeply rooted in plant phylogeny and it would be expected that photosynthesis in Eocene and Paleocene plants was fundamentally the same as in extant plants. The plant fossil record of the Neotropics suggests, therefore, that modern plants might already have the genetic variability to cope with increases in temperature and CO_2, as some have proposed (Lloyd & Farquhar, 2008).

4. Neogene

The Neogene represents a new chapter in the history of tropical biomes with the dramatic expansion of several biomes including savannas, dry forests, xerophytic forests, deserts, montane forests, and páramos (Figure 2a, 2b). Today, savannas occupy 30% of land on earth. They provide most of the food we consume and most of the land we inhabit (Jacobs et al., 1999). Grasses of tropical savannas comprise <2% of plant species (Sage et al., 1999), but nevertheless capture 20% of terrestrial carbon (Lloyd & Farquhar, 1994). Despite the importance of savannas, we still know very little about their origin and the factors that control them, especially in the South American tropics (Edwards et al., 2010).

The main factor that determines the type of vegetation within tropical lowland is precipitation rather than temperature. Variations in mean annual temperature within the tropical zone are minimal, from 23 to 28 °C, with very low variations throughout the year. In contrast, there are drastic variations in precipitation, both in the total amount throughout the year and in the length of the dry season. Biomes change as precipitation conditions changes (Jaramillo & Cárdenas, 2013; Lehmann et al., 2011), shifting from humid forest to dry forest, savanna, xerophytic forest, and desert as precipitation decreases (Jaramillo & Cárdenas, 2013). Another important factor during the Neogene is diminishing CO_2 levels. This trend began at the start of the Oligocene (ca. 34 Ma) and continued until the onset of the Pleistocene when CO_2 levels reached <200 ppm during glacial times (De Boer et al., 2010; Royer, 2006, 2010; Royer et al., 2011). There is a rapid increase during the middle Miocene climatic optimum (MMCO) ca. 17–14 Ma, characterized period of relative warmth, with global mean surface temperatures likely increasing by 2–3 °C (Zachos et al., 2001), and another during the late Pliocene (5–3 Ma) also characterized by warmer temperatures (Filippelli & Flores, 2009; Ravelo et al., 2006). During the glacial/interglacial times of the last 2.6 my, CO_2 has oscillated in concordance with global temperature, ranging from ~280 ppm during interglacial periods to 180 ppm during glacial periods (Lüthi et al., 2008; Monnin et al., 2001; Siegenthaler et al., 2005; Tripati et al., 2009).

Four main groups of plants are characteristic of dry environments: Cactaceae, Agavaceae, Poaceae, and the so–called "ice plants" of South Africa (Arakaki et al., 2011). Many of them have one of two paths for photosynthesis, either C4 or CAM, whereas most trees use C3 photosynthesis. Photosynthetic pathways C4 and CAM are much more efficient than C3 in areas where temperature is very high and there is hydric stress and/or low CO_2 levels (Edwards et al., 2010). Under such conditions, C3 photosynthesis becomes difficult because the water–loss by transpiration is too high (Edwards et al., 2010). The phylogeny of the aforementioned groups of plants indicates that they originated towards the end of the Eocene/beginning of the Oligocene, probably associated with the pronounced global decrease in CO_2 at the end of the Eocene, ca. 34–36 Ma (Arakaki et al., 2011). However, their radiation occurred millions of years later, during the late Miocene to Pleistocene (Arakaki et al., 2011; Edwards et al., 2010). This phylogenetic radiation seems to coincide with the expansion of the area occupied by savannas, as deduced from the fossil record.

Savanna expansion appears not to be coeval on a global scale, although the fossil record is still scarce (Edwards et al., 2010). Most empirical data indicate that 15 my ago savannas had not yet expanded (Edwards et al., 2010) (Figure 2a). In Kenya, the expansion of the savannas with C4–Poaceae occurs around 6–8 Ma (Uno et al., 2011). In Pakistan, the savannas C4 expand around 7 Ma (Morgan et al., 1994). In the Neotropics, the information about when the savannas developed is scarce (Wijmstra & van der Hammen, 1966). Areas that nowadays correspond to xerophytic/dry forests and savannas, like the Upper Magdalena Valley (Villavieja) (Figure 1), were humid forests 13–11 my ago (Kay et al., 1997) (Figure 2a). In Falcón province, northwestern Venezuela, fossil records of the upper Miocene (ca. 9 Ma) indicate the presence of a more humid forest, very different from the xerophytic vegetation present in the region today (Aguilera, 2004; Díaz de Gamero & Linares, 1989; Hambalek, 1993; Hambalek et al., 1994; Linares, 2004; Quiroz & Jaramillo, 2010; Sánchez–Villagra & Aguilera, 2006). The fossil record of the late Neogene and Quaternary in the Llanos Orientales of Colombia has mostly focused on the Holocene (Wijmstra & van der Hammen, 1966). Palynofloras of the Miocene, up to ca. 6 Ma, indicate that the region was not a savanna (Jaramillo et al., 2006, 2017b), therefore, the expansion of the savannas in the north of South America must have occurred very recently, at some point over the past 6 my (Figures 1, 2a).

What factors could have induced the expansion of the savanna in the Neotropics? The amount of precipitation, as well as its seasonality, determines in large part the presence of savannas (Lehmann et al., 2011). Precipitation on a macroscale in northern South America is controlled by the amplitude and

migration of the intertropical convergence zone (ITCZ). When summer occurs in the Southern Hemisphere, the ITCZ migrates to the south and positions itself over southern Colombia, Ecuador, and the basin of the Amazon (Poveda et al., 2006), leaving large portions of northern South America under dry conditions. Precipitation increases over northern South America when the ITCZ migrates north during the boreal summer (Poveda et al., 2006). This shift of the ITCZ produces a long dry season over the region occupied by savannas and xerophytic forests in northern South America. Therefore, the ITCZ must have shifted at some point within the last 6 my in order to yield the modern climate configuration.

Two mechanisms affecting the ITCZ have been proposed. First, the closure of the isthmus of Panamá during the late Pliocene, 4.2–3.5 Ma, enhanced the thermohaline circulation, which pushed the ITCZ southward to its modern position (Billups et al., 1999; Chaisson, 1995; Chaisson & Ravelo, 1997; Haug & Tiedemann, 1998; Haug et al., 2001; Hovan, 1995; Keigwin, 1982; Mikolajewicz et al., 1993). However, recent studies indicate that the onset of the thermohaline circulation was ca. 10–12 Ma, a consequence of the closure of the Central American Seaway (Bacon et al., 2015a; Jaramillo, 2018; Jaramillo et al., 2017a; Montes et al., 2015; Sepulchre et al., 2014). Second, the onset of permanent extensive ice in the Northern Hemisphere at 2.6 Ma would have pushed the ITZC south to its current position (Chiang & Bitz, 2005; Flohn, 1981; Shackleton et al., 1984).

An additional element that may have influenced the expansion of the savannas is the uplift of the Andes (Figure 2a). Models of climate sensibility (Sepulchre et al., 2010) indicate that the uplift of the northern Andes above 2000 m augmented the seasonality of northern South America, which could have facilitated expansion of the Neotropical savannas. Something similar occurred in southern South America, where precipitation from the Pacific Ocean is blocked by the western side of the Andes, enhancing the aridity in Patagonia (Sepulchre et al., 2010). Models of climate sensitivity have also shown that the rising the Central Andes above 2500 m may have intensified the Humboldt Current (Sepulchre et al., 2009). This current plays an important role in the regulation of the depth of the thermocline and the temperature of surficial waters of the eastern Pacific. Changes in the intensity of the Humboldt Current and/or in the depth of the thermocline in the tropical Pacific generate variations in the distribution and intensity of the atmospheric convection cells (circulation of Walker and Hadley), affecting the latitudinal position and intensity of the ITZC over the eastern Pacific (Chiang, 2009; Martínez, 2009; Rincón–Martínez et al., 2010).

The uplift of the Andes also produced substantial modifications in the landscape. While the majority of the riverine flux was northbound during most of the Cenozoic, the uplift of the Andes shifted the hydrographic system towards the east, producing the modern configuration of the Amazon and Orinoco hydrographic basins (Figueiredo et al., 2009; Hoorn, 1994a, 1994b; Hoorn et al., 1995, 2010, 2017; Jaramillo et al., 2010a). The process of uplifting also caused significant modifications in the patterns of subsidence across all Amazonian basins. The dynamic topography generated by the uplift/subsidence produced extensive floodplains in western Amazonia during most of the Cenozoic that, during the late Miocene, were shifted to the modern system of incisive rivers and reduced floodplains (Latrubesse et al., 2010; Sacek, 2014; Shephard et al., 2010).

Nowadays, floodplains constitute only 20% of the Amazon region (Toivonen et al., 2007), but during the Miocene they were much more extensive, allowing the existence of large reptiles and mammals, such as 3–m–long turtles (*Stupendemys*), crocodiles over 14 m long (*Purussaurus*), and rodents (*Phoberomys*) more than 1.8 m in length and weighing 700 kg (Antoine et al., 2007; Cozzuol, 2006; Frailey, 1986; Kay et al., 1997; Sánchez–Villagra, 2006; Sánchez–Villagra & Aguilera, 2006; Sánchez–Villagra et al., 2003). This high–subsidence system is called Pebas, and it is a biome that does not have a modern analogue (Jaramillo et al., 2017b), but it is closely related to the rainforest (Figure 2a). It is dominated by a unique depositional environment, termed "marginal," that includes greenish to gray–colored, laminated, bioturbated, and locally fossil–rich mudstones coarsening up to very fine to medium–grained sandstones with coal interbeds. The association of these lithofacies represents accumulation on deltaic plains, low–energy wetlands with swamps, ponds, and channels, and shallow fresh–water lacustrine systems (Jaramillo et al., 2017b) (Figure 1). Associated with the high–subsidence system, and probably eustasy, are two distinct marine intervals in the Llanos Basin, an early Miocene interval that lasted ca. 0.9 my (18.1 to 17.2 Ma) and a middle Miocene interval that lasted ca. 3.7 my (16.1 to 12.4 Ma) (Figure 2a). These two marine intervals are progressively later toward the southern basins of western Amazonia, and in the Amazonas/Solimões Basin are much shorter in duration, ca. 0.2 my (18.0 to 17.8 Ma) and ca. 0.4 my (14.1 to 13.7 Ma), respectively (Jaramillo et al., 2017b). The Miocene lake systems that are produced all along the Magdalena valley, e.g., La Cira beds and the Barzalosa Formation, may also be related to these two marine flooding periods but correlations are still uncertain. The disappearance of the Pebas system occurred at ca. 10–11 Ma (Jaramillo et al., 2017b), concomitant with the onset of the Amazon River (Hoorn et al., 2017). This major shift probably precipitated the extinction of flora associated with the "marginal" environment of the Pebas systems and its fauna of large reptiles and abundant mollusks.

The Andes reached their modern elevation by the end of the Miocene (ca. 5–6 Ma; Garzione et al., 2006, 2008, 2014; Ghosh et al., 2006; Kar et al., 2016; Wallis et al., 2016), thus generating two brand new biomes, the páramo and the cloud (montane) forest (Figure 2a). The species composition of these two biomes is roughly 50% derived from lowland tropical plants (tropical

Gondwanan lineages), ~25% from temperate latitudes in South America (temperate Gondwanan lineages), and ~25% from temperate latitudes in North America (temperate Laurasian lineages) (Gentry, 1982a, 1982b). The slopes of the Andes have also been considered a sort of engine of speciation because the topographic complexity generates diverse microenvironments (Gentry, 1982a; Hoorn et al., 2010). The history of the vegetation of the Andes during the late Neogene has been studied by professor van der Hammen and his team for more than four decades (Hooghiemstra & van der Hammen, 1998; Hooghiemstra et al., 2006; van der Hammen, 1989, 1995, 2003; van der Hammen & Hooghiemstra, 2000; van der Hammen et al., 1973; Wijninga, 1996). Nonetheless, when the extant páramo originated is still an open question.

The cool–mode climate of today, which emerged 2.6 my ago at the onset of the Pleistocene, is fundamentally different from the warm–mode, pre–Pleistocene climates (Fedorov et al., 2013). Four major characteristics define our modern climate: a permanent and extensive ice–cap at the North Pole, CO_2 levels below 200 ppm, a steep latitudinal temperature gradient pole–to–equator (~50 °C), and a steep longitudinal temperature gradient along the equatorial Pacific (Pagani et al., 2010). Understanding how those four components arose is fundamental to understanding our modern climate and making future predictions, yet we still lack satisfactory answers. The consequences of this major shift in climate mode are still being researched, but it seems to have greatly modified the extent and distribution of most biomes, including the expansion of savannas, páramos, and dry and xerophytic forests and the contraction of the rainforest (Jaramillo et al., 2015) (Figure 2a). One striking example of this shift is the Ware Formation in the northeastern region of the Guajira Peninsula (Figure 1). The Ware Formation is an upper Pliocene (3.4–2.78 Ma) fluvio–deltaic deposit (Hendy et al., 2015; Moreno et al., 2015) with a rich fossil record that includes sloths, cingulates, rodents, toxodontids, a procyonid, a camelid, large crocodiles, turtles, fossil wood, and a diverse fish assemblage (Aguilera et al., 2013a, 2013b, 2017; Amson et al., 2016; Cadena & Jaramillo, 2015; Carrillo et al., 2018; Carrillo et al., 2015; Forasiepi et al., 2014; Hendy et al., 2015; Jaramillo et al., 2015; Moreno–Bernal et al., 2016; Moreno et al., 2015; Pérez et al., 2017; Suárez et al., 2016), indicating that there were rivers with permanent water derived from local precipitation (Pérez–Consuegra et al., 2018); this is a stark contrast with the desertic environment of that region today. These profound changes, however, were not limited to terrestrial environments. The world's oceans, too, experienced a major extinction of marine megafauna at the onset of the Pleistocene (Pimiento et al., 2017).

The last large change in the history of the Neotropics occurred during the late Neogene with the terrestrial connection of Central America with South America across the Isthmus of Panamá, which facilitated a large–scale interchange of biota across the Americas, often known as GABI (the Great American Biotic Interchange) (MacFadden, 2006a; Simpson, 1983; Webb, 1976, 1978, 1994, 1995, 2006; Woodburne, 2010). Many studies have used 3.5 Ma as the a priori date for this event (Bacon et al., 2015a), although several genetic studies of taxa with low dispersal capabilities, including bees (Roubik & Camargo, 2011), tree frogs (Pinto–Sánchez et al., 2012), salamanders (Elmer et al., 2013), freshwater *Poecilia* fishes (Alda et al., 2013), and *Amazilia* hummingbirds (Ornelas et al., 2013), among many others, have reported evidence of earlier exchanges. A recent meta–analysis across a broad range of taxa, both marine and terrestrial, indicated a large increase in the rate of migrations/vicariance migration starting at 10 Ma, rather than at 3.5 Ma as was often assumed (Bacon et al., 2015a, b; Jaramillo, 2018; Jaramillo et al., 2017a). The fossil record of Panamá indicates a similar pattern in plants (Cody et al., 2010; Graham, 1988a, 1988b, 1991, 1992, 1999, 2010, 2011; Herrera et al., 2010, 2014a, 2014c; Jaramillo et al., 2014b; Jud et al., 2016; Rodríguez–Reyes et al., 2014, 2017a, 2017b) and vertebrates other than mammals (Cadena et al., 2012b; Hastings et al., 2013; Head et al., 2012; Scheyer et al., 2013). Panamanian mammals of the early – middle Miocene in contrast are dominated by North American lineages including camels, horses, peccaries, bear–dogs, anthracotheriums, rhinocerids, geomyoid rodents, dogs, oreodonts, and protoceratids (MacFadden, 2006a, 2006b, 2009; MacFadden & Higgins, 2004; MacFadden et al., 2010, 2012; Rincon et al., 2012, 2013; Slaughter, 1981; Whitmore & Stewart, 1965); there are only two South American lineages, a monkey (Bloch et al., 2016) and a bat. Recently O'Dea et al. (2016) proposed that findings of a Miocene closure of the Central American Seaway were unsupported and provided a new age for the formation of the Isthmus at 2.8 Ma. However, both conclusions have been rejected (Jaramillo et al., 2017a; Molnar, 2017).

Most of what is written about GABI in the paleontological literature is derived from the mammal fossil record. Therefore, the mammal–derived GABI has been accepted as the de facto pattern for all other organisms, even though mammals represent only ~0.02% of all species in the Americas. Both the fossil and genetic records show that mammal exchange starts at 10 Ma and accelerates greatly at ca. 2.5 Ma rather than at 3.5 Ma (Bacon et al., 2015a; Carrillo et al., 2015; Forasiepi et al., 2014; Jaramillo, 2018; Leite et al., 2014; Webb, 1976, 2006; Woodburne, 2010). The timing for the onset of massive GABI mammal migrations has been used to suggest that factors other than a land connection drove GABI, mainly the onset of the Pleistocene cool–climate mode and all the changes that produced in the hydrological patterns of the Americas as it was discussed above (Bacon et al., 2016; Leigh et al., 2013; Molnar, 2008; Smith et al., 2012; Webb, 1976, 1978, 2006).

The development of extant Neotropical biomes has been affected by a series of historical accidents, climate changes,

and tectonic processes, many of which are still unknown. They are, however, important if we are going to be able to predict how biomes will respond to the ongoing rapid perturbations of our climate.

Acknowledgments

Thanks to Felipe HINOJOSA and Alex CORREA–METRIO for reviewing the manuscript. Our studies have been sponsored by a number of funds and institutions including the Smithsonian Institution, Dr. David COFRIN, Anders Foundation, Fund 1923, Gregory D. and Jennifer WALSTON JOHNSON, Instituto Colombiano del Petróleo–Ecopetrol S.A., University of Florida, Missouri University of Science and Technology, Fondo para la Investigación de la Ciencia y la Tecnología del Banco de la República, USA National Science Foundation, Carbones del Cerrejón LLC., Isagén, Mark Tupper, National Geographic Society, Smithsonian Women's Committee, Agencia Nacional de Hidrocarburos, Servicio Geológico Colombiano, Colciencias, University of Zurich, and the Corporación Geológica Ares. Thanks to the PADILLA brothers and the Centro de Investigaciones Paleontológicas, Milton RUEDA and Paleoflora, and Carlos ROSERO. Thanks to the communities of la Victoria, Warpana, Patajau, Aulechit, Nazareth, Wososopo, Sillamana, Paraguachon, La Flor de la Guajira, and Ipapura for their support and knowledge. Thanks to Fernando ETAYO, Tomás VILLAMIL, Francisca OBOH–IKUENOBE, David DILCHER, and Scott WING for their training. Thanks to Natasha ATKINS and Camilo JARAMILLO for editing. Special thanks to M.I. BARRETO for her guidance and ideas, which have been critical to all our research over the past 25 years. This contribution is an updated and modified version of a contribution to the journal of ACCEFYN in 2012.

References

Aber, J., Neilson, R., McNulty, S., Lenihan, J.M., Bachelet, D. & Drapek, R.J. 2001. Forest processes and global environmental change: Predicting the effects of individual and multiple stressors. BioScience, 51(9): 735–751. https://doi.org/10.1641/0006-3568(2001)051[0735:FPAGEC]2.0.CO;2

Aguilera, O. 2004. Tesoros paleontológicos de Venezuela, Urumaco, patrimonio natural de la humanidad. Editorial Arte, 148 p. Caracas.

Aguilera, O., Lundberg, J., Birindelli, J., Sabaj–Pérez, M., Jaramillo, C.A. & Sánchez–Villagra, M.R. 2013a. Palaeontological evidence for the last temporal occurrence of the ancient western Amazonian River outflow into the Caribbean. PLOS ONE, 8(9): 1–17. https://doi.org/10.1371/journal.pone.0076202

Aguilera, O., Moraes–Santos, H., Costa, S., Ohe, F., Jaramillo, C.A. & Nogueira, A. 2013b. Ariid sea catfishes from the coeval Pirabas (Northeastern Brazil), Cantaure, Castillo (northwestern Venezuela), and Castilletes (North Colombia) Formations (early Miocene), with description of three new species. Swiss Journal of Palaeontology, 132(1): 45–68. https://doi.org/10.1007/s13358-013-0052-4

Aguilera, O., Andrade, G.O., Lopes, R.T., Machado, A.S., Dos Santos, T.M., Marques, G., Bertucci, T., Aguiar, T., Carrillo–Briceño, J., Rodríguez, F. & Jaramillo, C.A. 2017. Neogene proto–Caribbean porcupinefishes (Diodontidae). PLOS ONE, 12(7): 1–26. https://doi.org/10.1371/journal.pone.0181670

Alda, F., Reina, R.G., Doadrio, I. & Bermingham, E. 2013. Phylogeny and biogeography of the *Poecilia sphenops* species complex (Actinopterygii, Poeciliidae) in Central America. Molecular Phylogenetics and Evolution, 66(3): 1011–1026. https://doi.org/10.1016/j.ympev.2012.12.012

Amson, E., Carrillo, J.D. & Jaramillo, C.A. 2016. Neogene sloth assemblages (Mammalia, Pilosa) of the Cocinetas Basin (La Guajira, Colombia): Implications for the Great American Biotic Interchange. Palaeontology, 59(4): 563–582. https://doi.org/10.1111/pala.12244

Anderson, J.B., Warny, S., Askin, R.A., Wellner, J.S., Bohaty, S.M., Kirshner, A.E., Livsey, D.N., Simms, A.R., Smith, T.R., Ehrmann, W., Lawver, L.A., Barbeau, D., Wise, S.W., Kulhanek, D.K., Weaver, F.M. & Majewski, W. 2011. Progressive Cenozoic cooling and the demise of Antarctica's last refugium. Proceedings of the National Academy of Sciences of the United States of America, 108(28): 11356–11360. https://doi.org/10.1073/pnas.1014885108

Antoine, P.O., Salas–Gismondi, R., Baby, P., Benammi, M., Brusset, S., Francechi, D., Espurt, N., Goillot, C., Pujos, F., Tejada, J. & Urbina, M. 2007. The middle Miocene (Laventan) Fitzcarrald fauna, Amazonian Peru. Cuadernos del Museo Geominero, 8: 19–24. Madrid.

Arakaki, M., Christin, P.A., Nyffeler, R., Lendel, A., Eggli, U., Ogburn, R.M., Spriggs, E., Moore, M.J. & Edwards, E.J. 2011. Contemporaneous and recent radiations of the world's major succulent plant lineages. Proceedings of the National Academy of Sciences of the United States of America, 108(20): 8379–8384. https://doi.org/10.1073/pnas.1100628108

Archangelsky, S. & Taylor, T.N. 1993. The ultrastructure of in situ *Clavatipollenites* pollen from the Early Cretaceous of Patagonia. American Journal of Botany, 80(8): 879–885. https://doi.org/10.2307/2445507

Archer, D., Eby, M., Brovkin, V., Ridgwell, A., Cao, L., Mikolajewicz, U., Caldeira, K., Matsumoto, K., Munhoven, G., Montenegro, A. & Tokos, K. 2009. Atmospheric lifetime of fossil fuel carbon dioxide. Annual Review of Earth and Planetary Sciences, 37: 117–134. https://doi.org/10.1146/annurev.earth.031208.100206

Bacon, C.D., Silvestro, D., Jaramillo, C., Smith, B.T., Chakrabarty, P. & Antonelli, A. 2015a. Biological evidence supports an early and complex emergence of the Isthmus of Panama. Proceedings of the National Academy of Sciences of the United States of America, 112(19): 6110–6115. https://doi.org/10.1073/pnas.1423853112

Bacon, C.D., Silvestro, D., Jaramillo, C., Smith, B.T., Chakrabarty, P. & Antonelli, A. 2015b. Reply to Lessios and Marko et al.: Early and progressive migration across the Isthmus of Panama is robust to missing data and biases. Proceedings of the National Academy of Sciences of the United States of America, 112(43): E5767–E5768. https://doi.org/10.1073/pnas.1515451112

Bacon, C.D., Molnar, P., Antonelli, A., Crawford, A.J., Montes, C. & Vallejo–Pareja, M.C. 2016. Quaternary glaciation and the Great American Biotic Interchange. Geology, 44(5): 375–378. https://doi.org/10.1130/G37624.1

Bassow, S.L., McConnaughay, K.D. & Bazzaz, F.A. 1994. The response of temperate tree seedlings grown in elevated CO_2 to extreme temperature events. Ecological Applications, 4(3): 593–603. https://doi.org/10.2307/1941960

Bayona, G., Montes, C., Cardona, A., Jaramillo, C.A., Ojeda, G., Valencia, V. & Ayala–Calvo, C. 2011. Intraplate subsidence and basin filling adjacent to an oceanic arc–continent collision: A case from the southern Caribbean–South America plate margin. Basin Research, 23(4): 403–422. https://doi.org/10.1111/j.1365-2117.2010.00495.x

Beaulieu, J.M., O'Meara, B.C., Crane, P.R. & Donoghue, M.J. 2015. Heterogeneous rates of molecular evolution and diversification could explain the Triassic age estimate for angiosperms. Systematic Biology, 64(5): 869–878. https://doi.org/10.1093/sysbio/syv027

Bell, C.D., Soltis, D.E. & Soltis, P.S. 2010. The age and diversification of the angiosperms re–revisited. American Journal of Botany, 97(8): 1296–1303. https://doi.org/10.3732/ajb.0900346

Berry, J. & Björkman, O. 1980. Photosynthetic response and adaptation to temperature in higher plants. Annual Review of Plant Physiology, 31: 491–543. https://doi.org/10.1146/annurev.pp.31.060180.002423

Bice, K.L., Birgel, D., Meyers, P.A., Dahl, K.A., Hinrichs, K. & Norris, R.D. 2006. A multiple proxy and model study of Cretaceous upper ocean temperatures and atmospheric CO_2 concentrations. Paleoceanography and Paleoclimatology, 21(2): 1–17. https://doi.org/10.1029/2005PA001203

Billups, K., Ravelo, A.C., Zachos, J.C. & Norris, R.D. 1999. Link between oceanic heat transport, thermohaline circulation, and the intertropical convergence zone in the early Pliocene Atlantic. Geology, 27(4): 319–322. https://doi.org/10.1130/0091-7613(1999)027<0319:LBOHTT>2.3.CO;2

Bloch, J.I., Woodruff, E.D., Wood, A.R., Rincón, A.F., Harrington, A.R., Morgan, G.S., Foster, D.A., Montes, C., Jaramillo, C., Jud, N.A., Jones, D.S. & MacFadden, B.J. 2016. First North American fossil monkey and early Miocene tropical biotic interchange. Nature, 533(7602): 243–246. https://doi.org/10.1038/nature17415

Bowen, G.J. & Zachos, J.C. 2010. Rapid carbon sequestration at the termination of the Palaeocene – Eocene Thermal Maximum. Nature Geoscience, 3: 866–869. https://doi.org/10.1038/ngeo1014

Boyce, C.K. & Lee, J.E. 2010. An exceptional role for flowering plant physiology in the expansion of tropical rainforests and biodiversity. Proceedings of the Royal Society of London Series B: Biological Sciences, 277: 3437–3443. https://doi.org/10.1098/rspb.2010.0485

Bralower, T.J., Thomas, D.J., Zachos, J.C., Hirschmann, M.M., Röhl, U., Sigurdsson, H., Thomas, E. & Whitney, D.L. 1997. High–resolution records of the late Paleocene Thermal Maximum and circum–Caribbean volcanism: Is there a causal link? Geology, 25(11): 963–966. https://doi.org/10.1130/0091-7613(1997)025<0963:HRROTL>2.3.CO;2

Brenner, G. 1974. Palynostratigraphy of the Lower Cretaceous Gevar'am and Talme Yafe Formations in the Gever'am 2 well (southern coastal plain Israel). Geological Survey of Israel Bulletin, 59: 1–27.

Burnham, R.J. 2009. An overview of the fossil record of climbers: Bejucos, sogas, trepadoras, lianas, cipós, and vines. Revistra Brasileira de Paleontologia, 12(2): 149–160. https://doi.org/10.4072/rbp.2009.2.05

Burnham, R.J. & Graham, A. 1999. The history of Neotropical vegetation: New developments and status. Annals of the Missouri Botanical Garden, 86(2): 546–589. https://doi.org/10.2307/2666185

Burnham, R.J. & Johnson, K.R. 2004. South American palaeobotany and the origins of Neotropical rainforests. Philosophical Transactions of the Royal Society of London Series B: Biological Sciences, 359(1450): 1595–1610. https://doi.org/10.1098/rstb.2004.1531

Cadena, E.A. & Jaramillo, C. 2006. New Podocnemididae fossil turtles from the late Paleocene Cerrejón Formation, Guajira Peninsula, Colombia. 66th Annual Meeting of the Society of Vertebrate Paleontology. Unpublished Field Trip Guidebook, 43 p. Ottawa, Canada.

Cadena, E.A. & Jaramillo, C. 2015. The first fossil skull of *Chelus* (Pleurodira: Chelidae, Matamata turtle) from the early Miocene of Colombia. Palaeontologia Electronica, (18.2.32A): 1–10. https://doi.org/10.26879/545

Cadena, E.A. & Schweitzer, M.H. 2014. A pelomedusoid turtle from the Paleocene – Eocene of Colombia exhibiting preservation of blood vessels and osteocytes. Journal of Herpetology, 48(4): 461–465. https://doi.org/10.1670/13-046

Cadena, E.A., Bloch, J. & Jaramillo, C. 2012a. New bothremydid turtle (Testudines, Pleurodira) from the Paleocene of northeastern Colombia. Journal of Paleontology, 86(4): 688–698. https://doi.org/10.1666/11-128R1.1

Cadena, E.A., Bourque, J., Rincón, A., Bloch, J.I., Jaramillo, C. & MacFadden, B. 2012b. New turtles (Chelonia) from the late Eocene through late Miocene of the Panama Canal Basin. Journal of Paleontology, 86(3): 539–557. https://doi.org/10.1666/11-106.1

Cadena, E.A., Ksepka, D.T., Jaramillo, C. & Bloch, J.I. 2012c. New pelomedusoid turtles from the late Palaeocene Cerrejón Formation

of Colombia and their implications for phylogeny and body size evolution. Journal of Systematic Palaeontology, 10(2): 313–331. https://doi.org/10.1080/14772019.2011.569031

Carrillo, J.D., Forasiepi, A., Jaramillo, C. & Sánchez–Villagra, M.R. 2015. Neotropical mammal diversity and the Great American Biotic Interchange: Spatial and temporal variation in South America's fossil record. Frontiers in Genetics, 5(451): 1–12. https://doi.org/10.3389/fgene.2014.00451

Carrillo, J.D., Amson, E., Jaramillo, C., Sánchez, R., Quiroz, L., Cuartas, C., Rincón, A.F. & Sánchez–Villagra, M. 2018. The Neogene record of northern South American native ungulates. Smithsonian Contributions to Paleobiology 101, 67 p. Washington D.C. https://doi.org/10.5479/si.1943-6688.101

Carvalho, M.R., Herrera, F., Jaramillo, C.A., Wing, S. & Callejas, R. 2011. Paleocene Malvaceae from northern South America and their biogeographical implications. American Journal of Botany, 98(8): 1337–1355. https://doi.org/10.3732/ajb.1000539

Carvalho, M.R., Wilf, P., Barrios, H., Windsor, D.M., Currano, E., Labandeira, C. & Jaramillo, C. 2014. Insect leaf–chewing damage tracks herbivore richness in modern and ancient forests. PLOS ONE, 9(5): 1–9. https://doi.org/10.1371/journal.pone.0094950

Cernusak, L.A., Winter, K., Martínez, C., Correa, E., Aranda, J., García, M., Jaramillo, C. & Turner, B.L. 2011. Responses of legume versus nonlegume tropical tree seedlings to elevated CO_2 concentration. Plant Physiology, 157: 372–385. https://doi.org/10.1104/pp.111.182436

Cernusak, L.A., Winter, K., Dalling, J.W., Holtum, J.A.M., Jaramillo, C., Körner, C., Leakey, A.D.B., Norby, R.J., Poulter, B., Turner, B.L. & Wright, S.J. 2013. Tropical forest responses to increasing atmospheric CO_2: Current knowledge and opportunities for future research. Functional Plant Biology, 40(6): 531–551. https://doi.org/10.1071/FP12309

Chaisson, W.P. 1995. Planktonic foraminiferal assemblages and paleoceanographic change in the trans–tropical Pacific Ocean: A comparison of west (Leg 130) and east (Leg 138), latest Miocene to Pleistocene. In: Pisias, N.G., Mayer, L.A., Janecek, T.R., Palmer–Julson, A. & van Andel, T.H. (editors), Proceedings of the Ocean Drilling Program, Scientific Results 138, p. 555–597. https://doi.org/10.2973/odp.proc.sr.138.129.1995

Chaisson, W.P. & Ravelo, A.C. 1997. Changes in upper water–column structure at Site 925, late Miocene – Pleistocene: Planktonic foraminifer assemblage and isotopic evidence. In: Shackleton, N.J., Curry, W.B., Richter, C. & Bralower, T.J. (editors), Proceedings of the Ocean Drilling Program, Scientific Results 154, p. 255–268.

Chiang, J.C.H. 2009. The tropics in paleoclimate. Annual Review of Earth and Planetary Sciences, 37: 263–297. https://doi.org/10.1146/annurev.earth.031208.100217

Chiang, J.C.H. & Bitz, C.M. 2005. Influence of high latitude ice cover on the marine intertropical convergence zone. Climate Dynamics, 25(5): 477–496. https://doi.org/10.1007/s00382-005-0040-5

Clyde, W.C. & Gingerich, P.D. 1998. Mammalian community response to the latest Paleocene Thermal Maximum: An isotaphonomic study in the northern Bighorn Basin, Wyoming. Geology, 26(11): 1011–1014. https://doi.org/10.1130/0091-7613(1998)026<1011:MCRTTL>2.3.CO;2

Cody, S., Richardson, J.E., Rull, V., Ellis, C. & Pennington, R.T. 2010. The Great American Biotic Interchange revisited. Ecography, 33(2): 326–332. https://doi.org/10.1111/j.1600-0587.2010.06327.x

Connell, J.H. 1971. On the role of natural enemies in preventing competitive exclusion in some marine animals and in rain forest trees. In: den Boer, P.J. & Gradwell, G.R. (editors), Dynamics of populations. Centre for Agricultural Publication and Documentation, p. 298–312. Wageningen, the Netherlands.

Correa, E., Jaramillo, C., Manchester, S. & Gutiérrez, M. 2010. A fruit and leaves of rhamnaceous affinities from the Late Cretaceous (Maastrichtian) of Colombia. American Journal of Botany, 97(1): 71–79. https://doi.org/10.3732/ajb.0900093

Cozzuol, M. 2006. The Acre vertebrate fauna: Age, diversity, and geography. Journal of South American Earth Sciences, 21(3): 185–203. https://doi.org/10.1016/j.jsames.2006.03.005

Crane, P.R. & Lidgard, S. 1989. Angiosperm diversification and paleolatitudinal gradients in Cretaceous floristic diversity. Science, 246(4930): 675–678. https://doi.org/10.1126/science.246.4930.675

Crane, P.R. & Lidgard, S. 1990. Angiosperm radiation and patterns of Cretaceous palynological diversity. In: Taylor, P.D. & Larwood, G.P. (editors), Major evolutionary radiations 42, p. 377–407. Oxford.

Crifò, C., Currano, E.D., Baresh, A. & Jaramillo, C. 2014. Variations in angiosperm leaf vein density have implications for interpreting life form in the fossil record. Geology, 42(10): 919–922. https://doi.org/10.1130/G35828.1

Currano, E.D., Wilf, P., Wing, S.L., Labandeira, C.C., Lovelock, E.C. & Royer, D.L. 2008. Sharply increased insect herbivory during the Paleocene – Eocene Thermal Maximum. Proceedings of the National Academy of Sciences of the United States of America, 105(6): 1960–1964. https://doi.org/10.1073/pnas.0708646105

Davis, C., Webb, C.O., Wurdack, K.J., Jaramillo, C. & Donoghue, M.J. 2005. Explosive radiation of Malpighiales supports a mid–Cretaceous origin of modern tropical rain forests. The American Naturalist, 165(3): E36–E65. https://doi.org/10.1086/428296

De Boer, B., van de Wal, R.S.W., Bintanja, R., Lourens, L.J. & Tuenter, E. 2010. Cenozoic global ice–volume and temperature simulations with 1–D ice–sheet models forced by benthic $\delta^{18}O$ records. Annals of Glaciology, 51(55): 23–33. https://doi.org/10.3189/172756410791392736

De Boer, H.J., Lammertsma, E.I., Wagner–Cremer, F., Dilcher, D.L., Wassen, M.J. & Dekker, S.C. 2011. Climate forcing due to optimization of maximal leaf conductance in subtropical vegetation under rising CO_2. Proceedings of the National Acad-

emy of Sciences of the United States of America, 108(10): 4041–4046. https://doi.org/10.1073/pnas.1100555108

De la Parra, F. 2009. Palynological changes across the Cretaceous – Tertiary boundary in Colombia, South America. Master thesis, University of Florida, 105 p. Gainesville, USA.

De la Parra, F., Jaramillo, C. & Dilcher, D. 2008a. Paleoecological changes of spore producing plants through the Cretaceous – Paleocene boundary in Colombia. Palynology, 32: 258–259.

De la Parra, F., Jaramillo, C., Rueda, M. & Dilcher, D. 2008b. Has there been a plant mass extinction in the last 70 million years in the Neotropics? 12th International Palynological Congress. Proceedings, p. 59. Bonn, Germany.

Díaz de Gamero, M.L. & Linares, O.J. 1989. Estratigrafía y paleontología de la Formación Urumaco, del Mioceno tardío de Falcón noroccidental. 7th Congreso Geológico Venezolano. Proceedings, 1, p. 419–439. Caracas.

Dickens, G.R., O'Neil, J.R., Rea, D.K. & Owen, R.M. 1995. Dissociation of oceanic methane hydrate as a cause of the carbon isotope excursion at the end of the Paleocene. Paleoceanography and Paleoclimatology, 10(6): 965–971. https://doi.org/10.1029/95PA02087

Dickens, G.R., Bralower, T.J., Thomas, D.J., Thomas, E. & Zachos, J.C. 1998. High–resolution records of the late Paleocene Thermal Maximum and circum–Caribbean volcanism: Is there a causal link?: Comment and reply. Geology, 26(7): 670–671. https://doi.org/10.1130/0091-7613(1998)026<0670:HRROTL>2.3.CO;2

Doria, G., Jaramillo, C. & Herrera, F. 2008. Menispermaceae from the Cerrejón Formation, middle to late Paleocene, Colombia. American Journal of Botany, 95(8): 954–973. https://doi.org/10.3732/ajb.2007216

Doubinger, J. 1973. Pollen and spores from the Paleocene coal basin of Cerrejon (Guajira Province, Colombia). Comptes Rendus du 96 Congres National des Societes Savantes. Proceedings, 5, p. 253–262. Tolouse, France.

Doyle, J.A. 2012. Molecular and fossil evidence on the origin of angiosperms. Annual Review of Earth and Planetary Sciences, 40: 301–326. https://doi.org/10.1146/annurev-earth-042711-105313

Doyle, J.A. & Hickey, L.J. 1976. Pollen and leaves from the mid–Cretaceous Potomac Group and their bearing on early angiosperm evolution. In: Beck, C.B. (editor), Origin and early evolution of angiosperms. Columbia University Press, p. 139–206. New York.

Doyle, J.A., Biens, P., Doerenkamp, A. & Jardiné, S. 1977. Angiosperm pollen from the pre–Albian Lower Cretaceous of Equatorial Africa. Bulletin des Centres de Recherches Exploration–Production Elf–Aquitaine, 1: 451–473.

Doyle, J.A., Hotton, C. & Ward, J. 1990. Early Cretaceous tetrads, zonasulculate pollen, and Winteraceae. I. Taxonomy, morphology, and ultrastructure. American Journal of Botany, 77(12): 1544–1557. https://doi.org/10.1002/j.1537-2197.1990.tb11395.x

Edwards, E.J., Osborne, C.P., Strömberg, C.A.E., Smith, S.A., Bond, W.J., Christin, P.A., Cousins, A.B., Duvall, M.R., Fox, D.L., Freckleton, R.P., Ghannoum, O., Hartwell, J., Huang, Y., Janis, C.M., Keeley, J.E., Kellogg, E.A., Knapp, A.K., Leakey, A.D.B., Nelson, D.M., Saarela, J.M., Sage, R.F., Sala, O.E., Salamin, N., Still, C.J. & Tipple, B. 2010. The origins of C_4 grasslands: Integrating evolutionary and ecosystem science. Science, 328(5978): 587–591. https://doi.org/10.1126/science.1177216

Elmer, K.R., Bonett, R.M., Wake, D.B. & Lougheed, S. 2013. Early Miocene origin and cryptic diversification of South American salamanders. BMC Evolutionary Biology, 13(59): 1–16.

Erwin, D.H. 2008. Extinction: How life on earth nearly ended 250 million years ago. Princeton University Press, 320 p. Princeton.

Farris, D.W., Jaramillo, C., Bayona, G., Restrepo–Moreno, S.A., Montes, C., Cardona, A., Mora, A., Speakman, R.J., Glascock, M.D. & Valencia, V. 2011. Fracturing of the Panamanian Isthmus during initial collision with South America. Geology, 39(11): 1007–1010. https://doi.org/10.1130/G32237.1

Fedorov, A.V., Brierley, C.M., Lawrence, K.T., Liu, Z., Dekens, P.S. & Ravelo, A.C. 2013. Patterns and mechanisms of early Pliocene warmth. Nature, 496(7443): 43–49. https://doi.org/10.1038/nature12003

Feild, T.S., Brodribb, T.J., Iglesias, A., Chatelet, D.S., Baresh, A., Upchurch, G.R., Gómez, B., Mohr, B.A.R., Coiffard, C., Kvaček, J. & Jaramillo, C.A. 2011a. Fossil evidence for Cretaceous escalation in angiosperm leaf vein evolution. Proceedings of the National Academy of Sciences of the United States of America, 108(20): 8363–8366. https://doi.org/10.1073/pnas.1014456108

Feild, T.S., Upchurch, G.R., Chatelet, D.S., Brodribb, T.J., Grubbs, K.C., Samain, M.S. & Wanke, S. 2011b. Fossil evidence for low gas exchange capacities for Early Cretaceous angiosperm leaves. Paleobiology, 37(2): 195–213. https://doi.org/10.1666/10015.1

Figueiredo, J., Hoorn, C., van der Ven, P. & Soares, E. 2009. Late Miocene onset of the Amazon River and the Amazon deep–sea fan: Evidence from the Foz do Amazonas Basin. Geology, 37(7): 619–622. https://doi.org/10.1130/G25567A.1

Filippelli, G.M. & Flores, J.A. 2009. From the warm Pliocene to the cold Pleistocene: A tale of two oceans. Geology, 37(10): 959–960. https://doi.org/10.1130/focus102009.1

Fine, P.V.A. & Ree, R.H. 2006. Evidence for a time–integrated species–area effect on the latitudinal gradient in tree diversity. The American Naturalist, 168(6): 796–804. https://doi.org/10.1086/508635

Fine, P.V.A., Ree, R.H. & Burnham, R.J. 2008. Disparity in tree species richness between tropical, temperate and boreal biomes. The geographic area and age hypothesis. In: Carson, W.P. & Schnitzer, S.A. (editors), Tropical forest community ecology. Blackwell Scientific, p. 31–45. London.

Flohn, H. 1981. A hemispheric circulation asymmetry during late Tertiary. Geologische Rundschau, 70: 725–736.

Forasiepi, A.M., Soibelzon, L.H., Suárez, C., Sánchez, R., Quiroz, L.I., Jaramillo, C. & Sánchez–Villagra, M.R. 2014. Carnivorans at the Great American Biotic Interchange: New discoveries from the northern Neotropics. Naturwissenschaften, 101(11): 965–974. https://doi.org/10.1007/s00114-014-1237-4

Frailey, C.D. 1986. Late Miocene and Holocene mammals, exclusive of the Notoungulata, of the Rio Acre region, western Amazonia. Contribution in Sciences, 374: 1–46.

Frieling, J., Gebhardt, A., Hubert, M., Adekeye, O.A., Akande, S.O., Reichart, G.J., Middelburg, J.J., Schouten, S. & Sluijs, A. 2017. Extreme warmth and heat–stressed plankton in the tropics during the Paleocene – Eocene Thermal Maximum. Science Advances, 3(3): 1–9. https://doi.org/10.1126/sciadv.1600891

Friis, E.M., Crane, P.R., Pedersen, K.R., Stampanoni, M. & Marone, F. 2015. Exceptional preservation of tiny embryos documents seed dormancy in early angiosperms. Nature, 528: 551–554. https://doi.org/10.1038/nature16441

García, C. 1958. Investigación palinológica de la Formación Guaduas del Anticlinal de Guachetá–Lenguazaque–Tausa. Boletín de Geología, (2): 27–31.

Garzione, C.N., Molnar, P., Libarkin, J.C. & MacFadden, B.J. 2006. Rapid late Miocene rise of the Bolivian altiplano: Evidence for removal of mantle lithosphere. Earth and Planetary Science Letters, 241(3–4): 543–556. https://doi.org/10.1016/j.epsl.2005.11.026

Garzione, C.N., Hoke, G.D., Libarkin, J.C., Withers, S., MacFadden, B., Eiler, J., Ghosh, P. & Mulch, A. 2008. Rise of the Andes. Science, 320(5881): 1304–1307. https://doi.org/10.1126/science.1148615

Garzione, C.N., Auerbach, D.J., Smith, J.J.S., Rosario, J.J., Passey, B.H., Jordan, T.E. & Eiler, J.M. 2014. Clumped isotope evidence for diachronous surface cooling of the altiplano and pulsed surface uplift of the central Andes. Earth and Planetary Science Letters, 393: 173–181. https://doi.org/10.1016/j.epsl.2014.02.029

Gaston, K.J. 2000. Global patterns in biodiversity. Nature, 405: 220–227. https://doi.org/10.1038/35012228

Gehler, A., Gingerich, P.D. & Pack, A. 2016. Temperature and atmospheric CO_2 concentration estimates through the PETM using triple oxygen isotope analysis of mammalian bioapatite. Proceedings of the National Academy of Sciences of the United States of America, 113(28): 7739–7744. https://doi.org/10.1073/pnas.1518116113

Gentry, A.H. 1982a. Neotropical floristic diversity: Phytogeographical connections between Central and South America, Pleistocene climatic fluctuations, or an accident of the Andean Orogeny? Annals of the Missouri Botanical Garden, 69(3): 557–593. https://doi.org/10.2307/2399084

Gentry, A.H. 1982b. Patterns of Neotropical plant species diversity. Evolutionary Biology, 15: 1–84. https://doi.org/10.1007/978-1-4615-6968-8_1

Ghosh, P., Garzione, C.N. & Eiler, J.M. 2006. Rapid uplift of the altiplano revealed through ^{13}C–^{18}O bonds in paleosol carbonates. Science, 311(5760): 511–515. https://doi.org/10.1126/science.1119365

Gillett, J.B. 1962. Pest pressure, an underestimated factor in evolution. Systematics Association Publication, 4: 37–46.

Gingerich, P.D. 2006. Environment and evolution through the Paleocene – Eocene Thermal Maximum. Trends in Ecology & Evolution, 21(5): 246–253. https://doi.org/10.1016/j.tree.2006.03.006

Gómez–Navarro, C., Jaramillo, C., Herrera, F., Wing, S.L. & Callejas, R. 2009. Palms (Arecaceae) from a Paleocene rainforest of northern Colombia. American Journal of Botany, 96(7): 1300–1312. https://doi.org/10.3732/ajb.0800378

González, H., Lemoigne, I. & Martínez, J.O. 1977. Flora de la Formación Valle Alto, Jurásico en la cordillera Central de Colombia. Boletín de Ciencias de la Tierra, 2: 107–122.

González–Wevar, C.A., Hüne, M., Segovia, N.I., Nakano, T., Spencer, H.G., Chown, S.L., Saucède, T., Johnstone, G., Mansilla, A. & Poulin, E. 2016. Following the Antarctic Circumpolar Current: Patterns and processes in the biogeography of the limpet *Nacella* (Mollusca: Patellogastropoda) across the Southern Ocean. Journal of Biogeography, 44(4): 861–874. https://doi.org/10.1111/jbi.12908

Graham, A. 1988a. Studies in Neotropical paleobotany. VI. The lower Miocene communities of Panama–The Cucaracha Formation. Annals Missouri Botanical Garden, 75(4): 1467–1479.

Graham, A. 1988b. Studies in Neotropical paleobotany. V. The lower Miocene communities of Panama–The Culebra Formation. Annals Missouri Botanical Garden, 75(4): 1440–1466.

Graham, A. 1991. Studies in Neotropical paleobotany. X. The Pliocene communities of Panama–composition, numerical representations, and paleocommunity paleoenvironmental reconstructions. Annals Missouri Botanical Garden, 78(2): 465–475.

Graham, A. 1992. Utilization of the isthmian land bridge during the Cenozoic–paleobotanical evidence for timing, and the selective influence of altitudes and climate. Review of Palaeobotany and Palynology, 72(1–2): 119–128. https://doi.org/10.1016/0034-6667(92)90179-K

Graham, A. 1999. Late Cretaceous and Cenozoic history of North American vegetation. Oxford University Press, 350 p. New York.

Graham, A., editor. 2010. Late Cretaceous and Cenozoic history of Latin American vegetation and terrestrial environments. Missouri Botanical Garden Press, 618 p. Saint Louis, USA.

Graham, A. 2011. The age and diversification of terrestrial new world ecosystems through Cretaceous and Cenozoic time. American Journal of Botany, 98(3): 336–351. https://doi.org/10.3732/ajb.1000353

Gübeli, A.A., Hochuli, P. & Wildi, W. 1984. Lower Cretaceous turbiditic sediments from the Rif chain (northern Marocco)–palynology, stratigraphy and palaeogeographic setting. Geologische

Rundschau, 73(3): 1081–1114. https://doi.org/10.1007/BF01820889

Gutiérrez, N.M. & Jaramillo, C.A. 2007. Maastrichtian paleotemperature and paleoprecipitation from the Guaduas Formation, Colombia. Palynology, 32: 260.

Gutjahr, M., Ridgwell, A., Sexton, P.F., Anagnostou, E., Pearson, P.N., Pälike, H., Norris, R.D., Thomas, E. & Foster, G.L. 2017. Very large release of mostly volcanic carbon during the Palaeocene – Eocene Thermal Maximum. Nature, 548: 573–577. https://doi.org/10.1038/nature23646

Haffer, J. 1969. Speciation in Amazonian forest birds. Science, 165(3889): 131–137. https://doi.org/10.1126/science.165.3889.131

Hambalek, N. 1993. Palinoestratigrafía del Mioceno–Plioceno de la región de Urumaco, Falcón noroccidental. Bachelor thesis, Universidad Central de Venezuela, 168 p. Caracas.

Hambalek, N., Rull, V., Digiacomo, E. & Díaz de Gamero, M.L. 1994. Evolución paleoecológica y paleoambiental de la secuencia del Neógeno en el surco de Urumaco: Estudio palinológico y litológico. Boletín de la Sociedad Venezolana de Geología, 19: 7–19.

Haq, B.U., Hardenbol, J., Vail, P.R., Stover, L.E., Colin, J.P., Ioannides, N.S., Wright, R.C., Baum, G.R., Gombos–Jr, A.M., Pflum, C.E., Loutit, T.S., du Chêne, R.J., Romine, K.K., Sarg, J.F., Posamentier, H.W. & Morgan, B.E. 1988. Mesozoic and Cenozoic chronostratigraphy and cycles of sea–level change. In: Wilgus, C.K., Hastings, B.S., Posamentier, H., van Wagoner, J., Ross, C.A. & Kendall, C.G. (editors), Sea–level changes: An integrated approach. Society of Economic Paleontologists and Mineralogists, Special Publication 42, p. 71–108. https://doi.org/10.2110/pec.88.01.0071

Hastings, A., Bloch, J., Cadena, E. & Jaramillo, C. 2010. A new small short–snouted dyrosaurid (Crocodylomorpha, Mesoeucrocodylia) from the Paleocene of northeastern Colombia. Journal of Vertebrate Paleontology, 30(1): 139–162. https://doi.org/10.1080/02724630903409204

Hastings, A., Bloch, J. & Jaramillo, C. 2011. A new longirostrine dyrosaurid (Crocodylomorpha, Mesoeucrocodylia) from the Paleocene of north–eastern Colombia: Biogeographic and behavioural implications for new–world Dyrosauridae. Palaeontology, 54(5): 1095–1116. https://doi.org/10.1111/j.1475-4983.2011.01092.x

Hastings, A., Bloch, J., Jaramillo, C., Rincón, A. & MacFadden, B. 2013. Systematics and biogeography of crocodylians from the Miocene of Panama. Journal of Vertebrate Paleontology, 33(2): 239–263. https://doi.org/10.1080/02724634.2012.713814

Hastings, A., Bloch, J. & Jaramillo, C. 2014. A new blunt–snouted dyrosaurid, *Anthracosuchus balrogus* gen. et sp. nov. (Crocodylomorpha, Mesoeucrocodylia), from the Palaeocene of Colombia. Historical Biology: An International Journal of Paleobiology, 27(8): 998–1020. https://doi.org/10.1080/08912963.2014.918968

Haug, G. & Tiedemann, R. 1998. Effect of the formation of the Isthmus of Panama on Atlantic Ocean thermohaline circulation. Nature, 393: 673–676. https://doi.org/10.1038/31447

Haug, G.H., Hughen, K.A., Sigman, D.M., Peterson, L.C. & Röhl, U. 2001. Southward migration of the intertropical convergence zone through the Holocene. Science, 293(5533): 1304–1308. https://doi.org/10.1126/science.1059725

Head, J., Bloch, J., Hasting, A., Bourque, J., Cadena, E., Herrera, F., Polly, P.D. & Jaramillo, C. 2009a. Giant boid snake from the Palaeocene Neotropics reveals hotter past equatorial temperatures. Nature, 457(7230): 715–718. https://doi.org/10.1038/nature07671

Head, J., Bloch, J., Hasting, A., Bourque, J., Cadena, E., Herrera, F., Polly, P.D. & Jaramillo, C. 2009b. Head et al. reply. Nature, 460: E4–E5. https://doi.org/10.1038/nature08225

Head, J., Rincón, A., Suárez, C., Montes, C. & Jaramillo, C. 2012. Fossil evidence for earliest Neogene American faunal interchange: *Boa* (Serpentes, Boinae) from the early Miocene of Panama. Journal of Vertebrate Paleontology, 32(6): 1328–1334. https://doi.org/10.1080/02724634.2012.694387

Hendy, A.J.W., Jones, D.S., Moreno, F., Zapata, V. & Jaramillo, C. 2015. Neogene molluscs, shallow marine paleoenvironments, and chronostratigraphy of the Guajira Peninsula, Colombia. Swiss Journal of Palaeontology, 134(1): 45–75. https://doi.org/10.1007/s13358-015-0074-1

Herendeen, P.S., Friis, E.M., Pedersen, K.R. & Crane, P.R. 2017. Palaeobotanical redux: Revisiting the age of the angiosperms. Nature Plants, 3(17015): 1–8. https://doi.org/10.1038/nplants.2017.15

Herngreen, G.F.W. & Dueñas, H. 1990. Dating of the Cretaceous Une Formation, Colombia and the relationship with the Albian – Cenomanian African–South American microfloral province. Review of Palaeobotany and Palynology, 66(3–4): 345–359. https://doi.org/10.1016/0034-6667(90)90046-L

Herngreen, G.F.W., Kedves, M., Rovnina, L.V. & Smirnova, S.B. 1996. Cretaceous palynofloral provinces: A review. In: Jansonius, J. & McGregor, D.C. (editors), Palynology: Principles and applications. American Association of Stratigraphic Palynologists Foundation, 3, p. 1157–1188. Dallas.

Herrera, F., Jaramillo, C., Dilcher, D., Wing, S.L. & Gómez, C. 2008. Fossil Araceae from a Paleocene Neotropical rainforest in Colombia. American Journal of Botany, 95(12): 1569–1583. https://doi.org/10.3732/ajb.0800172

Herrera, F., Manchester, S., Jaramillo, C., MacFadden, B. & da Silva–Caminha, S. 2010. Phytogeographic history and phylogeny of the Humiriaceae. International Journal of Plant Sciences, 171(4): 2004–2017. https://doi.org/10.1086/651229

Herrera, F., Manchester, S.R., Hoot, S.B., Wefferling, K., Carvalho, M. & Jaramillo, C. 2011. Phytogeographic implications of fossil endocarps of Menispermaceae from the Paleocene of Colombia. American Journal of Botany, 98(12): 1–14. https://doi.org/10.3732/ajb.1000461

Herrera, F., Manchester, S., Vélez–Juarbe, J. & Jaramillo, C.A. 2014a. Phytogeographic history of the Humiriaceae (Part 2). International Journal of Plant Science, 175(7): 828–840. https://doi.org/10.1086/676818

Herrera, F., Manchester, S.R., Carvalho, M.R., Jaramillo, C. & Wing, S.L. 2014b. Paleocene wind–dispersed fruits and seeds from Colombia and their implications for early Neotropical rainforests. Acta Palaeobotanica, 54(2): 197–229. https://doi.org/10.2478/acpa-2014-0008

Herrera, F., Manchester, S.R., Koll, R. & Jaramillo, C. 2014c. Fruits of *Oreomunnea* (Juglandaceae) in the early Miocene of Panama. In: Stevens, W.D., Montiel, O.M. & Raven, P. (editors), Paleobotany and biogeography: A festschrift for Alan Graham in his 80th year. Missouri Botanical Garden Press, p. 124–133. Saint Louis, USA.

Hinojosa, F. & Villagrán, C. 2005. Did South American mixed paleofloras evolve under thermal equability or in the absence of an effective Andean barrier during the Cenozoic? Palaeogeography, Palaeoclimatology, Palaeoecology, 217(1–2): 1–23. https://doi.org/10.1016/j.palaeo.2004.11.013

Hooghiemstra, H. & van der Hammen, T. 1998. Neogene and Quaternary development of the Neotropical rain forest: The forest refugia hypothesis, and a literature overview. Earth–Science Reviews, 44(3–4): 147–183. https://doi.org/10.1016/S0012-8252(98)00027-0

Hooghiemstra, H., Wijninga, V.M. & Cleef, A.M. 2006. The paleobotanical record of Colombia: Implications for biogeography and biodiversity. Annals of the Missouri Botanical Garden, 93(2): 297–325.

Hoorn, C. 1994a. An environmental reconstruction of the palaeo–Amazon River system (middle – late Miocene, NW Amazonia). Palaeogeography, Palaeoclimatology, Palaeoecology, 112(3–4): 187–238. https://doi.org/10.1016/0031-0182(94)90074-4

Hoorn, C. 1994b. Fluvial palaeoenvironments in the intracratonic Amazonas Basin (early Miocene – early middle Miocene, Colombia). Palaeogeography, Palaeoclimatology, Palaeoecology, 109(1): 1–54. https://doi.org/10.1016/0031-0182(94)90117-1

Hoorn, C., Guerrero, J., Sarmiento, G.A. & Lorente, M.A. 1995. Andean tectonics as a cause for changing drainage patterns in Miocene northern South America. Geology, 23(3): 237–240. https://doi.org/10.1130/0091-7613(1995)023<0237:ATAACF>2.3.CO;2

Hoorn, C., Wesselingh, F.P., ter Steege, H., Bermúdez, M.A., Mora, A., Sevink, J., Sanmartín, I., Sánchez–Meseguer, A., Anderson, C.L., Figueiredo, J.P., Jaramillo, C., Riff, D., Negri, F.R., Hooghiemstra, H., Lundberg, J., Stadler, T., Särkinen, T. & Antonelli, A. 2010. Amazonia through time: Andean uplift, climate change, landscape evolution, and biodiversity. Science, 330(6006): 927–931. https://doi.org/10.1126/science.1194585

Hoorn, C., Bogotá, G.R., Romero–Báez, M., Lammertsma, E.I., Flantua, S.G.A., Dantas, E.L., Dino, R., do Carmo, D.A. & Chemale Jr., F. 2017. The Amazon at sea: Onset and stages of the Amazon River from a marine record, with special reference to Neogene plant turnover in the drainage basin. Global and Planetary Change, 153: 51–65. https://doi.org/10.1016/j.gloplacha.2017.02.005

Hotton, C.L. 2002. Palynology of the Cretaceous – Tertiary boundary in Central Montana: Evidence for extraterrestrial impact as a cause of the terminal Cretaceous extinctions. In: Hartman, J.H., Johnson, K.R. & Nichols, D.J. (editors), The Hell Creek Formation and the Cretaceous – Tertiary boundary in the northern great plains: An integrated continental record of the end of the Cretaceous. Geological Society of America, Special Paper 361, p. 473–502. Boulder, USA. https://doi.org/10.1130/0-8137-2361-2.473

Hovan, S. 1995. Late Cenozoic atmospheric circulation intensity and climatic history recorded by eolian deposition in the eastern equatorial Pacific Ocean, Leg 138. In: Pisias, N.G., Mayer, L.A., Janecek, T.R., Palmer–Julson, A. & van Andel, T.H. (editors), Proceedings of the Ocean Drilling Program. Scientific Results 138, p. 615–625. https://doi.org/10.2973/odp.proc.sr.138.132.1995

Huber, M. 2008. A hotter greenhouse? Science, 321(5887): 353–354. https://doi.org/10.1126/science.1161170

Huber, M. 2009. Snakes tell a torrid tale. Nature, 457: 669–671. https://doi.org/10.1038/457669a

Huber, M. & Caballero, R. 2011. The early Eocene equable climate problem revisited. Climate of the Past, 7: 603–633. https://doi.org/10.5194/cp-7-603-2011

Huber, M. & Sloan, L.C. 1999. Warm climate transitions: A general circulation modeling study of the late Paleocene Thermal Maximum (~56 Ma). Journal of Geophysical Research: Atmospheres, 104(D14): 16633–16655. https://doi.org/10.1029/1999JD900272

Huber, M. & Sloan, L.C. 2000. Climatic responses to tropical sea surface temperature changes on a "greenhouse" Earth. Paleoceanography and Paleoclimatology, 15(4): 443–450. https://doi.org/10.1029/1999PA000455

Huber, M., Sloan, L.C. & Shellito, C. 2003. Early Paleogene oceans and climate: A fully coupled modeling approach using the NCAR CCSM. In: Wing, S.L., Gingerich, P.D., Schmitz, B. & Thomas, E. (editors), Causes and consequences of globally warm climates in the early Paleogene. Geological Society of America, Special Paper 369, p. 25–47. Boulder, USA. https://doi.org/10.1130/0-8137-2369-8.25

Huertas, G. 2003. Flora fósil de Villa de Leyva y sus alrededores (Boyacá, Colombia, Suramérica). Camargo Editores, 151 p. Chía, Colombia.

Jablonski, D. 1993. The tropics as a source of evolutionary novelty through geological time. Nature, 364: 142–144. https://doi.org/10.1038/364142a0

Jacobs, B., Kingston, J. & Jacobs, L. 1999. The origin of grass–dominated ecosystems. Annals of the Missouri Botanical Garden, 86(2): 590–643. https://doi.org/10.2307/2666186

Jacques, F.M., Wang, W., Ortiz, R., Li, H.L., Zhou, Z.K. & Chen, Z. 2011. Integrating fossils in a molecular–based phylogeny and testing them as calibration points for divergence time estimates in Menispermaceae. Journal of Systematics and Evolution, 49(1): 25–49. https://doi.org/10.1111/j.1759-6831.2010.00105.x

Janzen, D.H. 1970. Herbivores and the number of tree species in tropical forests. The American Naturalist, 104(940): 501–528. https://doi.org/10.1086/282687

Jaramillo, C. 2002. Response of tropical vegetation to Paleogene warming. Paleobiology, 28(2): 222–243. https://doi.org/10.1666/0094-8373(2002)028<0222:ROTVTP>2.0.CO;2

Jaramillo, C. 2018. Evolution of the Isthmus of Panama: Biological, paleoceanographic, and paleoclimatological implications. In: Hoorn, C., Perrigo, A. & Antonelli, A. (editors), Mountains, climate and biodiversity. Wiley–Blackwell, p. 323–338. Chichester, UK.

Jaramillo, C. & Cárdenas, A. 2013. Global warming and Neotropical rainforests: A historical perspective. Annual Review of Earth and Planetary Sciences, 41: 741–766. https://doi.org/10.1146/annurev-earth-042711-105403

Jaramillo, C. & Dilcher, D.L. 2000. Microfloral diversity patterns of the late Paleocene – Eocene interval in Colombia, northern South America. Geology, 28(9): 815–818. https://doi.org/10.1130/0091-7613(2000)28<815:MDPOTL>2.0.CO;2

Jaramillo, C. & Dilcher, D.L. 2001. Middle Paleogene palynology of central Colombia, South America: A study of pollen and spores from tropical latitudes. Palaeontographica Abteilung B, 258(4–6): 87–213.

Jaramillo, C., Rueda, M. & Mora, G. 2006. Cenozoic plant diversity in the Neotropics. Science, 311(5769): 1893–1896. https://doi.org/10.1126/science.1121380

Jaramillo, C., Bayona, G., Pardo–Trujillo, A., Rueda, M., Torres, V., Harrington, G. & Mora, G. 2007. The palynology of the Cerrejón Formation (upper Paleocene) of northern Colombia. Palynology, 31(1): 153–189. https://doi.org/10.1080/01916122.2007.9989641

Jaramillo, C., Hoorn, C., Silva, S., Leite, F., Herrera, F., Quiroz, L., Dino, R. & Antonioli, L. 2010a. The origin of the modern Amazon rainforest: Implications of the palynological and palaeobotanical record. In: Hoorn, C. & Wesselingh, F.P. (editors), Amazonia: Landscape and species evolution: A look into the past. Wiley–Blackwell, John Wiley & Sons Ltd., Publication, p. 317–334. Chichester, UK. https://doi.org/10.1002/9781444306408.ch19

Jaramillo, C., Ochoa, D., Contreras, L., Pagani, M., Carvajal–Ortiz, H., Pratt, L.M., Krishnan, S., Cardona, A., Romero, M., Quiroz, L., Rodríguez, G., Rueda, M., De la Parra, F., Morón, S., Green, W., Bayona, G., Montes, C., Quintero, O., Ramírez, R., Mora, A., Schouten, S., Bermúdez, H., Navarrete, R.E., Parra, F., Alvarán, M., Osorno, J., Crowley, J.L., Valencia, V. & Vervoort, J. 2010b. Effects of rapid global warming at the Paleocene – Eocene boundary on Neotropical vegetation. Science, 330(6006): 957–961. https://doi.org/10.1126/science.1193833

Jaramillo, C., Cadena, E. & Herrera, F. 2014a. Diversidad fósil en el valle de Cerrejón. In: Báez, L. & Trujillo, F. (editors), Biodiversidad en Cerrejón. Carbones de Cerrejón, Fundación Omacha, Fondo para la Acción Ambiental y la Niñez. p. 39–55. Bogotá.

Jaramillo, C., Moreno, E., Ramirez, V., da Silva, S., de la Barrera, A., de la Barrera, A., Sánchez, C., Morón, S., Herrera, F., Escobar, J., Koll, R., Manchester, S.R. & Hoyos, N. 2014b. Palynological record of the last 20 million years in Panama. In: Stevens, W.D., Montiel, O.M. & Raven, P.H. (editors), Paleobotany and biogeography: A Festschrift for Alan Graham in his 80th year. Missouri Botanical Garden Press, p. 134–251. Saint Louis, USA.

Jaramillo, C., Moreno, F., Hendy, F., Sánchez–Villagra, M. & Marty, D. 2015. Preface: La Guajira, Colombia: A new window into the Cenozoic Neotropical biodiversity and the Great American Biotic Interchange. Swiss Journal of Palaeontology, 134: 1–4. https://doi.org/10.1007/s13358-015-0075-0

Jaramillo, C., Montes, C., Cardona, A., Silvestro, D., Antonelli, A. & Bacon, C.D. 2017a. Comment (1) on "Formation of the Isthmus of Panama" by O'Dea et al. Science Advances, 3(6): 1–8. https://doi.org/10.1126/sciadv.1602321

Jaramillo, C., Romero, I., D'Apolito, C., Bayona, G., Duarte, E., Louwye, S., Escobar, J., Luque, J., Carrillo–Briceno, J., Zapata, V., Mora, A., Schouten, S., Zavada, M., Harrington, G., Ortiz, J. & Wesselingh, F. 2017b. Miocene flooding events of western Amazonia. Science Advances, 3(5): 1–11. https://doi.org/10.1126/sciadv.1601693

Jud, N.A., Nelson, C.W. & Herrera, F. 2016. Fruits and wood of *Parinari* from the early Miocene of Panama and the fossil record of Chrysobalanaceae. American Journal of Botany, 103(2): 277–289. https://doi.org/10.3732/ajb.1500425

Kar, N., Garzione, C.N., Jaramillo, C., Shanahan, T., Carlotto, V., Pullen, A., Moreno, F., Anderson, V., Moreno, E. & Eiler, J. 2016. Rapid regional surface uplift of the northern Altiplano Plateau revealed by multiproxy paleoclimate reconstruction. Earth and Planetary Science Letters, 447: 33–47. https://doi.org/10.1016/j.epsl.2016.04.025

Kay, R.F., Madden, R.H., Cifelli, R.L. & Flynn, J.J., editors. 1997. Vertebrate paleontology in the Neotropics: The Miocene fauna of La Venta, Colombia. Smithsonian Institution Press, 608 p. Washington, D.C.

Keigwin, L.D. 1982. Isotopic paleoceanography of the Caribbean and East Pacific: Role of Panama uplift in late Neogene time. Science, 217(4557): 350–353. https://doi.org/10.1126/science.217.4557.350

Kemp, E.M. 1968. Probable angiosperm pollen from the British Barremian to Albian strata. Palaeontology, 11(3): 421–434.

Kennett, J.P. & Stott, L.D. 1991. Abrupt deep–sea warming, palaeoceanographic changes and benthic extinctions at the end of the Paleocene. Nature, 353: 225–229. https://doi.org/10.1038/353225a0

Krause, G.H., Winter, K., Krause, B., Jahns, P., García, M., Aranda, J. & Virgo, A. 2010. High–temperature tolerance of a tropical tree, *Ficus insipida*: Methodological reassessment and climate change considerations. Functional Plant Biology, 37(9): 890–900. https://doi.org/10.1071/FP10034

Kreft, H. & Jetz, W. 2007. Global patterns and determinants of vascular plant diversity. Proceedings of the National Academy of Sciences of the United States of America, 104(14): 5925–5930. https://doi.org/10.1073/pnas.0608361104

Lammertsma, E.I., Boer, H.J., Dekker, S.C., Dilcher, D.L., Lotter, A.F. & Wagner–Cremer, F. 2011. Global CO_2 rise leads to reduced maximum stomatal conductance in Florida vegetation. Proceedings of the National Academy of Sciences of the United States of America, 108(10): 4035–4040. https://doi.org/10.1073/pnas.1100371108

Latrubesse, E.M., Cozzuol, M., da Silva–Caminha, S.A., Rigsby, C.A., Absy, M.L. & Jaramillo, C. 2010. The late Miocene paleogeography of the Amazon Basin and the evolution of the Amazon River system. Earth–Science Reviews, 99(3–4): 99–124. https://doi.org/10.1016/j.earscirev.2010.02.005

Lefebvre, V., Donnadieu, Y., Sepulchre, P., Swingedouw, D. & Zhang, Z. 2012. Deciphering the role of southern gateways and carbon dioxide on the onset of the Antarctic Circumpolar Current. Paleoceanography and Paleoclimatology, 27(4): 1–9. https://doi.org/10.1029/2012PA002345

Lehmann, C.E., Archibald, S.A., Hoffmann, W.A. & Bond, W.J. 2011. Deciphering the distribution of the savanna biome. New Phytologist, 191(1): 197–209. https://doi.org/10.1111/j.1469-8137.2011.03689.x

Leigh, E.G., Davidar, P., Dick, C., Puyravaud, J., Terborgh, J., ter Steege, H. & Wright, S. 2004. Why do some tropical forests have so many species of trees? Biotropica, 36(4): 447–473. https://doi.org/10.1111/j.1744-7429.2004.tb00342.x

Leigh, E.G., O'Dea, A. & Vermeij, G.J. 2013. Historical biogeography of the Isthmus of Panama. Biological Reviews, 89(1): 148–172. https://doi.org/10.1111/brv.12048

Leighton, L.R. 2005. The latitudinal diversity gradient through deep time: Testing the "age of the tropics" hypothesis using Carboniferous productidine brachiopods. Evolutionary Ecology, 19(6): 563–581. https://doi.org/10.1007/s10682-005-1021-1

Leite, R.N., Kolokotronis, S.O., Almeida, F.C., Werneck, F., Rogers, D.S. & Weksler, M. 2014. In the wake of invasion: Tracing the historical biogeography of the South American cricetid radiation (Rodentia, Sigmodontinae). PLOS ONE, 9(6): 1–12. https://doi.org/10.1371/journal.pone.0100687

Lemoigne, Y. 1984. Données nouvelles sur la paléoflore de Colombie. Geobios, 17(6): 667–690. https://doi.org/10.1016/S0016-6995(84)80115-1

Lerdau, M.T. & Throop, H.L. 1999. Isoprene emission and photosynthesis in a tropical forest canopy: Implications for model development. Ecological Applications, 9(4): 1109–1117. https://doi.org/10.1890/1051-0761(1999)009[1109:IEAPIA]2.0.CO;2

Lewis, S.L., Malhi, Y. & Phillips, O.L. 2004. Fingerprinting the impacts of global change on tropical forests. Philosophical Transactions of the Royal Society of London Series B: Biological Sciences, 359(1443): 437–462. https://doi.org/10.1098/rstb.2003.1432

Linares, O. 2004. Bioestratigrafía de la fauna de mamíferos de las formaciones Socorro, Urumaco y Codore (Mioceno medio–Plioceno temprano, de la región de Urumaco, Falcón, Venezuela. Paleobiología Neotropical, 1: 1–26.

Liu, Z., Pagani, M., Zinniker, D., DeConto, R., Huber, B.T., Brinkhuis, H., Shah, S.R., Leckie, R.M. & Pearson, A. 2009. Global cooling during the Eocene – Oligocene climate transition. Science, 323(5918): 1187–1190. https://doi.org/10.1126/science.1166368

Lloyd, J. & Farquhar, G.D. 1994. ^{13}C discrimination during CO_2 assimilation by the terrestrial biosphere. Oecologia, 99(3–4): 201–215. https://doi.org/10.1007/BF00627732

Lloyd, J. & Farquhar, G.D. 2008. Effects of rising temperatures and [CO2] on the physiology of tropical forest trees. Philosophical Transactions of the Royal Society of London Series B: Biological Sciences, 363(1498): 1811–1817. https://doi.org/10.1098/rstb.2007.0032

Lupia, R., Lidgard, S. & Crane, P.R. 1999. Comparing palynological abundance and diversity: Implications for biotic replacement during the Cretaceous angiosperm radiation. Paleobiology, 25(3): 305–340. https://doi.org/10.1017/S009483730002131X

Lüthi, D., Le Floch, M., Bereiter, B., Blunier, T., Barnola, J.M., Siegenthaler, U., Raynaud, D., Jouzel, J., Fischer, H., Kawamura, K. & Stocker, T.F. 2008. High–resolution carbon dioxide concentration record 650 000–800 000 years before present. Nature, 453: 379–382. https://doi.org/10.1038/nature06949

MacFadden, B.J. 2006a. Extinct mammalian biodiversity of the ancient New World tropics. Trends in Ecology & Evolution, 21(3): 157–165. https://doi.org/10.1016/j.tree.2005.12.003

MacFadden, B.J. 2006b. North American Miocene land mammals from Panama. Journal of Vertebrate Paleontology, 26(3): 720–734. https://doi.org/10.1671/0272-4634(2006)26[720:NAMLMF]2.0.CO;2

MacFadden, B.J. 2009. Three–toed browsing horse *Anchiterium* (Echidae) from the Miocene of Panama. Journal of Paleontology, 83(3): 489–492.

MacFadden, B.J. & Higgins, P. 2004. Ancient ecology of 15–million–year–old browsing mammals within C3 plant communities from Panama. Oecologia, 140(1): 169–182. https://doi.org/10.1007/s00442-004-1571-x

MacFadden, B.J., Kirby, M.X., Rincon, A., Montes, C., Moron, S., Strong, N. & Jaramillo, C. 2010. Extinct peccary *"Cynorca" Occidentale* (Tayassuidae, Tayassuinae) from the Miocene of Panama and correlations to North America. Journal of Paleontology, 84(2): 288–298. https://doi.org/10.1666/09-064R.1

MacFadden, B.J., Foster, D.A., Rincón, A.F., Morgan, G.S. & Jaramillo, C. 2012. The New World tropics as a cradle of biodiversity

during the early Miocene: Calibration of the centenario fauna from Panama. Geological Society of America Abstracts with Programs, 44, p. 163.

Magallón, S. & Castillo, A. 2009. Angiosperm diversification through time. American Journal of Botany, 96(1): 349–365. https://doi.org/10.3732/ajb.0800060

Magallón, S., Crane, P.R. & Herendeen, P.S. 1999. Phylogenetic pattern, diversity, and diversification of eudicots. Annals of the Missouri Botanical Garden, 86(2): 297–372.

Martínez, C., Carvalho, M., Madriñan, S. & Jaramillo, C.A. 2015. A Late Cretaceous *Piper* (Piperaceae) from Colombia and diversification patterns for the genus. American Journal of Botany, 102(2): 273–289. https://doi.org/10.3732/ajb.1400427

Martínez, J.I. 2009. La historia cenozoica del fenómeno de El Niño. Revista de la Academia Colombiana de Ciencias Exactas, Físicas y Naturales, 33(129): 491–512.

McInerney, F.A. & Wing, S.L. 2011. The Paleocene – Eocene Thermal Maximum: A perturbation of carbon cycle, climate, and biosphere with implications for the future. Annual Review of Earth and Planetary Sciences, 39: 489–516. https://doi.org/10.1146/annurev-earth-040610-133431

Mejía–Velásquez, P.J. 2007. Floral composition of a Lower Cretaceous paleotropical ecosystem inferred from quantitative palynology. Master thesis, University of Florida, 85 p. Gainesville, USA.

Mejía–Velásquez, P., Dilcher, D., Jaramillo, C., Fortini, L. & Manchester, R.S. 2012. Palynological composition of a Lower Cretaceous South American tropical sequence: Climatic implications and diversity comparisons with other latitudes. American Journal of Botany, 99(11): 1819–1827. https://doi.org/10.3732/ajb.1200135

Mikolajewicz, U., Maier–Reimer, E., Crowley, T.J. & Kim, K.Y. 1993. Effect of Drake and Panamanian gateways on the circulation of an ocean model. Paleoceanography and Paleoclimatology, 8(4): 409–426. https://doi.org/10.1029/93PA00893

Miller, K.G., Kominz, M.A., Browning, J.V., Wright, J.D., Mountain, G.S., Katz, M.E., Sugarman, P.J., Cramer, B.S., Christie–Blick, N. & Pekar, S.F. 2005. The Phanerozoic record of global sea–level change. Science, 310(5752): 1293–1298. https://doi.org/10.1126/science.1116412

Molnar, P. 2008. Closing of the Central American Seaway and the ice age: A critical review. Paleoceanography and Paleoclimatology, 23(2): 1–15. https://doi.org/10.1029/2007PA001574

Molnar, P. 2017. Comment (2) on "Formation of the Isthmus of Panama" by O'Dea et al. Science Advances, 3(6): 1–4. https://doi.org/10.1126/sciadv.1602320

Monnin, E., Indermühle, A., Dällenbach, A., Flückiger, J., Stauffer, B., Stocker, T.F., Raynaud, D. & Barnola, J.M. 2001. Atmospheric CO_2 concentrations over the last glacial termination. Science, 291(5501): 112–114. https://doi.org/10.1126/science.291.5501.112

Montes, C., Bayona, G., Cardona, A., Buchs, D.M., Silva, C.A., Morón, S., Hoyos, N., Ramírez, D.A., Jaramillo, C. & Valencia, V. 2012a. Arc–continent collision and orocline formation: Closing of the Central American Seaway. Journal of Geophysical Research: Solid Earth, 117(B4): 25 p. https://doi.org/10.1029/2011JB008959

Montes, C., Cardona, A., McFadden, R.R., Morón, S., Silva, C.A., Restrepo–Moreno, S., Ramírez, D., Hoyos, N., Wilson, J., Farris, D.W., Bayona, G., Jaramillo, C., Valencia, V., Bryan, J. & Flores, J.A. 2012b. Evidence for middle Eocene and younger land emergence in Central Panama: Implications for isthmus closure. Geological Society of America Bulletin, 124(5–6): 780–799. https://doi.org/10.1130/B30528.1

Montes, C., Cardona, A., Jaramillo, C., Pardo, A., Silva, J.C., Valencia, V., Ayala, C., Pérez–Ángel, L.C., Rodríguez–Parra, L.A., Ramírez, V. & Niño, H. 2015. Middle Miocene closure of the Central American Seaway. Science, 348(6231): 226–229. https://doi.org/10.1126/science.aaa2815

Moore, M.J., Soltis, P.S., Bell, C.D., Burleigh, J.G. & Soltis, D.E. 2010. Phylogenetic analysis of 83 plastid genes further resolves the early diversification of eudicots. Proceedings of the National Academy of Sciences of the United States of America, 107(10): 4623–4628. https://doi.org/10.1073/pnas.0907801107

Moreno–Bernal, J.W., Head, J. & Jaramillo, C. 2016. Fossil crocodilians from the high Guajira Peninsula of Colombia: Neogene faunal change in northernmost South America. Journal of Vertebrate Paleontology, 36(3): 1–17. https://doi.org/10.1080/02724634.2016.1110586

Moreno, J.F., Hendy, A.J.W., Quiroz, L., Hoyos, N., Jones, D.S., Zapata, V., Zapata, S., Ballen, G.A., Cadena, E., Cárdenas, A.L., Carrillo–Briceño, J.D., Carrillo, J.D., Delgado–Sierra, D., Escobar, J., Martínez, J.I., Martínez, C., Montes, C., Moreno, J., Pérez, N., Sánchez, R., Suárez, C., Vallejo–Pareja, M.C. & Jaramillo, C. 2015. Revised stratigraphy of Neogene strata in the Cocinetas Basin, La Guajira, Colombia. Swiss Journal of Palaeontology, 134(1): 5–43. https://doi.org/10.1007/s13358-015-0071-4

Morgan, M.E., Kingston, J.D. & Marino, B.D. 1994. Carbon isotopic evidence for the emergence of C4 plants in the Neogene from Pakistan and Kenya. Nature, 367: 162–165. https://doi.org/10.1038/367162a0

Moritz, C., Patton, J.L., Schneider, C.J. & Smith, T.B. 2000. Diversification of rainforest faunas: An integrated molecular approach. Annual Review of Ecology and Systematics, 31: 533–563. https://doi.org/10.1146/annurev.ecolsys.31.1.533

Muller–Landau, H.C. 2010. The tolerance–fecundity trade–off and the maintenance of diversity in seed size. Proceedings of the National Academy of Sciences of the United States of America, 107(9): 4242–4247. https://doi.org/10.1073/pnas.0911637107

Near, T.J., Dornburg, A., Kuhn, K.L., Eastman, J.T., Pennington, J.N., Patarnello, T., Zane, L., Fernández, D.A. & Jones, C.D. 2012. Ancient climate change, antifreeze, and the evolutionary diversification of Antarctic fishes. Proceedings of the National

Academy of Sciences of the United States of America, 109(9): 3434–3439. https://doi.org/10.1073/pnas.1115169109

Nichols, D.J. & Johnson, K.G. 2008. Plants and the K–T boundary. Cambridge University Press, 292 p. Cambridge, UK. https://doi.org/10.1093/aob/mcp052

Niu, S., Wu, M., Han, Y., Xia, J., Li, L. & Wan, S. 2008. Water–mediated responses of ecosystem carbon fluxes to climatic change in a temperate steppe. New Phytologist, 177(1): 209–219. https://doi.org/10.1111/j.1469-8137.2007.02237.x

O'Dea, A., Lessios, H.A., Coates, A.H., Eytan, R., Restrepo–Moreno, S., Cione, A.L., Collins, L.S., De Queiroz, A., Farris, D.W., Norris, R.D., Stallard, R.F., Woodburne, M.O., Aguilera, O., Aubry, M., Berggren, W.A., Budd, A.F., Cozzuol, M.A., Coppard, S.E., Duque–Caro, H., Finnegan, S., Gasparini, G.M., Grossman, E.L., Johnson, K.G., Keigwin, L.D., Knowlton, N., Leigh, E.G., Leonard–Pingel, J.S., Marko, P.B., Pyenson, N.D., Rachello–Dolmen, P.G., Soibelzon, E., Soibelzon, L., Todd, J.A., Vermeij, G.J. & Jackson, J.B. 2016. Formation of the Isthmus of Panama. Science Advances, 2(8): 1–11. https://doi.org/10.1126/sciadv.1600883

Olson, D.M., Dinerstein, E., Wikramanayake, E.D., Burgess, N.D., Powell, G.V.N., Underwood, E.C., D'Amico, J.A., Itoua, I., Strand, H.E., Morrison, J.C., Loucks, C.J., Allnutt, T.F., Ricketts, T.H., Kura, Y., Lamoreux, J.F., Wettengel, W.W., Hedao, P. & Kassem, K.R. 2001. Terrestrial ecoregions of the world: A new map of life on Earth. BioScience, 51(11): 933–938. https://doi.org/10.1641/0006-3568(2001)051[0933:TEOTWA]2.0.CO;2

Ornelas, J.F., González, C., Espinosa de los Monteros, A., Rodríguez–Gómez, F. & García–Feria, L.M. 2013. In and out of Mesoamerica: Temporal divergence of *Amazilia* hummingbirds pre–dates the orthodox account of the completion of the Isthmus of Panama. Journal of Biogeography, 41(1): 168–181. https://doi.org/10.1111/jbi.12184

Pagani, M., Liu, Z.H., LaRiviere, J. & Ravelo, A.C. 2010. High Earth–system climate sensitivity determined from Pliocene carbon dioxide concentrations. Nature Geoscience, 3: 27–30. https://doi.org/10.1038/ngeo724

Pardo–Trujillo, A. 2004. Paleocene – Eocene palynology and palynofacies from northeastern Colombia and western Venezuela. Doctoral thesis, Université de Liège, 103 p. Liège, Belgium.

Pardo–Trujillo, A. & Jaramillo, C. 2002. New palynostratigraphical data of NW South America Paleocene – Eocene of the Middle Magdalena Valley, Colombia. International Journal of Tropical Geology, Geography and Ecology, 26(1): 1–10.

Pardo–Trujillo, A., Jaramillo, C. & Oboh–Ikuenobe, F. 2003. Paleogene palynostratigraphy of the eastern Middle Magdalena Valley, Colombia. Palynology, 27(1): 155–178. https://doi.org/10.1080/01916122.2003.9989585

Peppe, D.J., Royer, D.L., Cariglino, B., Oliver, S.Y., Newman, S., Leight, E., Enikolopov, G., Fernández–Burgos, M., Herrera, F., Adams, J.M., Correa, E., Currano, E.D., Erickson, J.M., Hinojosa, L.F., Hoganson, J.W., Iglesias, A., Jaramillo, C.A., Johnson, K.R., Jordan, G.J., Kraft, N.J.B., Lovelock, E.C., Lusk, C.H., Niinemets, U., Peñuelas, J., Rapson, G., Wing, S.L. & Wright, I.J. 2011. Sensitivity of leaf size and shape to climate: Global patterns and paleoclimatic applications. New Phytologist, 190(3): 724–739. https://doi.org/10.1111/j.1469-8137.2010.03615.x

Pérez–Consuegra, N., Cuervo–Gómez, A., Martínez, C., Montes, C., Herrera, F., Madriñán, S. & Jaramillo, C. 2017. Paleogene *Salvinia* (Salviniaceae) from Colombia and their paleobiogeographic implications. Review of Palaeobotany and Palynology, 246: 85–108. https://doi.org/10.1016/j.revpalbo.2017.06.003

Pérez–Consuegra, N., Parra, M., Jaramillo, C., Silvestro, D., Echeverri, S., Montes, C., Jaramillo, J.M. & Escobar, J. 2018. Provenance analysis of the Pliocene Ware Formation in the Guajira Peninsula, northern Colombia: Paleodrainage implications. Journal of South American Earth Sciences, 81: 66–77. https://doi.org/10.1016/j.jsames.2017.11.002

Pérez, M., Vallejo–Pareja, M.C., Carrillo, J.D. & Jaramillo, C. 2017. A new Pliocene capybara (Rodentia, Caviidae) from northern South America (Guajira, Colombia), and its implications for the Great American Biotic Interchange. Journal of Mammalian Evolution, 24(1): 111–125. https://doi.org/10.1007/s10914-016-9356-7

Pimiento, C., Griffin, J.N., Clements, C.F., Silvestro, D., Varela, S., Uhen, M. & Jaramillo, C. 2017. The Pliocene marine megafauna extinction and its impact on functional diversity. Nature Ecology & Evolution, 1: 1100–1106. https://doi.org/10.1038/s41559-017-0223-6

Pinto–Sánchez, N., Ibáñez, R., Madriñán, S., Sanjur, O., Bermingham, E. & Crawford, A.J. 2012. The Great American Biotic Interchange in frogs: Multiple and early colonization of Central America by the South American genus *Pristimantis* (Anura: Craugastoridae). Molecular Phylogenetics and Evolution, 62(3): 954–972. https://doi.org/10.1016/j.ympev.2011.11.022

Pons, D. 1988. Le Mesozoique de Colombie: Macroflores et microflores, Paris, Editions du Centre National de la Recherche Scientifique: Diffusion Presses du CNRS, Cahiers de paleontologie. Travaux de paliontologie est–africaine, 168 p.

Poveda, G., Waylen, P.R. & Pulwarty, R.S. 2006. Annual and inter–annual variability of the present climate in northern South America and southern Mesoamerica. Palaeogeography, Palaeoclimatology, Palaeoecology, 234(1): 3–27. https://doi.org/10.1016/j.palaeo.2005.10.031

Quiroz, L.I. & Jaramillo, C. 2010. Stratigraphy and sedimentary environments of Miocene shallow to marginal marine deposits in the Urumaco Trough, Falcon Basin, western Venezuela. In: Sánchez–Villagra, M., Aguilera, O. & Carlini, A.A. (editors), Urumaco and Venezuelan paleontology: The fossil record of the northern Neotropics. Indiana University Press, p. 153–172. Bloomington, USA.

Ramírez, S.R., Gravendeel, B., Singer, R.B., Marshall, C.R. & Pierce, N.E. 2007. Dating the origin of the Orchidaceae from a fossil

orchid with its pollinator. Nature, 448: 1042–1045. https://doi.org/10.1038/nature06039

Rangel, A., Moldowan, J.M., Nino, C., Parra, P. & Giraldo, B.N. 2002. Umir Formation: Organic geochemical and stratigraphic assessment as cosource for Middle Magdalena Basin oil, Colombia. American Association of Petroleum Geologists Bulletin, 86(12): 2069–2087. https://doi.org/10.1306/61EEDE04-173E-11D7-8645000102C1865D

Ravelo, A.C., Dekens, P.S. & McCarthy, M. 2006. Evidence for El Niño–like conditions during the Pliocene. Geological Society of America Today, 16(3): 4–11. https://doi.org/10.1130/1052-5173(2006)016<4:EFENLC>2.0.CO;2

Ricklefs, R.E. & Renner, S.S. 2012. Global correlations in tropical tree species richness and abundance reject neutrality. Science, 335(6067): 464–467. https://doi.org/10.1126/science.1215182

Rincon, A., Bloch, J.I., Suárez, C., MacFadden, B.J. & Jaramillo, C. 2012. New floridatragulines (Mammalia, Camelidae) from the early Miocene Las Cascadas Formation, Panama. Journal of Vertebrate Paleontology, 32(2): 456–475. https://doi.org/10.1080/02724634.2012.635736

Rincon, A., Bloch, J.I., MacFadden, B.J. & Jaramillo, C. 2013. First Central American record of Anthracotheriidae (Mammalia, Bothriodontinae) from the early Miocene of Panama. Journal of Vertebrate Paleontology, 33(2): 421–433. https://doi.org/10.1080/02724634.2013.722573

Rincón–Martínez, D., Lamy, F., Contreras, S., Leduc, G., Bard, E., Saukel, C., Blanz, T., Mackensen, A. & Tiedemann, R. 2010. More humid interglacials in Ecuador during the past 500 kyr linked to latitudinal shifts of the equatorial front and the intertropical convergence zone in the eastern tropical Pacific. Paleoceanography and Paleoclimatology, 25(2): 1–15. https://doi.org/10.1029/2009PA001868

Rodríguez–Reyes, O., Falcon–Lang, H.J., Gasson, P., Collinson, M.E. & Jaramillo, C. 2014. Fossil woods (Malvaceae) from the lower Miocene (early to mid–Burdigalian) part of the Cucaracha Formation of Panama (Central America) and their biogeographic implications. Review of Palaeobotany and Palynology, 209: 11–34. https://doi.org/10.1016/j.revpalbo.2014.05.006

Rodríguez–Reyes, O., Gasson, P., Falcon–Lang, H.J. & Collinson, M.E. 2017a. Fossil legume woods of the *Prioria*–clade (subfamily Detarioideae) from the lower Miocene (early to mid–Burdigalian) part of the Cucaracha Formation of Panama (Central America) and their systematic and palaeoecological implications. Review of Palaeobotany and Palynology, 246: 44–61. https://doi.org/10.1016/j.revpalbo.2017.06.005

Rodríguez–Reyes, O., Gasson, P., Thornton, C.V., Falcon–Lang, H.J. & Jud, N.A. 2017b. *Panascleroticoxylon crystallosa* gen. et sp. nov.: A new Miocene malpiguialean tree from Panama. IAWA Journal, 38(4): 437–455. https://doi.org/10.1163/22941932-20170178

Rosenzweig, M.L. 1995. Species diversity in space and time. Cambridge University Press, 460 p. Cambridge.

Roubik, D.W. & Camargo, J.M.F. 2011. The Panama microplate, island studies and relictual species of *Melipona (Melikerria)* (Hymenoptera: Apidae: Meliponini). Systematic Entomology, 37(1): 189–199. https://doi.org/10.1111/j.1365-3113.2011.00587.x

Royer, D. 2006. CO_2–forced climate thresholds during the Phanerozoic. Geochimica et Cosmochimica Acta, 70(23): 5665–5675. https://doi.org/10.1016/j.gca.2005.11.031

Royer, D. 2010. Fossil soils constrain ancient climate sensitivity. Proceedings of the National Academy of Sciences of the United States of America, 107(2): 517–518. https://doi.org/10.1073/pnas.0913188107

Royer, D. 2016. Climate sensitivity in the geologic past. Annual Review of Earth and Planetary Sciences, 44: 277–293. https://doi.org/10.1146/annurev-earth-100815-024150

Royer, D., Pagani, M. & Beerling, D.J. 2011. Geologic constraints on Earth system sensitivity to CO_2 during the Cretaceous and early Paleogene. Earth System Dynamic Discussions, 2: 211–240. https://doi.org/10.5194/esdd-2-211-2011

Royer, D. Pagani, M. & Beerling, D.J. 2012. Geobiological constraints on Earth system sensitivity to CO_2 during the Cretaceous and Cenozoic. Geobiology, 10(4): 298–310. https://doi.org/10.1111/j.1472-4669.2012.00320.x

Sacek, V. 2014. Drainage reversal of the Amazon River due to the coupling of surface and lithospheric processes. Earth and Planetary Science Letters, 401: 301–312. https://doi.org/10.1016/j.epsl.2014.06.022

Sage, R.F., Wedin, D.A. & Li, M. 1999. The biogeography of C_4 photosynthesis: Patterns and controlling factors. In: Sage, R.F. & Monson, R.K. (editors), C_4 plant biology. Academic Press, p. 313–373. San Diego, USA.

Sánchez–Villagra, M. 2006. Vertebrate fossils from the Neogene of Falcón state, Venezuela: Contributions on Neotropical palaeontology. Journal of Systematic Palaeontology, 4(3): 211. https://doi.org/10.1017/S1477201906001842

Sánchez–Villagra, M. & Aguilera, O. 2006. Neogene vertebrates from Urumaco, Falcón state, Venezuela: Diversity and significance. Journal of Systematic Palaeontology, 4(3): 213–220. https://doi.org/10.1017/S1477201906001829

Sánchez–Villagra, M., Aguilera, O. & Horovitz, I. 2003. The anatomy of the world's largest extinct rodent. Science, 301(5640): 1708–1710. https://doi.org/10.1126/science.1089332

Sarmiento, G. 1992. Palinología de la Formación Guaduas–estratigrafía y sistemática. Boletín Geológico, 32(1–3): 45–126.

Scheyer, T.M., Aguilera, O.A., Delfino, M., Fortier, D.C., Carlini, A.A., Sánchez, R., Carrillo–Briceño, J.D., Quiroz, L. & Sánchez–Villagra, M.R. 2013. Crocodylian diversity peak and extinction in the late Cenozoic of the northern Neotropics. Nature Communications, 4(1907): 1–9. https://doi.org/10.1038/ncomms2940

Schuettpelz, E. & Pryer, K.M. 2009. Evidence for a Cenozoic radiation of ferns in an angiosperm–dominated canopy. Proceedings of the National Academy of Sciences of the United States of America, 106(27): 11200–11205. https://doi.org/10.1073/pnas.0811136106

Schulte, P., Alegret, L., Arenillas, I., Arz, J.A., Barton, P.J., Bown, P.R., Bralower, T.J., Christeson, G.L., Claeys, P., Cockell, C.S., Collins, G.S., Deutsch, A., Goldin, T.J., Goto, K., Grajales–Nishimura, J.M., Grieve, R.A.F., Gulick, S.P.S., Johnson, K.R., Kiessling, W., Koeberl, C., Kring, D.A., MacLeod, K.G., Matsui, T., Melosh, J., Montanari, A., Morgan, J.V., Neal, C.R., Nichols, D.J., Norris, R.D., Pierazzo, E., Ravizza, G., Rebolledo–Vieyra, M., Reimold, W.U., Robin, E., Salge, T., Speijer, R.P., Sweet, A.R., Urrutia–Fucugauchi, J., Vajda, V., Whalen, M.T. & Willumsen, P.S. 2010. The Chicxulub asteroid impact and mass extinction at the Cretaceous – Paleogene boundary. Science, 327(5970): 1214–1218. https://doi.org/10.1126/science.1177265

Schultz, T.R. & Brady, S.G. 2008. Major evolutionary transitions in ant agriculture. Proceedings of the National Academy of Sciences of the United States of America, 105(14): 5435–5440. https://doi.org/10.1073/pnas.0711024105

Sepulchre, P., Sloan, L.C., Snyder, M. & Fiechter, J. 2009. Impacts of Andean uplift on the Humboldt Current system: A climate model sensitivity study. Paleoceanography and Paleoclimatology, 24(4): 1–11. https://doi.org/10.1029/2008PA001668

Sepulchre, P., Sloan, L.C. & Fluteau, F. 2010. Modelling the response of Amazonian climate to the uplift of the Andean mountain range. In: Hoorn, C. & Wesselingh, F.P. (editors), Amazonia: Landscape and species evolution: A look into the past. Wiley–Blackwell, John Wiley & Sons Ltd., Publication, p. 211–222. Chichester, UK.

Sepulchre, P., Arsouze, T., Donnadieu, Y., Dutay, J.C., Jaramillo, C., Le Bras, J., Martin, E., Montes, C. & Waite, A.J. 2014. Consequences of shoaling of the Central American Seaway determined from modeling Nd isotopes. Paleoceanography and Paleoclimatology, 29(3): 176–189. https://doi.org/10.1002/2013PA002501

Seton, M., Müller, R.D., Zahirovic, S., Gaina, C., Torsvik, T.H., Shephard, G., Talsma, A., Gurnis, M., Turner, M., Maus, S. & Chandler, M. 2012. Global continental and ocean basin reconstructions since 200 Ma. Earth–Science Reviews, 113(3–4): 212–270. https://doi.org/10.1016/j.earscirev.2012.03.002

Shackleton, N.J., Backman, J., Zimmerman, H., Kent, D.V., Hall, M.A., Roberts, D.G., Schnitker, D., Baldauf, J.G., Desprairies, A., Homrighausen, R., Huddlestun, P., Keene, J.B., Kaltenback, A.J., Krumsiek, K.A.O., Morton, A.C., Murray, J.W. & Westberg–Smith, J. 1984. Oxygen isotope calibration of the onset of ice–rafting and history of glaciation in the North Atlantic region. Nature, 307: 620–623. https://doi.org/10.1038/307620a0

Shellito, C.J., Sloan, L.C. & Huber, M. 2003. Climate model sensitivity to atmospheric CO_2 levels in the early – middle Paleogene. Palaeogeography, Palaeoclimatology, Palaeoecology, 193(1): 113–123. https://doi.org/10.1016/S0031-0182(02)00718-6

Shephard, G.E., Müller, R.D., Liu, L. & Gurnis, M. 2010. Miocene drainage reversal of the Amazon River driven by plate–mantle interaction. Nature Geoscience, 3: 870–875. https://doi.org/10.1038/ngeo1017

Siegenthaler, U., Stocker, T.F., Monnin, E., Lüthi, D., Schwander, J., Stauffer, B., Raynaud, D., Barnola, J.M., Fischer, H., Masson–Delmotte, V. & Jouzel, J. 2005. Stable carbon cycle–climate relationship during the late Pleistocene. Science, 310(5752): 1313–1317. https://doi.org/10.1126/science.1120130

Simpson, G.G. 1983. Splendid isolation: The curious history of South American mammals. Yale University Press, 275 p. New Haven, USA.

Slaughter, B.H. 1981. A new genus of geomyoid rodent from the Miocene of Texas and Panama. Journal of Vertebrate Paleontology, 1(1): 111–115. https://doi.org/10.1080/02724634.1981.10011884

Sloan, L.C. & Barron, E.J. 1992. A comparison of Eocene climate model results to quantified paleoclimatic interpretations. Palaeogeography, Palaeoclimatology, Palaeoecology, 93(3–4): 183–202. https://doi.org/10.1016/0031-0182(92)90096-N

Sloan, L.C. & Morrill, C. 1998. Orbital forcing and Eocene continental temperatures. Palaeogeography, Palaeoclimatology, Palaeoecology, 144(1–2): 21–35. https://doi.org/10.1016/S0031-0182(98)00091-1

Sloan, L.C. & Rea, D.K. 1996. Atmospheric carbon dioxide and early Eocene climate: A general circulation modeling sensitive study. Palaeogeography, Palaeoclimatology, Palaeoecology, 119(3–4): 275–292. https://doi.org/10.1016/0031-0182(95)00012-7

Sloan, L.C. & Thomas, E. 1998. Global climate of the late Paleocene epoch: Modeling the circumstances associated with a climatic "event". In: Aubry, M.P., Lucas, S.G. & Berggren, W.A. (editors), Late Paleocene – early Eocene climatic and biotic events in the marine and terrestrial records. Columbia University Press, p. 138–157. New York.

Sloan, L.C., Walker, J.C. & Moore Jr., T.C. 1995. Possible role of oceanic heat transport in early Eocene climate. Paleoceanography and Paleoclimatology, 10(2): 347–356. https://doi.org/10.1029/94PA02928

Slot, M. & Winter, K. 2017. Photosynthetic acclimation to warming in tropical forest tree seedlings. Journal of Experimental Botany, 68(9): 2275–2284. https://doi.org/10.1093/jxb/erx071

Smith, B.T., Amei, A. & Klicka, J. 2012. Evaluating the role of contracting and expanding rainforest in initiating cycles of speciation across the Isthmus of Panama. Proceedings of Royal Society of London Series B: Biological Sciences, 279(1742): 3520–3526. https://doi.org/10.1098/rspb.2012.0706

Sole de Porta, N. 1971. Algunos géneros nuevos de polen procedentes de la Formación Guaduas (Maastrichtiense–Paleoceno) de Colombia. Studia Geologica, 2: 133–143.

Stoskopf, N. 1981. Understanding crop production: Upper Saddle River, Reston, Virginia. Reston Publishing Company, Inc. 433 p.

Stull, G.W., Herrera, F., Manchester, S., Jaramillo, C. & Tiffney, B.H. 2012. Fruits of an "Old World" tribe (Phytocreneae; Icacinaceae) from the Paleogene of North and South America. Systematic Botany, 37(3): 784–794. https://doi.org/10.1600/036364412X648724

Suárez, C., Forasiepi, A.M., Goin, F.J. & Jaramillo, C. 2016. Insights into the Neotropics prior to the Great American Biotic Interchange: New evidence of mammalian predators from the Miocene of northern Colombia. Journal of Vertebrate Paleontology, 36(1): p. 1–10. https://doi.org/10.1080/02724634.2015.1029581

Sucerquia, P. & Jaramillo, C. 2008. Lower Cretaceous floras from central Colombia. Palynology, 32: 271–272.

Sun, G. & Dilcher, D. 2002. Early angiosperms from the Lower Cretaceous of Jixi, eastern Heilongjiang, China. Review of Palaeobotany and Palynology, 121(2): 91–112. https://doi.org/10.1016/S0034-6667(02)00083-0

Sun, G., Ji, Q., Dilcher, D.L., Zheng, S., Nixon, K.C. & Wang, X. 2002. Archaefructaceae, a new basal angiosperm family. Science, 296(5569): 899–904. https://doi.org/10.1126/science.1069439

Sun, G., Dilcher, D., Wang, H. & Chen, Z. 2011. A eudicot from the Early Cretaceous of China. Nature, 471: 625–628. https://doi.org/10.1038/nature09811

Tewksbury, J.J., Huey, R.B. & Deutsch, C.A. 2008. Putting the heat on tropical animals. Science, 320(5881): 1296–1297. https://doi.org/10.1126/science.1159328

Thomas, E. & Shackleton, N.J. 1996. The Paleocene – Eocene benthic foraminiferal extinction and stable isotope anomalies. In: Knox, R., Corfield, R.M. & Dunay, R.E. (editors), Correlations of the early Paleogene in Northwest Europe: An overview. Geological Society of London, Special Publication 101, p. 401–441. https://doi.org/10.1144/GSL.SP.1996.101.01.20

Thomas, W.W. 1999. Conservation and monographic research on the flora of tropical America. Biodiversity & Conservation, 8(8): 1007–1015. https://doi.org/10.1023/A:1008857429787

Toivonen, T., Mäki, S. & Kalliola, R. 2007. The riverscape of western Amazonia—A quantitative approach to the fluvial biogeography of the region. Journal of Biogeography, 34(8): 1374–1387. https://doi.org/10.1111/j.1365-2699.2007.01741.x

Tripati, A., Roberts, C. & Eagle, R. 2009. Coupling of CO_2 and ice sheet stability over major climate transitions of the last 20 million years. Science, 326(5958): 1394–1397. https://doi.org/10.1126/science.1178296

Ufnar, D.F., González, L.A., Ludvigson, G.A., Brenner, R.L. & Witzke, B.J. 2002. The mid–Cretaceous water bearer: Isotope mass balance quantification of the Albian hydrologic cycle. Palaeogeography, Palaeoclimatology, Palaeoecology, 188(1–2): 51–71. https://doi.org/10.1016/S0031-0182(02)00530-8

Ufnar, D.F., González, L.A., Ludvigson, G.A., Brenner, R.L. & Witzke, B.J. 2004. Evidence for increased latent heat transport during the Cretaceous (Albian) greenhouse warming. Geology, 32(12): 1049–1052. https://doi.org/10.1130/G20828.1

Ufnar, D.F., Ludvigson, G.A., González, L.A. & Gröcke, D.R. 2008. Precipitation rates and atmospheric heat transport during the Cenomanian greenhouse warming in North America: Estimates from a stable isotope mass–balance model. Palaeogeography, Palaeoclimatology, Palaeoecology, 266(1–2): 28–38. https://doi.org/10.1016/j.palaeo.2008.03.033

Uno, K.T., Cerling, T.E., Harris, J.M., Kunimatsu, Y., Leakey, M.G., Nakatsukasa, M. & Nakaya, H. 2011. Late Miocene to Pliocene carbon isotope record of differential diet change among east African herbivores. Proceedings of the National Academy of Sciences of the United States of America, 108(16): 6509–6514. https://doi.org/10.1073/pnas.1018435108

van der Hammen, T. 1958. Estratigrafía del terciario y Maastrichtiano continentales y tectogénesis de los Andes colombianos. Boletín Geológico, 6(1–3): 67–128.

van der Hammen, T. 1989. History of the montane forests of the northern Andes. Plant Systematics and Evolution, 162(1–4): 109–114.

van der Hammen, T. 1995. Plioceno y Cuaternario del altiplano de Bogotá y alrededores. Análisis Geográficos, 24: 1–142.

van der Hammen, T. 2003. Neógeno y Cuaternario del altiplano de Bogotá y alrededores. Análisis Geográficos, 26: 101–120.

van der Hammen, T. & Hooghiemstra, H. 2000. Neogene and Quaternary history of vegetation, climate, and plant diversity in Amazonia. Quaternary Science Reviews, 19(8): 725–742. https://doi.org/10.1016/S0277-3791(99)00024-4

van der Hammen, T., Werner, J.H. & van Dommelen, H. 1973. Palynological record of the upheaval of the northern Andes: A study of the Pliocene and lower Quaternary of the Colombian Eastern Cordillera and the early evolution of its high–Andean biota. Review of Palaeobotany and Palynology, 16(1–2): 1–122. https://doi.org/10.1016/0034-6667(73)90031-6

Wallis, G.P., Waters, J.M., Upton, P. & Craw, D. 2016. Transverse alpine speciation driven by glaciation. Trends in Ecology & Evolution, 31(12): 916–926. https://doi.org/10.1016/j.tree.2016.08.009

Wang, H., Moore, M.J., Soltis, P.S., Bell, C.D., Brockington, S.F., Alexandre, R., Davis, C.C., Latvis, M., Manchester, S. & Soltis, D.E. 2009. Rosid radiation and the rapid rise of angiosperm–dominated forests. Proceedings of the National Academy of Sciences of the United States of America, 106(10): 3853–3858. https://doi.org/10.1073/pnas.0813376106

van Waveren, I.M., van Konijnenburg–van Cittert, J.H.A., van der Burgh, J. & Dilcher, D.L. 2002. Macrofloral remains from the Lower Cretaceous of the Leiva region (Colombia). Scripta Geologica, 123: 1–39.

Webb, S.D. 1976. Mammalian faunal dynamics of the Great American Interchange. Paleobiology, 2(3): 220–234. https://doi.org/10.1017/S0094837300004802

Webb, S.D. 1978. A history of savanna vertebrates in the New World. Part II: South America and the great interchange. Annual Re-

view of Ecology and Systematics, 9: 393–426. https://doi.org/10.1146/annurev.es.09.110178.002141

Webb, S.D. 1994. Successful in spite of themselves. Natural History, 4: 50–53.

Webb, S.D. 1995. Biological implications of the middle Miocene Amazon seaway. Science, 269(5222): 361–362. https://doi.org/10.1126/science.269.5222.361

Webb, S.D. 2006. The Great American Biotic Interchange: Patterns and processes. Annals of the Missouri Botanical Garden, 93(2): 245–257. https://doi.org/10.3417/0026-6493(2006)93[245:TGABIP]2.0.CO;2

Westerhold, T., Röhl, U., McCarren, H.K. & Zachos, J.C. 2009. Latest on the absolute age of the Paleocene – Eocene Thermal Maximum (PETM): New insights from exact stratigraphic position of key ash layers +19 and –17. Earth and Planetary Science Letters, 287(3–4): 412–419. https://doi.org/10.1016/j.epsl.2009.08.027

Whitmore, F.C. & Stewart, R.H. 1965. Miocene mammals and Central American seaways: Fauna of the Canal zone indicates separation of Central and South America during most of the Tertiary. Science, 148(3667): 180–185. https://doi.org/10.1126/science.148.3667.180

Wijmstra, T.A. & van der Hammen, T. 1966. Palynological data on the history of tropical savannas in northern South America. Leidse Geologische Mededelingen, 38(1): 71–90.

Wijninga, V.M. 1996. Paleobotany and palynology of Neogene sediments from the High Plain of Bogota (Colombia). Evolution of the Andean flora from a paleoecological perspective. Doctoral thesis, University of Amsterdam, 370 p. Amsterdam, the Netherlands.

Wikström, N., Savolainen, V. & Chase, M.W. 2001. Evolution of the angiosperms: Calibrating the family tree. Proceedings of the Royal Society London B: Biological Sciences, 268(1482): 2211–2220. https://doi.org/10.1098/rspb.2001.1782

Williams, J.H. 2008. Novelties of the flowering plant pollen tube underlie diversification of a key life history stage. Proceedings of the National Academy of Sciences of the United States of America, 105(32): 11259–11263. https://doi.org/10.1073/pnas.0800036105

Wing, S.L. & Boucher, L. 1998. Ecological aspects of the Cretaceous flowering plant radiation. Annual Review of Earth and Planetary Sciences, 26: 379–421. https://doi.org/10.1146/annurev.earth.26.1.379

Wing, S.L., Hickey, L.J. & Swisher, C.C. 1993. Implications of an exceptional fossil flora for Late Cretaceous vegetation. Nature, 363: 342–344. https://doi.org/10.1038/363342a0

Wing, S.L., Harrington, G.J., Smith, F., Bloch, J.I., Boyer, D.M. & Freeman, K.H. 2005. Transient floral change and rapid global warming at the Paleocene – Eocene boundary. Science, 310(5750): 993–996. https://doi.org/10.1126/science.1116913

Wing, S.L., Herrera, F., Jaramillo, C., Gómez–Navarro, C., Wilf, P. & Labandeira, C.C. 2009. Late Paleocene fossils from the Cerrejón Formation, Colombia, are the earliest record of Neotropical rainforest. Proceedings of the National Academy of Sciences of the United States of America, 106(44): 18627–18632. https://doi.org/10.1073/pnas.0905130106

Woodburne, M.O. 2010. The Great American Biotic Interchange: Dispersals, tectonics, climate, sea level and holding pens. Journal of Mammalian Evolution, 17(4): 245–264. https://doi.org/10.1007/s10914-010-9144-8

Wright, S., Keeling, J. & Gillman, L. 2006. The road from Santa Rosalia: A faster tempo of evolution in tropical climates. Proceedings of the National Academy of Sciences of the United States of America, 103(20): 7718–7722. https://doi.org/10.1073/pnas.0510383103

Wright, J.S., Fu, R., Worden, J.R., Chakraborty, S., Clinton, N.E., Risi, C., Sun, Y. & Yin, L. 2017. Rainforest–initiated wet season onset over the southern Amazon. Proceedings of the National Academy of Sciences of the United States of America, 114(32): 8481–8486. https://doi.org/10.1073/pnas.1621516114

Zachos, J.C., Pagani, M., Sloan, L., Thomas, E. & Billups, K. 2001. Trends, rhythms, and aberrations in global climate 65 Ma to present. Science, 292(5517): 686–693. https://doi.org/10.1126/science.1059412

Zachos, J.C., Wara, M.W., Bohaty, S., Delaney, M.L., Petrizzo, M.R., Brill, A., Bralower, T.J. & Premoli–Silva, I. 2003. A transient rise in tropical sea surface temperature during the Paleocene – Eocene Thermal Maximum. Science, 302(5650): 1551–1554. https://doi.org/10.1126/science.1090110

Explanation of Acronyms, Abbreviations, and Symbols:

CAM	Crassulacean acid metabolism
DNA	Deoxyribonucleic acid
ETM	Eocene Thermal Maximum
GABI	Great American Biotic Interchange
ITCZ	Intertropical convergence zone
MMCO	Middle Miocene climatic optimum
PETM	Paleocene Eocene Thermal Maximum
WUE	Water use efficiency
WWF	World Wildlife Fund

Author's Biographical Notes

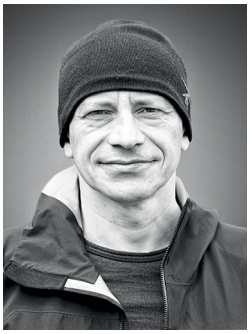

Carlos JARAMILLO investigates the causes, patterns, and processes of tropical biodiversity at diverse temporal and spatial scales, as well as the evolution of tropical landscapes over geological time. He intends to address questions from a paleontological perspective (mainly using fossil pollen, spores and dinoflagellates), a point of view that is vital for understanding and predicting the behavior of biota in tropical ecosystems. He is also interested in energy exploration, Cretaceous – Cenozoic biostratigraphy of low latitudes, developing methods for high–resolution biostratigraphy and the paleobiogeography of Tethys.

Chapter 7

https://doi.org/10.32685/pub.esp.36.2019.07
Published online 27 May 2020

Tectonostratigraphic Terranes in Colombia: An Update Second Part: Oceanic Terranes

Jean–François TOUSSAINT[1] and Jorge Julián RESTREPO[2]*

1 jftoussaint@hotmail.com
Universidad Nacional de Colombia
Sede Medellín
Medellín, Colombia

2 jjrestrepoa@gmail.com
Universidad Nacional de Colombia
Sede Medellín
GEMMA Research Group
Medellín, Colombia

* Corresponding author

Abstract In Colombia, several oceanic, allochthonous terranes exist west of the San Jerónimo Fault, which is the western limit of large continental terranes. The main terranes are the Calima and Cuna in the Western Cordillera, the Tumaco Suspect Terrane in the southern Western Cordillera and the Tairona Terrane in the Sierra Nevada de Santa Marta. All of them are oceanic terranes that formed in the Pacific Ocean and moved northward to their present positions, where they were emplaced from Late Cretaceous to Miocene times. At least the Calima and Cuna are believed to be part of the Caribbean Plateau. Smaller oceanic terranes are found in the Cauca–Romeral Fault Zone (CRFZ).

Keywords: *Colombian tectonostratigraphic terranes, oceanic terranes, allochthonous terranes, Caribbean Plateau, transpressional collisional metamorphism.*

Resumen En Colombia existen varios terrenos oceánicos alóctonos al oeste de la Falla de San Jerónimo, límite occidental de los grandes terrenos continentales. Los principales son el Calima y Cuna en la cordillera Occidental, el presunto Terreno Tumaco en la parte sur de la cordillera Occidental y el Terreno Tairona en la Sierra Nevada de Santa Marta. Todos son terrenos oceánicos que se formaron en el océano Pacífico y migraron hacia el norte hasta sus posiciones actuales desde el Cretácico Tardío al Mioceno. Se cree que por lo menos los terrenos Calima y Cuna son parte del Plateau del Caribe. Pequeños terrenos oceánicos se encuentran dentro del Sistema de Fallas Cauca–Romeral.

Palabras clave: *terrenos tectonoestratigráficos colombianos, terrenos oceánicos, terrenos alóctonos, Plateau del Caribe, metamorfismo colisional transpresional.*

1. Introduction

Oceanic basement terranes (Figure 1) exist west of the San Jerónimo Fault, which marks the eastern edge of the Cauca–Romeral Fault Zone (CRFZ) (Figure 2). These terranes include the Calima and Cuna Terranes (Toussaint & Restrepo, 1989). Similarly, several oceanic terranes are mixed with continental terranes in the CRFZ located on the western flank of the Central Cordillera and on the eastern flank of the Western Cordillera. These terranes include the Ebéjico (Quebradagrande) and Pozo (Arquía) Terranes, among others. The newly defined Tairona Terrane, composed of oceanic basement, occurs in the Sierra Nevada de Santa Marta (SNSM) and on La Guajira Peninsula.

In this chapter, the boundaries and characteristics of the known oceanic terranes are determined, and new terranes are defined. Some of the names have been changed to comply with the recommendation of the initiators of the terranes tectonics (i.e., Coney et al., 1980; Howell, 1989) that the names of strati-

Citation: Toussaint, J.F. & Restrepo, J.J. 2020. Tectonostratigraphic terranes in Colombia: An update. Second part: Oceanic terranes. In: Gómez, J. & Pinilla–Pachon, A.O. (editors), The Geology of Colombia, Volume 2 Mesozoic. Servicio Geológico Colombiano, Publicaciones Geológicas Especiales 36, p. 237–260. Bogotá. https://doi.org/10.32685/pub.esp.36.2019.07

Figure 1. Schematic map of the tectonostratigraphic terranes in Colombia: (An) Andaquí Terrane; (Ch) Chibcha Terrane; (Y) Yalcón Terrane; (Ta) Tahamí Terrane; (K) Kogi Terrane; (Ca) Calima Terrane; (Tu) Tumaco Terrane; (Tai) Tairona Terrane; (Cu) Cuna Terrane; (CRUT) Cauca–Romeral Undifferentiated Terranes: strips formed by smaller continental and oceanic terranes, such as the Pozo (Arquía), Ebéjico (Quebradagrande) and Sinifaná–Amagá Terranes, among others.

graphic units not be used to name terranes. Following the common usage for naming terranes, we use names from the first indigenous cultures of America. The discussion of the continental terranes is presented in a different chapter of this book (see Restrepo & Toussaint, 2020).

2. The Calima Terrane

2.1. Introduction

The Calima Terrane is located in the Western Cordillera and probably also forms the basement of El Plato depression to the north of the Central Cordillera. The review by Etayo–Serna et al. (1983) suggests that several terranes named Buriticá, Sinú, and San Jacinto form this zone in the north and that the Dagua Terrane occurs in the south. Restrepo & Toussaint (1988) initially grouped all units with oceanic affinity into the *Western Andean Terrane*, and then Toussaint & Restrepo (1989) renamed it the Calima Terrane after a pre–Columbian culture of the Cisneros region in the Valle del Cauca. In Gómez et al. (2015a) practically all regions with oceanic basement were grouped into a single megaterrane called the Caribbean Terrane. The smaller oceanic terranes, such as the Pozo (Arquía) and Ebéjico (Quebradagrande) Terranes, which occur in a strip between the oceanic and continental terranes, were initially included in the Calima Terrane and were later separated from it (Restrepo et al., 2009a). Two smaller oceanic areas that are newly defined here, the Bocaná and Aburrá Terranes within the Tahamí Terrane, are also discussed.

The northern and southern parts of the Calima Terrane are composed of basement rocks with oceanic affinity (Case et al., 1971). The difference between the regions is that the southern part was affected by an important tectono–metamorphic event in the Late Cretaceous, but in the north, this event is featured only on the eastern border with the Quirimará Terrane (newly defined here), which includes the Sabaletas Schists (see below). Apparently, the transition from one area to another is progressive (Parra, 1983). The westernmost faults of the CRFZ mark the eastern boundary of the extensive oceanic terranes that are composed mainly of mafic rocks and deep–water sedimentites (Case et al., 1971; Irving, 1971).

Because the nomenclature, and possibly the nature of the rocks, is different in the northern and southern parts, with a transition at approximately latitude 4° 40' N, we describe the two areas separately.

2.2. Distinguishing Features of the Northern Part of the Calima Terrane

The most important unit of the Calima Terrane, forming the basement, is the Cañasgordas Group, which comprises a basal basaltic unit called the Barroso Formation and a sedimentary unit called the Penderisco Formation that seems to be on top of and intercalated with the basalts (Álvarez & González, 1978; Irving, 1971; González, 2001). The original Barroso Formation included pillow lavas, flows, tuffs, and breccias but, as discussed below, has been subdivided into two units.

Since the work of Case et al. (1971), it has been known that the westernmost faults of the CRFZ are the eastern boundary of the large oceanic terranes that are composed mainly of mafic rocks and deep–water sedimentites. These authors also hypothesized that the oceanic basement of western Colombia was allochthonous and related to the Caribbean basement.

Based on the petrological and geochronological characteristics, Restrepo & Toussaint (1976) proposed that the basic volcanic rocks, mostly pillow lavas assigned to the Barroso Formation that are intruded by the Altamira Gabbro and the Sabanalarga Batholith, presently called the Santa Fé Batholith, represent an island arc that developed on top of oceanic crust.

Recently, it was proposed that the basic rocks that have been termed "Barroso" actually belong to two different units: the mainly pyroclastic Barroso Formation considered to represent a basic volcanic arc, and the San José de Urama Diabases, which are interpreted as part of an oceanic plateau (Rodríguez & Arango, 2013).

Although pillow lavas that are indicative of submarine eruptions are quite common, subaerial eruptions composed of red and green tuffs and breccias have been found near Altamira, Antioquia. For these rocks, geochemical analyses indicate an oceanic–crustal origin followed by gabbroic intrusions associated with an incipient arc (Zapata et al., 2017a).

The age of the volcanic rocks has been determined by several methods as Cretaceous, but dating with the K–Ar and Ar–Ar systems has been somewhat erratic. Ages from these systems range from 105 to 73 Ma (González, 2010; Sinton et al., 1998; Toussaint & Restrepo, 1981), and an abnormally old Ar–Ar age of 155 Ma was obtained for the San José de Urama Diabases (Rodríguez & Arango, 2013). Some of these ages, specifically the age from San José de Urama Diabases, could be unreliable due to the very low K content in the analyzed minerals. A better indicator of the minimum age of the Barroso Formation is the ages of the stocks that intrude the sequence, as discussed below.

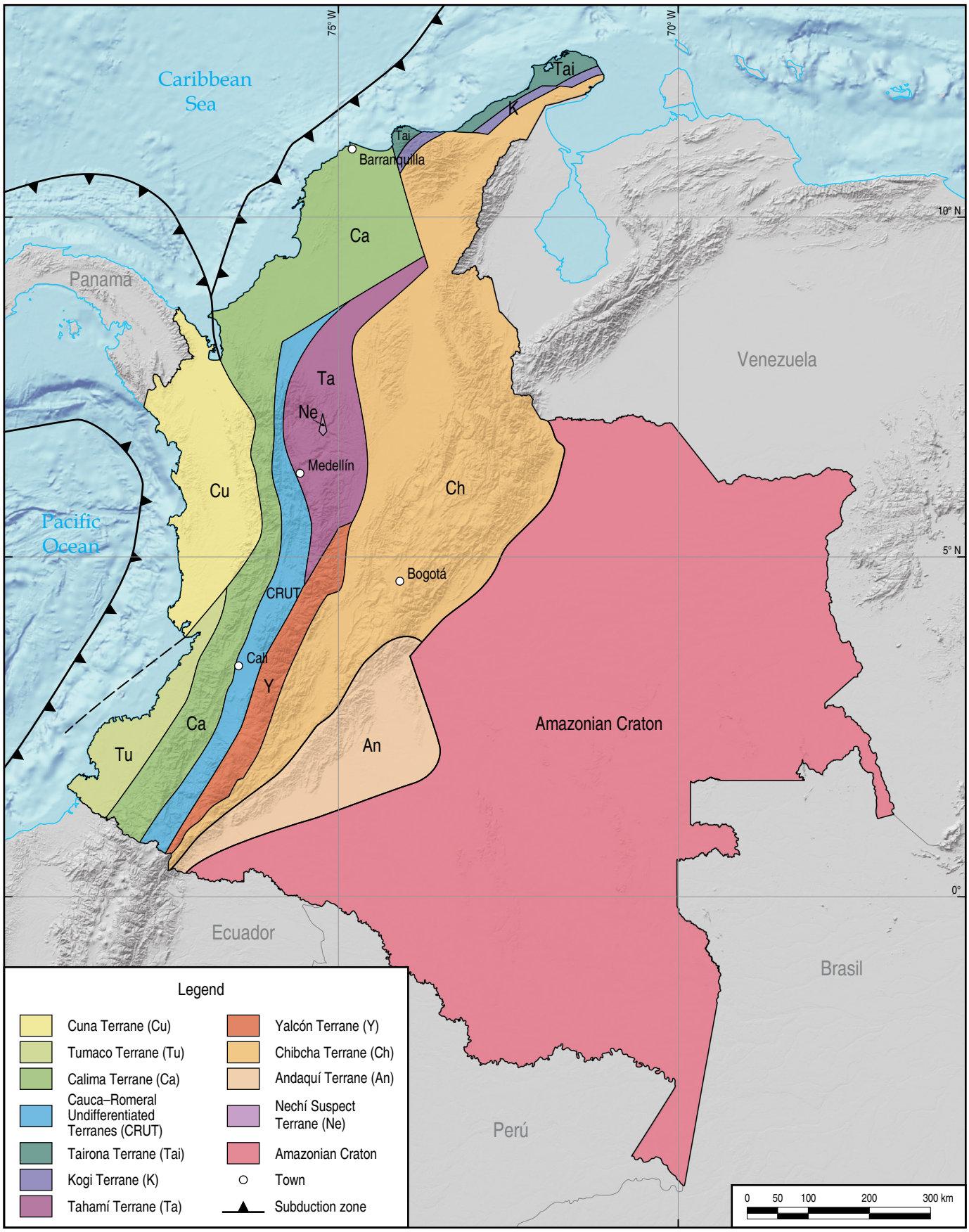

Neogene
Paleogene
Cretaceous

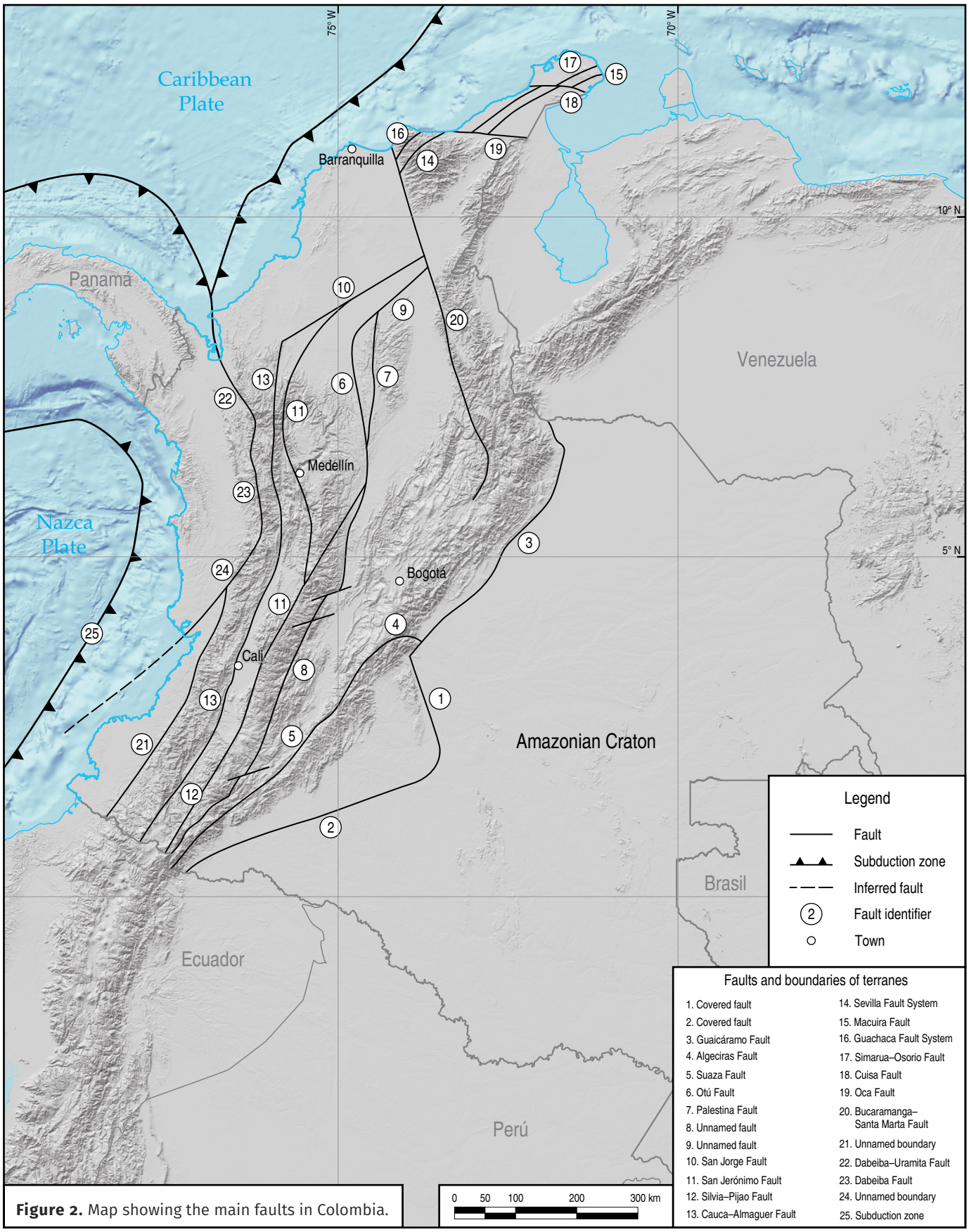

Figure 2. Map showing the main faults in Colombia.

The sedimentary succession contained within the Cañasgordas Group, named the Penderisco Formation, has been divided into a clastic sequence (the Urrao Member) and a mainly cherty sequence (the Nutibara Member), Álvarez & González (1978).

The Urrao Member is composed of several meter–thick turbiditic successions that are repeated for hundreds of meters, whereas the Nutibara Member is composed of cherts and lithographic limestones. The Urrao Member is predominant on the eastern side of the range, while the Nutibara Member is predominant on the western side. However, the relationships between them are not clear.

In Dabeiba, near the Calima–Cuna suture marked by the Dabeiba–Uramita Fault, Paleocene to Eocene fauna have been discovered in the Río Verde Unit, which is composed of basalts, radiolarites, calcareous cherts, and limestones (Bourgois et al., 1982a). This finding suggests that at least a portion of the Nutibara Member would not be Calima but rather would be related to a Paleocene – Eocene magmatism event of the Cuna Terrane, which accreted in the Miocene. It is currently unclear whether all the calcareous cherts that are attributed to the Nutibara Member in this area are Paleocene and belong to the Cuna Terrane or whether a Cretaceous portion remains in the Calima Terrane. Additionally, the only zone in the north where slates have been found is close to Dabeiba (Restrepo et al., 1979). This low–grade metamorphism was probably produced by the collision of the Cuna with the Calima Terrane.

The Paleocene siliceous limestones and cherts were highly deformed by Miocene tectogenesis, which is responsible for the main deformation of the sedimentary rocks of the Penderisco Formation. However, the presence of a Late Cretaceous to Paleocene event is not discarded.

Fossils are not very common, but those found have yielded ages that range from Albian to Maastrichtian (Etayo–Serna et al., 1980; González, 2001 and references therein). Ammonites near Buriticá are assigned to the mid–Albian (Etayo–Serna et al., 1980), and they likely represent interstratified cherts and fine clastic rocks within the Barroso Formation rather than the Penderisco Formation as previously thought (González, 2001). This age is confirmed by the intrusion of the Buriticá Stock into the sequence, forming a contact aureole (Feininger in Etayo–Serna et al., 1980); this stock has been dated at 100.5 Ma (Weber et al., 2015) and 93.9 Ma (Giraldo–Ramírez, 2017) by U–Pb in zircons. These ages agree well with a K–Ar date of 105 ± 10 Ma obtained from the Barroso Formation (Restrepo et al., 1991). If all of the basic volcanic rocks of the Barroso Formation formed in a short time, it is probable that they were completely established by the beginning of deposition associated with the Penderisco Formation. For this unit, Etayo–Serna (1989) reports Campanian to Maastrichtian fossils in turbidites near Peque on the western side of the sequence; recently, Turonian to Maastrichtian fossils have also been found at Ciudad Bolívar and Carmen de Atrato (Etayo–Serna cited by Rodríguez & Arango, 2013). The Cañasgordas Group was intruded by several plutons. On the eastern side, these plutons include the Buriticá Stock and the Santa Fé Gabbro (formerly the Sabanalarga Batholith); the Caicedo Gabbro and Altamira Gabbro mostly intrude the Barroso Formation. These plutons have been dated between 110.5 Ma and 71.6 Ma by U–Pb in zircons (Correa et al., 2017; Giraldo–Ramírez, 2017; Zapata et al., 2017b).

2.3. Features of the Southern Part of the Calima Terrane

To the east of the southern part of the Calima Terrane are the Bolívar and the Riofrío Complexes, which consist of dunites, peridotites, banded pyroxenites, and gabbros cut by several hornblende pegmatites that have been dated between 112 and 95 Ma using Ar–Ar and U–Pb (Kerr et al., 2004; Villagómez, 2010). According to Bourgois et al. (1982b), the Bolívar Complex forms the base of the Diabasic Group and represents a portion of the proto–Caribbean basin that was overthrust onto the continent. Likewise, Nivia (1993, 1996) interpreted that these complexes represent the base of an obducted plateau.

Most of the southern part of the Calima Terrane is composed of basic volcanic rocks of the Diabasic Group or Volcanic Formation and by sedimentary and metasedimentary rocks of the Dagua Group, which has been divided into two formations: the Cisneros Formation, which is composed of metamorphic rocks, mainly phyllites and slates, and the Espinal Formation, which is composed of marine sedimentites, mostly mudrocks and turbiditic sandstones (Nelson, 1962). Several authors have proposed changing this nomenclature (Parra, 1983; Aspden, 1984) without reaching a consensus.

The Diabasic Group consists of spilitized diabase, K–poor tholeiitic basalts, and tuffs with interspersed cherts, siltstones, graywackes, and limestones. Trace element and REE analyses indicate a T–MORB that represents an oceanic plateau or a rift disturbed by a hotspot (Desmet, 1994; Kerr et al., 1997). The sedimentites that are interspersed with the basic rocks contain a few fossils from the Aptian – Campanian range (Etayo–Serna et al., 1982). Some small gabbro stocks associated with volcanic rocks have been dated at 99.7 Ma by U–Pb in El Palmar (Villagómez et al., 2011) and 94 ± 17 Ma by Rb–Sr isochron in El Tambor (Brook, 1984).

The Amaime Formation (McCourt, 1984), located on the western border of the Central Cordillera near Sevilla, is similar in composition and age to the Diabasic Group (Nivia, 1989). However, this formation could be an independent unit because it is separated from the Diabasic Group by an important fault network (Aspden & McCourt, 1986; Moreno–Sánchez & Pardo–Trujillo, 2003). According to the paleomagnetic studies of Estrada (1995), the Amaime Formation was probably generated in the Pacific at an equatorial paleolatitude.

The Cisneros Formation consists of siliceous phyllites and carbonaceous slates interspersed with metacherts, metagraywackes, and metalimestones that formed from low–grade metamorphism of pelagic sedimentites, particularly distal turbidites (Barrero, 1979). In the phyllites, *Zoophycus* ichnofossils are abundant. Bivalve molds indicate a Turonian – Maastrichtian age (Etayo–Serna et al., 1982). Some authors consider that the metamorphism was exclusively dynamic and that the phyllites are cataclasites (McCourt et al., 1984). The presence of schistosity affected by isoclinal folding that is associated with a second schistosity shows that large portions of the phyllites were produced by low–grade regional metamorphism, even though the presence of superimposed cataclasis is certain in several areas (Bourgois et al., 1982b).

The Espinal Formation is composed of siliceous shales, siltstones, and graywacke with rare cherts and limestones. Foraminifera and *Inoceramus* fossils suggest Campanian – Maastrichtian ages (Etayo–Serna, 1989).

However, the present apparent stratigraphy may be tectonically induced. Etayo–Serna et al. (1982) suggested that the Dagua Group can be divided into three segments with different textures and compositions, which were deposited contemporaneously and later tectonically stacked.

An important Late Cretaceous tectono–metamorphic event was caused by the oblique collision between plateau material of the Caribbean Plate and continental basement of the South American continent. At first, the collision was quite frontal, but later, major dextral movements occurred. Indeed, initially, the collision produced tectonic phases marked mainly by isoclinal folding, overthrust faults associated with schistosity and regional metamorphism, but the convergence then became more oblique, producing the great strike–slip faults that cut the previous structures (Toussaint, 1996).

Barrero (1979) assumed that the main tectonic phase that affected this region was Late Cretaceous and noted that phyllite of the Cisneros Formation dips mainly to the east, suggesting this observation as evidence of eastward subduction. Subsequent work by Bourgois et al. (1982b) indicated that the center of the Western Cordillera is formed by tectonic stacking of overthrust units based on the presence of folds that affect a first schistosity associated with isoclinal folds. The second schistosity, with a dip generally less than 30 degrees, is associated with folds dipping to the east. McCourt et al. (1984) placed a special emphasis on the large NNE faults that crosscut the previous structures. These authors attributed the faulting to Late Cretaceous tectonogenesis, but Toussaint (1996) argued that the inverse direction movements are subsequent to the Late Cretaceous regional metamorphism and are responsible for dynamic metamorphism that produced the cataclasites in the region. In the north, it is difficult to separate the Late Cretaceous tectonic event from the collision between the Cuna and Calima Terranes, which occurred during the Miocene.

The final accretion of the Calima Terrane to the continent appears to have occurred close to the Late Cretaceous – Paleogene boundary, beginning at approximately 70 Ma (the age of the youngest igneous zircons found in the Sabaletas Schists) and concluding before 58 Ma (the age of a dike that intrudes the schists; Zapata & Cardona, 2017). This age agrees well with the age determined in the southern part of the terrane, where Paleocene and Eocene sedimentary units partially cover the terrane borders with little to no deformation (see Geologic Map of Colombia by Gómez et al., 2015b).

2.4. Extent and Boundaries of the Calima Terrane

Broadly speaking, the transition between the oceanic basement of the Calima Terrane and continental crust occurs along what is presently the CRFZ. However, it is important to note that the area has been subject to diverse tectonic phases with compressional, extensional, and especially large horizontal movements due to dextral–inverse transpression. The right–lateral faults were active during most of the Cenozoic. Thus, the limit is presently represented by the Cauca–Almaguer Fault (the westernmost fault of the CRFZ), but this fault is not necessarily the original boundary. This fault separates the Calima and Pozo (Arquía) Terranes.

The origin of the Caribbean Plateau has generally been attributed to the paleo–Galápagos hotspot, south of its present position (for a discussion regarding the paleo–Galápagos hotspot, see Nerlich et al., 2014, and references therein). The latitude of formation of the basic rocks was determined from paleomagnetic data to be nearly equatorial (Estrada, 1995) or between 2° S and 4° S (Hincapié–Gómez et al., 2018). Since its formation at that southerly location, there has been a northeasterly drift of the plateau that has resulted in the accretion of oceanic crust to the continental borders of the northern Andes and the Caribbean margin of South America (i.e., Kennan & Pindell, 2009). The interaction of the oceanic and continental terranes has produced slivers of both types of crust, dispersing large and small terranes that were accreted to the north. An example of these accretions is observed west of Medellín. The San Jerónimo Fault runs in a N–NE direction from Ecuador to an approximate latitude of 4° 40' N, where it turns to a N–NW direction. After the change in direction, many microterranes, such as the Anacona, Quirimará, and Ebéjico Terranes, were left stranded in this area. Additionally, at the flexure point, extensive mylonites occur that were mapped as regional metamorphic rocks (González, 1980).

In the northernmost part of Colombia, the Calima Terrane is limited by an inverse fault that dips toward the south and confines the folded belt of the Caribbean within the Caribbean Plate (Toussaint & Restrepo, 1989). The location of the Calima Terrane in the Sinú region and El Plato depression is

unclear. Research prior to Mora–Bohórquez et al. (2017) assumed that the Cauca–Almaguer Fault, also called the Romeral Fault in this region (Grosse, 1926), represents the boundary between the continental and oceanic materials to the E and W, respectively. However, geophysical research by Mora–Bohórquez et al. (2017) showed that between the Romeral or Cauca–Almaguer Fault and the San Jerónimo Fault with a NE direction in this region, the basement is composed of oceanic material. These authors consider that such basement may be associated with the Quebradagrande Complex, but we propose that it is more likely associated with the Calima Terrane; quite clearly, this basement is not from the Tahamí Terrane.

2.5. Post–Accretion Events in the Calima–Continental Terranes Supraterrane

An Oligocene to early Miocene magmatic belt including the Piedrancha Granodioritic Batholith (23 Ma; Álvarez & Linares, 1981), the Anchicayá Batholith (18 Ma; Brook, 1984), the Cumbitara Stock, El Vergel Stock (23 Ma to 22 Ma; Leal–Mejía, 2011) and the Tatamá Pluton (19 to 17 Ma; Brook, 1984) intrudes the previous rock associations. It is feasible that the final magmatic event of this belt is represented by the Tatamá Pluton, intruded shortly prior to the collision of the Cuna and Calima Terranes, which would have changed the position of the subduction zone.

Marine sediments were deposited during the Cenozoic in the Cauca River valley, for example, the Campanian – Paleocene Nogales Formation and the Eocene Chimborazo Formation (Pardo–Trujillo et al., 2003) on the western edge of the southern part of the Western Cordillera, and are similar to the sediments of the Pacific Group (van der Hammen, 1958) north of the Western Cordillera in the Sinú and San Jacinto regions, such as the Paleocene – Eocene San Cayetano Formation (Duque–Caro, 1984).

An important deformed belt developed in the northernmost part of the Calima Terrane, related to the Cenozoic subduction of the Caribbean Plate beneath the Northern Andes. Some of the sediments associated with this belt are exposed on the Caribbean Colombian coast, in Sinú, where they rest on the Calima Terrane units (see B&G Unión Temporal, 2006).

3. The Tumaco Suspect Terrane (Gorgona Terrane and Western Flank of the Southern Region of the Western Cordillera)

3.1. Introduction

A set of dunites, wehrlites, gabbros, and basalt flows that are covered by basic tuffs with *Inoceramus* in the Gorgona and Gorgonilla Islands were denominated the Igneous Complex of Gorgona by Gansser (1973). Etayo–Serna et al. (1983) considered that this assemblage represents the Gorgona Terrane.

The Guapi Ultramafic Complex, associated with a volcano–sedimentary sequence located to the west of the Western Cordillera (in a sparsely studied area), raises the question of whether the complex is associated with the Calima Terrane, with a southern extension of the Cuna Terrane, or with a new terrane that remains undefined. Due to a lack of thorough geological knowledge in this region, it is difficult to select among the hypotheses. In this article, these various units are included in the Tumaco Suspect Terrane, named after an important pre–Columbian culture.

3.2. Features of the Tumaco Terrane

The Igneous Complex of Gorgona includes mafic and ultramafic rocks with dunites, wehrlites, poikilitic or troctolitic gabbros, komatiites, basalt flows, volcanic breccias, and basic tuffs that contain *Inoceramus* (Gansser, 1973). Echeverría (1982) documented komatiites with spinifex textures, which are characteristic of the partial fusion of the mantle at a temperature of more than 1400 °C. Ages between 86 and 66 Ma reflect a seemingly continuous magmatic episode of ca. 20 Ma, with dates similar to those of the Caribbean Plateau (Espinosa–Baquero et al., 1982; Serrano et al., 2011; Walker et al., 1999). According to Estrada (1995), basalts with K–Ar dates of 86 ± 3 Ma had a paleolatitude of 25° S to 35° S. On the other hand, Serrano et al. (2011) considered that the Gorgona magmatism was due to the mixing of asthenospheric mantle material that was metasomatized by the subducted material of the proto–Caribbean Plate beneath the Antilles Arc. These authors discarded the hypothesis of magmatism related to the Galápagos Hotspot, considering that the continuity of Gorgona magmatism over 20 Ma was inconsistent with a moving plate passing over a hotspot.

The Guapi Ultramafic Complex includes harzburgites, lherzolites, serpentinized dunites, wehrlites, and gabbros associated with volcano–sedimentary formations that include basalts, breccias, and tuffs interbedded with cherts, siltstones, and Paleocene – Eocene limestones of the Timbiquí Formation (McCourt et al., 1990; Agencia Nacional de Hidrocarburos & Geología Regional y Prospección, 2011). Their presence on the west flank of the Western Cordillera prompts questions regarding which terrane these rocks belong to. This complex is intruded by smaller plutons, such as the Balsitas and El Salto Plutons, which are composed of hornblendic gabbro, quartz diorites, andesite porphyries, and tonalites for which McCourt et al. (1990) obtained ten K–Ar ages between 53 and 41 Ma. A more robust age of 53.25 ± 0.27 was obtained by U–Pb in zircons from a dike that crosscuts the complex (Agencia Nacional de Hidrocarburos & Geología Regional y Prospección, 2011), so a minimum Eocene age is indicated. The magmatism of the complex seems to be

representative of oceanic arc activity developed on an oceanic basement, possibly disturbed by a high heat flow.

The Late Cretaceous to early Eocene age of the Gorgona Igneous Complex and the Guapi Ultramafic Complex (associated with volcano–sedimentary units) suggests that they constitute a different terrane from the Calima and Cuna Terranes. A similar hypothesis was suggested in a map presented by Guiral–Vega et al. (2015). However, until new data are available, the temporal relationships between the location of these ultramafic complexes and the accretion of the Calima Terrane remain unknown. Although the Calima Terrane includes the Miocene Alto Condoto Ultramafic Complex (Salinas & Tistl, 1992; Tistl et al., 1994), the Late Cretaceous to Eocene age excludes a similar origin between the two.

3.3. Accretion and Extent of the Tumaco Terrane

An approximately N–S–oriented fault network separates the Tumaco Terrane from the Calima Terrane. These faults have no specific names in the most recent map published by the Servicio Geológico Colombiano (Gómez et al., 2015b). The faults are covered by recent sediments south of Buenaventura, continue south in Nariño near the town of El Charco, then extend near Ricaurte and finally end in Ecuador at the limit between the Piñón and Piñón–Macuchi Terranes (Litherland et al., 1993). Currently, it is difficult to specify the age and type of suture; however, an undated pluton attributed to the Piedrancha Batholith appears to crosscut the border. Although K–Ar ages ranging from 62 to 21 Ma have been reported from this batholith (González et al., 2002), the U–Pb age of 22.53 ± 0.18 Ma (Agencia Nacional de Hidrocarburos & Geología Regional y Prospección, 2011) would place the age of accretion as pre–Miocene. According to McGeary & Ben–Avraham (1985), the accretion of the Gorgona Terrane occurred before the early Miocene. The accretion of the Tumaco Suspect Terrane occurred after the mid–Eocene based on the age of 41 Ma of the youngest pluton mentioned above and before the early Miocene accretion of the Cuna Terrane.

The boundary between this terrane and the Cuna Terrane is represented by a NNE fault that crosses Buenaventura bay and extends offshore to the west of Gorgona Island. This fault was identified using seismology by McGeary & Ben–Avraham (1985), who assumed it represents a suture between two terranes.

3.4. Other Possibilities

The existence of a Tumaco Terrane is feasible, but the hypothesis that these geological assemblages represent a southern extension of the Cuna Terrane (which is described later) cannot be discarded. Similarly, we cannot completely eliminate the possibility that the Guapi Ultramafic Complex is associated with the Calima Terrane, although it would be difficult to explain the in situ generation of the Guapi Ultramafic Complex.

4. The Cuna Terrane

4.1. Introduction

The Cuna Terrane is located in the western part of Colombia, cropping out on the western flank of the Western Cordillera and in the Serranía de Baudó. It forms the basement of the Atrato River and Chucunaque Basins in Colombia and Panamá, respectively. This terrane extends to the Isthmus of Panamá.

For this area, the Ingeominas review by Etayo–Serna et al. (1983) considered that the west flank of the Western Cordillera is part of the Cañasgordas Terrane, that the Atrato River valley belongs to the Atrato–San Juan Terrane and that the Serranía de Baudó is associated with the Baudó Terrane. Restrepo & Toussaint (1988) initially named it the Panamá–Baudó–Mandé Terrane, and later, Toussaint & Restrepo (1989) defined it as the Cuna Terrane. Duque–Caro (1990) called it the Panamá–Chocó Block or Chocó Block. Gómez et al. (2015a) did not separate this area as a distinct terrane but associated it with a Caribbean Megaterrane that includes all terranes that contain oceanic basement. The Gorgona Terrane defined by Estrada (1995) may be a small terrane between the Calima and Cuna Terranes or may belong either to the Tumaco Suspect Terrane or to the Cuna Terrane. This research considers the Gorgona Terrane to be part of the Tumaco Suspect Terrane.

4.2. Features of the Cuna Terrane

The Cuna Terrane includes a Cretaceous oceanic basement that was intruded in the NE by a magmatic arc of intermediate to acidic composition. It is represented by the Mandé Batholith with tuffs and breccias of the Santa Cecilia–La Equis Formation, the Acandí Batholith, and the Eocene Río Pito Pluton in Panamá. A thick succession of marine sedimentites was deposited in the Atrato River Basin, mainly between the Eocene and Miocene.

Bourgois et al. (1982a) argued that the oldest units in the Baudó Range are massive basalts, some with amygdules, and pillow lavas, diabases, and gabbros, dated at 70 Ma by K–Ar. Using Ar–Ar dating, Kerr et al. (1997) obtained ages between 77.9 Ma for a gabbro and 71.8 Ma for a basalt near Bahía Solano. These authors consider the rocks to be plateau basalts similar to those of the Caribbean Plateau. Planktonic foraminifera that were detected in sedimentary rocks interlayered with basalts suggest Coniacian to Maastrichtian ages (Bandy, 1970). These units are covered by chaotic volcano–sedimentary se-

quences characterized by basalts interspersed with limestones, radiolarites, and graywackes. Faunal ages range from Paleocene to lower Miocene (Bourgois et al., 1982a).

In the east and northeast region, volcanic rocks including basalts, andesites, latites, breccias, and tuffs are associated with cherts, siltstones, mudstone, and limestones that contain Paleocene – Eocene fossils, such as the Río Verde Formation (Bourgois et al., 1982a), the Santa Cecilia Formation, and La Equis Formation (Calle & Salinas, 1986). The Santa Cecilia–La Equis Complex, defined by Salazar et al. (1991), is composed of interlayered basic to intermediate lava flows and pyroclastic sequences. These authors initially included the Mandé Batholith in this complex, but the name was later limited to the volcanic portion. Near Dabeiba, a trachyandesite was dated at 41.5 Ma using K–Ar (Restrepo et al., 1991), whereas rocks of this unit dated with Ar–Ar produced ages between 55 and 37 Ma (Buchely et al., 2009). This magmatism also features the quartz diorite porphyries of Murindó and Pantanos, dated between 54.7 and 42.7 Ma by K–Ar, which contain important copper deposits (Sillitoe et al., 1982). Intense granodioritic to quartz monzonitic plutonism, which occurred during the Eocene, is represented mainly by the Mandé and Acandí Batholiths. The Mandé Batholith was dated by U–Pb in zircons at 45.3 ± 1.2 and 44.6 ± 0.9 Ma (Leal–Mejía, 2011), while other methods such as Ar–Ar and K–Ar produced ages between 55 and 45 Ma (Sillitoe et al., 1982; Buchely et al., 2009). This entire complex represents an island arc that developed over the Caribbean Plate, which was displaced dextrally compared to the NW corner of South America. In the northern part of the Cuna Terrane between the magmatic arc and the border of the Cuna Terrane with the Caribbean Plateau, the north Panamá deformed belt developed. This belt is composed of thick sequences of marine sedimentites deformed during the subduction of the Caribbean Plate beneath the Cuna Terrane. According to Montes et al. (2012), the emergence of the Panamá Arc, transported by the Caribbean Plate, commenced in the Eocene, although the arc collided with the NW corner of South America in the early Miocene (Toussaint & Restrepo, 1989). A younger age of collision is proposed by Restrepo–Moreno et al. (2017).

More than 6000 meters of marine sedimentary sequences were deposited in the Atrato River Basin between the Eocene and middle Miocene. The deposits include the Clavo, Salaquí, Uva, Napipí, and Sierra Formations (Haffer, 1967).

The Alto Condoto Ultramafic Complex, Viravira Complex, the Mumbú Ultramafic Complex, the Mutatá Ultramafic Complex, and La Cristalina Complex occur to the east of the Cuna Terrane and are composed of platinum–rich dunites, harzburgites, and lherzolites. They are Ural–Alaska–type complexes, products of the partial melting of an oceanic crust in a volcanic arc environment (Tistl et al., 1994). K–Ar isotopic dating of hornblende ranges from 21 to 18 Ma, or late Oligocene to early Miocene (Tistl et al., 1994). In the Viravira Complex, a few kilometers south of the Alto Condoto Ultramafic Complex, upper Eocene – lower Miocene cherts and limestones are intercalated with basalts.

The northeastern part of the Cuna Terrane features two important gravimetric highs of 90 mgal in the Serranía de Baudó and 130 mgal in the eastern region of the Cuna Terrane. These highs were interpreted to be the result of tectonic uplift in this region during collision with the Northern Andes (Case et al., 1971).

4.3. Extent and Boundaries of the Cuna Terrane

The Cuna Terrane is separated from the Caribbean Plate by a fault where the north Panamá deformed belt overrides the Caribbean Plate. This situation corresponds to the convergence between the Caribbean Plate and the Cuna Terrane that makes part of the Panamá Plate (Case & Holcombe, 1980; Bird, 2003). The border with the Calima Terrane features inverse faults with eastern and western dips, such as those of Dabeiba–Pueblo Rico and Uramita Faults (Restrepo & Toussaint, 1988). This fault system was generated during the collision of the Cuna Terrane with the NW corner of South America, when the Cuna Terrane attempted to subduct under the NW corner of South America. However, in some regions, such as around Dabeiba and along El Toro River on the road between Medellín and Quibdó, the most superficial area of the Cuna Terrane overthrust onto the Calima Terrane units (Bourgois et al., 1982a; Toussaint, 1999). In the Gulf of Urabá and around Buenaventura bay, the boundary is covered by late Miocene and Quaternary sediments. The boundary in the southern part of the Cuna Terrane, oriented N–NE, is marked by a nameless inverse dextral fault (see Gómez et al., 2015b) that segments the original suture.

The western boundary of the Cuna Terrane includes the subduction zone associated with subduction of the Nazca Plate beneath the Northern Andes and, in the northernmost region, a transform fault that borders the south Panamá deformed belt.

4.4. Accretion of the Cuna Terrane

The collision of the Cuna Terrane with the Northern Andes apparently occurred in the early Miocene both because the intense Eocene magmatism affected only the eastern edge of the Cuna Terrane but not the Calima Terrane and because the Miocene – Pliocene sedimentites cover the border in the Gulf of Urabá. In addition, the late Miocene – Pliocene Quibdó Formation discordantly overlies the early to middle Miocene Sierra Formation. Near Dabeiba, the Guineales Formation (Botero, 1936), deposited on the 9.3 Ma basalt of El Botón (Restrepo et al., 1991; Zapata & Rodríguez, 2011), appears to cover the border.

Duque–Caro (1985) and Montes et al. (2012) suggested that deep–water circulation between the Caribbean Sea and the Pacific Ocean was interrupted during the early Miocene, although O'Dea et al. (2016) argued that the interruption of marine exchange between the Caribbean Sea and the Pacific Ocean occurred only 2.8 Ma ago. In addition, Toussaint & Restrepo (1989) and Toussaint (1996) suggested that the collision of the Cuna Terrane with the Andean Block not only was responsible for the folding of the Cretaceous sedimentites of the Calima Terrane but also was a major cause of Miocene – Pliocene tectonogenesis that affected the entirety of the Colombian Andes, unlike the previous tectonogenesis that affected only specific terranes. Gómez–Vargas et al. (2017) suggested that the Penderisco Formation, associated with the Calima Terrane, was detached from its oceanic basement and was obducted during the collision.

Additionally, an important late Miocene to Pliocene magmatic event affected the whole Western Cordillera, at that moment already constituted by the accreted Cuna Terrane and the Calima Terrane. A shoshonitic belt that includes El Botón Trachybasalt, dated at 9.3 Ma by K–Ar (Restrepo et al., 1991) and at 11 ± 0.3 Ma by Ar–Ar (Rodríguez & Zapata, 2012), and several intrusives dated between 12 and 9 Ma by K–Ar and Ar–Ar (Rodríguez & Zapata, 2012 and references therein), mostly of monzonitic composition, extends between latitudes 5° 30' N and 7° 15' N. The magmatic belt migrated to the east and affected the Cauca River valley during the Combia magmatism between 10 and 6 Ma, which was responsible for the Au–Cu porphyries of the well–known "Middle–Cauca belt".

The late Miocene to Pliocene belt in the central and southern parts of the Calima Terrane is different from the early Oligocene – Miocene belt described above. The former includes the Piedrancha and Anchicayá Batholiths and El Pital and Tatamá Plutons, which are intrusions into the Calima Terrane prior to collision with the Cuna Terrane. Presumably, the two magmatic events were associated with different subduction zones.

The age range of the accretion of the Cuna Terrane to the Calima Terrane can be restricted because this event seems to have occurred after the intrusion of the Tatamá Pluton, dated at 17 Ma (Brook, 1984), and before the intrusion of El Boton Trachybasalt, dated at 11 Ma (Rodríguez & Zapata, 2012).

The Cuna Terrane represents an island arc generated on top of the Caribbean Plate farther south of its current position (Kennan & Pindell, 2009), which entered as a wedge between North and South America. The dextral movement in the Colombian west was blocked when the arc collided, allowing accretion of the Cuna Terrane to the Northern Andes. It is possible that the collision changed the direction of the fault displacement in the boundary zone between the Cuna and Calima Terranes. The formation of a bridge between North and South America allowed terrestrial faunal exchange between the two continents and implied an evolutionary mismatch between the Pacific Ocean marine faunas and those of the Caribbean Sea (Duque–Caro, 1985; Montes et al., 2012).

5. The Oceanic Terranes in the Cauca–Romeral Strip

5.1. Introduction

As stated in the continental terranes chapter, the Cauca–Romeral strip is composed of continental and oceanic microterranes (Figure 3) resulting from the rupture of the collision zone between these domains. All of the recognized terranes form long N–S oriented strips, some only a few kilometers long and others several tens of kilometers. Within this strip, continental slivers correlatable with the Tahamí Terrane may be present as well as ultramafic bodies that have not yet been classified as terranes.

5.2. Ebéjico Terrane (Quebradagrande)

We propose using the name Ebéjico Terrane instead of Quebradagrande Terrane to avoid confusion with the Quebradagrande Formation (Botero, 1963) or the Quebradagrande Complex (Maya & González, 1995). An additional reason for the change is to use a name related to pre–Columbian tribes or places, as has been common in past works.

The boundaries of the terrane are two faults of the CRFZ. To the east, the San Jerónimo Fault separates Quebradagrande from continental terranes such as the Tahamí, Anacona, and Yalcón Terranes, and to the west, the Silvia–Pijao Fault separates it from the Pozo (Arquía) Terrane south of the Arma Fault. North of this area, the Romeral Fault (sensu Grosse, 1926) separates the Ebéjico Terrane from the Amagá–Sinifaná Terrane (Restrepo et al., 2009a).

The lithology of the Ebéjico Terrane corresponds completely to the Quebradagrande Complex (Maya & González, 1995). It is composed of flows, pillow lavas, breccias, and tuffs of basaltic to andesitic composition interbedded with sedimentary rocks, including shales, arkoses, and cherts (González, 2001; Jaramillo et al., 2017; Rodríguez & Cetina, 2016). Manganese minerals that presumably formed on the ocean floor occur near Santa Bárbara, Antioquia (Durango, 1978). The basic rocks have undergone strong spilitization, forming abundant pumpellyite and chlorite that impart a green color to the greenstones (Restrepo & Toussaint, 1984). The unit forms a narrow and discontinuous belt with a maximum width of approximately 15 km that extends from Ecuador, where it is known as the Alao Terrane (Litherland et al., 1993), to the town of Liborina, Antioquia (Gómez et al., 2015a). The continuation of the terrane to the north of the Central Cordillera is not completely clear. Some authors (Mora–Bohórquez et al., 2017) have suggested

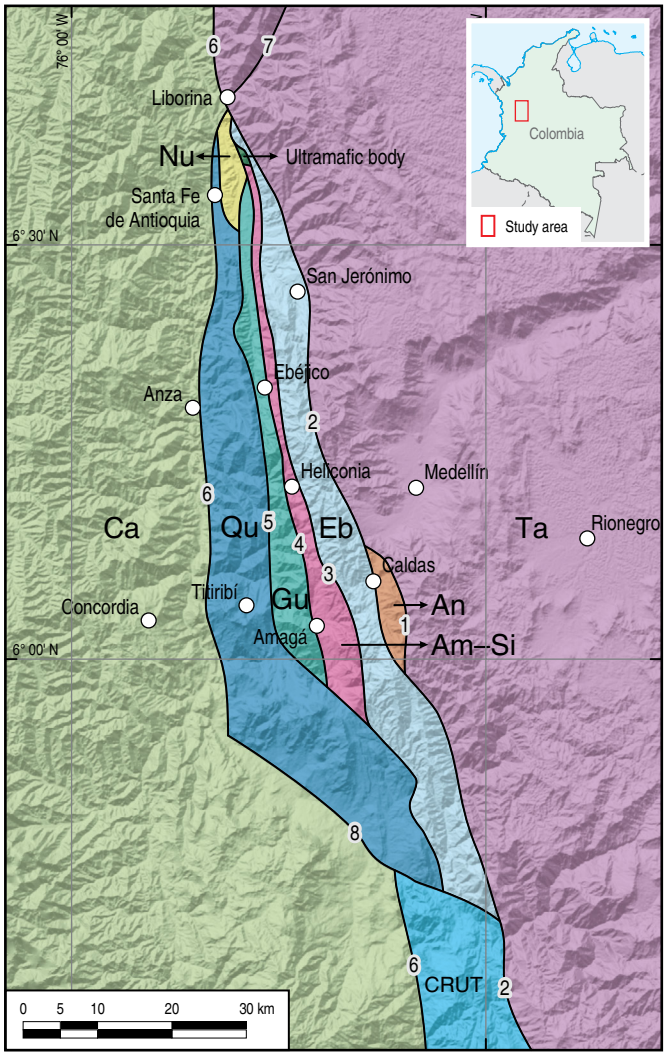

Figure 3. Schematic map of the small terranes in the Cauca–Romeral Fault Zone.

that it extends northward under the sedimentary cover of the Caribbean lowlands, but this continuity has not been proven. Cardona et al. (2012) seem to imply that the Quebradagrande Complex is not present in this area. On the surface, this terrane has not been mapped north of Liborina in the northern part of the Central Cordillera (Gómez et al., 2015a; Hall et al., 1972). However, recent unpublished mapping in the Liborina–Sabanalarga area has demonstrated the presence of low– to medium–grade metamorphic rocks that could be the northward continuation of the Quebradagrande Complex, although the nature of the metamorphism as dynamothermal or dynamic is debated. Guiral–Vega et al. (2015) and Jaramillo et al. (2017) suggest that metamorphism is dynamic in character and is associated with the important wrench faults that are present in the area. However, a close examination of thin sections shows that the mineralogy and microstructures of greenschists and muscovite–quartz schists correspond to dynamothermal metamorphism, followed by shearing and mylonitization along these faults. The San Jerónimo Fault proper also ends at Liborina. This truncation is probably because the Tahamí has a prong (the Liborina prong proposed here), the most westerly occurrence of the terrane, that seems to have squeezed the several CRFZ faults so that here they are separated by only a few kilometers. The possibility exists that a metamorphic Quebradagrande has been included in the Cajamarca Complex in previous mapping efforts. In fact, in the detailed mapping by Grosse (1926), this part of the diabases was considered to be a metamorphic variant, but this feature was apparently forgotten by subsequent field geologists. In a somewhat similar way, extensive mylonitic rocks produced by the shearing of the Quebradagrande Complex along the CRFZ, at an approximate latitude of 5° N, were mapped as regional metamorphic rocks equivalent to the Cajamarca Complex (González, 1980). Detailed mapping and petrological and geochronological studies are necessary to clarify this possibility.

The age of the Quebradagrande Complex based on fossils is Aptian – Albian (González, 1980) or Hauterivian – Albian (Botero et al., 1974). The unit has been difficult to date using K–Ar and Ar–Ar methods due to the alteration and very–low–grade metamorphism that is present almost everywhere, as well as the scarcity of zircons that has extensively hampered U–Pb dating. However, a U–Pb zircon date from a metatuff yielded an age of 114.3 ± 3.8 Ma (Villagómez et al., 2011), and a dioritic dike that is thought to be associated with Quebradagrande yielded a similar age of 112.6 ± 3.1 Ma (Cochrane et al., 2014). As such, an Early Cretaceous age is indicated for the unit. This age is valid both for the sedimentary rocks and for the volcanics because in the Arma fossiliferous locality, the authors collected volcanic rocks with *Trigonia* imprints and samples of volcanic rocks intercalated with sedimentary rocks; photos of these two samples were published by González (1980; see Figure 18). Some Late Cretaceous ages have also been reported. Botero (1963) considered the algal remains of the genus *Archeolithothamnion* to be indicative of a Late Cretaceous age, but in fact, the range of this genus extends from Late Jurassic to Neogene (Johnson, 1963). An age of 93.41 ± 0.51 Ma was obtained from a gabbroic

intrusion supposedly related to the Quebradagrande volcanics, indicating a probable continuation of the magmatism to the Late Cretaceous (Jaramillo et al., 2017).

The origin of the Quebradagrande Complex is still debated. Although an island arc magmatic origin with possible remnants of a basal oceanic crust is recognized by most authors, the environment where the arc was formed is unclear. Nivia et al. (2006) suggested that the continental margin of South America was rifted in the Early Cretaceous, forming a marginal basin and a suprasubduction zone arc with Neoproterozoic (?) metamorphic rocks on both sides of the basin, followed by a final compressional event that closed the basin. This model was criticized for several reasons by Restrepo et al. (2009b), one of the reasons being the presence of belts exclusively composed of Quebradagrande or Arquía Complexes and completely limited by faults, with no intermingling between them. This condition is easily explained by a terrane model but is quite difficult to explain in an autochthonous model. On the other hand, models such as the one proposed by Villagómez & Spikings (2013) suggest that the arc was intraoceanic and related to a subduction zone that formed the Arquía Complex and that after the formation of these rocks, they were accreted to the continental border. Jaramillo et al. (2017) also argued for an oceanic arc but with a thickened crust; a major variation in this model is that the age of the arc is considered Late Cretaceous based on dating of granitoid rocks intruding the basic rocks.

The name of the terrane is taken from the present municipality of Ebéjico, Antioquia, where good exposures of the Quebradagrande Complex are found. This word is an indigenous term that was originally applied to a valley in the Western Cordillera where the city of Antioquia was first founded in 1541 (Aguilar–Rodas, 2001; Duque, 1967).

5.3. Pozo Terrane (Arquía)

The name of the Pozo Terrane is proposed for the terrane known by some authors as the Arquía Terrane because the names Arquía Group (Restrepo & Toussaint, 1976) and Arquía Complex already exist in the literature (Maya & González, 1995). Pozo is the name of an ethnic group that lived near the Arquía area, on the border between the Antioquia and Caldas Departments.

The Arquía Group (Restrepo & Toussaint, 1976) is a narrow belt of metamorphic rocks that include garnet amphibolites, serpentinites, greenschists, graphite–muscovite schists and quartzites. The units are crosscut by several faults and thus form discrete blocks. Some authors have called it a mélange (i.e., González, 2001; Rodríguez & Arango, 2013), but this term is not an adequate name since the definition of mélange requires a fine matrix that surrounds the blocks (Festa et al., 2010), which is not present in the area.

For the most part, the K–Ar and Ar–Ar ages of the Arquía garnet amphibolites yield Early Cretaceous ages (Restrepo et al., 2008; Villagómez & Spikings, 2013; Ruiz–Jiménez, 2014). The unit has been considered allochthonous, with the rocks formed in a subduction zone (Restrepo & Toussaint, 1976; Villagómez et al., 2011). However, P–T measurements by Garcia–Casco et al. (2011) have shown that the temperature gradient that formed these rocks is higher than those found in subduction zones, so a collisional origin has been proposed by these authors. Nonetheless, the association of metamorphic serpentinites with garnet amphibolites favors a subduction zone environment. In this same sense, Ríos–Reyes et al. (2017) proposed that the garnet amphibolites are retrograded eclogites similar to those found at Pijao and Barragán. An alternative autochthonous origin was proposed by Nivia et al. (2006), as discussed above for the Ebéjico Terrane, where the metamorphic Arquía rocks are considered Neoproterozoic rocks that formed part of the continental margin that was rifted during the Cretaceous. A similar autochthonous model was proposed by Cochrane et al. (2014).

The name of the group was extended by Maya & González (1995) to cover a complex that includes this unit, as well as several other metamorphic and even basic igneous rocks. The complex is located close to the Cauca River, extending along the western side of the Central Cordillera and the Cauca valley. Units such as the Bugalagrande Schists, the Sabaletas Schists, the Palestina–Balboa Schists, the Sucre Amphibolites, the Bolo Azul Complex, the Buesaco Schists, and the Complejo Río Rosario have been included in the complex. In Ecuador, its equivalent is the Alao Terrane (Litherland et al., 1994). In the original definition, high–P rocks such as the Pijao eclogites and Barragán blueschists and eclogites were not included, but modern usage has incorporated them within the complex.

Lithogeochemical analyses indicate that tholeiitic basalts with a MORB origin were the predominant protoliths of the basic rocks (Villagómez et al., 2011; García–Ramírez et al., 2017), although a small negative Nb anomaly indicates some affinity with IAT (Ruiz–Jiménez, 2014; Ruiz–Jiménez et al., 2012).

Due to the application of the name Arquía to different rank units, specifying in any article whether it is related to the Arquía "Group" (using the original definition and name given by Restrepo & Toussaint, 1976) or to the Arquía Complex is necessary. For example, the Sabaletas Schists (Toussaint et al., 1981) are considered part of the Arquía Complex, but in our opinion, they would not be part of the Arquía "Group". A similar situation is found for the newly defined Quimbaya Terrane (Chinchiná Gneiss) near Manizales (Restrepo & Toussaint, 2020). It may be part of the Arquía Complex but not of the Arquía "Group".

The terrane is separated from the Ebéjico Terrane to the east by the Silvia–Pijao Fault and to the west from the Calima Terrane by the Cauca–Almaguer Fault (Figure 4); both faults are part of the CRFZ (Maya & González, 1995).

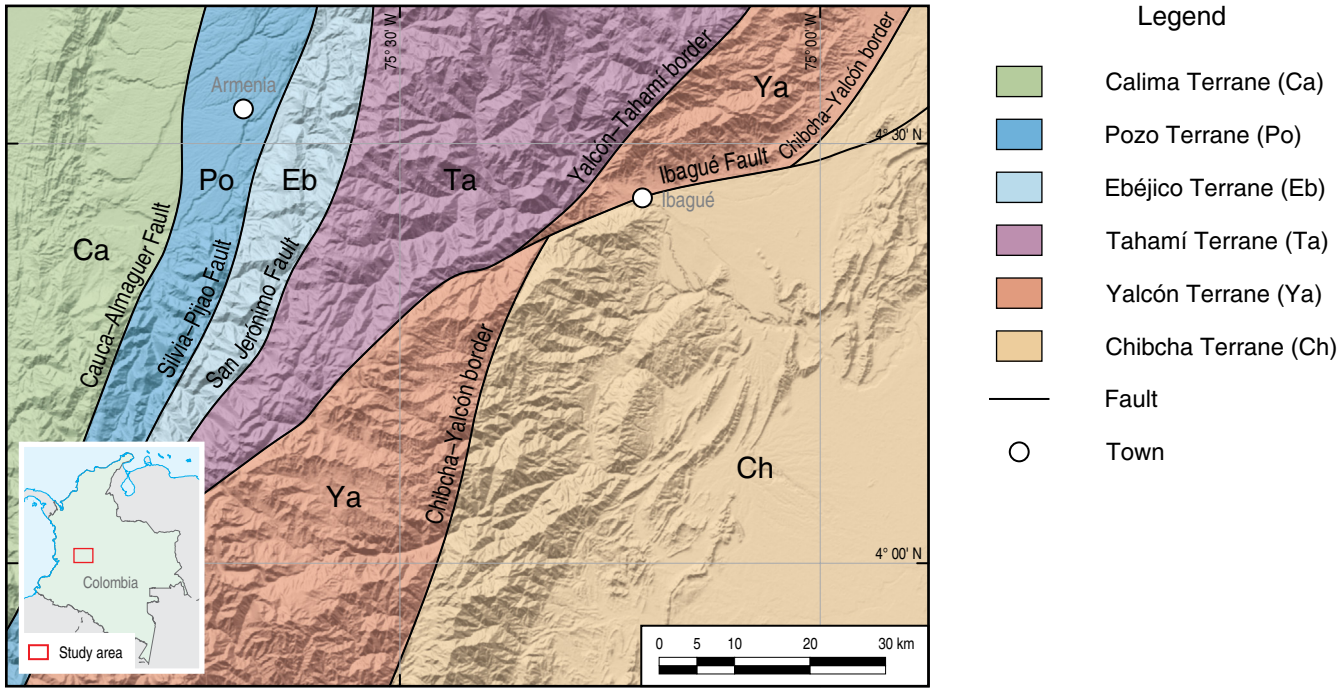

Figure 4. Schematic map of terranes and faults in the Ibagué area.

5.4. Bocaná Suspect Terrane

This suspect terrane occurs on the eastern side of the Aburrá valley (Medellín) and is composed mainly by amphibolites.

The main unit is the Santa Elena Amphibolite, which is composed of amphibolites, some of which are garnetiferous, and interbedded with quartz–biotite–graphite schists and some of which are associated ultramafic rocks (Restrepo, 2008). According to recent U–Pb zircon ages, metamorphism occurred in the mid–Cretaceous (Restrepo et al., 2012). This age is in contrast with the Triassic age of the contiguous La Espadera–Chupadero Amphibolites that compose part of the Triassic Aburrá Terrane (see below). The Santa Elena Amphibolites are geochemically different from La Espadera–Chupadero Amphibolites and are richer in incompatible elements (Restrepo, 2008). The age and composition are similar to those of the garnet amphibolites of the Arquía Complex, so perhaps they could be related in origin. The limits of the terrane are denoted by an inferred thrust fault that occurs at the base of the unit. The eastern side of the terrane was intruded by the Antioqueño Batholith, and on the western side, the Rodas Fault separates it from the Aburrá Terrane.

Bocaná was the name of Santa Elena Creek, which crosses the city of Medellín from east to west, in the indigenous language and means brackish water (Figure 5).

5.5. Aburrá Terrane

A dismembered ophiolite crops out along the Aburrá valley, composed of a large ultramafic body, El Picacho Metagabbros, and La Espadera–Chupadero Amphibolite. The ultramafic rock is composed mainly of olivine, in part serpentinized, chromium spinel and variable amounts of tremolite, talc, and chlorite. The presence of these three minerals is interpreted as the replacement of ortho– and clinopyroxenes during metamorphism (Correa–Martínez, 2007; Restrepo, 2008). Hence, the name Medellín metaharzburgitic unit is proposed for this unit (Garcia–Casco et al., 2020).

The metagabbros occur mostly on the western side of the valley, with Picacho Peak hosting the best exposure. They also appear as boulders in the extensive mass–movement deposits that are found on the western side of the Medellín valley. Metamorphic plagioclase and amphibole are the main minerals, with reddish–brown hornblende as a probable relict igneous mineral. The microstructures vary from granular gabbroic relict structures to well–foliated rocks that are practically lineated amphibolites. The unit is named the Picacho Metagabbros (Correa–Martínez et al., 2005). Hornblende–plagioclase metapegmatites are found in several places.

Fine–grained amphibolites underlie the ultramafic body, although the outcrops are difficult to observe due to the geometry of the ultramafic body and the abundant mass–movement deposits that cover the slopes of the Medellín valley. Lithogeochemical analyses of La Espadera–Chupadero Amphibolites show that these are of incipient island arc affinity (Restrepo, 2008), whereas the Santa Elena Amphibolites are richer in incompatible elements, representing a probable MORB origin. U–Pb analyses of La Espadera Amphibolite, metagabbros and metapegmatites yield Triassic ages (Restrepo et al., 2007; Restrepo et al., 2012). Apparently, the ages of approximately

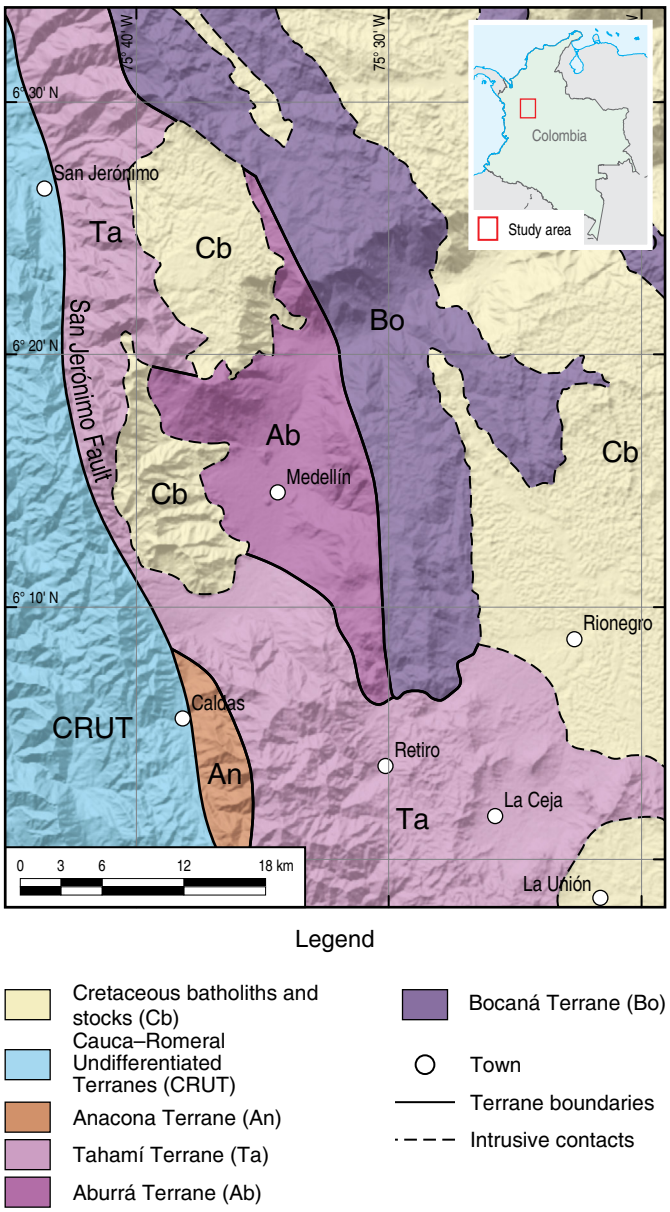

Figure 5. Schematic map of the terranes in the Medellín valley area.

228 Ma indicate the igneous formation of the mafic materials. The complex was named the Aburrá Ophiolitic Complex (Correa–Martínez et al., 2005).

Aburrá was the name of the natives that lived in the Medellín valley when the spaniards arrived. It is also the name of the valley where the city of Medellín and neighboring towns are located.

5.6. Quirimará Terrane (Sabaletas Schists)

This thin belt of intercalated greenschists and "blackschists", located between latitudes 6° 00' N and 6° 35' N, has been generally included in the Arquía Complex (i.e., Maya & González, 1995; Gómez et al., 2015a). The rocks in this belt are composed of albite–epidote–chlorite–actinolite schists intercalated with graphite–muscovite–quartz schists; according to Grosse (1926), garnet may also occur. They compose the wallrock of the famous Zancudo gold mines in Titiribí. In this unit, we also include the schists found at the western margin of the Cauca River near Santa Fé de Antioquia that were recently named the "Santa Fé de Antioquia Mylonites" (Correa et al., 2017).

The unit was named the Sabaletas Schists by Toussaint et al. (1981), who obtained Early Cretaceous ages (127 ± 5 Ma) from a greenschist using K–Ar dating; an age of 104 ± 5 Ma was also obtained using this method from actinolite in a metagabbro (Restrepo et al., 1991), and a younger age of 71 ± 3 Ma was obtained from actinolite (K–Ar) in a retrograded amphibolite (Ruiz–Jiménez, 2014). Vinasco & Cordani (2012) obtained an age of 127.5 ± 2 Ma by Ar–Ar dating. However, the real age of the unit has been debated. Rodríguez–Jiménez (2010) argued that the schists are intruded by dikes related to the Pueblito Diorite, dated at 233 Ma, whereas Giraldo–Arroyave (2010) dated by U–Pb zircons obtained from the greenschists at 72 Ma, which she considered a magmatic age. Similar Cretaceous ages were obtained using the same method by Correa et al. (2017) and Zapata & Cardona (2017). These apparently incompatible ages can be reconciled when it is observed that the Pueblito dioritic body and some schists lie to the east of the important Quirimará Fault, which is part of the CRFZ, whereas the Sabaletas Schists are on the western side of the fault. In this sense, the schists intruded by the Pueblito Dike would have no relation with the Sabaletas Schists; we propose that they would belong to different terranes, so the ages of the schists cannot be compared. As discussed in Restrepo & Toussaint (2020), the Pueblito Diorite and its surrounding schists are included in a new terrane named Guaca.

The age of metamorphism is post–70 Ma, but an exact age is unknown. However, it is quite likely close to the Cretaceous – Paleocene boundary, as discussed in the chapter on terranes with continental basement, for the accretion of the Cuna Terrane to the Tahamí Terrane (Restrepo & Toussaint, 2020). The Early Cretaceous K–Ar and Ar–Ar ages obtained from this unit remain unexplained; a possibility is that rocks with different ages but similar compositions were mingled during the accretion processes.

The unit has been considered to be composed mainly of mylonitic rocks (i.e., Correa et al., 2017; Zapata & Cardona, 2017), but a close petrographic inspection shows that they are actually dynamothermal schists affected locally by intense shearing and mylonitization (i.e., see Grosse's classic study, 1926, for petrographic descriptions). A shearing–related origin for the unit that would be associated with the accretion of the Calima Terrane to the western side of South America has been attributed by these authors. The dynamothermal nature of the schists probably implies a more complicated scenario, where the rocks underwent heating within the greenschist facies and even the epidote–amphibolite facies in addition to deformation produced by the accretion. Ruiz–Jiménez (2014) measured pressure con-

ditions for an amphibolite found within the schists, finding a pressure between 6.7 and 7.0 kbar; under these conditions, the metamorphic rocks would have formed at depths on the order of 22–23 km. To explain this deep burial and subsequent exhumation, it is hypothesized here that these materials could have penetrated into the subduction zone that existed during the Late Cretaceous on the western side of the Tahamí Terrane. This subduction zone accommodated transpressional stress with strong right–lateral horizontal movement. Thus, this metamorphism could be called a *transpressional collisional metamorphism*, limited to a small area as opposed to normal collisional metamorphism. Subsequently, the right–lateral movement that had a vertical component could have exhumed the sliver. In this way, schists with mineralogic and microstructural dynamothermal characteristics would have been formed in a small area but with characteristics similar to those of regional metamorphism. Near the bordering faults, local mylonitization would have been intense. Presently, the nature of the protoliths is unknown. Although the mineralogical compositions of the rocks point to an ocean floor, rocks from this environment of approximately 70 Ma are unknown in the area. The limits of the sliver are the Quirimará Fault to the east, which separates it from the Guaca Terrane, and the Cauca–Almaguer Fault to the west, which separates it from the Calima Terrane. It should be noted that the Cauca–Almaguer Fault is considered the fault that places the oceanic rocks of the Calima Terrane in contact with other units of the Cauca–Romeral Terranes or even the Tahamí Terrane. Quirimará is an indigenous name applied to a hill formed by the schists west of the town of Ebéjico (Rodríguez–Pulgarín, 2011).

5.7. Nutabe Terrane (Sucre Amphibolite)

These amphibolites or metagabbros are strongly lineated rocks associated with serpentinized ultramafic rocks. The name Nutabe corresponds to a pre–Spanish tribe.

A hornblende K–Ar age of 284 ± 30 Ma has been reported (Restrepo et al., 1991), and more recently, ages of 260.7 ± 16.3 and 267.5 ± 16.2 Ma were obtained by U–Pb in magmatic zircons from these amphibolites (Correa et al., 2017). The body extends to the western margin of the Cauca River, where it is in fault contact with the northern extension of the Sabaletas Schists (also called the Santa Fé de Antioquia Mylonites) along one of the Cauca Faults. The history of metamorphism and accretion of this block has not yet been determined. The age is similar but somewhat older than the age of metamorphic rocks of the Tahamí Terrane.

5.8. Ultramafic Slivers

Several ultramafic slivers bounded by faults occur in this area, with the larger ones being the Heliconia and Sucre bodies. No special name is assigned for these very small terranes.

The Heliconia body is spatially associated with gabbros and the Pueblito Diorite. Several different origins have been proposed for ultramafic rocks. Rodríguez–Jiménez (2010) proposed that the three units are the components of a zoned body related to a suprasubduction zone, whereas according to Montoya & Peláez (1993), only the gabbro and the ultramafics are related, as parts of an ophiolite. Recently, the ultramafic unit was studied by González–Ospina (2016), who considered that it is an ophiolitic body related to the Medellín Metaharzburgitic Unit (Garcia–Casco et al., 2020). Neither the age of formation nor the age of emplacement have been defined for these rocks, although the fact that the Sucre body is spatially related to the Permian Sucre Amphibolites suggests a probable similar age.

In the CRFZ, several other similar slivers exist, such as the Planeta Rica Peridotites in the Córdoba Department (Dueñas & Duque–Caro, 1981), where an important nickel mine is located, and the Ginebra, Venus, La Tetilla, and Los Azules Ophiolitic Complexes (De Souza et al., 1984; Espinosa–Baquero, 1985; Nivia, 1987, 1991, 2001; Spadea et al., 1987) in the Cauca and Valle del Cauca Departments.

5.9. Nechí Terrane (Campamento)

Etayo–Serna et al. (1983) defined the Campamento Terrane to include these rocks. The name Nechí Suspect Terrane (Figure 6) seems to be a better name because it is based on the term "Nechí", an indigenous name; it is also the name that was used originally for the basic–ultrabasic complex by Estrada (1967).

The terrane is composed of an ophiolitic complex located in the northern part of the Tahamí Terrane near the Nechí River between the towns of Yarumal and Campamento. It crops out along the axis of the Central Cordillera, on the northern side of the Antioqueño Batholith, and it is not part of the Cauca–Romeral Terranes.

This terrane is composed of serpentinized ultramafic rocks, gabbros, and basalts that are covered by flysch sedimentites known as the San Pablo Formation. All of the rocks are affected by very low– to low–grade metamorphism. The exact age is unknown. The age is pre–Late Cretaceous because the Antioqueño Batholith intrudes these rocks, but a maximum age is uncertain (Hall et al., 1972). The sequence was interpreted by Estrada (1967) as the Nechí Mafic–Ultramafic Complex, whereas Restrepo & Toussaint (1973) considered that it was part of a large obduction complex that emplaced ophiolitic bodies over the Tahamí Terrane during the Cretaceous. Presently, a portion of these bodies are included in the Aburrá Terrane. Mejía et al. (2017) considered that a marginal basin was formed in the area in Early Cretaceous before the intrusion of the Antioqueño Batholith; however, the details were not described.

According to Etayo–Serna et al. (1983), the eastern limit of the terrane is the San Lorencito–Corrales Fault, the western limit is the San Juan–Nechí Fault and the southern limit is de-

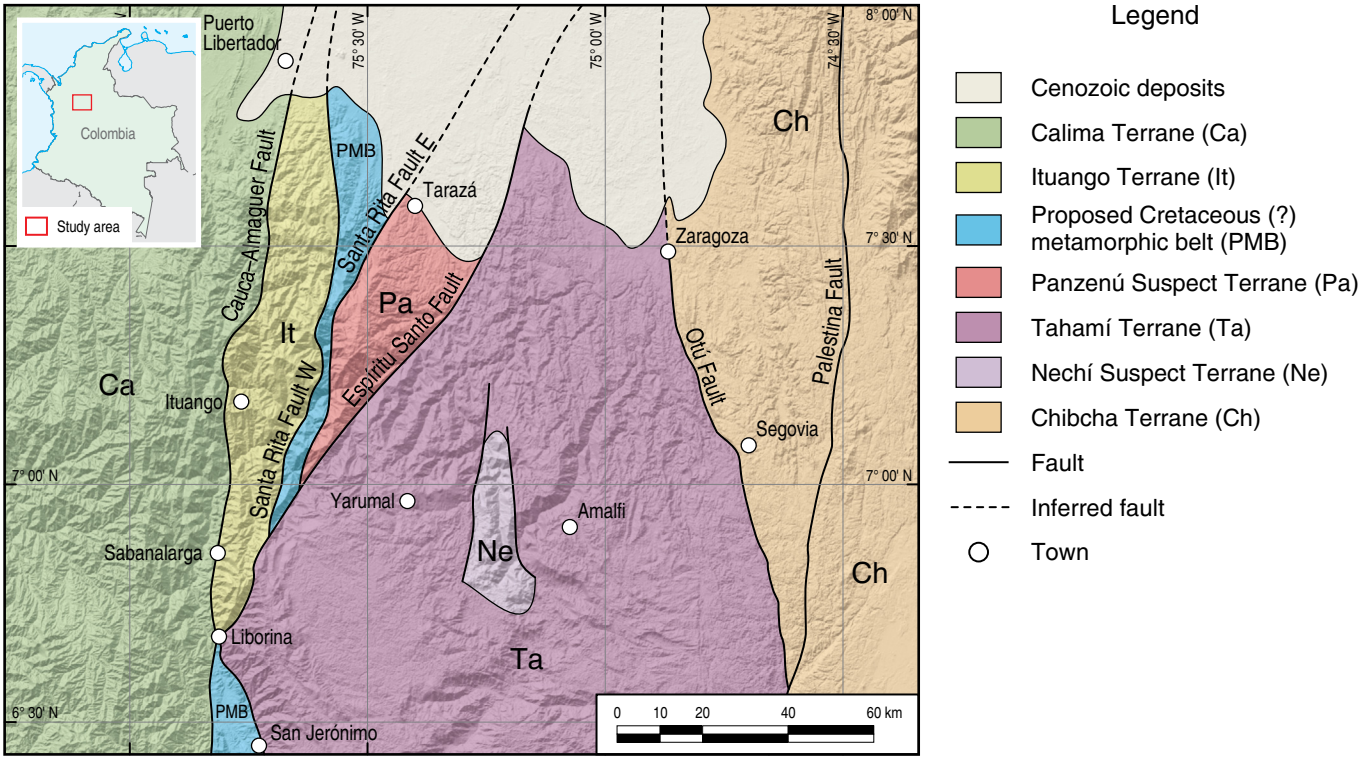

Figure 6. Schematic map of the Nechí Terrane.

fined by the Antioqueño Batholith. More field work is needed to determine whether the mafic–ultramafic complex is in situ or allochthonous.

6. The Tairona Terrane in the SNSM and La Guajira Peninsula

In a review by Etayo–Serna et al., (1983), the terranes with oceanic basement in northern Colombia are Santa Marta in the SNSM and Ruma in the LGP. Restrepo & Toussaint (1988) argued that these terranes are associated with the Calima Terrane, and Gómez et al. (2015a) suggested that they are associated with the Caribbean Megaterrane. This work groups them as a single Tairona Terrane, named after an important pre–Columbian culture in the SNSM (Figure 1).

The NW part of the SNSM corresponds to the Tairona Terrane formed mainly of muscovite and chlorite quartz schists, phyllites, slates, and some marbles. These rocks have been given several local names, such as La Gaira Schists, the Taganga Phyllites, and the San Lorenzo Schists. They were grouped as the Santa Marta Schists, whose magmatic age was dated by U–Pb in zircons between 91 and 80 Ma (Cardona et al., 2010). This metamorphism has been geochronologically difficult to determine, but these authors believe that metamorphism had already ended at 65 Ma. The granodioritic to quartz–monzonitic Santa Marta Batholith intrudes the previous metamorphic set and was dated by U–Pb between 56 and 50 Ma (Mejía–Herrera et al., 2008; Duque, 2010). Another stock, the Toribio Pluton, is also considered Paleocene. In the SNSM, the Tairona Terrane is linked to the Kogi Terrane (see Restrepo & Toussaint, 2020) by the inverse Guachaca Fault System. Several of these faults are oblique relative to the original boundary. The Buritaca Pluton, dated by U–Pb as 50 ± 1.5 Ma (Duque, 2010), appears to intrude the boundary between the terranes, which suggests their accretion in the early Paleocene–Eocene. In the LGP, the Tairona Terrane, limited to the SE by the Simarua–Osorio Fault that produced a strong mylonitization, overrides the Kogi Terrane. According to the Geological Map of Colombia (Gómez et al., 2015b), reef limestones associated with marls, mudstone, and sandstone of the Eocene Uitpa Formation cover the border, which suggests that the suturing between the Tairona and Kogi Terranes occurred in the Late Cretaceous – Paleocene.

In LGP, the Tairona Terrane includes the presumably Late Cretaceous Etpana Metamorphic Complex and is intruded by the Parashi Granodioritic Pluton that has been dated by U–Pb at 49 ± 1 Ma (Cardona et al., 2014). The presence of serpentinites with rodingite dikes is noted in the Etpana Complex and in the Cabo de la Vela. Schists, amphibolites, and phyllites from the Jarara and Carpintero Ranges are also found in this area. Cardona et al. (2014) hypothesized that an intraoceanic island arc environment developed in an allochthonous position during the Cretaceous and was accreted before the Eocene intrusion of the Parashi Pluton. Piraquive et al. (2017) suggested that units with oceanic affinity such as the Jarara Formation from the Tairona Terrane override continental units similar to the Macuira Gneiss

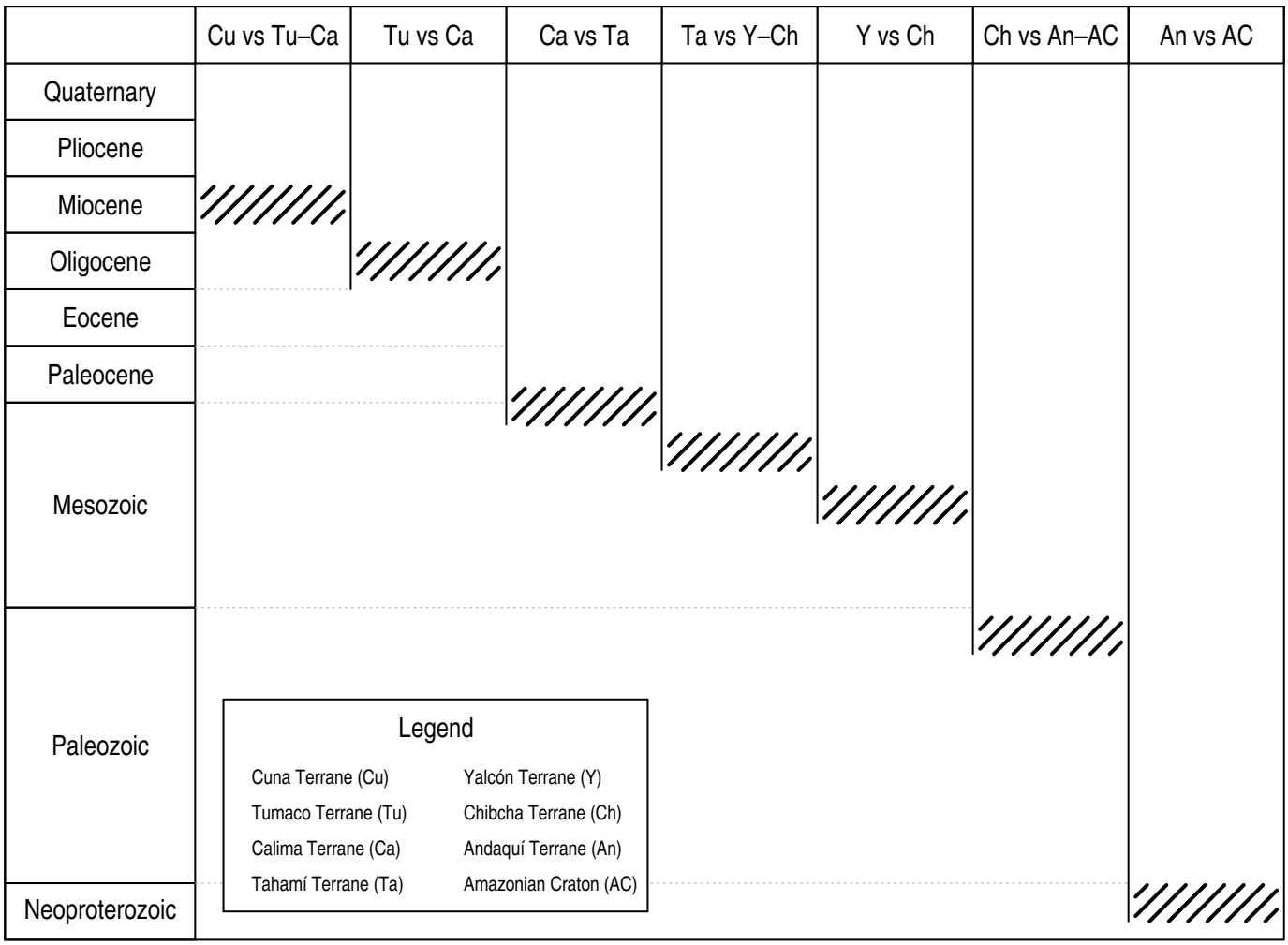

Figure 7. Timing of accretions of Colombian Terranes.

from the Kogi Terrane. These authors proposed that accretion occurred between the Late Cretaceous and the Paleocene.

The Tairona Terrane has certain similarities to the Calima and Tumaco Terranes. All have Cretaceous oceanic basements, but until more information is available, it seems more appropriate to treat them as different terranes.

7. Conclusions

With few exceptions, all the terranes west of the San Jerónimo Fault have oceanic crust. They probably formed south of their present positions and then moved northward to collide with the Tahamí Terrane in Late Cretaceous time or later (Figure 7). The accretion of the Calima Terrane occurred close to the Cretaceous – Paleogene boundary. Then, between the mid–Eocene and early Miocene, the Tumaco Suspect Terrane was accreted. Finally, the Cuna Terrane collided with the rest of the terranes during the Miocene (17–11 Ma), causing important changes in the geology of Colombia (Figure 7). Most of the terranes are part of the Caribbean Plateau. A special type of metamorphism is described here as collisional transpressional metamorphism, which produces dynamothermal metamorphism in small areas.

Acknowledgments

We wish to thank Gómez et al. (2015c) for the excellent compilation of isotopic dates in Colombia. Without them, this work would have been much more difficult.

We are also grateful to Andrés PARDO–TRUJILLO and Yamirka ROJAS–AGRAMONTE, reviewers of this chapter. Their suggestions greatly improved the manuscript.

The authors especially wish to thank Professor Oswaldo ORDOÑEZ–CARMONA for the interesting discussions about the geology of western Colombia while sharing the teaching of geological field work. Although in some cases we do not agree, the difficult questions posed by professor ORDOÑEZ–CARMONA motivated new ideas regarding the numerous geological problems we discussed. The possibility of a Cretaceous unit between the Ituango Block and the Tahamí and Panzenú Terranes was discussed several times, as well as the importance of collisional metamorphism in the CRFZ.

We also want to thank Fernando ALCÁRCEL for drawing the final versions of the figures.

References

Agencia Nacional de Hidrocarburos & Geología Regional y Prospección. 2011. Cartografía geológica a escala 1:100 000 de las planchas 340, 362, 385 y 409 localizadas en la Cuenca Tumaco, así como el inherente levantamiento de columnas estratigráficas y muestreo litológico para los análisis petrográficos, bioestratigráficos, geoquímicos, petrofísicos y radiométricos. Contrato 084 de 2010, unpublished report. 207 p.

Aguilar–Rodas, R. 2001. Fundación de la ciudad de Antioquia–1541. Academia Antioqueña de Historia, 144 p. Medellín.

Álvarez, J. & González, H. 1978. Geología y geoquímica del cuadrángulo I–7 Urrao. Ingeominas, Internal report 1761, 347 p. Medellín.

Álvarez, J. & Linares, E. 1981. Edades K/Ar del Batolito de Piedrancha y el Stock de Arboledas, departamento de Nariño. Boletín de Ciencias de la Tierra, (5–6): 113–118.

Aspden, J. 1984. The geology of the Western Cordillera and Pacific coastal plain in the departament of Valle del Cauca (sheets 261, 278, 279, 280 and 299). Ingeominas–Misión Británica, Internal report 1959, 61 p. Cali.

Aspden, J.A. & McCourt, W.J. 1986. Mesozoic oceanic terrane in the central Andes of Colombia. Geology, 14(5): 415–418. https://doi.org/10.1130/0091-7613(1986)14<415:MOTITC>2.0.CO;2

Bandy, O.L. 1970. Upper Cretaceous–Cenozoic paleobathymetric cycles, eastern Panamá and northern Colombia. American Association of Petroleum Geologists Bulletin, 54 (9): 1782.

Barrero, D. 1979. Geology of the central Western Cordillera, west of Buga and Roldanillo, Colombia. Publicaciones Geológicas Especiales del Ingeominas, (4): 1–75. Bogotá.

Bird, P. 2003. An updated digital model of plate boundaries. Geochemistry, Geophysics, Geosystems, 4(3): 1–52. https://doi.org/10.1029/2001GC000252

Botero, G. 1936. Bosquejo de la paleontología colombiana. Bachelor thesis, Universidad Nacional de Colombia, 116 p. Medellín.

Botero, G. 1963. Contribución al conocimiento de la geología de la zona central de Antioquia. Universidad Nacional de Colombia, Anales de la Facultad de Minas, 57, 101 p. Medellín.

Botero, G., Toussaint, J.F., Ospina, H., Ortiz, F. & Gómez, J. 1974. Yacimiento fosilífero de Arma. Universidad Nacional de Colombia, Anales de la Facultad de Minas, 58, p. 1–12. Medellín.

Bourgois, J., Azéma, J., Tournon, J., Bellon, H., Calle, B., Parra, E., Toussaint, J.F., Glaçon, G., Feinberg, H., De Wever, P. & Origlia, I. 1982a. Ages et structures des complexes basiques et ultrabasiques de la façade pacifique entre 3º N et 12º N (Colombie, Panama et Costa Rica). Bulletin de la Société Géologique de France, 24(3): 545–554. https://doi.org/10.2113/gssgfbull.S7-XXIV.3.545

Bourgois, J., Calle, B., Tournon, J. & Toussaint, J.F. 1982b. The andean ophiolitic megastructures on the Buga–Buenaventura transverse (Western Cordillera–Valle, Colombia). Tectonophysics, 82(3–4): 207–229. https://doi.org/10.1016/0040-1951(82)90046-4

Brook, M. 1984. New radiometric age data from SW Colombia. Ingeominas–Misión Británica, unpublished report 10, 25 p. Cali.

Buchely, F., Parra, E., Castillo, H., González, F., Dávila, C.F. & Romero, Ó.A. 2009. Realización de la cartografía geológica y muestreo geoquímico en las planchas 144, 145, 128, 129, 113 y 114 (1580 km²). Contrato No. 390 de 2007. Ingeominas & GRP Ltda., 172 p. Bogotá.

B&G Unión Temporal. 2006. Cartografía geológica en los cinturones plegados Sinú–San Jacinto. Agencia Nacional de Hidrocarburos, unpublished report, 46 p. Bogotá.

Calle, B. & Salinas, R. 1986. Memoria explicativa: Geología y geoquímica de la plancha 165 Carmen de Atrato. Scale 1:100 000. Ingeominas, Internal report 1987, 140 p. Medellín.

Cardona, A., Valencia, V., Bustamante, C., García–Casco, A., Ojeda, G., Ruiz, J., Saldarriaga, M. & Weber, M. 2010. Tectonomagmatic setting and provenance of the Santa Marta Schists, northern Colombia: Insights on the growth and approach of Cretaceous Caribbean oceanic terranes to the South American continent. Journal of South American Earth Sciences, 29(4): 784–804. https://doi.org/10.1016/j.jsames.2009.08.012

Cardona, A., Montes, C., Ayala, C., Bustamante, C., Hoyos, N., Montenegro, O., Ojeda, C., Niño, H., Ramirez, V., Valencia, V., Rincón, D., Vervoort, J. & Zapata, S. 2012. From arc–continent collision to continuous convergence, clues from Paleogene conglomerates along the southern Caribbean–South America Plate boundary. Tectonophysics, 580: 58–87. https://doi.org/10.1016/j.tecto.2012.08.039

Cardona, A., Weber, M., Valencia, V., Bustamante, C., Montes, C., Cordani, U. & Muñoz, C.M. 2014. Geochronology and geochemistry of the Parashi granitoid, NE Colombia: Tectonic implication of short–lived early Eocene plutonism along the SE Caribbean margin. Journal of South American Earth Sciences, 50: 75–92. https://doi.org/10.1016/j.jsames.2013.12.006

Case, J.E. & Holcombe, T.L. 1980. Geologic–tectonic map of the Caribbean region. Scale 1:2 500 000. U.S. Geological Survey, series 1100. https://doi.org/10.3133/i1100

Case, J.E., Durán, L.G., López, A. & Moore, W.R. 1971. Tectonic investigations in western Colombia and eastern Panama. Geological Society of America Bulletin, 82(10): 2685–2712. https://doi.org/10.1130/0016-7606(1971)82[2685:TIIWCA]2.0.CO;2

Cochrane, R., Spikings, R., Gerdes, A., Winkler, W., Ulianov, A., Mora, A. & Chiaradia, M. 2014. Distinguishing between in–situ and accretionary growth of continents along active margins. Lithos, 202–203: 382–394. https://doi.org/10.1016/j.lithos.2014.05.031

Coney, P.J., Jones, D.L. & Monger, J.W.H. 1980. Cordilleran suspect terranes. Nature, 288: 329–333. https://doi.org/10.1038/288329a0

Correa–Martínez, A.M. 2007. Petrogênese e evolução do Ofiolito de Aburrá, Cordilhera Central dos Andes colombianos. Doctoral thesis, Universidade de Brasilia, 178 p. Brasilia.

Correa–Martínez, A.M., Martens, U., Restrepo, J.J., Ordóñez–Carmona, O. & Pimentel, M.M. 2005. Subdivisión de las metamorfitas básicas de los alrededores de Medellín–cordillera Central de Colombia. Revista de la Academia Colombiana de Ciencias Exactas, Físicas y Naturales, 29(112): 325–344.

Correa, T., Zapata, J.P., Rincón, A.V., Obando, M.G., Ortiz, F.H. & Rodríguez, G. 2017. Edades U–Pb y Ar–Ar obtenidas durante la cartografía 1:50 000 del borde occidental de la plancha 130 Medellín Occidental. XVI Congreso Colombiano de Geología. Memoirs, p. 1223–1228. Santa Marta.

Desmet, A. 1994. Ophiolites et séries basaltiques crétacées des regions caraibes et nordandines: Bassins marginaux, dorsales ou plateaux océaniques? Doctoral thesis, Université Henri Poincaré, 597 p. Nancy, France.

De Souza, H.A.F., Espinosa, A. & Delaloye, M. 1984. K–Ar ages of basic rocks in the Patia valley, southwest Colombia. Tectonophysics, 107(1–2): 135–145. https://doi.org/10.1016/0040-1951(84)90031-3

Dueñas, H. & Duque–Caro, H. 1981. Geología del cuadrángulo F–8 Planeta Rica. Boletín Geológico, 24(1), 35 p. Bogotá.

Duque–Caro, H. 1984. Structural style, diapirism, and accretionary episodes of the Sinú–San Jacinto terrane, northwestern Caribbean borderland. In: Bonini, W.E., Hargraves, R.B. & Shagam, R. (editors), The Caribbean–South American plate boundary and regional tectonics. Geological Society of America, Memoir 162, p. 303–316. https://doi.org/10.1130/MEM162-p303

Duque–Caro, H. 1985. La Cuenca del Atrato en el bloque del Chocó (Sudamérica noroccidental) y sus implicaciones estratigráficas y estructurales. VI Congreso Latinoamericano de Geología. Proceedings, 1, p. 61. Bogotá.

Duque–Caro, H. 1990. The Choco Block in the northwestern corner of South America: Structural, tectonostratigraphic, and paleogeographic implications. Journal of South American Earth Sciences, 3(1): 71–84. https://doi.org/10.1016/0895-9811(90)90019-W

Duque, F. 1967. Historia del departamento de Antioquia. Imprenta departamental, 1175 p. Medellín.

Duque, J.F. 2010. Geocronología (U/Pb y $^{40}Ar/^{39}Ar$) y geoquímica de los intrusivos paleógenos de la Sierra Nevada de Santa Marta y sus relaciones con la tectónica del Caribe y el arco magmático circun–caribeño. Master thesis, Universidad Nacional Autónoma de México, 189 p. México D.F.

Durango, J. 1978. Prospección geoquímica de las quebradas La Loma y Frías, Santa Bárbara, Antioquia. Ingeominas. Internal report 1770, 45 p. Bogotá.

Echeverría, L.M. 1982. Komatiites from Gorgona Island, Colombia. In: Arndt, N.T. & Nisbet, E.G. (editors), Komatiites. George Allen & Unwin, p. 199–209. London, UK.

Espinosa–Baquero, A. 1985. El Macizo de Ginebra, Valle, una nueva secuencia ofiolítica sobre el flanco occidental de la cordillera Central. VI Congreso Latinoamericano de Geología. Proceedings, 3, p. 46–57. Bogotá.

Espinosa–Baquero, A., Delaloye, M. & Wagner, J.J. 1982. Radiometric ages of the Gorgona Island (Colombia), Komatiitic ophiolite. Ofioliti, 7(2–3): 237–238.

Estrada, A. 1967. Asociación magmática básica del Nechí. Bachelor thesis, Universidad Nacional de Colombia, 88 p. Medellín.

Estrada, J.J. 1995. Paleomagnetism and accretion events in the northern Andes. Doctoral thesis, State University of New York at Binghamton, 170 p. New York, USA.

Etayo–Serna, F. 1989. Campanian to Maastrichtian fossils in the northeastern Western Cordillera, Colombia. Geología Norandina, (11): 23–31.

Etayo–Serna, F., González, H. & Álvarez, E. 1980. Mid–Albian ammonites from northern Western Cordillera, Colombia, S.A. Geología Norandina, (2): 25–30.

Etayo–Serna, F., Parra, E. & Rodríguez, G. 1982. Análisis facial del "Grupo del Dagua" con base en secciones aflorantes al oeste de Toro (Valle del Cauca). Geología Norandina, (5): 3–12.

Etayo–Serna, F., Barrero, D., Lozano, H., Espinosa, A., González, H., Orrego, A., Ballesteros, I., Forero, H., Ramírez, C., Zambrano–Ortiz, F., Duque–Caro, H., Vargas, R., Núñez, A., Álvarez, J., Ropaín, C., Cardozo, E., Galvis, N., Sarmiento, L., Alberts, J.P., Case, J.E., Singer, D.A., Bowen, R.W., Berger, B.R., Cox, D.P. & Hodges, C.A. 1983. Mapa de terrenos geológicos de Colombia. Publicaciones Geológicas Especiales del Ingeominas, 14(1): 1–135 p. Bogotá.

Festa, A., Pini, G.A., Dilek, Y. & Codegone, G. 2010. Mélanges and mélange–forming processes: A historical overview and new concepts. International Geology Review, 52(10–12): 1040–1105. https://doi.org/10.1080/00206810903557704

Gansser, A. 1973. Facts and theories on the Andes. Journal of the Geological Society of London, 129(2): 93–13l. https://doi.org/10.1144/gsjgs.129.2.0093

Garcia–Casco, A., Blanco–Quintero, I.F., Ruiz–Jiménez, E.C., Toro–Toro, L.M., Moreno–Sánchez, M., Gómez–Cruz, A.J. & Vinasco–Vallejo, C.J. 2011. Thermobarometry of amphibolites from the Arquía Complex (Central Colombia): Geodynamic implications. XIV Congreso Latinoamericano de Geología y XIII Congreso Colombiano de Geología. Memoirs, p. 435. Medellín.

Garcia–Casco, A., Restrepo, J.J., Correa–Martínez, A.M., Blanco–Quintero, I.F., Proenza, J.A., Weber, M. & Butjosa, L. 2020. The petrologic nature of the "Medellín Dunite" revisited: An algebraic approach and proposal of a new definition of the geological body. In: Gómez, J. & Pinilla–Pachon, A.O. (editors), The Geology of Colombia, Volume 2 Mesozoic. Servicio Geológico Colombiano, Publicaciones Geológicas Especiales 36, p. 45–75. Bogotá. https://doi.org/10.32685/pub.esp.36.2019.02

García–Ramírez, C.A., Ríos–Reyes, C.A., Castellanos–Alarcón, O.M. & Mantilla–Figueroa, L.C. 2017. Petrology, geochemistry and geochronology of the Arquía Complex´s metabasites at the Pijao–Génova sector, Central Cordillera, Colombian Andes. Boletín de Geología, 39(1): 105–126. http://dx.doi.org/10.18273/revbol.v39n1-2017005

Giraldo–Arroyave, M.I. 2010. Esquema geodinámico de la parte noroccidental de la cordillera Central de Colombia. Master thesis, Universidad Nacional de Colombia, 146 p. Medellín.

Giraldo–Ramírez, W.E. 2017. Novas idades U–Pb (LA–ICP–MS) de rochas granitoides na região de Sabanalarga (Colômbia) e sua correlação com a evolução da Placa do Caribe. Master thesis, Universidade de Rio de Janeiro, 88 p. Rio de Janeiro.

Gómez, J., Nivia, Á., Montes, N.E., Diederix, H., Almanza, M.F., Alcárcel, F.A. & Madrid, C.A. 2015a. Explanatory notes: Geological Map of Colombia. In: Gómez, J & Almanza, M.F. (editors), Compilando la geología de Colombia: Una visión a 2015. Servicio Geológico Colombiano, Publicaciones Geológicas Especiales 33, p. 35–60, Bogotá.

Gómez, J., Montes, N., Nivia, Á. & Diederix, H., compilers. 2015b. Geological Map of Colombia 2015. Scale 1:1 000 000. Servicio Geológico Colombiano, 2 sheets. Bogotá. https://doi.org/10.32685/10.143.2015.936

Gómez, J., Montes, N.E., Alcárcel, F.A. & Ceballos, J.A. 2015c. Cátálogo de dataciones radiométricas de Colombia en ArcGIS y Google Earth. In: Gómez, J & Almanza, M.F. (editors), Compilando la geología de Colombia: Una visión a 2015. Servicio Geológico Colombiano, Publicaciones Geológicas Especiales 33, p. 63–419, Bogotá.

Gómez–Vargas, D., Duque, J. & Molina–Garza, R. 2017. Deformación de los sedimentos pertenecientes a la Formación Penderisco, en respuesta a la colisión del Bloque Chocó, flanco oriental de la cordillera Occidental. XVI Congreso Colombiano de Geología. Memoirs, p. 1827–1830. Santa Marta.

González, H. 1980. Geología de las planchas 167 Sonsón y 187 Salamina. Scale 1:100 000. Boletín Geológico, 23(1): 1–174.

González, H. 2001. Memoria explicativa: Mapa geológico del departamento de Antioquia. Scale 1:400 000. Ingeominas, 240 p. Medellín.

González, H. 2010. Geoquímica, geocronología de las unidades litológicas asociadas al sistema de fallas Cauca–Romeral, sector centro–sur. Tomo I. Ingeominas, unpublished report, 412 p. Medellín.

González, H., Zapata, G. & Montoya, D.M. 2002. Memoria explicativa: Geología y geomorfología de la plancha 428 Túquerres, departamento de Nariño. Ingeominas, 168 p. Medellín.

González–Ospina, L.J. 2016. Petrogénesis de los complejos ultramáficos de Heliconia–Angelópolis y del oriente de Medellín, Antioquia, Colombia. Master thesis, Universidad Nacional de Colombia, 108 p. Bogotá.

Grosse, E. 1926. Estudio geológico del terciario carbonífero de Antioquia en la parte occidental de la cordillera Central de Colombia, entre el río Arma y Sacaojal, ejecutado en los años de 1920–1923. Dietrich Reimer, 361 p. Berlin.

Guiral–Vega, J.S., Rincón–Gamero, J.J. & Ordoñez–Carmona, O. 2015. Geología de la porción sur del Batolito de Sabanalarga: Implicaciones para la teoría de terrenos al occidente de Colombia. Boletín de Ciencias de la Tierra, (38): 41–48. https://doi.org/10.15446/rbct.n38.46367

Haffer, J. 1967. On the geology of the Uraba and northern Choco regions, NW Colombia. Colombian Petroleum Company, COLPET. Internal report GR–351, 106 p. Bogotá.

Hall, R., Álvarez, J. & Rico, H. 1972. Geología de los departamentos de Antioquia y Caldas–Subzona II–A. Boletín Geológico, 20(1): 1–85.

Hincapié–Gómez, S., Cardona, A., Jiménez, G., Monsalve, G., Ramírez–Hoyos, L. & Bayona, G. 2018. Paleomagnetic and gravimetrical reconnaissance of Cretaceous volcanic rocks from the western Colombian Andes: Paleogeographic connections with the Caribbean Plate. Studia Geophysica et Geodaetica, 62(3): 485–511. https://doi.org/10.1007/s11200-016-0678-y

Howell, D.G. 1989. Tectonics of suspect terranes: Mountain building and continental growth. Chapman and Hall, 231 p. London, UK.

Irving, E.M. 1971. La evolución estructural de Los Andes más septentrionales de Colombia. Boletín Geológico, 19(2): 1–90.

Jaramillo, J.S., Cardona, A., León, S., Valencia, V. & Vinasco, C. 2017. Geochemistry and geochronology from Cretaceous magmatic and sedimentary rocks at 6°35' N, western flank of the Central Cordillera (Colombian Andes): Magmatic record of arc growth and collision. Journal of South American Earth Sciences, 76: 460–481. https://doi.org/10.1016/j.jsames.2017.04.012

Johnson, J.H. 1963. The algal genus *Archaeolithothamnium* and its fossil representatives. Journal of Paleontology, 37(1): 175–211.

Kennan, L. & Pindell, J.L. 2009. Dextral shear, terrane accretion and basin formation in the northern Andes: Best explained by interaction with a Pacific–derived Caribbean Plate? In: James, K.H., Lorente, M.A. & Pindell, J.L. (editors), The origin and evolution of the Caribbean Plate. Geological Society of London, Special Publication 328, p. 487–531. https://doi.org/10.1144/SP328.20

Kerr, A.C., Marriner, G.F., Tarney, J., Nivia, Á., Saunders, A.D., Thirlwall, M.F. & Sinton, C.W. 1997. Cretaceous basaltic terranes in western Colombia: Elemental, chronological and Sr–Nd isotopic constraints on petrogenesis. Journal of Petrology, 38(6): 677–702. https://doi.org/10.1093/petroj/38.6.677

Kerr, A.C., Tarney, J., Kempton, P.D., Pringle, M. & Nivia, Á. 2004. Mafic pegmatites intruding oceanic plateau gabbros and ultramafic cumulates from Bolívar, Colombia: Evidence for a 'wet' mantle plume? Journal of Petrology, 45(9): 1877–1906. https://doi.org/10.1093/petrology/egh037

Leal–Mejía, H. 2011. Phanerozoic gold metallogeny in the Colombian Andes: A tectono–magmatic approach. Doctoral thesis, Universitat de Barcelona, 989 p. Barcelona.

Litherland, M., Aspden, J.A. & Egüez, A. 1993. The geotectonics evolution of Ecuador in the Phanerozoic. Second ISAG, 21–23: 215–218. Oxford, United Kingdom.

Litherland, M., Aspden, J.A. & Jemielita, R.A. 1994. The metamorphic belts of Ecuador. Overseas Memoir of the British Geological Survey 11, 147 p. Nottingham, England.

Maya, M. & González, H. 1995. Unidades litodémicas en la cordillera Central de Colombia. Boletín Geológico, 35(2–3): 43–57.

McCourt, W.J. 1984. Geología de la plancha 262 Génova. Scale 1:100 000. Ingeominas. Bogotá.

McCourt, W.J., Aspden, J.A. & Brook, M. 1984. New geological and geochronological data from the Colombian Andes: Continental growth by multiple accretion. Journal of the Geological Society, 141(5): 831–845. https://doi.org/10.1144/gsjgs.141.5.0831

McCourt, W.J., Muñoz, C.A. & Villegas, H. 1990. Regional geology and gold potential of the Guapi–Napi drainage basin and upper Timbiquí River, Cauca Department, SW Colombia, phase II. Ingeominas–British Geological Survey, unpublished report, 62 p. Cali.

McGeary, S. & Ben–Avraham, Z. 1985. The accretion of Gorgona Island, Colombia: Multichannel seismic evidence. In: Howell, D.G. (editor), Tectonostratigraphic terranes of the Circum–Pacific region. Circum–Pacific Council for Energy and Mineral Resources, Earth Sciences Series, 1: 543–554.

Mejía, D., Cardona, M., Serna, S. & Valencia, V. 2017. Metasedimentitas de San Luis, formación y cierre de las cuencas marginales del Cretáceo Inferior en la cordillera Central? XVI Congreso Geológico Colombiano. Memoirs, p. 1849–1850. Santa Marta.

Mejía–Herrera, P., Santa–Escobar, M., Ordoñez–Carmona, O. & Pimentel, M.M. 2008. Consideraciones petrográficas, geoquímicas y geocronológicas de la parte occidental del Batolito de Santa Marta. DYNA, 75(155): 223–236.

Montes, C., Bayona, G., Cardona, A., Buchs, D.M., Silva, C.A., Morón, S., Hoyos, N., Ramírez, D.A., Jaramillo, C.A. & Valencia, V. 2012. Arc–continent collision and orocline formation: Closing of the Central American seaway. Journal of Geophysical Research: Solid Earth, 117(B4): 1–25 p. https://doi.org/10.1029/2011JB008959

Montoya, D. & Peláez, I. 1993. Ultramafitas y rocas relacionadas de Heliconia, Antioquia. Bachelor thesis, Universidad Nacional de Colombia, 223 p. Medellín.

Mora–Bohórquez, A., Ibañez–Mejia, M., Oncken, O., de Freitas, M., Vélez, V., Mesa, A. & Serna, L. 2017. Structure and age of the Lower Magdalena Valley Basin basement, northern Colombia: New reflection–seismic and U–Pb–Hf insights into the termination of the central Andes against the Caribbean Basin. Journal of South American Earth Sciences, 74: 1–26. https://doi.org/10.1016/j.jsames.2017.01.001

Moreno–Sánchez, M. & Pardo–Trujillo, A. 2003. Stratigraphical and sedimentological constraints on western Colombia: Implications on the evolution of the Caribbean Plate. In: Bartolini, C., Buffler, R.T. & Blickwede, J. (editors), The circum–Gulf of Mexico and the Caribbean: Hydrocarbon habitats, basin formation, and plate tectonics. American Association of Petroleum Geologists, Memoir 79, p. 891–924. Tulsa, USA. https://doi.org/10.1306/M79877C40

Nelson, H.W. 1962. Contribución al conocimiento de la cordillera Occidental: Sección carretera Cali–Buenaventura. Boletín Geológico, 10(1–3): 81–108.

Nerlich, R., Clark, S.R. & Bunge, H.P. 2014. Reconstructing the link between the Galapagos hotspot and the Caribbean Plateau. GeoResJ, 1–2: 1–7. https://doi.org/10.1016/j.grj.2014.02.001

Nivia, Á. 1987. Geochemistry and origin of the Amaime and volcanic sequences southwestern Colombia. Master of Philosophy thesis, University of Leicester, 164 p. Leicester, UK.

Nivia, Á. 1989. El terreno Amaime–Volcánica una provincia acrecionada de basaltos de meseta oceánica. V Congreso Colombiano de Geología. Memoirs, I, p. 1–30. Bucaramanga.

Nivia, Á. 1991. Memoria explicativa: Mapa geológico departamento del Valle del Cauca. Ingeominas, 149 p. Bogotá.

Nivia, Á. 1993. Evidencia de obducción en el Complejo Ultramáfico de Bolívar. VI Congreso Colombiano Geología. Memoirs, I, p. 63–79. Medellín.

Nivia, Á. 1996. The Bolívar mafic–ultramafic complex, SW Colombia: The base of an obducted oceanic plateau Journal of South American Earth Sciences, 9(1–2): 59–68. https://doi.org/10.1016/0895-9811(96)00027-2

Nivia, Á. 2001. Memoria explicativa: Mapa geológico departamento del Valle del Cauca. Scale 1:250 000. Ingeominas, 148 p. Bogotá.

Nivia, Á., Marriner, G.F., Kerr, A.C. & Tarney, J. 2006. The Quebradagrande Complex: A Lower Cretaceous ensialic marginal basin in the Central Cordillera of the Colombian Andes. Journal of South American Earth Sciences, 21(4): 423–436. https://doi.org/10.1016/j.jsames.2006.07.002

O'Dea, A., Lessios, H.A., Coates, A.G., Eytan, R., Restrepo–Moreno, S.A., Cione, A.L., Collins, L.S., de Queiroz, A., Farris, D.W., Norris, R.D., Stallard, R.F., Woodburne, M.O., Aguilera, O., Aubry, M.P., Berggren, W.A., Budd, A.F., Cozzuol, M.A., Coppard, S.E., Duque–Caro, H., Finnegan, S., Gasparini, G.M., Grossman, E.L., Johnson, K.G., Keigwin, L.D., Knowlton, N., Leigh, E.G., Leonard–Pingel, J.S., Marko, P.B., Pyenson, N.D., Rachello–Dolmen, P.G., Soibelzon, E., Soibelzon, L., Todd, J.A., Vermeij, G.J. & Jackson, J.B.C. 2016. Formation of the Isthmus of Panama. Science Advances, 2(8): 1–11. https://doi.org/10.1126/sciadv.1600883

Pardo–Trujillo, A., Jaramillo, C.A. & Oboh–Ikuenobe, F.E. 2003. Paleogene palynostratigraphy of the eastern Middle Magdalena Valley, Colombia. Palynology, 27(1): 155–178. https://doi.org/10.1080/01916122.2003.9989585

Parra, E. 1983. Geología y geoquímica de la plancha 223 El Cairo. Scale 1:100 000. Ingeominas, Internal report 1914, 138 p. Bogotá.

Piraquive, A., Kammer, A., Bernet, M. & von Quadt, A. 2017. Exhumación del basamento metamórfico de las serranías de Jarara y Macuira a partir de termocronología y geocronología U–Pb LA–ICP–MS en circones. XVI Congreso Colombiano de Geología. Memoirs, p. 1509–1510. Santa Marta.

Restrepo, J.J. 2008. Obducción y metamorfismo de ofiolitas triásicas en el flanco occidental del terreno Tahamí, cordillera Central de Colombia. Boletín de Ciencias de la Tierra, (22): 49–100.

Restrepo, J.J. & Toussaint, J.F. 1973. Obducción cretácea en el occidente colombiano. Publicación Especial de Geología, (3): 1–26. Medellín.

Restrepo, J.J. & Toussaint, J.F. 1976. Edades radiométricas de algunas rocas de Antioquia, Colombia. Publicación Especial Geológica, (6): 1–15. Medellín.

Restrepo, J.J. & Toussaint, J.F. 1984. Unidades litológicas de los alrededores de Medellín. Primera conferencia sobre riesgos geológicos del Valle de Aburrá. Sociedad Colombiana de Geología. Memoirs, p. 1–26. Medellín.

Restrepo, J.J. & Toussaint, J.F. 1988. Terranes and continental accretion in the Colombian Andes. Episodes, 11(3): 189–193. https://doi.org/10.18814/epiiugs/1988/v11i3/006

Restrepo, J.J. & Toussaint, J.F. 2020. Tectonostratigraphic terranes in Colombia: An update. First part: Continental terranes. In: Gómez, J. & Mateus–Zabala, D. (editors), The Geology of Colombia, Volume 1 Proterozoic – Paleozoic. Servicio Geológico Colombiano, Publicaciones Geológicas Especiales 35, p. 37–63. Bogotá. https://doi.org/10.32685/pub.esp.35.2019.03

Restrepo, J.J., Toussaint, J.F., Zuluaga, J. & Hoyos, P. 1979. Algunas consideraciones sobre la geología de la parte septentrional de la cordillera Occidental. Publicación Especial (20): 1–26. Medellín.

Restrepo, J.J., Toussaint, J.F., González, H., Cordani, U., Kawashita, K., Linares, E. & Parica, C. 1991. Precisiones geocronológicas sobre el occidente colombiano. Simposio sobre Magmatismo Andino y su Marco Tectónico. Memoirs, I, 21 p. Manizales.

Restrepo, J.J., Frantz, J.C., Ordóñez–Carmona, O., Correa–Martínez, A.M., Martens, U. & Chemale, F. 2007. Edad triásica de formación de la Ofiolita de Aburrá, flanco occidental de la cordillera Central. XI Congreso Colombiano de Geología. Abstracts, p. 49. Bucaramanga.

Restrepo, J.J., Dunlap, W.J., Martens, U., Ordoñez–Carmona, O. & Correa, A.M. 2008. Ar–Ar ages of amphibolites from the Central Cordillera of Colombia and their implications for tectonostratigraphic terrane evolution in the northwestern Andes. VI South American Symposium on Isotope Geology. Proceedings in CD ROM, p. 1–6. Bariloche, Argentina.

Restrepo, J.J., Ordóñez–Carmona, O., Martens, U. & Correa, A.M. 2009a. Terrenos, complejos y provincias en la cordillera Central de Colombia. Ingeniería, Investigación y Desarrollo, 9(2): 49–56.

Restrepo, J.J., Ordóñez–Carmona, O. & Moreno–Sánchez, M. 2009b. A comment on ‘‘The Quebradagrande Complex: A Lower Cretaceous ensialic marginal basin in the Central Cordillera of the Colombian Andes” by Nivia et al. Journal of South American Earth Sciences, 28(2): 204–205. https://doi.org/10.1016/j.jsames.2009.03.004

Restrepo, J.J., Ibañez–Mejia, M. & García–Casco, A. 2012. U–Pb zircon ages of the Medellín Amphibolites (Central Cordillera of Colombia) reveal mid–Cretaceous tectonic juxtaposition of Triassic and mid–Cretaceous metamorphic complexes. VIII South American Symposium on Isotope Geology. Presentaciones memoria USB, 33 diapositivas. Medellín.

Restrepo–Moreno, S.A., O´Dea, A., Coates, A.G., Eytan, R., Farris, D.W., Jackson, J.B.C., Lessios, H.A., Collins, L.S., Stallard, R.F., Duque–Caro, H., Marko, P.B., Rachello–Dolmen, P.G., Keigwin, L.D. & Vermeij, G.J. 2017. Perspectives on the formation of Panamanian Isthmus. XVI Congreso Colombiano de Geología. Memoirs, p. 1872–1874. Santa Marta.

Ríos–Reyes, C.A., Castellanos–Alarcón, O.M. & García–Ramírez, C.A. 2017. Petrogenetic significance of the eclogites from the Arquía Complex on southwestern Pijao, Central Cordillera (Colombia Andes). DYNA, 84(200): 291–301. https://doi.org/10.15446/dyna.v84n200.48166

Rodríguez, G. & Arango, M.I. 2013. Formación Barroso: Arco volcánico toleítico y diabasas de San José de Urama: Un prisma acrecionario T–MORB en el segmento norte de la cordillera Occidental de Colombia. Boletín de Ciencias de la Tierra, (33): 17–38.

Rodríguez, G. & Cetina, L.M. 2016. Caracterización petrográfica y química de rocas de corteza oceánica del Complejo Quebradagrande y comparación con rocas de la unidad Diabasas de San José de Urama. Boletín de Geología, 38(3): 15–29. https://doi.org/10.18273/revbol.v38n3-2016001

Rodríguez, G. & Zapata, G. 2012. Características del plutonismo Mioceno superior en el segmento norte de la cordillera Occidental e implicaciones tectónicas en el modelo geológico del noroccidente colombiano. Boletín de Ciencias de la Tierra, (31): 5–22.

Rodríguez–Jiménez, J.V. 2010. Fábrica y emplazamiento de la Diorita de Pueblito, NW cordillera Central de Colombia: Análisis de fábrica magnética y mineral. Master thesis, Universidad Nacional de Colombia, 60 p. Medellín.

Rodríguez–Pulgarín, E.A. 2011. Identificación del municipio de Ebéjico (II). Revista Vinculando: Web versión. http://vinculando.org/vacaciones_viajes/turismo_sostenible/7_identificacion_del_municipio_de_ebejico_ii.html (consulted in October 2018).

Ruiz–Jiménez, E.C. 2014. Geoquímica y trayectorias P–T de las rocas metamórficas del Complejo Arquía, entre los municipios de Santafé de Antioquia, Antioquia y el río Arquía, Caldas. Master thesis, Universidad de Caldas, 132 p. Manizales.

Ruiz–Jiménez, E.C., Blanco–Quintero, I.F., Toro–Toro, L.M., Moreno–Sánchez, M., Vinasco, C.J., García–Casco, A., Morata, D. & Gómez–Cruz, A. 2012. Geoquímica y petrología de las metabasitas del Complejo Arquía (municipio de Santafé de An-

tioquia y río Arquía, Colombia): Implicaciones geodinámicas. Boletín de Ciencias de la Tierra, (32): 65–79.

Salazar, G., James, M. & Tistl, M. 1991. El Complejo Santa Cecilia–La Equis: Evolución y acreción de un arco magmático en el norte de la cordillera Occidental, Colombia. Simposio sobre Magmatismo Andino y su Marco Tectónico. Memoirs, II, p. 142–160. Manizales.

Salinas, R. & Tistl, M. 1992. A tertiary zoned ultramafic complex and komatiitic basalts from Condoto, Choco, NW Colombia. Zentralblatt Fur Geologie Und Palaontologie, 1(6), p. 1659–1676. Stuttgart, Germany.

Serrano, L., Ferrari, L., López–Martínez, M., Petrone, C.M. & Jaramillo, C. 2011. An integrative geologic, geochronologic and geochemical study of Gorgona Island, Colombia: Implications for the formation of the Caribbean Large Igneous Province. Earth and Planetary Science Letters, 309(3–4): 324–336. https://doi.org/10.1016/j.epsl.2011.07.011

Sillitoe, R.H., Jaramillo, L., Damon, P.E., Shafiqullah, M. & Escovar, R. 1982. Setting, characteristics, and age of the Andean porphyry copper belt in Colombia. Economic Geology, 77(8): 1837–1850. https://doi.org/10.2113/gsecongeo.77.8.1837

Sinton, C.W., Duncan, R.A., Storey, M., Lewis, J. & Estrada, J.J. 1998. An oceanic flood basalt province within the Caribbean Plate. Earth and Planetary Science Letters, 155(3–4): 221–235. https://doi.org/10.1016/S0012-821X(97)00214-8

Spadea, P., Delaloye, M., Espinosa, A., Orrego, A. & Wagner, J.J. 1987. Ophiolite Complex from La Tetilla, southwestern Colombia, South America. The Journal of Geology, 95(3): 377–395. https://doi.org/10.1086/629136

Tistl, M., Burgath, K.P., Höhndorf, A., Kreuzer, H., Muñoz, R. & Salinas, R. 1994. Origin and emplacement of tertiary ultramafic complexes in northwest Colombia: Evidence from geochemistry and K–Ar, Sm–Nd and Rb–Sr isotopes. Earth and Planetary Science Letters, 126(1–3): 41–59. https://doi.org/10.1016/0012-821X(94)90241-0

Toussaint, J.F. 1996. Evolución geológica de Colombia: 3, Cretácico. Universidad Nacional de Colombia, 277 p. Medellín.

Toussaint, J.F. 1999. Evolución geológica de Colombia durante el Cenozoico. Universidad Nacional de Colombia. CD ROM, 222 p. Medellín.

Toussaint, J.F. & Restrepo, J.J. 1981. Edad K/Ar de dos rocas básicas del flanco noroccidental de la cordillera Central. Boletín de Ciencias de la Tierra, (5–6): 71.

Toussaint, J.F. & Restrepo, J.J. 1989. Acreciones sucesivas en Colombia: Un nuevo modelo de evolución geológica. V Congreso Colombiano de Geología, Memoirs, I, p. 127–146. Bucaramanga.

Toussaint, J.F., González, H., Restrepo, J.J. & Linares, E. 1981. Edad K/Ar de tres rocas metamórficas del flanco noroccidental de la cordillera Central. Boletín de Ciencias de la Tierra, (5–6): 63–69.

van der Hammen, T. 1958. Estratigrafía del Terciario y Maastrichtiano continentales y tectogénesis de los Andes colombianos. Boletín Geológico, 6(1–3): 67–128.

Villagómez, D. 2010. Thermochronology, geochronology and geochemistry of the Western and Central Cordilleras and Sierra Nevada de Santa Marta, Colombia: The tectonic evolution of NW South America. Doctoral thesis, University of Geneva, 143 p. Geneva.

Villagómez, D. & Spikings, R. 2013. Thermochronology and tectonics of the Central and Western Cordilleras of Colombia: Early Cretaceous – Tertiary evolution of the northern Andes. Lithos, 160–161: 228–249. https://doi.org/10.1016/j.lithos.2012.12.008

Villagómez, D., Spikings, R., Magna, T., Kammer, A., Winkler, W. & Beltrán, A. 2011. Geochronology, geochemistry and tectonic evolution of the Western and Central Cordilleras of Colombia. Lithos, 125(3–4): 875–896. https://doi.org/10.1016/j.lithos.2011.05.003

Vinasco, C.J. & Cordani, U. 2012. Reactivation episodes of the Romeral Fault System in the northwestern part of Central Andes, Colombia, through ^{39}Ar–^{40}Ar and K–Ar results. Boletín de Ciencias de la Tierra, (32): 111–123.

Walker, R.J., Storey, M., Kerr, A.C., Tarney, J. & Arndt, N.T. 1999. Implications of ^{187}Os isotopic heterogeneities in a mantle plume: evidence from Gorgona Island and Curaçao. Geochimica et Cosmochimica Acta, 63(5): 713–728. https://doi.org/10.1016/S0016-7037(99)00041-1

Weber, M., Gómez, J., Cardona, A., Duarte, E., Pardo–Trujillo, A. & Valencia, V.A. 2015. Geochemistry of the Santa Fé Batholith and Buriticá Tonalite in NW Colombia–Evidence of subduction initiation beneath the Colombian Caribbean Plateau. Journal of South American Earth Sciences, 62: 257–274. https://doi.org/10.1016/j.jsames.2015.04.002

Zapata, G. & Rodríguez, G. 2011. Basalto de El Botón: Arco volcánico Mioceno de afinidad shoshonítica al norte de la cordillera Occidental de Colombia. Boletín de Ciencias de la Tierra, (30): 77–91.

Zapata, J.P. & Cardona, A. 2017. Unidades miloníticas asociadas a eventos colisionales del Cretácico Superior en el margen occidental de la cordillera Central. XVI Congreso Colombiano de Geología. Memoirs, p. 1889–1891. Santa Marta.

Zapata, J.P., Restrepo, J.J., Cardona, A. & Martens, U. 2017a. Geoquímica y geocronología de las rocas volcánicas básicas y el Gabro de Altamira, cordillera Occidental (Colombia): Registro de ambientes de plateau y arco oceánico superpuestos durante el Cretácico. Boletín de Geología, 39(2): 13–30. https://doi.org/10.18273/revbol.v39n2-2017001

Zapata, J.P., Correa, T., Obando, M., Rincón, A., Ortiz, F. & Rodríguez, G. 2017b. Redefinición cronoestratigráfica del Batolito de Sabanalarga. XVI Congreso Geológico Colombiano. Memoirs, p. 1472–1477. Santa Marta.

Explanation of Acronyms, Abbreviations, and Symbols:

CRFZ	Cauca–Romeral Fault Zone	REE	Rare earth element
IAT	Island arc tholeiite	SNSM	Sierra Nevada de Santa Marta
MORB	Mid–ocean ridge basalt	T–MORB	Transicional mid–ocean ridge basalt

Authors' Biographical Notes

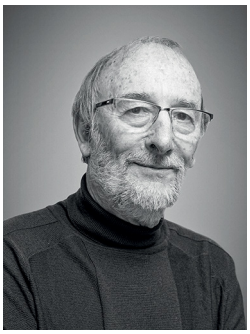

Jean–François TOUSSAINT has a Doctorate degree from the Université de Paris. After working in Bolivia for some time, he arrived at Medellín to teach at the Universidad Nacional de Colombia, Sede Medellín, where he taught courses such as Structural Geology, Geotectonics, Regional Geology, and Geology of Colombia for approximately 35 years. He was awarded the titles of Honorary Professor and "Maestro Universitario" by the Universidad Nacional. Some of his interests are the geological evolution of the Colombian Andes in terms of plate tectonics and tectonostratigraphic terranes, playing tennis, and the history of human evolution.

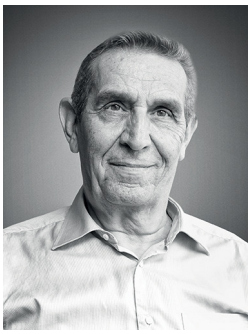

Jorge Julián RESTREPO obtained a degree in mining engineering and metallurgy at the Universidad Nacional de Colombia in 1968 and a Master of Science degree in geology at the Colorado School of Mines in 1973. He was a faculty member of the Universidad Nacional de Colombia, Sede Medellín, for over 40 years and currently holds the titles of Emeritus Professor and "Maestro Universitario". He taught Mineralogy, Metamorphic Petrology, Regional Geology, Field Geology, and Geochronology. His research focused on plate tectonics applied to the geology of Colombia, tectonostratigraphic terranes, geochronology, and the geologic evolution of metamorphic and mafic/ultramafic complexes of the Central Cordillera. Other interests are photography, genealogy, and the study of passifloras.

Volume 2

Chapter 8

Detrital U–Pb Provenance, Mineralogy, and Geochemistry of the Cretaceous Colombian Back–Arc Basin

https://doi.org/10.32685/pub.esp.36.2019.08
Published online 25 November 2020

Javier GUERRERO[1]*, Alejandra MEJÍA–MOLINA[2], and José OSORNO[3]

1 jguerrerod@unal.edu.co
Universidad Nacional de Colombia
Sede Bogotá
Departamento de Geociencias
Carrera 30 n.° 45–03
Bogotá, Colombia

2 amejia@yachaytech.edu.ec
Universidad Yachay Tech
Hacienda Urcuquí s/n y Proyecto Yachay
Urcuquí, Ecuador

3 jose.osorno@anh.gov.co
Agencia Nacional de Hidrocarburos
Calle 26 n.° 59–65, segundo piso
Bogotá, Colombia

* Corresponding author

Supplementary Information:

S: https://www2.sgc.gov.co/LibroGeologiaColombia/tgc/sgcpubesp36201908s.pdf

Abstract The geology of the Cretaceous Colombian back–arc basin is reviewed considering detrital U–Pb provenance ages, mineralogy, and geochemistry of samples collected from outcrop sections and wells at several localities in the core of the Eastern Cordillera, Middle Magdalena Valley, and Catatumbo areas. The data set supports previous studies indicating a basin with main grabens in the present–day Eastern Cordillera between the Guaicáramo/Pajarito and Bituima/La Salina border faults, which operated as normal faults during the Cretaceous. Limestones are common on the western and northern sides of the basin, whereas terrigenous strata predominate on the eastern and southern sides. After the Berriasian, grabens were connected by marine flooding during the Valanginian, with two main source areas documented by distinct element and mineral contents, one in the Central Cordillera magmatic arc and the other in the Guiana Shield. Some elements present in Lower Cretaceous shales, including scandium, vanadium, and beryllium, are not related to the sediment supply areas for the basin but instead are linked to Valanginian to Cenomanian hydrothermal activity and dikes of gabbro, diorite, and tonalite emplaced during the main phase of extension in the basin.

Keywords: *Cretaceous, back–arc, Colombia, U–Pb provenance, geochemistry.*

Resumen La geología de la Cuenca Cretácica Colombiana de back–arc se revisa considerando edades de procedencia U–Pb, mineralogía y geoquímica de muestras colectadas en secciones de afloramientos y pozos de varias localidades en el núcleo de la cordillera Oriental, Valle Medio del Magdalena y Catatumbo. El conjunto de datos respalda estudios previos que indican una cuenca cuyos principales grábenes se encontraban en la cordillera Oriental actual, entre las fallas de Guaicáramo/Pajarito y Bituima/La Salina, que durante el Cretácico fueron fallas normales. Las calizas son comunes en los lados occidental y norte de la cuenca, mientras que los estratos terrígenos predominan en el lado este y sur de la misma. Después que los grábenes berriasianos de la cuenca se conectaron por inundación marina durante el Valanginiano, se pueden documentar dos áreas fuente con elementos y minerales distintivos, una en el arco magmático de la cordillera Central y otra en el Escudo de Guayana. Algunos elementos presentes en los *shales* del Cretácico Inferior, incluidos escandio, vanadio y berilio, no están relacionados con las áreas de aporte de los sedimentos de la cuenca,

Citation: Guerrero, J., Mejía–Molina, A. & Osorno, J. 2020. Detrital U–Pb provenance, mineralogy, and geochemistry of the Cretaceous Colombian back–arc basin. In: Gómez, J. & Pinilla–Pachon, A.O. (editors), The Geology of Colombia, Volume 2 Mesozoic. Servicio Geológico Colombiano, Publicaciones Geológicas Especiales 36, p. 261–297. Bogotá. https://doi.org/10.32685/pub.esp.36.2019.08

sino que están ligados con la actividad hidrotermal relacionada a los diques de gabro, diorita y tonalita, emplazados durante la extensión principal de la cuenca desde el Valanginiano hasta el Cenomaniano.

Palabras clave: *Cretácico, back–arc, Colombia, procedencia U–Pb, geoquímica.*

1. Introduction

The main depocenter of the Cretaceous Colombian back–arc basin is located in the present–day Eastern Cordillera, including the Cundinamarca, Boyacá, and Santander Departments, where several stratigraphic wells, oil wells, and field sections were studied (Figure 1). These areas include the Eastern Emerald Belt (Cinturón Esmeraldífero Oriental "CEOR"), Western Emerald Belt (Cinturón Esmeraldífero Occidental "CEOC"), Villeta, and Barichara/Bucaramanga. Three localities outside the main depocenter were also studied, including the Catatumbo area on the NE side of the basin and the Infantas oil well and Aguachica area (Middle Magdalena Valle "MMV") on the NW side of the basin.

The paleogeography and tectonic setting of the basin were initially documented using field–measured sections, sedimentary petrography, grain size distribution, and sequence stratigraphy (Guerrero, 2002a, 2002b; Guerrero et al., 2000). The presence of a magmatic arc delineating the western border of the basin during the entire Cretaceous Period is demonstrated using petrographic evidence that documents volcanic and metamorphic particles sourced from the Central Cordillera (Guerrero et al., 2000). Sandstones and biosparites have coarser grain sizes (very coarse to conglomeratic) along the eastern and western margins of the basin, where the thicknesses of coarse–grained units may reach hundreds of meters; these facies change gradually to finer–grained strata toward the center of the basin (Figures 2–4). Offshore biomicrites, marls, and shales are thicker toward the basin center, where they reach thicknesses of hundreds of meters.

Terrigenous sandstones and sandy biosparites on the western margin are volcanic and metamorphic litharenites sourced from the Central Cordillera; sandstones on the eastern basin margin are quartz arenites sourced mostly from recycled Paleozoic and older strata from the Guiana Shield. In fact, most Cretaceous sections rest in angular unconformity on Paleozoic strata along the eastern basin margin, whereas on the opposite, western margin of the basin, they rest in angular unconformity on Jurassic rocks. There is no sedimentological or structural continuity between Upper Jurassic and Lower Cretaceous strata in any place throughout the present–day Eastern Cordillera, so that there is not a continuous "Mesozoic basin". The basal sandstones of the Cretaceous system exposed near Girón and Zapatoca, which rest in angular unconformity on older basement and are transitionally covered by genetically related marine strata, were originally included in the Girón strata by Hettner (1892). Later, these beds were erroneously assigned to the Jurassic, based only on stratigraphic position, but in fact, they correspond to fluvial and shoreface transgressive sandstones of Berriasian and Valanginian age, which are now included in the Tambor, Tibasosa, Arcabuco, Buenavista, and Batá Formations (e.g., Etayo–Serna et al., 2003). There is no temporal or structural relationship between the basin and the Jurassic separation of Pangea, which affected parts of Brasil and Venezuela in northern South America. Actually, the Jurassic strata and igneous rocks, parallel to the Central Cordillera, are associated with a magmatic arc related to subduction along the western border of the continent (e.g., Bustamante et al., 2010; Zapata et al., 2016). The Cretaceous back–arc and forearc basins are also related to subduction of the Pacific Oceanic Plate beneath the western margin of South America. The Cretaceous succession from the Eastern Cordillera of Colombia was deposited in a back–arc basin related to subduction instead of a Mesozoic rift related to the breakup of Pangea. The Cretaceous strata that rest in angular unconformity on previously accreted oceanic crust in the Western Cordillera and on the western side of the Central Cordillera are assigned to the forearc basin and are not included in this study.

The main back–arc basin rift exposed in the Eastern Cordillera was controlled by NNE–striking normal faults that were active throughout the Cretaceous, as indicated by the great thickness (5000 m) and wide age range (Berriasian to Maastrichtian) of strata W of the Guaicáramo Fault compared to the reduced thickness (500 m) and restricted age range (only Turonian to Maastrichtian) of strata E of the fault (Guerrero, 2002b). After the Berriasian to Cenomanian synrift stage, subsidence continued to be greater in the central rift than in areas E of the Guaicáramo Fault, as indicated by the reduced thickness (ca. 500 m) of Turonian to Maastrichtian strata in the present–day Llanos Foothills and Putumayo areas compared to the approximately 1500 m of equivalent strata (Chipaque Formation, Guadalupe Group, and Guaduas Formation) W of the fault (Guerrero, 2002b; Guerrero & Sarmiento, 1996). Other evidence that supports the age of synrift subsidence is the presence of Valanginian to Cenomanian dikes of gabbro, diorite, and tonalite (Gómez

Figure 1. Study area in part of the Cretaceous Colombian back–arc basin, including the locations of wells and field sections from the CEOR (GA, MSP), Villeta (QP, RC), CEOC (BB, O), Barichara (QLP, QAD), Aguachica (CAB, CES), and Catatumbo (QLL, RR). The highest contents of zirconium (average percentages per locality) are in the SE part of the basin.

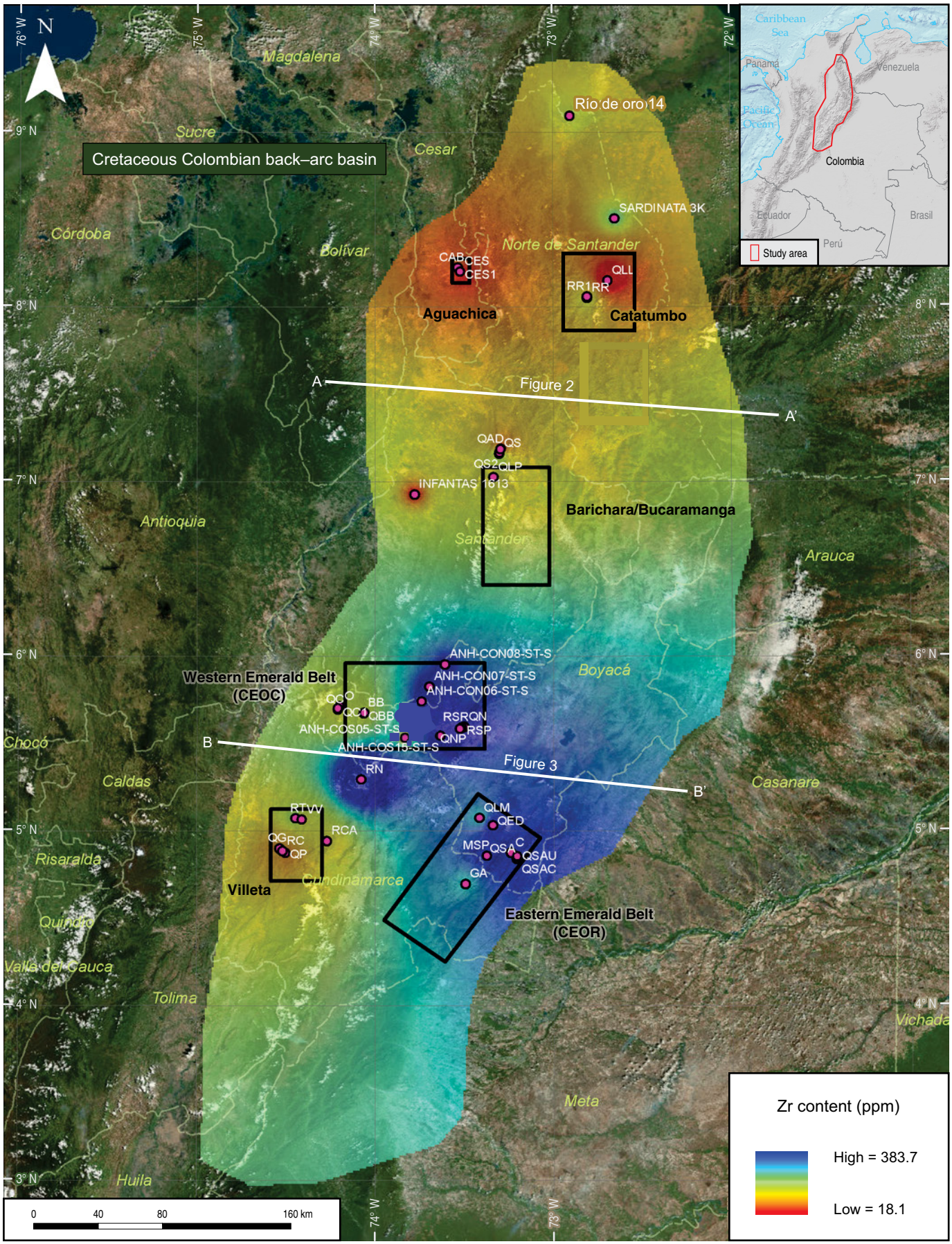
Cretaceous Colombian back–arc basin
Río de oro 14
SARDINATA 3K
CAB
CES
CES1
Aguachica
QLL
RR1
RR
Catatumbo
Norte de Santander
Bolívar
Córdoba
Sucre
Cesar
Magdalena
A
A'
Figure 2
QAD
QS
QS2
QLP
INFANTAS 1613
Barichara/Bucaramanga
Santander
Antioquia
Arauca
Boyacá
ANH-CON08-ST-S
ANH-CON07-ST-S
ANH-CON06-ST-S
Western Emerald Belt
(CEOC)
QC
QCO
BB
QBB
RSR
QN
RSP
QNP
ANH-COS05-ST-S
ANH-COS15-ST-S
RN
B
B'
Figure 3
Chocó
Caldas
Casanare
RTW
RCA
QG
RC
QP
Villeta
Cundinamarca
QLM
QED
MSP
QSA
C
QSAU
QSAC
GA
Eastern Emerald Belt
(CEOR)
Risaralda
Quindío
Valle del Cauca
Tolima
Huila
Meta
Vichada
Caribbean Sea
Panamá
Venezuela
Pacific Ocean
Colombia
Ecuador
Brasil
Perú
Study area
Zr content (ppm)
High = 383.7
Low = 18.1
0
40
80
160 km
76° W
75° W
74° W
73° W
72° W
9° N
8° N
7° N
6° N
5° N
4° N
3° N

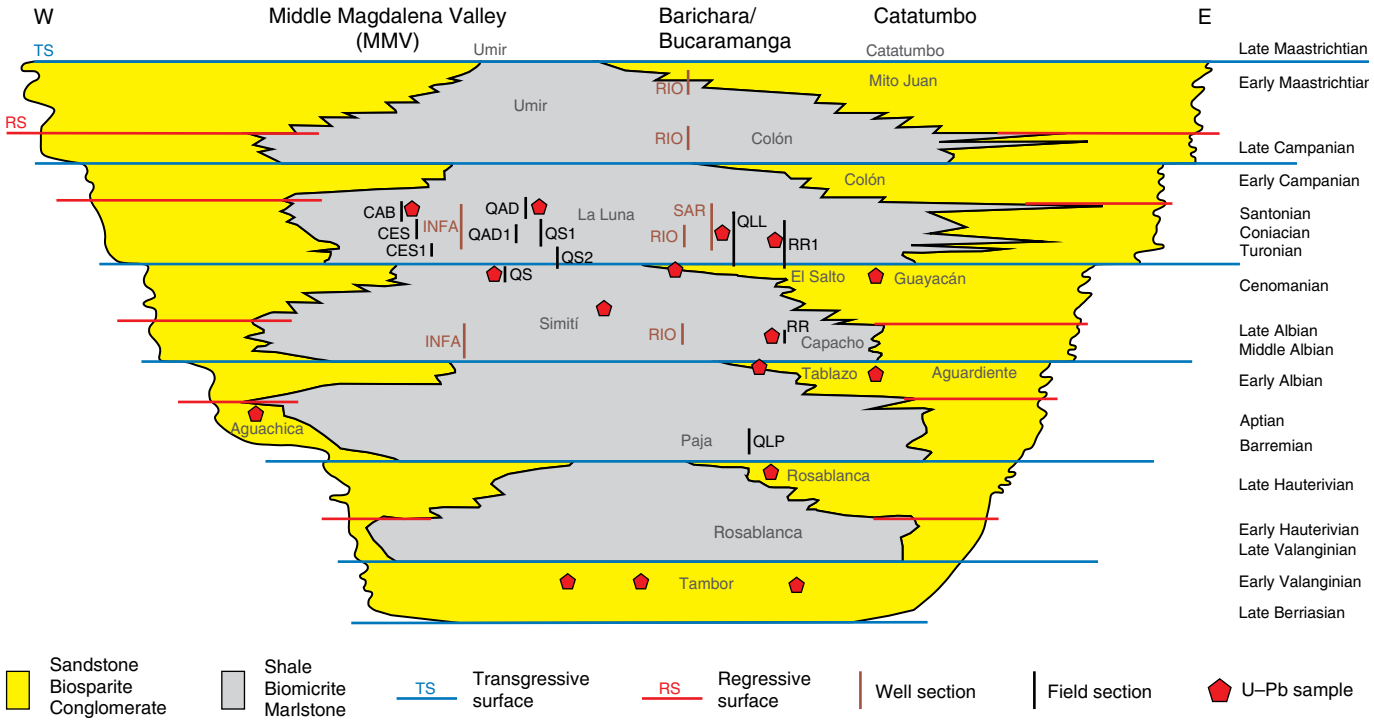

Figure 2. Units studied in the N sector of the basin, including the MMV, Barichara/Bucaramanga, and Catatumbo areas. Locations projected to line AA' of Figure 1 are: (CAB) Caño Agua Blanca; (CES) Caño El Salto; (QAD) Aguadulce Creek; (QS) La Sorda Creek; (QLL) La Leche Creek; (RR) Riecito River; (QLP) La Paja Creek. Oil wells are (INFA) Infantas; (RIO) Río de Oro; (SAR) Sardinata. Cross section modified from Guerrero (2002a).

et al., 2015; Vásquez et al., 2005, 2010), which intruded Lower Cretaceous strata during the main extensional phase of the basin. Subsequently, during the Turonian to Maastrichtian thermal subsidence of the basin, magmatic and hydrothermal activity stopped in the central rift.

The main rift was initially subdivided into grabens separated during the Berriasian but connected by the late Valanginian when the present–day Santander, Floresta, and Quetame Massifs were completely flooded by offshore marine strata. The role of Cretaceous normal faults and their Cenozoic inversion was initially discussed by Cooper et al. (1995) and has been recognized by Sarmiento–Rojas et al. (2006), Horton et al. (2010), and Mora et al. (2010), and among others. Tesón et al. (2013) documented several grabens, including Guatiquía, Pisba, Cocuy, and Tablazo, which were bounded by the Guaicáramo, Pajarito, Pesca, Servitá, Lengupá, Soapaga, Boyacá, Bituima, and La Salina normal faults.

The purposes of this chapter are to better document the two source areas and the evolution of the Cretaceous Colombian back–arc basin and to characterize the rock types from successions at several localities. We present new results on XRD mineralogy and ICP–MS/OES geochemistry mainly from shales and biomicrites, along with U–Pb ages of zircon grains contained in sandstones from both sides of the basin.

2. Materials and Methods

Fine–grained strata including biomicrites, marls, and shales, as well as coarse–grained strata including sandstones and biosparites, were collected mainly from 9 wells and 35 field sections of key localities within the basin (Figures 1–4; Tables 1–3). Table 1 contains the initial and final coordinates of stratigraphic sections exposed along creeks, rivers, and roads. Table 2 displays the coordinates of sampled oil and stratigraphic wells, with the depth information in feet for each unit. Table 3 contains the stratigraphic information and the coordinates of sandstone samples collected outside the main stratigraphic sections.

Selected samples of sandstone, volcanic tuff, and limestone were processed for detrital zircon U–Pb dating with a single collector quadrupole LA–ICP–MS Agilent 7700x instrument at the laboratories of Apatite to Zircon, Inc., in Viola, Idaho, USA. Details of the procedures, statistics, and standards employed are presented by Chew & Donelick (2012), Moore (2014), and Moore et al. (2015). According to the report provided by Apatite to Zircon, Inc., the approach was the modeling of background–corrected signal intensities for each isotope in each scan. U–Pb age standards for which independently accepted ages are published were designated primary, secondary, and tertiary for purposes of age calibration. A minimum of

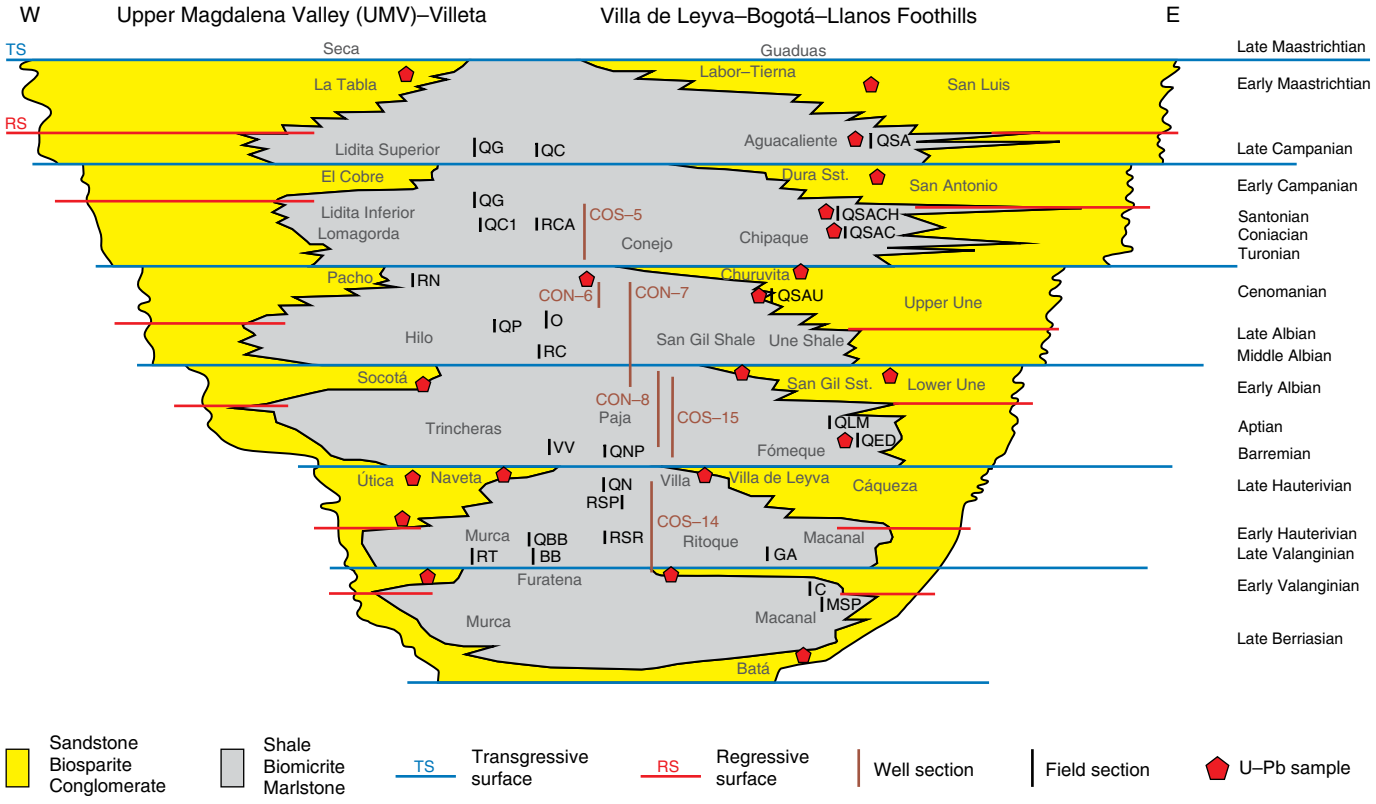

Figure 3. Units studied in the S sector of the basin. Locations projected to line BB' of Figure 1. Sections are from (R) rivers; (Q) creeks; and road cuts, including (MSP) San Pedro Mine; (C) Cachipay; (GA) Gachalá; (RT) Tobia River; (QBB) Buriburi Creek; (RS) Samacá River; (QN) Negra Creek; (VV) Caiquero; (QED) El Dátil Creek; (QLM) Los Monos Creek; (QSA) San Antonio Creek; (RC) Contador River; (QP) Piñal Creek; (O) Otanche; (RN) Negro River; (QC) Cobre Creek; (RCA) Cañas River; (QG) Guate Creek. Stratigraphic Agencia Nacional de Hidrocarburos (ANH) wells are COS–14, COS–15, CON–8, CON–7, CON–6, and COS–5. Cross–section modified from Guerrero (2002a).

two primary and two secondary standard spots were analyzed prior to and following each group of ca. 25–40 tertiary standards and/or unknown sample spots. Tertiary standards were also analyzed with the primary and secondary standards. For a particular isotopic ratio (e.g., $^{206}Pb/^{238}U$), the fractionation factor equals the accepted isotopic ratio divided by the measured ratio (radiogenic Pb only). For zircon U–Pb standards, common Pb was assumed to be negligible, and fractionation factors and their absolute errors were determined directly for the isotopes of interest. Fractionation factors and their errors for each spot were smoothed to yield session–wide spot fractionation factors and their errors. Fractionation factors were calculated based on the following assumptions: (a) ^{235}U values were calculated from measured ^{238}U values (Steiger & Jäger, 1977) and (b) zero fractionation was assumed between ^{206}Pb and ^{207}Pb. For common Pb correction, the Stacey & Kramers (1975) common Pb model for the Earth was used. Ages and common Pb ratios were determined iteratively using an arbitrary, session–wide minimum common Pb age value (the default minimum common Pb age was arbitrarily set equal to the age of the oldest age standard in the current session). For each scan, U–Pb ages and their asymmetrical errors were calculated. For a sum of N scans, the U–Pb age and its error were calculated from the sum of the respective isotopes and a fractionation factor calculated as a weighted sum of N fractionation factors, one fractionation factor for each scan, and each fractionation factor was weighted by the amount of uranium or thorium for the scan.

In total, 110 inclusion–free zircon grains were processed from most samples, obtaining an average of 100 dates per sample. The reported results consist of a single date for each analyzed zircon grain. Data are plotted as age histograms and age probability distribution functions. Detailed data are presented in Tables 1 and 2 of the Supplementary Information.

Heavy minerals were processed by HM Research Associates in St. Ishmaels, Pembrokeshire, UK. Elemental analyses were conducted at ACME Analytical Laboratories in Bogotá, Colombia, using a Thermo 6500 DUO equipment for ICP–OES of major elements and an Agilent 7500cx system for ICP–MS of minor elements and REE. Samples were previously fused with lithium borate salts using a Claisse M4 Fluxer.

3. Results

The results from U–Pb provenance analyses are displayed in Table 4 and Tables 1, 2 of the Supplementary Information. The youngest ages are in the interval of 50 to 150 Ma and corre-

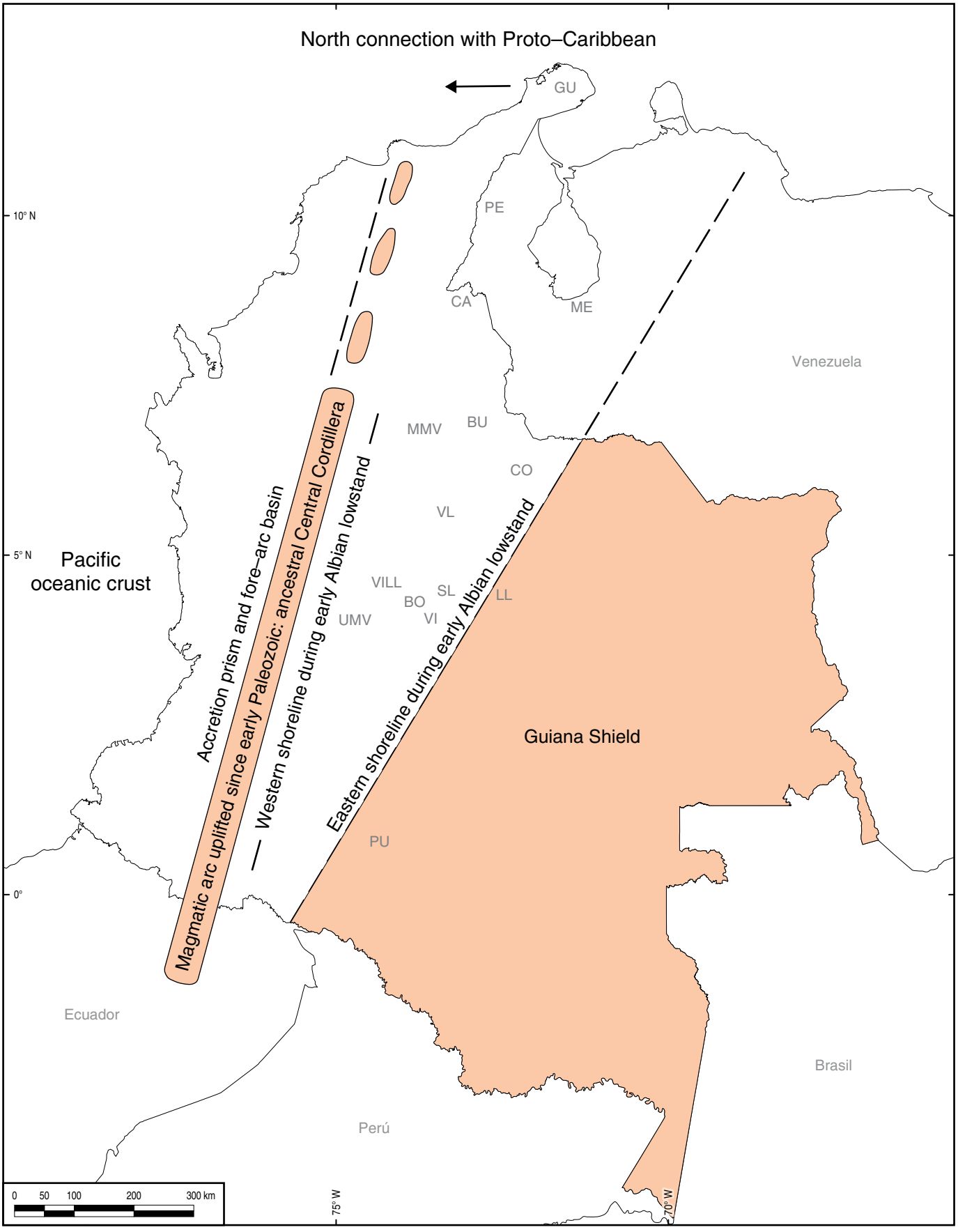
North connection with Proto–Caribbean
GU
PE
CA
ME
Venezuela
10° N
5° N
0°
MMV
BU
CO
VL
VILL
SL
LL
BO
VI
UMV
PU
Pacific
oceanic crust
Accretion prism and fore–arc basin
Magmatic arc uplifted since early Paleozoic: ancestral Central Cordillera
Western shoreline during early Albian lowstand
Eastern shoreline during early Albian lowstand
Guiana Shield
Ecuador
Perú
Brasil
0 50 100 200 300 km
75° W
70° W

Figure 4. Location of the Cretaceous Colombian back–arc basin between the Central Cordillera and the Guiana Shield. The studied sections include the CEOR (SL, VI); Villeta (VILL); CEOC/Villa de Leyva (VL); Barichara/Bucaramanga (BU); Aguachica (MMV); Catatumbo (CA). Referenced sections include: (PU) Putumayo; (UMV) Upper Magdalena Valley; (LL) Llanos; (BO) Bogotá; (CO) Cocuy; (PE) Périja; (ME) Mérida. La Guajira Peninsula (GU) was aligned with the Santa Marta Massif and the Central Cordillera. Modified from Guerrero (2002a) and Guerrero et al. (2000).

spond to coeval Cretaceous particles present in strata from the Magdalena Valley and W side of the Eastern Cordillera. Important age peaks of 150 to 200 Ma (Jurassic) and 200 to 250 (Triassic) are also present on the W side of the basin.

Older peaks, present in samples from both the E and W sides of the study area, are centered around 250 to 550 Ma (Paleozoic) and 900 to 1200 Ma (late Mesoproterozoic to early Neoproterozoic); however, these ages are more common in samples from the E side of the Eastern Cordillera. Other important provenance ages are around 1500 Ma (early Mesoproterozoic) and 1800 Ma (late Paleoproterozoic), which are also more common on the E side of the Eastern Cordillera. The oldest grains, 3250 to 3950 Ma (Paleoarchean and Eoarchean), are present in very minor amounts, usually 1 or 2 particles per sample.

XRD mineralogical results from selected units are displayed in Table 5. The highest contents of kaolinite and montmorillonite correspond mainly to the Llanos Foothills, CEOR, Villa de Leyva, and Barichara areas. The highest contents of illite and chlorite are mainly from the CEOC, Villeta, and Magdalena Valley areas. The percentages displayed are averages per formation in a particular section. The majority are field sections, except for wells COS–5, COS–14, COS–15, CON–6, CON–7, CON–8, SAR 3K, and INFA–1613. Most samples were processed from shales, but there are also marlstones, biomicrites, and cherts. The lowest clay mineral contents (1 to 5 %) are from biomicrites and cherts of La Luna Formation; the highest contents (69%) are from the Chipaque Formation shales. The last column reports the sum of phyllosilicates, including illite, pyrophyllite, kaolinite, chlorite, and montmorillonite.

ICP–OES major element percentages of selected shale beds are displayed in Table 6. Samples with the highest Al_2O_3 contents are mainly from units with high amounts of mudstone and clay shale, including the Paja, San Gil, Chipaque, Conejo, Fómeque, and Macanal Formations. In these units, most clay–sized particles correspond to clay minerals, as indicated by XRD analyses. Samples with the highest contents of titanium (COS–15–2054 Paja Formation), chromium (O–75 Hilo Formation), and scandium (C–12 Macanal Formation) are included.

The ICP–OES major element percentages of limestone and chert units (with less than 5% Al_2O_3) are displayed in Table 7. Samples with the highest CaO contents include mainly examples from La Luna Formation biomicrites. The highest SiO_2 contents correspond to diagenetic cherts of the Lidita Inferior, Lidita Superior, Hilo, and La Luna Formations. The samples with the highest contents of nickel (SAR–7443) and phosphorus (QLL–55) in the study are from La Luna Formation in the Catatumbo area.

Minor elements of selected biomicrite and shale units are presented in ppm in Table 8. The highest contents of vanadium are from shale samples (QP–440 and O–05) of the Hilo Formation from the Villeta and CEOC areas. The highest contents of uranium (SAR–7443) and strontium (QLL–55) are from biomicrite samples of La Luna Formation in the Catatumbo area. The highest values of scandium are from the Macanal (C–12 and MSP–25), Villa de Leyva (COS14–459), and Fómeque (QED–35) Formations. The highest zirconium value is from a sample (COS15–2054) of the Paja Formation in the Villa de Leyva area. The regional distribution of zirconium is also presented in Figure 1.

Table 9 presents the REE in ppm. The highest cerium content is present in a sample (COS14–1575) from the Arcabuco Formation in the Villa de Leyva area. High cerium values are present mostly in the Paja and San Gil Shales from the Villa de Leyva area, along with the Aguacaliente and Une Formations from the Llanos Foothills. The highest content of yttrium is from a sample (RT–10) of the Murca Formation in the Villeta area. The heavy REE are generally associated with the Murca, Trincheras, and Pacho Formations from the Villeta area.

4. Discussion

4.1. Provenance and Paleogeography of the Basin from Detrital Zircon U–Pb Ages

Zircon U–Pb dates obtained from samples collected at several stratigraphic positions and various localities (Figures 1–4) confirm previous paleogeographic reconstructions based on petrography and sandstone distribution (Guerrero, 2002a, 2002b; Guerrero et al., 2000), indicating a back–arc basin sourced from the magmatic arc in the W and the Guiana Shield in the E during the entire Cretaceous time span. Samples are mainly sandstones, but finer–grained strata, including a few siltstones, shales, and biomicrites, are included. Most formations were sampled several times, so a few representative examples are presented here to illustrate the source areas.

4.1.1. Llanos Foothills and CEOR

In the SE sector of the basin, along the periphery of Bogotá, Villavicencio, and San Luis, the Cretaceous succession and Paleozoic sedimentary basement were sampled. The youngest zircon particles in Paleozoic strata are 300 to 350 Ma (Figure 5), which confirms the Carboniferous age of the Farallones Group.

Table 1. Location of field sections.

Sample	Section	Area	Formation	Age	Latitude N	Longitude W
BB–00	Buriburi	CEOC	Furatena (Lower)	Berriasian – early Hauterivian	5° 40’ 28.931”	74° 03’ 54.439”
BB–10	Buriburi	CEOC	Furatena (Lower)	Berriasian – early Hauterivian	5° 40’ 27.833”	74° 03’ 53.743”
C–00	Cachipay	CEOR	Macanal	Berriasian – early Hauterivian	4° 52’ 24.791”	73° 14’ 18.525”
C–48	Cachipay	CEOR	Macanal	Berriasian – early Hauterivian	4° 52’ 23.458”	73° 14’ 16.868”
CAB–00	Agua Blanca Creek	Aguachica	La Luna (Upper)	Coniacian to Santonian	8° 13’ 28.226”	73° 32’ 07.428”
CAB–128	Agua Blanca Creek	Aguachica	La Luna (Upper)	Coniacian to Santonian	8° 13’ 25.764”	73° 32’ 11.248”
CAB–130	Agua Blanca Creek	Aguachica	Umir (Lower)	Early Campanian	8° 13’ 25.725”	73° 32’ 11.306”
CES–00	El Salto Creek	Aguachica	La Luna	Turonian to Santonian	8° 12’ 08.312”	73° 31’ 18.000”
CES–82	El Salto Creek	Aguachica	La Luna	Turonian to Santonian	8° 12’ 05.444”	73° 31’ 20.457”
CES1–00	El Salto Creek	Aguachica	La Luna	Turonian to Santonian	8° 12’ 08.911”	73° 31’ 13.229”
CES1–20	El Salto Creek	Aguachica	La Luna	Turonian to Santonian	8° 12’ 08.853”	73° 31’ 13.827”
GA–00	Gachalá	CEOR	Macanal	Berriasian – early Hauterivian	4° 41’ 44.416”	73° 29’ 43.044”
GA–62	Gachalá	CEOR	Macanal	Berriasian – early Hauterivian	4° 41’ 45.454”	73° 29’ 46.375”
MSP–00	M. San Pedro	CEOR	Macanal	Berriasian – early Hauterivian	4° 51’ 23.858”	73° 22’ 28.851”
MSP–36	M. San Pedro	CEOR	Macanal	Berriasian – early Hauterivian	4° 51’ 24.804”	73° 22’ 30.268”
O–00	Otanche	CEOC	Hilo	Middle and late Albian	5° 42’ 50.420”	74° 11’ 54.956”
O–96	Otanche	CEOC	Hilo	Middle and late Albian	5° 42’ 49.222”	74° 11’ 51.865”
QAD–00	Aguadulce Creek	Barichara	La Luna	Turonian to Santonian	7° 11’ 06.173”	73° 17’ 40.617”
QAD–77	Aguadulce Creek	Barichara	La Luna	Turonian to Santonian	7° 11’ 06.670”	73° 17’ 43.550”
QAD1–00	Aguadulce Creek 1	Barichara	La Luna	Turonian to Santonian	7° 11’ 18.134”	73° 17’ 32.182”
QAD1–60	Aguadulce Creek 1	Barichara	La Luna	Turonian to Santonian	7° 11’ 18.037”	73° 17’ 34.405”
QBB–00	Buriburi Creek	CEOC	Furatena (Lower)	Berriasian – early Hauterivian	5° 40’ 36.746”	74° 03’ 41.176”
QBB–12	Buriburi Creek	CEOC	Furatena (Lower)	Berriasian – early Hauterivian	5° 40’ 36.717”	74° 03’ 40.604”
QC–00	Cobre Creek	CEOC	Lidita Inferior	Late Santonian	5° 41’ 41.386”	74° 12’ 27.255”
QC–50	Cobre Creek	CEOC	Lidita Inferior	Late Santonian	5° 41’ 39.970”	74° 12’ 26.572”
QC1–00	Cobre Creek 1	CEOC	Lomagorda	Turonian to Santonian	5° 42’ 04.020”	74° 12’ 27.205”
QC1–54	Cobre Creek 1	CEOC	Lomagorda	Turonian to Santonian	5° 42’ 02.266”	74° 12’ 25.176”
QED–00	El Dátil Creek	CEOR	Fómeque	Barremian and Aptian	5° 01’ 54.296”	73° 20’ 25.292”
QED–36	El Dátil Creek	CEOR	Fómeque	Barremian and Aptian	5° 01’ 55.929”	73° 20’ 24.462”
QG–00	Guate Creek	Villeta	Lidita Inf.	Late Santonian	4° 53’ 59.292”	74° 32’ 03.307”
QG–137	Guate Creek	Villeta	Lidita Inf.	Late Santonian	4° 54’ 01.026”	74° 32’ 08.472”
QG–251	Guate Creek	Villeta	Lidita Sup.	Late Campanian	4° 54’ 00.408”	74° 32’ 13.807”
QG–292	Guate Creek	Villeta	Lidita Sup.	Late Campanian	4° 54’ 00.354”	74° 32’ 15.777”
QLL–00	La Leche Creek	Catatumbo	Guayacán	Cenomanian	8° 08’ 56.797”	72° 41’ 31.315”
QLL–02	La Leche Creek	Catatumbo	Guayacán	Cenomanian	8° 08’ 57.311”	72° 41’ 30.412”
QLL–04	La Leche Creek	Catatumbo	La Luna	Turonian to Santonian	8° 08’ 57.822”	72° 41’ 29.509”
QLL–63	La Leche Creek	Catatumbo	La Luna	Turonian to Santonian	8° 09’ 09.873”	72° 41’ 14.692”
QLM–00	Los Micos Creek	CEOR	Fómeque	Barremian and Aptian	5° 04’ 22.882”	73° 24’ 53.983”
QLM–53	Los Micos Creek	CEOR	Fómeque	Barremian and Aptian	5° 04’ 20.588”	73° 24’ 57.524”
QLP–00	La Paja Creek	Barichara	Paja	Barremian and Aptian	7° 01’ 26.468”	73° 20’ 04.444”
QLP–66	La Paja Creek	Barichara	Paja	Barremian and Aptian	7° 01’ 25.114”	73° 20’ 08.359”
QN–00	Negra Creek	CEOC	Villa de Leyva	Late Hauterivian	5° 35’ 40.402”	73° 30’ 02.088”

Table 1. Location of field sections (*continued*).

Sample	Section	Area	Formation	Age	Latitude N	Longitude W
QN–10	Negra Creek	CEOC	Villa de Leyva	Late Hauterivian	5° 35' 39.696"	73° 30' 02.193"
QNP–00	Negra Creek	CEOC	Paja	Barremian and Aptian	5° 35' 38.593"	73° 29' 56.222"
QNP–34	Negra Creek	CEOC	Paja	Barremian and Aptian	5° 35' 37.967"	73° 29' 54.923"
QP–00	Piñal Creek	Villeta	Hilo	Middle and late Albian	4° 52' 25.191"	74° 30' 09.671"
QP–465	Piñal Creek	Villeta	Hilo	Middle and late Albian	4° 52' 06.673"	74° 29' 55.123"
QS–00	La Sorda Creek	Barichara	El Salto	Cenomanian	7° 09' 38.294"	73° 18' 05.373"
QS–16	La Sorda Creek	Barichara	El Salto	Cenomanian	7° 09' 38.753"	73° 18' 05.597"
QS1–02	La Sorda Creek 1	Barichara	La Luna (Lower)	Turonian	7° 09' 50.411"	73° 18' 04.775"
QS1–36	La Sorda Creek 1	Barichara	La Luna (Lower)	Turonian	7° 09' 48.200"	73° 18' 06.301"
QS2–00	La Sorda Creek 2	Barichara	El Salto	Cenomanian	7° 09' 57.080"	73° 18' 00.931"
QS2–20	La Sorda Creek 2	Barichara	El Salto	Cenomanian	7° 09' 58.418"	73° 18' 01.340"
QS2–22	La Sorda Creek 2	Barichara	La Luna (Lower)	Turonian	7° 09' 58.552"	73° 18' 01.379"
QS2–52	La Sorda Creek 2	Barichara	La Luna (Lower)	Turonian	7° 10' 00.565"	73° 18' 01.991"
QSA–00	San Antonio Creek	CEOR	Aguacaliente	Late Campanian	4° 50' 15.031"	73° 12' 25.203"
QSA–100	San Antonio Creek	CEOR	Aguacaliente	Late Campanian	4° 50' 11.838"	73° 12' 25.178"
QSAC–00	S. Antonio Creek C	CEOR	Chipaque	Turonian to Santonian	4° 50' 34.658"	73° 12' 23.685"
QSAC–48	S. Antonio Creek C	CEOR	Chipaque	Turonian to Santonian	4° 50' 33.001"	73° 12' 23.408"
QSACH–00	S. Antonio Creek Ch	CEOR	Chipaque	Turonian to Santonian	4° 50' 27.921"	73° 12' 24.635"
QSACH–30	S. Antonio Creek Ch	CEOR	Chipaque	Turonian to Santonian	4° 50' 26.784"	73° 12' 24.231"
QSAU–00	S. Antonio Creek U	CEOR	Une (Upper)	Late Cenomanian	4° 51' 13.714"	73° 12' 14.776"
QSAU–18	S. Antonio Creek U	CEOR	Une (Upper)	Late Cenomanian	4° 51' 13.752"	73° 12' 14.292"
RC–00	Contador River	Villeta	Hilo (Lower)	Middle Albian	4° 52' 59.887"	74° 31' 09.813"
RC–44	Contador River	Villeta	Hilo (Lower)	Middle Albian	4° 52' 59.100"	74° 31' 08.615"
RCA–00	Cañas River	Villeta	Conejo	Turonian to Santonian	4° 56' 31.704"	74° 16' 10.733"
RCA–80	Cañas River	Villeta	Conejo	Turonian to Santonian	4° 56' 28.080"	74° 16' 02.777"
RN–00	Negro River	CEOC	Pacho	Cenomanian	5° 17' 35.949"	74° 04' 43.213"
RN–112	Negro River	CEOC	Pacho	Cenomanian	5° 17' 33.238"	74° 04' 52.281"
RR–02	Riecito River	Catatumbo	Capacho	Middle and late Albian	8° 03' 02.089"	72° 48' 26.230"
RR–20	Riecito River	Catatumbo	Capacho	Middle and late Albian	8° 03' 05.512"	72° 48' 26.056"
RR1–00	Riecito River 1	Catatumbo	Guayacán	Cenomanian	8° 03' 30.022"	72° 48' 26.355"
RR1–10	Riecito River 1	Catatumbo	Guayacán	Cenomanian	8° 03' 30.158"	72° 48' 27.350"
RR1–18	Riecito River 1	Catatumbo	La Luna	Turonian to Santonian	8° 03' 30.265"	72° 48' 28.150"
RR1–60	Riecito River 1	Catatumbo	La Luna	Turonian to Santonian	8° 03' 30.834"	72° 48' 32.337"
RSP–00	Samacá River	CEOC	Villa de Leyva	Late Hauterivian	5° 35' 19.005"	73° 30' 44.572"
RSP–32	Samacá River	CEOC	Villa de Leyva	Late Hauterivian	5° 35' 17.562"	73° 30' 43.650"
RSR–00	Samacá River	CEOC	Ritoque	Late Valanginian – early Hauterivian	5° 35' 30.385"	73° 30' 54.584"
RSR–34	Samacá River	CEOC	Ritoque	Late Valanginian – early Hauterivian	5° 35' 31.205"	73° 30' 51.049"
RT–00	Tobia River	Villeta	Murca (Lower)	Berriasian – early Hauterivian	5° 04' 16.218"	74° 26' 44.287"
RT–62	Tobia River	Villeta	Murca (Lower)	Berriasian – early Hauterivian	5° 04' 14.781"	74° 26' 40.134"
VV–00	Caiquero	Villeta	Trincheras	Barremian and Aptian	5° 03' 51.475"	74° 24' 41.054"
VV–89	Caiquero	Villeta	Trincheras	Barremian and Aptian	5° 03' 47.484"	74° 24' 32.936"

Table 2. Location of wells.

Sample and depth in feet	Well	Area	Formation	Age	Latitude N	Longitude W
CON–06–360	ANH–CON–06	CEOC	Churuvita	Cenomanian	5° 44' 26.202"	73° 44' 14.826"
CON–06–1470	ANH–CON–06	CEOC	Churuvita	Cenomanian	5° 44' 26.202"	73° 44' 14.826"
CON–07–134	ANH–CON–07	CEOC	Churuvita	Cenomanian	5° 49' 30.758"	73° 41' 47.587"
CON–07–240	ANH–CON–07	CEOC	Churuvita	Cenomanian	5° 49' 30.758"	73° 41' 47.587"
CON–07–485	ANH–CON–07	CEOC	San Gil Shale	Middle and late Albian	5° 49' 30.758"	73° 41' 47.587"
CON–07–1810	ANH–CON–07	CEOC	San Gil Shale	Middle and late Albian	5° 49' 30.758"	73° 41' 47.587"
CON–07–1880	ANH–CON–07	CEOC	San Gil Sandstone	Early Albian	5° 49' 30.758"	73° 41' 47.587"
CON–07–2420	ANH–CON–07	CEOC	San Gil Sandstone	Early Albian	5° 49' 30.758"	73° 41' 47.587"
CON–08–287	ANH–CON–08	CEOC	San Gil Sandstone	Early Albian	5° 57' 12.630"	73° 36' 31.512"
CON–08–1310	ANH–CON–08	CEOC	San Gil Sandstone	Early Albian	5° 57' 12.630"	73° 36' 31.512"
CON–08–1376	ANH–CON–08	CEOC	Paja	Barremian and Aptian	5° 57' 12.630"	73° 36' 31.512"
CON–08–2575	ANH–CON–08	CEOC	Paja	Barremian and Aptian	5° 57' 12.630"	73° 36' 31.512"
COS–05–261	ANH–COS–05	Villa de Leyva	Conejo	Turonian to Santonian	5° 31' 54.705"	73° 49' 49.929"
COS–05–1059	ANH–COS–05	Villa de Leyva	Conejo	Turonian to Santonian	5° 31' 54.705"	73° 49' 49.929"
COS–14–370	ANH–COS–14	Villa de Leyva	Villa de Leyva	Late Hauterivian	5° 35' 01.356"	73° 31' 30.586"
COS–14–650	ANH–COS–14	Villa de Leyva	Villa de Leyva	Late Hauterivian	5° 35' 01.356"	73° 31' 30.586"
COS–14–678	ANH–COS–14	Villa de Leyva	Ritoque	Late Valanginian – early Hauterivian	5° 35' 01.356"	73° 31' 30.586"
COS–14–1506	ANH–COS–14	Villa de Leyva	Ritoque	Late Valanginian – early Hauterivian	5° 35' 01.356"	73° 31' 30.586"
COS–15–893	ANH–COS–15	Villa de Leyva	San Gil Sandstone	Early Albian	5° 32' 37.037"	73° 38' 06.689"
COS–15–1323	ANH–COS–15	Villa de Leyva	San Gil Sandstone	Early Albian	5° 32' 37.037"	73° 38' 06.689"
COS–15–1330	ANH–COS–15	Villa de Leyva	Paja	Barremian and Aptian	5° 32' 37.037"	73° 38' 06.689"
COS–15–2220	ANH–COS–15	Villa de Leyva	Paja	Barremian and Aptian	5° 32' 37.037"	73° 38' 06.689"
INFA–4727	Infantas–1613	MMV	La Luna	Turonian to Santonian	6° 55' 38.423"	73° 46' 43.388"
INFA–6243	Infantas–1613	MMV	La Luna	Turonian to Santonian	6° 55' 38.423"	73° 46' 43.388"
INFA–6396	Infantas–1613	MMV	El Salto	Cenomanian	6° 55' 38.423"	73° 46' 43.388"
INFA–6472	Infantas–1613	MMV	El Salto	Cenomanian	6° 55' 38.423"	73° 46' 43.388"
INFA–6480	Infantas–1613	MMV	Simití	Middle and late Albian	6° 55' 38.423"	73° 46' 43.388"
INFA–8840	Infantas–1613	MMV	Simití	Middle and late Albian	6° 55' 38.423"	73° 46' 43.388"
INFA–8650	Infantas–1613	MMV	Tablazo	Early Albian	6° 55' 38.423"	73° 46' 43.388"
INFA–9358	Infantas–1613	MMV	Paja	Barremian and Aptian	6° 55' 38.423"	73° 46' 43.388"
INFA–9364	Infantas–1613	MMV	Paja	Barremian and Aptian	6° 55' 38.423"	73° 46' 43.388"
RIO–3496	Río de oro–14	Catatumbo	Mito Juan	Early Maastrichtian	9° 05' 37.499"	72° 54' 04.926"
RIO–4220	Río de oro–14	Catatumbo	Mito Juan	Early Maastrichtian	9° 05' 37.499"	72° 54' 04.926"
RIO–4780	Río de oro–14	Catatumbo	Colón (Lower)	Early Campanian	9° 05' 37.499"	72° 54' 04.926"
RIO–5392	Río de oro–14	Catatumbo	Colón (Lower)	Early Campanian	9° 05' 37.499"	72° 54' 04.926"
RIO–5768	Río de oro–14	Catatumbo	La Luna	Turonian to Santonian	9° 05' 37.499"	72° 54' 04.926"
RIO–5775	Río de oro–14	Catatumbo	La Luna	Turonian to Santonian	9° 05' 37.499"	72° 54' 04.926"
RIO–6259	Río de oro–14	Catatumbo	Capacho	Middle and late Albian	9° 05' 37.499"	72° 54' 04.926"
SAR–7336	Sardinata–n2	Catatumbo	La Luna	Turonian to Santonian	8° 30' 15.474"	72° 39' 04.879"
SAR–7460	Sardinata–n2	Catatumbo	La Luna	Turonian to Santonian	8° 30' 15.474"	72° 39' 04.879"

Table 3. Sandstone samples located outside of main sections.

Sample	Area	Formation	Age	Latitude N	Longitude W
GPS–89	Barichara	Tablazo	Early Albian	7° 10' 51.343"	73° 16' 47.387"
GPS–270	Aguachica	Aguachica	Late Aptian	8° 13' 01.122"	73° 31' 10.134"
GPS–500	Llanos Foothills	San Luis	Early Maastrichtian	4° 50' 00.469"	73° 12' 28.233"
GPS–501	Llanos Foothills	San Antonio	Early Campanian	4° 50' 11.561"	73° 12' 50.548"
GPS–502	Llanos Foothills	Chipaque	Turonian to Santonian	4° 50' 31.771"	73° 12' 59.524"
GPS–506	Llanos Foothills	Alto de Caqueza	Late Hauterivian	4° 51' 51.308"	73° 14' 02.402"
GPS–510	Llanos Foothills	Batá	Berriasian	4° 51' 42.523"	73° 16' 07.012"
GPS–511	Llanos Foothills	Farallones	Carboniferous	4° 52' 55.098"	73° 16' 15.635"
GPS–518	Llanos Foothills	Fómeque	Barremian and Aptian	5° 00' 14.466"	73° 30' 14.414"
GPS–520	Llanos Foothills	Une (Middle)	Middle and late Albian	5° 03' 09.896"	73° 31' 38.813"
GPS–526	Llanos Foothills	Une (Upper)	Cenomanian	5° 04' 52.142"	73° 37' 09.574"
GPS–540	Barichara	Tambor	Berriasian to Valanginian	6° 31' 31.234"	73° 02' 37.969"
GPS–541	Barichara	Tambor	Berriasian to Valanginian	6° 36' 23.379"	73° 02' 47.256"
GPS–543	Barichara	Rosablanca (Upper)	Late Hauterivian	6° 25' 11.723"	73° 09' 31.939"
GPS–549	Barichara	Tambor	Berriasian to Valanginian	6° 53' 59.656"	73° 20' 58.413"
GPS–551	Barichara	Tambor	Berriasian to Valanginian	6° 53' 54.205"	73° 21' 50.441"
GPS–553	Barichara	Tablazo	Early Albian	6° 56' 30.482"	73° 22' 40.936"
GPS–555	Barichara	Simití	Middle and late Albian	7° 08' 32.549"	73° 17' 56.712"
GPS–556	Aguachica	Aguachica	Late Aptian	8° 14' 00.073"	73° 31' 56.083"
GPS–564	Catatumbo	Aguardiente	Early Albian	7° 57' 38.309"	72° 49' 36.168"
GPS–568	Catatumbo	Guayacán	Cenomanian	7° 53' 32.915"	72° 42' 04.787"
GPS–571	Barichara	Tambor	Berriasian to Valanginian	6° 52' 00.669"	73° 03' 21.267"
GPS–572	Barichara	Tambor	Berriasian to Valanginian	6° 54' 57.911"	73° 01' 53.909"
GPS–579	Villeta	La Naveta	Late Hauterivian	4° 30' 23.637"	74° 34' 11.221"
GPS–599	Villeta	Socotá	Early Albian	5° 01' 03.675"	74° 31' 02.152"
GPS–602	Villeta	Útica	Late Hauterivian	5° 11' 14.769"	74° 27' 57.707"
GPS–619	Villeta	Murca	Berriasian to Hauterivian	5° 04' 07.443"	74° 26' 00.059"
GPS–1210	Villa de Leyva	San Gil Shale	Middle and late Albian	5° 34' 30.881"	73° 30' 19.854"
GPS–1211	Villa de Leyva	Villa de Leyva	Late Hauterivian	5° 35' 06.535"	73° 30' 52.170"
GPS–1220	Llanos Foothills	Macanal (Middle)	Early Valanginian	4° 45' 07.809"	73° 33' 38.372"
GPS–1238	Llanos Foothills	Une (Lower)	Early Albian	4° 25' 03.396"	73° 59' 13.992"
OU	CEOC	La Tabla	Early Maastrichtian	5° 41' 00.988"	74° 11' 15.624"

Other important ages present in both Paleozoic and Cretaceous strata (Figures 5–7; Table 4) are in the ranges of 450 to 650 Ma (Ediacaran to Ordovician) and 900 to 1100 Ma, which correspond with the late Mesoproterozoic to early Neoproterozoic Grenvillian Orogeny. Middle and early Mesoproterozoic particles around 1300 and 1500 Ma and a few Paleoproterozoic and Archean particles are also present, clearly indicating a cratonic source area to the E. There are no particles of Jurassic or Cretaceous age. The lower part of the Cretaceous section contains more abundant Paleozoic particles than the upper part because Proterozoic particles became dominant as the Paleozoic sedimentary basement was eroded. These results are similar to those reported from the E side of the Eastern Cordillera by Horton et al. (2010), who indicated that Paleozoic grains in the range of 500 to 400 Ma are more common in the lower part of the Cretaceous section, whereas Paleoproterozoic and Mesoproterozoic grains of 2000 to 950 Ma become dominant in the upper part.

4.1.2. Villeta area, CEOC, and MMV

Along the W margin of the basin, the source areas of the Cretaceous strata were quite different from those for the Llanos Foothills on the E basin margin. Mesoproterozoic and Paleozoic particles were also present in the Central Cordillera but in lower

Table 4. Detrital zircon U–Pb provenance ages (Ma).

Sample	Number of particules	Formation	Area	Youngest ages	Youngest ages group	Important age groups			Oldest ages group
GPS–500	108	San Luis	Llanos Foothills	477 ± 22	450–500	1000–1050	1550–1600	1750–1800	2500–2550
QSA–92	73	Aguacaliente	Llanos Foothills	462 ± 22	450–500	1000–1050	1200–1250	1450–1500	3900–3950
GPS–501	103	San Antonio	Llanos Foothills	548 ± 28	450–550	900–950	1300–1350	1650–1700	2000–2050
GPS–502	102	Chipaque	Llanos Foothills	435 ± 26	400–450	1000–1050	1150–1200	1450–1500	2500–2550
GPS–526	96	Une (Upper)	Llanos Foothills	410 ± 18	400–450	1000–1050	1300–1350	1800–1850	2100–2150
GPS–520	95	Une (Middle)	Llanos Foothills	463 ± 12	450–500	950–1000	1250–1300	1450–1500	2750–2800
GPS–1238	99	Une (Lower)	Llanos Foothills	304 ± 26	300–350	550–600	950–1000	1450–1500	2350–2400
GPS–518	79	Fómeque	Llanos Foothills	335 ± 12	300–350	600–650	900–950	1550–1600	1950–2000
GPS–506	108	Cáqueza Sandstone	Llanos Foothills	480 ± 54	450–500	950–1000	1150–1200	1450–1500	2600–2650
GPS–1220	105	Macanal	Llanos Foothills	282 ± 26	250–300	400–450	900–950	1400–1450	1900–1950
GPS–510	108	Batá	Llanos Foothills	312 ± 10	300–350	400–450	900–950	1050–1100	1750–1800
GPS–511	98	Farallones	Llanos Foothills	311 ± 12	300–350	500–550	1000–1050	1150–1200	3500–3550
CON6–1322	87	Churuvita	Villa de Leyva	445 ± 17	400–450	1000–1050	1450–1500	1800–1850	2200–2250
GPS–1210	99	San Gil Shale	Villa de Leyva	525 ± 24	500–550	1250–1300	1500–1550	2650–2700	2050–2100
CON8–1181	76	San Gil Sandstone	Villa de Leyva	332 ± 30	300–350	550–600	850–900	1350–1400	1800–1850
GPS–1211	83	Villa de Leyva	Villa de Leyva	428 ± 14	400–450	850–900	950–1000	1150–1200	1950–2000
COS14–1550	102	Arcabuco	Villa de Leyva	401 ± 12	400–450	900–950	950–1000	1450–1500	2650–2700
QAD–15	84	La Luna	Barichara	86 ± 5	50–100	200–250	1000–1100	1450–1500	2050–2100
QS–14.8	84	El Salto	Barichara	536 ± 30	500–550	1300–1350	1750–1800	1900–1950	2650–2700
GPS–555	83	Simití	Barichara	473 ± 25	450–500	950–1000	1500–1550	1750–1800	2000–2050
GPS–553	92	Tablazo	Barichara	401 ± 17	400–450	450–500	1500–1550	1750–1800	2600–2650
GPS–89	91	Tablazo	Barichara	361 ± 13	600–650	900–1000	1500–1550	1750–1800	2750–2800
GPS–543	103	Rosablanca	Barichara	269 ± 19	400–450	500–550	900–1000	1150–1200	2100–2150
GPS–540	109	Tambor	Barichara	373 ± 18	350–400	450–550	900–1000	1400–1450	2100–2150
GPS–541	94	Tambor	Barichara	139 ± 9	100–150	150–200	200–250	400–450	2000–2050
GPS–571	104	Tambor	Barichara	287 ± 13	350–400	500–550	950–1000	1400–1450	2050–2100
GPS–572	104	Tambor	Barichara	158 ± 8	150–200	200–250	400–450	950–1000	2000–2050
GPS–551	104	Tambor	Barichara	256 ± 11	250–300	400–450	1000–1050	1500–1550	1800–1850
GPS–549	100	Tambor	Barichara	145 ± 6	150–200	200–250	350–400	400–450	2100–2150
RR1–15	100	La Luna	Catatumbo	90 ± 4	50–100	100–150	150–200	1000–1050	1400–1450
GPS–568	99	Guayacán	Catatumbo	487 ± 77	450–600	1300–1350	1500–1550	1700–1750	3250–3300
RR–00	82	Capacho	Catatumbo	442 ± 18	400–450	1300–1350	1550–1600	1750–1800	2000–2050
GPS–564	106	Aguardiente	Catatumbo	420 ± 16	500–550	950–1000	1150–1200	1450 –1500	2100–2150
GPS–556	89	Aguachica	Aguachica (MMV)	145 ± 8	100–150	150–200	900–950	1000–1100	1700–1750
GPS–270	106	Aguachica	Aguachica (MMV)	164 ± 6	170–186	150–200	200–250	600–650	950–1000
OU	28	La Tabla	CEOC	78 ± 6	50–100	100–150	1200–1250	1550–1600	2100–2150
GPS–599	99	Socotá	Villeta	142 ± 10	100–150	150–200	950–1000	1150–1200	2500–2550
GPS–602	102	Útica	Villeta	138 ± 7	100–150	150–200	250–300	1150–1200	3000–3050
GPS–579	64	La Naveta	Villeta	128 ± 13	100–150	150–200	200–250	950–1000	1200–1250
GPS–619	98	Murca	Villeta	135 ± 6	100–150	150–200	250–300	950–1000	2850–2900

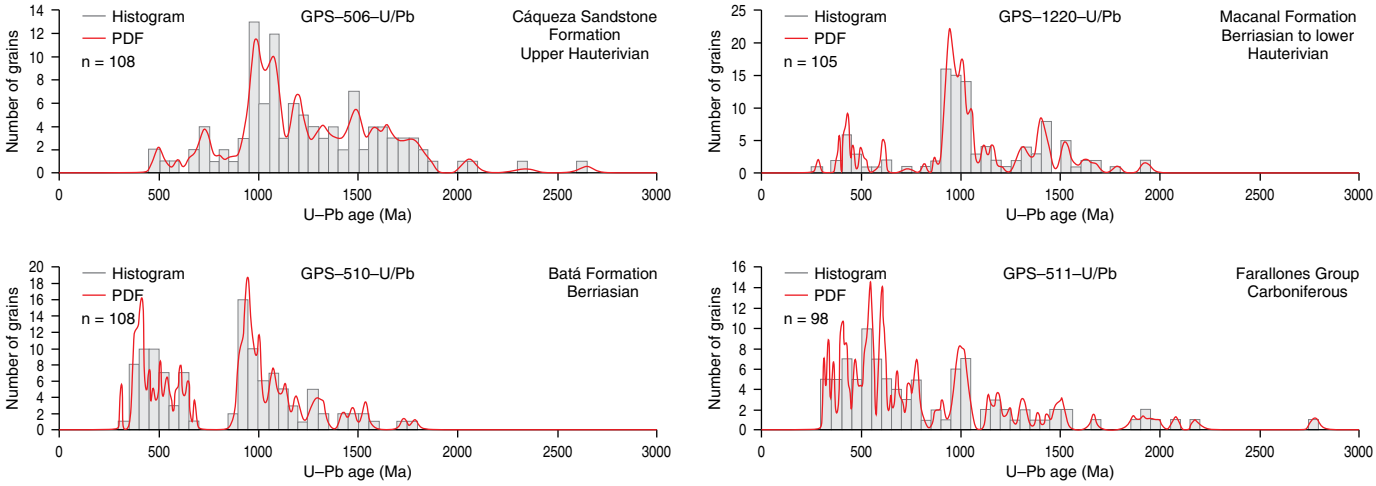

Figure 5. Detrital zircon U–Pb ages from the Paleozoic sedimentary basement and Berriasian to Hauterivian units from the E foothills of the Eastern Cordillera.

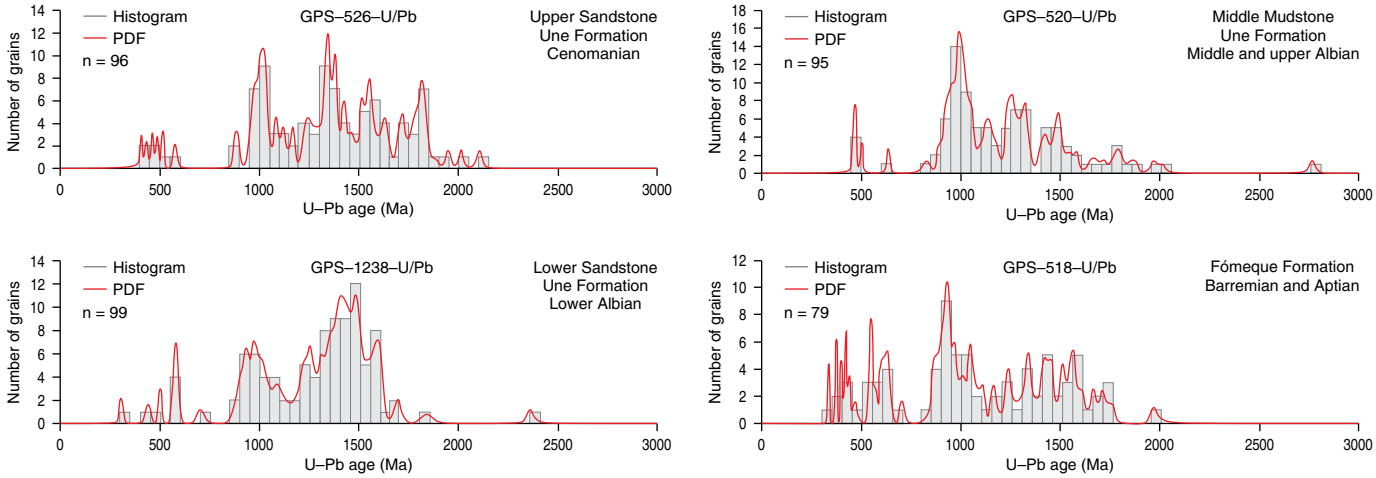

Figure 6. Detrital zircon U–Pb ages of Barremian to Cenomanian units from the E foothills of the Eastern Cordillera.

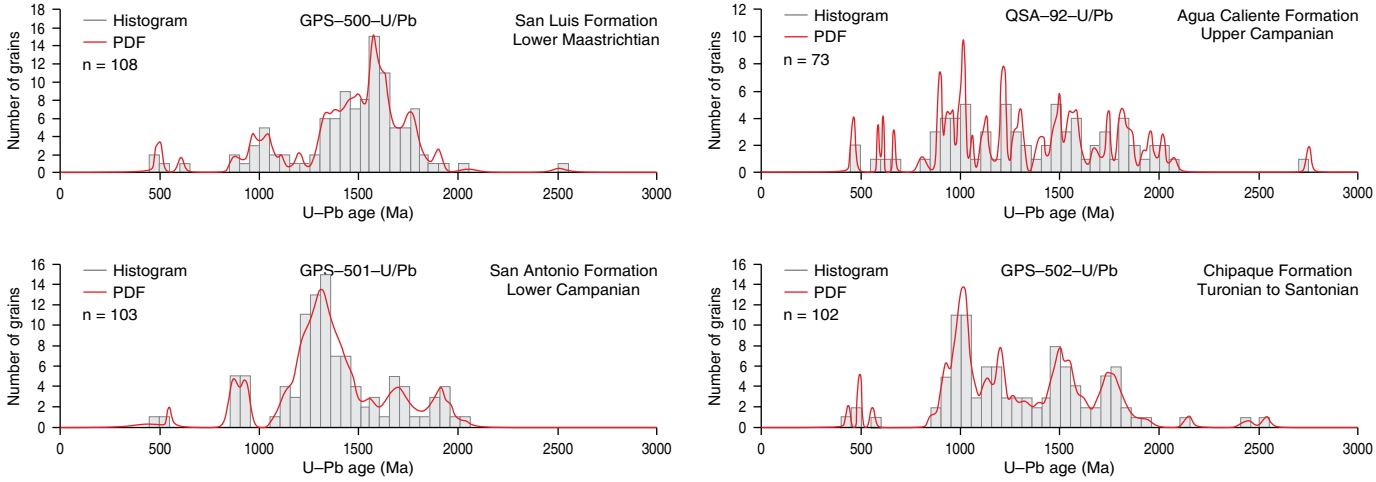

Figure 7. Detrital zircon U–Pb ages of Turonian to lower Maastrichtian units from the E foothills of the Eastern Cordillera.

proportions than in the E sources. The age of zircon particles (Figures 8, 9; Table 4) is dominated by Lower Cretaceous rocks derived from magmatic and volcanic activity in the Central Cordillera and by abundant Jurassic rocks exhumed before and during the development of the Cretaceous basin. Sample GPS–619 from the Murca Formation contains 27 particles that cluster at 135 ± 6 Ma, which is within the Berriasian to Hauterivian biostratigraphic age range of the unit. The highest frequency includes 37 particles in the 150 to 200 Ma Jurassic age range. Sample GPS–579 from La Naveta Formation contains 11 particles concentrated at 128 ± 13 Ma and 35 particles (highest frequency) in the 150 to 200 Ma Jurassic age range. The Útica Formation (GPS–602) contains 12 grains focused at 138 ± 7 Ma and the highest frequency (35 grains) in the 150 to 200 Ma Jurassic age range. The upper sandstone/conglomerate members of the Murca, La Naveta, and Útica Formations are contemporaneous regressive units of late Hauterivian age, which include shoreface and fluvial deposits sourced from the Central Cordillera magmatic arc. The names have been inconsistently used to include upper Hauterivian regressive conglomerates and sandstones of fluvial and shoreface origin and Berriasian to lower Hauterivian mudstones with minor sandstone interbeds of marine origin. The ages of zircon grains presented here are consistent with the Berriasian to Hauterivian biostratigraphic range of the units. The sedimentary petrography and the grain size paleogeography of the sandstones (Guerrero, 2002a; Moreno, 1990, 1991) also indicate provenance from the Central Cordillera.

The lower Albian sandstones of the Socotá Formation show the same pattern of Jurassic to Early Cretaceous grains. Sample GPS–599 includes 5 particles centered at 142 ± 10 Ma and 12 particles in the 150 to 200 Ma Jurassic age interval. Interestingly, it also includes a number of Proterozoic dates at approximately 1150 ± 29 Ma, which could be interpreted as derived from the Guiana Shield, but Jurassic and Cretaceous sources are not represented there, so the source area should not have been the shield. The unit was deposited in a regressive shoreface dominated by storms, with sediments sourced from rivers draining the Central Cordillera.

The lower Maastrichtian La Tabla Formation from the CEOC (sample OU) contains 3 zircon grains at 78 ± 6 Ma (Campanian) and 139 ± 5 Ma (Berriasian to Valanginian), along with 2–4 grains around 1200 Ma and 1500 to 1900 Ma (Figure 9).

The western provenance of zircon particles from the Central Cordillera is also observed for samples from the Magdalena Valley. The basal sandstones in the Aguachica area, which are outside the central rift of the basin, are of late Aptian age. Older Cretaceous strata of Berriasian to early Aptian age from the main rift of the basin (present–day Eastern Cordillera) are nonexistent in the Aguachica area. The stratigraphy is similar to that exposed in the Upper Magdalena Valley (UMV), where the oldest Cretaceous strata of the Yaví Formation and the Lower and Middle Members of the Caballos Formation are of Aptian age (Guerrero, 2002b; Guerrero et al., 2000). These Aptian units also rest unconformably on Jurassic igneous and volcaniclastic rocks: the Saldaña Formation in the UMV and the Noreán Formation in the northern sector of the MMV. The oldest ammonites collected from the marine beds transitionally overlying the conglomerates and sandstones of the Aguachica section are of late Aptian age, so that the section is definitely younger than the succession from the western foothills of the Eastern Cordillera near Bucaramanga. The Aguachica section was deposited on the W side of the basin, unlike the Barichara–Bucaramanga section, which was supplied from the E side of the basin. Consequently, the Tambor, Rosablanca, Paja, and Tablazo Formations are not present. A different stratigraphic nomenclature should be used for those areas of the Magdalena Valley west of the Early Cretaceous border faults. We propose the name Aguachica Formation for the transgressive upward–fining fluvial succession of conglomerates, sandstones, and red mudstones of Aptian age, which rest unconformably on the Noreán Formation and are overlain transitionally by marine strata of late Aptian to Maastrichtian age. The Aguachica Formation name is applied only to the fluvial strata; the overlying marine beds should receive formal names different from those of rocks in the Barichara–Bucaramanga.

The youngest zircon grains from the Aguachica Formation (Figure 9; Table 4) at the base of the Cretaceous section near Aguachica in the Cesar Department (GPS–556) are in the range of 145 ± 8 Ma; the highest age frequency of the sample (70 grains) is in the Jurassic interval from 150–200 Ma. Of these, 37 grains are clustered at 174 ± 8 Ma. A few grains with Triassic and older ages are also present.

Sample GPS–270 contains 102 grains in the 150–200 Jurassic interval; of these, 84 grains are within the age of 178 ± 8 Ma. The youngest grain has an age of 164 ± 6 Ma, and only 4 grains are older than Jurassic.

The provenance ages of the basal Cretaceous section from the MMV coincide with the ages reported by Horton et al. (2015) from the Cocuyo, Guane, and Cagui wells. They recognized peaks at 170 to 185 Ma for the coarse–grained nonmarine section (Aguachica Formation) and 175 to 190 Ma for the finer–grained marine deposits.

Proterozoic U–Pb ages have been reported from several localities on the E flank of the Central Cordillera; for instance, Villagómez et al. (2011) reported zircon crystals from La Miel Orthogneiss with ages of 1700 to 450 Ma and a major peak at approximately 1200 Ma. They also reported zircon crystals from a quartzite in the Cajamarca Complex with a peak age of approximately 240 Ma and 500 to 600 Ma and 1000 to 1200 Ma populations. Ordóñez–Carmona et al. (2006) reported Sm/Nd TDM ages of approximately 1710 and 1790 Ma from El Vapor Gneiss, which also has a metamorphic Rb/Sr age of 894 ± 36 Ma. The Tierradentro amphibolite has a K/Ar age of 1360 ± 270 Ma (Vesga & Barrero, 1978). El Hígado Amphibolite has an Ar/Ar age

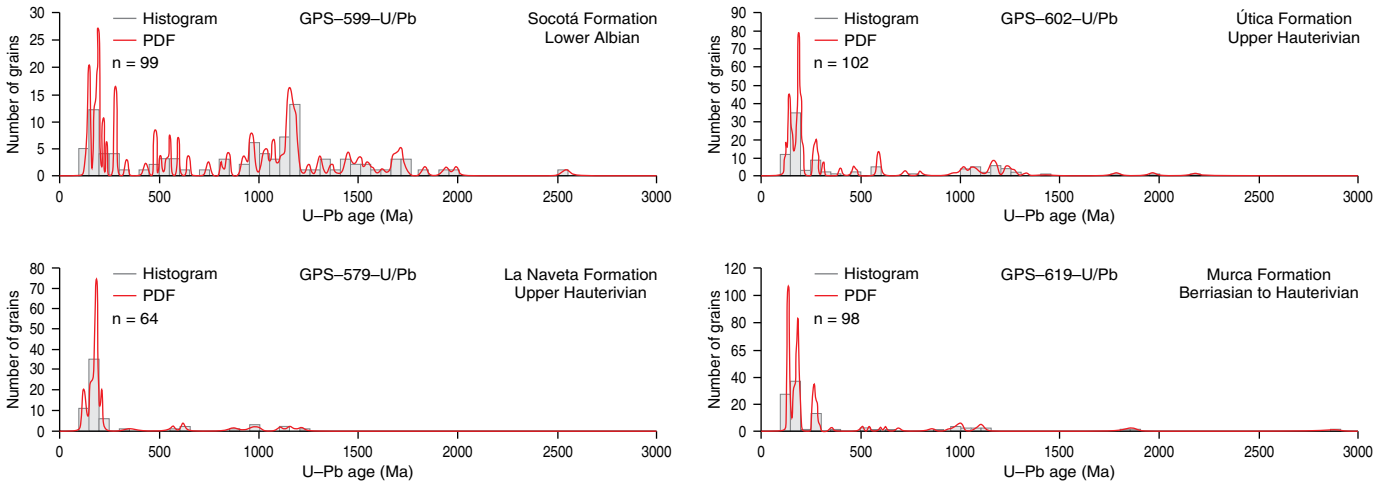

Figure 8. Detrital zircon U–Pb ages of Berriasian to lower Albian units from the Villeta Area.

of 911 ± 2 Ma (Restrepo–Pace et al., 1997). Granulites from the San Lucas Gneiss yield a U–Pb age of 1124 ± 22 Ma and a Sm/Nd TDM age of 1600 Ma, as reported by Clavijo et al. (2008).

It is evident that Proterozoic ages are not exclusive to eastern sources in the Guiana Shield but are also present in western sources today along the E flank of the Central Cordillera, which was the uplifted magmatic/metamorphic arc and constituted the western margin of the Cretaceous Colombian back–arc basin. The Central Cordillera as the source of Proterozoic particles was also indicated by Horton et al. (2015), but they concluded that the Cretaceous strata at the MMV were supplied from both E and W sources, including the Central Cordillera serranía de San Lucas, the Eastern Cordillera Santander Massif, and the Guiana Shield.

We postulate that although the Proterozoic particles could have been derived either from the Guiana Shield or from the Central Cordillera, there is certainly a notable difference in the frequency of the Proterozoic particles, which are far more abundant when the source area is the Guiana Shield. However, what is markedly different and unique in the western source area (Central Cordillera) is the presence of Jurassic and Cretaceous particles, which are not present to the E in the Guiana Shield. Therefore, we prefer to interpret our data from the Villeta and MMV areas as indicating a single source area in the Central Cordillera.

The possibility of units derived from both the E and W flanks of the basin would only be conceivable for a trunk fluvial system along the basin axis during the early rifting (Berriasian to Valanginian) stage, as discussed below for the Tambor Formation. However, the units studied are shoreface marine sandstones with younger ages that could not possibly be sourced from both sides of the basin because the E and W shorefaces of the basin had already been separated since the late Valanginian by the deeper offshore muds and marls in the center of the basin. It is impossible for particles to cross from one side of the basin to the deepest axis of the seaway and subsequently reach the opposite shoreface. Eastern Cordillera sources in exposed horsts are impossible because the present–day massifs (Santander, Floresta, and Quetame) were already covered by marine strata during the late Valanginian. The crystalline basement of those massifs was covered by Lower Cretaceous to middle Miocene strata and was only exposed again during the late Miocene to the present due to uplift of the Eastern Cordillera. Since late Valanginian times, the only possible sources for the Cretaceous back–arc basin were the Guiana Shield and the Central Cordillera, supplying the opposite E and W shorelines.

4.1.3. Villa de Leyva Area

The central portions of the Eastern Cordillera repeat the pattern from the SE of the basin in the Bogotá–Villavicencio–San Luis area and show provenance from the Guiana Shield.

Samples from the ANH stratigraphic wells CON and COS were collected, along with outcrop samples, from the proximities of Villa de Leyva in Boyacá Department. The samples processed include the Arcabuco, Villa de Leyva, Paja, San Gil Inferior Sandstone, and Churuvita Formations (Figure 10; Table 4). The Villa de Leyva area is dominated by zircon particles of Paleozoic, Proterozoic, and Neoarchean ages, from 300 to 2700 Ma. There are neither Jurassic nor Cretaceous particles. The samples include peaks at 1000 Ma, 1500 Ma, and 1700 Ma, related to rocks from the late Mesoproterozoic to early Neoproterozoic Grenvillian Orogeny, and particles from the late Paleoproterozoic to early Mesoproterozoic Río Negro–Juruena Province.

4.1.4. Barichara Area

Cretaceous samples from Santander Department (Figures 11–13) were collected on both flanks of Los Cobardes Anticline and on both margins of the Sogamoso River valley near the type section of the units. The Cretaceous succession, which begins with a cobble to pebble conglomerate included in the

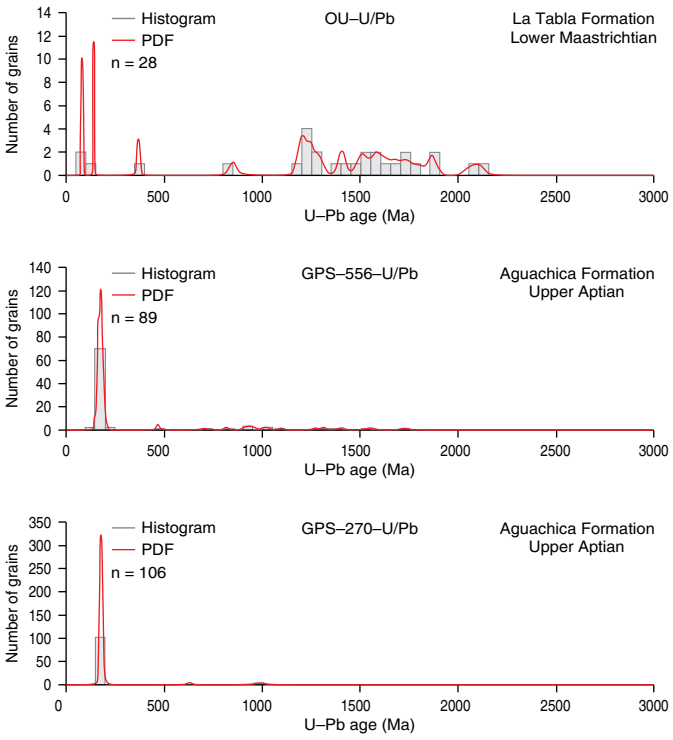

Figure 9. Detrital zircon U–Pb ages of units from the CEOC (Otanche) and MMV (Aguachica).

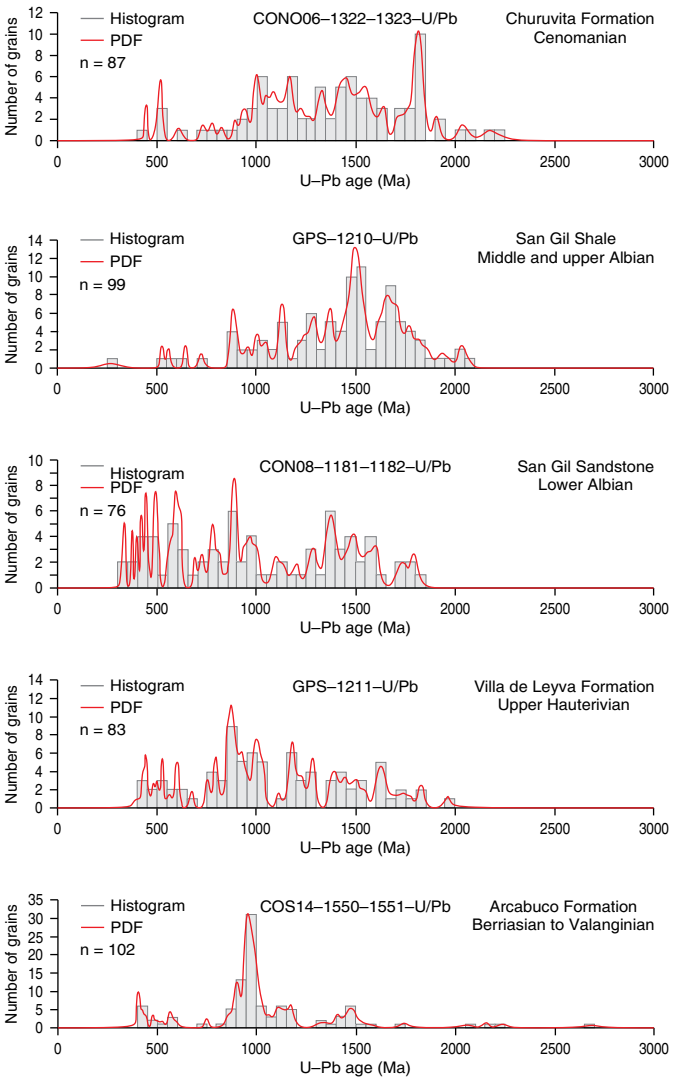

Figure 10. Detrital zircon U–Pb ages of Berriasian to Cenomanian units from the Villa de Leyva area.

fluvial strata of the lower part of the Tambor Formation, rests unconformably on older igneous, metamorphic, and sedimentary units. Prior to the back–arc subsidence that originated the Cretaceous basin, older units were faulted and exhumed through the Late Jurassic Andean orogeny. During early rift development of the Cretaceous back–arc system, rivers from both the E and W sides of the basin fed a trunk river that drained northward toward the Caribbean.

Samples GPS–549 and GPS–551 collected along the road from Zapatoca to San Vicente indicate both a source from the Central Cordillera and a source from the Guiana Shield (Figure 11). The sample with the lower stratigraphic position (GPS–549) was derived from the Central Cordillera because it contains 23 Jurassic grains from 150 to 200 Ma and 9 Triassic grains from 200 to 250 Ma. The youngest particle has an age of 145 ± 6 Ma in the Tithonian to Berriasian time span. An Early Jurassic age peak is placed at 190 ± 9 Ma, and an Early Devonian peak is placed at 410 ± 12 Ma, which are the main age populations of the sample. The stratigraphically higher sample (GPS–551) contains Proterozoic particles with 1000 to 1500 Ma age peaks along with a few Paleozoic but no Jurassic particles, suggesting derivation from the Guiana Shield.

Samples GPS–571 and 5 GPS-572 were collected from Mesa de Los Santos, which exhibits a good reference section of the Tambor Formation. Sample GPS–571 contains Proterozoic and Paleozoic age peaks but no Jurassic grains, consistent with derivation from the Guiana Shield. Sample GPS–572 has a mixture of Jurassic, Paleozoic, and Proterozoic ages, so it was sourced from the Central Cordillera. The particle with the youngest age is Late Jurassic (158 ± 8 Ma). In total, 13 Triassic and Jurassic particles are present, with a peak at approximately 196 ± 6 Ma. The highest frequency, with a total of 21 grains, occurs in the range of 400 to 450 Ma (Silurian and Early Devonian).

Samples GPS–540 and GPS–541 were collected from a monocline structure near Curití, on the San Gil to Mogotes road, from strata of the Tambor Formation resting unconformably over the early Paleozoic Silgará Schist and Mogotes Batholith. The sample (GPS–540) was sourced from the Guiana Shield; it contains Proterozoic particles, mainly 900 to 1000 Ma, and early Paleozoic particles but no Jurassic or Cretaceous particles (Figure 12). The Curití sample (GPS–541) was sourced from the Central Cordillera and contains 3 Early Cretaceous grains with a central age of 139 ± 9 Ma, consistent

with the Berriasian to Valanginian age range of the unit. The highest frequency (33 grains) is in the Triassic to Jurassic age interval, with a peak at 202 ± 13 Ma.

The Tambor Formation is transitionally covered by offshore marine strata of the lower part of the Rosablanca Formation, which includes marlstones and biomicrites deposited during late Valanginian to early Hauterivian progressive flooding of the basin. The shoreline and the rivers definitely migrated to the W because the overlying units contain particles derived only from the Guiana Shield. Sample GPS–543 from the upper Hauterivian regressive shoreface sandstones and sandy biosparites of the upper part of the Rosablanca Formation includes Proterozoic grains in the 900–1000 Ma age interval (highest frequency), along with a few Paleozoic grains with a youngest age of 269 ± 19 Ma (Figure 12; Table 4). Since there are no Mesozoic particles, we conclude that the unit was sourced from the Guiana Shield.

During the Barremian and Aptian, the basin was again extensively flooded, reaching farther to the E and W and also to the S, covering a larger area of Colombia and parts of Venezuela and Ecuador. Shale and marlstone beds (Fómeque, Paja, and Yuruma Formations) reach thicknesses of 600 m in the basin center. Basal conglomerates and sandstones were deposited along the basin margins in the present–day Magdalena Valley (Yaví and Aguachica Formations) and Llanos Foothills. Strata overlying the Paja Formation, including the Tablazo, Simití, and El Salto Formations, contain particles derived from the Guiana Shield.

Sample GPS–89 of the lower Albian Tablazo Formation contains age populations of approximately 400–450 Ma, 900–1000 Ma, and 1500–1550 Ma; the youngest particle is 361 ± 13 Ma (Figure 12; Table 4). Sample GPS–553 from the same unit has age populations of 450–500 Ma, 1500–1550 Ma, and 1750–1800 Ma; the youngest particle is 401 ± 17 Ma (Figure 13).

Sample GPS–555 from a very fine sandstone within the middle and upper Albian Simití shale has age peaks of approximately 450–500 Ma, 950–1000 Ma, 1500–1550 Ma, and 1750–1800 Ma (Figure 13; Table 4). The youngest particle has an age of 473 ± 25 Ma. The ages from El Salto Formation have peak populations at 1750–1800 Ma and 1900–1950 Ma, with a youngest age of 536 ± 30 Ma. None of the samples from the Tablazo, Simití, and El Salto Formations contain Mesozoic particles, so these units were sourced from the Guiana Shield.

Sample QAD–15 from the upper part of La Luna Formation is a pale gray bentonite claystone that contains 69 zircon particles with a central age of 86 ± 5 Ma (Figure 13; Table 4), which we interpret as volcanic ash falls transported by wind from the Central Cordillera magmatic arc during a time close to the Coniacian/Santonian boundary. The sample also includes a few Proterozoic particles (12 in total) that we believe were derived from the Guiana Shield, as well as other Albian and Cenomanian samples. We postulate that the Late Cretaceous zircon particles from La Luna Formation were not transported by rivers draining the Central Cordillera because of the absence of Jurassic particles, which are a unique mark of this source area.

The rocks of La Luna Formation from the QAD section include mainly biomicrites of foraminifera, transformed into diagenetic cherts with 50 to 70 % quartz and 20 to 45 % calcite plus dolomite. Minor storm beds of phosphatic bio–pelmicrites are also present with fluorapatite contents up to 60% and P_2O_5 contents up to 18%. The illite contents range from 3 to 5 %, with an exceptional value of approximately 16%, so the terrigenous contribution was generally very low, except for the wind–transported volcanic ash beds, which were dispersed on both sides of the basin. The U–Pb dating of distal volcanic ash zircons transported by wind has also been reported from the Cretaceous of Australia by Barham et al. (2016) and from the Miocene of North America by Smith et al. (2018).

4.1.5. Catatumbo Area

Finally, the areas south of Cúcuta exhibit a high frequency of Proterozoic particles derived from the Guiana Shield. Important peaks present in the Aguardiente, Capacho, and Guayacán Formations are approximately 1000 Ma, 1500 Ma, and 1800 Ma (Figure 14; Table 4). An exception is a volcanic tuff sample (RR1–15) that comes from the lower part of La Luna Formation at Riecito River and contains a high frequency of particles (94 zircon grains) with an age of 90 ± 4 Ma, near the Turonian/Coniacian time boundary. These particles are interpreted as wind–transported volcanic ash. The terrigenous content of La Luna Formation biomicrites is generally very low, so there are very few zircon particles (only 6) of older ages, which could have been transported by fluvial streams and storm currents to lower offshore depths.

ICP–OES analyses of the foraminiferal biomicrites from Riecito River reveal very low aluminum (Al_2O_3) contents less than 1%, with 46 to 55 % calcium (CaO) and 40 to 43 % volatile components, (mostly CO_2) loss on ignition (LOI), indicating 86 to 98 % calcite contents. The partially silicified biomicrites contain 42 to 49 % SiO_2, 2 to 4 % Al_2O_3, and 43 to 50 % calcite. The terrigenous clay and silt contents are very low except in the wind–transported volcanic ash beds present in the unit.

4.2. XRD, Heavy Minerals, and ICP–MS/OES Analyses

XRD mineral analyses, heavy mineral analyses, ICP–OES, and ICP–MS elemental analyses (Tables 5–9) from several localities and stratigraphic positions also help in the identification of the source areas for the basin.

Diagenesis during sediment burial modifies the crystallinity of clay minerals, but there is no documented evidence of metamorphism or clay neomorphism in the strata, so the clay mineralogy depends mostly on the rock types from the source areas

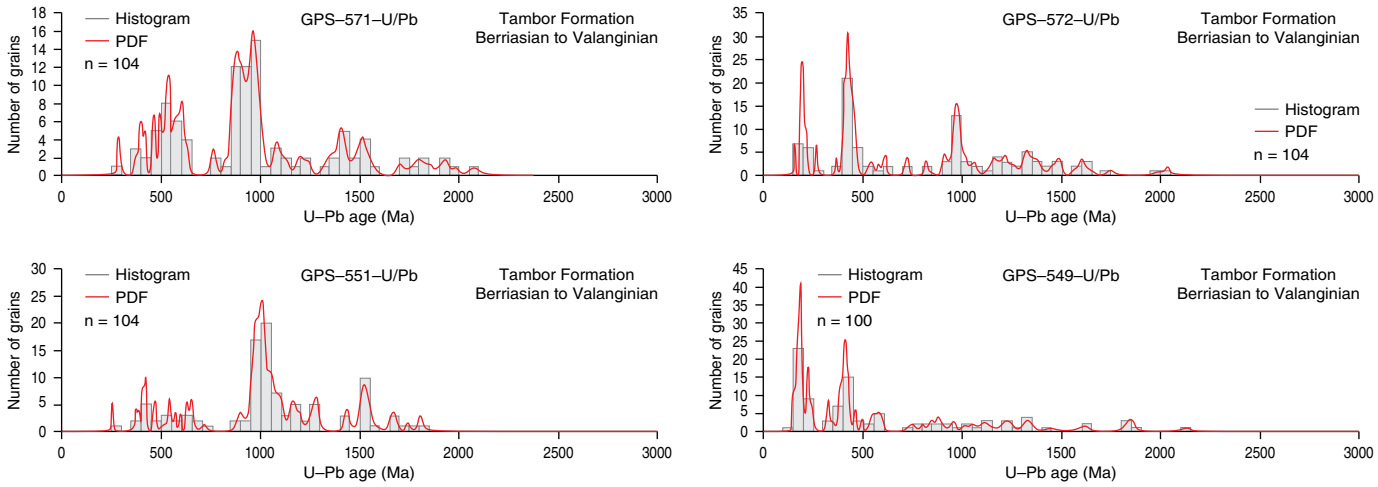

Figure 11. Detrital zircon U–Pb ages of the Tambor Formation from the Barichara area.

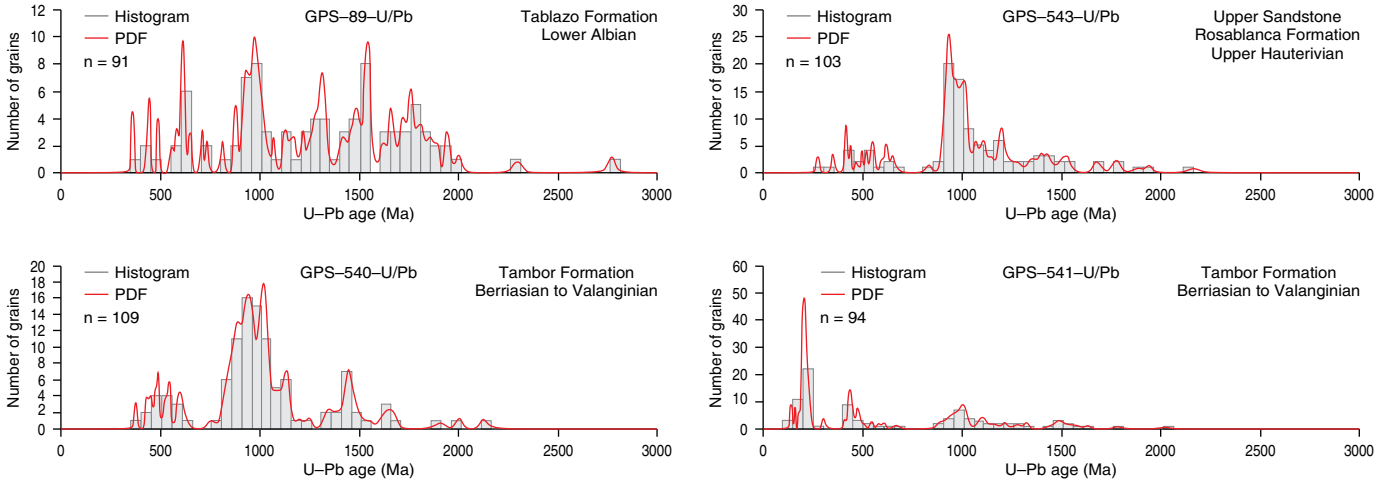

Figure 12. Detrital zircon U–Pb ages of Berriasian to lower Albian units from the Barichara area.

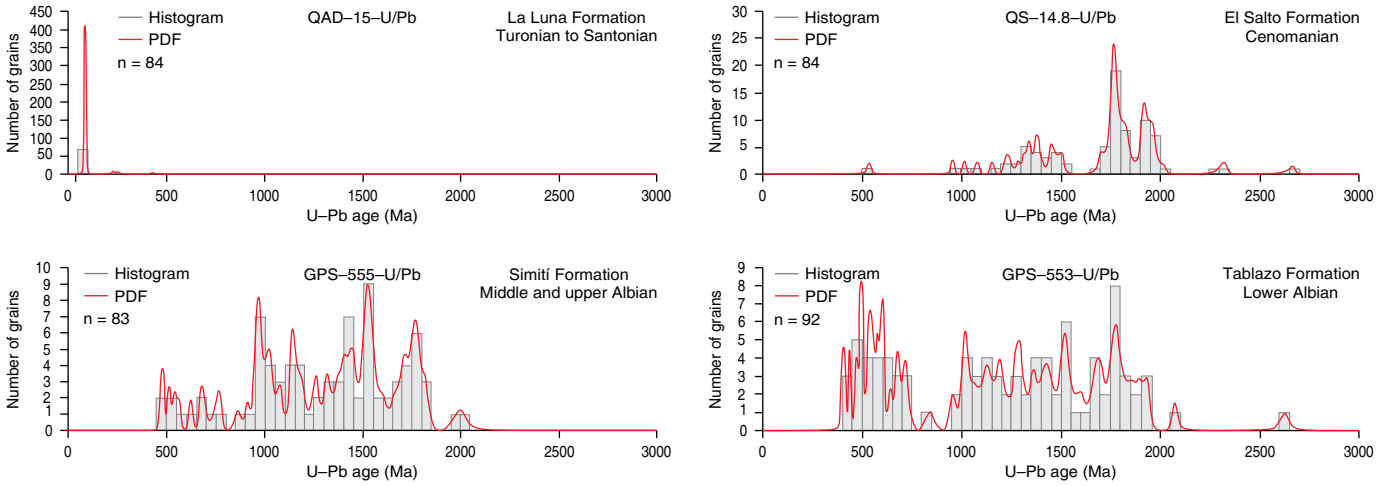

Figure 13. Detrital zircon U–Pb ages of lower Albian to Santonian units from the Barichara area.

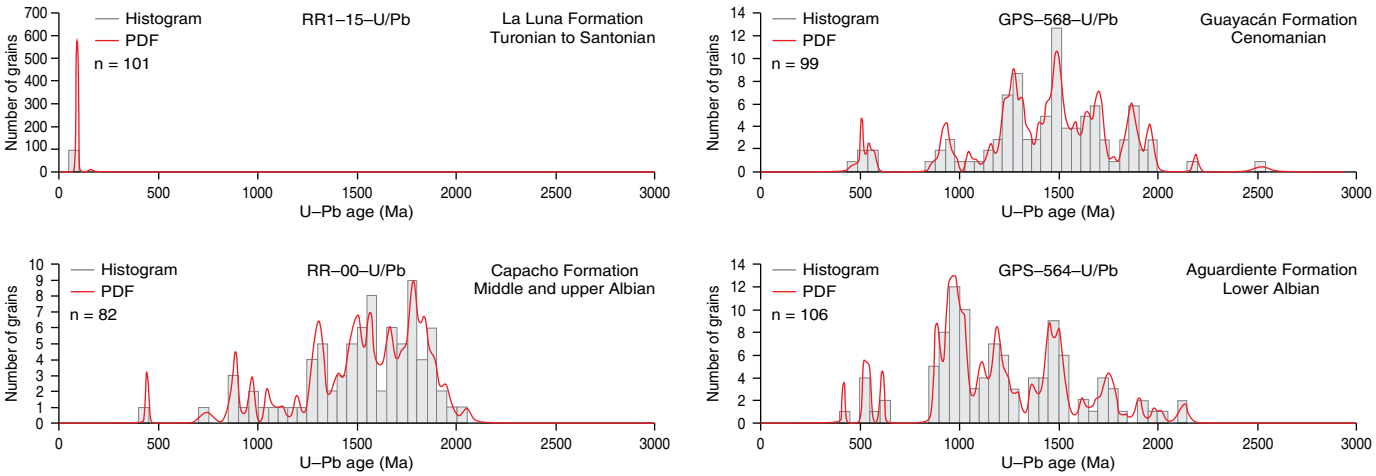

Figure 14. Detrital zircon U–Pb ages of lower Albian to Santonian units from the Catatumbo area.

of the basin. For instance, Bonilla et al. (2011) documented low degrees of kaolinite and illite crystallinity for Maastrichtian strata of the Upper Guadalupe Group and lower part of the Guaduas Formation, indicating slight diagenesis. For illite, they reported a Kubler crystallinity index of approximately 0.9 to 1.1, which would indicate a temperature of approximately 100 °C and correspond to burial diagenesis at approximately 3 km, which also matches the approximate 3 km thickness of the overlying Paleogene section. Considering an average geothermal gradient of 25 °C/km and the thickness of the underlying Campanian to Berriasian strata of approximately 4 km, the temperature of the basal strata from the Cretaceous section was approximately 200 °C, still within the diagenetic zone. Because of these observations, we consider that the clay mineralogy primarily reflects the nature of the rocks from the provenance areas. The clay mineralogy of source areas from the Guiana Shield should reflect the weathering of granites and recycled Paleozoic strata. The clay mineralogy of source areas from the Central Cordillera should reflect the weathering of continental igneous and metamorphic rocks, along with accreted oceanic basalt and gabbro.

The XRD analyses presented here show that clay minerals are common in shale units with source areas on the eastern side of the basin but are also present along the western side. The highest average percentages of kaolinite (Al_2O_3 $2SiO_2$ $2H_2O$) of approximately 50 to 55 % (Figure 15; Table 5) are from the Paja Formation in its type section (QLP) and the Une and Chipaque Formations along the San Antonio Creek (QSAU and QSAC). These shale intervals include lower average percentages of quartz silt (18 to 28 %) and illite (7 to 18 %). The high percentages of kaolinite would indicate several cycles of weathering in the tropical rainforest of the Guiana Shield.

The highest average percentages of illite in the range of 60 to 65 % (Figure 16; Table 5) are from shales of the Simití and El Salto Formations in the Infantas (INFA) 1613 well and from the Hilo Formation in the Otanche section (O); both are located toward the W side of the basin. These shale units contain lower average percentages of quartz silt (37 to 38 %) and no kaolinite. Since illite includes K, Mg, and Fe in the structure, high values of these elements are also found in the ICP–OES analyses of Otanche samples, approximately 9% Fe_2O_3 and 6% K_2O, which are among the highest values of these elements in the basin. The highest K_2O content in the study (6.4%) is from a sample (O–85) of the Otanche section.

Chlorite is present in minor amounts compared to kaolinite and illite. The highest average percentage of chlorite (22%) from XRD analyses comes from the shales in the lower part of the Murca Formation at the Tobia River section (RT) in the Villeta area. These samples include an average of 34% quartz silt particles, with lesser amounts of illite (11%), calcite (10%), kaolinite (8%), and dolomite (7%). Chlorite is most likely derived from low–grade metamorphic rocks sourced from the Central Cordillera.

Montmorillonite is present in very minor amounts in sections from the SE side of the basin, usually associated with kaolinite. The highest average percentages of montmorillonite (3 to 5 %) come from the Chipaque and Aguacaliente Formations at the San Antonio Creek sections.

The total ICP–OES distribution of aluminum (expressed as Al_2O_3) is highest in the central sector of the basin and in the Llanos Foothills (Figure 17; Table 6). It is coincident with the distribution of kaolinite and illite, which are the most abundant clay minerals. The highest Al_2O_3 individual values (26 to 30 %) are from the central and SE areas of the basin in wells COS–15, CON–7, CON–8, CON–6, and COS–5, La Paja Creek in Santander (QLP), and the Llanos Foothills along San Antonio Creek (QSAU and QSAC).

There are several important elements associated with the clay content of black shales from the basin, which also help to discriminate between western and eastern sources. The highest contents of titanium (1.7% TiO_2), zirconium (1337 ppm),

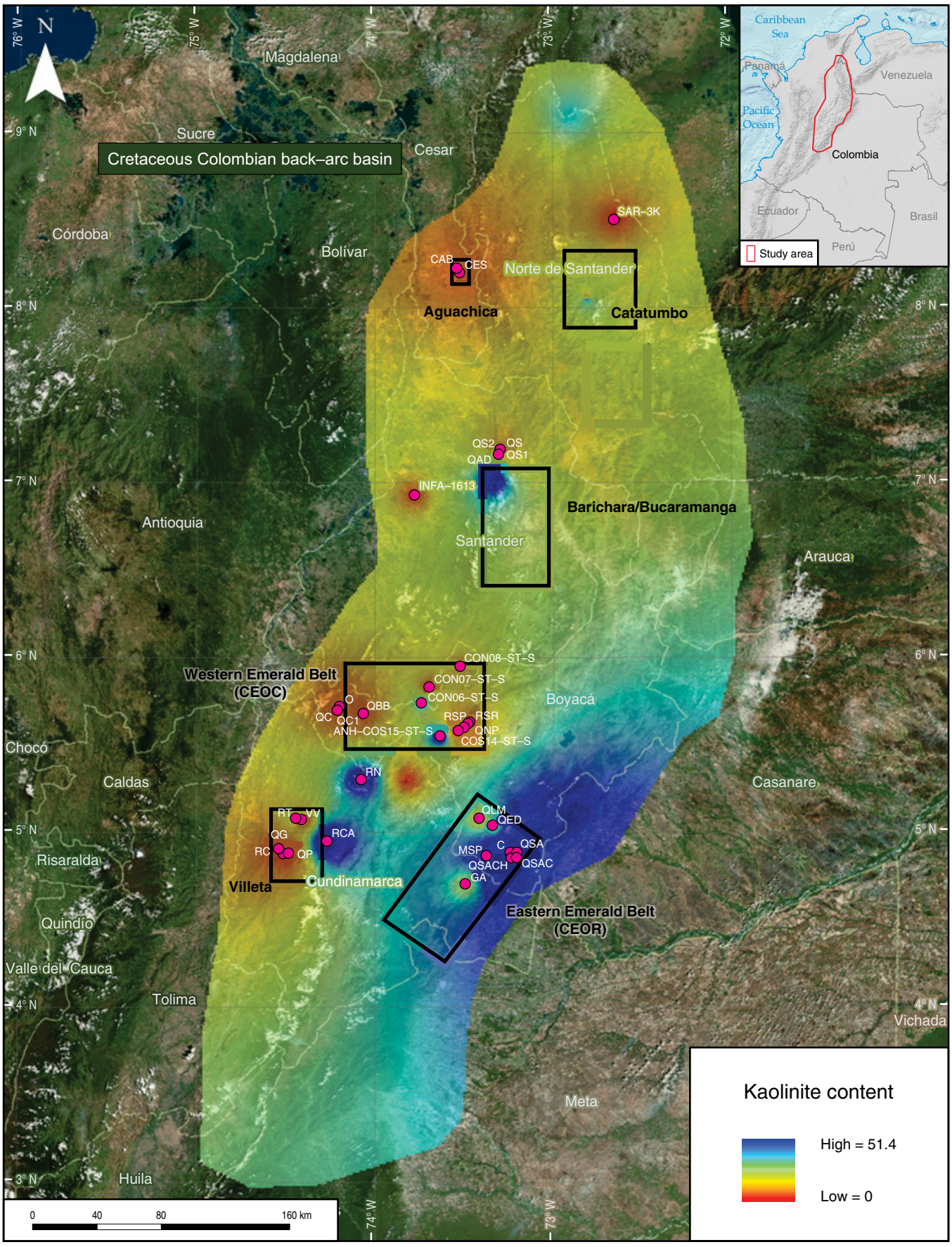

Figure 15. Kaolinite contents from XRD. Values plotted are average percentages per locality.

Table 5. XRD mineralogy (average percentage per section).

Section	Area	Formation	Quartz	Dolomite	Illite/Muscovite	Pyrophyllite	Kaolinite	Calcite	Chlorite	Pyrite	Rutile	Koenenite	Siderite	Gypsum	Ankerite	Albite	Anatase	Montmorillonite	Fluorapatite	Total phyllosilicates
QSAC	Llanos Foothills	Chipaque	27.5		11.1		54.1				2.0							3.8		69.0
QSAU	Llanos Foothills	Une	26.7		6.5		52.3					0.6	13.3				0.6			58.8
QLP	Barichara	Paja	17.5		17.5		50.0	1.4		4.6		1.7					7.3			67.5
QSACH	Llanos Foothills	Chipaque	55.6		9.1		28.9		0.4	0.8							0.4	4.8		43.2
QSA	Llanos Foothills	Aguacaliente	50.6		9.7		26.7		2.1	1.5	1.2		1.8					2.8		41.3
RN	Villeta	Pacho	37.6	0.4	6.4	8.3	23.2	9.1	7.5	4.7	0.6	0.2		0.6	0.3		1.2			45.4
COS–15	Villa de Leyva	Paja	18.6		26.8	18.4	17.3			5.8	2.1	3.7	0.5	2.0	2.4					62.5
C	CEOR	Macanal	39.4		31.5		12.2			0.5	0.2	0.4	15.8							43.7
QED	CEOR	Fómeque	28.9	2.1	9.5	11.3	10.4	24.8	3.3	0.7	0.5				0.9	4.5	0.6			34.5
CON–7	Villa de Leyva	San Gil Shale	38.8	0.5	15.0	13.2	10.3	2.3	5.1	2.7	0.4	1.5	1.6		5.0		0.3			43.6
COS–5	Villa de Leyva	Conejo	58.0	5.5	5.7	5.8	8.8	7.8		2.4	0.5	1.4	1.2		2.9					20.3
CON–6	Villa de Leyva	Churuvita	64.0		15.5		7.8	2.4	3.2	0.9		0.9	2.6	0.3	1.8		0.3			26.5
CON–8	Villa de Leyva	Paja	22.5	2.3	11.8	27.4	7.7	14.8	0.1	3.2	0.3	2.8	1.8	2.6	2.4					47.0
CAB	Aguachica	La Luna	59.5		1.8	0.3	1.7	31.3	0.3	2.3			0.3						2.5	4.1
QS2	Barichara	La Luna	23.0		0.6		0.5	70.6		1.2			0.2		1.3				2.6	1.1
QAD	Barichara	La Luna	50.1	4.8	4.5		0.5	30.1		1.5		0.5							8.0	5.0
SAR–3K	Catatumbo	La Luna	26.7	1.6	3.7			61.3		1.4	0.7	0.4		1.0					3.2	3.7
RT	Villeta	Murca	33.7	6.5	11.2		7.7	9.7	21.9	2.3	1.0	1.9		0.2	3.9					40.8
QP	Villeta	Hilo	46.4	1.8	14.5		0.4	26.5	3.7	3.6		1.5		1.2	0.2					18.6
QC	UMV	Lidita Inferior	59.3		26.9		3.0	0.7	8.8			0.7	0.4				0.2			38.7
GA	CEOR	Macanal	33.2		35.2		7.4	4.6	8.6	4.7	0.7			5.6						51.2
MSP	CEOR	Macanal	28.9		35.2			0.2			1.6					33.6				35.2
RSP	Villa de Leyva	Villa de Leyva	27.9		35.8	16.5	2.2		7.0	4.3	2.1	4.2								61.5
COS–14	Villa de Leyva	Ritoque	40.2	2.9	38.0		2.1	3.0	7.1	2.4	1.6	0.6		0.1	2.0					47.2
QBB	CEOC	Furatena	49.4		39.6		1.4		9.6											50.6
QNP	Villa de Leyva	Paja	29.2	11.1	42.2	0.8		4.8	4.1	1.6				0.4	5.8					47.1
O	CEOC	Hilo	38.4		59.7					0.8		1.1								59.7
INFA–1613	MMV	Simití	37.0	0.5	62.5															62.5
INFA–1613	MMV	El Salto	37.1		62.9															62.9

thorium (52 ppm), niobium (46 ppm), hafnium (36 ppm), and tantalum (4 ppm) in the study come from a shale sample (COS15–2054) of the Paja Formation in the Villa de Leyva area (Tables 6–8). As indicated before, the unit was sourced from the eastern side of the basin, which has more differentiated continental crust than the western sources.

In contrast, the highest contents of chromium (0.105% Cr_2O_3), copper (825 ppm), molybdenum (372 ppm), arsenic (121 ppm), antimony (94 ppm), selenium (79 ppm), thallium (13 ppm), and silver (9 ppm) in the study come from the shales of the Hilo Formation in the Otanche section (O–05, 15, 25, 40, 45, and 75), which also have very high illite contents. The unit was sourced from the western side of the basin, which included the magmatic/metamorphic arc and accreted oceanic crust.

The light REE of the cerium group have the maximum values (Figure 18; Table 9) of the study in a siltstone sample (COS14–1575) from the upper part of the Arcabuco Formation, in the ANH COS–14 well, in the vicinity of Villa de Leyva: Ce (619

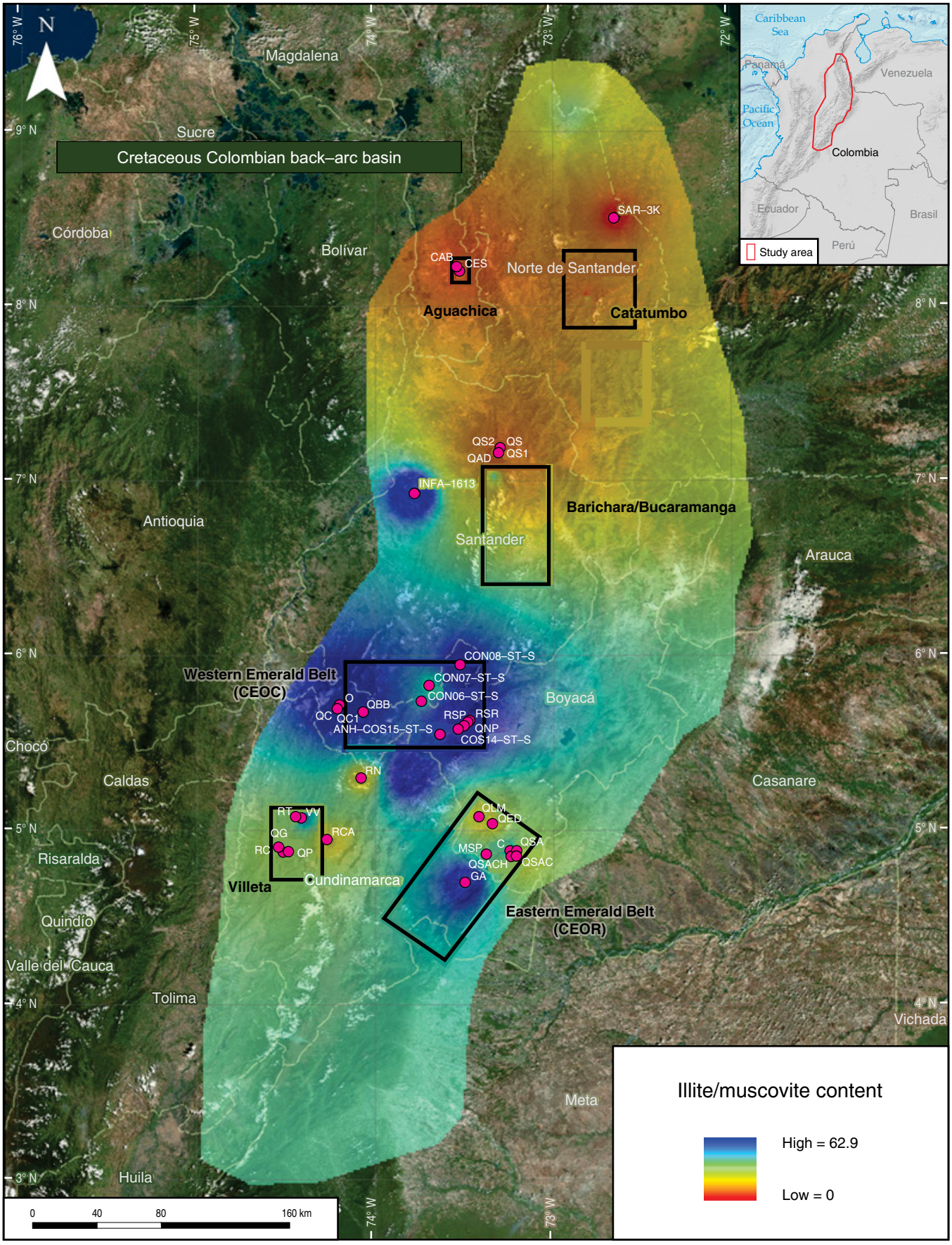

Figure 16. Illite/muscovite contents from XRD. Values are average percentages per locality.

ppm), Nd (315 ppm), La (276 ppm), Pr (82 ppm), Sm (50 ppm), and Eu (8 ppm). In contrast, the heavy REE of the yttrium group have the maximum values of the study in a sample (RT–10) from the lower part of the Murca Formation in the Tobia River section: Y (231 ppm), Dy (40 ppm), Gd (27 ppm), Er (19), Yb (11 ppm), Ho (8 ppm), Tb (6 ppm), and Tm (2 ppm). The high contents of the yttrium group would indicate an ultramafic source in accreted oceanic crust situated along the western flank of the basin, while the cerium group indicates more differentiated continental crust on the eastern flank of the basin.

Another important mineral that indicates provenance is apatite, which shows higher percentages (Figure 19) in the western part of the basin and is related to igneous and metamorphic sources in the Central Cordillera. Samples with heavy mineral analyses containing high percentages of terrigenous apatite come from the Murca, Trincheras, Socotá, Hilo, and Pacho Formations from the western side of the Eastern Cordillera.

An important part of the reported apatite is related to phosphatic biomicrites and has an authigenic origin because of biological accumulation in fish. The highest percentages of fluorapatite from XRD analyses are from La Luna Formation in the Aguadulce Creek (8%) and La Sorda Creek (3%) near Bucaramanga, the Sardinata 3K well near Cúcuta (3%), and Caño Agua Blanca near Aguachica (3%). The highest contents of P_2O_5 from ICP–OES analyses (Table 7) are from La Luna Formation at La Leche Creek near Cúcuta (26%) and Aguadulce Creek (18%).

The distribution of apatite in La Luna Formation is related to the distributions of quartz and calcite (Figures 20, 21; Tables 5–7) because the unit consists mostly of biomicrites composed of planktonic foraminifera and fish remains (containing authigenic fluorapatite), along with diagenetic cherts. Since the unit was deposited during the Turonian to Santonian transgressive and highstand sea levels, the terrigenous clay input was very low or completely absent, and the rocks consist of microfossil particles deposited offshore. Textures include wackestone and packstone beds; the latter could originate from high productivity but are usually the result of repetitive storm events that concentrate the available particles. Quartz enters the system much later during diagenesis, replacing calcite. The foraminifera and the calcareous mud matrix are partially to totally replaced by quartz, and the rock becomes a diagenetic chert, as illustrated for the Lidita Inferior and Lidita Superior Formations of the UMV (Guerrero et al., 2000). The quartz is obtained from the terrigenous units above and below the original calcareous strata. These terrigenous units are in turn partially replaced by calcite mobilized from the limestones in a two–way exchange of calcite and quartz during diagenesis. All cherts from the basin are diagenetic, including those of the Hilo, Lomagorda, La Luna, La Frontera, Lidita Inferior, and Lidita Superior Formations. Radiolaria and diatoms are almost completely absent, so no oceanic cherts are present.

The highest calcium (CaO) contents of the study (40 to 55 %), obtained from ICP–OES analyses (Table 7), come from biomicrite limestones of La Luna Formation in the N part of the basin (Catatumbo, Aguachica, and Barichara areas). These samples have CO_2 loss on ignition (LOI) of 33 to 43 %, except for those with higher phosphate content (3 to 26 % P_2O_5) or are partially replaced by diagenetic quartz (1 to 19 % SiO_2). The content of Al_2O_3 is less than 3% because of the nearly complete absence of clay minerals; the content of Fe, Mg, Na, and K is usually less than 1%. Samples from the same sections that are extensively replaced by quartz to create diagenetic cherts have increased SiO_2 contents (49 to 66 %) and decreasing percentages of CaO (12 to 22 %) and LOI (16 to 22 %).

The highest contents of SiO_2 (59 to 79 %) in diagenetic cherts (Table 7) are from La Luna Formation (Barichara, Aguachica, and MMV), Lidita Inferior and Lidita Superior Formations (UMV), Hilo Formation (Villeta), and La Frontera Member of the Conejo Formation (Villa de Leyva).

Associated with the phosphates biologically concentrated by fish in the biomicrites and cherts of La Luna Formation (Tables 7, 8) are the highest contents of uranium (27 to 89 ppm), nickel (231 to 468 ppm), and strontium (1521 to 2506 ppm) in the study. The SAR–7443 sample from the Catatumbo area contains the highest values of uranium and nickel. The highest values of vanadium in the study (1901 to 3865 ppm) are present in cherts and biomicrites of the Hilo Formation (QP from the Villeta area) and La Luna Formation (QLL, RR1, and QS2 from the Catatumbo and Barichara areas).

4.3. Elements Related to Gabbro–Diorite–Tonalite Intrusions and Valanginian to Cenomanian Hydrothermal Activity During the Synrift Stage

The highest contents of scandium come from the southeastern side of the basin in the sections at Vereda Cachipay (29 ppm) and the San Pedro emerald mine (24 ppm). In these areas, the anomalous content of scandium in the Berriasian to lower Hauterivian shales of the Macanal Formation (Tables 6, 8) does not seem to be related to the source areas of sediment; instead, it would be related to hydrothermal activity linked to the Early Cretaceous intrusion of several gabbro, diorite, and tonalite bodies documented by Vásquez et al. (2005, 2010). Scandium was originally present in the structure of pyroxenes and amphiboles of the gabbroic bodies because of its affinity with minerals in mafic melts. The XRD analyses of the rocks related to the San Pedro emerald mine reveal a very anomalous 34% albite content, which is also the highest percentage in the study. The highest contents of sodium (2 to 7 % Na_2O) in the basin come from the San Pedro emerald mine area because of the high content of hydrothermal albite ($NaAlSi_3O_8$). The

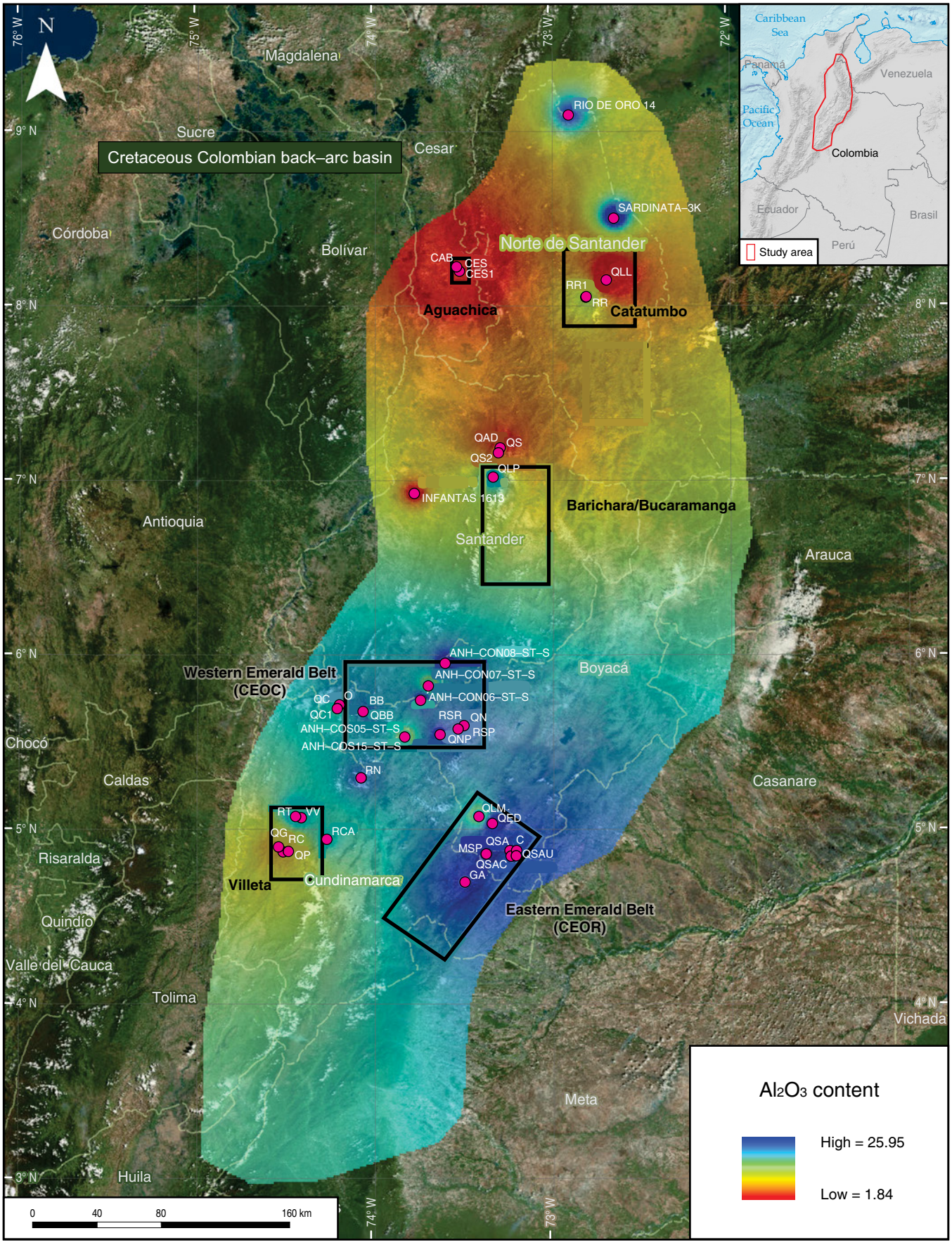

Figure 17. Aluminum distribution from ICP–OES analyses. Values are average percentages per locality.

Table 6. Major elements percentages (shale/siltstone samples).

Sample	Area	Formation	SiO_2	Al_2O_3	Fe_2O_3	MgO	CaO	Na_2O	K_2O	TiO_2	P_2O_5	MnO	Cr_2O_3	Ni	Sc	LOI	Total
COS15–1553	Villa de Leyva	Paja	50.76	29.95	4.49	0.47	0.60	0.89	2.95	0.96	0.18	0.01	0.015	40	19	8.5	99.78
CON7–1125	Villa de Leyva	San Gil Shale	47.54	29.18	6.45	1.03	0.34	0.56	2.30	0.91	0.12	0.02	0.015	45	20	11.3	99.77
CON8–1796	Villa de Leyva	Paja	46.58	28.16	4.25	0.67	2.26	0.68	2.82	0.82	0.17	0.01	0.018	52	18	13.3	99.74
QSAU–18	Llanos Foothills	Une	47.99	27.32	6.22	0.97	0.28	0.04	2.88	1.03	0.10	0.08	0.012	39	19	12.9	99.82
QLP–35	Barichara	Paja	46.41	26.42	4.36	0.62	2.57	0.19	1.92	0.80	0.14	0.01	0.021	66	18	16.2	99.66
QSAC–40	Llanos Foothills	Chipaque	47.69	26.35	7.04	1.12	0.60	0.23	1.95	0.99	0.11	0.05	0.026	24	19	13.7	99.86
CON6–1405	Villa de Leyva	Churuvita	50.05	25.82	6.82	1.06	0.54	0.26	2.95	1.04	0.18	0.04	0.012	35	19	11.0	99.77
COS5–269	Villa de Leyva	Conejo	50.86	25.65	4.50	0.77	0.48	0.59	2.06	0.87	0.12	<0.01	0.016	24	16	13.9	99.82
RSP–30	Villa de Leyva	Villa de Leyva	50.53	25.46	6.80	0.99	0.32	0.83	3.53	1.06	0.22	0.02	0.021	69	21	10.0	99.78
QED–30	CEOR	Fómeque	51.84	25.11	4.89	1.18	2.18	0.62	3.60	1.23	0.15	0.05	0.016	<20	21	8.9	99.77
O–85	CEOC	Hilo	57.18	25.06	1.05	1.13	0.02	0.13	6.43	0.78	0.13	<0.01	0.023	<20	21	7.7	99.63
QED–35	CEOR	Fómeque	51.93	24.98	6.53	1.04	0.24	0.60	3.34	1.28	0.17	<0.01	0.016	22	22	9.6	99.73
RN–60	Villeta	Pacho	52.08	24.89	6.24	1.17	1.91	0.42	2.25	0.91	0.17	0.01	0.017	43	17	9.7	99.77
C–40	CEOR	Macanal	55.40	24.09	3.25	0.98	0.29	0.46	4.41	1.07	0.12	0.03	0.015	41	17	9.7	99.82
COS14–522	Villa de Leyva	Villa de Leyva	51.97	23.98	6.10	1.15	1.17	0.92	4.12	0.89	0.15	0.02	0.017	66	20	9.3	99.79
O–55	CEOC	Hilo	48.10	23.82	5.04	1.00	0.03	0.17	5.15	0.65	0.14	<0.01	0.066	35	16	15.4	99.57
QNP–05	Villa de Leyva	Paja	47.40	23.77	6.01	1.22	4.26	0.58	3.27	0.93	0.16	0.07	0.025	92	18	12.1	99.80
QBB–00	CEOC	Furatena	55.10	23.71	3.89	1.11	0.35	1.30	3.51	0.87	0.16	<0.01	0.019	85	20	9.6	99.62
RT–15	Villeta	Murca	53.61	22.46	6.06	1.52	1.95	1.41	2.30	0.76	0.11	0.02	0.010	43	16	9.6	99.81
O–75	CEOC	Hilo	59.16	22.20	1.00	1.02	0.02	0.18	6.03	1.00	0.05	<0.01	0.105	<20	12	8.8	99.57
MSP–25	CEOR	Macanal	63.22	21.99	1.26	0.83	0.08	0.93	5.78	1.25	0.03	<0.01	0.016	<20	24	4.4	99.79
QSACH–25	Llanos Foothills	Chipaque	55.63	21.82	4.45	1.25	0.65	0.21	2.06	0.78	0.04	<0.01	0.025	24	15	12.9	99.82
COS14–1575	Villa de Leyva	Arcabuco	57.78	21.29	5.78	0.92	0.47	0.20	5.92	1.05	0.18	0.09	0.015	56	21	5.9	99.60
INFA–7359	MMV	Simití	55.83	21.18	5.60	1.20	0.45	0.50	1.55	0.84	0.23	0.02	0.015	36	15	12.4	99.82
GA–10	CEOR	Macanal	55.20	21.18	6.09	1.28	2.22	0.69	3.72	0.90	0.10	0.03	0.014	80	17	8.4	99.82
QSA–40	Llanos Foothills	Aguacaliente	54.09	19.84	5.98	1.83	1.30	0.19	2.08	0.69	0.20	0.03	0.028	<20	13	13.5	99.76
QP–20	Villeta	Hilo	54.15	19.53	3.37	0.84	5.12	0.33	1.49	0.58	0.29	0.01	0.018	143	15	13.8	99.53
GA–60	CEOR	Macanal	59.23	19.47	7.03	1.59	0.98	0.58	3.30	0.96	0.08	0.02	0.015	56	17	6.5	99.76
RT–10	Villeta	Murca	50.14	18.78	5.39	1.61	7.65	1.10	1.90	0.65	0.16	0.04	0.009	38	14	12.4	99.83
MSP–15	CEOR	Macanal	65.97	17.54	3.26	0.24	0.15	6.89	1.47	1.11	0.12	<0.01	0.014	<20	13	3.1	99.86
COS15–2054	Villa de Leyva	Paja	58.69	16.39	6.91	0.56	1.36	0.90	1.96	1.66	0.18	0.01	0.016	39	14	10.9	99.54
C–12	CEOR	Macanal	34.94	10.72	27.54	2.30	1.21	0.20	1.56	0.62	0.19	0.37	0.009	<20	29	20.2	99.86

shales of the Macanal Formation from the Gachalá section (GA) have the maximum contents of beryllium (6 to 9 ppm) in the basin. A younger unit from the same area that has a high content of albite (4.5%) according to the XRD analyses is the Barremian and Aptian Fómeque Formation from El Dátil Creek section (QED), which also has relatively high scandium (18 to 21 ppm) and beryllium (2 to 4 ppm) contents. The scandium and beryllium anomalies would be better explained by the Early Cretaceous hydrothermal activity that formed the emerald ($Be_3Al_2(SiO_3)_6$) mineralization.

The highest scandium values are restricted to Early Cretaceous sections that present some hydrothermal influence with calcite veins and intense micro fracturing. In addition to the Cachipay section (C) near Santa María de Bata (29 ppm), the San Pedro emerald mine (24 ppm), and El Dátil (22 ppm) from the Macanal and Fómeque Formations, high scandium values (20 to 23 ppm) are present in other units at other localities. Good examples are the Arcabuco and Villa de Leyva Formations from well COS–14 near Simijaca, the Villa de Leyva Formation (21 ppm) from the Samacá River section near Villa de Leyva, the Paja Formation (20 ppm) from well COS–15 near Ráquira, and the San Gil Superior Shales from well CON–7 near Puente Nacional. Relatively high scandium values are also present in the Berriasian to Hauterivian lower part of the Murca Formation

Table 7. Major elements percentages (biomicrite and chert samples).

Sample	Area	Formation	SiO_2	Al_2O_3	Fe_2O_3	MgO	CaO	Na_2O	K_2O	TiO_2	P_2O_5	MnO	Cr_2O_3	Ni	Sc	LOI	Total
SAR–7459	Catatumbo	La Luna	0.83	0.07	0.05	0.69	54.93	0.02	0.01	<0.01	0.10	<0.01	0.002	<20	<1	43.2	99.90
RR1–20	Catatumbo	La Luna	1.45	0.06	<0.04	0.36	54.79	<0.01	<0.01	<0.01	0.02	<0.01	<0.002	<20	<1	43.2	99.88
QLL–00	Catatumbo	La Luna	2.58	0.47	0.14	0.30	53.39	0.05	0.06	0.02	0.08	<0.01	<0.002	21	<1	42.8	99.89
CES1–00	Aguachica	La Luna	1.81	0.39	0.32	0.61	53.35	0.01	0.04	0.02	0.32	<0.01	0.005	24	<1	43.0	99.88
QLL–55	Catatumbo	La Luna	8.95	0.81	0.46	0.16	49.54	0.21	0.10	0.03	25.63	<0.01	0.021	45	5	13.4	99.31
QS2–35	Barichara	La Luna	10.93	0.58	0.23	0.49	47.92	0.01	0.08	0.03	0.13	<0.01	0.004	36	<1	39.4	99.80
QAD–65	Barichara	La Luna	15.17	1.32	0.35	0.17	44.47	0.07	0.15	0.05	18.32	<0.01	0.020	41	6	19.6	99.69
CAB–40	Aguachica	La Luna	12.8	2.56	0.71	0.43	44.45	0.04	0.41	0.10	3.37	0.02	0.017	37	4	34.9	99.81
CES1–10	Aguachica	La Luna	12.45	2.61	0.50	0.47	42.03	0.03	0.33	0.11	0.63	<0.01	0.017	63	3	40.4	99.58
SAR–7443	Catatumbo	La Luna	19.49	0.91	0.59	0.34	41.18	0.07	0.15	0.04	3.26	<0.01	0.019	468	2	33.0	99.05
QS2–50	Barichara	La Luna	18.24	1.78	0.44	0.40	39.77	0.06	0.27	0.07	0.42	<0.01	0.016	291	2	37.7	99.17
QP–270	Villeta	Hilo	21.42	2.53	2.54	0.48	39.24	0.02	0.21	0.08	0.15	0.05	0.009	126	5	33.0	99.73
CES–25	Aguachica	La Luna	19.28	3.37	0.92	0.42	38.19	0.07	0.41	0.14	0.48	<0.01	0.014	263	3	36.0	99.29
SAR–7410	Catatumbo	La Luna	21.10	2.91	0.95	0.59	37.53	0.32	0.49	0.08	0.77	<0.01	0.016	183	3	34.6	99.36
QS2–45	Barichara	La Luna	22.21	2.48	0.71	0.42	35.87	0.06	0.35	0.10	0.37	<0.01	0.019	357	2	34.8	97.39
CES–70	Aguachica	La Luna	28.05	1.65	0.46	0.29	34.79	0.04	0.22	0.06	0.38	<0.01	0.013	63	2	33.7	99.65
QLM–24	CEOR	Fómeque	29.54	4.45	2.36	0.61	33.24	0.12	0.48	0.33	0.10	0.06	0.003	<20	4	28.5	99.79
QAD–70	Barichara	La Luna	30.77	3.97	1.14	0.38	31.98	0.06	0.56	0.16	4.18	<0.01	0.021	108	4	26.5	99.72
QLP–10	Barichara	Paja	7.30	3.78	9.50	7.19	31.6	0.06	0.28	0.13	0.14	0.07	0.012	49	3	39.6	99.66
SAR–7379	Catatumbo	La Luna	34.37	3.04	0.93	0.45	29.92	0.39	0.54	0.11	0.73	<0.01	0.040	231	4	29.0	99.52
QAD–50	Barichara	La Luna	42.08	3.84	0.93	0.25	24.54	0.07	0.47	0.13	9.92	<0.01	0.021	75	7	16.4	98.65
QLL–10	Catatumbo	La Luna	44.03	2.85	0.91	0.42	23.89	0.19	0.38	0.07	0.31	<0.01	0.017	172	2	26.3	99.37
QLL–15	Catatumbo	La Luna	46.07	4.49	1.42	0.49	21.58	0.28	0.62	0.12	1.14	<0.01	0.028	227	3	22.9	99.14
RR1–35	Catatumbo	La Luna	48.71	4.00	1.22	0.34	21.57	0.05	0.46	0.11	1.23	<0.01	0.029	130	4	21.6	99.32
QG–257	UMV	Lidita Superior	59.43	3.33	1.21	1.42	16.20	0.24	0.40	0.12	0.35	<0.01	0.013	38	3	17.1	99.81
QAD–25	Barichara	La Luna	65.74	1.30	0.26	0.17	15.29	0.04	0.13	0.04	0.17	<0.01	0.018	87	<1	16.7	99.86
QP–445	Villeta	Hilo	57.62	4.57	1.03	0.28	14.82	0.02	0.47	0.20	0.23	0.01	0.027	187	5	19.9	99.18
CAB–115	Aguachica	La Luna	65.93	3.94	0.93	0.28	11.72	0.08	0.61	0.16	0.28	0.07	0.022	87	3	15.6	99.62
INFA–4724	MMV	La Luna	73.19	2.17	0.35	0.21	11.07	0.15	0.26	0.07	0.12	<0.01	0.010	53	2	12.2	99.80
COS5–985	Villa de Leyva	La Frontera	72.11	3.85	0.51	0.13	10.05	0.07	0.35	0.06	0.28	<0.01	0.011	70	2	12.3	99.72
QG–00	UMV	Lidita Inferior	78.91	4.55	1.20	0.42	5.49	0.26	0.61	0.18	0.39	<0.01	0.013	42	5	7.9	99.92

(14 to 16 ppm) at the Tobia River section (RT) and the lower part of the Furatena Formation (16 to 20 ppm) at Buriburi Creek (QBB) in the western part of the basin. The samples from QBB also have relatively high (2 to 4 ppm) beryllium contents. The presence of scandium in fluid inclusions in emeralds was also reported by Mantilla et al. (2008).

On the southwestern side of the basin, a vanadium anomaly (Table 8) is present in the shales from the upper part of the Hilo Formation at the Otanche section (O), near the emerald mines. The highest vanadium contents in the basin (2523 to 3865 ppm) come from the shales, marls, biomicrites, and diagenetic cherts of the middle and upper Albian Hilo Formation at the Piñal Creek (QP) and Otanche sections. The presence of vanadium was reported from emeralds of the CEOC by Pignatelli et al. (2015) in Valanginian to Hauterivian black shales and marlstones, assigned here to the Furatena Formation.

Other associated minerals in the shales include ankerite ($Ca(Fe,Mg,Mn)(CO_3)_2$) and dolomite ($CaMg(CO_3)_2$). According to XRD analyses (Table 5), the highest percentages are present in the Paja Formation shales (QNP) from the Villa de Leyva area, which contain 11.1% dolomite and 5.8% ankerite. The

Table 8. Minor elements in ppm (biomicrite and shale).

Sample	Area	Formation	Sc	Ba	Be	Hf	Nb	Rb	Sr	Th	U	V	Zr	Mo	Cu	As	Sb	Ag	Tl	Se
QLL–15	Catatumbo	La Luna	3	178	1	0.8	3.1	28.6	835.1	4.7	25.4	2404	26.9	97.4	73.9	28.5	9.2	1.0	0.8	10.4
QS2–45	Barichara	La Luna	2	136	<1	0.5	2.1	19.2	1394.2	2.5	20.5	2225	25.1	209.0	73.6	39.1	13.7	1.2	0.7	15.1
RR1–35	Catatumbo	La Luna	4	135	1	0.7	2.4	22.9	768.8	3.8	23.9	2125	30.8	63.1	88.5	50.2	9.9	0.7	0.7	8.5
QLL–10	Catatumbo	La Luna	2	282	1	0.4	1.9	16.1	683.6	2.7	12.7	1901	17.1	79.1	62.1	14.8	5.9	0.6	<0.1	16.7
CES–25	Aguachica	La Luna	3	865	<1	1.1	2.5	21.9	1510.8	2.7	24.4	1578	33.7	114.7	39.2	27.2	5.4	1.1	1.1	16.7
SAR–7443	Catatumbo	La Luna	2	73	1	0.4	0.5	6.2	1549.2	1.2	89.0	1421	13.9	177.1	46.9	34.6	17.1	1.6	0.8	26.2
CAB–115	Aguachica	La Luna	3	1909	<1	1.3	4.4	26.2	491.7	4.4	6.9	138	44.1	7.9	18.8	3.2	0.5	1.0	<0.1	2.0
QAD–50	Barichara	La Luna	7	2042	3	2.5	4.2	20.8	1182.2	7.4	36.6	115	100.7	7.0	17.5	2.6	0.8	0.8	<0.1	9.1
QLL–55	Catatumbo	La Luna	5	2390	2	0.3	0.6	6.0	2505.9	11.2	85.4	104	16.8	2.7	11.4	9.8	2.3	0.8	0.3	2.6
QAD–65	Barichara	La Luna	6	504	<1	0.3	1.0	7.1	1439.0	9.2	58.0	86	15.1	3.3	9.9	3.5	0.8	0.4	<0.1	2.8
QP–440	Villeta	Hilo	9	576	2	1.4	8.7	58.9	259.9	10.2	14.5	3865	61.4	163.1	59.2	45.1	11.8	1.7	1.7	34.4
O–05	CEOR	Hilo	16	1158	<1	3	10.4	119.1	79.0	11.7	55.6	2811	110.5	372.2	653.8	16.1	94.2	8.8	3.7	11.4
QP–435	Villeta	Hilo	7	567	<1	1.3	7.4	44.0	372.7	7.9	12.5	2535	55.0	121.0	33.4	52.2	18.4	1.3	1.9	45.2
QP–290	Villeta	Hilo	10	759	2	1.9	8.0	52.2	133.7	10.0	16.7	2205	59.7	108.2	53.1	57.5	7.6	2.1	2.3	37.4
O–15	CEOC	Hilo	13	1090	3	3.5	11.1	124.2	26.0	11.7	15.3	2033	121.4	97.8	824.7	16.5	15.8	6.9	0.6	9.9
O–40	CEOC	Hilo	16	595	2	3.6	11.6	146.5	18.6	12.7	16.0	2000	119.8	120.8	201.3	25.8	16.0	2.4	12.6	11.3
O–25	CEOC	Hilo	14	702	3	3.4	11.4	122.9	23.9	10.6	11.1	1576	117.5	75.6	48.0	48.2	21.7	1.9	1.8	79.3
O–45	CEOC	Hilo	15	556	<1	3.4	9.7	131.3	16.3	10.0	9.0	1296	109.0	60.6	101.5	120.6	38.1	2.7	3.0	74.1
C–12	CEOR	Macanal	29	194	2	5.2	10.9	75.8	101.0	8.6	2.0	94	187.9	1.0	60.3	15.5	<0.1	<0.1	<0.1	<0.5
MSP–25	CEOR	Macanal	24	453	4	7.1	23.6	242.8	28.2	12.2	3.9	182	231.1	1.2	55.0	16.2	2.2	<0.1	<0.1	0.5
COS14–459	Villa de Leyva	Villa de Leyva	23	265	3	2.9	10.6	137.6	286.4	10.7	5.4	272	144.1	7.6	19.8	11.5	0.8	<0.1	0.8	2.2
QED–35	CEOR	Fómeque	22	369	2	5.5	25.0	170.9	250.7	22.4	4.2	143	230.7	0.9	14.0	6.4	<0.1	<0.1	<0.1	<0.5
RSP–30	Villa de Leyva	Villa de Leyva	21	400	3	5.5	20.8	214.8	214.9	18.8	4.6	299	193.8	13.7	42.0	15.1	0.1	0.1	0.5	0.7
QED–00	CEOR	Fómeque	20	389	4	6.8	26.9	177.5	251.4	21.1	3.7	127	251.1	0.9	72.2	7.8	<0.1	<0.1	<0.1	<0.5
COS15–1553	Villa de Leyva	Paja	19	481	5	3.9	25.7	152.0	291.9	35.4	4.2	108	134.3	1.7	18.5	5.6	<0.1	<0.1	<0.1	<0.5
C–30	CEOR	Macanal	19	576	6	6.0	22.1	238.8	160.7	19.6	3.0	153	196.3	1.5	72.2	1.9	<0.1	<0.1	<0.1	<0.5
GA–60	CEOR	Macanal	17	528	9	6.6	20.6	193.7	137.4	17.2	4.2	181	220.9	14.9	20.9	10.9	0.2	<0.1	0.2	1.6
CON7–671	Villa de Leyva	San Gil Shale	13	270	7	11.8	33.4	91.6	237.2	31.9	5.4	56	416.3	1.3	11.7	8.1	<0.1	<0.1	<0.1	<0.5
RN–55	Villeta	Pacho	8	152	3	21.5	20.5	38.6	92.1	18.0	4.5	108	803.0	7.8	6.5	3.9	0.1	<0.1	0.3	1.0
CON6–674	Villa de Leyva	Churuvita	12	389	3	28.5	42.6	118.1	217.7	34.3	6.9	93	1058.1	1.6	7.1	8.7	<0.1	<0.1	0.1	<0.5
COS15–1739	Villa de Leyva	Paja	11	240	2	32.8	34.5	82.4	206.5	39.7	7.7	72	1232.4	1.0	19.0	15.5	0.2	<0.1	<0.1	<0.5
COS15–2054	Villa de Leyva	Paja	14	359	4	36.3	45.8	98.3	301.9	52.1	9.0	130	1336.5	2.9	13.2	14.6	0.1	<0.1	<0.1	<0.5

Murca Formation shales from the Tobia River (RT) of the Villeta area contain 6.5% dolomite and 3.9% ankerite. These two minerals have been reported as solid inclusions in emeralds (Pignatelli et al., 2015) and are associated with albite in hydrothermal veins and breccias that contain the emerald mineralization (Mantilla et al., 2008).

Mantle–derived Cretaceous gabbroic bodies were emplaced during the early extensional phases of the back–arc basin and

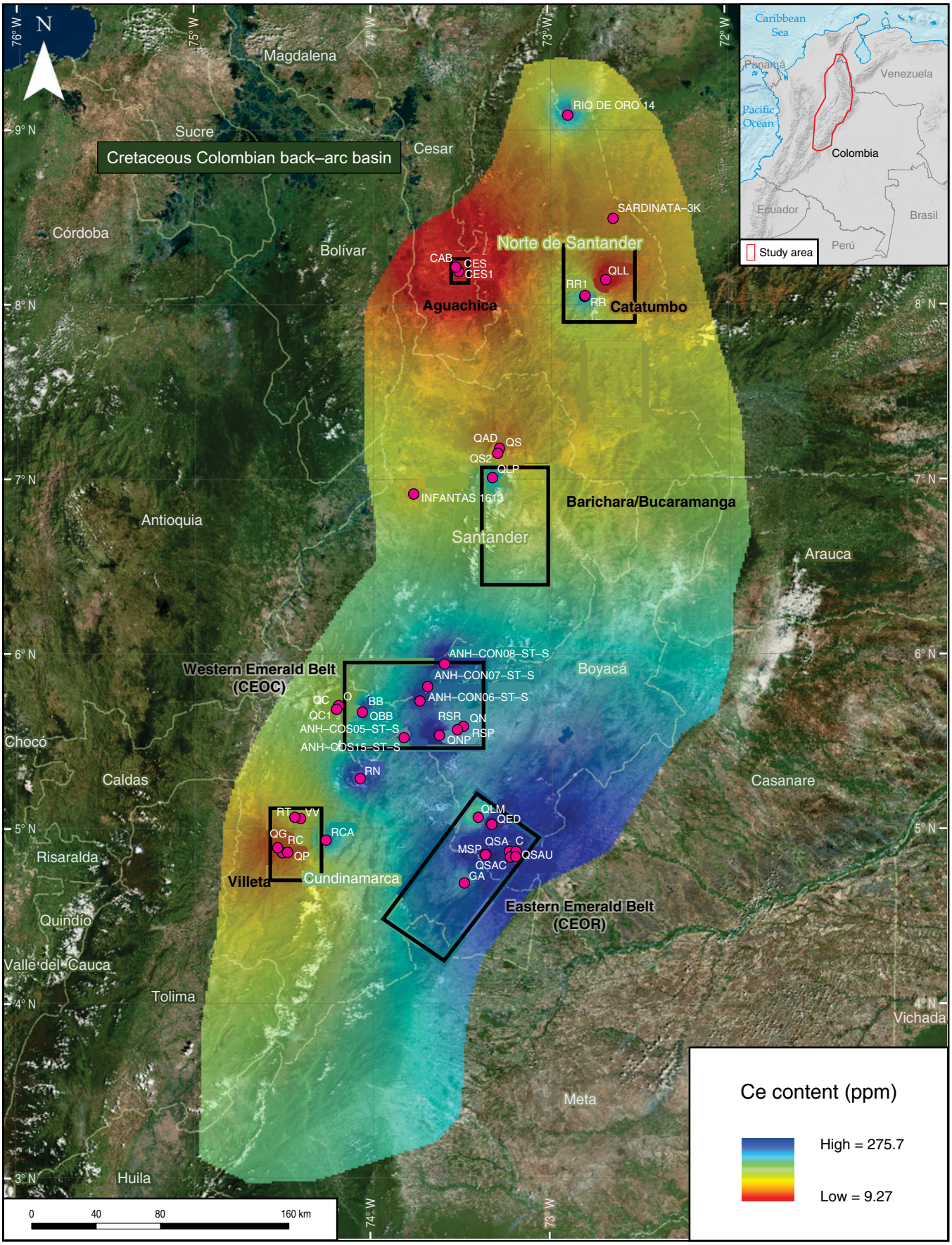

Figure 18. Cerium distribution from ICP–MS analyses. Values are average ppm per locality.

Table 9. Rare earth elements in ppm.

Sample	Area	Formation	Sc	Y	La	Ce	Pr	Nd	Sm	Eu	Gd	Tb	Dy	Ho	Er	Tm	Yb	Lu
COS14–1575	Villa de Leyva	Arcabuco	21	52.4	276.2	618.8	82.09	315.2	50.13	7.97	21.7	2.32	11.55	1.75	4.50	0.72	4.85	0.71
QBB–00	CEOC	Furatena	20	32.6	233.2	502.5	61.08	217.8	31.65	4.9	16.14	1.68	7.78	1.19	3.15	0.46	3.09	0.41
MSP–30	CEOR	Macanal	22	45.5	205.0	374.1	40.35	150.1	22.43	3.68	12.03	1.53	8.73	1.55	4.08	0.61	4.31	0.63
COS15–2054	Villa de Leyva	Paja	14	89.9	161.3	359.5	41.09	154.5	26.18	4.07	18.96	2.57	15.8	3.25	10.00	1.61	10.93	1.72
QSA–65	Villa de Leyva	Aguacaliente	12	104.5	118.7	299.3	35.17	133.8	25.49	4.30	22.58	3.59	19.18	3.32	8.71	1.17	6.96	1.01
COS15–1490	Villa de Leyva	Paja	13	38.6	119.8	287.6	30.62	109.9	17.09	2.70	12.33	1.52	7.64	1.46	4.08	0.62	4.12	0.62
O–75	CEOC	Hilo	12	52.9	142.1	233.0	29.09	99.8	11.24	1.67	7.51	0.78	4.36	1.14	3.96	0.59	4.00	0.68
MSP–35	CEOR	Macanal	21	43.3	119.3	214.9	23.72	88.6	15.19	2.71	10.64	1.57	8.39	1.72	4.82	0.68	4.57	0.65
CON7–485	Villa de Leyva	San Gil Shale	18	45.0	106.3	212.9	24.45	87.0	14.81	2.45	11.79	1.69	9.50	1.80	5.11	0.72	4.74	0.69
COS15–1360	Villa de Leyva	Paja	15	49.8	98.8	210.5	23.59	87.1	14.95	2.48	11.09	1.51	9.25	1.90	5.78	0.96	6.48	0.93
QSAU–18	Villa de Leyva	Une	19	39.7	95.6	199.2	21.95	76.5	13.28	2.25	10.08	1.51	8.32	1.55	4.46	0.68	4.37	0.68
CON6–1405	Villa de Leyva	Churuvita	19	45.6	94.9	198.3	22.50	83.2	15.32	2.60	12.97	1.91	9.88	1.83	4.66	0.70	4.35	0.67
CON7–1014	Villa de Leyva	San Gil Shale	20	41.2	101.2	198.0	22.80	80.1	13.42	2.28	9.77	1.26	7.60	1.55	4.94	0.73	4.62	0.70
QSAU–0	Villa de Leyva	Une	18	45.6	98.6	195.7	22.53	80.0	13.57	2.31	10.24	1.67	9.38	1.76	4.99	0.76	5.05	0.75
CON8–1958	Villa de Leyva	Paja	17	54.9	92.4	193.3	21.70	79.6	13.55	2.32	11.46	1.75	10.28	1.95	5.63	0.87	5.58	0.85
CON8–2025	Villa de Leyva	Paja	17	47.6	90.9	184.9	20.85	75.6	13.63	2.44	12.21	1.73	9.63	1.78	5.14	0.75	4.93	0.76
COS15–1739	Villa de Leyva	Paja	11	51.2	84.7	180.4	20.34	74.7	12.9	2.00	9.23	1.35	8.45	1.81	6.11	1.04	7.28	1.15
QS–00	Villa de Leyva	Salto	13	53.1	75.9	174.4	19.02	70.0	12.58	2.02	11.58	1.75	10.32	1.97	5.94	0.86	5.54	0.86
CON7–1655	Villa de Leyva	San Gil Shale	17	50.8	79.2	161.5	18.45	67.5	12.28	2.14	10.10	1.61	9.93	2.05	6.06	0.91	5.55	0.86
CON6–674	Villa de Leyva	Churuvita	12	54.6	74.1	158.4	17.60	63.6	9.91	1.47	7.08	1.22	8.33	1.92	6.00	1.05	7.19	1.14
COS15–1819	Villa de Leyva	Paja	13	47.4	79.1	156.7	18.05	66.5	11.96	1.96	9.86	1.36	8.09	1.64	4.97	0.82	5.78	0.90
CON8–1712	Villa de Leyva	Paja	15	48.5	72.9	147.8	16.59	61.0	11.39	2.11	10.49	1.63	9.25	1.80	5.21	0.81	5.38	0.85
QNP–00	Villa de Leyva	Paja	16	38.7	59.8	131.7	15.21	60.0	15.14	3.25	18.97	2.43	10.11	1.54	3.63	0.51	3.29	0.44
CON8–2296	Villa de Leyva	Paja	10	53.0	59.2	126.7	14.91	55.1	9.50	1.64	8.46	1.46	8.70	1.76	5.22	0.86	5.76	0.88
RN–40	Villa de Leyva	Pacho	12	41.1	52.3	105.0	13.08	50.8	11.13	2.13	12.03	1.68	8.51	1.56	4.46	0.63	4.39	0.64
O–85	CEOC	Hilo	21	29.1	46.7	90.0	13.01	52.4	15.12	3.34	12.44	1.81	9.62	1.66	4.29	0.59	3.82	0.49
QAD–50	Villa de Leyva	La Luna	7	130.0	67.7	88.3	11.81	44.1	8.26	1.58	9.12	1.6	10.71	2.54	8.15	1.19	7.78	1.19
QLL–55	Villa de Leyva	La Luna	5	223.7	97.2	75.7	15.15	64.0	12.80	3.13	17.18	2.52	16.16	3.89	12.09	1.66	10.25	1.73
C–12	CEOR	Macanal	29	29.0	31.6	63.8	7.65	30.8	6.65	1.23	6.42	0.99	4.88	1.09	3.32	0.43	3.19	0.47
QAD–65	Villa de Leyva	La Luna	6	168.6	73.2	61.2	11.06	44.4	9.73	2.27	12.73	1.89	11.47	2.80	8.65	1.25	7.62	1.25
COS14–459	Villa de Leyva	Villa de Leyva	23	20.7	28.8	56.6	7.03	28.0	5.90	1.72	5.84	0.83	4.19	0.74	2.16	0.33	2.36	0.36
VV–80	Villa de Leyva	Trincheras	10	50.5	29.8	55.7	6.57	26.6	4.96	1.14	7.23	1.37	8.11	1.89	4.73	0.66	3.92	0.55
RN–70	Villa de Leyva	Pacho	14	52.0	24.9	54.8	6.68	27.1	7.30	1.60	9.61	1.67	9.56	2.05	6.02	0.86	5.69	0.90
RT–10	Villa de Leyva	Murca	14	231.3	25.5	50.4	5.96	23.7	10.01	3.77	26.90	5.88	39.66	7.74	18.58	2.24	11.43	1.39
MSP–25	CEOR	Macanal	24	34.6	21.2	37.7	6.23	24.1	5.64	1.37	6.51	1.05	6.70	1.31	3.88	0.55	4.22	0.59

intruded Lower Cretaceous shales. These rocks include dikes of gabbro, diorite, and tonalite associated with hydrothermal activity that carried fluids related to the emerald mineralization. The ages reported by Vásquez et al. (2010) and the Radiometric Dating Catalog of Colombia, compiled by Gómez et al. (2015), indicate that the gabbros span Valanginian to Cenomanian time. The K–Ar and Ar–Ar ages from whole–rock and hornblende samples, which would reflect the ages of emplacement, are Valanginian to Hauterivian (Pacho), Barremian to Cenomanian (Cáceres), Aptian (Pajarito), Albian to Cenomanian (Rodrigoque), and Cenomanian (La Corona).

Vásquez et al. (2005, 2010) documented the geochemistry of the mafic to intermediate bodies, indicating tholeiitic affinity (MORB–like) from Cáceres and Pacho on the western side of the Eastern Cordillera and alkaline affinity (OIB–like) from Rodrigoque and Pajarito on the eastern side. The tonalite from La Corona in the western part of the Eastern Cordillera, near Cáceres and Pacho, also shows alkaline affinity. The authors

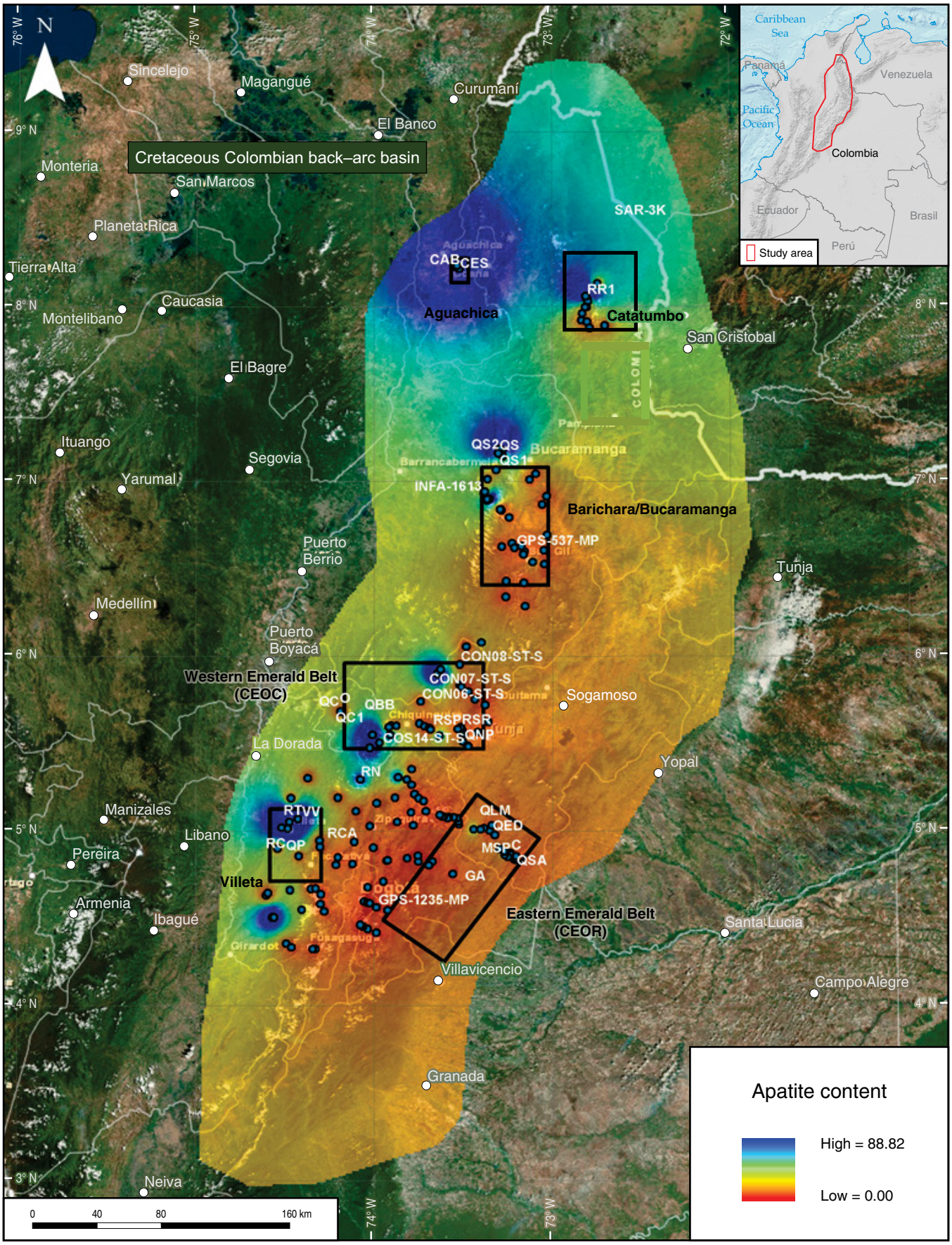

Figure 19. Regional distribution of apatite from heavy mineral analyses.

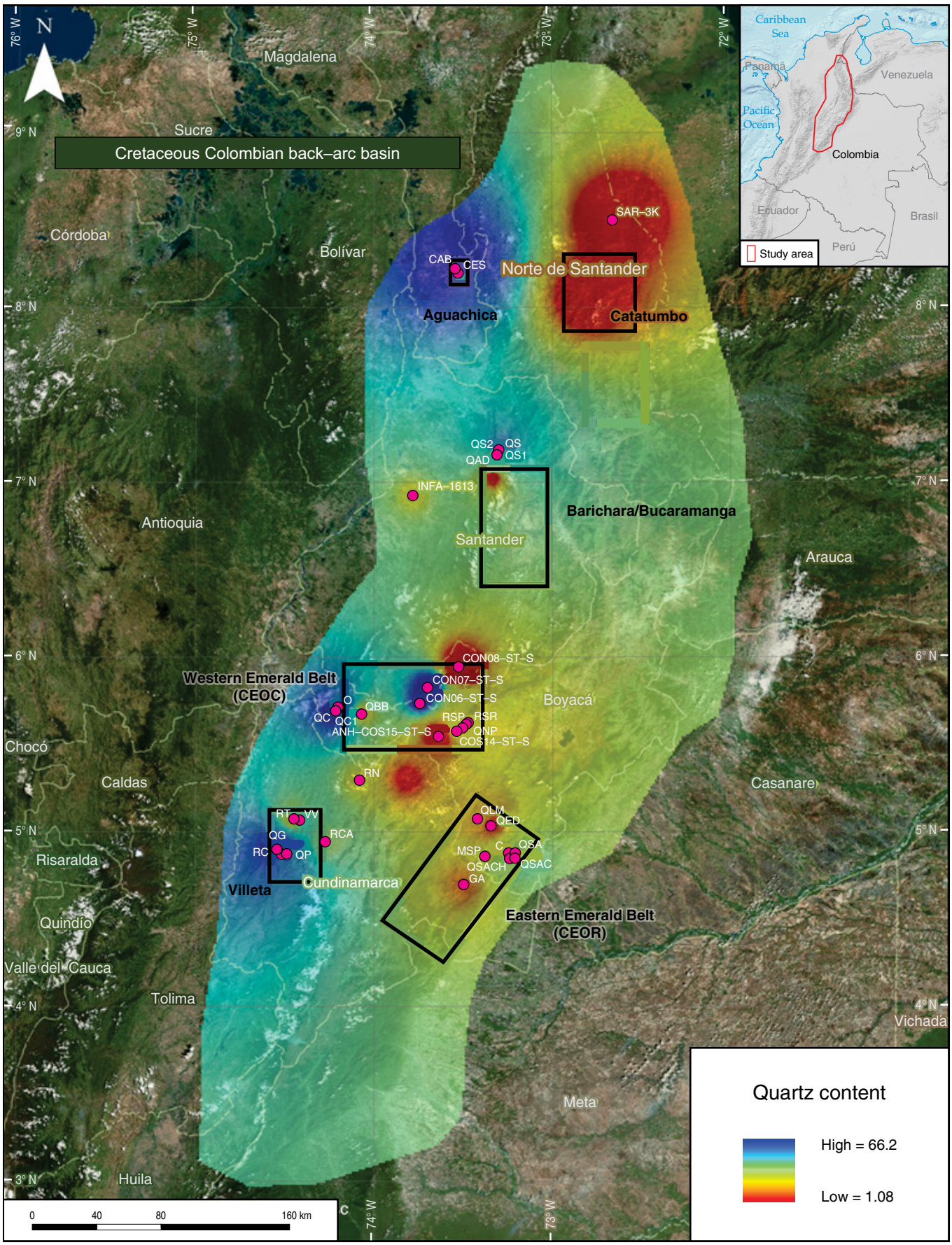

Figure 20. Quartz contents from XRD. Values plotted are average percentages per locality.

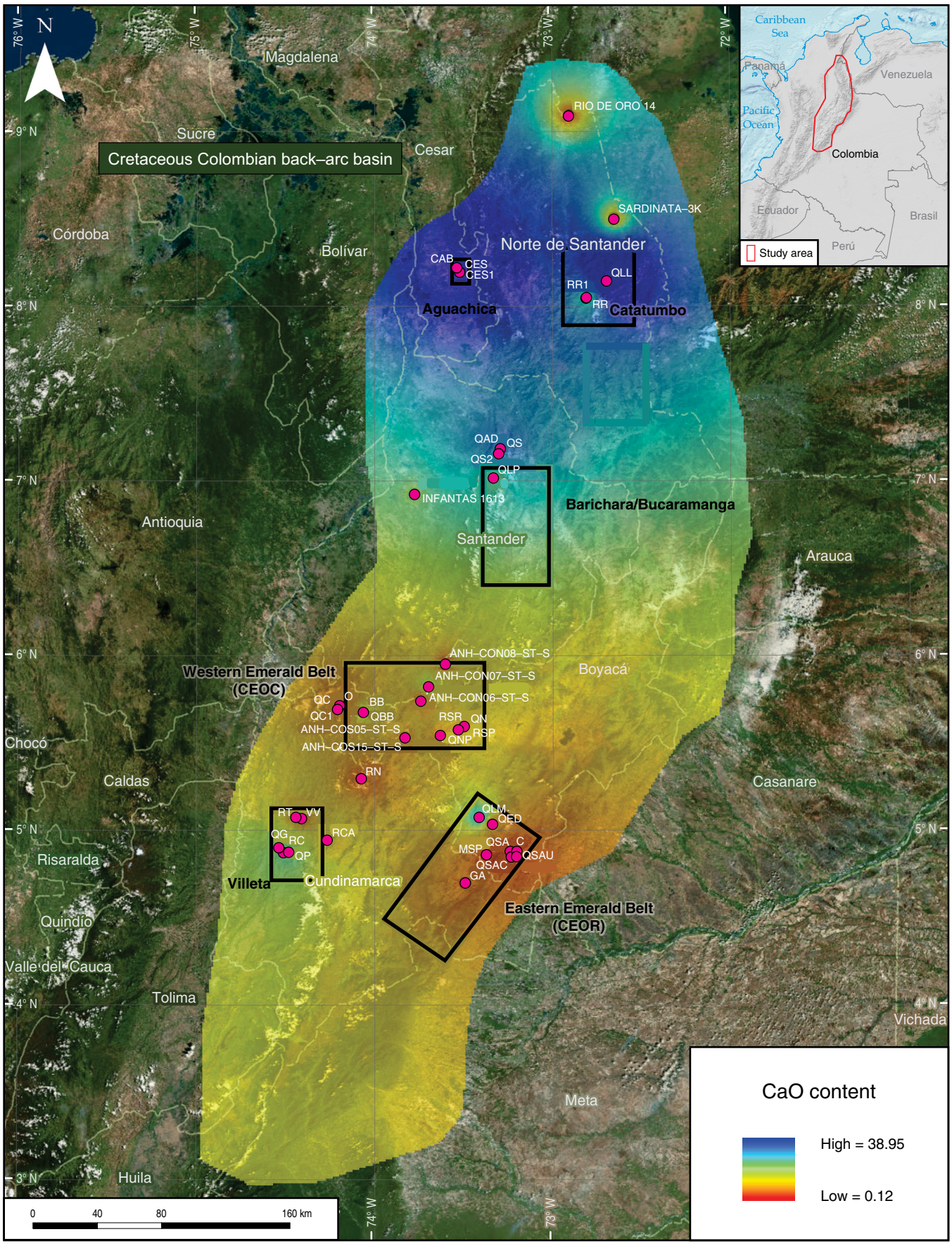

Figure 21. CaO contents from ICP–OES. Values plotted are average percentages per locality.

indicated a transition from a low to a high degree of partial melting and crustal contamination of mantle–derived magmas.

The wide range of muscovite K–Ar and Ar–Ar ages (Cheilletz et al., 1994, 1997; Gómez et al., 2015) of the mineralized emerald zones from the Macanal Formation: 76 ± 2.4 Ma to 58.4 ± 5.3 Ma (early Campanian to late Paleocene) and the Furatena Formation: 37.3 ± 0.1 Ma to 31.4 ± 0.3 Ma (late Eocene to early Oligocene), could indicate that not all the mineral systems were completely closed with respect to Ar due to the Early Cretaceous hydrothermal activity in the basin. For instance, the Cáceres Gabbro yields plagioclase Ar–Ar ages (Gómez et al., 2015; Vásquez et al. 2010) of 81.7 ± 0.8 Ma to 27 ± 1.9 Ma (early Campanian to late Oligocene), which are too young, considering the Early Cretaceous biostratigraphic ages of the strata intruded across the basin. The oldest whole–rock K–Ar age of the Cáceres Gabbro is 113.0 ± 16.0 Ma (early Barremian to early Cenomanian), which is closer to the age of emplacement. The Rodrigoque Gabbro presents the same situation; the youngest Ar–Ar age in plagioclase is 49.9 ± 0.2 Ma (early Eocene), but the oldest whole–rock K–Ar age is 106.5 ± 5.5 Ma (Albian). In the Corona Gabbro, the youngest Ar–Ar age in plagioclase is 64.3 ± 2.3 Ma (late Maastrichtian to Paleocene), but the oldest Ar–Ar age in hornblende is 97.8 ± 0.1 Ma (early Cenomanian). The muscovite and plagioclase ages younger than hornblende ages could indicate different closure temperatures, but the wide range of ages could also indicate argon loss during the Early Cretaceous hydrothermal activity, producing misleading younger ages.

We infer that the magmatic activity which affected the Lower Cretaceous strata in the basin produced several episodes of mineralization. The hydrothermal fluids that carried the scandium, vanadium, and beryllium were emplaced during Valanginian to Cenomanian rifting of the back–arc basin. Emeralds are present mostly in strata of Berriasian to Hauterivian age on both sides of the basin, so emerald mineralizing fluids must have been emplaced during the rifting stage when the basin experienced peak magmatic and hydrothermal activity. If the main mineralizing episode had occurred during the Cenozoic, then the emeralds would also have crystallized in younger strata and not primarily in Berriasian to Hauterivian shales. The Lower Cretaceous shales from the opposite eastern and western sides of the basin have different clay and REE signatures because of different source areas but share similar geochemical features because of the elements introduced during magmatic and hydrothermal activity.

Two other lines of evidence have been explored regarding the origin of emerald mineralization. One line is the maximum temperature reached by burial of the Berriasian to Hauterivian strata that host the main emerald mineralization, and the other line is the temperature of the mineralization itself. Silva et al. (2010) concluded that the chlorite (clinochlore) associated with the emerald mineralization hosted in Berriasian rocks with hydrothermal activity (which also contain hydrothermal albite and dolomite) crystallized at ca. 354 °C and that such a temperature was consistent with the temperature (ca. 335 °C) of fluid inclusions in the emeralds reported by Mantilla et al. (2008). On the other hand, Mora et al. (2013) established that cleavage was produced at maximum paleotemperatures (ca. 220 °C deduced from ZFT and vitrinite reflectance) during the late Oligocene; fold–related calcite–filled veins and late stages of cleavage were produced at temperatures between 220 °C and 160 °C during the early Miocene, indicating that the strata accumulated strain for a few million years before first–order thrusting, which was produced during the late Miocene and Pliocene uplift of the Eastern Cordillera. The temperatures obtained from the two data sets were attained during different events: One temperature (ca. 354 °C) is that of chlorite and emerald mineralization during Valanginian to Cenomanian hydrothermal activity, and the other temperature (220 to 160 °C) represents the maximum burial at which the strata began accumulating strain before thrust movement occurred during late Miocene uplift.

We postulate that at a micro scale, the normal faults and extensional fractures that controlled the basin during the Early Cretaceous were the main conduits for the hydrothermal fluids that formed the emeralds. Many but not all of these normal faults and fracture planes were later inverted during the Miocene thrusting and uplifting of the basin. For instance, Mantilla et al. (2008) indicate that in the Oriente mine of the CEOR, fragments of hydrothermal veins with emeralds are present in fractures produced during a recent tectonic event that destroyed the emerald mineralization. Mora et al. (2013) indicated that most of the planar fabrics, veins, and fractures are correlated with the main folds that affected the Cretaceous rocks during the late Oligocene and early Miocene, but in the mining area of El Porvenir in the Gachalá dome, orthogonal veins filled with calcite have no parallelism or symmetry with any contractional fold.

Since there are no igneous bodies of Campanian to Oligocene age intruding the strata of the basin, which could support the hypothesis of hydrothermal activity during this time span, and since the temperature produced by burial diagenesis was not high enough (less than 220 °C for the oldest strata), we prefer the interpretation of emerald mineralization during Early Cretaceous hydrothermal activity with temperatures higher than 350 °C.

5. Conclusions

Detrital zircon U–Pb ages document two source areas for the back–arc Cretaceous Colombian Basin. One source on the E side of the basin has Archean, Proterozoic, and Paleozoic ages derived from the Guiana Shield, and the other source on the W side of the basin has Triassic to Cretaceous ages, including very abundant Jurassic particles derived from the Central Cordillera magmatic arc. Other important particles derived from the Central Cordillera have Paleozoic ages, along with a small number of Proterozoic particles. No Mesozoic particles are present in the samples from the E side of the Eastern Cordillera.

The fluvial system of Berriasian to Valanginian age that deposited the Tambor Formation and time–equivalent fluvial units in the center of the basin contained particles sourced from both the E and W sides of the basin, including distributary streams feeding a trunk river flowing northward to the Caribbean. The central rift of the basin was completely flooded during the late Valanginian, as indicated by the offshore shales, marlstones, and biomicrites deposited in large areas of Cundinamarca, Boyacá, and Santander Departments. The horsts that separated the early grabens of the basin were definitely covered during the late Valanginian. After this time, the Cretaceous seaway was separated into two shorelines supplied from E and W sources on opposite sides of the basin. Fluvial environments during the rest of Cretaceous time were also separated on the opposite E and W margins of the basin. No mixing of particles from opposite E and W source areas or from local horsts occurred in the basin after the Valanginian.

XRD analyses show that black shale mudstones of the basin are composed mainly of clay minerals and quartz silt. The highest contents of kaolinite (50 to 55 %) are from the Paja Formation in the Santander area and the Une and Chipaque Formations in the Llanos Foothills, both sourced from the Guiana Shield. The highest average illite contents (60 to 65 %) are from shales of the Simití and El Salto Formations in the Infantas well and from the Hilo Formation in the Otanche section; both are situated toward the W side of the basin. Chlorite is present in minor amounts compared to kaolinite and illite; the highest average percentage of chlorite (22%) comes from the lower part of the Murca Formation in the Tobia River section of the Villeta area. Chlorite was derived from low–grade metamorphic rocks sourced from the Central Cordillera.

ICP–MS analyses reveal several important elements associated with the clay content of black shales from the basin, which also help to discriminate between eastern and western sources. The highest contents of titanium, zirconium, thorium, niobium, hafnium, and tantalum in the study come from a shale sample of the Paja Formation in the Villa de Leyva area. The unit was sourced from the eastern side of the basin, which has more differentiated continental crust than the western sources. In contrast, the highest contents of chromium, copper, molybdenum, arsenic, antimony, selenium, thallium, and silver in the study come from the shales of the Hilo Formation in the Otanche section, which also have very high contents of illite. This unit was sourced from the western side of the basin, which included the magmatic/metamorphic arc and accreted oceanic crust.

The light REE of the cerium group have the maximum values for this study in a siltstone sample from the upper part of the Arcabuco Formation in the ANH COS–14 well in the vicinity of Villa de Leyva. In contrast, the heavy REE of the yttrium group have the maximum values for this study in a sample from the lower part of the Murca Formation in the Tobia River section. The high contents of the yttrium group indicate an ultramafic source in accreted oceanic crust along the western basin margin, while the cerium group indicates more differentiated continental crust on the eastern basin margin.

Another important mineral that indicates provenance is apatite, which shows higher percentages in the western part of the basin and is related to igneous and metamorphic sources in the Central Cordillera. Samples with heavy mineral analyses containing high percentages of terrigenous apatite come from the Murca, Trincheras, Socotá, Hilo, and Pacho Formations in the Villeta area. Another important fraction of the reported apatite is related to phosphatic biomicrites and has an authigenic origin because of biological accumulation in fish. The highest percentages of fluorapatite from XRD analyses are from La Luna Formation. The highest contents of uranium in the study are associated with the biologically concentrated phosphates of La Luna Formation.

The highest calcium (CaO) contents (40 to 55 %), obtained from ICP–OES analyses, come from the biomicrite limestones of La Luna Formation on the W and N sides of the basin. The highest contents of SiO_2 (59 to 79 %) in diagenetic cherts are also from La Luna Formation, in addition to the Lidita Inferior and Lidita Superior Formations, Hilo Formation, and La Frontera Member of the Conejo Formation.

Mantle–derived gabbroic to intermediate bodies emplaced during the early extensional synrift phase of the back–arc basin intruded Lower Cretaceous shales. The former rocks include dikes of gabbro, diorite, and tonalite, associated with important hydrothermal activity that carried the fluids that produced the emerald mineralization. The highest values of scandium are found in shales of the CEOR, whereas the highest values of vanadium are present in shales of the CEOC. The wide range of muscovite and plagioclase ages from the mineralized emerald zones (early Campanian to late Oligocene), much younger than the hornblende and whole–rock ages of emplacement of the gabbros (Valanginian to Cenomanian), might indicate that the systems were not closed with respect to Ar, producing misleading younger ages. Argon loss could be due to several factors, including Early Cretaceous hydrothermal activity, increasing temperature during Late Cretaceous to Oligocene sedimentation, and compressional strain during Miocene uplift of the Eastern Cordillera. There are no igneous bodies or other known sources of heat, which could support the hypothesis of hydrothermal activity during the Campanian to Oligocene.

Acknowledgments

We thank the Agencia Nacional de Hidrocarburos for permission to publish their data. The field work and analyses were conducted within project 299–12 to evaluate the unconventional hydrocarbon potential of fine–grained strata from the Cretaceous Colombian Basin. The project was directed by Javier GUERRERO and supervised by Alejandra MEJÍA–MOLINA.

We also thank Dr. Brian HORTON from the University of Texas, Dr. Andres MORA from ICP, and an anonymous reviewer for valuable suggestions that helped us improve the paper.

References

Barham, M., Kirkland, C.L., Reynolds, S., O'Leary, M.J., Evans, N.J., Allen, H., Haines, P.W., Hocking, R.M., McDonald, B.J., Belousova, E. & Goodall, J. 2016. The answers are blowin' in the wind: Ultra–distal ashfall zircons, indicators of Cretaceous super–eruptions in eastern Gondwana. Geology, 44 (8): 643–646. https://doi.org/10.1130/G38000.1

Bonilla, G.E., Sarmiento, G.A. & Gaviria, S. 2011. Proveniencia y transformación diagenética de minerales arcillosos del Maastrichtiano–Paleoceno al norte de Bogotá, cordillera Oriental de Colombia. Geología Colombiana, 36(1): 179–196.

Bustamante, C., Cardona, A., Bayona, G., Mora, A., Valencia, V., Gehrels, G. & Vervoort, J. 2010. U–Pb LA–ICP–MS geochronology and regional correlation of Middle Jurassic intrusive rocks from the Garzón Massif, Upper Magdalena Valley and Central Cordillera, southern Colombia. Boletín de Geología, 32(2): 93–109.

Cheilletz, A., Féraud, G., Giuliani, G. & Rodriguez, C.T. 1994. Time–pressure and temperature constraints on the formation of Colombian emeralds: An $^{40}Ar/^{39}Ar$ laser microprobe and fluid inclusion study. Economic Geology, 89(2): 361–380. https://doi.org/10.2113/gsecongeo.89.2.361

Cheilletz, A., Giuliani, G., Branquet, Y., Laumonier, B., Sanchez, A.J., Féraud, G. & Arhan, T. 1997. Datation K–Ar et $^{40}Ar/^{39}Ar$ à 65 + 3 Ma des gisements d'émeraude du district de Chivor–Macanal: Argument en faveur d'une déformation précoce dans la Cordillère Orientale de Colombie. Comptes–Rendus de l'Académie des Sciences, 324(5): 369–377. Paris, France.

Chew, D.M. & Donelick, R.A. 2012. Combined apatite fission track and U–Pb dating by LA–ICP–MS and its application in apatite provenance analysis. Mineralogical Association of Canada, Short Course 42: 219–247.

Clavijo, J., Mantilla, L., Pinto, J., Bernal, L. & Pérez, A. 2008. Evolución geológica de la serranía de San Lucas, norte del Valle Medio del Magdalena y noroeste de la cordillera Oriental. Boletín de Geología, 30(1): 45–62.

Cooper, M.A., Addison, F.T., Álvarez, R., Coral, M., Graham, R.H., Hayward, A.B., Howe, S., Martínez, J., Naar, J., Peñas, R., Pulham, A.J. & Taborda, A. 1995. Basin development and tectonic history of the Llanos Basin, Eastern Cordillera, and Middle Magdalena Valley, Colombia. American Association of Petroleum Geologists Bulletin, 79(10): 1421–1443.

Etayo–Serna, F., De Porta, N.S., De Porta, J. & Gaona, T. 2003. The Batá Formation of Colombia is truly Cretaceous, not Jurassic. Journal of South American Earth Sciences, 16(3): 113–117. https://doi.org/10.1016/S0895-9811(03)00048-8

Gómez, J., Montes, N.E., Alcárcel, F.A. & Ceballos, J.A. 2015. Catálogo de dataciones radiométricas de Colombia en ArcGIS y Google Earth. In: Gómez, J. & Almanza, M.F. (editors), Compilando la geología de Colombia: Una visión a 2015. Servicio Geológico Colombiano, Publicaciones Geológicas Especiales 33, p. 63–419. Bogotá.

Guerrero, J. 2002a. A proposal on the classification of systems tracts: Application to the allostratigraphy and sequence stratigraphy of the Cretaceous Colombian Basin. Part 1: Berriasian to Hauterivian. Geología Colombiana, (27): 3–25.

Guerrero, J. 2002b. A proposal on the classification of systems tracts: Application to the allostratigraphy and sequence stratigraphy of the Cretaceous Colombian Basin. Part 2: Barremian to Maastrichtian. Geología Colombiana, (27): 27–49.

Guerrero, J. & Sarmiento, G. 1996. Estratigrafía física, palinológica, sedimentológica y secuencial del Cretácico Superior y Paleoceno del Piedemonte Llanero: Implicaciones en exploración petrolera. Geología Colombiana, 20: 3–66.

Guerrero, J., Sarmiento, G. & Navarrete, R. 2000. The stratigraphy of the W side of the Cretaceous Colombian Basin in the Upper Magdalena Valley. Reevaluation of selected areas and type localities including Aipe, Guaduas, Ortega, and Piedras. Geología Colombiana, (25): 45–110.

Hettner, A. 1892. Die Kordillere von Bogotá. Gotha: Justus Perthes, 131 p.

Horton, B.K., Saylor, J.E., Nie, J., Mora, A., Parra, M., Reyes–Harker, A. & Stockli, D.F. 2010. Linking sedimentation in the northern Andes to basement configuration, Mesozoic extension, and Cenozoic shortening: Evidence from detrital zircon U–Pb ages, Eastern Cordillera, Colombia. Geological Society of America Bulletin, 122(9–10): 1423–1442. https://doi.org/10.1130/B30118.1

Horton, B.K., Anderson, V.J., Caballero, V., Saylor, J.E., Nie, J., Parra, M. & Mora, A. 2015. Application of detrital zircon U–Pb geochronology to surface and subsurface correlations of provenance, paleodrainage and tectonics of the Middle Magdalena Valley Basin of Colombia. Geosphere, 11(6): 1790–1811. https://doi.org/10.1130/GES01251.1

Mantilla, L.C., Silva, A., Conde, J., Gaviria, J.A., Gallo, F.H., Torres, D.A., Ortegon, J.M., Silva, E.N., Tarazona, C.A., Castro, B.J. & Garcia, C.A. 2008. Estudio de los procesos de interacción fluido–roca en el cinturón esmeraldífero oriental (cordillera Oriental, Colombia) y su importancia en la exploración de nuevos yacimientos hidrotermales. Ingeominas–Universidad Industrial de Santander, unpublished report, 496 p. Bogotá.

Moore, T.E. 2014. U–Pb zircon age data for selected sedimentary, metasedimentary, and igneous rocks from northern and central Alaska. U.S. Geological Survey Data Series 899, 4 p. https://doi.org/10.3133/ds899

Moore, T.E., O'Sullivan, P.B., Potter, C.J. & Donelick, R.A. 2015. Provenance and detrital zircon geochronologic evolution of lower Brookian foreland basin deposits of the western Brooks Range,

Alaska, and implications for early Brookian tectonism. Geosphere, 11(1): 93–122. https://doi.org/10.1130/GES01043.1

Mora, A., Horton, B.K., Mesa, A., Rubiano, J., Ketcham, R.A., Parra, M., Blanco, V., Garcia, D. & Stockli, D.F. 2010. Migration of Cenozoic deformation in the Eastern Cordillera of Colombia interpreted from fission track results and structural relationships: Implications for petroleum systems. American Association of Petroleum Geologists Bulletin, 94(10): 1543–1580. https://doi.org/10.1306/01051009111

Mora, A., Blanco, V., Naranjo, J., Sanchez, N., Ketcham, R.A., Rubiano, J., Stockli, D.F., Quintero, I., Nemčok, M., Horton, B.K. & Davila, H. 2013. On the lag time between internal strain and basement involved thrust induced exhumation: The case of the Colombian Eastern Cordillera. Journal of Structural Geology, 52: 96–118. https://doi.org/10.1016/j.jsg.2013.04.001

Moreno, J.M. 1990. Stratigraphy of the Lower Cretaceous Rosablanca and Cumbre Formations, Útica Sandstone and Murca Formation, west flank, Eastern Cordillera, Colombia. Geología Colombiana, 17: 65–86.

Moreno, J.M. 1991. Provenance of the Lower Cretaceous sedimentary sequences, central part, Eastern Cordillera, Colombia. Revista de la Academia Colombiana de Ciencias Exactas, Físicas y Naturales, 18(69): 159–173.

Ordóñez–Carmona, O., Restrepo, J.J. & Pimentel, M.M. 2006. Geochronological and isotopical review of pre–Devonian crustal basement of the Colombian Andes. Journal of South American Earth Sciences, 21(4): 372–382. https://doi.org/10.1016/j.jsames.2006.07.005

Pignatelli, I., Giuliani, G., Ohnenstetter, D., Agrosi, G., Mathieu, S., Morlot, C. & Branquet, Y. 2015. Colombian trapiche emeralds: Recent advances in understanding their formation. Gems & Gemology, 51(3): 222–259. http://dx.doi.org/10.5741/GEMS.51.3.222

Restrepo–Pace, P.A., Ruiz, J., Gehrels, G. & Cosca, M. 1997. Geochronology and Nd isotopic data of Grenville–age rocks in the Colombian Andes: New constraints for late Proterozoic – early Paleozoic paleocontinental reconstructions of the Americas. Earth and Planetary Science Letters, 150(3–4): 427–441. https://doi.org/10.1016/S0012-821X(97)00091-5

Sarmiento–Rojas, L.F., van Wess, J.D. & Cloetingh, S. 2006. Mesozoic transtensional basin history of the Eastern Cordillera, Colombian Andes: Inferences from tectonic models. Journal of South American Earth Sciences, 21(4): 383–411. https://doi.org/10.1016/j.jsames.2006.07.003

Silva, A., Mantilla, L.C., Terraza, R. 2010. Clasificación química y geotermometría de las cloritas de las formaciones cretácicas Santa Rosa y Lutitas de Macanal, cinturón esmeraldífero oriental, cordillera Oriental, Colombia. Boletín de Geología, 32 (2): 45–54.

Smith, J.J., Turner, E., Möller, A., Joeckel, R.M. & Otto, R.E. 2018. First U–Pb zircon ages for late Miocene Ashfall Konservat–Lagerstätte and Grove Lake ashes from eastern Great Plains, USA. PLOS ONE 13(11): e0207103. https://doi.org/10.1371/journal.pone.0207103

Stacey, J.S. & Kramers, J.D. 1975. Approximation of terrestrial lead isotope evolution by a two–stage model. Earth and Planetary Science Letters, 26(2): 207–221. https://doi.org/10.1016/0012-821X(75)90088-6

Steiger, R.H. & Jäger, E. 1977. Subcommission on geochronology: Convention on the use of decay constants in geo– and cosmochronology. Earth and Planetary Science Letters, 36(3): 359–362. https://doi.org/10.1016/0012-821X(77)90060-7

Tesón, E., Mora, A., Silva, A., Namson, J., Teixell, A., Castellanos, J., Casallas, W., Julivert, M., Taylor, M., Ibañez–Mejia, M. & Valencia, V. 2013. Relationship of Mesozoic graben development, stress, shortening magnitude, and structural style in the Eastern Cordillera of the Colombian Andes. In: Nemčok, M., Mora, A. & Cosgrove, J.W. (editors), Thick–skin–dominated orogens: From initial inversion to full accretion. Geological Society of London, Special Publication 377, p. 257–283. London. https://doi.org/10.1144/SP377.10

Vásquez, M., Altenberger, U., Romer, R.L. & Moreno, J.M. 2005. Extension–related magmatism during mid–Cretaceous times in the Eastern Cordillera, Colombia. 6th International Symposium on Andean Geodynamics, Extended Abstracts, p. 770–772. Barcelona, Spain.

Vásquez, M., Altenberger, U., Romer, R.L., Sudo, M. & Moreno–Murillo, J.M. 2010. Magmatic evolution of the Andean Eastern Cordillera of Colombia during the Cretaceous: Influence of previous tectonic processes. Journal of South American Earth Sciences, 29(2): 171–186. https://doi.org/10.1016/j.jsames.2009.02.003

Vesga, C.J. & Barrero, D. 1978. Edades K/Ar en rocas ígneas y metamórficas de la cordillera Central de Colombia y su implicación geológica. II Congreso Colombiano de Geología. Abstracts, p. 19. Bogotá.

Villagómez, D., Spikings, R., Magna, T., Kammer, A., Winkler, W. & Beltrán, A. 2011. Geochronology, geochemistry and tectonic evolution of the Western and Central Cordilleras of Colombia. Lithos, 125(3–4): 875–896. https://doi.org/10.1016/j.lithos.2011.05.003

Zapata, S., Cardona, A., Jaramillo, C., Valencia, V. & Vervoort, J. 2016. U–Pb LA–ICP–MS geochronology and geochemistry of Jurassic volcanic and plutonic rocks from the Putumayo region (southern Colombia): Tectonic setting and regional correlations. Boletín de Geología, 38(2): 1–38. https://doi.org/10.18273/revbol.v38n2-2016001

Explanation of Acronyms, Abbreviations, and Symbols:

ANH	Agencia Nacional de Hidrocarburos
CEOC	Western Emerald Belt
CEOR	Eastern Emerald Belt
ICP–MS	Inductively coupled plasma mass spectrometry
ICP–OES	Inductively coupled plasma optical emission spectrometry
LA–ICP–MS	Laser ablation inductively coupled plasma mass spectrometry
LOI	Loss on ignition
MMV	Middle Magdalena Valley
MORB	Mid–ocean ridge basalt
OIB	Ocean island basalt
REE	Rare earth element
UMV	Upper Magdalena Valley
XRD	X–ray powder diffraction
ZFT	Zircon fission track

Authors' Biographical Notes

Javier GUERRERO is a geologist from the Universidad Nacional de Colombia. He obtained a Master of Science degree and a PhD from Duke University (USA) in the areas of stratigraphy, sedimentology, and paleomagnetism. He participated with a multidisciplinary group of geologists and paleontologists from several American universities in a project on biostratigraphy, sedimentology, and magnetostratigraphy of the Honda Group in the Tatacoa Desert. He worked at the stratigraphy section of the Servicio Geológico Colombiano on various projects on the Cenozoic from the Magdalena River Valley. Recently, he has been a professor in the Departamento de Geociencias at the Universidad Nacional de Colombia, lecturing in courses on sedimentology, sequence stratigraphy, and regional geology. Javier has conducted research and consulting projects for several petroleum companies and for the Agencia Nacional de Hidrocarburos (ANH) on rocks of the Cretaceous Colombian back–arc basin and the Cenozoic foreland basin.

Alejandra MEJÍA–MOLINA is a geologist from the Universidad de Caldas (Colombia) who has been working during the last decade in paleontology, paleoecology, paleoceanography, and paleoclimatology as a member of the Grupo de Geociencias Oceánicas (GGO) at the Universidad de Salamanca (España). Her Master's thesis was on Quaternary marine/continental variability in North Africa and her Doctoral thesis was on calcareous nannofossils, both at the Universidad de Salamanca. Alejandra worked for the Agencia Nacional de Hidrocarburos (ANH) on several projects to obtain new geological data and evaluate the Colombian exploratory potential of both conventional (Pacific and Caribbean offshore basins) and unconventional hydrocarbons (Cretaceous from the Eastern Cordillera). She currently works for the Escuela de Ciencias Geológicas e Ingeniería at the Universidad Yachay Tech, Ecuador.

José OSORNO is a geologist from the Universidad de Caldas with a specialization in project management from the Universidad Piloto de Colombia. He recently completed a Master of Science in energy management at Universidad Sergio Arboleda and an Executive MBA at the Universitat Politècnica de València, España. José Fernando worked for 18 years at the Servicio Geológico Colombiano in the División de Geología Regional y Estratigrafía. Recently, he has been working at the Agencia Nacional de Hidrocarburos (ANH) in project design and evaluation, including the definition of oil systems in Colombia and geochemical evaluation of the Sinú–San Jacinto area. He is currently responsible for "yet–to–find" projects focused on calculating the potential of hydrocarbons yet to be discovered in the sedimentary basins of Colombia. José is also responsible for projects on the potential of unconventional hydrocarbons in the country.

Chapter 9

https://doi.org/10.32685/pub.esp.36.2019.09
Published online 25 November 2020

Biomicrite, Marlstone, and Shale Properties: Exploration of Nonconventional Hydrocarbons in the Cretaceous Colombian Back–Arc Basin

Javier GUERRERO[1]*, Alejandra MEJÍA–MOLINA[2], and José OSORNO[3]

1 jguerrerod@unal.edu.co
Universidad Nacional de Colombia
Sede Bogotá
Departamento de Geociencias
Carrera 30 n.° 45–03
Bogotá, Colombia

2 amejia@yachaytech.edu.ec
Universidad Yachay Tech
Hacienda Urcuquí s/n y Proyecto Yachay
Urcuquí, Ecuador

3 jose.osorno@anh.gov.co
Agencia Nacional de Hidrocarburos
Calle 26 n.° 59–65, segundo piso
Bogotá, Colombia

* Corresponding author

Abstract The nonconventional hydrocarbon potential of the Cretaceous Colombian back–arc basin is explored taking into consideration the properties of fine–grained units, including biomicrite, marlstone, and shale, in terms of total organic carbon content, gas content, vitrinite reflectance, porosity, permeability, pyrolysis, and organic geochemistry of samples collected from outcrop sections and wells in several localities in the core of the Eastern Cordillera, Middle Magdalena Valley, and Catatumbo. The best properties are from the Turonian to Santonian limestones of La Luna Formation and time–equivalent units, but other limestones of Albian and Campanian ages, including the Hilo Formation and the Oliní Group, have potential. La Luna Formation was deposited during a transgressive and relatively high sea level interval; it is composed of biomicrites of planktonic foraminifera, with minor interbedding of marlstones. Diagenetic cherts resulting from replacement of calcite by quartz are also present. The average total organic carbon values of the formation are excellent, between 4.9 and 11.6% for sections in the area of Aguachica, 5.4 to 8.6% in the area of Barichara, and 6.1 to 7.2% in the area of Cúcuta. These high values of total organic carbon are systematically associated with moderate values of thermal maturity, between 0.8 and 1.3% Ro; the interval contains mainly type II kerogen, with minor mixtures of types II–III.

Keywords: *Cretaceous, back–arc, nonconventional hydrocarbons, limestones.*

Resumen El potencial de hidrocarburos no convencionales de la Cuenca Cretácica Colombiana de back–arc se explora teniendo en cuenta las propiedades de unidades de grano fino, incluyendo biomicrita, marga y lodolita, en términos de contenido de carbono orgánico total, contenido de gas, reflectancia de vitrinita, porosidad, permeabilidad, pirólisis y geoquímica orgánica de muestras recolectadas de secciones de afloramiento y pozos en varias localidades del núcleo de la cordillera Oriental, Valle Medio del Magdalena y Catatumbo. Las mejores propiedades provienen de las calizas del Turoniano al Santoniano de la Formación La Luna y unidades equivalentes en tiempo, pero otras calizas de edades albianas y campanianas, incluyendo la Formación Hilo y el Grupo Oliní, tienen potencial. La Formación La Luna se depositó durante un intervalo transgresivo y relativamente alto del nivel del mar; está compuesta por biomicritas de foraminíferos planctónicos, con intercalaciones menores de margas. Cherts diagenéticos resultantes del reemplazo de calcita por cuarzo también están presentes. Los valores promedio de carbono orgánico total de la formación son excelentes, entre 4,9 y 11,6 % para seccio-

Citation: Guerrero, J., Mejía–Molina, A. & Osorno, J. 2020. Biomicrite, marlstone, and shale properties: Exploration of nonconventional hydrocarbons in the Cretaceous Colombian back–arc basin. In: Gómez, J. & Pinilla–Pachon, A.O. (editors), The Geology of Colombia, Volume 2 Mesozoic. Servicio Geológico Colombiano, Publicaciones Geológicas Especiales 36, p. 299–333. Bogotá. https://doi.org/10.32685/pub.esp.36.2019.09

nes en el área de Aguachica, 5,4 a 8,6 % en el área de Barichara y 6,1 a 7,2 % en el área de Cúcuta. Estos altos valores de carbono orgánico total se asocian sistemáticamente con valores moderados de madurez térmica, entre 0,8 y 1,3 % Ro; el intervalo contiene principalmente kerógeno tipo II, con mezclas menores de los tipos II–III.

Palabras clave: *Cretácico, back–arc, hidrocarburos no convencionales, calizas.*

1. Introduction

The distribution of calcareous and terrigenous units, source areas, geochemistry, U–Pb ages, and mineralogy of the Cretaceous Colombian back–arc basin were reported in previous studies (Guerrero 2002a, 2002b; Guerrero et al., 2000, 2020), indicating that the main depositional axis was located in the present day Eastern Cordillera. Limestones are common on the western and northern sides of the basin; in contrast, terrigenous strata predominate on the eastern and southern sides of the basin. Berriasian and Valanginian strata from the lower part of the succession in the main rift were buried at depths of approximately 8 to 9 km and are overmature for oil and gas. Cretaceous strata of younger ages, deposited outside the main rift, in the modern E and W foothills of the Eastern Cordillera, Llanos, and Magdalena Valley, were buried to lower depths and contain most of the hydrocarbons of the basin.

Sandstones and sandy biosparites of the western border are metamorphic and volcanic lithic arenites sourced from the Central Cordillera; sandstones from the eastern side of the basin are quartz arenites sourced mostly from recycled Paleozoic and older strata from the Guiana Shield. In fact, most of the Cretaceous sections rest with angular unconformity on Paleozoic strata on the eastern border of the basin, while they rest with angular unconformity on igneous and volcanoclastic rocks of Jurassic age on the western border of the basin. The Cretaceous strata present today in the Eastern Cordillera of the Colombian Andes were deposited in a back–arc basin (Figure 1) related to subduction perpendicular to the western border of the continent. The remains of the Cretaceous fore–arc basin include strata that overlie accreted oceanic basalts of MORB affinity, present in the Western Cordillera and western side of the Central Cordillera.

The limestones, diagenetic cherts, and marlstones present on the W and N sides of the basin are of major interest because they include important source rocks and constitute nonconventional reservoirs of hydrocarbons. They have a much better quality of marine organic matter than the shales from the S and E sides of the basin. The type and quality of organic matter was controlled by the offshore sedimentary environments (including mud and silt sedimentation under fair weather climate and sporadic storms) and by the availability of terrigenous particles, including clay minerals and silt–sized quartz particles. The terms gas–shale and oil–shale have been imprecisely applied to fine–grained rocks in the range of silt– and clay–sized particles, which could have either biogenic or terrigenous origin. However, many of those fine–grained rocks include important carbonate contents and are limestones (mainly biomicrites) instead of shales, so it is a better strategy to explore biomicrites instead of shales and to recognize the major differences between those types of rocks. One very important difference is that the biomicrites are more brittle (and respond better to fracking) than the plastic shales, which contain large amounts of clay minerals; the other difference is that organic matter particles of terrestrial origin, including plant debris, are more common in the shales than in the biomicrites, so that they are more prone to produce gas than the biomicrites that generate mainly oil hydrocarbons. In fact, the presence of centimeter–scale regressive marlstone beds within the dominantly transgressive and high–stand biomicrite parasequences is very important because it introduces large amounts of organic matter of terrestrial origin, producing mixtures of type II and type III organic matter.

The geographic location and stratigraphic position of the studied sections are presented in Figures 1–3 and Tables 1 and 2.

2. Materials and Methods

Fine–grained strata, including biomicrites, marlstones, and shales, were collected from 9 wells and 35 field sections at key localities in the basin. Best exposures with published stratigraphy were picked to minimize stratigraphic mistakes. Pyrolysis, total organic carbon (TOC), porosity, permeability, and organic geochemistry analyses were performed at the Antek S.A. laboratories. A total of 1500 samples were processed for TOC, 1500 for vitrinite reflectance, 500 for pyrolysis, 500 for petrophysics, 500 for biomarkers, and 200 for gas content and chromatography.

3. Results

The total organic carbon (TOC) and thermal maturity (Ro) results of 3000 samples are presented as averages per stratigraphic section, displayed in Table 3. The highest average content (11.6% TOC) in the upper part of the table corre-

Figure 1. Paleogeography of the Cretaceous Colombian back–arc basin during the early Albian. La Guajira was aligned with Santa Marta and the Central Cordillera. Sections are: (PU) Putumayo; (UMV) Upper Magdalena Valley; (LL) Llanos; (VI) Villavicencio; (SL) San Luis; (BO) Bogotá; (VILL) Villeta; (VL) Villa de Leyva; (CO) Cocuy; (BU) Bucaramanga; (MMV) Middle Magdalena Valley; (CA) Catatumbo; (ME) Mérida; (PE) Perijá; (GU) Guajira. Modified from Guerrero (2002a).

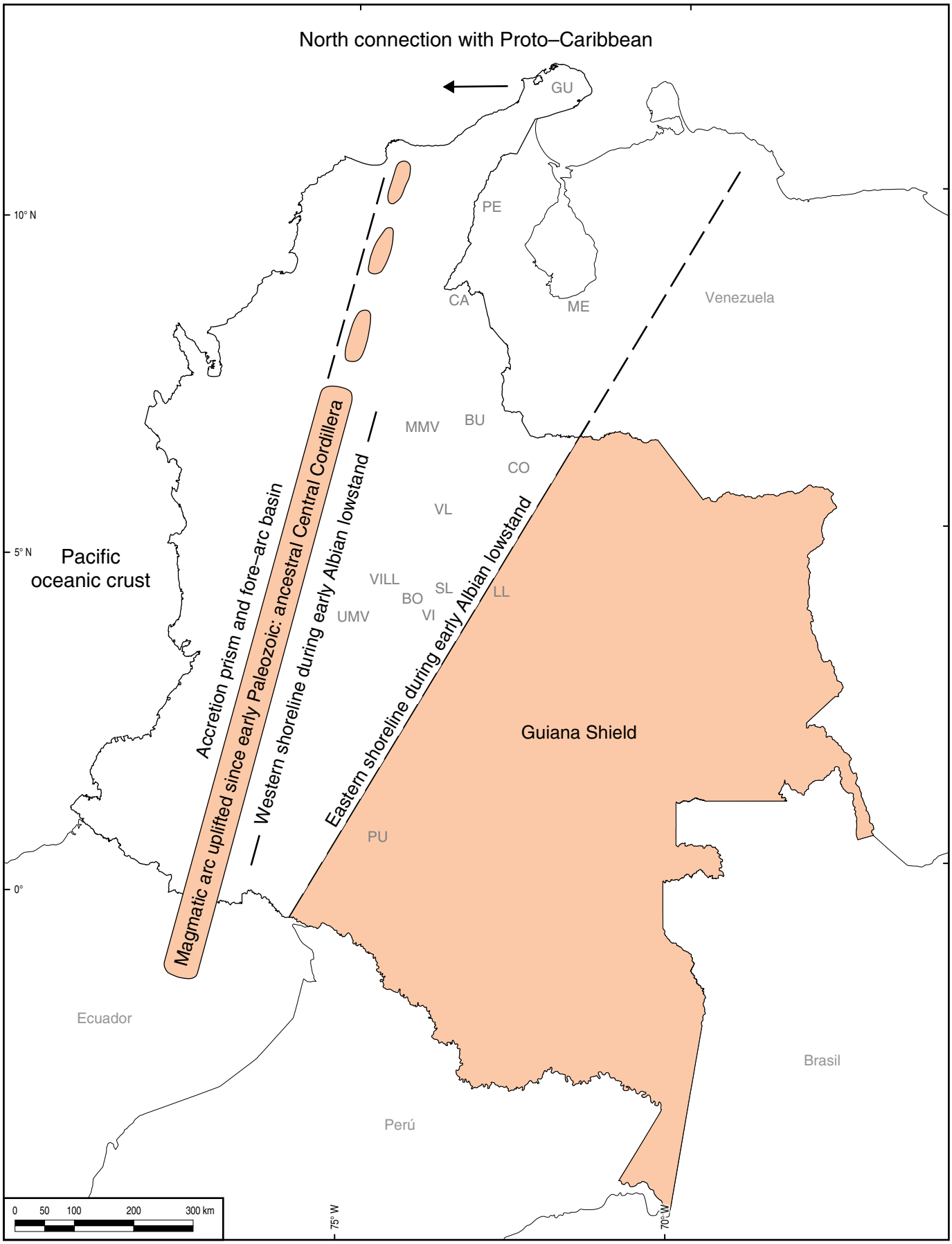
North connection with Proto–Caribbean
GU
PE
CA
ME
Venezuela
10° N
5° N
0°
Pacific
oceanic crust
Accretion prism and fore–arc basin
Magmatic arc uplifted since early Paleozoic: ancestral Central Cordillera
Western shoreline during early Albian lowstand
Eastern shoreline during early Albian lowstand
MMV
BU
CO
VL
VILL
BO
SL
LL
UMV
VI
PU
Guiana Shield
Ecuador
Perú
Brasil
0 50 100 200 300 km
75° W
70° W

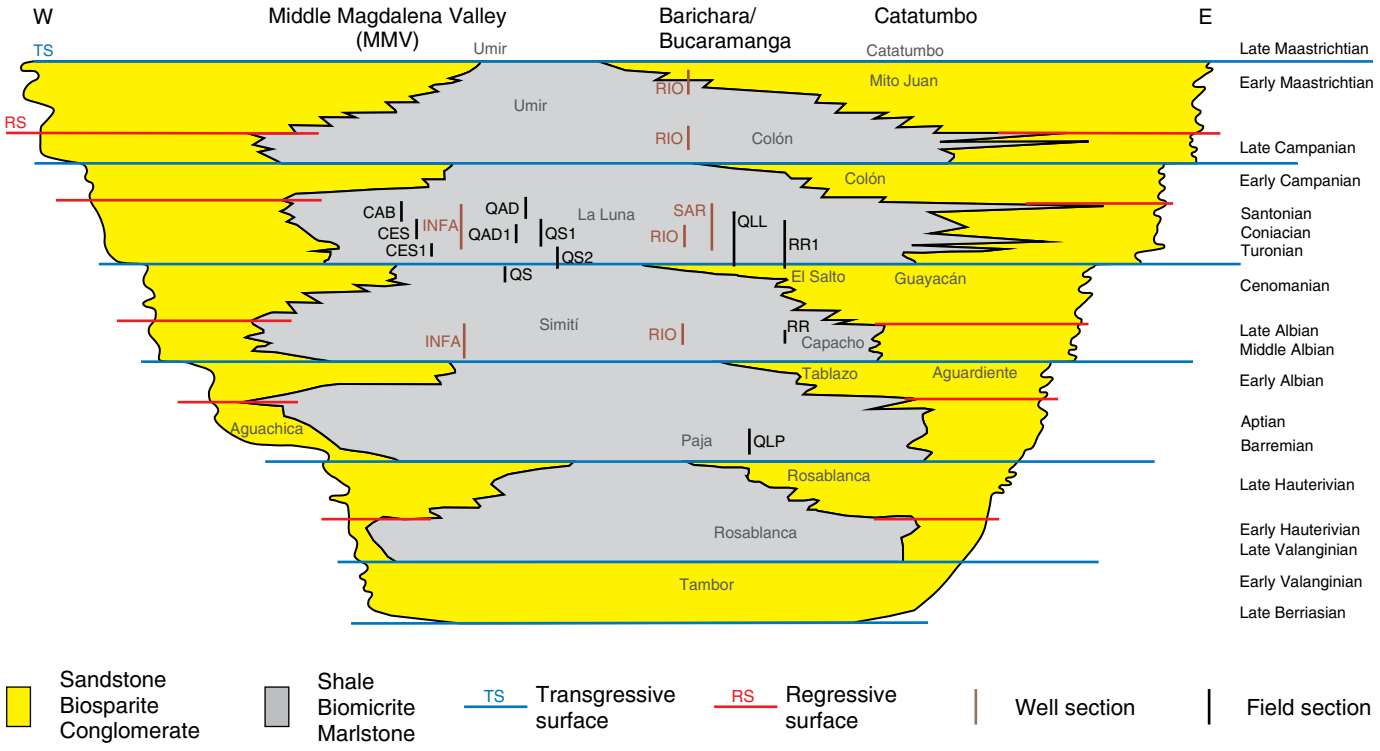

Figure 2. Sections studied in the N sector of the basin, including the Middle Magdalena Valley, Barichara/Bucaramanga, and Catatumbo areas. Modified from Guerrero (2002a).

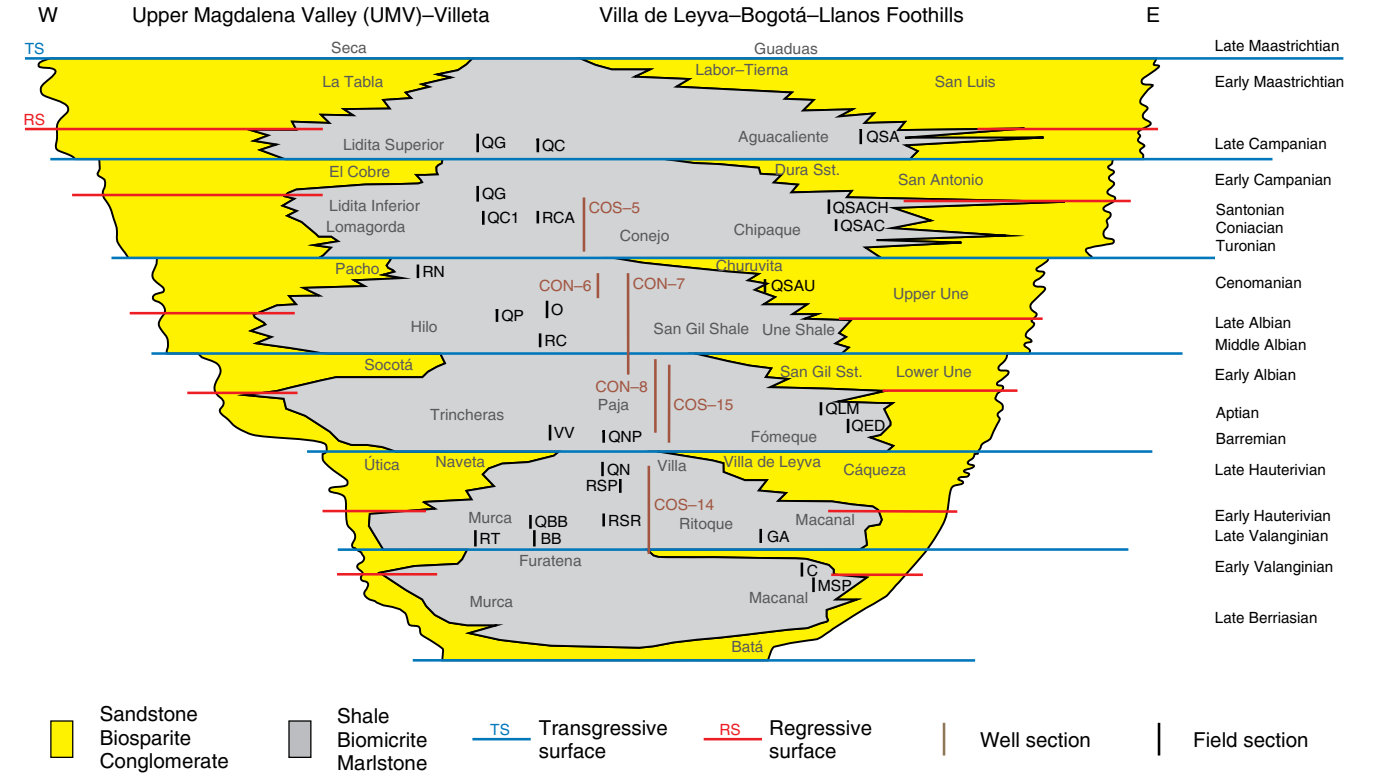

Figure 3. Sections studied in the S sector of the basin, including the Eastern and Western Emerald belts and the Villeta, Villa de Leyva, and Bogotá areas. Modified from Guerrero (2002a).

Table 1. Location of field sections.

Sample	Section	Area	Formation	Age	Latitude N	Longitude W
BB–00	Buriburi	CEOC	Furatena (Lower)	Berriasian – early Hauterivian	5° 40' 28.931"	74° 03' 54.439"
BB–10	Buriburi	CEOC	Furatena (Lower)	Berriasian – early Hauterivian	5° 40' 27.833"	74° 03' 53.743"
C–00	Cachipay	CEOR	Macanal	Berriasian – early Hauterivian	4° 52' 24.791"	73° 14' 18.525"
C–48	Cachipay	CEOR	Macanal	Berriasian – early Hauterivian	4° 52' 23.458"	73° 14' 16.868"
CAB–00	Agua Blanca Creek	Aguachica	La Luna (Upper)	Coniacian to Santonian	8° 13' 28.226"	73° 32' 07.428"
CAB–128	Agua Blanca Creek	Aguachica	La Luna (Upper)	Coniacian to Santonian	8° 13' 25.764"	73° 32' 11.248"
CAB–130	Agua Blanca Creek	Aguachica	Umir (Lower)	Early Campanian	8° 13' 25.725"	73° 32' 11.306"
CES–00	El Salto Creek	Aguachica	La Luna	Turonian to Santonian	8° 12' 08.312"	73° 31' 18.000"
CES–82	El Salto Creek	Aguachica	La Luna	Turonian to Santonian	8° 12' 05.444"	73° 31' 20.457"
CES1–00	El Salto Creek	Aguachica	La Luna	Turonian to Santonian	8° 12' 08.911"	73° 31' 13.229"
CES1–20	El Salto Creek	Aguachica	La Luna	Turonian to Santonian	8° 12' 08.853"	73° 31' 13.827"
GA–00	Gachalá	CEOR	Macanal	Berriasian – early Hauterivian	4° 41' 44.416"	73° 29' 43.044"
GA–62	Gachalá	CEOR	Macanal	Berriasian – early Hauterivian	4° 41' 45.454"	73° 29' 46.375"
MSP–00	M. San Pedro	CEOR	Macanal	Berriasian – early Hauterivian	4° 51' 23.858"	73° 22' 28.851"
MSP–36	M. San Pedro	CEOR	Macanal	Berriasian – early Hauterivian	4° 51' 24.804"	73° 22' 30.268"
O–00	Otanche	CEOC	Hilo	Middle and late Albian	5° 42' 50.420"	74° 11' 54.956"
O–96	Otanche	CEOC	Hilo	Middle and late Albian	5° 42' 49.222"	74° 11' 51.865"
QAD–00	Aguadulce Creek	Barichara	La Luna	Turonian to Santonian	7° 11' 06.173"	73° 17' 40.617"
QAD–77	Aguadulce Creek	Barichara	La Luna	Turonian to Santonian	7° 11' 06.670"	73° 17' 43.550"
QAD1–00	Aguadulce Creek 1	Barichara	La Luna	Turonian to Santonian	7° 11' 18.134"	73° 17' 32.182"
QAD1–60	Aguadulce Creek 1	Barichara	La Luna	Turonian to Santonian	7° 11' 18.037"	73° 17' 34.405"
QBB–00	Buriburi Creek	CEOC	Furatena (Lower)	Berriasian – early Hauterivian	5° 40' 36.746"	74° 03' 41.176"
QBB–12	Buriburi Creek	CEOC	Furatena (Lower)	Berriasian – early Hauterivian	5° 40' 36.717"	74° 03' 40.604"
QC–00	Cobre Creek	CEOC	Lidita Inferior	Late Santonian	5° 41' 41.386"	74° 12' 27.255"
QC–50	Cobre Creek	CEOC	Lidita Inferior	Late Santonian	5° 41' 39.970"	74° 12' 26.572"
QC1–00	Cobre Creek 1	CEOC	Lomagorda	Turonian to Santonian	5° 42' 04.020"	74° 12' 27.205"
QC1–54	Cobre Creek 1	CEOC	Lomagorda	Turonian to Santonian	5° 42' 02.266"	74° 12' 25.176"
QED–00	El Dátil Creek	CEOR	Fómeque	Barremian and Aptian	5° 01' 54.296"	73° 20' 25.292"
QED–36	El Dátil Creek	CEOR	Fómeque	Barremian and Aptian	5° 01' 55.929"	73° 20' 24.462"
QG–00	Guate Creek	Villeta	Lidita Inf.	Late Santonian	4° 53' 59.292"	74° 32' 03.307"
QG–137	Guate Creek	Villeta	Lidita Inf.	Late Santonian	4° 54' 01.026"	74° 32' 08.472"
QG–251	Guate Creek	Villeta	Lidita Sup.	Late Campanian	4° 54' 00.408"	74° 32' 13.807"
QG–292	Guate Creek	Villeta	Lidita Sup.	Late Campanian	4° 54' 00.354"	74° 32' 15.777"
QLL–00	La Leche Creek	Catatumbo	Guayacán	Cenomanian	8° 08' 56.797"	72° 41' 31.315"
QLL–02	La Leche Creek	Catatumbo	Guayacán	Cenomanian	8° 08' 57.311"	72° 41' 30.412"
QLL–04	La Leche Creek	Catatumbo	La Luna	Turonian to Santonian	8° 08' 57.822"	72° 41' 29.509"
QLL–63	La Leche Creek	Catatumbo	La Luna	Turonian to Santonian	8° 09' 09.873"	72° 41' 14.692"
QLM–00	Los Micos Creek	CEOR	Fómeque	Barremian and Aptian	5° 04' 22.882"	73° 24' 53.983"
QLM–53	Los Micos Creek	CEOR	Fómeque	Barremian and Aptian	5° 04' 20.588"	73° 24' 57.524"
QLP–00	La Paja Creek	Barichara	Paja	Barremian and Aptian	7° 01' 26.468"	73° 20' 04.444"
QLP–66	La Paja Creek	Barichara	Paja	Barremian and Aptian	7° 01' 25.114"	73° 20' 08.359"
QN–00	Negra Creek	CEOC	Villa de Leyva	Late Hauterivian	5° 35' 40.402"	73° 30' 02.088"

Table 1. Location of field sections (*continued*).

Sample	Section	Area	Formation	Age	Latitude N	Longitude W
QN–10	Negra Creek	CEOC	Villa de Leyva	Late Hauterivian	5° 35' 39.696"	73° 30' 02.193"
QNP–00	Negra Creek	CEOC	Paja	Barremian and Aptian	5° 35' 38.593"	73° 29' 56.222"
QNP–34	Negra Creek	CEOC	Paja	Barremian and Aptian	5° 35' 37.967"	73° 29' 54.923"
QP–00	Piñal Creek	Villeta	Hilo	Middle and late Albian	4° 52' 25.191"	74° 30' 09.671"
QP–465	Piñal Creek	Villeta	Hilo	Middle and late Albian	4° 52' 06.673"	74° 29' 55.123"
QS–00	La Sorda Creek	Barichara	El Salto	Cenomanian	7° 09' 38.294"	73° 18' 05.373"
QS–16	La Sorda Creek	Barichara	El Salto	Cenomanian	7° 09' 38.753"	73° 18' 05.597"
QS1–02	La Sorda Creek 1	Barichara	La Luna (Lower)	Turonian	7° 09' 50.411"	73° 18' 04.775"
QS1–36	La Sorda Creek 1	Barichara	La Luna (Lower)	Turonian	7° 09' 48.200"	73° 18' 06.301"
QS2–00	La Sorda Creek 2	Barichara	El Salto	Cenomanian	7° 09' 57.080"	73° 18' 00.931"
QS2–20	La Sorda Creek 2	Barichara	El Salto	Cenomanian	7° 09' 58.418"	73° 18' 01.340"
QS2–22	La Sorda Creek 2	Barichara	La Luna (Lower)	Turonian	7° 09' 58.552"	73° 18' 01.379"
QS2–52	La Sorda Creek 2	Barichara	La Luna (Lower)	Turonian	7° 10' 00.565"	73° 18' 01.991"
QSA–00	San Antonio Creek	CEOR	Aguacaliente	Late Campanian	4° 50' 15.031"	73° 12' 25.203"
QSA–100	San Antonio Creek	CEOR	Aguacaliente	Late Campanian	4° 50' 11.838"	73° 12' 25.178"
QSAC–00	S. Antonio Creek C	CEOR	Chipaque	Turonian to Santonian	4° 50' 34.658"	73° 12' 23.685"
QSAC–48	S. Antonio Creek C	CEOR	Chipaque	Turonian to Santonian	4° 50' 33.001"	73° 12' 23.408"
QSACH–00	S. Antonio Creek Ch	CEOR	Chipaque	Turonian to Santonian	4° 50' 27.921"	73° 12' 24.635"
QSACH–30	S. Antonio Creek Ch	CEOR	Chipaque	Turonian to Santonian	4° 50' 26.784"	73° 12' 24.231"
QSAU–00	S. Antonio Creek U	CEOR	Une (Upper)	Late Cenomanian	4° 51' 13.714"	73° 12' 14.776"
QSAU–18	S. Antonio Creek U	CEOR	Une (Upper)	Late Cenomanian	4° 51' 13.752"	73° 12' 14.292"
RC–00	Contador River	Villeta	Hilo (Lower)	Middle Albian	4° 52' 59.887"	74° 31' 09.813"
RC–44	Contador River	Villeta	Hilo (Lower)	Middle Albian	4° 52' 59.100"	74° 31' 08.615"
RCA–00	Cañas River	Villeta	Conejo	Turonian to Santonian	4° 56' 31.704"	74° 16' 10.733"
RCA–80	Cañas River	Villeta	Conejo	Turonian to Santonian	4° 56' 28.080"	74° 16' 02.777"
RN–00	Negro River	CEOC	Pacho	Cenomanian	5° 17' 35.949"	74° 04' 43.213"
RN–112	Negro River	CEOC	Pacho	Cenomanian	5° 17' 33.238"	74° 04' 52.281"
RR–02	Riecito River	Catatumbo	Capacho	Middle and late Albian	8° 03' 02.089"	72° 48' 26.230"
RR–20	Riecito River	Catatumbo	Capacho	Middle and late Albian	8° 03' 05.512"	72° 48' 26.056"
RR1–00	Riecito River 1	Catatumbo	Guayacán	Cenomanian	8° 03' 30.022"	72° 48' 26.355"
RR1–10	Riecito River 1	Catatumbo	Guayacán	Cenomanian	8° 03' 30.158"	72° 48' 27.350"
RR1–18	Riecito River 1	Catatumbo	La Luna	Turonian to Santonian	8° 03' 30.265"	72° 48' 28.150"
RR1–60	Riecito River 1	Catatumbo	La Luna	Turonian to Santonian	8° 03' 30.834"	72° 48' 32.337"
RSP–00	Samacá River	CEOC	Villa de Leyva	Late Hauterivian	5° 35' 19.005"	73° 30' 44.572"
RSP–32	Samacá River	CEOC	Villa de Leyva	Late Hauterivian	5° 35' 17.562"	73° 30' 43.650"
RSR–00	Samacá River	CEOC	Ritoque	Late Valanginian – early Hauterivian	5° 35' 30.385"	73° 30' 54.584"
RSR–34	Samacá River	CEOC	Ritoque	Late Valanginian – early Hauterivian	5° 35' 31.205"	73° 30' 51.049"
RT–00	Tobia River	Villeta	Murca (Lower)	Berriasian – early Hauterivian	5° 04' 16.218"	74° 26' 44.287"
RT–62	Tobia River	Villeta	Murca (Lower)	Berriasian – early Hauterivian	5° 04' 14.781"	74° 26' 40.134"
VV–00	Caiquero	Villeta	Trincheras	Barremian and Aptian	5° 03' 51.475"	74° 24' 41.054"
VV–89	Caiquero	Villeta	Trincheras	Barremian and Aptian	5° 03' 47.484"	74° 24' 32.936"

Table 2. Location of wells.

Sample	Well	Area	Formation	Age	Latitude N	Longitude W
CON–06–360	ANH–CON–06	CEOC	Churuvita	Cenomanian	5° 44' 26.202"	73° 44' 14.826"
CON–06–1470	ANH–CON–06	CEOC	Churuvita	Cenomanian	5° 44' 26.202"	73° 44' 14.826"
CON–07–134	ANH–CON–07	CEOC	Churuvita	Cenomanian	5° 49' 30.758"	73° 41' 47.587"
CON–07–240	ANH–CON–07	CEOC	Churuvita	Cenomanian	5° 49' 30.758"	73° 41' 47.587"
CON–07–485	ANH–CON–07	CEOC	San Gil Shale	Middle and late Albian	5° 49' 30.758"	73° 41' 47.587"
CON–07–1810	ANH–CON–07	CEOC	San Gil Shale	Middle and late Albian	5° 49' 30.758"	73° 41' 47.587"
CON–07–1880	ANH–CON–07	CEOC	San Gil Sandstone	Early Albian	5° 49' 30.758"	73° 41' 47.587"
CON–07–2420	ANH–CON–07	CEOC	San Gil Sandstone	Early Albian	5° 49' 30.758"	73° 41' 47.587"
CON–08–287	ANH–CON–08	CEOC	San Gil Sandstone	Early Albian	5° 57' 12.630"	73° 36' 31.512"
CON–08–1310	ANH–CON–08	CEOC	San Gil Sandstone	Early Albian	5° 57' 12.630"	73° 36' 31.512"
CON–08–1376	ANH–CON–08	CEOC	Paja	Barremian and Aptian	5° 57' 12.630"	73° 36' 31.512"
CON–08–2575	ANH–CON–08	CEOC	Paja	Barremian and Aptian	5° 57' 12.630"	73° 36' 31.512"
COS–05–261	ANH–COS–05	Villa de Leyva	Conejo	Turonian to Santonian	5° 31' 54.705"	73° 49' 49.929"
COS–05–1059	ANH–COS–05	Villa de Leyva	Conejo	Turonian to Santonian	5° 31' 54.705"	73° 49' 49.929"
COS–14–370	ANH–COS–14	Villa de Leyva	Villa de Leyva	Late Hauterivian	5° 35' 01.356"	73° 31' 30.586"
COS–14–650	ANH–COS–14	Villa de Leyva	Villa de Leyva	Late Hauterivian	5° 35' 01.356"	73° 31' 30.586"
COS–14–678	ANH–COS–14	Villa de Leyva	Ritoque	Late Valanginian – early Hauterivian	5° 35' 01.356"	73° 31' 30.586"
COS–14–1506	ANH–COS–14	Villa de Leyva	Ritoque	Late Valanginian – early Hauterivian	5° 35' 01.356"	73° 31' 30.586"
COS–15–893	ANH–COS–15	Villa de Leyva	San Gil Sandstone	Early Albian	5° 32' 37.037"	73° 38' 06.689"
COS–15–1323	ANH–COS–15	Villa de Leyva	San Gil Sandstone	Early Albian	5° 32' 37.037"	73° 38' 06.689"
COS–15–1330	ANH–COS–15	Villa de Leyva	Paja	Barremian and Aptian	5° 32' 37.037"	73° 38' 06.689"
COS–15–2220	ANH–COS–15	Villa de Leyva	Paja	Barremian and Aptian	5° 32' 37.037"	73° 38' 06.689"
INFA–4727	Infantas–1613	MMV	La Luna	Turonian to Santonian	6° 55' 38.423"	73° 46' 43.388"
INFA–6243	Infantas–1613	MMV	La Luna	Turonian to Santonian	6° 55' 38.423"	73° 46' 43.388"
INFA–6396	Infantas–1613	MMV	El Salto	Cenomanian	6° 55' 38.423"	73° 46' 43.388"
INFA–6472	Infantas–1613	MMV	El Salto	Cenomanian	6° 55' 38.423"	73° 46' 43.388"
INFA–6480	Infantas–1613	MMV	Simití	Middle and late Albian	6° 55' 38.423"	73° 46' 43.388"
INFA–8840	Infantas–1613	MMV	Simití	Middle and late Albian	6° 55' 38.423"	73° 46' 43.388"
INFA–8650	Infantas–1613	MMV	Tablazo	Early Albian	6° 55' 38.423"	73° 46' 43.388"
INFA–9358	Infantas–1613	MMV	Paja	Barremian and Aptian	6° 55' 38.423"	73° 46' 43.388"
INFA–9364	Infantas–1613	MMV	Paja	Barremian and Aptian	6° 55' 38.423"	73° 46' 43.388"
RIO–3496	Río de oro–14	Catatumbo	Mito Juan	Early Maastrichtian	9° 05' 37.499"	72° 54' 04.926"
RIO–4220	Río de oro–14	Catatumbo	Mito Juan	Early Maastrichtian	9° 05' 37.499"	72° 54' 04.926"
RIO–4780	Río de oro–14	Catatumbo	Colón (Lower)	Early Campanian	9° 05' 37.499"	72° 54' 04.926"
RIO–5392	Río de oro–14	Catatumbo	Colón (Lower)	Early Campanian	9° 05' 37.499"	72° 54' 04.926"
RIO–5768	Río de oro–14	Catatumbo	La Luna	Turonian to Santonian	9° 05' 37.499"	72° 54' 04.926"
RIO–5775	Río de oro–14	Catatumbo	La Luna	Turonian to Santonian	9° 05' 37.499"	72° 54' 04.926"
RIO–6259	Río de oro–14	Catatumbo	Capacho	Middle and late Albian	9° 05' 37.499"	72° 54' 04.926"
SAR–7336	Sardinata–n2	Catatumbo	La Luna	Turonian to Santonian	8° 30' 15.474"	72° 39' 04.879"
SAR–7460	Sardinata–n2	Catatumbo	La Luna	Turonian to Santonian	8° 30' 15.474"	72° 39' 04.879"

sponds to La Luna Formation in the Aguachica area; the lowest content (0.2% TOC) is from the Ritoque Formation in the Villa de Leyva area.

Thermal maturity values are derived from vitrinite reflectance and pyrolysis. The limestones include Ro data that have at least 10 particles of vitrinite per sample. The shales include Ro data that have at least 40 particles of vitrinite per sample. Thermal maturity from pyrolysis comes from reliable Tmax values from samples with more than 0.2 mg HC/g at S2.

The Ro values from La Luna Formation are in the oil and early gas generation windows (0.8–1.3 % Ro). The highest thermal maturity values obtained from pyrolysis are from the Upper Cretaceous Oliní Group (2.4–2.8 % Ro) and Conejo Formation (2.9% Ro). The highest thermal maturity values obtained from vitrinite are from the Lower Cretaceous Murca, Trincheras, and Hilo Formations from the Villeta area (4.0–4.2 % Ro) and the Paja Formation from the Villa de Leyva area (4.3% Ro).

Table 4 shows the average values of gas collected in the 200 canister samples cored from field exposures, along with the TOC average values per section. The samples with the highest TOC and gas contents in the upper part of the table are from La Luna, Guayacán, Hilo, and Paja Formations. The values correspond to total gas, which includes lost and desorbed gas before fracturing and grinding the rock and residual gas after these procedures. Total gas includes hydrocarbons, CO_2, nitrogen, and oxygen. The results are ordered by gas content.

Table 5 displays the gas chromatography results with the best sample of each section in terms of the highest contents of gaseous hydrocarbons released in the 200 canister tests, along with the averages of TOC and Ro per section. The table includes the contents of the most abundant gases, including methane, ethane, and propane. The results are ordered by the total percentage of gas hydrocarbons; the highest ones are in the upper part of the table and correspond to La Luna, Lidita Inferior, Lidita Superior, Hilo, Guayacán, and Paja Formations.

Table 6 presents the samples with the highest volumes of hydrocarbons, along with the residual versus desorbed gas ratio and the CO_2 content. The results from a total of 200 samples are ordered by hydrocarbon percentage. The highest values in the upper part of the table correspond to La Luna, Lidita Inferior, Lidita Superior, Hilo, Guayacán, and Paja Formations.

Table 7 shows the porosity and permeability average values per section, along with the average gas hydrocarbon content. The results from a total of 500 samples are ordered by porosity values; the lowest ones are in the upper part of the table and correspond to the units with the highest hydrocarbon content.

Table 8 displays the pyrolysis results, along with the TOC and thermal maturity values per section. The samples are ordered by the average content of hydrocarbons released at the S2 peak. The TOC averages included in the table are those of the 500 samples processed for pyrolysis and are in general higher than those compiled in Table 3, which correspond to the total 1500 samples of the study. This is because the samples with higher TOC from each section were chosen for the pyrolysis analysis.

4. Discussion

4.1. TOC and Thermal Maturity

The best values of TOC and thermal maturity are found in the biomicrites and diagenetic cherts of La Luna Formation, the Hilo Formation, and the Oliní Group, from the N and W sides of the basin (Figures 4–7; Tables 3–5).

The Ro values obtained from vitrinite reflectance and pyrolysis data (Figures 6, 7; Table 3) are present in two lithological groups, calcareous and terrigenous, which have very different properties in terms of maturity and TOC contents. Because the particles of vitrinite are of terrigenous origin, the rocks that contain more analyzed points and yield more reliable results are the mudstones and shales that have higher contents of clay minerals and organic matter of terrestrial origin. In this shale (and marlstone) group, the San Gil Superior Shale from well CON–7 and the Paja Formation from wells CON–8 and COS–15 are notable because they have between 40 and 70 vitrinite particles analyzed.

The biomicrites, as well as the biosparites and siltstones with low amounts of terrigenous mud, are placed in the other group, with very few or no particles of vitrinite. The most notable rocks of this group are the foraminiferal biomicrites of La Luna Formation, which have very few particles, usually 1 or 2 per sample, and do not produce reliable average Ro results. In these rocks, the pyrolysis results yield a better approximation of thermal maturity. The biomicrites of the Hilo and Lomagorda Formations, along with the Oliní Group, also have very few vitrinite particles, approximately 3 to 6 on average. For instance, there is a huge difference between the vitrinite (0.8% Ro) and pyrolysis (2.4–2.8 % Ro) values of the Oliní Group due to the scarcity of vitrinite particles. A few siltstones, muddy sandstones, and biosparites interbedded in the Ritoque (well COS–14), Churuvita (well CON–6), and Conejo Formations (well COS–5) are also good examples of nonreliable thermal maturity values from vitrinite.

The best TOC results are those of La Luna Formation biomicrite (Turonian to Santonian TST and HST), which has averages per section between 4.9 and 11.6% TOC. These averages are even higher than the 4–8 % TOC averages compiled by Kennedy et al. (2016) from the prolific Eagle Ford biomicrite of Texas, which has the same age as La Luna Formation and is currently producing nonconventional oil and gas. Very high individual values were obtained from samples at caño El Salto (CES–1) from Aguachica (21.7% TOC), Aguadulce Creek (QAD) from the W foothills of the Eastern Cordillera (18.2% TOC), and caño Aguablanca (CAB) also from Aguachica

Table 3. TOC vs. Thermal maturity.

Formation	Alloformation age	Stratigraphic section	Area	TOC average (%)	Ro average (%) Vitrin – Pyrol
La Luna	Turonian to Santonian	CES1	Aguachica	11.6	PYR 0.8
Guayacán	Cenomanian	QLL	Catatumbo	8.7	PYR 1.2
La Luna	Turonian to Santonian	CES	Aguachica	8.6	PYR 0.8
La Luna	Turonian to Santonian	QS2	Barichara	8.6	PYR 0.9
La Luna	Turonian to Santonian	RIO–14	Catatumbo	8.1	VIT 0.3 PYR 1.0
La Luna	Turonian to Santonian	SAR–N2	Catatumbo	7.7	VIT 1.0 PYR 1.3
La Luna	Turonian to Santonian	RR1	Catatumbo	7.2	VIT 0.8 PYR 1.1
La Luna	Turonian to Santonian	QS1	Barichara	7	VIT 0.4 PYR 0.9
La Luna	Turonian to Santonian	QAD1	Barichara	6.5	VIT 0.4 PYR 0.8
La Luna	Turonian to Santonian	QLL	Catatumbo	6.1	VIT 0.6 PYR 1.2
Hilo	Middle and late Albian	QP	Villeta	5.8	VIT 4.0
Paja	Barremian and Aptian	QNP	Villa de Leyva	5.8	VIT 3.1
La Luna	Turonian to Santonian	INFAN–1613	Middle Magdalena Valley	5.6	PYR 0.9
La Luna	Turonian to Santonian	QAD	Barichara	5.4	VIT 0.4 PYR 0.8
Furatena (lower section)	Berriasian to early Hauterivian	QBB	W Emerald B	5.3	VIT 3.1
Hilo	Middle and late Albian	O	W Emerald B	5.3	VIT 3.5
Hilo	Middle and late Albian	RC	Villeta	4.9	VIT 3.4
La Luna	Turonian to Santonian	CAB	Aguachica	4.9	PYR 0.8
Lomagorda	Turonian to Santonian	QC1	UMV–W Foothills	4.5	VIT 2.4
Furatena (lower section)	Berriasian to early Hauterivian	BB	W Emerald B	4.4	VIT 3.1
Paja	Barremian and Aptian	QLP	Barichara	3.8	PYR 1.9
Guayacán	Cenomanian	RR1	Catatumbo	3.7	PYR 1.1
Trincheras	Barremian and Aptian	VV	Villeta	3.5	VIT 4.0
Lidita Superior	Late Campanian	QG	UMV–Villeta	3.1	VIT 0.8 PYR 2.4
Lidita Inferior	Late Santonian	QC	UMV–W Foothills	3	VIT 2.4
Lidita Inferior	Late Santonian	QG	UMV–Villeta	2.7	VIT 0.8 PYR 2.8
Paja	Barremian and Aptian	CON–8	Villa de Leyva	2.7	VIT 3.1
El Salto	Cenomanian	QS2	Barichara	2.4	PYR 0.9
San Gil Sandstone	Early Albian	CON–8	Villa de Leyva	2.4	VIT 2.5
Paja	Barremian and Aptian	COS–15	Villa de Leyva	2.3	VIT 4.3
Macanal	Berriasian to early Hauterivian	GA	E Emerald B	2.1	VIT 3.7
San Gil Sandstone	Early Albian	COS–15	Villa de Leyva	1.9	VIT 3.8
Villa de Leyva	Late Hauterivian	COS–14	Villa de Leyva	1.8	VIT 3.4
Conejo	Turonian to Santonian	COS–5	Villa de Leyva	1.7	VIT 2.9
Conejo	Turonian to Santonian	RCA	Villeta	1.6	PYR 2.9
Murca (lower Section)	Berriasian to early Hauterivian	RT	Villeta	1.4	VIT 4.2
San Gil Shale	Middle and late Albian	CON–7	Villa de Leyva	1.4	VIT 2.6
San Gil Sandstone	Early Albian	CON–7	Villa de Leyva	1.2	VIT 3.2
El Salto	Cenomanian	QS	Barichara	1.1	PYR 0.9
Capacho	Middle and late Albian	RR	Catatumbo	0.8	PYR 1.2
Churuvita	Cenomanian	CON–7	Villa de Leyva	0.7	VIT 2.5
Chipaque	Turonian to Santonian	QSACH	Llanos Foothills	0.6	PYR 0.6
Une (upper section)	Cenomanian	QSAU	Llanos Foothills	0.6	PYR 0.9
Chipaque	Turonian to Santonian	QSAC	Llanos Foothills	0.5	PYR 0.6
Churuvita	Cenomanian	CON–6	Villa de Leyva	0.5	VIT 2.2
Aguacaliente	Late Campanian	QSA	Llanos Foothills	0.4	PYR 0.6
Ritoque	Berriasian to early Hauterivian	COS–14	Villa de Leyva	0.2	VIT 3.9

Table 4. Gas content vs. TOC.

Formation	Alloformation Age	Stratigraphic Section	Area	Total Gas (feet³/ton)	TOC (%)
Guayacán	Cenomanian	RR1	Catatumbo	16.18	3.7
La Luna	Turonian to Santonian	QS2	Barichara	15.63	8.6
La Luna	Turonian to Santonian	RR1	Catatumbo	14.59	7.2
Murca (lower section)	Berriasian to early Hauterivian	RT	Villeta	14.42	1.4
Capacho	Middle and late Albian	RR	Catatumbo	13.74	0.8
Furatena (lower section)	Berriasian to early Hauterivian	BB	W Emerald B	13.68	4.4
La Luna	Turonian to Santonian	CAB	Aguachica	13.51	4.9
El Salto	Cenomanian	QS2	Barichara	13.01	2.4
Paja	Barremian and Aptian	QLP	Barichara	12.89	3.8
Lidita Inferior	Late Santonian	QC	UMV–W foothills	12.51	3
La Luna	Turonian to Santonian	CES1	Aguachica	12.04	11.6
Hilo	Middle and late Albian	O	W Emerald B	11.84	5.3
La Luna	Turonian to Santonian	QAD1	Barichara	11.67	6.5
Une (upper section)	Cenomanian	QSAU	Llanos Foothills	11.63	0.6
La Luna	Turonian to Santonian	CES	Aguachica	11.59	8.6
Villa de Leyva	Late Hauterivian	RSP	Villa de Leyva	11.48	1.3
Macanal	Berriasian to early Hauterivian	GA	E Emerald B	10.9	2.1
La Luna	Turonian to Santonian	QS1	Barichara	10.3	7
Chipaque	Turonian to Santonian	QSACH	Llanos Foothills	9.91	0.6
La Luna	Turonian to Santonian	QAD	Barichara	9.1	5.4
La Luna	Turonian to Santonian	QLL	Catatumbo	9.02	6.1
Macanal	Berriasian to early Hauterivian	C	E Emerald B	8.89	1.4
Aguacaliente	Late Campanian	QSA	Llanos Foothills	8.5	0.4
Hilo	Middle and late Albian	QP	Villeta	8.47	5.8
Chipaque	Turonian to Santonian	QSAC	Llanos Foothills	7.8	0.5
Ritoque	Berriasian to early Hauterivian	RSR	Villa de Leyva	7.79	0.6
Trincheras	Barremian and Aptian	VV	Villeta	7.67	3.5
Fómeque	Barremian and Aptian	QLM	E Emerald B	7.43	1.1
Macanal	Berriasian to early Hauterivian	MSP	E Emerald B	7.34	0.6
Conejo	Turonian to Santonian	RCA	Villeta	7.33	1.6
Fómeque	Barremian and Aptian	QED	E Emerald B	6.93	1.4
Lidita Superior	Late Campanian	QG	UMV–Villeta	6.46	3.1
Hilo	Middle and late Albian	RC	Villeta	6.39	4.9
Guayacán	Cenomanian	QLL	Catatumbo	6.25	8.7
Lidita Inferior	Late Santonian	QG	UMV–Villeta	6.23	2.7
El Salto	Cenomanian	QS	Barichara	5.52	1.1
Villa de Leyva	Late Hauterivian	QN	Villa de Leyva	4.88	0.8
Paja	Barremian and Aptian	QNP	Villa de Leyva	4.78	5.8

(13.9% TOC). The Ro maturity values of La Luna Formation (from Tmax) are also excellent, between 0.8 and 1.3%, in the oil and early gas generation windows.

The TOC average percentages presented here from 212 samples of La Luna Formation, collected from 9 field sections

Figure 4. Distribution of average TOC values per section from 1500 samples. The highest percentages are on the N and W sides of the basin.

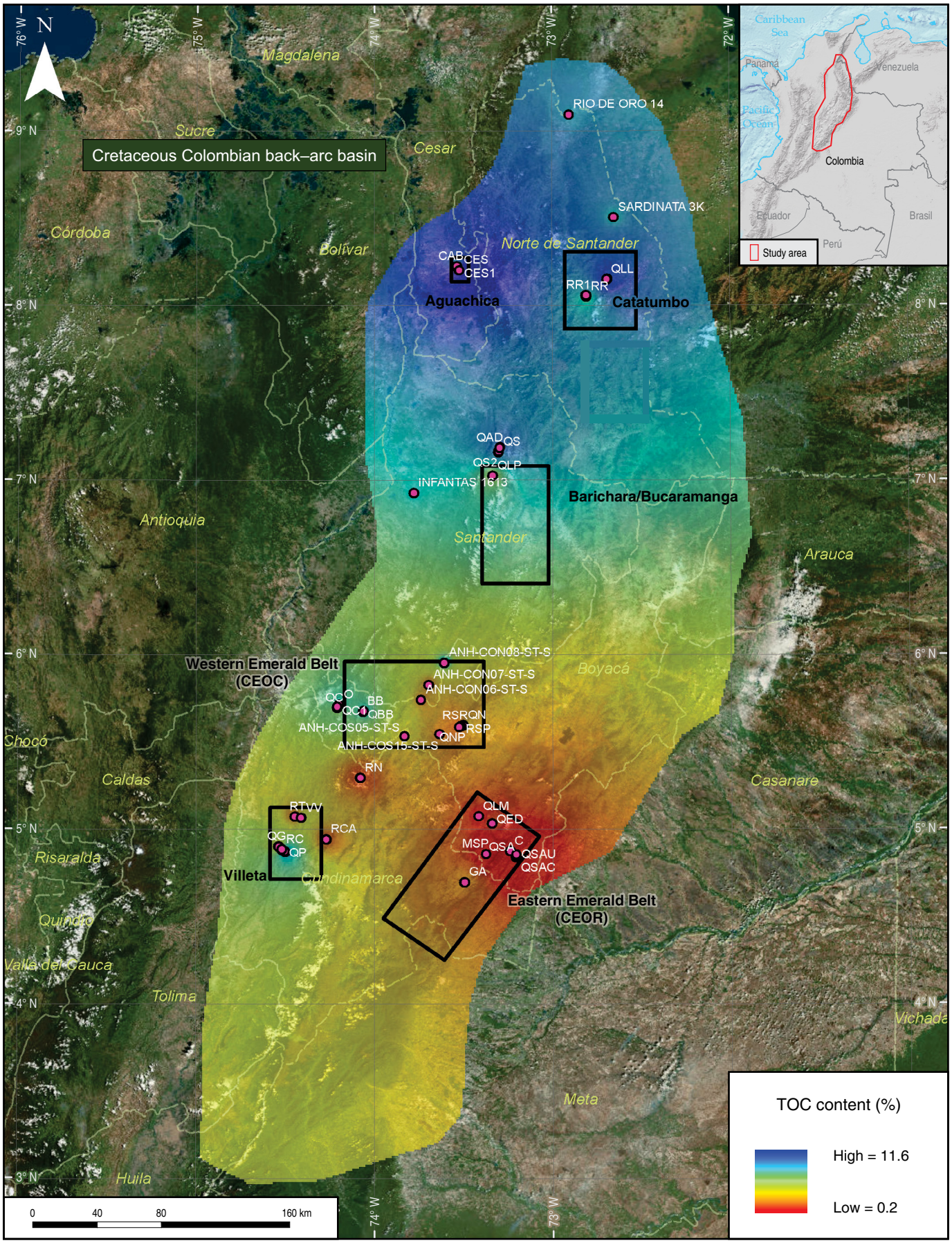
N
Cretaceous Colombian back–arc basin
Magdalena
Sucre
Cesar
Córdoba
Bolívar
Norte de Santander
Antioquia
Santander
Arauca
Boyacá
Chocó
Caldas
Casanare
Risaralda
Cundinamarca
Quindío
Valle del Cauca
Tolima
Meta
Huila
Vichada
RIO DE ORO 14
SARDINATA 3K
CAB
CES
CES1
Aguachica
QLL
RR1
RR
Catatumbo
QAD
QS
QS2
QLP
INFANTAS 1613
Barichara/Bucaramanga
ANH-CON08-ST-S
ANH-CON07-ST-S
ANH-CON06-ST-S
Western Emerald Belt
(CEOC)
QCO
BB
CC4
QBB
RSRQN
RSP
ANH-COS05-ST-S
QNP
ANH-COS15-ST-S
RN
RTW
RCA
QGRC
QP
Villeta
QLM
QED
MSP
QSA
C
QSAU
QSAC
GA
Eastern Emerald Belt
(CEOR)
76° W
75° W
74° W
73° W
72° W
9° N
8° N
7° N
6° N
5° N
4° N
3° N
0
40
80
160 km
Caribbean Sea
Panamá
Venezuela
Pacific Ocean
Colombia
Ecuador
Brasil
Perú
Study area
TOC content (%)
High = 11.6
Low = 0.2

and three wells (Table 3), are also higher than the 4.0% TOC documented by Liborius & Slatt (2014) from 20 data points from a well in the Maracaibo area of Venezuela and higher than the values of 4.3% TOC (Zumberge, 1984) and 4.0% TOC (Casadiego & Rios, 2016) from exposures W of Bucaramanga. Torres et al. (2015) also reported values as high as 11.9% TOC from an area W of Bucaramanga, but the average of 34 data points appears to be approximately 2.5% TOC. Galvis–Portilla et al. (2014) reported TOC data from a 120–feet interval of a well in the Middle Magdalena Valley (MMV), with 11 values between 1.3 and 5.3% TOC and an average of approximately 3.0% TOC. Veiga & Dzelalija (2014) reported TOC values between 2 and 5% TOC with thermal maturity from 0.8–1.3 % Ro from Catatumbo and between 2 and 6% TOC with thermal maturity from 0.5–1.3 % Ro from the MMV, which match our maximum thermal maturity results but are below our TOC averages. Most of the TOC values from La Luna in the Catatumbo area compiled by Aguilera et al. (2010) are in the range of 4–6 % TOC, with 10 points between 6 and 8% TOC, which are within the range of the 6.1–8.1 % TOC averages presented here from 80 samples from the Cúcuta/Catatumbo area; most of their thermal maturity values are between 0.8 and 1.5% Ro. Aguilera et al. (2010) also compiled data from the MMV, showing that most TOC data points are between 2 and 4% TOC, with 7 samples between 4 and 6% TOC, which are lower than the 4.9–11.6 % TOC averages presented here; most of their Ro values are between 0.6–0.9 % Ro with a few between 0.9–1.3 % Ro, which present a wider range than the 0.8–0.9 % Ro presented here for the MMV from 132 samples (Table 3).

Most of the Turonian to Santonian limestones of the basin, including La Luna and Lomagorda Formations, are biomicrites of planktonic foraminifera (Figure 5) deposited in a deep–sea offshore environment, between 150 and 200 m depths, and far from terrigenous sources. Centimeter–scale chert beds are present as a diagenetic transformation of these biomicrites. There are also minor amounts of impure biomicrites (10–35 % clay minerals and silt–sized quartz particles) and minor amounts of marlstones (a nearly equal mixture of calcareous and terrigenous mud particles), as indicated by the petrography, XRD, and ICP–MS chemical analysis (Guerrero et al., 2000, 2020). In general, the Lomagorda and La Luna Formations have very little contribution of terrigenous material, including clay minerals, silt–sized quartz particles, and vitrinite particles.

Other rock names, such as "fossiliferous claystone", "siliceous claystone", "calcareous claystone", "fossiliferous shale", "siliceous shale", "calcareous shale", "argillaceous limestone", "siliceous mudstone", "argillaceous mudstone", "calcareous mudstone", and so on, have been inaccurately used for La Luna Formation and are either the result of inappropriate rock classification or misidentification of the unit.

In the first case, concerning inappropriate rock classification, the dark–colored, organic–rich calcareous mud matrix

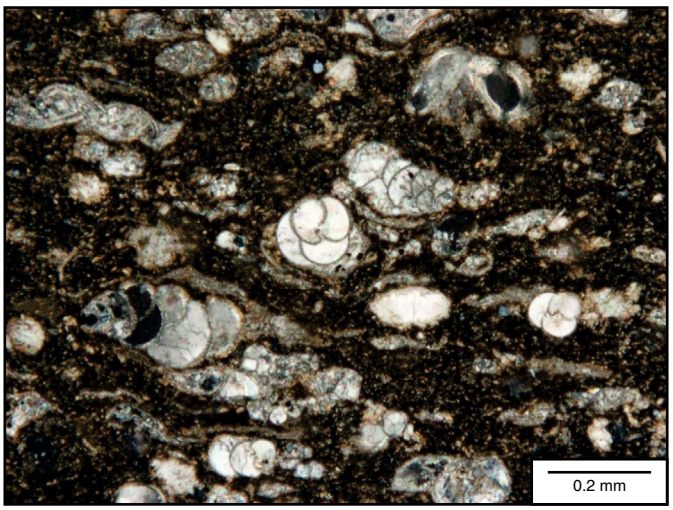

Figure 5. Thin section photograph of a silicified biomicrite (sample QAD–20) from La Luna Formation at the Aguadulce Creek W of Bucaramanga. Large foraminifera have a length of 100 to 200 µm. The matrix is composed of organic matter and quartz–replaced calcareous mud (silt– and clay–sized fragments of foraminifera and calcareous algae). The sample contains 5% terrigenous mud (clay minerals and silt–sized quartz particles), 60% diagenetic quartz, and 35% calcite.

(fragments of foraminifera, calcareous algae, and coccoliths), and the diagenetically silicified chert matrix, are erroneously identified as terrigenous claystones and/or mudstone shales, although in those rocks, the only observable framework particles in the petrographic microscope are foraminifera, fish bones, and fecal pellets in the range of coarse silt and sand–sized bioclasts. The petrography and the chemical ICP–MS and XRD analysis of these rocks indicate a dominance of calcite and quartz (diagenetic quartz instead of terrigenous quartz), with very little or no clay minerals.

In the second case, concerning the misidentification of the unit, the shale beds of the upper part of the Simití Formation were erroneously included in the "salada" and "pujamana" members of La Luna Formation at a proposed type locality (Morales et al., 1958) W of Bucaramanga, where La Luna biomicrite and the Simití shale are in faulted contact. Since then, researchers have tried to identify three members in La Luna Formation, creating difficulties in the identification of the unit and major correlation problems; for example, Casadiego & Rios (2016) indicated that the "pujamana" member of other authors corresponds to the "galembo" member at the Aguablanca section W of Bucaramanga. The enormous thickness of approximately 3000 feet from cores reported by Galvis–Portilla et al. (2014) also suggests that the authors may have included strata from more than one unit in their definition of La Luna Formation. The thickness of the Turonian to Santonian limestones exposed at the type locality of La Luna Formation in Venezuela and in the rest of the basin in Colombia (Guerrero,

2002b) reaches a maximum measured thickness of 700 to 900 feet, so it is difficult to believe that the unit could reach 2500 to 3000 feet in oil wells.

Other rocks laterally adjacent (on the same Turonian to Santonian TST and HST facies belts) have maturity data slightly lower in the early oil generation window, such as the Chipaque Formation shales of the Llanos Foothills (0.6% Ro), but very low contents of organic matter (0.5–0.6 % TOC).

The Conejo Formation, which is located closer to the center of the basin than the Chipaque Formation, has much higher thermal maturity, between 2.6 and 2.9% Ro (well COS–5), in the late generation gas window, with TOC values between 1.6 and 1.7%, which are also somewhat low. However, one sample from La Frontera Member in the lower part of the Conejo Formation at the COS–5 well had the highest TOC (24.8%) of the whole study.

Toward the west, the Lomagorda Formation from the Cobre Creek (QC1) in the W foothills of the Eastern Cordillera has maturity values of approximately 2.4% Ro, which are also in the late generation gas window, but has average values of TOC (4.5%) comparable with the lowest values of La Luna Formation. The highest content from the Lomagorda Formation in the study area was 7.4% TOC. Veiga & Dzelalija (2014) reported TOC values from 5 wells of the Lomagorda Formation in the UMV (they used the name "la luna") of between 1.45 and 2.75% TOC. However, the enormous reported thicknesses in some wells (up to 2650 feet) and the absence of the Lidita Inferior and Lidita Superior of the Oliní Group introduces doubts regarding the identification of the units. Aguilera et al. (2010) compiled values between 1 and 9% TOC from the Lomagorda Formation of the UMV (they also used the name "la luna") with immature organic matter showing values below 0.5% Ro.

The late Santonian Lidita Inferior Unit has essentially the same lithology as the Lomagorda Formation (biomicrites of planktonic foraminifera) but is partially replaced by diagenetic quartz (Guerrero et al., 2000) due to its proximity with the regressive terrigenous strata of Campanian age (middle part of the Oliní Group). The TOC average values of the Lidita Inferior are between 2.7 (QG) and 3.0% (QC); the highest TOC of the Lidita Inferior at the Cobre Creek was 6.8%.

The biomicrites, diagenetic cherts, marlstones, and shales of the middle and late Albian transgressive and high sea level intervals (Tetuán, Hilo, San Gil Superior, Simití, and Capacho) present significant differences in terms of TOC and Ro. The best TOC values correspond to the Hilo Formation, whose averages are very good and range from 4.9–5.8 % TOC, but the unit is apparently overmature, with Ro vitrinite values between 3.4 and 4.0%. The highest TOC of the Hilo Formation was 12.1% at the Otanche (O) section. The San Gil Superior Shale of well CON–7 is on the late gas generation window (2.6% Ro), but it has a low average value of TOC (1.4%). The Capacho Formation of the Catatumbo area is in the early gas generation window (1.2% Ro) and has a low content of organic matter (0.8% TOC). Veiga & Dzelalija (2014) reported TOC values of the Tetuán Formation between 1.78 and 4.42% TOC from 5 wells of the UMV. Aguilera et al. (2010) also compiled abundant data between 2–10 % TOC and 0.5–0.8 % Ro from the Tetuán Formation.

Units of Barremian and Aptian transgressive and high sea levels (Paja, Fómeque, and Trincheras Formations) have acceptable values for TOC, between 2.3 and 5.8% but are generally overmature, with values between 3.1 and 4.3% Ro in wells CON–8 and COS–15. There is, however, an interesting exception at the type locality of the Paja Formation in the W foothills of the Eastern Cordillera, where it has 3.8% TOC and 1.9% Ro, putting it in the gas generation window.

The oldest units of the succession, in the Berriasian to Hauterivian interval, are even more overmature, with 3.7% Ro in the Macanal Formation from Gachalá (GA), 4.2% Ro in the Murca Formation of the Tobia River (RT), 3.9% Ro in the Ritoque Formation from COS–14 well, and 3.4% Ro in the overlying Villa de Leyva Formation in the same well COS–14.

In general, biomicrites of foraminifera have much higher contents of TOC than shales, so that instead of gas shales, the gas biomicrites constitute a far better target. Because biomicrites have lower clay contents (down to zero) than claystone and mudstone shales, it is expected that the biomicrites have a more brittle behavior than shales during the process of fracking. In addition, the plastic behavior of the clay shales will more easily close the induced fractures than the brittle behavior of the biomicrite limestones.

Thermal maturity values in the oil and early gas windows are good in the E and W borders and very good in the N side of the basin, where it opened to the proto–Caribbean. The strata from the axis of the basin are thermally overmature, especially in the areas proximal to the gabbroic intrusions and associated hydrothermal activity, which increased the thermal gradient during the Berriasian to Cenomanian main extension of the back–arc basin (Guerrero et al., 2020).

4.2. Gas Content in Canister Samples

The volumes of gas released from 200 canister samples taken from field exposures are compared with the TOC and Ro values of several formations (Figures 8, 9; Tables 5, 6). Airtight cylindrical containers of metal (canisters) were used to collect and measure gases in drilled cores of approximately 1 foot in length and 1.6–inch diameter, taken at a depth of 3 m below the surface. Most of the units measured are from transgressive and high sea level (TST and HST) biomicrites, marlstones, and shales, with some exceptions in regressive sea level (RST) shale units.

Gas chromatography revealed the presence of methane, ethane, propane, isobutane, butane, neopentane, isopentane, pentane, and hexane. In most of the samples studied, methane

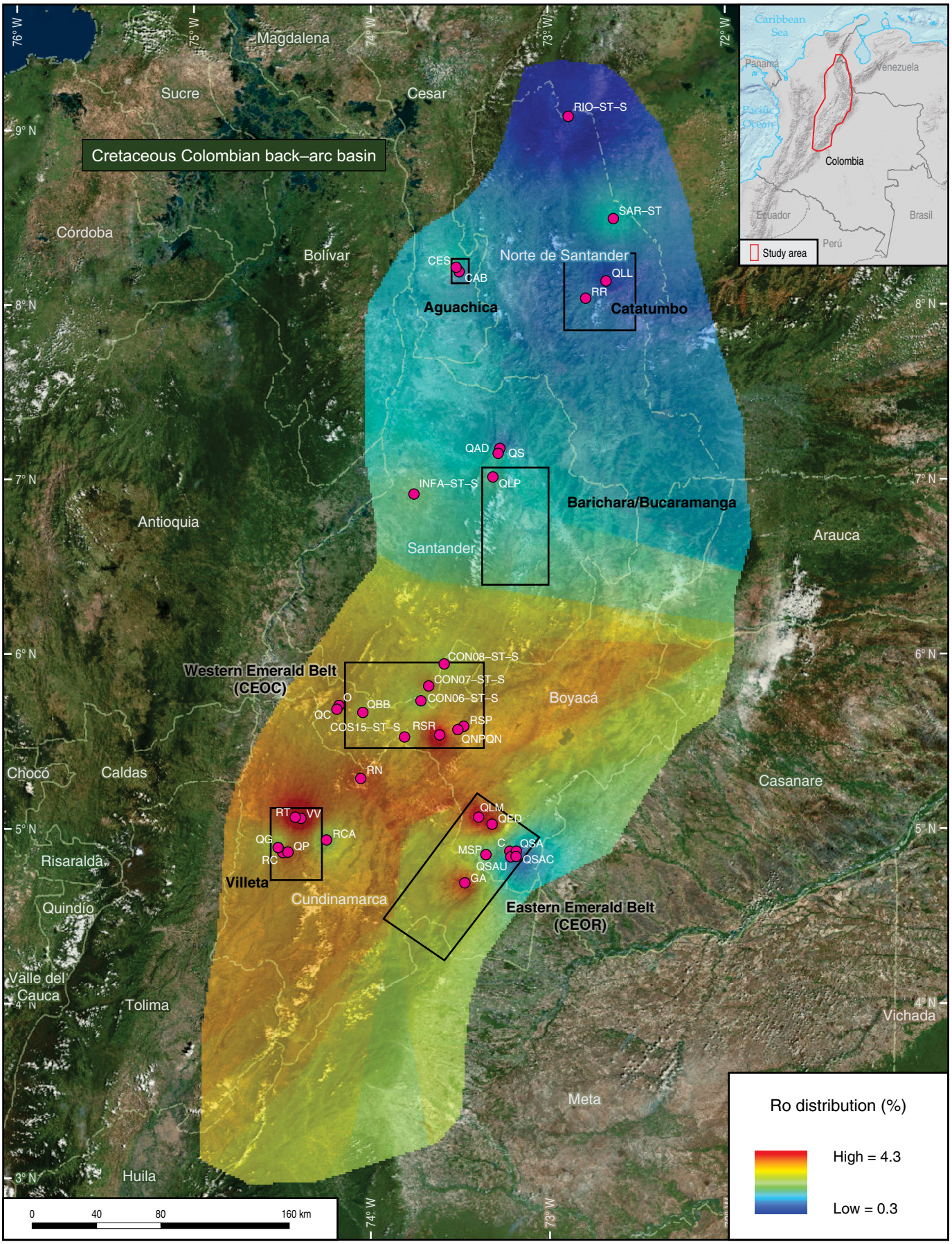
Cretaceous Colombian back–arc basin
Magdalena
Sucre
Cesar
Córdoba
Bolívar
Norte de Santander
Antioquia
Santander
Arauca
Boyacá
Casanare
Chocó
Caldas
Risaralda
Quindío
Valle del Cauca
Tolima
Cundinamarca
Meta
Huila
Vichada
Aguachica
Catatumbo
Barichara/Bucaramanga
Western Emerald Belt (CEOC)
Eastern Emerald Belt (CEOR)
Villeta
RIO–ST–S
SAR–ST
CES
CAB
QLL
RR
QAD
QS
INFA–ST–S
QLP
CON08–ST–S
CON07–ST–S
CON06–ST–S
QBB
QC
COS15–ST–S
RSR
RSP
QNP
QN
RN
RT
VV
RCA
QG
QP
RC
QLM
QED
MSP
C
QSA
QSAC
QSAU
GA
9° N
8° N
7° N
6° N
5° N
4° N
3° N
76° W
75° W
74° W
73° W
72° W
Caribbean Sea
Panamá
Venezuela
Pacific Ocean
Colombia
Ecuador
Perú
Brasil
Study area
0
40
80
160 km
Ro distribution (%)
High = 4.3
Low = 0.3

Figure 6. Distribution of thermal maturity (vitrinite reflectance) average values per section. The strata of the N area of the basin have lower thermal maturity than those of the central and SW areas. 1500 samples.

constitutes the main volume of gaseous hydrocarbons (Figures 9, 10; Table 5), followed by ethane and propane. All samples also contained a mixture of nitrogen and oxygen obtained from air exposure near the surface. This mixture varies between 19 and 91% of the total gases collected, so many samples had high contents of air instead of gaseous hydrocarbons; the samples with the highest air contamination (nitrogen and oxygen) were the shales of the Ritoque, Villa de Leyva, Paja, Macanal, Fómeque, Chipaque, and Aguacaliente Formations. CO_2 was also present in significant volumes that reached 15.3%, with the highest percentages obtained in samples of the Conejo, El Salto, La Luna, Macanal, Fómeque, Une, Chipaque, Aguacaliente, Murca, Trincheras, and Hilo Formations.

Samples with the lowest CO_2 contents (3.0–11.5 %) were associated with the highest hydrocarbon contents (15.0–77.8 %), which include the limestones and cherts of La Luna, Lidita Inferior, Lidita Superior, Hilo, Guayacán, and Paja Formations (Figure 11; Table 6). The results are important because although these rocks have lost important amounts of gas during uplift fracturing and have also been near the surface for some time, they still contain hydrocarbons stored in micropores and microfossil cavities.

Notably, gas contents are present in the biomicrites of La Luna Formation (TST and HST of the Turonian to Santonian time span), with average contents of total gas per section between 9.02 and 15.63 cubic feet per ton (feet^3/ton). The best sample of the whole study (QLL–40 from La Leche Creek) released 5.10 feet^3/ton of hydrocarbons, corresponding to 77.8% of its total gas content.

Additionally, in these areas, the TOC average values per section are excellent, ranging from 11.6% in El Salto Creek (CES1) in the Aguachica area, 8.6% in La Sorda Creek (QS2) in the Barichara area, and 7.2% in the Riecito River (RR1) in the Cúcuta area. In addition to the very high averages per section, individual samples have amazing organic carbon contents that range from 21.7 (sample CES1–02 from the Aguachica area) to 18.2% TOC (sample QAD–64 from the Barichara area) and 11.1% TOC (sample RR1–30 from the Cúcuta area).

In contrast, laterally adjacent units composed mainly of mudstone and shale have very low contents of gaseous hydrocarbons and TOC, such as the Chipaque Formation of the Llanos Foothills, which only reaches 0.5% TOC (QSAC) and 0.6% TOC (QSACH) in San Antonio Creek, with maximum hydrocarbon contents of 0.004% to 0.1%. The Conejo Formation at the Cañas River (RCA) in the Villeta area is slightly better, with a maximum 3.3% gaseous hydrocarbon content and TOC average of 1.6%. The three units belong to the same interval of time (Turonian to Santonian), constitute source rock and still contain hydrocarbons, but the biomicrites of La Luna Formation are much richer in TOC and release more gaseous hydrocarbons than the shales of the other units. Therefore, La Luna Formation constitutes the most promising unit for unconventional hydrocarbons, not only because of its high content of gas and its very high content of TOC but also because the biomicrite limestones break better and maintain open fractures better than muddy units with high contents of clay minerals. The mudstones and shales do not break easily due to their plastic behavior, and the induced fractures close more quickly than in the biomicrites.

The Guayacán Formation (Cenomanian) from the Cúcuta area also presents high values of hydrocarbons and TOC. Total gaseous hydrocarbons comprise up to 27.2% of the gases measured (6.25 feet^3/ton), with a TOC average of 8.7% (QLL). The highest TOC value (9.4%) of the unit is from sample RR1–02 at the Riecito River. The Guayacán Formation is a regressive unit (RST) that contains shales similar to those of the underlying Capacho Formation (TST and HST of the middle and late Albian) but differs by its content of minor interbedding of bivalve biosparites and arenites deposited in a progradational set of offshore to shoreface parasequences. The upper part of the Guayacán Formation can also serve as a conventional reservoir filled with hydrocarbons generated by the Capacho Formation and the lower part of the Guayacán Formation. The seal of this reservoir is made by the biomicrites and marlstones of La Luna Formation.

Other units that deserve special mention are the late Santonian to Campanian biomicrites and cherts of the Lidita Inferior and Lidita Superior of the Oliní Group from the Guate Creek (QG), west of the Bituima Fault. The highest gaseous hydrocarbon canister contents are between 34.3 and 37.3% of their total gas content (10.47 to 12.71 feet^3/ton), with TOC values between 2.7 and 3.1%. The highest hydrocarbon contents from the Oliní Group were between 3.91 and 4.36 feet^3/ton. The highest methane content of the whole study (4.35 feet^3/ton) comes from sample QG–251 of the Lidita Superior (Figures 9, 10, 12; Table 5). The data of gas released from the Oliní Group are very important because the same units are present over a large area in the UMV, along with other thick biomicrite units, which include the Lomagorda (Turonian to Santonian) and Tetuán (middle and late Albian) Formations.

The biomicrites and cherts of the Hilo Formation (middle and late Albian TST and HST) reached a high value of 1.93 feet^3/ton of hydrocarbons (27.9% out of 6.93 feet^3/ton), with a 4.9% TOC average value at the Contador River (RC) in the Villeta area. At Piñal Creek (QP), the hydrocarbon content reached 7.7%, with a 5.8% TOC average value. At Otanche

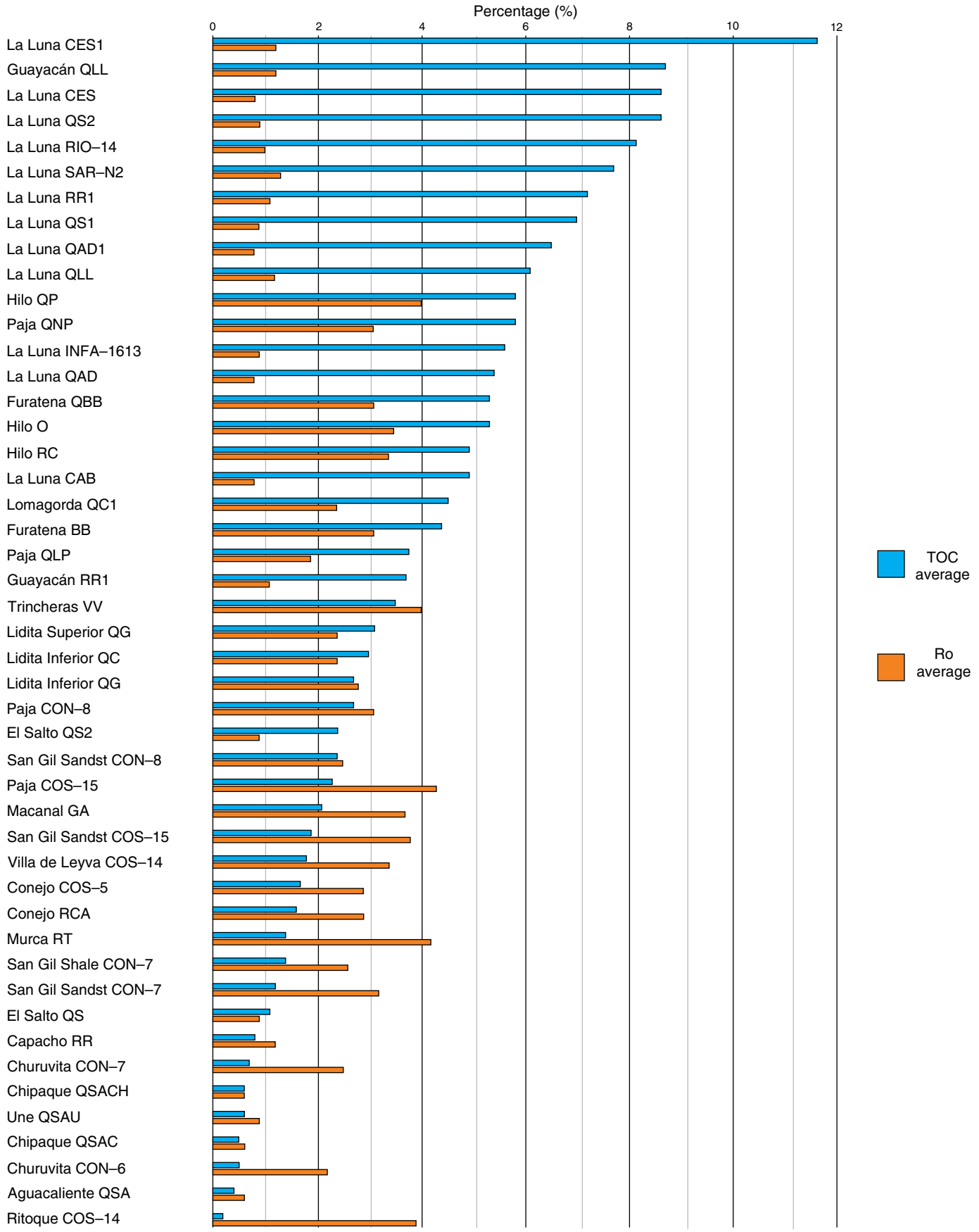
Percentage (%)
0
2
4
6
8
10
12
La Luna CES1
Guayacán QLL
La Luna CES
La Luna QS2
La Luna RIO–14
La Luna SAR–N2
La Luna RR1
La Luna QS1
La Luna QAD1
La Luna QLL
Hilo QP
Paja QNP
La Luna INFA–1613
La Luna QAD
Furatena QBB
Hilo O
Hilo RC
La Luna CAB
Lomagorda QC1
Furatena BB
Paja QLP
Guayacán RR1
Trincheras VV
Lidita Superior QG
Lidita Inferior QC
Lidita Inferior QG
Paja CON–8
El Salto QS2
San Gil Sandst CON–8
Paja COS–15
Macanal GA
San Gil Sandst COS–15
Villa de Leyva COS–14
Conejo COS–5
Conejo RCA
Murca RT
San Gil Shale CON–7
San Gil Sandst CON–7
El Salto QS
Capacho RR
Churuvita CON–7
Chipaque QSACH
Une QSAU
Chipaque QSAC
Churuvita CON–6
Aguacaliente QSA
Ritoque COS–14
TOC average
Ro average

Figure 7. TOC and Ro average values per section. The highest TOC contents (11.6–2.1 %) are from La Luna, Guayacán, Hilo, Paja, Furatena, Lomagorda, Trincheras, Lidita Inferior, Lidita Superior, San Gil Sandstone, and Macanal Formations. The best Ro values (0.8–1.3 %) are from La Luna Formation biomicrites. Number of samples: 1500.

Table 5. Gas chromatography from canisters.

Formation	Sample	Total Gas (feet³/ton)	TOC (%)	Ro (%)	Methane % (mol)	Ethane % (mol)	Propane % (mol)	Total HC % (mol)
La Luna	QLL–40	6.56	6.1	PYR 1.2	30.6	15.1	12.1	77.8
La Luna	RR1–25	6.66	7.2	PYR 1.1	19.8	12.6	5.1	47.9
Lidita Inferior	QG–35	10.47	2.7	PYR 2.8	35.1	1.9	0.3	37.3
Lidita Superior	QG–251	12.71	3.1	PYR 2.4	34.2	0	0	34.3
Hilo	RC–16	6.93	4.9	VIT 3.4	27.8	0.1	0	27.9
Guayacán	QLL–00	6.25	8.7	PYR 1.2	13.6	6.6	3	27.2
La Luna	CES1–00	10.55	11.6	PYR 0.8	4.2	3.7	6.4	18.6
Paja	QLP–36	12.61	3.8	PYR 1.9	15.4	1.4	0.2	17.3
Lidita Inferior	QC–13	19.19	3	VIT 2.4	14.6	0.2	0	14.8
La Luna	CES–51	9.34	8.6	PYR 0.8	3.5	2	4.7	13.4
La Luna	CAB–85	12.85	4.9	PYR 0.8	10.6	0	0	10.6
La Luna	QS2–50	15.18	8.6	PYR 0.9	1.8	1.6	2.4	8.5
Hilo	QP–313	13.68	5.8	VIT 4.0	7.7	0	0	7.7
La Luna	QAD–64	8.56	5.4	PYR 0.8	1.6	1	1.9	6.3
La Luna	QAD1–10	13.88	6.5	PYR 0.8	0.9	0.8	1.2	3.7
Conejo	RCA–47	9.66	1.6	PYR 2.9	3.2	0.1	0	3.3
Capacho	RR–00	10.1	0.8	PYR 1.2	0.9	0.2	0.2	1.9
Hilo	O–33	6.02	5.3	VIT 3.5	1.4	0.2	0	1.6
La Luna	QS1–26	8.42	7	PYR 0.9	0.3	0.3	0.4	1.3
Furatena	BB–00	12.8	4.4	VIT 3.1	0.7	0	0	0.7
El Salto	QS2–12	11.6	2.4	PYR 0.9	0.2	0.1	0.2	0.7
Murca (lower section)	RT–29	11.26	1.4	VIT 4.2	0.6	0	0	0.6
Macanal	C–50	8.66	1.4	VIT 2.9	0.5	0	0	0.6
El Salto	QS–03	6.74	1.1	PYR 0.9	0.6	0	0	0.6
Aguacaliente	QSA–93	3.24	0.4	PYR 0.6	0.4	0	0	0.4
Macanal	GA–62	12.42	2.1	VIT 3.7	0.1	0	0.2	0.3
Guayacán	RR1–02	26.55	3.7	PYR 1.1	0.1	0	0	0.2
Macanal	MSP–30	8.67	0.6	VIT 3.0	0.2	0	0	0.2
Trincheras	VV–30	2.2	3.5	VIT 4.0	0.1	0	0	0.2
Une (upper section)	QSAU–19	9.73	0.6	PYR 0.9	0.1	0	0	0.1
Chipaque	QSAC–08	8.38	0.5	PYR 0.6	0.1	0	0	0.1
Fómeque	QED–00	7.22	1.4	VIT 4.2	0.1	0	0	0.1
Fómeque	QLM–00	5.16	1.1	VIT 4.3	0.1	0	0	0.1
Villa de Leyva	RSP–15	12.4	1.3	VIT 3.9	0.004	0	0	0.004
Chipaque	QSACH–22	11.81	0.6	PYR 0.6	0.004	0	0	0.004
Ritoque	RSR–16	9.13	0.6	VIT 3.4	0.004	0	0	0.004
Paja	QNP–06	7.57	5.8	VIT 3.1	0.004	0	0	0.004
Villa de Leyva	QN–00	6.19	0.8	VIT 3.8	0.004	0	0	0.004

Table 6. Gas contents in canister samples (feet³/ton).

Formation	Sample	Lost	Desorbed	Residual	Total Gas	HC (%)	CO_2 (%)	Total HC	Residual vs. desorbed
La Luna	QLL–40	0.15	1.18	5.24	6.56	77.8	3	5.1	4.5
La Luna	RR1–25	0.08	1.29	5.29	6.66	47.9	7.1	3.19	4.1
Lidita Inferior	QG–35	0.01	0.74	9.72	10.47	37.3	8.5	3.91	13.2
Lidita Superior	QG–251	0.08	6.03	6.6	12.71	34.3	8.9	4.36	1.1
Lidita Inferior	QG–25	0	1.11	6.07	7.17	33.1	9.1	2.37	5.5
Hilo	RC–16	0	1.24	5.69	6.93	27.9	9.8	1.93	4.6
La Luna	QLL–17	0.19	1.11	7.73	9.03	27.6	9.8	2.49	7
Guayacán	QLL–00	0.01	1.27	4.96	6.25	27.2	9.9	1.7	3.9
Lidita Inferior	QG–137	0.01	0.27	4.35	4.63	19.6	10.9	0.91	16.1
La Luna	CES1–00	0.17	1.32	9.06	10.55	18.6	11	1.96	6.9
Lidita Inferior	QG–00	0	0.73	6.9	7.63	18.6	9.9	1.42	9.5
Lidita Superior	QG–261	0.02	0.36	5.7	6.08	18.4	8.4	1.12	15.9
Paja	QLP–36	0.04	0.64	11.92	12.61	17.3	11.2	2.18	18.5
La Luna	RR1–60	0	1.79	13.45	15.24	17.2	11.2	2.62	7.5
La Luna	CES1–21	0.02	1.88	10.54	12.44	15	11.5	1.87	5.6
Lidita Inferior	QC–13	0.05	1.04	18.1	19.19	14.8	11.5	2.84	17.4
La Luna	QLL–09	0.04	1.13	7.33	8.5	13.9	11.7	1.18	6.5
La Luna	CES–51	0.26	1.47	7.61	9.34	13.4	11.7	1.25	5.2
Lidita Inferior	QG–128	0	0.58	4.62	5.21	12.8	10	0.67	7.9
Lidita Inferior	QG–12	0.01	5.03	7.75	12.79	11.7	11.4	1.5	1.5
La Luna	QLL–56	0.63	1.88	8.93	11.44	11.3	11.5	1.29	4.7
La Luna	CES1–10	0.28	2.64	12.2	15.11	10.6	12.1	1.6	4.6
La Luna	CAB–85	0.07	1.35	11.44	12.85	10.6	12.1	1.36	8.5
La Luna	QS2–50	0	1.97	13.21	15.18	8.5	12	1.29	6.7
Lidita Inferior	QG–55	0	0.39	3.06	3.45	8.2	12.4	0.28	7.8
Paja	QLP–55	0.03	0.98	8.29	9.31	8	12.4	0.74	8.4
La Luna	CAB–32	0.05	1.3	16.77	18.13	7.8	12.5	1.41	12.9
Hilo	QP–313	0.02	3.83	9.84	13.68	7.7	12.5	1.05	2.6
La Luna	CES–24	0.61	2.22	12.47	15.3	7.6	12.5	1.16	5.6
La Luna	CES–15	0.16	1.77	8.67	10.6	6.9	12.6	0.73	4.9
Paja	QLP–44	0.01	0.86	9.81	10.68	6.8	12.6	0.73	11.4
La Luna	RR1–35	0.16	2.17	12	14.32	6.4	12.7	0.92	5.5
La Luna	QAD–64	0.15	1.34	7.08	8.56	6.3	12.9	0.54	5.3
La Luna	CAB–15	0.13	1.27	6.67	8.07	5.8	12.4	0.47	5.3
La Luna	QS2–38	0.04	1.9	12.33	14.28	4.4	12.9	0.63	6.5
La Luna	QAD–53	0.12	1.13	10.31	11.56	4.4	13.1	0.51	9.2
La Luna	QS2–25	0.02	1.29	16.14	17.45	4.4	13.1	0.77	12.6
La Luna	QAD1–10	0.05	1.12	12.71	13.88	3.7	13.1	0.51	11.4
Conejo	RCA–47	0	0.03	9.63	9.66	3.3	12.7	0.32	367.3
La Luna	QAD1–60	0.28	1.71	10.86	12.85	3	13.2	0.39	6.4
Conejo	RCA–59	0.05	0.21	3.91	4.17	2.1	13.3	0.09	19
Capacho	RR–00	0.26	1.32	8.52	10.1	1.9	11.7	0.19	6.5
Hilo	O–33	0.07	0.81	5.14	6.02	1.6	13.3	0.1	6.4

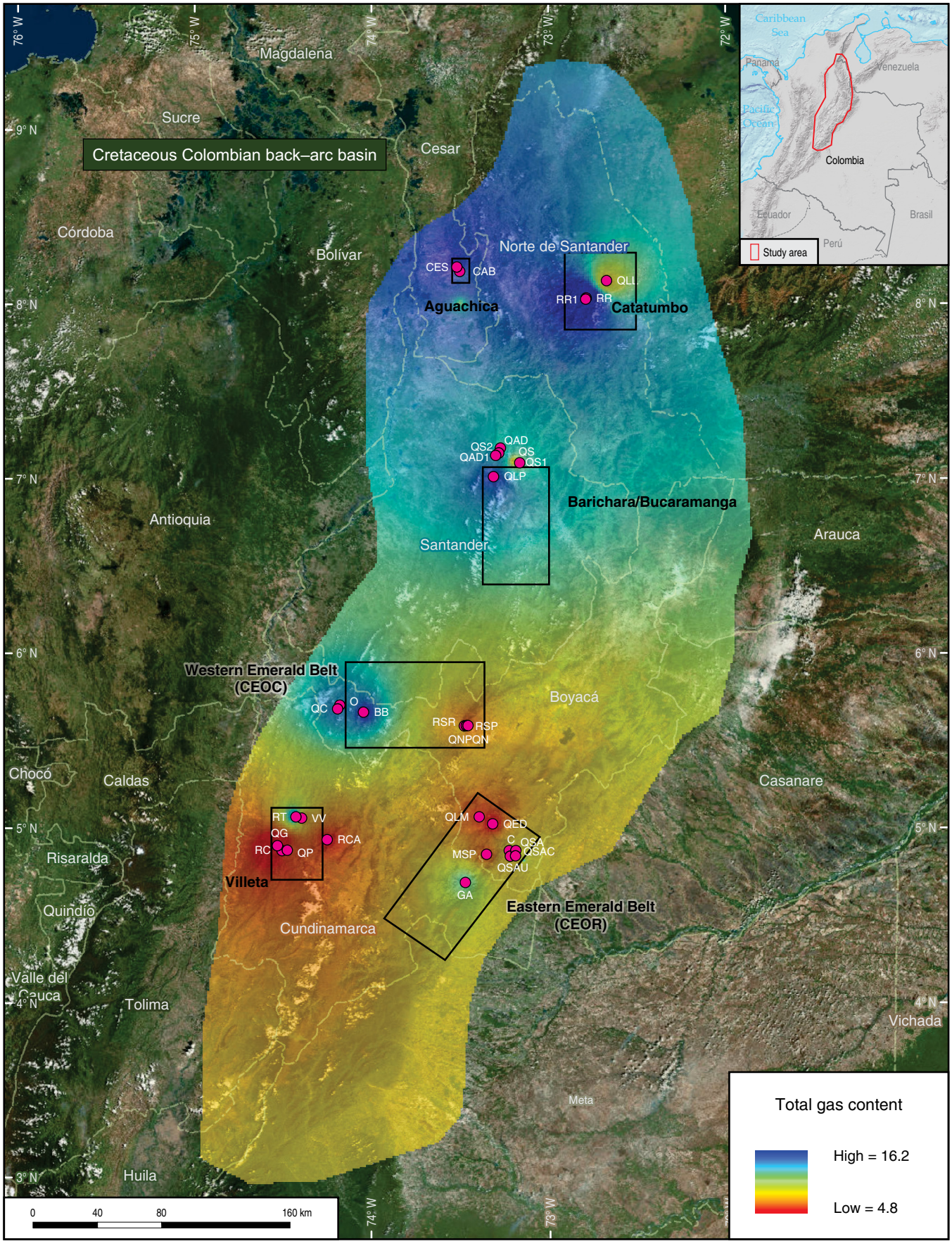

Figure 8. Total gas content average per section (feet³/ton), including hydrocarbons, CO_2, nitrogen, and oxygen. Number of samples: 200.

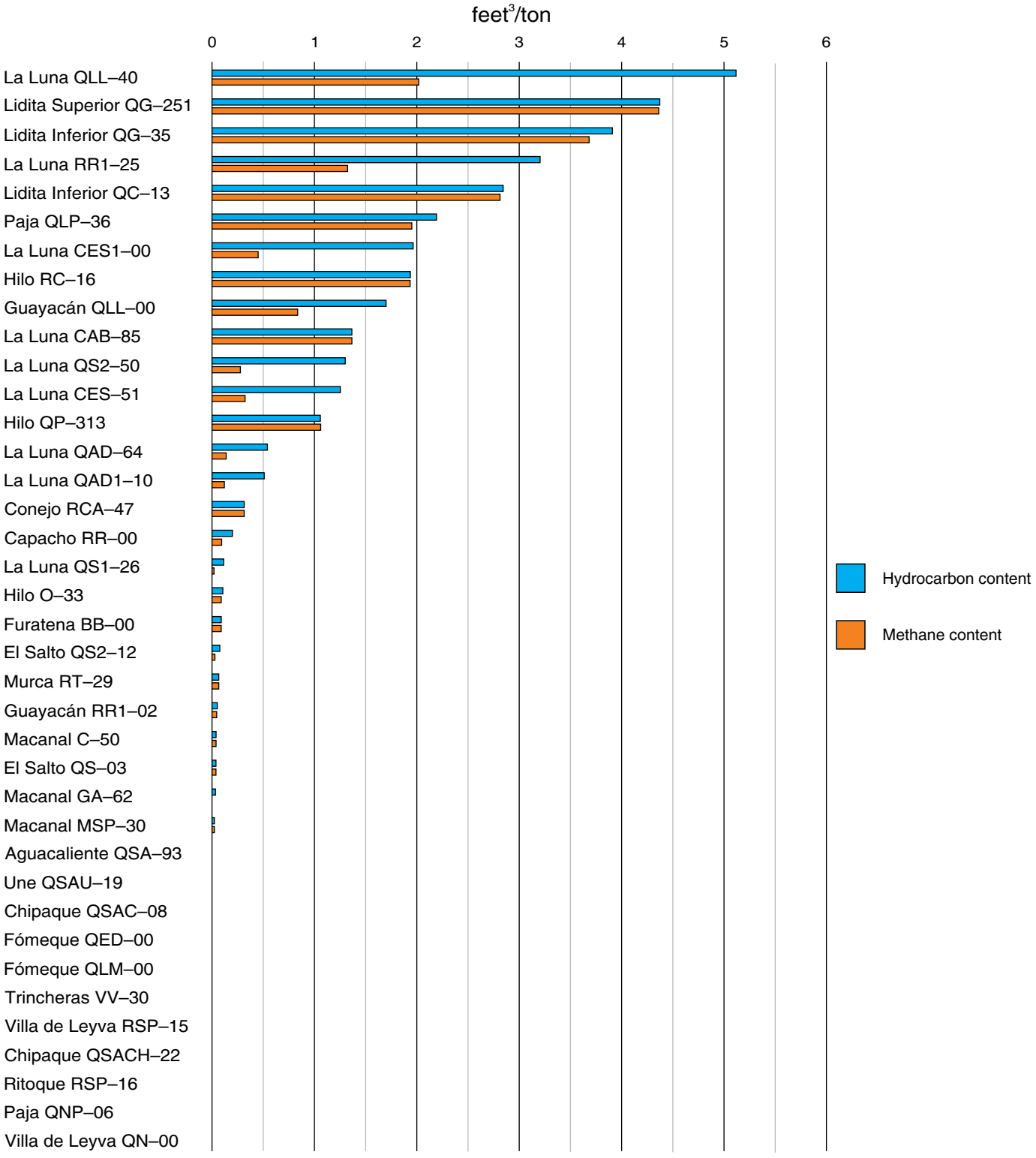

Figure 9. Samples with the highest hydrocarbon volume (feet³/ton), along with their methane content. The best samples are from La Luna, Lidita Superior, Lidita Inferior, Paja, Hilo, and Guayacán Formations.

(O), the hydrocarbon content reached 1.6%, with a 5.3% TOC average. The highest TOC value of the Hilo Formation (12.1%) comes from sample O–10 at the Otanche section. The Capacho Formation shales from the same time span in the Cúcuta area present lower values: 1.9% for the highest hydrocarbon content and only 0.8% TOC average.

The best sample of the Paja Formation (Barremian and Aptian TST and HST) from the type section at the Paja Creek

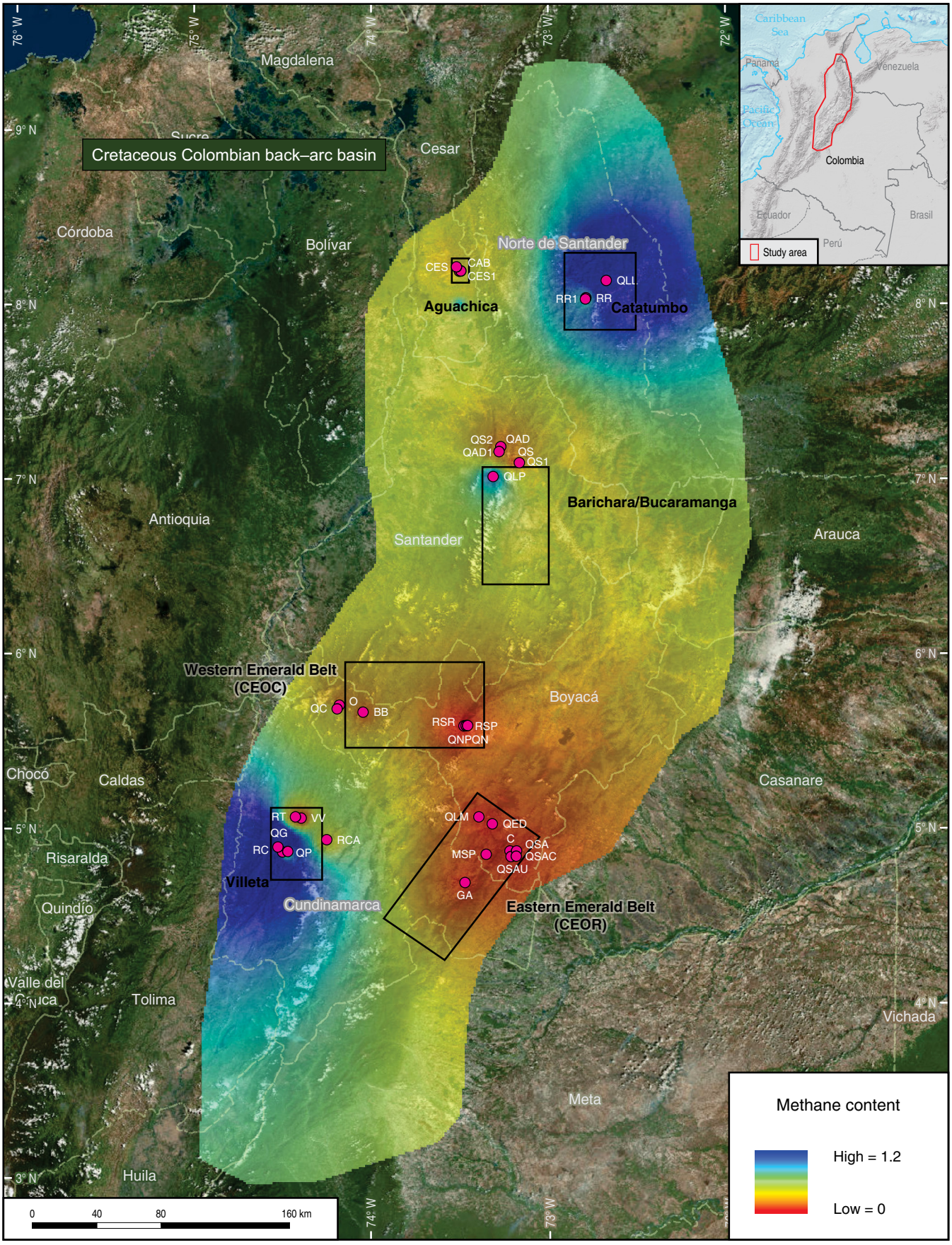

Figure 10. Methane average volumes per section (feet³/ton). Total number of samples: 200.

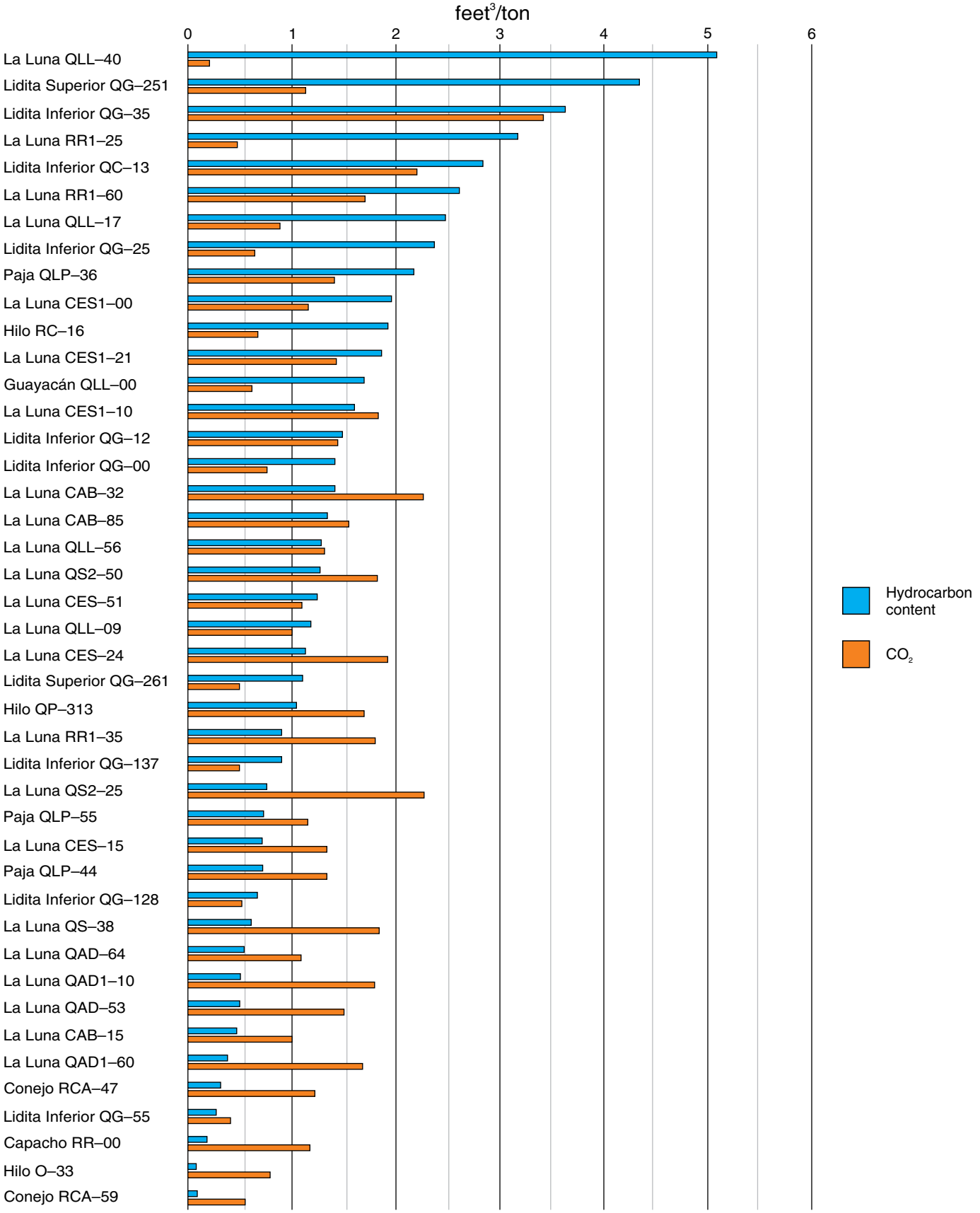

Figure 11. Samples with the highest hydrocarbon volume (feet³/ton), along with their CO_2 content. The best hydrocarbon contents are from La Luna, Lidita Superior, Lidita Inferior, Paja, Hilo, and Guayacán Formations.

(QLP–36) released 12.61 feet^3/ton of gas, of which 17.3% (2.18 feet^3/ton) are hydrocarbons; the average TOC of the section is 3.8%, but the highest value of the unit is 9.7% TOC from sample QLP–08. Thermal maturity from pyrolysis is 1.9%, so the unit is in the gas window.

All the other units had very low percentages of hydrocarbons in the gas contents in the canister measurements, ranging from 0.004 to 0.7% in the Furatena, Murca, Trincheras, Paja, El Salto, Guayacán, Macanal, Fómeque, Une, Chipaque, Aguacaliente, Ritoque, and Villa de Leyva Formations (Figure 9; Table 6). These units are composed mainly of shale, with minor interbedding of marlstone and biomicrite. In most samples, the gas measured was a mixture of oxygen and nitrogen introduced during air exposure close to the surface.

In samples with the highest contents of hydrocarbons from La Luna Formation, the volumes of residual gas released after fracturing the canister samples were always higher (4.1 to 12.9 times, with an average of 6.8 times) than the volumes of gas desorbed before fracturing and milling (Table 6). This means that these rocks still have hydrocarbons stored in micropores and microfossil cavities that can be released by fracturing, simulating the induced fracking process at depth. The sample with the highest volume of hydrocarbons (5.10 feet^3/ton) was QLL–40 from La Luna Formation in the Cúcuta area, which released 4.5 times more residual than desorbed gas. According to ICP–MS elemental analyses and petrography, QLL–40 is a partially silicified biomicrite composed of foraminifera with 65% calcite, 30% quartz, and less than 1% Al_2O_3. Sample RR1–60 from La Luna Formation in the Cúcuta area, which is also a partially silicified biomicrite with 47% calcite, 47% quartz, and less than 2% Al_2O_3, contained a hydrocarbon volume of 2.62 feet^3/ton and a ratio of 7.5 residual versus desorbed gas.

Sample CES1–00 from the Aguachica area, which is a pure biomicrite with 96% calcite and less than 1% Al_2O_3, released a hydrocarbon volume of 1.96 feet^3/ton and had a ratio of 6.9 times residual versus desorbed gas. Samples CAB–85 from Aguachica and QS2–50 from Barichara are partially silicified biomicrites with 75% calcite, 13–15 % quartz, 4–5 % clay minerals, 2–3 % fluorapatite phosphates, 1% ankerite, and 1–2 % pyrite. Sample CAB–85 released gas hydrocarbons in a concentration of 1.36 feet^3/ton and had a ratio of residual versus desorbed gas of 8.5. Sample QS2–50 released 1.29 feet^3/ton and had a ratio of residual versus desorbed gas of 6.7. This means that regardless of the partial replacement of calcite by quartz, La Luna Formation biomicrites and diagenetic cherts (with clay mineral contents below 5%) have similar properties and contain important volumes of hydrocarbons of marine origin.

The best samples of the Lidita Inferior and Lidita Superior of the Oliní Group present a less uniform ratio of residual versus desorbed gas. At Guate Creek (QG), the residual to desorbed gas ratio varies from 1.1 to 16.1 times, and at Cobre Creek (QC), it is 17.4 times. The volumes of gas hydrocarbons

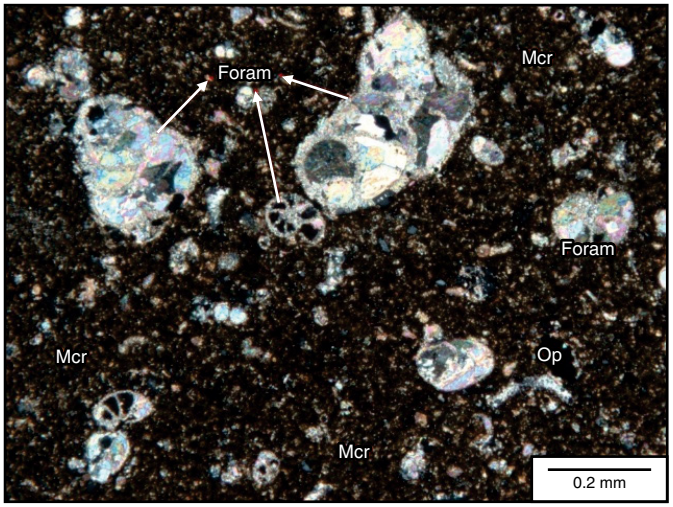

Figure 12. Thin section photograph of a silicified biomicrite (sample QG–251) from the Lidita Superior at Guate Creek west of the Bituima Fault. Large foraminifera have a length of 100 to 300 µm. The matrix is composed of organic matter and partially silicified calcareous mud (silt–sized fragments of foraminifera and calcareous algae). The sample contains 15% terrigenous mud (clay minerals and silt–sized quartz particles), 50% diagenetic quartz, and 35% calcite.

range from 0.28 to 4.36 feet^3/ton, which are similar to those of La Luna Formation, but there are fewer samples with gas in this unit than in La Luna. The lithology of the Lidita Units at Guate Creek (Figure 12) is slightly different from that of La Luna, with a higher clay mineral content between 10 and 30%, a calcite content of 25 to 45%, and a quartz content (in the form of diagenetic chert and silt–sized particles) of 20–75 %. The section QC contains an average of 59% quartz (diagenetic chert and silt–sized particles), 39% clay minerals, and less than 1% calcite.

The best samples of the Hilo Formation from the Contador River (RC) and Piñal Creek (QP) released gas hydrocarbons in similar concentrations to La Luna, but there are very few of them compared with the number from La Luna. The RC samples are impure biomicrites and marlstones with 20–30 % clay minerals, 25–55 % calcite, and 32–58 % quartz (diagenetic chert and silt–sized particles). The sample RC–16 released 1.93 feet^3/ton and had a ratio of 4.6 residual versus desorbed gas. The QP samples are impure biomicrites and marlstones with 10–40 % clay minerals, 10–70 % calcite, and 21–77% quartz (diagenetic chert and silt–sized particles). Sample QP–313 released 1.05 feet^3/ton and had a ratio of 2.6 residual versus desorbed gas.

Other units that released hydrocarbons include the Paja, Capacho, and Conejo Formations. Sample QLP–55 from the type section of the Paja Formation is a marlstone with 50% calcite, 25% clay minerals, 20% silt–sized quartz particles, and 5% pyrite; the sample released gas hydrocarbons with a concentration

of 0.74 feet^3/ton. The Paja Formation is composed of shale with minor marlstone and biomicrite; the samples of the QLP section contain 10–75 % clay minerals, 2–60% calcite, 5–30 % quartz, and 3–10% pyrite. Sample QLP–36 released gas hydrocarbons with a concentration of 2.18 feet^3/ton, which is comparable with good samples from La Luna Formation.

The samples RCA–47 and RR–00 from the Conejo and Capacho Formations released smaller amounts of hydrocarbons (0.32 and 0.19 feet^3/ton) than samples from La Luna Formation. The Conejo Formation from section RCA is composed of shale with minor marlstone and chert; it contains 10–60 % clay minerals, 20–70 % quartz (in silt particles and diagenetic chert), 2–32 % calcite, and 2–5 % pyrite. The Capacho Formation is composed of shales with less than 2% calcite, 40–50 % clay minerals, and 50–60 % silt–sized quartz particles.

The samples of the units with higher clay contents tend to have an erratic relationship of residual versus desorbed gas. This was especially notable in the Conejo Formation (19.0 to 367.3 times), which is very different from the more uniform relationship (4.1 to 12.9 times) of the biomicrites and cherts from La Luna Formation. It seems that the shales exposed near the surface (3 m depth) are more fractured and weathered than the biomicrites, so the relationship of residual versus desorbed gas (mostly air in the Conejo Formation) is less uniform.

The residual gas contents (Table 6) of samples from field exposures of the Paja, Capacho, Guayacán, La Luna, Lidita Inferior, and Lidita Superior Formations (3.06 to 18.10 feet^3/ton) are comparable with the residual gas contents (3.13 to 24.33 feet^3/ton) of samples from a well (534 to 564 m depth) in a Paleozoic shale in Indiana by Mastalerz et al. (2016). However, the ratios of desorbed to residual gas content are not comparable because the amount of desorbed gas was always higher than the amount of residual gas (a ratio of 1.1 to 7.4) in the well samples from Indiana (Mastalerz et al., 2016), but in our samples, it was the opposite: the amount of residual gas was always higher than the amount of desorbed gas (a ratio of 1.1 to 18.5). We conclude that most of the total desorbed gas originally present in our samples was lost during uplift decompression and fracturing and during weathering close to the surface (3 m depth). If the relationship of residual gas in our best samples (in terms of hydrocarbon and residual gas content) from La Luna, Paja, and Lidita Inferior Formations (CES1–00, QLP–36, and QC–13) is extrapolated to the total gas they should contain at depth, using the average ratio of total to residual gas (approximately 5) of Mastalerz et al. (2016), total gas values between 45.5 and 90.5 feet^3/ton could be reached. A clear relationship of increasing gas content (18.8 to 67.8 feet^3/ton) with increasing organic matter content (1.22 to 15.61% TOC) was documented by Mastalerz et al. (2016), who indicated that the gas was contained mainly within the micropores of the organic matter. We also found that the samples with the highest TOC generally contained the highest amounts of gas hydrocarbons.

Table 7. Porosity and permeability.

Formation	Section	Porosity (%)	Permeability (μD)	Hydrocarbons (% molar)
Guayacán	QLL	0.28	0.01	27.15
Lidita Inferior	QG	0.43	0.08	15.03
Lidita Superior	QG	0.89	2.12	16.94
La Luna	CES	0.96	0.68	3.51
Ritoque	RSR	0.97	0.17	0
La Luna	RR1	1.18	0.09	18.24
La Luna	CAB	1.31	11.01	2
Conejo	RCA	1.34	14.92	2.28
La Luna	CES1	1.47	0.52	11.93
Furatena (lower section)	BB	1.55	0.21	0.46
Villa de Leyva	RSP	1.8	0.56	0
La Luna	QAD	1.93	6.14	4.05
Macanal	C	2.01	26.27	0.11
Fómeque	QED	2.06	13.15	0.02
Murca (lower section)	RT	2.44	24	0.23
La Luna	QLL	2.56	3.04	26.21
La Luna	QS1	2.67	0.2	1.02
La Luna	QAD1	2.67	0.24	1.89
La Luna	QS2	3	4.85	5.77
Villa de Leyva	QN	3.03	247.33	0
Hilo	QP	3.05	62.33	1.12
Macanal	MSP	3.23	17.88	0.07
Macanal	GA	3.27	23.56	0.08
Fómeque	QLM	3.44	118.63	0.02
Une (upper section)	QSAU	3.65	0	0.03
Lidita Inferior	QC	3.83	7.72	3.38
Trincheras	VV	4.09	57.54	0.07
Guayacán	RR1	4.32	2235.26	0.1
Aguacaliente	QSA	4.59	64.58	0.05
Capacho	RR	4.66	16 560.92	1.09
El Salto	QS	5.22	26.63	0.41
El Salto	QS2	5.27	4094.03	0.51
Chipaque	QSAC	5.38	36 853.87	0.01
Chipaque	QSACH	5.65	45.28	0
Hilo	RC	7.43	0.76	7.47
Paja	QNP	10.01	61.09	0
Hilo	O	20.8	255.87	0.38

4.3. Porosity and Permeability

The limestones and cherts of the Guayacán, La Luna, Lidita Inferior, and Lidita Superior Formations, which released the

highest average percentages of gaseous hydrocarbons (11.93–27.15 %), have porosity values below 3% and absolute permeability below 3 microdarcys (Table 7). In contrast, the shale units have higher and nonreliable values, which reached 20.8% porosity in shales of the Hilo Formation and 36 854 microdarcys (36.85 millidarcys) in shales of the Chipaque Formation. These abnormal porosity and permeability values for the shales should correspond to free space produced during fracturing and weathering and to noneffective porosity related to water bounded to clay minerals. On the other hand, the low porosity and very low permeability values of the limestones, which have the highest contents of gas, do not necessarily account for all the nonconnected pores and fossil cavities, which can preserve hydrocarbons.

La Luna Formation biomicrites have uniform porosity values between 1 and 3%, with permeability values between 0.1 and 11 microdarcys. The biomicrites and cherts of the Lidita Inferior and Lidita Superior Formations also have uniform values of porosity (below 4%) and permeability (below 8 microdarcys). There are also shale units (Murca, Macanal, Fómeque, and Conejo Formations) with comparable values of porosity (below 4%) and permeability (13 to 26 microdarcys), but those units contained very little or no hydrocarbons.

The values presented here for La Luna Formation are comparable with those obtained by Cerón et al. (2013) and Walls et al. (2014) for the MMV and Catatumbo areas; the authors also showed that La Luna average values are comparable to those of the Eagle Ford reservoir from Texas. They used a high resolution microCT scanner and SEM imaging to obtain average porosity values of 4.8–6.3 % and average horizontal permeability values of 733 to 920 nanodarcys (0.73 to 0.92 microdarcys). They also reported solid organic material of 7.7–8.1 % and porosity values of 20–29 % within that organic material.

The very low permeability values that we obtained from the limestones of the Guayacán, La Luna, Lidita Inferior, and Lidita Superior Formations are very good because they mean that the units still retain hydrocarbons in organic matter, nonconnected pores, and fossil cavities, which could be released by fracking.

4.4. Pyrolysis and Organic Geochemistry

The pyrolysis results reveal that La Luna Formation limestones have the best indicators in terms of hydrocarbon content, type II organic matter, and thermal maturity (Figures 13, 14; Table 8). The best sections (QAD1, QAD, CES, INFAN–1613, CES1, CAB, QS1, and QS2) are in the NW sector of the basin, in the areas of Aguachica and Barichara/Bucaramanga, in the MMV and W foothills of the Eastern Cordillera, followed by the Cúcuta sections in the Catatumbo area (RIO–14, SAR–N2, RR1, and QLL), in the NE sector of the basin. Older units, with a higher shale and marlstone content, including the Paja, Simití, El Salto, Capacho, and Guayacán, are also in the oil and gas generation windows and have significant amounts of type III and type II kerogens.

Table 8 compiles the parameters of pyrolysis of units with higher hydrocarbon contents, which in La Luna Formation from the MMV and W flank of the Eastern Cordillera reach averages between 9.48 and 23.29 mg HC/g at the S2 peak. The best S2 average values of sections from La Luna Formation are above the average values reported from the Aguablanca section (4.54 mg HC/g) W of Bucaramanga (Casadiego & Rios, 2016) and 13.21 mg HC/g from a well in the Maracaibo area of Venezuela (Liborius & Slatt, 2014). The last one is comparable with the average (13.02 mg HC/g) from La Sorda Creek (QS1) W of Bucaramanga. The S2 averages from the Catatumbo area are lower (2.14 to 7.93 mg HC/g) because the sections have a higher thermal maturity (451 to 473 °C Tmax) and have released more hydrocarbons than the ones from the MMV and W foothills of the Eastern Cordillera (440 to 446 °C Tmax). Aguilera et al. (2010) reported S2 values from the MMV between 1 and 20 mg HC/g, with most data points between 5 and 15 mg HC/g, with Tmax values between 430 and 450 °C. Aguilera et al. (2010) also reported S2 values from Catatumbo below 10 mg HC/g.

Values lower than 0.2 mg HC/g at S1 and S2 are present in overmature units that have lost nearly all hydrocarbons; in those samples, the values of Tmax are unreliable and do not permit deducing the thermal maturity of the units (e.g., Nuñez–Betelu & Baceta, 1994). For example, the Paja Formation from well COS–15 presents very low average values of S1 (0.16 mg HC/g) and S2 (0.13 mg HC/g) so that the values of Tmax are erroneously low, approximately 322 °C, which would indicate that the unit has not entered the generation window. However, the correct value of vitrinite reflectance (4.3% Ro) indicates that the unit is overmature. The same goes for the other units of the Agencia Nacional de Hidrocarburos (ANH) wells from the Eastern Cordillera, which in general are overmature and have already released most of their hydrocarbons.

The hydrogen index (HI) averages are generally higher in the biomicrite limestones, which have a greater marine contribution of organic matter, than in the shales, which have a more terrestrial contribution along with the clay minerals (Figures 15–17; Table 8). The average values of La Luna Formation biomicrites in the MMV on the NW side of the basin ranged from 81 to 292, suggesting mixtures of types II–III of marine and continental origin. The average HI values of La Luna from the Catatumbo area in the NE side of the basin ranged from 24 to 112, suggesting a higher contribution of organic matter type III of continental origin; the Catatumbo samples also have higher production index (PI) values and higher thermal maturity (Ro 1–1.3 %) than those of the MMV (Ro 0.8–0.9 %). Aguilera et al. (2010) reported that most samples from the Catatumbo area had poor generation potential, with HI values below 200 and S2 values below 5, indicating

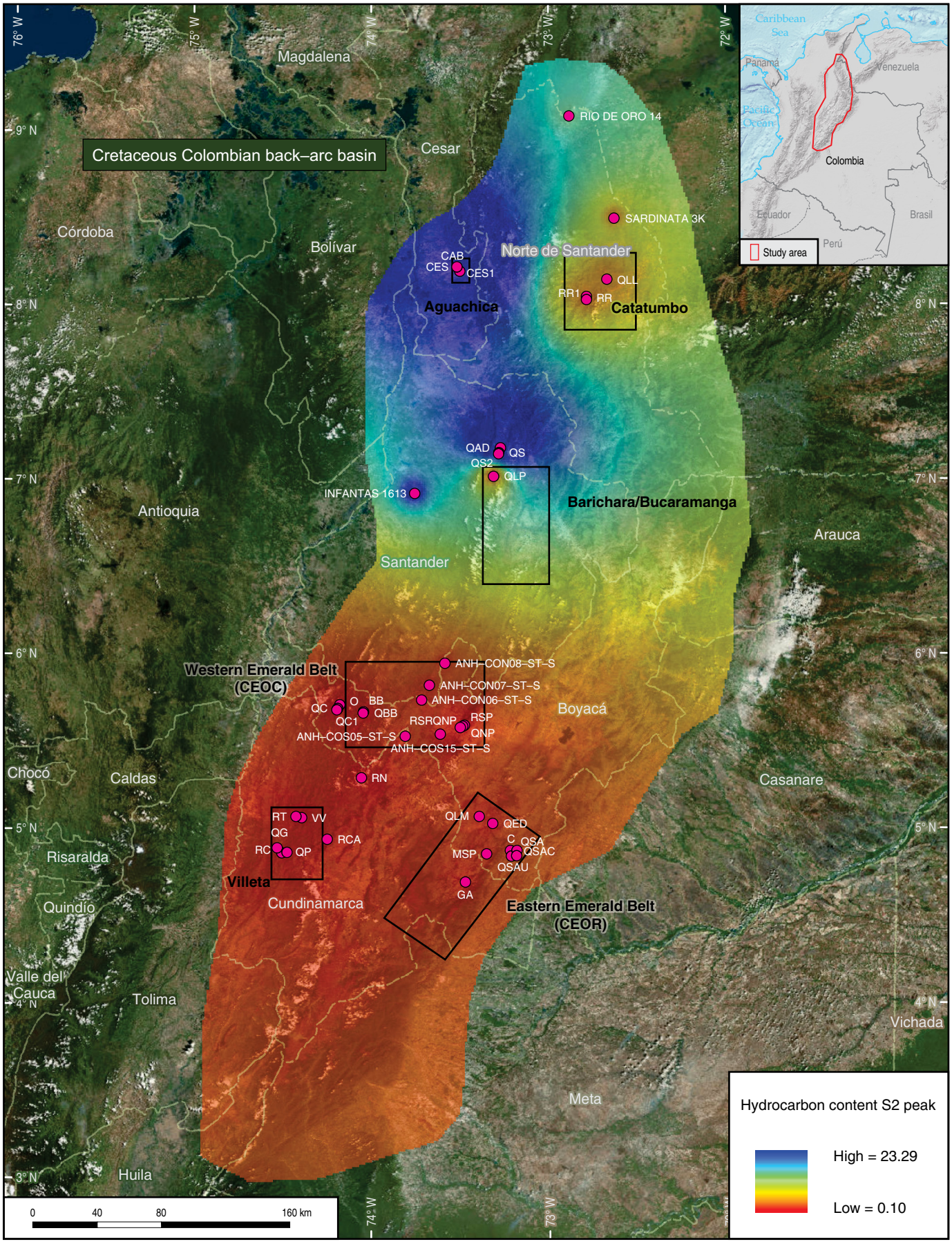
Cretaceous Colombian back–arc basin
RIO DE ORO 14
SARDINATA 3K
CAB
CES
CES1
Aguachica
Norte de Santander
QLL
RR1
RR
Catatumbo
QAD
QS
QS2
QLP
Barichara/Bucaramanga
INFANTAS 1613
Santander
ANH–CON08–ST–S
ANH–CON07–ST–S
ANH–CON06–ST–S
Western Emerald Belt (CEOC)
QC
O
BB
QBB
QC1
RSRQNP
RSP
QNP
ANH–COS05–ST–S
ANH–COS15–ST–S
Boyacá
RN
RT
VV
QG
RCA
RC
QP
Villeta
Cundinamarca
QLM
QED
C
QSA
QSAC
MSP
QSAU
GA
Eastern Emerald Belt (CEOR)
Magdalena
Cesar
Córdoba
Bolívar
Antioquia
Arauca
Casanare
Chocó
Caldas
Risaralda
Quindío
Valle del Cauca
Tolima
Huila
Meta
Vichada
9° N
8° N
7° N
6° N
5° N
4° N
3° N
76° W
75° W
74° W
73° W
72° W
0
40
80
160 km
Caribbean Sea
Panamá
Venezuela
Pacific Ocean
Colombia
Ecuador
Perú
Brasil
Study area
Hydrocarbon content S2 peak
High = 23.29
Low = 0.10

Figure 13. Average hydrocarbon contents (mg HC/g) per section at the S2 peak. The best values are located in the NW sector of the basin. Total number of samples: 500.

Table 8. Pyrolysis.

Formation	Section	TOC (%)	Ro (%) VIT–PYR	S1 (mg HC/g)[a]	S2 (mg HC/g)[b]	Tmax (ºC)[c]	HI	PI
La Luna	QAD1	8.3	PYR 0.8	4.69	23.29	444	281	0.17
La Luna	QAD	7.2	PYR 0.8	4.46	19.45	443	292	0.18
La Luna	CES	10.5	PYR 0.8	2.06	19.06	440	182	0.1
La Luna	INFA–1613	7.7	PYR 0.9	4.04	18.81	446	250	0.18
La Luna	CES1	11.9	PYR 0.8	1.34	17.67	441	149	0.07
La Luna	CAB	6.8	PYR 0.8	1.47	16.15	442	252	0.08
La Luna	QS1	8.6	PYR 0.9	2.61	13.02	445	151	0.17
La Luna	QS2	10.9	PYR 0.9	1.17	9.48	446	81	0.13
La Luna	RIO–14	8.1	PYR 1.0	2.53	7.93	451	112	0.24
La Luna	SAR–N2	9.6	PYR 1.3	1.3	2.68	468	28	0.34
La Luna	RR1	9.8	PYR 1.1	0.73	2.37	457	24	0.26
La Luna	QLL	8.6	PYR 1.2	0.64	2.14	473	25	0.24
Chipaque	QSACH	0.8	PYR 0.6	0.05	1.23	431	123	0.08
Paja	QLP	6	PYR 1.9	0.19	0.85	502	15	0.2
Aguacaliente	QSA	0.5	PYR 0.6	0.04	0.85	430	152	0.07
Lidita Superior	QG	3.6	PYR 2.4	0.16	0.61	530	17	0.2
Lidita Inferior	QG	3.7	PYR 2.8	0.11	0.54	551	15	0.19
Chipaque	QSAC	0.6	PYR 0.6	0.04	0.54	431	90	0.08
Capacho	RR	1.2	PYR 1.2	0.25	0.44	464	38	0.36
Conejo	RCA	2.6	PYR 2.9	0.09	0.27	560	11	0.26
Paja	COS–15	3.3	VIT 4.3	0.16	0.13	322	4	0.52
Paja	CON–8	5.1	VIT 3.1	0.09	0.11	345	2	0.46
Villa de Leyva	COS–14	1.9	VIT 3.4	0.08	0.11	336	6	0.42
Conejo	COS–5	4.3	VIT 2.9	0.08	0.11	409	5	0.42
San Gil Shale	CON–7	1.7	VIT 2.6	0.07	0.1	373	6	0.4

[a] Volume of hydrocarbons that formed during thermal pyrolysis at ca. 300 °C.

[b] Volume of hydrocarbons that formed during thermal pyrolysis at Tmax.

[c] Temperature of maximum hydrocarbon generation.

that it could also reflect the depletion effect caused by the high thermal maturity of the Cretaceous rocks.

The hydrogen index values should be treated with caution when interpreting the type of organic matter because the samples that released the highest amounts of hydrocarbons are silicified biomicrites composed of foraminifera, with less than 5% terrigenous particles. For instance, sample QAD1–20 from the W foothills of the Eastern Cordillera, which had a TOC of 8.2%, released 4.13 mg HC/g at S1 and 18.22 mg HC/g at an S2 peak Tmax of 444 °C and had an HI of 221, which would indicate a mixture of terrestrial and continental type II–III organic matter. However, the sample has less than 5% clay minerals, 50% calcite, 5% dolomite, and 40% diagenetic quartz, according to the petrography, XRD, and ICP–MS analyses; the framework of the rock was composed of planktonic foraminifera and fish bones. It is difficult to believe that a rock that has so little terrigenous particles could have important amounts of type III organic matter. As indicated by Nuñez–Betelu & Baceta (1994), it is possible to chemically degrade organic matter type II into type II–III due to variations in the mineral matrix and organic enrichment. We believe that the main reason for the low HI values is the relatively high thermal maturity of the samples, but it is also possible that the exchange of calcite by quartz and fluorapatite during diagenesis could have affected the carbon

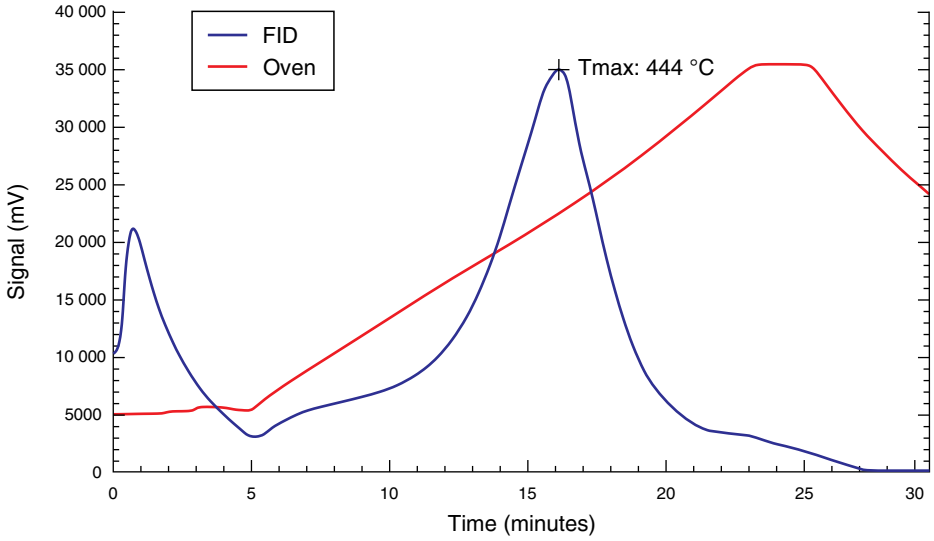

Figure 14. Pyrogram of sample QAD1–20 from La Luna Formation in the Aguadulce Creek section of the Barichara area.

and hydrogen relationships of La Luna Formation biomicrites and diagenetic cherts. The highest hydrogen index value from the Aguadulce Creek section is 450, from sample QAD1–46, which released 37.65 mg HC/g at an S2 peak Tmax of 440 °C, indicating fully marine–origin type II organic matter.

An interesting example of a very low hydrogen index of 14, erroneously indicating a terrestrial type III organic matter, comes from sample QLL–40 from the Catatumbo area. It had a TOC of 7.4%, released 0.51 mg HC/g at S1 and 1.04 mg HC/g at an S2 Tmax of 471 °C. According to ICP–MS elemental analyses and petrography, QLL–40 is a partially silicified biomicrite of foraminifera with 65% calcite, 30% diagenetic quartz, and less than 1% Al_2O_3. Again, it is difficult to believe that a rock made of planktonic foraminifera and with so little clay mineral content could have important amounts of type III continental organic matter. As indicated before, sample QLL–40 released the highest amounts of gaseous hydrocarbons (canister measurements) in the entire study. This is not because of the type of organic matter but because La Luna Formation in the Catatumbo area is more mature (1.3% Ro) than that in the Magdalena Valley. We believe that in addition to the relatively high thermal maturity of the samples, the diagenetic changes involving quartz and phosphate replacement of calcite affected the carbon and hydrogen relationships of the samples. In La Leche Creek section, the highest HI is 60, from sample QLL–10, which is again a partially silicified biomicrite of foraminifera with 50% calcite, 40% diagenetic quartz, 3% pyrite and dolomite, and 5% clay minerals, which could not have had enough terrestrial influx to predominantly incorporate type III organic matter of continental origin.

Another indication of the type of organic matter from the Catatumbo area is expressed by the ratio of tricyclic terpanes (Figure 18), indicating the relative presence of carbonates and clay minerals or marine versus terrestrial organic matter. In oils with organic matter of marine origin, C_{23} is the dominant terpane, and C_{25} is more abundant than C_{26} (e.g., Peters & Moldowan, 1993). However, it is interesting to consider the known mineralogy of the samples, according to the available petrography, ICP–MS elemental analyses, and XRD. Sample RR1–02 from the Guayacán Formation (on the right side of the Figure 18) is a shale with 60% clay minerals and 40% silt–sized quartz particles. Samples RR–6, 18, and 20 from the Capacho Formation (at the center of the Figure 18) are also shales with 50–60 % clay minerals and 40–50 % silt–sized quartz particles. Samples RR1–20 to RR1–40 from La Luna Formation are partially silicified biomicrites of foraminifera with 40–98 % calcite, 2–50 % diagenetic quartz, and 2–8 % clay minerals; all of them fall on the left (carbonate) side of the Figure 18, except for RR1–28. Samples QLL–04 to QLL–40 from La Luna Formation are also partially silicified biomicrites composed of foraminifera with 45–65 % calcite, 30–50 % diagenetic quartz, and 2–12 % clay minerals; all of them fall on the left (carbonate) side of the Figure 18, except for QLL–40. This means that except for a few samples, the type of organic matter is better expressed by the ratio of tricyclic terpanes than by using the hydrogen index previously discussed.

The tricyclic terpane ratio of the samples from the MMV and W foothills of the Eastern Cordillera (Figure 19) indicates a predominance of marine organic matter. Most samples fall on the left side of the Figure 19, except for some samples of the Paja (QLP) and La Luna (CAB, CES1) Formations. According to the available petrography, ICP–MS elemental analyses, and XRD, the Paja Formation at its type section is composed of marlstones and shales with minor biomicrite interbedding,

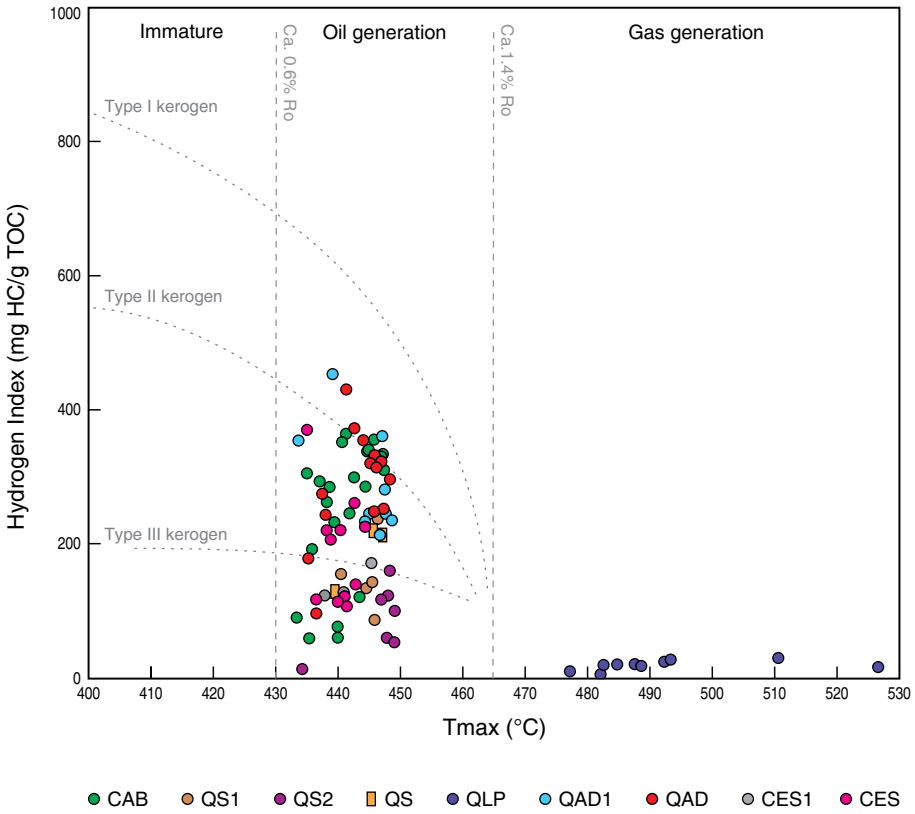

Figure 15. HI vs. Tmax of the Paja (QLP), Simití (QS), El Salto (QS2), and La Luna (QAD, QAD1, CES, CES1, CAB, QS1, QS2) Formations from the MMV and W foothills of the Eastern Cordillera.

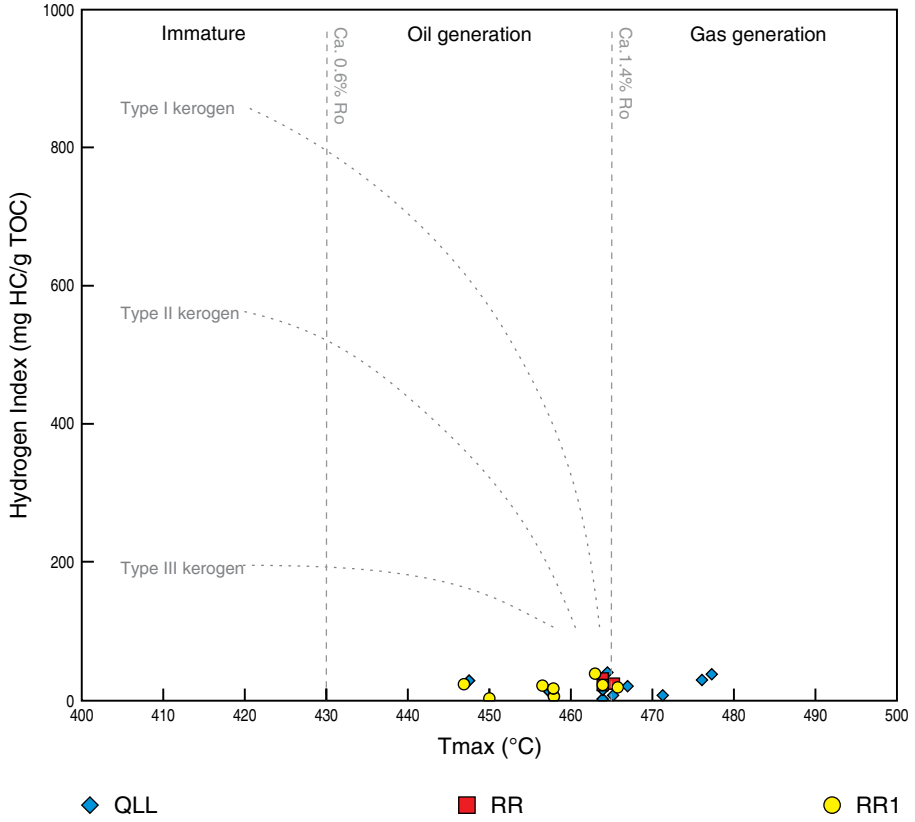

Figure 16. HI vs. Tmax of the Capacho (RR), Guayacán (RR1), and La Luna (QLL, RR1) Formations in the Catatumbo area.

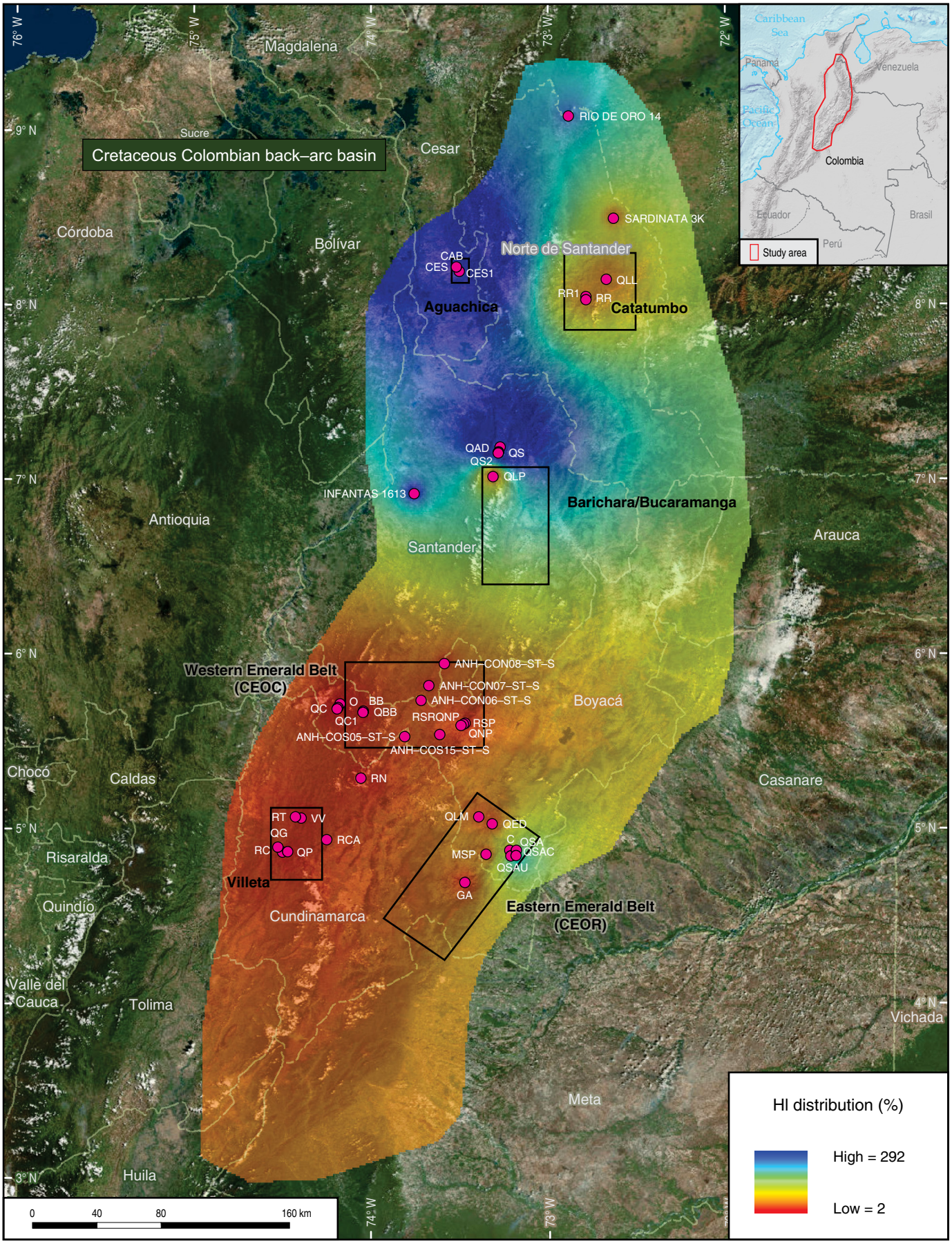
Cretaceous Colombian back–arc basin
Magdalena
Sucre
Cesar
Córdoba
Bolívar
Norte de Santander
Antioquia
Santander
Arauca
Boyacá
Casanare
Chocó
Caldas
Risaralda
Quindío
Cundinamarca
Tolima
Valle del Cauca
Huila
Meta
Vichada
RIO DE ORO 14
SARDINATA 3K
CAB
CES
CES1
Aguachica
QLL
RR1
RR
Catatumbo
QAD
QS2
QS
QLP
INFANTAS 1613
Barichara/Bucaramanga
ANH–CON08–ST–S
ANH–CON07–ST–S
ANH–CON06–ST–S
Western Emerald Belt (CEOC)
QC
O
BB
QBB
QC1
RSRQNP
RSP
QNP
ANH–COS05–ST–S
ANH–COS15–ST–S
RN
RT
VV
QG
RCA
RC
QP
Villeta
QLM
QED
C
QSA
QSAC
MSP
QSAU
GA
Eastern Emerald Belt (CEOR)
Caribbean Sea
Panamá
Venezuela
Pacific Ocean
Colombia
Ecuador
Brasil
Perú
Study area
HI distribution (%)
High = 292
Low = 2
0
40
80
160 km
76° W
75° W
74° W
73° W
72° W
9° N
8° N
7° N
6° N
5° N
4° N
3° N

Figure 17. Hydrogen index averages per section. The highest values are present in La Luna Formation from the NW side of the basin, at the MMV and W foothills of the Eastern Cordillera. Total number of samples: 500.

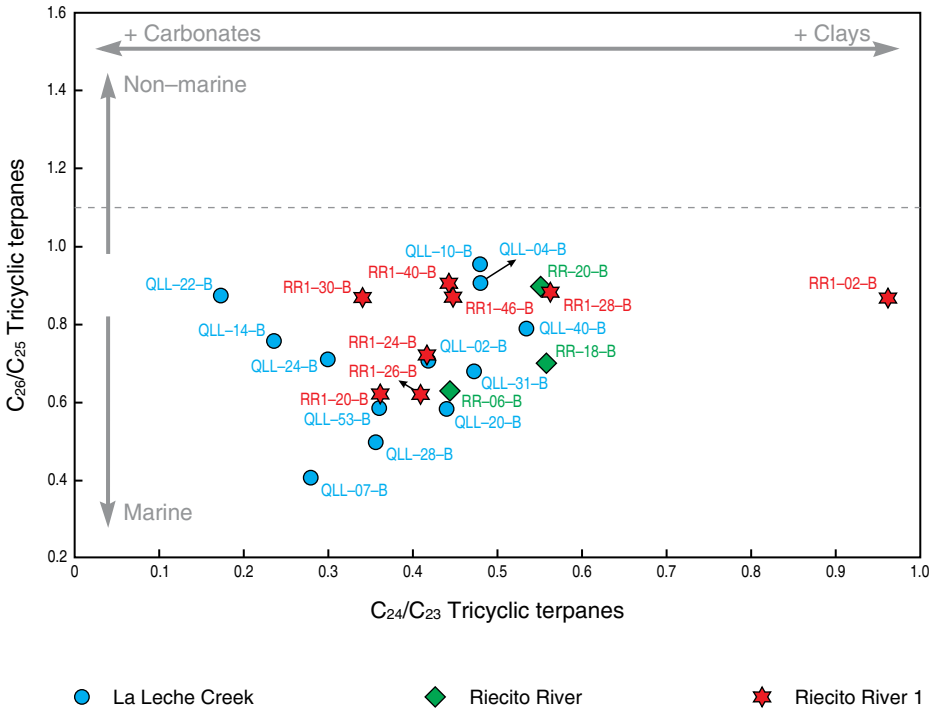

Figure 18. Relationship of tricyclic terpanes indicating the relative presence of marine organic matter related to carbonate rocks versus continental organic matter related to clay mineral content in the Capacho (RR), Guayacán (RR1–02), and La Luna (QLL, RR1) Formations from three localities in the Catatumbo area.

which explain the position of the shale QLP–38 on the right side of the Figure 19, indicating a predominance of continental organic matter. La Luna Formation of the CAB section is composed of partially silicified biomicrites and marlstones composed of foraminifera with 10–80 % calcite, 10–60 % diagenetic quartz, 5–30 % clay minerals, and 5–30 % silt–sized quartz particles. One of the samples toward the right side of the Figure 19, with the highest content of clay minerals (30%), is CAB–50, which is a marlstone and has a mixture of marine and continental organic matter. However, a few samples fall in a field that does not correspond with their lithology.

For instance, the shales of the Simití Formation (QS) contain 35–50 % clay minerals, 40–55 % silt–sized quartz particles, and less than 2% calcite, so they are completely terrigenous and should fall in the field of continental organic matter instead of carbonate marine. The biomicrite limestones of section CES1 have less than 7% clay minerals, so those samples should fall more toward the left, in the carbonate organic matter field, instead of the clay side. In any case, except for the samples mentioned above, the type of organic matter is better expressed by the ratio of tricyclic terpanes than by using the hydrogen index. Based on mineralogy, fossil content, and organic geochemistry, we conclude that La Luna Formation biomicrite limestones predominantly have type II organic matter of marine origin. Rangel et al. (2017) performed an assessment of the Colombian oils and identified an oil family in the UMV and MMV that suggested an origin in calcareous marine source rocks, which they considered probably related to La Luna Formation limestones.

The mixture of various types of fine–grained rocks (biomicrites, marlstones, and shales) and the type of organic matter (marine versus continental) are very important in the production of unconventional hydrocarbons because they determine the micro scale properties of the rocks, such as fracturing (biomicrites) versus plasticity (marlstones and shales), along with the tendency to produce predominantly oil or gas.

5. Conclusions

The highest average TOC contents of the whole basin correspond to La Luna Formation biomicrites at several localities, including caño El Salto (CES–1) in the Aguachica area in the MMV (11.6% TOC), La Sorda Creek (QS2) section in the

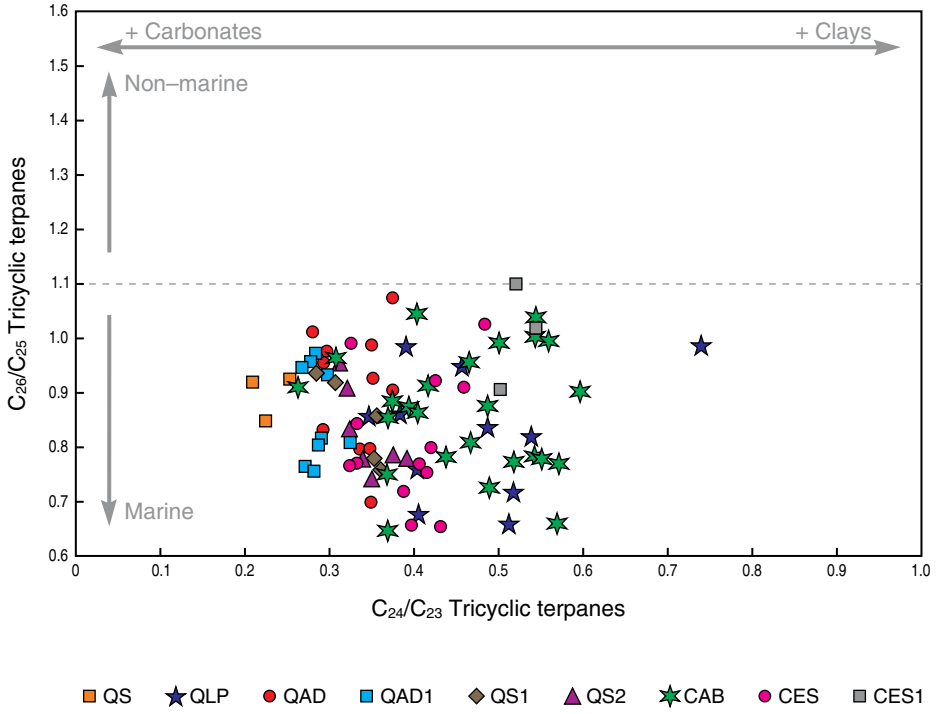

Figure 19. Relationship of tricyclic terpanes indicating the relative presence of marine versus continental organic (carbonate versus clay mineral) content in the Paja (QLP), Simití (QS), and La Luna Formations (QAD, QAD1, CES, CES1, CAB, QS1, QS2) from the MMV.

Barichara area in the W foothills of the Eastern Cordillera (8.6% TOC), and the Rio de Oro oil well (RIO–14) in the Cúcuta/Catatumbo area (8.1% TOC).

Very high TOC values were obtained from individual samples at section CES–1 (21.7% TOC), the Aguadulce Creek (QAD) section in the W foothills of the Eastern Cordillera (18.2% TOC), and caño Aguablanca (CAB) in Aguachica (13.9% TOC). Other units with very high TOC values include La Frontera Member of the Conejo Formation from ANH well COS–5 (24.8% TOC), the Hilo Formation at the Otanche (O) section (12.1% TOC), and the Lomagorda Formation from Cobre Creek (QC) section (7.4% TOC).

The Ro values from La Luna Formation are in the oil and early gas generation windows (0.8–1.3 % Ro). The highest thermal maturity values obtained from pyrolysis are from the Upper Cretaceous Oliní Group (2.4–2.8 % Ro) and Conejo Formation (2.9% Ro). The highest thermal maturity values obtained from vitrinite are from the Lower Cretaceous Murca, Trincheras, and Hilo Formations from the Villeta area (4.0–4.2 % Ro) and the Paja Formation from the Villa de Leyva area (4.3% Ro).

The highest hydrocarbon contents (mainly methane, ethane, and propane) collected in the canister samples cored from field exposures correspond to the Paja, Hilo, Guayacán, La Luna, Lidita Inferior, and Lidita Superior Formations, which contained 1.29 to 5.10 feet^3/ton. The samples with the lowest CO_2 contents (3.0–11.5 %) were associated with the highest hydrocarbon contents (15.0–77.8 %). The samples with the highest gaseous hydrocarbon contents after grinding the samples (residual gas) come from La Luna Formation in La Leche Creek (QLL) and Riecito River (RR1) sections in the Cúcuta/Catatumbo area, La Luna Formation in the caño El Salto (CES1) and caño Aguablanca (CAB) sections in the Aguachica area in the MMV, La Luna Formation in La Sorda Creek (QS2) section in the W foothills of the Eastern Cordillera, the Lidita Inferior and Lidita Superior Formations in the Cobre Creek (QC) and Guate Creek (QG) sections in the W foothills of the Eastern Cordillera, the Paja Formation in La Paja Creek (QLP) section in the western foothills of the Eastern Cordillera, the Hilo Formation in the Contador River (RC) section in the Villeta area, and the Guayacán Formation in the QLL section in the Cúcuta/Catatumbo area.

If the relationship of residual gas of the best samples from La Luna, Paja, and Lidita Inferior Formations (9.1 to 18.1 feet^3/ton) is extrapolated to estimate the total gas at depth using an average ratio of total to residual gas of approximately 5 (as found in other basins), they should exhibit total gas values of between 45.5 and 90.5 feet^3/ton.

The limestones and cherts of the Guayacán, La Luna, Lidita Inferior, and Lidita Superior Formations, which released the highest average percentages of gaseous hydrocarbons after fracturing and grinding the samples (11.93 to 27.15% of total gas content), have porosity values below 3% and permeability values below 3 microdarcys. The biomicrites and cherts of La Luna Formation have uniform porosities between 1 and 3%,

with permeability values between 0.1 and 11 microdarcys. The biomicrites and cherts of the Lidita Inferior and Lidita Superior also have uniform values of porosity (below 4%) and permeability (below 8 microdarcys). The very low permeability values obtained from the limestones are very good because these mean that the units still retain hydrocarbons in organic matter, nonconnected pores, and fossil cavities, which could be released by fracking.

The pyrolysis and organic geochemistry results reveal that La Luna Formation limestones present the best indicators in terms of hydrocarbon content, type II organic matter, and thermal maturity. The best sections are in the NW sector of the basin, in the areas of Aguachica and Barichara, in the MMV and W foothills of the Eastern Cordillera, followed by the sections from the Catatumbo area in the NE sector of the basin. Older units, with a higher shale and marlstone content, including the Paja, Simití, El Salto, Capacho, and Guayacán, are also in the oil and gas generation windows and have significant amounts of type III and type II kerogen.

Foraminiferal biomicrites, marlstones, and diagenetic cherts have higher contents of TOC than shales, so instead of exploring gas shales, gas biomicrites would constitute a better target. Because the biomicrites have lower or no clay content compared with the claystone and mudstone shales, it is expected that the biomicrites have a more brittle behavior than shales during the process of fracking. In addition, the plastic behavior of the clay shales will more easily close the induced fractures than the biomicrite limestones.

Acknowledgments

We thank the Colombia ANH for permission to publish their data. The field work and analyses were conducted in the frame of project 299–12 to evaluate the nonconventional hydrocarbon potential of fine–grained strata from the Cretaceous Colombian Basin. The project was directed by Javier GUERRERO and supervised by Alejandra MEJÍA–MOLINA. We also appreciate the comments and suggestions of Professor Dr. Yucel AKKUTLU from Texas A&M University and an anonymous reviewer, who helped us to improve the chapter.

References

Aguilera, R.C., Sotelo, V.A., Burgos, C.A., Arce, C., Gómez, C., Mojica, J., Castillo, H., Jiménez, D. & Osorno, J. 2010. Organic Geochemistry Atlas of Colombia. Earth Sciences Research Journal, Special Edition 14, 174 p.

Casadiego, E. & Rios, C. 2016. Lithofacies analysis and depositional environment of the Galembo Member of La Luna Formation. Ciencia, Tecnología y Futuro, 4(1): 37–56.

Cerón, M.R., Walls, J.D. & Diaz, E. 2013. Comparison of reservoir quality from La Luna, Gacheta, and Eagle Ford Shale Formations using digital rock physics. Search and Discovery Article 50875. 15 p.

Galvis–Portilla, H.A., Higuera–Diaz, I., Cespedes, S., Ballesteros, C., Forero, S., Marfisi, N., Cantisano, M., Pineda, E., Pachon, Z., Slatt, R.M., Ramirez, R., Guzman, G. & Torres, A. 2014. Regional sequence stratigraphy of the Upper Cretaceous La Luna Formation in the Magdalena Valley Basin, Colombia. Unconventional Resources Technology Conference, paper 1934959, 10 p. Denver. https://doi.org/10.15530/URTEC–2014–1934959

Guerrero, J. 2002a. A proposal on the classification of systems tracts: Application to the allostratigraphy and sequence stratigraphy of the Cretaceous Colombian Basin. Part 1: Berriasian to Hauterivian. Geología Colombiana, (27): 3–25.

Guerrero, J. 2002b. A proposal on the classification of systems tracts: Application to the allostratigraphy and sequence stratigraphy of the Cretaceous Colombian Basin. Part 2: Barremian to Maastrichtian. Geología Colombiana, (27): 27–49.

Guerrero, J., Sarmiento, G. & Navarrete, R. 2000. The stratigraphy of the W side of the Cretaceous Colombian Basin in the Upper Magdalena Valley. Reevaluation of selected areas and type localities including Aipe, Guaduas, Ortega, and Piedras. Geología Colombiana, (25): 45–110.

Guerrero, J., Mejía–Molina, A. & Osorno, J. 2020. Detrital U–Pb provenance, mineralogy, and geochemistry of the Cretaceous Colombian back–arc basin. In: Gómez, J. & Pinilla–Pachon, A.O. (editors), The Geology of Colombia, Volume 2 Mesozoic. Servicio Geológico Colombiano, Publicaciones Geológicas Especiales 36, p. 261–297. Bogotá. https://doi.org/10.32685/pub.esp.36.2019.08

Kennedy, R., Luo, L.X. & Kuuskra, V. 2016. The unconventional basins and plays–North America, the rest of the world, and emerging basins. In: Ahmed, U. & Meehan, D.N. (editors), Unconventional oil and gas resources: Exploitation and development. CRC Press, p. 76–111. Boca Raton, USA.

Liborius, A. & Slatt, R. 2014. Geological characterization of La Luna Formation as an unconventional resource in Lago de Maracaibo Basin, Venezuela. Unconventional Resources Technology Conference, paper 2461968. 20 p. Denver, CO, USA. https://doi.org/10.15530/urtec-2016-2461968

Mastalerz, M., Karayigit, A.I., Hampton, L. & Drobniak, A. 2016. Variations in gas content in organic matter–rich low maturity shale; example from the New Albany Shale in the Illinois Basin. Jacobs Journal of Petroleum and Natural Gas, 1: 1–16.

Morales, L.G., Podesta, D., Hatfield, W., Tanner, H.H., Jones, S.H., Barker, M.H.S., O'Donoghue, D.J., Mohler, C.E., Dubois, E.P., Jacobs, C. & Goss, C.R. 1958. General geology and oil occurrences of Middle Magdalena Valley, Colombia: South America. In: Weeks, L.G. (editor), Habitat of Oil Symposium. American Association of Petroleum Geologists, p. 641–695. Tulsa, USA.

Nuñez–Betelu, L. & Baceta, J.I. 1994. Basics and application of rock–eval/TOC pyrolysis: An example from the uppermost

Paleocene/lowermost Eocene in the Basque Basin, Western Pyrenees. Natur Zientziak, (46): 43–62.

Peters, K.E. & Moldowan, J.M. 1993. The biomarker guide: Interpreting molecular fossils in petroleum and ancient sediments. Prentice Hall, 699 p. New Jersey.

Rangel, A., Osorno, J.F., Ramirez, J.C., De Bedout, J., González, J.L. & Pabón, J.M. 2017. Geochemical assessment of the Colombian oils based on bulk petroleum properties and biomarker parameters. Marine and Petroleum Geology, 86: 1291–1309. https://doi.org/10.1016/j.marpetgeo.2017.07.010

Torres, E.J., Slatt, R., Philp, P., O'Brien, N.R.O. & Rodriguez, H.L. 2015. Unconventional resources assessment of La Luna Formation in the Middle Magdalena Valley Basin, Colombia. Search and Discovery Article 80469. Denver, CO, USA.

Veiga, R. & Dzelalija, F. 2014. A regional overview of the La Luna Formation and the Villeta Group as shale gas/shale oil in the Catatumbo, Magdalena Valley and Eastern Cordillera Regions, Colombia. Search and Discovery Article 10565. Cartagena.

Walls, J.D., Cerón, M.R. & Anderson, J. 2014. Characterizing unconventional resource potential in Colombia; a digital rock physics project. Unconventional Resources Technology Conference, paper 1913256, 9 p. Denver. https://doi.org/10.15530/urtec–2014–1913256

Zumberge, J. 1984. Source rocks of the La Luna Formation (Upper Cretaceous) in the Middle Magdalena Valley, Colombia. In: Palacas, J. (editor), Petroleum Geochemistry and Source Rock Potential of Carbonate Rocks. American Association of Petroleum Geologists, Special volumes, 18, p. 127–133.

Explanation of Acronyms, Abbreviations, and Symbols:

ANH	Agencia Nacional de Hidrocarburos
HC	Hydrocarbon
HI	Hydrogen index
HST	Highstand systems tract
ICP–MS	Inductively coupled plasma mass spectrometry
MMV	Middle Magdalena Valley
MORB	Mid–ocean ridge basalt
PI	Production index
Ro	Thermal maturity
RST	Regressive systems tract
SEM	Scanning Electron Microscope
Tmax	Temperature of maximum hydrocarbon generation
TOC	Total organic carbon
TST	Transgressive systems tract
UMV	Upper Magdalena Valley
XRD	X–ray diffraction

Authors' Biographical Notes

Javier GUERRERO is a geologist from the Universidad Nacional de Colombia. He obtained a Master of Science degree and a PhD from Duke University (USA) in the areas of stratigraphy, sedimentology, and paleomagnetism. He participated with a multidisciplinary group of geologists and paleontologists from several American universities in a project on biostratigraphy, sedimentology, and magnetostratigraphy of the Honda Group in the Tatacoa Desert. He worked at the stratigraphy section of the Servicio Geológico Colombiano on various projects on the Cenozoic from the Magdalena River Valley. Recently, he has been a professor in the Departamento de Geociencias at the Universidad Nacional de Colombia, lecturing in courses on sedimentology, sequence stratigraphy, and regional geology. Javier has conducted research and consulting projects for several petroleum companies and for the Agencia Nacional de Hidrocarburos (ANH) on rocks of the Cretaceous Colombian back–arc basin and the Cenozoic foreland basin.

Alejandra MEJÍA–MOLINA is a geologist from the Universidad de Caldas (Colombia) who has been working during the last decade in paleontology, paleoecology, paleoceanography, and paleoclimatology as a member of the Grupo de Geociencias Oceánicas (GGO) at the Universidad de Salamanca (España). Her Master's thesis was on Quaternary marine/continental variability in North Africa and her Doctoral thesis was on calcareous nannofossils, both at the Universidad de Salamanca. Alejandra worked for the Agencia Nacional de Hidrocarburos (ANH) on several projects to obtain new geological data and evaluate the Colombian exploratory potential of both conventional (Pacific and Caribbean offshore basins) and unconventional hydrocarbons (Cretaceous from the Eastern Cordillera). She currently works for the Escuela de Ciencias Geológicas e Ingeniería at the Universidad Yachay Tech, Ecuador.

José OSORNO is a geologist from the Universidad de Caldas with a specialization in project management from the Universidad Piloto de Colombia. He recently completed a Master of Science in energy management at Universidad Sergio Arboleda and an Executive MBA at the Universitat Politècnica de València, España. José Fernando worked for 18 years at the Servicio Geológico Colombiano in the División de Geología Regional y Estratigrafía. Recently, he has been working at the Agencia Nacional de Hidrocarburos (ANH) in project design and evaluation, including the definition of oil systems in Colombia and geochemical evaluation of the Sinú–San Jacinto area. He is currently responsible for "yet–to–find" projects focused on calculating the potential of hydrocarbons yet to be discovered in the sedimentary basins of Colombia. José is also responsible for projects on the potential of unconventional hydrocarbons in the country.

Volume 2

Chapter 10

Cretaceous Record from a Mariana– to an Andean–Type Margin in the Central Cordillera of the Colombian Andes

Agustín CARDONA[1]* , Santiago LEÓN[2], Juan S. JARAMILLO[3], Victor A. VALENCIA[4], Sebastian ZAPATA[5], Andrés PARDO–TRUJILLO[6], Axel K. SCHMITT[7], Dany MEJÍA[8], and Juan Camilo ARENAS[9]

Abstract The Cretaceous tectonic evolution of the western margin of South America involves a shift from an extensional convergent margin toward a more compressional setting that marks the beginning of the Andean Orogeny. In the Colombian Andes, this changing scenario is recorded in the Cretaceous sedimentary and magmatic rocks of the Central Cordillera. A review of field relationships, together with analysis of integrated provenance constraints, including sandstone petrography and detrital zircon geochronology from various localities, suggests that during the Early Cretaceous until the Aptian – Albian, siliciclastic basin fills were characterized by transgressive fining–upward trends, with prominent first–cycle quartzose provenances that indicate strong chemical weathering in the source areas. Jurassic, Triassic, and older detrital zircon U–Pb ages suggest that the igneous and metamorphic rocks forming the basement of the Central Cordillera were the main sources. Furthermore, the presence of Early Cretaceous detrital ages between 120 and 100 Ma, together with interlayered volcanic rocks at the top of the sequence characterized by mixed arc–like, MORB, and E–MORB geochemical signatures, can be related to the evolution of an extensional arc with associated back–arc basin formation. Plutonic rocks with ca. 98 Ma crystallization ages show Nd, Sr, Hf, and O isotope evidence for the existence of thinned continental crust that may account for the dominant mantle signature. By ca. 93 Ma, the Early Cretaceous sedimentary sequences were deformed and intruded by plutonic rocks, which conversely show isotopic fingerprints characteristic of crustal signatures that can be explained by the involvement of thicker crust that promoted melt interaction with the more radiogenic host rocks.

This tectonic change from a Mariana– to an Andean–type subduction style was probably triggered by regional–scale plate kinematic reorganizations, as suggested by similar coeval tectonic scenarios along the entire South American margin, and set the conditions for the construction of the Andean chain.

Keywords: *Cretaceous, back-arc, intra–arc, Andean Orogeny, Geochemistry.*

Resumen La evolución tectónica del borde occidental de Suramérica durante el Cretácico está marcada por el cambio de un margen convergente extensional hacia una configuración más compresiva que marca el inicio de la Orogenia Andina. En los Andes

Citation: Cardona, A., León, S., Jaramillo, J.S., Valencia, V., Zapata, S., Pardo–Trujillo, A., Schmitt, A.K., Mejía, D. & Arenas, J.C. 2020. Cretaceous record from a Mariana– to an Andean–type margin in the Central Cordillera of the Colombian Andes. In: Gómez, J. & Pinilla–Pachon, A.O. (editors), The Geology of Colombia, Volume 2 Mesozoic. Servicio Geológico Colombiano, Publicaciones Geológicas Especiales 36, p. 335–373. Bogotá. https://doi.org/10.32685/pub.esp.36.2019.10

https://doi.org/10.32685/pub.esp.36.2019.10

Published online 15 May 2020

1 agcardonamo@unal.edu.co
Universidad Nacional de Colombia
Sede Medellín
Facultad de Minas
Departamento de Procesos y Energía
Grupo de Investigación en Geología y Geofísica (EGEO)
Medellín, Colombia

2 sleonva@gmail.com
Universidad Nacional de Colombia
Sede Medellín
Grupo de Investigación en Geología y Geofísica (EGEO)
Medellín, Colombia
Smithsonian Tropical Research Institute
Ancón, Panamá

3 jusjaramillori@unal.edu.co
Universidad Nacional de Colombia
Sede Medellín
Facultad de Minas
Departamento de Materiales y Minerales
Grupo de Investigación en Geología y Geofísica (EGEO)
Medellín, Colombia

4 victor.valencia@wsu.edu
Washington State University
School of the Environment
Pullman, USA

5 szapatah@gmail.com
Smithsonian Tropical Research Institute
Ancón, Panamá
Missouri University of Science and Technology
Department of Geology and Geophysics
USA

6 andres.pardo@ucaldas.edu.co
Universidad de Caldas
Instituto de Investigaciones en Estratigrafía (IIES)
Manizales, Colombia

7 Axel.Schmitt@geow.uni-heidelberg.de
Heidelberg University
Institute of Earth Sciences
Heidelberg, Germany

8 dymejiav@unal.edu.co
Universidad Nacional de Colombia
Sede Medellín
Facultad de Minas
Departamento de Materiales y Minerales
Grupo de Investigación en Geología y Geofísica (EGEO)
Medellín, Colombia

9 Universidad Nacional de Colombia
Sede Medellín
Departamento de Geociencias y Medio Ambiente
Medellín, Colombia

* Corresponding author

Supplementary Information:

S: https://www2.sgc.gov.co/LibroGeologiaColombia/tgc/sgcpubesp36201910s.pdf

colombianos, este cambio está registrado en las rocas sedimentarias y magmáticas cretácicas de la cordillera Central. La revisión de las relaciones de campo, junto con el análisis de procedencia de rocas siliciclásticas (petrografía de areniscas y geocronología en circones detríticos de varias localidades), sugiere que durante el Cretácico Temprano hasta el Aptiano–Albiano el relleno siliciclástico de la cuenca se caracterizó por tener un carácter transgresivo granodecreciente y una composición cuarzosa con componentes de primer ciclo asociados a condiciones de meteorización intensa en el área fuente. Las edades U–Pb en circón jurásicas, triásicas y más antiguas sugieren que las fuentes principales fueron las rocas ígneas y metamórficas que conforman el basamento de la cordillera Central. Además, la presencia de edades detríticas del Cretácico Temprano entre 120 y 100 Ma, junto con la de rocas volcánicas intercaladas al tope de la secuencia que se caracterizan por una mezcla de firmas geoquímicas de arco, MORB y E–MORB, puede estar relacionada con la evolución de un arco extensional y la formación de una cuenca de retroarco. Las rocas plutónicas con edades de cristalización de ca. 98 Ma muestran evidencias isotópicas de Nd, Sr, Hf y O de afinidad mantélica que estarían asociadas a la existencia de una corteza continental adelgazada. A los ca. 93 Ma, las secuencias sedimentarias del Cretácico Temprano fueron deformadas e intruidas por rocas plutónicas, las cuales en cambio muestran características isotópicas corticales que pueden explicarse por la participación de una corteza más gruesa que promovió la interacción del fundido con las rocas caja más radiogénicas.

Este cambio tectónico de un estilo de subducción de tipo Marianas a uno de tipo andino es común en toda la margen continental suramericana y estaría asociado con reorganizaciones cinemáticas a escala de placas que marcarían el inicio de la construcción de la cadena andina.

Palabras clave: *Cretácico, retroarco, intraarco, Orogenia Andina, geoquímica.*

1. Introduction

During the Cretaceous, the western margin of South America experienced a major change from a dominantly extensional system (Mariana–type) toward a more compressional tectonic style (Chile–type; Uyeda & Kanamori, 1979; Stern, 2012), which marks the initiation of the Andean orogeny (see reviews in Tunik et al., 2010; Horton, 2018). Whereas the Mesozoic – Cenozoic tectonic evolution of the central and southern Andean segments was characterized by a subduction–dominated orogeny, the northern Andes constitutes a classic accretionary orogen in which interspersed terrane accretion and subduction tectonics were responsible for orogenic growth (see a review in Ramos, 2009). With such a complex scenario and the continuous superimposition of tectonic events, clear discrimination between subduction–dominated extensional and compressional tectonics remains a major challenge.

The long–term spatiotemporal and compositional changes in magmatic rocks integrated with the stratigraphic and provenance evolution of contemporaneous basins are sensitive markers of the evolution of convergent margins and can be used to address alternating settings between extension and compression (Busby, 2012; Cawood et al., 2009; Marsaglia, 2012).

In this contribution, we present a review of published field observations and petrographic, geochronological, and geochemical data, together with new results from magmatic and detrital zircon U–Pb geochronology, whole–rock geochemistry, zircon Hf and O isotopes, sandstone petrography, and field relationships of Cretaceous units from selected localities exposed between the two flanks of the Central Cordillera of the Colombian Andes (Figure 1). The analysis of available data and the new data presented here allows documenting an Aptian – Albian extensional margin associated with the formation of different intra–arc and back–arc extensional domains, which were inverted and deformed before 90 Ma and subsequently experienced the formation of a younger Late Cretaceous arc and the collision of an intra–oceanic terrane.

The Early to Late Cretaceous record in the Central Cordillera provides additional constraints on the continental–scale transition from extension to compression that gave rise to the Andean Orogeny (Horton, 2018; Tunik et al., 2010).

2. Geological Setting

Within the Colombian Andes, the Cretaceous geological record is found in three different tectonostratigraphic domains, which closely coincide with major morphostructural features represented by the three main cordilleras and the intervening Magdalena and Cauca valleys (Figures 1, 2).

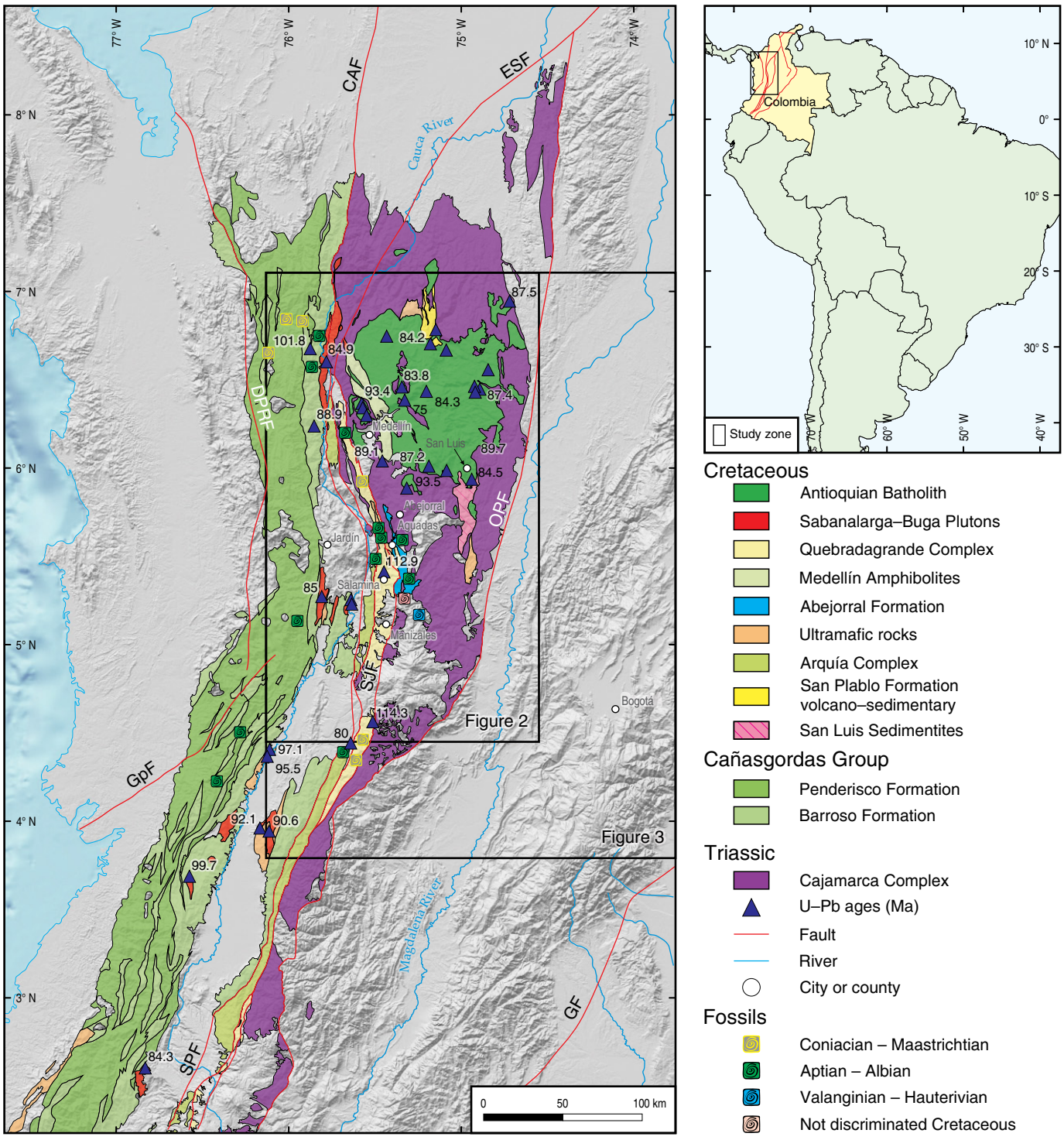

Figure 1. Regional geological map of the Colombian Andes showing the locations of the pre–Cretaceous and Cretaceous units, as well as the published U–Pb geochronology from the magmatic units (modified after Gómez et al., 2015; Jaramillo et al., 2017). (CAF) Cauca–Almaguer Fault; (ESF) Espíritu Santo Fault; (DPRF) Dabeiba–Pueblo Rico Fault; (OPF) Otú–Pericos Fault; (SJF) San Jerónimo Fault; (GpF) Garrapata Fault; (SPF) Silvia–Pijao Fault; (GF) Guaicáramo Fault.

In the Magdalena valley and the Eastern Cordillera, Cretaceous sedimentary rocks accumulated over Jurassic volcanic and siliciclastic units and correspond to a former extensional basin filling interval that ended in the Berriasian (Kammer & Sánchez, 2006; Sarmiento–Rojas et al., 2006). These units are considered para–autochthonous and/or northward–transported domains that nearly achieved their modern paleogeographic positions west of the reference craton during the Late Jurassic

(Bayona et al., 2006). The Early Cretaceous extension–dominated setting switched to eustatic–dominated sedimentation with coeval tectonic quiescence and thermal subsidence. This sedimentary record can be traced eastward in the Llanos Basin and includes associated volcanogenic clays and tuffs ranging in age from the Hauterivian to the Turonian (Villamil & Arango, 1998; Villamil, 1999; Sarmiento–Rojas et al., 2006), as well as minor gabbroic bodies with Ar–Ar ages between 136 and 74 Ma (Vásquez et al., 2010).

In the Central Cordillera, the Early Cretaceous units are represented by a series of discontinuous siliciclastic sequences that crop out on both flanks and along its axis (Figure 2). These sequences overlie Permian – Triassic and Jurassic metamorphic rocks and are characterized by an apparent fining–upward pattern from predominantly sandstone/conglomeratic beds toward a mudstone–dominated sequence (see review in Nivia et al., 2006; Zapata et al., 2018). Fossil remnants, including ammonites, bivalves, and gastropods, have shown that sedimentary accumulation extended from the Berriasian to the Aptian (see compilation in Botero & González, 1983; González, 2001). Volcanic flows and small gabbroic bodies have been found in association with some of these sedimentary sequences (Rodríguez & Celada–Arango, 2018; Zapata et al., 2018).

Two different hypothetical geodynamic settings have been considered for the evolution of the Central Cordillera sedimentites: a passive margin that collided with an intra–oceanic arc (Toussaint, 1996; Moreno–Sánchez et al., 2008) or a back–arc basin that formed during the Early Cretaceous (Nivia et al., 2006; Villagómez et al., 2011; Cochrane et al., 2014a; Spikings et al., 2015; Zapata et al., 2018). The paleogeographic position where these basins accumulated also remains controversial, with some authors considering an autochthonous origin connected to depocenters located in the Eastern Cordillera domains (Etayo–Serna et al., 1969) and other authors arguing for exotic positions farther to the south probably correlated with coeval terranes in Ecuador (Toussaint, 1996; Pindell & Kennan, 2009).

In the western flank of the Central Cordillera and the Cauca Valley that separates it from the Western Cordillera, a series of highly deformed volcano–sedimentary units also considered Aptian – Albian in age crop out and are affected by a major fault system (Cauca–Romeral; Nivia et al., 2006). These units include gabbroic rocks associated with serpentinized peridotites (Álvarez, 1987; González, 2001) and are in fault contact with intermediate– to high–pressure metamorphic rocks with Lu–Hf and Ar–Ar peaks and cooling ages between 137 and 110 Ma (García–Ramírez et al., 2017), as well as younger ages of ca. 64 Ma (Bustamante et al., 2011). These units are also interspersed with Triassic and older igneous and metamorphic rocks (Vinasco et al., 2006; Cochrane et al., 2014a; Zapata et al., 2018). The volcano–sedimentary units have been considered either as part of a fringing arc associated with the formation of a back–arc basin (Nivia et al., 2006; Villagómez et al., 2011; Cochrane et al., 2014b; Spikings et al., 2015) or as an allochthonous oceanic arc that collided with a passive margin (Toussaint, 1996; Moreno–Sánchez & Pardo–Trujillo, 2003).

Following the formation of these extensional basins related to a back–arc or intra–arc setting, prominent plutonic activity formed intrusions with ages between 98 and 72 Ma in the Early Cretaceous and older basement of the Central Cordillera (Ibañez–Mejia et al., 2007; Ordóñez–Carmona et al., 2007; Restrepo–Moreno et al., 2007; Leal–Mejía, 2011; Villagómez et al., 2011). This magmatism represents the construction of a continental arc that was active until the Maastrichtian – Paleocene collision of the South American margin with an intra–oceanic arc (Villagómez et al., 2011; Spikings et al., 2015; Jaramillo et al., 2017). Several plutonic bodies with ages between 90 Ma and 78 Ma also intrude the Cretaceous extensional related volcano–sedimentary unit exposed to the west (Villagómez et al., 2011; Jaramillo et al., 2017).

In contrast, the Western Cordillera includes a high–density basaltic sequence characterized by deformed and undeformed lava flows, pillow lavas, and minor pyroclastic rocks, which have been interpreted as remnants of an oceanic plateau likely related to the Caribbean Large Igneous Province that formed in southern latitudes (CLIP; Kerr et al., 1997; Villagómez et al., 2011; Zapata et al., 2017; Hincapié–Gómez et al., 2018). This basaltic province presents minor intercalations of mudstones and cherts with Berriasian to Albian fossil remnants that are intruded by plateau–related gabbroic and tonalitic bodies with ca. 98 Ma crystallization ages (Villagómez et al., 2011; Weber et al., 2015). These units are also intruded by arc–related granitoids and gabbroic rocks with zircon U–Pb ages between 80 and 90 Ma (Villagómez et al., 2011; Zapata et al., 2017), which are locally associated with volcanic units of Campanian age (Spadea & Espinosa, 1996). Late Cretaceous and younger sandstones with quartz–rich compositions overlie these volcanic units and represent the stratigraphic record of their juxtaposition against the continental margin (León et al., 2018).

Several lines of evidence, including exhumation trends in the Central and Western Cordilleras (Villagómez & Spikings, 2013), changes in the nature of the magmatic record along the western flank of the Central Cordillera (Jaramillo et al., 2017) and major changes in the sedimentary environments and the associated provenances in the eastern basins (Villamil, 1999), have suggested that during the Late Cretaceous – Paleocene, the different units described above were fully juxtaposed (Toussaint, 1996; Villagómez et al., 2011; Spikings et al., 2015) and subsequently segmented and dispersed by strike–slip fault systems along the margin (Pindell & Kennan, 2009; Montes et al., 2010).

3. Methods and Approach

In this contribution, we present a review of published geological constraints from Lower to Upper Cretaceous sedimentary

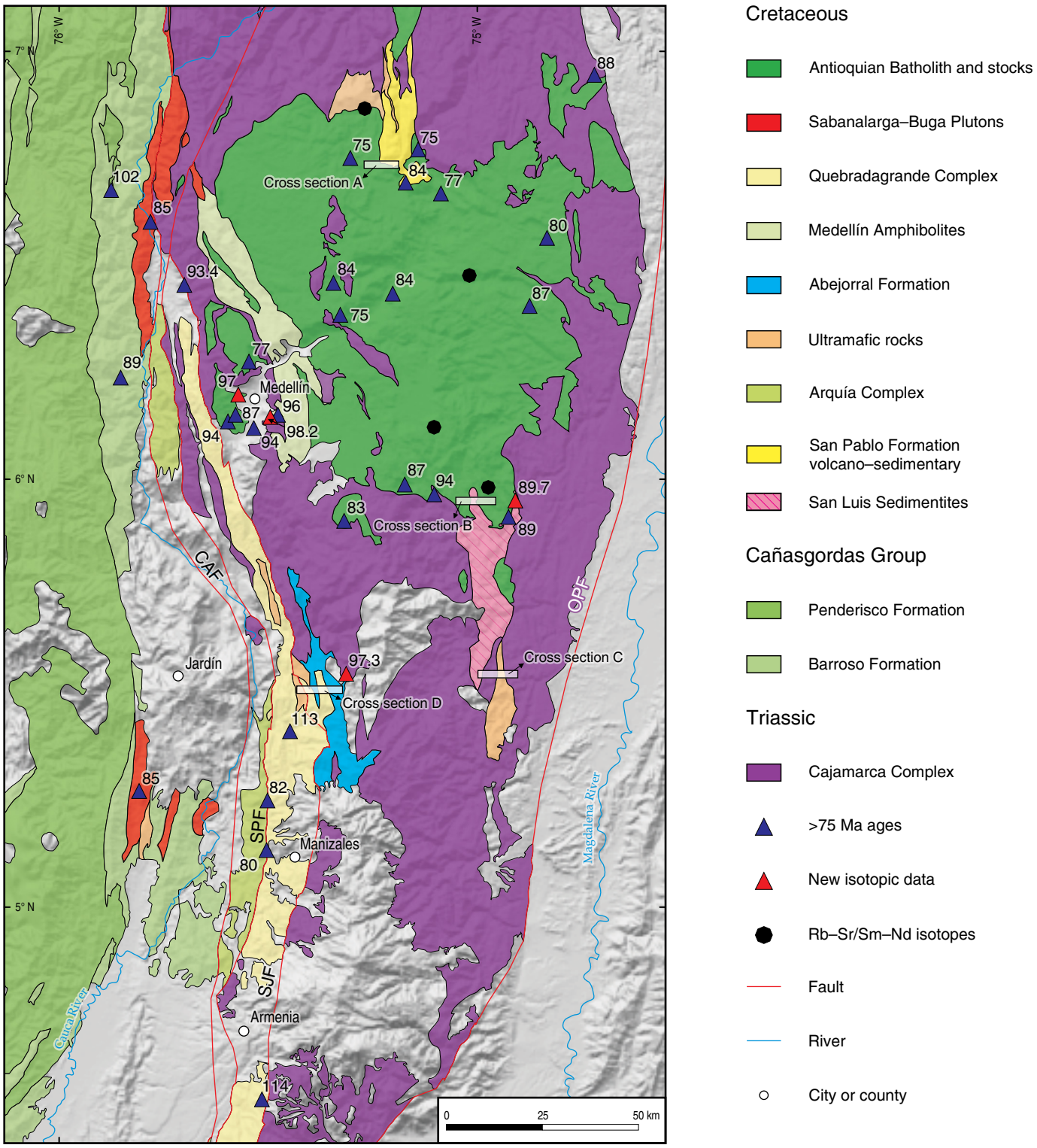

Figure 2. Geological map of the sampled and discussed regions in the Central Cordillera (modified after Gómez et al., 2015). (CAF) Cauca–Almaguer Fault; (OPF) Otú–Pericos Fault; (SJF) San Jerónimo Fault; (SPF) Silvia–Pijao Fault. See the cross sections A, B, C, and D in Figure 4.

and magmatic rocks of the Central Cordillera. Although some of the available constraints are mainly from basic geological cartography, the descriptions are remarkably objective and remain valid. These results are integrated with new field observations together with sandstone petrography, geochemical analyses, U–Pb zircon geochronology, and zircon oxygen and

hafnium isotopes from two localities of the Cretaceous units exposed in the western and eastern flanks of the Central Cordillera in the Department of Antioquia near the city of Medellín and cross section B (Figures 2 and 3).

Our approach follows the concept of tectonic facies (Robertson, 1994), which integrates field and laboratory analysis to identify tectonostratigraphic associations, which can be used to recognize discrete tectonic settings and test their geological evolution.

To avoid repetition, we integrated both the published and the new data in a single section. The locations of the samples analyzed in this study are presented in Table 1, and the results from sandstone petrography of samples from the San Luis Sedimentites in Table 2.

3.1. Zircon U–Pb LA–ICP–MS Geochronology

After zircon separation using conventional techniques, including crushing, pulverization, water table, and heavy liquid gravity concentration, LA–ICP–MS U–Pb zircon analyses were obtained from 4 granitic rocks and 4 sandstone samples at the Washington State University Geoanalytical Lab, using a New Wave Nd:YAG UV 213–nm laser coupled to a Thermo Finnigan Element 2 single collector, double–focusing, magnetic sector ICP–MS following the analytical protocol of Chang et al. (2006). For this study, the Plešovice zircon was used as the main standard, which is characterized by a $^{238}U/^{206}Pb$ age of 337.13 ± 0.37 Ma (Sláma et al., 2008). Common Pb represents a large proportion of the total Pb in Mesozoic and younger U–poor zircons. However, common Pb is typically not significant in LA–ICP–MS analyses, most likely because it is concentrated in cracks and inclusions, which can be avoided by appropriately selecting the crystals. When this is not possible, the influence of common Pb is easy to recognize on Tera–Wasserburg diagrams because analyses tend to line up on a steep linear trajectory that can be anchored at a reasonable $^{207}Pb/^{206}Pb$ common lead composition (y–intercept) (DeGraaff–Surpless et al., 2002). Common Pb corrections were made on these analyses using the ^{207}Pb method (Williams, 1998). Uranium–lead ages were processed and calculated using Isoplot 4.15 (Ludwig, 2003). Analytical data from the detrital zircons are presented in Table 1, Supplementary Information, and data from the magmatic rocks are presented in Table 3.

3.2. Whole–Rock Geochemistry

Whole–rock geochemical analyses of five magmatic rocks from the Cretaceous Altavista Stock and San Diego Gabbro were conducted at the ALS Minerals Laboratories (the results are presented in Table 4).

After crushing, splitting, and pulverizing, an aliquot of 0.1 g is added to a $LiBO_2/Li_2B4O_7$ flux, mixed and fused in a furnace at 1000 °C. The resulting melt is then cooled and dissolved in 100 mL of $4\%HNO_3/2\%HCl$. This solution is then analyzed for major oxides by inductively coupled plasma atomic emission spectroscopy (ICP–AES), and the results are corrected for spectral interelement interferences. For trace and rare earth elements, an aliquot of 0.1 g is added to a $LiBO_2/Li_2B_4O_7$ flux (1.8 g), mixed and fused in a furnace at 1025 °C. The resulting melt is cooled and dissolved in a mixture containing HNO_3, HCl, and HF. This solution is then analyzed by ICP–MS. Data handling, plotting, and interpretation are performed using the software GCD Toolkit 4.1 (Janoušek et al., 2006).

3.3. Hafnium Isotopes

Hf isotope geochemistry was determined at the GeoAnalytical Lab of Washington State University using a Thermo Finnigan Neptune™ MC–ICP–MS equipped with 9 Faraday collectors interfaced with a New Wave™ 213 nm UP Nd–YAG laser. The results are presented in Table 5.

The laser was operated at a pulse rate of 10 Hz and a fluence of 10–12 J/cm^2. The laser spot size was 30 μm. The carrier gas consisted of purified He plus small quantities of N_2 to minimize oxide formation and increase Hf sensitivity. The total Hf signal achieved was between 2 and 6 V. The data were acquired in static mode with 60 s integrations. Details of the analytical procedures and data treatment were after (Vervoort et al., 2004; Dufrane et al., 2007). For the Hf–depleted mantle model ages (Hf TDM), we used $^{176}Hf/^{177}Hf$ and $^{176}Lu/^{177}Hf$ for the individual zircon samples to determine their initial $^{176}Hf/^{177}Hf$ ratios at their crystallization ages. Projection back from zircon crystallization was calculated using a present value of 0.0093 for $^{176}Lu/^{177}Hf$ in the crust (Vervoort & Patchett, 1996; Amelin et al., 2002). The depleted mantle Hf evolution curve was calculated from present–day depleted mantle values of $^{176}Hf/^{177}Hf$ DM(0) = 0.283225 and $^{176}Lu/^{177}Hf$ DM(0) = 0.038512 (Vervoort & Blichert–Toft, 1999).

3.4. Oxygen Isotopes

Oxygen isotopes in zircon were analyzed using the CAMECA IMS 1280–HR ion microprobe at Heidelberg University. The procedures of multicollection analysis of oxygen isotopes (^{16}O and ^{18}O) using two Faraday cup (FC) detectors were similar to those presented in Trail et al. (2007) as modified by Schmitt et al. (2017).

A 2–3 nA Cs^+ primary beam was focused to 10–15 μm using a focused beam rastered over 10 μm. FC backgrounds were recorded during an initial 30 s of presputtering and averaged over the duration of the analysis session. Mass fractionation was corrected by analyzing the 91 500 reference zircon in pairs with interspersed blocks of six unknowns (91500 $\delta^{18}O$ = +9.86‰; Wiedenbeck et al., 2004; δ values are relative to Vien-

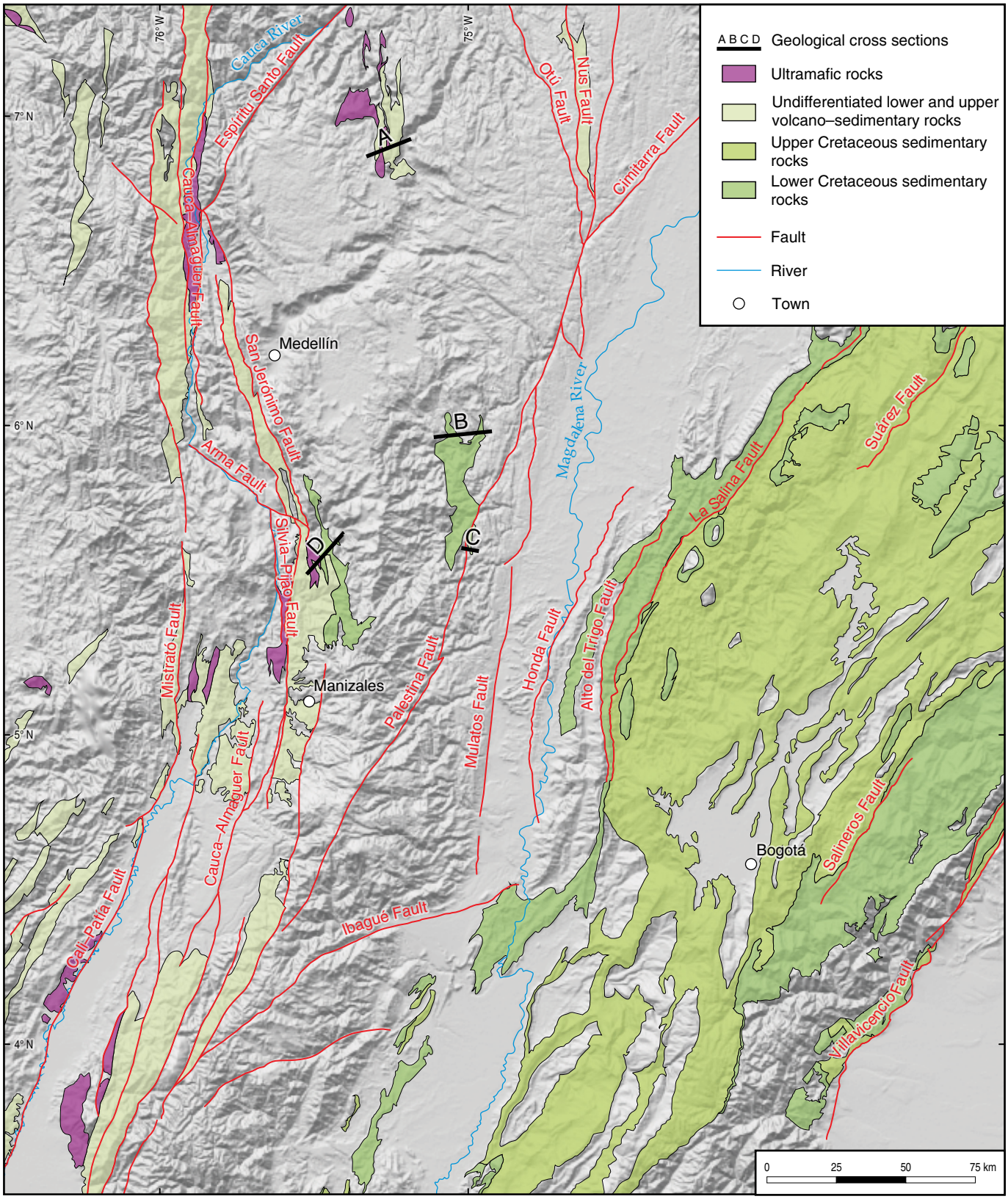

Figure 3. Distribution of Cretaceous rocks in the Colombian Andes (modified after Gómez et al., 2015). Geological cross sections A, B, C, and D are presented in Figure 4.

Table 1. Sample locations.

Sample code	N	W	Geologic unit	Lithology	Analysis
JCA–045	6.27423	–75.62193	Altavista Stock	Qartz monzonite	U–Pb LA–ICP–MS
JCA–046	6.22818	–75.56890	San Diego Gabbro	Gabbroic diorite	U–Pb LA–ICP–MS
DM–056	5.57991	–75.36080		Porphyry andesitic	U–Pb LA–ICP–MS and Hf
AG–01	6.01612	–74.94476	Antioquian Batholith	Quartz diorite	U–Pb LA–ICP–MS
QG–W–01	5.07222	–75.44886	Quebradagrande Complex	Sandstone	Detrital U–Pb LA–ICP–MS
MQA–4A	5.07197	–75.44895	Quebradagrande Complex	Quartz conglomerate	Detrital U–Pb LA–ICP–MS
JCA036	6.27423	–75.62193	Altavista Stock	Quartz diorite	Geochemistry
JCA037	6.27423	–75.62193	Altavista Stock	Gabbro	Geochemistry
JCA038	6.27423	–75.62193	Altavista Stock	Andesitic porphyry	Geochemistry
JCA043	6.22818	–75.56890	San Diego Gabbro	Gabbro	Geochemistry
DM–TM–084	5.99307	–75.03510	San Luis Sedimentites	Sandstone	Petrography
DM–TM–076	5.99593	–75.02480	San Luis Sedimentites	Sandstone	Petrography

Table 2. Petrographical results from the San Luis Sedimentites.

Sample	Qzm	Qzi	Qzmet	Ltmet	Ltsed	Pg	K
DM–TM–084	85	85	46	3	8	22	8
DM–TM–076	70	65	29	1	3	18	3

(Qzm) monocrystalline quartz; (Qzi) polycrystalline igneous quartz; (Qzmet) polycrystalline metamorphic quartz; (Ltmet) metamorphic lithic; (Ltsed) sedimentary lithic; (Pg) plagioclase; (K) alkaline feldspar.

na standard mean ocean water, VSMOW; $^{18}O/^{16}O = 0.0020052$; Baertschi, 1976). The reproducibility in $\delta^{18}O$ was 0.15‰ (1 standard deviation, n = 24). A secondary reference zircon FC1 ($\delta^{18}O = 5.4$‰; Ickert et al., 2008) was analyzed under the same conditions, and a $\delta^{18}O$ value of 5.56 ± 0.15‰ (n = 6) was obtained, attesting to the accuracy of the method within stated uncertainties.

4. Results

4.1. Review of the Early Cretaceous Sedimentary Record in the Central Cordillera and New Observations

Several discontinuous belts of fossiliferous siliciclastic Lower Cretaceous rocks are exposed along the axis and both flanks of the Central Cordillera (Figure 2). All of them are overlying Triassic or Jurassic schist and gneissic rocks that have been included in the Cajamarca Complex (Vinasco et al., 2006; Blanco–Quintero et al., 2014; Cochrane et al., 2014b; Bustamante et al., 2017; Rodríguez et al., 2018) and show local evidence of intense deformation by folding and faulting, as well as local low–grade metamorphic overprinting that formed slates and flattened metaconglomerates. In some segments of the cordillera, the eastern and western belts are separated more than 50 km by the pre–Cretaceous metamorphic basement.

In the western flank of the Central Cordillera, between the Departments of Antioquia and Caldas, different names have been used to refer units with similar lithofacies, including the Abejorral Formation (González, 1980), the Aranzázu–Manizales Metasedimentary Complex (Lozano et al., 1975), the "Valle Alto", "San Félix", and "El Establo" units (Rodríguez & Rojas, 1985), and the "Eastern" interval near the city of Manizales (Gómez–Cruz et al., 1995).

These sequences include basal oligomictic quartzose conglomerates and coarse–grained sandstones with thicknesses between 40 and 240 m. Interlayered fine–grained sandstones, mudstones, siliceous mudstones, and chert with polymictic conglomerate beds overlie the coarse–grained units and may reach thicknesses between 160 and 1910 m. The greater stratigraphic thicknesses may be an artifact of repetition associated with the superimposed deformation (Figure 4). These units yield Berriasian to middle Albian fossil fauna and have been interpreted as transgressive successions that evolved from fluvial–deltaic to marine platform environments (Lozano et al., 1975; Etayo–Serna, 1985; Rodríguez & Rojas, 1985; Gómez–Cruz et al., 1995; Quiroz, 2005; Zapata et al., 2018). Magmatic activity associated with fine–grained facies has recently been recognized in the form of interlayered tuffs and dikes near the town of Abejorral (Antioquia), which suggests that sedimentation and volcanism were contemporaneous (Zapata et al., 2018). In this contribution, we report the presence of a porphyritic body that intrudes a sequence of mudstones and siltstones of the Abejorral Formation near the town of Salamina in the state Caldas Department.

Several segmented and deformed siliciclastic units also crop out along the eastern flank of the Central Cordillera approximately 50 km to the east and both north and south from the main exposures of the Abejorral Formation. These sequences trend N–S,

Table 3. U–Pb LA–ICP–MS geochronological results from the analyzed intrusive bodies (Altavista, San Diego, and Antioquia).

Department of the Environment, Washington State University			Isotopic ratios									Ages							
Sample			Pb 207 Corrected					Non Corrected				$^{207}Pb/^{235}U$	2σ Abs error	$^{206}Pb/^{238}U$	2σ Abs error	$^{207}Pb/^{206}Pb$	2σ Abs error	Best age	2σ Abs error
Name	U (ppm)	U/Th	$^{207}Pb/^{235}U$	2σ Abs error	$^{206}Pb/^{238}U$	2s Abs error	Corr. Coef.	$^{238}U/^{206}Pb$	2σ Abs error	$^{207}Pb/^{206}Pb$	2σ Abs error	(Ma)	(Ma)	(Ma) (207 Corr)	(Ma)	(Ma)	(Ma)	(Ma)	(Ma)
JCA–045_1	1241	0.3	0.10276	0.00468	0.01485	0.00046	0.825	67.1453	2.0541	0.0502	0.0013	99.3	4.3	95.0	2.9	203.7	30.5	95.0	2.9
JCA–045_2	1372	0.3	0.10170	0.00453	0.01521	0.00047	0.837	65.6973	2.0198	0.0485	0.0012	98.3	4.2	97.3	3.0	123.2	29.4	97.3	3.0
JCA–045_3	1014	0.4	0.10415	0.00485	0.01551	0.00050	0.828	64.4056	2.0550	0.0487	0.0013	100.6	4.5	99.2	3.2	133.2	31.3	99.2	3.2
JCA–045_4	1859	0.2	0.10669	0.00445	0.01512	0.00046	0.866	65.8769	1.9861	0.0512	0.0011	102.9	4.1	96.7	2.9	249.2	24.7	96.7	2.9
JCA–045_5	955	0.5	0.11109	0.00535	0.01517	0.00049	0.817	65.4894	2.1001	0.0531	0.0015	107.0	4.9	97.1	3.1	333.7	31.9	97.1	3.1
JCA–045_6	1132	0.3	0.10328	0.00463	0.01543	0.00047	0.833	64.7666	1.9875	0.0485	0.0012	99.8	4.3	98.7	3.0	126.1	30.0	98.7	3.0
JCA–045_7	1728	0.4	0.10264	0.00423	0.01530	0.00047	0.874	65.2928	1.9836	0.0486	0.0010	99.2	3.9	97.9	3.0	130.7	24.3	97.9	3.0
JCA–045_8	500	0.9	0.10600	0.00594	0.01594	0.00058	0.791	62.7350	2.2947	0.0482	0.0017	102.3	5.4	101.9	3.7	111.1	41.0	101.9	3.7
JCA–045_9	1530	0.3	0.10124	0.00471	0.01487	0.00045	0.811	67.1098	2.0367	0.0494	0.0014	97.9	4.3	95.2	2.9	165.2	32.6	95.2	2.9
JCA–045_10	2021	0.3	0.10001	0.00428	0.01504	0.00049	0.886	66.4656	2.1818	0.0482	0.0010	96.8	4.0	96.2	3.1	110.6	24.0	96.2	3.1
JCA–045_11	547	0.6	0.10732	0.00611	0.01544	0.00053	0.761	64.5841	2.1908	0.0504	0.0019	103.5	5.6	98.7	3.3	214.8	43.4	98.7	3.3
JCA–045_12	3223	0.2	0.10364	0.00416	0.01564	0.00047	0.880	63.9292	1.9038	0.0481	0.0010	100.1	3.8	100.1	3.0	102.1	23.3	100.1	3.0
JCA–045_13	3670	0.3	0.10383	0.00444	0.01532	0.00053	0.912	65.1954	2.2474	0.0492	0.0009	100.3	4.1	98.0	3.4	155.9	21.1	98.0	3.4
JCA–045_14	2536	0.3	0.09994	0.00414	0.01505	0.00047	0.887	66.4295	2.0951	0.0482	0.0010	96.7	3.8	96.3	3.0	107.3	23.3	96.3	3.0
JCA–045_15	3443	0.2	0.10148	0.00438	0.01513	0.00050	0.888	66.0270	2.1954	0.0486	0.0010	98.1	4.0	96.8	3.2	130.5	24.0	96.8	3.2
JCA–045_16	1667	0.4	0.10327	0.00440	0.01484	0.00047	0.869	67.1516	2.1007	0.0505	0.0011	99.8	4.0	95.0	3.0	216.2	25.1	95.0	3.0
JCA–045_17	1209	0.3	0.10833	0.00470	0.01608	0.00048	0.836	62.1391	1.8396	0.0489	0.0012	104.4	4.3	102.8	3.0	141.7	28.7	102.8	3.0
JCA–045_18	882	0.4	0.10116	0.00544	0.01490	0.00059	0.848	67.0016	2.6686	0.0492	0.0014	97.8	5.0	95.3	3.8	159.4	33.6	95.3	3.8
JCA–045_19	426	0.7	0.10443	0.00546	0.01477	0.00049	0.790	67.4305	2.2382	0.0513	0.0017	100.9	5.0	94.5	3.1	254.1	37.3	94.5	3.1
JCA–045_20	459	1.1	0.10569	0.00574	0.01484	0.00050	0.778	67.0791	2.2567	0.0517	0.0018	102.0	5.3	94.9	3.2	270.6	39.7	94.9	3.2
JCA–046_1	1085	0.4	0.10397	0.00540	0.01543	0.00048	0.772	64.7219	2.0253	0.0489	0.0017	100.4	5.0	98.7	3.1	141.0	39.5	98.7	3.1
JCA–046_2	1282	0.4	0.10477	0.00490	0.01576	0.00051	0.828	63.4334	2.0321	0.0482	0.0013	101.2	4.5	100.8	3.2	109.7	31.7	100.8	3.2
JCA–046_3	1354	0.6	0.10514	0.00492	0.01541	0.00052	0.847	64.7781	2.1739	0.0495	0.0013	101.5	4.5	98.6	3.3	171.1	29.6	98.6	3.3
JCA–046_4	605	1.1	0.10372	0.00560	0.01523	0.00054	0.796	65.5443	2.3173	0.0494	0.0017	100.2	5.1	97.4	3.4	166.7	38.7	97.4	3.4
JCA–046_5	1829	0.3	0.14750	0.00705	0.01472	0.00054	0.876	65.7814	2.3297	0.0727	0.0017	139.7	6.2	94.2	3.3	1004.7	23.1	94.2	3.3
JCA–046_6	367	1.1	0.18299	0.01245	0.01472	0.00062	0.763	64.2634	2.5666	0.0901	0.0038	170.6	10.6	94.2	3.8	1428.6	40.1	94.2	3.8
JCA–046_7	401	0.8	0.12206	0.00751	0.01558	0.00063	0.786	63.4533	2.5255	0.0568	0.0022	116.9	6.8	99.7	4.0	484.2	41.9	99.7	4.0
JCA–046_8	2132	0.3	0.09888	0.00443	0.01493	0.00051	0.878	66.9584	2.2837	0.0480	0.0011	95.7	4.1	95.6	3.2	100.4	25.9	95.6	3.2
JCA–046_9	893	0.7	0.10581	0.00565	0.01527	0.00056	0.815	65.2950	2.3863	0.0503	0.0016	102.1	5.2	97.7	3.6	206.9	36.3	97.7	3.6
JCA–046_10	486	0.7	0.10092	0.00595	0.01545	0.00050	0.734	64.7761	2.1005	0.0474	0.0020	97.6	5.5	98.8	3.2	68.1	48.7	98.8	3.2
JCA–046_11	511	0.5	0.11094	0.00583	0.01570	0.00052	0.783	63.4248	2.0749	0.0512	0.0017	106.8	5.3	100.4	3.3	251.8	38.2	100.4	3.3

Cretaceous

Table 3. U–Pb LA–ICP–MS geochronological results from the analyzed intrusive bodies (Altavista, San Diego, and Antioquia) *(continued)*.

Department of the Environment, Washington State University			Isotopic ratios									Ages							
Sample			Pb 207 Corrected					Non Corrected				$^{207}Pb/^{235}U$	2σ Abs error	$^{206}Pb/^{238}U$	2σ Abs error	$^{207}Pb/^{206}Pb$	2σ Abs error	Best age	2σ Abs error
Name	U (ppm)	U/Th	$^{207}Pb/^{235}U$	2σ Abs error	$^{206}Pb/^{238}U$	2s Abs error	Corr. Coef.	$^{238}U/^{206}Pb$	2σ Abs error	$^{207}Pb/^{206}Pb$	2σ Abs error	(Ma)	(Ma)	(Ma) (207 Corr)	(Ma)	(Ma)	(Ma)	(Ma)	(Ma)
JCA–046_12	515	0.7	0.10312	0.00566	0.01526	0.00052	0.774	65.4367	2.2113	0.0490	0.0018	99.7	5.2	97.6	3.3	148.1	41.4	97.6	3.3
JCA–046_13	930	0.6	0.10398	0.00475	0.01563	0.00049	0.832	63.9668	2.0123	0.0483	0.0013	100.4	4.4	100.0	3.1	111.8	30.6	100.0	3.1
JCA–046_14	460	0.9	0.10374	0.00561	0.01565	0.00055	0.791	63.8983	2.2340	0.0481	0.0016	100.2	5.2	100.1	3.5	103.1	39.7	100.1	3.5
JCA–046_15	1224	0.5	0.09936	0.00449	0.01500	0.00046	0.830	66.6674	2.0542	0.0480	0.0013	96.2	4.1	96.0	2.9	101.6	30.5	96.0	2.9
JCA–046_16	480	0.7	0.10477	0.00562	0.01465	0.00052	0.803	67.9338	2.4174	0.0519	0.0017	101.2	5.2	93.7	3.3	280.5	36.9	93.7	3.3
JCA–046_17	3108	0.3	0.10236	0.00410	0.01542	0.00047	0.895	64.8489	1.9930	0.0482	0.0009	99.0	3.8	98.6	3.0	106.9	21.8	98.6	3.0
JCA–046_18	1161	0.7	0.10237	0.00465	0.01547	0.00050	0.849	64.6331	2.1068	0.0480	0.0012	99.0	4.3	99.0	3.2	98.6	29.0	99.0	3.2
JCA–046_19	999	0.7	0.10153	0.00461	0.01539	0.00049	0.839	64.9936	2.0676	0.0478	0.0012	98.2	4.2	98.4	3.1	91.8	30.0	98.4	3.1
JCA–046_20	1029	0.6	0.10785	0.00556	0.01545	0.00058	0.843	64.5014	2.4115	0.0506	0.0014	104.0	5.1	98.8	3.7	223.7	32.4	98.8	3.7
AG–01_1	442	0.3	0.09151	0.00519	0.01388	0.00047	0.758	72.0371	2.4205	0.0478	0.0018	88.9	4.8	88.9	3.0	89.9	44.6	88.9	3.0
AG–01_2	955	0.3	0.09564	0.00484	0.01408	0.00045	0.791	70.8804	2.2699	0.0493	0.0016	92.7	4.5	90.1	2.9	160.1	36.9	90.1	2.9
AG–01_3	310	0.3	0.09829	0.00622	0.01405	0.00051	0.743	70.9108	2.5870	0.0507	0.0022	95.2	5.7	89.9	3.3	228.9	49.4	89.9	3.3
AG–01_4	422	0.3	0.12867	0.01543	0.01277	0.00050	0.650	75.7602	2.8662	0.0731	0.0070	122.9	13.8	81.8	3.2	1015.8	94.2	81.8	3.2
AG–01_5	279	0.3	0.20064	0.02189	0.01352	0.00071	0.675	68.3075	3.3098	0.1076	0.0083	185.7	18.2	86.6	4.3	1759.5	68.7	86.6	4.3
AG–01_6	360	0.3	0.09565	0.00600	0.01397	0.00051	0.746	71.4332	2.6114	0.0497	0.0021	92.7	5.6	89.4	3.3	179.6	49.3	89.4	3.3
AG–01_7	301	0.3	0.09530	0.00631	0.01439	0.00051	0.721	69.4940	2.4824	0.0480	0.0023	92.4	5.8	92.1	3.3	101.6	55.1	92.1	3.3
AG–01_8	629	0.3	0.10049	0.00647	0.01377	0.00054	0.759	72.1494	2.8303	0.0529	0.0023	97.2	6.0	88.2	3.5	325.9	47.7	88.2	3.5
AG–01_9	231	0.3	0.09640	0.00678	0.01398	0.00055	0.729	71.3235	2.8221	0.0500	0.0025	93.5	6.3	89.5	3.5	195.4	56.4	89.5	3.5
AG–01_10	388	0.3	0.09013	0.00553	0.01405	0.00050	0.743	71.2944	2.5173	0.0465	0.0020	87.6	5.1	89.9	3.2	25.0	50.2	89.9	3.2
AG–01_11	317	0.3	0.10078	0.00728	0.01428	0.00057	0.720	69.7401	2.7550	0.0512	0.0026	97.5	6.7	91.4	3.6	249.5	58.2	91.4	3.6
AG–01_12	435	0.3	0.09130	0.00542	0.01397	0.00049	0.755	71.6075	2.5232	0.0474	0.0019	88.7	5.0	89.4	3.1	69.1	47.1	89.4	3.1
AG–01_13	375	0.3	0.10117	0.00734	0.01376	0.00050	0.700	72.1606	2.6214	0.0533	0.0028	97.9	6.8	88.1	3.2	342.7	59.3	88.1	3.2
AG–01_14	542	0.4	0.09123	0.00595	0.01363	0.00063	0.817	73.2973	3.4070	0.0485	0.0019	88.6	5.5	87.3	4.0	125.9	44.4	87.3	4.0
AG–01_15	677	0.3	0.09247	0.00466	0.01390	0.00044	0.791	71.8793	2.2939	0.0482	0.0015	89.8	4.3	89.0	2.8	110.8	37.1	89.0	2.8
AG–01_16	631	0.3	0.09657	0.00531	0.01458	0.00050	0.777	68.5634	2.3473	0.0480	0.0017	93.6	4.9	93.3	3.2	100.8	41.6	93.3	3.2
AG–01_17	436	0.2	0.09206	0.00583	0.01358	0.00050	0.746	73.5011	2.7205	0.0492	0.0021	89.4	5.4	87.0	3.2	155.7	49.9	87.0	3.2
AG–01_18	388	0.2	0.09041	0.00579	0.01379	0.00051	0.743	72.5375	2.7009	0.0475	0.0021	87.9	5.4	88.3	3.3	76.9	51.6	88.3	3.3
AG–01_19	595	0.3	0.10576	0.00633	0.01413	0.00056	0.791	70.2030	2.7475	0.0543	0.0020	102.1	5.8	90.4	3.5	383.4	41.2	90.4	3.5
AG–01_20	554	0.3	0.09369	0.00622	0.01413	0.00066	0.807	70.7667	3.2861	0.0481	0.0019	90.9	5.8	90.4	4.2	104.3	46.4	90.4	4.2
AG–01_21	553	0.4	0.09683	0.00481	0.01458	0.00046	0.794	68.5701	2.1676	0.0482	0.0015	93.8	4.4	93.3	2.9	107.7	36.4	93.3	2.9

Table 3. U–Pb LA–ICP–MS geochronological results from the analyzed intrusive bodies (Altavista, San Diego, and Antioquia) *(continued).*

Department of the Environment, Washington State University			Isotopic ratios									Ages							
Sample			Pb 207 Corrected					Non Corrected				$^{207}Pb/^{235}U$	2σ Abs error	$^{206}Pb/^{238}U$	2σ Abs error	$^{207}Pb/^{206}Pb$	2σ Abs error	Best age	2σ Abs error
Name	U (ppm)	U/Th	$^{207}Pb/^{235}U$	2σ Abs error	$^{206}Pb/^{238}U$	2s Abs error	Corr. Coef.	$^{238}U/^{206}Pb$	2σ Abs error	$^{207}Pb/^{206}Pb$	2σ Abs error	(Ma)	(Ma)	(Ma) (207 Corr)	(Ma)	(Ma)	(Ma)	(Ma)	(Ma)
DM–056_1	100	1.8	0.09562	0.00907	0.01527	0.00071	0.724	65.7082	3.0561	0.0454	0.0032	92.7	8.4	97.7	4.5	0.0	49.1	97.7	4.5
DM–056_2	290	1.0	0.09663	0.00605	0.01516	0.00051	0.779	66.0890	2.2307	0.0462	0.0019	93.7	5.6	97.0	3.3	8.7	49.9	97.0	3.3
DM–056_3	189	1.3	0.10458	0.00668	0.01544	0.00056	0.785	64.6646	2.3241	0.0491	0.0021	101.0	6.1	98.8	3.5	153.5	48.4	98.8	3.5
DM–056_4	152	1.0	0.12042	0.01383	0.01464	0.00068	0.700	67.2831	3.0872	0.0597	0.0052	115.5	12.5	93.7	4.3	591.2	92.0	93.7	4.3
DM–056_5	135	1.2	0.09890	0.00820	0.01508	0.00078	0.786	66.3443	3.4457	0.0476	0.0025	95.8	7.6	96.5	5.0	77.7	61.8	96.5	5.0
DM–056_6	100	1.4	0.10365	0.00988	0.01532	0.00069	0.719	65.1730	2.9118	0.0491	0.0034	100.1	9.1	98.0	4.4	150.8	80.3	98.0	4.4
DM–056_7	106	1.8	0.10589	0.00909	0.01507	0.00063	0.732	66.1030	2.7610	0.0510	0.0032	102.2	8.3	96.4	4.0	239.0	69.9	96.4	4.0
DM–056_8	94	1.6	0.10229	0.01370	0.01542	0.00084	0.692	64.8431	3.5524	0.0481	0.0050	98.9	12.6	98.6	5.4	104.9	118.3	98.6	5.4
DM–056_9	121	1.8	0.10199	0.00879	0.01526	0.00066	0.735	65.4732	2.8372	0.0485	0.0030	98.6	8.1	97.7	4.2	121.8	71.1	97.7	4.2
DM–056_10	109	1.1	0.10138	0.00933	0.01547	0.00077	0.742	64.6707	3.2182	0.0475	0.0031	98.0	8.6	99.0	4.9	75.4	74.9	99.0	4.9
DM–056_11	109	1.6	0.10275	0.00990	0.01549	0.00085	0.750	64.5614	3.5290	0.0481	0.0032	99.3	9.1	99.1	5.4	105.1	76.3	99.1	5.4
DM–056_12	214	1.2	0.10310	0.00831	0.01480	0.00077	0.798	67.3376	3.4976	0.0505	0.0025	99.6	7.6	94.7	4.9	218.9	56.8	94.7	4.9
DM–056_13	110	1.7	0.10926	0.00969	0.01561	0.00078	0.754	63.8484	3.1824	0.0508	0.0031	105.3	8.8	99.8	5.0	230.5	68.3	99.8	5.0
DM–056_14	136	1.5	0.09880	0.00851	0.01537	0.00078	0.766	65.1912	3.3105	0.0466	0.0027	95.7	7.9	98.3	5.0	30.6	67.6	98.3	5.0
DM–056_15	104	1.5	0.10388	0.01254	0.01537	0.00117	0.771	64.9912	4.9583	0.0490	0.0039	100.4	11.5	98.3	7.5	149.3	89.6	98.3	7.5
DM–056_16	138	1.7	0.09700	0.00831	0.01535	0.00080	0.775	65.3406	3.4102	0.0458	0.0026	94.0	7.7	98.2	5.1	0.0	56.0	98.2	5.1
DM–056_17	110	1.6	0.10746	0.00906	0.01504	0.00059	0.729	66.1518	2.5977	0.0518	0.0032	103.6	8.3	96.2	3.8	277.2	68.9	96.2	3.8
DM–056_18	95	2.1	0.10809	0.00958	0.01490	0.00060	0.723	66.7323	2.6817	0.0526	0.0034	104.2	8.8	95.3	3.8	312.9	72.6	95.3	3.8
DM–056_19	98	1.3	0.10098	0.00929	0.01542	0.00070	0.728	64.8919	2.9543	0.0475	0.0032	97.7	8.5	98.6	4.5	74.1	77.4	98.6	4.5
DM–056_20	146	0.6	0.10435	0.00776	0.01551	0.00065	0.769	64.4212	2.7079	0.0488	0.0024	100.8	7.1	99.2	4.2	138.6	57.5	99.2	4.2
DM–056_21	108	1.6	0.09602	0.00734	0.01516	0.00064	0.760	66.1276	2.7911	0.0459	0.0024	93.1	6.8	97.0	4.1	0.4	55.7	97.0	4.1
DM–056_22	97	1.6	0.10395	0.00916	0.01493	0.00067	0.735	66.7764	2.9791	0.0505	0.0032	100.4	8.4	95.5	4.3	218.5	71.2	95.5	4.3
DM–056_23	66	2.4	0.09748	0.01054	0.01503	0.00078	0.713	66.6121	3.4411	0.0470	0.0038	94.4	9.7	96.2	5.0	51.2	92.9	96.2	5.0
DM–056_24	174	2.0	0.10609	0.00805	0.01514	0.00056	0.744	65.8070	2.4430	0.0508	0.0027	102.4	7.4	96.9	3.6	232.6	61.2	96.9	3.6
DM–056_25	190	1.3	0.10585	0.00746	0.01497	0.00054	0.756	66.4981	2.3692	0.0513	0.0025	102.2	6.8	95.8	3.4	252.9	55.6	95.8	3.4
DM–056_26	113	2.1	0.10162	0.00768	0.01508	0.00058	0.748	66.2409	2.5293	0.0489	0.0026	98.3	7.1	96.5	3.7	142.1	61.4	96.5	3.7
DM–056_27	141	1.7	0.10283	0.00900	0.01499	0.00070	0.742	66.5727	3.0824	0.0498	0.0031	99.4	8.3	95.9	4.4	184.1	70.0	95.9	4.4
DM–056_28	93	2.0	0.11843	0.01050	0.01566	0.00072	0.738	63.2963	2.8963	0.0548	0.0034	113.6	9.5	100.2	4.6	406.0	68.3	100.2	4.6
DM–056_29	121	1.5	0.10360	0.00830	0.01505	0.00059	0.738	66.2812	2.5859	0.0499	0.0029	100.1	7.6	96.3	3.8	191.6	65.6	96.3	3.8
DM–056_30	104	1.8	0.09789	0.00820	0.01522	0.00060	0.730	65.8208	2.6156	0.0467	0.0029	94.8	7.6	97.4	3.9	31.4	71.9	97.4	3.9
DM–056_31	94	2.0	0.09949	0.00934	0.01585	0.00071	0.721	63.2773	2.8272	0.0455	0.0032	96.3	8.6	101.4	4.5	0.0	53.7	101.4	4.5

Cretaceous

Table 4. Whole–rock geochemistry from the Altavista and San Diego Plutons.

Sample	JCA036	JCA037	JCA038	JCA043
Rock type	Quartz diorite	Gabbro	Andesitic porphyry	Gabbro
Unit	Altavista	Altavista	Altavista	San Diego
SiO_2	67.4	63.9	56.9	54.6
Al_2O_3	16.8	15.6	15.8	16.15
Fe_2O_3	4.12	5.36	6.71	7.19
MgO	0.83	2.67	3.42	5.93
CaO	2.87	5.23	7.48	9.36
Na_2O	6.51	5.48	2.99	3.73
K_2O	1.59	0.67	0.8	0.43
TiO_2	0.51	0.92	0.76	0.85
P_2O_5	0.15	0.2	0.23	0.12
MnO	0.06	0.14	0.15	0.14
Cr_2O_3		0.01	0.01	0.01
Ni	0	0	0	0
Sc	0	0	0	0
LOI	0.36	0.44	4.5	1.03
Sum	101.28	100.67	99.85	99.59
Cr	30	60	60	100
Pb				
Ba	487	193.5	356	169.5
Co	0	0	0	0
Cs	2.05	1.25	0.59	0.49
Ga	21.2	18.9	18.2	14.7
Hf	8.4	4	3.4	2.7
Nb	10.6	14.4	4.3	5
Rb	48.6	27.8	18.1	9.4
Sn	3	3	2	2
Sr	243	240	493	289
Ta	0.6	0.9	0.3	0.3
Th	4.42	3.26	1.64	1.41
U	1.99	1.39	0.73	0.47
V	87	95	148	172
W	1	1	1	1
Zr	406	168	122	98
Y	25	37.2	21	22
La	21.2	14.4	10.3	8.5
Ce	43.3	37.7	23.4	21.2
Pr	4.96	4.98	3.23	2.93
Nd	18.3	20.9	14.1	13.3
Sm	4.02	4.87	3.02	3.23
Eu	1.31	1.21	1	1.28
Gd	4.28	5.64	3.68	4.13
Tb	0.65	0.9	0.63	0.75
Dy	3.82	6.11	3.44	4.35
Ho	0.9	1.28	0.73	0.8
Er	2.66	4.13	2.42	2.4
Tm	0.41	0.62	0.32	0.35
Yb	2.96	4.67	2.18	2.27
Lu	0.49	0.62	0.36	0.39
Rb/Sr	0.20	0.12	0.04	0.03
Sr/Y	9.72	6.45	23.48	13.14
Sr/Y thickness	18.84	15.21	34.11	22.63

have received different lithostratigraphic names (e.g., San Luis, Amalfi, and Berlin Sedimentites, and the San Pablo and La Soledad Formations), overlie Triassic and older metamorphic rocks of the Cajamarca Complex, and are also intruded by Upper Cretaceous plutons (Feininger et al., 1972; Hall et al., 1972; Barrero & Vesga, 1976; Naranjo, 1983). The fossil content of mudstones from these units suggests Valanginian to Aptian – Albian accumulation ages. Although precise stratigraphic analysis from these units is still missing, cartographic and field observations indicate that they are represented by fining–upward sequences in which coarse–grained conglomeratic and sandstone levels are overlain by upper fine–grained siliciclastic facies associations.

The coarse–grained association includes intercalations of sandstones and conglomerates, which in the *S*an Luis Sedimentites are characterized by thicknesses of a few centimeters to hundreds of meters (Feininger et al., 1972). Sandstones are mainly quartzose in composition, whereas conglomerates include oligomictic (white quartz and chert) or polymictic conglomerates that may include metavolcanic, schist, and/or gabbroic clasts in the San Luis Sedimentites, as well as in the San Pablo Formation and the Berlin Sedimentites (Feininger et al., 1972; Hall et al., 1972; Naranjo, 1983). The quartzose conglomerates have been reported overlying the metamorphic basement (Feininger et al., 1972; Hall et al., 1972; Naranjo, 1983; Pimiento, 2011).

The fine–grained facies include mostly fossiliferous Lower Cretaceous black shales (up to 80%; see review in González, 2001) intercalated with chert, siltstones, graywackes, and intraformational conglomerates with shale and sandstone fragments, which may reach thicknesses of 600–1000 m (Feininger et al., 1972; Hall et al., 1972; Gómez & Lizcano, 1990). Significant variations and lateral differences in the stratigraphic thickness between distinct localities is a commonly reported feature. The La Soledad Formation, which is one of the northern expressions

Table 5. Hf isotope results for zircons from the Aguadas porphyritic unit.

	measured	corrected															
Sample	$^{176}Hf/^{177}Hf$	$^{176}Hf/^{177}Hf$	2SE	$^{176}Lu/^{177}Hf$	2SE	$^{176}Yb/^{177}Hf$	2SE	$^{178}Hf/^{177}Hf$	2SE	$^{180}Hf/^{177}Hf$	2SE	Total Hf beam	Age	$^{176}Hf/^{177}Hfi$	EHf0	2SE	EHfi
DM56_1	0.282958	0.2830121	0.000036	0.002089	0.000067	0.0504	0.0018	1.467149	0.000041	1.88694	0.0001	14.5	94.4	0.283008412	8.0	1.3	10.0
DM56_2	0.282949	0.2830031	0.00003	0.001171	0.000018	0.0263	0.0004	1.467186	0.000042	1.887079	0.000091	16.44	97.2	0.283000967	7.7	1.1	9.8
DM56_3	0.282937	0.2829911	0.000026	0.000881	0.000039	0.01948	0.00082	1.46717	0.000033	1.887001	0.000084	17.68	98.7	0.282989468	7.3	0.9	9.4
DM56_4	0.282966	0.2830201	0.000026	0.001068	0.00005	0.0232	0.001	1.467173	0.000032	1.88699	0.00011	17.41	93.9	0.283018224	8.3	0.9	10.3
DM56_5	0.283019	0.2830731	0.000028	0.00319	0.00025	0.0805	0.0064	1.467178	0.000031	1.887	0.000082	14.78	99.0	0.283067207	10.2	1.0	12.2
DM56_6	0.282946	0.2830001	0.000033	0.001426	0.000071	0.0336	0.0017	1.467165	0.000037	1.88695	0.000081	18.13	98.0	0.282997483	7.6	1.2	9.7
DM56_7	0.282946	0.2830001	0.000025	0.001099	0.000022	0.02485	0.00048	1.467187	0.000035	1.886991	0.000081	15.49	98.5	0.282998071	7.6	0.9	9.7
DM56_8	0.282928	0.2829821	0.000024	0.001542	0.000048	0.037	0.0014	1.467171	0.000035	1.88695	0.000071	15.9	97.2	0.282979289	7.0	0.8	9.0
DM56_9	0.282965	0.2830191	0.000036	0.00128	0.000093	0.0306	0.0021	1.467153	0.000042	1.88694	0.00012	18.56	96.2	0.283016797	8.3	1.3	10.3
DM56_10	0.282955	0.2830091	0.000029	0.001196	0.000021	0.02749	0.00065	1.467133	0.000031	1.887	0.00011	16.33	99.6	0.28300687	7.9	1.0	10.1
DM56_11	0.282972	0.2830261	0.00003	0.00195	0.00024	0.0476	0.0061	1.467147	0.000032	1.886874	0.000095	15.13	97.2	0.283022557	8.5	1.1	10.6
DM56_12	0.282974	0.2830281	0.000023	0.00176	0.00012	0.0406	0.0029	1.467179	0.000034	1.886947	0.000084	16.97	97.2	0.283024902	8.6	0.8	10.6
DM56_13	0.282982	0.2830361	0.000032	0.001103	0.000059	0.0243	0.0013	1.46714	0.000031	1.886876	0.00009	17.18	97.2	0.283034097	8.9	1.1	11.0

of the Lower Cretaceous sedimentites of the Central Cordillera, presents interlayered spilitized basaltic lava flows at its top, which include embedded fragments of the host sedimentary rocks (Hall et al., 1972).

All the units described above are intruded by Upper Cretaceous granodioritic to quartz dioritic rocks, which are part of the composite Antioquian Batholith with a protracted magmatic history spanning from 97 Ma to 84 Ma (Figures 2, 3; Ibañez–Mejia et al., 2007; Leal–Mejía, 2011; Villagómez et al., 2011; Duque–Trujillo et al., 2018). Our new field and petrographic observations of the San Luis Sedimentites, together with similar published results in the same unit as well as in the La Soledad Formation and Berlin Sedimentites (Feininger et al., 1972; Hall et al., 1972), have shown that granitoid bodies intrude formerly folded and foliated low–grade Lower Cretaceous metasedimentary rocks (Figure 4), producing an undeformed thermal aureole. In the San Luis Sedimentites, petrographic observations of andalusite porphyroblasts and mica needles cut the schistose fabric defined by the orientation of white mica and suggest that contact metamorphism reached the hornblende–hornfels facies.

Field observations in the Abejorral Formation and in the San Luis Sedimentites near the towns of Aguadas and San Luis, as well as previously published maps and reports from correlatable units (Zapata et al., 2018), show that all of these rocks are characterized by the presence of asymmetric folding with relatively steep limbs and are commonly faulted against the metamorphic basement (Figure 4).

West of the Abejorral Formation, in the western flank of the Central Cordillera, a series of Cretaceous siliciclastic sequences crops out and is characterized by interlayered fine–grained sandstones and mudstones with volcanic (pyroclastic and effusive) rocks (Gómez–Cruz et al., 1995; Tamayo & Correa, 2010; Zapata et al., 2018). These sequences are often exclusively composed of volcanic rocks with basaltic composition, including pillow lavas, and are locally associated with gabbroic bodies and highly deformed serpentinized peridotites, which have been included in the Quebradagrande Complex and/or the Cauca Ophiolitic Complex (González, 1980, 2001; Álvarez, 1987; Rodríguez & Cetina, 2016; Zapata et al., 2018).

4.2. Sandstone Petrography

Quantitative published petrographic data from the Abejorral Formation and Quebradagrande Complex were reviewed (Quiroz, 2005; Tamayo & Correa, 2010; Zapata et al., 2018), together with two newly analyzed samples from the San Luis Sedimentites. Additionally, qualitative descriptions were revised in order to assess the compositional character and provenance of the Lower Cretaceous sedimentary units exposed in the Central Cordillera of Colombia. Both the Folk (1974) and Garzanti (2016) classification and provenance diagrams were used to analyze sandstone compositions.

Sandstones from the Abejorral Formation and the upper segment of the Valle Alto Formation are medium– to coarse–grained, with angular to subangular and low–sphericity particles dominantly composed of monocrystalline and polycrystalline quartz and metamorphic lithic fragments, with minor muscovite and sedimentary lithic fragments (Gómez–Cruz et al., 1995; Quiroz, 2005; Tamayo & Correa, 2010; Zapata et al., 2018). In the QFL diagram of Folk (1974), samples plot within the litharenite, sublitharenite, and quartzarenite fields, whereas in the tectonic discrimination diagram of Garzanti (2016), they plot within the recycled orogen and continental block fields (Figure 5).

The Lower Cretaceous sandstones included in the Quebradagrande Complex and the upper Abejorral segment include

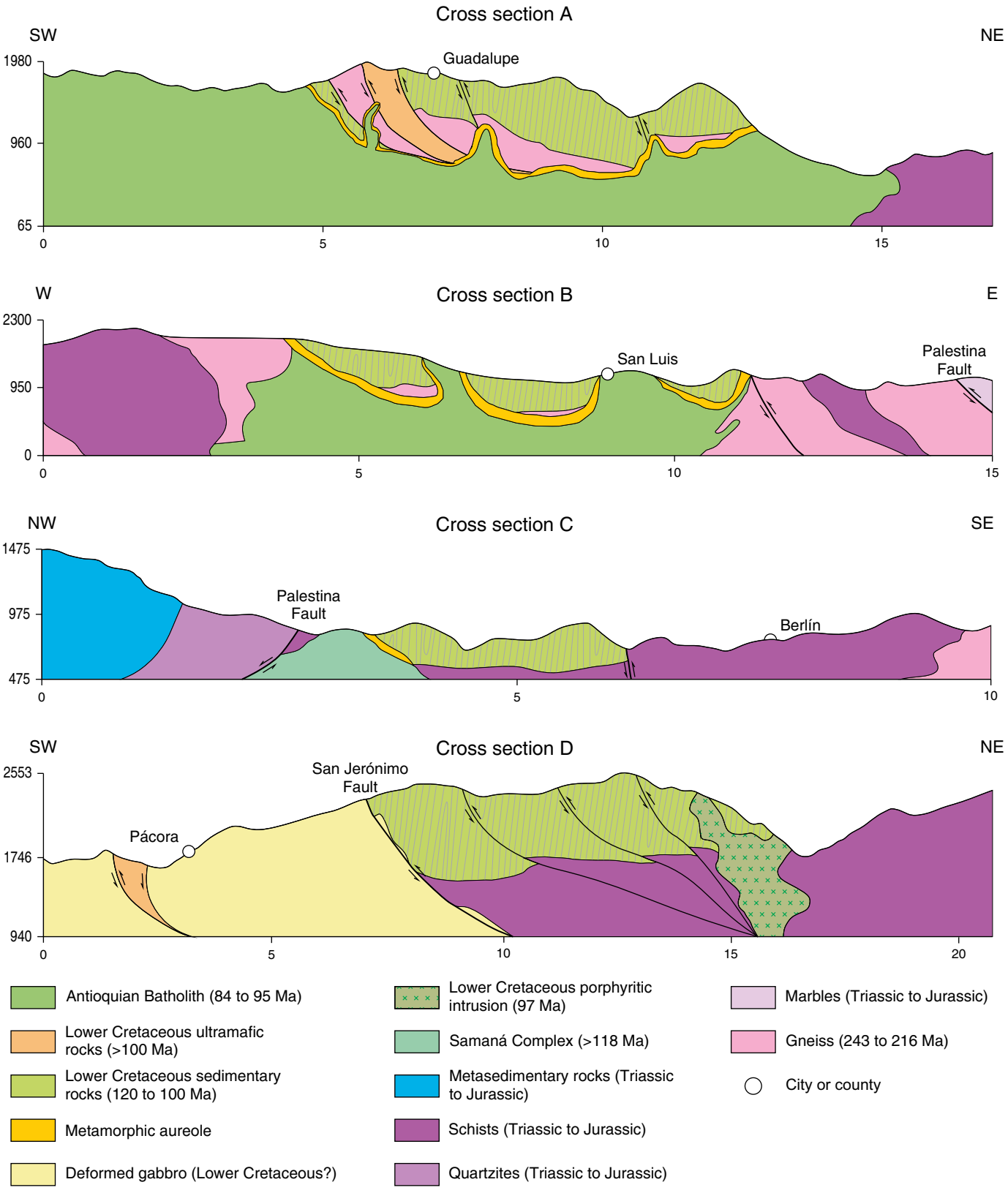

Figure 4. Geological cross sections from the Lower Cretaceous units showing the relation between deformation and magmatic intrusions. The cross–section locations are given in Figure 2. Cross section A includes the San Pablo Formation in the northern segment of the Central Cordillera (after Álvarez et al., 1975). Cross section B includes the San Luis Sedimentites in the eastern segment of the Central Cordillera (new field data, after Feininger et al., 1972). Cross section C includes the Berlin Sedimentites on the eastern flank of the Central Cordillera (after Barrero & Vesga, 1976). Cross section D includes the Abejorral Formation on the western flank of the Central Cordillera (new field data).

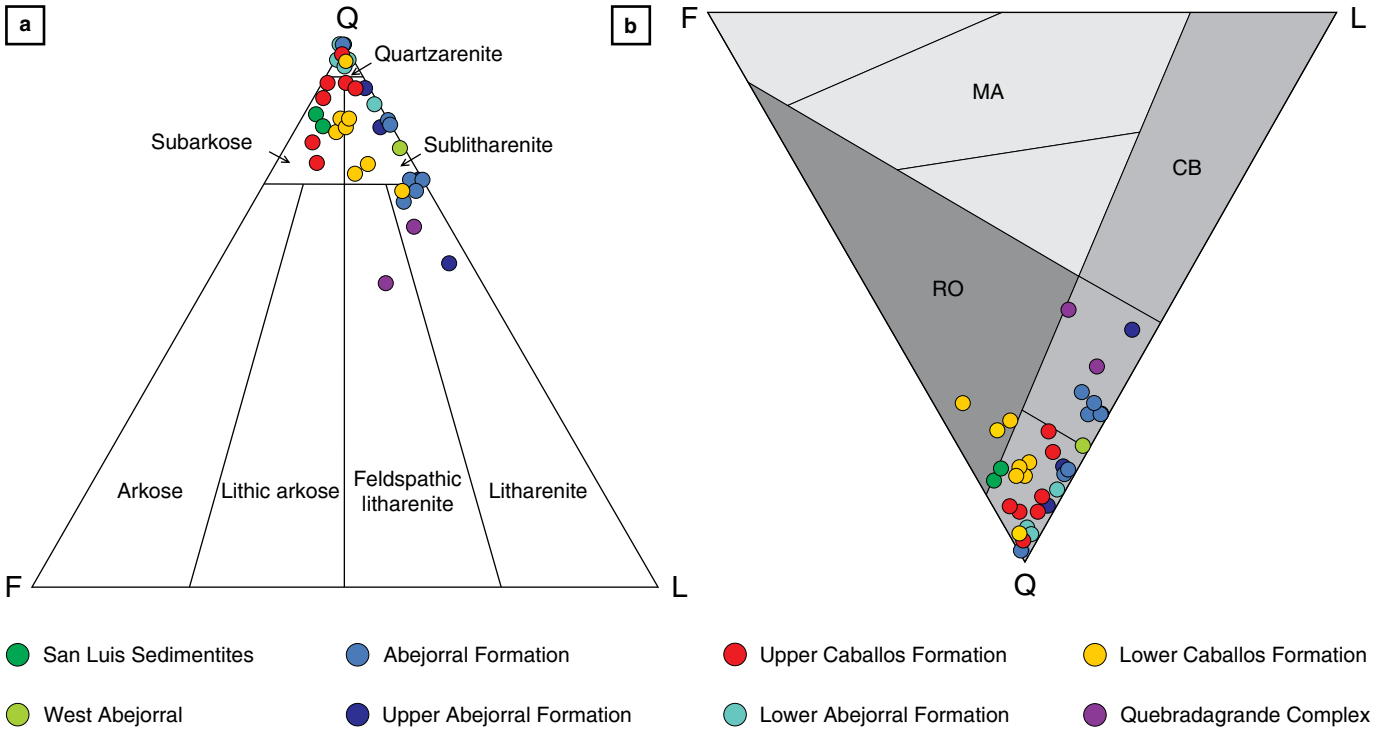

Figure 5. Sandstone petrography compilation and new data from the Abejorral Formation (Tamayo & Correa, 2010) and the San Luis Sedimentites. **(a)** Sandstone classification after Folk (1974). **(b)** Sandstone classification diagram after Garzanti (2016). Abbreviations: (MA) magmatic arc; (RO) recycled orogen; (CB) continental block.

schistose and volcanic lithics, as well as abundant (<70%) foliated polycrystalline and monocrystalline quartz with undulatory and straight extinction (Tamayo & Correa, 2010; Jaramillo et al., 2017; Zapata et al., 2018).

The San Luis Sedimentites include medium– to coarse–grained sandstones, with angular to subangular and low–sphericity particles, also dominantly composed of monocrystalline igneous and polycrystalline metamorphic quartz, with minor sedimentary and metamorphic lithic fragments and feldspar. In the QFL diagram of Folk (1974), the samples plot within the subarkose field, whereas in the tectonic discrimination diagram of Garzanti (2016), they plot within the continental block field (Figure 5).

Descriptions of sandstones from the San Pablo and La Soledad Formations in the northern segment of the Central Cordillera, as well as the Berlin Sedimentites, suggest that they are fine– to medium–grained rocks, with angular particles mainly composed of quartz, which is consistent with a sialic continental block affinity. However, more definitive details are missing and waiting for new provenance research.

4.3. Detrital Zircon Geochronology

The results of four new detrital zircon U–Pb analyses are presented and compared with previously published geochronological data to complement the sedimentary provenance of the Lower Cretaceous units exposed in both the western and eastern flanks of the Central Cordillera. We report the maximum accumulation age based on the three youngest overlapping grains approach of Dickinson & Gehrels (2009), but only when it is close to the stratigraphic age previously suggested by the fossil content, since older ages are meaningless for the purpose of analyzing accumulation ages. Single– or two–grain ages are also noted when necessary, although we are aware that such types of ages are not statistically robust (Dickinson & Gehrels, 2009).

One sample collected from the Quebradagrande Complex exposed northwest of the city of Medellín (Figures 1, 2) yielded only seven individual zircon U–Pb ages clustered at approximately 190 Ma, with additional Early Cretaceous, Paleozoic, and Neoproterozoic ages (Figure 6).

Two samples were analyzed from the Abejorral Formation and the Quebradagrande Complex (eastern and western intervals in the sense of Gómez–Cruz et al., 1995) exposed in the western flank of the Central Cordillera near the city of Manizales (Figures 1, 2). A total of 95 individual zircon grains were dated from the eastern interval (Abejorral Formation equivalent). The sample is characterized by major age peaks in the Permian – Triassic (240–296 Ma), early Paleozoic (340–530 Ma), and Proterozoic (ca. 630–1400 Ma). Thirty–six individual grains were analyzed from a sample from the western interval. This sample has a major Early Cretaceous peak (ca. 105 Ma) with additional Permian – Triassic, Paleozoic, and Proterozoic

zircon ages and a well–defined maximum accumulation age of 103.4 ± 1.1 Ma (Figure 6).

One hundred and twenty–seven individual zircon U–Pb ages were also obtained from one sample collected from the San Luis Sedimentites close to the town of San Luis (Figure 6). The sample is characterized by Late Jurassic (145–150 Ma), Permian – Triassic (ca. 220–270 Ma), Paleozoic (ca. 340–540 Ma), and Proterozoic ages (ca. 560–1800 Ma). Although this sample also includes minor Early Cretaceous ages of ca. 120–127 Ma and 136–137 Ma, the three youngest overlapping grains suggest a maximum accumulation age of 146.1 ± 2.0 Ma.

4.4. Zircon Geochronology of Magmatic Rocks

Early Cretaceous magmatic rocks from the Central Cordillera have yielded ca. 129 Ma U–Pb crystallization ages obtained from stock–sized plutons in the eastern flank of the cordillera, which intrude Jurassic metamorphic rocks of the Cajamarca Complex (Bustamante et al., 2016) and are exposed immediately to the south of the San Luis and Berlin Sedimentites.

Cretaceous magmatism in the Central Cordillera of Colombia includes both plutonic and volcanic units. The plutonic record is widely exposed in a ca. 8000 km^2 trapezoidal body that has been defined as the Antioquian Batholith (Figures 1, 2; Feininger & Botero, 1982). Compositionally, it varies between gabbro and monzogranite, although it is mainly composed of medium– to coarse–grained tonalite and granodiorite facies. The mafic minerals are hornblende and biotite, which are typical of hydrated sources for magmas generated at convergent margins. These plutons intrude Triassic and older metamorphic rocks of the Cajamarca Complex as well as the Lower Cretaceous sedimentary rocks, forming well–defined contact aureoles (Botero, 1963; Feininger et al., 1972; González, 2001). Different small bodies with similar tonalite, granodiorite, and gabbro compositions include the La Union, La Culebra, Ovejas, Belmira, San Diego, and Altavista Stocks, which have also been interpreted as associated with the different pulses that formed the Antioquian Batholith.

Available U–Pb zircon crystallization ages obtained by multigrain TIMS and single grain LA–ICP–MS analyses have yielded ages between 95 and 59 Ma (Correa et al., 2006; Ibañez–Mejia et al., 2007; Restrepo–Moreno et al., 2007; Leal–Mejía, 2011; Villagómez et al., 2011), without any particular spatial trend. Although areas of this broad plutonic province remain to be analyzed, available whole–rock geochemical data have indicated a typical convergent margin setting for its origin with a well–defined calc–alkaline signature and Nb–Ti anomalies that suggest a magmatic arc affinity (Leal–Mejía, 2011; Villagómez et al., 2011). Farther to the south, Leal–Mejía (2011) described ca. 90 Ma plutonic rocks that intrude the Lower Cretaceous rocks of the Mariquita Stock (Bustamante et al., 2016) and therefore extend the latitudinal distribution of the Late Cretaceous magmatism.

Volcanic rocks are exposed in the western flank of the Central Cordillera, forming a quasi–continuous and highly deformed belt that has been grouped as the Quebradagrande Complex (Maya & González, 1995). This unit is within the San Jerónimo Fault system that separates it from the eastern Lower Cretaceous and Triassic metamorphic rocks of the cordillera and is also in fault contact with ultrabasic units. Its lithostratigraphy includes basaltic to andesitic lavas and pyroclastic rocks with intercalated mudstones and fine–grained sandstones (Nivia et al., 2006; Villagómez et al., 2011; Jaramillo et al., 2017). A coarser siliciclastic sequence, including sandstones and conglomerates, has also been reported (González, 1980). This unit is in fault contact to the west with Lower Cretaceous greenschist– to amphibolite–facies metamorphic rocks included in the Arquía Complex (Maya & González, 1995), as well as Triassic meta–igneous bodies and metasedimentary rocks that resemble those found to the east in the Central Cordillera (Vinasco et al., 2006; Cochrane et al., 2014a).

Published geochemical data suggest the existence of multiple compositional groups within the Quebradagrande Complex. A MORB to E–MORB character (Nivia et al., 2006; Villagómez et al., 2011; Rodríguez & Cetina, 2016) and an arc–like signature are represented by lavas and pyroclastic rocks (review in Jaramillo et al., 2017). These geochemical patterns have been interpreted in terms of the evolution of a single back–arc system that might have resulted from the progressive reduction of the supra–subduction zone mantle signature (Nivia et al., 2006). Nevertheless, Jaramillo et al. (2017) suggested that the compositional evolution followed a trend from MORB–like signatures toward arc–related signatures as a consequence of ongoing crustal thickening.

Available temporal constraints for the magmatic units of the Quebradagrande Complex include local stratigraphic relations with Aptian – Albian mudstone levels (Grosse, 1926; Botero, 1963; González, 1980; Botero & González, 1983; Arévalo et al., 2001), in which basaltic volcanic rocks intrude and are deposited over the fossiliferous strata (Grosse, 1926; Botero, 1963; Arévalo et al., 2001). Zircon U–Pb ages from diorite and tuff samples have yielded ages between 112 Ma and 114 Ma (Villagómez et al., 2011; Cochrane et al., 2014b). Zapata et al. (2018) also documented U–Pb crystallization ages between 103 Ma and 115 Ma in different tuffs and andesitic bodies that are related to the Abejorral Formation and the Quebradagrande Complex. Although a more extensive discussion is beyond the scope of this contribution, it is arguable that the Aptian – Albian volcanic and sedimentary records exposed in the western flank of the Central Cordillera (Quebradagrande Complex and Abejorral Formation) are part of a continuous Aptian – Albian domain.

Elsewhere, Upper Cretaceous fossil content has been recognized in two localities where a sequence of interlayered pyroclastic rocks and mudstones associated with the Que-

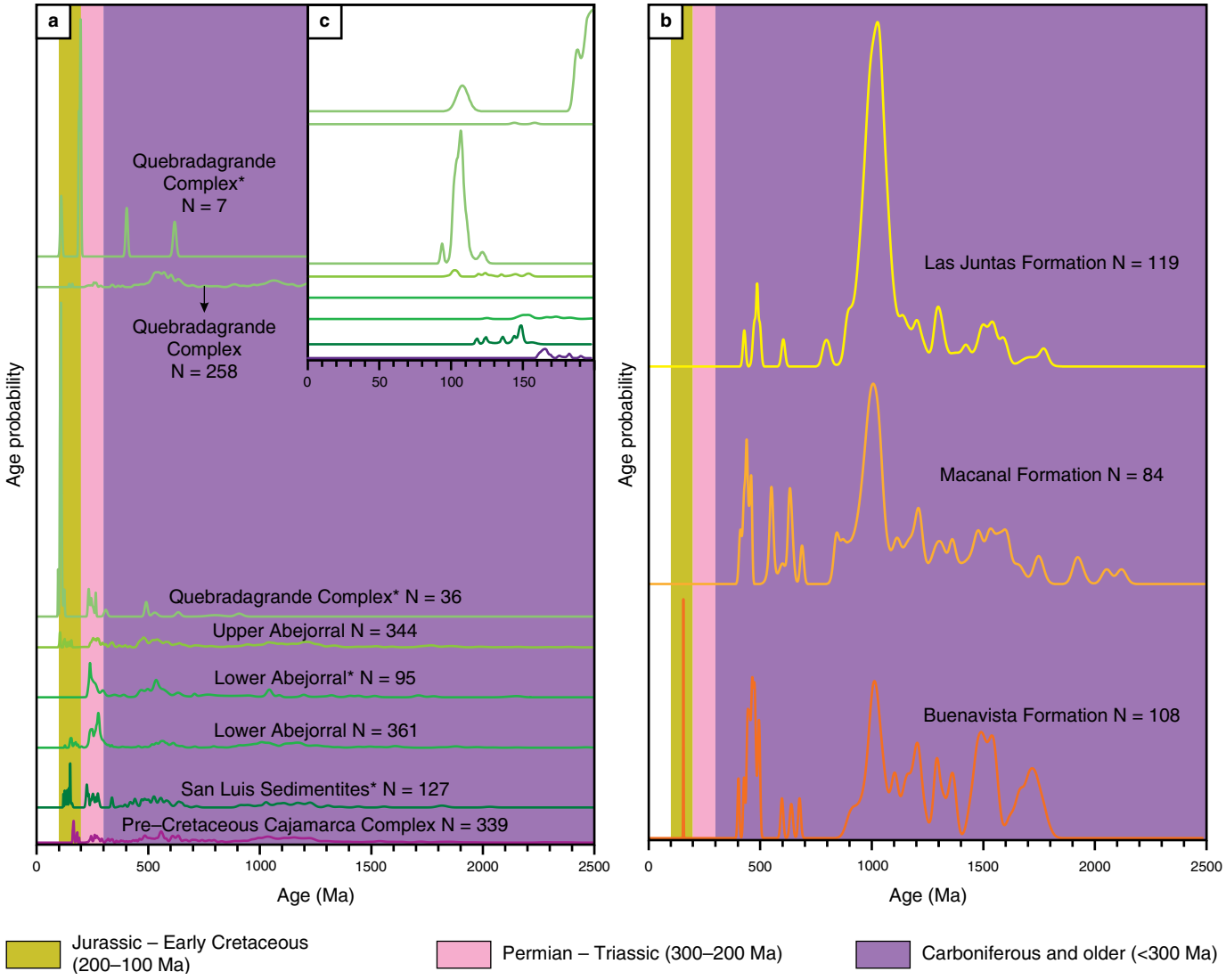

Figure 6. (a) U–Pb zircon geochronology of detrital samples from the Abejorral Formation, Quebradagrande Complex, and San Luis Sedimentites. **(b)** Published results from the same units and the Eastern Cordillera are also included (see text for references). **(c)** Expanded view of panel a showing the distribution of detrital ages between 0 and 200 Ma. *New data presented in this contribution.

bradagrande Complex is found (Botero & González, 1983; Gómez–Cruz et al., 2002). Although these rocks are not extensively discussed, Cochrane (2013) reported U–Pb zircon ages of 80.2 ± 0.7 Ma and 82.1 ± 0.7 Ma from deformed agglomerates near the city of Manizales. These agglomerates are also associated with cherts that include *Hastigerinoides watersi* Cushman, foraminifera characteristic of the Turonian – Campanian (Hall et al., 1972). Similarly, Zapata et al. (2018) documented the existence of ca. 80 Ma volcanic rocks overlying the Early Cretaceous volcano–sedimentary sequence.

Several plutonic bodies of tonalitic and gabbroic compositions with an arc–related geochemical affinity and intrusive relations with volcanic rocks of the Quebradagrande Complex have yielded U–Pb zircon crystallization ages of ca. 80 Ma and 90 Ma (Villagómez et al., 2011; Jaramillo et al., 2017).

It is therefore concluded that the magmatic record of the Quebradagrande Complex represents long–term Cretaceous magmatic evolution between 114 Ma and 80 Ma, which likely occurred through different tectonic scenarios.

Although scarcely studied, in the northern axial zone of the Central Cordillera, in association with the La Soledad Formation, two different volcanic units have been reported: an eastern basaltic unit interlayered with the upper levels of the siliciclastic rocks (Hall et al., 1972) and a prominent pyroclastic unit that includes agglomerates and tuffs, as well as several porphyritic intrusive rocks. The latter is located west of La Soledad Formation, is limited to the west by ultramafic bodies and apparently Triassic gneisses and has been correlated with the Quebradagrande Complex and tentatively assigned to the Late Cretaceous (Hall et al., 1972).

4.5. New U–Pb Zircon Geochronology of Plutonic Rocks

U–Pb LA–ICP–MS ages were obtained from four samples that intruded the Cajamarca Complex (2 samples) and the Lower Cretaceous sedimentary rocks exposed in the western and eastern flank of the Central Cordillera (2 samples; see red triangles in Figure 2). We attempted to refine the timing of the Cretaceous magmatic history and test the temporal relations among magmatism, sedimentation, and deformation.

4.5.1. San Diego Gabbro and Altavista Stock

Both units crop out on the western flank of the Central Cordillera in the city of Medellín (Figures 1, 2). The Altavista Stock intrudes micaceous schists with graphite, biotitic gneisses, and amphibolites, which are part of the pre–Cretaceous Cajamarca Complex (Rodríguez & Montoya, 1993), whereas the San Diego Gabbro intrudes only Triassic gneisses (Rendón, 1999).

In the sampled area, two different facies are recognized in the Altavista Stock; one facies has a predominantly medium–grained granodioritic composition represented by andesine plagioclase (40%), quartz (20%), K–feldspar (15%), hornblende (15%), and biotite (8%), with accessory minerals including apatite, zircon, titanite, and opaque minerals. A second and more mafic diorite facies commonly found as enclaves within the felsic facies is characterized by intermediate plagioclase (40%), quartz (10%), amphibole (40%), biotite (10%), and ~3% accessory minerals including titanite, opaque minerals, and apatite.

The San Diego Gabbro is characteristically a medium–grained, highly altered rock that includes saussuritized plagioclase (50%), hornblende altered to actinolite (45%), and quartz (2%) with titanite, apatite, and opaque minerals as accessory minerals.

Twenty zircon crystals in a granodiorite sample from the Altavista Stock (JCA–045) and twenty more in a diorite sample from the San Diego Gabbro (JCA–046) were analyzed. Crystal sizes vary between 40 and 200 μm and exhibit prismatic habits with (length:width) L:W ratios of 3:1 and 2:1. Cathodoluminescence images are characterized by a single oscillatory zoning pattern that is characteristic of igneous–related zircons (Vavra et al., 1999). The Th/U ratio varies between 0.91 and 5.05 and can also be related to zircons with a magmatic origin (Rubatto, 2002). U–Pb zircon crystallization ages from the two stocks are strongly similar, with weighted mean ages of 97.0 ± 1.4 Ma and 98.2 ± 1.4 Ma, Altavista Stock and San Diego Gabbro, respectively (Figure 7). Previously published multigrain TIMS analyses yield ages of 96 ± 0.4 Ma and 87 ± 0.5 Ma for a mafic and a felsic facies, respectively, of the Altavista Stock and 94 ± 0.9 Ma for the San Diego Gabbro (Correa et al., 2006). Whereas the older TIMS ages for the Altavista Stock overlap with our new results, the other two ages are younger and may reflect a protracted magmatic history.

4.5.2. Aguadas Porphyritic Andesite

Thirty–one zircons were analyzed from a porphyritic andesite with hornblende phenocrysts that intrudes a sequence of interlayered gray and black mudstones from the Abejorral Formation (sample DM–056), located farther to the south of the Altavista Stock and San Diego Gabbro. Zircon crystal sizes range between 60 and 300 μm and show prismatic shapes with L:W of 3:1. Cathodoluminescence images show single oscillatory zoning patterns characteristic of igneous zircons (Vavra et al., 1999). The Th/U ratio varies between 0.4 and 1.6, consistent with a magmatic character for the analyzed zircons (Rubatto, 2002). The analyzed individual grains yield a weighted mean age of 97.3 ± 1.3 Ma (Figure 7), which is related to the magmatic crystallization. No previous geochronological data are available for this porphyritic unit, which has been related to the Sonsón Batholith, considered Eocene in age based on U–Pb zircon geochronology (Ordóñez–Carmona et al., 2001; Leal–Mejía, 2011).

4.5.3. Antioquian Batholith

We analyzed the zircon U–Pb geochronology of a quartz diorite sample with hornblende and biotite from the Antioquian Batholith near the Samaná River (AG–01), where it intrudes the Lower Cretaceous San Luis Sedimentites and the Triassic Samaná Gneiss. The twenty analyzed zircon crystals range from 75 to 200 μm in size and have a L:W ratio of 2:1. Cathodoluminescence images show a single oscillatory zoning pattern characteristic of igneous zircons (Vavra et al., 1999). The Th/U ratio varies between 0.91 and 3.67, which may suggest a magmatic character for the analyzed grains (Rubatto, 2002). Zircons yield a weighted average age of 89.7 ± 1.3 Ma (Figure 7), which is related to the magmatic crystallization. Three U–Pb ages between 84.5 Ma and 93.5 Ma have previously been obtained by single–grain LA–ICP–MS and multigrain TIMS within the same region and are consistent with the new results presented in this contribution (Ibañez–Mejia et al., 2007; Villagómez et al., 2011).

4.6. Whole–Rock Geochemistry from Plutonic Rocks: New and Published Data

Four whole–rock geochemical analyses were conducted on three samples from the Altavista Stock and one from the San Diego Gabbro. SiO_2 varies between 54.6 and 67.4 wt %; total alkalis ($Na_2O + K_2O$), between 3.79 and 8.1 wt %; and CaO and MgO, from 2.87 to 9.36 wt % and 0.83 to 5.93 wt %, respectively. Al_2O_3 and Fe_2O_3 range from 15.6 to 16.8 wt % and 4.12

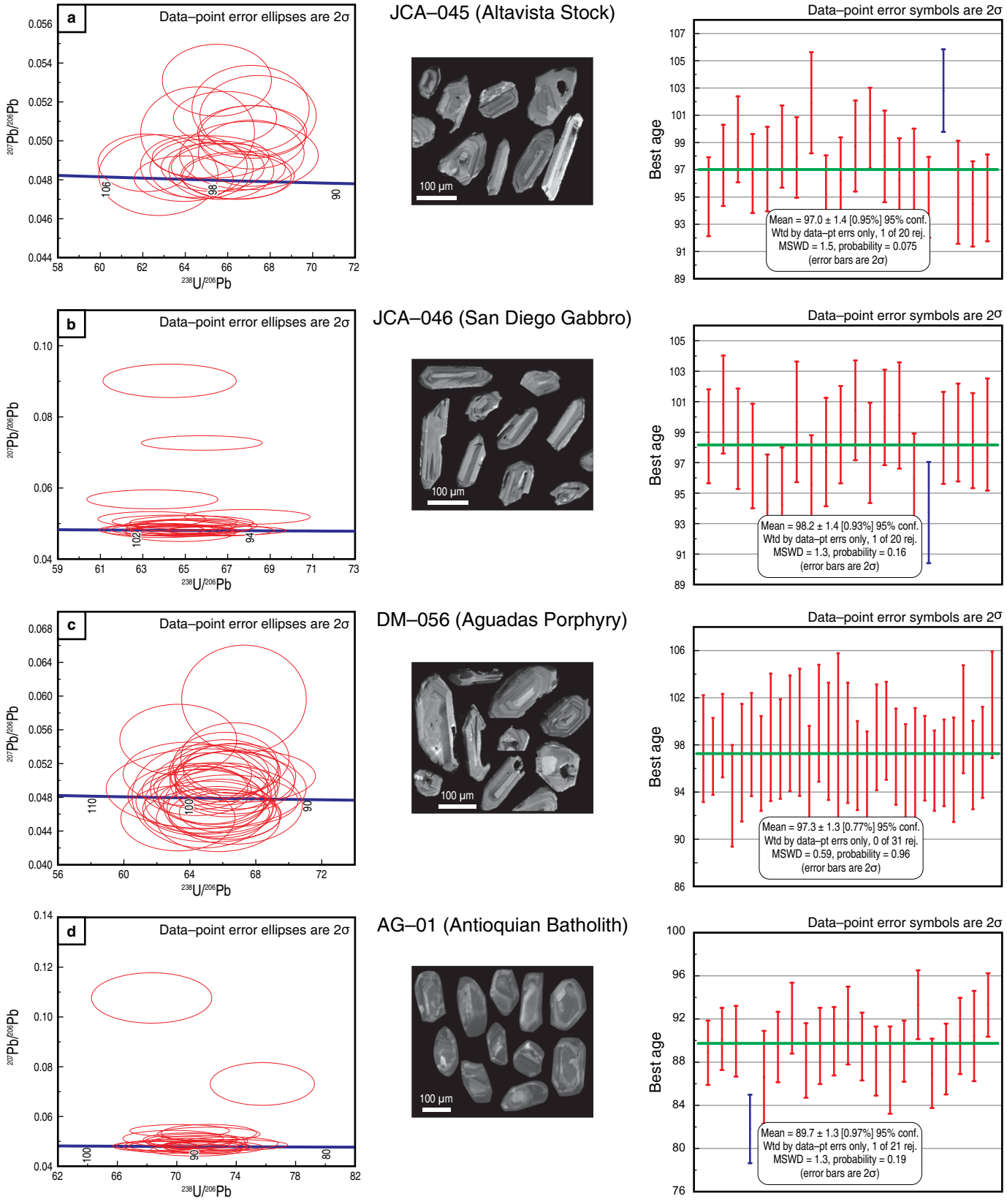

Figure 7. U–Pb zircon geochronology and cathodoluminescence images for: **(a)** Altavista Stock, **(b)** San Diego Gabbro, **(c)** porphyritic rock near Aguadas, and **(d)** Antioquian Batholith.

to 7.19 wt %, respectively, and these values are characteristic of basic to acidic compositions, which allows the classification of these rocks as diorite–gabbro to quartz monzonite (Figure 8a; TAS diagram after Middlemost, 1994), associated with the calc–alkaline magmatic series (Figure 8b, 8c; AFM diagram after Irvine & Baragar, 1971).

REE patterns normalized to the chondrite composition of Nakamura (1974) are characterized by enrichments in light rare earth elements (LREE), with $(La/Sm)_N$ ratios between 1.64 and 3.29, $(La/Yb)_N$ between 2.06 and 4.79, and a flat trend in the heavy rare earth elements (Figure 9; HREE). Only one sample presents a negative Eu anomaly with a Eu/Eu* value of 0.71, while the other three samples show flat trends in the MREE and HREE with Eu/Eu* between 0.92 and 1.08.

Multielemental patterns, normalized to the N–MORB composition of Sun & McDonough (1989), are characterized by negative anomalies in some high field strength elements (HFSE) such as Nb and Ti and enrichments in large ion lithophile elements (LILE), such as Cs, Ba, Th, and K, which may be correlated to subduction–related magmas (Figure 9; Pearce et al., 1984).

The available geochemical data for the Antioquian Batholith show that this body ranges in composition between gabbro and granite (Figure 8; TAS diagram after Middlemost, 1994) and exhibits a typical calc–alkaline affinity (Figure 8; AFM diagram after Irvine & Baragar, 1971). REE patterns normalized to the chondrite composition of Nakamura (1974) are characterized by a well–defined enrichments in LREE and depletions in HREE with both negative and positive Eu anomalies, which could be related to plagioclase fractionation (Figure 9). Multielemental patterns normalized to N–MORB (Sun & McDonough, 1989) show negative anomalies in some HFSE such as Nb and Ti, together with enrichments in LILE such as Cs, Rb, Ba, Th, and K, which suggest the geochemical signature of a magmatic arc (Figure 9; Pearce et al., 1984).

It is noteworthy that the Altavista Stock and San Diego Gabbro, when compared with samples from the Antioquian Batholith, show flatter HREE patterns and more limited enrichments in LREE and Th (Figure 9).

In the tectonic discrimination diagrams, all samples plot in the arc–related pluton field (Figure 10; Pearce et al., 1984). The Th/Yb and Nb/Yb relations also suggest a continental magmatic arc setting. However, the older plutons, including Altavista and San Diego, show relatively less Th enrichment (Figure 10).

4.7. Isotopic Constraints

Isotopic analyses of plutonic rocks from the Cretaceous magmatism are still scarce (Ordóñez–Carmona & Pimentel, 2001; Correa et al., 2006; Leal–Mejía, 2011); however, with the available data, some general observations are possible regarding the temporal changes in isotopic fingerprints and their potential relations with changes in tectonic scenarios.

We have considered data from those samples whose crystallization ages are within the ca. 90–100 Ma time span in order to avoid those that could be related to younger magmatic phases, which are preferentially exposed along the northwestern and northeastern flanks of the Central Cordillera (Jaramillo et al., 2017).

Published Nd–Sr results from the Altavista Stock at 98 Ma are characterized by $\varepsilon Nd_{(98\ Ma)}$ values between +7.4 and +9.8 and initial $^{87}Sr/^{86}Sr$ values ranging from 0.70402 to 0.70456, whereas the values for the San Diego Gabbro vary between +2.8 and +6.2 and 0.70326–0.70331, respectively (Ordóñez–Carmona & Pimentel, 2001; Correa et al., 2006). Conversely, available data from younger samples (ca. 90 Ma) of the Antioquian Batholith on the western and eastern flanks of the cordillera, including samples near the San Diego and Altavista Plutons, yield more radiogenic values with $\varepsilon Nd_{(90\ Ma)}$ varying between –2.47 and +2.6 and initial $^{87}Sr/^{86}Sr$ between 0.70405 and 0.70734 (Ordóñez–Carmona et al., 2001; Leal–Mejía, 2011).

We obtained zircon Hf isotope data from the above–described porphyritic andesite sample that intrudes the Abejorral Formation (DM–056), which yield a U–Pb crystallization age of ca. 97 Ma. The initial $^{176}Hf/^{177}Hf$ ratios in thirteen zircons range from 0.282989 to 0.283067, with positive values of initial $\varepsilon Hfi_{(97\ Ma)}$ ranging from 9.0 to 12.2 (Figure 11).

As Hf and Nd isotopes behave in a similar fashion, we can use them for the same petrogenetic considerations (Chapman et al., 2017). Therefore, older plutons (ca. 98 Ma) are characterized by a more depleted mantle source and differ from the younger Upper Cretaceous magmatic units, which are more radiogenic and may include additional older crustal input.

4.8. Oxygen Isotopes

Oxygen isotope analyses were conducted on zircons from the samples of the Altavista Stock, San Diego Gabbro (98 Ma), and the Antioquian Batholith (90 Ma) dated by U–Pb LA–ICP–MS geochronology. The $\delta^{18}O$ values for the Altavista Stock (24 magmatic crystals) range between 4.9‰ and 6.1‰, and those for the San Diego Gabbro (24 magmatic crystals) show similar values between 5.0‰ and 5.9‰, with mean values of 5.6‰ and 5.5‰, respectively. In the case of the Antioquian Batholith, the 13 analyzed crystals have $\delta^{18}O$ values between 6.8‰ and 7.9‰. (Table 6). These results show that the older plutons have values characteristic of mantle–derived oxygen isotope compositions, whereas a stronger crustal signature characterizes the younger Antioquian Batholith (Figure 12), buttressing the considerations drawn from the radiogenic isotopes.

5. Discussion

The Jurassic to Early Cretaceous tectonic evolution of the northwestern margin of South America has been related to

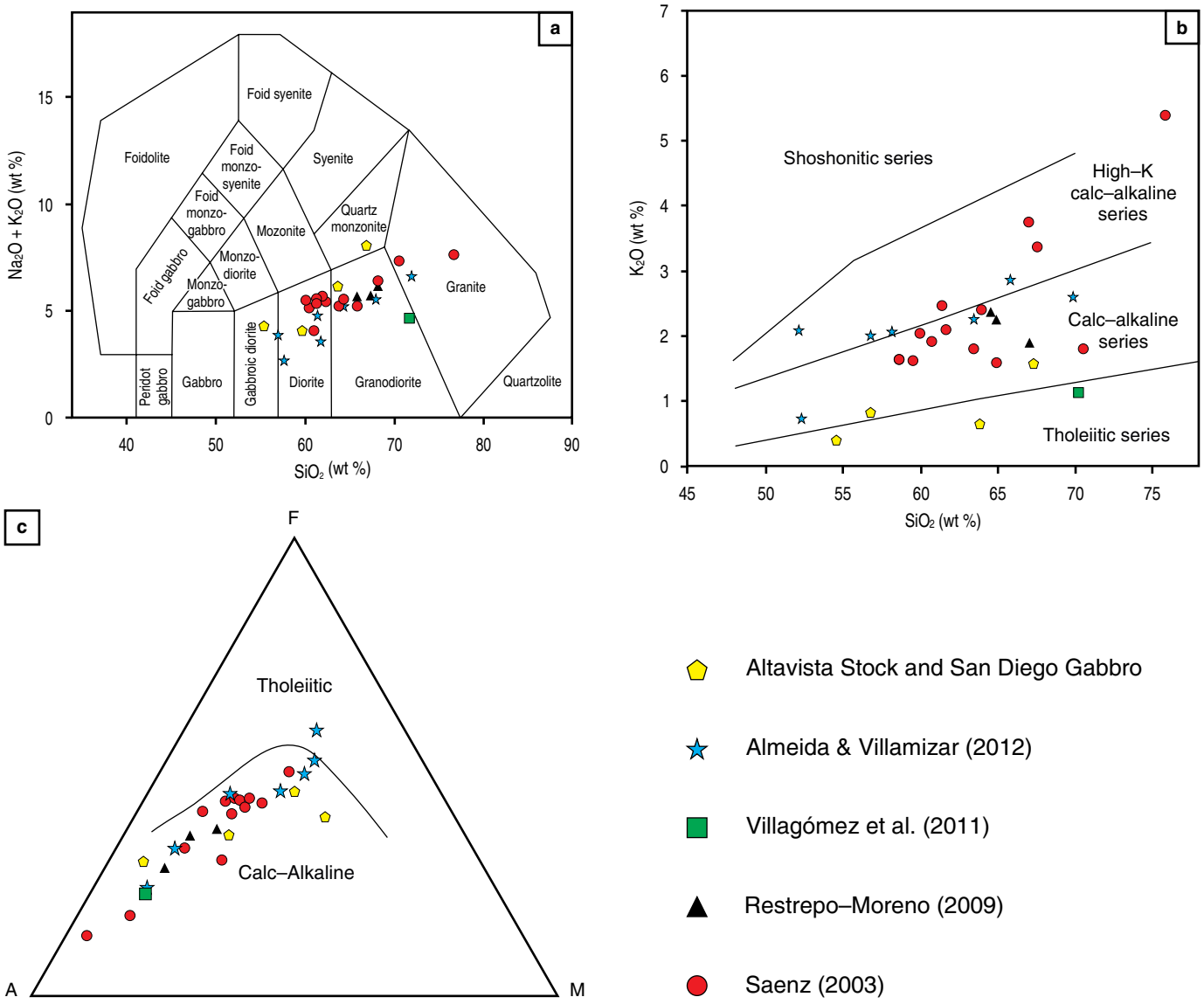

Figure 8. Whole–rock geochemical results from the Altavista Stock and San Diego Gabbro compared with published data from the Antioquian Batholith (see text for references). **(a)** TAS classification diagram (Middlemost, 1994). **(b)** Alkaline series (Peccerillo & Taylor, 1976), **(c)** AFM diagram (Irvine & Baragar, 1971).

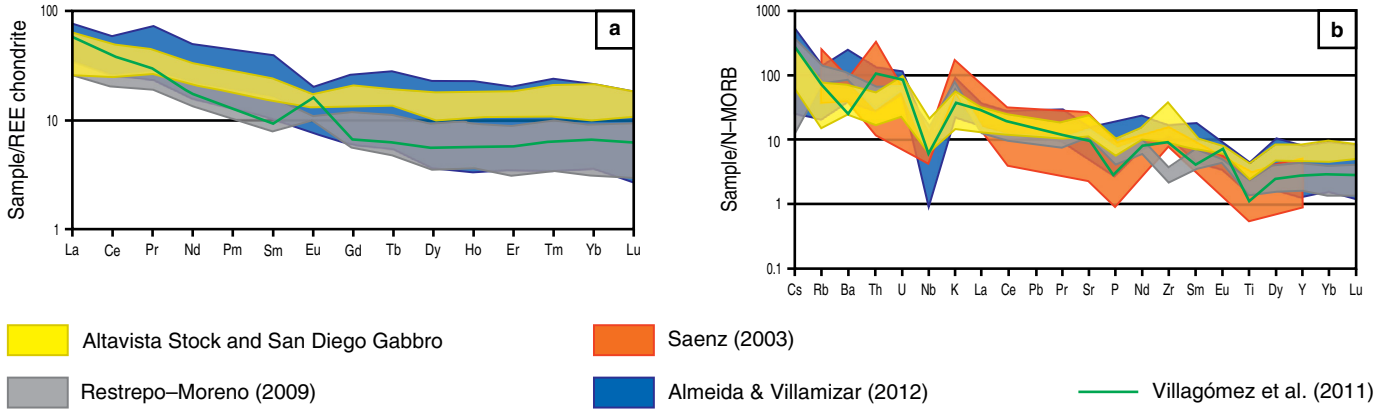

Figure 9. Trace element patterns from the Altavista Stock and San Diego Gabbro compared with published data from the Antioquian Batholith (see text for references). **(a)** REE diagram normalized to chondrites (Nakamura, 1974). **(b)** Multielemental patterns normalized to N–MORB (Sun & McDonough, 1989).

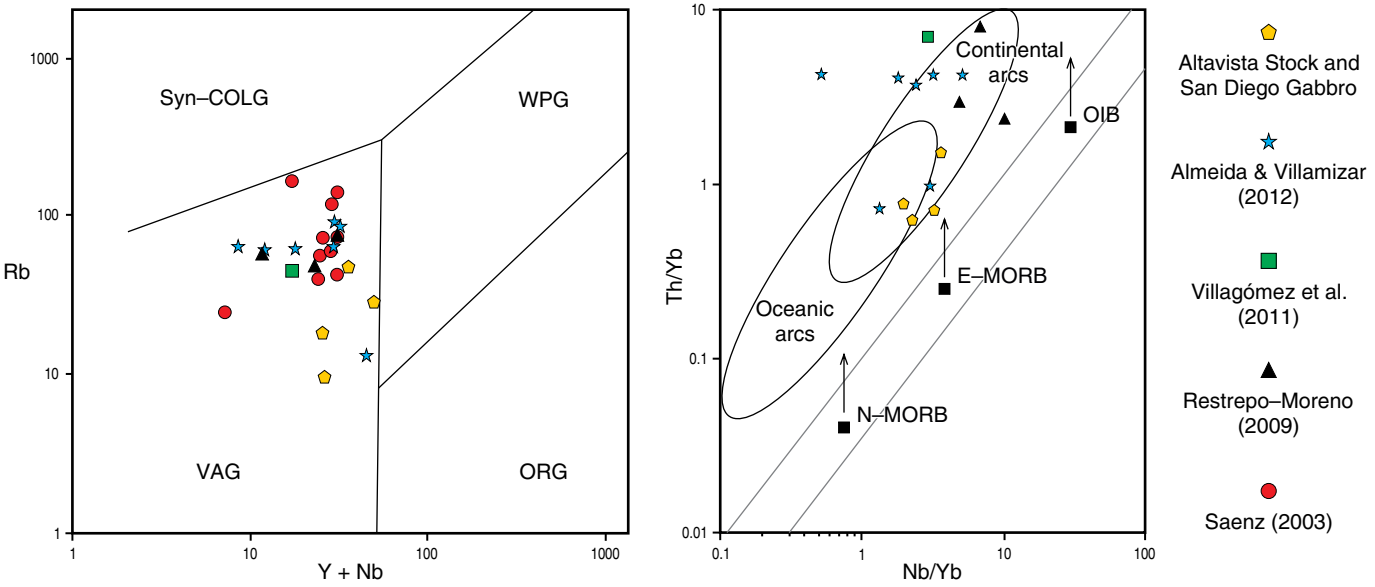

Figure 10. Geotectonic discrimination diagrams from the Altavista Stock and San Diego Gabbro compared with published data from the Antioquian Batholith (see text for references). **(a)** Granitoid discrimination diagram after Pearce et al. (1984). **(b)** Th/Yb vs. Nb/Yb discrimination diagram for subduction input and mantle reservoirs after Pearce (2008). (Syn–COLG) Syn–collisional granite; (WPG) Within–plate granite; (ORG) Ocean ridge granite; (VAG) Volcanic arc granite.

the growth of a series of magmatic arcs, which record major spatial and compositional changes related to modifications in the obliquity of plate convergence as well as in the subduction angle (recent reviews in Spikings et al., 2015; van der Lelij et al., 2016; Bustamante et al., 2017). During this time interval and until the Early Cretaceous, along–strike translation of Jurassic arc–related units from southern latitudes toward the Colombian margin has also been suggested by paleomagnetic data (Bayona et al., 2006, 2010). Conversely, metamorphic rocks included within the Cajamarca and Arquía Complexes on both flanks of the Central Cordillera have been related to different accretionary events at ca. 157–146 Ma (Blanco–Quintero et al., 2014) and between 137 and 112 Ma (Toussaint, 1996; Villagómez et al., 2011). Although we are aware that the Jurassic magmatic evolution and the Early Cretaceous metamorphic record of the Arquía Complex must have influenced the younger magmatic and sedimentary record presented in this contribution, in the next paragraphs, we consider them as already incorporated into a common domain that formed part of the Central Cordillera when the units discussed in this contribution were forming.

5.1. Early Cretaceous Sedimentary Provenance and Tectonostratigraphic Implications

Although more stratigraphic constraints are still necessary, the Early Cretaceous siliciclastic record found in the different belts exposed along the Central Cordillera is characterized by a well–defined fining–upward trend with interlayered chert levels that implies a basin–deepening pattern. The fossiliferous record extends from the Berriasian to the Aptian for these sedimentary successions, which are characterized by initial coarse–grained sequences that most likely accumulated in fluvial–deltaic environments (particularly well defined on the western flank). A major environmental change is registered upward in the sequence when sedimentation began to reflect marine turbiditic settings (Feininger et al., 1972; Hall et al., 1972; Etayo–Serna, 1985; Rodríguez & Rojas, 1985; Gómez–Cruz et al., 1995; González, 2001; Gómez–Cruz et al., 2002; Quiroz, 2005) and may include relatively distal subenvironments, as suggested by the presence of interlayered chert levels.

Although sedimentation may be as old as the Berriasian, the most abundant paleontological record, the estimated maximum accumulation ages from zircon U–Pb data, and geochronological constraints from associated volcanism (see former temporal considerations), coincide between the Aptian and Albian (126.3 to 100.5 Ma after Gradstein et al., 2012), and we therefore consider this time interval for the main Early Cretaceous tectonostratigraphic evolution of the transgressive basin discussed in this contribution.

Petrographic constraints from different sandstone levels are characterized by significant textural immaturity and dominantly quartz–rich compositions. Lithic fragments are mostly metamorphic (schists) with minor sedimentary (sandstones and mudstones) rocks. Such components can be related to proximal depocenters adjacent to first–cycle crystalline metamorphic rocks as well as siliciclastic sedimentary sources that were being eroded and rapidly buried.

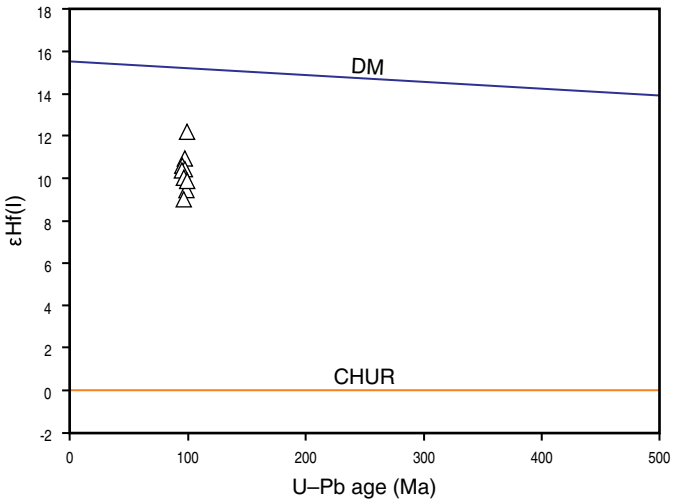

Figure 11. Hf isotope data for zircons from the Aguadas porphyritic body.

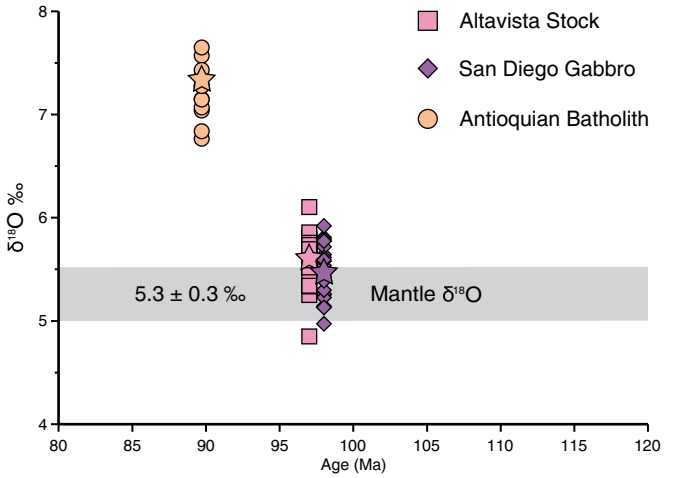

Figure 12. Oxygen isotope data for zircons from the Altavista Stock, San Diego Gabbro, and Antioquian Batholith (after Lackey et al., 2005). The stars are the weight average for each sample.

The origin of quartz–rich compositions in sandstones is commonly a consequence of multiple parameters (Dott, 2003; Smyth et al., 2008), as it may reflect sedimentary recycling in the source area, intense chemical weathering conditions, diagenetic modifications, or strong eolian or littoral derivation. In the case of the Cretaceous sandstones from the Central Cordillera, diagenetic and environmental controls on composition are discarded since petrographic evidence of intense cementation, mineral replacement, or extreme roundness is not observed. Therefore, some recycling (as suggested by the sedimentary lithic fragments) and particularly relatively high weathering rates in the source areas are considered the major controls for the observed quartz enrichment. Similar high quartz contents have been documented in the eastern basins of Colombia within the Upper Magdalena Valley and the Eastern Cordillera (Figure 13; Moreno, 1990, 1991; Duarte et al., 2018), as well as in several deformed Cretaceous siliciclastic units from the Cordillera Real of Ecuador (Litherland et al., 1994), which may be temporally and geologically related (Spikings et al., 2015). Chemical and fossil data have shown that during the Early Cretaceous, particularly the Aptian – Albian, climate conditions in some of the eastern Colombian basins were characterized by high humidity (Campos–Álvarez & Roser, 2007; Suárez et al., 2010; Mejía–Velásquez et al., 2012), which favored strong chemical weathering that facilitated the formation of stable quartzose sediments, as discussed for the origin of high quartz contents in the northern Andean basins.

A comparison shows that the detrital geochronological signatures of the San Luis Sedimentites, the Abejorral Formation, and the Quebradagrande Complex are characterized by similar pre–Jurassic zircon U–Pb age distributions (Figure 6; Cochrane et al., 2014b; Jaramillo et al., 2017), which suggests that they probably shared common regional source areas and could have been part of the same crustal domain. Published zircon U–Pb geochronological data from metasedimentary rocks of the Cajamarca Complex are included in Figure 6 to test whether they could be considered the main source areas (Martens et al., 2012; Cochrane et al., 2014a; Bustamante et al., 2017; Jaramillo et al., 2017).

The Permian – Triassic detrital zircon age peaks found in the Early Cretaceous sedimentites resemble those yielded by the meta–igneous basement of the Central Cordillera (Cajamarca Complex; Vinasco et al., 2006; Restrepo et al., 2011; Villagómez et al., 2011; Bustamante et al., 2017), which borders the basins at present. Likewise, the older Paleozoic and Proterozoic detrital ages are also associated with the erosion of both gneissic and metasedimentary units of the same complex (Cochrane et al., 2014a; Martens et al., 2014; Jaramillo et al., 2017).

The Middle and Upper Jurassic detrital ages are likely derived either from a long–lived magmatic arc exposed along the axis and the eastern flank of the Central Cordillera (i.e., Ibagué Batholith, Mariquita Stock; Villagómez et al., 2011; Rodríguez et al., 2018; Bustamante et al., 2016 and references therein) or from the recently identified Jurassic metavolcano–sedimentary belt and hidden arc, which crop out in the core of the Central Cordillera (Blanco–Quintero et al., 2014; Bustamante et al., 2017).

The Early Cretaceous detrital ages between 127 Ma and 105 Ma identified in sandstones from the Abejorral Formation and the Quebradagrande Complex (Cochrane et al., 2014b; Zapata et al., 2018; this contribution) suggest that active magmatism accompanied basin filling. Stratigraphic relationships in the Abejorral Formation (Quiroz, 2005; Zapata et al. 2018), the Quebradagrande Complex (Arévalo et al., 2001), and the San Pablo Formation (Hall et al., 1972; Rodríguez & Celada–Arango, 2018) show that volcanic rocks with Early

Table 6. Oxygen isotope results for zircons from the Altavista, San Diego, and Antioquia plutonic units.

Sample	^{16}O	^{18}O	$^{18}O/^{16}O$ Raw	$^{18}O/^{16}O$ Raw 1σ	$^{18}O/^{16}O$ Corr	$^{18}O/^{16}O$ Corr 1σ	$\delta^{18}O$	$\delta^{18}O$ 1σ (internal)	$\delta^{18}O$ 1σ (external)	Age (Ma)
Altavista Stock										
Altavista_1	3688114048	7449863.765	0.002019966	1.02055E-07	0.002016377	1.01874E-07	5.574058437	0.050523335	0.145198714	97
Altavista_2	3664205016	7402418.776	0.002020198	1.00256E-07	0.002016609	1.00078E-07	5.689597941	0.049626932	0.145198714	97
Altavista_3	3682975462	7440542.502	0.002020253	8.3584E-08	0.002016664	8.34355E-08	5.717133239	0.041373026	0.145198714	97
Altavista_4	3654928559	7382951.554	0.002019999	1.01673E-07	0.00201641	1.01493E-07	5.59058503	0.050333378	0.145198714	97
Altavista_5	3651019532	7372580.95	0.002019321	8.60402E-08	0.002015734	8.58874E-08	5.253203371	0.042608494	0.145198714	97
Altavista_6	3684495700	7444167.771	0.002020403	9.55637E-08	0.002016814	9.5394E-08	5.791985504	0.047299339	0.145198714	97
Altavista_7	3666162780	7404152.036	0.002019592	1.03906E-07	0.002015902	1.03717E-07	5.337225934	0.051449243	0.145198714	97
Altavista_8	3559797233	7189990.625	0.002019775	8.61823E-08	0.002016085	8.60249E-08	5.428619019	0.042669253	0.145198714	97
Altavista_9	3779521491	7636316.983	0.002020445	9.07805E-08	0.002016754	9.06147E-08	5.762198472	0.044930934	0.145198714	97
Altavista_10	3677779704	7428959.815	0.002019958	1.10197E-07	0.002016268	1.09996E-07	5.519454125	0.054554033	0.145198714	97
Altavista_11	3766601349	7610365.013	0.002020486	1.07642E-07	0.002016795	1.07445E-07	5.782349073	0.053275372	0.145198714	97
Altavista_12	3616035500	7302963.015	0.002019605	8.24489E-08	0.002015915	8.22982E-08	5.343781496	0.040824248	0.145198714	97
Altavista_13	3647100442	7370919.576	0.002021036	8.18711E-08	0.002017445	8.17256E-08	6.10637449	0.040509483	0.145198714	97
Altavista_14	3733251978	7541150.441	0.002019995	1.007E-07	0.002016406	1.00521E-07	5.588237328	0.049851515	0.145198714	97
Altavista_15	3642221912	7358367.421	0.002020296	1.13869E-07	0.002016706	1.13666E-07	5.73821049	0.056362361	0.145198714	97
Altavista_16	3651394559	7376470.8	0.002020179	1.19009E-07	0.002016589	1.18798E-07	5.679846786	0.058910187	0.145198714	97
Altavista_17	3682717208	7439367.36	0.002020076	7.37248E-08	0.002016486	7.35938E-08	5.628529859	0.036496049	0.145198714	97
Altavista_18	3656727727	7388212.236	0.002020444	9.40272E-08	0.002016854	9.38601E-08	5.811715483	0.04653789	0.145198714	97
Altavista_19	3704404268	7477398.233	0.002018516	9.78316E-08	0.002014929	9.76578E-08	4.851967357	0.048467115	0.145198714	97
Altavista_20	3683194245	7442038.138	0.002020539	1.30672E-07	0.002016949	1.3044E-07	5.859263637	0.064671709	0.145198714	97
Altavista_21	3623706784	7321114.318	0.002020338	8.93737E-08	0.002016749	8.92149E-08	5.759379322	0.044237004	0.145198714	97
Altavista_22	3643404245	7360750.653	0.002020295	9.66362E-08	0.002016705	9.64645E-08	5.737468393	0.047832709	0.145198714	97
Altavista_23	3734672516	7544317.434	0.002020075	9.61603E-08	0.002016485	9.59894E-08	5.627894597	0.047602352	0.145198714	97
Altavista_24	3693810456	7462291.118	0.002020215	8.2551E-08	0.002016625	8.24043E-08	5.69771896	0.040862491	0.145198714	97
San Diego Gabbro										
SanDiego_1	3650642115	7372414.213	0.002019484	8.98598E-08	0.002016082	8.97084E-08	5.426775849	0.044496419	0.145198714	98
SanDiego_2	3634562415	7340497.673	0.002019637	1.05268E-07	0.002016015	1.05079E-07	5.39360339	0.052122045	0.145198714	98
SanDiego_3	3646294898	7363187.8	0.002019362	8.98188E-08	0.00201574	8.96577E-08	5.256364219	0.044478816	0.145198714	98
SanDiego_4	3632609938	7337608.241	0.002019927	1.04179E-07	0.002016305	1.03992E-07	5.538023628	0.05157555	0.145198714	98
SanDiego_5	3679460339	7430391.551	0.002019424	6.88846E-08	0.002016022	6.87685E-08	5.396925428	0.034111011	0.145198714	98
SanDiego_6	3644024017	7359343.877	0.002019565	1.14924E-07	0.002016163	1.1473E-07	5.467053992	0.056905228	0.145198714	98
SanDiego_7	3676308415	7427076.792	0.002020254	8.86218E-08	0.00201685	8.84725E-08	5.810012987	0.04386668	0.145198714	98
SanDiego_8	3671901676	7417947.225	0.002020192	1.15873E-07	0.002016789	1.15678E-07	5.779257241	0.057357541	0.145198714	98
SanDiego_9	3664735153	7403568.957	0.002020219	9.3783E-08	0.002016816	9.3625E-08	5.792772709	0.046422186	0.145198714	98
SanDiego_10	3628969778	7329395.226	0.00201969	9.11728E-08	0.002016068	9.10093E-08	5.420030348	0.045141967	0.145198714	98
SanDiego_11	3664209716	7399398.551	0.002019371	1.00423E-07	0.002015749	1.00242E-07	5.261018193	0.049729639	0.145198714	98
SanDiego_12	3675246379	7424036.598	0.002020011	1.04105E-07	0.002016388	1.03918E-07	5.579449645	0.051536869	0.145198714	98
SanDiego_13	3593837725	7255573.938	0.002018893	7.50014E-08	0.002015514	7.48759E-08	5.143402247	0.037149788	0.145198714	98
SanDiego_14	3629458641	7328088.292	0.002019058	7.67725E-08	0.002015683	7.66442E-08	5.227903504	0.038023917	0.145198714	98
SanDiego_15	3580149828	7227834.793	0.002018864	1.40919E-07	0.002015489	1.40684E-07	5.131096342	0.069801207	0.145198714	98
SanDiego_16	3614330705	7298068.753	0.002019203	1.14343E-07	0.002015828	1.14151E-07	5.300172878	0.056627566	0.145198714	98
SanDiego_17	3607217243	7286212.498	0.002019898	7.39302E-08	0.002016517	7.38065E-08	5.643966011	0.036600952	0.145198714	98
SanDiego_18	3702243622	7473173.912	0.002018553	1.10825E-07	0.002015174	1.10639E-07	4.97396946	0.054902959	0.145198714	98
SanDiego_19	3644848397	7362778.447	0.002020051	1.19558E-07	0.002016669	1.19358E-07	5.719754622	0.059185539	0.145198714	98
SanDiego_20	3658102880	7391030.78	0.002020455	1.40003E-07	0.002017073	1.39769E-07	5.920856995	0.069292906	0.145198714	98

Table 6. Oxygen isotope results for zircons from the Altavista, San Diego, and Antioquia plutonic units *(continued)*.

Sample	^{16}O	^{18}O	$^{18}O/^{16}O$ Raw	$^{18}O/^{16}O$ Raw 1σ	$^{18}O/^{16}O$ Corr	$^{18}O/^{16}O$ Corr 1σ	$\delta^{18}O$	$\delta^{18}O$ 1σ (internal)	$\delta^{18}O$ 1σ (external)	Age (Ma)
SanDiego_21	3613283980	7296616.05	0.002019386	9.77497E-08	0.002016006	9.75861E-08	5.388969282	0.048405652	0.145198714	98
SanDiego_22	3633779270	7339641.028	0.002019837	9.81263E-08	0.00201646	9.79623E-08	5.615527566	0.048581299	0.145198714	98
SanDiego_23	3646412845	7366328.834	0.002020158	7.59605E-08	0.002016781	7.58335E-08	5.775282021	0.037601279	0.145198714	98
SanDiego_24	3613042799	7297587.514	0.00201979	1.07292E-07	0.002016413	1.07113E-07	5.592208601	0.053120614	0.145198714	98
Antioquian Batholith										
Antioquia_1	3632822808	7363514.284	0.00202694	1.01491E-07	0.002023144	1.01301E-07	8.94877152	0.050070925	0.145198714	89.7
Antioquia_2	3285597305	6650625.361	0.002024175	9.42455E-08	0.002020385	9.4069E-08	7.572598937	0.046559929	0.145198714	89.7
Antioquia_3	1828915444	3700092.154	0.002023107	1.85592E-07	0.002019318	1.85244E-07	7.040904134	0.091735979	0.145198714	89.7
Antioquia_4	3224101918	6520936.4	0.002022559	1.24489E-07	0.002018771	1.24256E-07	6.767993465	0.061550385	0.145198714	89.7
Antioquia_5	3312559147	6700331.775	0.002022706	1.07826E-07	0.002018917	1.07624E-07	6.840934748	0.053307695	0.145198714	89.7
Antioquia_6	3390186708	6858919.049	0.002023169	1.05978E-07	0.00201938	1.0578E-07	7.07138988	0.052382315	0.145198714	89.7
Antioquia_7	3353470156	6784748.313	0.002023202	9.8269E-08	0.002019799	9.81037E-08	7.280617887	0.048571027	0.145198714	89.7
Antioquia_8	3354500943	6787460.026	0.002023389	1.0839E-07	0.002019985	1.08207E-07	7.373559824	0.053568451	0.145198714	89.7
Antioquia_9	3340687423	6758026.56	0.002022945	1.09166E-07	0.002019542	1.08982E-07	7.152496341	0.053963836	0.145198714	89.7
Antioquia_10	3359762175	6799979.233	0.002023947	9.35875E-08	0.002020542	9.34301E-08	7.651211355	0.046240102	0.145198714	89.7
Antioquia_11	3367941785	6813126.447	0.002022935	9.02515E-08	0.002019532	9.00997E-08	7.147442904	0.044614147	0.145198714	89.7
Antioquia_12	3326712333	6731638.28	0.002023511	8.66576E-08	0.002020107	8.65118E-08	7.434233581	0.042825362	0.145198714	89.7
Antioquia_13	3330684484	6738635.218	0.002023198	1.2408E-07	0.002019795	1.23871E-07	7.278663753	0.061328642	0.145198714	89.7

Cretaceous ages are interspersed and overlying the coeval siliciclastic rocks, confirming the appearance of volcanic activity in the history of the basin. Several discontinuous segments of predominantly volcanic rocks, which are locally associated with gabbros and/or serpentinized peridotite lenses, present different calc–alkaline, MORB, and E–MORB geochemical signatures (Nivia et al., 2006; Villagómez et al., 2011; Rodríguez & Cetina, 2016; Rodríguez & Celada–Arango, 2018; Zapata et al., 2018). Although precise geochronological constraints for each of the geochemical units are still lacking, by assuming probable Cretaceous ages, heterogeneous geochemical fingerprints, the existence of ophiolite–type associations, and the discussed transgressive nature of the Aptian – Albian sedimentation, it is possible to interpret a tectonic setting in which a magmatic arc was affected by a major extensional episode with associated back–arc basin formation (Figure 14a, 14b; Nivia et al., 2006; Cochrane et al., 2014b; Zapata et al., 2018). The presence of pre–Cretaceous detrital zircons in the Quebradagrande Complex suggests that this arc formed adjacent to a continental basement as part of a fringing arc that records the Early Cretaceous back–arc formation (Nivia et al., 2006; Cochrane et al., 2014b; Spikings et al., 2015; Jaramillo et al., 2017), eliminating its origin as an allochthonous oceanic arc.

Several authors have argued that the lack of volcanic material of the Abejorral Formation precludes its relation to the magmatism associated with the Quebradagrande Complex (Toussaint, 1996; Moreno–Sánchez et al., 2008; Restrepo et al., 2009). However, we suggest that such an interpretation was biased by the observed stratigraphic sections and samples. The observations presented by Quiroz (2005) have shown that whereas the lower segment of the Abejorral Formation is in fact highly quartzose and lacks related magmatism, toward the top, intercalations of volcanic rocks are remarkably common, similar to what is reported for the La Soledad Formation (Hall et al., 1972).

Plutonic activity at ca. 98 Ma, such as that recorded by the three analyzed plutons (Altavista Stock, San Diego Gabbro, and Aguadas porphyritic andesite), is characterized by a significant juvenile mantle isotopic fingerprint, which is compatible with the existence of a thinned lithosphere associated with the extensional setting discussed above.

An extension–dominated tectonic setting that temporally extended until the Albian suggests that models of back–arc basin closure and compression by 114 Ma (Cediel et al., 2003; Villagómez & Spikings, 2013; Cochrane et al., 2014a; Spikings et al., 2015) are not sustainable.

Extension–controlled sedimentation and tectonics have also been reported in the stratigraphic record of the Eastern Cordillera, the Middle and Upper Magdalena Valley, and the Putumayo region, as well as in Ecuador (Sarmiento–Rojas et al., 2006; Baby et al., 2013). In the Eastern Cordillera, magmatism is restricted to minor gabbroic bodies (Vásquez et al., 2010) and distal volcanism represented by a series of lapilli tuffs altered to clay, which have been reported in the post–Hauterivian sedimentites (Sarmiento–Rojas et al., 2006).

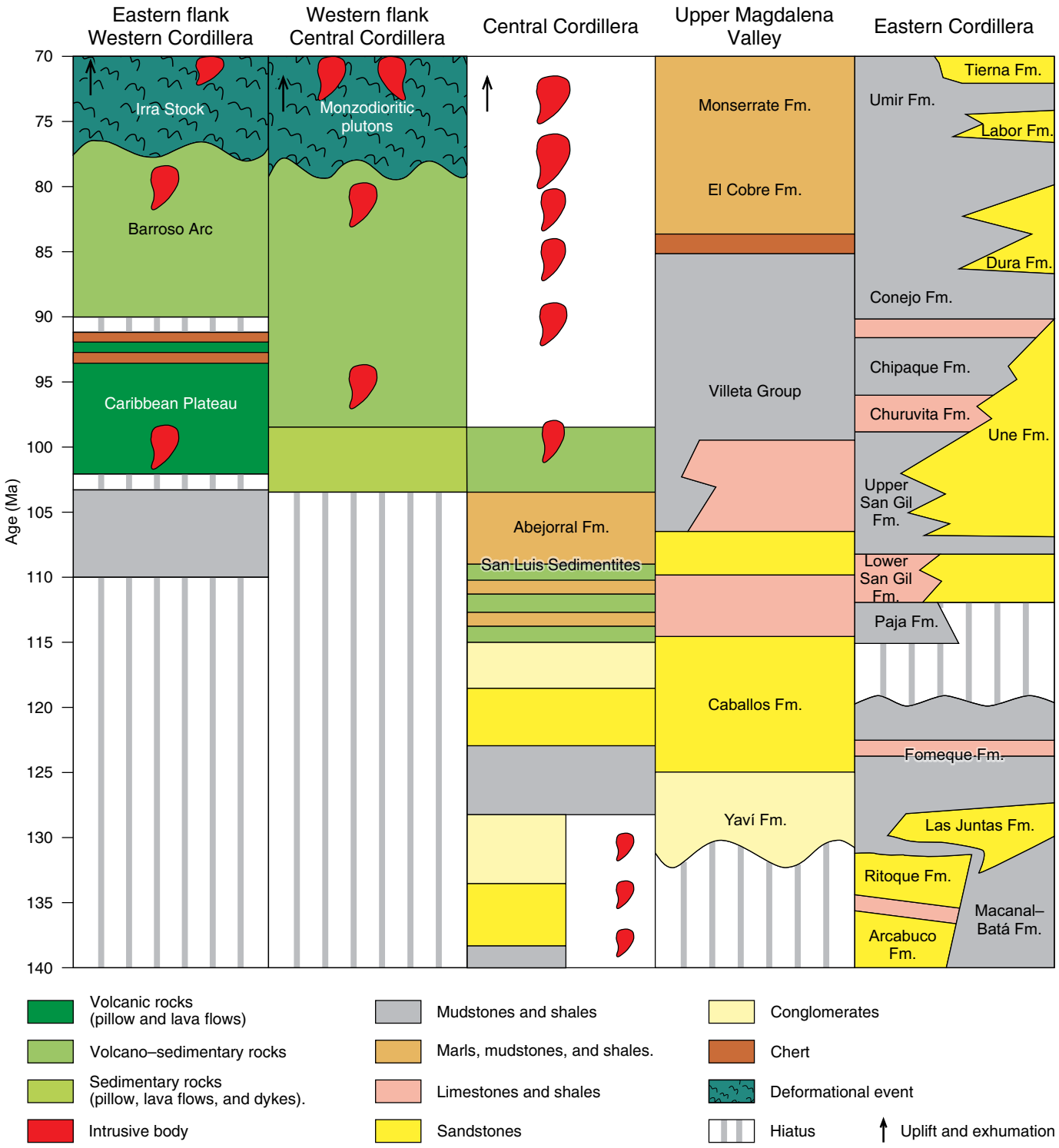

Figure 13. Simplified chronostratigraphic chart of Cretaceous events (after Sarmiento–Rojas et al., 2006; Barrero et al., 2007; Jaramillo et al., 2017). (Fm.) Formation.

Published detrital zircon geochronological data from the Lower Cretaceous units of the Eastern Cordillera (Horton et al., 2010) show a well–defined dominance of Paleozoic and older sources (>400 Ma), with a prominent Grenvillian age peak (ca. 1000 Ma) and only one individual age from the Early Cretaceous yielded by the Buenavista Formation (Figure 6). Paleozoic and older zircon U–Pb ages found in the Lower Cretaceous units of the Eastern Cordillera were probably sourced from magmatic and metasedimentary units included as part of the continental basement of eastern Colombia, which is exposed

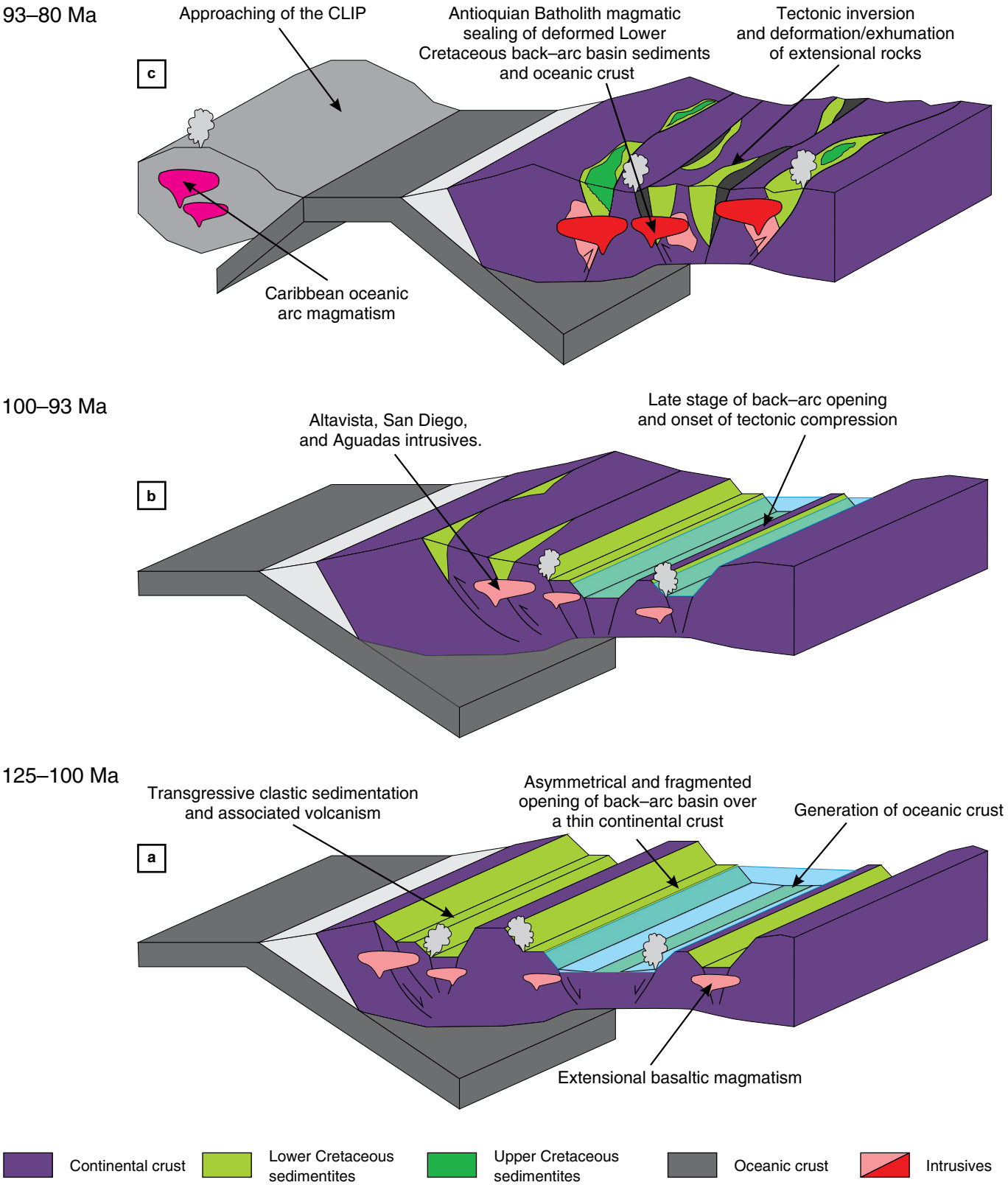

Figure 14. Proposed Cretaceous tectonic scenarios and paleogeography (this contribution; and modifications from Jaramillo et al. (2017) and Zapata et al. (2018)). (CLIP) Caribbean Large Igneous Province.

in the Floresta, Santander, and Quetame Massifs (Horton et al., 2010; Cardona et al., 2016). The diachronic Early Cretaceous opening of basins in the central and eastern Colombian sedimentary systems, together with the remarkable differences in the detrital zircon age populations of the two domains, suggests that these basins were not connected and may represent independent depocenters formed by regional–scale upper–plate asymmetric extension.

Generally, the extensional record of the northern Andes is represented by characteristic marine sedimentation and the quartz–rich compositions of sandstones, which may reflect strong weathering in which not only the climate but also the lack of strong relief and the proximity to the sea level must play major roles.

The formation of extensional basins related to mafic volcanism and ophiolite associations in the Central Cordillera record both intra–arc extension (San Pablo Formation along the axis of the cordillera) and back–arc basin formation (Quebradagrande Complex – Abejorral Formation on the western flank). As the basin opened, a remnant arc was probably left to the east, as suggested by the ca. 129–143 Ma plutons exposed on the eastern flank of the Central Cordillera (Bustamante et al., 2017) and by the detrital geochronology of the Abejorral and San Luis Sedimentites discussed above. The existence of fragments of a western Jurassic remnant arc remains to be discovered.

Similar back–arc scenarios have been proposed from the Upper Jurassic to Lower Cretaceous volcano–sedimentary record of the Cordillera Real of Ecuador (Litherland et al., 1994; Cochrane et al., 2014b; Spikings et al., 2015), as well as from the thermal histories recorded in the Triassic basements of Colombia and Ecuador (Paul et al., 2018). Such correlations suggest that a regional–scale extensional back–arc system was common in the northern Andes during the Early Cretaceous.

Early Cretaceous extensional basins have also been recognized along the entire Andean chain, including the Celica–Lancones and Casma Basins in Perú (Jaillard et al., 1999) as well as other basins in central and southern Chile (Fildani & Hessler, 2005; Ramos, 2010).

The existence of regional–scale back–arc basins, which characterized a Cenozoic Mariana–type style of subduction in the Pacific (Uyeda & Kanamori, 1979), can be related to upper plate motions that favor trench rollback (reviews in Ramos, 2010), the subduction of old oceanic plates, or lateral variations in the buoyancy of the subducted slab (Sdrolias & Müller, 2006; Seton et al., 2016).

In the Andean case, it has been suggested that this tectonic regime is likely related to upper plate kinematic changes associated with the opening of the Atlantic during the Early Cretaceous (Torsvik et al., 2009; Moulin et al., 2010; Ramos, 2010).

5.2. Late Cretaceous Magmatism and Deformation

Both along the axis and on the eastern flank of the Central Cordillera, the Lower Cretaceous siliciclastic rocks from the San Luis Sedimentites, the San Pablo Formation, and the Berlin Sedimentites are folded and affected by low–grade metamorphism with associated neoformation of mica and are also intruded by the Antioquian Batholith with ages of ca. 90–93 Ma (Leal–Mejía, 2011; Villagómez et al., 2011; this contribution). Such intrusive activity has left a clear contact metamorphic imprint, as evidenced by the growth of metamorphic minerals (e.g., andalusite) lacking any preferentially oriented texture that is imposed over a previously existing foliated fabric. Such cross–cutting relationships clearly constrain a major deformational event that occurred between ca. 100 Ma (Aptian age of sedimentation) and 93 Ma, i.e., the age of the intrusive bodies that cut these units (Figure 14c). As already discussed, there are clear and distinct geochemical and isotopic signals from the older (ca. 98 Ma) plutonic units compared with the youngest <93 Ma granitoid pulses, with the latter showing increased enrichment in the LREE and Th, together with more radiogenic Nd–Sr and $\delta^{18}O$ values of zircons. This compositional trend reflects more extensive interaction with the older continental basement, which may be in part related to increased crustal thickness caused by the deformational event, as also suggested by relatively steeper La/Yb_N values in the younger rocks. Arc–related volcanism and plutonism continued in the axis and western flank of the Central Cordillera, intruding or overlying rocks from the Quebradagrande Complex between 93 Ma and 78 Ma (Villagómez et al., 2011; Jaramillo et al., 2017; Zapata et al., 2018), and may also have been related to the protracted compressional event that affected former extensional domains.

Although some authors have considered the Late Cretaceous magmatism in the Central Cordillera to represent the record of subduction initiation (Pindell & Kennan, 2009) or to be related to a plume (Whattam & Stern, 2015), the long–term arc–related Cretaceous units discussed here, as well as the continental nature of the host rocks, refute both hypotheses and suggest that an east–vergent subduction zone was active in the northern Andean margin during this time.

5.2.1. On the Discussion of Plausible Tectonic Mechanisms

To date, two different models have been proposed to explain the tectonic mechanisms responsible for this post–Albian event in the Central Cordillera. One model involves the collision of an oceanic arc terrane (Quebradagrande Complex) during which the obduction of a major ophiolitic complex that is currently exposed on the western flank and along the axis of the Cen-

tral Cordillera took place, consequently deforming the Lower Cretaceous siliciclastic sequences (reviews in Toussaint, 1996). The other model suggests that an Early Cretaceous back–arc basin was closed by 114 Ma (Villagómez et al., 2011; Spikings et al., 2015) and was followed by the occurrence of minor magmatism along the continental margin during the Late Cretaceous (Pindell & Kennan, 2009; Spikings et al., 2015).

The results presented in this contribution and the review of published geological, geochemical, and geochronological data favor a model of back–arc basin closure, in which the related ophiolitic bodies represent oceanic crust formed in a supra–subduction zone environment during the back–arc and intra–arc extension. Nevertheless, our interpretation differs in timing from the previously proposed models because in the light of the new data presented here, the time may have been later than ca. 100 Ma, as suggested by the presence of Albian detrital and magmatic zircon U–Pb ages (Cochrane et al., 2014b; Zapata et al., 2018; this contribution). It is also suggested that basin closure caused folding and thickening of the crust, as recorded in the Aptian – Albian sedimentary units, and could also have been responsible for the ca. 100 Ma metamorphism identified on the western flank of the Central Cordillera near the city of Medellín (Restrepo et al., 2012; Rodríguez & Correa–Martínez, 2015).

Similar to the Early Cretaceous event, the Late Cretaceous compressional event in the northern Andes left evidence of its regional–scale nature in the Upper Magdalena Valley of Colombia, where Albian to Cenomanian deformation has been documented by seismic lines (Jaimes & De Freitas, 2006). In addition, in the Ecuadorian Andes, including the eastern Amazon region (Ruiz et al., 2007; Jaillard et al., 2008; Baby et al., 2013), and in Perú and Chile, former extensional and back–arc basins were closed (Atherton & Aguirre, 1992; Fildani et al; 2003).

Geochronological data from the Cretaceous plutonic rocks of the Central Cordillera (Leal–Mejía, 2011; Villagómez et al., 2011; this contribution) as well as the distal pyroclastic record found in the eastern basins of Colombia (Figure 13; Villamil, 1999) suggest that Late Cretaceous (ca. 94–75 Ma) arc magmatism, which ended the ca. 100 Ma deformational episode, was significant in the evolution of the margin. This deformational event and the reinstallation of a productive magmatic arc have been recognized along most of the 85–100 Ma Andean record (Tunik et al., 2010) and may also have resulted from regional–scale plate kinematic modifications, including changes in upper plate velocity, increases in the subduction rates, and changes to more orthogonal convergence between the South American and Caribbean Plates (Ramos, 2010; Matthews et al., 2012; Seton et al., 2012).

The 100–90 Ma subduction initiation along the margins of the Caribbean oceanic plateau, which was part of the Pacific Plate (Whattam & Stern, 2015), must have also changed the mantle flow associated with eastward subduction underneath South America, which likely prompted plate coupling and deformation in the northern Andes.

Finally, another younger compressional episode in the northern Andes has been related to the ca. 75–70 Ma collision of an allochthonous oceanic terrane against the continental margin (Figure 13; Villagómez & Spikings, 2013; Jaramillo et al., 2017). This exotic oceanic domain includes a Lower to Upper Cretaceous plateau and an associated island arc, which were formed in southern latitudes (Figure 14c; reviews in Zapata et al., 2017; Hincapié–Gómez et al., 2018).

5.3. Paleogeographic Restrictions

Paleogeographic reconstructions of the multiple Cretaceous tectonostratigraphic domains of the northern Andes remain an exciting field of discussion, as the oblique nature of the convergence through the Mesozoic and Cenozoic, including the collision with the Caribbean Plate, provides the possibility of dextral terrane translation along the continental margin (Toussaint, 1996; Pindell et al., 2005; Bayona et al., 2006, 2010; Pindell & Kennan, 2009).

Although specific palinspastic restorations, including the amounts of displacement during the Cretaceous and Cenozoic, have not been precisely quantified, several considerations can constrain the margin–scale configuration.

The Cretaceous oceanic terranes that constitute most of the Western Cordillera were in southwestern positions until ca. 89 Ma, as suggested by their intra–oceanic plateau and arc–related origin as well as some of the available paleomagnetic constraints (reviews in Hincapié–Gómez et al., 2018).

Provenance constraints from the Cretaceous units of the Central Cordillera, including those associated with the Quebradagrande Complex, have shown that these units were associated with a continental domain having a pre–Cretaceous basement similar to that exposed in the cordillera (Nivia et al., 2006; Villagómez et al., 2011; Cochrane et al., 2014b; Jaramillo et al., 2017; Zapata et al., 2018). Moreover, the Cretaceous and older records of the Central Cordillera show remarkable similarities with those of the Cordillera Real in Ecuador (Litherland et al., 1994; Toussaint, 1996; Cochrane et al., 2014b; Spikings et al., 2015).

Therefore, Cretaceous domains in the Central Cordillera would have been located in southern positions (Toussaint, 1996; Pindell & Kennan, 2009), and both the back–arc opening and closure and the subsequent Cenozoic tectonic movements would have contributed to their northward displacements.

6. Conclusions

The integration of new and published data from the Cretaceous record of the Central Cordillera of Colombia provides insights into the feasible regional tectonic scenarios responsible for the

geological evolution of this segment of the northern Colombian Andes during this time. Nevertheless, as one of the main goals of this contribution, specific areas are also identified where the acquisition of more geological data is required in order to test the tectonic evolution discussed here.

Major conclusions that can be reached following the discussion of the results presented in this work are as follows:

- Lithostratigraphic trends and provenance characteristics of the Early Cretaceous siliciclastic units of the Central Cordillera record transgressive basin filling and the erosion of the adjacent metamorphic basement. The high quartz contents of the sandstones are most likely related to intense chemical weathering in the source areas and some sedimentary recycling.
- Detrital zircons and stratigraphic relationships between magmatic and sedimentary rocks of the described units suggest that volcanic activity became significant at the top of the sequence.
- The basin–deepening trend, the geochemical heterogeneity of associated magmatic rocks (arc–like, MORB, and E–MORB signatures), and the relation with ophiolite remnants are interpreted as records of back–arc basin formation.
- The Early Cretaceous arc and back–arc basin system was subsequently deformed and intruded by ca. 90 Ma undeformed arc–related granitoids.
- Similar Early Cretaceous upper–plate basin formation and subsequent Late Cretaceous closure and deformation are documented in eastern Colombia and along most of the entire Andean margin, suggesting regional–scale plate kinematic control for the switch from Mariana– to Andean–style tectonics.

Acknowledgments

We acknowledge the Fundación para la Promoción de la Investigación y la Tecnología del Banco de la República de Colombia project 3451 and the Sistema de Investigación (Hermes) from the Universidad Nacional de Colombia projects 30362 and 25452. The HIP facility at Heidelberg University is operated under the auspices of the DFG Scientific Instrumentation and Information Technology program. Students and researchers associated with EGEO between 2014 and 2018 are especially thanked for fruitful discussions and help during fieldwork. Thoughtful and key reviews and comments from the editor, Victor A. RAMOS, and Robert J. STERN are gratefully acknowledged.

References

Almeida, J. J. & Villamizar, F. 2012. Petrografía y geoquímica del Batolito Antioqueño en un sector del municipio Santa Rosa de Osos, Antioquia. Bachelor thesis, Universidad Industrial de Santander, 88 p. Bucaramanga.

Álvarez, J. 1987. Geología del Complejo Ofiolítico de Pácora y secuencias relacionadas de arco de islas (Complejo Quebradagrande), Colombia. Ingeominas, Internal report 2027, 81 p. Medellín.

Álvarez, J., Rico, H., Vásquez, H., Hall, R. & Blade, L. 1975. Geologic map of the Yarumal quadrangle (H–8) and part of the Ituango quadrangle (H–7), Colombia. Scale 1:100 000. Ingeominas & U.S. Geological Survey. https://doi.org/10.3133/i842

Amelin, Y., Krot, A.N., Hutcheon, I.D. & Ulyanov, A.A. 2002. Lead isotopic ages of chondrules and calcium–aluminum–rich inclusions. Science, 297(5587): 1678–1683. https://doi.org/10.1126/science.1073950

Arévalo, O.J, Mojica, J. & Patarroyo, P. 2001. Sedimentitas del Aptiano tardío al sur de Pijao, quebrada La Maizena, flanco occidental de la cordillera Central, departamento del Quindío, Colombia. Geología Colombiana, 26: 29–43.

Atherton, M. & Aguirre, L. 1992. Thermal and geotectonic setting of Cretaceous volcanic rocks near Ica, Perú, in relation to Andean crustal thinning. Journal of South American Earth Sciences, 5(1): 47–69. https://doi.org/10.1016/0895-9811(92)90059-8

Baby, P., Rivadeneira, M., Barragan, R. & Christophoul, F. 2013. Thick–skinned tectonics in the Oriente foreland basin of Ecuador. In: Nemčok, M., Mora, A. & Cosgrove, J.W. (editors), Thick–skinned–dominated orogens: From initial inversion to full accretion. Geological Society of London, Special Publication 377, p. 59–76. https://doi.org/10.1144/SP377.1

Baertschi, P. 1976. Absolute ^{18}O content of standard mean ocean water. Earth and Planetary Science Letters, 31(3): 341–344. https://doi.org/10.1016/0012-821X(76)90115-1

Barrero, D. & Vesga, C.J. 1976. Mapa geológico del cuadrángulo K–9 Armero y mitad sur del J–9 La Dorada. Scale 1:100 000. Ingeominas. Bogotá.

Barrero, D., Pardo, A., Vargas, C. A., & Martínez, J. F. 2007. Colombian sedimentary basins: Nomenclature, boundaries and petroleum geology, a new proposal. Agencia Nacional de Hidrocarburos, 92 p. Bogotá.

Bayona, G., Rapalini, A. & Costanzo–Álvarez, V. 2006. Paleomagnetism in Mesozoic rocks of the northern Andes and its implications in Mesozoic tectonics of northwestern South America. Earth, Planets and Space, 58(10): 1255–1272. https://doi.org/10.1186/BF03352621

Bayona, G., Jiménez, G., Silva, C., Cardona, A., Montes, C., Roncancio, J. & Cordani, U. 2010. Paleomagnetic data and K–Ar ages from Mesozoic units of the Santa Marta massif: A preliminary interpretation for block rotation and translations. Journal of South American Earth Sciences, 29(4): 817–831. https://doi.org/10.1016/j.jsames.2009.10.005

Blanco–Quintero, I.F., García–Casco, A., Toro–Toro, L.M., Moreno, M., Ruiz, E.C., Vinasco, C.J., Cardona, A., Lázaro, C. & Morata, D. 2014. Late Jurassic terrane collision in the northwestern margin of Gondwana (Cajamarca Complex, eastern flank of the Central Cordillera, Colombia). International Geology

Review, 56(15): 1852–1872. https://doi.org/10.1080/00206814.2014.963710

Botero, G. 1963. Contribución al conocimiento de la geología de la zona central de Antioquia. Universidad Nacional de Colombia, Anales de la Facultad de Minas, 57, 101 p. Medellín.

Botero, G. & González, H. 1983. Algunas localidades fosilíferas cretáceas de la cordillera Central, Antioquia y Caldas, Colombia. Geología Norandina, (7): 15–28.

Busby, C.J. 2012. Extensional and transtensional continental ARC basins: Case studies from the southwestern United States. In: Busby, C. & Azor, A. (editors), Tectonics of sedimentary basins: Recent advances. Wiley–Blackwell, p. 382–404. https://doi.org/10.1002/9781444347166.ch19

Bustamante, A., Juliani, C.M., Hall, C.M. & Essene, E.J. 2011. $^{40}Ar/^{39}Ar$ ages from blueschists of the Jambaló region, Central Cordillera of Colombia: Implications on the styles of accretion in the Northern Andes. Geologica Acta, 9(3–4): 351–362. http://dx.doi.org/10.1344/105.000001697

Bustamante, C., Archanjo, C.J., Cardona, A. & Vervoort, J.D. 2016. Late Jurassic to Early Cretaceous plutonism in the Colombian Andes: A record of long–term arc maturity. Geological Society of America Bulletin, 128(11–12): 1762–1779. https://doi.org/10.1130/B31307.1

Bustamante, C., Archanjo, C.J., Cardona, A., Bustamante, A. & Valencia, V. 2017. U–Pb ages and Hf isotopes in zircons from parautochthonous Mesozoic terranes in the western margin of Pangea: Implications for the terrane configurations in the northern Andes. The Journal of Geology, 125(5): 487–500. https://doi.org/10.1086/693014

Campos–Álvarez, N.O. & Roser, B.P. 2007. Geochemistry of black shales from the Lower Cretaceous Paja Formation, Eastern Cordillera, Colombia: Source weathering, provenance, and tectonic setting. Journal of South American Earth Sciences, 23(4): 271–289. https://doi.org/10.1016/j.jsames.2007.02.003

Cardona, A., Valencia, V.A., Lotero, A., Villafañez, Y. & Bayona, G. 2016. Provenance of middle to late Palaeozoic sediments in the northeastern Colombian Andes: Implications for Pangea reconstruction. International Geology Review, 58(15): 1914–1939. https://doi.org/10.1080/00206814.2016.1190948

Cawood, P.A., Kröner, A., Collins, W.J., Kusky, T.M., Mooney, W.D. & Windley, B.F. 2009. Accretionary orogens through Earth history. In: Cawood, P.A. & Kröner, A. (editors), Earth Accretionary Systems in Space and Time. Geological Society of London, Special Publication 318, p. 1–36. https://doi.org/10.1144/SP318.1

Cediel, F., Shaw, R.P. & Cáceres. C. 2003. Tectonic assembly of the northern Andean block. In: Bartolini, C., Buffer, R.T. & Blickwede, J. (editors), The circum–Gulf of Mexico and the Caribbean: Hydrocarbon habitats, basin formation, and plate tectonics. American Association of Petroleum Geologists, Memoir 79, 815–848. Tulsa, USA.

Chang, Z., Vervoort, J.D., McClelland, W.C. & Knaack, C. 2006. U–Pb dating of zircon by LA–ICP–MS. Geochemistry, Geophysics, Geosystems, 7(5): 1–14. https://doi.org/10.1029/2005GC001100

Chapman, J.B., Ducea, M.N., Kapp, P., Gehrels, G.E. & DeCelles, P.G. 2017. Spatial and temporal radiogenic isotopic trends of magmatism in Cordilleran orogens. Gondwana Research, 48: 189–204. https://doi.org/10.1016/j.gr.2017.04.019

Cochrane, R. 2013. U–Pb thermochronology, geochronology and geochemistry of NW South America: Rift to drift transition, active margin dynamics and implications for the volume balance of continents. Doctoral thesis, University of Geneva, 118 p. Geneva.

Cochrane, R., Spikings, R., Gerdes, A., Ulianov, A., Mora, A., Villagómez, D., Putlitz, B. & Chiaradia, M. 2014a. Permo–Triassic anatexis, continental rifting and the disassembly of western Pangaea. Lithos, 190–191: 383–402. https://doi.org/10.1016/j.lithos.2013.12.020

Cochrane, R., Spikings, R., Gerdes, A., Winkler, W., Ulianov, A., Mora, A. & Chiaradia, M. 2014b. Distinguishing between in–situ and accretionary growth of continents along active margins. Lithos, 202–203: 382–394. https://doi.org/10.1016/j.lithos.2014.05.031

Correa, A.M., Pimentel, M., Restrepo, J.J., Nilson, A., Ordoñez, O., Martens, U., Laux, J.E. & Junges, S. 2006. U–Pb zircon ages and Nd–Sr isotopes of the Altavista Stock and the San Diego Gabbro: New insights on Cretaceous arc magmatism in the Colombian Andes. V South American Symposium on Isotope Geology. Memoirs, p. 84–86. Punta del Este, Uruguay.

DeGraaff–Surpless, K., Graham, S.A., Wooden, J.L. & McWilliams, M.O. 2002. Detrital zircon provenance analysis of the Great Valley Group, California: Evolution of an arc–forearc system. Geological Society of America Bulletin, 114(12): 1564–1580. https://doi.org/10.1130/0016-7606(2002)114<1564:DZPAOT>2.0.CO;2

Dickinson, W.R. & Gehrels, G.E. 2009. Use of U–Pb ages of detrital zircons to infer maximum depositional ages of strata: A test against a Colorado Plateau Mesozoic database. Earth and Planetary Science Letters, 288(1–2): 115–125. https://doi.org/10.1016/j.epsl.2009.09.013

Dott Jr., R.H. 2003. The importance of eolian abrasion in supermature quartz sandstone and the paradox of weathering on vegetation–free landscapes. The Journal of Geology, 111(4): 387–405. https://doi.org/10.1086/375286

Duarte, E. Cardona, A., Lopera, S., Valencia, V. & Estupiñan, H., 2018. Provenance and diagenesis from two stratigraphic sections of the Lower Cretaceous Caballos Formation in the Upper Magdalena Valley: Geological and reservoir quality implications. Ciencia, Tectonología y Futuro, 8 (1): 5–29.

Dufrane, S.A., Vervoort, J.D. & Hart, G.L. 2007. Uncertainty of Hf isotope analysis in zircon using LA–MC–ICPMS techniques: Full disclosure. 17th Annual V.M. Goldschmidt Conference, Cologne, Germany. Geochimica et Cosmochimica Acta, 71(15): 241.

Duque–Trujillo, J., Bustamante, C., Solari, L., Gómez–Mafla, Á., Toro–Villegas, G., & Hoyos, S. 2018. Reviewing the Antioquia Batholith and satellite bodies: A record of Late Cretaceous to Eocene syn– to post–collisional arc magmatism in the Central Cordillera of Colombia: Andean Geology, 46(1): 82–101. http://dx.doi.org/10.5027/andgeoV46n1–3120

Etayo–Serna, F. 1985. Documentación paleontológica del Infracretácico de San Felix y Valle Alto, cordillera Central. In: Etayo–Serna, F. & Laverde, F. (editors), Proyecto Cretácico: Contribuciones. Publicaciones Geológicas Especiales del Ingeominas 16, p. XXV–1–XXV–7. Bogotá.

Etayo–Serna, F., Renzoni, G. & Barrero, D. 1969. Contornos sucesivos del mar cretáceo en Colombia. Primer Congreso Colombiano de Geología. Memoirs, p. 217–252. Bogotá.

Feininger, T. & Botero, G. 1982. The Antioquian Batholith, Colombia. Publicaciones Geológicas Especiales del Ingeominas 12, p. 1–50. Bogotá.

Feininger, T., Barrero, D. & Castro, N. 1972. Geología de parte de los departamentos de Antioquia y Caldas (sub–zona II–B). Boletín Geológico, 20(2): 1–173.

Fildani, A. & Hessler, A.M. 2005. Stratigraphic record across a retroarc basin inversion: Rocas Verdes–Magallanes Basin, Patagonian Andes, Chile. Geological Society of America Bulletin, 117(11–12): 1596–1614. https://doi.org/10.1130/B25708.1

Fildani, A., Cope, T.D., Graham, S.A. & Wooden, J.L. 2003. Initiation of the Magallanes Foreland Basin: Timing of the southernmost Patagonian Andes Orogeny revised by detrital zircon provenance analysis. Geology, 31(12): 1081–1084. https://doi.org/10.1130/G20016.1

Folk, R. 1974. Petrology of sedimentary rocks. Hemphill Publishing Company, 182 p. Austin, USA.

García–Ramírez, C.A., Ríos–Reyes, C.A., Castellanos–Alarcón, O.M. & Mantilla–Figueroa, L.C. 2017. Petrology, geochemistry and geochronology of the Arquía Complex's metabasites at the Pijao–Génova sector, Central Cordillera, Colombian Andes. Boletín de Geología, 39(1): 105–126. http://dx.doi.org/10.18273/revbol.v39n1-2017005

Garzanti, E. 2016. From static to dynamic provenance analysis–sedimentary petrology upgraded. Sedimentary Geology, 336: 3–13. https://doi.org/10.1016/j.sedgeo.2015.07.010

Gómez–Cruz, A.d.J., Moreno–Sánchez, M. & Pardo–Trujillo, A. 1995. Edad y origen del "Complejo Metasedimentario Aranzazu–Manizales" en los alrededores de Manizales (departamento de Caldas, Colombia). Geología Colombiana, 19: 83–93.

Gómez–Cruz, A.d.J., Moreno–Sánchez, M. & Pardo–Trujillo, A. 2002. Afloramientos fosilíferos del Cretácico Superior en el municipio de Pijao (borde occidental de la cordillera Central, Colombia). Geo–Eco–Trop, 26(2): 41–50.

Gómez, J., Montes, N., Nivia, Á. & Diederix, H., compiladores. 2015. Geological Map of Colombia 2015. Scale 1:1 000 000. Servicio Geológico Colombiano, 2 sheets. Bogotá.

Gómez, P.D. & Lizcano, A. 1990. Estudio tectónico–estratigráfico de la franja sedimentaria cretácea de Berlín, Caldas, cordillera Central. Bachelor thesis, Universidad Industrial de Santander, 120 p. Bucaramanga.

González, H. 1980. Geología de las planchas 167 Sonsón y 187 Salamina. Scale 1:100 000. Ingeominas, Internal report 1760, 262 p. Medellín.

González, H. 2001. Memoria explicativa: Mapa geológico del departamento de Antioquia. Scale 1:400 000. Ingeominas, 240 p. Medellín.

Gradstein, F.M., Ogg, J.G. & Hilgen, F.J. 2012. On the geologic time scale. Newsletters on Stratigraphy, 45(2): 171–188. https://doi.org/10.1127/0078-0421/2012/0020

Grosse, E. 1926. Estudio geológico del terciario carbonífero de Antioquia en la parte occidental de la cordillera Central de Colombia, entre el río Arma y Sacaojal, ejecutado en los años de 1920–1923. Dietrich Reimer, 361 p. Berlin.

Hall, R.B., Álvarez, J. & Rico, H. 1972. Geología de los departamentos de Antioquia y Caldas (subzona II–A). Boletín Geológico, 20(1): 1–85.

Hincapié–Gómez, S., Cardona, A., Jiménez, G., Monsalve, G., Ramírez–Hoyos, L. & Bayona, G. 2018. Paleomagnetic and gravimetrical reconnaissance of Cretaceous volcanic rocks from the western Colombian Andes: Paleogeographic connections with the Caribbean Plate. Studia Geophysica et Geodaetica, 62(3): 485–511. https://doi.org/10.1007/s11200-016-0678-y

Horton, B.K. 2018. Tectonic regimes of the central and southern Andes: Responses to variations in plate coupling during subduction. Tectonics, 37(2): 402–429. https://doi.org/10.1002/2017TC004624

Horton, B.K., Saylor, J.E., Nie, J., Mora, A., Parra, M., Reyes–Harker, A. & Stockli, D.F. 2010. Linking sedimentation in the northern Andes to basement configuration, Mesozoic extension, and Cenozoic shortening: Evidence from detrital zircon U–Pb ages, Eastern Cordillera, Colombia. Geological Society of America Bulletin, 122(9–10): 1423–1442. https://doi.org/10.1130/B30118.1

Ibañez–Mejia, M., Tassinari, C.C.G. & Jaramillo–Mejía, J.M. 2007. U–Pb zircon ages of the "Antioquian Batholith": Geochronological constraints of late Cretaceous magmatism in the central Andes of Colombia. XI Congreso Colombiano de Geología. Abstracts, 11 p. Bucaramanga.

Ickert, R.B., Hiess, J., Williams, I.S., Holden, P., Ireland, T.R., Lanc, P., Schram, N., Foster, J.J. & Clement, S.W. 2008. Determining high precision, in situ, oxygen isotope ratios with a SHRIMP II: Analyses of MPI–DING silicate–glass reference materials and zircon from contrasting granites. Chemical Geology, 257(1–2): 114–128. https://doi.org/10.1016/j.chemgeo.2008.08.024

Irvine, T.N. & Baragar, W.R.A. 1971. A guide to the chemical classification of the common volcanic rocks. Canadian Journal of Earth Sciences, 8(5): 523–548.https://doi.org/10.1139/e71-055

Jaillard, E., Laubacher, G., Bengston, P., Dhondt, A.V. & Bulot, L.G. 1999. Stratigraphy and evolution of the Cretaceous forearc Celica–Lancones Basin of southwestern Ecuador. Journal of South American Earth Sciences, 12(1): 51–68. https://doi.org/10.1016/S0895-9811(99)00006-1

Jaillard, E., Bengston, P., Ordóñez, M., Vaca, W., Dhondt, A., Suárez, J. & Toro, J. 2008. Sedimentary record of terminal Cretaceous accretions in Ecuador: The Yunguilla Group in the Cuenca area. Journal of South American Earth Sciences, 25(2): 133–144. https://doi.org/10.1016/j.jsames.2007.08.002

Jaimes, E. & De Freitas, M. 2006. An Albian–Cenomanian unconformity in the northern Andes: Evidence and tectonic significance. Journal of South American Earth Sciences, 21(4): 466–492. https://doi.org/10.1016/j.jsames.2006.07.011

Janoušek, V., Farrow, C.M. & Erban, V. 2006. Interpretation of whole–rock geochemical data in igneous geochemistry: Introducing geochemical data toolkit (GCDkit). Journal of Petrology, 47(6): 1255–1259. https://doi.org/10.1093/petrology/egl013

Jaramillo, J.S., Cardona, A., León, S., Valencia, V. & Vinasco, C. 2017. Geochemistry and geochronology from Cretaceous magmatic and sedimentary rocks at 6° 35' N, western flank of the Central Cordillera (Colombian Andes): Magmatic record of arc growth and collision. Journal of South American Earth Sciences, 76: 460–481. https://doi.org/10.1016/j.jsames.2017.04.012

Kammer, A. & Sánchez, J. 2006. Early Jurassic rift structures associated with the Soapaga and Boyacá faults of the Eastern Cordillera, Colombia: Sedimentological inferences and regional implications. Journal of South American Earth Sciences, 21(4): 412–422. https://doi.org/10.1016/j.jsames.2006.07.006

Kerr, A.C., Marriner, G.F., Tarney, J., Nivia, Á., Saunders, A.D., Thirlwall, M.F. & Sinton, C.W. 1997. Cretaceous basaltic terranes in western Colombia: Elemental, chronological and Sr–Nd isotopic constraints on petrogenesis. Journal of Petrology, 38(6): 677–702. https://doi.org/10.1093/petrology/38.6.677

Lackey, J.S., Valley, J.W. & Saleeby, J.B. 2005. Supracrustal input to magmas in the deep crust of Sierra Nevada Batholith: Evidence from high–$\delta^{18}O$ zircon. Earth and Planetary Science Letters, 235(1–2): 315–330. https://doi.org/10.1016/j.epsl.2005.04.003

Leal–Mejía, H. 2011. Phanerozoic gold metallogeny in the Colombian Andes: A tectono–magmatic approach. Doctoral thesis, Universitat de Barcelona, 989 p. Barcelona.

León, S., Cardona, A., Parra, M., Sobel, E.R., Jaramillo, J.S., Glodny, J., Valencia, V., Chew, D., Montes, C., Posada, G., Monsalve, G. & Pardo–Trujillo, A. 2018. Transition from collisional to subduction–related regimes: An example from Neogene Panama–Nazca–South–America interactions. Tectonics, 37(1): 119–139. https://doi.org/10.1002/2017TC004785

Litherland, M., Aspden, J.A. & Jemielita, R.A. 1994. The metamorphic belts of Ecuador. Overseas Memoir of the British Geological Survey 11, 147 p. Nottingham, England.

Lozano, H., Pérez, H. & Mosquera, D. 1975. Prospección geoquímica en los municipios de Salento, Quindio y Cajamarca, Tolima. Ingeominas, Internal report 1692, 103 p. Bogotá.

Ludwig, K.R. 2003. "User's Manual for Isoplot/Ex, Version 3.00. A Geochronological Toolkit for Microsoft Excel," Berkeley Geochronology Center. Special Publication 4(2), 70 p. Berkeley, USA.

Marsaglia, K.M. 2012. Sedimentation at plate boundaries in transition. In: Busby, C. & Azor, A. (editors), Tectonics of sedimentary basins: Recent advances. Blackwell Publishing Ltd, p 291–309. https://doi.org/10.1002/9781444347166.ch14

Martens, U.C., Restrepo, J.J. & Solari, L.A. 2012. Sinifaná metasedimentites and relations with Cajamarca paragneisses of the Central Cordillera of Colombia. Boletín de Ciencias de la Tierra, (32): 99–110.

Martens, U., Restrepo, J.J., Ordóñez–Carmona, O. & Correa–Martínez, A.M. 2014. The Tahamí and Anacona Terranes of the Colombian Andes: Missing links between the South American and Mexican Gondwana margins. The Journal of Geology, 122(5): 507–530. https://doi.org/10.1086/677177

Matthews, K.J., Seton, M. & Müller, R.D. 2012. A global–scale plate reorganization event at 105–100 Ma. Earth and Planetary Science Letters, 355–356: 283–298. https://doi.org/10.1016/j.epsl.2012.08.023

Maya, M. & González, H. 1995. Unidades litodémicas en la cordillera Central de Colombia. Boletín Geológico, 35(2–3): 43–57.

Mejía–Velásquez, P.J., Dilcher, D.L., Jaramillo, C.A., Fortini, L.B. & Manchester, .S.R. 2012. Palynological composition of a Lower Cretaceous South American tropical sequence: Climatic implications and diversity comparisons with other latitudes. American Journal of Botany, 99(11): 1819–1827. https://doi.org/10.3732/ajb.1200135

Middlemost, E.A.K. 1994. Naming materials in the magma/igneous rock system. Earth–Science Reviews, 37(3–4): 215–224. https://doi.org/10.1016/0012-8252(94)90029-9

Montes, C., Guzmán, G., Bayona, G., Cardona, A., Valencia, V. & Jaramillo, C. 2010. Clockwise rotation of the Santa Marta Massif and simultaneous Paleogene to Neogene deformation of the Plato–San Jorge and Cesar–Ranchería Basins. Journal of South American Earth Sciences, 29(4): 832–848. https://doi.org/10.1016/j.jsames.2009.07.010

Moreno, J.M. 1990. Stratigraphy of the Lower Cretaceous Rosablanca and Cumbre Formations, Utica Sandstone and Murca Formation, west flank, Eastern Cordillera, Colombia. Geología Colombiana, 17: 65–86.

Moreno, J.M. 1991. Provenance of the Lower Cretaceous sedimentary sequences, central part, Eastern Cordillera, Colombia. Revista de la Academia Colombiana de Ciencias Exactas, Físicas y Naturales, 18(69): 159–173.

Moreno–Sánchez, M. & Pardo–Trujillo, A. 2003. Stratigraphical and sedimentological constraints on western Colombia: Implications on the evolution of the Caribbean Plate. In: Bartolini,

C., Buffler, R.T. & Blickwede, J. (editors), The circum–Gulf of Mexico and the Caribbean: Hydrocarbon habitats, basin formation, and plate tectonics. American Association of Petroleum Geologists, Memoir 79, p. 891–924. Tulsa, USA.

Moreno–Sánchez, M., Gómez–Cruz, A.d.J. & Toro–Toro, L.M. 2008. Proveniencia del material clástico del Complejo Quebradagrande y su relación con los complejos estructurales adyacentes. Boletín de Ciencias de la Tierra, (22): 27–38.

Moulin, M., Aslanian, D. & Unternehr, P. 2010. A new starting point for the south and equatorial Atlantic Ocean. Earth–Science Reviews, 98(1–2): 1–37. https://doi.org/10.1016/j.earscirev.2009.08.001

Nakamura, N., 1974. Determination of REE, Ba, Fe, Mg, Na, and K in carbonaceous and ordinary chondrites. Geochimica et Cosmochimica Acta, 38(5): 757–775. https://doi.org/10.1016/0016-7037(74)90149-5

Naranjo, J.L. 1983. Investigación del potencial uranífero en los shales negros del Sinclinal de Berlín, departamento de Caldas. Bachelor thesis, Universidad Nacional de Colombia, 98 p. Bogotá.

Nivia, Á., Marriner, G.F., Kerr, A.C. & Tarney, J. 2006. The Quebradagrande Complex: A Lower Cretaceous ensialic marginal basin in the Central Cordillera of the Colombian Andes. Journal of South American Earth Sciences, 21(4): 423–436. https://doi.org/10.1016/j.jsames.2006.07.002

Ordóñez–Carmona, O. & Pimentel, M.M. 2001. Consideraciones geocronológicas e isotópicas del Batolito Antioqueño. Revista de la Academia Colombiana de Ciencias Exactas, Físicas y Naturales, 25(94): 27–35.

Ordóñez–Carmona, O., Pimentel, M.M. & Angel–Cárdenas, P. 2001. Consideraciones geocronológicas e isotópicas preliminares del magmatismo cretáceo–paleoceno en el norte de la cordillera Central. VIII Congreso Colombiano de Geología. Memoirs, 5 p. Manizales.

Ordóñez–Carmona, O., Pimentel, M.M., Frantz, J.C. & Chemale, F.F. 2007. Edades U–Pb convencionales de algunas intrusiones colombianas. XI Congreso Colombiano de Geología. Abstracts, p. 45. Bucaramanga.

Paul, A.N., Spikings, R.A., Ulianov, A. & Ovtcharova, M. 2018. High temperature (>350° C) thermal histories of the long lived (>500 Ma) active margin of Ecuador and Colombia: Apatite, titanite and rutile U–Pb thermochronology. Geochimica et Cosmochimica Acta, 228: 275–300. https://doi.org/10.1016/j.gca.2018.02.033

Pearce, J.A. 2008. Geochemical fingerprinting of oceanic basalts with applications to ophiolite classification and the search for Archean oceanic crust. Lithos, 100(1–4): 14–48. https://doi.org/10.1016/j.lithos.2007.06.016

Pearce, J.A., Harris, N.B.W. & Tindle, A.G. 1984. Trace element discrimination diagrams for the tectonic interpretation of granitic rocks. Journal of Petrology, 25(4): 956–983. https://doi.org/10.1093/petrology/25.4.956

Peccerillo, A. & Taylor, S.R. 1976. Geochemistry of Eocene calc–alkaline volcanic rocks from the Kastamonu area, northern Turkey. Contributions to Mineralogy and Petrology, 58(1): 63–81. https://doi.org/10.1007/BF00384745

Pimiento, R. 2011. Mineralogía y petrografía de la mineralización de uranio en fosforitas del Cretácico Inferior, Sinclinal de Berlín, cordillera Central (departamento de Caldas, Colombia). Bachelor thesis, Universidad Industrial de Santander, 156 p. Bucaramanga.

Pindell, J., Kennan, L., Maresch, W.V., Stanek, K.P., Draper, G. & Higgs, R. 2005. Plate–kinematics and crustal dynamics of circum–Caribbean arc–continent interactions: Tectonic controls on basin development in proto–Caribbean margins. In: Avé–Lallemant, H.G. & Sisson, V.B. (editors), Caribbean–South American Plate interactions, Venezuela. Geological Society of America, Special Paper 394, p. 7–52. https://doi.org/10.1130/0-8137-2394-9.7

Pindell, J.L. & Kennan, L. 2009. Tectonic evolution of the Gulf of Mexico, caribbean and northern South America in the mantle reference frame: An update. In: James, K.H., Lorente, M.A. & Pindell, J.L. (editors), The origin and evolution of the Caribbean Plate. Geological Society of London, Special Publication 328, p. 1–55. https://doi.org/10.1144/SP328.1

Quiroz, L. 2005. Cartografía y análisis estratigráfico de las formaciones Valle Alto y Abejorral en la región de San Félix, departamento de Caldas, Colombia. Bachelor thesis, Universidad Nacional de Colombia, 53 p. Bogotá.

Ramos, V.A. 2009. Anatomy and global context of the Andes: Main geologic features and the Andean orogenic cycle. In: Kay, S.M., Ramos, V.A. & Dickinson, W.R. (editors), Backbone of the Americas: Shallow subduction, plateau uplift, and ridge and terrane collision. Geological Society of America, Memoirs 204, p. 31–65. https://doi.org/10.1130/2009.1204(02)

Ramos, V.A. 2010. The tectonic regime along the Andes: Present–day and Mesozoic regimes. Geological Journal, 45(1): 2–25. https://doi.org/10.1002/gj.1193

Rendón, D.A. 1999. Cartografía y caracterización de las unidades geológicas de la zona urbana de Medellín. Bachelor thesis, Universidad Nacional de Colombia, 113 p. Medellín.

Restrepo, J.J., Ordóñez–Carmona, O. & Moreno–Sánchez, M. 2009. A comment on ‘‘The Quebradagrande Complex: A Lower Cretaceous ensialic marginal basin in the Central Cordillera of the Colombian Andes” by Nivia et al. Journal of South American Earth Sciences, 28(2): 204–205. https://doi.org/10.1016/j.jsames.2009.03.004

Restrepo, J.J., Ordóñez–Carmona, O., Armstrong, R. & Pimentel, M.M. 2011. Triassic metamorphism in the northern part of the Tahamí Terrane of the Central Cordillera of Colombia. Journal of South American Earth Sciences, 32(4): 497–507. https://doi.org/10.1016/j.jsames.2011.04.009

Restrepo, J.J., Ibañez–Mejia, M. & García–Casco, A. 2012. U–Pb zircon ages of the Medellín Amphibolites (Central Cordillera

of Colombia) reveal mid–Cretaceous tectonic juxtaposition of Triassic and mid–Cretaceous metamorphic complexes. VIII South American Symposium on Isotope Geology. USB memory device, 33 slides. Medellín.

Restrepo–Moreno, S.A. 2009. Long–term morphotectonic evolution and denudation chronology of the Antioqueño Plateau, Cordillera Central, Colombia. Doctoral Thesis. University of Florida, 223 p. Gainesville, USA.

Restrepo–Moreno, S., Foster, D.A. & Kamenov, G. 2007. Formation age and magma sources for the Antioqueño Batholith derived from LA–ICP–MS uranium–lead dating and hafnium–isotope analysis of zircon grains. GSA Meeting 2007, 39(6): p. 493. Denver, CO, USA.

Robertson, A.H.F. 1994. Role of the tectonic facies concept in orogenic analysis and its application to Tethys in the eastern Mediterranean region. Earth–Science Reviews, 37(3–4): 139–213. https://doi.org/10.1016/0012-8252(94)90028-0

Rodríguez, C. & Rojas, R. 1985. Estratigrafía y tectónica de la serie infracretácica en los alrededores de San Felix, cordillera Central de Colombia. In: Etayo–Serna, F. & Laverde–Montaño, F. (editors), Proyecto Cretácico: Contribuciones. Publicaciones Geológicas Especiales del Ingeominas 16, p. XXIV–1–XXI–21. Bogotá.

Rodríguez, G. & Celada–Arango, C.M. 2018. Basaltos de San Pablo: un bloque de un arco de islas en el norte de la cordillera Central de Colombia. Caracterización petrográfica y química. Boletín de Geología, 40(2): 69–85. https://doi.org/10.18273/revbol.v40n2-2018004

Rodríguez, G. & Cetina, L.M. 2016. Caracterización petrográfica y química de rocas de corteza oceánica del Complejo Quebradagrande y comparación con rocas de la unidad Diabasas de San José de Urama. Boletín de Geología, 38(3): 15–29. https://doi.org/10.18273/revbol.v38n3-2016001

Rodríguez, G. & Correa–Martínez, A.M. 2015. Edades U–Pb en circón de varias unidades metamórficas al este y noreste de la ciudad de Medellín, cordillera Central de Colombia. XV Congreso Colombiano de Geología. Memoirs, p. 287–289. Bucaramanga.

Rodríguez, G. & Montoya, T. 1993. Evolución magmática del Stock de Altavista. VI Congreso Colombiano de Geología. Memoirs, II, p. 497–514. Medellín.

Rodríguez, G., Arango, M.I, Zapata, G. & Bermúdez, J.G. 2018. Petrotectonic characteristics, geochemistry, and U–Pb geochronology of Jurassic plutons in the Upper Magdalena Valley–Colombia: Implications on the evolution of magmatic arcs in the NW Andes. Journal of South American Earth Sciences, 81: 10–30. https://doi.org/10.1016/j.jsames.2017.10.012

Rubatto, D. 2002. Zircon trace element geochemistry: Partitioning with garnet and the link between U–Pb ages and metamorphism. Chemical Geology, 184(1–2): 123–138. https://doi.org/10.1016/S0009-2541(01)00355-2

Ruiz, G.M.H., Seward, D. & Winkler, W. 2007. Evolution of the Amazon Basin in Ecuador with special reference to hinterland tectonics: Data from zircon fission–track and heavy mineral analysis. In: Mange, M.A. & Wright, D.T. (editors), Heavy Minerals in Use. Developments in Sedimentology, 58: 907–934. https://doi.org/10.1016/S0070-4571(07)58036-2

Saenz, E.A. 2003. Fission track thermochronology and denudational response to tectonics in the north of the Colombian Central Cordillera. Master Thesis, Shimane University, 138 p. Shimane, Japan.

Sarmiento–Rojas, L.F., van Wess, J.D. & Cloetingh, S. 2006. Mesozoic transtensional basin history of the Eastern Cordillera, Colombian Andes: Inferences from tectonic models. Journal of South American Earth Sciences, 21(4): 383–411. https://doi.org/10.1016/j.jsames.2006.07.003

Schmitt, A.K., Konrad, K., Andrews, G.D.M., Horie, K., Brow, S.R., Koppers, A.A.P., Pecha, M., Busby, C.J. & Tamura, Y. 2017. $^{40}Ar/^{39}Ar$ ages and zircon petrochronology for the rear arc of the Izu–Bonin–Marianas intra–oceanic subduction zone. International Geology Review, 60(8): 956–976. https://doi.org/10.1080/00206814.2017.1363675

Sdrolias, M. & Müller, R.D. 2006. Controls on back–arc basin formation. Geochemistry, Geophysics, Geosystems, 7(4): 1–40. https://doi.org/10.1029/2005GC001090

Seton, M., Müller, R.D., Zahirovic, S., Gaina, C., Torsvik, T.H., Shephard, G., Talsma, A., Gurnis, M., Turner, M., Maus, S. & Chandler, M. 2012. Global continental and ocean basin reconstructions since 200 Ma. Earth–Science Reviews, 113(3–4): 212–270. https://doi.org/10.1016/j.earscirev.2012.03.002

Seton, M., Mortimer, N., Williams, S., Quilty, P., Gans, P., Meffre, S., Micklethwaite, S., Zahirovic, S., Moore, J. & Matthews, K.J. 2016. Melanesian back–arc basin and arc development: Constraints from the eastern Coral Sea. Gondwana Research, 39: 77–95. https://doi.org/10.1016/j.gr.2016.06.011

Sláma, J., Kosler, J., Condon, D.J., Crowley, J.L., Gerdes, A., Hanchar, J.M., Horstwood, M.S.A., Morris, G.A., Nasdala, L., Norberg, N., Schaltegger, U., Schoene, B., Tubrett, M.N. & Whitehouse, M.J. 2008. Plešovice zircon–A new natural reference material for U–Pb and Hf isotopic microanalysis. Chemical Geology, 249(1–2): 1–35. https://doi.org/10.1016/j.chemgeo.2007.11.005

Smyth, H.R., Hall, R. & Nichols, G.J. 2008. Significant volcanic contribution to some quartz–rich sandstones, east Java, Indonesia. Journal of Sedimentary Research, 78(5): 335–356. https://doi.org/10.2110/jsr.2008.039

Spadea, P. & Espinosa, A. 1996. Petrology and chemistry of late Cretaceous volcanic rocks from the southernmost segment of the Western Cordillera of Colombia (South America). Journal of South American Earth Sciences, 9(1–2): 79–90. https://doi.org/10.1016/0895-9811(96)00029-6

Spikings, R., Cochrane, R., Villagómez, D., van der Lelij, R., Vallejo, C., Winkler, W. & Beate, B. 2015. The geological history of northwestern South America: From Pangaea to the early collision of the Caribbean Large Igneous Province (290–75 Ma).

Gondwana Research, 27(1): 95–139. https://doi.org/10.1016/j.gr.2014.06.004

Stern, R.J. 2012. Subduction zones. Reviews of Geophysics, 40(4): 3–38. https://doi.org/10.1029/2001RG000108

Suárez, M.B., González, L.A. & Ludvigson, G.A. 2010. Estimating the oxygen isotopic composition of equatorial precipitation during the mid–Cretaceous. Journal of Sedimentary Research, 80(5): 480–491. https://doi.org/10.2110/jsr.2010.048

Sun, S.S. & McDonough, W.F. 1989. Chemical and isotopic systematics of oceanic basalts: Implications for mantle composition and processes. In: Saunders, A.D. & Norry, M.J. (editors), Magmatism in the ocean basins. Geological Society of London, Special Publication 42, p. 313–345. https://doi.org/10.1144/GSL.SP.1989.042.01.19

Tamayo, J. & Correa, V. 2010. Petrografía y datación de circones detríticos en las facies cuarzosas del complejo Quebradagrande (Cretácico Inferior) de la cordillera Central. Bachelor thesis, Universidad de Caldas, 76 p. Manizales.

Torsvik, T.H., Rousse, S., Labails, C. & Smethurst, M.A. 2009. A new scheme for the opening of the South Atlantic Ocean and the dissection of an Aptian salt basin. Geophysical Journal International, 177(3): 1315–1333. https://doi.org/10.1111/j.1365-246X.2009.04137.x

Toussaint, J.F. 1996. Evolución geológica de Colombia: 3 Cretácico. Universidad Nacional de Colombia, 277 p. Medellín.

Trail, D., Mojzsis, S.J., Harrison, T.M., Schmitt, A.K., Watson, E.B. & Young, E.D. 2007. Constraints on Hadean zircon protoliths from oxygen isotopes, Ti–thermometry, and rare earth elements. Geochemistry, Geophysics, Geosystems, 8(6): 1–22. https://doi.org/10.1029/2006GC001449

Tunik, M., Folguera, A., Naipauer, M., Pimentel, M. & Ramos, V.A. 2010. Early uplift and orogenic deformation in the Neuquén Basin: Constraints on the Andean uplift from U–Pb and Hf isotopic data of detrital zircons. Tectonophysics, 489(1–4): 258–273. https://doi.org/10.1016/j.tecto.2010.04.017

Uyeda, S. & Kanamori, H. 1979. Back–arc opening and the mode of subduction. Journal of Geophysical Research: Solid Earth, 84(B3): 1049–1061. https://doi.org/10.1029/JB084iB03p01049

van der Lelij, R., Spikings, R. & Mora, A. 2016. Thermochronology and tectonics of the Mérida Andes and the Santander Massif, NW South America. Lithos, 248–251: 220–239. https://doi.org/10.1016/j.lithos.2016.01.006

Vásquez, M., Altenberger, U., Romer, R.L., Sudo, M. & Moreno–Murillo, J.M. 2010. Magmatic evolution of the Andean Eastern Cordillera of Colombia during the Cretaceous: Influence of previous tectonic processes. Journal of South American Earth Sciences, 29(2): 171–186. https://doi.org/10.1016/j.jsames.2009.02.003

Vavra, G., Schmid, R. & Gebauer, D. 1999. Internal morphology, habit and U–Th–Pb microanalysis of amphibolite–to–granulite facies zircons: Geochronology of the Ivrea zone (southern Alps). Contribution to Mineralogy and Petrology, 134(4): 380–404. https://doi.org/10.1007/s004100050492

Vervoort, J.D. & Blichert–Toft, J. 1999. Evolution of the depleted mantle: Hf isotope evidence from juvenile rocks through time. Geochimica et Cosmochimica Acta, 63(3–4): 533–556. https://doi.org/10.1016/S0016–7037(98)00274–9

Vervoort, J.D. & Patchett, P.J. 1996. Behavior of hafnium and neodymium isotopes in the crust: Constraints from Precambrian crustally derived granites. Geochimica et Cosmochimica Acta, 60(19): 3717–3733. https://doi.org/10.1016/S0016-7037(98)00274-9

Vervoort, J.D., Patchett, P.J., Söderlund, U. & Baker, M. 2004. Isotopic composition of Yb and the determination of Lu concentrations and Lu/Hf ratios by isotope dilution using MC–ICPMS. Geochemistry, Geophysics, Geosystems, 5(11): 1–15. https://doi.org/10.1029/2004GC000721

Villagómez, D. & Spikings, R. 2013. Thermochronology and tectonics of the Central and Western Cordilleras of Colombia: Early Cretaceous–Tertiary evolution of the northern Andes. Lithos, 160–161: 228–249. https://doi.org/10.1016/j.lithos.2012.12.008

Villagómez, D., Spikings, R., Magna, T., Kammer, A., Winkler, W. & Beltrán, A. 2011. Geochronology, geochemistry and tectonic evolution of the Western and Central Cordilleras of Colombia. Lithos, 125(3–4): 875–896. https://doi.org/10.1016/j.lithos.2011.05.003

Villamil, T. 1999. Campanian–Miocene tectonostratigraphy, depocenter evolution and basin development of Colombia and western Venezuela. Palaeogeography, Palaeoclimatology, Palaeoecology, 153(1–4): 239–275. https://doi.org/10.1016/S0031-0182(99)00075-9

Villamil, T. & Arango, C. 1998. Integrated stratigraphy of latest Cenomanian and Early Turonian facies of Colombia. In: Pindell, J.L. & Drake, C.L. (editors), Paleogeographic evolution and non–glacial eustacy, northern South America. Society for Sedimentary Geology, Special Publication 58, p. 129–159. https://doi.org/10.2110/pec.98.58.0129

Vinasco, C.J., Cordani, U.G., González, H., Weber, M. & Peláez, C. 2006. Geochronological, isotopic, and geochemical data from Permo–Triassic granitic gneisses and granitoids of the Colombian central Andes. Journal of South American Earth Sciences, 21(4): 355–371. https://doi.org/10.1016/j.jsames.2006.07.007

Weber, M., Gómez–Tapias, J., Cardona, A., Duarte, E., Pardo–Trujillo, A. & Valencia, V. 2015. Geochemistry of the Santa Fé Batholith and Buriticá Tonalite in NW Colombia—Evidence of subduction initiation beneath the Colombian Caribbean Plateau. Journal of South American Earth Sciences, 62: 257–274. https://doi.org/10.1016/j.jsames.2015.04.002

Whattam, S.A. & Stern, R.J. 2015. Late Cretaceous plume–induced subduction initiation along the southern margin of the Caribbean and NW South America: The first documented example with implications for the onset of plate tectonics.

Gondwana Research, 27(1): 38–63. https://doi.org/10.1016/j.gr.2014.07.011

Wiedenbeck, M., Hanchar, J.M., Peck, W.H., Sylvester, P., Valley, J., Whitehouse, M., Kronz, A., Morishita, Y., Nasdala, L., Fiebig, J., Franchi, I., Girard, J.P., Greenwood, R.C., Hinton, R., Kita, N., Mason, P.R.D., Norman, M., Ogasawara, M., Piccoli, P.M., Rhede, D., Satoh, H., Schulz–Dobrick, B., Skår, O., Spicuzza, M.J., Terada, K., Tindle, A., Togashi, S., Vennemann, T., Xie, Q. & Zheng, Y.F. 2004. Further characterisation of the 91 500 zircon crystal. Geostandards and Geoanalytical Research, 28(1): 9–39. https://doi.org/10.1111/j.1751-908X.2004.tb01041.x

Williams, I.S. 1998. U–Th–Pb geochronology by ion microprobe. In: Mckibben, M.A., Shanks III, W.C. & Ridley, W.I. (editors.), Applications of microanalytical techniques to understanding mineralizing processes. Reviews in Economic Geology 7, p. 1–35. Littleton, USA.

Zapata, J.P., Restrepo, J.J., Cardona, A. & Martens, U. 2017. Geoquímica y geocronología de las rocas volcánicas básicas y el Gabro de Altamira, cordillera Occidental (Colombia): Registro de ambientes de plateau y arco oceánico superpuestos durante el Cretácico. Boletín de Geología, 39(2): 13–30. https://doi.org/10.18273/revbol.v39n2-2017001

Zapata, S., Cardona, A., Jaramillo, J. S., Patiño, A., Valencia, V., Leon, S., Mejía, D., Pardo–Trujillo, A. & Castañeda, J. P. 2018. Cretaceous extensional and compressional tectonics in the Northwestern Andes, prior to the collision with the Caribbean oceanic plateau. Gondwana Research, 66: 207–226. https://doi.org/10.1016/j.gr.2018.10.008

Explanation of Acronyms, Abbreviations, and Symbols:

CLIP	Caribbean Large Igneous Province
E–MORB	Enriched mid–ocean ridge basalt
FC	Faraday cup
DM	Depleted mantle
HFSE	High field strength element
HREE	Heavy rare earth element
ICP–AES	Inductively coupled plasma atomic emission spectroscopy
ICP–MS	Inductively coupled plasma mass spectrometry
LA–ICP–MS	Laser ablation inductively coupled plasma mass spectrometry
LILE	Large–ion lithophile element
LREE	Light rare earth element
MORB	Mid–ocean ridge basalt
MREE	Middle rare earth element
TDM	Depleted mantle model ages
TIMS	Thermal ionization mass spectrometry
VSMOW	Vienna standard mean ocean water

Authors' Biographical Notes

Agustín CARDONA is graduated with a degree in geology from Universidad EAFIT in 1999. He obtained MS and PhD degrees in geochemistry and geotectonics, respectively, from the Universidade de São Paulo, Brasil. Subsequently, he was a postdoctoral fellow at the Smithsonian Tropical Research Institute 2006–2011), working in several paleogeogeographic–oriented projects in northern Colombia and Panamá. Since 2012, he has served as full–time professor at the Universidad Nacional de Colombia in Medellín. His main interest is related to regional tectonics of convergent margins, especially the Andean and Caribbean Orogens.

Santiago LEÓN is graduated with a degree in geological engineering from the Universidad Nacional de Colombia in 2015 and obtained a MS degree in geochemistry and geotectonics from the Universidade de São Paulo, Brasil in 2017. He is currently enrolled as a PhD student at the Universidad Nacional de Colombia and as a predoctoral fellow at the Smithsonian Tropical Research Institute in Panamá. Santiago uses zircon U–Pb geochronology, petrography, geochemistry, and low–temperature thermochronology to reconstruct the Neogene tectono–stratigraphic and magmatic record of northwesternmost Colombia as the product of changing collisional and subduction–related tectonics.

Juan S. JARAMILLO is graduated as a geological engineer from the Universidad Nacional de Colombia in 2016 and master of mineral resources in 2018 from the same university. He is interested in the tectono–magmatic evolution of the northern Andes and the integration of geological mapping, geochemistry, and the geochronological and the stratigraphic evolution of magmatic arcs. He has examined the reconstruction of the Cretaceous, Paleocene, and Miocene volcanic arcs of the northern Andes. Currently, Juan is studying the tectono–magmatic processes of the Miocene compositional arc variation of the Colombian Andes.

Victor A. VALENCIA is currently a research scientist at the School of the Environment, Washington State University, he received his BEng in geosciences from CESUES, México, MS in geology from the Universidad de Sonora, and PhD from the Department of Geosciences, University of Arizona. His research interests include U–Pb geochronology, economic geology, and the magmatic evolution of convergent margins. He has been involved in various regional projects examining the Mesozoic – Cenozoic tectonomagmatic and metallogenetic evolution of the Andes and México.

Sebastian ZAPATA is a geologist, who received his PhD from the University of Potsdam (Germany). He performed his undergraduate and master's studies at the Universidad Nacional de Colombia Sede Medellín. He is interested in examining the structural, sedimentological, and thermochronological characteristics of exposed orogenic systems in rock sequences that are generated at shallow–to–intermediate depths of the Earth. His research approach involves the application of multitechnique methodologies that are oriented towards a better understanding and the reconstruction of paleogeographic and tectonic conditions during the evolution of convergent margins. In particular, he aims to understand the processes responsible for mountain building, topographic evolution, and relief development in combination with climate–driven impacts on surface processes and structural patterns in orogeny development. The research of Sebastian ZAPATA has been focused on "source–to–sink" topics along the Andean flanks in the northern and central Andes but also includes the Caribbean Plateau, using low–temperature thermochronology, U/Pb geochronology, tectonostratigraphy, structural geology, and sediment provenance analysis.

Andrés PARDO–TRUJILLO is a geologist in the Departamento de Ciencias Geológicas at the Universidad de Caldas (Manizales, 1998). Andres obtained his MS in vegetal micropaleontology in 1997 and his PhD in Science from Liège University (Belgium, 2004). He has worked since 1989 as a professor in the Departamento de Ciencias Geológicas at Universidad de Caldas, Colombia, in sedimentology, regional geology, palynology, and field geology. From 2006–2009, he worked as an advisor at the Agencia Nacional de Hidrocarburos (ANH), where he participated in the geological study of several Colombian sedimentary basins. Andres is currently the director of the Instituto de Investigaciones en Estratigrafía (IIES) and of the Grupo de Investigación en Estratigrafía y Vulcanología (GIEV) at the Universidad de Caldas. His main interest is the study of the geological and biological evolution of the NW corner of South America during the Cretaceous – Cenozoic.

Axel K. SCHMITT is currently a professor at the Institute of Earth Sciences at Ruprecht–Karls–Universität Heidelberg, Germany and is part of the petrology and isotope geology research group. He was formerly a professor and researcher at the University of California, Los Angeles, USA. Some major lines of research include, among others, the analysis of the time scales of magmatic processes; the origin, growth, and recycling of the continental crust; continental rifting and magmatism, magma–driven geothermal systems and their thermal history; and geoarchaeology.

Dany MEJÍA as an MS student of mineral resources at the Facultad de Minas at the Universidad Nacional de Colombia Sede Medellín, he is studying Jurassic metamorphism at the Central Cordillera of Colombia, using structural geology, mineral chemistry, whole–rock geochemistry, and isotope geology to understand Andean continental arc growth and responses to changes in the subduction angle and convergence obliquity. Dany obtained his degree as an engineer geologist from the same university in 2015 and has experience in structural geology, geological mapping, petrology, heavy mineral analysis, geochronology, geochemistry, and low–to–medium–grade thermobarometry.

Juan Camilo ARENAS has worked as a geologist engineer since 2018. He obtained his degree from the Universidad Nacional de Colombia, where he developed his work in geochemistry and geochronology from north zone of Central Cordillera to understand the Cretaceous tectonic evolution in this region. He is currently engaged in hydrogeological modulation as an employee of a private company dedicated to the development of environmental impact studies.

Volume 2

Chapter 11

https://doi.org/10.32685/pub.esp.36.2019.11
Published online 25 November 2020

Dinosaur Footprints from the Lower Cretaceous, Batá Formation, Colombia (South America), and the Possible Interchange of Large Ornithopods between Southern Laurasia and Northern Gondwana

Leslie F. NOÈ[1]*, Marcela GÓMEZ–PÉREZ[2], José Vicente RODRÍGUEZ[3], Alejandro CORRALES–GARCÍA[4], and William G. CARANTON–MATEUS[5]

Abstract Dinosaur remains from northwestern South America are rare, with only extremely scarce fossil evidence recovered from Colombia. Here we report six dinosaur footprints preserved on a sub–vertical bedding plane of the upper Valanginian – lower Hauterivian Batá Formation, Santa María, Boyacá Department, Colombia. The Batá Formation consists of a thick succession of conglomerates and sandstones with shale intercalations interpreted as deposited along the palaeoshoreline of an epicontinental seaway. Four of the footprints form a trackway made by a single dinosaur, which is interpreted as a sub–adult ornithopod, estimated at 8 m in length, weighing around 2.5 metric tons, and travelling at an average walking speed of almost 5 km/h. The footprints are assigned to the ichnogenus *Iguanodontipus*, and were probably produced by an iguanodontian dinosaur. Prior to this work, *Iguanodontipus* was considered an exclusively European taxon, making this a unique record of the ichnogenus in Gondwana. The presence of *Iguanodontipus* in northern South America suggests an Early Cretaceous sweepstake, with dinosaurs crossing Tethys Ocean into modern–day northern Africa, and migrating along the northern shores of Gondwana into modern–day South America. Range extension of iguanodontian ornithopods southwards into Gondwana during the Early Cretaceous was apparently prevented by the Central Gondwana Desert Belt, possibly as a result of the palaeoecology of these dinosaurs, which seem to have had an affinity for environments rich in water and lush vegetation. A migration route across Tethys and the Central Gondwana Desert Belt helps explain similarities between northern Gondwanan and southern Laurasian dinosaurs, and the differences between northern and southern Gondwanan faunas, during the Early Cretaceous.

Keywords: *dinosaur, ichnofossils, Lower Cretaceous, Gondwana, Laurasia, faunal interchange.*

Resumen Los restos de dinosaurio del noroeste de Suramérica son raros, con muy pocas evidencias fósiles recuperadas en Colombia. Aquí reportamos seis huellas de dinosaurio preservadas en una capa subvertical del Valanginiano superior–Hauteriviano inferior de la Formación Batá, Santa María, departamento de Boyacá, Colombia. La Formación

1 l.noe@uniandes.edu.co
Universidad de los Andes
Facultad de Ciencias
Departamento de Geociencias
Carrera 1 n.° 18A–12
Bogotá, Colombia

2 mgomezp@sgc.gov.co
Servicio Geológico Colombiano
Dirección de Geociencias Básicas
Diagonal 53 n.° 34–53
Bogotá, Colombia

3 jv.rodriguez@uniandes.edu.co
Universidad de los Andes
Facultad de Ciencias
Departamento de Geociencias
Carrera 1 n.° 18A–12
Bogotá, Colombia

4 a.corrales10@uniandes.edu.co
Universidad de los Andes
Facultad de Ciencias
Departamentos de Geociencias y Biología
Carrera 1 n.° 18A–12
Bogotá, Colombia

5 wg.caranton10@uniandes.edu.co
Universidad de los Andes
Facultad de Ciencias
Departamento de Geociencias
Carrera 1 n.° 18A–12
Bogotá, Colombia

* Corresponding author

Citation: Noè, L.F., Gómez–Pérez, M., Rodríguez, J.V., Corrales–García, A. & Caranton–Mateus, W.G. 2020. Dinosaur footprints from the Lower Cretaceous, Batá Formation, Colombia (South America), and the possible interchange of large ornithopods between southern Laurasia and northern Gondwana. In: Gómez, J. & Pinilla–Pachon, A.O. (editors), The Geology of Colombia, Volume 2 Mesozoic. Servicio Geológico Colombiano, Publicaciones Geológicas Especiales 36, p. 375–401. Bogotá. https://doi.org/10.32685/pub.esp.36.2019.11

Batá consiste en una secuencia espesa de conglomerados y areniscas con intercalaciones de lodolitas interpretadas como depósitos de la línea de costa de un antiguo mar epicontinental. Cuatro de las huellas forman una pista dejada por un único dinosaurio, interpretado como un ornitópodo subadulto, con una longitud estimada de 8 m, un peso de 2,5 toneladas métricas y que viajaba a un ritmo normal de casi 5 km/h. Las huellas se asignaron al icnogénero *Iguanodontipus*, y fueron probablemente hechas por un dinosaurio tipo iguanodontiano. Antes de este trabajo, *Iguanodontipus* se consideraba como un taxón exclusivamente europeo, por lo que este registro sería el único en Gondwana. La presencia de *Iguanodontipus* en el norte de Suramérica sugiere la existencia de una comunicación terrestre durante el Cretácico Temprano, con dinosaurios cruzando el océano Tetis hacia el norte de África actual, y migrando a lo largo de la costa norte de Gondwana hasta lo que hoy es Suramérica. La extensión del rango de los ornitópodos iguanodontes hasta el sur de Gondwana durante el Cretácico Temprano no ocurrió debido a la presencia del Cinturón del Desierto de Gondwana Central, posiblemente como un resultado de la paleoecología de los ornitópodos, los cuales tenían afinidad por el agua y la vegetación exuberante. Una ruta de migración a través del Tetis y una barrera en el Cinturón del Desierto de Gondwana Central explicarían las similitudes entre los dinosaurios del norte de Gondwana y el sur de Laurasia, y las diferencias entre las faunas de norte y sur de Gondwana, durante el Cretácico Temprano.

Palabras clave: *dinosaurio, icnofósiles, Cretácico Inferior, Gondwana, Laurasia, intercambio faunístico.*

1. Introduction

Considering the first evidence for dinosaurs from South America came from Colombia (Buffetaut, 2000; Degenhardt in Mahlmann, 1840), body and trace fossils of these large terrestrial Mesozoic reptiles are tantalizingly rare in this country. Most South American dinosaurs are known from Argentina and Brasil (e.g., Bittencourt & Langer, 2011; Costa da Silva et al., 2012; de la Fuente et al., 2007; Díaz–Martínez et al., 2016; Francischini et al., 2015; Leonardi, 1989; Pazos et al., 2012; Weishampel et al., 2004), and indicate taxonomic dissimilarity from Laurasian dinosaurs (Cox, 1974; Gheerbrant & Rage, 2006; Canudo et al., 2009). This leaves a considerable gap in our understanding of the dinosaurs from northwestern Gondwana, and their relationships with the more southerly Gondwanan and southern Laurasian realms. Here, we report on the discovery of six footprints from the Lower Cretaceous Batá Formation of Colombia, northern South America, four of which are attributed to a large ornithopod dinosaur. The Batá Formation footprints apparently demonstrate affinities with Laurasian iguanodontian ichnofossils, rather than with dinosaur footprints from southern South America, therefore these findings have important implications for the palaeobiogeography of Early Cretaceous ornithopod dinosaurs.

1.1. Dinosaurs in Colombia

The first evidence for dinosaurs in South America were footprints reported in the *Gesellschaft für Erdkunde zu Berlin* (the Berlin Society for Geography) on the 17 March 1839 (Buffetaut, 2000; Degenhardt in Mahlmann, 1840). Although originally correctly cited as originating from Colombia, subsequent reports erroneously indicated the footprints had been discovered in México (Degenhardt, 1840; Winkler, 1886; see also Buffetaut, 2000). These tracks were never figured, and were originally described as the footprints of giant birds (Degenhardt in Mahlmann, 1840). However, this was prior to Richard OWEN coining the term Dinosauria (Owen, 1841), so the Colombian footprints were almost certainly traces of dinosaurs (Buffetaut, 2000). These ichnofossils, now lost, came from a Lower Cretaceous locality near Oiba, Santander Department, Colombia (Degenhardt in Mahlmann, 1840), and remain one of only a handful of reports of dinosaur body and trace fossils from Colombia (Table 1).

Skeletal remains of Colombian dinosaurs are rare, with confirmed reports limited to Late Jurassic/Early Cretaceous sauropods (Carballido et al., 2015; Langston, 1953; Langston & Durham, 1955) and Late Cretaceous theropods (Table 1; Ezcurra, 2009). However, dinosaur footprints, although rare, are more common, with reports (in addition to those of Degenhardt in Mahlmann (1840)) of unidentified footprints from the Jurassic; titanosaurid sauropod, theropod, and rare ornithopod footprints from the uppermost Jurassic/lowermost Cretaceous; and theropod footprints from the Lower Cretaceous (Moreno–Sánchez & Gómez–Cruz, 2013; Moreno–Sánchez et al., 2011). Hence, most dinosaurs reported from Colombia have been attributed to Saurischia, either members of Theropoda or Sauropoda (although some of these taxonomic assignments have been

Table 1. Tabulation of dinosaur remains discovered in Colombia, showing the year of discovery, fossil type, material discovered, location of discovery, the geological formation, and geological age of the find, and the published reference to the discovery.

Year	Type	Material	Locality	Fm/Age	Reference(s)/Notes
1839	T	'Bird footprints' ?Theropod.	Summit of 'Cuchillas de las Pezuñas del Venado', Oiba, Santander.	Cretaceous, probably Paja Fm.	[1, 2]
1937	B	?Theropod, teeth.	Huila and Payandé, Tolima.	Cretaceous, unspecified Fm.	[3], considered crocodilian [4].
1943	B	Sauropod, anterior/mid–thoracic vertebra, UCMP 37689	East of La Paz, Cesar valley, Magdalena.	Pre–upper Aptian (Cretaceous), probably La Luna Fm.	[4]
1949	B	3 Theropod teeth, (2 abelisauridae, 1 ?dromaeosaurid), UCMP 39649a, b (2 teeth), UCMP 39650.	Upper Magdalena Basin, near Ortega, Tolima.	Late Cretaceous (?Maastrichtian), Fm. not specified (probably La Tabla Fm. or Oliní Group).	[5–7]
2008	T	Ornithopod, theropod and titanosaurid sauropod, footprints.	Santuario de Fauna y Flora de Iguaque, Chíquiza, Boyacá	Pre–Valanginian (uppermost Jurassic – Lower Cretaceous), Arcabuco Fm.	[8]
–	T	Theropod, footprints.	Circa de Villa de Leyva, Boyacá.	Aptian, Paja Fm; idenfication questionable as Paja Fm. is fully marine [9].	[8, 10]
–	T	Dinosaur, footprints.	Near Zapatoca, Santander.	Jurassic, Girón Fm.	[8, 10]
–	T	Theropod, footprints.	A quarry near Alpujarra, Tolima, Upper Magdalena Valley.	Early Cretaceous (?Barremian), Alpujarra Fm. [11], now Hondita y Loma Fm.	[8, 10]
–	B	?Dinosaur, bone fragments.	Dolores Sector, Tolima.	Yaví Fm., ?Jurassic – Early Cretaceous.	[8]
–	B	?Ornithopod, bone fragments.	North of Media Luna Syncline, Aipe.	?Jurassic – Early Cretaceous, Yaví Fm.	[8, 10]
–	B	Theropod, ?tooth.	South of Cuiza Fault, Alta Guajira.	Early Cretaceous, Moina Fm.	[8]
–	T	Ornithopod, traces.	Venado River, Huila.	Jurassic, Saldaña Fm.	[10]
–	B	Sauropod, 14 vertebrae, 'JACVM 0001'; correctly MJACM 1 [9].	'La Tordolla', vereda Monquirá, Villa de Leyva, Boyacá; La Tordolla lies within vereda El Roble [9].	Late Barremian, Paja Fm.	*Padillasaurus leivaensis* a brachiosaurid [12]; a non–titanosauriform somphospondylian [13].
2020	T	Large iguanodontid footprints	Río Batá, Santa María, Boyacá	Early Cretaceous, Batá Fm.	This work

References: [1] Degenhardt (1840); [2] Buffetaut (2000); [3] Botero–Arango (1937, 39, pls 64, 65); [4] Langston & Durham (1955); [5] Ezcurra (2009); [6] Langston (1953); [7] Langston (1965); [8] Moreno–Sánchez et al. (2011); [9] Noè & Gómez–Pérez (2020); [10] Moreno–Sánchez & Gómez–Cruz (2013); [11] Flórez & Carrillo (1994); [12] Carballido et al. (2015); [13] Mannion et al. (2017).

(B) Body fossil (skeletal remains); (Fm.) Formation; (T) trace fossil.

questioned; de Valais et al., 2015), whereas only a small number of footprints have been ascribed to small– or medium–sized ornithopods (Moreno–Sánchez et al., 2011).

1.2. The Cretaceous World

The Cretaceous was a time of profound, but often poorly understood, global tectonic and environmental change, both on land and within the marine realm (Lehmann et al., 2015; Tennant et al., 2016). The break–up of Pangaea, which commenced in the Early Jurassic, continued apace (McLoughlin, 2001). During the Early Cretaceous, Laurasia remained essentially complete, whereas the opening and widening of the Central Atlantic, and its connection to Tethys Ocean separated Gondwana from Laurasia (Canudo, 2006; Cox, 1974; Rage, 1988; Riccardi, 1991; Sereno et al., 1994; Tennant et al., 2016), producing an equatorial marine seaway along the northern margin of Gondwana (Rage, 1988), extending from modern–day Indonesia to México, linking the Central Atlantic to both western and eastern Panthalassa (Riccardi, 1991). The Central Atlantic–Tethys connection thereby acted as a barrier that apparently brought about continental isolation of Laurasia from Gondwana, breaking the

former terrestrial connection between modern–day Europe and North America, and northern Africa and South America by at least the earliest Cretaceous (Sereno et al., 1994; however, see also Bosellini, 2002).

The complex and gradually accelerating breakup of Gondwana occurred throughout the Cretaceous (Heine et al., 2015; McLoughlin, 2001; Sereno et al., 1994; Torsvik & Cocks, 2017). This initially led to the separation of western Gondwana (Africa and South America) (Gheerbrant & Rage, 2006) from southeastern Gondwana (Antarctica, Australia, India, and Madagascar) through the opening of the South Atlantic, and later to the gradual development of essentially modern continental configurations (Torsvik & Cocks, 2017). The breakup of Gondwana led to constantly moving plates with significantly increased absolute velocities compared to earlier in the Mesozoic (Torsvik & Cocks, 2017). At various times in the Cretaceous, Gondwana was subjected to extensive plume related volcanic activity, doming and rifting, Large Igneous Provinces (LIPs), emplacement of kimberlites, subduction, orogenesis, and occasional meteorite impacts (Jaillard et al., 1995; McLoughlin, 2001; Tennant et al., 2016; Torsvik & Cocks, 2017).

Cretaceous climates were generally warm and humid, with relatively high global temperatures and high atmospheric partial pressures of carbon dioxide (pCO_2) (McLoughlin, 2001; Torsvik & Cocks, 2017). For much of the Cretaceous, the world exhibited high global sea levels, with extensive epicontinental seaways (Cox, 1974), caused in part by long mid–ocean ridges with rapid spreading rates, and in Gondwana by movement of the plates to areas of lower dynamic topography (Torsvik & Cocks, 2017). Hence, superimposed over typically high sea levels, were complex patterns of transgression and regression, which led to constantly changing continental shelves, and the repeated opening (flooding) and closure (isolation or draining) of epicontinental seaways (Cox, 1974; Gheerbrant & Rage, 2006; Lehmann et al., 2015; Tennant et al., 2016). In addition, Early Cretaceous seas and oceans were affected by global or regional oceanic anoxic events (OAEs), leading to widespread deposition of black shales (Erba et al., 2004; Owens et al., 2018; Tennant et al., 2016).

1.2.1. The Early Cretaceous

The Berriasian, Valanginian, and Hauterivian ("Neocomian" of previous authors; Lockley et al., 2009; Torsvik & Cocks, 2017) were times of major global upheaval, and increasing continental isolation of Gondwana (Sereno et al., 1994). During the Valanginian – Hauterivian interval, globally important events included emplacement of the Paraná–Etendeka continental flood basalts (LIP volcanism) in Brasil and Namibia (Erba, 2004; McLoughlin, 2001; Svensen et al., 2018), which initiated rifting of the South Atlantic, and ultimately led to a marine link between the South and Central Atlantic (Rage, 1988; Tennant et al., 2016). This rifting produced eastward doming of the future South American continental landmass (Jaillard et al., 1995), leading to the deposition of the Batá Formation and other diachronous Lower Cretaceous sediments over the Palaeozoic basement in Colombia (Moreno et al., 2009). On the northern margins of Gondwana, in the Mediterranean realm, there was subduction, folding, emplacement of ophiolites, rotation and rifting of the Iberian Peninsula, and flexure of the Arabian Plate (Gong et al., 2008; Torsvik & Cocks, 2017).

Early Cretaceous, global sea levels were highly variable, falling in the Valanginian – Hauterivian to their lowest for the entire Cretaceous, but rising thereafter, which produced substantial continental flooding (Heine et al., 2015; Lehmann et al., 2015; Miller et al., 2005; Tennant et al., 2016; Torsvik & Cocks, 2017). During the Early Cretaceous, there was a general increase in global temperatures, with the first true greenhouse (globally warm and humid) climatic conditions commencing during the late Valanginian – early Hauterivian (Erba, 2004; Gröcke et al., 2005). However, during the Early Cretaceous there were major climatic fluctuations (Meissner et al., 2015; Tennant et al., 2016), with the general warming punctuated by shorter, cooler episodes. Hence, although many authors consider the Early Cretaceous to have been entirely ice free (e.g., Canudo, 2006; McLoughlin, 2001; Torsvik & Cocks, 2017), there is increasing evidence for dramatically cooler climatic intervals, including sub–freezing temperatures and ice advances during the Valanginian – Hauterivian (Alley et al., 2019; Tennant et al., 2016). Although sea level changes in the Cretaceous are not generally attributed to glaciations (Canudo, 2006; Torsvik & Cocks, 2017), some authors consider Early Cretaceous sea level rises and falls, at least in the Central Atlantic Tethyian realm, the result of global, but relatively time–restricted, ice advances and retreats (Gröcke et al., 2005; McLoughlin, 2001; Tennant et al., 2016).

1.2.2. The Río Batá Footprints: Geological and Palaeoenvironmental Setting

During the Mesozoic, modern–day Colombia straddled the palaeo–equator, and during the Early Cretaceous lay on the northern shores of the rapidly dividing supercontinent of Gondwana. The dinosaur footprints reported here were discovered in a deep gorge of the Río Batá, Boyacá Department, Colombia (Figure 1), in the Batá Formation (Ulloa & Rodríguez, 1979; Etayo–Serna et al., 2003). The Batá Formation forms part of the Lower Cretaceous in Colombia, although these rocks were long considered Early Jurassic in age (Bürgl, 1958, 1964; Irving, 1975; Mojica & Kammer, 1995). The type section of the Batá Formation lies in the valley of the Río Batá, and along the adjacent Guateque–Santa María road, close to Santa María, Boyacá (Ulloa & Rodríguez, 1979). The Batá Formation (Ulloa & Rodríguez, 1979) was formally designated for beds originally described by Bürgl (1958),

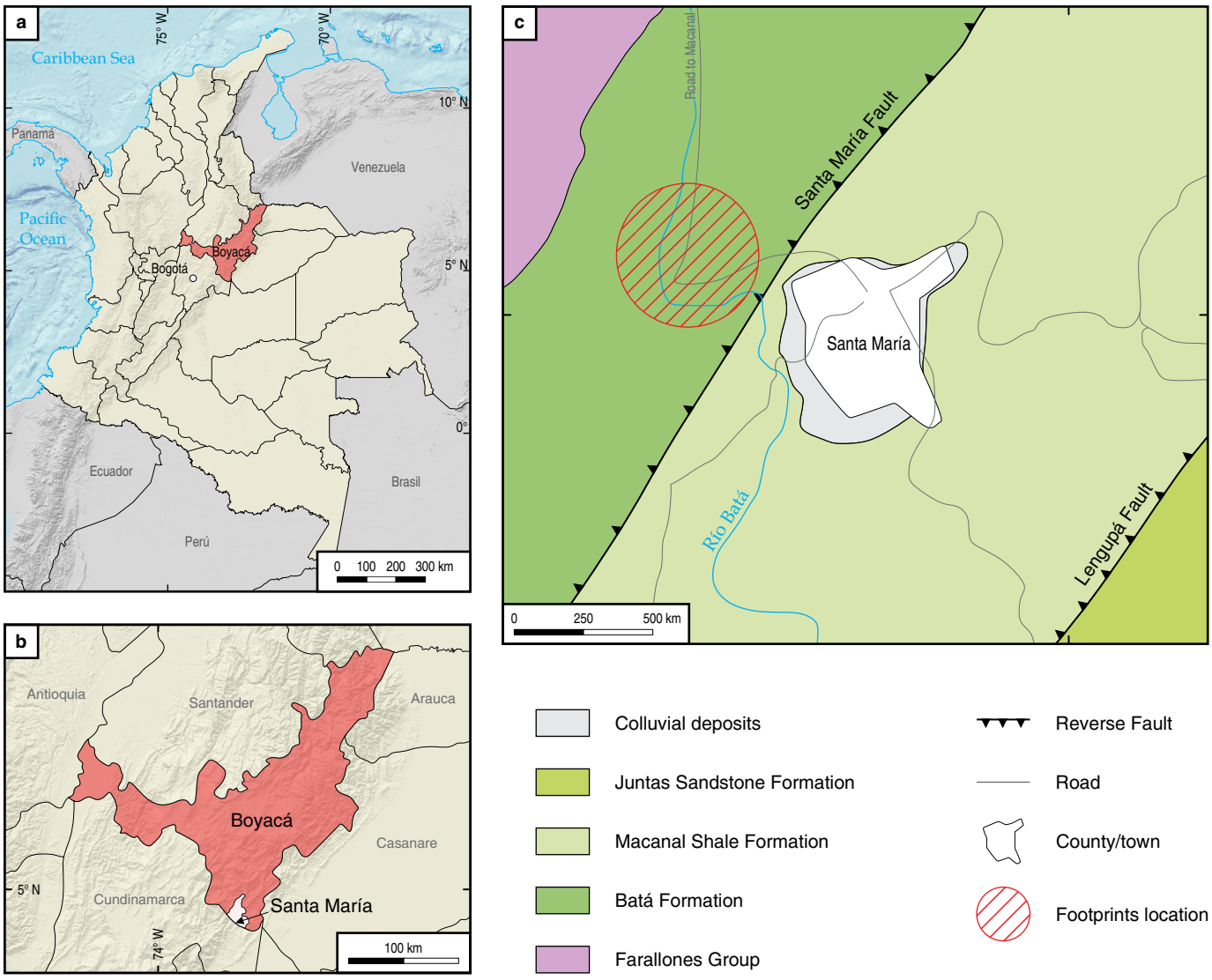

Figure 1. Geographical location of the Río Batá dinosaur footprints. **(a)** Political map of Colombia showing the locations of the capital Bogotá and Boyacá Department. **(b)** Geographical map of the Boyacá Department showing the locality of the municipality of Santa María. **(c)** Geological map of the region around the town of Santa María (modified from Montoya et al., 2008), indicating the approximate position of the dinosaur footprints (hatched red circle).

although previously the name "Batá Formation" had been used informally (Geyer, 1967, 61). At the type locality, the Batá Formation unconformably overlies the Palaeozoic Farallones Group, and is separated from the overlying Cretaceous Macanal Formation by the Santa María Fault (Terraza et al., 2013). The Batá Formation consists of more than 1000 m of conglomerates, quartz arenites, siliceous siltstones, claystones, and mudstones, and is divided into four units lettered A–D from base to top (Ulloa & Rodríguez, 1979). The Batá Formation sediments indicate alternating terrestrial to shallow marine palaeoenvironments (Etayo–Serna et al., 2003; Ulloa & Rodríguez, 1979), with the dinosaur ichnofossils formed along a tidally influenced palaeo–shoreline on the margin of an epicontinental seaway. The palynological evidence is indicative of a warm and humid regional climate (Etayo–Serna et al., 2003).

2. Materials and Methods

There are six dinosaur footprints, here designated DF1–DF6 (Figure 2), four of which (DF1–4) form a single trackway; the remaining two footprints (DF5–6) are isolated, and lie approximately perpendicular to the trackway. The footprints are preserved on a sub–vertical bedding surface above a deep rock pool of the Río Batá, and although additional footprints may be preserved below the water line, no further footprints were observed higher on the cliff face. Due to the difficulty of accessing the site, descriptions and measurements were obtained from field sketches and scaled photographs taken during two site visits. The trackway and footprints were described using standard variables (both metrical and non–metrical) for large tridactyl dinosaur footprints (Figures 3, 4; following Castanera et al., 2013; Lockley, 1991,

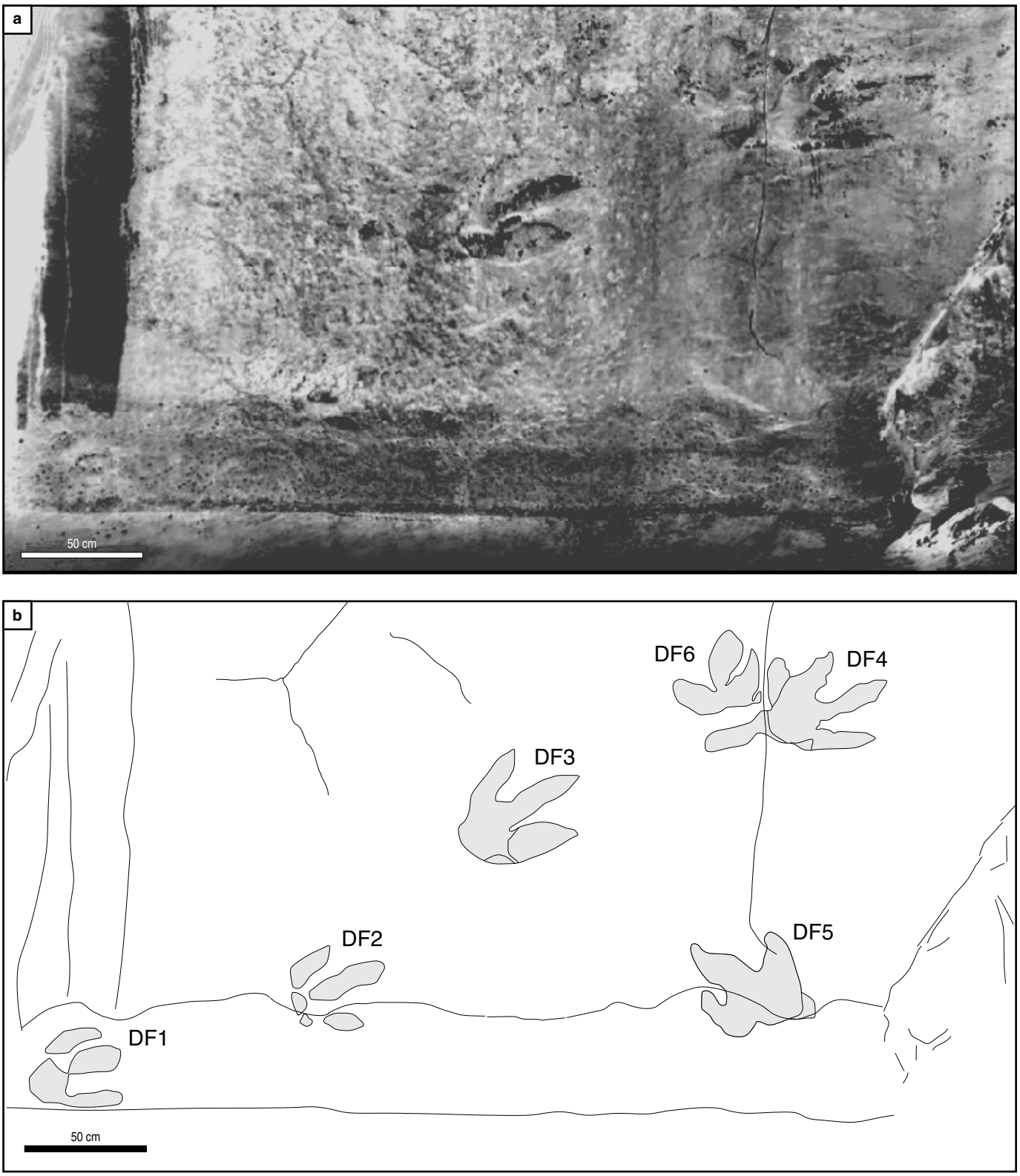

Figure 2. The Río Batá dinosaur footprints. **(a)** Photograph of the outcrop showing the dinosaur footprints preserved in convex hyporelief on the underside of a thick, subvertical, sandstone bed within segments C–D (Ulloa & Rodríguez, 1979) of the Lower Cretaceous (upper Valanginian – lower Hauterivian) Batá Formation. The footprints are exposed along the Río Batá, Boyacá Department, on the eastern flank of the Eastern Cordillera of Colombia. **(b)** Interpretive drawing of the footprints. The dinosaur footprints are indicated with the acronym DF, DF1–4 belong to a single trackway.

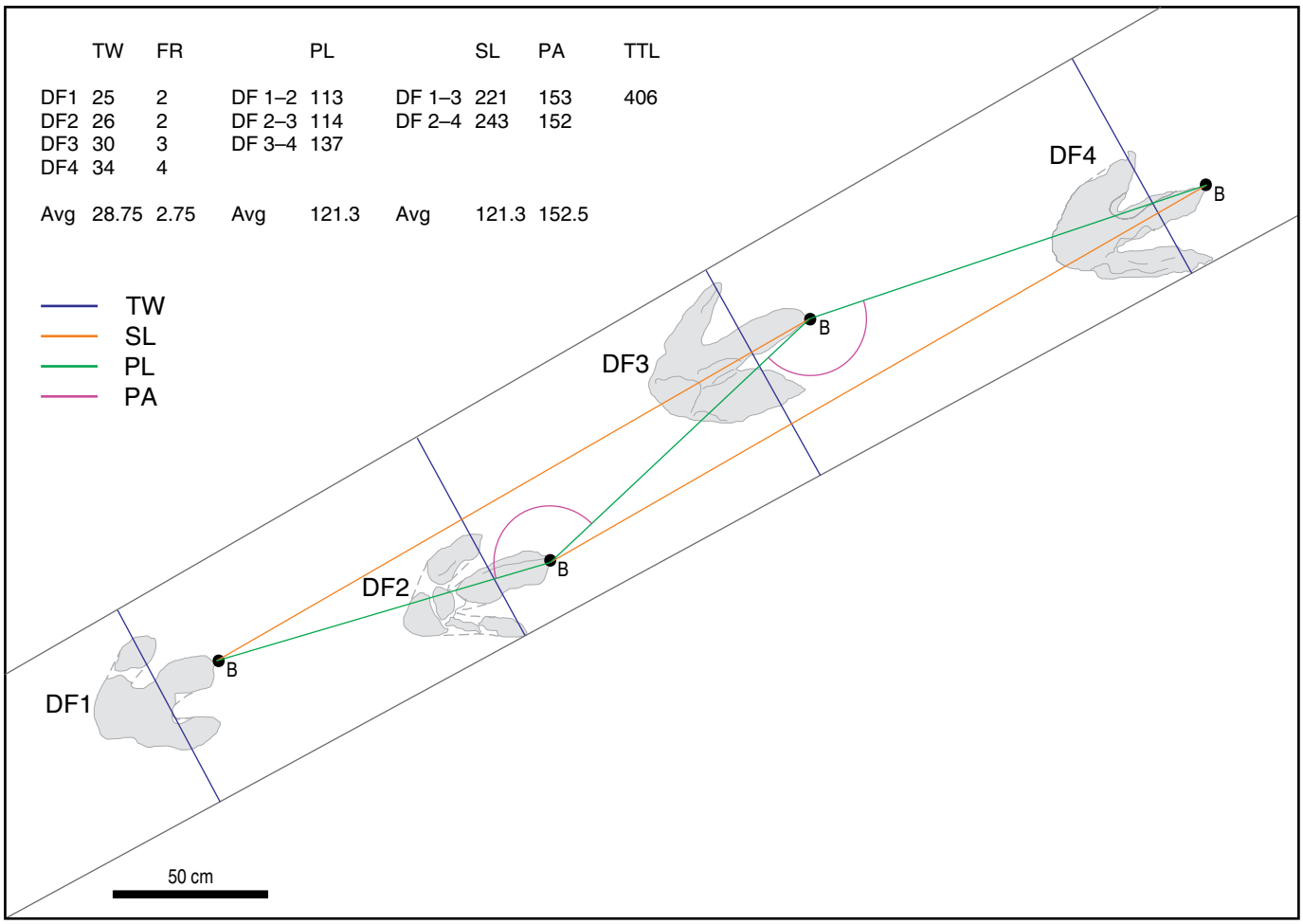

Figure 3. Metrics used to study the Río Batá dinosaur trackway, superimposed over a map of footprints DF1–4 with measurements (in cm) of the footprints. (DF1–4) Dinosaur footprints forming the trackway; (B) tip of digit III; (TW) trackway width; (FR) footprint rotation (not illustrated); (PL) pace length; (SL) stride length; (PA) pace angulation; (TTL) total trackway length; (Avg) average (arithmetic mean). Details of metrics given in the Abbreviations section of the text.

2009; Lockley et al., 2014; Martinez et al., 2015; Moratalla et al., 1988; Romilio & Salisbury, 2011; Thulborn, 1990).

The Río Batá dinosaur footprints remain in situ and are an important part of Colombian National Heritage, protected by the Colombian Constitution (1991) and Decree 1353 (2018). The competent national and regional authorities (the Servicio Geológico Colombiano (SGC), and the Alcaldía, or local mayor of Santa María) have been informed of the exact location to aid their long–term preservation.

3. Systematic Ichnology

3.1. Ichnofamily

Iguanodontipodidae Vialov, 1988 sensu Lockley et al., 2014, and as emended by Martinez et al., 2015.

Diagnosis: Tridactyl, mesaxonic, and subsymmetrical pedal imprints of a digitigrade dinosaur; tracks typically as wide or wider than long; when preserved, one digital pad impression per digit, longer than wide, and one metatarsophangeal pad forming the "heel"; well–developed notches on the latero–proximal margins of digits II and IV; manus tracks when present are much smaller than pedal tracks (modified from Martinez et al., 2015; see also Lockley et al., 2014; Martinez et al., 2015).

3.2. Ichnogenus

Iguanodontipus Sarjeant et al., 1998, as emended by Martinez et al., 2015: 23.

Diagnosis: Iguanodontipodidae tracks with a metatarsophalangeal ("heel") pad impression that is small (only as wide as the proximal impression of digit III), rounded, centred, and narrow; digits long and narrow; digits with sharp distal ends (modified from Martinez et al., 2015).

3.3. Type Ichnospecies

Iguanodontipus burreyi Sarjeant et al., 1998.

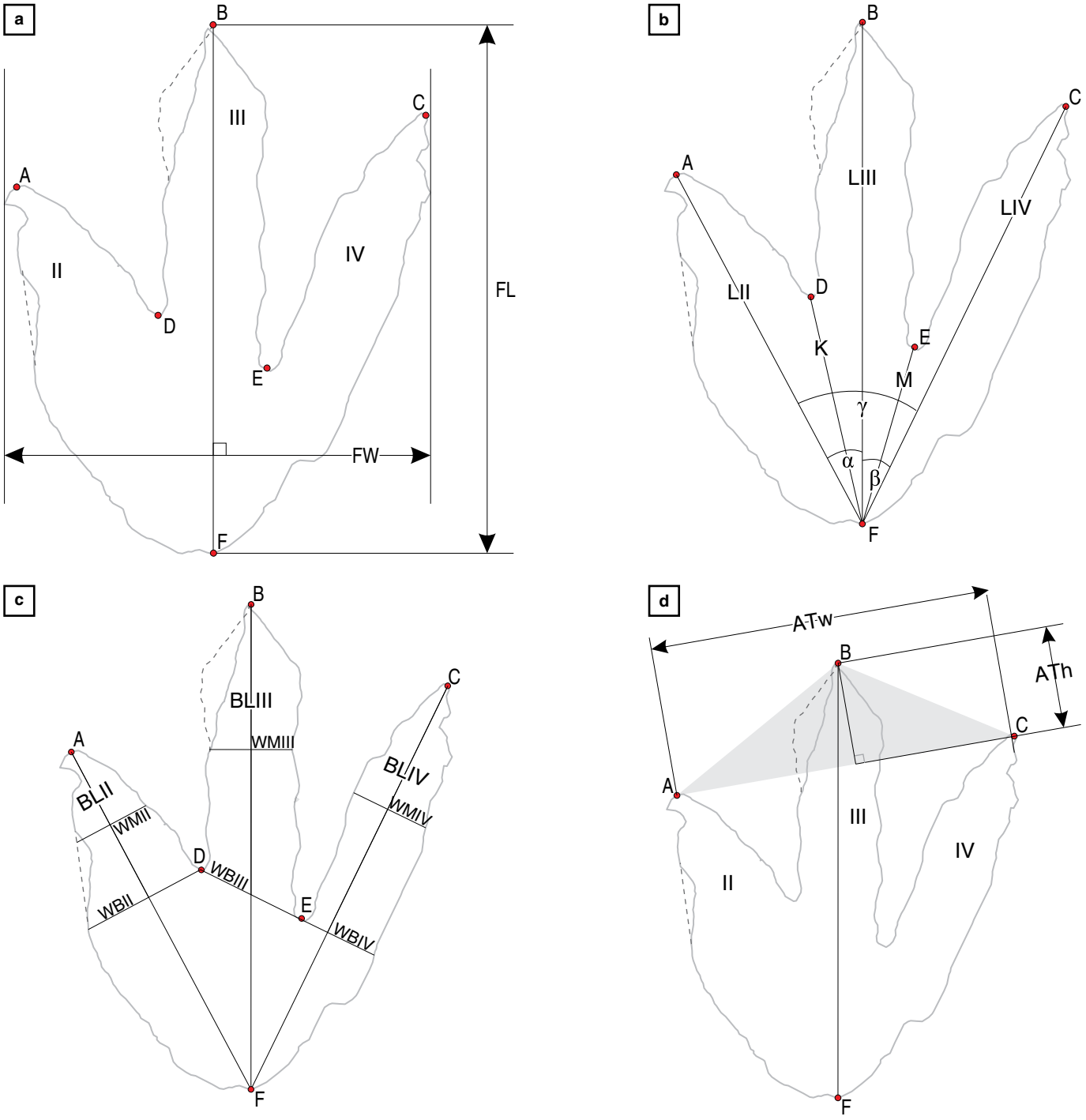

Figure 4. Parameters used to study the Río Batá dinosaur footprints, superimposed over an illustration of footprint DF4. **(a)** Footprint length, width, and key landmarks. **(b)** Digit lengths and angular measurements. **(c)** Digit free segment lengths. **(d)** Anterior triangle. (A, B, C, D, E, F) key footprint landmarks; (ATh, ATw) height and width of the anterior triangle; (BLII, BLIII, BLIV) length of free segment of toe; (FL) footprint length; (FW) footprint width; (LII, LIII, LIV) digit lengths; (K, M) length to hypex; (WBII, WBIII, WBIV) width at base of free segment of toe; (WMII, WMIII, WMIV) width at middle of free segment of toe; (II, III, IV) digit numbers; (α, β, γ) divarication angles. Details of metrics given in the Abbreviations section of the text, and numerical values in Tables 2, 4.

Diagnosis: *Iguanodontipus* is a monotypic ichnospecies containing only *Iguanodontipus burreyi*, which has the same diagnosis as the ichnogenus (Martinez et al., 2015).

3.3.1. Referred Material

Six ornithopod dinosaur footprints, DF1–DF6 (Figure 2).

3.3.2. Emended Distribution

Iguanodontipus: Cretaceous, Berriasian to Hauterivian of western Europe and northern South America. Prior to this work, *Iguanodontipus burreyi* was only known from the Lower Durlston Beds (Berriasian) of England, UK; the Bückeburg Formation (Berriasian) of Germany; and the Oncala Group (Berriasian – Valanginian) of Spain (Castanera et al., 2013; Díaz–Martínez et al., 2015; Lockley et al., 2004; Pascual–Arribas et al., 2009; Sarjeant et al., 1998). The new find extends the geographic range to the Batá Formation (Valanginian – Hauterivian) of Colombia, northern South America.

3.3.3. Locality and Horizon

The referred dinosaur footprints are exposed on the original underside of a now sub–vertically oriented massive sandstone bed within the upper part (segments C–D) of the Lower Cretaceous Batá Formation along Río Batá, Boyacá Department, on the eastern flank of the Eastern Cordillera of Colombia (Figure 1). Segments C and D of the Batá Formation consist of a series of fining–upward successions, commonly including ripple marked sandstone levels, some of which preserve bivalve fossils and palynomorphs (Etayo–Serna et al., 2003; Terraza et al., 2008). The bedding plane preserving the footprints strikes NE–SW is now sub–vertical and elevated to a present–day altitude of 840 m above sea level due to the uplift of the northern Andes. Exact geographic coordinates of the locality are withheld to aid site preservation, but are available from the Servicio Geológico Colombiano upon request.

3.3.4. Geological Age

Late Valanginian to early Hauterivian, ca. 132.9 Ma (Cohen et al., 2013; updated 2019/05). Based on the presence of the bivalve *Syrotrigonia*, palynomorphs, and other unspecified fossils, segments C and D of the Batá Formation were assigned a late Valanginian to early Hauterivian age (Etayo–Serna et al., 2003; although Berriasian is also mentioned without context, page 115). Recently, the Batá Formation has been considered Berriasian in age, based on stratigraphic and unspecified biostratigraphic comparison with the Cumbre Formation of the Middle Magdalena River valley (Moreno et al., 2009; Terraza et al., 2008, 2013). However, it is likely that the Batá and Cumbre Formations are of different ages due to diachronic Early Cretaceous transgression and deposition over underlying Palaeozoic basement of the Farallones Group (Terraza et al., 2013). Hence, here we accept the late Valanginian to early Hauterivian age for the Batá Formation based on the published palaeontological evidence (Etayo–Serna et al., 2003, page 115, arguments 1, 3), rather than the less well supported (and largely unpublished) comparisons with the more spatially distant Cumbre Formation (Etayo–Serna et al., 2003, page 115, argument 2).

4. Description

The Río Batá dinosaur footprints are tridactyl and digitigrade pedal tracks with no evidence for manus prints, tail drag marks, or interdigital webbing (Figure 2). The orientations of the two isolated footprints DF5 and DF6 make it highly unlikely these form part of a second trackway. The relative timings of production of the trackway and the isolated footprints are unclear, despite footprints DF4 and DF6 partially coinciding.

4.1. Preservation

The Río Batá footprints are preserved in convex hyporelief (Lockwood et al., 2014); i.e., as natural infills of the original footprints (the trace fossils), or as natural casts of the foot of the original dinosaur track maker. The topographically lower footprints (DF1, 2) are less well preserved than those higher up the cliff face (DF3, 4), as they have been partially eroded by running water from Río Batá. As preservation of the footprints on the lower surface of a massive sandstone bed, it is improbable that they are underprints; the Río Batá footprints thereby most likely represent natural casts of "true tracks" (Lockley, 1991; Platt et al., 2018). However, preservation of the Río Batá footprints is sub–optimal, as no distinct metatarsophalangeal "heel" pad, hallux prints, or skin impressions are preserved. DF4 exhibits what may be a "heel" drag mark (Thulborn, 1990), or much less likely a metatarsal impression (Farlow et al., 1995). However, the close proximity of DF4 to DF6, and their similar size, suggests that the "drag mark" may be the "heel" impression of DF6, or possibly the remnants of another poorly preserved footprint coinciding with both DF4 and DF6 (Figure 2). The aligned footprints (DF1–4) were produced by a single individual dinosaur, but show morphological variation along the trackway. This variation may be the result of differences in original footprint morphology (natural differences between the left and right feet), influenced by extra–morphological effects such as dinosaur behaviour (including locomotion pattern and speed), substrate characteristics (including type, consistency, humidity, and local irregularities), taphonomy, or recent subaerial weathering and erosion (Lockley, 2009; Lockley et al., 2014; Moratalla et al., 1988; Pazos et al., 2012; Romilio & Salisbury, 2011), all of which may be applicable to the Río Batá footprints.

4.2. Trackway (DF1–4)

The four aligned footprints form an approximately four metres long trackway. This trackway exhibits average (arithmetic mean) values of: stride length, 2.32 m; pace length, 1.21 m; pace angulation, 152.5°; external track width, 0.38 m; and slight positive

(outward) footprint rotation (sensu Lockley, 1991; we note that Thulborn, 1990 uses the terminology in the opposite sense) of 2–4° (Figure 3). After correction for subsequent tilt of the sub–vertically orientated bedding plane on which the footprints are preserved, the direction of travel (estimated to 5° increments) for the trackway is 255°; and the orientations of footprints DF5 and DF6 are 5° and 325° from north respectively.

4.3. Footprints

Footprints DF3 and DF4 are the best preserved, and therefore are used as the basis for this description (Figure 4). The footprints are large, measuring an average of 51.5 cm from the anterior tip of digit III to rear of the metatarsophalangeal "heel", and are tridactyl, with no digit I (laterally directed hallux) or digit V impressions preserved. The digits are generally straight, although the distal end digit III of DF3 is curved slightly medially; other toes may also exhibit a slight curvature. Digit III is the longest and forms the anteroposterior axis of the footprints. Digits II and IV are arranged approximately symmetrically either side of, and shorter than, digit III, but sub–equal in length to each other; the mesaxonic condition. Digit II is the widest, stout, robust, and tapering; digit IV is narrower and tapered, and as preserved, is slightly longer than digit II in DF4 but shorter in DF3; digit III is intermediate in form, with approximately sub–parallel lateral and medial margins. None of the digits are constricted. Footprints DF3–4 are longer than wide, with an average length:width ratio of 1.22, an average total digital (II–IV) divarication of 58.5° and individual interdigital angles of 26–33°. The average height:width ratios of the anterior triangles (Lockley, 2009) of DF1–2 are 0.41 (Table 4).

The distal ends of the digits are bluntly tapered, with sub–acute (pointed) tips, and no distinct ungual (hoof or claw) impressions. The hypices (the posterior–most points of separation between the toes) in DF3 are rounded, but the angle is slightly more acute between digits II and III. In DF4, the hypex between digits II and III is more deeply incised but this is likely an artefact of preservation, whereas between digits III–IV it is similar to DF3. In both DF3 and DF4, the lateral margin of the posterior of digit IV (somewhat posterior of the level of the hypicies) preserves what may be a slight lateral notch (Martinez et al., 2015). However, this is of a different form, and in a slightly different position in the two footprints, so may be an artefact of preservation. The posterior margin of the metatarsophalangeal "heel" pad impression is rounded in DF4, but sub–quadrangular in DF3, although both metatarsophalangeal pads lack marked medial or lateral indentations.

5. Interpretation and Discussion

Individual footprints represent the original foot morphology of the dinosaur trackmaker (Moratalla et al., 1988), although the footprint is modified by the effects of behaviour, substrate consistency, preservation, diagenesis, and recent and ancient weathering, requiring considerable caution in interpretation. However, extra–morphological variation in ichnology can be minimized by utilizing data from a series of aligned footprints (a trackway), where available (e.g., Lockley, 1991; Thulborn, 1990). The Río Batá footprints only preserve a short trackway segment (DF1–4) and two additional prints (DF5, 6), so here we focus on metrics from the two best–preserved trackway footprints (DF3–4), supplemented by data DF1–2. We cautiously compare the trackway to the isolated footprints (DF5, 6), although these were most likely produced by one or more different individuals or taxa.

A large ornithopod or theropod dinosaur produced the Río Batá dinosaur footprints. Size definitions are inherently arbitrary, general categories (Lallensack et al., 2016), however, the term "large" for tridactyl dinosaur footprints is only loosely defined. In ichnological studies, organism size is determined by footprint length (FL), and "large" has been considered both >30 cm and >25 cm (Thulborn, 1990 pages 52, 265, 268), although FL >25 cm has also been consistently used (Dalla–Vecchia, 1998, 2008). Medium size for tridactyl dinosaur footprints has been regarded as FL = 20–30 cm (Castanera et al., 2013), implying a large animal has a FL >30 cm. However, other authors (e.g., Martinez et al., 2015) appear to consider large as >25 cm (following Thulborn, 1990), although no clear definition is provided. Here we define "large" tridactyl dinosaur footprints as exhibiting FL >300 mm.

5.1. Ornithopod vs. Theropod Footprints

Distinguishing between large, tridactyl footprints produced by bipedal ornithopod and theropod dinosaurs has frequently proven problematic (e.g., Lallensack et al., 2016; Lockwood et al., 2014; Moratalla et al., 1988; Platt et al., 2018; Romilio & Salisbury, 2011). This difficulty is due to the similar, although osteologically distinct, original foot morphology, which in both groups is digitigrade, functionally 3–toed with the central digit (III) most prominent, and digits II and IV shorter than digit III (Lockley et al., 2009). Hence, the trace fossils produced by both ornithopods and theropods are similar: Relatively wide, tridactyl, and mesaxonic. The difficulty in distinguishing ornithopod from theropod ichnites applies especially to isolated footprints, short trackway segments, or when preservation is sub–optimal (e.g., Moratalla et al., 1988; Thulborn, 1990), all of which apply to the Río Batá footprints.

A number of studies have attempted to resolve the problems of distinguishing between large ornithopod and theropod footprints, however there is no single, unique criterion that clearly separates the trace fossils of these two groups of dinosaurs (Lallensack et al., 2016; Moratalla et al., 1988). Here we use two approaches in an attempt to determine the most likely

Table 2. Measurements for the Río Batá dinosaur footprints, in cm.

Track			Digit length			Free segment length			Basal toe width			Mid–toe width			Hypicies		Divicariance		
	FL	FW	LII	LIII	LIV	BLII	BLIII	BLIV	WBII	WBIII	WBIV	WMII	WMIII	WMIV	K	M	α	β	γ (α+β)
DF1	44	41	40	44	34	16	25	17	10	17	8	10	12	10	24	18	33	31	64
DF2	52	38	39	52	39	21	35	23	10	8	7	9	10	6	18	17	27	26	53
DF3	56	45	48	56	41	22	31	20	17	13	10	12	11	7	27	23	29	30	59
DF4	54	44	43	54	50	18	33	31	14	13	9	9	9	9	25	20	28	26	54
DF5	48	45	35	48	36	18	28	11	15	15	14	8	12	11	19	25	41	30	71
DF6	37	40	29	37	28	18	22	10	12	11	11	11	13	8	13	19	52	34	86

Note: (DF with number) Río Batá footprint number; (FL) footprint length; (FW) footprint width; (LII, LIII, LIV) digit lengths; (BLII, BLIII, BLIV) length of free segment of toe; (WBII, WBIII, WBIV) width at base of free segment of toe; (WMII, WMIII, WMIV) width at middle of free segment of toe; (K, M) length to hypex; (α, β, γ) divarication angles.

See Figure 4 for locations of metrics; details of metrics given in the Abbreviations section of the text.

track maker for the Río Batá footprints. Firstly, a compilation of ichnological characteristics, based on an updated version of parameters used to distinguish ornithopod from theropod footprints (Dalla–Vecchia & Tarlao, 2000), and modified in the light of subsequent research. Secondly, we compare the Río Batá footprints to ornithopod–theropod threshold values for a series of bivariate ratios (Moratalla et al., 1988).

A compilation of ichnological characteristics (Dalla–Vecchia & Tarlao, 2000), indicates the Río Batá footprints forming the trackway (DF1–4), share more than half (12/21) of the features characterizing large ornithopod dinosaur footprints. However, two features are indicative of large theropods, and slightly more than one–third (7/21) cannot be applied to the Río Batá footprints (Table 3). Of the features indicative of ornithopod footprints digits relatively straight with little curvature, the rounded to quadrangular metatarsophalangeal "heel", sub–symmetrical footprint, and trackway pace angulation (PA) <160°, fall within the typical ornithopod range (Table 3, coloured green). However, other features show overlap between the ornithopod and theropod values, and require discussion. For the best preserved footprints (DF3–4), the height:width ratio of the anterior triangle (Table 4) is within the range reported for large ornithopods (Lockley, 2009). However, when all four footprints in the trackway (DF1–4) are averaged, the value slightly exceeds the ornithopod maximum. Nevertheless, the lowest value for DF3–4 also lies outside the reported theropod range, although the average value is higher, it lies at the extreme lower range for large theropods. Hence, the best preserved, and therefore probably most reliable, data indicates ornithopod affinity, whereas the probably less reliable aggregated data lies at the lower end of the large theropods range. As a result of the above, we consider the anterior triangle date more indicative of ornithopod than theropod dinosaurs. The pedal footprint length:width ratio (FL:FW) is greater than one, indicating a footprint that is longer than wide, a feature considered typical of theropod dinosaurs (Thulborn, 1990). However, DF3–4 fall within the ornithopod range, although considering all footprints in the trackway, the average does not fall within the ornithopod range. Stride length to foot length (SL:FL) lies within the range most common for ornithopods, but outside that considered most frequently associated with theropods, although the ranges for both groups exhibit considerable overlap (Thulborn, 1990).

Another relevant feature is a notch between digit II and the metatarsophalangeal "heel", considered a theropod feature. However, the "notch" in Río Batá footprints occurs between digit IV and the "heel". This is probably a poorly preserved remnant of the double notch observed in ornithopod dinosaur footprints (Martinez et al., 2015). The digits in the Río Batá footprints are relatively long and somewhat pointed; this is often considered a typical theropod feature. However, this is also characteristic of Group 1 ornithopods (Martinez et al., 2015). Hence, many parameters (digit curvature; "heel" shape; trackway pace angulation; anterior triangle height:width ratio; footprint length:width ratio), exhibit overlap between footprints considered to belong to ornithopods and theropods, although for the Río Batá footprints many of these features are closer to the ornithopod state.

Two features of the Río Batá trackway falls within the normal theropod range (Table 3, coloured red). A total divarication between digits II and IV of <60° is considered typically theropodan, although one of the less well–preserved footprints (DF1) shows a typical ornithopod total divarication 64° (Table 2). However, divarication of the digits varies with numerous factors including original foot morphology, substrate consistency, and patterns of behaviour (Platt et al., 2018). In addition, variation is seen when a large number of footprints form a track single attributable to the same individual (Lallensack et al., 2016). Footprint rotation is normally negative (inward facing) in ornithopod dinosaurs, but is weakly positive (outwardly directed) in theropods; the Río Batá footprints exhibit thero-

Table 3. Characteristics of the Río Batá dinosaur footprints compared to a range of criteria used to differentiate large ornithopod from large theropod dinosaur ichnofossils.

Footprint characteristic	Large ornithopod footprints	Río Batá footprints	Large theropod footprints
Anterior triangle, h:w ratio.	Low (0.28–0.47)	Low (0.30–0.36/0.49)	High (0.31–1.43)
Bipedality	Manus prints sometimes present	Manus prints absent	Manus prints almost always absent
Claw impressions	Blunt, "hooves".	Absent	Sharp, laterally compressed.
Digit impressions (especially DIII)	Wider, parallel–sided, often u–shaped, with a relatively short free segment.	DII wide, tapering; DIII–IV relatively narrow, parallel–sided, u–shaped.	Slender, tapered, often v– shaped, with relatively long free segment.
Digit relative lengths	DIII slightly longer, DII and DIV subequal in length.	DIII slightly longer, DII and DIV subequal in length.	DIII substantially longer, DII shorter and wider than DIV.
Digit I (hallux) impression, medially directed at base of DII.	Lacking in most	Absent	Occasionally present
Digit III form	Symmetrical, straight, with little or no curvature.	Symmetrical, straight, with little or no curvature.	May be curved, sinuous or with a marked medial displacement.
Digital curvature medially, distal.	Little or none	Little, slight in DIII of DF3.	Frequent in DIII, less in DIV, sometimes in DII.
Digital offsets	Digit IV frequently offset and widely divergent	None	Digit II offset from DIII– IV
Divarication, DII–DIII: DIII–DIV.	Angles between DII–DIII and DIII–DIV similar	DII–DIII, 28–29° (27–33°); DIII–DIV, 26–30° (31°).	DII–DIII (35–39°) > DIII–DIV (20–37°)
Divarication, total (DII–DIV)	Wider (?>60°)	54°–59° (64°)	Narrower, usually <60°
Footprint rotation (orientation of DIII)	Normally inward (–ve)	Slightly +ve, ≤4°	Normally weakly +ve
Footprint symmetry	Symmetrical	Symmetrical	Asymmetrical
Heel shape	Relatively large, symmetrical, u–shaped.	Rounded to quadrangular, u–shaped.	Relatively small, elongate, asymmetrical, v–shaped.
Indent medially between DII and heel	Absent	Absent	Present
Pes print FL:FW ratio	FW=FL or FW>FL, range 0.92–1.36	FW>FL 1.23–1.24 (1.07–1.37)	FL>FW, range 1.03–2.64
Phalangeal pad impressions	Almost always lacking when FL>30 cm	Absent	Often well–defined
PL:SL	Shorter	1.91	Longer
PA	Lower, ?<160°	152–153°	High, 160–180°
SL:FL (much overlap)	Low	4.14–4.30 (5.27)	High
TW	Consistently wider	68 cm	Consistently narrower

Source: Data from Dalla–Vecchia & Tarlao (2000) and modified with additions from Hasiotis et al. (2007), Lallensack et al. (2016), Lockley (2009), Milner et al. (2006), Moreno et al. (2012), and Thulborn (1990).

Note: The Río Batá footprints exhibit 12/21 characteristics that indicate an ornithopod affinity (highlighted in green), whereas only 2/21 coincides with the characteristics that that indicate a theropod footprint (highlighted in red); seven characteristics are not comparable (not highlighted). See text for further details. (h) Height; (w) width; (D with roman numeral) digit number; (FL) footprint length; (FW) footprint width; (PL) pace length; (SL) stride length; (+ve) positive; (–ve) negative; (PA) pace angulation; (TW) trackway width.

See Figures 3, 4 for locations of metrics; details of metrics given in the Abbreviations section of the text.

pod–like positive rotation, although this also varies depending on speed of locomotion (Day et al., 2002).

Seven of the 21 characteristics are non–applicable (Table 3, uncoloured). Of these features, three cannot be compared with certainty due to lack of excellent preservation (presence/absence of manus prints; claw impressions; presence/absence of a hallux mark), one is a feature which does not match the diagnostic features of either group (digital offsets), and two lack sufficient comparable metrics in the literature (PL:SL and TW). Hence, on balance (12 features to two in favour, with seven not comparable) we consider the values exhibited by the Río Batá trackway footprints, most likely, to be ornithopod in nature.

Our second approach is to compare the Río Batá footprints to ornithopod–theropod threshold values for a series of bivar-

Table 4. Measurements of the anterior triangle (Lockley, 2009) for the Río Batá dinosaur footprints, in cm.

Track	ATh	ATw	ATh/ATw
DF1	13	40	0.33
DF2	17	35	0.49
DF3	16	45	0.36
DF4	13	43	0.30
DF5	19	41	0.46
DF6	16	39	0.41

Note: Green, large ornithopod range (0.28–0.47); orange, ambiguous (overlaps both large ornithopod and large theropod ranges); red, large theropod range (0.31–1.43); threshold values from Lockley (2009).

(ATh) anterior triangle height; (ATw) anterior triangle width.

See Figure 4d for locations of metrics; details of metrics given in the Abbreviations section of the text.

iate ratios (Figure 5; Table 5; Moratalla et al., 1988). These ratios have been applied graphically by a variety of authors (Figueiredo et al., 2017; Mateus & Milán, 2008; Platt et al., 2018; Romilio & Salisbury, 2011), and have the advantage of utilizing ratios, which minimize the effects of organism size on the analysis (Lallensack et al., 2016). Comparison between the threshold values proposed (Moratalla et al., 1988) and those for the Río Batá trackway, show that the two best–preserved footprints (DF3–4) fall within the ornithopod thresholds for just 3/9 values, whereas 6/9 are considered typically theropodan (Table 5). Including data from all four trackway footprints (DF1–4), shows no unequivocally ornithopod features, 6/9 exhibit overlap between ornithopod and theropod values, and 3/9 indicate a theropod trackmaker. However, the two isolated footprints, DF5 (values for DF6 in brackets) are more clearly ornithischian with 6/9 (8/9) indicating an ornithischian trackmaker, and only 3/9 (1/9) indicating a theropod trackmaker. The second technique would therefore suggest that the trackway was produced by a theropod dinosaur, and the two isolated footprints are ornithischian in nature.

Based on the first of the two techniques employed, we attribute the Río Batá footprints to a large ornithopod dinosaur, whereas the results of the second technique indicate the trackway was produced by a large theropod. We interpret this to indicate that a wide range of descriptive and metrical characteristics are more reliable than comparison to a small sample of time restricted and tentatively proposed threshold values (Moratalla et al., 1988). This is despite the Río Batá footprints concurring in geological age (Early Cretaceous) and organism size ("large" dinosaur) comparable with the original sample (Moratalla et al., 1988); although the Colombian footprints lie outside the original geographical range studied. Hence, our analysis appears to question the applicability of threshold values as a technique to determine dinosaur affinities in ichnological studies (e.g., as used by Figueiredo et al., 2017; Lallensack et al., 2016; Mateus & Milán, 2008; Platt et al., 2018; Romilio & Salisbury, 2011), as previously argued (Thulborn, 2013). In addition, despite compensating for body size using ratios, biological scaling affects (e.g., allometry, ontogeny; Castanera et al., 2013; Lockley, 2009) may have an important effect on this type of analysis.

5.2. Attribution to Ichnotaxon and Taxon

The somewhat confusing ichnotaxonomy of large ornithopod tracks has recently been revised (Martinez et al., 2015; see also Lockley et al., 2014). Based on the small, rounded metatarsophalangeal "heel" pad (rather than a large rounded or bilobed "heel"), and relatively elongate, narrow digits (as opposed to short, wide digits), the Río Batá footprints can be attributed to the Group 1 ornithopod morphology (Martinez et al., 2015). Group 1 contains only the ichnogenus *Iguanodontipus* and ichnospecies *I. burreyi*. The only other valid ichnospecies, formerly within *Iguanodontipus*, was "*I.*" *billsarjeanti*, now attributed to the ichnogenus *Caririchnium* (Martinez et al., 2015). Thus, the Colombian footprints, as tridactyl, mesaxonic, and subsymmetrical pedal imprints of a digitigrade ornithischian dinosaur, can be attributed to the ichnofamily Iguanodontipodidae, based on the morphological characteristics available (Martinez et al., 2015). However, the tracks are somewhat longer than wide, and do not preserve pad or manus impressions, and only faintly show (on the lateral margins of DF3–4) evidence for the well–developed notches on the latero–proximal margins of digits II and IV, characteristic of the ichnofamily (Martinez et al., 2015). Nevertheless, this lack of data are most likely a result of preservational biases. However, with regard to the ichnogenus *Iguanodontipus*, the "heel" impression of the Río Batá footprints is relatively narrow, rounded, and centred, and the digits are long and narrow with somewhat pointed distal ends, matching the diagnosis of the ichnogenus (Martinez et al., 2015).

Iguanodontipus ichnofossils are universally attributed iguanodontid (or iguanodontian) ornithischian dinosaur track makers (e.g., Lockley et al., 2014; Lockwood et al., 2014; Martinez et al., 2015; Santos et al., 2013; Sarjeant et al., 1998). Body fossils of iguanodontian ornithopods are widely distributed across Laurasia and Gondwana, and have been recovered from the Upper Jurassic to uppermost Cretaceous rocks (Llandres–Serrano et al., 2013; Norman, 2004, 2013). However, prior to this work, the geographic and temporal distribution of *Iguanodontipus* was strictly limited, with the ichnogenus only reported from the Berriasian – Valanginian of Europe (Díaz–Martínez et al., 2015). Hence, the Río Batá *Iguanodontipus* ichnofossils were likely produced by a large iguanodontian ornithischian dinosaur, and thereby have important palaeogeographical implications for dinosaur biogeography.

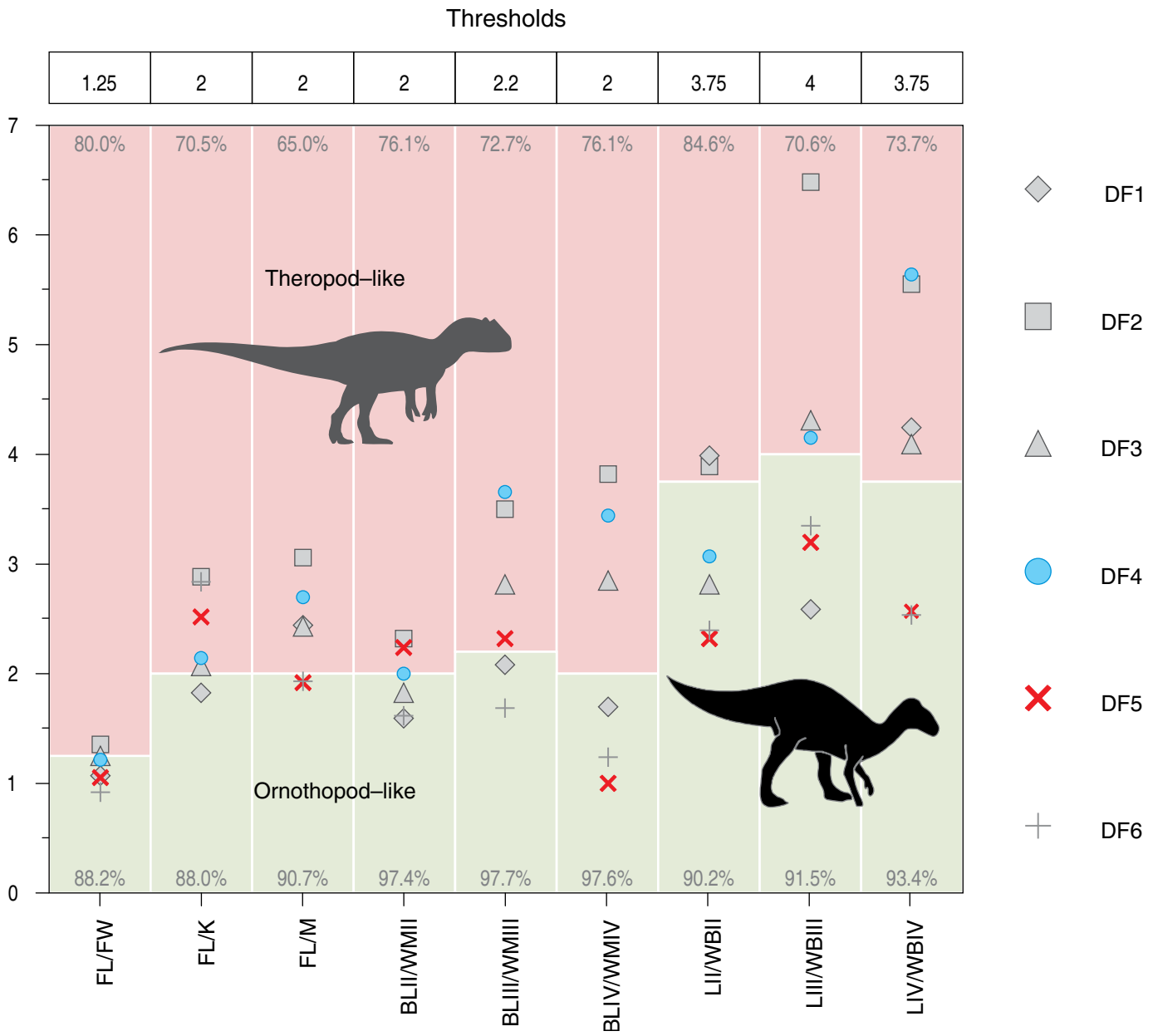

Figure 5. Ratios from the Río Batá footprints (DF1–6) shown as a graphical representation (modified from Romilio & Salisbury, 2011) for comparison to the proposed threshold values (top) used to distinguish between ornithopod and theropod dinosaur footprints (Moratalla et al., 1988). Green, large ornithopod range; red, large theropod range. (BLII, BLIII, BLIV) Length of free segment of toe; (DF1–6) dinosaur footprints; (FL) footprint length; (FW) footprint width; (LII, LIII, LIV) digit lengths; (K, M) length to hypex; (WBII, WBIII, WBIV) width at base of free segment of toe; (WMII, WMIII, WMIV) width at middle of free segment of toe. See Figure 4 for locations of metrics; details of metrics given in the Abbreviations section of the text. See Table 5 for numerical values for the ratios presented.

5.3. Size and Speed Estimates

Ichnofossils can be used to determine the approximate body size and speed of movement of the Río Batá trackmaker by using foot length to obtain hip height, and incorporating stride length (Hutchinson, 2005; Lockley, 1991; Thulborn, 1990). Hip height (HH) can be estimated by assuming the hip was an average of four times the length of the footprint (FL) (McNeil Alexander, 1976; Henderson, 2003). However, although a range of metrics have been proposed for different dinosaurian groups (Thulborn, 1990), HH = FL × 4 is the most widely used metric (Platt et al., 2018), and is considered the most accurate for large dinosaurs (Henderson, 2003). The Río Batá trackway has an average FL (DF1–4) = 51.5 cm, which produces an estimated HH = 2.06 m (Table 6). Comparison with well–known skeletons of the Barremian iguanodontian ornithopod *Iguanodon bernissartensis* provides a body length estimate of approximately 8.0 m and an estimated body mass of 2.500

Table 5. Ratios from the Río Batá footprints for comparison to the proposed threshold values (beneath each metric) for ornithopod and theropod dinosaur footprints (Moratalla et al., 1988), for individual footprints (DF1–6), the range for the best preserved footprints in the trackway (DF3–4), and the range for all footprints in the trackway (DF1–4).

Track	FL:FW 1.25	FL:K 2.0	FL:M 2.0	BLII:WMII 2.0	BLIII:WMIII 2.2	BLIV:WMIV 2.0	LII:WBII 3.75	LIII:WBIII 4.0	LIV:WBIV 3.75
DF1	1.07	1.83	2.44	1.60	2.08	1.70	4.00	2.59	4.25
DF2	1.37	2.89	3.06	2.33	3.50	3.83	3.90	6.50	5.57
DF3	1.24	2.07	2.43	1.83	2.82	2.86	2.82	4.31	4.10
DF4	1.23	2.16	2.70	2.00	3.67	3.44	3.07	4.15	5.56
DF5	1.07	2.53	1.92	2.25	2.33	1.00	2.33	3.20	2.57
DF6	0.93	2.85	1.95	1.64	1.69	1.25	2.42	3.36	2.55
DF3–4	1.23–1.24	2.07–2.16	2.43–2.70	1.83–2.00	2.82–3.67	2.86–3.44	2.82–3.07	4.15–4.31	4.10–5.56
DF1–4	1.07–1.37	1.83–2.89	2.43–3.06	1.60–2.33	2.08–3.67	1.70–3.83	2.82–4.00	2.59–6.50	4.10–5.57

Note: Green, large ornithopod range; orange, ambiguous (overlaps both large ornithopod and large theropod ranges); red, large theropod range; threshold values, shown in bold beneath the headings, from Moratalla et al. (1988).

(DF with number) Río Batá dinosaur footprint number; (FL) footprint length; (FW) footprint width; (K, M) length to hypex; (BLII, BLIII, BLIV) length of free segment of toe; (WMII, WMIII, WMIV) width at middle of free segment of toe; (LII, LIII, LIV) digit lengths; (WBII, WBIII, WBIV) width at base of free segment of toe.

See Figures 3, 4 for locations of metrics; details of metrics given in the Abbreviations section of the text. See Figure 5 for a graphical representation of the data for the individual footprints.

Table 6. Trackway metrics the Río Batá footprints, showing the values used, and the results obtained, for the velocity calculations, using $V \approx 0.25g^{0.5}.SL^{1.67}.HH^{-1.17}$ (McNeil Alexander, 1976).

Track	FL (m)	SL (m)	HH (m)	SL/HH	V m/s	V km/h
DF1	0.44		1.76			
DF2	0.52		2.08			
DF3	0.56		2.24			
DF4	0.54		2.16			
DF1–3		2.21	2.03	1.09	1.29	4.64
DF2–4		2.43	2.16	1.13	1.40	5.04
Avg	0.52	2.32	2.06	1.13	1.37	4.93

Note: (DF with number) Río Batá dinosaur footprint number; (FL) footprint length, in metres; (SL) stride length, in metres; (m) metres; (HH) hip height (4 × FL), in metres; (V) velocity of the trackmaker in both m/s and km/h; (m/s) metres per second; (km/h) kilometres per hour; (Avg) arithmetic mean (average); g, acceleration due to gravity (9.81 m/s).

kg for the Río Batá ornithopod (Henderson, 2003; Norman, 1980; Seebacher, 2001). This would indicate that the Colombian iguanodontian was of moderate to large size, possibly a small adult or a sub–adult approaching adult size, depending upon the species of original trackmaker.

The speed of travel for the Colombian dinosaur can be estimated from the Río Batá trackway (DF1–4), using average (arithmetic mean) trackway metrics, SL (2.32 m) and calculated HH (2.06 m) (Table 6). As average SL/HH (1.13) is ≤2.0 (walking pace; Thulborn, 1990), it is appropriate to use $V \approx 0.25g^{0.5}.SL^{1.67}.HH^{-1.17}$ (McNeil Alexander, 1976), where V = velocity in m/s, g = acceleration due to gravity (9.81 m/s), SL = stride length in metres, and HH = hip height in metres. However, this equation is thought to underestimate dinosaur locomotion rates at moderate speeds (Thulborn, 1990). Using the velocity equation above, the estimated speed of the Río Batá trackmaker is 1.37 m/s (or 4.93 km/h) (Table 6). This is within the range of estimated average walking speeds for iguanodontian dinosaurs of 4.61–5.27 km/h (Thulborn, 1990). The apparent lack of manus prints along the Río Batá trackway indicates the animal was travelling either bipedally, or with little weight upon the manus. Adult iguanodontians were probably facultatively bipedal, but may have walked quadrupedally, using their hands in locomotion only at very slow speeds, or when running at greater velocities (Norman, 1980, 2004).

5.4. Dinosaur Biogeography

During the Jurassic, dinosaurs were widely distributed (Barrett et al., 2011; Canudo, 2006; Carballido et al., 2012; Cox, 1974; Rage, 1988; Sereno et al., 1994), with biotic interchange of terrestrial organisms possible due to the geographic competency of Pangaea. However, the latest Jurassic witnessed the opening of the Central Atlantic, which severed the previously persistent Jurassic land connection between Laurasia and Gondwana (Cox, 1974; Rage, 1988; Riccardi, 1991; Tennant et al., 2016). In addition, extinctions at the end of the Jurassic led to major ecosystem upheavals and terrestrial biotic reor-

ganization (Tennant et al., 2016). Tethys ocean thereby began to act both as a conduit for the east–west migration of marine organisms, and as an increasingly effective barrier to the north–south migrations of terrestrial fauna and flora (Canudo, 2006; Gheerbrant & Rage, 2006; Torsvik & Cocks, 2017). As a result, faunal exchanges continued across the northern (Laurasian) and southern (Gondwanan) continents, whereas free faunal exchange between the northern and southern continents was largely precluded (Cox, 1974; Canudo, 2006; Canudo et al., 2009; Francischini et al., 2015; Rage, 1988).

With the isolation of Laurasia and Gondwana, differences began to develop in the Early Cretaceous between the faunas and floras of the two continental landmasses (Cox, 1974; Canudo et al., 2009; Rage, 1988). Hence, continental isolation is seen by many as both a major impediment to north–south dinosaur migrations (e.g., Mao et al., 2012; Sereno et al., 1994), and as a driver of vicariance between the faunas of Gondwana and Laurasia (Canudo, 2006). However, although differences are generally recognised between the Early Cretaceous faunas of Laurasia and Gondwana (Canudo et al., 2009; Cox, 1974; Sereno et al., 1994), a simplistic view of organismal distributions, primarily driven by plate tectonics, is constantly being questioned (e.g., Gheerbrant & Rage, 2006; Rage, 1988). Despite the separation of Gondwana and Laurasia, by perhaps as much as several 100 km of deep ocean in the Early Cretaceous (Canudo et al., 2009), there is a growing body of evidence for faunal and floral exchanges between the northern and southern landmasses (Ezcurra & Agnolín, 2012; Gheerbrant & Rage, 2006; Rage, 1988). This makes the simple distinction between the Early Cretaceous faunas of Laurasia and Gondwana an oversimplification (Gheerbrant & Rage, 2006). However, distinguishing between vicariance–evolution from an ancestral stock following continental separation (Canudo, 2006; Carballido et al., 2012) – and migrations, can prove problematic, especially with an incomplete fossil record and flux in the taxonomy and phylogeny of dinosaurian and other groups. However, between the latest Jurassic and the Barremian – Aptian transition there is growing fossil evidence for biotic exchanges between Gondwana and Laurasia (Canudo et al., 2009).

5.4.1. Migration Routes and Barriers to Dispersal

Limits to continental organismal migrations typically include physical barriers such as deep ocean basins and mountain ranges; and to a lesser extent epicontinental seas and continental flood basalts (Canudo, 2006; Cox, 1974; Lehmann et al., 2015; Sereno et al., 1994). However, climatic gradients such as temperature, water availability, and desert belts also exert profound effects on organismal distributions (Canudo, 2006; Cox, 1974; Gallina et al., 2014). Hence, a deep and wide Tethys Ocean between Laurasia and Gondwana would have acted as an effective barrier to dinosaur migrations (Canudo, 2006). However, increasing data suggests at least an intermittent connection between Laurasia and Gondwana (Barrett et al., 2011; Canudo et al., 2009; de Klerk et al., 2000; Gallina et al., 2014; Gheerbrant & Rage, 2006; Naish et al., 2004; Nicosia et al., 2007; Rage, 1988), even though this goes against current palaeogeographic received wisdom (e.g., Torsvik & Cocks, 2017). Even if faunal exchanges occurred, it is clear that there was not complete homogenization of northern and southern continental faunas during the Early Cretaceous (Gheerbrant & Rage, 2006), although the reasons for this remain unclear.

Three routes crossing between Laurasia and Gondwana have been hypothesised, although the detailed connections between Mesozoic landmasses are often poorly constrained (Ezcurra & Agnolín, 2012; Rage, 1988). The first is a western corridor via modern–day southern North America and northern South America; the second is a central route between modern–day Europe and northern Africa; and the third is an eastern route between modern–day Asia and Australia (Cox, 1974; Ezcurra & Agnolín, 2012; Gheerbrant & Rage, 2006). Although favoured by some palaeobiogeographic models based on phylogenetic inferences (Barrett et al., 2011; Poropat et al., 2016), the Australia–Asia route has no support based on past or current palaeogeographic continental reconstructions for the Mesozoic (e.g., Scotese & Golonka, 1992; Smith et al., 1994; Torsvik & Cocks, 2017). The long–standing hypothesis that the North America–South America route was more likely than the circuitous route through Europe and Africa (Cox, 1974; Ezcurra & Agnolín, 2012) seems to be the most likely for the dinosaurs forming the Río Batá footprints. However, a North America–South America migration route is not supported by the well–studied dinosaur bearing beds of North America, that lack evidence for *Iguanodontipus* footprints. Hence, despite assertions to the contrary (Cox, 1974; Mao et al., 2012), there is little evidence for migrations across the southwestern margin of Laurasia (modern–day North America) into north–western Gondwana (modern–day northern South America) during the Early Cretaceous (e.g., Torsvik & Cocks, 2017).

The third route suggest dinosaurs migrated across Tethys from modern–day Europe into northern Africa. This route has the greatest support, although sampling remains poor (Dalla–Vecchia, 1998; Ezcurra & Agnolín, 2012; Pazos et al., 2012; Rage, 1988). It has been hypothesised that the most likely routes were through Apulia and/or Alboran, possibly via the Iberian Peninsula (Bosellini, 2002; Canudo, 2006; Gallina et al., 2014; Gheerbrant & Rage, 2006). Dinosaurs could have crossed oceanic Tethys, onto the passive north African margin (Torsvik & Cocks, 2017) and there is growing evidence for temporary connections between European Laurasian and African Gondwana (Canudo et al., 2009; Dalla–Vecchia, 1994, 2008; Nicosia et al., 2007). This migration route is supported by the apparently substantial Laurasian origin of Early Creta-

ceous Gondwanan (northern African) organisms (Gheerbrant & Rage, 2006) and recent palaeogeographic reconstructions (van Hinsbergen et al., 2020). This suggests biotic exchanges occurred between Gondwana and Laurasia (Ezcurra & Agnolín, 2012), although prior to the Barremian the faunas of the two supercontinents remain distinct (Barrett et al., 2011; Canudo et al., 2009). However, it has also been argued that dispersal prior to the division of Pangaea, followed by later independent evolution, is a more plausible explanation for observed dinosaur distributions (Poropat et al., 2016; Sereno et al., 1994).

During the Early Cretaceous, Europe was an archipelago within a shallow epicontinental sea (Canudo, 2006; Canudo et al., 2009; Gheerbrant & Rage, 2006), and dinosaur movements between these islands could have been facilitated by global climatic and environmental changes (Kujau, 2012). Periodically lowered Early Cretaceous sea levels, possibly due to polar ice sheets (Canudo, 2006), would have produced a complex series of emergent land masses that facilitated movement of terrestrial organisms across Tethys in the Central Atlantic region between modern–day Europe and North Africa (Bosellini, 2002; Dalla–Vecchia, 2008; Gheerbrant & Rage, 2006). Although there was no land bridge across Tethys, Gondwana and Laurasia were in relatively close proximity (Rage, 1988). Island hopping across now accreted or subducted microcontinents, volcanic islands, or emergent carbonate platforms may have been possible via the mid–Tethys sill (Canudo, 2006; Canudo et al., 2009; Dalla –Vecchia, 1994, 1998; Ezcurra & Agnolín, 2012; Mao et al., 2012), or Greater Adria (van Hinsbergen et al., 2020). This would indicate biotic exchange across Tethys was a temporary sweepstake between islands, facilitated by lowered sea levels, during times of climatic cooling and may have allowed large animals, such as dinosaurs, to occasionally wade or swim across the intervening body of water. This would have produced an inconsistent, perhaps somewhat directional (north to south), intercontinental selective filter between the two major Early Cretaceous landmasses (Canudo et al., 2009; Ezcurra & Agnolín, 2012; Gheerbrant & Rage, 2006; Rage, 1988).

Considering all the evidence, a Europe–North Africa migration route across Tethys is currently the most plausible explanation for the presence of iguanodotians in northern South America. Hence, the Río Batá footprints would indicate an Early Cretaceous ornithischian dinosaur migration route westwards along the northern shores of Gondwana from modern–day Africa into Colombia. This scenario would predict the future discovery of Lower Cretaceous *Iguanodontipus* footprints, and iguanodontian skeletal remains, in northern Africa and elsewhere in modern northern South America (Figure 6).

5.4.2. Dinosaur Palaeobiology

The remains of dinosaurs are some of the best–studied fossils of the Early Cretaceous (Tennant et al., 2016), and there are undoubted similarities between the ornithischian dinosaurs of central–southern Laurasia and northern–central Gondwana (Canudo, 2006; Canudo et al., 2009; Gheerbrant & Rage, 2006). Following the end–Jurassic extinctions, terrestrial vertebrate numbers declined, however, the ornithischian dinosaurs were only moderately affected, the ornithopods were virtually unaffected, and the iguanodontians became abundant in the Early Cretaceous (Tennant et al., 2016). It has been hypothesised that the dinosaurs that survived the end–Jurassic extinctions had key morphological adaptations, and possibly more generalized morphologies (Tennant et al., 2016). In addition, terrestrial life may have benefited from the generally warm and humid conditions during times of climatic amelioration, which produced widespread vegetation cover (Charbonnier et al., 2017; McLoughlin, 2001; Mao et al., 2012). This may have allowed the surviving herbivorous dinosaurs to radiate during the Early Cretaceous, taking advantage of broadly distributed, gymnosperm dominated, vegetation (Charbonnier et al., 2017; Mao et al., 2012).

The ecology of the iguanodontian dinosaurs may also have improved their chances of crossing Tethys. The iguanodontian, and other dinosaurian, fauna lived on an archipelago (modern Europe), which led to frequent migrations along coastal areas (Dalla–Vecchia, 1994, 1998; Santos et al., 2013), and probably necessitated occasional or regular wading or swimming between islands. This may have given these dinosaurs a propensity to cross shallow seas (Canudo, 2006), which at appropriate times may have included crossing Tethys. Indeed the Río Batá footprints, many *Iguanodontipus* and Lower Cretaceous dinosaur ichnofossils more generally, are commonly found on or close to palaeoshoreline or other water–rich deposits (e.g., Castanera et al., 2013; Dalla–Vecchia & Tarlao, 2000; Farlow et al., 1995; Kim et al., 2009; Pazos et al., 2012; Santos et al., 2013). In addition, during periods of Early Cretaceous cooling, there may have been additional environmental pressure for dinosaurs to move southwards towards more equatorial climates, thereby tracking both ecological and vegetational changes.

5.4.3. Gondwanan Dinosaur Provincialism

A migration route across Tethys for large, mobile dinosaurs such as iguanodontians fails to explain the absence of *Iguanodontipus* footprints in the more southerly parts of Gondwana. The best–known Gondwanan dinosaur faunas are those from southwest South America: Argentina and Brasil (e.g., Bittencourt & Langer, 2011; Costa da Silva et al., 2012; de la Fuente et al., 2007; de Valais et al., 2015; Moreno et al., 2012; Pazos et al., 2012). However, Gondwanan dinosaurs are also known from South Africa (de Klerk et al., 2000; Haughton, 1915) and Australia (Poropat et al., 2016; Romilio & Salisbury, 2011; Thulborn, 2016), whereas the dinosaurian faunas from northern South America are much more poorly known (Sereno et al., 1994; Weishampel et al., 2004). As a result of substantial connections between the southern continental

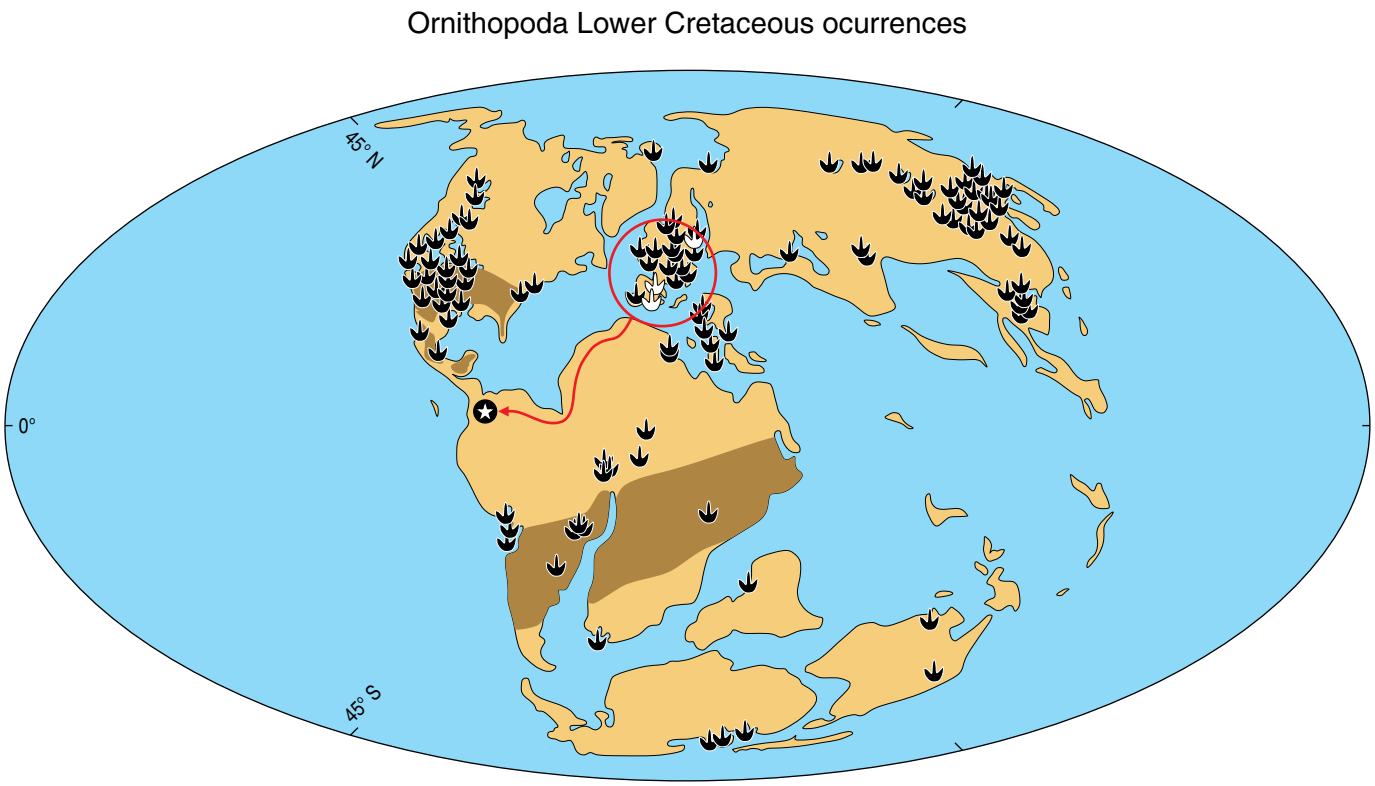

Figure 6. Early Cretaceous palaeogeographic map showing global distribution of ornithopod dinosaurs (footprint symbols, Iguanodontipus in white) and proposed migration route for the Río Batá *Iguanodontipus* trackmakers from the European archipelago (red circle), across Tethys Ocean, and along the northern shores of modern–day Africa and South America (red line), and into the modern–day Río Batá locality in Colombia (white star in black circle). Note the Central Gondwanan Desert Belt (dark brown) that probably restricted free southward migration of iguanodontians into southern Gondwana, which has its own endemic dinosaurian fauna, and the desert in the modern southern USA and Central America that precluded the water–adapted iguanodontians from migrating to South America via North America. Dinosaur data from downloaded from The Palaeobiology Database (https://paleobiodb.org/#/) using the clade name "Ornithopoda" (04 June 2018); Early Cretaceous base map from Matthews et al. (2016). Blue, water bodies; pale brown, land; dark brown, desert belts.

landmasses during the Early Cretaceous (de Klerk et al., 2000), it has often been assumed Gondwanan dinosaurs were widely distributed, continuing the trend from the Jurassic (e.g., Barrett et al., 2011; Cox, 1974; Sereno et al., 1994). Indeed there is good evidence for a broad distribution of high latitude southern Gondwanan dinosaurian taxa (Gallina et al., 2014) with migrations possible between modern southern South America, South Africa, Antarctica, and Australia, and probably encompassing India and Madagascar (Gheerbrant & Rage, 2006). This was despite (or perhaps because of) strong annual photoperiod variations and a flattened thermal gradient (McLoughlin, 2001; Poropat et al., 2016). On the other hand, there is relatively limited direct evidence for south–north migrations across Gondwana, although these have often been hypothesised based on taxonomic or phylogenetic evidence (e.g., Barrett et al., 2011; Naish et al., 2004). However, during much of the Jurassic, and continuing into the Early Cretaceous, Gondwana extended from the palaeo–equator to southern high latitudes, and the continent is known to have exhibited a well–marked, latitudinally determined, climatic gradient (McLoughlin, 2001).

Across a supercontinent the size of Gondwana, it is inconceivable that climatic gradients did not affect dinosaur distributions and migrations. This would lead to regional variations in dinosaurian faunas (Francischini et al., 2015), controlled by climate and geographical barriers, as with global faunal distributions today (Davies et al., 2011). During the Early Cretaceous, continuing from earlier in the Jurassic, there is considerable evidence for a Central Gondwanan Desert Belt (Gallina et al., 2014; de Valais et al., 2015; Francischini et al., 2015; McLoughlin, 2001; Naish et al., 2004; Philippe et al., 2004; Remes et al., 2009; Svensen et al., 2018). The Central Gondwanan Desert Belt was centred around 30 degrees south of the equator (Philippe et al., 2004, Figure 1), coinciding with the modern descending limbs of the Hadley and Ferrell atmospheric cells (Ziegler et al., 2003). This is in contrast to the northern hemisphere, where an extensive Laurasian (northern) desert belt did not develop, possibly due to widespread epicontinental seaways (e.g., the proto–Western Interior Sea, the central (European) archipelago, and the Turgai Sea), although desert conditions were present in the southern extent of western Laurasia (Philippe

et al., 2004). In Gondwana, the extensive Central Gondwanan Desert Belt crossed the continent from what are today northern Argentina, Uruguay, Paraguay, Brasil, and Namibia (Francischini et al., 2015; Gallina et al., 2014; Iglesias et al., 2011) and undoubtedly restricted the latitudinal migrations of dinosaurs, although occasional faunal interchanges were possible during periods of climatic amelioration (Gallina et al., 2014). Hence, the environment across the wide latitudinal geographic spread of Gondwana was uneven, undoubtedly affected biotic interchanges between northern and southern Gondwana, and prevented the southward migration of the possibly water–loving iguanodontians into southern Gondwana.

6. Conclusions

Six dinosaur footprints discovered in the upper Valanginian to lower Hauterivian Batá Formation along the Río Batá, Boyacá Department, Colombia, South America are interpreted as formed by a large (>30 cm foot length) ornithischian dinosaur. Four footprints form an approximately four metre long trackway generated by a dinosaur attributed to the ichnospecies *Iguanodontipus burreyi*, which prior to this work was an exclusively Laurasian ichnogenus. The trackmaker is interpreted as an iguanodontian dinosaur with a hip height of greater than two metres, possibly suggesting a sub–adult individual of approximately eight metres in length and weighting 2.5 metric tons. The dinosaur was moving at an average walking pace for iguanodontians of almost five kilometres per hour. The Río Batá dinosaur footprints are the first evidence for large ornithopod dinosaurs in Colombia, and represent the best–preserved dinosaur footprints, yet discovered in the country.

The Río Batá footprints, situated close to the northern shore of west Gondwana, suggest biotic interchange across Tethys Ocean between southern Laurasia (modern Europe) and northern Gondwana (modern North Africa), despite many modern palaeogeographic reconstructions showing no direct land connection during the Early Cretaceous. The separation of Pangaea during the latest Jurassic into northern Laurasia and southern Gondwana coincided in time with the end–Jurassic mass extinction event. This resulted in the radiation of iguanodontian dinosaurs into vacant ecological space during the Early Cretaceous. These dinosaurs appear to have been adapted to water–rich environments in the European archipelago and variable climates during the Early Cretaceous, probably related to relatively small–scale ice advances and retreats, which resulted in lowered global sea levels that permitted iguanodontian dinosaurs to cross Tethys Ocean, perhaps via the Iberian Peninsula, Apulia and/or Albora or Greater Adria.

Once in Gondwana, the iguanodontian dinosaurs probably tracked lush tropical vegetation and water–rich environments along the northern margins of the continent. However, a lack of evidence for *Iguanodontipus* footprints in southern Gondwana implies a geographical barrier between northern and southern Gondwana. To the south lay the Central Gondwanan Desert Belt, which posed a considerable, and possibly impenetrable, barrier to southward movements of the water–loving iguanodontians, and precluded range extension into southern Gondwana. Hence, a variety of geographic and climatic factors drove Early Cretaceous northern Gondwanan dinosaur distributions, and as a result, we predict the discovery of both iguanodontian dinosaur skeletal remains, and further *Iguanodontipus* ichnofossils, in northern Africa and northern South America, but not in southern Gondwana.

The discovery of large ornithopod footprints along the Río Batá thereby adds considerably to the evidence for Colombian and northwestern South American dinosaurs and their movements. The identification of these footprints as attributable to the ichnogenus *Iguanodontipus*, is the first evidence for this ichnotaxon outside modern Europe, and has important implications for the palaeogeographic distribution of *Iguanodontipus* trackmakers. The Río Batá footprints thereby indicate we have much to learn about the palaeobiology, palaeoecology, and palaeogeography of Early Cretaceous dinosaurs in northern South America.

Acknowledgments

We extend our grateful thanks Jorge GÓMEZ TAPIAS for inviting us to contribute to this exciting and unique volume on The Geology of Colombia. We also thank: Diego GÓMEZ and Daniela GARCÍA for indicating the locality of the footprints that commenced this research; Eric BUFFETAUT for providing references to DEGENHARDT's work; and Eliana ARAQUE–SANABRIA (Servicio Geológico Colombiano) for developing Figure 1. LFN, JVR–J, AC–G, and WGC–M acknowledge the stimulating academic environment of the Departamento de Geociencias, Universidad de los Andes, and MG–P acknowledges the support and collegiate atmosphere of the Museo Geológico Nacional José ROYO Y GÓMEZ, of the SGC. Funding for LFN was provided by a "Fondo de Apoyo para Profesores Asistentes" grant (FAPA n° P12–160422.006/01) awarded by Universidad de los Andes; writing of the manuscript was undertaken during the tenure of a project entitled "The Paja Formation Lagerstätte of the alto Ricaurte: Access, palaeoenvironment and taphonomy" (Programas de Investigación para Profesores de Planta Asociados, Titulares y Emeritos n.o P18.160322.001/23) from the Facultad de Ciencias, Universidad de los Andes. The authors gratefully acknowledge the patience and support of our families during the preparation of this manuscript. We extend our sincere thanks to Fabio Marco DALLA–VECCHIA (Institut Català de Paleontologia Miguel Crusafont, Sabadell, Cataluña, Spain) and Anthony ROMILIO (School of Chemistry and Molecular Biosciences, The University of Queensland, St. Lucia, Australia) for insightful reviews, which considerably improved an earlier version of this contribution.

References

Alley, N.F., Hore, S.B. & Frakes, L.A. 2019. Glaciations at high–latitude southern Australia during the Early Cretaceous. Australian Journal of Earth Sciences, 66(4): 1–51. https://doi.org/10.1080/08120099.2019.1590457

Barrett, P.M., Benson, R.B.J., Rich, T.H. & Vickers–Rich, P. 2011. First spinosaurid dinosaur from Australia and the cosmopolitanism of Cretaceous dinosaur faunas. Biology Letters, 7: 933–936. https://doi.org/10.1098/rsbl.2011.0466

Bittencourt, J.S. & Langer, M.C. 2011. Mesozoic dinosaurs from Brazil and their biogeographic implications. Anais da Academia Brasileira de Ciências, 83(1): 23–60. http://dx.doi.org/10.1590/S0001-37652011000100003

Bosellini, A. 2002. Dinosaurs "re–write" the geodynamics of the eastern Mediterranean and the paleogeography of the Apulia Platform. Earth Science Reviews, 59(1–4): 211–234. https://doi.org/10.1016/S0012-8252(02)00075-2

Botero–Arango, G. 1937. Bosquejo de paleontología colombiana, 2nd edition. Imprenta Nacional, 84 p. Bogotá.

Buffetaut, E. 2000. A forgotten episode in the history of dinosaur ichnology: Carl Degenhardt's report on the first discovery of fossil footprints in South America (Colombia, 1839). Bulletin de la Société Géologique de France, 171(1): 137–140.

Bürgl, H. 1958. El Jurásico e Infracretáceo del río Batá, Boyacá. Boletín Geológico, 6(1–3): 169–211.

Bürgl, H. 1964. El "Jura–Triásico" de Colombia. Boletín Geológico, 12(1–3): 5–31.

Canudo, J.I. 2006. La ambigüedad paleobiogeográfica de los dinosaurios ibéricos durante el Cretácico Inferior. In: Salense, E. (editor), Actas de las III Jornadas sobre Dinosaurios y su Entorno, Colectivo Arqueológica–Paleontológico: 21–45. Salas de los Infantes, Burgos, España.

Canudo, J.I., Barco, J.L., Pereda–Suberbiola, X., Ruiz–Omeñaca, J.I., Salgado, L., Fernández–Baldor, F.T. & Gasulla, J.M. 2009. What Iberian dinosaurs reveal about the bridge said to exist between Gondwana and Laurasia in the Early Cretaceous. Bulletin de la Société Géologique de France, 180(1): 5–11. https://doi.org/10.2113/gssgfbull.180.1.5

Carballido, J.L., Salgado, L., Pol, D., Canudo, J.I. & Garrido, A. 2012. A new basal rebbachisaurid (Sauropoda, Diplodocoidea) from the Early Cretaceous of the Neuquén Basin: Evolution and biogeography of the group. Historical Biology, 24(6): 631–654. https://doi.org/10.1080/08912963.2012.672416

Carballido, J.L., Pol, D., Parra–Ruge, M.L., Padilla–Bernal, S., Páramo–Fonseca, M.E. & Etayo–Serna, F. 2015. A new Early Cretaceous brachiosaurid (Dinosauria, Neosauropoda) from northwestern Gondwana (Villa de Leiva, Colombia). Journal of Vertebrate Paleontology, 35(5): 1–12. https://doi.org/10.1080/02724634.2015.980505

Castanera, D., Pascual, C., Razzolini, N.L., Vila, B., Barco, J.L. & Canudo, J.I. 2013. Discriminating between medium–sized tridactyl trackmakers: Tracking ornithopod tracks in the base of the Cretaceous (Berriasian, Spain). PLOS ONE, 8(11): e81830. https://doi.org/10.1371/journal.pone.0081830

Charbonnier, G., Morales, C., Duchamp–Alphonse, S., Westermann, S., Adatte, T. & Föllmi, K.B. 2017. Mercury enrichment indicates volcanic triggering of Valanginian environmental change. Scientific Reports, 7(40808): 1–6. https://doi.org/10.1038/srep40808

Cohen, K.M., Finney, S.C., Gibbard, P.L. & Fan, J.X. 2013 (updated v2019/05). The ICS International Chronostratigraphic Chart. Episodes, 36(3): 199–204.

Costa da Silva, R., Barboni, R., Dutra, T., Marques–Godoy, M. & Barros–Binotto, R. 2012. Footprints of large theropod dinosaurs and implications on the age of Triassic biotas from southern Brazil. Journal of South American Earth Sciences, 39: 16–23. https://doi.org/10.1016/j.jsames.2012.06.017

Cox, C.B. 1974. Vertebrate palaeodistributional patterns and continental drift. Journal of Biogeography, 1(2): 75–94.

Dalla–Vecchia, F.M. 1994. Jurassic and Cretaceous sauropod evidence in the Mesozoic carbonate platforms of the southern Alps and Dinarids. Gaia, (10): 65–73.

Dalla–Vecchia, F.M. 1998. Theropod footprints in the Cretaceous Adriatic–Dinaric carbonate platform, Italy and Croatia. Gaia, (15): 355–367.

Dalla–Vecchia, F.M. 2008. The impact of dinosaur palaeoichnology in palaeoenvironmental and paleogeographic reconstructions: The case of the Periadriatic carbonate platforms. Oryctos, 8: 89–106.

Dalla–Vecchia, F.M. & Tarlao, A. 2000. New dinosaur track sites in the Albian (Early Cretaceous) of the Istrian Peninsula, Croatia–Part II. Memorie di Scienze Geologiche, 52(2): 227–292.

Davies, T.J., Buckley, L.B., Grenyer, R. & Gittleman, J.L. 2011. The influence of past and present climate on the biogeography of modern mammal diversity. Philosophical Transactions of the Royal Society B, 366(1577): 2526–2535. https://doi.org/10.1098/rstb.2011.0018

Day, J.J., Norman, D.B., Upchurch, P. & Powell, H.P. 2002. Dinosaur locomotion from a new trackway. Nature, 415(6871): 494–495. https://doi.org/10.1038/415494a

Degenhardt, C. 1840. Fuss–Spuren eines Vogels im rothen Sandstein in Mexiko. Neues Jahrbuch für Mineralogie, Geognosie, Geologie und Petrefaktenkunde Jahrgang 1840, p. 485.

de Klerk, W.J., Forster, C.A., Sampson, S.D., Chinsamy, A. & Ross, C.F. 2000. A new coelurosaurian dinosaur from the Early Cretaceous of South Africa. Journal of Vertebrate Paleontology, 20(2): 324–332. https://doi.org/10.1671/0272-4634(2000)020[0324:ANCDFT]2.0.CO;2

de la Fuente, M.S., Salgado, L., Albino, A., Báez, A.M., Bonaparte, J.F., Calvo, J.O., Chiappe, L.M., Codorniú, L.S., Coria, R.A., Gasparini, Z., González–Riga, B.J., Novas, F.E. & Pol, D. 2007. Tetrápodos continentales del Cretácico de la Argentina: Una síntesis actualizada. Asociación Paleontológica Argentina, Publicación Especial, 11: 137–153.

de Valais, S., Candeiro, C.R., Tavares, L.F., Alves, Y.M. & Cruvinel, C. 2015. Current situation of the ichnological locality of São Domingos from the Corda Formation (Lower Cretaceous), northern Tocantins state, Brazil. Journal of South American Earth Sciences 61: 142–146. https://doi.org/10.1016/j.jsames.2014.09.023

Díaz–Martínez, I., Pereda–Suberbiola, X., Pérez–Lorente, F. & Canudo, J.I. 2015. Ichnotaxonomic review of large ornithopod dinosaur tracks: Temporal and geographic implications. PLOS ONE, 10(2): e0115477. https://doi.org/10.1371/journal.pone.0115477

Díaz–Martínez, I., de Valais, S. & Cónsole–Gonella, C. 2016. First evidence of *Hadrosauropodus* in Gondwana (Yacoraite Formation, Maastrichtian – Danian), northwestern Argentina. Journal of African Earth Sciences, 122: 79–87. https://doi.org/10.1016/j.jafrearsci.2016.02.012

Erba, E. 2004. Calcareous nannofossils and Mesozoic oceanic anoxic events. Marine Micropaleontology, 52(1–4): 85–106. https://doi.org/10.1016/j.marmicro.2004.04.007

Erba, E., Bartolini, A. & Larson, R.L. 2004. Valanginian Weissert oceanic anoxic event. Geology, 32(2): 149–152. https://doi.org/10.1130/G20008.1

Etayo–Serna, F., De Porta, N.S., De Porta, J. & Gaona, T. 2003. The Batá Formation of Colombia is truly Cretaceous, not Jurassic. Journal of South American Earth Sciences, 16(3): 113–117. https://doi.org/10.1016/S0895-9811(03)00048-8

Ezcurra, M.D. 2009. Theropod remains from the uppermost Cretaceous of Colombia and their implications for the palaeozoogeography of western Gondwana. Cretaceous Research, 30(5): 1339–1344. https://doi.org/10.1016/j.cretres.2009.08.004

Ezcurra, M.D. & Agnolín, F.L. 2012. A new global palaeobigeographical model for the late Mesozoic and early Tertiary. Systematic Biology, 61(4): 553–566. https://doi.org/10.1093/sysbio/syr115

Farlow, J.O., Dodson, P. & Chinsamy, A. 1995. Dinosaur biology. Annual Review of Ecology and Systematics, 26: 445–471.

Figueiredo, S., Dinis, P., Belo, J., Rosina, P. & Bachtsevanidou–Strantzali, I. 2017. A new record of a possible ornithopod footprint from the Lower Cretaceous of Cabo Espichel, Sesimbra, Portugal. Bollettino della Società Paleontologica Italiana, 56 (2): 217–231.

Flórez, M. J. & Carrillo, G. 1994. Estratigrafía de la sucesión litológica basal del Cretácico del Valle Superior del Magdalena. In: Etayo–Serna, F. (editor), Estudios geológicos del Valle Superior del Magdalena. Universidad Nacional de Colombia, p. II–1–II–26. Bogotá.

Francischini, H., Dentzien–Dias, P.C., Fernandes, M.A. & Schultz, C.L. 2015. Dinosaur ichnofauna of the Upper Jurassic/Lower Cretaceous of the Paraná Basin (Brazil and Uruguay). Journal of South American Earth Sciences, 63: 180–190. https://doi.org/10.1016/j.jsames.2015.07.016

Gallina, P.A., Apesteguía, S., Haluza, A. & Canale, J.I. 2014. A diplodocid sauropod survivor from the Early Cretaceous of South America. PLOS ONE, 9(5): e97128. https://doi.org/10.1371/journal.pone.0097128

Geyer, O.F. 1967. Das Typus–Profil der Morrocoyal–Formation, Unterlias; Depto. Bolívar, Kolumbien. Mitteilungen aus dem Instituto Colombo Alemán de Investigaciones Científicas, 1: 53–63.

Gheerbrant, E. & Rage, J.C. 2006. Paleobiogeography of Africa: How distinct from Gondwana and Laurasia? Palaeogeography, Palaeoclimatology, Palaeoecology, 241(2): 224–246. https://doi.org/10.1016/j.palaeo.2006.03.016

Gong, Z., Langereis, C.G. & Mullender, T.A.T. 2008. The rotation of Iberia during the Aptian and the opening of the Bay of Biscay. Earth and Planetary Science Letters 273(1–2), 80–93. https://doi.org/10.1016/j.epsl.2008.06.016

Gröcke, D.R., Price, G.D., Robinson, S.A., Baraboshkin, E.Y., Mutterlose, J. & Ruffell, A.H. 2005. The upper Valanginian (Early Cretaceous) positive carbon–isotope event recorded in terrestrial plants. Earth and Planetary Science Letters, 240(2): 495–509. https://doi.org/10.1016/j.epsl.2005.09.001

Hasiotis, S.T., Platt, B.F., Hembree, D.I. & Everhart, M.J. 2007. The trace–fossil record of vertebrates. In: Miller III, W. (editor), Trace fossils: Concepts, problems, prospects. Elsevier, p. 196–218. Amsterdam. https://doi.org/10.1016/B978-044452949-7/50138-8

Haughton, S.H. 1915. On some dinosaur remains from Bushmanland. Transactions of the Royal Society of South Africa 5(1): 259–264. https://doi.org/10.1080/00359191509519723

Heine, C., Yeo, L.G. & Müller, R.D. 2015. Evaluating global paleoshoreline models for the Cretaceous and Cenozoic. Australian Journal of Earth Sciences, 62(3): 275–287. https://doi.org/10.1080/08120099.2015.1018321

Henderson, D.M. 2003. Footprints, trackways, and hip heights of bipedal dinosaurs: Testing hip height predictions with computer models. Ichnos, 10(2–4): 99–114. https://doi.org/10.1080/10420940390257914

Hutchinson, J.R. 2005. Dinosaur locomotion. Encyclopedia of Life Sciences. John Wiley & Sons, Ltd., p. 1–7. https://doi.org/10.1038/npg.els.0003320

Iglesias, A., Artabe, A.E. & Morel, E.M. 2011. The evolution of Patagonian climate and vegetation from the Mesozoic to the present. Biological Journal of the Linnean Society, 103(2): 409–422. https://doi.org/10.1111/j.1095-8312.2011.01657.x

Irving, E.M. 1975. Structural evolution of the northernmost Andes, Colombia. U.S. Geological Survey, Professional Paper 846, p. 1–47. Washington, USA. https://doi.org/10.3133/pp846

Jaillard, E., Sempere, T., Soler, P., Carlier G. & Marocco, R. 1995. The role of Tethys in the evolution of the northern Andes between late Permian and late Eocene times. In: Nairn, A.E.M., Ricou, L.–E., Vrielynck, B. & Dercourt, J. (editors), The ocean basins and margins, Volume 8: The Tethys Ocean. Plenum Press: 463–492. New York. https://doi.org/10.1007/978-1-4899-1558-0_15

Kim, J.Y., Lockley, M.G., Kim, H.M, Lim, J.D. & Kim, K.S. 2009. New dinosaur tracks from Korea, *Ornithopodichnus masanensis* ichnogen. et ichnosp. nov. (Jindong Formation, Lower Cretaceous): Implications for polarities in ornithopod foot morphology. Cretaceous Research, 30(6): 1387–1397. https://doi.org/10.1016/j.cretres.2009.08.003

Kujau, A. 2012. Climatic and environmental dynamics during the Valanginian carbon isotope event: Evidence from geochemistry and palynology. Doctoral thesis, Ruhr–Universität Bochum, 175 p. Bochum, Germany.

Lallensack, J.N., van Heteren, A.H. & Wings, O. 2016. Geometric morphometric analysis of intratrackway variability: A case study on theropod and ornithopod dinosaur trackways from Münchehagen, Lower Cretaceous, Germany. PeerJ 4: e2059, p. 1–42. https://doi.org/10.7287/peerj.preprints.2004v1

Langston, W.J. 1953. Cretaceous terrestrial vertebrates from Colombia, South America. GSA Bulletin, 64(12): 1519.

Langston, W. 1965. Fossil crocodilians from Colombia and the Cenozoic history of the crocodylia in South America. University of California Publications in Geological Sciences, 52, 157 p. Berkeley, USA.

Langston, W.J. & Durham, J.W. 1955. A sauropod dinosaur from Colombia. Journal of Paleontology, 29(6): 1047–1051.

Lehmann, J., Ifrim, C., Bulot, L. & Frau, C. 2015. Paleobiogeography of Early Cretaceous ammonoids. In: Klug, C., Korn, D., De Baets, K., Kruta, I. & Mapes, R.H. (editors), Ammonoid paleobiology: From macroevolution to paleogeography. Topics in Geobiology, 44. Springer Netherlands, p. 229–257. Dordrecht, The Netherlands. https://doi.org/10.1007/978-94-017-9633-0_9

Leonardi, G. 1989. Inventory and statistics of the South American dinosaurian ichnofauna and its paleobiological interpretation. In: Gillette, D.D. & Lockley, M.G. (editors), Dinosaur tracks and traces. Cambridge University Press, p. 165–178. Oakland, USA.

Llandres–Serrano, M., Vullo, R., Marugán–Lobón, J., Ortega, F. & Buscalioni, Á.D. 2013. An articulated hindlimb of a basal iguanodont (Dinosauria, Ornithopoda) from the Early Cretaceous Las Hoyas Lagerstätte (Spain). Geological Magazine, 150(3): 572–576. https://doi.org/10.1017/S0016756813000095

Lockley, M.G. 1991. Tracking dinosaurs: A new look at an ancient world. Cambridge University Press, 238 p. Cambridge, UK.

Lockley, M.G. 2009. New perspectives on morphological variation in tridactyl footprints: Clues to widespread convergence in developmental dynamics. Geological Quarterly, 53(4): 415–432.

Lockley, M.G., Wright, J.L. & Thies, D. 2004. Some observations on the dinosaur tracks at Münchenhagen (Lower Cretaceous), Germany. Ichnos, 11(3–4): 262–274. https://doi.org/10.1080/10420940490428805

Lockley, M.G., McCrea, R.T. & Matsukawa, M. 2009. Ichnological evidence for small quadrupedal ornithischians from the basal Cretaceous of SE Asia and North America: Implications for a global radiation. In: Buffetaut, E., Cuny, G., Le Loeuff, J. & Suteethorn, V. (editors), Late Palaeozoic and Mesozoic continental ecosystems in SE Asia. Geological Society of London, Special Publication 315, p. 255–269. https://doi.org/10.1144/SP315.18

Lockley, M.G., Xing, L., Lockwood, J.A.F. & Pond, S. 2014. A review of large Cretaceous ornithopod tracks, with special reference to their ichnotaxonomy. Biological Journal of the Linnean Society, 113(3): 721–736. https://doi.org/10.1111/bij.12294

Lockwood, J.A.F., Lockley, M.G. & Pond, S. 2014. A review of footprints from the Wessex Formation (Wealden Group, Lower Cretaceous) at Hanover Point, the Isle of Wight, southern England. Biological Journal of the Linnean Society, 113(3): 707–720. https://doi.org/10.1111/bij.12349

Mahlmann, W. 1840. Geognostische und meteorologische Notizen aus einem Schreiben des Bergwerks–Directors Carl Degenhardt an Herrn A. v. Humboldt, d. d. Marmato (Prov. Popayan) d. 1. November 1839. Monatsberichte über die Verhandlungen der Gesellschaft für Erdkunde zu Berlin, 1(11–12): 206–208.

Mannion, P.D., Allain, R. & Moine, O. 2017. The earliest known titanosauriform sauropod dinosaur and the evolution of Brachiosauridae. PeerJ, 5: e3217, p. 1–82. https://doi.org/10.7717/peerj.3217

Mao, K., Milne, R.I., Zhang, L., Peng, Y., Liu, J., Thomas, P., Mill, R.R. & Renner, S.S. 2012. Distribution of living Cupressaceae reflects the breakup of Pangea. Proceedings of the National Academy of Sciences of the United States of America, 109(20): 7793–7798. https://doi.org/10.1073/pnas.1114319109

Martinez, M., Deconinck, J.F., Pellenard, P., Riquier, L., Company, M., Reboulet, S. & Moiroud, M. 2015. Astrochronology of the Valanginian – Hauterivian stages (Early Cretaceous): Chronological relationships between the Paraná–Etendeka Large Igneous Province and the Weissert and Faraoni events. Global and Planetary Change, 131: 158–173. https://doi.org/10.1016/j.gloplacha.2015.06.001

Mateus, O. & Milán, J. 2008. Ichnological evidence for giant ornithopod dinosaurs in the Upper Jurassic Lourinhã Formation, Portugal. ORYCTOS, 8: 47–52.

Matthews, K.J., Maloney, K.T., Zahirovic, S., Williams, S.E., Seton, M. & Müller, R.D. 2016. Global plate boundary evolution and kinematics since the late Paleozoic. Global and Planetary Change, 146: 226–250. https://doi.org/10.1016/j.gloplacha.2016.10.002

McLoughlin, S. 2001. The breakup history of Gondwana and its impact on pre–Cenozoic floristic provincialism. Australian Journal of Botany, 49(3): 271–300. https://doi.org/10.1071/BT00023

McNeil Alexander, R. 1976. Estimates of speeds of dinosaurs. Nature, 261(5556): 129–130. https://doi.org/10.1038/261129a0

Meissner, P., Mutterlose, J. & Bodin, S. 2015. Latitudinal temperature trends in the Northern Hemisphere during the Early Cretaceous (Valanginian – Hauterivian). Palaeogeography, Palaeoclimatology, Palaeoecology, 424: 17–39. https://doi.org/10.1016/j.palaeo.2015.02.003

Miller, K.G., Kominz, M.A., Browning, J.V., Wright, J.D., Mountain, G.S., Katz, M.E., Sugarman, P.J., Cramer, B.S., Christie–Blick, N. & Pekar, S.F. 2005. The Phanerozoic record of global sea–level change. Science, 310(5752): 1293–1298. https://doi.org/10.1126/science.1116412

Milner, A.R.C. Vice, G.S, Harris, J.D. & Lockley, M.G. 2006. Dinosaur tracks from the Upper Cretaceous Iron Springs Formation, Iron County, Utah. In: Lucas, S.G. & Sullivan, R.M. (editors), Late Cretaceous vertebrates from the Western Interior. New Mexico Museum of Natural History and Science, Bulletin 35, p 105–113.

Mojica, J. & Kammer, A. 1995. Eventos jurásicos en Colombia. Geología Colombiana, (19): 165–172.

Montoya, D., Terraza, R., Reyes, G., Moreno, G. & Fúquen, J. 2008. Geología del Cinturón Esmeraldífero Oriental. Planchas 210, 229 y 228. Scale 1:100 000. Ingeominas. Bogotá.

Moratalla, J.J., Sanz, J.L. & Jimenez, S. 1988. Multivariate analysis on Lower Cretaceous dinosaur footprints: Discrimination between ornithopods and theropods. Geobios, 21(4): 395–408. https://doi.org/10.1016/S0016-6995(88)80042-1

Moreno, G., Terraza, R. & Montoya, D. 2009. Geología del cinturón esmeraldífero oriental (CEOR). Boletín de Geología, 31(2): 51–67.

Moreno, K., de Valais, S., Blanco, N., Tomlinson, A.J., Jacay, J. & Calvo, J.O. 2012. Large theropod dinosaur footprint associations in western Gondwana: Behavioural and palaeogeographic implications. Acta Palaeontologica Polonica, 57(1): 73–83. https://doi.org/10.4202/app.2010.0119

Moreno–Sánchez, M. & Gómez–Cruz, A.d.J. 2013. Huellas de dinosaurios en Colombia: Revisión y nuevos hallazgos. II Simposio Latinoamericano de Icnología. Abstract, p. 49. Santa Rosa de la Pampa, Argentina.

Moreno–Sánchez, M., Gómez, A.d.J. & Gómez, J. 2011. Reporte de huellas de dinosaurios en el Santuario de Fauna y Flora de Iguaque, en cercanías de Chíquiza, Boyacá, Colombia. Boletín de Geología, 33(2): 107–118.

Naish, D., Martill, D.M. & Frey, E. 2004. Ecology, systematics and biogeographical relationships of dinosaurs, including a new theropod, from the Santana Formation (?Albian, Early Cretaceous) of Brazil. Historical Biology, 16(2–4): 57–70. https://doi.org/10.1080/08912960410001674200

Nicosia, U., Massimo–Petti, F., Perugini, G., D'Orazi–Porchetti, S., Sacchi, E., Conti, M.A., Mariotti, N. & Zarattini, A. 2007. Dinosaur tracks as paleogeographic constraints: New scenarios for the Cretaceous geography of the Periadriatic region. Ichnos, 14(1–2): 69–90. https://doi.org/10.1080/10420940601006859

Noè, L.F. & Gómez–Pérez, M. 2020. Plesiosaurs, palaeoenvironments, and the Paja Formation Lagerstätte of central Colombia: An overview. In: Gómez, J. & Pinilla–Pachon, A.O. (editors), The Geology of Colombia, Volume 2 Mesozoic. Servicio Geológico Colombiano, Publicaciones Geológicas Especiales 36, p. 441–483. Bogotá. https://doi.org/10.32685/pub.esp.36.2019.13

Norman, D.B. 1980. On the ornithischian dinosaur Iguanodon bernissartensis from the Lower Cretaceous of Bernissart, Belgium. Institut Royal des Sciences Naturelles de Belgique, Mémoire 178, 103 p. Brussels, Belgium.

Norman, D.B. 2004. Basal Iguanodontia. In: Weishampel, D.B., Dodson, P. & Osmólska, H. (editors), The Dinosauria, 2nd edition. University of California Press, p. 413–437. Berkeley, USA.

Norman, D.B. 2013. On the taxonomy and diversity of Wealden iguanodontian dinosaurs (Ornithischia: Ornithopoda). Revue de Paléobiologie, 32(2): 385–404.

Owen, R. 1841. Report on British fossil reptiles: Part II. Report of the British Association for the Advancement of Science for 1841, p. 60–204. London, UK.

Owens, J.D., Lyons, T.W. & Lowery, C.M. 2018. Quantifying the missing sink for global organic carbon burial during a Cretaceous oceanic anoxic event. Earth and Planetary Science Letters, 499: 83–94. https://doi.org/10.1016/j.epsl.2018.07.021

Pascual–Arribas, C., Hernández–Medrano, N., Latorre–Macarrón, P. & Sanz–Pérez, E. 2009. El Icnogénero *Iguanodontipus* en el yacimiento de "Las Cuestas I", Santa Cruz de Yanguas, Soria. España. Studia Geologica Salmanticensia, 45(2): 105–128.

Pazos, P.J., Lazo, D.G., Tunik, M.A., Marsicano, C.A., Fernández, E.E. & Aguirre–Urreta, M.B. 2012. Paleoenvironmental framework of dinosaur tracksites and other ichnofossils in Early Cretaceous mixed siliciclastic–carbonate deposits in the Neuquén Basin, northern Patagonia, Argentina. Gondwana Research, 22(3–4): 1125–1140. https://doi.org/10.1016/j.gr.2012.02.003

Philippe, M., Bamford, M., McLoughlin, S., Alves, L.S.R., Falcon–Lang, H.J., Gnaedinger, S., Ottone, E.G., Pole, M., Rajanikanth, A., Shoemaker, R.E., Torres, T. & Zamuner, A. 2004. Biogeographic analysis of Jurassic – Early Cretaceous wood assemblages from Gondwana. Review of Palaeobotany and Palynology, 129(3): 141–173. https://doi.org/10.1016/j.revpalbo.2004.01.005

Platt, B.F., Suarez, C.A., Boss, S.K., Williamson, M., Cothren, J. & Kvamme, J.A.C. 2018. LIDAR–based characterization and conservation of the first theropod dinosaur trackways from Arkansas, USA. PLOS ONE, 13(1): e0190527. https://doi.org/10.1371/journal.pone.0190527

Poropat, S.F., Mannion, P.D., Upchurch, P., Hocknull, S.A., Kear, B.P., Kundrát, M., Tischler, T.R., Sloan, T., Sinapius, G.H.K., Elliott, J.A. & Elliott, D.A. 2016. New Australian sauropods shed light on Cretaceous dinosaur palaeobiogeography. Scientific Reports, 6: 34467. https://doi.org/10.1038/srep34467

Rage, J.C. 1988. Gondwana, Tethys, and terrestrial vertebrates during the Mesozoic and Cainozoic. Geological Society of London, Special Publication 37(1): 255–273. https://doi.org/10.1144/GSL.SP.1988.037.01.18

Remes, K., Ortega, F., Fierro, I., Joger, U., Kosma, R., Marín–Ferrer, J.M., Ide, O.A. & Maga, A. 2009. A new basal sauropod dinosaur from the Middle Jurassic of Niger and the early evo-

lution of Sauropoda. PLOS ONE, 4(9): e6924. https://doi.org/10.1371/journal.pone.0006924

Riccardi, A.C. 1991. Jurassic and Cretaceous marine connections between the southeast Pacific and Tethys. Palaeogeography, Palaeoclimatology, Palaeoecology, 87(1–4): 155–189. https://doi.org/10.1016/0031-0182(91)90134-D

Romilio, A. & Salisbury, S.W. 2011. A reassessment of large theropod dinosaur tracks from the mid–Cretaceous (late Albian – Cenomanian) Winton Formation of Lark Quarry, central–western Queensland, Australia: A case for mistaken identity. Cretaceous Research, 32(2): 135–142. https://doi.org/10.1016/j.cretres.2010.11.003

Santos, V.F., Callapez, P.M. & Rodrigues, N.P.C. 2013. Dinosaur footprints from the Lower Cretaceous of the Algarve Basin, Portugal: New data on the ornithopod palaeoecology and palaeobiogeography of the Iberian Peninsula. Cretaceous Research, 40: 158–169. https://doi.org/10.1016/j.cretres.2012.07.001

Sarjeant, W.A.S., Delair, J.B. & Lockley, M.G. 1998. The footprints of *Iguanodon*: A history and taxonomic study. Ichnos, 6(3): 183–202. https://doi.org/10.1080/10420949809386448

Scotese, C.R. & Golonka, J. 1992. Paleogeographic atlas. PALEOMAP Progress Report 20. University of Texas at Arlington, p. 1–34.

Seebacher, F. 2001. A new method to calculate allometric length–mass relationships of dinosaurs. Journal of Vertebrate Paleontology, 21(1): 51–60. https://doi.org/10.1671/0272-4634(2001)021[0051:ANMTCA]2.0.CO;2

Sereno, P.C., Wilson, J.A., Larsson, H.C.E., Dutheil, D.B. & Sues, H.D. 1994. Early Cretaceous dinosaurs from the Sahara. Science, 266(5183): 267–271. https://doi.org/10.1126/science.266.5183.267

Smith, A.G., Smith, D.G. & Funnell, B.M. 1994. Atlas of Mesozoic and Cenozoic coastlines. Cambridge University Press, 99 p. Cambridge, UK.

Svensen, H.H., Torsvik, T.H., Gallegaro, S., Augland, L., Heimdal, T.H., Jerram, D.A., Planke, S. & Pereira, E. 2018. Gondwana Large Igneous Provinces: Plate reconstructions, volcanic basins and sill volumes. In: Sensarma, S. & Storey, B.C. (editors), Large Igneous Provinces from Gondwana and adjacent regions. Geological Society of London, Special Publications 463: 17–40. https://doi.org/10.1144/SP463.7

Tennant, J.P., Mannion, P.D., Upchurch, P., Sutton, M.D. & Price, G.D. 2016. Biotic and environmental dynamics through the Late Jurassic – Early Cretaceous transition: Evidence for protracted faunal and ecological turnover. Biological Reviews, 92(2): 776–814. https://doi.org/10.1111/brv.12255

Terraza, R., Montoya, D., Reyes, G., Moreno, G., Fúquen, J. & Etayo–Serna, F. 2008. Geología del cinturón esmeraldífero oriental planchas 210, 228 y 229. Ingeominas, Internal report 2877, 129 p. Bogotá.

Terraza, R., Montoya, D., Reyes, G., Moreno, G., Fúquen, J., Torres, E., López, M., Nivia, A. & Etayo–Serna, F. 2013. Memoria explicativa: Geología de la plancha 229 Gachalá. Scale 1:100 000. Servicio Geológico Colombiano, Unpublished report, 296 p. Bogotá.

Thulborn, R.A. 2013. Lark Quarry revisited: A critique of the methods used to identify a large dinosaurian track–maker in the Winton Formation (Albian – Cenomanian), western Queensland, Australia. Alcheringa, 37(3): 312–330. https://doi.org/10.1080/03115518.2013.748482

Thulborn, T. 1990. Dinosaur tracks. Chapman and Hall, 410 p. London, UK.

Thulborn, T. 2016. Behaviour of dinosaurian track–makers in the Winton Formation (Cretaceous, Albian – Cenomanian) at Lark Quarry, western Queensland, Australia: running or swimming? Ichnos, 24(1): 1–18. https://doi.org/10.1080/10420940.2015.1129326

Torsvik, T.H. & Cocks, L.R.M. 2017. Earth history and palaeogeography. Cambridge University Press, 317 p. Cambridge, UK. https://doi.org/10.1017/9781316225523

Ulloa, C. & Rodríguez, E. 1979. Geología del cuadrángulo K–12 Guateque. Boletín Geológico, 22(1): 3–55.

van Hinsbergen, D.J.J., Torsvik, T.H., Schmid, S.M., Maţenco, L.C., Maffione, M., Vissers, R.L.M., Gürer, D. & Spakman, W. 2020. Orogenic architecture of the Mediterranean region and kinematic reconstruction of its tectonic evolution since the Triassic. Gondwana Research, 81: 79–229. https://doi.org/10.1016/j.gr.2019.07.009

Vialov, O.S. 1988. On the classification of dinosaurian traces. Ezhegodnik Vsesoyuznogo Paleontologicheskogo Obshchestva, 31: 322–325.

Weishampel, D.B., Barrett, P.M., Coria, R.A., le Loeuff, J., Xing, X., Xijin, Z., Sahni, A., Gomani, E.M.P. & Noto, C.R. 2004. Dinosaur distribution. In: Weishampel, D.B., Dodson, P. & Osmólska, H. (editors), The Dinosauria. 2nd edition, University of California Press, p. 517–606. Berkeley, USA.

Winkler, T.C. 1886. Histoire de l'ichnologie. Étude ichnologique sur les empreintes de pas d'animaux fossils, suivie de la description des plaques à impressions d'animaux, qui se trouvent au musée Teyler. Les Héritiers Loosjes, 200 p. Haarlem, the Netherlands.

Ziegler, A.M., Eshel, G., McAllister–Rees, P., Rothfus, T.A., Rowley, D.B. & Sunderlin, D. 2003. Tracing the tropics across land and sea: Permian to present. Lethaia, 36(3): 227–254. https://doi.org/10.1080/00241160310004657

Explanation of Acronyms, Abbreviations, and Symbols:

α, β, γ	Divarication angles (between II–III, III–IV, II–IV (= total divarication) respectively)
A, B, C	Anterior–most points of II, III, IV respectively
AC–G	Alejandro CORRALES–GARCÍA
AT	Anterior triangle (triangle connecting points A, B, C)
ATh	Anterior triangle height (length of the line passing through B and perpendicular to A–C)
ATw	Anterior triangle width (length A–C)
Avg	Average
BLII, BLIII, BLIV	Length of toe free segment (A, B, C along lines A–F, B–F, C–F to the intersection with lines through D (perpendicular to A–F), D–E, E (perpendicular to C–F) respectively)
D, E	Posteriormost points of hypices (between II–III, III–IV respectively)
DF (with number)	Río Batá dinosaur fooprints
F	Rear of metatarsophalangeal ("heel") pad impression (the posterior–most point of the footprint)
FA	Footprint axis (line B–F)
FL	Footprint length (distance B–F [≡ LIII])
FR	Footprint rotation (the angle between FA and TA)
FW	Footprint width (maximum width perpendicular to FL)
HH	Hip height (4 × FL)
II, III, IV	Digit number (also prefixed by B)
JVR–J	José Vicente RODRÍGUEZ
K, M	"heel"–hypex lengths (D–F, E–F respectively)
LFN	Leslie Francis NOÈ
LII, LIII, LIV	Digital lengths (lengths of II, III, and IV along A–F, B–F, and C–F respectively)
LIPs	Large Igneous Provinces
MG–P	Marcela GÓMEZ–PÉREZ
OAE	Oceanic anoxic events
PA	Pace angulation (angle between points B of three consecutive footprints)
pCO_2	Partial pressures of carbon dioxide
PL	Pace length (line joining points B of consecutive left and right footprints)
SGC	Servicio Geológico Colombiano
SL	Stride length (the line joining points B on consecutive footprints on the same (left or right) side)
TA	Trackway axis (the line midway between the lateral–most points of the left and right footprints)
TTL	Total trackway length (distance from F of DF1 to B of DF4)
TW	External trackway width (distance between the lines joining the lateral–most point of the footprints forming the trackway, and approximately parallel to TA)
WBII, WBIII, WBIV	Width at base of free segment of toe (length of line passing through D perpendicular to A–F, D–E, length of line passing through E perpendicular to C–F)
WGC–M	William G. CARANTON–MATEUS
WMII, WMIII, WMIII	Width at middle of free segment of toe (length half way between BLII, BLIII, BLIV, and perpendicular to A–F, B–F, C–F, respectively)

Authors' Biographical Notes

Leslie F. NOÈ is a vertebrate palaeontologist, stratigrapher, and historian of science, with special interests in the palaeobiology and evolution of the Sauropterygia. Leslie undertook his undergraduate studies in the School of Environmental and Applied Sciences at the University of Derby, UK, and graduated with honours with a Combined Subjects (Biology, Geology, and Physical Geography) degree. Leslie subsequently undertook doctoral studies, at the University of Derby, under the supervision of Dr. Don SMITH, Dr. Arthur CRUICKSHANK (Leicester Museums), and Dr. Derek WALTON, and wrote his PhD thesis on the cranial osteology of the Callovian (Middle Jurassic) Oxford Clay Formation pliosaurian genera *Liopleurodon*, *Simolestes*, and *Pachycostasaurus*. Leslie gained a wide range of experience during seven years in the Sedgwick Museum, University of Cambridge, UK, as well as undertaking undergraduate and postgraduate supervision, and undergraduate teaching in both the Department of Earth Sciences and the Department of Zoology. A curatorship at Thinktank, the Birmingham Science Museum, UK, followed, together with an honorary position at the University of Birmingham. Leslie returned to Cambridge as curator of the globally important Harland Collection of rocks, fossils, and minerals, before moving to Colombia, where he is currently Associate Professor in the Departamento de Geociencias, Universidad de los Andes in Bogotá. As the first geologist in the newly formed Geociencias Department, Leslie has written numerous undergraduate courses, and continues to publish on Mesozoic marine reptiles, with special reference to Colombian Cretaceous faunas.

Marcela GÓMEZ–PÉREZ is a vertebrate palaeontologist and sedimentary geologist with special interests in pliosauromorph marine reptiles, museology, and geological outreach. Marcela undertook her undergraduate studies in the Departamento de Geociencias of the Universidad Nacional de Colombia Sede Bogotá, where she graduated with honours. Marcela then received the Joven Investigador Colciencias and worked for the Departamento de Geología of the Universidad EAFIT, Medellín, implementing the Alkenone protocol for surface seawater temperatures during the Holocene. Marcela worked on a voluntary basis at the Sedgwick Museum of Earth Sciences in Cambridge, where her enthusiasm for museology started. She joined the Department of Earth Sciences, University of Cambridge, UK, for her doctoral studies under the supervision of Dr. David NORMAN with a prestigious Gates Cambridge Scholarship and a UK government Overseas Research Fellowship, at Newnham College. Following completion of her PhD studies, Marcela worked as a sedimentologist for CASP in Cambridge, before returning to Colombia to work on fine–grained sediment geochemistry for oil prospection. Marcela undertook post–doctoral research work, focusing on Colombian plesiosaur faunas, and teaching, in the Departamento de Geociencias, Universidad de los Andes. Currently Marcela is the vertebrate palaeontologist in the Museo Geológico José Royo y Gómez of the Servicio Geológico Colombiano in Bogotá, contributing to the development of vertebrate palaeontology and professionalizing all aspects of the museum.

José Vicente RODRÍGUEZ received a BS degree in geology and a MEng in materials from the Universidad Nacional de Colombia in Bogotá. He has extensive first–hand knowledge of Colombian geology which stems from wide–ranging field–work experience including geological mapping, stratigraphy, and sampling. He also has laboratory expertise in sedimentological core studies of Colombian Cretaceous rocks, and on magnetic fabric studies of igneous rocks. His most recent work is related to a tectonic study of the Triassic Pueblo Pluton in the Central Cordillera, and participation in the discovery of a section crossing the Cretaceous – Paleogene boundary in the easternmost Pacific (Gorgona Island).

Alejandro CORRALES–GARCÍA is an undergraduate student in the Departments of Geosciences and Biology at Universidad de los Andes, Bogotá. Alejandro is interested in palaeontology, geochronology, taxonomy, arthropods, reptiles, and amphibians. Starting in his first semester, Alejandro worked in the Museo de Historia Natural ANDES at Universidad de los Andes. For his undergraduate thesis Alejandro worked on the palaeoecology of Cambrian trilobites.

William G. CARANTON–MATEUS is an undergraduate student in the Department of Geosciences, with minors in biology and astronomy, at Universidad de los Andes, Bogotá. William's academic interests include structural geology, geochronology, and the effects of tectonic configurations on climate, global circulation, and life. During his early semesters, William was part of the La Venta Palaeontology project, which focused on primates along the Magdalena valley, Colombia, supported by the National Geographical Society and directed by Siobhan COOKE, PhD in physical anthropology at City University, New York. For his undergraduate thesis, William studied deformation events in the northwest margin of the Sierra Nevada de Santa Marta.

Volume 2

Chapter 12

Barremian Deposits of Colombia: A Special Emphasis on Marine Successions

https://doi.org/10.32685/pub.esp.36.2019.12
Published online 8 May 2020

Dr. *rer. nat*. Pedro PATARROYO[1]*

In memory of Prof. Dr. Jost WIEDMANN (31.03.1931–02.12.1993), Prof. Dr. Wolfram BLIND (11.10.1929–02.07.2017), Dr. Hermann DUQUE CARO (22.03.1935–20.09.2015), and Dr. José Ignacio MARTÍNEZ RODRÍGUEZ (15.05.1956–17.12.2016)

1 pcpatarroyog@unal.edu.co
Universidad Nacional de Colombia
Sede Bogotá
Departamento de Geociencias
Carrera 30 n.° 45–03
Bogotá, Colombia

* Corresponding author

Abstract Marine Barremian deposits are represented in different lithostratigraphic units in Colombia, from the central part of the country to the north. Up to the Upper Magdalena Valley, continental deposits have been reported in the Yaví Formation; although until now, only Aptian plant remains have been recognized.

Marine deposits include the shales and biomicrites of the Trincheras Formation to the west and southwest of Bogotá; the shales and biomicrites of the Fómeque Formation to the east and northeast of Bogotá; the biomicrites, biosparites, and shales of the Upper Calcareous Member of the Tibasosa Formation to the north of Bogotá; the shales and biomicrites of the Paja Formation near Villa de Leyva and to the northwest of Bogotá in the Middle Magdalena Valley; and in some cases, the biomicrites of the "Rosablanca" Formation.

Sporadic occurrences of Barremian ammonites have been reported in the biomicrites of the Yuruma Formation, that occurs in northern Colombia near Venezuela; in the *Cretácico del* Río *Cañas* (La Guajira) deposits; and in the central and western regions of the Central Cordillera. Nevertheless, these have been poorly studied.

Other lithostratigraphic units that have been cited as being related to the Barremian deposits, albeit without biostratigraphic support, are the Tibú–Mercedes Formation and, possibly, the Río Negro Formation. Barremian ammonites have been reported in the La Naveta Formation but with controversial stratigraphic control.

Different fossil fauna and flora have been reported in these units, but ammonite biostratigraphy is the principal tool used to identify chronostratigraphic levels. Tethyan fauna allows one to correlate Barremian successions with standard biozones and biohorizons from the Mediterranean area, based on the *Psilotissotia*, *Nicklesia*, *Pulchellia*, *Gerhardtia*, *Heinzia*, etc.

The sedimentary and ecological variations in the lithological units are the consequence of environmental factors, paleoecology, and basin differentiation that have recorded tectonic or subsidence influxes due to their local paleogeographic positions.

Keywords: *Barremian deposits, biostratigraphy, lithostratigraphy, Colombia.*

Resumen Los depósitos marinos del Barremiano en Colombia están representados en diferentes unidades litoestratigráficas desde la parte central del país y hacia el norte. Para el Valle Superior del Magdalena han sido reportados depósitos continentales de la Formación Yaví, aunque allí hasta ahora se han reconocido restos vegetales del Aptiano.

Citation: Patarroyo, P. 2020. Barremian deposits of Colombia: A special emphasis on marine successions. In: Gómez, J. & Pinilla–Pachon, A.O. (editors), The Geology of Colombia, Volume 2 Mesozoic. Servicio Geológico Colombiano, Publicaciones Geológicas Especiales 36, p. 403–439. Bogotá. https://doi.org/10.32685/pub.esp.36.2019.12

Los depósitos marinos incluyen las lodolitas y biomicritas de la Formación Trincheras al oeste y al suroeste de Bogotá; las lodolitas y biomicritas de la Formación Fómeque al este y noreste de Bogotá; las biomicritas, bioesparitas y lodolitas del Miembro Calcáreo Superior de la Formación Tibasosa al norte de Bogotá; las lodolitas y biomicritas de la Formación Paja cerca de Villa de Leyva y al noroeste de Bogotá en el Valle Medio del Magdalena; y en algunos casos las biomicritas de la Formación "Rosablanca".

Para las biomicritas de la Formación Yuruma que se presentan al norte de Colombia, cerca de Venezuela; los depósitos del *Cretácico del Río Cañas* (La Guajira); y las regiones central y occidental de la cordillera Central se han reportado ocurrencias esporádicas de amonitas del Barremiano. Sin embargo, estas han sido muy poco estudiadas.

La Formación Tibú–Mercedes y posiblemente la Formación Río Negro son otras unidades litoestratigráficas que han sido relacionadas con los depósitos del Barremiano, aunque sin soporte bioestratigráfico. En la Formación La Naveta se reportaron amonitas del Barremiano, pero con control estratigráfico insuficiente.

Diferentes fósiles de fauna y flora han sido mencionados dentro de las unidades referidas, pero la bioestratigrafía de las amonitas es la principal herramienta para identificar los niveles cronoestratigráficos. La fauna del Tetis permite correlacionar las sucesiones del Barremiano con las biozonas y biohorizontes estándar del área del Mediterráneo con base en *Psilotissotia*, *Nicklesia*, *Pulchellia*, *Gerhardtia*, *Heinzia*, etc.

Las variaciones sedimentarias y ecológicas de las unidades litológicas son consecuencia de factores ambientales, la paleoecología y la diferenciación de la cuenca que puede tener influencia tectónica o de subsidencia debido a la posición paleogeográfica local.

Palabras clave: *depósitos del Barremiano, bioestratigrafía, litoestratigrafía, Colombia.*

1. Introduction

Barremian marine deposits in Colombia outcrop in different locations; they principally outcrop along the Eastern Cordillera, although some occur in the Central Cordillera, and others occur in northern Colombia (La Guajira province). It may be possible to find other deposits, such as those in the continental successions to the north of the Upper Magdalena Valley and the serranía del Perijá (Figure 1), but there are not enough data to indicate that they comprise a Barremian range.

Von Buch (1838, 1839) first showed the existence of Lower Cretaceous deposits in Colombia based on the paleontological collection of von Humboldt and Degenhardt, which is kept in the Museum of Natural History in Berlin (Germany). Thus, the first allusion to the Villeta denomination (von Humboldt, 1816, 66; 1823; 1853; 1888) was Villeta shales (Thonschiefer). Thereafter, Uhlig (1882, 94–95) provided the first mention of Barremian deposits in Colombia.

The most investigated succession in Colombia is represented near Villa de Leyva (Boyacá) in the Paja Formation (cf. Bürgl, 1954, 1956; Etayo–Serna, 1968a, 1968b, 1968c; Patarroyo, 2000a, 2000b, 2000c, 2004), which is used here as a reference to other marine lithostratigraphic units that include Barremian deposits. Ammonites, wood, bivalves, gastropods, echinoids, serpulids, foraminifera, and vertebrates have been recognized in the Barremian successions.

The Barremian ammonites from Colombia record a Tethyan influence, but not all genera and species from the western Mediterranean province are present in Colombian deposits (Patarroyo, 2000a, 2000b, 2004).

The Barremian boundary with the upper Hauterivian in Colombia remains unclear. *Crioceratites* can be found in upper Hauterivian and lower Barremian deposits. In the upper part of the upper Barremian, *Colchidites* and then *Pseudocrioceras* (Kakabadze & Sharikadze, 2004) appear, whereas in the lower Aptian, *Prochelonicera*s (Kakabadze & Sharikadze, 2004),

Figure 1. Location map with the main places mentioned, as follows: (1) Yuruma Hill, (2) Uribia, (3) Riohacha, (4) Santa Marta, (5) Mingueo (Dibulla), (6) Becerril, (7) Pailitas, (8) Ábrego, (9) Cúcuta, (10) Simití, (11) Gramalote, (12) Bucaramanga, (13) Betulia, (14) Yarumal, (15) San Andrés (Santander), (16) Barichara, (17) Curití, (18) Socorro, (19) El Cocuy, (20) Ebéjico, (21) Medellín, (22) Oiba, (23) La Estrella, (24) Belén, (25) Vélez, (26) Betéitiva, (27) Abejorral, (28) Tibasosa, (29) Corrales, (30) Villa de Leyva, (31) Firavitoba, (32) Berlín, (33) Muzo, (34) Tunja, (35) Pesca, (36) Pajarito, (37) Rondón, (38) San Félix, (39) Valle Alto, (40) Garagoa, (41) Villeta, (42) La Vega, (43) Sasaima, (44) Gachalá, (45) Bogotá, (46) Apulo, (47) Fómeque, (48) Tocaima, (49) Viotá, (50) Cáqueza, and (51) El Cobre Creek (San Luis, Tolima). (LMV) Lower Magdalena Valley; (MMV) Middle Magdalena Valley; (UMV) Upper Magdalena Valley; (SNSM) Sierra Nevada de Santa Marta; (SP) Serranía del Perijá; (EC) Eastern Cordillera; (CC) Central Cordillera; (WC) Western Cordillera.

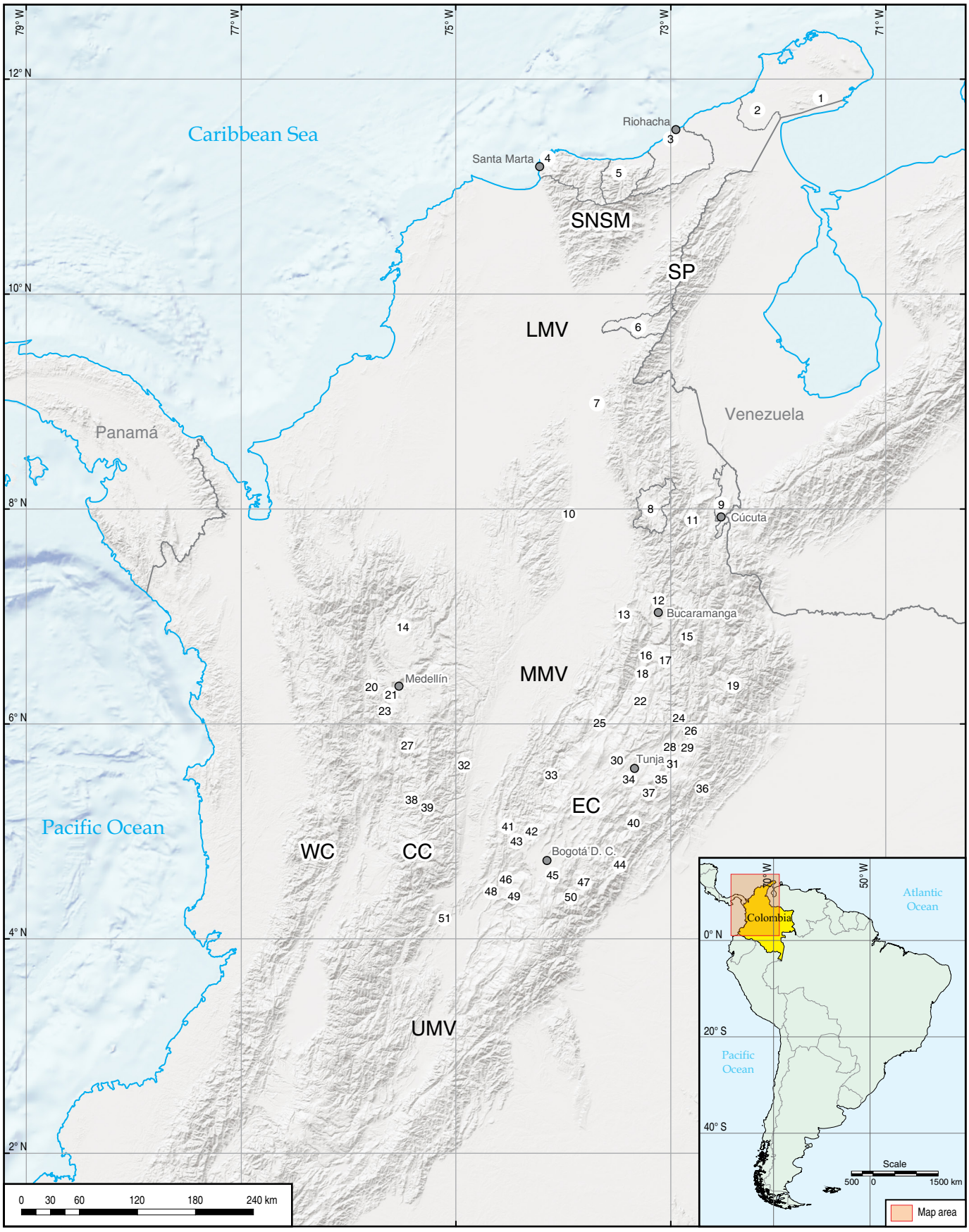
79° W
77° W
75° W
73° W
71° W
12° N
10° N
8° N
6° N
4° N
2° N
Caribbean Sea
Pacific Ocean
Panamá
Venezuela
Riohacha
Santa Marta
Cúcuta
Bucaramanga
Medellín
Tunja
Bogotá D. C.
SNSM
SP
LMV
MMV
EC
WC
CC
UMV
1
2
3
4
5
6
7
8
9
10
11
12
13
14
15
16
17
18
19
20
21
22
23
24
25
26
27
28
29
30
31
32
33
34
35
36
37
38
39
40
41
42
43
44
45
46
47
48
49
50
51
0 30 60 120 180 240 km
90° W
50° W
Atlantic Ocean
Colombia
0° N
20° S
40° S
Pacific Ocean
Scale
500 0 1500 km
Map area

Dufrenoyia, and *Cheloniceras* appear. Between these intervals, the fossil record is poor. Unfortunately, Bürgl (1956) introduced three–fold divisions of the Barremian in Colombia (lower, middle, and upper); therefore, international researchers believe that this is among the best places to recognize these marine deposits. Although Mutterlose et al. (2014, 260) officially used the mid–Barremian as the boundary interval between the upper lower–lower upper Barremian and the lower/upper Barremian, the International Commission on Stratigraphy only recognizes the lower and upper Barremian.

2. Barremian Stage

Coquand (1861) originally introduced the Barremian denomination near Barrême (Alpes–de–Haute–Provence, SE France), which is the type locality. Busnardo (1965) clarified the definition of the Barremian Stage using the outcrops along the way to Angles (SE France) because, according to Coquand, it actually included the upper Hauterivian and Barremian succession.

Although the Global Boundary Stratotype Section and Point (GSSP) of the Barremian Stage has not been established until now, its ammonite biostratigraphy has been used to recognize its subdivisions in the lower and upper Barremian following the western Mediterranean successions (Figure 2). The lower Barremian substage includes 5 biozones (Reboulet et al., 2014, 2018), some subzones and biohorizons (Reboulet et al., 2014, Table 1); the upper Barremian substage includes 4 biozones (Reboulet et al., 2014, 2018), more subzones and one biohorizon (Reboulet et al., 2014, Table 1). A candidate for the GSSP (Company et al., 1995; Ogg et al., 2012; Rawson et al., 1996) is a succession in Río Argos (near Caravaca, Murcia province, Spain) with the first apparition data (FAD) of the *Taveraidiscus hugii* auctorum formerly termed "*Spitidiscus*" *hugii* (Company et al., 1995; Hoedemaeker et al., 1993, 2003) and the *Avramidiscus vandeckii* ammonite group (cf. Company et al., 1995; Rawson et al., 1996). The boundary interval in Italy falls within the uppermost part of magnetic polarity zone M4n (at approximately Chron M4n.8 ¼ "M5n.8") (Bartolocci et al., 1992; Channell et al., 1995; as cited in Ogg et al., 2012).

The boundary between the lower and upper Barremian is related to the FAD of the ammonite "*Ancyloceras*" *vendenheckii* (Rawson et al., 1996, 28; Reboulet et al., 2009, 2011, 2014, 2018; Ogg et al., 2012). A GSSP substage is proposed near Caravaca, Spain (Ogg et al., 2012; Company et al., 1995). This substage boundary level is within the uppermost part of the magnetic polarity zone M3r (at approximately Chron M3r.8) in Italy (Bartolocci et al., 1992; Channell et al., 1995; as cited in Ogg et al., 2012).

2.1. Biostratigraphy

"Biostratigraphic units (biozones) are bodies of strata that are defined or characterized on the basis of their contained fossils. Biostratigraphic units only exist where the particular diagnostic feature or attribute on which they are based has been identified. Biostratigraphic units, therefore, are objective units based on the identification of fossil taxa" (Murphy & Salvador, 1999, 261).

This means that taxonomy affects the denominations of biozones; however, taxonomy may be artificial because generic determination principally depends on the interpretation of the specialist. Therefore, some citations here related to biostratigraphy and taxonomy do not follow some postulates that have recently been recognized (Reboulet et al., 2011, 2014, 2018), such as some species of "*Heinzia*" and "*Gerhardtia*". In taxonomic hierarchy, only the species is tangible; the other categories are artificial and are dependent on the author (cf. Vermeulen & Klein, 2006). Therefore, the specific determination, which is independent of the generic designation, allows one to identify stratigraphic levels that can be correlated. Therefore, it may be considered that only one or two authors have established synonym lists of Barremian ammonites (cf. Vermeulen & Klein, 2006).

In this study, some Barremian generic denominations follow those of classical publications, such as *Psilotissotia* sensu Hyatt (1900), *Gerhardtia* and *Carstenia* sensu Hyatt (1903), and *Heinzia* sensu Bürgl (1956).

The Barremian Stage in the western Mediterranean province (Reboulet et al., 2014, Table 1; 2018, Table 1b) is officially divided into the lower and upper Barremian. To Reboulet et al., (2014, Table 1), the lower Barremian includes 5 biozones, some subzones and biohorizons (Figure 2), including *Taveraidiscus hugii* auctorum (*T. hugii* auctorum and *Psilotissotia colombiana* Subzones), *Kotetishvilia nicklesi*, *Nicklesia pulchella*, *Kotetishvilia compressissima* (*Holcodiscus fallax*, *Nicklesia didayana*, "*Heinzia*" *communis*, and *Subtorcapella defayae* Horizons), and *Moutoniceras moutonianum* (*Coronites darsi* and "*Heinzia*" *caicedi* Horizons). The upper Barremian includes 4 biozones, some subzones and horizons (Figure 2), such as *Toxancyloceras vandenheckii* (*T. vandenheckii* and *Barrancyloceras barremense* Subzones), *Gerhardtia sartousiana* (*G. sartousiana*, "*G.*" *provincialis*, and *Hemihoplites feraudianus* Subzones), *Imerites giraudi* (*I. giraudi* and *Heteroceras emerici* Subzones), and *Martelites sarasini* (*M. sarasini* (*Anglesites puzosianum* Horizon) and *Pseudocrioceras waagenoides* Subzones). Recently, Reboulet et al. (2018) introduced new considerations related to ammonite taxonomy and biostratigraphy of the Barremian (Figure 2), in which they did not use biohorizons. Moreover, they referred that the meeting in Vienna of 2017 deleted the term "auctorum" from the *Taveraidiscus hugii* index species (cf. Figure 2) and stated the problematic identification of *Psilotissotia colombiana* in the Mediterranean forms.

In Colombia, most Barremian ammonites record a Tethyan influence that allows one to correlate these deposits with the western Mediterranean successions. *Psilotissotia malladae*, *Nicklesia pulchella*, *Pulchellia communis*, "*P*". *caicedi*, *Heinzia provincialis,* and *Carstenia lindigii* are present in both areas.

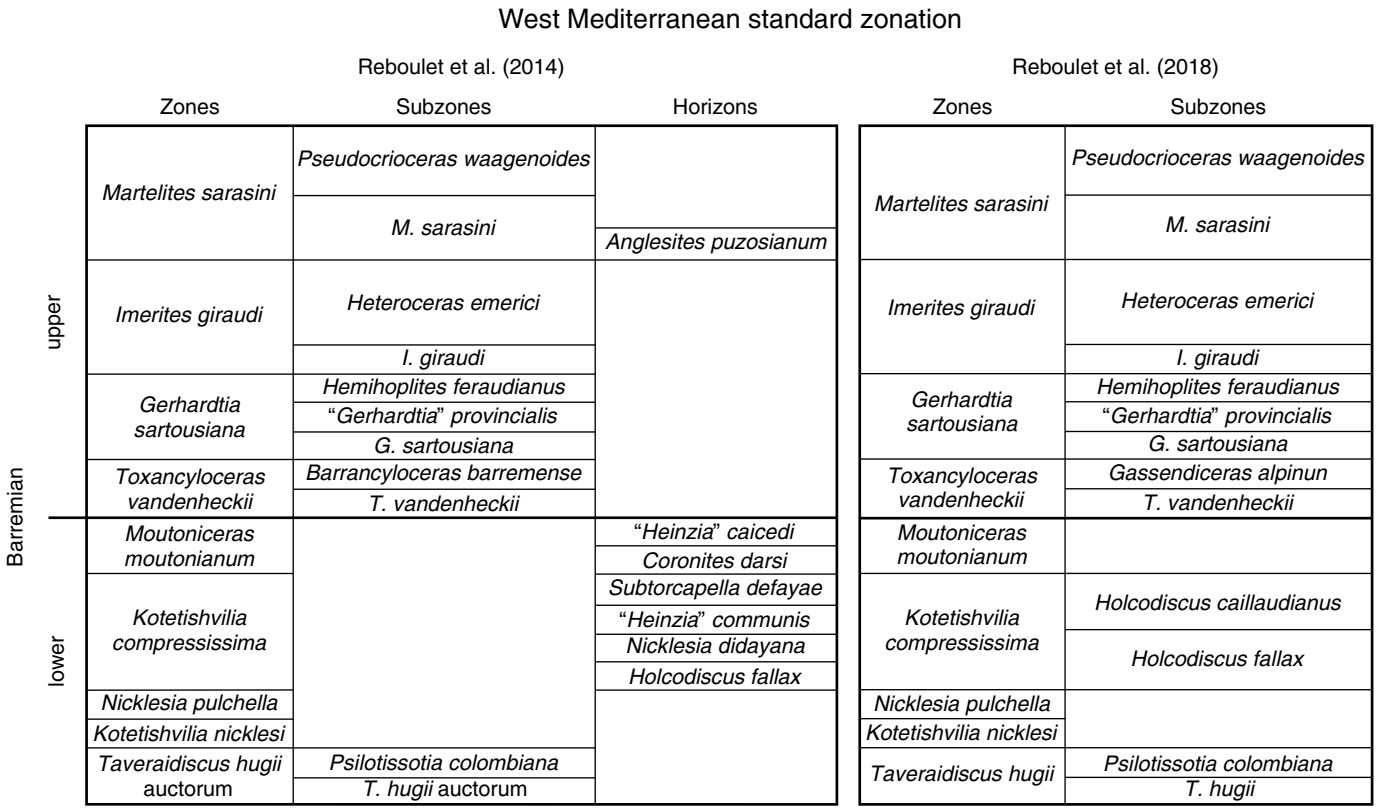

Figure 2. Western Mediterranean standard zonation of the Barremian Stage (Taken from Reboulet et al., 2014, 2018).

Following the best exposed Barremian deposits in Colombia, as a part of the Paja Formation (Hauterivian – Aptian) in the Villa de Leyva area (Figures 3, 4, 5), it is possible to affirm that the faunal representation is better in the lower Barremian deposits than in those of the upper Barremian deposits. Ammonites from the lower Barremian are represented by *Psilotissotia colombiana* (d'Orbigny, 1842); *P. malladae* (Nicklès, 1894); *Pedioceras caquesense*; *Crioceratites* sp., *C.* (*Paracrioceras*) *leyvaensis* Kakabadze & Hoedemaeker, 2004; *Buergliceras buerglii* Etayo–Serna, 1968c; *Acanthoptychoceras* ? *trumpyi* Kakabadze & Thieuloy, 1991 (cf. Klein et al., 2007); *Nicklesia pulchella* (d'Orbigny, 1840); *N. nodosa* Bürgl, 1956; *N. karsteni* Hyatt; 1903; *Parasaynoceras horridum* (d'Orbigny, 1840); *Acrioceras julivertii* Etayo–Serna, 1968c; *Valdedorsella inca* (Forbes, 1845); *Karsteniceras beyrichi* (Karsten, 1858); *Phylloceras* sp.; *Lytoceras* sp.; *Pulchellia galeata* (von Buch, 1838); *P. communis* Bürgl, 1956; *P. hettneri* Gerhardt, 1897; *P. fasciata* Gerhardt, 1897; *P. selecta* Gerhardt, 1897; and "*P*". *caicedi* (Karsten, 1858). Ammonites from the upper Barremian are represented by *Gerhardtia veleziensis* (Hyatt, 1903); *G. galeatoides* (Karsten, 1858); *Heinzia provincialis* (d'Orbigny, 1850); *H. colleti* (Bürgl, 1956); *Carstenia lindigii* (Karsten, 1858); *Colchidites breistrofferi* Kakabadze & Thieuloy, 1991; *Pseudohaploceras* cf. *liptoviense* (Zeuschner 1856); *Pseudocrioceras anthulai* (Eristavi, 1955); *Ancyloceras* sp., *Heteroceras* sp., *Kutatissites* sp., and *Moutoniceras* cf. *moutonianum* (d'Orbigny, 1850).

Until now, it has not been clear if *Spitidiscus* (*S. ursulae* (Riedel, 1938), *S. simitiensis* (Haas, 1960)), *Toxancyloceras,* and *Imerites* are present in the Barremian deposits.

Patarroyo (2000a, 2000b, 2004) introduced interval zones to the Colombian Barremian deposits (Figure 6) following the first appearance data of lower Barremian taxa, such as *Psilotissotia colombiana*, *Nicklesia pulchella*, and *Pulchellia galeata*, and upper Barremian taxa, such as *Heinzia* (*Gerhardtia*) *veleziensis* (actually *Gerhardtia veleziensis,* Figure 7) and *Colchidites breistrofferi*. However, some intervals in this succession include poor fossil recovery or there are no fossils at all. Thus, the upper part of the zones can be considered intrazones with respect to *Pulchellia galeata*, *Gerhardtia veleziensis,* and *Colchidites breistrofferi* (Figure 6). However, directly above the *Colchidites breistrofferi* Zone, Kakabadze & Sharikadze (2004) suggested three biostratigraphical levels, the first is the succession with *Pseudocrioceras anthulai* (uppermost Barremian), the second with *Procheloniceras albrechtiaustriae* (lowest Aptian), and the third with *Cheloniceras kiliani* (Figure 7), that are below the first Aptian assemblage zone of Etayo–Serna (1979). But directly above *Colchidites breistrofferi* Zone there are no sufficient outcrops (containing rich ammonites fauna) and therefore to solve the problem of determination of the uppermost Barremian *Pseudocrioceras anthulai* Horizon still needs further additional palaeontological and lithological data (cf. Kakabadze & Sharikadze, 2004).

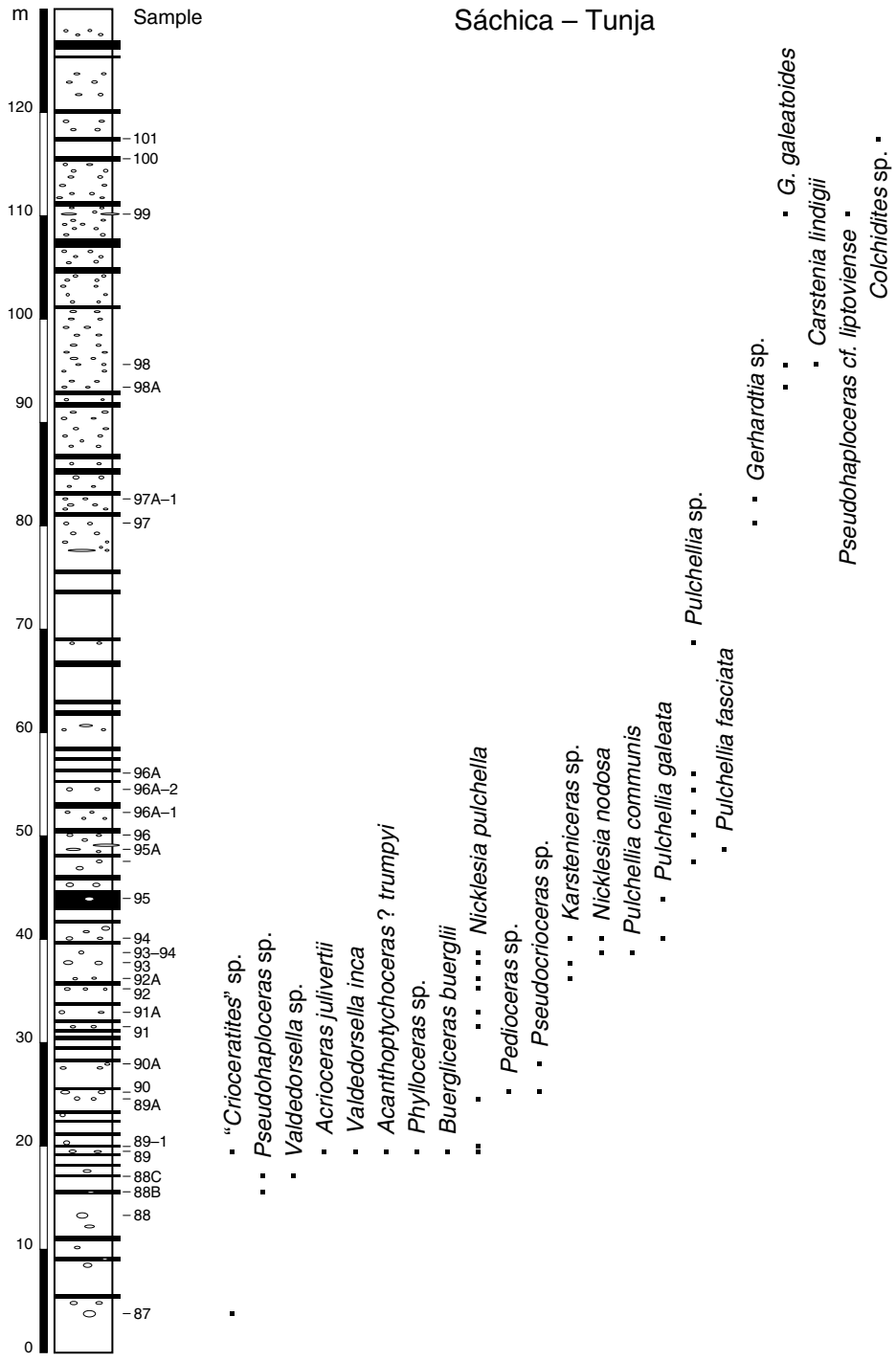

Figure 3. Succession of the Sáchica–Tunja way with the Barremian ammonite distribution of the Paja Formation (Boyacá province).

2.2. Lithostratigraphy

Although the Cretaceous successions along the Eastern Cordillera in Colombia have been studied in different investigations, they are poorly understood. Homonymies, synonymies, and stratigraphic generalization are the most important problems related to the differentiation of the basin.

In central Colombia, Barremian deposits are included in the Paja Formation (cf. Basse, 1928; Bürgl, 1954, 1956; Collet, 1924; Etayo–Serna, 1964, 1968a, 1968b, 1968c; Gerhardt, 1897; Haas, 1960; Karsten, 1858; Patarroyo, 1997, 2000a, 2000b, 2000c, 2004), the Trincheras Formation (cf. Basse, 1950; Cáceres & Etayo–Serna, 1969a, 1969b; Patarroyo, 2011; von Buch, 1838, 1839), the Fómeque Formation (cf. Bürgl, 1956;

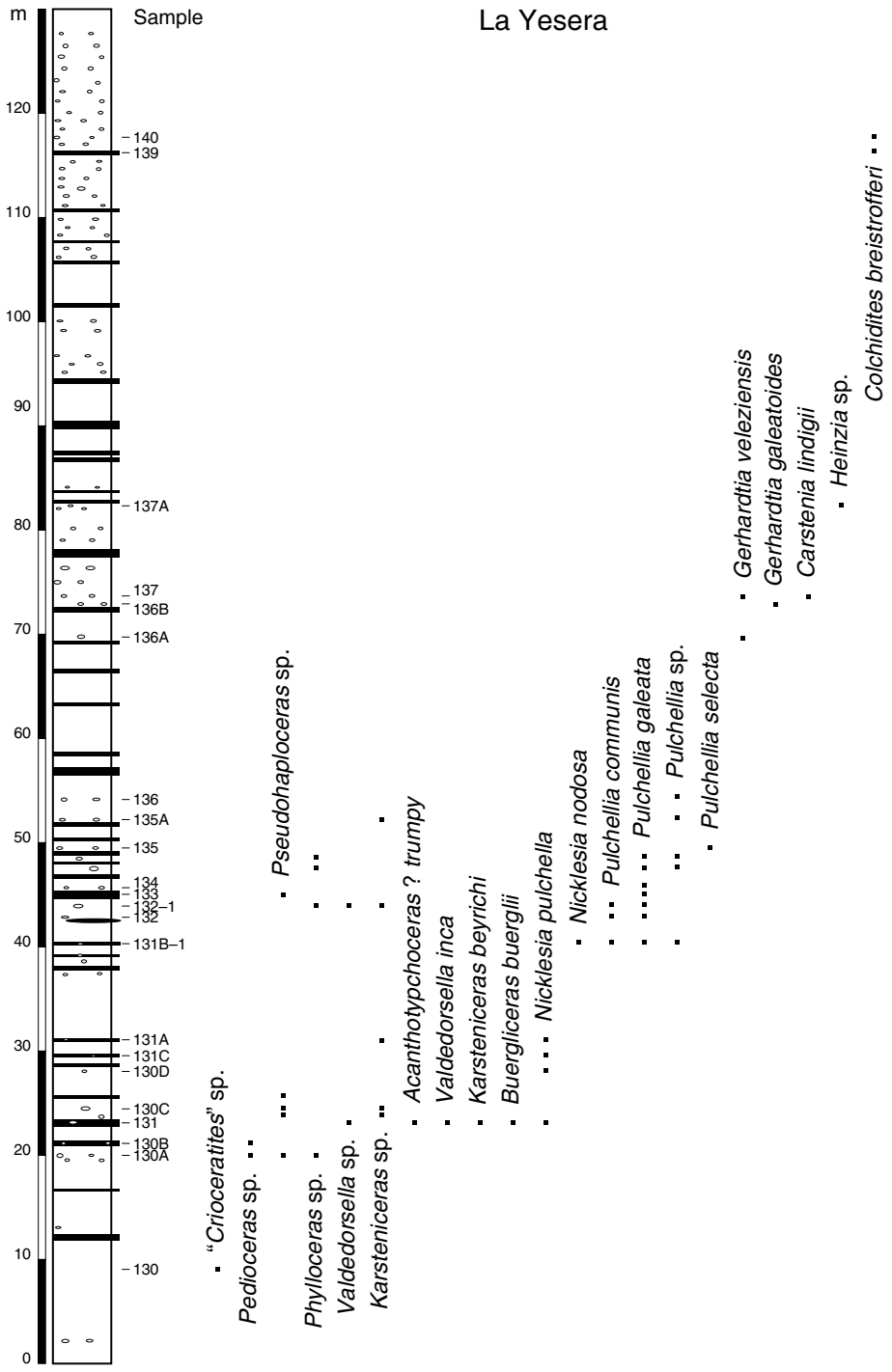

Figure 4. Succession of La Yesera Hill with the Barremian ammonite distribution of the Paja Formation in Villa de Leyva (Boyacá province).

Etayo–Serna, 1964; Karsten, 1858; Royo y Gómez, 1945a; Ramos–Gámez, 2016; Ulloa et al., 2000), the Upper Calcareous Member of the Tibasosa Formation (Patarroyo, 2005, 2017), in some areas of the Central Cordillera in the Quebradagrande Complex (cf. Etayo–Serna, 1985a; Grosse, 1926), and occasionally in the "Rosablanca" Formation (Blau, 1993; Gaona–Narváez et al., 2013; Etayo–Serna in Mantilla–Figueroa et al., 2006; Morales et al., 1958; Patarroyo, 2017). They have also been found in northern Colombia in La Guajira province, in the poorly known successions of the *Cretácico del Río Cañas* (Colmenares et al., 2007) and the Yuruma Formation (Bürgl, 1958; Patarroyo, 2011; Renz, 1960; Rollins, 1965). Following Fabre (1985) and Etayo–Serna (1985b), the "Areniscas de Las Juntas" Formation comprises Barremian deposits, and in the serranía del

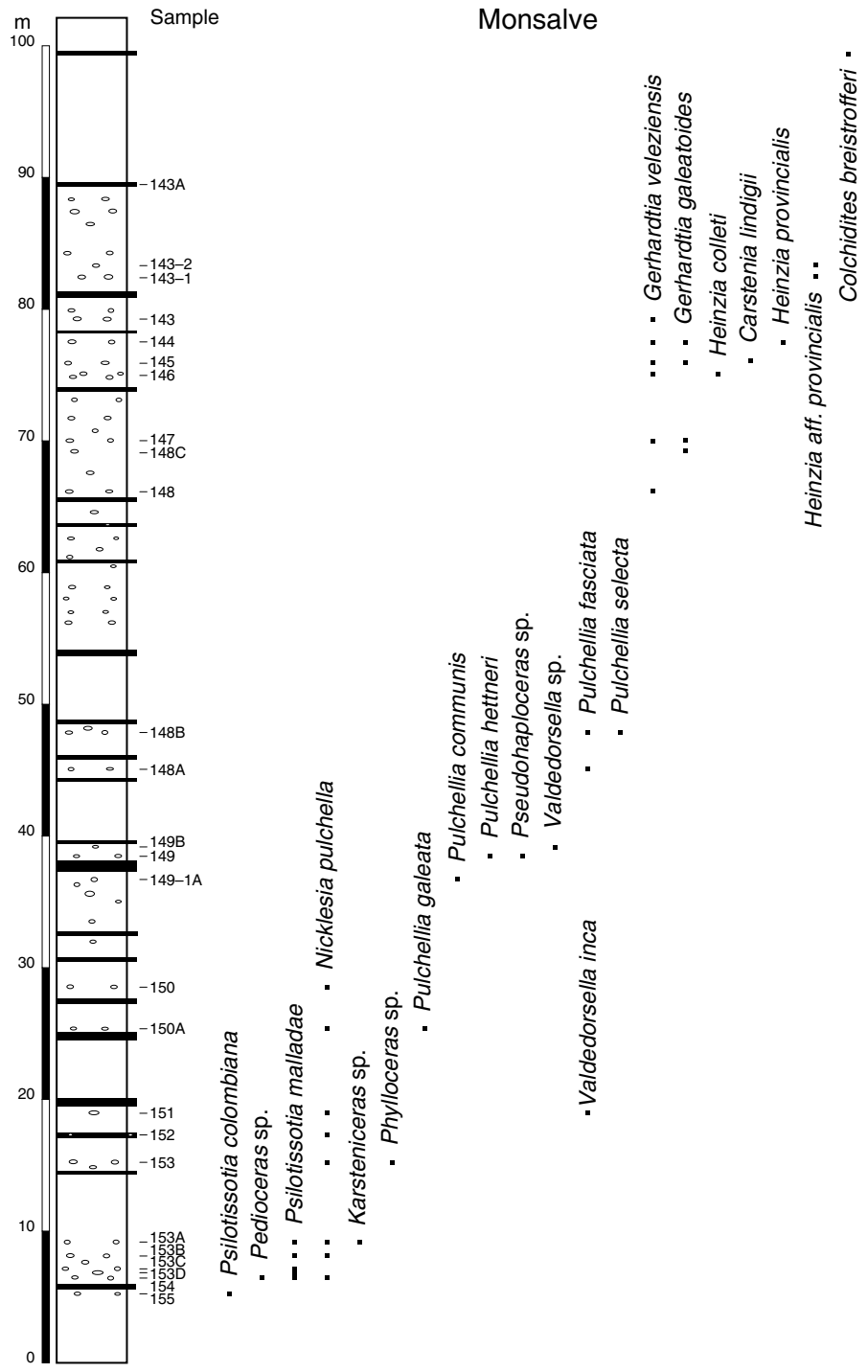

Figure 5. Succession of the Monsalve Hill with the Barremian ammonite distribution of the Paja Formation in Villa de Leyva (Boyacá province).

Perijá and Catatumbo areas, the Río Negro Formation contains sandy Barremian deposits (Julivert, 1968, 415–417; Petrash et al., 2016, Figure 2; Renz, 1959, 6; Sutton, 1946; van Andel, 1958), given the existence of Aptian ammonites in the overlying Cogollo Formation or Group in Venezuela and, probably, in some places in Colombia. Barremian ammonites have been reported between Ábrego and Gramalote near Cúcuta (Norte de Santander) (Royo y Gómez in Botero–Restrepo & Sarmiento–Rojas, 1947, 36; Bürgl, 1956, 32) are now considered to be part of the Tibú and Mercedes Formations (Vargas & Arias, 1981). Some citations without illustrations related to Barremian fauna are found in Petters (1954) in Becerril and Pailitas (Cesar province), in Langston & Durham (1955) and in Etayo–Serna et al. (1969, 232). Other citations have mentioned Barremian

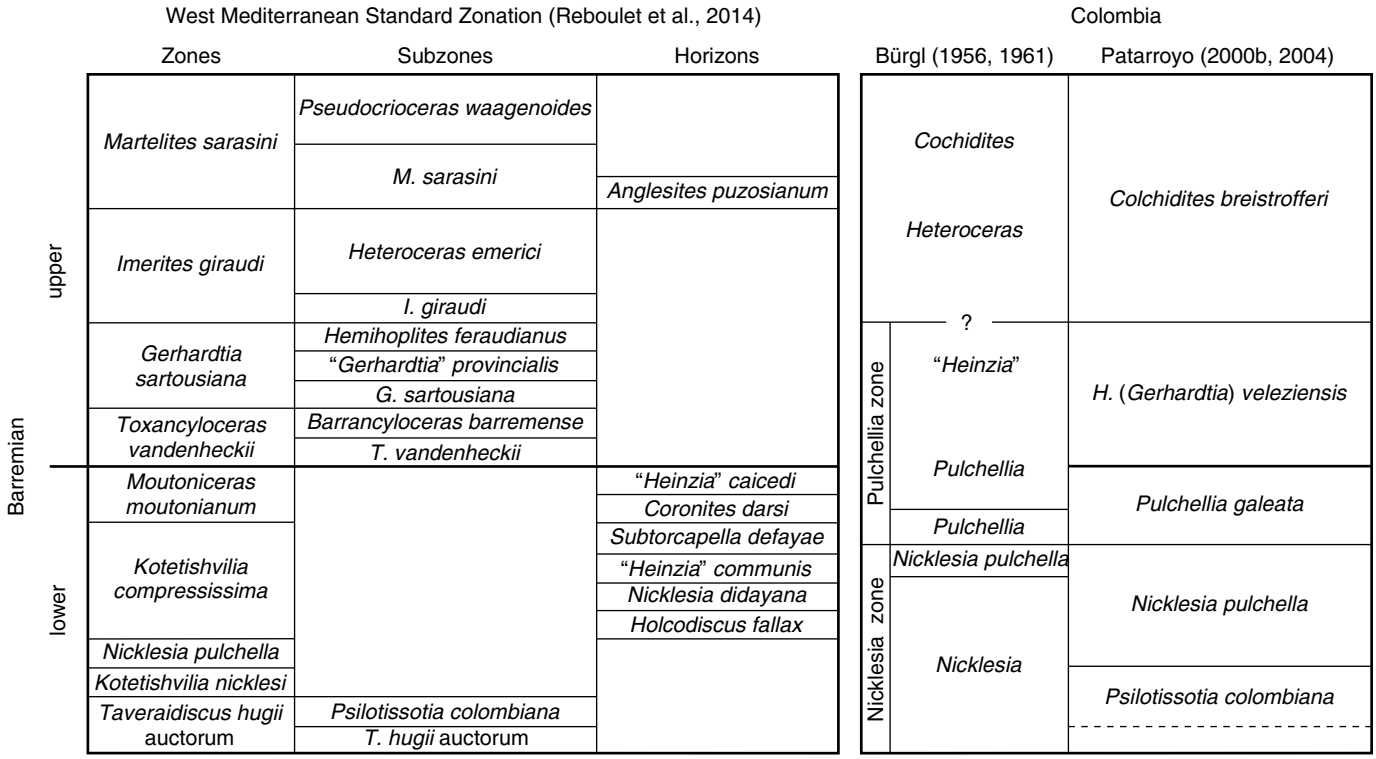

Figure 6. Western Mediterranean standard zonation of the Barremian Stage (Taken from Reboulet et al., 2014) and biostratigraphy correlated to the Colombian Barremian.

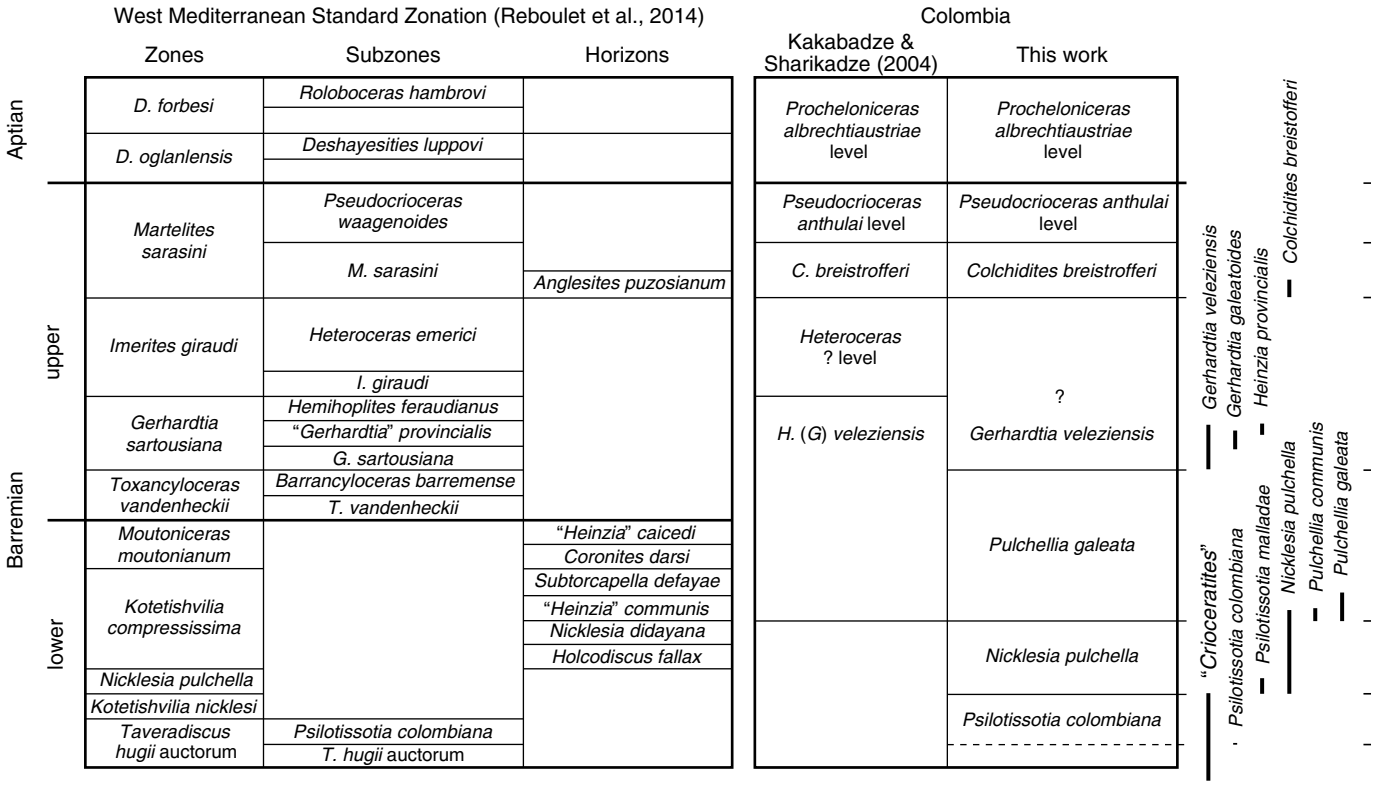

Figure 7. Western Mediterranean standard zonation of the Barremian Stage (Taken from Reboulet et al., 2014) and the new correlations of the biostratigraphy to the Colombian Barremian.

deposits in El Cobre Creek from San Luis (Tolima province), in San Andres (Santander province) by Acosta (1960, 36) and in central Colombia in the denominated Muzo Formation and El Peñón Formation (Reyes et al., 2006). The continental deposits extending from the Yaví Formation to the northern Upper Magdalena Valley and the Río Negro Formation of the serranía del Perijá likely represent Barremian successions.

2.2.1. Paja Formation

The Paja Formation was informally introduced by Wheeler (1929, 5) as the "La Paja" Formation; however, since Morales et al. (1958, 648), it has been better known by its formal name as the Paja Formation. Because this denomination has been more widely diffused, it is not convenient to readopt the old denomination following the priority recommendation of the International Commission on Stratigraphy: "Publication of a properly proposed, named, and described unit has priority. However, priority alone does not justify displacing a well–established name by one not well known or rarely used; nor should an inadequately established name be preserved merely because of priority" (Murphy & Salvador, 1999, 258). There is not a type section designation or description for the Paja Formation; therefore, a lectostratotype is necessary to typify this lithostratigraphic unit, although its name originates from La Paja Creek (in the Middle Magdalena Valley to the NW of Bogotá), which is a stream that principally follows the bed direction (Figure 8). Shales, biomicrites, and calcareous concretions represent the succession, which is 625 m in thickness at the type locality (Morales et al., 1958, 650). Barremian and Aptian fossils are included in the Paja Formation at the type locality (Tablazo area, Santander province). *Nicklesia pulchella*, *Psilotissotia* sp., *Valdedorsella cf. inca*, *Pulchellia galeata*, *Karsteniceras* sp., and *Gerhardtia veleziensis* have been recovered near Barichara (Santander province) in the Barremian deposits of the Paja Formation (Figures 9, 10, 11). The lower boundary with the Rosablanca Formation is sharp (Valanginian – Hauterivian, cf. Etayo–Serna in Guzmán, 1985; Schemm–Gregory et al., 2012), although near Barichara (Santander province), the lowest Barremian ammonites, including *Valdedorsella* or *Pseudohaploceras* sp. and *Pedioceras* sp. (Figure 12), were found towards the top of the Rosablanca Formation. The upper boundary of the Paja Formation is transitional to the Tablazo Formation (Aptian – Albian). However, in the Villa de Leyva area (Boyacá province), the Paja Formation (Figure 13) includes deposits ranging from the Hauterivian to the Aptian (Etayo–Serna, 1968a, 1968b, 1968c; Patarroyo, 2000a, 2000b, 2004); as in the Vélez area (Patarroyo, 2009), they overlie the Ritoque Formation (Valanginian – Hauterivian) and underlie the "San Gil inferior" Formation (Aptian – Albian). *"Crioceratites"* sp., *Paracrioceras leyvaense*, *Psilotissotia colombiana*, *P. malladae*, *Buergliceras buerglii*, *Acanthoptychoceras*? *trumpyi*, *Pedioceras caquesense*, *Nicklesia pulchella*, *N. nodosa*, *Lamellapthycus* ? sp., *Valdedorsella inca*; *Karsteniceras beyrichi*, *Phylloceras* sp.; *Pseudohaploceras* sp., *Pulchellia galeata*, *P. communis*, *P. hettneri*, *P. fasciata*, *P. selecta*, *Gerhardtia veleziensis, G. galeatoides*, *Heinzia provincialis*, *H. colleti, Carstenia lindigii*, and *Colchidites breistrofferi* (Figures 12, 14, 15, 16, 17) have been found in the Barremian deposits of the Paja Formation (Figures 3, 4, 5) in the Villa de Leyva area (Boyacá province). Moreover, in the Vélez area (Santander province), "*Pulchellia*" *caicedi* and *Lytoceras* sp. (Figures 18, 19) have also been found (Bustos, 2017). To the Middle Magdalena Valley (Tablazo–Magdalena Sub–basin) area, exceptional Barremian deposits are recognized in the "Rosablanca" Formation (Blau, 1993; Gaona–Narváez et al., 2013; Patarroyo, 2017) because of the presence of *Gerhardtia veleziensis*, *G. galeata*, *Kutatissites* sp., and *Ancyloceras*? sp. (Figure 20) and in the eastern Central Cordillera (Etayo–Serna in Mantilla–Figueroa et al., 2006; Morales et al., 1958) near Simití (south Bolivar province).

Figure 8. La Paja Creek valley (Betulia, Santander province near Puente El Tablazo). South margin of the Sogamoso River or Dam.

2.2.2. Fómeque Formation

The Fómeque Formation (Hubach, 1931) to the east and northeast of Bogotá contains shales, sandstones, biomicrites, biosparites, and calcareous concretions that range from the upper Hauterivian to the Aptian (Bürgl, 1959; Ramos–Gámez, 2016; Royo y Gómez, 1945b, 116). Unfortunately, this lithostratigraphic unit does not have a type section; therefore, its description is very poor. However, it clearly contains Barremian fossils (Breistroffer, 1936; Bürgl, 1956; Campbell & Bürgl, 1965; Haas, 1960; Hubach, 1957a, 1957b; Karsten, 1858; Ramos–Gámez, 2016; Royo y Gómez, 1945b). *Nicklesia pulchella*, *Gerhardtia* cf. *galeatoides,* and *Atherfieldastacus*? sp. (Figures 12, 21) have been recovered in the Barremian deposits of the Fómeque Formation (Ramos–Gámez, 2016).

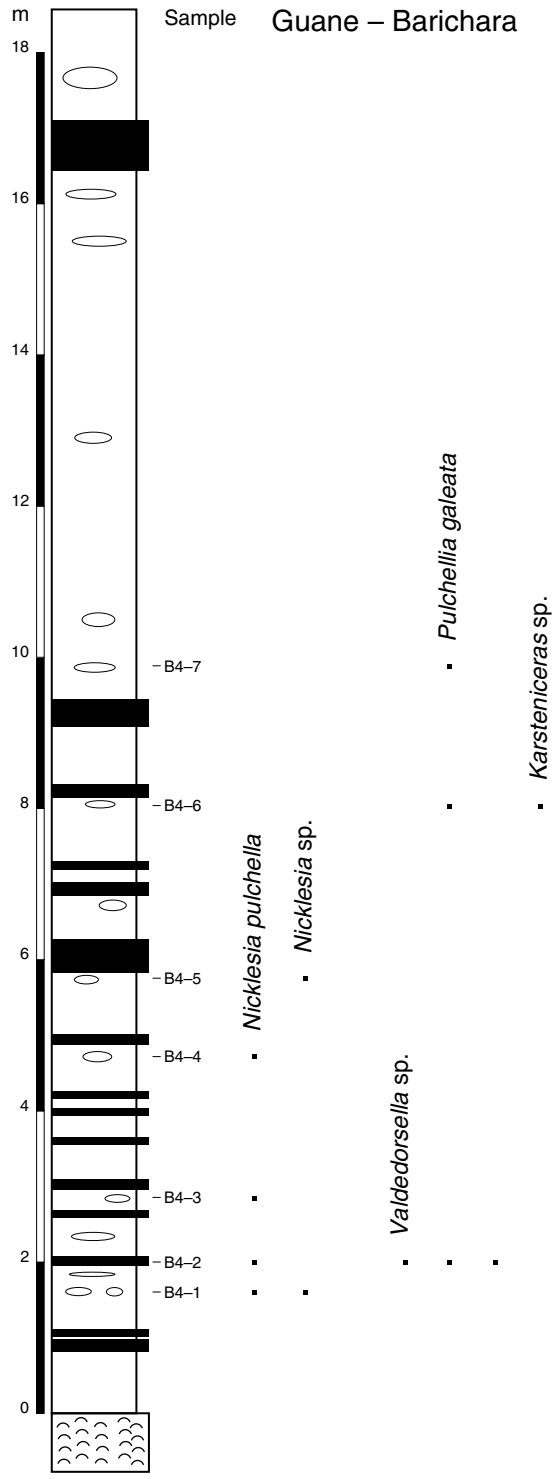

Figure 9. Lower Barremian succession of the Barichara–Guane with the ammonite distribution of the Paja Formation (Santander province).

2.2.3. Trincheras Formation

The Trincheras Formation (Cáceres & Etayo–Serna, 1969a) contains shales, biomicrites, and calcareous concretions that range from the upper Hauterivian to the Aptian (Patarroyo, 2013). Unfortunately, this lithostratigraphic unit does not have a type section description; therefore, its reconnaissance is very poor, but it clearly contains Barremian fossils (Bürgl, 1956; Collet, 1924; Cáceres & Etayo–Serna, 1969a, 1969b; Gerhardt, 1897; Patarroyo, 2013; Riedel, 1938; Royo y Gómez, 1945a; von Buch, 1838, 1839). The deposits of the underlying La Naveta Formation are considered to be Barremian (Bürgl, 1955; Cáceres & Etayo–Serna, 1969a, 1969b; Olsson, 1956; Petters, 1954) however, deposits in its upper part may be considered Hauterivian (cf. Patarroyo, 2013) because the lower deposits of the overlying Trincheras Formation represent Hauterivian deposits (cf. Etayo–Serna in Moreno, 1993; Patarroyo, 2013). *Nicklesia pulchella* and *Pulchellia galeata* (Figure 21) have been found in the Barremian deposits of the middle part of the Trincheras Formation (Patarroyo, 2013).

2.2.4. Upper Calcareous Member (Calcáreo Superior Member of the Tibasosa Formation)

The Tibasosa Formation (Renzoni & Ospina, 1969) includes a succession with four members that likely ranges from the Berriasian to the Aptian and clearly includes Valanginian, Hauterivian, Barremian, and Aptian ammonites (Patarroyo, 2002, 2003, 2005, 2017; Patarroyo & Salamanca–Saavedra, 2013). The type section is along Guadube Creek (known as Manecuche) in Tibasosa (Boyacá province). Its Upper Calcareous Member ranges from the Barremian to the Aptian (Patarroyo, 2005, 2017), and is principally represented by biomicrites, biosparites, poor sandstones, shales, and calcareous concretions towards the upper part.

Nicklesia pulchella, *Pedioceras caquesense*, *Pulchellia galeata*, *P. fasciata*, and *"Crioceratites"* sp. (Figure 22) have been recovered in Barremian deposits of the Upper Calcareous Member of the Tibasosa Formation.

2.2.5. Yuruma Formation

The Yuruma Formation, which was proposed by geologists from the Richmond Exploration Company (1947 in Rollins, 1965, 25), was formalized by Renz (1956 in Julivert, 1968) as a calcareous succession that included two parts: the lower and upper Yuruma. Renz (1960) restricted the Yuruma Formation to the upper Yuruma and redefined the lower Yuruma deposits of Renz (1956 in Julivert, 1968) as the Moina Formation. The Yuruma denomination originates from Yuruma Hill (Figure 23) in the high Guajira (La Guajira province); its type section is west of this hill (Renz, 1960, 331), and it includes Barremian deposits. The Yuruma Formation comprises marls, shales, and marly limestones with oysters, other bivalves, equinoids, and ammonites (Rollins, 1965, 26).

Nicklesia, *Pulchellia*, *Pedioceras*, *Gerhardtia* and *Heinzia* have been reported but without illustrations; therefore, their stratigraphic position is poor understood.

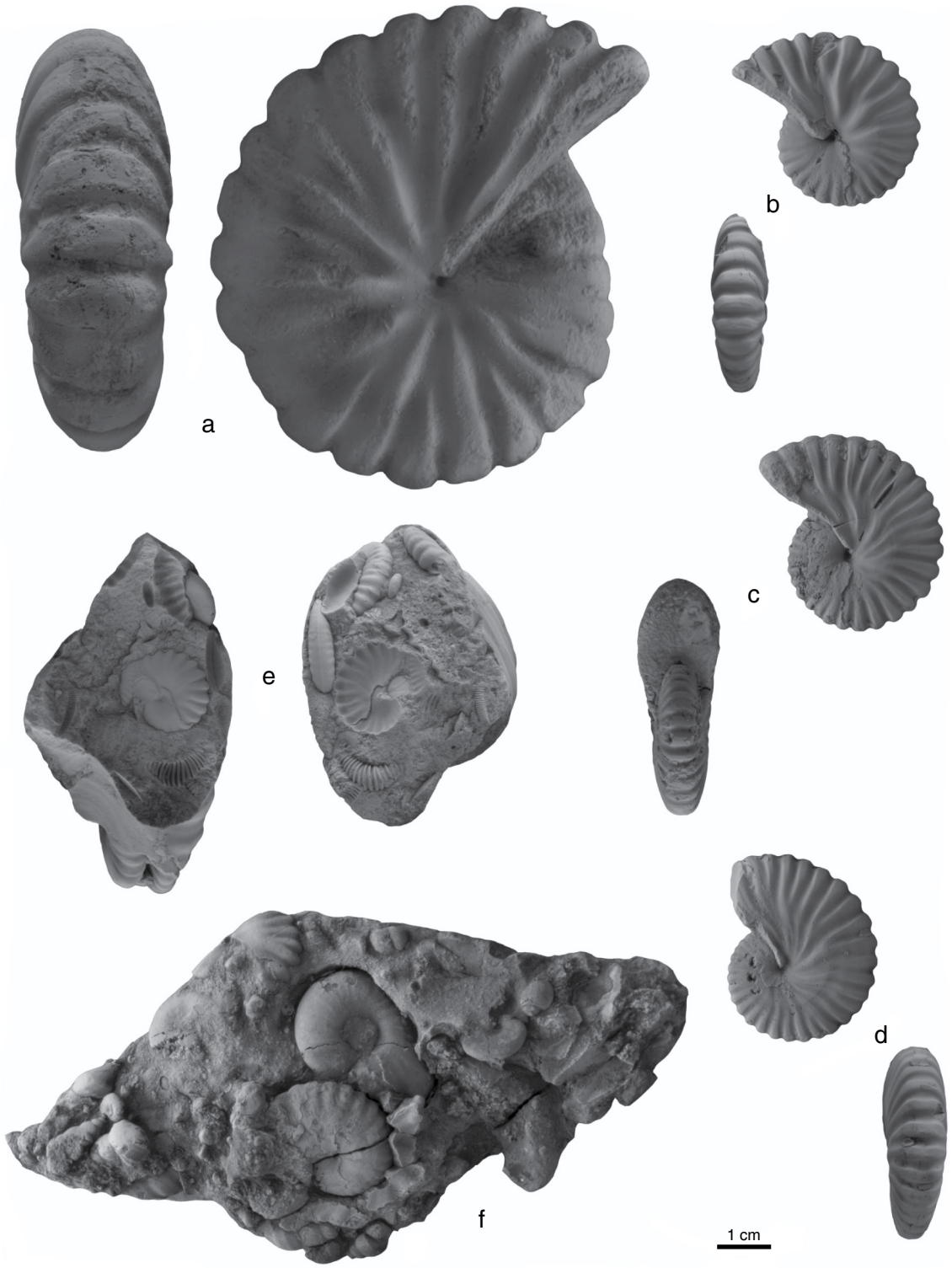

Figure 10. (a) *Nicklesia pulchella* (d'Orbigny). Lower Barremian. Guane by Barichara (Santander province). Sample G5-6-1. **(b)** *Nicklesia pulchella* (d'Orbigny). Lower Barremian. Guane by Barichara (Santander province). Sample G4-6. **(c)** *Nicklesia pulchella* (d'Orbigny). Lower Barremian. Guane by Barichara (Santander province). Sample G4-3. **(d)** *Nicklesia pulchella* (d'Orbigny). Lower Barremian. Guane by Barichara (Santander province). Sample G4-2. **(e)** Fragment of body chamber ammonite with *Nicklesia pulchella* (d'Orbigny), *Psilotissotia* sp., *Karsteniceras* sp., and gastropods. Lower Barremian. Guane by Barichara (Santander province). Sample Pt-2. **(f)** *Nicklesia pulchella* (d'Orbigny), *Pseudohaploceras*? sp., and gastropods. Lower Barremian. Guane by Barichara (Santander province). Sample B4-2-2.

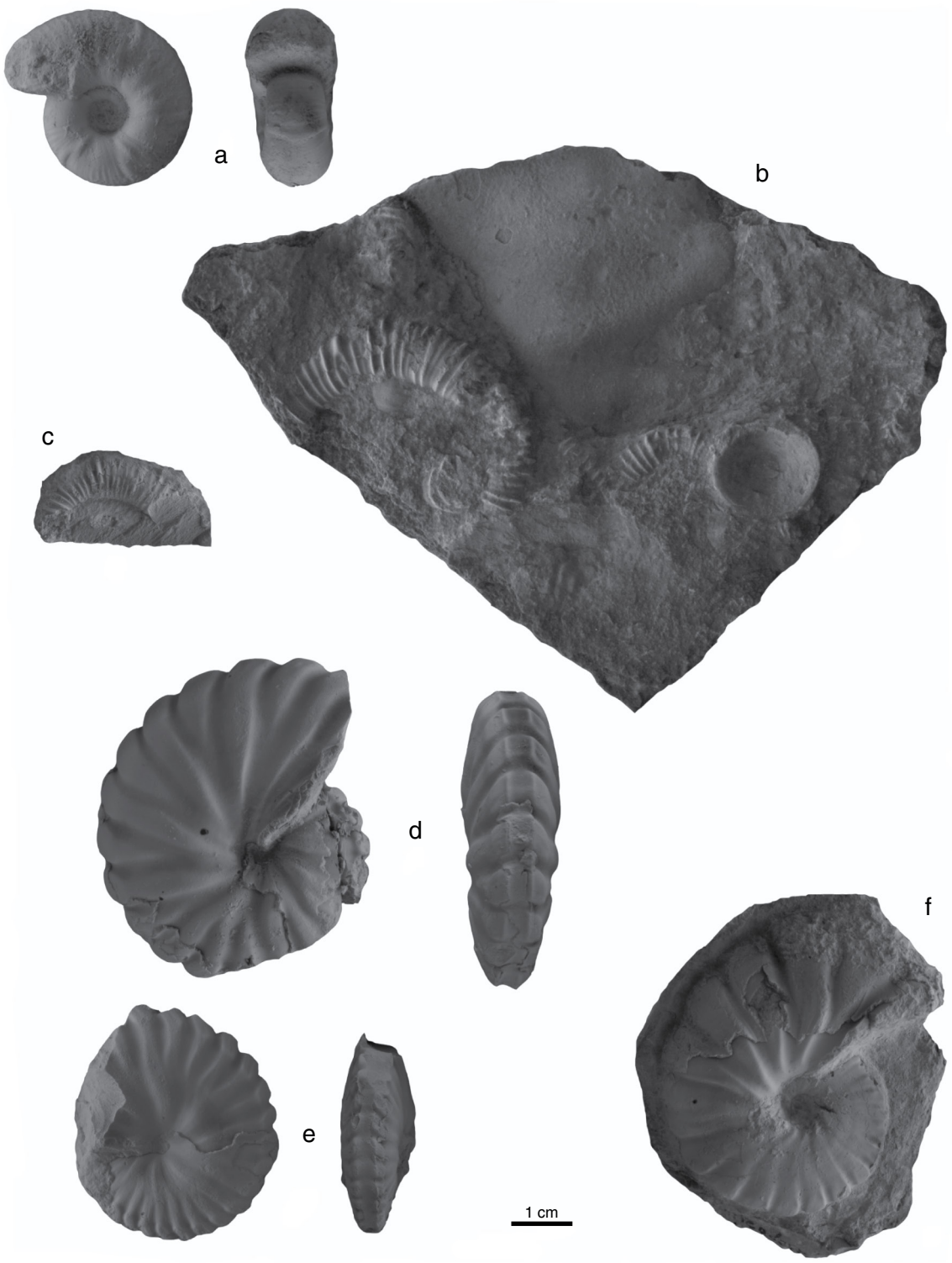

Figure 11. (a) *Valdedorsella* cf. *inca* (Forbes). Lower Barremian. Guane by Barichara (Santander province). Sample B4–2–1. **(b)** *Karsteniceras* sp., *Valdedorsella*? sp. and fish vertebrae. Lower Barremian. Guane by Barichara (Santander province). Sample B4–6. **(c)** *Karsteniceras* sp. Lower Barremian. Guane by Barichara (Santander province). Sample G–7. **(d)** *Pulchellia galeata* (von Buch). Lower Barremian. Guane by Barichara (Santander province). Sample B4–7–1. **(e)** *Pulchellia galeata* (von Buch). Lower Barremian. Guane by Barichara (Santander province). Sample B4–7–2. **(f)** *Gerhardtia veleziensis* (Hyatt). Upper Barremian. Guane by Barichara (Santander province). Sample Pt 10.

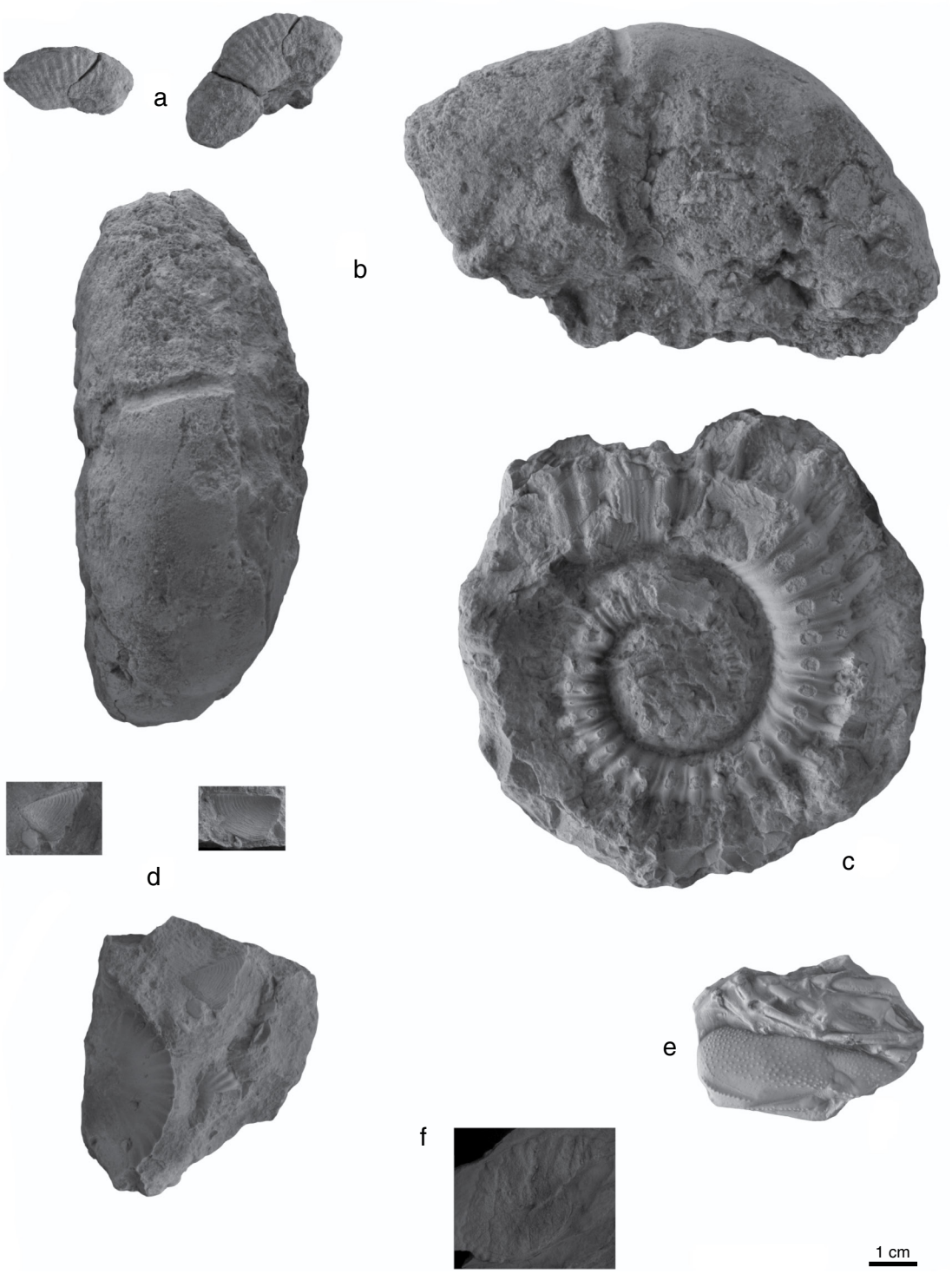

Figure 12. (a) *Pedioceras* sp. Lower Barremian. Villanueva section (Santander province). Sample VNR–1. **(b)** *Valdedorsella* or *Pseudohaploceras* sp. Lower Barremian. Barichara–Punteadero section (Santander province). Sample Pt–1. **(c)** *Paracrioceras leyvaense* (Kakabadze & Hoedemaeker). Ex situ. Lower Barremian. Villa de Leyva area (Boyacá province). Sample VL–49. **(d)** *Lamellapthycus*? sp. and *Nicklesia pulchella* (d'Orbigny). Lower Barremian. Monsalve section by Villa de Leyva area (Boyacá province). Pp151–L. **(f)** *Atherfieldastacus*? sp. Lower Barremian. Cáqueza section (Cundinamarca province). Sample E7. **(g)** *Nicklesia pulchella* (d'Orbigny). Lower Barremian. Punta Espada – Uribia area (La Guajira province). Sample PEY–1.

Figure 13. La Yesera section of the Paja Formation to the south of Villa de Leyva (Boyacá province).

2.2.6. Quebradagrande Complex

Botero–Arango (1963) first presented the Quebradagrande Formation along the central western margin of the Central Cordillera (La Estrella, Antioquia province); it is related to a volcano–sedimentary succession that is now recognized as the Quebradagrande Complex (González, 2001, 117). Successions such as those near Ebéjico (Antioquia province) in Loma Hermosa (Steinmann in Grosse, 1926) are included in the Quebradagrande lithostratigraphic unit (Mejía, 1984, 115), i.e., the Abejorral Formation (Valanginian – Albian) in González (1980) the San Felix Stratigraphic Tectonic Interval (Etayo–Serna 1985a, 3; Rodríguez–Rodríguez & Rojas–Ladino, 1985) and probably, the San Luis and Aquitania sedimentites (Giraldo et al., 2015) that contain Upper Jurassic and Lower Cretaceous fossils, some of which are Barremian ammonites. Steinmann in Grosse (1926) only listed "*Pulchellia* cf. *didayi*", cf. "*Desmoceras charrierianum*", and cf. "*Lytoceras subfimbriatum*".

2.2.7. Other Reported Barremian Deposits

Cretácico del Río Cañas which contains Barremian ammonites, has been reported to the south of the Oca Fault near Mingueo (La Guajira province). There, mudstones with calcareous concretions probably contain more *Nicklesia* than *Pulchellia* (cf. Colmenares et al., 2007, photography 128, 267).

In the serranía del Perijá and the Catatumbo area, the Río Negro Formation includes Barremian deposits (Julivert, 1968, 415–417; Petrash et al., 2016, Figure 2; Renz, 1959, 6; Sutton, 1946) based on the existence of Aptian ammonites in the overlying Cogollo Formation or Group in Venezuela. In the Catatumbo area (Colombia), Notestein et al. (1944) used the Tibú and Mercedes Members of the Uribante Formation, a succession that is equivalent to the Apón Formation (Sutton, 1946). Renz (1959) used the Tibú Formation, a proposition that was followed by Richards (1968) and a petroleum industry geologist. Some authors such as Julivert (1968) believe that under the Tibú Formation or Apón Formation is the underlying Río Negro Formation. Aptian ammonites are included in the Tibú or Apón Formation (Sutton, 1946) in the Catatumbo area and it is not clear if these rocks are older (Barremian) in Venezuela because of its thickening in the serranía del Perijá and Lara State (Venezuela) following Renz (1959, 9).

Between Ábrego and Gramalote (Norte de Santander province), Barremian ammonites have been reported (Bürgl, 1956, 32; Royo y Gómez in Botero–Restrepo & Sarmiento–Rojas, 1947, 36) that are probably erroneously considered to be part of the Tibú and Mercedes Formations (Vargas & Arias 1981). Some citations without illustrations related to Barremian fauna have been presented by Petters (1954) from Becerril and Pailitas (Cesar province). Langston & Durham (1955) also cited Barremian ammonites in Becerril; references that are used in Etayo–Serna et al. (1969, 232) and in this investigation to extend the Barremian deposits to north–central Colombia (Figure 24). Barremian deposits may extend to San Andrés (Santander province) based on the reported presence of Valanginian and Aptian ammonites in the "Rosablanca" Formation (cf. Acosta, 1960, 36); however, according to Vargas et al. (1976), this succession corresponds to the Tibú–Mercedes Formation.

To the north of the Upper Magdalena Valley, continental deposits of the Yaví Formation may be of Barremian age based on the transgressive sedimentary tendency from the north (central Colombia) to south within the overlying Caballos Formation sedimentites, which include Aptian ammonites in their middle part, although "*Ancyloceras* sp." have been mentioned in El Cobre Creek from San Luis (Tolima province) within an upper Barremian – lower Aptian range (cf. Etayo–Serna et al., 1969, 224). However, Durham (1946), Julivert (1968, 69) and Vega et al. (2008) indicated that they have an Aptian range.

The Muzo Formation is a recent informal lithostratigraphic unit that was introduced by Reyes et al. (2006) and includes Barremian deposits. Additionally, the El Peñon Formation of Reyes

et al. (2006, 37–40) following Ulloa (1982 in Acosta–Garay & Ulloa–Melo, 1996) represents Barremian and Aptian deposits, although this unit is correlated or equivalent to the Socotá Formation that overlies the Trincheras Formation, which is Hauterivian, Barremian, and Aptian in range. However, the El Peñón Formation of Reyes et al. (2006) overlies the Furatena Formation (Valanginian) and underlies the Capotes Formation (Albian).

3. Results

Based on this bibliographic compilation, combined with the conducted investigations and new field data presented here, correlations are proposed for the lithostratigraphic units of Colombia that include Barremian deposits. A proposed distribution of the deposits of the sub–basins that integrate the Cretaceous Colom-

Figure 14. (a) *Psilotissotia colombiana* (d'Orbigny). Lower Barremian. Monsalve section by Villa de Leyva (Boyacá province). Sample Pp155-1. **(b)** *Psilotissotia malladae* (Nickles). Lower Barremian. Monsalve section by Villa de Leyva (Boyacá province). Sample Pp154-5. **(c)** *Psilotissotia colombiana* (d'Orbigny). Lower Barremian. Monsalve section by Villa de Leyva (Boyacá province). Sample Pp155-2. **(d)** *Psilotissotia malladae* (Nickles). Lower Barremian. Monsalve section by Villa de Leyva (Boyacá province). Sample Pp154-1. **(e)** *Psilotissotia malladae* (Nickles). Lower Barremian. Monsalve section by Villa de Leyva (Boyacá province). Sample Pp153B-4. **(f)** *Buergliceras buerglii* Etayo-Serna. Lower Barremian. Yuca Hill near Villa de Leyva (Boyacá province). Sample Mp00. **(g)** *Pedioceras caquesense* (Karsten). Lower Barremian. Sáchica-Tunja section near Villa de Leyva (Boyacá province). Sample Pp90-1. **(h)** *Crioceratites*? sp. Lower Barremian. Sáchica-Tunja section near Villa de Leyva (Boyacá province). Sample Pp89-5. **(i)** *Nicklesia pulchella* (d'Orbigny). Lower Barremian. Monsalve section by Villa de Leyva (Boyacá province). Sample Pp153-1. **(j)** *Nicklesia pulchella* (d'Orbigny). Lower Barremian. Monsalve section by Villa de Leyva (Boyacá province). Sample Pp151-2. **(k)** *Valdedorsella inca* (Forbes). Lower Barremian. La Yesera section near Villa de Leyva (Boyacá province). Sample Pp131-5. **(l)** *Acanthoptychoceras*? *trumpyi* Kakabadze & Thieuloy. Lower Barremian. Monsalve section by Villa de Leyva (Boyacá province). Sample Pp131-6. **(m)** *Acanthoptychoceras*? *trumpyi* Kakabadze & Thieuloy. Lower Barremian. Monsalve section by Villa de Leyva (Boyacá province). Sample Pp131-7. **(n)** *Acanthoptychoceras*? *trumpyi* Kakabadze & Thieuloy. Lower Barremian. Sáchica-Tunja section near Villa de Leyva (Boyacá province). Sample Pp88-5. **(o)** *Acrioceras (A.) julivertii* Etayo-Serna. Lower Barremian. Sáchica-Tunja section near Villa de Leyva (Boyacá province). Sample Pp89-6. **(p)** *Crioceratites*? sp. Lower Barremian. Sáchica-Tunja section near Villa de Leyva (Boyacá province). Sample Pp88-6.

bian Basin is also presented. The fossil fauna and the sedimentary characteristics of the Barremian deposits are the key to determine the variations in the depth of the bottom of the deposit to understand paleogeographic variations.

3.1. Correlation

As previously stated, most of the Colombian Barremian ammonites record a Tethyan influx that allows one to correlate these deposits with the western Mediterranean successions. *Psilotissotia colombiana*, *P. malladae*, *Nicklesia pulchella*, *Pulchellia communis*, "*P*". *caicedi*, *Heinzia provincialis,* and *Carstenia lindigii* are present in both areas.

The base of the Barremian is defined in the Mediterranean region by the first occurrence of *Taveraidiscus hugii* (formerly "*Spitidiscus*" *hugii* (Ooster)), and the base of the Aptian is defined by the first occurrence of *Deshayesites oglanlensis* Bogdanova (Reboulet et al., 2009, 2011, 2014, 2018). Both genera and species are not represented in Colombia, although some publications have recognized these genera but with erroneous determinations (cf. Bürgl, 1954, 1957; Etayo–Serna, 1964; Haas, 1960; Riedel, 1938) that were clarified by Etayo–Serna (1979).

Moreover, the boundaries of the Barremian and Aptian have still not been identified in Colombia. *Crioceratites* fossils have been found in the upper Hauterivian and lower Barremian (Figure 7). *Procheloniceras*, *Cheloniceras,* and *Dufrenoyia* fossils are the first representatives of Aptian deposits.

Western Mediterranean Barremian ammonite standard zones (e.g., Avram, 1983; Birkelund et al., 1984; Kakabadze, 1987, 1989; Rawson et al., 1996; Reboulet et al., 2009, 2011, 2014, 2018) may not be completely correlated to those in Colombia because of the absence of some index fossil zones.

However, it may be stated that Bürgl's subdivision of the Colombian Barremian deposits (Bürgl, 1956) in Colombia is partially accepted, although the vertical range of the ammonites of the Pulchelliidae family is mainly used to identify the lower and upper Barremian. *Pulchellia* is found after Bürgl in the upper part of the lower Barremian and in the lower part of the "middle" Barremian. Furthermore, the middle Barremian of Bürgl (1956) could not be recognized in relation to the association of *Pulchellia–Heinzia*. For Bürgl (1956), the lower limit of the upper middle Barremian was represented by the occurrence of "*Heinzia*", which nearly corresponded to the lower limit of the upper Barremian in the western Mediterranean province (Hoedemaeker & Leereveld, 1995, 219). Reboulet et al. (2009, 2011, 2014, 2018) present new interpretations related to *Heinzia* and *Gerhardtia* that changed the boundaries and biostratigraphic proposals.

The *Psilotissotia colombiana* Zone can be partially correlated to the upper *Taveraidiscus hugii* Standard Zone (Figures 6, 7), which contains the *P. colombiana* Subzone (Reboulet et al., 2009, 2011, 2014, 2018). The index species and genera of the *Kotetishvillia nicklesi* Standard Zone are not found in the Colombian Barremian deposits. The *Nicklesia pulchella* Zone is present in both areas, but the range in Colombia is broader than that in the Mediterranean standard zone. The *Kotetishvillia compressissima* Standard Zone cannot be recognized in Colombia because of the absence of the index species; however, with the inclusion of the "*Heinzia*" *communis* Horizon (Reboulet et al., 2014), it is possible to correlate it to the Colombian successions because of the presence of *Pulchellia communis* in the lower part of the Colombian *Pulchellia galeata* Zone (Figure 6). The "*Heinzia*" *caicedi* Horizon of the *Moutoniceras moutonianum* Standard Zone (Reboulet et al., 2014) can be correlated to Colombia because of the existence of "*Pulchellia*" *caicedi* (Karsten, 1858), which, until now, did not have a defined stratigraphic position in the Villa de Leyva area (Patarroyo, 2000b, 2004). However, near Vélez (Santander province), "*P*". *caicedi* (Figure 19b) was found together with *Pulchellia selecta* (Bustos, 2017) in the upper lower Barremian deposits.

To recognize the lower boundary of the upper Barremian in Colombia (cf. Patarroyo, 2000a, 2000b, 2004), we used the

Figure 15. (a) *Nicklesia nodosa* Bürgl. Lower Barremian. La Yesera section by Villa de Leyva (Boyacá province). Sample Pp131B-1-1. **(b)** *Phylloceras* sp. Lower Barremian. Sáchica-Tunja section near Villa de Leyva (Boyacá province). Pp88-9. **(c)** *Pulchellia communis* Bürgl. Lower Barremian. Monsalve section by Villa de Leyva (Boyacá province). Sample Pp149-1A-2. **(d)** *Pulchellia galeata* (von Buch). Lower Barremian. Monsalve section by Villa de Leyva (Boyacá province). Sample Pp132-4. **(e)** *Pulchellia communis* Bürgl. Lower Barremian. Monsalve section by Villa de Leyva (Boyacá province). Sample Pp149-1A-2. **(f)** *Karsteniceras beyrichi* (Karsten). Lower Barremian. La Yesera section by Villa de Leyva (Boyacá province). **(g)** *Pulchellia selecta* Gerhardt. Lower Barremian. Monsalve section by Villa de Leyva (Boyacá province). Sample Pp148B-2. **(h)** *Pulchellia fasciata* Gerhardt. Lower Barremian. Monsalve section by Villa de Leyva (Boyacá province). Sample Pp148A-1. **(i)** *Pulchellia fasciata* Gerhardt. Lower Barremian. Monsalve section by Villa de Leyva (Boyacá province). Sample Pp148A-2. **(j)** *Pulchellia hettneri* Gerhardt. Lower Barremian. Monsalve section by Villa de Leyva (Boyacá province). Sample Pp149-1. **(k)** *Pseudohaploceras* sp. Lower Barremian. Monsalve section by Villa de Leyva (Boyacá province). Sample Pp149-2.

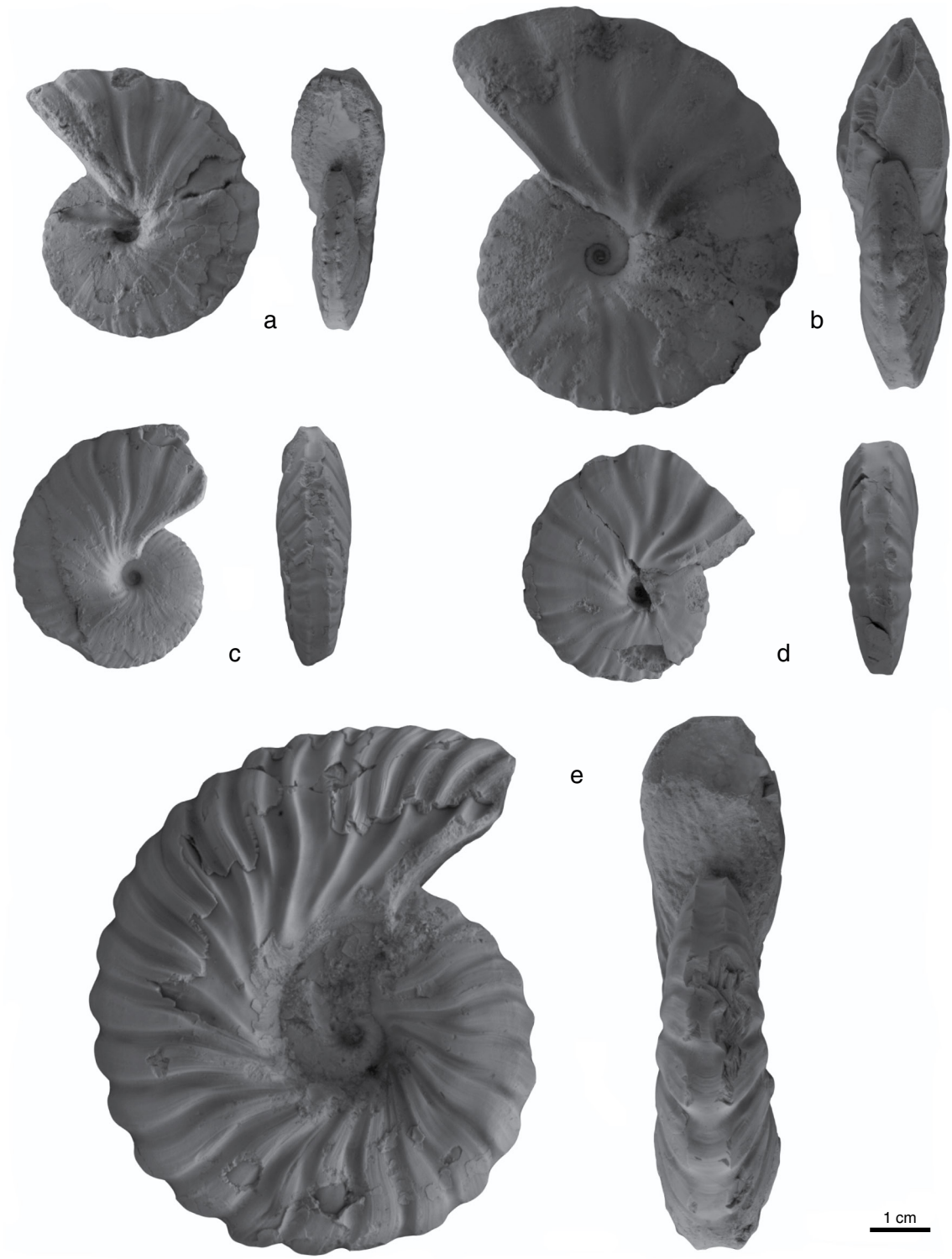

Figure 16. (a) *Gerhardtia veleziensis* Hyatt. Upper Barremian. La Yesera section by Villa de Leyva (Boyacá province). Sample Pp137-3. **(b)** *Gerhardtia veleziensis* Hyatt. Upper Barremian. Monsalve section by Villa de Leyva (Boyacá province). Sample Pp148-1. **(c)** *Gerhardtia veleziensis* Hyatt. Upper Barremian. Monsalve section by Villa de Leyva (Boyacá province). Sample Pp146-1. **(d)** *Gerhardtia veleziensis* Hyatt. Upper Barremian. La Yesera section by Villa de Leyva (Boyacá province). Sample Pp137-4. **(e)** *Gerhardtia galeatoides* (Karsten). Upper Barremian. Santo Ecce Homo section near Villa de Leyva (Boyacá province). Sample SEH-00.

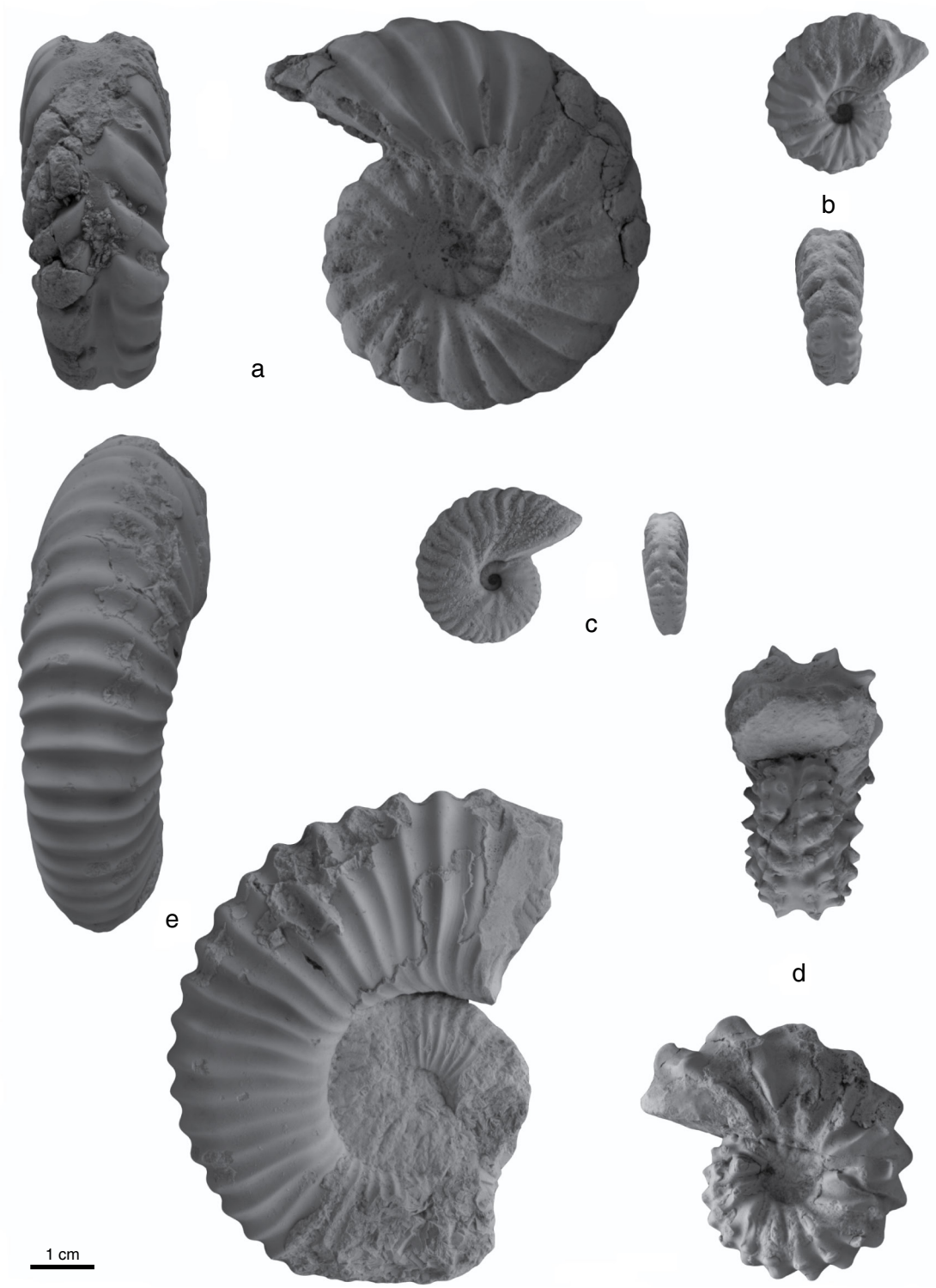

Figure 17. (a) *Heinzia colleti* Bürgl. Upper Barremian. Monsalve section by Villa de Leyva (Boyacá province). Pp146-3. **(b)** *Heinzia provincialis* (d'Orbigny). Upper Barremian. Monsalve section by Villa de Leyva (Boyacá province). Pp144-1. **(c)** *Heinzia provincialis* (d'Orbigny). Upper Barremian. Monsalve section by Villa de Leyva (Boyacá province). Pp144-3. **(d)** *Carstenia lindigii* (d'Orbigny). Upper Barremian. La Yesera section by Villa de Leyva (Boyacá province). Pp137-5. **(e)** *Colchidites breistrofferi* Kakabadze & Thieuloy. Upper Barremian. La Yesera section by Villa de Leyva (Boyacá province). Pp140-1.

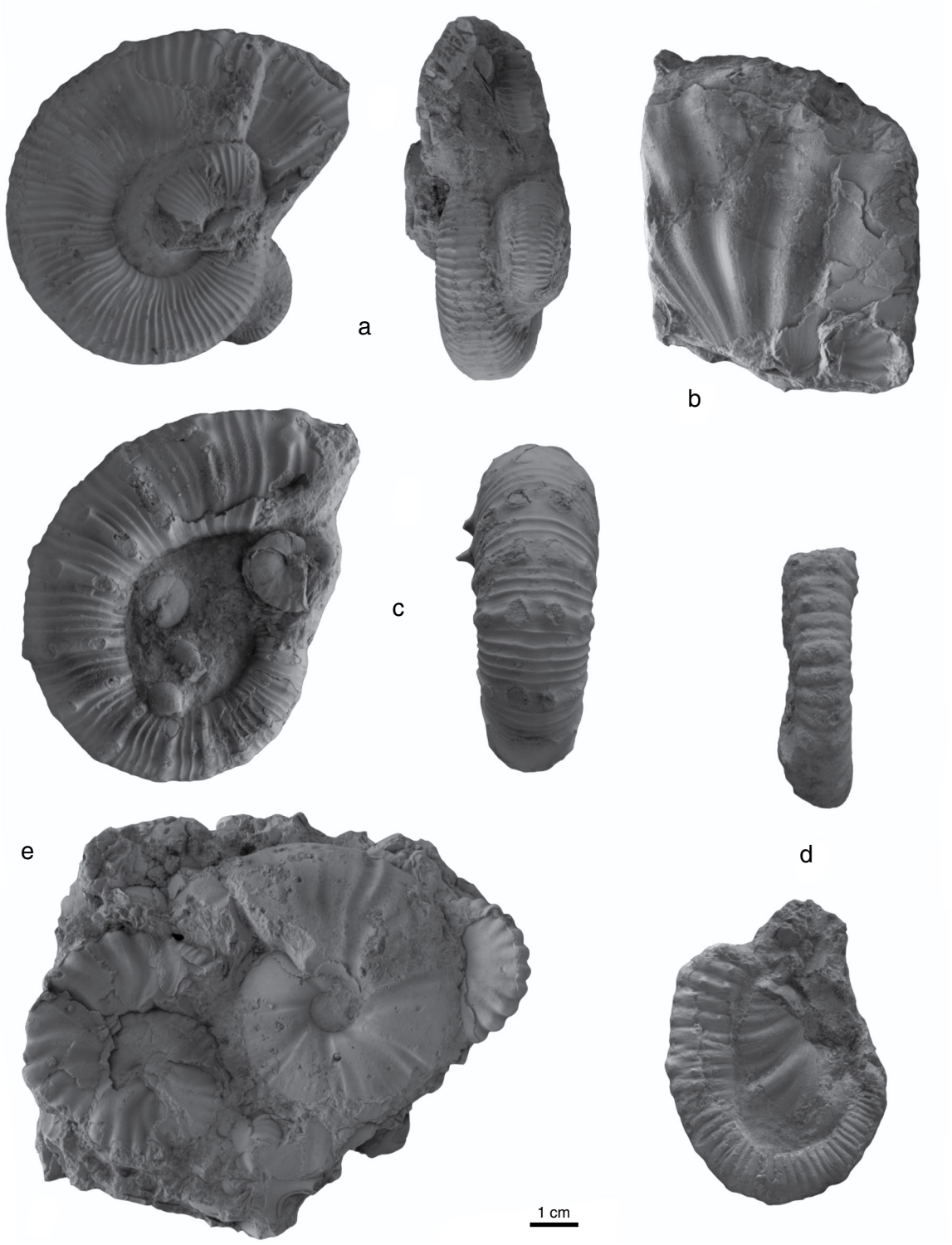

Figure 18. (a) *Pedioceras caquesense* (Karsten). Lower Barremian. Vélez-Chipatá area (Santander province). Sample VCh1. **(b)** *Buergliceras* cf. *buerglii* Etayo-Serna. Lower Barremian. Vélez-Chipatá area (Santander province). Sample VCh2. **(c)** *Paracrioceras leyvaense* (Kakabadze & Hoedemaeker). Lower Barremian. Vélez-Chipatá area (Santander province). Sample VCh3. **(d)** *Acanthoptychoceras*? *trumpyi* Kakabadze & Thieuloy. Lower Barremian. Vélez-Chipatá area (Santander province). Sample VCh4. **(e)** *Nicklesia pulchella* (d'Orbigny) and *Valdedorsella inca* (Forbes). Lower Barremian. Vélez-Chipatá area (Santander province). Sample VCh5.

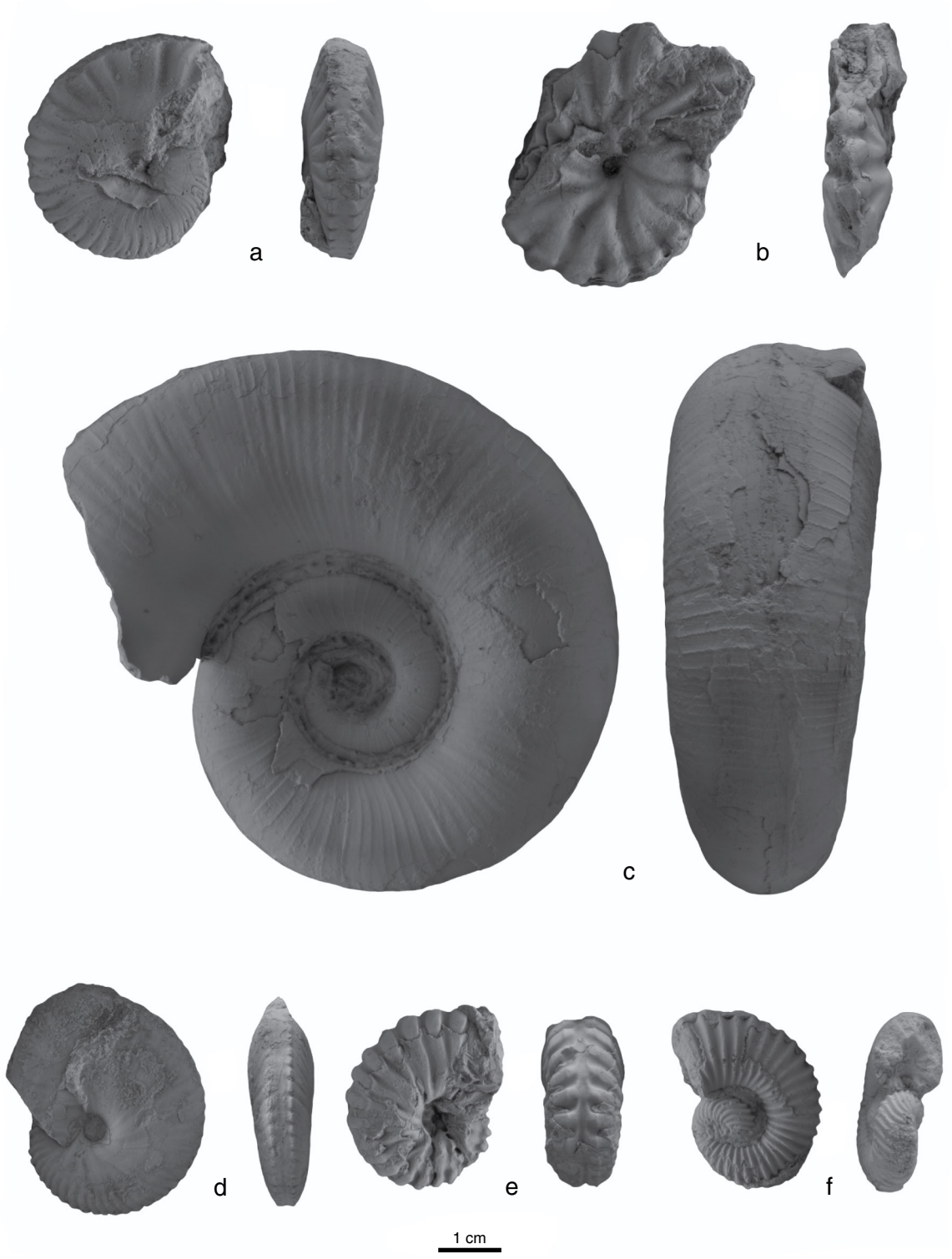

Figure 19. (a) *Pulchellia fasciata* Gerhardt. Lower Barremian. Vélez section (Santander province). Sample S2C9–5. **(b)** *"Pulchellia" caicedi* (Karsten). Lower Barremian. Vélez section (Santander province). Sample S2C7–1. **(c)** *Lytoceras* sp. Lower Barremian. Vélez section (Santander province). Sample S3C1–4. **(d)** *Gerhardtia veleziensis* Hyatt. Upper Barremian. Vélez section (Santander province). Sample S3C1–2. **(e)** *Carstenia lindigii* (Karsten). Upper Barremian. Vélez section (Santander province). Sample S3C1–1. **(f)** *Colchidites* sp. Upper Barremian. Vélez section (Santander province). Sample S4C5–3

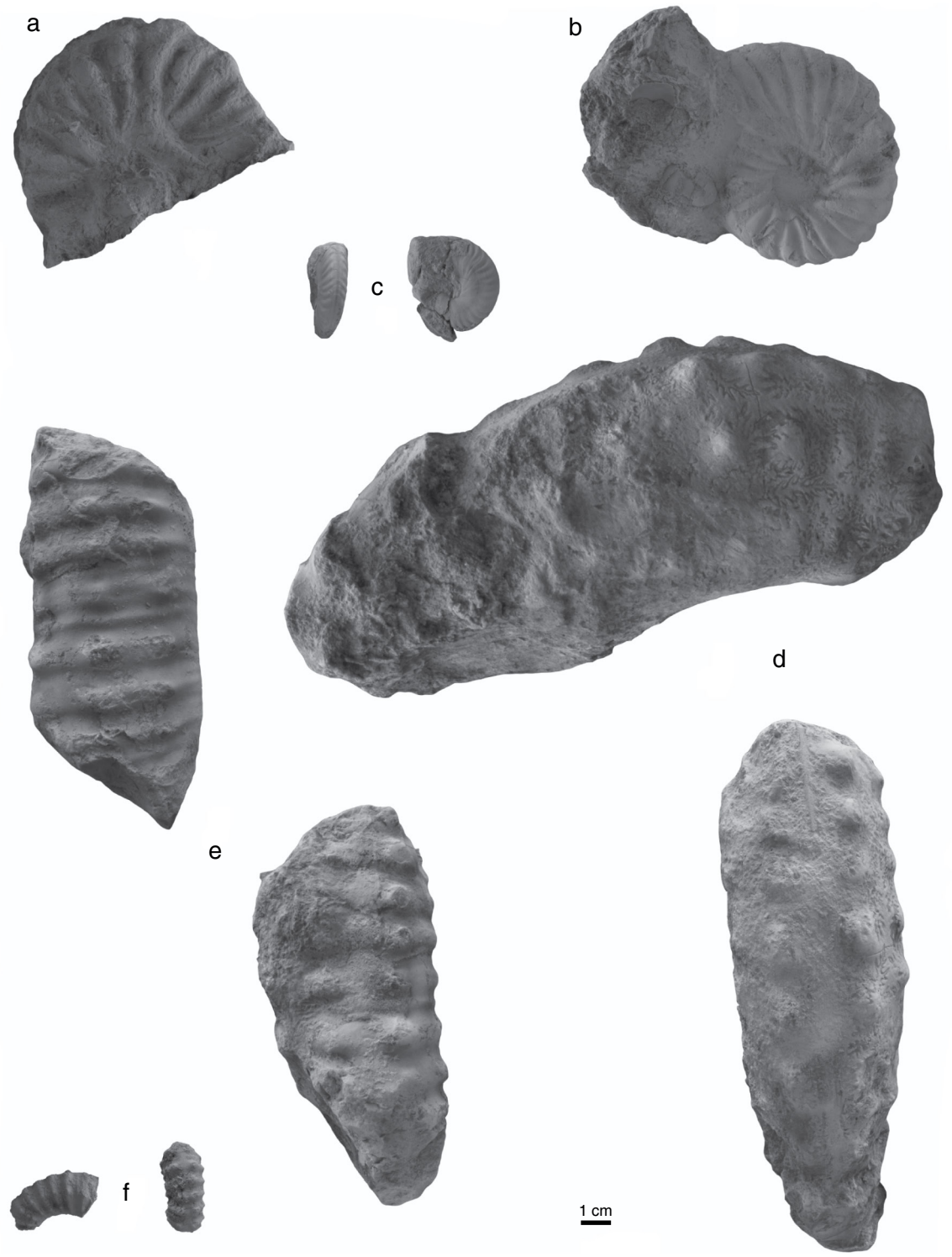

Figure 20. (a) *Gerhardtia* cf. *galetoides* (Karsten). Upper Barremian. Curití (Santander province). Sample Cr1. **(b)** *Gerhardtia galetoides* (Karsten). Upper Barremian. Curití (Santander province). Sample Cr2. **(c)** *Gerhardtia* cf. *veleziensis* Hyatt. Upper Barremian. Curití (Santander province). Sample Cr3. **(d)** *Ancyloceras*? sp. Upper Barremian. Curití (Santander province). Sample Cr4. **(e)** *Ancyloceras*? sp. Upper Barremian. Curití (Santander province). Sample Cr5. **(f)** *Kutatissites* sp. Upper Barremian. Curití (Santander province). Sample Cr6.

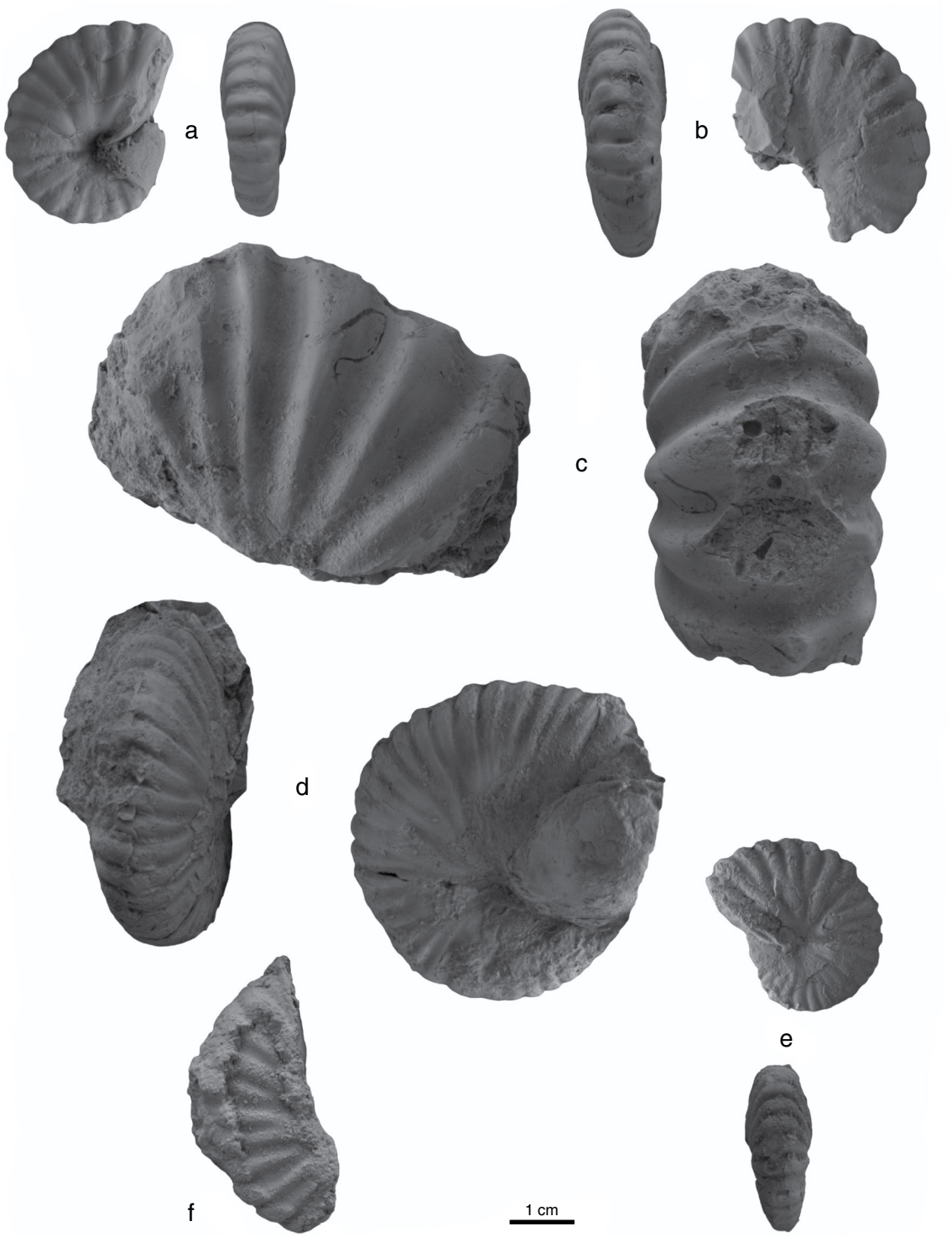

Figure 21. (a) *Nicklesia pulchella* (d'Orbigny). Lower Barremian. Cáqueza section (Cundinamarca province). Sample C-14. **(b)** *Nicklesia pulchella* (d'Orbigny). Lower Barremian. Cáqueza section (Cundinamarca province). Sample E5. **(c)** *Gerhardtia* cf. *galeatoides* (Karsten). Upper Barremian. Cáqueza section (Cundinamarca province). Sample E4. **(d)** *Nicklesia pulchella* (d'Orbigny). Lower Barremian. Nocaima section (Cundinamarca province). Sample FTN-1. **(e)** *Nicklesia pulchella* (d'Orbigny). Lower Barremian. Nocaima section (Cundinamarca province). Sample FTN-2. **(f)** *Pulchellia galeata* (von Buch). Lower Barremian. Nocaima section (Cundinamarca province). Sample FTN-3.

Figure 22. (a) *Nicklesia pulchella* (d'Orbigny). Lower Barremian. Tibasosa area (Boyacá province). Sample Sc1. **(b)** *Pedioceras caquesense* (Karsten). Lower Barremian. Firavitoba section (Boyacá province). Sample F1. **(c)***"Crioceratites"* sp. Lower Barremian. Firavitoba section (Boyacá province). Sample F2. **(d)** *Pulchellia galeata* (von Buch). Lower Barremian. Firavitoba section (Boyacá province). Sample F3. **(e)** *Pulchellia fasciata* Gerhardt. Lower Barremian. Firavitoba section (Boyacá province). Sample F4.

Figure 23. Type locality of the Yuruma Formation. Yuruma Hill is to the right. To the left is the succession of the Hauterivian Moina Formation (La Guajira province).

first occurrence of "*Heinzia* (*Gerhardtia*) *veleziensis*" (now *Gerhardtia veleziensis*). In the western Mediterranean zone, the first occurrence of this genus is related to the *Gerhardtia sartousiana* Zone, which immediately overlies the *Toxancyloceras vandenheckii* Zone of the lowest upper Barremian. *T. vandenheckii* has not been reported clearly in Colombia because of its assignation to *Ancyloceras* (cf. Etayo–Serna, 1964; Royo y Gómez, 1945a), which may be present in Aptian deposits (Kakabadze & Hoedemaeker, 2004). This now means that it is not possible to differentiate the boundary between the lower and upper Barremian deposits in Colombia because the *Gerhardtia veleziensis* Zone in Colombia does not start at the lower Barremian limit, therefore it may be possibly to correlate it with the standard *Gerhardtia sartousiana* Zone in the western Mediterranean area (Figure 7).

Heinzia provincialis is present in Colombia and in the middle part of the *Gerhardtia sartousiana* Zone. Based on this, the "*Gerhardtia*" *provincialis* Subzone was established in the western Mediterranean area, allowing correlation of the successions in both regions.

Kakabadze (1989) reported the presence of "*Heinzia*" (*Carstenia*) *lindigii* (Karsten) in the lower and upper Barremian deposits, and Company et al. (1995) found "*H.*" (*Carstenia*) *lindigii* (Karsten) in the *Moutoniceras moutonianum* Zone from the upper lower Barremian deposits of Spain. However, in Colombia, *Carstenia lindigii* is related to the Colombian upper Barremian *Gerhardtia veleziensis* Zone.

The occurrence of *Colchidites* presented by Kakabadze (1989) and Hoedemaeker & Leereveld (1995, 219) is associated with the base of the *Imerites giraudi* Standard Zone up to the *Martelites sarasini* Standard Zone (Figures 6, 7). In this sense, the Colombian *Colchidites breistrofferi* Zone can be partially correlated to these biostratigraphic levels.

Based on study of Colombian ammonites (Paja Formation; Villa de Leyva, Sáchica, Guane, etc.), Kakabadze & Sharikadze (2004) noted that above the *Colchidites breistrofferi* Zone a level with *Pseudocrioceras anthulai* can be identified; and by ammonite composition (representatives of *Pseudocrioceras, Hemihoplites*, *Audouliceras, Kutatissites,* etc.), this level apparently corresponds to the uppermost Barremian *Pseudocrioceras waagenoides* Subzone of the standard Mediterranean scheme by Hoedemaeker & Rawson (2000).

Following the ammonite biostratigraphy, it is possible to locally correlate our Barremian marine successions (Figure 25) into the Cretaceous Colombian Basin independent of the differentiation of sub–basins (Figures 24, 26), where variable sedimentary environments developed and accumulating and preserving these successions.

Epistomina caracolla, *Platypterygius sachicarum* (Páramo–Fonseca, 1997; Maxwell et al., 2019), *Stenorhynchosaurus munozi* (Páramo–Fonseca et al., 2016), *Acostasaurus pavachoquensis* (Gómez–Pérez & Noè, 2017), *Atherfieldastacus*? sp. (cf. González–León et al., 2018), *Ceratostreon* sp., gastropods, equinoids, and wood, among others, are found together with

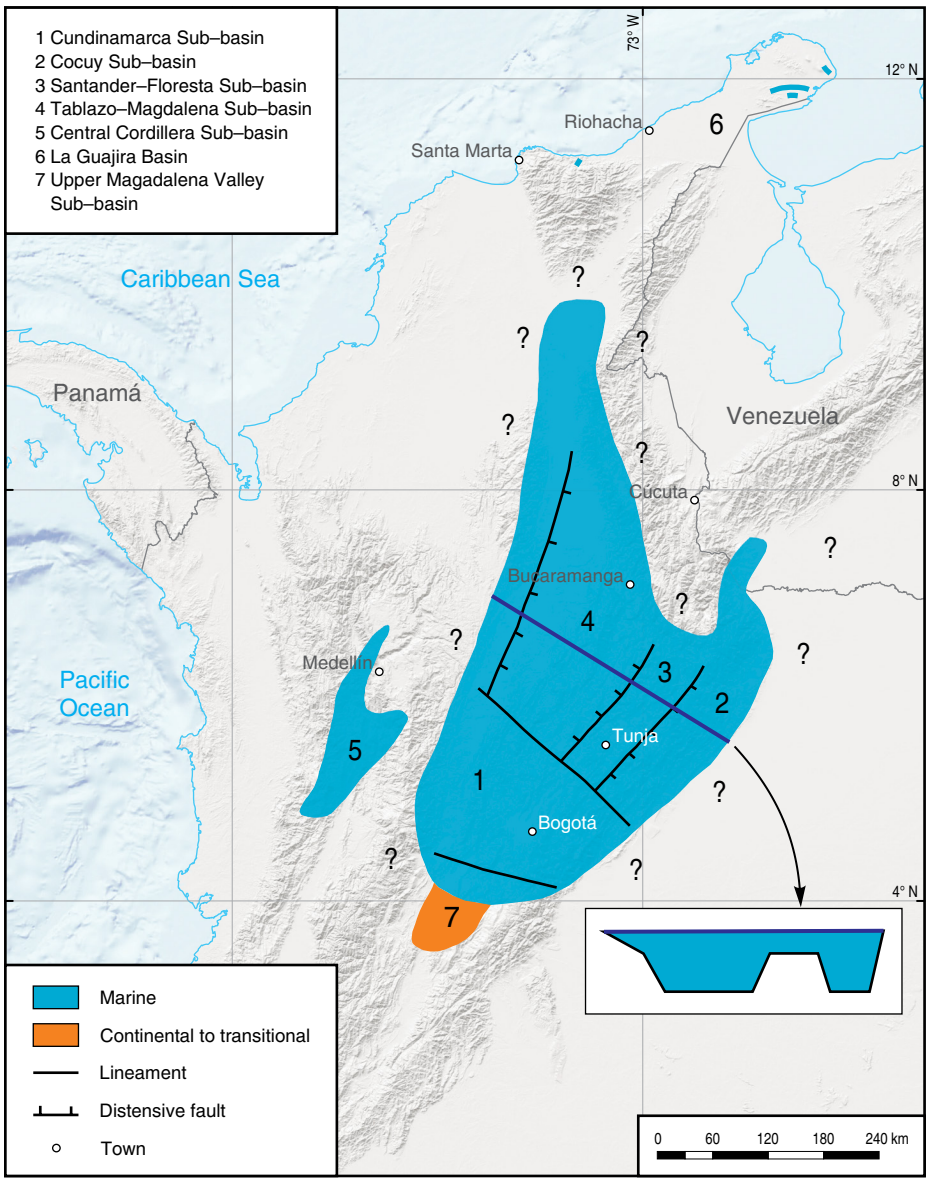

Figure 24. Colombian Barremian deposits with a geographic distribution that does not represent a real paleogeographic reconstruction. Question marks indicate absence of evidence for continental or transitional deposits.

Barremian ammonites, but some of these are not good elements to establish a correlation.

3.2. Paleogeography and Paleoecology

The Cretaceous Colombian Basin was near the equatorial zone as part of an epicontinental sea (Figures 24, 26); although some authors believe that it was a pericratonic sea, the Guayana Shield is to the east. The central Cretaceous Colombian Basin included different geological provinces, including the Amazonia Craton border (Río Negro–Juruena Province sensu Gómez et al., 2015); the Andaquí, Chibcha, Tahamí, and Calima terranes; and the lower and upper Guajira terranes, which are to the north.

Hauterivian deposits in Colombia are principally associated with a lowstand systems tract, in which there are recognized sandstones, shales, biosparites, etc. (cf. La Naveta, Útica, Murca, Rosablanca, Moina, Arenisca de Cáqueza Formations, Lutitas negras inferiores interval, Arenáceo intermedio Member of the Tibasosa Formation, etc.; Figure 25). Overlying these successions a sharp boundary appears as a transgressive surface, which can be associated with lower Barremian deposits as biomicrites, shales with concretions (Paja, Trincheras, Fómeque, and Yuruma Formations), and in some cases biosparites (Upper Calcareous Member of the Tibasosa Formation, "Rosablanca" Formation in Curití; Figure 25) occur.

In the middle stratigraphic level of the Paja Formation in the Villa de Leyva area, it is possible to recognize a bed or a

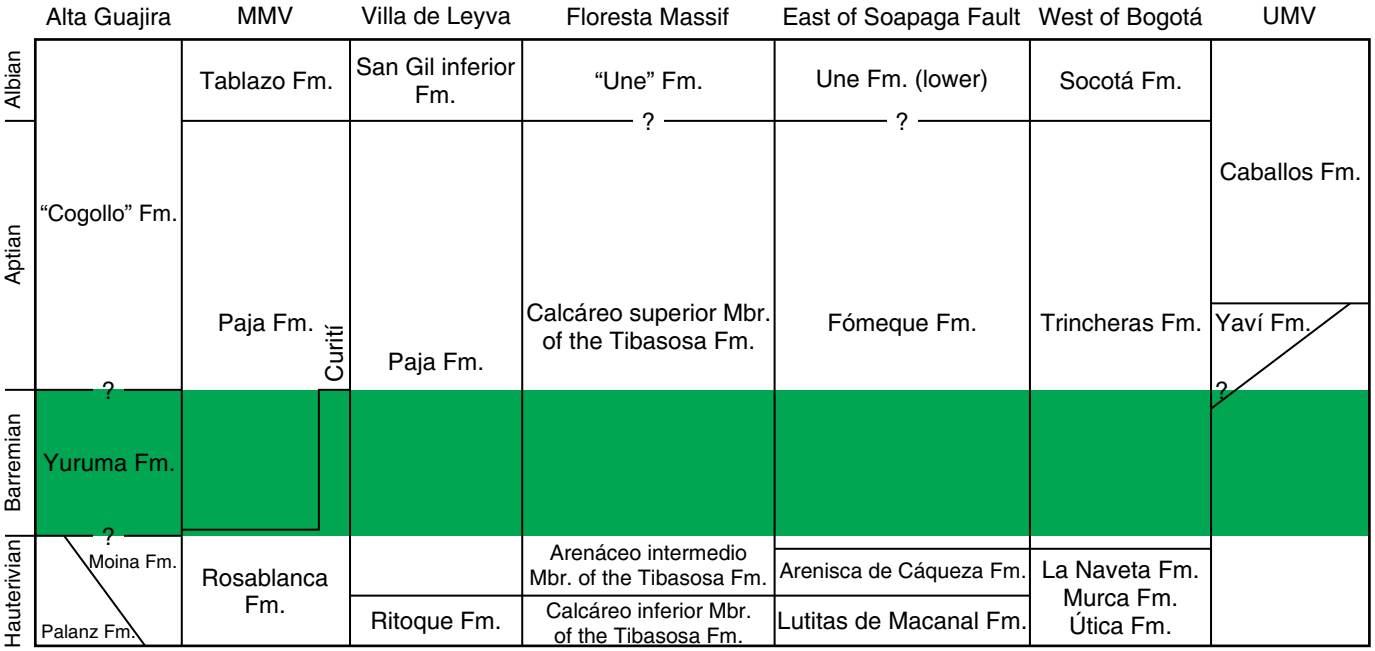

Figure 25. Colombian lithostratigraphic correlation chart of Barremian deposits.

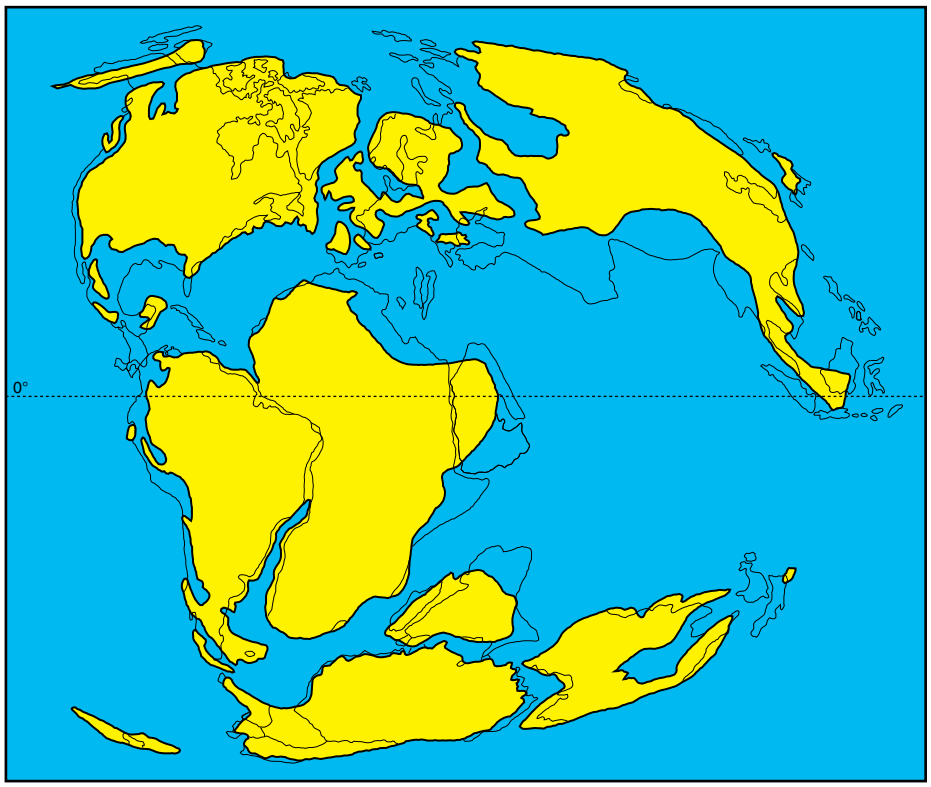

Figure 26. Barremian paleogeographic map (modified from Smith et al., 1994). Positive relief is in yellow.

bed set of biomicrites with fossil wood, ammonites, and benthic foraminifera with a chaotic disposition that has been recognized as a high–energy lower Barremian level (Patarroyo, 2009) that may be associated with a rapid and high sea level rise.

Hoedemaeker (2004) interpreted the sequences in the "monotonous Barremian succession" of Loma de La Yesera to the south of the Villa de Leyva, believing them to be missed lowstand systems tracts (hiatus) between each sequence (Hoede-

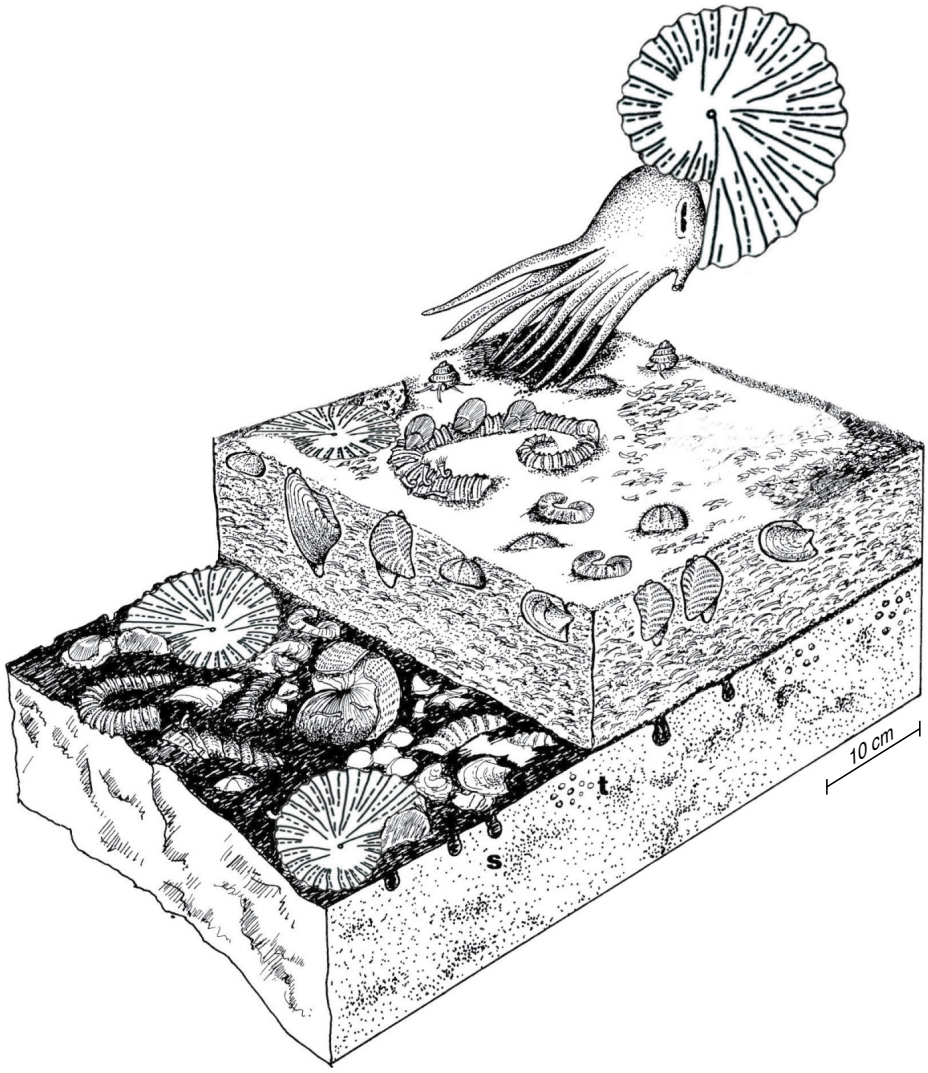

Figure 27. Diagram showing paleoecological deposit conditions of the Upper Calcareous Member of the Tibasosa Formation, "Rosablanca" Formation (Curití, Simití, etc.), and some beds of the Yuruma Formation (taken and modified from McKerrow, 1981).

maeker, 2004, Figure 3), and proposed that the sequences in Europe and Colombia "are precisely time equivalent" using biostratigraphy and stated "that the sequences are incited by global sea–level fluctuations" following the ten Barremian sequence boundaries from Río Argos in Spain (Hoedemaeker & Herngreen, 2003).

The deposits of the Upper Calcareous Member of the Tibasosa Formation contain more infaunal and epifaunal individuals than planktonic and nektonic fossils (Figure 27) in the predominantly calcareous facies of the Santander–Floresta paleo–Massif, as in some locations in the Tablazo–Magdalena (cf. "Rosablanca" Formation in Curití, Simití, etc.) Sub–basin and the La Guajira Basin in some beds of the Yuruma Formation (Figures 23, 24, 27). The disarticulation and fragmentation of thick and strong ornamented shells and carapaces is common in the biomicrites and biosparites, and the bioturbation of infaunal individuals is primarily present in the scarce muddy sediments. This type of deposit and its fossil content is characteristic of the Barremian deposits of the "Rosablanca" Formation in Curití (Santander province) or on the eastern border of the Central Cordillera (cf. Simití area following Mantilla–Figueroa et al., 2006), in some beds of the Yuruma Formation deposits (Bürgl, 1958; Renz, 1960; Rollins, 1965), in the "Cogollo" Formation (Becerril), in some beds of the Fómeque Formation, and probably between Ábrego and Gramalote near Cúcuta (Norte de Santander province).

However, the fine grained sediments (predominantly siliciclastic facies) of the Paja, Trincheras and Fomeque Formations (Figure 28) include scarce calcareous beds but more calcareous concretions with nektonic and poor benthic fauna, wood, and leaves. Thin tabular beds with a predominant plane parallel lamination can be laterally followed as a consequence of low energy regime deposits. Therefore, it is possible to interpret that these deposits were deeper (Figure 24) than those

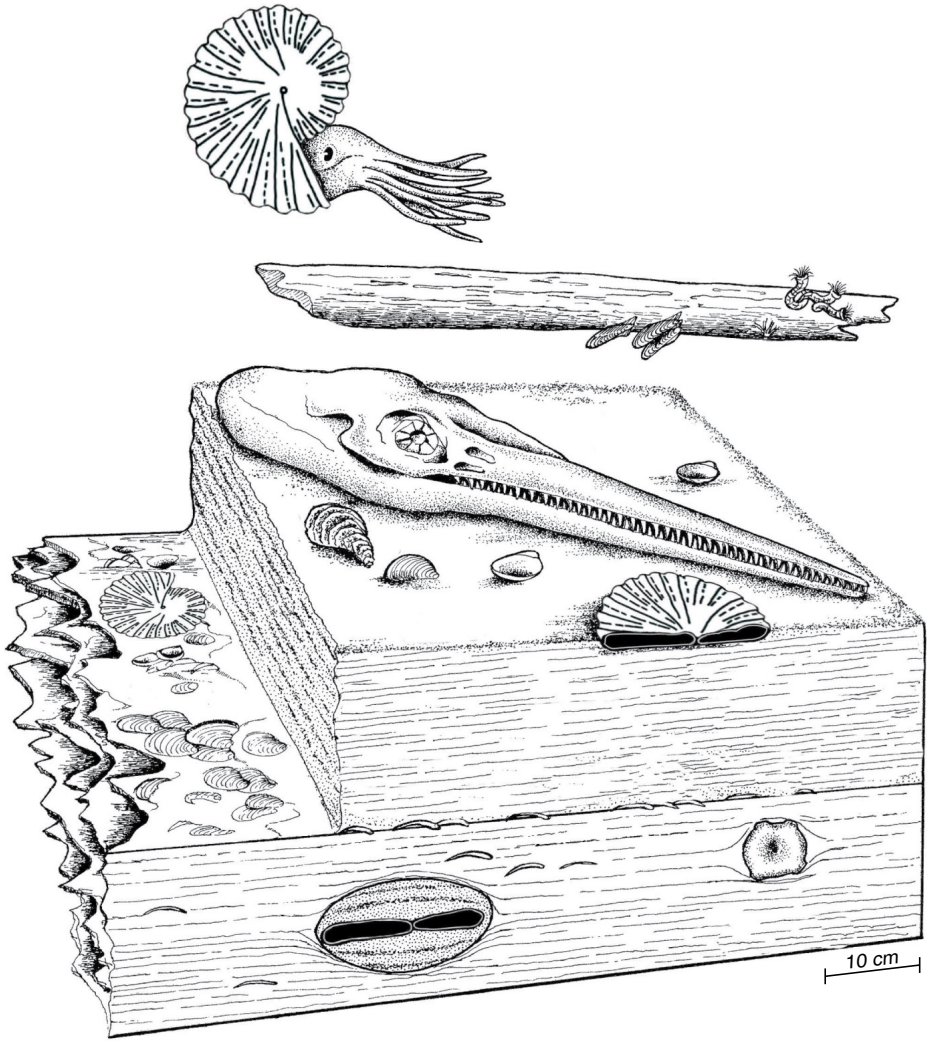

Figure 28. Diagram showing paleoecological deposit conditions of the Paja, Trincheras, and Fómeque Formations (taken and modify from McKerrow, 1981).

of the Upper Calcareous Member of the Tibasosa Formation, the "Rosablanca" Formation in Curití (Santander province) and Simití (Bolivar province), the "Cogollo" Formation in Becerril (Cesar province), and in some beds of the Yuruma Formation (La Guajira province) because the floors of the Tablazo–Magdalena, Cundinamarca, and Cocuy Sub–basins were deeper (Figure 24). However, some authors believe that the sea level during the Barremian was shallow at times (cf. Forero–Onofre & Sarmiento 1985; Hoedemaeker, 2004). Therefore, the hiatus proposition in the Colombian Barremian succession has to be proven using sufficient arguments.

3.3. Future Investigations

Chemostratigraphy, magnetostratigraphy, and sequence stratigraphy may be carefully investigated in the Barremian successions in Colombia and integrated with lithostratigraphic and biostratigraphic data to integrally understand the evolution of the Cretaceous Colombian Basin.

Interregional and intercontinental correlations can be performed to recognize biostratigraphic levels with different fossil groups, chemostratigraphic spikes, magnetic chrons, and effective hydrocarbon sources.

4. Discussion

The Paja Formation, the Barremian "Rosablanca" Formation, the Upper Calcareous Member of the Tibasosa Formation, the Yuruma Formation, and the Quebradagrande Complex are lithostratigraphic units with clear and differentiable characteristics that developed in recognized sub–basins of the Cretaceous Colombian Basin (Figures 24, 25, 27, 28) based on their sedimentological conditions, fossil contents, organic contents, thicknesses, and geographical restrictions.

Although the Barremian successions of the Fómeque and Trincheras Formations are associated with the Cundinamarca Sub–basin (Figure 24), until now it has not been possible to confirm or dispute the lateral continuity of these lithological bodies because of the absence of wells and seismic data. Therefore, they may be considered to comprise independent lithostratigraphic units.

The deposits included in the "Rosablanca" or Tibú–Mercedes Formations near Gramalote (Norte de Santander province) and San Andrés (Santander province) may be carefully investigated to clarify the paleogeographic position of the basin and to determine its actual lithostratigraphic denomination, association, and geographic distribution.

5. Conclusions

The best–investigated unit that includes marine Barremian deposits has been the Paja Formation of the Villa de Leyva area. This lithostratigraphic unit allows one to recognize other Barremian marine deposits, such as the Fómeque, Trincheras, "Rosablanca", "Cogollo", Yuruma, and "Tibú–Mercedes" Formations, as well as the Upper Calcareous Member of the Tibasosa Formation. These lithostratigraphic units differ because the developed sub–basins of the Cretaceous Colombian Basin were subject to seafloor variations, where some areas were deep and others were shallow. The surrounding continental deposits in some cases are preserved while others were eroded as a result of tectonic exhumation.

Ammonites are the most important biostratigraphic markers that can be used to correlate local sections and regional and intercontinental successions with marine Barremian deposits.

It may be possible that Colombian basin areas with continental Barremian deposits from around the Cretaceous period have been preserved, but currently, there is no biostratigraphic support.

Acknowledgments

I would like to thank the Universidad Nacional de Colombia (Sede Bogotá) for financing the project "Amonitas del Barremiano, parte central de Colombia" (Grant 803529); my advisors Prof. Dr. Jost WIEDMANN (†), Prof. Dr. Wolfram BLIND (†), Priv. Doc. Dr. Joachim BLAU (Goethe–Universität Frankfurt) under DAAD grant (A/95/01865); and Dr. Hermann DUQUE–CARO (†) and José Ignacio MARTÍNEZ (†) who compelled me to start studying ammonite stratigraphy. I would also like to thank my students who helped me during many field trips, the Servicio Geológico Colombiano and the editorial staff that allowed me to present this contribution. Particular thanks go to Dr. María Beatriz AGUIRRE–URRETA and Dr. Mikhail KAKABADZE who reviewed my preliminary report and who strongly contributed to the final version.

References

Acosta, C.E. 1960. Estratigrafía de García Rovira. Boletín de Geología, (5): 33–40.

Acosta–Garay, J. & Ulloa–Melo, C.E. 1996. Geología de la plancha 208 Villeta. Scale 1:100 000. Memoria explicative. 83 p. Ingeominas. Bogotá.

Avram, E.A. 1983. Barremian ammonite zonation in the Carpathian area. Zitteliana, 10: 509–514.

Bartolocci, P., Beraldini, M., Cecca, F., Faraoni, P., Marini, A. & Pallini, G. 1992. Preliminary results on correlation between Barremian ammonites and magnetic stratigraphy in Umbria–Marche Apennines (central Italy). Palaeopelagos, 2: 63–68.

Basse, E. 1928. Quelques invertébrés crétacés de la Cordillére Andine. Bulletin de la Société Géologique de France, 28(4): 113–147.

Basse, E. 1950. Quelques du Crétacé de Colombie. Bulletin de la Société Géologique de France, 20(5): 245–255.

Birkelund, T., Hancock, J.M., Hart, M.B., Rawson, P., Remane, J., Robaszynski, F., Schmid, F. & Surlyk, F. 1984. Cretaceous stages boundaries–Proposals. Bulletin of the Geological Society of Denmark, 33(1–2): 3–20.

Blau, J. 1993. *Parinvolutina aquitanica* Pelissié & Peybernès (Foraminifere) aus der Unterkreide (Fm. Rosablanca) von Kolumbien. Neus Jahrbuch für Geologie und Paläontologie, Monatshefte, 5: 292–304.

Botero–Restrepo, G. & Sarmiento, A. 1947. Reconocimiento geológico en la carretera Ocaña–Abrego–Sardinata, departamento de Norte de Santander. Servicio Geológico Nacional, Internal report 612, 79 p. Bogotá.

Botero–Arango, G. 1963. Contribución al conocimiento de la geología de la zona central de Antioquia. Anales de la Facultad de Minas, 57, 101 p. Medellín.

Breistroffer, M. 1936. Sur quelques Céphalopodes du Crétacé de Colombie. Comptes Rendus Sommaires de la Société Géologique de France, 9, p. 155–157. Paris.

Bürgl, H. 1954. El Cretáceo Inferior en los alrededores de Villa de Leyva, Boyacá. Boletín Geológico, 2(1): 5–22.

Bürgl, H. 1955. El Anticlinal de Apulo. Boletín Geológico, 3(2): 2–22.

Bürgl, H. 1956. Catálogo de las amonitas de Colombia. Parte I. Pulchelliidae. Boletín Geológico, 4(1): 1–119.

Bürgl, H. 1957. Bioestratigrafía de la Sabana de Bogotá y sus alrededores. Boletín Geológico, 5(2): 113–185.

Bürgl, H. 1958. Geología de la península de La Guajira. Boletín Geológico, 6(1–3): 129–168.

Bürgl, H. 1959. Sedimentación cíclica en el geosinclinal Cretáceo de la Cordillera Oriental de Colombia. Boletín Geológico, 7(1–3): 85–118.

Bürgl, H. 1961. Historia geológica de Colombia. Revista Academia Colombiana de Ciencias Exactas, Físicas y Naturales, 11(43): 137–191. Bogotá.

Busnardo, R. 1965. Le stratotyp du Barrémien. Lithologie et macrofaune. Mémories du Bureau de Recherches Géologiques et Minières, 34, p. 101–116.

Bustos, J. 2017. Caracterización estratigráfica, tafonómica y geoquímica de algunos niveles fosilíferos de la Formación Paja en el municipio de Vélez–Santander. Bachelor thesis, Universidad Nacional de Colombia, 126 p. Bogotá.

Cáceres, C. & Etayo–Serna, F. 1969a. Bosquejo geológico de la región del Tequendama. Opúsculo guía de la excursión pre–congreso. Primer Congreso Colombiano de Geología, 23 p. Bogotá.

Cáceres, C. & Etayo–Serna, F. 1969b. Memoria explicativa del cuadrángulo L–10 Fusagasugá. Universidad Nacional de Colombia, 50 p. Bogotá.

Campbell, C.J. & Bürgl, H. 1965. Section through the Eastern Cordillera of Colombia, South America. Geological Society of America SA Bulletin, 76(5): 567–590. Doi: https://doi.org/10.1130/0016-7606(1965)76[567:STTECO]2.0.CO;2

Channell, J.E.T., Cecca, F. & Erba, E. 1995. Correlations of Hauterivian and Barremian (early Cretaceous) stage boundaries to polarity chrons. Earth and Planetary Science Letters, 134(1–2): 125–140. https://doi.org/10.1016/0012-821X(95)00111-O

Collet, L.W. 1924. Sur quelques Ammonites du Barrémien de Colombie: Remarques sur les genres Carstenia Hyatt et Pluchellia Uhlig. Eclogae Geologicae Helvetiae, 18(4): 485–493.

Colmenares, F., Mesa, A.M., Roncancio, J.H., Arciniegas, E.G., Pedraza, P.E., Cardona, A., Romero, A.J., Silva, C.A., Alvarado, S.I., Romero, O.A. & Vargas, A.F. 2007. Geología de las planchas 11, 12, 13, 14, 18, 19, 20, 21, 25, 26, 27, 33, 34 y 40. Proyecto: Evolución geohistórica de la Sierra Nevada de Santa Marta. Ingeominas, 401 p. Bogotá.

Company, M., Sandoval, J. & Tavera, J.M. 1995. Lower Barremian ammonite biostratigraphy in the Subbetic Domain (Betic Cordillera, southern Spain). Cretaceous Research, 16(2–3): 243–256. https://doi.org/10.1006/cres.1995.1018

Coquand, H. 1861. Sur la convenance d'établir dans le groupe inférieur de la formation cretacée un nouvel étage entre le Néocomien proprement dit (couches à Toxaster complanatus et à Ostrea couloni) et le Néocomien supérieur (étage Urgonien de d'Orbigny). Mémoires de la Société d'Emulation de Provence, I, p. 127–139. Marseille, France.

d'Orbigny, A. 1840. Paléontologie française. Terrains Crétacés. Céphalopodes. Tome I. Masson Editorial, 662 p. Paris.

d'Orbigny, A. 1842. Coquilles et échinodermes fossiles de Colombie (Nouvelle–Grenade), recuellis de 1821 à 1883, par M. Boussingault et décrits par Alcide d'Orbigny. Chez P. Bertrand Editorial, 64 p. Paris.

d'Orbigny, A. 1850. Prodrome de Paléontologie stratigraphique universelle des animaux mollusques & rayonnés, faisant suite au Cours élémentaire de paléontologie et de géologie stratigraphiques. Volume 1. Victor Masson Editorial, 392 p. Paris. https://doi.org/10.5962/bhl.title.45605

Durham, J.W. 1946. Upper Aptian nautiloids from Colombia. Journal of Paleontology, 20(5): 428–434.

Eristavi, M. 1955. Lower Cretaceous fauna of Georgia. Akademiya Nauk Gruzinskoi GSSR. Monograph, 6: 224 p. (in Russiam).

Etayo–Serna, F. 1964. Posición de las faunas en los depósitos cretácicos colombianos y su valor en la subdivisión cronológica de los mismos. Boletín de Geología, 16–17: 5–142.

Etayo–Serna, F. 1968a. Sinopsis estratigráfica de la región de Villa de Leyva y zonas próximas. Boletín de Geología, 21: 19–32.

Etayo–Serna, F. 1968b. El sistema Cretácico en la región de Villa de Leyva y zonas próximas. Geología Colombiana, 5: 5–74.

Etayo–Serna, F. 1968c. Apuntaciones acerca de algunas amonitas interesantes del Hauteriviano y del Barremiano de la región de Villa de Leyva (Boyacá, Colombia, S.A.). Boletín de Geología, 24: 51–70.

Etayo–Serna, F. 1979. Zonation of the Cretaceous of central Colombia by ammonites. Publicaciones Geológicas Especiales del Ingeominas 2, p. 1–186. Bogotá.

Etayo–Serna, F. 1985a. Documentación paleontológica del infracretácico de San Felix y Valle Alto, Cordillera Central. In: Etayo–Serna, F. & Laverde–Montaño, F. (editors), Proyecto Cretácico. Publicaciones Geológicas Especiales del Ingeominas 16, p. XXV–1–XXV–7. Bogotá.

Etayo–Serna, F. 1985b. Paleontología estratigráfica del sistema Cretácico en la Sierra Nevada del Cocuy. In: Etayo–Serna, F. & Laverde–Montaño, F. (editors), Proyecto Cretácico. Publicaciones Geológicas Especiales del Ingeominas 16, p. XXIV–1–XXV–47. Bogotá.

Etayo–Serna, F., Renzoni, G. & Barrero, D. 1969. Contornos sucesivos del mar Cretáceo en Colombia. Primer Congreso Colombiano de Geología. Memoirs, p. 217–252. Bogotá.

Fabre, A. 1985. Dinámica de la sedimentación cretácica en la región de la Sierra Nevada del Cocuy (Cordillera Oriental de Colombia). In: Etayo–Serna, F. & Laverde–Montaño, F. (editors), Proyecto Cretácico. Publicaciones Geológicas Especiales del Ingeominas 16, p. XIX–1–XXV–20. Bogotá.

Forbes, E. 1845. Report on the fossils from Santa Fe de Bogotá, presented to the Geological Society by Evan Hopkins, Esq. F.G.S. Quarterly Journal of the Geological Society, 1(1): 174–179. https://doi.org/10.1144/GSL.JGS.1845.001.01.47

Forero–Onofre, H. & Sarmiento–Rojas, L. 1985. La facies evaporítica de la Formación Paja en la región de Villa de Leyva. In: Etayo–Serna, F. & Laverde–Montaño, F. (editors), Proyecto Cretácico. Publicaciones Geológicas Especiales del Ingeominas 16, p. XVII–1–XVII–16. Bogotá.

Gaona–Narváez, T., Maurrasse, F.J.M.R. & Etayo–Serna, F. 2013. Geochemistry, palaeoenvironments and timing of Aptian organic–rich beds of the Paja Formation (Curití, Eastern Cordillera, Colombia). In: Bojar, A.V., Melinte–Dobrinescu, M.C. & Smit, J. (editors), Isotopic studies in Cretaceous research.

Geological Society of London, Special Publication 382, p. 31–48. https://doi.org/10.1144/SP382.6

Gerhardt, K. 1897. Beitrag zur Kenntniss der Kreide–formation in Venezuela und Peru. In: G. Steinmann (editor), Beiträge zur Geologie und Paleontologie von Südamerika, 5. Neues Jahrbuch Mineralogie, Geologie und Palaleontologie B–Bd 11, S. 65–117. Stuttgart, Germany.

Giraldo, W., Patarroyo, P. & Restrepo J.J. 2015. Sedimentitas de Aquitania, Antioquia: Edad y correlaciones. XV Congreso Colombiano de Geología. Poster. Bucaramanga.

Gómez, J., Nivia–Guevara, Á., Montes–Ramírez, N.E., Diederix, H., Almanza–Meléndez, M.F., Alcárcel–Gutiérrez, F.A. & Madrid–Montoya, C.A. 2015. Explanatory notes: Geological Map of Colombia. In: Gómez, J. & Almanza–Meléndez, M.F. (editors), Compilando la geología de Colombia: Una visión a 2015. Servicio Geológico Colombiano, Publicaciones Geológicas Especiales 33, p. 35–60. Bogotá.

Gómez–Pérez, M. & Noè, L.F. 2017. Cranial anatomy of a new pliosaurid Acostasaurus pavachoquensis from the Lower Cretaceous of Colombia, South America. Palaeontographica Abteilung A: Palaeozoology–Stratigraphy, 310(1–2): 5–42. https://doi.org/10.1127/pala/2017/0068

González, H. 1980. Geología de las planchas 167 Sonsón y 187 Salamina. Scale 1:100 000. Boletín Geológico, 23 (1): 174 p.

González, H. 2001. Memoria explicativa: Mapa geológico del departamento de Antioquia. Scale 1:400 000. Ingeominas, 240 p. Bogotá.

González–León, O., Moreno–Bedemar, J.A., Vega, F.J., Oviedo–García, A. & Franco–Rubio, M. 2018. Review of *Meyeria Mexicana* Rathbun, 1935 (Glypheidea, Mecochiridae) from the upper Aptian (Cretaceous) of Chihuahua, northern Mexico. Cretaceous Research, 91: 111–125. https://doi.org/10.1016/j.cretres.2018.05.009

Grosse, E. 1926. Das Kohlentertiär Antioquias. Dietrich Reimer/Ernst Vohsen, 361 p. Berlin.

Guzmán, G. 1985. Los grifeidos infracretácicos *Aetostreon couloni* y *Ceratostreon boussingaulti*, de la Formación Rosablanca, como indicadores de oscilaciones marinas. In: Etayo–Serna, F. & Laverde–Montaño, F. (editors), Proyecto Cretácico. Publicaciones Geológicas Especiales del Ingeominas 16, p. XII–1–XII–16. Bogotá.

Haas, O. 1960. Lower Cretaceous ammonites from Colombia, South America. American Museum Novitates 2005, 62 p. New York.

Hoedemaeker, P.J. 2004. On the Barremian–lower Albian stratigraphy of Colombia. Scripta Geologica, 128: 3–15.

Hoedemaeker, P.J. & Herngreen, G.F.W. 2003. Correlation of the Tethyan and Boreal Berriasian–Barremian strata with emphasis on strata in the subsurface of the Netherlands. Cretaceous Research, 24(3): 253–275. https://doi.org/10.1016/S0195-6671(03)00044-2

Hoedemaeker, P.J. & Leevereld H. 1995. Biostratigraphy and sequence stratigraphy of the Berriasian–lowest Aptian (Lower Cretaceous) of the Río Argos succession, Caravaca, SE Spain. Cretaceous Research, 16(2–3): 195–230. https://doi.org/10.1006/cres.1995.1016

Hoedemaeker, P.J. & Rawson, P.F. 2000. Report on the 5th International Workshop of the Lower Cretaceous Cephalopod Team (Vienna, 5 September 2000). Cretaceous Research, 21(6): 857–860. https://doi.org/10.1006/cres.2000.0233

Hoedemaeker, P.J., Company, M., Aguirre–Urreta, M.B., Avram, E., Bogdanova, T., Bujtor, T., Bulot, L., Cecca, F., Delanoy, G., Ettachfini, M., Memmi, L., Owen, H., Rawson, P., Sandoval, J., Tavera, J., Thieuloy, J.P., Tovbina, S.V. & Vašíček, Z. 1993. Ammonite zonation for the Lower Cretaceous of the Mediterranean region: Basis for the stratigraphic correlations within IGCP–Project 262. Revista Española de Paleontología, 8(1): 117–120.

Hoedemaeker, P.J., Reboulet, S., Aguirre–Urreta, M.B., Alsen, P., Aoutem, M., Atrops, F., Barragan, R., Company, M., González–Arreola, C., Klein, J., Lukeneder, A., Ploch, I., Raisossadat, N., Rawson, P.F., Ropolo, P., Vašiček, Z., Vermeulen, J. & Wippich, M.G.E. 2003. Report on the 1st International Workshop of the IUGS Lower Cretaceous Ammonite Working Group, the 'Kilian Group' (Lyon, 11 July 2002). Cretaceous Research, 24(1): 89–94. https://doi.org/10.1016/S0195-6671(03)00018-1

Hubach, E. 1931. Geología petrolífera del departamento Norte de Santander. Servicio Geológico Nacional, Internal report 176, p. 461 p. Bogotá.

Hubach, E. 1957a. Contribución a las unidades estratigráficas de Colombia. Servicio Geológico Nacional, Internal report 1212, 166 p. Bogotá.

Hubach, E. 1957b. Estratigrafía de la Sabana de Bogotá y alrededores. Boletín Geológivo, 5(2): 93–112.

Hyatt, A. 1900. Cephalopoda. In: Zittel, K.A. (editor), Texbook of palaeontology, 1st edition. Macmillan Education, p. 502–592. London, New York.

Hyatt, A. 1903. Pseudoceratites of the Cretaceous. Monographs of the United States Geological Survey 44, 250 p. Washington. https://doi.org/10.5962/bhl.title.45347

Julivert, M. 1968. Lexique Stratigraphique Internacional, Amérique Latine. Colombie (première partie), Précambrien, Paléozoïque, Mésozoïque, et intrusions d'âge mésozoïque–tertiaire. Centre National de la Recherche Scientifique 5, p. 1–651. Paris.

Kakabadze, M.V. 1987. On stratigraphical position of the Heinzia matura zone (Barremian, Georgia). Bulletin of Georgian Academy of Sciences, 126(3): 577–580.

Kakabadze, M.V. 1989. The Barremian biostratigraphical subdivisions of Georgia (USSR) and comparision with some Western Mediterranean regions. In: Wiedmann, J. (editor), Cretaceous of the Western Tethys. 3rd International Cretaceous Symposium Tübingen. Proceedings, p. 551–560. Stuttgart.

Kakabadze, M.V. & Hoedemaeker, P.J. 2004. Heteromorphic ammonites from the Barremian and Aptian strata of Colombia. Scripta Geologica, 128: 39–182.

Kakabadze, M.V. & Sharikadze, M.Z. 2004. Comparative biostratigraphical analyses of the Late Barremian and Early Aptian ammonites (Cephalopoda) of the Caucasus and Colombia. Proceedings of A. Janelidze Geological Institute of Georgian Academy of Sciences. New Series, 119: 248–256 (in Russian).

Kakabadze, M.V. & Thieuloy, J.P. 1991. Ammonites hétéromorphes du Barrémien et de l'Aptien de Colombie. Géologie Alpine, 67: 81–113.

Karsten, H. 1858. Über die geognostischen Verhältnisse des westlischen Columbien, der heutigen Republiken Neu–Granada und Equador. Amtlicher Bericht über die 32 Versammlung der Deutschen Naturforscher und Ärzte zu Wien, 1856: 80–116.

Klein, J., Busnardo, R., Company, M., Delanoy, G., Kakabadze, M., Reboulet, S., Ropolo, P., Vašiček, Z. & Vermeulen, J. 2007. Lower Cretaceous ammonites III Bochianitoidea, Protancyloceratoidea, Ancyloceratoidea, Ptychoceratoidea. In: Riegraf, W. (editor), Fossilium Catalogus I: Animalia. Pars 144. Backhuys Publishers, p. 1–381. Leiden, The Netherlands.

Langston, W.Jr. & Durham, J.W. 1955. A sauropod dinosaur from Colombia. Journal of Paleontology, 29(6): 1047–1051.

Mantilla–Figueroa, L.C., Clavijo, J., Pinto, J.E., Páez, L.A., Pérez, A., Quintero, I., García, M., Correa, K.J., Serrano, J.J., Gaviria, J.A., Niz, L.D., Navas, G. & Silva A. 2006. Memoria explicativa: Plancha 85 Simití, sur de los departamentos de Bolívar y Cesar. Ingeominas, 140 p. Bogotá.

Maxwell, E.E., Cortés, D., Patarroyo, P. & Parra–Ruge, M.L. 2019. A new specimen of Platypterygius sachicarum (Reptilia, Ichthyosauria) from the Early Cretaceous of Colombia and its phylogenetic implications. Journal of Vertebrate Paleontology. 12 p. https://doi.org/10.1080/02724634.2019.1577875

McKerrow, W.S. 1981. Palökologie: Lebensräume, Vergesellschaftungen, Lebensweise und Funktion ausgestorbener Tiere und ihre Veränderungen im Laufe der Erdgeschichte. (Übersetzung von Franz Fürsich). Franckh'sche Verlagshandlung, W. Keller & Co., p. 1–248. Eicklingen, Germany.

Mejía, M. 1984. Memoria explicativa: Geología y geoquímica de las planchas 130 (Santa Fe de Antioquia) y 146 (Medellín occidental). Scale 1:100 000. Ingeominas, Internal report 1950. 370 p. Medellín.

Morales, L.G., Tanner, H.H., Jones, S.H., Barker, M.H.S., O'Donoghue, D.J., Mohler, C.E., Dubois, E.P., Jacobs, C. & Goss, C.R. 1958. General geology and oil occurrences of Middle Magdalena Valley, Colombia: South America. In: Weeks, L.G. (editor), Habitat of oil Symposium. American Association of Petroleum Geologists, p. 641–695. Tulsa, USA.

Moreno, J.M. 1993. Contribución al conocimiento de las unidades del Cretácico Inferior, parte central de la cordillera Oriental, Colombia. VI Congreso Colombiano de Geología. Memorias, I, p. 235–247. Medellín.

Murphy, M.A. & Salvador, A. 1999. International stratigraphic guide–An abridged version. Episodes, 22(4): 255–271. https://doi.org/10.18814/epiiugs/1999/v22i4/002

Mutterlose, J., Bodin, S. & Fähnrich, L. 2014. Strontium–isotope stratigraphy of the early Cretaceous (Valanginian–Barremian): Implications for Boreal–Tethys correlation and paleoclimate. Cretaceous Research, 50: 252–263. https://doi.org/10.1016/j.cretres.2014.03.027

Nicklès, R. 1894. Contributions à la paléontologie du sud–est de l'Espagne. Mémoires de la Société Géologique de France, 4: 27–59. Paris.

Notestein, F.B, Hubman, C.W. & Bowler, J.W. 1944. Geology of the Barco Concession, Republic of Colombia, South America. Geological Society of America Bulletin, 55(10): 1165–1216. https://doi.org/10.1130/GSAB-55-1165

Ogg, J.G., Hinnov, L.A. & Huang, C. 2012. Cretaceous. In: Gradstein, F.M., Ogg, J.G., Schmitz, M.D. & Ogg, G.M. (editors), The geological time scale 2012. Elsevier, p. 793–853. https://doi.org/10.1016/B978-0-444-59425-9.00027-5

Olsson, A. 1956. Colombia. In: Jenks, W.F. (editor), Handbook of South American Geology. Geological Society of America, Memoirs 65, p. 293–326. https://doi.org/10.1130/MEM65-p293

Páramo–Fonseca, M.E. 1997. Platypterygius sachicarum (Reptilia, Ichthyosauria) nueva especie del Cretácico de Colombia. Revista Ingeominas, 6: 1–12.

Páramo–Fonseca, M.E., Gómez–Pérez, M., Noé, L.F. & Etayo–Serna, F. 2016. Stenorhynchosaurus munozi, gen. et sp. nov. a new pliosaurid from the upper Barremian (Lower Cretaceous) of Villa de Leyva, Colombia, South America. Revista de la Academia Colombiana de Ciencias Exactas, Físicas y Naturales, 40(154): 84–103. https://doi.org/10.18257/raccefyn.239

Patarroyo, P. 1997. Barremiano inferior en la base de la Formación Paja, Barichara, Santander–Colombia. Geología Colombiana, 22: 135–138.

Patarroyo, P. 2000a. Amonitas del Barremiano en Villa de Leyva–Boyacá (Colombia–Sur America): Datos bioestratigráficos preliminares. Zentralblatt der Geologie und Paläontologie, I, p. 789–798. Stuttgart, Germany.

Patarroyo, P. 2000b. Distribución de amonitas del Barremiano de la Formación Paja en el sector de Villa de Leyva (Boyacá, Colombia): Bioestratigrafía. Geología Colombiana, 25: 149–162.

Patarroyo, P. 2000c. Primer registro de un áptico, asociado con *Nicklesia pulchella* (D'Orbigny), en Villa de Leyva–Boyacá (Colombia–Sudamérica). Revista de la Academia Colombiana de Ciencias Exactas, Físicas y Naturales, 24(91): 279–283.

Patarroyo, P. 2002. Equinoideos del Miembro Calcáreo Superior Formación Tibasosa, en el área de Firavitoba (Boyacá, Colombia). Morfología y fauna asociada. Geología Colombiana, 27: 95–107.

Patarroyo, P. 2003. Fossils of the Barremian–Aptian, associated to the Upper Calcareous Member of the Tibasosa Formation,

in Firavitoba–Boyacá (Colombia–SA). 18° Lateinamerika Kolloquium–Freiberg. Terra Nostra, II, p. 57.

Patarroyo, P. 2004. Die Entwicklung der Ammoniten der Familie Pulchelliidae aus dem Barrême von Zentral–Kolumbien. Révue de Paléobiologie, 23(1): 1–65.

Patarroyo, P. 2005. Fauna fósil del Barremiano–Aptiano, asociada al Miembro Calcáreo Superior de la Formación Tibasosa, en Firavitoba–Boyacá (Colombia–S.A.). X Congreso Colombiano de Geología. Abstracts, p. 42. Bogotá.

Patarroyo, P. 2009. Reconocimiento estratigráfico del Cretácico Inferior de la provincia de Vélez (Santander). XII Congreso Colombiano de Geología. Memoirs in CD ROM, p. 129. Paipa, Boyacá.

Patarroyo, P. 2011. Observaciones sobre la geología de las sedimentitas del Cretácico (Barremiano–Coniaciano) del sector de Punta Espada, Alta Guajira (Uribia–Guajira–Colombia). XIV Congreso Latinoamericano de Geología y XIII Congreso Colombiano de Geología. Memoirs, p. 366. Medellín.

Patarroyo, P. 2013. Nicklesia y Pulchellia, Barremiano inferior, de la parte media de la Formación Trincheras, Nocaima (Cundinamarca–Colombia). XIV Congreso Colombiano de Geología. Memoirs, p. 61. Bogotá.

Patarroyo, P. 2017. Depósitos del Barremiano–Aptiano: Comparación entre el Macizo de Floresta y Curití (Santander). XVI Congreso Colombiano de Geología. Memoirs, p. 429–433. Santa Marta.

Patarroyo, P. & Salamanca–Saavedra, A.F. 2013. Estratigrafía del Miembro Calcáreo Inferior de la Formación Tibasosa, en el área de Tibasosa. Valanginiano–Hauteriviano. XIV Congreso Colombiano de Geología. Memoirs, p. 60. Bogotá.

Petrash, D.A., Gueneli, N., Brocks, J.J., Méndez–Dot, J.A., González–Arismendi, G., Poulton, S.W. & Konhauser, K.O. 2016. Black shale deposition and early diagenetic dolomite cementation during Oceanic Anoxic Event 1: The mid Cretaceous Maracaibo platform, northwestern South America. American Journal of Science, 316(7): 669–711. https://doi.org/10.2475/07.2016.03

Petters, V. 1954. Typical foraminiferal horizons in the Lower Cretaceous of Colombia, S.A. Contributions from the Cushman Foundation for Foraminiferal Research, 5(3): 128–137.

Ramos–Gámez, M.A. 2016. Estratigrafía de la Formación Fómeque al occidente del Municipio de Cáqueza, Cundinamarca. Bachelor thesis, Universidad Nacional de Colombia, 38 p. Bogotá.

Rawson, P.F., Avram, E., Baraboschkin, E.J., Cecca, F., Company, M., Delanoy, G., Hoedemaeker, P.J., Kakabadze, M.V., Kotetishvili, E., Leereveld, H., Mutterlose, J., von Salis, K., Sandoval, J., Tavera, J.M. & Vašiček, Z. 1996. The Barremian stage. In: Rawson, P.F., Dhondt, A.V., Hancock, J.M., Kennedy, W.J. (editors), Proceedings Second International Symposium on Cretaceous Stage Boundaries. Bulletin de l'Institut Royal des Sciences Naturelles de Belgique, Sciences de la Terre, 66, p. 25–30.

Reboulet, S., Klein, J., Barragán, R., Company, M., González–Arreola, C., Lukeneder, A., Raisossadat, S.N., Sandoval, J., Szives, O., Tavera, J.M., Vašiček, Z. & Vermeulen, J. 2009. Report on the 3rd International Meeting of the IUGS Lower Cretaceous Ammonite Working Group, the "Kilian Group" (Vienna, Austria, 15 April 2008). Cretaceous Research, 30(2): 496–502. https://doi.org/10.1016/j.cretres.2008.12.009

Reboulet, S., Rawson, P.F., Moreno–Bedmar, J.A., Aguirre–Urreta, M.B., Barragán, R., Bogomolov, Y., Company, M., González–Arreola, C., Stoyanova, V.I., Lukeneder, A., Matrion, B., Mitta, V., Randrianaly, H., Vašiček, Z., Baraboshkin, E.J., Bert, D., Bersac, S., Bogdanova, T.N., Bulot, L.G., Latil, J.L., Mikhailova, I.A., Ropolo, P. & Szives, O. 2011. Report on the 4th International Meeting of the IUGS Lower Cretaceous Ammonite Working Group, the "Kilian Group" (Dijon, France, 30 August 2010). Cretaceous Research, 32(6): 786–793. Doi: https://doi.org/10.1016/j.cretres.2011.05.007

Reboulet, S., Szives, O., Aguirre–Urreta, B., Barragán, R., Company, M., Idakieva, V., Ivanov, M., Kakabadze, M.V., Moreno–Bedmar, J.A., Sandoval, J., Baraboshkin, E.J., Çağlar, M.K., Főzy, I., González–Arreola, C., Kenjo, S., Lukeneder, A., Raisossadat, S.N., Rawson, P.F. & Tavera, J.M. 2014. Report on the 5th International Meeting of the IUGS Lower Cretaceous Ammonite Working Group, the Kilian Group (Ankara, Turkey, 31 August 2013). Cretaceous Research, 50: 126–137. https://doi.org/10.1016/j.cretres.2014.04.001

Reboulet, S., Szives, O., Aguirre–Urreta, B., Barragán, R., Company, M., Frau, C., Kakabadze, M.V., Klein, J., Moreno–Bedmar, J.A., Lukeneder, A., Pictet, A., Ploch, I., Raisossadat, S.N., Vašíček, Z., Baraboshkin, E.J. & Mitta, V.V. 2018. Report on the 6th International Meeting of the IUGS Lower Cretaceous Ammonite Working Group, the Kilian Group (Vienna, Austria, 20 August 2017). Cretaceous Research, 91: 100–110. https://doi.org/10.1016/j.cretres.2018.05.008

Renz, O. 1959. Estratigrafía del Cretácico en Venezuela occidental. Boletín de Geología, 5(10): 3–48. Caracas, Venezuela.

Renz, O. 1960. Geología de la parte sureste de la península de La Guajira (República de Colombia). Boletín de Geología, Publicación Especial 3, 1, p. 317–347. Caracas, Venezuela.

Renzoni, G. & Ospina, C. 1969. Geología del cuadrángulo J–12. Servicio Geológico Nacional, Internal report 1546, p. 1–30. Bogotá.

Reyes, G., Montoya, D., Terraza, R., Fuquen, J., Mayorga, M., Gaona, T. & Etayo–Serna, F. 2006. Geología del cinturón esmeraldífero occidental, planchas 169, 170, 189 y 190. Ingeominas, unpublished report, 114 p. Bogotá.

Richards, H.G. 1968. Cretaceous section in the Barco area of northeastern Colombia. America Association of Petroleum Geologists Bulletin, 52(12): 2324–2336. https://doi.org/10.1306/5D25C57F-16C1-11D7-8645000102C1865D

Riedel, L. 1938. Amonitas del Cretácico Inferior de la Cordillera Oriental. In: Scheibe, R. (editor), Estudios geológicos y pa-

leontológicos sobre la Cordillera Oriental de Colombia, 2, p. 7–78. Bogotá.

Rodríguez–Rodríguez, C. & Rojas–Ladino, R. 1985. Estratigrafía y tectónica de la serie infracretácica en los alrededores de San Felix, Cordillera Central de Colombia. In: Etayo–Serna, F. & Laverde–Montaño, F. (editors), Proyecto Cretácico. Publicaciones Geológicas Especiales del Ingeominas 16, p. XXI–1–XXI–21. Bogotá.

Rollins, J.F. 1965. Stratigraphy and structure of the Guajira Peninsula, northwestern Venezuela and northeastern Colombia. University of Nebraska Studies, 30, 102 p. Lincoln, Nebraska.

Royo y Gómez, J. 1945a. Fósiles del Barremiense colombiano. Servicio Geológico Colombiano. Compilación de los Estudios Geológicos Oficiales en Colombia 6, p. 455–494. Bogotá.

Royo y Gómez, J. 1945b. Fósiles carboníferos e infracretácicos del oriente de Cundinamarca. Servicio Geológico Nacional. Compilación de los Estudios Geológicos Oficiales en Colombia 6, p. 193–246. Bogotá.

Schemm–Gregory, M., Rojas–Briceño, A., Patarroyo, P. & Jaramillo, C. 2012. First report of *Hadrosia* Cooper, 1983 in South America and its biostratigraphical and palaeobiogeographical implications. Cretaceous Research, 34: 257–267. https://doi.org/10.1016/j.cretres.2011.11.005

Smith, A.G., Smith, D.G. & Funnell, B.M. 1994. Atlas of Mesozoic and Cenozoic coastlines. Cambridge University Press, 99 p. Cambridge.

Sutton, F.A. 1946. Geology of the Maracaibo Basin, Venezuela: Part 1. American Association of Petroleum Geologists Bulletin, 30(10): 1621–1741. https://doi.org/10.1306/3D933870-16B1-11D7-8645000102C1865D

Uhlig, V. 1882. Die Wernsdorfer Schichten und ihre Äquivalente. Sitzungsberichte der kaiserlichen Akademie der Wissenschaften. Mathematisch–Naturwissenschaftliche Classe 86, p. 86–117.

Ulloa, C.E., Arias, A. & Solano, F. 2000. Caracterización de unidades geológicas y geomorfológicas de Colombia: Formación Fómeque. Ingeominas, 57 p. Bogotá.

van Andel, T.H. 1958. Origin and classification of Cretaceous, Paleocene and Eocene sandstones of western Venezuela. American Association of Petroleum Geologists Bulletin, 42(4): 734–763. https://doi.org/10.1306/0BDA5ABF-16BD-11D7-8645000102C1865D

Vargas, R. & Arias, A. 1981. Geología de la plancha 86 Ábrego. Scale 1:100 000. Ingeominas. Bogotá.

Vargas, R., Arias, A., Jaramillo, L. & Téllez, N. 1976. Geología de la plancha 136 Málaga. Scale 1:100 000. Ingeominas. Bogotá.

Vega, F.J., Feldmann, R.M., Etayo–Serna, F., Bermúdez–Aguirre, H.D. & Gómez, J. 2008. Occurrence of *Meyeria magna* M'Coy, 1849 in Colombia: A widely distributed species during Aptian times. Boletín de la Sociedad Geológica Mexicana, 60(1): 1–10.

Vermeulen, J. & Klein, J. 2006. Lower Cretaceous Ammonites II: Endemoceratacеae: Pulchellidae. In: W. Riegraf (editor), Fossilium Catalogus I: Animalia 141. Backhuys Publishers, p. 187–255. Leiden, the Netherlands.

von Buch, L. 1838. Über den zoologischen Character der Secundär–Formationen in Süd–Amerika. Bericht über die zur Bekanntmachung geeigneten Verhandlungen der Königlichen Preussischen Akademie der Wissenschaften zu Berlin, p. 54–67.

von Buch, F.C.L. 1839. Pétrifications recueillies en Amérique par Mr. Alexandre de Humboldt et par Mr. Charles Degenhardt. Imprimé de l'Académie royale des sciences, 4: 519–542.

von Humboldt, A. 1816. Vues des cordillères, et monuments des peoples indigènes de l'Amérique. Tome premier, Chez N. Maze, Libraire592 p. Paris. https://doi.org/10.5962/bhl.title.82451

von Humboldt, A. 1823. Geognostischer Versuch über die Lagerung der Gebirgsarten in beiden Erdhälften. Levrault, Edniglichem Buchbruder und Buchhändler, 383 p. Strassburg, France. https://doi.org/10.3931/e-rara-22308

von Humboldt, A. 1853. Über die Hochebene von Bogota. Kleinere Schriften. Erster Band. Geognostische und physikalische Erinnerungen, p. 100–132. Stuttgart and Tübingen, Germany.

von Humboldt, A. 1888. Memoria razonada de las salinas de Zipaquirá. Dispuesta para uso de los visitantes por Luis Orjuela, 43 p. Bogotá.

Wheeler, O.C. 1929. Report on the Palmira series with notes on stratigraphy of the Umir, Lisama, and La Paz formations near the east part of the Mares Concession. Ecopetrol, internal report, p. 1–18.

Zeuschner, L. 1856. Geognostische Beschreibung des Liaskalkes in der Tatra und in den angrenzenden Gebirgen. Sitzungsberichte der Akademie der Wissenschaften Mathematisch–Naturwissenschaftliche Klasse 19: p. 13–182.

Explanation of Acronyms, Abbreviations, and Symbols:

FAD First apparition datum

GSSP Global Boundary Stratotype Section and Point

Author's Biographical Notes

Pedro PATARROYO born in Bogotá in 1961. He graduated in geology from Universidad Nacional de Colombia, Sede Bogotá, in 1988. He has a PhD from Justus–Liebig Universität Giessen (Germany, 1999) and a Posdoc from Ruprecht-Karls Universität Heidelberg (Germany, 2011). He has worked in the Universidad Nacional de Colombia, Sede Bogotá, since 1992. His research includes invertebrate paleontology, stratigraphy, paleoecology, paleogeography, and regional geology.

Chapter 13

https://doi.org/10.32685/pub.esp.36.2019.13
Published online 22 April 2020

Plesiosaurs, Palaeoenvironments, and the Paja Formation Lagerstätte of Central Colombia: An Overview

Leslie F. NOÈ[1]* and Marcela GÓMEZ–PÉREZ[2]

1 l.noe@uniandes.edu.co
Universidad de los Andes
Departamento de Geociencias
Facultad de Ciencias
Carrera 1 n.° 18A–12
Bogotá, Colombia

2 mgomezp@sgc.gov.co
Servicio Geológico Colombiano
Dirección de Geociencias Básicas
Diagonal 53 n.° 34–53
Bogotá, Colombia

* Corresponding author

Abstract The Cretaceous Paja Formation of the alto Ricaurte of the Eastern Cordillera of central Colombia was laid down under an epicontinental sea during Hauterivian – Aptian times. The Paja Formation epicontinental sea was home to a diverse, and now well–preserved, pelagic marine fauna that includes members of Plesiosauria, other marine reptiles, fish, and ammonites. However, the benthic fauna is depauperate, preserving just a few thin–shelled bivalves and evidence of microbial mats. This suggests dysoxic–anoxic bottom waters, separated from oxic surface waters by a chemocline–pycnocline. The exceptional preservation of the Paja Formation fauna makes the alto Ricaurte a unique Lower Cretaceous marine vertebrae Lagerstätte. Previous palaeoenvironmental interpretations of the Paja Formation, based on observations of the gypsiferous, dark mudrock sequence, suggested an intertidal evaporitic (sabkha) environment. However, integration of sedimentological, palaeobiological, taphonomic, and diagenetic data provides evidence for deeper water conditions. The exquisite preservation and articulation of the skeletons of large marine reptiles, three–dimensionally preserved fish, beautifully ornamented ammonites, and delicate plants, do not accord with a sabkha environment. Sabkha is typical of mid–latitude, dryer climates under the descended limb of the Hadley atmospheric cell, rather than a wet tropical equatorial location of the Paja Formation. Mineralogical arguments used to infer the presence of sabkha are not primary depositional features, but due to secondary migration of mineral–rich fluids. These fluids probably had their source in the earliest Cretaceous topographic high now beneath the Sabana de Bogotá, and were driven by hydraulic pressure generated by volumetric changes due to hydration of anhydrite into gypsum due to the post–Cretaceous rise of the northern Andes mountain chain. The separation of primary and secondary diagenetic features is thereby critical for understanding the evolution of the Paja Formation sedimentary basin in the alto Ricaurte.

Keywords: *Lagerstätte, Lower Cretaceous, Paja Formation, palaeoenvironments, Plesiosauria.*

Resumen La Formación Paja de la región del alto Ricaurte en la cordillera Oriental de Colombia se depositó en un mar epicontinental durante el Hauteriviano–Aptiano. Este mar tenía una fauna marina pelágica diversa que se encuentra hoy en día muy bien preservada e incluye miembros del orden Plesiosauria, otros reptiles marinos, peces y amonitas. Sin embargo, la fauna bentónica está empobrecida, se conservan solo algunos bivalvos de conchilla delgada y evidencia de tapetes microbiales. Esto sugiere que las aguas profundas eran de carácter disóxico–anóxico, separadas de las aguas

Citation: Noè, L.F. & Gómez–Pérez, M. 2020. Plesiosaurs, palaeoenvironments, and the Paja Formation Lagerstätte of central Colombia: An overview. In: Gómez, J. & Pinilla–Pachon, A.O. (editors), The Geology of Colombia, Volume 2 Mesozoic. Servicio Geológico Colombiano, Publicaciones Geológicas Especiales 36, p. 441–483. Bogotá. https://doi.org/10.32685/pub.esp.36.2019.13

superficiales oxigenadas por la quimoclina–picnoclina. La preservación excepcional de la fauna de la Formación Paja hace que el alto Ricaurte sea un Lagerstätte de vertebrados marinos del Cretácico Inferior único a nivel mundial. Interpretaciones previas del paleoambiente de la Formación Paja, basadas en observaciones de la secuencia de lodolitas oscuras yesosas, sugirieron un ambiente evaporítico intermareal (*sabkha*). Sin embargo, la integración de datos sedimentológicos, paleobiológicos, tafonómicos y diagenéticos proporciona evidencia de condiciones de aguas más profundas. La exquisita preservación y la articulación de los esqueletos de grandes reptiles marinos, peces, amonitas bellamente ornamentadas y plantas delicadas no concuerdan con un ambiente de *sabkha*. Los *sabkhas* son característicos de latitudes medias y climas más secos, localizados bajo la rama descendente de la celda atmosférica de Hadley, antes que típicos de la localización más ecuatorial tropical húmeda de la Formación Paja. Los argumentos mineralógicos utilizados para inferir la presencia del *sabkha* no son característicos de deposición primaria, sino debido a la migración secundaria de fluidos ricos en minerales. Estos fluidos probablemente tenían su origen en la topografía alta del Cretácico más temprano, ahora debajo de la Sabana de Bogotá, y fueron impulsados por la presión hidráulica generada por los cambios volumétricos debidos a la hidratación de la anhidrita en yeso como un resultado del levantamiento pos–Cretácico de la cadena montañosa norte de los Andes. Por lo tanto, la separación entre características diagenéticas primarias y secundarias es crítica para comprender la evolución de la cuenca sedimentaria de la Formación Paja en el alto Ricaurte.

Palabras clave: *Lagerstätte, Cretácico Inferior, Formación Paja, paleoambientes, Plesiosauria.*

1. Introduction

The Cretaceous was a "greenhouse" world (Hu et al., 2012; Larson & Erba, 1999) with high partial pressure of atmospheric carbon dioxide, high global temperatures, high rates of plate tectonic (mid–ocean ridge) activity, and no or very restricted polar ice caps (Fluteau et al., 2007; Hay, 2008; Mann & Stein, 1997; Miller et al., 2003b; Poulsen et al., 2007). These conditions resulted in high global sea levels which, associated with the generally subdued Cretaceous terrestrial topography, brought about flooding of large areas of the low lying continental margins, producing numerous shallow epicontinental, epeiric, or epicratonic seas (Bornemann et al., 2005; Immenhauser, 2009; Miller, et al., 1988). These epicontinental seas were especially prevalent in tropical and subtropical regions, with water depths typically in the range of 100 m or less, and sluggish circulation compared to modern shallow marine shelf settings (e.g., Miller & Foote, 2009). Epicontinental seas were dominated by the deposition of fine–grained siliciclastic mudrocks (silt and clay grade in varying proportions, variably termed mudstones, claystones, siltstones, and shales), and/or carbonate–rich sediments (Ruppel & Loucks, 2008), which were highly susceptible to water column stratification and bottom water and/or sediment dysoxia or anoxia (Mann & Stein, 1997; Miller & Foote, 2009; Weissert, 1981; Wignall, 1989). These oxygen–poor epicontinental seafloor conditions, associated with occasional oceanic anoxic events (OAEs) (Jenkyns, 1980, 1997; Schlanger & Jenkyns, 1976), led to frequent preservation of appreciable amounts of organic carbon (C_{org}). Total organic carbon was typically >1%, but commonly much more (Tourtelot, 1979; Tyson & Pearson, 1991; Weissert, 1981), producing black mudrock successions, which often resulted in exceptional fossil preservation.

The Paja Formation forms part of the exposures within the Eastern Cordillera of modern–day central Colombia (Figure 1). The depositional environment of the Eastern Cordillera of Colombia (ECC) is interpreted as part of a shallow, epicontinental sea lying over an extensional back–arc basin (Martínez et al., 2007) due to subduction of the Farallón Plate under the South American Plate. Roll–back of the overlying continental plate led to crustal stretching and thinning, with downwarping, which generated a low lying marine sedimentary basin (Macellari, 1988). Later inversion of this extensional tectonic regime formed a compressional zone as the proto–Andes mountain range began to rise, resulting in uplift and ultimate unroofing and exposure of the ECC Cretaceous sedimentites (Mosolf et al., 2010). Today, the Paja Formation preserves "typical" epicontinental sea deposits, with a lithology of predominantly dark–coloured organic–rich mudrocks and a rich fossil fauna.

The thickest known outcrops of the Paja Formation are approximately 940 m (Etayo–Serna, 1979), and occur in Villa de Leiva, Sáchica, and Sutamarchán, an area known as the alto Ricaurte (Figure 1d), Boyacá Department which forms part of the altiplano Cundiboyacense of the ECC (Etayo–Serna, 1968). Around alto Ricaurte, the Paja Formation is a sequence of typically finely laminated mudrocks (shales) with occasional ar-

gillaceous limestones, fine–grained sandstones, and abundant calcareous concretions; intercalations of gypsum and calcite are frequent, and pyrite is abundant (Etayo–Serna, 1979). The Paja Formation of the alto Ricaurte is richly fossiliferous, preserving both autochthonous marine and allochthonous terrestrial faunas (Carballido et al., 2015; Etayo–Serna, 1968, 1979; Huertas, 1970). The number of fossils preserved in national and local museums, and private collections, indicates the richness of the fossiliferous deposits of alto Ricaurte.

The warm Cretaceous "waterworld" produced ideal conditions for marine organisms to flourish. Cretaceous epicontinental seas teemed with life, including the large marine reptiles and their prey: numerous fish, and uncountable invertebrates. One of the longest–lived groups of marine reptiles were Sauropterygia (Early Triassic – Late Cretaceous; Bardet, 1995; Carroll, 1988). Plesiosauria are advanced members of Sauropterygia, which during the Jurassic and Cretaceous acquired a global distribution (Bardet et al., 2014), and as large (>2 m length) marine predators and mega–predators, were important faunal elements of Cretaceous oceans (Massare, 1984, 1997). However, our understanding of Lower Cretaceous Plesiosauria is very limited (e.g., Benson & Druckenmiller, 2014; Gasparini & Goñi, 1985; Hampe, 1992), producing a major lacuna in our understanding of Cretaceous seas, and leading to the designation of this interval as the "Lower Cretaceous Gap" (Gómez–Pérez & Noè, 2017). In addition to plesiosaurs, a wide range of marine reptiles inhabited Early Cretaceous seas: the fish–shaped Ichthyosauria (ichthyosaurs), the marine Chelonia (turtles), and marine members of Crocodylia (crocodiles). Of the invertebrates, the ammonites are so abundant that it has become a tradition in alto Ricaurte to use their fossils in local buildings, and the genus *Dufrenoyia* has become a symbol of the region (Figure 2).

The Early Cretaceous is a key time for understanding the evolution of marine life, following the extinctions at the end of the Jurassic (Benson & Druckenmiller, 2014). However, relatively few complete or well–preserved Lower Cretaceous sections exist worldwide. The deposits of the alto Ricaurte preserve a comparatively complete Lower Cretaceous sedimentary sequence, of which the Hauterivian – Aptian Paja Formation forms part. The Paja Formation thereby represents one of the few epicontinental sea deposits recording the history of the Lower Cretaceous Gap. The Paja Formation preserves both a marine and terrestrial fossil fauna that is exceptional in terms of the quantity and quality. Hence, the Paja Formation is a fossil *Lagerstätte* (Gómez–Pérez & Noè, 2017; Maxwell et al., 2016), a geological formation that exhibits great diversity and exceptional fidelity of preserved palaeobiodiversity (Selden & Nudds, 2012). Of the numerous invertebrates and vertebrates recovered from the Paja Formation, some of the most important are the ammonites, which are used for global correlation, and Plesiosauria, which have begun to fill the marine reptile Lower Cretaceous Gap. This combination of completeness of the deposits, and the exceptional fossil fauna, makes the Paja Formation of the alto Ricaurte globally important.

1.1. The Problem

The Paja Formation of the alto Ricaurte is one of the best–studied sedimentary sections in Colombia, yet numerous questions remain unanswered. Much of the primary work is in the form of unpublished undergraduate theses (e.g., Espinel–Arias & Hurtado–Henao, 2010; Galvis–Arenas & Valencia–Escobar, 2009), or has been presented as conference abstracts of restricted availability, and without full supporting data (e.g., Etayo–Serna et al., 1978; Patarroyo–Camargo et al., 2011). The environment of deposition of the Paja Formation has been interpreted as a marginal marine succession, with water depths ranging from outer–shelf to upper shore slope (e.g., Huber & Wiedmann, 1986). Interpretations based on sedimentological studies have concluded that the Paja Formation was lain down in a closed basin with restricted circulation and tranquil sedimentation, including periods of subaerial exposure resulting in an evaporitic sabkha environment (Etayo–Serna, 1968; Forero–Onofre & Sarmiento–Rojas, 1985). However, a greater water depth, comparable to the Tethyian Vocontian Basin (Bornemann et al., 2005; Mattioli et al., 2008), has been proposed based on palaeontological studies (Maxwell et al., 2016; Welles, 1962). However, this relatively deep bathymetric interpretation has been countered by evidence from the presence of turtle eggs and benthic algal mats (Etayo–Serna et al., 2015), suggesting a nearshore, terrestrial breeding ground for the turtles, and a shallow water, nearshore, subtidal environment for algal growth. In this model, marine reptile carcasses are interpreted as having floated into the Paja Formation Basin after death (Etayo–Serna, 1968), yet the often exceptional, fully articulated nature of the large vertebrates argues against a "float and bloat" model of post–mortem transport and deposition (Schäfer, 1972). Currently, these major discrepancies in interpretation remain unresolved, and hinder our understanding of Paja Formation palaeoenvironments. Hence, former interpretations require critical reappraisal based on a combination of sedimentological and palaeontological data.

1.2. Materials and Methods

In this contribution, we concentrate on the Paja Formation exposed within the alto Ricaurte, in Sáchica, Sutamarchán, and Villa de Leiva. We base our interpretations on published and other widely available data, both sedimentological (including mineralogical) and palaeobiological (vertebrate, invertebrate, and microfossil; marine and terrestrial), supplemented by personally collected specimens. We combine palaeontological, sedimentological, and diagenetic data with published studies on the modern shallow marine realm and ancient epicontinental

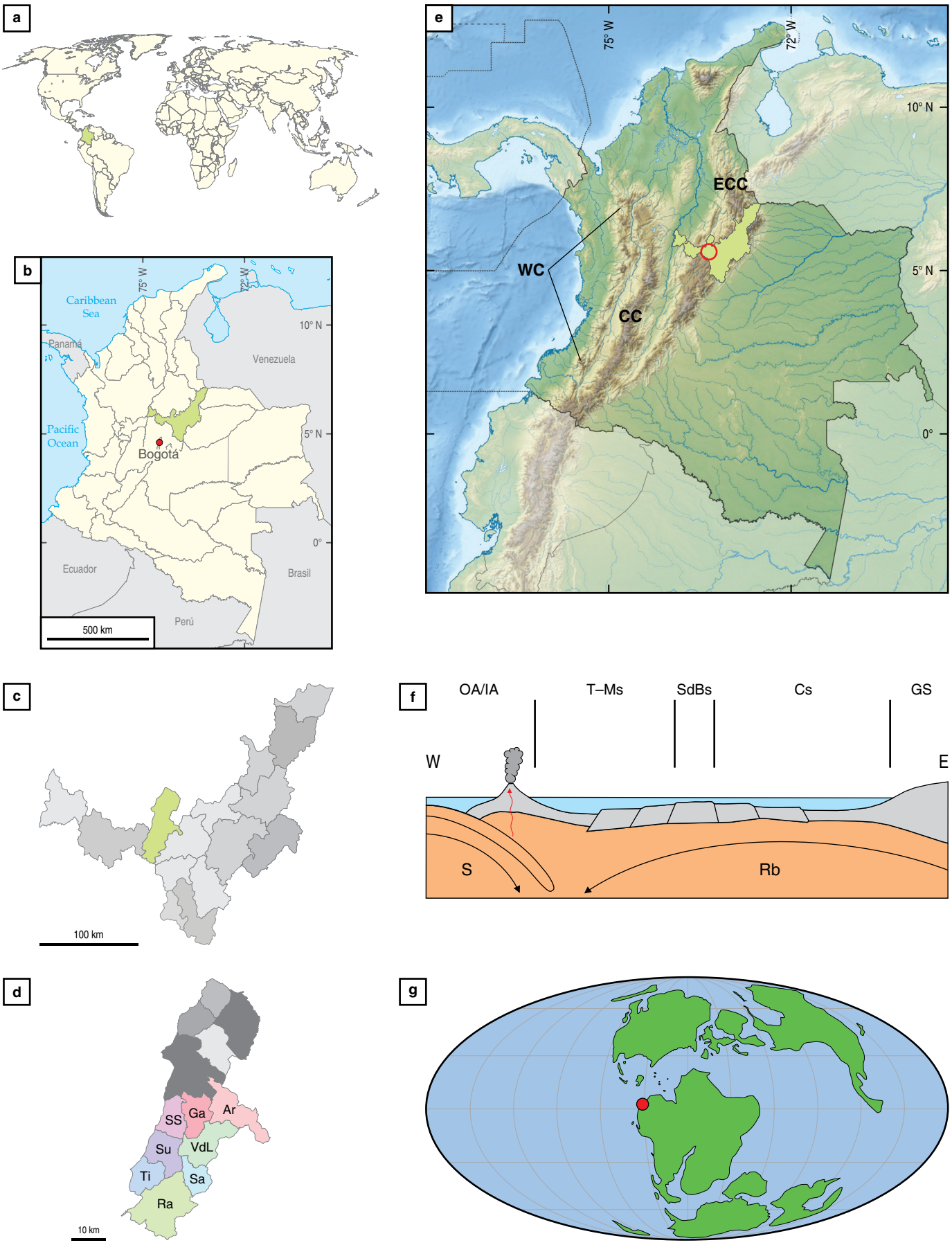
a
b
Caribbean Sea
Panamá
Pacific Ocean
Venezuela
Bogotá
Ecuador
Brasil
Perú
500 km
75° W
72° W
10° N
5° N
0°
e
WC
CC
ECC
c
100 km
f
OA/IA
T–Ms
SdBs
Cs
GS
W
E
S
Rb
d
SS
Ga
Ar
Su
VdL
Ti
Sa
Ra
10 km
g

Figure 1. Maps and cross–section showing the location of the Paja Formation Basin and palaeogeological interpretations. **(a)** World map showing the position of Colombia (green). **(b)** Map of Colombia showing the departments (Department of Boyacá, green; Bogotá, red). **(c)** Department of Boyacá showing the provinces (Ricaurte Province, green). **(d)** Ricaurte Province showing municipalities (alto Ricaurte coloured showing the municipalities: (Ar) Arcabuco, (Ga) Gachantivá, (Ra) Ráquira, (Sa) Sáchica, (SS) Santa Sofía, (Su) Sutamarchán, (Ti) Tinjacá; (VdL) Villa de Leiva), and bajo Ricaurte, greys. **(e)** Topographic map showing the three Colombia cordilleras (mountain chains): (WC) Western Cordillera, the currently active volcanic mountain chain resulting from subduction of the Nazca Plate to the west; (CC) Central Cordillera, separated from the Western Cordillera by the Cauca River, the former island arc to the west of the Eastern Cordillera Basin; and (ECC) Eastern Cordillera of Colombia within which the Paja Formation lies (approximate position of Paja Formation Seas, red circle). **(f)** Conceptual model showing a cross–section through the Eastern Cordillera Basin sedimentary basin during the Early Cretaceous: (Cs) Cocuy Sub–basin, a series of half–grabens; (E) east; (GS) Guiana Shield of the South American Plate; (OA/IA) open ocean/island arc (the future Central Cordillera); Rb—roll–back of the edge of the South American Plate, leading to lithospheric stretching, thinning, and downwarping; (S) subduction of the Farallón Plate under the South American Plate; (SdBs) Sabana de Bogotá (or Cundinamarca) Sub–basin, a horst over which salts were deposited during the earliest Cretaceous; (T–Ms) Tablazo–Magdalena Sub–basin, a series of half–grabens, of which the Paja Formation deposits form part; (W) west. **(g)** Hauterivian – Barremian palaeogeography, with the approximate position of Paja Formation Seas, red circle; land, green; seas and oceans, blue. Base maps (a–e) from various government websites; (f) original; (g) modified from Smith et al. (1994; map 18).

Figure 2. Ammonite sculpture mounted in the alto Ricaurte. Ammonites are so abundant, that the genus *Dufrenoyia* has become a symbol of the region. Sculpture located along the Villa de Leiva–Sutamarchán road (location indicated by an asterisk on Figure 3).

sea deposits, and thereby provide a comprehensive and integrated overview of the Paja Formation.

2. Overview of Paja Sedimentology and Palaeoenvironmental Interpretations

2.1. Tectonic Setting

The Paja Formation rocks of the ECC form part of the Chibcha Terrane (Gómez & Almanza, 2015). The regional tectonic structure of the ECC is broadly a horst (comprising the Sabana de Bogotá or Cundinamarca Sub–basin), which lies between a pair of half grabens, the Tablazo–Magdalena Sub–basin to the west and the Cocuy Sub–basin to the east (Gaona–Narváez, 2015; Jiménez et al., 2014; Teixell et al., 2015); the Paja Formation of the alto Ricaurte forms part of the Tablazo–Magdalena Sub–basin (Gaona–Narváez, 2015). The majority of the ECC Cretaceous rocks are of marine origin, with the (presumably deeper) western margin dominated by mudrocks (Teixell et al., 2015).

Early Cretaceous sedimentation of the ECC occurred in an extensional back–arc basin (Martínez et al., 2007), the result of complex interactions between the Caribbean, Nazca (a remnant of the Farallón), and South American plates. Subduction of the oceanic Farallón Plate beneath the continental South American Plate (Teixell et al., 2015) caused roll–back and extension of the western margin of the South American Plate (Figure 1f). This extensional regime resulted in normal faulting, which produced a "block–basin" topography; however, it is not known if extension was sufficiently great to produce rifting and emplacement of mid–ocean ridge basalt–type magmas. The extensional regime initially caused thermal expansion, followed by thermal sag (Jiménez et al., 2014) which produced a tectonically controlled deepening of the basin. Although the Cretaceous has been hypothesised as a time of generally subdued topographic relief, this does not accord well with a hypothesised increase in mid–ocean ridge spreading rates, which would have led to increased rates of subduction and elevated topography in the form of the Central Cordillera island arc to the west of Paja Formation Seas. Paja Formation sedimentation was therefore controlled by tectonically induced normal faulting, and bounded by a magmatic arc to the west (the future Central Cordillera), and the Guiana Shield to the east, both of which acted as potential sediment sources (Gaona–Narváez, 2015).

2.2. The Paja Formation

The type section for the Paja Formation lies on the north bank of the La Paja Creek, where it enters the Sogamoso River, close to Bucaramanga, Santander Department, in the Middle Magdalena Valley on the western flank of the ECC (Etayo–Serna, 1965, 1979; Guerrero, 2002b). The Paja Formation was first described by WHEELER (in Morales, 1958), as composed of black shales with abundant calcareous concretions, which preserves a Hauterivian to Aptian ammonite fauna including the genera *Nicklesia*, *Pulchellia*, *Heteroceras*, *Santandericeras*, *Cheloniceras,* and *Colombiceras* (Guerrero, 2002b; Renzoni, 1981). In the type locality, the Paja Formation overlies the coarse–grained limestones of the Rosablanca Formation, and underlies the mixed carbonate and clastic sedimentites of the Tablazo Formation, the lateral time equivalent of the lower part of the San Gil Group of the alto Ricaurte (Guerrero, 2002b; Moreno et al., 2013).

Within alto Ricaurte, the Paja Formation overlies the Ritoque Formation. Although the contact between the Ritoque and Paja Formations was originally thought to be conformable (Etayo–Serna, 1979; Guerrero, 2002a; Huber & Wiedmann, 1986), it is now considered a paraconformity due to missing upper Valanginian ammonite biozones (Etayo–Serna et al., 2015). The upper contact of the Paja Formation with the Lower San Gil Formation (San Gil Group) is gradational (Etayo–Serna, 1979; Guerrero, 2002b). The Paja Formation crops out almost continuously along road cuttings (e.g., Tunja–Sáchica), rivers (e.g., Samacá River), creeks (such as Negra Creek) and hillsides (loma La Yuca, loma Monsalve, loma La Cabrera, loma La Catalina, loma La Yesera, and loma Blanca) and is divided into three members, which in ascending stratigraphic order are: Lutitas Negras Inferiores, Arcillolitas Abigarradas, and Arcillolitas con Nódulos Huecos (Etayo–Serna, 1965) (Figure 3). These deposits surround the Upper Jurassic or lowest Cretaceous sandstones of the Arcabuco Anticline (Etayo–Serna, 1968; Huber & Wiedmann, 1986). However, despite the complex tectonic environment that has raised the alto Ricaurte sections of the Paja Formation to around 2150 m above modern day sea levels, the deposits are well–exposed and exhibit limited structural complications (Etayo–Serna, 1968).

2.2.1. Sedimentology

2.2.1.1. Lutitas Negras Inferiores (LNI)

The lowermost member of the Paja Formation is the LNI, and it is this unit on which the town of Villa de Leiva lies (Etayo–Serna, 1968). The LNI has a sharp contact with the underlying grey siltstones of the Ritoque Formation (Etayo–Serna, 1965, 1968; Guerrero, 2002a) and is subdivided into five lettered segments, A–E. Along the Cucaita–Samacá Road the LNI exhibits a thickness of 340–380 m, and the sedimentites are mainly black, fissile claystones with intercalations of micrite, and occasional sandier interbeds in the middle of the unit (Etayo–Serna, 1965, 1968, 1979; Etayo–Serna et al., 2015). The LNI has been considered a distinct lithostratigraphic unit, the Villa de Leiva Formation (Guerrero, 2002a), as the LNI is absent from Paja Formation type area near Bucaramanga. The proposed type section for the Villa de Leiva Formation is 5 km south–southeast

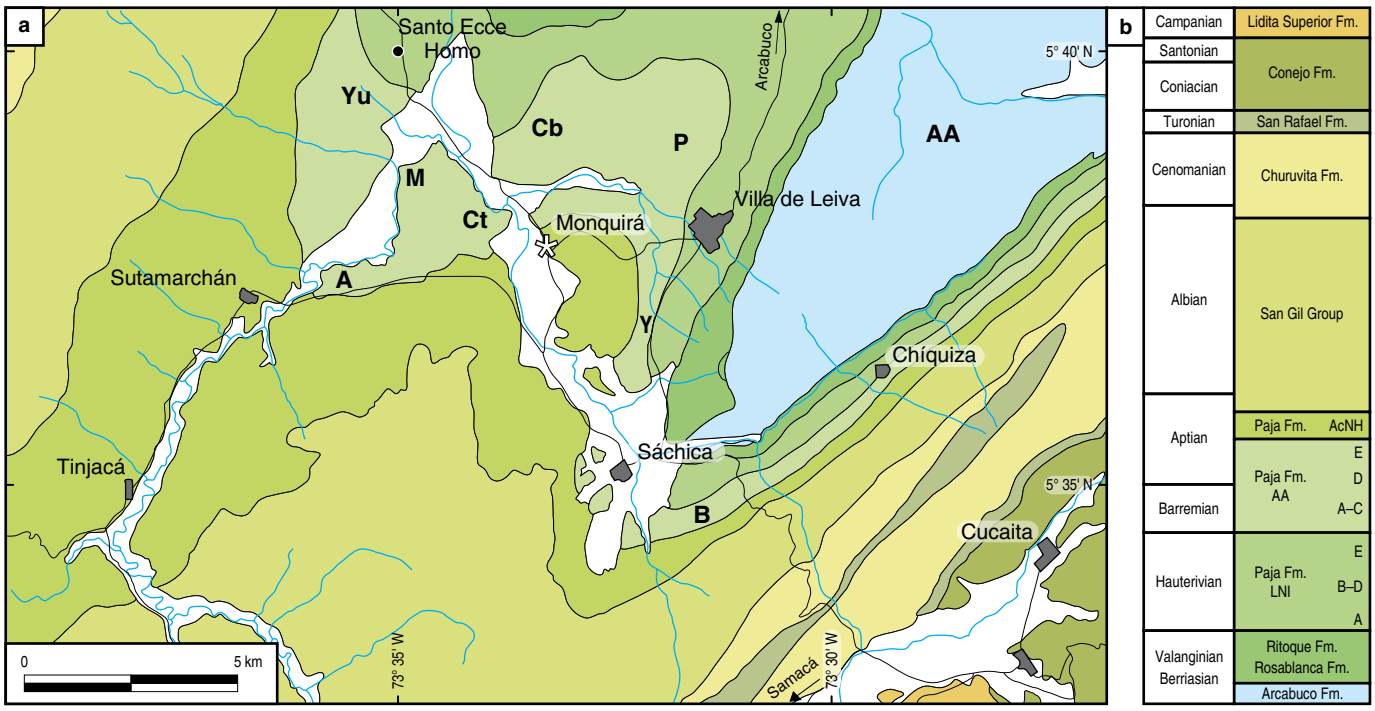

Figure 3. The southern alto Ricaurte. **(a)** Geological map and **(b)** stratigraphic column, indicating localities mentioned in the text. The map extends from Tinjacá in the west to Cucaita in the east and is centred on Sáchica–Villa de Leiva with directions to Arcabuco and Samacá indicated (alluvium, white; asterisk, location of ammonite sculpture (Figure 2); rivers, blue; towns, grey; principal roads, black). Abbreviations: (A) loma La Asomada; (AA) Arcabuco Anticline; (B) loma Blanca; (Cb) loma La Cabrera; (Ct) loma La Catalina; (M) loma Monsalve; (P) loma Pedro Luis; (Y) loma La Yesera; (Yu) loma La Yuca; (Fm.) Formation. The stratigraphic column shows geological age (left), formation or group (centre), with members and lettered segments for the Paja Formation. Modified from Etayo–Serna et al. (2015).

of Villa de Leiva along Negra Creek to the southeast of the Arcabuco Anticline (Guerrero, 2002a). However, this proposal of an independent Villa de Leiva Formation has not been widely adopted (however, see Patarroyo, 2009).

Segment A of the LNI comprises 110–120 m of black, red–weathering, normally finely–laminated claystones that are sandier towards the base (Etayo–Serna, 1965, 1968). Calcareous concretions are dispersed throughout the segment and are occasionally concentrated into bands; gypsum is present in the segment but is more common higher in the sequence. Fossils are scarce, although some concretions are fossiliferous and some fossils are covered with or shattered by gypsum (Etayo–Serna, 1968).

Segment B of the LNI consists of 20 m of dark–coloured, very fine–grained sandy clay–shales. The base and top of the segment are formed by two bands of very fine–grained sandstone, and between these marker horizons, the shales exhibit "swirling" boundaries (Etayo–Serna, 1968), possibly representing dewatering structures. The segment also contains both calcareous concretions and gypsum (Etayo–Serna, 1968). Segment C is 30 m of black shales, with calcareous concretions up to 250 mm in diameter, and occasional fossils some of which are pyritized. Approximately in the middle of the segment is a 1.3 m thick, contorted sandy–shale bed, which may represent slump folding, with intercalations of gypsum (Etayo–Serna, 1968). Segment D is 15 m of very fine–grained, compact, siliceous sandstone, which is banded and apparently forms banks (Etayo–Serna, 1968). Some calcareous concretions are present.

Segment E of the LNI, consists of 165 m of predominantly dark mudstones, occasionally finely–laminated, with some micaceous siltstone intercalations (Etayo–Serna, 1965, 1968). Concretions are common, many calcareous, but others are small and clay–rich. Towards the top of the segment the concretions are occasionally fossiliferous and coated, or radially crossed, by layers of gypsum (Etayo–Serna, 1968). Fossils are generally scarce in this segment, although most abundant towards the top.

2.2.1.1.1. Environment of Deposition

The LNI has been considered a period of relative geological stability, with nearly uniform environmental conditions prevailing during deposition of the member (Etayo–Serna, 1968). By LNI times, the generation of accommodation space and rates of sedimentation are considered to have been subequal, with environmental conditions remaining approximately uniform throughout deposition (Etayo–Serna, 1968). The black shale units (segments A, E) are considered to have been deposited in a low energy, reducing environment with little or no bottom currents (Etayo–Serna, 1968). However, it has been speculated that

this was not the result of deep marine conditions (Etayo–Serna, 1968), but due to restricted access to the open sea. This suggested the LNI black shales did not represent deep water deposition, but rather sedimentation in anoxic conditions below storm wave base (Etayo–Serna et al., 2015). The sandier segments (B, the centre of C, D) have been seen as the edges of a northward thickening sandstone unit, representing former offshore littoral marine bars lying parallel to the palaeocoastline (Etayo–Serna, 1968, 1979; Etayo–Serna et al., 2015). The presence of littoral sand bars is equivocal, as it was based on lithological correlation between segments B–D of the LNI, and an unnamed thick sandstone unit lying west of the town of Arcabuco (Etayo–Serna, 1965, 1968, 1979; Etayo–Serna et al., 2015). Correlation was also based on both units overlying sedimentites containing *Olcostephanus* ammonites (Etayo–Serna, 1968).

2.2.1.2. Arcillolitas Abigarradas (AA)

The middle unit of the Paja Formation is the AA Member, which along the Cucaita–Samacá Road exhibits a thickness of 480 m (Etayo–Serna, 1965, 1968, 1979). The AA is predominantly composed of fissile, light–coloured claystones, sandier in the lower part, and exhibiting intercalations of calcareous claystones and gypsum higher in the succession (Etayo–Serna, 1979). This unit is subdivided into five segments lettered A–E.

Segment A of the AA, is up to 57 m of weathered black claystones, with intercalations of harder calcareous clayey–sandstones, some of which preserve evidence of cross–bedding (Etayo–Serna, 1965, 1968, 1979). The segment contains calcareous concretions 0.5 m or more in maximum dimension and often clay coated, some of which are septarian and crossed internally by veins of calcite. The surrounding beds arch both above and below the concretions. Gypsum forms interstratified, bedding parallel layers, but also cuts the bedding and forms coatings around concretions. In places it is possible to observe layers of fibrous calcite, especially along the margins of the clayey–sandstone beds. The base of the segment preserves an event horizon consisting of a mixture of ammonites (some fragmentary), wood, and benthic foraminiferans (Patarroyo–Camargo et al., 2009; Patarroyo, 2009). In the top few metres of segment A at lomas La Yesera and Blanca, fossils and concretions are poorly preserved due to accumulations of gypsum.

Segment B of the AA is a marker horizon, 1.6 m thick, formed from very compact clay–rich limestones in thin beds, some separated by thin clay lenses towards the top; these beds contain some poorly preserved concretions and fossils (Etayo–Serna, 1968). Segment C comprises 86 m of grey claystones, with calcareous concretions, and harder marlstone intercalations. Gypsum fills fissures throughout the segment, with marl layers overlain by bedding parallel layers of gypsum up to 10 mm thick. Calcareous concretions are frequently surrounded by layers of gypsum and iron oxides (Etayo–Serna, 1968). Except for the base, segment C typically preserves no fossils. Segment D is formed from 102 m of claystones, less sandy than the underlying layers, and with a white clay–rich bed towards the top (Etayo–Serna, 1968); this may be a bentonite (Bürgl, 1954). The middle of the segment preserves gypsum exploited by local farmers, and smaller gypsum veins fill cracks and fissures. The segment preserves abundant small, calcareous concretions and prominent, hard calcite levels (Etayo–Serna, 1968). Fossils are rare at the base of the segment, but occur sporadically above; fossils in the white clay layer are strongly compressed and covered in gypsum.

Segment E of the AA comprises 235 m of weathered claystones, some finely laminated, and intercalated with thin calcareous clays bands. The claystones are interstratified with gypsum, which in places has been exploited by local farmers; gypsum–filled cracks and fissures are frequently present. Calcareous concretions are dispersed throughout the segment (Figure 4) together with hard bands of calcite (Etayo–Serna, 1968). The entire segment is richly fossiliferous, with many concretions full of well–preserved ammonites; fossils are often at the centres of the concretions.

2.2.1.2.1. Environmental Interpretation

The base of segment A of the AA, has been interpreted as showing the action of density driven (turbidity) currents, which flowed from east to west (Etayo–Serna, 1968). These turbidity currents were interpreted as reworking previously deposited organic remains (principally cephalopod shells and wood) and produced little sorting in terms of size of the transported materials. Large ammonites were deposited parallel to the stratification, with the remains of smaller ammonites within the living chambers of the larger specimens. The east–west direction of the flow was based on a westerly reduction in calcium carbonate deposition, which resulted in an increase in the size and richness of cephalopod fragments, an increase in heteromorphic ammonites, and a reduction in fossil wood towards the east. Hence, segment A of the AA was seen as having mobile bottom conditions that inhibited benthic fauna (Etayo–Serna, 1968). However, although turbidity currents may have affected the Paja Formation Basin, no data is available on the flow direction(s) indicated by the cross–bedding within the hard bands of segment A, and as intermittent events, turbidity currents would not have produced constantly shifting bottom conditions. The variation in ammonites considered current transported (Etayo–Serna, 1968), is only marginally statistically significant, and the distances are probably too short for reliable analysis. The preservation of delicate organic structures, such as spines on ammonite shells, strongly argues against dynamic transport of these organisms from within or outside the Paja Formation Basin. In addition, supporting arguments based on fossils being located at the centres of the concretions, or the possibility of concretions concentrated by current action (Etayo–Serna, 1968), are

Figure 4. Concretion from the alto Ricaurte (UADG LM 15.57f) with a mixture of autochthonous ammonites (a) and allochthonous terrestrial plant material (b). Collected from loma La Cabrera.

fallacious as concretions are of early diagenetic origin (Lash & Blood, 2004; Witkowska, 2012), and therefore not related to depositional processes.

Segments B–E of the AA were interpreted as representing a wide, shallow bay in the neritic zone of a platform sea, with alternating restriction and access to the open ocean (Etayo–Serna, 1968). Restriction was seen as the result of more complete development of the littoral bars hypothesised for LNI times. This periodic restriction was hypothesised to lead to changes in bottom waters, with west–east flowing currents that produced oscillating bottom water dynamics. During times of restriction there were gentle bottom currents with deposition of mostly complete and well–preserved ammonites, and increased salinity which led to development of sabkha and deposition of gypsum (Etayo–Serna, 1968; Forero–Onofre & Sarmiento–Rojas, 1985). Times of greater access to the open sea produced more dynamic bottom currents, with winnowing of ammonites by shell shape, and the introduction of decomposing marine reptile carcasses in from the west, which floated belly up into shallow Paja Formation waters, to become beached and preserved (Etayo–Serna, 1968). However, salinity increase would have led to the deposition of halite (NaCl) prior to gypsum, for which there is no evidence in the Paja Formation. In addition, many of the characteristic features of sabkha (e.g., birdseyes, boudinage, scour and fill, ripples, cross–bedding; Townson, 1975) are absent from the AA, and setulfs (Sarkar et al., 2011), although reported from the Paja Formation are not supported by images or locations (Forero–Onofre & Sarmiento–Rojas, 1985), casting doubt on their validity. Sabkha development requires hypersalinity for gypsum to be deposited, leading to a sparse fauna (Townson, 1975) and this is at odds with abundant, unbroken, three–dimensionally preserved ammonites in segments B–E of the AA. The floating of decomposing vertebrate carcasses does not match the taphonomy of fully articulated fossils, many of which (e.g., *Callawayasaurus*) are also associated with the presence of gypsum (Welles, 1962).

2.2.1.3. Arcillolitas con Nódulos Huecos (AcNH)

The uppermost unit of the Paja Formation is the 80 m thick and undivided AcNH Member, which consists of claystones, with intercalations of shiny white clays, although the deposits become more micaceous and sandy towards the top of the unit. Numerous hollow concretions, up to 200 mm in diameter, and smaller massive clay concretions up to 50 mm in diameter, characterize the unit (Etayo–Serna, 1968). Fossils occur sporadically within the claystones, white clays, and concretions. Although vertebrate fossils are rare in the AcNH, one of the authors (M.G.–P.) has found indeterminate fragments of a very weathered vertebrate in this member.

2.2.1.3.1. Environmental Interpretation

The environmental conditions of the AcNH are interpreted as a similar to the AA, but without the calcite– and gypsum–rich layers. This suggested more access to the open sea, with reduced deposition of evaporitic minerals (Etayo–Serna, 1968). The white clays have been considered volcanic ash deposits (Bürgl, 1954), although these were not subsequently recognised as such (Etayo–Serna, 1968).

2.2.2. Palaeontology

Fossils, especially marine reptiles, fish, and ammonites (Figures 5–7), are common in the Paja Formation around the alto Ricaurte (Huber & Wiedmann, 1986). Here we summarize the palaeontology of the Paja Formation, with special emphasis on the autochthonous marine reptiles (plesiosaurs, ichthyosaurs, marine turtles), followed more briefly by fish, invertebrates, and microfossils.

2.2.2.1. Plesiosaurs

The Paja Formation, in terms of abundance, variety, and exceptional preservation of Plesiosauria, is the most important Lower Cretaceous plesiosaur assemblage in the world. In pre–cladistic studies, Plesiosauria was divided into two groups, the long–necked plesiosauromorphs (Figure 5a) and the short–necked pliosauromorphs (Figure 5b). Rather confusingly, both Plesiosauria and the plesiosauromorphs have been referred to as "plesiosaurs"; however, here we use the term "plesiosaur" to refer only to Plesiosauria. Both plesiosauromorph and pliosauromorph plesiosaurs are represented in the Paja Formation deposits of the alto Ricaurte. Plesiosauria are the second most common large vertebrate faunal elements after the ichthyosaurs,

a

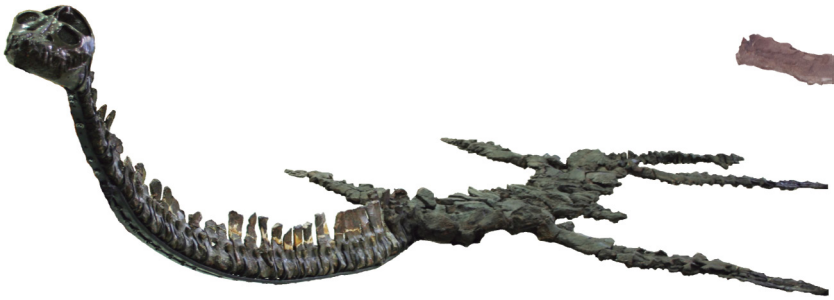

b

c

d

e

f

Figure 5. Representative marine reptile fossils from the alto Ricaurte. **(a)** The Bogotá specimen of the plesiosauromorph plesiosaur *Callawayasaurus colombiensis* (SGC MGJRG.2018.V.1), the skull is a replica based on combined information from the original of this specimen and the holotype (UCMP 38349); length along the vertebral column 7 m. **(b)** The pliosauromorph plesiosaur *Kronosaurus boyacensis* (MJACM 1) in situ where discovered, preserved length 7.35 m. **(c)** Skull of the opthalmosaurid ichthyosaur *Platypterygius sachicarum* (SGC DON–19671), length 890 mm. **(d)** Skull and anterior vertebral column of the opthalmosaurid ichthyosaur *Muiscasaurus catheti* (CIP–FGC–CBP–74), length 800 mm. **(e)** The protostegid marine turtle *Desmatochelys padillai* (CIP–FGC–CBP 01), length 1.44 m along the midline; it is likely the eggs illustrated in Figures 9, 10 belong to this species. **(f)** The sandownid marine turtle *Leyvachelys cipadi* (CIP–FGC–CBP–71), length 1 m.

represented by four published genera, all of which are currently monospecific, although further specimens await description.

The first published plesiosaurs from the Paja Formation were two substantially complete skeletons of the plesiosauromorph *Callawayasaurus colombiensis* (Welles, 1962) Carpenter, 1999, the holotype (UCMP 38349) and second specimen (SGC MGJRG.2018.V.1; Figure 5a). The two specimens were originally described as new species of the North American genus *Alzadasaurus* Welles, 1943, as *Alzadasaurus colombiensis* Welles, 1962, although following revision, the species was transferred to the new genus *Callawayasaurus* (Carpenter, 1999), as *Callawayasaurus colombiensis* (Welles, 1962) Carpenter, 1999. Unfortunately, during this revision, both the name of the country ("Columbia") and the original species name ("*C. columbiensis*") were misspelt (Carpenter, 1999, 172).

The two skeletons of *Callawayasaurus* were excavated from grey–coloured red–weathering siltstones of segment E of the AA Member of the Paja Formation by teams led by Ruben Arthur STIRTON of the UCMP (Páramo–Fonseca, 2015; Welles, 1962). The holotype was recovered from loma La Catalina, approximately 6 km to the west of Villa de Leiva, and about 300 m to the north of the Villa de Leiva–Chiquinquirá road (Welles, 1962). The second specimen (or "paratype") was discovered approximately 100 m to the north, and stratigraphically 10 m from the holotype; however, there is confusion as to the exact relative positions of the two skeletons, as the original description records conflicting locality information (see Welles, 1962, 1, 13, 32), although this discrepancy is in the process of being resolved. The holotype of *Callawayasaurus* was transferred to the University of California, Berkeley under the 1944–1945 Comisión de Vertebrados (Espinosa, 2016), whilst the second specimen remained in Bogotá (Welles, 1962, 17, 32); the skull, formerly registered to the museum in Berkeley as UCMP 125328, has recently been returned to the Servicio Geológico Colombiano (SGC).

The preservation of the holotype and second specimens of *Callawayasaurus colombiensis* are remarkably similar. Both skeletons were found in the supine ("belly–up") position, are almost complete and articulated, and exhibit minimal crushing (Páramo–Fonseca, 2015; Welles, 1962). The holotype is missing the ilia, ischia, tail, and some distal limb elements, all of which can be attributed to recent weathering and/or collection failure due to digging for gypsum (Welles, 1962). The second specimen of *Callawayasaurus* (Figure 5a) is somewhat more complete, although the skull is imperfect, missing the left mid–portion between the external naris and orbit, which was not found in the field. Both specimens are largely articulated, with the holotype exhibiting slight movement of the right paddles, ribs, gastralia, and a few other elements (Welles, 1962), all attributable to the settling of the carcass during decomposition. Both specimens are mostly uncrushed, with the holotype exhibiting slight compression of the skull (a pit in the snout, between the orbits, the parietal crest, part of lower temporal arch, and the palate), the left scapula, right coracoid, and a few distal limb elements (Welles, 1962).

Both the holotype and Bogotá specimens of *Callawayasaurus* are remarkably well–preserved (Welles, 1962). Using the holotype as an example, the skeleton preserves the jaws tightly closed, most of the teeth in situ in their alveoli, the delicate hyoid bones under the skull, and gastroliths in and around the rib cage. The bone surface is excellently preserved, with the internal spongy bone texture present in many places without mineral infill; this has been attributed to rapid burial by fine–grained sediments that sealed the carcass from permineralizing groundwaters (Welles, 1962). The casts of bivalves and ammonites are common in the surrounding matrix. The bones are frequently surrounded by extensive limestone concretions, especially the skull, shoulder girdle, and vertebral column, which has reduced the crushing from subsequent overburden. The bones are typically chocolate brown–coloured and coated in red–coloured iron oxide, or surrounded by cm scale red– or yellow–weathering iron oxide–rich concretions. In addition, gypsum is common as crystals in the sedimentary matrix, and infilling veins and cracks (Figure 8). A layer of gypsum approximately 6 mm thick covered the skull and palate, with gypsum penetrating the skull and other bones.

After the discovery of *Callawayasaurus*, two incomplete plesiosauromorph specimens, exhibiting good three–dimensional preservation, have been recovered from the alto Ricaurte, and attributed to the genus (Goñi & Gasparini, 1983; Jerez–Jaimes & Narváez–Parra, 2001). The first was the anterior of a skull and mandible preserved to level with the rear of the orbits (UN ICNMHNR–081) recovered from loma La Cabrera, some 4 km to the west of Villa de Leiva (Goñi & Gasparini, 1983). The second was a much more complete, and at least partially articulated, skeleton discovered at an unrecorded locality and horizon in the Paja Formation near Villa de Leiva. Discovered

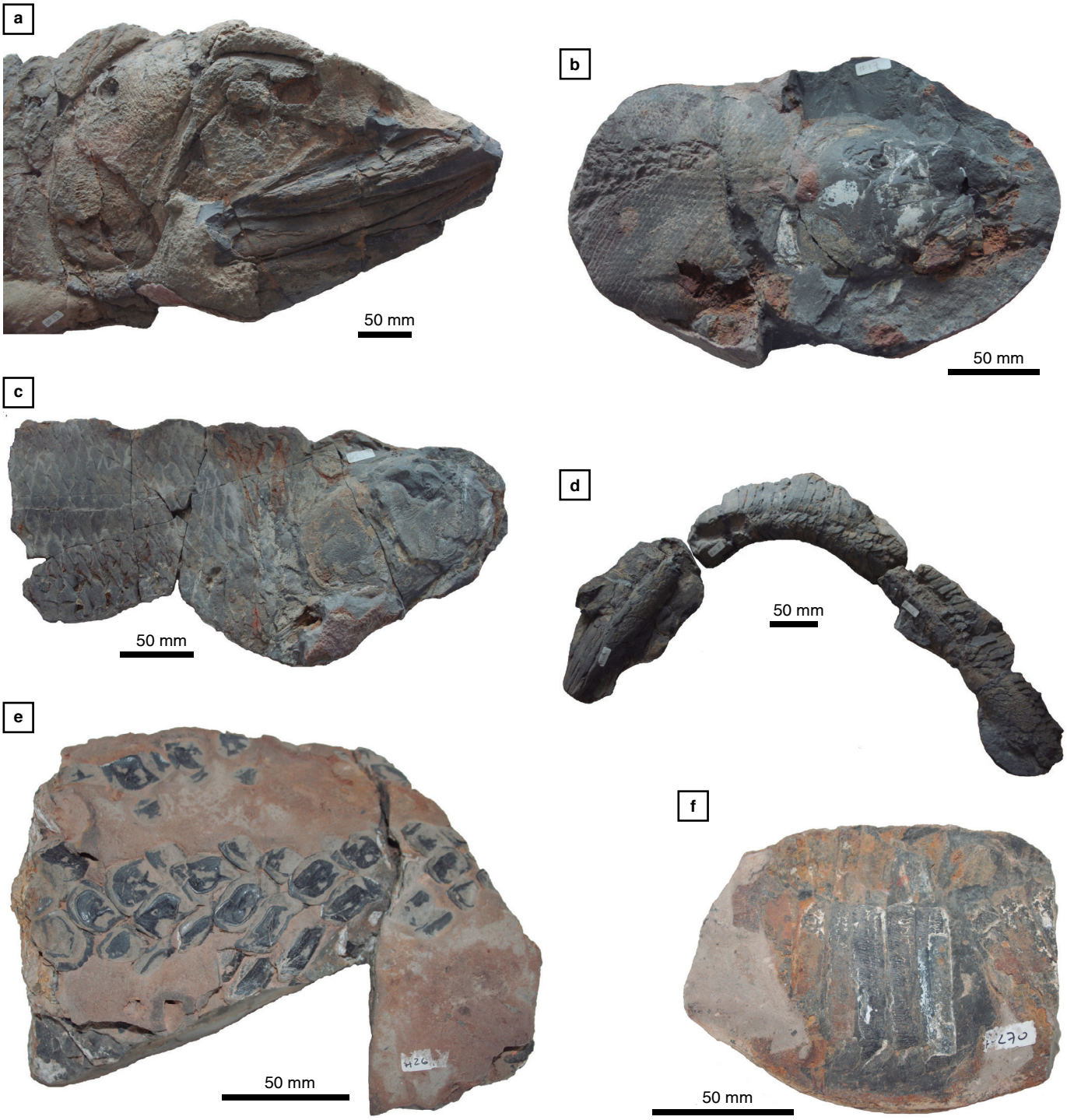

Figure 6. Fish remains preserved in three–dimensions from the alto Ricaurte showing a range of sizes and morphotypes, none of which have been formerly described. Specimen numbers **(a)** MJACM 13; **(b)** MJACM 17; **(c)** MJACM 29; **(d)** MJACM 16a–c, a complete specimen of *Vinctifer* species; **(e)** MJACM 269, scales from the flanks of a large fish; **(f)** MJACM 270, scales of *Vinctifer* species. No collection localities recorded, but all specimens are likely derived from Paja Formation, vereda Monquirá.

Figure 7. Ammonites from the alto Ricaurte showing a range of sizes and morphotypes (both planispiral and heteromorphic forms), none of which have yet been formerly described. Specimen numbers **(a)** MJACM 35, large planispiral ammonite missing central whorls and **(b)** detail of the boxed area showing suture pattern; **(c)** MJACM 202, a smaller planispiral ammonite; **(d)** MJACM 117, a criocone (open planispiral) heteromorph ammonite; **(e)** MJACM 112, "hairpin–shaped" heteromorph ammonite preserved in association with two planispiral ammonites; **(f)** MJACM 137, a moderately sized planispiral ammonite missing the central whorls, and **(g)** detail of the boxed area showing suture pattern. No collection localities recorded, but all specimens are likely derived from Paja Formation, vereda Monquirá.


a
50 mm
b
c
#202
50 mm
d
#117
50 mm
e
50 mm
f
50 mm
g

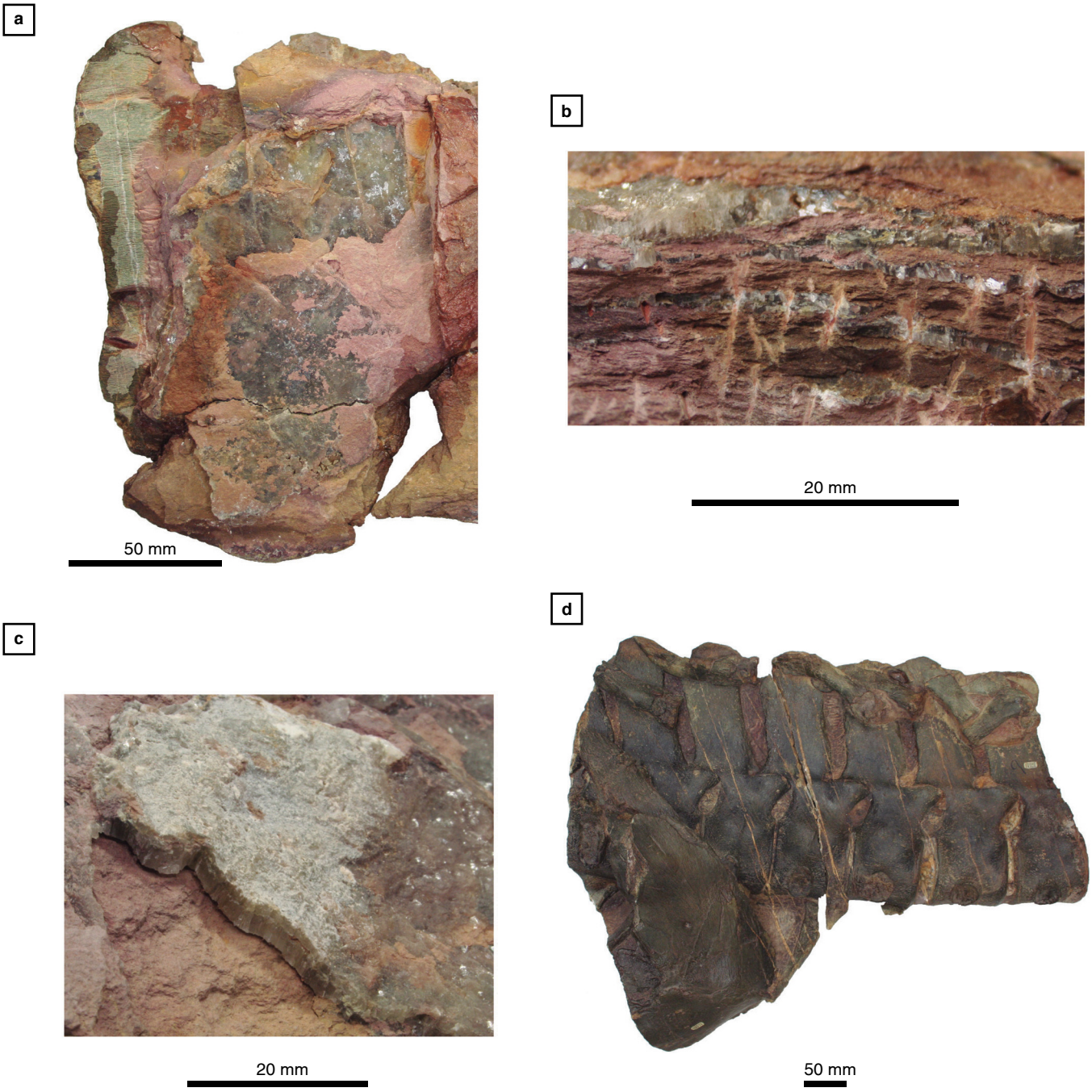

Figure 8. Gypsum "beef" associated with the holotype of *Callawayasaurus colombiensis* (UCMP 38349) showing **(a)** the unprepared (originally upper) surface of cervical vertebra 22 (anterior, left; dorsal, top) showing a gypsum sheet sub–parallel to the bone surface, that splits into two to the left; notice also the vertical veins of gypsum cutting the bone and matrix. **(b)** Layers of gypsum "beef" within the sediments as seen from anterior view (i.e., to the left of (a)). **(c)** Bi–layered sheet of gypsum "beef" on the unprepared (original upper) surface of a block containing cervical vertebra 29 (pars) to 31. **(d)** Prepared (originally lower) surface of posterior cervical and ?anterior "pectoral" vertebrae partly covered by the coracoid of the shoulder girdle (anterior, right; dorsal, top), showing vertical veins of gypsum cutting the bones. Collected by a party from the Tropical Oil Company and Ruben Arthur STIRTON (UCMP) from loma La Catalina.

in 1999, the specimen was tentatively attributed to *Callawayasaurus* (Jerez–Jaimes & Narváez–Parra, 2001), although the current whereabouts is unknown. Numerous additional specimens of plesiosauromorphs, some probably attributable to *Callawayasaurus* but others that represent new genera, are held by various institutions and await formal scientific description (Gómez–Pérez & Noè, 2017; Páramo–Fonseca, 2015).

The second described plesiosaur from the Paja Formation of the alto Ricaurte was a pliosauromorph (MJACM 1) discovered in June 1977 (Acosta et al., 1979), and later described as

the new species *Kronosaurus boyacensis* Hampe, 1992 (Figure 5b). The skeleton was discovered by local farmers in the upper Aptian segment E of the AA Member of the Paja Formation in Monquirá, 4 km to the west of Villa de Leiva (Acosta et al., 1979). The skeletal remains are currently the centrepiece of the community run Museo El Fósil built over the site of the find. MJACM 1 lies in the prone (dorsal up) position, is substantially complete and mostly articulated, although the skeleton is missing the upper surface of the posterior of the skull, some elements of the posterior of the pelvis, the rear right limb beyond the femur, the tail, and numerous distal limb elements (Hampe, 1992). However, all missing elements can be attributed to recent weathering or collection failure. The skull is somewhat crushed and some elements such as the ribs and some vertebrae are slightly displaced due to post–mortem movement of the carcass. However, the skeleton is mostly articulated, with the teeth in their alveoli, and the bones preserved in three–dimensions; there is no evidence of scavenging or colonization by epibionts. The surrounding sediments are fine–grained, grey–weathering, and fissile (Acosta et al., 1979), and many of the bones are surrounded by calcareous and/or iron–rich concretions (Hampe & Leimkuehuler, 1996), which helped to maintain the original three–dimensional shape of the animal.

The third plesiosaur described from the Paja Formation of alto Ricaurte was *Stenorhynchosaurus munozi* Páramo–Fonseca et al., 2016 (SGC VL17052004–1), discovered on the land of Jorge MUÑOZ on the eastern slope of loma La Cabrera, some 4 km to the west of Villa de Leiva. The specimen was originally published as *Brachauchenius* sp. (Hampe, 2005), whilst under the study of María Eurídice PÁRAMO–FONSECA and colleagues. *Stenorhynchosaurus* was recovered from segment C of the AA Member of the Paja Formation, and ammonite biostratigraphy permitted dating of the specimen to the early late Barremian (Páramo–Fonseca et al., 2016). The skeleton was discovered in a variegated clay–grade, calcareous and kaolinitic, laminated mudstone. The animal was articulated and substantially complete, lying in the prone position with the paddles spread out laterally. The bone surface is generally very well–preserved. *Stenrohynchosaurus* is missing the tip of the snout, distal elements of the left anterior paddle, the entire right posterior paddle, and the tail. There is some crushing to the rear of the skull and neural arches, and some of the ribs and posterior elements are displaced, but there is no evidence of scavenging or epibionts.

The fourth plesiosaur from the alto Ricaurte Paja Formation is the newly described genus and species of pliosauromorph, *Acostasaurus pavachoquensis* Gómez–Pérez & Noè, 2017 (UNDG R–1000). This specimen was recovered in 1967 by a French Technical Cooperation team working with the Hydrology Section of the Ministry of Public Works of Colombia; however, no contemporary collection records exist (Acosta et al., 1979). The specimen was recovered close to the Santo Ecce Homo Convent, in Sutamarchán. The specimen consists of a largely complete and articulated pliosauromorph from the lower Barremian segment A at the base of the AA Member of the Paja Formation. The specimen was surrounded by a fine–grained, very dark–coloured matrix, and encased in a single large, non–septarian concretion which preserved ammonites, used for biostratigraphically dating the skeleton. No gypsum was preserved with this specimen. Currently only the skull and anterior cervical vertebrae are prepared; however, the skull is substantially complete and three–dimensional, with delicate structures such as sclerotic plates well–preserved, which are only infrequently encountered in plesiosaurs (Andrews, 1913; Gómez–Pérez & Noè, 2017). *Acostasaurus* is therefore one of the most complete members of Plesiosauria from the Lower Cretaceous, and one of the best preserved pliosauromorphs anywhere in the world.

2.2.2.2. Ichthyosaurs

The second common group of marine reptiles reported from the Paja Formation of alto Ricaurte are the ichthyosaurs. Numerous examples of ichthyosaurs are known, but the majority remain unpublished (e.g., Páramo–Fonseca, 2015); however, many specimens represent new taxa, and are likely to completely re–write our current understanding of post–Jurassic ichthyosaur diversity and evolution, and deserve publication in the highest–quality international journals. The work reinterpreting Cretaceous ichthyosaur diversity and evolution has begun on other faunas worldwide (e.g., Fernández & Aguirre–Urreta, 2005; Fernández et al., 2005; Fischer et al., 2014; Zammit, 2012), and the Colombian specimens from the Paja Formation are likely to prove key to this work.

The first named ichthyosaur from Colombia was the opthalmosaurid *Platypterygius sachicarum* Páramo–Fonseca, 1997 (SGC DON–19671), recovered from loma Pedro Luis, 1.5 km northwest of Villa de Leiva by Jorge CÁRDENAS and presented to the SGC Museum in 1967 (Figure 5c). No detailed stratigraphic information is available; however, the specimen was recovered from the lower part, probably segment A, of the AA Member (see Páramo–Fonseca, 1997, Figure 1). The specimen consists of a substantially complete skull, originally preserved in a hard calcareous–rich matrix (probably a non–septarian concretion), which permitted acid preparation of the left side of the skull; the right side was earlier mechanically prepared. The specimen is essentially three–dimensionally preserved, with some lateral crushing, and is largely complete, but missing the tips of the jaws. The skull bones are articulated, with the sclerotic rings partly preserved in life position, and almost all teeth on the left side in situ; the teeth on the right are more disordered. Bone preservation is generally good on the left of the skull, although the surfaces of some bones are incomplete or fractured, whereas the right side is much more heavily weathered, indicating the specimen lay in the sediment

on its left side, with the right side exposed to weathering prior to collection. The surrounding matrix is organic–rich, with some carbonized plant remains preserved in and around the tightly closed jaws. No ammonites or other macrofossils, palynomorphs or foraminiferans, were encountered in the matrix during preparation (Páramo–Fonseca, 1997).

Muiscasaurus catheti Maxwell et al., 2016 (CIP–FGC–CBP–74) was the second described opthalmosaurid ichthyosaur from the alto Ricaurte Paja Formation, preserving an incomplete cranium associated with 10 articulated cervical vertebrae with attached neural arches and some ribs (Figure 5d). The specimen was recovered from vereda Arrayanes, municipio de Sáchica, from an unspecified horizon within the AA Member of the Paja Formation. The remains were preserved in two calcareous concretions; however, the orientation of discovery was not recorded. Although the skull is essentially three–dimensionally preserved, there is some lateral compression. The anterior of the snout of *Muiscasaurus* is unnaturally curved to the right; this curvature has been attributed to arrival of the carcass head first on the sea floor (Maxwell et al., 2016). However, there is no known mechanism for plastic deformation (rather than breakage) of fresh bone due to impact, making it more likely the deformed snout was due to diagenetic concretionary growth or overburden pressure. As with most of the alto Ricaurte vertebrate specimens, the jaws are preserved tightly closed, the teeth are in position, and delicate structures including sclerotic rings and probable hyoid elements are preserved in or close to their original life positions. The vertebral centra of *Muiscasaurus* are exceptionally well–preserved (Maxwell et al., 2016), the bone retaining the open, porous texture observed in *Callawayasaurus* (Welles, 1962).

2.2.2.3. Marine Turtles

Turtles are abundant in many Cretaceous marine deposits (Cadena & Parham, 2015), although they are most commonly found disarticulated (Cadena, 2014); however, articulated turtles are well represented in the Paja Formation deposits of alto Ricaurte. The first published turtle remains, attributed to a eucryptodire, were a cranial mould and associated mandible (UN ICN–MHNR–083) discovered at loma La Asomada. However, the first turtle named from the Paja Formation was *Desmatochelys padillai* Cadena & Parham, 2015, a member of the Protostegidae, a group of specialized marine turtles that radiated during the Early Cretaceous (Figure 5e); this specimen was considered the oldest known marine turtle, depending on the definition of this group (Cadena & Parham, 2015). The holotype (CIP–FGC–CBP 01) includes a complete skull with articulated lower jaw, a partial hyoid, some cervical vertebrae, both forelimbs (missing most of the phalanges), a left scapula and coracoid, a nearly complete carapace, and parts of the plastron (Cadena & Parham, 2015). Referred specimens include both adults and juveniles with complete or near complete skulls, all with the lower jaws articulated (CIP–FCG–CBP 13, 15, 39, 40, and UCMP 38346), an incomplete vertebral column with attached fragmentary carapace (UCMP 38245A), and a posterior fragment of a carapace (UCMP 38245B). The specimens were found in dark grey limestone concretions, the bones covered, and cavities filled, with a layer of iron oxides. UCMP 38245B preserves possible evidence of predation, in the form of two sub–circular holes, that have been attributed to the teeth marks of a predatory pliosauromorph (Cadena & Parham, 2015). Most specimens were recovered from loma La Catalina, but one (FCG–CBP 15) was found nearby at loma La Cabrera. Although the exact locality of the Berkeley specimens (UCMP 38345A, B, and 38346) was assumed to be from the alto Ricaurte region (Cadena & Parham, 2015), examination of the UCMP archives (by LFN) indicates all three turtle remains were recovered from loma La Catalina, at the same date and site as the holotype of *Callawayasaurus*. All three remains, therefore, most probably belong to the same individual. Hence the UCMP referred specimens, and probably all the material mentioned above, were derived from segment E of the AA Member of the Paja Formation.

The second new genus and species of turtle described from the Paja Formation was *Leyvachelys cipadi* Cadena, 2015, the most complete sandownid turtle (Tong & Meylan, 2013) thus far known (Figure 5f). The holotype skeleton (CIP–FGC–CBP–71) was discovered in 2009 at loma La Catalina in a calcareous claystone, surrounded by abundant calcareous–iron nodules and concretions, presumably from segment E of the AA Member of the Paja Formation. The specimen consists of an incomplete but articulated skeleton, including the united skull and lower jaw, cervical and caudal vertebrae, parts of both limb–girdles, distal limb elements, and an almost complete carapace (Cadena, 2015). The preservation and preparation is sub–optimal, due to the attached iron–rich nodules, with some erosion of the bone surface. The skull is three–dimensionally preserved, with the jaws articulated and minimal evidence of distortion; however, the postcrania is generally flattened.

The Paja Formation of the alto Ricaurte has revealed several spherical objects (UMCP 38348) interpreted as fossilized turtle eggs (Etayo–Serna et al., 2015; Páramo–Fonseca, 2015), which are closely associated with the bones of the mother (Figures 9, 10). The eggs were discovered in segment E of the AA Member at loma La Catalina, the locality that produced the holotype of *Callawayasaurus*, and at the same time as the *Leyvachelys cipadi* specimens (UCMP 38245A, B, 38346); it is therefore probable the eggs belonged to the same individual. The eggs are spherical, a common shape for modern sea turtle eggs (Mikhailov, 1997), and three measurable specimens have diameters of 50, 61, and 64 mm, which is slightly larger than modern sea turtle eggs which range between 32.1–55.2 mm in diameter (Dodd Jr, 1988; Hirth, 1980; Miller et al., 2003a; Pritchard & Mortimer, 1999). The outer surfaces of the preserved eggs exhibit irregularly arranged, sub–millimetric, raised swellings, different to the

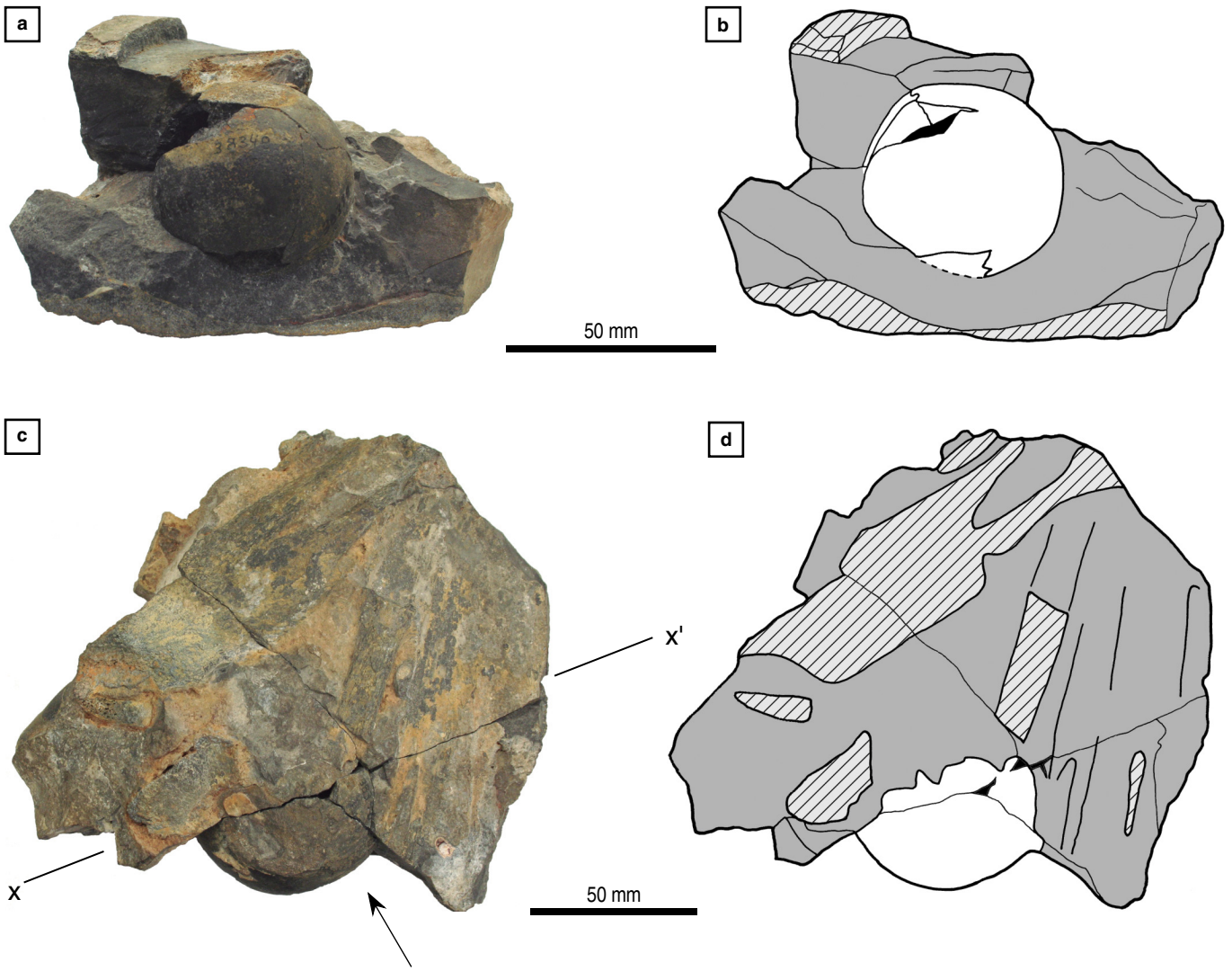

Figure 9. Two turtle eggs preserved in non–septarian concretions, which also preserve the bones of the mother enclosing the eggs (UCMP 38340), **(a, c)** photographs and **(b, d)** interpretive drawings. The eggs, probably belong to *Desmastochelys padillai*, were collected in 1945 by a party from the Tropical Oil Company and Ruben Arthur STIRTON (UCMP) from loma La Catalina, at the same time as the holotype of *Callawayasaurs colombiensis*. Line x–x' represents the section of the surface shown in Figure 10 (a, c), as viewed from the direction of the arrow. In the drawings: bones, hatched; concretion, grey; eggs, white. Scale bars represent 50 mm.

smooth shelled eggs of modern marine turtles (Imai et al., 2016; Mikhailov, 1997). The eggs are preserved with approximately 3 mm thick calcite "shells", which are much thicker than the leathery shells of modern turtle eggs (Nuamsukon et al., 2009; Phillott & Parmenter, 2006), although in contrast to modern turtles, the fossil eggs are likely to have been hard–shelled (Winkler & Sánchez–Villagra, 2006). Two distinctly coloured calcite layers form the "shell", a dark outer layer and a lighter inner layer, and the eggs are more–or–less completely filled with dark–coloured, coarsely crystalline (sparry) calcite. The mammilated structure, "shell" thickness, and bi–coloured external layering suggests the preserved external surface of the eggs is a result of calcite crystals lining the inside of the original aragonite shell (Isaji et al., 2006; Mikhailov, 1997), which was later lost during diagenesis.

2.2.2.4. Fish

Planktonic fish are numerous and diverse from the Paja Formation of alto Ricaurte (Álvarez–León et al., 2013; Etayo–Serna, 1968), are preserved in numerous collections, but are currently understudied (Figure 6). A specimen of the aspidorhynchid fish *Vinctifer* (MB f. 3500), was recovered from Aptian strata of loma Blanca near Sáchica in segment E of the AA Member of the Paja Formation (Schultze & Stöhr, 1996). The specimen is incomplete, but preserved in three–dimensions. In addition, numerous fish in a range of institutions await formal description, but appear to include amiids, "semionotiforms", ichthyodectiforms, pachyrhizodontids, aspidorhynchids, and araripichthyids which are similar to, or possibly congeneric with, fish collected

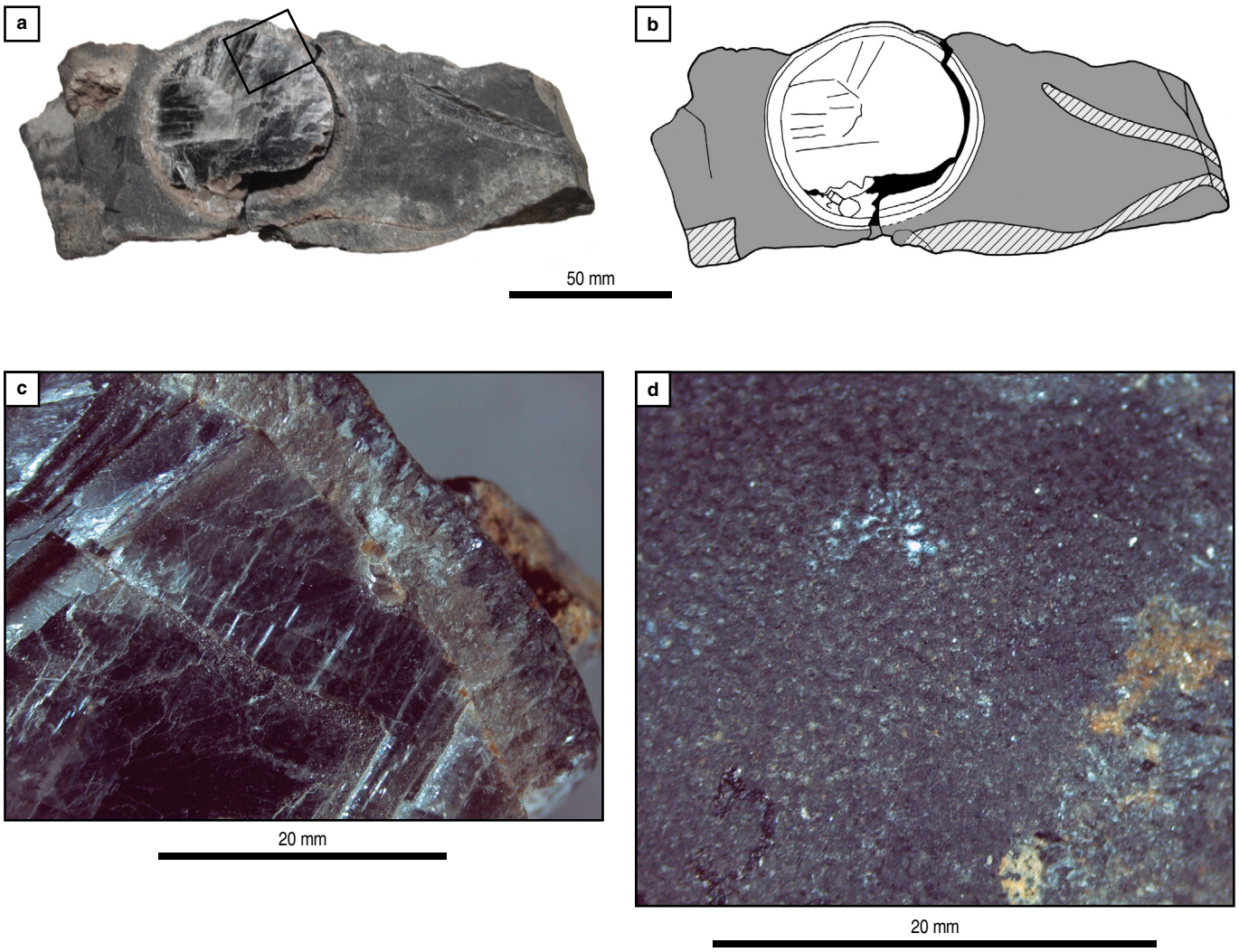

Figure 10. Cross–section through the turtle egg (UCMP 38340) shown in Figure 9c, probably belonging to *Desmatochelys padillai* **(a)** photograph and **(b)** interpretive drawing; in the drawing: bone, hatched; concretion, grey; egg, white; voids, black. **(c)** Photomicrograph close up of section of the "shell" boxed in (a), notice the "shell" is a double layer of differentially coloured calcite, and the coarsely crystalline (sparry) calcite infill. **(d)** Photomicrograph of the external surface of the "shell". In (c, d) the "shell" most likely represents calcite lining the inner surface of the original aragonite invested shell, which is not now preserved. Collected by a party from the Tropical Oil Company and Ruben Arthur STIRTON (UCMP) from loma La Catalina.

from the slightly younger Santana Formation of Brazil (Selden & Nudds, 2012).

2.2.2.5. Marine Macro–invertebrates

Here we briefly summarize the marine invertebrate palaeontology of the Paja Formation, with special emphasis on the range of organisms present. In contrast to the taxonomic treatment of the vertebrates above, we explore the macroinvertebrates in stratigraphic order to show the range of organisms living in the Paja palaeoenvironments at any one time. As with much of the Mesozoic marine world, ammonites (Figure 7) are key elements for Colombian and Paja Formation biostratigraphy (e.g., Etayo–Serna, 1964, 1979; Hoedemaeker & Kakabadze, 2004; Kakabadze & Hoedemaeker, 1997), and include diverse planispiral and heteromorphic forms (Bogdanova & Hoedemaeker, 2004; Etayo–Serna, 1968; Kakabadze & Hoedemaeker, 1997, 2004; Sharikadze et al., 2004; Vašíček & Hoedemaeker, 2003). The age of the Paja Formation had been ascertained as Hauterivian to part way through the late Aptian (Etayo–Serna, 1965), with one of the most intractable problems being the definition of the lower Barremian boundary (Etayo–Serna, 1964; Patarroyo, 1997, 2000b, 2009). Biostratigraphic work has included ammonites from the Creutzberg Collection (see the volume prefaced by Hoedemaeker & Kakabadze, 2004), however these specimens were not collected with robust stratigraphic horizons, with inferred geological ages assigned based on comparison to European ammonite

faunas. Details of the complex ammonite zonation are not discussed here.

2.2.2.5.1. Lutitas Negras Inferiores (LNI)

Ammonite biostratigraphy indicates a late Hauterivian age for the LNI (Etayo–Serna, 1965), although the lowermost part of segment A has occasional preserved lower Hauterivian ammonites (Etayo–Serna et al., 2015). Segment A of the LNI preserves occasional accumulations of invertebrates, which are mostly preserved flattened in the mudstones, rather than within the concretions. Occasional accumulations of large sized *Olcostephanus* ammonites occur (Etayo–Serna, 1968), and the segment also preserves a few other indeterminate cephalopod fossils (Etayo–Serna et al., 2015), but no bivalves or gastropods. Segment C also preserves a few *Olcostephanus* ammonites (Etayo–Serna, 1968). Within segment E fragments or impressions of indeterminate ammonites are occasionally locally abundant (Etayo–Serna, 1968), with *Crioceratites* present close to the top of the segment (Etayo–Serna, 1968). Rare thin–shelled bivalve molluscs are also found at this horizon (Etayo–Serna, 1968).

2.2.2.5.2. Arcillolitas Abigarradas (AA)

The ammonite fauna preserved in the AA indicates an age range from Barremian to early Aptian (Etayo–Serna, 1968). The fossils in segment A of the AA are distributed across a series of localities; however, not all fossils are found at all sites, and when present the genera are found in varying proportions (Etayo–Serna, 1968). The lower part of the segment preserves a rich ammonite fauna, often with very well–preserved delicate organic structures, including *Acrioceras*, *Ancyloceras*, *Hamulina*, *Heteroceras*, *Paracrioceras*, *Phylloceras*, Pulchelliidae, *Pseudohaploceras*, *Spitidiscus,* and *Valdedorsella* ammonites typical for the base of the local Barremian (Etayo–Serna, 1964). This horizon has also yielded a rare example of an ammonite aptychus, attributed to *Nicklesia pulchella* (Patarroyo, 2000a). The ammonites are found together with a few turritellid gastropods, fragments of bivalve molluscs, but notably no echinoderms (which are stenohaline taxa; Townson, 1975) and some benthic foraminiferans (Etayo–Serna, 1968). The middle of the segment preserves ammonites typical of the Colombian Barremian, including *Crioceratites*, *Karsteniceras*, *Nicklesia*, *Pedioceras*, *Phylloceras,* and *Pseudohaploceras*, together with indeterminate, thin–shelled bivalves and a few gastropods. Towards the top of the segment, the upper lower Barremian ammonites *Phylloceras*, *Pulchellia*, *Karsteniceras*, *Parasaynoceras*, and *Pseudohaploceras* are found, together with other heteromorphs and some indeterminate bivalves. The fossils are frequently three–dimensionally preserved when in the centres of the concretions, whereas those in the mudstones are more commonly compressed and fragmented (Etayo–Serna, 1968).

Segment B of the AA preserves a few poorly preserved enrolled and heteromorph ammonites, whereas segment C has revealed various, well–preserved ammonites, mostly belonging to Pulchelliidae, including the genera *Colchidites*, *Heinzia*, *Phylloceras*, *Pseudohaploceras*, *Pulchellia*, *Karsteniceras*. Segment D has produced *Cheloniceras*, *Neodeshayesites,* and *Procheloniceras* ammonites (Etayo–Serna, 1968).

Ammonite fossils are incredibly abundant within the concretions of segment E of the AA. Large forms are often found isolated, whereas smaller specimens are frequently preserved complete and in dense accumulations, and may be associated with fragments. The ammonites recovered from segment E include the genera *Acanthohoplites*, *Australiceras*, *Colombiceras*, *Cheloniceras*, *Epicheloniceras*, *Dufrenoyia*, *Gargasiceras*, *Neodeshayesites*, *Phylloceras*, *Pseudoaustraliceras*, *Riedelites*, and *Zurcherella* (Etayo–Serna, 1964, 1979, 1981). In addition to the ammonites, marine Teredinidae bivalves (or "shipworms") that live by boring into floating wood (Evans, 1999; Gingras et al., 2004) are common in the segment (Figure 11). Towards the top of segment E, a fibrous calcite band, when split along the middle, reveals extremely abundant remains of inoceramid bivalves, representing the preservation of a short–lived event horizon (Figure 12).

2.2.2.5.3. Arcillolitas con Nódulos Huecos (AcNH)

The ammonite fauna of the AcNH indicates a late Aptian age (Etayo–Serna, 1968). Ammonites are frequently preserved as internal moulds within the mudstones and concretions, and dense accumulations of thin–shelled bivalves and occasional gastropods occur at some horizons. The fauna was taken to indicate well–oxygenated waters with a soft bottom that limited the development of benthic life (Etayo–Serna, 1968). This in turn was used as evidence to infer abundant life throughout the AcNH, which was concentrated by currents, but only sporadically fossilized due to unspecified taphonomic effects (Etayo–Serna, 1968).

2.2.2.6. Marine Microorganisms

Within the Paja Formation, finely–laminated wavy, somewhat dome–like, sedimentary structures are common at some horizons. These structures, with 92% micrite and parallel lamination have been interpreted as cryptalgal mats (Etayo–Serna et al., 2015), providing evidence for shallow water conditions, as marine algae usually live in the permanently wet, but well–lit zone immediately below the low tide mark. Other microfossils are rarely preserved in the Paja Formation; however, an event horizon at the base of the AA (segments A–B) preserves the calcareous benthic foraminifera *Epistomina caracolla* (Patarroyo–Camargo et al., 2009; Patarroyo, 2009). The low diversity of *Epistomina* was used to support an anoxic nearshore evapo-

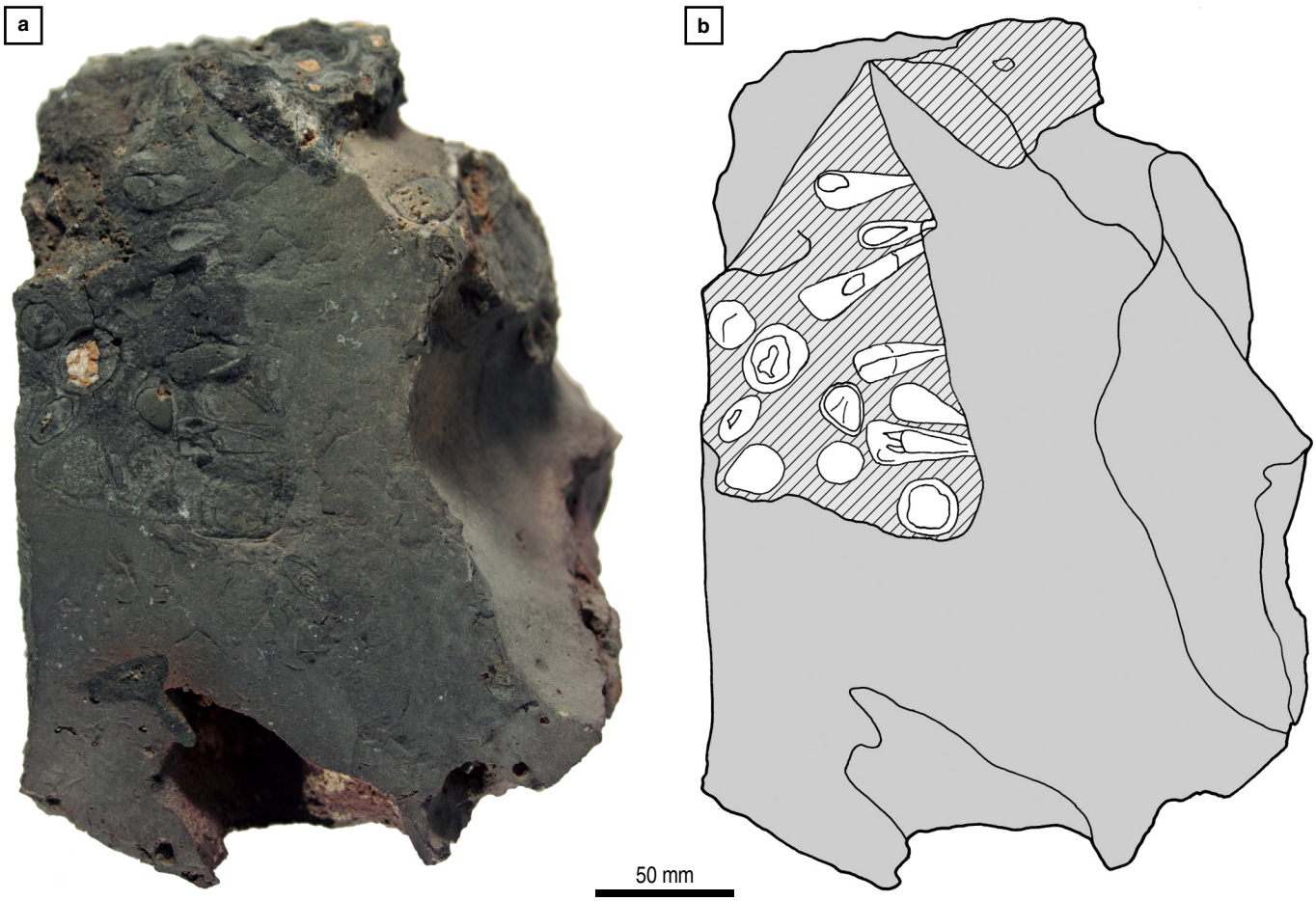

Figure 11. *Teredolites* "wood–ground" ichnofossils, with body fossils of the original bivalves that inhabited the burrows, preserved in a non–sepatarian concretion (UADG LM 15.10), **(a)** photograph and **(b)** interpretive drawing of. In (b) calcite replaced wood, hatched; concretion, grey; ichnofossils and inhabitants, white. Collected by LFN from loma La Cabrera.

ritic environment for the AA; however, *Epistomina caracolla* is typical of oxic watermasses (Gradstein et al., 1999) from mid–shelf neritic to bathyal depths (Decker & Rögl, 1988; Wightman, 1992), and hence cannot support this conclusion. It is more likely this assemblage represents temporary seafloor oxygenation following a storm event (Figure 13).

2.2.2.7. Terrestrial Organisms

In addition to the autochthonous marine fauna of the Paja Formation, alto Ricaurte rocks preserve abundant remains of allochthonous terrestrial plants and occasional terrestrial vertebrates and invertebrates.

2.2.2.7.1. Terrestrial Vertebrates

Mesozoic terrestrial vertebrates are extremely uncommon in Colombia, with the only diagnostic dinosaur being the sauropod *Padillasaurus leivaensis* Carballido et al., 2015 from the Paja Formation of the alto Ricaurte (MJACM 4; originally published as JAVCM 0001). Although originally considered a brachiosaurid titanosauriform (Carballido et al., 2015) *Padillasaurus* is now considered to be a basal member of the non–brachiosaurid titanosauriform clade Somphospondyli (Mannion et al., 2017). The exact geographical location where *Padillasaurus* was found is not known, although the source of the specimen is reported as the La Tordoya area of vereda Monquirá (Carballido et al., 2015); however La Tordoya is located in vereda El Roble, northeast of Villa de Leiva. Based on the presence of *Gerhardtia galeatoides* and *Lytoceras* sp. ammonites (JAVCM 2, 3, and 4 of Carballido et al., 2015) the remains have an early late Barremian age, and were derived from an unspecified segment (but probably segment C) of the AA Member of the Paja Formation.

The remains of *Padillasaurus* consist of three non–articulating units that contain the incomplete posterior dorsal, sacral, and anterior caudal regions interpreted as the parts of a single animal (Carballido et al., 2015). The first unit consists of part of an isolated mid– to posterior dorsal cervical centrum, the second (unprepared) unit is interpreted as the last dorsal and two anterior sacral vertebrae, and the third unit consists of two posterior sacral and eight anterior caudal vertebrae in articulation. Although incomplete, the vertebrae are well–preserved

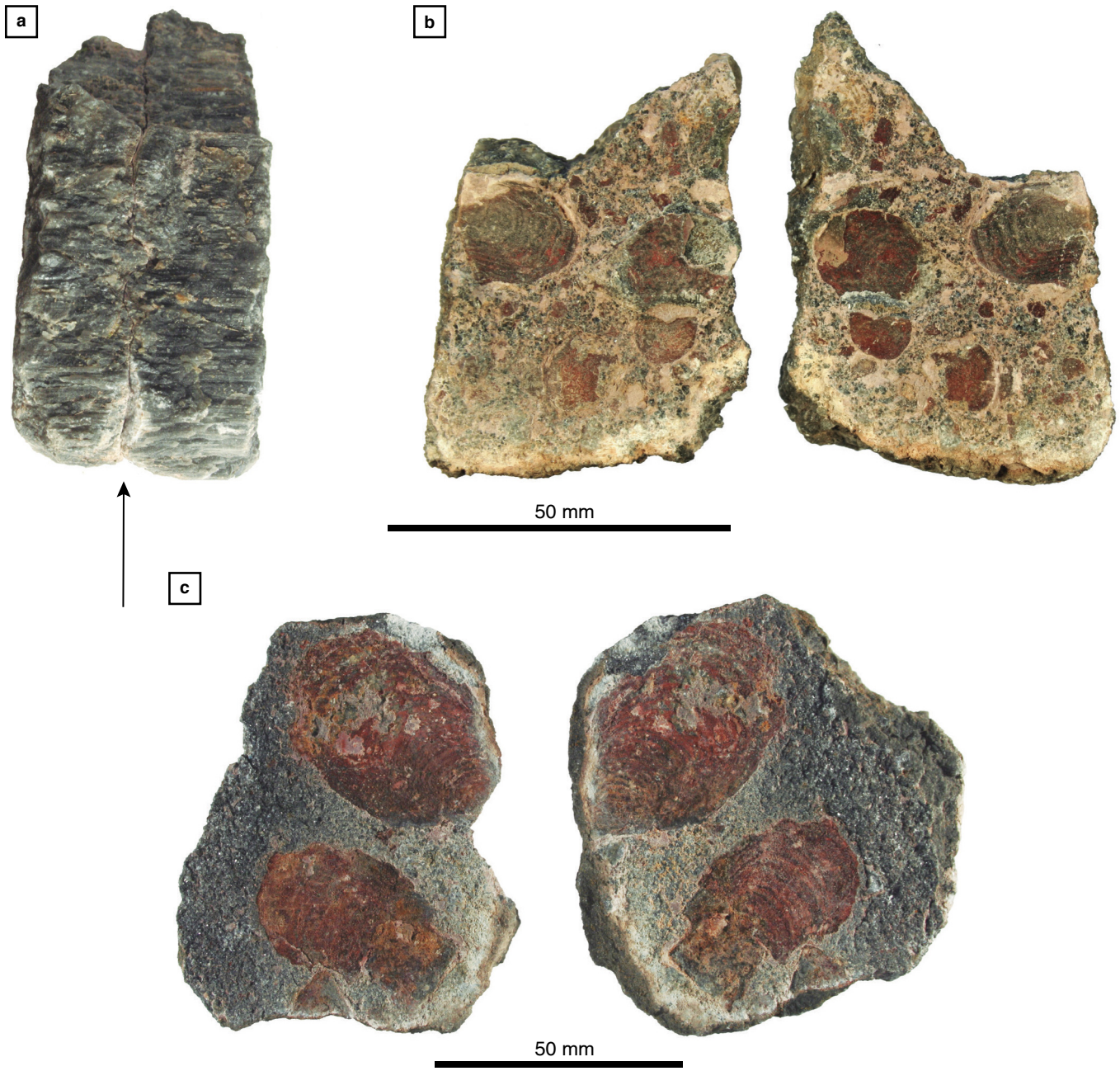

Figure 12. Bivalves preserved in calcite "beef". **(a)** Bi–layered calcite "beef" showing the "fibrous" nature of the mineral, with the calcite crystals oriented normal to the edges of the vein (UADG LM 17.560). **(b)** The same specimen split open along the central "suture" (arrowed in (a)), showing the preservation of inoceramid bivalve shells within the "beef". **(c)** A second specimen showing somewhat larger inoceramid shells (UADG LM 17.564). The presence of the bivalves in the centres of the veins indicates antitaxial (from the centre outwards) growth of the calcite. Presumably, the bivalves colonized the seafloor following an environmental perturbation that temporally oxygenated the seafloor, and after lithification the vein nucleated along the calcium carbonate of the shells. Collected by LFN from loma La Cabrera.

including large pleurocoels and some delicate vertebral laminae (Carballido et al., 2015). The almost complete posterior dorsal vertebra is better preserved on its right, suggesting this part of the specimen was discovered sediment side down. This dinosaur fossil appears to be the incomplete remains of a floated carcass, with only the most tightly fused (sacral) or ligamentously tied (anterior caudal) regions remaining articulated.

2.2.2.7.2. Terrestrial Invertebrates

The only reported insect remains from the Paja Formation belong to the family Aeschnidiidae (Insecta: Odonata), the group to which dragonflies belong (McGavin, 2001). The material includes a beautifully preserved four–winged insect collected from the upper part of segment E of AA. Although no full de-

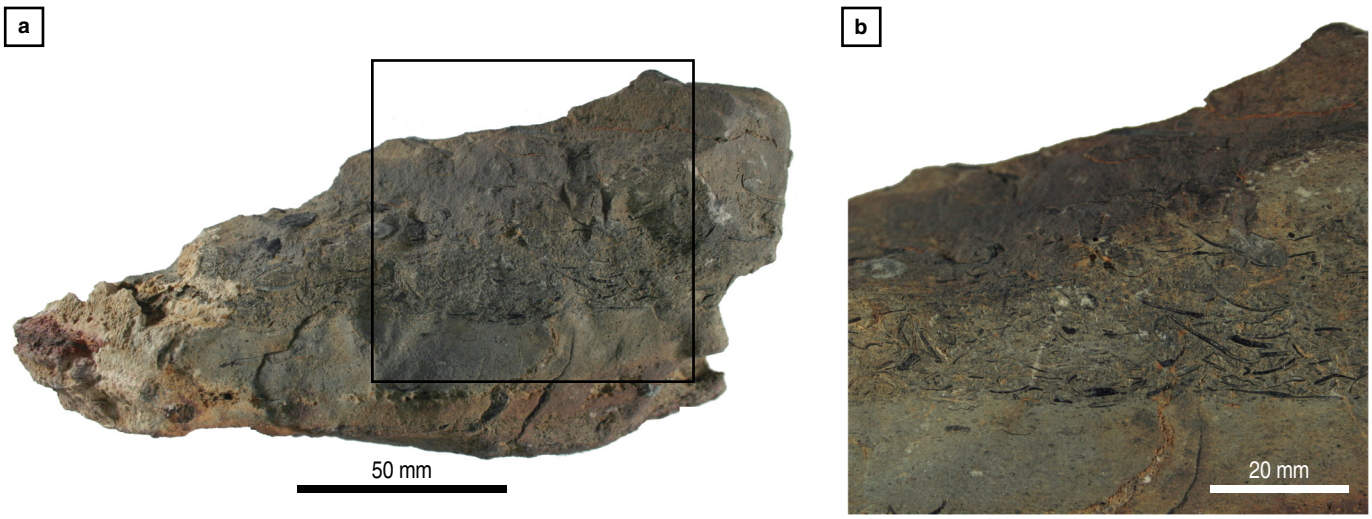

Figure 13. A non–septarian concretion containing a horizon rich in chaotically arranged bivalve fragments, interpreted as a storm bed (UADG LM 17.478). **(a)** Complete block, **(b)** close up of boxed section indicated in (a). Way up interpreted as to the top of the page, based on relatively sharp base and more defuse upper boundary, but uncertain as the specimen was recovered as a loose block. Collected by LFN from Salto y La Lavendera.

scription is yet available, the environment of deposition has been interpreted as very shallow marine (Gómez–Cruz et al., 2011). However, this does not account for taphonomic aspects such as transportation and burial, so it is uncertain how the specimen was preserved in the Paja Formation Basin. It is possible the insect either flew or was blown into Paja Formation Seas and was deposited in the basin after becoming water saturated and sinking. Preservation of the relatively delicate soft parts, such as the wings, indicates rapid burial, and an absence of oxygen and bioturbation.

2.2.2.7.3. Terrestrial Plants

Allochthonous terrestrial plants (Pteridophyta) are relatively common elements of the Paja Formation deposits of alto Ricuarte. LNI segments A and E preserve some scattered plant remains (Etayo–Serna, 1968; Etayo–Serna et al., 2015), but plants are most abundant in the concretions of segment E of the AA (Etayo–Serna, 1968). Described taxa include ferns (Polypodiopsida, part of the former "Pteridophyta"), and seed plants (Spermatophyta) including Bennettitales and cycads (Cycadophyta), conifers (Pinophyta) (the latter two forming part of the former "Gymnospermae"), and angiosperms (Magnoliophyta) (Willis & McElwain, 2002). The ferns are referred to the Weichseliaceae genus *Paradoxopteris* (van Waveren et al., 2002), and Cycadophtya include the genera *Macrotaeniopteris*, *Nilssonia* (Huertas, 1967, 1970), *Pterophyllum,* and *Taeniopteris* (van Waveren et al., 2002). Pinophyta includes a range of families: *Cupressinocladus* (formerly referred to *Thuites* and *Brachyphyllum*; Huertas, 1967, 1970), *Brachyphyllum,* and *Pagiophyllum* (van Waveren et al., 2002) (family Cupressineae); *Frenelopsis* (Moreno–Sánchez et al., 2007) (family Cheirolepidiaceae); *Araucariostrobus* (Huertas, 1970, 1976; van Waveren et al., 2002), *Conites* (van Waveren et al., 2002), and *Damarites* (Huertas, 1976) (family Araucarineae); *Pinostrobus* and *Pityostrobus* (Huertas, 1967; van Waveren et al., 2002) (family Pinaceae); and *Podozamites* (Huertas, 1967; van Waveren et al., 2002) (family Podocarpaceae). Magnoliophyta includes the genus *Ficus* (family Moraceae) (Huertas, 1967) and the putative angiosperms *Sterculiocarpus* (Huertas, 1967) and *Carpolithes* (van Waveren et al., 2002); however, the latter two may be conifers with large seeds (van Waveren et al., 2002). In addition to the species named above, fossil wood, which cannot easily be attributed to a genus (van Waveren et al., 2002), is extremely common in the Paja Formation. Many of the plant remains are extremely well–preserved externally, often as casts filled with black, macrocrystalline calcite (sparite) (Huertas, 1967; van Waveren et al., 2002), but with no original internal structure (Figure 14); however some wood in the Paja Formation is silicified (Figure 15), and preserves detail to the cellular level.

3. Discussion

The Paja Formation is a thick sequence of fine–grained siliclastic, predominantly dark–coloured pyrite–enriched mudrocks with some calcareous and sandier interbeds, and abundant fossils. Such "monotonous" mudrock successions (Mann & Stein, 1997), make up 75–80 % of crustal strata (Ruppel & Loucks, 2008); however, black mudrock deposits like the Paja Formation are poorly understood, although with the advent of hydraulic fracturing ("fracking") an increasing number of studies are being undertaken (e.g., Ruppel & Loucks, 2008; Sageman et al., 1991; Schieber, 2016; Tourtelot, 1979). Organic–rich

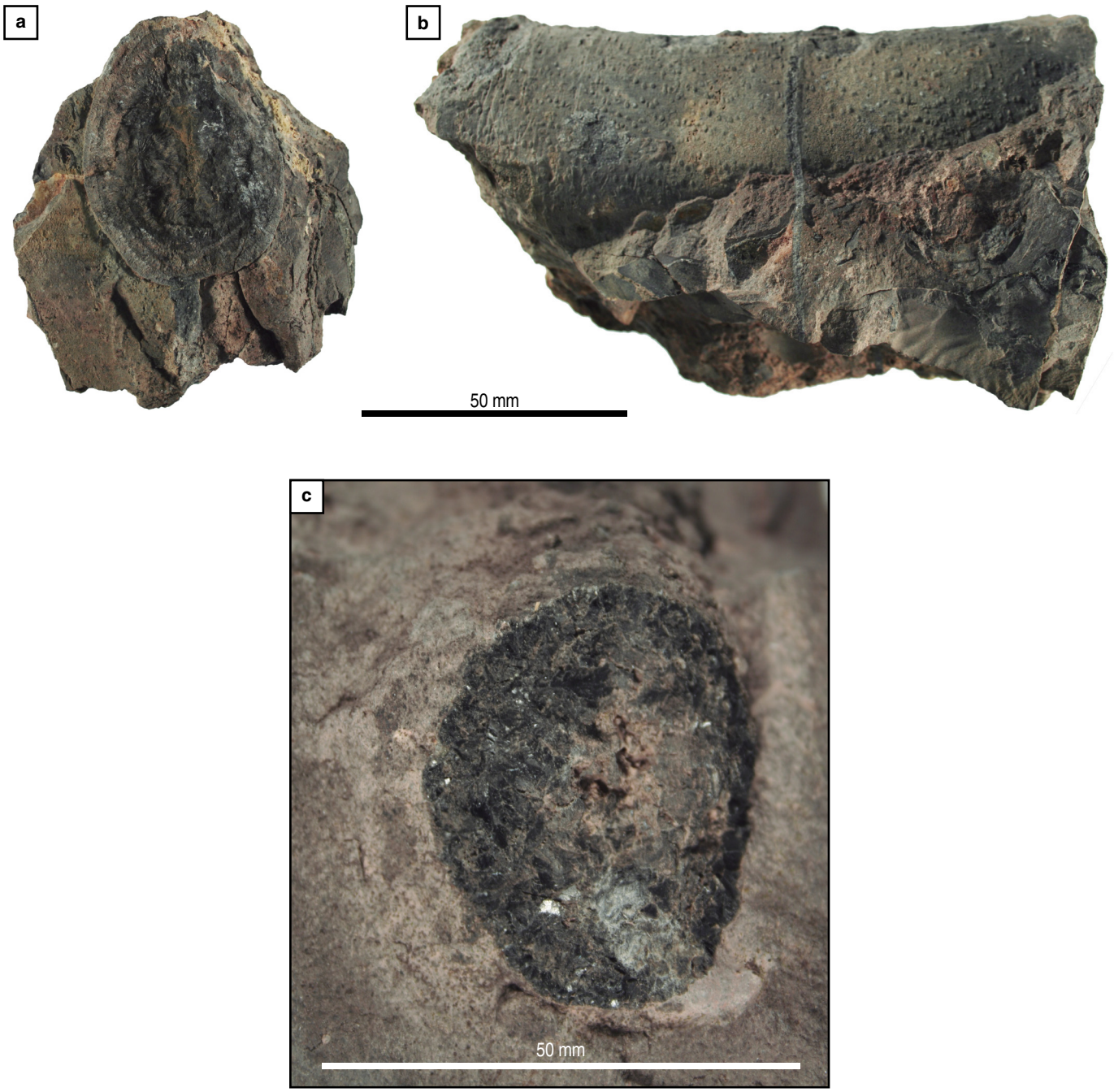

Figure 14. Wood preserved as external moulds filled with coarsely crystalline (sparry) black calcite. **(a)** Cross–section showing the internally layered calcite infill, and **(b)** lateral surface with well–preserved external surface ornamentation of small rugosities (UADG LM 14.50h). **(c)** A second specimen with coarser external ornamentation, filled with non–layered, coarsely crystalline black calcite (UADG 17.537). Both specimens preserved within non–sectarian concretions. Collected by LFN from loma La Cabrera.

mudrocks accumulate in a wide range of depositional settings, many of which are highly complex to understand (Ruppel & Loucks, 2008), in part due to a lack of modern analogues for Cretaceous high–stand epicontinental seas (Algeo et al., 2008; Schieber, 2016; Wignall, 1991a). Hence, to understand the dynamics of former Paja Formation Seas, and the organisms that inhabited them, it is essential to consider diverse evidence for physical water body properties, sedimentary environments, and biogeochemical parameters (Sageman et al., 1991; Tyson & Pearson, 1991).

3.1. Reinterpretation of the Physical and Biotic Environment of the Paja Formation

Deposition of the Paja Formation in the alto Ricaurte took place during Hauterivian – Aptian times, in a world with high global

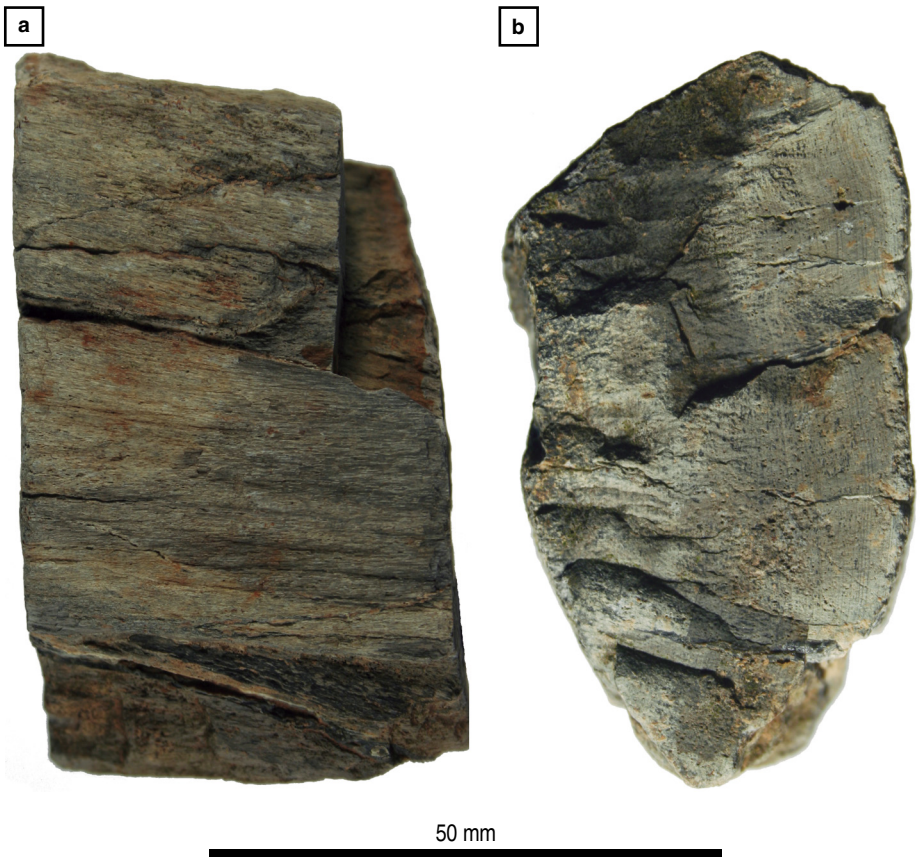

Figure 15. Silicified wood, **(a)** showing external fibrous woody texture and **(b)** rotated 90 degrees to show the cross–section with the outer surface (a) to the right (UADG LM 17.407a). Note the faint growth lines to the right of (b) with coarser textured (heart) wood to the left. The preservation of the internal structure contrasts markedly with specimens preserved in calcite (Figure 14). Collected by LFN from El Roble.

sea levels, warm and equitable global temperatures (Tyson & Pearson, 1991; van Helmond et al., 2015; Weissert, 1981), and seas dominated by marine reptiles, fish, and ammonites. The Paja Formation Basin lay in an equatorial location, 5–7° north of the equator (Smith et al., 1994), beneath the ascending limb of the Hadley atmospheric cell (Ziegler et al., 2003). This location, associated with high solar insolation and warm sea surface temperatures, enhanced the hydrological cycle (Poulsen et al., 2007; Ufnar et al., 2002) and produced high evaporation and precipitation rates (van Helmond et al., 2015). Modern tropical shelf seas are well–mixed by the action of tides and/or wind driven waves; although tides would have been damped by friction over shallow epicontinental sea floors (Bádenas & Aurell, 2008). Hence, most energy in Cretaceous tropical epicontinental seas came from the wind (Tyson & Pearson, 1991), and this atmospheric disturbance incorporated abundant O_2 and CO_2 into surface waters, despite a decrease in atmospheric gas solubility in sea water with increasing temperature (Tyson & Pearson, 1991; van Helmond et al., 2015).

3.1.1. Water Depth in Paja Formation Seas

Water depth is a key environmental parameter, and yet absolute palaeowater depths are one of the most poorly constrained boundary conditions of epicontinental seas (Immenhauser, 2009; Ruppel & Loucks, 2008; Tyson & Pearson, 1991; Wignall, 1991a). The Paja Formation Seas flooded continental lithosphere, producing a marine incursion extending into the continental interior (Immenhauser, 2009). Hence, water depth in Paja Seas would have been "shallow" compared to abyssal depths, as high global sea levels increase the aerial extent of continental flooding more rapidly than water depth (Tyson & Pearson, 1991). Modern shelf seas range in depth from 0 m (at the shoreline) to around 200 m (close to the continental slope) (Immenhauser, 2009), but are typically <130 m deep. Anoxia does not occur in waters shallower than about 10–15 m (due to atmospheric surface mixing), and does not normally occur below 60 m, the depth where organic matter is fully degraded in oxic waters (Tyson & Pearson, 1991). The thermocline typically lies at 10–40 m water depth, and a pycnocline may occur at 1–10 m above the sediment–water interface (Tyson & Pearson, 1991). However, with their unique characteristics, Cretaceous epicontinental seas are not directly comparable to modern peri–continental (shelf) seas (Immenhauser, 2009; Meyer & Kump, 2008).

Water depths in epicontinental seas undoubtedly varied in space and time. Estimates of water depth vary from a few to tens to hundreds of metres (Etayo–Serna, 1968; Forero–Onofre & Sarmiento–Rojas, 1985; Miller et al., 1988; Sageman et al., 1991; Wignall, 1991a), but maximum water depth is commonly cited as <100 m (e.g., Miller & Foote, 2009; Mutterlose et al., 2009). Water depth is controlled, and modified, by global sea–levels, and rates of sedimentation and subsidence (Wig-

nall, 1991a). However, anoxic bottom waters must be below fair weather wave base (typically around 15 m water depth), and the generally fine–grained mudrocks of the Paja Formation (Etayo–Serna, 1965, 1968) suggest a water depth below normal storm wave base (Miller et al., 1988), which is typically around 30–60 m (Bádenas & Aurell, 2008). However, occasional distal tempestites (Figure 13) indicate the Paja Formation sediment–water interface was within reach of exceptional storms, which in modern seas may affect waters below 100 m (Tyson & Pearson, 1991). This is corroborated by a lack of shallow water sedimentary structures (desiccation cracks, wave–formed ripples, seafloor mineralization) or common tempestite deposits (erosive bases, coarse–grained lags, hummocky cross stratification) (Immenhauser, 2009; Miller et al., 1988), and may be further constrained by the presence of sandownid turtles that have been considered to inhabit the near shore–littoral zone (Cadena, 2015). Hence, we suggest a water depth for Paja Formation Seas in the range of 60–130 m.

3.1.2. Paja Formation Surface Waters

Cretaceous atmospheric (and oceanic) partial pressures of carbon dioxide (pCO_2) were high (Zhang et al., 2016), which together with high water temperatures and a well–lit equatorial location (due to daytime solar input being directly overhead; Sageman et al., 1991), led to elevated rates of marine photosynthesis (Caplan & Bustin, 1998; van Helmond et al., 2015). In modern seas, nutrient availability, water temperature, salinity, and water clarity all control photosynthetic rate (Tourtelot, 1979), so for continued primary productivity in Paja Seas, constant input or recycling of biologically limiting nutrients (especially N, K, Fe) was essential (Moore et al., 2013). Most nutrients in the modern shallow marine realm come from continental weathering and are delivered by freshwater runoff (Keller, 2008). For Paja Formation Seas, sediments and nutrients were sourced from neighbouring landmasses or topographic highs forming islands, which included the Guiana Shield to the east, and the Central Cordillera island arc to the west (Campos–Álvarez & Roser, 2007). The island arc may also have contributed volcanic ash during eruptions (Hoedemaeker & Kakabadze, 2004), and thus influenced Cretaceous ocean fertility (Petrash et al., 2016; van Helmond et al., 2015). Wind–blown continental dust may also have contributed nutrients (Schieber, 2016), but as Paja Formation Seas were outside the desert climatic belt, this was likely to have been a minimal input.

The climate of adjacent landmasses controls the rate of terrestrial organic matter input into a marine basin (Weissert, 1981). During Paja Formation times, elevated pCO_2, equatorial temperatures, and abundant water availability enhanced rates of terrestrial tropical deep weathering (Petrash et al., 2016; van Helmond et al., 2015). There is ample evidence from the Paja Formation that these nearby landmasses, like the Paja Seas, exhibited high primary productivity, and were therefore covered in an abundance of vegetation. Terrestrial vegetation acts to stabilize weathering products, especially if land surface gradients are subdued (Schieber, 2016), although vegetation may also have generated high levels of weathering, both physical (through root action) and chemical (through release of organic acids). There is abundant evidence for higher plant input into Paja Formation Seas (e.g., Huertas, 1967, 1970), and this abundance of terrestrially sourced vegetation indicates high levels of run off, which would have brought abundant detrital grains and nutrients, as ions in solution, into the Paja Formation Basin (Tyson & Pearson, 1991), together with the organic material. These terrestrially sourced weathering products, together with the organic material, were presumably delivered to Paja Formation Seas via rivers (Tyson & Pearson, 1991; van Helmond et al., 2015) as a result of high tropical precipitation rates and following intense runoff resulting from storms. Once in the shallow marine realm, high sea surface temperatures ensured rapid biochemical recycling of biological limiting nutrients. High nutrient input, associated with elevated temperatures may also have been a key factor in bottom water anoxia (Meyer & Kump, 2008).

There is no absolute method for determining Paja Formation palaeosalinity (Tyson & Pearson, 1991). Rainfall and freshwater runoff from adjacent landmasses can decrease surface seawater salinity, but wind mixing would have limited this to local variability near–shore (Sageman et al., 1991; Tyson & Pearson, 1991). The abundant ammonite fossils (e.g., Etayo–Serna, 1979; Patarroyo, 2000b), members of Cephalopoda, are indicative of marine conditions with near normal salinity, as all modern cephalopods are intolerant to greatly increased or lowered salinities (Moore, 2001). That most ammonites are autochthonous to the Paja Formation Basin, and did not experience significant post–mortem transport, is demonstrated by their frequent exceptional preservation, including the most delicate shell structures such as spines (e.g., Etayo–Serna, 1968; Patarroyo, 2000a). Hence, near normal marine conditions, as indicated by the fossil fauna, implies an open connection to wider Cretaceous oceans which maintained normal marine salinity. Thus, surface waters of Paja Formation Seas would have been warm, well–lit, and well mixed, with abundant O_2 and CO_2, and normal marine salinity.

3.1.3. Pelagic Fauna

Interpreting a living community from fossil evidence requires rigorous analysis, but this is only partly possible for Paja Formation Seas due to lack of study. Paja Formation Seas were home to a diverse, autochthonous pelagic fauna consisting of numerous marine reptiles, fish, and ammonites (Figures 5–7), although marine crocodiles and belemnites, common in other Lower Cretaceous marine deposits (Mutterlose et al., 2009), are entirely absent from the Colombian Cretaceous. Marine rep-

tiles, all air breathing, are represented by abundant and diverse plesiosaurs (both plesiosauromorphs and pliosauromorphs), ichthyosaurs, and marine turtles. Fish are abundant and diverse, and ammonites, both planispiral and heteromorphic, some large, are incredibly abundant. The fish and ammonites, both of which obtain O_2 for respiration dissolved in the water column, provide evidence for abundant oxygenation of surface waters. The high pelagic biodiversity is also an indication of the productivity of Paja Formation Sea surface waters, as all organisms are ultimately dependent on phytoplankton as a source of energy. The organic–rich Paja Formation sediments are thus indicative of rich phytoplankton and zooplankton in the oxic, photic zone waters of this former epicontinental sea.

Marine reptiles may have been attracted to Paja Formation Seas to exploit feeding grounds rich in fish and ammonites. Additionally, Paja Formation Seas may have acted as relatively safe breeding– or birthing–grounds for marine reptiles (cf. to the Posidonien–schiefer deposits of Holzmaden, Germany; Bottjer et al., 2002). However, gravid females and juveniles are rare in the fossil record, and poorly known from the Paja Formation, so the topic requires additional research. Currently, the only direct evidence for marine reptile reproduction in Paja Formation Seas is the presence of turtle eggs (Figures 9, 10), and juveniles of *Desmatochelys padillai* (Cadena & Parham, 2015). However, as the turtle eggs are surrounded by the bones of the mother, this excludes the possibility the eggs had been laid. Hence, the current data cannot support the hypothesis of a turtle breeding ground (Etayo–Serna et al., 2015), and in any case, marine turtle eggs require both water from the environment (Wallace et al., 2006) and low salinity (Miller et al., 2003a) to develop. Hence, the previously hypothesised sabkha environment for the Paja Formation (Forero–Onofre & Sarmiento–Rojas, 1985) is incompatible with the terrestrial deposition of turtle eggs, which in an evaporitic environment will rapidly dehydrate and die.

In addition to the free–swimming pelagic organisms, the Paja Formation preserves abundant evidence of pseudoplanktonic bivalves, or lignophagous "shipworms" (Evans, 1999; Gingras et al., 2004) that lived by burrowing into floating driftwood (Figure 11). That this is pseudoplankton, rather than bottom living bivalves colonizing wood falls, is clear from the presence of boring bivalves all around the wood, which would not be the case for bottom colonization, where wood in contact with the sediment surface would be free of boring organisms. The presence of xylic bivalves is also evidence that woody plant material was a common resource in Paja Formation Seas, and that some floated for a considerable time. In addition to the preserved pseudoplankton, it is likely other organisms hitched a ride on swimming marine reptiles, fish, and cephalopods, or floating objects, as occurs in modern oceans (Wignall & Myers, 1988). However, this is aspect of Paja Formation palaeoecology requires additional research.

3.1.4. Paja Formation Bottom Waters

The sedimentology of the Paja Formation is predominantly fine–grained mudrocks, which are frequently finely–laminated, but exhibit limited evidence for abiotic sedimentary structures, and typically lack coarse–grained clastic materials (Tyson & Pearson, 1991). These muddy sediments are indicative of a low energy depositional environment (Townson, 1975; Wignall & Myers, 1988), with sediments gradually settling through a tranquil water column, and little disturbed by bottom currents (cf. Etayo–Serna, 1968). This is supported by the low–level of mechanical fragmentation and disarticulation observed in many invertebrate and vertebrate fossils, but which may also be due to the rarity of scavengers on the sea floor (Wignall & Myers, 1988). However, infrequent silt laminae and sandier interbeds indicate occasional high–energy events that deposited coarser–grained material in the Paja Formation Basin. These event horizons produced large, infrequent perturbations of Paja Formation Seas, likely generated by very large tropical storms, tsunamis or turbidity currents. Tectonic activity probably produced earthquakes (Wignall, 1989) from the nearby subduction zone beneath the Central Cordillera island arc to the west (Gaona–Narváez, 2015), or as a result of extensional crustal faulting beneath the Paja Formation sedimentary basin (Jiménez et al., 2014).

The predominantly dark colour of Paja Formation sedimentites is indicative of a high organic carbon (C_{org}) content (Tourtelot, 1979). Total organic carbon (TOC) values in the Paja Formation are on average >1%, and in some exceptionally horizons TOC reaches >15% in (Campos–Álvarez et al., 2002). However, C_{org} is only incorporated into seafloor sediments when organic matter supply is greater than biochemical breakdown. Aerobic metabolism consumes O_2, and when consumption is higher than supply, dysoxic or anoxic bottom waters and/or sediments, together with enhanced preservation of C_{org} result (Caplan & Bustin, 1998; Tourtelot, 1979; Tyson & Pearson, 1991). In addition, the dark mudrocks of the Paja Formation frequently preserve iron pyrite (Fe_2S) (Etayo–Serna, 1979). In the absence of O_2, photosynthetic (green, purple) or non–photosynthetic sulphate–reducing bacteria thrive, decompose organic matter, invade the sediments, and generate hydrogen sulphide (H_2S) (Tourtelot, 1979; Tyson & Pearson, 1991). The organic matter thereby acts as fuel for seawater sulphate reduction. H_2S is produced close to the sediment–water interface, combines with iron derived from sediments, and is ultimately preserved in the form of iron pyrite (Fe_2S) (Schieber, 2011). Hence, the common presence of iron pyrite (Etayo–Serna, 1979) is evidence for the anoxic nature of Paja Formation epicontinental sea sediments. The less–common silt–rich and sandier interbeds, on the other hand, are of lighter colour as they contain much less C_{org}, and little or no Fe_2S. These lighter coloured beds were probably the result of

low–frequency high–energy perturbations that stirred up the water column, introducing both coarser sediments and dissolved oxygen into the benthic realm. Short–term oxidation of the sea floor permitted oxidative decomposition of organic matter raining down from the surface waters, and temporally changed biological seafloor dynamics.

The muddy Paja Formation Sea floor was probably soft, possibly with a "soupy" (water–rich) consistency (Martill, 1993). Muds, when initially deposited, typically contain a high percentage of water (Nicholls & Russell, 1990), leading to a fluidized upper sedimentary pile. These muds may contain up to 80% water by volume, which can be reduced to as little as 30% upon compaction (Nichols, 2009). It is possible to estimate the volume of dewatering for the Paja Formation by comparing the thickness of bedding preserved within early diagenetic concretions, to the compacted sediments that wrap around those concretions; this differential compaction indicates a loss of original sediment thickness of at least 80% (Figure 16). In addition to the sedimentary evidence, the fully articulated nature of many Paja Formation marine reptile skeletons (plesiosaurs, ichthyosaurs, turtles) suggest the carcasses sank into soft muds (Martill, 1985, 1988), partially or completely burying the organisms. This would have aided their preservation, and may help explain differential preservation on the two sides of the ichthyosaur *Platypterygius sachicarum* (SGC DON–19671), and the titanosauriform dinosaur *Padillasaurus leivaensis* (MJACM 4) (Carballido et al., 2015; Páramo–Fonseca, 1997). The numerous articulated fish, many bearing scales and/or preserved in three–dimensions (Figure 6), also strongly argues for rapid burial close to the site of death, and preservation in anoxic sediments (Martill, 1993). The presence of soft or soupy sediments inhibited the growth of "normal" marine benthos, except perhaps for a few reclining species of inoceramid bivalves, dysoxia–anoxia at the base of the water column prevented the growth of epifauna on exposed skeletal elements (Etayo–Serna, 1965), and minimized the action of scavengers.

3.1.5. Benthic Fauna

The Paja Formation preserves a depauperate benthic fossil fauna compared to the pelagic realm (Macellari & de Vries, 1987), with typically low levels of bottom–living macrofossil diversity and abundance. This indicates non–normal bottom conditions, most likely lacking in oxygen, but also possibly with toxic H_2S generated on the sea floor or periodically released from within the sediments. However, some thin–shelled, epifaunal bivalve molluscs (e.g., inoceramids) are tolerant of low oxygen tensions, and even small amounts of H_2S (Wignall, 1991b; Wignall & Myers, 1988), and it is probably these species that are preserved in the Paja Formation (Etayo–Serna, 1968). In addition, the Paja Formation occasionally preserves gastropods, and extremely rarely echinoderms, crustaceans, and benthic foraminiferans (Etayo–Serna, 1968; Patarroyo, 2009). Hence, as with the sedimentology, there is good biological evidence for short–term benthic oxidation of the Paja Sea floor. These oxygenation events are recorded as occasional bivalve–rich horizons (Figure 12), and the rare presence of "normal" marine benthic faunal elements (Etayo–Serna, 1968). Periodically oxygenated Paja Formation bottom waters is in line with our developing more general understanding of epicontinental seas dynamics (e.g., Brady & Bowie, 2017; Sageman et al., 1991; Selden & Nudds, 2012).

Wavy, finely laminated sedimentary structures preserved with cubes of iron pyrite (Fe_2S) are common within the Paja Formation of alto Ricaurte. These sedimentary structures have been interpreted as algal mats (Etayo–Serna et al., 2015), living in shallow, well–lit (euphotic) waters that permitted sufficient light penetration to maintain photosynthesis. However, the lack of grazing macrofauna, normally abundantly associated with Phanerozoic well–lit, well–oxygenated algal mat ecosystems (Eriksson et al., 2007), indicates dysoxic–anoxic conditions at least at the sediment–water interface. Hence, although microbial mat communities may at times have had oxic photosynthetic microorganisms (such as cyanobacteria) on the surface, it is likely that at most times these environments were dysoxic–anoxic and consisted of surface–living, sulphate–reducing microbial mat communities (e.g., green sulphur bacteria; Hay, 2008), producing H_2S to which algae are entirely intolerant. Hence, the Paja Formation microbial laminates, with the common presence of pyrite, are not necessarily indicative of well–lit, shallow–water, oxic conditions, but are better interpreted as deeper water, low oxygen, possibly H_2S–rich environments dominated by sulphate–reducing microbes. However, even in the presence of somewhat oxygenated near–bottom waters, anoxic microbial mats may flourish, with a strong O_2 (and H_2S) gradient immediately above the sediment water interface. The interpretation of wavy lamination as anoxic microbialites, rather than oxic cryptoalgal structures, is of importance as it accords more closely with the deeper, anoxic interpretation of the fine–grained organic–rich sediments generally observed in the Paja Formation.

The well–laminated fabric of many Paja Formation beds, and the scarcity of ichnofossils, indicates an almost entire lack of bioturbating infauna. Absence of burrowing forms implies anoxia at the sediment water interface (Mann & Stein, 1997; Wignall & Myers, 1988), most likely with the presence of H_2S, which produces conditions chemically hostile to most macro–infaunal and epifaunal life (Macellari & de Vries, 1987; Sageman et al., 1991). However, laminated sediments may not be entirely lifeless (Tyson & Pearson, 1991), although the organisms are likely to be soft–bodied polychaetes, which are unlikely to leave evidence of their presence in the sedimentary or fossil records.

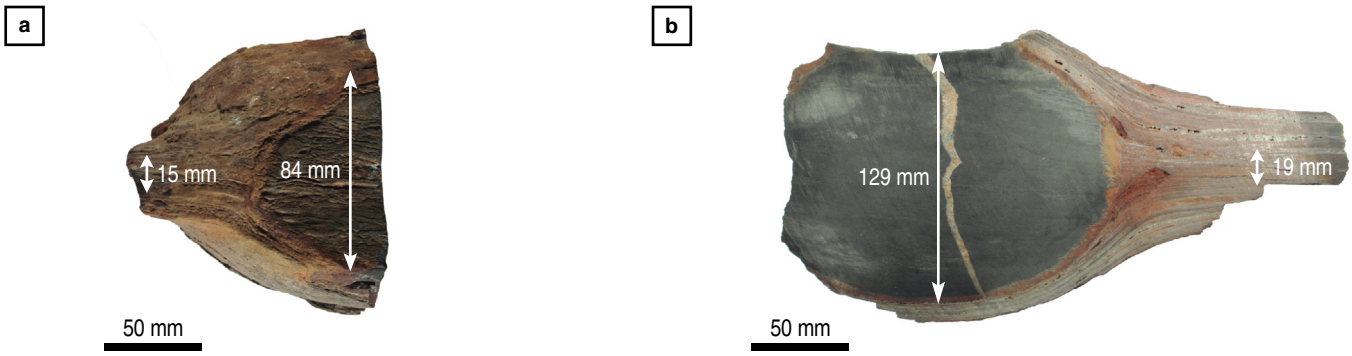

Figure 16. Non–septarian, early diagenetic concretion surrounded by non–concretionary sediments that "wrap around" the concretion (UADG LM 17.369). **(a)** "End" of the concretion showing the bedding (picked out by recent weathering) passing through the concretion, whereas the surrounding non–concretionary sediments "wrap" around the concretion. **(b)** Cut, right side, of (a) showing the lack of obvious bedding within the concretion (but which is faintly visible in the original specimen), the wrapping of sediments not invested by early diagenetic concretion growth, and a later phase calcite vein cutting the concretion sub–vertically. This specimen gives details of both pre– and post–compaction thicknesses of the sediment pile; in (a) concretion 84 mm, same laminae 15 mm post–compaction gives 82.14% compaction (100 – (15/84 × 100)); in (b) concretion 129 mm (minimum), same laminae 19 mm post–compaction gives a minimum of 85.27% compaction (100 – (19/129 × 100)). Collected by LFN from Salto y La Lavendera, way up not known but overburden pressure was in the sense top–bottom.

3.1.6. A Tripartite Division of Paja Formation Waters

Dark, laminated mudrocks largely devoid of benthic macrofauna and trace fossils, beneath a stratified water mass were episodically developed in shallow epicontinental seas during the Jurassic and Cretaceous (Petrash et al., 2016; van Helmond et al., 2015). Paja Formation Seas were thereby divided into a three–phase environment (Tyson & Pearson, 1991): firstly, near–normal marine surface waters; secondly, non–normal dysoxic–anoxic bottom waters and anoxic sediments; and thirdly, these two semi–independent water masses were separated by a chemocline or pycnocline (density interface). However, development of a chemocline–pycnocline will trap nutrients in the bottom waters, which, unless nutrients are available from elsewhere, will lead to reduced surface water primary productivity (Tyson & Pearson, 1991), however, abundant nutrients appear to have been available in Paja Formation Seas from terrestrial sources as argued above. The interface between the upper and lower waters was not a sharp line, but rather a transition zone, which restricted vertical mixing of oxygen–rich surface waters and nutrient–rich but oxygen–poor bottom waters (Sageman, 1985; Wignall, 1991a). Hence, the development of a semi–permanent chemocline–pycnocline acted as a control on both fauna and C_{org} burial (Pacton et al., 2011; Sageman et al., 1991).

With water depth greater than fair weather atmospheric mixing, an oxygen and temperature gradient can develop due to incomplete mixing. With highly productive surface waters, the degradation of dead organic matter settling through the water column is incomplete, and below the well–mixed zone organic matter degradation consumes more oxygen than can be replaced by diffusion, especially in periods of high global temperatures such as the Cretaceous (Meyer & Kump, 2008; Tourtelot, 1979). This generates an oxygen gradient, and an oxygen minimum zone at or above the sediment–water interface (Jenkyns, 1980). Hence, dead organic matter normally oxidized within the water column, reaches the sediment–water interface, using up dissolved oxygen as it goes. Any aerobic decomposition on the seafloor further reduces benthic oxygen availability, and low oxygen tensions gradually reduce benthic faunal species richness, biomass, and body size. The elimination of thick–shelled forms occurs first, although some smaller shelly forms can survive in dysoxic environments (Wignall & Myers, 1988). In the Paja Formation, the thickness of the lower (sub chemocline–pycnocline) dysoxic–anoxic water layer was probably in the order of centimetres to a metre (cf. Tyson & Pearson, 1991).

Ultimately, organic matter on the seafloor becomes incorporated into sediments, as it can no longer be completely consumed by aerobic epifauna. In organic–rich sediments without infauna, even in the presence of partially oxic bottom waters, anoxic conditions will exist a few millimetres below the sediment–water interface (May & Harvey, 1995). In anoxic conditions, sulphate–reducing bacteria act on the organic matter, producing hydrogen sulphide, which is preserved in the rock record as iron pyrite (Tourtelot, 1979). Indeed, the incomplete breakdown of organic matter may produce compounds that preferentially act as substrates for anaerobic bacteria on the seafloor (Tourtelot, 1979). These conditions are most likely to occur in the deepest part of the basin, producing an oxygen–deficient "puddle" (Wignall, 1991a). However, oxygen levels also depend on the rate of surface organic primary productivity, clastic sedimentation rates (so as not to over dilute organic matter), oxygen diffusion rates (lower in warmer waters), and the intensity of oxidation (Tourtelot, 1979).

The interface between the upper and lower water masses developed due to differences between surface and bottom water bodies in terms of (Hay, 2008; Meyer & Kump, 2008; Wignall, 1989): temperature as a result of solar heating of surface waters (likely); chemical differences due to slow oxygen diffusion and high nutrient availability (likely); and/or salinity differences (less likely). In modern environments, shelf anoxia is normally due to thermal stratification of the water column, but can be a result of dense saline bottom waters (Tyson & Pearson, 1991). In Paja Formation Seas, salinity differences seem an unlikely cause because, although salinity is a potent stratifying agent, it is improbable a halocline could develop across an entire epicontinental sea basin (Tyson & Pearson, 1991). However, sediment cracking is observed in the Paja Formation, and underwater this could be related to syneresis (sub–aqueous sediment shrinkage due to osmotic dewatering into a halocline). However, the cracking seen in Paja Formation sediments seems more likely to be a result of diagenetic sediment dewatering and shrinkage (cf. to septarian nodule formation). Hence, thermal stratification of Paja Formation Seas, associated with oxygen starvation of the bottom waters and high nutrient input into surface waters (and hence high primary productivity), leading to biochemical water mass differences, seems the most likely reason for Paja Formation chemocline–pycnocline development and maintenance.

Shallow water black mudrock facies are often considered broadly transgressive (Tourtelot, 1979). However, although transgression may help explain the initial development of anoxia in Paja Formation Seas, it cannot explain the maintenance of that system. Paja Formation Seas existed from Hauterivian to Aptian times (approximately 18 Ma based on current understanding, Cohen et al., 2013; updated 2017/02), and marine transgression did not continue unabated throughout this time (Guerrero, 2002a, 2002b). In modern subtropical and temperate seas, stratification is commonly linked to seasonality, with summer primary productivity sufficient to induce bottom water dysoxia–anoxia, and winter storms sufficiently strong to breakdown the chemocline–pycnocline (Bádenas & Aurell, 2008; Miller et al., 1988). However, the latitudinal position of the Paja Formation Seas indicates a non–seasonal equatorial climate, with constant high primary productivity and therefore continual organic matter loading.

The majority of modern, and many ancient, dysoxic–bottom marine environments are enclosed, but it is perhaps possible to develop shelf anoxia in an open setting. However, the Paja Formation is best seen as a semi–enclosed sea, bordered by land to the east (and at different times to the north and south), with an incomplete barrier to the west formed by the Central Cordillera island arc. Hence, none of the commonly cited causes of density stratification appears to apply to Paja Formation Seas, and this reinforces the uniqueness of each individual epicontinental sea. Hence, the tripartite division of Paja Formation waters initially developed, and was later maintained, through surface water heating, and differential surface and bottom water biochemical processes (Meyer & Kump, 2008). Once developed, dysoxic or anoxic bottom conditions are self–perpetuating. Some phytoplankton live along the chemocline–pycnocline, obtaining sunlight for photosynthesis from above and nutrients for growth from below (Tyson & Pearson, 1991). The gill–bearing fish and cephalopods will not enter dysoxic bottom waters, as they require oxygenated waters to survive. Marine reptiles, as air breathing organisms, could potentially cross the chemocline–pycnocline to enter dysoxic bottom waters, but a lack of prey items would normally restrict these organisms to the well–mixed surface waters. This lack of macroscopic predators in Paja Formation bottom waters, together with soft sediments, helps to explain the absence of scavenging on marine reptile skeletons and fish carcasses preserved in the Paja Formation. A "snapshot" model for the environment for the Paja Formation is presented in Figure 17.

3.1.7. Dynamics of Paja Formation Seas

Epicontinental seas were dynamic places (Sageman et al., 1991). Modern shallow seas are rarely beyond the reach of storm mixing (Tyson & Pearson, 1991), and Paja Formation Seas were undoubtedly affected by storms, and possibly earthquakes, tsunamis, and turbidity currents. Equatorial regions are subject to short but intense thunderstorms, and at 5–7° north of the equator (Smith et al., 1994), Paja Formation Seas were on the lower latitudinal limits of the tropical storm (hurricane–typhoon–cyclone) belt, but were undoubtedly occasionally affected by these large atmospheric perturbations (Emanuel, 2003). In shallow shelf or epicontinental seas, storms affect a large proportion of the water column (Tyson & Pearson, 1991). Exceptional storms may completely break down chemical or density interfaces (Wignall & Myers, 1988) although the greater the depth of water, the greater the energy required to breakdown stratification, making permanency of the chemocline–pycnocline a depth dependant parameter (Wignall, 1991a). Large storms that breach the chemocline–pycnocline will temporally introduce oxygen into normally dysoxic–anoxic bottom waters (Miller et al., 1988; Wignall & Myers, 1988), but may also release toxic H_2S from bottom waters or sediments (Meyer & Kump, 2008).

Evidence for storms in deep water environments are typically preserved as distal tempestites (Figure 13), often just a few mm thick, characterized by graded rip–up clasts, silt laminae, and thin graded mud horizons (Miller et al., 1988; Wignall, 1989). The aftermath of storm events may be recognised in the rock record by the presence of brief colonization events preserved as shell pavements (Figure 12), surrounded above and below by dysoxic–anoxic sediments (Miller et al., 1988; Wignall, 1989). In addition, the wide range of terrestrial material within the Paja Formation Basin (including logs, branches, leaves, fruit, insects,

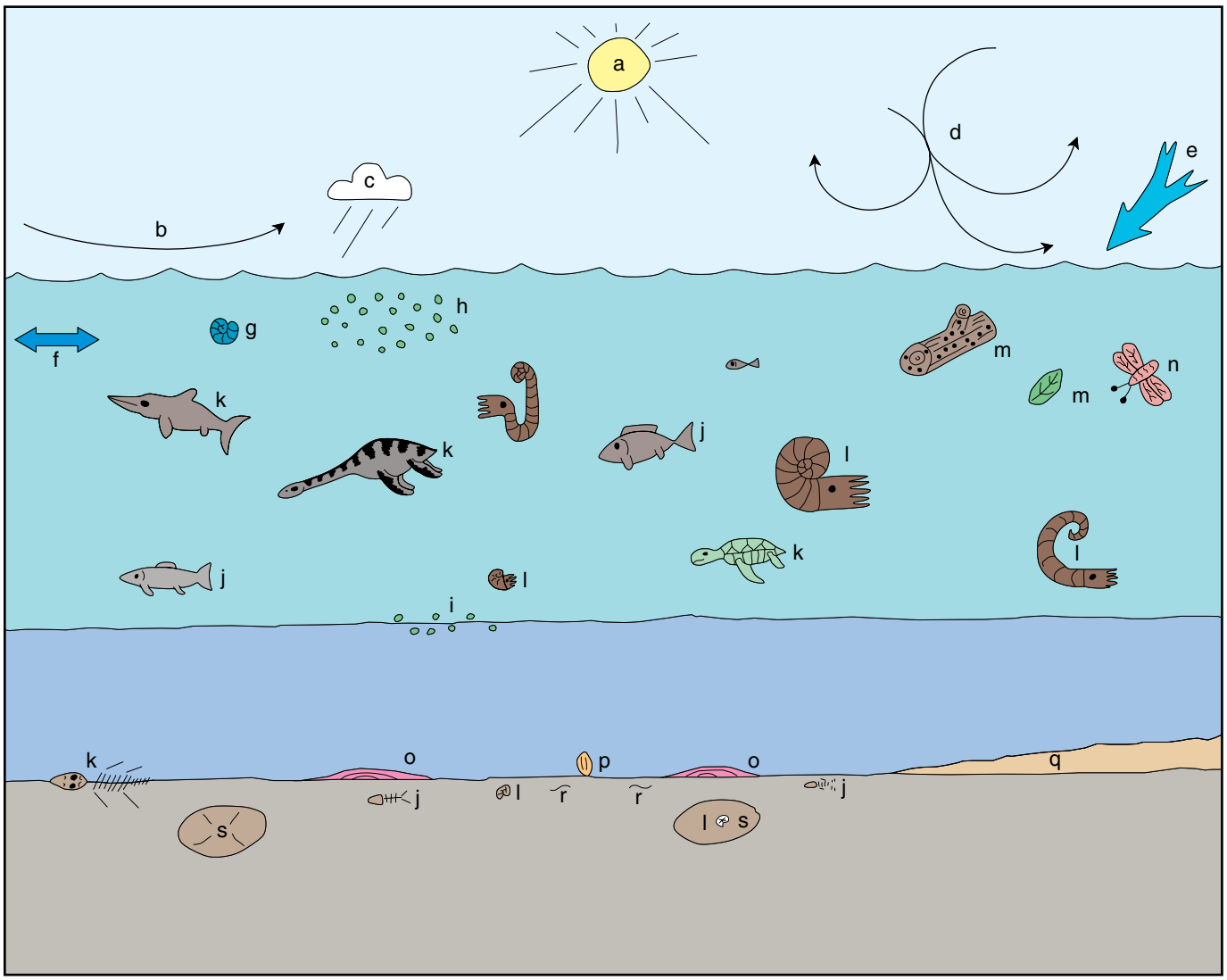

Figure 17. A diagrammatic representation of Paja Formation Seas, with inputs from sun, rain, wind, storms, and the terrestrial realm. Surface waters with a restricted circulation and tidal influence, and with a diverse pelagic fauna. Dysoxic–anoxic bottom waters with a depauperate benthic fauna of a few thin–shelled bivalves, separated from the surface waters by a chemocline–pycnocline. The dysoxic–anoxic bottom waters largely excluded burrowing and surface living organisms and permitted exceptional fossil preservation. Abbreviations: (a) solar input; (b) wind; (c) rain; (d) tropical storms; (e) terrestrial freshwater and organic matter; (f) subdued tidal or current action; (g) zooplankton; (h) surface water phytoplanton; (i) phytoplankton exploiting the chemocline–pycnocline; (j) fish and their fossils; (k) marine vertebrates and their fossils; (l) ammonites and their fossils; (m) floating logs with boring bivalves ("shipworms"), and other terrestrial plant material; (n) insects; (o) sulphate–reducing bacterial mats; (p) depauperate benthic fauna; (q) occasional storm deposits; (r) low oxygen tension and hydrogen sulphide–tolerant annelid worms; (s) early diagenetic concretions, which may or may not contain fossils, and/or be septarian in nature. Water depths not to scale, with chemocline–pycnocline a transition zone. See text for details.

and a dinosaur) is evidence for intense tropical storms blowing or washing terrestrial faunal and floral elements into Paja Formation Seas. However, it is worth noting, that no pterosaur or bird remains have yet been reported from the Paja Formation, although both of these groups should be expected to be occasionally found. Storms may mix the water column to the seafloor (Tyson & Pearson, 1991); however, high–energy storm events are the rarest (Wignall, 1989). With the perturbation over, the seafloor may remain oxygenated for a period of years, depending on water depth and surface water primary productivity, which allowed the development of short–term post–event biofacies (e.g., Figure 12). However, the chemocline–pycnocline was self–restoring and with time bottom water dysoxia–anoxia developed, re–establishing the former tripartite division. A model for the possible development and dynamics of the Paja Formation epicontinental sea is presented in Figure 18.

Hence, Paja Formation Seas had surface waters that were warm and buoyant, well–lit, well–oxygenated, and with a near–normal salinity. Surface waters had strong solar input, a freshwater contribution derived from precipitation and runoff

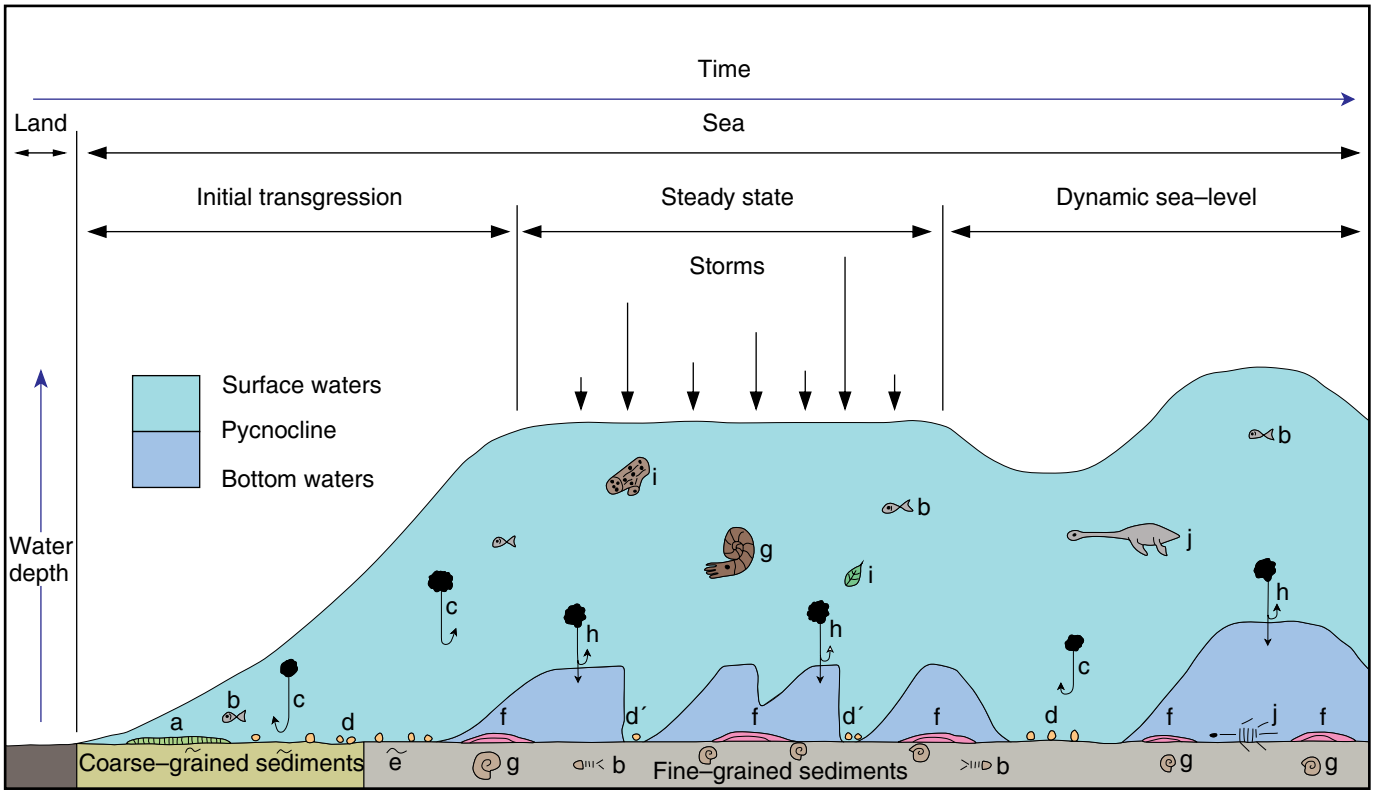

Figure 18. Conceptual diagram for the development, maintenance, breakdown, and re–initiation of a chemocline–pycnocline and dysoxic–anoxic bottoms water in Paja Formation epicontinental seas. Left to right: transgression over the land surface deposited coarse–grained nearshore sediments and a shallow water fauna developed. Organic carbon is almost completely recycled, either within the water column, or on or close to the seafloor. As sea level continues to rise, finer–grained sediments are deposited, and bottom waters are no longer well mixed or oxygenated. With high surface water primary productivity, organic carbon is incompletely degraded, and in the lower water column oxygen demand is greater than availability leading to bottom water dysoxia–anoxia. The two water masses are separated by a chemocline–pycnocline zone, which was reinforced by a relative lack of solar heating of bottom waters. With steady–state (non–fluctuating) sea levels, large storms may lower or breakdown the chemocline–pycnocline briefly oxygenating the sea floor, however, the chemocline–pycnocline is self–restoring. With fluctuating sea levels, regression may lead to the lowering or complete removal of the chemocline–pycnocline, and transgression may raise the chemocline–pycnocline. Paja Formation Seas were probably affected by a combination of fluctuating sea levels and storm events producing a complex, everchanging dynamic. Abbreviations: (a) algal mats; (b) fish and their fossils; (c) recycled organic matter; (d) bottom living epifauna, d' epifaunal invasions due to brief oxygenation events; (e) infauna; (f) sulphate reducing microbial mats; (g) ammonites and their fossils; (h) incompletely recycled organic matter; (i) floating logs with boring bivalves ("shipworms"), and other terrestrial plant material; (j) marine vertebrates and their fossils. Horizontal and vertical axes not to scale. See text for details.

(which provided nutrients and terrestrial organic matter), and were mixed by wind and to a lesser extent tidal action. The surface waters were home to a pelagic flora of phytoplankton, with high rates of photosynthetic primary productivity (Pacton et al., 2011), and a fauna of zooplankton, which acted as the base of a complex food web dominated by ammonites, fish, and marine reptiles (Figures 5–7). In addition, floating terrestrial wood acted as a substrate for pseudoplanktonic, wood–boring bivalves (Figure 11). By contrast, the bottom waters of Paja Seas were C_{org}–rich, oxygen–starved (anoxic–dysoxic), and affected by the production of H_2S. This led to a low diversity, low abundance depauperate benthos, dominated by microbial mat communities that thrived at low oxygen tensions. These two water masses were separated by a chemocline–pycnocline, making the Paja Formation a Type II, pelagic dominated facies (Sageman et al., 1991). However, Paja Formation Seas were highly dynamic, leading to periodic breakdown of the boundary between surface and bottom waters by large–impact physical perturbations such as passing tropical storms, tsunamis or turbidity currents (Hay, 2008; Miller et al., 1988). Nonetheless, the tripartite division of Paja Seas was re–established through the same biochemical and physical processes that initiated the system (Sageman et al., 1991), producing a dynamic equilibrium that did not rely upon sluggish circulation of bottom currents (Meyer & Kump, 2008).

3.2. Taphonomy and Diagenesis

Preservation affects both sediments and fossils, and many processes are common to both inorganic particles and organic remains. Taphonomy is commonly divided into two comple-

mentary studies: biostratinomy, the biological, chemical, and physical processes occurring prior to final burial, or organisms (or their parts) acting as sedimentary particles; and diagenesis, the chemical and physical processes which affect both rocks and enclosing fossils following final burial (Lash & Blood, 2004; e.g., Martin, 1999; Witkowska, 2012). The taphonomy of the Paja Formation is understudied (but see Etayo–Serna, 1968); however, below we discuss the taphonomy of the marine reptiles, knowing that further work is required to fully understand Paja Formation deposits, post–depositional history, and the preservation of diverse faunal elements.

3.2.1. Biostratinomy

Following death, a vertebrate carcass may float, beach or sink. In the taphonomic model proposed for the Paja Formation (Etayo–Serna, 1968), marine reptile decomposing carcasses floated in from the west, eventually beaching along the palaeoshoreline. The assumption that marine reptile carcasses floated may or may not be true. For instance, humans have hunted modern marine mammals, preferring "right" whales—those that floated when harpooned, over other species that sank (Clapham, 1997; Würtz & Repetto, 1998)—but it is not known whether marine reptiles floated or sank upon death, or if like modern marine mammals it varied between species. However, marine mammals are insulated with a thick layer of low–density blubber, which increases their propensity to float, whereas modern reptiles typically have little subcutaneous fat deposits (Shirihai & Jarrett, 2006). If Mesozoic marine reptiles were akin to modern reptiles, it is more likely they sank upon death, at least until the gases of decomposition developed to a sufficient degree to re–float the carcass. However, the beautifully preserved specimens of marine reptiles from the Paja Formation are often fully articulated (Figure 5), with the jaws tightly closed, teeth in their alveoli, and delicate structures such as sclerotic plates and hyoid apparatus preserved in situ (e.g., Maxwell et al., 2016; Páramo–Fonseca, 1997; Welles, 1962). Based on actualistic taphonomic studies of modern mammals, floating carcasses rapidly decay and are subject to scavenging and disarticulation, and the lower jaw is one of the first elements to drop from a carcass (Schäfer, 1972). Hence, assuming similar patterns of necrolysis in Mesozoic marine reptiles and modern mammals, a "float and bloat" model for marine reptile preservation in the Paja Formation (Etayo–Serna, 1968) would predict loss of elements, starting with the lower jaw, distal limb elements, and the tail, and carcasses would present evidence of scavenging. However, modern mammal and Mesozoic marine reptile taphonomy are not the same, with examples of ichthyosaurs known that "nose–dived" into sediments with the lower jaws intact (Martill, 1993; Wahl, 2009). However, the residence times in water (i.e., when sinking occurred) of these carcasses after death, are not known. Equally, beaching of marine reptiles following death (as proposed by Etayo–Serna, 1968) would predict that, as a large potential food supply, the body would be rapidly consumed by aerial, marine or terrestrial predator–scavengers, and that the bones would become scattered by wave action (Schäfer, 1972), which this is not seen in Paja Formation fossils.

The exceptionally well–preserved, articulated, little crushed preservation of the Paja vertebrates, including the preservation of delicate structures such as hyoid bones, sclerotic rings, scales, and eggs, requires a different explanation, where normal biostratinomic decay and destructive processes were "short–circuited". The articulated nature of the skeletons argues strongly for rapid burial (Brenchley & Harper, 1998), which may have been due to rapid sedimentation rates, but is more likely a result of a soft or soupy substrate consistency (Martill, 1993). Complete or partial burial in soft sediments would also decrease the chances of re–flotation of a carcass during the generation of gases of decomposition, depending on the weight of the overlying water column. The presence of organic carbon–rich sediments and dysoxic–anoxic bottom waters would also have precluded scavenging by fish and cephalopods, reduced or prevented epibiont encrustation, and minimized the possibility of scavenging by air–breathing marine reptiles.

3.2.2. Diagenesis

Following final burial, diagenetic processes begin. The soft tissues of a dead organism are a vast potential energy source for microorganisms, which rapidly reduce oxygen availability around the carcass, and produce dysoxic–anoxic conditions at or close to the sediment–water interface. The subsequent anaerobic breakdown of soft tissues and interaction with seawater releases H_2S, which reacts with iron released from sediments to produce iron pyrite (Fe_2S). Hence, the presence of pyrite in alto Ricaurte sediments strongly suggests anoxic pore waters, and future study of pyrite morphology may be indicative of the oxygen content of Paja Formation bottom waters (Gallego–Torres et al., 2015; Roychoudhury et al., 2003).

Calcareous– and iron–rich concretions are abundant throughout the Paja Formation (Figure 4). Concretions are often richly fossiliferous (Etayo–Serna, 1968), but even those devoid of macrofossils are likely to have nucleated around microfossils or amorphous C_{org}. Concretions are also indicative of reduced sedimentation rates (Martin, 1999), and localized, pre–compaction diagenesis at shallow depths within the sediment pile, prior to dewatering. The early diagenetic nature of Paja Formation concretions can be ascertained by the "wrapping" of enclosing sediments (Figure 16), which is indicative of concretionary growth within the sediment body and later differential dewatering and compaction of the surrounding non–concretionary sediments. As burial depth increased, early diagenetic concretions resisted compaction of the sediments and, where they formed around fossils, led to exceptional three–dimensional preservation (Páramo–Fonseca, 1997; Welles, 1962).

Gypsum and calcite are common in many parts of the Paja Formation, and have been considered syndepositional (Etayo–Serna, 1968; Forero–Onofre & Sarmiento–Rojas, 1985). Both calcite and gypsum are encountered as sheet–like bodies (gypsum veins are commonly 1–2 mm thick, whereas calcite veins are often 10 mm or more in thickness; Figures 8, 12), with internal bi–layered fibrous–like crystals ("satin spar" for gypsum or "sparite" for calcite), distributed approximately symmetrically around a central junction (Cobbold et al., 2013; Philipp, 2008). As the crystals lie approximately normal to the edges of the mineral sheets, this form of gypsum or calcite is commonly termed "beef" as it has the appearance of cut meat (Cobbold et al., 2013); cone–in–cone calcite is also occasionally present. The calcite and gypsum sheets may follow bedding, but also commonly cross or cut sedimentary layers and concretions, or divide to surround fossils (Etayo–Serna, 1968). In addition, antitaxial growth (from the vein centre) means fossils may be found in the centre of calcite "beef" (Figure 12), and as the crystals of the minerals are arranged perpendicular to the centre of the vein, vague impressions or "shadows" of the fossils may be visible on both outer surfaces of the mineral veins (Cobbold et al., 2013).

The perpendicular arrangement of gypsum and calcite fibres is evidence for extensional vein growth, with cracking and deposition from hydrothermal fluids occurring along the vein walls (Philipp, 2008). The fracturing of mudrocks indicates vein growth and deposition must have taken place in consolidated sediments. Gypsum "beef" typically forms at temperatures of up to 60 °C, whereas calcite "beef" is deposited at temperatures of 70–120 °C or within the "oil window" (Cobbold et al., 2013). Thus, formation of gypsum and calcite "beef" occurs at temperatures (and pressures) higher than those at the surface of the earth (Kershaw & Guo, 2016), so interpretations of sheet gypsum or calcite as syndepositional, are erroneous. The temperatures of formation of gypsum and calcite "beef" suggest emplacement of gypsum after the calcite, probably during relatively recent unroofing of the ECC (Mosolf et al., 2010), although further work is required to determine the cross–cutting relationships of gypsum and calcite in the Paja Formation, and hence the relative timing of vein emplacement. However, as gypsum deposition did not occur during Paja Formation times, this leaves open the source of the calcium sulphate. One possible source is vertical migration from underlying or now missing overlying sediments, rich in calcium sulphate. However, contiguous formations show no evidence of extensive original gypsum precipitation (Etayo–Serna, 1965, 1968), which suggests lateral migration of calcium sulphate–rich fluids from a geographically more distal source.

3.3. A Regional and Global Overview

During the Cretaceous, sea levels were globally high compared to today (Haq et al., 1987; Miller et al., 2005). Flooding of the Early Cretaceous western basins of Colombia commenced during the Berriasian, gradually extending from west to east (Gaona–Narváez, 2015). During this time, the Cundinamarca or Sabana de Bogotá Sub–basin horst was periodically flooded, as a result of constantly changing global sea levels (Haq et al., 1988; Müller et al., 2008), which led to the deposition of evaporitic deposits (Cortés et al., 2006). Evaporation of seawater is likely to have produced a range of salts, including calcium carbonate, gypsum (hydrated calcium sulphate), and halite (sodium chloride). However, as sea levels were constantly changing, repeated flooding and evaporation would have built complex salt deposits. Following tectonic inversion, these salts may have been the source of the post–depositional minerals (gypsum and possibly calcite) in the Paja Formation.

During Paja Formation times (Hauterivian to early Albian) global sea levels continued to fluctuate (Haq et al., 1988; Müller et al., 2008), leading to complex and dynamic cycles that affected the Paja Formation depositional environment (Mann & Stein, 1997). The causes (and effects) of these high but constantly changing sea levels have been the subject of much debate with increased seafloor spreading rates and superplume induced large igneous province volcanism (e.g., the Ontong Java Plateau) evoked as possible mechanisms (Keller, 2008; Kominz, 2001; Seton et al., 2009). Superimposed over global sea–level changes, where a series of oceanic anoxic events (OAEs), which occurred throughout the Cretaceous (Hesselbo et al., 2007; Jenkyns, 2010). The Paja Formation of alto Ricaurte is likely to record evidence for two of these events. The OAE 1a (Selli) event of the early Aptian (Jenkyns, 2010; Leckie et al., 2002; Pictet et al., 2015) probably occurred in segment D (or possibly the base of segment E) of the AA Member. OAE 1b (the Paquier event), which occurred close to the Aptian – Albian boundary (Jenkyns, 2010; Zhang et al., 2016), is likely to have occurred in the AcNH Member. The causes of OAEs may have been many and varied, but possibly include increased mid–ocean ridge volcanism producing gasses and nutrients, and release of methane gas hydrates, both leading to higher than normal ocean primary productivity (Jones & Jenkyns, 2001; Larson & Erba, 1999; Méhay et al., 2009; Petrash et al., 2016; van Helmond et al., 2015; Zhang et al., 2016). In northern South America, facies changes appear to broadly match these global trends in sea–level and ocean dynamics (Macellari, 1988).

During the latest Cretaceous, collision of the Pacific Plate with the South American Shield began the process of tectonic inversion of the ECC Basin, producing an intracontinental doubly vergent mountain chain (Jiménez et al., 2014; Teixell et al., 2015). This compression resulted in a combination of thick– and thin–skinned faulting (Babault et al., 2013; Moreno et al., 2013), with a major decollement (basal detachment fault) in the lowermost Cretaceous salt–rich layers, that today lie at around 4 km depth (Teixell et al., 2015). Inversion of the ECC resulted in halite diapirs (e.g., at Nemocón and Zipaquirá; Babault et al., 2013), and may have been the source for the lateral migration of

mineral–rich fluids that gave rise to both Colombian emeralds (Cobbold et al., 2013) and the gypsum "beef" in the Paja Formation. The calcite "beef" could have been sourced from the same fluids, intrabasinally, or a combination of both. Hence, rapid Miocene uplift of the Andes (Babault et al., 2013; Bayona et al., 2013), may have been the trigger for fracturing, vertical salt dome diapirism, and lateral migration of over pressurized, calcium– and sulphate–rich fluids.

One salt deposited during the Berriasian was presumably calcium sulphate, originally in the form of gypsum, but at depth converted by dehydration to anhydrite, which produces a reduction of the original volume of around 10% (Philipp, 2008). Following tectonic inversion, the anhydrite was exposed to circulating groundwaters, causing hydration to gypsum, and a volume increase of 60% (Philipp, 2008), generating fluid over pressurisation and salt mobilization. Over pressurisation would have led to hydrothermal fluid movement along faults and fractures reactivated or produced due to crustal shortening, or developed as a result of natural hydraulic fracturing, and along bedding planes between the largely impermeable mudrocks within the Tablazo–Magdalena Sub–basin. Successive mineral–rich fluid flows, over a period of several millions of years (Cobbold et al., 2013), would thereby have deposited fibrous gypsum (and possibly calcite) "beef" within Paja Formation rocks. Hence, the source of the over pressurization is likely to have been conversion of anhydrite to gypsum (Philipp, 2008), driven by deep water circulation as a result of changing precipitation and runoff resulting from the rise of the Andes mountain chain (Mora et al., 2008).

Ultimately, uplift of the Andes brought Paja Formation rocks to 2150 m above sea level, and unroofing led to modern subaerial weathering and erosion. This produced recent oxidation of iron–rich clay minerals, leading to the typically variegated colours of the Paja Formation outcrops. A small amount of gypsum in the Paja Formation may have been produced close to the surface by recent weathering.

4. Conclusions

The Paja Formation was deposited in a moderately deep (~60–130 m) marine basin, formed as a result of extensional tectonics and high sea levels during Hauterivian to Aptian times. By uniting sedimentological, paleobiological, taphonomic, and tectonic data with literature on modern shelf and ancient epicontinental seas, we have been able to reconstruct and reinterpret the palaeoenvironment of the Paja Formation of alto Ricaurte. The Paja Formation Seas were tripartite, with normal marine surface waters inhabited by a diverse pelagic fauna of marine reptiles (plesiosauromorph and pliosauromorph plesiosaurs, ichthyosaurs, and marine turtles), numerous fish, and extremely abundant ammonites. The food web is inferred to have been based on abundant phyto– and zoo–plankton. Surface waters were warm, well–lit, well–mixed, and of normal salinity. This was in marked contrast to the bottom waters, which were dysoxic–anoxic, and inhabited by low oxygen– and hydrogen sulphide–tolerant species, such as thin–shelled bivalves, probable annelid worms, and sulphide reducing bacteria that formed seafloor mats. Dysoxia–anoxia in the sediments and lower water column was due to the accumulation of incompletely degraded organic matter. The upper and lower portions of the water column seem to have been separated by a chemocline–pycnocline, which may have arisen due to temperature driven chemical or density differences between surface and deeper waters, but could (less probably) have been due to differences in salinity, or a combination of factors. However, Paja Seas were dynamic, and occasional breakdown of the chemocline–pycnocline occurred as a result of large tropical storms, but Paja Formation Seas may also have been affected by earthquake generated tsunamis and/or turbidity currents.

A paucity of Lower Cretaceous marine reptile bearing strata has long been noticed (e.g., Hampe, 1992). However, the Paja Formation of the alto Ricaurte, Eastern Cordillera of Colombia is a very complete succession of Hauterivian to Aptian rocks, which preserves an exceptional pelagic fauna. The excellent preservation of the fossil fauna around alto Ricaurte opens a new window on marine reptile, and particularly plesiosaur, diversity in the Early Cretaceous. The Paja Formation can therefore be considered one of very few Lower Cretaceous marine reptile Lagerstätte.

Data supporting an evaporitic environment for the Paja Formation, based on the presence of gypsum, is shown to be erroneous and the result of secondary, diagenetic processes. Gypsum (and possibly calcite) "beef" is likely to have been emplaced as the result of hydrothermal fluid migration, with the gypsum probably sourced from Berriasian salts deposited over the Sabana de Bogotá high. Fluid migration was likely driven by over pressurisation due to rehydration of anhydrite to gypsum as a result of Andean uplift, unroofing, and resultant changing climatic patterns. Hence, two aspects critical to a full understanding of the geological history of the Paja Formation, are the taphonomy of the fossil remains, and the clear separation of original depositional features from the products of diagenesis. This work thereby suggests that although the deposits of the alto Ricaurte region are some of the best studied in Colombia, there remains much to understand about these fascinating rocks, and the times in which they were deposited.

Acknowledgments

We thank Jorge GÓMEZ TAPIAS for inviting us to contribute to this exciting volume on *The Geology of Colombia*. We extend our grateful thanks to Charles MARSHALL, Mark GOODWIN and Pat HOLROYD (UCMP), Leopoldo GONZÁLEZ OVIEDO and Lina TORRES (SGC Museum, Bogotá), Javier GONZALEZ, Humberto SÁCHICA, and Alberto DELGADO

(MJACM), and Santiago PADILLA and Juan de DIOS PARRA (CIP) for access to, and permission to publish photographs of, specimens in their care. We extend special thanks to: Alejandra CARDONA (SGC) for the *Kronosaurus boyacensis* photograph (Figure 5b); Matt FRIEDMAN (Department of Earth and Environmental Sciences, College of Literature, Science, and the Arts, University of Michigan, USA) for preliminary identifications of fish specimens; José Vicente RODRIGUEZ JIMÉNEZ (Departamento de Geociencias, Universidad de los Andes, Colombia) for proof reading and comments; and to numerous colleagues for providing us with literature. We acknowledge lively discussions with various colleagues, not all of whom agree with our conclusions, and in particular Dr. Fernando ETAYO SERNA who has displayed exceptional kindness to LFN and acted as mentor and inspiration for MG–P. LFN acknowledges the stimulating academic environment of the Departamento de Geociencias, Universidad de los Andes, and MG–P acknowledges the support and collegiate atmosphere of the Museo José Royo y Gomez, SGC. Funding for LFN was provided by a "Fondo de Apoyo para Profesores Asistentes" grant (FAPA n° P12–160422.006/01) awarded by Universidad de los Andes; writing of the manuscript was undertaken during the tenure of a grant entitled "The Paja Formation Lagerstätte of the alto Ricaurte: Access, palaeoenvironment and taphonomy" grant (Programas de Investigación para Profesores de Planta Associados, Titulares y Emeritos n° P18.160322.001/23) from the Facultad de Ciencias, Universidad de los Andes. We extend our sincere thanks to Judy MASSARE (Department of Earth Sciences, State University of New York College at Brockport, USA) and John NUDDS (School of Earth and Environmental Sciences, Manchester University, UK) for thoughtful and insightful reviews, which considerably improved a manuscript version of this contribution. The authors gratefully acknowledge the patience and support of our families during the preparation of this manuscript.

References

Acosta, C.E., Huerta, G. & Ruiz, P.M. 1979. Noticia preliminar sobre el hallazgo de un presunto *Kronosaurus* (Reptilia: Dolichorhynchopidae) en el Aptiano superior de Villa de Leyva, Colombia. Lozania (Acta Zoológica Colombiana), 28: 1–7.

Algeo, T.J., Heckel, P.H., Maynard, B., Blakey, R.C. & Rowe, H. 2008. Modern and ancient epeiric seas and the super–estuarine circulation model of marine anoxia. In: Pratt, B.R. & Holmden, C. (editors), Dynamics of epeiric seas. Geological Association of Canada, Special Paper 48, p. 7–38. Toronto.

Álvarez–León, R., Orozco–Rey, R.H., Páramo–Fonseca, M.E. & Restrepo–Santamaría, D. 2013. Lista de los peces fósiles y actuales de Colombia: Nombres científicos válidos, distribución geográfica, diagnosis de referencia & nombres comunes e indígenas. Eco Prints Diseño Gráfico y Audiovisual Ltda., 346 p. Bogotá.

Andrews, C.W. 1913. A descriptive catalogue of the marine reptiles of the Oxford Clay: Based on the Leeds Collection in the British Museum (Natural History), London. British Museum, II, 206 p. London. https://doi.org/10.5962/bhl.title.61785

Babault, J., Teixell, A., Struth, L., van den Driessche, J., Arboleya, M.L. & Tesón, E. 2013. Shortening, structural relief and drainage evolution in inverted rifts: Insights from the Atlas Mountains, the Eastern Cordillera of Colombia and the Pyrenees. In: Nemčok, M., Mora, A. & Cosgrove, J.W. (editors), Thick–skin–dominated orogens: From initial inversion to full accretion. Geological Society of London, Special Publication 377, p. 141–158. London. https://doi.org/10.1144/SP377.14

Bádenas, B. & Aurell, M. 2008. Kimmeridgian epeiric sea deposits of northeastern Spain: Sedimentary dynamics of a storm–dominated carbonate ramp. In: Pratt, B.R. & Holmden, C. (editors), Dynamics of epeiric seas. Geological Association of Canada, Special Paper 48, p. 55–71. Toronto.

Bardet, N. 1995. Evolution et extinction des reptiles marins au cours du Mésozoïque. Palaeovertebrata, 24(3–4): 177–283.

Bardet, N., Falconnet, J., Fischer, V., Houssaye, A., Jouve, S., Pereda–Superbiola, X., Pérez–García, A., Rage, J.C. & Vincent, P. 2014. Mesozoic marine reptile palaeobiogeography in response to drifting plates. Gondwana Research, 26(3–4): 869–887. https://doi.org/10.1016/j.gr.2014.05.005

Bayona, G., Cardona, A., Jaramillo, C., Mora, A., Montes, C., Caballero, V., Mahecha, H., Lamus, F., Montenegro, O., Jiménez, G., Mesa, A. & Valencia, V. 2013. Onset of fault reactivation in the Eastern Cordillera of Colombia and proximal Llanos Basin; Response to Caribbean–South American convergence in early Palaeogene time. In: Nemčok, M., Mora, A. & Cosgrove, J.W. (editors), Thick–skin–dominated orogens: From initial inversion to full accretion. Geological Society of London, Special Publication 377, p. 285–314. London. https://doi.org/10.1144/SP377.5

Benson, R.B.J. & Druckenmiller, P.S. 2014. Faunal turnover of marine tetrapods during the Jurassic – Cretaceous transition. Biological Reviews: Cambridge Philosophical Society, 89(1): 1–23. https://doi.org/10.1111/brv.12038

Bogdanova, T.N. & Hoedemaeker, P.J. 2004. Barremian – early Aptian Deshayesitidae, Oppeliidae, Desmoceratidae and Silesitidae of Colombia. Scripta Geologica, 128: 183–312.

Bornemann, A., Pross, J., Reichelt, K., Herrle, J.O., Hemleben, C. & Mutterlose, J. 2005. Reconstruction of short–term palaeoceanographic changes during the formation of the late Albian 'Niveau Breistroffer' black shales (Oceanic Anoxic Event 1d, SE France). Journal of the Geological Society, 162(4): 623–639. https://doi.org/10.1144/0016-764903-171

Bottjer, D.J., Etter, W., Hagadorn, J.W. & Tang, C.M., editors. 2002. Exceptional fossil preservation: A unique view on the evolution of marine life. Columbia University Press, 403 p. New York.

Brady, M. & Bowie, C. 2017. Discontinuity surfaces and microfacies in a storm–dominated shallow epeiric sea, Devonian Cedar Valley Group, Iowa. The Depositional Record, 3(2): 136–160. https://doi.org/10.1002/dep2.26

Brenchley, P.J. & Harper, D.A.T. 1998. Palaeoecology: Ecosystems, environments and evolution. Chapman & Hall, 402 p. London. https://doi.org/10.1002/gj.810

Bürgl, H. 1954. El Cretáceo Inferior en los alrededores de Villa de Leiva, Boyacá. Boletín Geológico, 2(1): 5–22.

Cadena, E.A. 2014. The fossil record of turtles in Colombia: A review of the discoveries, research and future challenges. Acta Biológica Colombiana, 19(3): 333–339. https://doi.org/10.15446/abc.v19n3.42223

Cadena, E.A. 2015. The first South American sandownid turtle from the Lower Cretaceous of Colombia. PeerJ, 3(e1431): 1–24. https://doi.org/10.7717/peerj.1431

Cadena, E.A. & Parham, J.F. 2015. Oldest known marine turtle? A new protostegid from the Lower Cretaceous of Colombia. PaleoBios, 32(1): 1–42.

Campos–Álvarez, N.O. & Roser, B.P. 2007. Geochemistry of black shales from the Lower Cretaceous Paja Formation, Eastern Cordillera, Colombia: Source weathering, provenance, and tectonic setting. Journal of South American Earth Sciences, 23(4): 271–289. https://doi.org/10.1016/j.jsames.2007.02.003

Campos–Álvarez, N.O., Roser, B.P. & Sampei, Y. 2002. Organic carbon and carbonate contents of black shales from the Lower Cretaceous Paja Formation (Colombia) by loss on ignition and CHNS analysis: Comparison of methods. Geoscience Reports of Shimane University, 21: 9–16.

Caplan, M.L. & Bustin, R.M. 1998. Palaeoceanographic controls on geochemical characteristics of organic–rich Exshaw mudrocks: Role of enhanced primary production. Organic Geochemistry, 30(2–3): 161–188. https://doi.org/10.1016/S0146-6380(98)00202-2

Carballido, J.L., Pol, D., Parra–Ruge, M.L., Padilla–Bernal, S., Páramo–Fonseca, M.E. & Etayo–Serna, F. 2015. A new Early Cretaceous brachiosaurid (Dinosauria, Neosauropoda) from northwestern Gondwana (Villa de Leiva, Colombia). Journal of Vertebrate Paleontology, 35(5): 1–12. https://doi.org/10.1080/02724634.2015.980505

Carpenter, K. 1999. Revision of North American elasmosaurs from the Cretaceous of the Western Interior. Paludicola, 2(2): 148–173.

Carroll, R.L. 1988. Vertebrate paleontology and evolution. W.H. Freeman and Company, 698 p. New York.

Clapham, P. 1997. Whales. Colin Baxter Photography, 132 p. Scotland.

Cobbold, P.R., Zanella, A., Rodrigues, N. & Løseth, H. 2013. Bedding–parallel fibrous veins (beef and cone–in–cone): Worldwide occurrence and possible significance in terms of fluid overpressure, hydrocarbon generation and mineralization. Marine and Petroleum Geology, 43: 1–20. https://doi.org/10.1016/j.marpetgeo.2013.01.010

Cohen, K.M., Finney, S.C., Gibbard, P.L. & Fan, J.X. 2013. The ICS International Chronostratigraphic Chart. Episodes, 36(3): 199–204.

Cortés, M., Colletta, B. & Angelier, J. 2006. Structure and tectonics of the central segment of the Eastern Cordillera of Colombia. Journal of South American Earth Sciences, 21(4): 437–465. https://doi.org/10.1016/j.jsames.2006.07.004

Decker, K. & Rögl, F. 1988. Early Cretaceous agglutinated foraminifera from limestone–marl rhythmites of the Gresten Klippen Belt, eastern Alps (Austria). Abhandlungen der Geologischen Bundesanstalt, 41: 41–59.

Dodd Jr, C.K. 1988. Sinopsis of the biological data on the loggerhead sea turtle *Caretta caretta* (Linnaeus 1758). U.S. Department of the Interior. Fish and Wildlife Service. Biological Report, 88(14), 110 p. Washington D.C.

Emanuel, K. 2003. Tropical cyclones. Annual Review of Earth and Planetary Sciences, 31: 75–104. https://doi.org/10.1146/annurev.earth.31.100901.141259

Eriksson, P.G., Schieber, J., Bouougri, E., Gerdes, G., Porada, H., Banerjee, S., Bose, P.K. & Sarkar, S. 2007. Classification of structures left by microbial mats in their host sediments. In: Schieber, J., Bose, P.K., Eriksson, P.G., Banerjee, S., Sarkar, S., Altermann, W. & Catuneau, O. (editors), Atlas of microbial mat features preserved within the siliciclastic rock record. Elsevier, Atlases in geoscience, 2, p. 39–52. Oxford, UK.

Espinel–Arias, V. & Hurtado–Henao, J.A. 2010. Petrografía y análisis facial de las rocas calcáreas aflorantes de la sección Tunja–Villa de Leiva, Boyacá. Bachelor thesis, Universidad de Caldas, 117 p. Manizales.

Espinosa, A. 2016. El Servicio Geológico Colombiano 1916–2016: Cien años al servicio de Colombia. Servicio Geológico Colombiano, 261 p. Bogotá.

Etayo–Serna, F. 1964. Posición de las faunas en los depósitos cretácicos colombianos y su valor en la subdivisión cronológica de los mismos. Boletín de Geología, (16–17): 5–142.

Etayo–Serna, F. 1965. Sinopsis estratigráfica de la región de Villa de Leiva y zonas próximas. Boletín de Geología, (21): 19–32.

Etayo–Serna, F. 1968. El sistema Cretáceo en la región de Villa de Leiva y zonas próximas. Geología Colombiana, 5: 5–74.

Etayo–Serna, F. 1979. Zonation of the Cretaceous of central Colombia by ammonites. Publicaciones Geológicas Especiales del Ingeominas 2, 186 p. Bogotá.

Etayo–Serna, F. 1981. On the supposed Aptian occurrence of the ammonite genus *Neodeshayesites* in Colombia and Venezuela; with an appendix on *Neodeshayesites karsteni* (Marcou). Geología Norandina, (3): 45–51.

Etayo–Serna, F. Acosta, C.E., Ruiz, P.M. & Huertas, G. 1978. Un posible *Kronosaurus* en el Aptiano de Villa de Leiva. II Congreso Colombiano de Geología. Abstracts, p. 40. Bogotá.

Etayo–Serna, F., Montoya, D.M. & Terraza, M.R. 2015. Patrimonio geológico y paleontológico Villa de Leiva y zonas próximas:

Un caso único. Servicio Geológico Colombiano, unpublished report, 42 p. Bogotá.

Evans, S. 1999. Wood–boring bivalves and boring linings. Bulletin of the Geological Society of Denmark, 45: 130–134.

Fernández, M.S. & Aguirre–Urreta, M.B. 2005. Revision of *Platypterygius hauthali* von Huene, 1927 (Ichthyosauria: Ophthalmosauridae) from the Early Cretaceous of Patagonia, Argentina. Journal of Vertebrate Paleontology, 25(3): 583–587. https://doi.org/10.1671/0272-4634(2005)025[0583:ROPHVH]2.0.CO;2

Fernández, M.S., Archuby, F., Talevi, M. & Ebner, R. 2005. Ichthyosaurian eyes: Paleobiological information content in the sclerotic ring of *Caypullisaurus* (Ichthyosauria, Ophthalmosauria). Journal of Vertebrate Paleontology, 25(2): 330–337. https://doi.org/10.1671/0272-4634(2005)025[0330:IEPICI]2.0.CO;2

Fischer, V., Bardet, N., Guiomar, M. & Godefroit, P. 2014. High diversity in Cretaceous ichthyosaurs from Europe prior to their extinction. PLOS ONE, 9(1): 1–26. https://doi.org/10.1371/journal.pone.0084709

Fluteau, F., Ramstein, G., Besse, J., Guiraud, R. & Masse, J.P. 2007. Impacts of palaeogeography and sea level changes on mid–Cretaceous climate. Palaeogeography, Palaeoclimatology, Palaeoecology, 247(3–4): 357–381. https://doi.org/10.1016/j.palaeo.2006.11.016

Forero–Onofre, H. & Sarmiento–Rojas, L. 1985. La facies evaporítica de la Formación Paja en la región de Villa de Leiva. In: Etayo–Serna, F. & Laverde–Montaño, F. (editors), Proyecto Cretácico: Contribuciones. Publicaciones Geológicas Especiales del Ingeominas 16, p. XVII-1–XVII-16. Bogotá.

Gallego–Torres, D., Reolid, M., Nieto–Moreno, V. & Martínez–Casado, F.J. 2015. Pyrite framboid size distribution as a record for relative variations in sedimentation rate: An example on the Toarcian oceanic anoxic event in southiberian palaeomargin. Sedimentary Geology, 330: 59–73. https://doi.org/10.1016/j.sedgeo.2015.09.013

Galvis–Arenas, B.E. & Valencia–Escobar, J.L. 2009. Contribución en la determinación de los posibles paleoambientes de las rocas cretáceas tempranas sobre la vía Tunja–Villa de Leyva (entre alto del Arrayan–Peaje Sáchica) y sectores aledaños, departamento de Boyacá. Bachelor thesis, Universidad de Caldas, 144 p. Manizales.

Gaona–Narváez, T. 2015. El Cretácico sedimentario al este de la Falla de San Jerónimo: Compilación para el Mapa Geológico de Colombia. In: Gómez, J. & Almanza, M.F. (editors), Compilando la geología de Colombia: Una visión a 2015. Servicio Geológico Colombiano, Publicaciones Geológicas Especiales 33, p. 421–429. Bogotá.

Gasparini, Z. & Goñi, R. 1985. Los plesiosaurios cretácicos de América del Sur y del continente antártico. Coletânea de Trabalhos Paleontologicos: Trabalhos apresentados no VIII Congresso Brasileiro de Paleontologia 1983, Série Geologia 27(2), p. 55–63. Brasilia.

Gingras, M.K., Maceachern, J.A. & Pickerill, R.K. 2004. Modern perspectives on the *Teredolites* ichnofacies: Observations from Willapa Bay, Washington. PALAIOS, 19(1): 79–88. https://doi.org/10.1669/0883-1351(2004)019<0079:MPOTTI>2.0.CO;2

Gómez–Cruz, A.d.J., Moreno–Sánchez, M. & Vallejo, L. 2011. Fósiles de Insecta (Odonata) del Aptiano tardío en la Formación Paja. Boletín Científico. Centro de Museos. Museo de Historia Natural. Novedades en Historia Natural, 15(2): p. 222.

Gómez, J. & Almanza, M.F., editors. 2015. Compilando la geología de Colombia: Una visión a 2015. Servicio Geológico Colombiano, Publicaciones Geológicas Especiales 33, 401 p. Bogotá.

Gómez–Pérez, M. & Noè, L.F. 2017. Cranial anatomy of a new pliosaurid *Acostasaurus pavachoquensis* from the Lower Cretaceous of Colombia, South America. Palaeontographica, 310(1–2): 5–42. https://doi.org/10.1127/pala/2017/0068

Goñi, R. & Gasparini, Z. 1983. Nuevos restos de "*Alzadasaurus colombiensis*" (Reptilia, Plesiosauria) del Cretácico Temprano de Colombia. Geología Norandina, (7): 49–54.

Gradstein, F.M., Kaminski, M.A. & Agterberg, F.P. 1999. Biostratigraphy and paleoceanography of the Cretaceous seaway between Norway and Greenland. Earth–Science Reviews, 46(1–4): 27–98. https://doi.org/10.1016/S0012-8252(99)00018-5

Guerrero, J. 2002a. A proposal on the classification of systems tracts: Application to the allostratigraphy and sequence stratigraphy of the Cretaceous Colombian Basin. Part 1: Berriasian to Hauterivian. Geología Colombiana, 27: 3–25.

Guerrero, J. 2002b. A proposal on the classification of systems tracts: Application to the allostratigraphy and sequence stratigraphy of the Cretaceous Colombian Basin. Part 2: Barremian to Maastrichtian. Geología Colombiana, 27: 27–49.

Hampe, O. 1992. Ein großwüchsiger Pliosauride (Reptilia: Plesiosauria) aus der Unterkreide (oberes Aptium) von Kolumbien. Courier Forschungsinstitut Senckenberg, 145: 1–25.

Hampe, O. 2005. Considerations on a *Brachauchenius* skeleton (Pliosauroidea) from the lower Paja Formation (late Barremian) of Villa de Leyva area (Colombia). Fossil Record, 8(1): 37–51. https://doi.org/10.1002/mmng.200410003

Hampe, O. & Leimkühler, C. 1996. Die anwendung der photogrammetrie in der wirbeltierpaläontologie am beispiel eines *Kronosaurus*–fundes in Kolumbien. Mainzer Geowissenschaftliche Mitteilungen, 25: 55–78.

Haq, B.U., Hardenbol, J. & Vail, P.R. 1987. Chronology of fluctuating sea levels since the Triassic. Science, 235: 1156–1167.

Haq, B.U., Hardenbol, J., Vail, P.R., Stover, L.E., Colin, J.P., Ioannides, N.S., Wright, R.C., Baum, G.R., Gombos–Jr, A.M., Pflum, C.E., Loutit, T.S., du Chêne, R.J., Romine, K.K., Sarg, J.F., Posamentier, H.W. & Morgan, B.E. 1988. Mesozoic and Cenozoic chronostratigraphy and cycles of sea–level change. In: Wilgus, C.K., Hastings, B.S., Posamentier, H., van Wagoner, J., Ross, C.A. & Kendall, C.G. (editors), Sea–level changes: An integrated approach. Society Economic Paleon-

tologists and Mineralogists SEPM, Special Publication 42, p. 71–108. https://doi.org/10.2110/pec.88.01.0071

Hay, W.W. 2008. Evolving ideas about the Cretaceous climate and ocean circulation. Cretaceous Research, 29(5–6): 725–753. https://doi.org/10.1016/j.cretres.2008.05.025

Hesselbo, S.P., Jenkyns, H.C., Duarte, L.V. & Oliveira, L.C.V. 2007. Carbon–isotope record of the Early Jurassic (Toarcian) oceanic anoxic event from fossil wood and marine carbonate (Lusitanian Basin, Portugal). Earth and Planetary Science Letters, 253(3–4): 455–470. https://doi.org/10.1016/j.epsl.2006.11.009

Hirth, H.F. 1980. Some aspects of the nesting behavior and reproductive biology of sea turtles. American Zoologist, 20(3): 507–523. https://doi.org/10.1093/icb/20.3.507

Hoedemaeker, P.J. & Kakabadze, M.V. 2004. Preface: Early Cretaceous ammonites from Colombia. Scripta Geologica, 128: 1–2.

Huber, K. & Wiedmann, J. 1986. Sobre el límite Jurásico–Cretácico en los alrededores de Villa de Leiva, departamento de Boyacá, Colombia. Geología Colombiana, 15: 81–92.

Huertas, G. 1967. Sertum florulae fossilis Villae de Leivae. Caldasia, 10(46): 59–75.

Huertas, G. 1970. Sertum florulae fossilis Villae de Leivae II. Caldasia, 10(50): 595–602.

Huertas, G. 1976. Sertum florulae fossilis Villae de Leiva. Caldasia, 11(54): 17–23.

Hu, X., Wagreich, M. & Yilmaz, I.O. 2012. Marine rapid environmental/climatic change in the Cretaceous greenhouse world. Cretaceous Research, 38: 1–6. https://doi.org/10.1016/j.cretres.2012.04.012

Imai, T., Jintasakul, P., Azuma, Y., Noda, Y. & Chokchaloemwong, D. 2016. First confirmed fossil turtle eggshells (Oogenus *Testudoolithus*) from the Lower Cretaceous of Thailand. Memoir of the Fukui Prefectural Dinosaur Museum, 15: 1–6.

Immenhauser, A. 2009. Estimating palaeo–water depth from the physical rock record. Earth–Science Reviews, 96(1–2): 107–139. https://doi.org/10.1016/j.earscirev.2009.06.003

Isaji, S., Matsushita, A. & Hirayama, R. 2006. Chelonian eggshells from the Lower Cretaceous Kuwajima Formation of the Tetori Group, central Japan. Paleontological Research, 10(1): 29–36. https://doi.org/10.2517/prpsj.10.29

Jenkyns, H.C. 1980. Cretaceous anoxic events: From continents to oceans. Journal of the Geological Society, 137(2): 171–188. https://doi.org/10.1144/gsjgs.137.2.0171

Jenkyns, H.C. 1997. Mesozoic anoxic events and palaeoclimate. Zentralblatt für Geologie und Paläontologie, 1(7–9): 943–949.

Jenkyns, H.C. 2010. Geochemistry of oceanic anoxic events. Geochemistry, Geophysics, Geosystems, 11(3): 1–30. https://doi.org/10.1029/2009GC002788

Jerez–Jaimes, J.H. & Narváez–Parra, E.X. 2001. *Callawayasaurus colombiensis* (Welles) Carpenter 1999 el plesiosaurio de Villa de Leyva (Boyacá, Colombia). ¿Un nuevo espécimen? Boletín de Geología, 23(38): 9–19.

Jiménez, G., Speranza, F., Faccenna, C., Bayona, G. & Mora, A. 2014. Paleomagnetism and magnetic fabric of the Eastern Cordillera of Colombia: Evidence for oblique convergence and nonrotational reactivation of a Mesozoic intracontintental rift. Tectonics, 33(11): 2233–2260. https://doi.org/10.1002/2014TC003532

Jones, C.E. & Jenkyns, H.C. 2001. Seawater strontium isotopes, oceanic anoxic events, and seafloor hydrothermal activity in the Jurassic and Cretaceous. American Journal of Science, 301(2): 112–149. https://doi.org/10.2475/ajs.301.2.112

Kakabadze, M.V. & Hoedemaeker, P.J. 1997. New and less known Barremian – Albian ammonites from Colombia. Scripta Geologica, 114: 57–117.

Kakabadze, M.V. & Hoedemaeker, P.J. 2004. Heteromorphic ammonites from the Barremian and Aptian strata of Colombia. Scripta Geologica, 128: 39–182.

Keller, G. 2008. Cretaceous climate, volcanism, impacts, and biotic effects. Cretaceous Research, 29 (5–6): 754–771. https://doi.org/10.1016/j.cretres.2008.05.030

Kershaw, S. & Guo, L. 2016. Beef and cone–in–cone calcite fibrous cements associated with the end–Permian and end–Triassic mass extinctions: Reassessment of processes of formation. Journal of Palaeogeography, 5(1): 28–42. https://doi.org/10.1016/j.jop.2015.11.003

Kominz, M.A. 2001. Sea level variations over geologic time. In: Steele, J.H., Thorpe, S.A, & Turekian, K.K. (editors), Encyclopedia of ocean sciences. Elsevier, p. 2605–2613. https://doi.org/10.1006/rwos.2001.0255

Larson, R.L. & Erba, E. 1999. Onset of the mid–Cretaceous greenhouse in the Barremian – Aptian: Igneous events and the biological, sedimentary, and geochemical responses. Paleoceanography and Paleoclimatology, 14(6): 663–678. https://doi.org/10.1029/1999PA900040

Lash, G.G. & Blood, D. 2004. Geochemical and textural evidence for early (shallow) diagenetic growth of stratigraphically confined carbonate concretions, Upper Devonian Rhinestreet black shale, western New York. Chemical Geology, 206(3–4): 407–424. https://doi.org/10.1016/j.chemgeo.2003.12.017

Leckie, R.M., Bralower, T.J. & Cashman, R. 2002. Oceanic anoxic events and plankton evolution: Biotic response to tectonic forcing during the mid–Cretaceous. Paleoceanography and Paleoclimatology, 17(3): 13–1-13–29. https://doi.org/10.1029/2001PA000623

Macellari, C.E. 1988. Cretaceous paleogeography and depositional cycles of western South America. Journal of South American Earth Sciences, 1(4): 373–418. https://doi.org/10.1016/0895-9811(88)90024-7

Macellari, C.E. & de Vries, T.J. 1987. Late Cretaceous upwelling and anoxic sedimentation in northwestern South America. Palaeogeography, Palaeoclimatology, Palaeoecology, 59: 279–292. https://doi.org/10.1016/0031-0182(87)90086-1

Mannion, P.D., Allain, R. & Moine, O. 2017. The earliest known titanosauriform sauropod dinosaur and the evolution of Brachiosauridae. PeerJ 5(e3217): 1–82. https://doi.org/10.7717/peerj.3217

Mann, U. & Stein, R. 1997. Organic facies variations, source rock potential, and sea level changes in Cretaceous black shales of the quebrada Ocal, Upper Magdalena Valley, Colombia. American Association of Petroleum Geologists Bulletin, 81(4): 556–576.

Martill, D.M. 1985. The preservation of marine vertebrates in the Lower Oxford Clay (Jurassic) of central England. Philosophical Transactions of the Royal Society of London B: Biological Sciences, 311(1148): 155–165. https://doi.org/10.1098/rstb.1985.0147

Martill, D.M. 1988. Preservation of fish in the Cretaceous Santana Formation of Brazil. Palaeontology, 31(1): 1–18.

Martill, D.M. 1993. Soupy substrates: A medium for the exceptional preservation of ichthyosaurs of the Posidonia Shale (Lower Jurassic) of Germany. Kaupia–Darmstädter Beiträge zur Naturgeschichte, 2: 77–97.

Martínez, F., Okino, K., Ohara, Y., Reysenbach, A.L. & Goffredi, S.K. 2007. Back–arc basins. Oceanography, 20(1): 116–127. https://doi.org/10.5670/oceanog.2007.85

Martin, R.E. 1999. Taphonomy a process approach. Cambridge Paleobiology Series 4. Cambridge University Press, 524 p. Cambridge.

Massare, J.A. 1984. Ecology and evolution of Mesozoic marine reptiles. Doctoral thesis, John Hopkins University, 182 p. Baltimore, USA.

Massare, J.A. 1997. Faunas, behavior, and evolution. In: Callaway, J.M. & Nicholls, E.L. (editors), Ancient marine reptiles. Academic Press, p. 401–421. San Diego.

Mattioli, E., Gardin, S., Giraud, F., Olivero, D., Pittet, B. & Reboulet, S. 2008. Guidebook for the post–congress fieldtrip in the Vocontian Basin, SE France (September 11–13, 2008). 12th Meeting of the International Nannoplankton Association, 26 p.

Maxwell, E.E., Dick, D., Padilla, S. & Parra, M.L. 2016. A new opthalmosaurid ichthyosaur from the Early Cretaceous of Colombia. Palaeontology, 2(1): 59–70. https://doi.org/10.1002/spp2.1030

May, R.M. & Harvey, P.H., editors. 1995. Ecology and evolution in anoxic worlds. Oxford University Press, 276 p. Oxford.

McGavin, G.C. 2001. Essential entomology: An order–by–order introduction. Oxford University Press, 328 p. Oxford.

Méhay, S., Keller, C.E., Bernasconi, S.M., Weissert, H., Erba, E., Bottini, C. & Hochuli, P.A. 2009. A volcanic CO_2 pulse triggered the Cretaceous oceanic anoxic event 1a and a biocalcification crisis. Geology, 37(9): 819–822. https://doi.org/10.1130/G30100A.1

Meyer, K.M. & Kump, L.R. 2008. Oceanic euxinia in Earth history: Causes and consequences. Annual Review of Earth and Planetary Sciences, 36: 251–288. https://doi.org/10.1146/annurev.earth.36.031207.124256

Mikhailov, K.E. 1997. Fossil and recent eggshell in amniotic vertebrates: Fine structure, comparative morphology and classification. Special Papers in Palaeontology, (56): 1–80.

Miller, A.I. & Foote, M. 2009. Epicontinental seas versus open–ocean settings: The kinetics of mass extinction and origination. Science, 326(5956): 1106–1109. https://doi.org/10.1126/science.1180061

Miller, J.D., Limpus, C.J. & Godfrey, M.H. 2003a. Nest site selection, oviposition, eggs, development, hatching, and emergence of loggerhead turtles. In: Bolten, A.B. & Witherington, B.E. (editors), Loggerhead sea turtles. Smithsonian Books, p. 125–143. Washington D.C.

Miller, K.B. Brett, C.E. & Parsons, K.M. 1988. The paleoecologic significance of storm–generated disturbance within a Middle Devonian muddy epeiric sea. PALAIOS, 3(1): 35–52. https://doi.org/10.2307/3514543

Miller, K.G., Sugarman, P.J., Browning, J.V., Kominz, M.A., Hernández, J.C., Olsson, R.K., Wright, J.D., Feigenson, M.D. & van Sickel, W. 2003b. Late Cretaceous chronology of large, rapid sea–level changes: Glacioeustasy during the greenhouse world. Geology, 31(7): 585–588. https://doi.org/10.1130/0091-7613(2003)031<0585:LCCOLR>2.0.CO;2

Miller, K.G., Kominz, M.A., Browning, J.V., Wright, J.D., Mountain, G.S., Katz, M.E., Sugarman, P.J., Cramer, B.S., Christie–Blick, N. & Pekar, S.F. 2005. The Phanerozoic record of global sea–level change. Science, 310(5752): 1293–1298. https://doi.org/10.1126/science.1116412

Moore, C.M., Mills, M.M., Arrigo, K.R., Berman–Frank, I., Bopp, L., Boyd, P.W., Galbraith, E.D., Geider, R.J., Guieu, C., Jaccard, S.L., Jickells, T.D., La Roche, J., Lenton, T.M., Mahowald, N.M., Marañón, E., Marinov, I., Moore, J.K., Nakatsuka, T., Oschlies, A., Saito, M.A., Thingstad, T.F., Tsuda, A. & Ulloa, O. 2013. Processes and patterns of oceanic nutrient limitation. Nature Geoscience, 6: 701–710. https://doi.org/10.1038/ngeo1765

Moore, J. 2001. An introduction to the invertebrates. Cambridge University Press, 355 p. Cambridge.

Mora, A., Parra, M., Strecker, M.R., Sobel, E.R., Hooghiemstra, H., Torres, V. & Vallejo–Jaramillo, J. 2008. Climatic forcing of asymmetric orogenic evolution in the Eastern Cordillera of Colombia. Geological Society of America Bulletin, 120(7–8): 930–949. https://doi.org/10.1130/B26186.1

Morales, L.G. 1958. General geology and oil occurrences of Middle Magdalena Valley, Colombia. In: Weeks, L.G. (editor), Habitat of oil. American Association of Petroleum Geologists, p. 641–695. Tulsa, USA.

Moreno, N., Silva, A., Mora, A., Tesón, E., Quintero, I., Rojas, L.E., López, C., Blanco, V., Castellanos, J., Sánchez, J., Osorio, L., Namson, J., Stockli, D. & Casallas, W. 2013. Interaction between thin– and thick–skinned tectonics in the foothill areas of an inverted graben: The Middle Magdalena Foothill belt. In: Nemčok, M., Mora, A. & Cosgrove, J.W. (editors), Thick–

skin–dominated orogens: From initial inversion to full accretion. Geological Society of London, Special Publication 377, p. 221–255. London. https://doi.org/10.1144/SP377.18

Moreno–Sánchez, M., Gómez–Cruz, A.d.J. & Castillo–González, H. 2007. *Frenelopsis* y *Pseudofrenelopsis* (Coniferales: Cheirolepidiaceae) en el Cretácico Temprano de Colombia. Boletín de Geología, 29(2): 13–19.

Mosolf, J.G., Horton, B.K., Heizler, M.T. & Matos, R. 2010. Unroofing the core of the central Andean fold–thrust belt during focused late Miocene exhumation: Evidence from the Tipuani–Mapiri wedge–top basin, Bolivia. Basin Research, 23: 346–360. https://doi.org/10.1111/j.1365-2117.2010.00491.x

Müller, R.D., Sdrolias, M., Gaina, C., Steinberger, B. & Heine, C. 2008. Long–term sea–level fluctuations driven by ocean basin dynamics. Science, 319(5868): 1357–1362. https://doi.org/10.1126/science.1151540

Mutterlose, J., Pauly, S. & Steuber, T. 2009. Temperature controlled deposition of Early Cretaceous (Barremian – early Aptian) black shales in an epicontinental sea. Palaeogeography, Palaeoclimatology, Palaeoecology, 273(3–4): 330–345. https://doi.org/10.1016/j.palaeo.2008.04.026

Nicholls, E.L. & Russell, A.P. 1990. Paleobiogeography of the Cretaceous Western Interior Seaway of North America: The vertebrate evidence. Palaeogeography, Palaeoclimatology, Palaeoecology, 79(1–2): 149–169. https://doi.org/10.1016/0031-0182(90)90110-S

Nichols, G. 2009. Sedimentology and stratigraphy, second edition. Wiley–Blackwell, 419 p. Chichester, UK.

Nuamsukon, S., Chuen–Im, T., Rattanayuvakorn, S., Panishkan, K., Narkkong, N. & Areekijseree, M. 2009. Thai marine turtle eggshell: Morphology, ultrastructure and composition. Journal of Microscopy Society of Thailand, 23(1): 52–56.

Pacton, M., Schmid, T., Gorin, G., Massault, M. & Stadler, J. 2011. Cretaceous black shale: A window into microbial life adaptation. Terra Nova, 23(6): 362–368. https://doi.org/10.1111/j.1365-3121.2011.01020.x

Páramo–Fonseca, M.E. 1997. *Platypterygius sachicarum* (Reptilia, Ichthyosauria) nueva especie del Cretácico de Colombia. Revista Ingeominas, 6: 1–12.

Páramo–Fonseca, M.E. 2015. Estado actual del conocimiento de los reptiles marinos cretácicos de Colombia. Publicación Electrónica de la Asociación Paleontológica Argentina, 15(1): 40–57. https://doi.org/10.5710/PEAPA.12.06.2015.98

Páramo–Fonseca, M.E., Gómez–Pérez, M., Noè, L.F. & Etayo–Serna, F. 2016. *Stenorhynchosaurus munozi*, gen. et sp. nov. a new pliosaurid from the upper Barremian (Lower Cretaceous) of Villa de Leiva, Colombia, South America. Revista de la Academia Colombiana de Ciencias Exactas, Físicas y Naturales, 40(154): 84–103. http://dx.doi.org/10.18257/raccefyn.239

Patarroyo–Camargo, G.D., Patarroyo, P. & Sánchez–Quiñónez, C.A. 2009. Foraminíferos bentónicos en el Barremiano inferior de la Formación Paja (Boyacá–Santander, Colombia): Evidencias preliminares de un posible bioevento. Geología Colombiana, 34: 111–122.

Patarroyo–Camargo, G., Patarroyo, P. & Sánchez–Quiñónez, C.A. 2011. Benthic foraminiferal biostratigraphy of northern South America: Problems and perspectives. 22nd Colloquium on Latin American Earth Sciences. Abstract, 28 p. Heidelberg Institute of Earth Sciences. Heidelberg, Germany.

Patarroyo, P. 1997. Barremiano inferior en la base de la Formación Paja, Barichara, Santander–Colombia. Geología Colombiana, 22: 135–138.

Patarroyo, P. 2000a. Primer registro de un áptico, asociado con *Nicklesia pulchella* (D'Orbigny), en Villa de Leiva–Boyacá (Colombia–Sudamérica). Revista de la Academia Colombiana de Ciencias Exactas, Físicas y Naturales, 24(91): 279–283.

Patarroyo, P. 2000b. Distribución de amonitas del Barremiano de la Formación Paja en el sector de Villa de Leiva (Boyacá, Colombia). Bioestratigrafía. Geología Colombiana, 25: 149–162.

Patarroyo, P. 2009. Amonitas de un nivel de alta energía del Barremiano inferior en la Formación Paja de los sectores de Villa de Leiva (Boyacá) y de Vélez (Santander). Boletín de Geología, 31(2): 15–21.

Petrash, D.A., Gueneli, N., Brocks, J.J., Méndez–Dot, J.A., González–Arismendi, G., Poulton, S.W. & Konhauser, K.O. 2016. Black shale deposition and early diagenetic dolomite cementation during oceanic anoxic event 1: The mid–Cretaceous Maracaibo platform, northwestern South America. American Journal of Science, 316(7): 669–711. https://doi.org/10.2475/07.2016.03

Philipp, S.L. 2008. Geometry and formation of gypsum veins in mudstones at Watchet, Somerset, SW England. Geological Magazine, 145(6): 831–844. https://doi.org/10.1017/S0016756808005451

Phillott, A.D. & Parmenter, C.J. 2006. The ultrastructure of sea turtle eggshell does not contribute to interspecies variation in fungal invasion of the egg. Canadian Journal of Zoology, 84(9): 1339–1344. https://doi.org/10.1139/z06-125

Pictet, A., Delanoy, G., Adatte, T., Spangenberg, J.E., Baudouin, C., Boselli, P., Boselli, M., Kindler, P. & Föllmi, K.B. 2015. Three successive phases of platform demise during the early Aptian and their association with the oceanic anoxic Selli episode (Ardèche, France). Palaeogeography, Palaeoclimatology, Palaeoecology, 418: 101–125. https://doi.org/10.1016/j.palaeo.2014.11.008

Poulsen, C.J., Pollard, D. & White, T.S. 2007. General circulation model simulation of the $\delta^{18}O$ content of continental precipitation in the middle Cretaceous: A model–proxy comparison. Geology, 35(3): 199–202. https://doi.org/10.1130/G23343A.1

Pritchard, P.C.H. & Mortimer, J.A. 1999. Taxonomy, external morphology, and species identification. In: Eckert, K.L., Bjorndal, K.A., Abreu–Grobois, F.A. & Donnelly, M. (editors), Research and management techniques for the conservation of sea turtles. IUCN/SSC Marine Turtle Specialist Group 4, p. 21–38. Washington D.C.

Renzoni, G. 1981. Geología del cuadrángulo J–12 Tunja. Boletín Geológico, 24(2): 31–48.

Roychoudhury, A.N., Kostka, J.E. & van Cappellen, P. 2003. Pyritization: A palaeoenvironmental and redox proxy reevaluated. Estuarine, Coastal and Shelf Science, 57(5–6): 1183–1193. https://doi.org/10.1016/S0272-7714(03)00058-1

Ruppel, S.C. & Loucks, R.G. 2008. Black mudrocks: Lessons and questions from the Mississippian Barnett Shale in the southern midcontinent. The Sedimentary Record, 6(2): 4–8.

Sageman, B.B. 1985. High–resolution stratigraphy and paleobiology of the Hartland Shale Member: Analysis of an oxygen–deficient epicontinental sea. In: Pratt, L.M., Kauffman, E.G. & Zelt, F.B. (editors), Fine–grained deposits and biofacies of the Cretaceous Western Interior Seaway: Evidence of cyclic sedimentary processes. Society of Economic Paleontologists and Mineralogists SEPM, Field Trip Guidebook 4, p. 110–121. Tulsa, USA. https://doi.org/10.2110/sepmfg.04.110

Sageman, B.B., Wignall, P.B. & Kauffman, E.G. 1991. Biofacies models for oxygen–deficient facies in epicontinental seas: Tool for paleoenvironmental analysis. In: Einsele, G., Ricken, W. & Seilacher, A. (editors), Cycles and events in stratigraphy. Springer–Verlag, p. 542–564. Berlin.

Sarkar, S., Samanta, P. & Altermann, W. 2011. Setulfs, modern and ancient: Formative mechanism, preservation bias and palaeoenvironmental implications. Sedimentary Geology, 238(1–2): 71–78. https://doi.org/10.1016/j.sedgeo.2011.04.003

Schäfer, W. 1972. Ecology and palaeoecology of marine environments. University of Chicago Press, 568 p. Edinburgh, Scotland.

Schieber, J. 2011. Iron sulfide formation. In: Reitner, J. & Thiel, V. (editors), Encyclopedia of Geobiology. Encyclopedia of Earth Science Series. Springer, p. 486–502. Dordrecht, the Netherlands. https://doi.org/10.1007/978-1-4020-9212-1_118

Schieber, J. 2016. Mud re–distribution in epicontinental basins–exploring likely processes. Marine and Petroleum Geology, 71: 119–133. https://doi.org/10.1016/j.marpetgeo.2015.12.014

Schlanger, S.O. & Jenkyns, H.C. 1976. Cretaceous oceanic anoxic events: Causes and consequences. Geologie en Mijnbouw, 55(3–4): 179–184.

Schultze, H.P. & Stöhr, D. 1996. *Vinctifer* (Pisces, Aspidorhynchidae) aus der Unterkreide (oberes Aptium) von Kolumbien. Neues Jahrbuch für Geologie und Paläeontologie, Abhandlungen, 199(3): 395–415.

Selden, P.A. & Nudds, J.R. 2012. Evolution of fossil ecosystems. Academic Press, 288 p. London.

Seton, M., Gaina, C., Müller, R.D. & Heine, C. 2009. Mid–Cretaceous seafloor spreading pulse: Fact or fiction? Geology, 37(8): 687–690. https://doi.org/10.1130/G25624A.1

Sharikadze, M.Z., Kakabadze, M.V. & Hoedemaeker, P.J. 2004. Aptian and early Albian Douvilleiceratidae, Acanthohoplitidae and Parahoplitidae of Colombia. Scripta Geologica, 128: 313–514.

Shirihai, H. & Jarrett, B. 2006. Whales dolphins and seals: A field guide to the marine mammals of the world. A & C Black Publishers Ltd., 384 p. London.

Smith, A.G., Smith, D.G. & Funnell, B.M. 1994. Atlas of Mesozoic and Cenozoic coastlines. Cambridge University Press, 99 p. Cambridge.

Teixell, A., Ruiz, J.C., Teson, E. & Mora, A. 2015. The structure of an inverted back–arc rift: Insights from a transect across the Eastern Cordillera of Colombia near Bogotá. In: Bartolini, C. & Mann, P. (editors), Petroleum geology and potential of the Colombian Caribbean margin. American Association of Petroleum Geologists, Memoir 108, p. 499–516. https://doi.org/10.1306/M1081307

Tong, H. & Meylan, P. 2013. Morphology and relationships of *Brachyopsemys tingitana* gen. et sp. nov. from the early Paleocene of Morocco and recognition of the new eucryptodiran turtle family: Sandownidae. In: Brinkman, D.B., Holroyd, P.A. & Gardner, J.P. (editors), Morphology and evolution of turtles: Vertebrate Paleobiology and Paleoanthropology. Springer, p. 187–212. Dordrecht, the Netherlands. https://doi.org/10.1007/978-94-007-4309-0_13

Tourtelot, H.A. 1979. Black shale–its deposition and diagenesis. Clays and Clay Minerals, 27(5): 313–321.

Townson, W.G. 1975. Lithostratigraphy and deposition of the type Portlandian. Journal of the Geological Society, 131(6): 619–638. https://doi.org/10.1144/gsjgs.131.6.0619

Tyson, R.V. & Pearson, T.H. 1991. Modern and ancient continental shelf anoxia: An overview. In: Tyson, R.V. & Pearson, T.H. (editors), Modern and ancient continental shelf anoxia. Geological Society of London, Special Publication 58, p. 1–24. https://doi.org/10.1144/GSL.SP.1991.058.01.01

Ufnar, D.F., González, L.A., Ludvigson, G.A., Brenner, R.L. & Witzke, B.J. 2002. The mid–Cretaceous water bearer: Isotope mass balance quantification of the Albian hydrologic cycle. Palaeogeography, Palaeoclimatology, Palaeoecology, 188(1–2): 51–71. https://doi.org/10.1016/S0031-0182(02)00530-8

van Helmond, N.A.G.M., Sluijs, A., Sinninghe–Damsté, J.S., Reichart, G.J., Voigt, S., Erbacher, J., Pross, J. & Brinkhuis, H. 2015. Freshwater discharge controlled deposition of Cenomanian – Turonian black shales on the NW European epicontinental shelf (Wunstorf, northern Germany). Climate of the Past, 11(3): 495–508. https://doi.org/10.5194/cp-11-495-2015

van Waveren, I.M., van Konijnenburg–van Cittert, J.H.A., van der Burgh, J. & Dilcher, D.L. 2002. Macrofloral remains from the Lower Cretaceous of the Leiva region (Colombia). Scripta Geologica, 123: 1–39.

Vašíček, Z. & Hoedemaeker, P.J. 2003. A new *Karsteniceras* from the Barremian (Lower Cretaceous) of Colombia. Scripta Geologica, 125: 141–143.

Wahl, W.R. 2009. Taphonomy of a nose dive: Bone and tooth displacement and mineral accretion in an ichthyosaur skull. Paludicola, 7(3): 107–116.

Wallace, B.P., Sotherland, P.R., Tomillo, P.S., Bouchard, S.S., Reina, R.D., Spotila, J.R. & Paladino, F.V. 2006. Egg components, egg size, and hatchling size in leatherback turtles. Comparative Biochemistry and Physiology Part A: Molecular & Integrative Physiology, 145(4): 524–532. https://doi.org/10.1016/j.cbpa.2006.08.040

Weissert, H. 1981. The environment of deposition of black shales in the Early Cretaceous: An ongoing controversy. In: Warme, J.E., Douglas, R.G. & Winterer, E.L. (editors), The deep sea drilling project: A decade of progress. Society of Economic Paleontologists and Mineralogists SEPM, Special Publication 32, p. 547–560. https://doi.org/10.2110/pec.81.32.0547

Welles, S.P. 1943. Elasmosaurid plesiosaurs with description of new material from California and Colorado. Memoirs of the University of California, Berkeley, 13(3): 125–254.

Welles, S.P. 1962. A new species of elasmosaur from the Aptian of Colombia and a review of the Cretaceous plesiosaurs. University of California Publications in Geological Sciences, 44(1): 1–96.

Wightman, W.G. 1992. Reworked benthic foraminifers from Site 802, East Mariana Basin, western equatorial Pacific. In: Larson, R.L., Lancelot, Y., Fisher, A., Abrams, L., Behl, R., Busch, W.H., Cameron, G., Castillo, P.R., Covington, J.M., Dürr, G., Erba, E., Floyd, P.A., France–Lanord, C., Hauser, E.H., Karl, S.M., Karpoff, A.M., Matsuoka, A., Molinie, A., Ogg, J.G., Salimullah, A.R.M., Steiner, M., Wallick, B.P. & Wightman, W. (editors), Proceedings of the Ocean Drilling Program, Scientific Results 129, p. 229–245. College Station, USA.

Wignall, P.B. 1989. Sedimentary dynamics of the Kimmeridge Clay: Tempests and earthquakes. Journal of the Geological Society, 146(2): 273–284. https://doi.org/10.1144/gsjgs.146.2.0273

Wignall, P.B. 1991a. Model for transgressive black shales? Geology, 19(2): 167–170. https://doi.org/10.1130/0091-7613(1991)019<0167:MFTBS>2.3.CO;2

Wignall, P.B. 1991b. Dysaerobic trace fossils and ichnofabrics in the Upper Jurassic Kimmeridge Clay of southern England. PALAIOS, 6(3): 264–270. https://doi.org/10.2307/3514906

Wignall, P.B. & Myers, K.J. 1988. Interpreting benthic oxygen levels in mudrocks: A new approach. Geology, 16(5): 452–455. https://doi.org/10.1130/0091-7613(1988)016<0452:IBOLIM>2.3.CO;2

Willis, K.J. & McElwain, J.C. 2002. The evolution of plants. Oxford University Press, 378 p. Oxford.

Winkler, J.D. & Sánchez–Villagra, M.R. 2006. A nesting site and egg morphology of a Miocene turtle from Urumaco, Venezuela: Evidence of marine adaptations in Pelomedusoides. Palaeontology, 49(3): 641–646. https://doi.org/10.1111/j.1475-4983.2006.00557.x

Witkowska, M. 2012. Palaeoenvironmental significance of iron carbonate concretions from the Bathonian (Middle Jurassic) ore–bearing clays at Gnaszyn, Kraków–Silesia homocline, Poland. Acta Geologica Polonica, 62(3): 307–324.

Würtz, M. & Repetto, N. 1998. Whales & dolphins: A guide to the biology and behaviour of cetaceans. Swan Hill Press, 167 p. Shrewsbury, UK.

Zammit, M. 2012. Cretaceous ichthyosaurs: Dwindling diversity, or the empire strikes back? Geosciences, 2(2): 11–24. https://doi.org/10.3390/geosciences2020011

Zhang, X., Chen, K., Hu, D. & Sha, J. 2016. Mid–Cretaceous carbon cycle perturbations and oceanic anoxic events recorded in southern Tibet. Scientific Reports, 6(39643): 1–6. https://doi.org/10.1038/srep39643

Ziegler, A.M., Eshel, G., McAllister–Rees, P., Rothfus, T., Rowley, D. & Sunderlin, D. 2003. Tracing the tropics across land and sea: Permian to present. Lethaia, 36(3): 227–254. https://doi.org/10.1080/00241160310004657

Explanation of Acronyms, Abbreviations, and Symbols:

AA	Arcillolitas Abigarradas
AcNH	Arcillolitas con Nódulos Huecos
CIP	Centro de Investigaciones Paleontológicas km 4, vía Santa Sofía, Villa de Leiva, Boyacá, Colombia
ECC	Eastern Cordillera of Colombia
JAVCM	Junta de Acción Comunal, vereda Monquirá (now MJACM)
LFN	Leslie Francis NOÈ
LNI	Lutitas Negras Inferiores
MG–P	Marcela GÓMEZ–PÉREZ
MJACM	Museo El Fósil, vereda Monquirá, Boyacá, Colombia
OAEs	Oceanic anoxic events
SGC	Servicio Geológico Colombiano Dirección de Geociencias Básicas Museo Geológico José Royo y Gómez Diagonal 53 n.° 34–53, Bogotá D. C., Colombia
TOC	Total organic carbon
UCMP	University of California Museum of Palaeontology 1101 Valley Life Sciences Building, Berkeley California 94720, USA
UN	Universidad Nacional de Colombia Departamento de Geociencias Carrera 45 n.° 26–85, Bogotá D. C., Colombia

Authors' Biographical Notes

Leslie F. NOÈ is a vertebrate palaeontologist, stratigrapher, and historian of science, with special interests in the palaeobiology and evolution of the Sauropterygia. Leslie undertook his undergraduate studies in the School of Environmental and Applied Sciences at the University of Derby, UK, and graduated with honours with a Combined Subjects (Biology, Geology, and Physical Geography) degree. Leslie subsequently undertook doctoral studies, at the University of Derby, under the supervision of Dr. Don SMITH, Dr. Arthur CRUICKSHANK (Leicester Museums), and Dr. Derek WALTON, and wrote his PhD thesis on the cranial osteology of the Callovian (Middle Jurassic) Oxford Clay Formation pliosaurian genera *Liopleurodon*, *Simolestes,* and *Pachycostasaurus*. Leslie gained a wide range of experience during seven years in the Sedgwick Museum, University of Cambridge, UK, as well as undertaking undergraduate and postgraduate supervision, and undergraduate teaching in both the Department of Earth Sciences and the Department of Zoology. A curatorship at Thinktank, the Birmingham Science Museum, UK, followed, together with an honorary position at the University of Birmingham. Leslie returned to Cambridge as curator of the globally important Harland Collection of rocks, fossils, and minerals, before moving to Colombia, where he is currently Associate Professor in the Departamento de Geociencias, Universidad de los Andes in Bogotá. As the first geologist in the newly formed Geociencias Department, Leslie has written numerous undergraduate courses, and continues to publish on Mesozoic marine reptiles, with special reference to Colombian Cretaceous faunas.

Marcela GÓMEZ–PÉREZ is a vertebrate palaeontologist and sedimentary geologist with special interests in pliosauromorph marine reptiles, museology, and geological outreach. Marcela undertook her undergraduate studies in the Departamento de Geociencias of the Universidad Nacional de Colombia, Bogotá, where she graduated with honours. Marcela then received the Joven Investigador Colciencias and worked for the Departamento de Geología of the Universidad EAFIT, Medellín, implementing the Alkenone protocol for surface seawater temperatures during the Holocene. Marcela worked on a voluntary basis at the Sedgwick Museum of Earth Sciences in Cambridge, where her enthusiasm for museology started. She joined the Department of Earth Sciences, University of Cambridge, UK, for her doctoral studies under the supervision of Dr. David NORMAN with a prestigious Gates Cambridge Scholarship and a UK government Overseas Research Fellowship, at Newnham College. Following completion of her PhD studies, Marcela worked as a sedimentologist for CASP in Cambridge, before returning to Colombia to work on fine–grained sediment geochemistry for oil prospection. Marcela undertook post–doctoral research work, focusing on Colombian plesiosaur faunas, and teaching, in the Departamento de Geociencias, Universidad de los Andes. Currently Marcela is the Director the Museo Geológico José Royo y Gómez of the Servicio Geológico Colombiano in Bogotá, contributing to the development of vertebrate palaeontology and professionalizing all aspects of the museum.

Volume 2

Chapter 14

https://doi.org/10.32685/pub.esp.36.2019.14
Published online 6 December 2019

Two Cretaceous Subduction Events in the Central Cordillera: Insights from the High P–Low T Metamorphism

Camilo BUSTAMANTE[1]* and Andres BUSTAMANTE[2]

1 cbustam3@eafit.edu.co
Universidad EAFIT
Carrera 49 n.° 7 sur–50
Medellín, Colombia

2 andresbl@aim.com
Universidade Federal de Pernambuco
Departamento de Geologia
Recife, PE, Avenida da Arquitetura s/n, CEP 50740–550
Recife–PE, Brasil

* Corresponding author

Abstract The scarcity of high–pressure metamorphic rocks at the Earth's surface due to the specific conditions required for their formation and preservation makes it difficult to access the information about subduction zones that they can provide. The northern Andes are characterized by several occurrences of blueschists and, in minor proportions, eclogites, whose origins are yet to be unraveled. The metamorphic rocks found herein include the Pijao amphibolitized eclogites, Barragán blueschists and associated garnet–amphibolites, and Jambaló blueschists found in Colombia as well as the Raspas Metamorphic Complex in Ecuador. All these rocks have been correlated into a single Early Cretaceous high–pressure metamorphic belt based on regional geochemistry and geochronological data. A compilation of the most recent whole–rock geochemistry and Ar–Ar and Lu–Hf ages from the three high–pressure sequences in Colombia indicates that at least two different subduction events have been recorded in the Central Cordillera of Colombia. The first event, involving subduction and collision, occurred at ca. 130–120 Ma and is represented by the Pijao, Barragán, and Raspas high–pressure rocks, which have N–MORB–like protoliths and are contemporaneous with the end of the arc–related magmatism of the northern Andes, related to an oblique convergence between the Farallón Plate and the continental margin of South America. The second event of subduction is represented only by the Jambaló blueschists at ca. 70–60 Ma, whose protolith is akin to basalt formed in a plume–influenced intra–oceanic arc that was accreted to the continental margin. No reliable correlation is possible for these rocks as yet.

Keywords: *blueschist, eclogite, northern Andes, high–pressure metamorphism.*

Resumen Las rocas metamórficas de alta presión son escasas en la superficie de la Tierra debido a sus condiciones especiales de formación y conservación. Esta escasez dificulta el acceso a la información que este tipo de rocas puede proporcionar sobre las zonas de subducción. Los Andes del norte se caracterizan por varias ocurrencias de esquistos azules y, en menor proporción, eclogitas cuyo origen aún no es claro. Entre estas ocurrencias se incluyen las eclogitas anfibolitizadas de Pijao, los esquistos azules y anfibolitas granatíferas asociadas de Barragán, y los esquistos azules de Jambaló en Colombia, así como el Complejo Metamórfico Raspas en Ecuador. Todas se han correlacionado como un único cinturón metamórfico de alta presión del Cretácico Temprano sobre la base de datos regionales de geoquímica y geocronología. Una recopilación de los datos más recientes de geoquímica en roca total y las edades Ar–Ar y Lu–Hf de

Citation: Bustamante, C. & Bustamante, A. 2019. Two Cretaceous subduction events in the Central Cordillera: Insights from the high P–low T metamorphism. In: Gómez, J. & Pinilla–Pachon, A.O. (editors), The Geology of Colombia, Volume 2 Mesozoic. Servicio Geológico Colombiano, Publicaciones Geológicas Especiales 36, p. 485–498. Bogotá. https://doi.org/10.32685/pub.esp.36.2019.14

las tres manifestaciones de alta presión en Colombia registra al menos dos eventos de subducción diferentes en la cordillera Central de Colombia. El primer evento de subducción y colisión ocurrió a ca. 130–120 Ma y está representado por las rocas de alta presión de Pijao, Barragán y Raspas, las cuales tienen protolitos tipo N–MORB y son contemporáneas con el final del magmatismo de arco de los Andes del norte, relacionado con una convergencia oblicua entre la Placa de Farallón y el margen continental de Suramérica. El segundo evento de subducción solo está representado por los esquistos azules de Jambaló con edades de ca. 70–60 Ma, cuyo protolito es afín a basaltos formados en un arco intraoceánico con influencia de una pluma mantélica y acrecionados a la margen continental. Hasta ahora no existe una correlación confiable entre estas rocas y otras similares.

Palabras clave: *esquisto azul, eclogita, Andes del norte, metamorfismo de alta presión.*

1. Introduction

Blueschists and eclogites represent some of the main lithological vestiges from which we can understand convergent margin processes since they are unequivocal evidence for paleo–subduction zones and collision between lithospheric plates (e.g., Ernst, 1988; Maruyama et al., 1996). Unfortunately, these rocks are rarely exposed at the Earth's surface owing to the difficulties involved in their exhumation and preservation, which are attributed to their high density and low buoyancy when compared with lower crustal materials (Agard et al., 2009).

The Mesozoic to Cenozoic orogenesis in the northern Andes including Ecuador and Colombia is characterized by a series of collisions of island arcs and oceanic plateau with the South American continental margin, accompanied by the formation of several subduction zones and the thrusting of oceanic crustal fragments, both on the continental margin and in the intra–oceanic domains (e.g., Cardona et al., 2012; Ramos, 2009; Restrepo & Toussaint, 1988; Spikings et al., 2015). These processes have resulted in the formation of ophiolitic complexes along with low–, medium, and high–pressure metamorphic rocks via the amalgamation of tectonostratigraphic terranes (Kerr et al., 1997; Pindell & Kennan, 2009; Ramos, 2009). Blueschist and eclogite defining suture zones have been identified in the Cordillera Real of Ecuador (Raspas Metamorphic Complex sensu Feininger, 1980) and in the Central Cordillera of Colombia (Figure 1; Arquía Complex sensu Maya & González, 1995).

The Arquía Complex is located in the Central Cordillera of Colombia, where high–pressure metamorphic rocks crop out in the Pijao, Barragán, and Jambaló areas (Figures 2, 3, 4 respectively; Bustamante et al., 2011, 2012; Feininger, 1982; Núñez & Murillo, 1978; Orrego et al., 1980a). The Jambaló rocks are limited in their distribution to the east by the Cajamarca Complex, comprising Jurassic metapelitic and amphibolic schists (Blanco–Quintero et al., 2014; Bustamante et al., 2017a), and to the west by Lower Cretaceous volcanic rocks of the Quebradagrande Complex (Figure 5; Botero, 1963; Kerr et al., 1997; Maya & González, 1995). The Pijao and Barragán rocks are within the Arquía Complex (Figure 5).

The tectonic significance of the abovementioned rocks is still under debate as relatively few geological data from selected occurrences have been used in existing interpretations. These rocks have been interpreted as being related to subduction events (Aspden & McCourt, 1986; Aspden et al., 1995; Bourgois et al., 1987) and exhumed during the Early Cretaceous, according to cooling ages varying between 132 and 110 Ma (Aspden & McCourt, 1986; Feininger, 1982). Furthermore, rocks from the Raspas Metamorphic Complex (Ecuador) and those in the Central Cordillera (Colombia) have been correlated due to their similar tectonic positions and regional geochemical data and thereby assigned Early Cretaceous metamorphic ages (Spikings et al., 2015; Villagómez & Spikings, 2013; Villagómez et al., 2011). Other studies (Bustamante et al., 2011, 2012) have suggested that blueschists from the Jambaló area have a volcanic arc protolith and a Late Cretaceous to Paleogene age of metamorphism.

Although high–pressure rocks of the Central Cordillera have long been recognized, no tectonic model combining their occurrences has been developed as yet. This study, therefore, aims to give an updated review of the high–pressure metamorphic rocks of Colombia, describing their distributions, ages of metamorphism, and differences in protoliths. We challenge current models that consider a single Lower Cretaceous high–pressure metamorphic belt in Colombia and Ecuador with an exclusively N–MORB protolith (García–Ramírez et al., 2017; Spikings et al., 2015; Villagómez & Spikings, 2013). Pressure and temperature constraints, together with metamorphic ages and whole–rock geochemistry, suggest that Barragán and Pijao eclogites have N–MORB protoliths with Early Cretaceous metamorphic ages (Bustamante et al., 2012; García–Ramírez et al., 2017), whereas the Jambaló area records Late Cretaceous metamorphism with a volcanic arc–like protolith (Bustamante, 2008). Thus, we propose a tectonic model for the Cretaceous to Paleogene evolution of the western margin of the northern Andes, with special emphasis in the high–pressure metamorphic record.

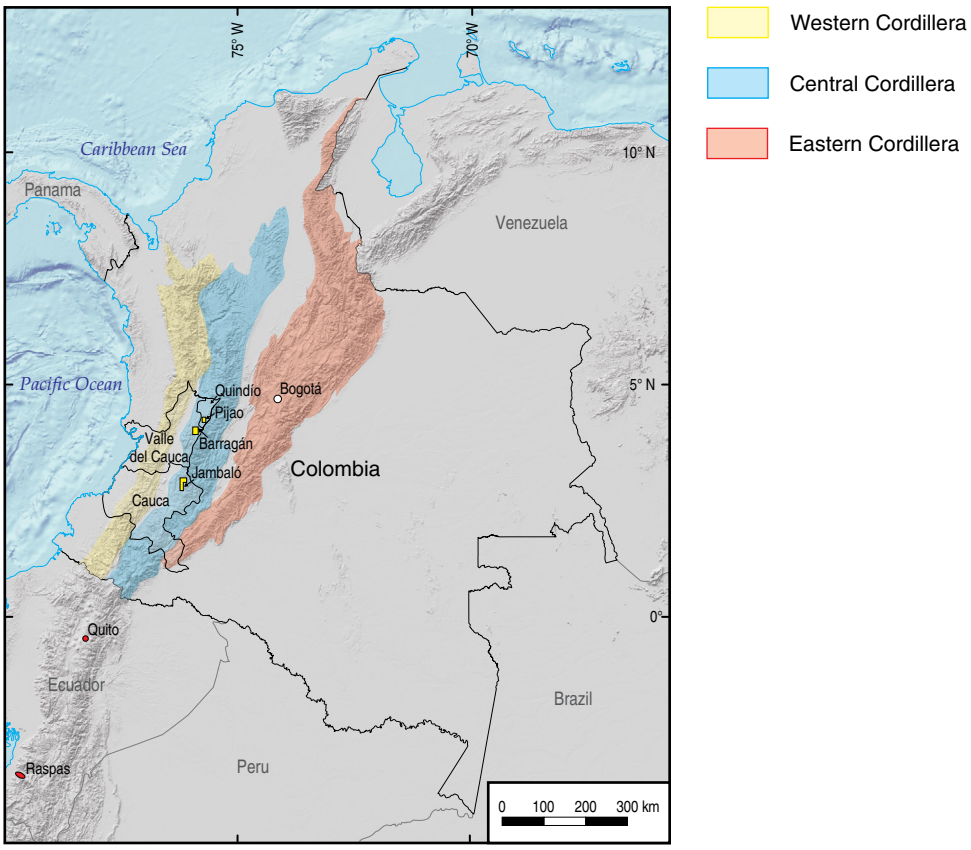

Figure 1. Map of Colombia showing the distribution of high–pressure rocks along the Central Cordillera. The Raspas Metamorphic Complex (Ecuador) is also shown as a reference.

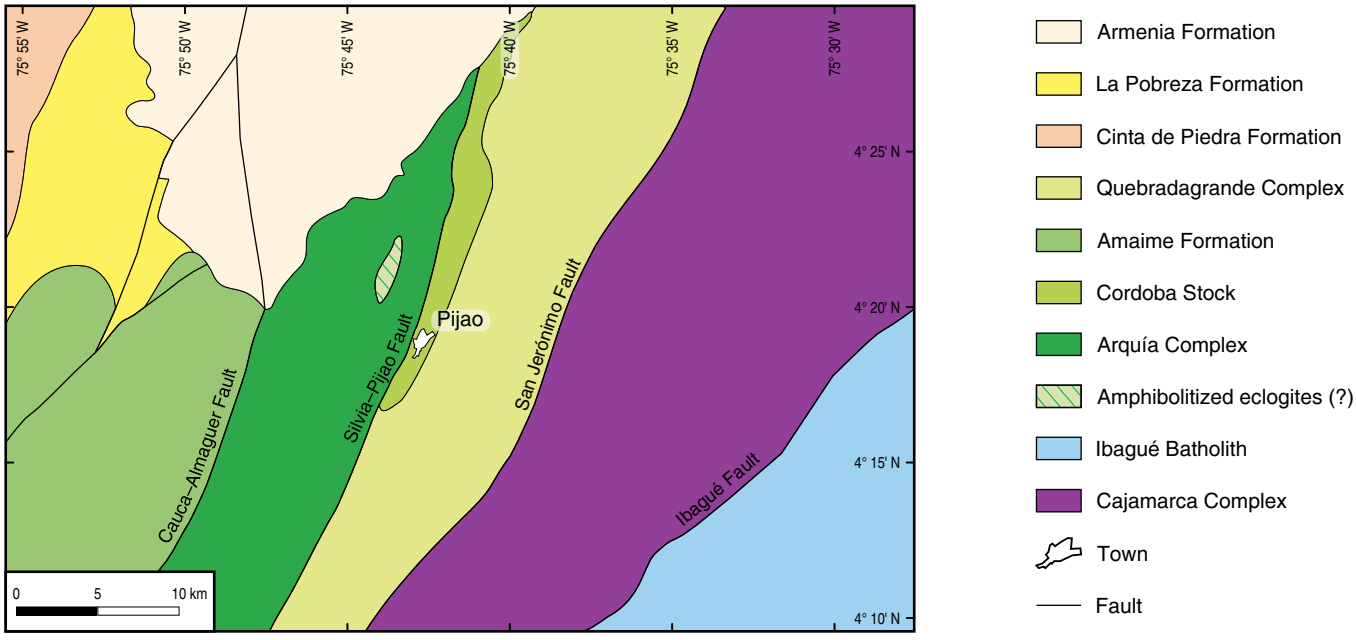

Figure 2. Simplified geological map of the Pijao area (Alcárcel & Gómez 2019).

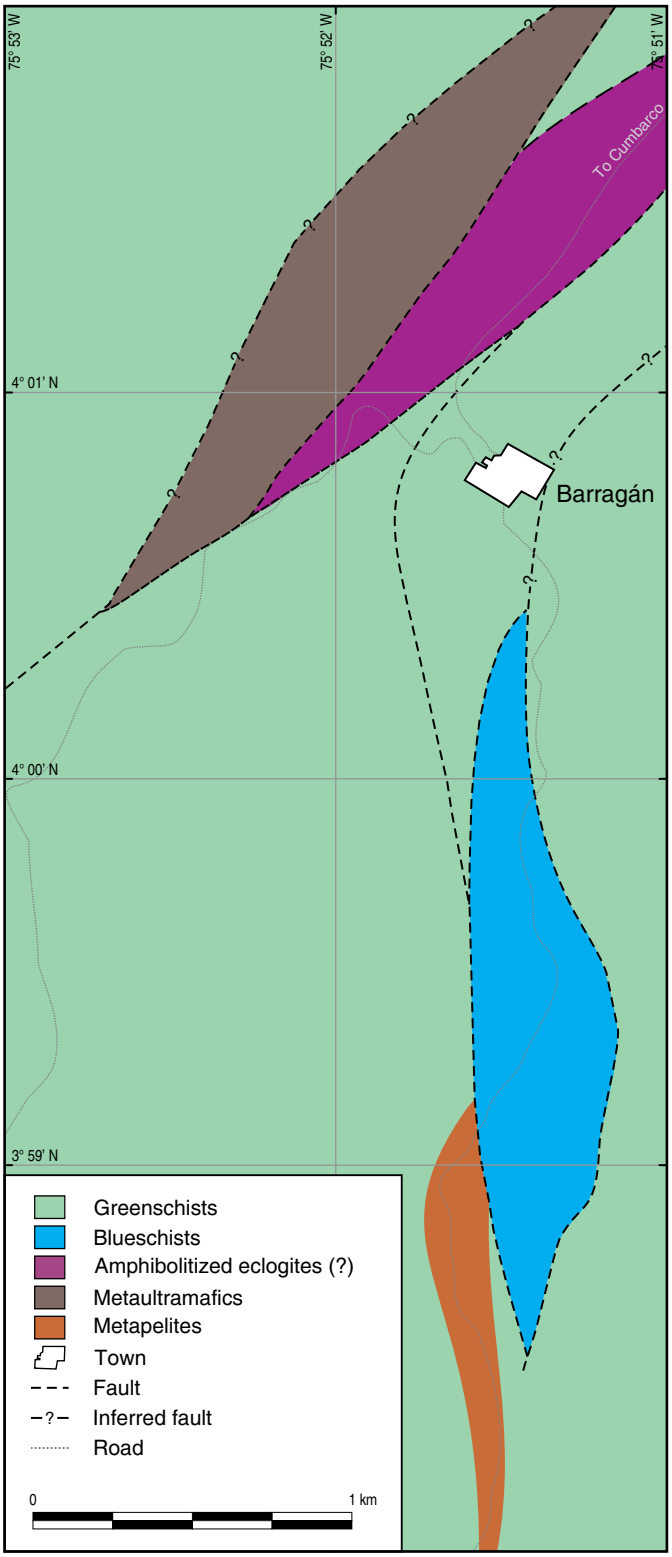

Figure 3. Simplified geological map of the Barragán area.

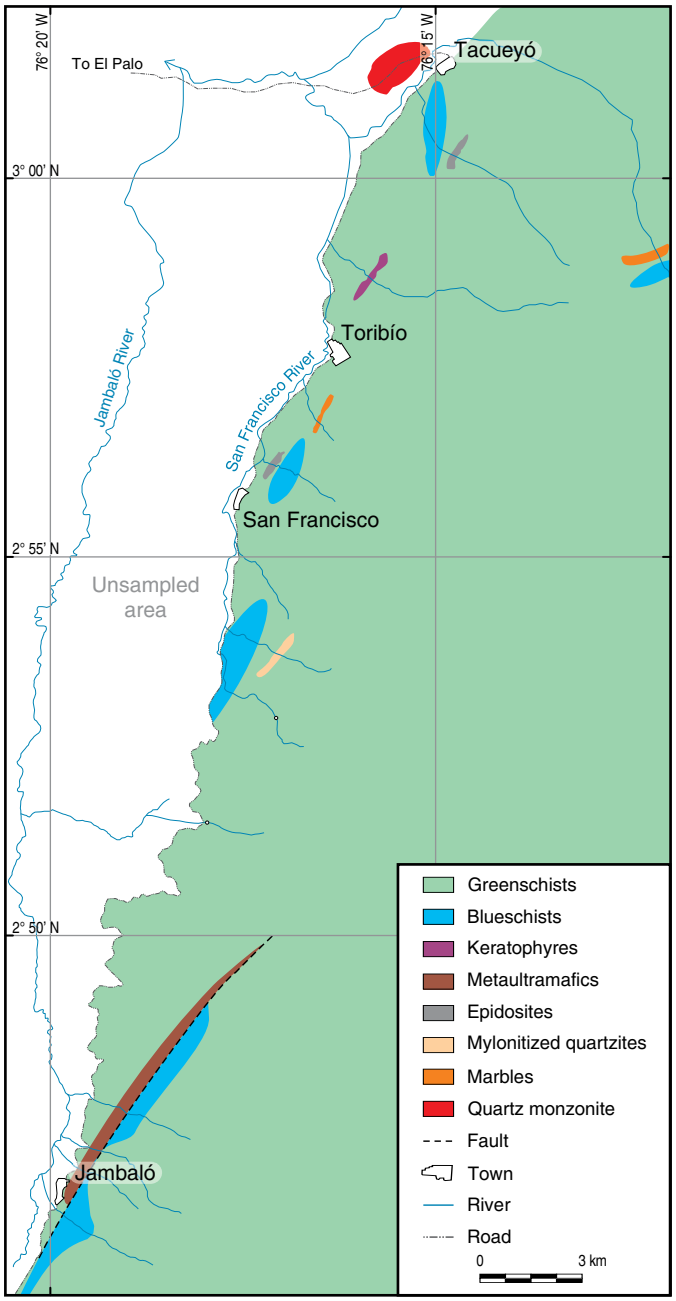

Figure 4. Simplified geological map of the Jambaló area.

2. Materials and Methods

Whole–rock geochemistry and geochronology have been previously published and peer reviewed: Details of the sampling and methodologies are provided in Bustamante (2008) for the Barragán and Jambaló blueschists, and in García–Ramírez et al. (2017) for the Pijao eclogites. Table 1 compiles the mineralogy, geochemistry, and ages of northern Andes high–pressure rocks available up to the present study. Table 2 compiles whole–rock geochemical data reported from Barragán blueschists (Bustamante et al., 2012), Pijao eclogites (García–Ramírez et al., 2017), and Jambaló blueschists (Bustamante, 2008).

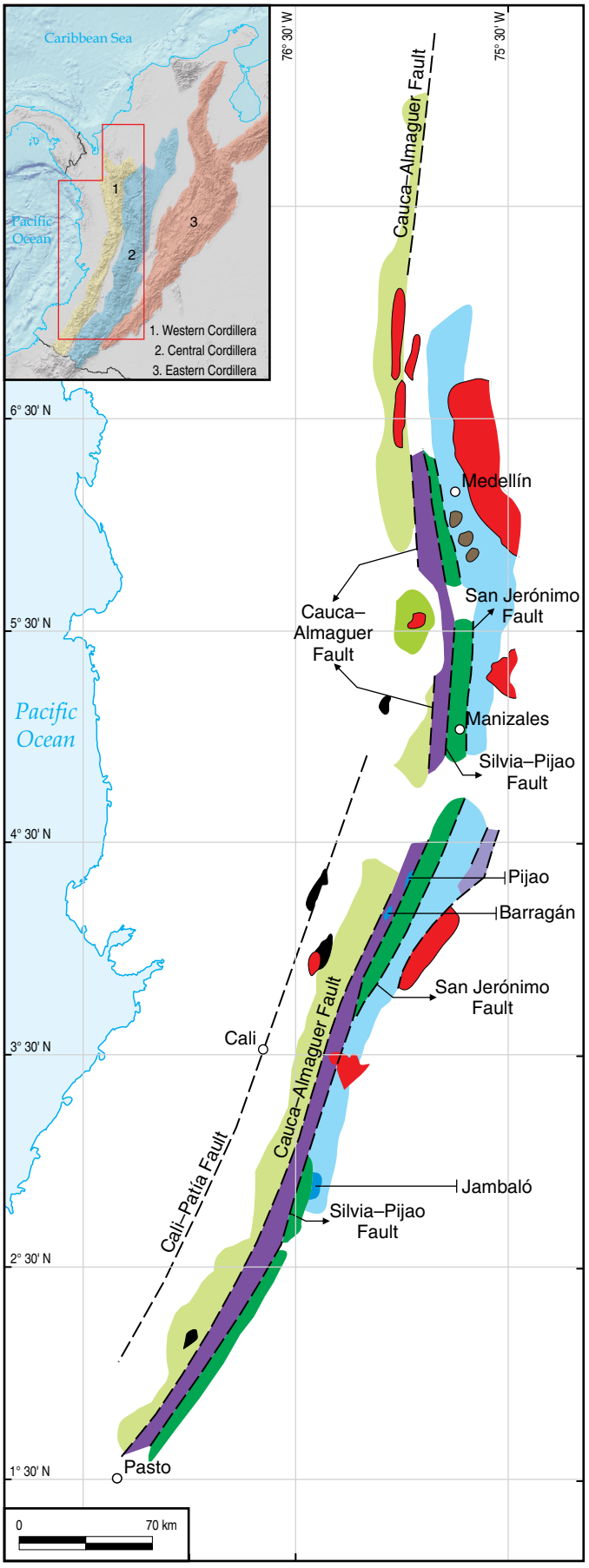

Miocene volcanic rocks
Mesozoic oceanic–related rocks
Mesozoic igneous rocks
High–pressure metamorphic rocks (Cretaceous – Paleogene)
Ultramafic rocks (Cretaceous?)
Quebradagrande Complex (Cretaceous)
Arquía Complex (Paleozoic – Cenozoic)
Cajamarca Complex (Paleozoic – Mesozoic)
Paleozoic – Triassic gneisses
Proterozoic high–grade metamorphic rocks

Figure 5. Geological map of the occurrences of high–pressure rocks in the Central Cordillera and their tectonic position related to the Quebradagrande and Cajamarca Complexes (Maya & González, 1995).

3. Results

Herein, we briefly summarize present knowledge of the high–pressure metamorphic rocks from the Central Cordillera and provide the current geochronological data along with the whole–rock geochemistry that has been used to define the protolith.

3.1. Pijao Eclogites

García–Ramírez et al. (2017) and Avellaneda et al. (2017) reported eclogites south of the Pijao region (Figures 2, 5) and described meter–scale lenses of eclogites, amphibolitized eclogites, and garnet–bearing amphibolites enveloped by chlorite–actinolite schists in faulted contact with amphibolites.

The geochemistry reported by García–Ramírez et al. (2017) indicates a basaltic protolith for the Pijao eclogites (Figure 6), similar to that of the Barragán blueschist and amphibolite–facies rocks. Chondrite–normalized rare earth elements (REE) define a flat pattern (Figure 7a), further supporting this finding. A subtle Nb anomaly is seen in the trace element variation plots normalized to N–MORB (Figure 8a; Table 1; Sun & McDonough, 1989).

A garnet–derived $^{176}Lu/^{177}Hf$ isochron age of 128.7 ± 3.5 Ma (MSWD = 4.0) has been reported for Pijao eclogite samples (Table 1; García–Ramírez et al., 2017). García–Ramírez et al. (2017) interpreted this age as that at which the Pijao rocks reached eclogite facies, which is related to a slab roll–back process characterizing the western margin of the northern Andes since the Jurassic (Spikings et al., 2015). García–Ramírez et al. (2017) also suggested that along with the Pijao eclogites, the entire Arquía Complex (Maya &

Table 1. Mineralogy, geochemical constraints, and ages of the high–pressure rocks of northern Andes, including the Raspas Metamorphic Complex (Ecuador).

Region	Pijao[1]	Barragán[2]		Jambaló[3]	Raspas[4, 5]	
Rock Type	Ecl (?) and Amp–ecl	BS	Amp–ecl (?)	BS	Ecl	BS
Mineralogy	Hbl, Pl*, Phg, Qtz, Ep, Czo, Zo, Ttn, Rt, Grt, Omp	Gln, Lws, Ilm, Pg, Phg, Ep, Czo, Chl, Pl*, Carb, Ttn, Pmp, Py	Hbl, Pl*, Phg, Qtz, Ep, Czo, Zo, Ttn, Rt, Scp	Gln, Brs, Act, Pg, Ep, Czo, Chl, Pl*, Carb, Ttn, Rt, Zrn, Ap, Grt, Ilm, Py	Omp, Grt, Brs, Qtz, Zo, Rt, Ap, Ilm	Gln, Phg, Pg, Qtz, Carb, Ttn, Rt, Grt, Ap, Pl*, Ilm
Geochemistry	MORB[1]	MORB[2]		MORB + OIB	MORB + seamounts[6]	
Age	ca. 130 Ma[1, A]	ca. 120 Ma[2, B]		71–63Ma[3, C]	ca. 130 Ma[6, D]	

(Ecl) eclogite; (BS) blueschist; (Amp–ecl) amphibolitized eclogites; (MORB) Mid Ocean Ridge Basalt; (OIB) Ocean Island Basalts; (Act) actinolite; (Ap) apatite; (Brs) barroisite; (Carb) carbonate; (Chl) chlorite; (Czo) clinozoisite; (Ep) epidote; (Gln) glaucophane; (Grt) garnet; (Hbl) hornblende; (Ilm) ilmenite; (Lws) lawsonite; (Omp) omphacite; Opaque minerals; (Pg) paragonite; (Phg) phengite; (Pl) plagioclase* (An contents varying from 2 to 28); (Pmp) pumpellyite; (Py) pyrite; (Qtz) quartz; (Rt) rutile; (Scp) scapolite; (Ttn) titanite; (Zo) zoisite; (Zrn) zircon.

[1]García–Ramírez et al. (2017); [2]Bustamante et al. (2012); [3]Bustamante et al. (2011); [4]Aspden et al. (1995); [5]Bosch et al. (2002); [6]John et al. (2010).

[A] Whole rock from metabasites using Lu–Hf method. Age of metamorphism; [B]Muscovite and separates from graphite–chlorite–muscovite–quartz schist associated with the blueschist–facies rocks using $^{40}Ar/^{39}Ar$ method. Age of exhumation event; [C]Paragonite and phengite from a blueschist using $^{40}Ar/^{39}Ar$ method. Age of metamorphism; [D]Whole rocks and mineral separates from an eclogite using Lu–Hf method. Age of metamorphism.

González, 1995) has the same basaltic protolith and was subjected to the same slab roll–back process.

3.2. Barragán Blueschists

Discontinuous outcrops of blue–gray fine–grained epidote–glaucophane and chlorite–lawsonite schists occur in the Barragán region. These outcrops are associated with hornblende and chlorite schists and metapelites made up of muscovite, graphite, and quartz, together with serpentinized ultramafic rocks (Figures 3, 5). Possible amphibolitized eclogites mainly comprising hornblende and garnet have also been described in the area (González, 1997; McCourt & Feininger 1984).

Whole–rock geochemistry of the blueschist– and amphibolite–facies rocks (Bustamante et al., 2012) indicates a basaltic protolith (Figure 6). Chondrite–normalized REE patterns (Figure 7b) show a slight depletion in the lightest rare earth elements (LREE) and an almost flat pattern in the middle rare earth elements (MREE) and heavy rare earth elements (HREE). Within the trace element variation plots normalized to N–MORB (Figure 8b; Sun & McDonough, 1989), Nb and Th show negative anomalies.

Bustamante et al. (2012) reported ^{40}Ar–^{39}Ar ages using muscovite and separates from a graphite–chlorite–muscovite–quartz schist associated with the blueschist facies rocks, obtaining plateau ages of 119.4 ± 3.8 Ma, 120.1 ± 1.0 Ma, and 120.8 ± 0.3 Ma (Table 1); the error–weighted average of these three plateau ages is 120.7 ± 0.3 Ma (MSWD = 0.29).

Both the geochemistry and geochronology were interpreted by Bustamante et al. (2012) to indicate a basaltic protolith metamorphosed under high–pressure conditions at ca. 120 Ma, representing the exhumation event associated with the development of a mylonitic foliation.

3.3. Jambaló Blueschists

The Jambaló blueschists constitute a series of blueschist–facies lenses embedded in greenschist–facies rocks. These rocks are associated with impure marbles, serpentinized peridotites, and quartzites (Figures 4, 5).

Geochemical results suggest that the Jambaló blueschists have a slightly more differentiated protolith compared with the high–pressure rocks from Pijao and Barragán (Figure 6). Additionally, chondrite–normalized REE patterns of the blueschists show a slight enrichment of LREE (Figure 7c). Eu anomalies are slightly negative in these blueschists (Eu/Eu* from 0.7 to 1.2). Trace element variation plots normalized to N–MORB (Sun & McDonough, 1989) are characterized by negative Nb, Zr, Hf, Ti, and Ta anomalies (Figure 8c).

Orrego et al. (1980b) reported a minimum whole–rock (from sericite schist) K–Ar age for the metamorphism of 125 ± 15 Ma, and De Souza et al. (1984) obtained ages of 104 ± 14

Table 2. Whole–rock geochemistry from the Pijao eclogites[1], Barragán blueschists[2], and Jambaló blueschists[2].

Region	Pijao	Pijao	Pijao	Barragán	Barragán	Barragán	Barragán	Barragán	Barragán	Barragán	Barragán	Barragán	Barragán	Barragán	Jambaló	Jambaló	Jambaló	Jambaló	Jambaló	Jambaló	Jambaló	Jambaló
Rock type	Ecl (?)	Ecl (?)	Ecl (?)	Amp–Ecl	Amp–Ecl	Amp–Ecl	Amp–Ecl	Amp–Ecl	BS	BS	BS	BS	BS	BS	BS	BS	BS	BS	BS	BS	BS	BS
Sample	ARQ–214	ARQ–378	ARQ–379	187A	187AA	187BA	188A	189A	195BS	196BS	196ABS	196DBS	197ABS	199BS	121B	123A	124G	124J	125I	125K	125M	129A
SiO_2	49.3	47.2	49.0	47.7	50.8	50.0	51.3	49.4	50.0	48.4	48.4	49.1	49.2	48.3	51.7	50.4	56.9	52.0	53.3	53.1	56.3	51.4
Al_2O_3	13.5	15.2	14.1	15.1	14.3	15.0	13.4	14.7	14.5	14.5	15.4	13.9	16.3	14.4	15.6	17.8	15.6	18.1	17.2	19.8	17.8	14.4
Fe_2O_3	4.5	2.4	2.7	14.5	10.8	10.6	12.2	12.2	11.2	10.3	11.7	10.8	10.4	12.7	9.7	9.8	9.5	8.8	9.1	10.9	8.1	9.5
MnO	0.230	0.160	0.200	0.519	0.222	0.176	0.230	0.190	0.187	0.157	0.200	0.161	0.168	0.158	0.441	0.139	0.123	0.145	0.240	0.080	0.103	0.129
MgO	7.680	7.480	8.390	7.990	7.910	8.240	6.010	8.720	6.180	9.280	6.740	6.600	8.590	7.600	3.490	3.270	4.020	4.480	5.410	2.590	4.680	5.330
CaO	8.0	13.4	9.0	8.8	10.3	11.2	9.4	8.8	8.4	8.1	8.7	10.8	4.2	7.6	5.8	11.6	2.9	3.5	3.7	1.7	1.6	4.0
Na_2O	2.6	2.4	3.6	2.6	2.4	2.3	3.9	2.6	2.0	2.7	3.4	2.4	0.2	3.3	4.8	2.6	4.5	5.6	5.1	3.4	5.7	5.2
K_2O	0.1	0.2	0.1	0.2	0.1	0.1	0.1	0.2	<0.01	0.6	0.1	0.5	0.0	0.1	0.3	0.4	0.8	0.7	0.5	2.9	0.7	0.2
TiO_2	2.390	1.230	1.860	1.300	1.230	1.270	2.040	1.370	1.980	1.400	1.730	1.480	1.240	1.920	1.430	1.460	1.710	1.480	1.530	2.080	1.170	1.840
P_2O_5	0.210	0.100	0.160	0.100	0.080	0.120	0.220	0.100	0.200	0.140	0.130	0.200	0.090	0.190	0.290	0.410	0.290	0.230	0.210	0.150	0.130	0.230
LOI	0.70	3.10	0.50	1.40	2.08	1.23	1.15	2.05	5.21	4.52	3.45	3.27	8.48	3.87	6.60	2.58	3.80	4.18	3.50	3.20	3.74	7.84
Total	99.8	99.9	99.9	100.1	100.2	100.3	100.0	100.3	99.9	100.1	99.8	99.3	98.9	100.1	100.1	100.4	100.2	99.2	99.7	99.8	100.0	100.0
Sc	41	39	44	44	43	45	42	44	46	43	47	42	35	42	29	20	27	25	30	31	28	37
V	428	263	377	285	275	305	395	331	418	315	386	334	290	380	214	184	238	185	252	170	194	278
Co	51.8	45.1	47.6	72	61	40	53	41	51	45	51	51	48	52	33	36	32	51	34.4	39.5	34	35
Ni	19.3	54	17	90	80	70	60	80	80	80	90	80	120	120	30	70	–	30	59.7	3.5	30	30
Cu	33.2	104.8	33.1	30	20	30	30	80	60	50	50	110	<10	70	–	50	–	–	3.3	1.1	50	30
Zn	24	16	17	110	80	90	140	130	150	100	130	110	130	140	70	80	130	130	125	41	110	130
Ga	18.1	14.3	18.5	14	16	18	18	19	21	17	21	18	18	19	17	25	20	22	18	24.7	19	20
Rb	0.8	2.8	0.3	4	2	4	<1	3	<1	11	3	12	<1	7	5	6	20	16	11.1	91.1	14	3
Sr	104.4	182.3	109.7	37	113	152	113	120	9	73	142	201	73	91	166	574	68	80	113.2	69.5	83	163
Y	49.3	27	41.2	37.5	29.2	30.3	48.8	33.2	51	30.9	41.9	38.3	21.9	40.8	33	23.5	35.8	48.6	39.7	32.7	23.8	38.4
Zr	164.2	82.4	117.4	59	62	69	134	68	123	80	107	88	53	120	126	224	186	264	139	230.2	147	175
Nb	3.0	2.5	1.8	2.0	1.1	1.0	2.5	0.9	4.2	3.4	4.1	3.6	2.2	5.0	5.3	15.4	7.2	9.5	6.2	9.1	4.9	7.7
Cs	0.9	0.3	<0.1	0.2	<0.1	0.1	<0.1	0.2	<0.1	0.8	0.2	0.7	<0.1	0.4	1.2	0.3	0.4	0.4	0.5	1.2	0.5	0.3
Ba	22	11	20	78	374	323	17	38	38	73	49	383	18	110	66	71	119	108	222	259	191	25
La	5.5	3.6	3.8	3.4	2.2	2.5	5.0	2.0	5.9	4.5	7.3	6.0	2.8	6.5	10.4	22.3	15.6	14.8	11.5	17.4	12.4	9.2
Ce	16.30	10.40	12.80	7.28	6.45	6.81	16.00	7.13	15.60	12.10	17.10	13.00	8.69	17.30	25.90	46.60	35.40	40.40	24.20	36.60	28.10	24.00
Pr	2.82	1.64	2.18	1.59	1.26	1.35	2.63	1.35	2.69	1.88	2.86	2.29	1.42	2.72	3.62	5.86	4.71	5.65	3.81	4.52	3.36	3.38
Nd	15.5	8.5	11.5	8.8	7.5	8.1	14.4	8.0	14.6	9.9	14.5	11.7	8.1	14.4	17.5	24.4	20.4	24.3	17.8	19.8	14.2	16.2
Sm	5.21	2.74	4.24	2.95	2.70	2.79	4.87	2.93	4.81	3.13	4.46	3.69	2.82	4.62	4.59	5.31	5.02	6.04	4.52	4.42	3.51	4.74
Eu	1.90	1.07	4.24	1.08	1.12	1.14	1.81	1.27	1.85	1.27	1.76	1.49	1.10	1.77	1.83	1.98	1.70	1.95	1.53	1.07	1.18	1.58
Gd	7.20	4.02	5.69	3.95	3.79	3.86	6.52	4.15	6.33	4.04	5.85	5.07	3.45	5.80	5.27	5.17	5.45	6.76	5.61	4.88	3.81	5.32
Tb	1.310	0.690	1.050	0.830	0.760	0.790	1.300	0.890	1.250	0.800	1.140	0.990	0.630	1.140	0.940	0.840	0.990	1.270	1.020	0.910	0.710	1.020
Dy	8.88	4.34	6.95	5.91	5.10	5.24	8.51	5.84	8.17	5.23	7.39	6.42	3.90	7.35	5.92	4.74	6.23	8.01	6.19	5.48	4.55	6.74
Ho	1.870	0.910	1.520	1.270	1.060	1.070	1.750	1.150	1.640	1.050	1.450	1.290	0.780	1.470	1.180	0.860	1.280	1.630	1.310	1.160	0.890	1.400

Cretaceous

Table 2. Whole–rock geochemistry from the Pijao eclogites[1], Barragán blueschists[2], and Jambaló blueschists[2] *(continued)*.

Region	Pijao	Pijao	Barragán	Barragán	Barragán	Barragán	Barragán	Barragán	Barragán	Barragán	Barragán	Jambaló	Jambaló	Jambaló	Jambaló	Jambaló	Jambaló	Jambaló
Rock type	Ecl (?)	Ecl (?)	Amp–Ecl	Amp–Ecl	Amp–Ecl	Amp–Ecl	BS	BS	BS	BS	BS	BS	BS	BS	BS	BS	BS	BS
Sample	ARQ–214	ARQ–378	ARQ–379	187A	187AA	187BA	188A	189A	195BS	196BS	196ABS	196DBS	197ABS	199BS	121B	123A	124G	124J	125I	125K	125M	129A
Er	5.38	2.80	4.47	4.06	3.17	3.24	5.19	3.44	4.87	3.12	4.26	3.86	2.30	4.34	3.51	2.35	3.74	4.88	3.96	3.58	2.66	4.16
Tm	0.850	0.410	0.680	0.635	0.482	0.495	0.787	0.514	0.730	0.463	0.639	0.589	0.342	0.652	0.532	0.327	0.542	0.721	0.550	0.550	0.396	0.631
Yb	5.62	2.75	4.87	4.14	3.10	3.21	5.02	3.27	4.69	2.92	4.06	3.73	2.26	4.13	3.45	2.03	3.48	4.53	3.33	3.52	2.55	4.14
Lu	0.790	0.400	0.680	0.656	0.464	0.509	0.766	0.512	0.700	0.457	0.609	0.566	0.353	0.624	0.516	0.290	0.550	0.683	0.520	0.570	0.377	0.635
Hf	4.60	<0.01	3.50	2.10	1.90	1.90	3.90	2.20	3.60	2.40	3.00	2.50	2.00	3.40	3.30	4.90	4.50	6.40	3.90	6.60	3.70	4.30
Ta	0.300	0.100	<0.1	1.460	0.860	0.040	0.670	0.030	0.520	0.440	0.550	0.760	0.400	0.680	1.120	2.210	1.460	1.390	0.600	1.200	1.010	1.290
W	<0.1	<0.1	<0.1	208	230	3	137	2	94	66	90	163	93	97	258	333	322	230	107	220	171	107
Th	<0.2	<0.2	<0.2	0.11	0.06	0.06	0.19	0.06	0.29	0.23	0.28	0.24	0.20	0.37	1.00	1.48	3.64	3.74	1.70	5.10	3.09	1.20
U	<0.1	<0.1	<0.1	0.05	0.04	0.04	0.09	0.05	0.25	0.14	0.70	0.29	1.83	0.24	0.39	0.34	0.93	1.38	0.60	1.10	0.75	0.52

[1] García–Ramírez et al. (2017)

[2] Bustamante (2008)

Ma and 217 ± 10 Ma using the same method in glaucophane. The K–Ar method has several limitations concerning the dating of metamorphic rocks since argon losses or excesses cannot be determined and the thermal history of minerals (i.e., white micas) cannot be discriminated (Clauer & Chaudhuri, 1999; Dallmeyer & Takasu, 1992). In addition, the use of glaucophane K–Ar geochronology may be unreliable since potassium contents could be attributed to very fine inclusions of K–bearing minerals (i.e., K–micas and barroisite). Recently, Bustamante et al. (2011) reported Ar–Ar ages in white micas from six samples of blueschist–facies rocks. The age range obtained was very different ca. 70 to 60 Ma (Table 1) and was interpreted as the record of the mylonitic event responsible for the exhumation of the blueschist–facies rocks.

Although high–pressure metamorphic rocks are presented as independent bodies, the available geochemistry data of the possibly amphibolitized eclogites (Avellaneda et al., 2017; García–Ramírez et al., 2017) and their estimated ages suggest a strong correlation with Barragán rock occurrences (Bustamante et al., 2012) that could represent subduction–collision complexes (e.g., Avellaneda et al., 2017; Bustamante et al., 2012) and need not be related to the roll–back processes proposed by Spikings et al. (2015) and García–Ramírez et al. (2017).

4. Discussion

4.1. Age of Metamorphism and Protoliths

The most recent and precise ages of the high–pressure metamorphic rocks of the Central Cordillera compiled in this review (Table 1) indicate that at least two different high–pressure metamorphic events occurred during the Cretaceous – Paleogene in the northern Andes, and are recorded at the western flank of the Central Cordillera. The first occurred between 128 and 120 Ma (Early Cretaceous) and is represented by the Barragán blueschists (Bustamante et al., 2012) and Pijao eclogites (García–Ramírez et al., 2017). The second occurred between 70 and 60 Ma (Late Cretaceous to Paleogene) when the Jambaló blueschists were formed (Bustamante et al., 2011). This hypothesis opposes models that consider the entirety of the high–pressure metamorphic rocks of the Central Cordillera to have been formed in a single Early Cretaceous event (De Souza et al., 1984; García–Ramírez et al., 2017; Orrego et al., 1980b; Spikings et al., 2015; Villagómez & Spikings, 2013).

Available whole–rock geochemistry from the Pijao, Barragán, and Jambaló high–pressure rocks shows that a basaltic protolith is common for the three, although in Jambaló a basaltic andesite may have been present (Figure 6). Despite similar mafic protoliths, we postulate that the Barragán and Pijao high–pressure rocks share the same N–MORB signature (Figures 7, 8) as suggested in the Zr–Nb–Y diagram (Figure 9). The Jambaló rocks may represent an intra–oceanic arc that

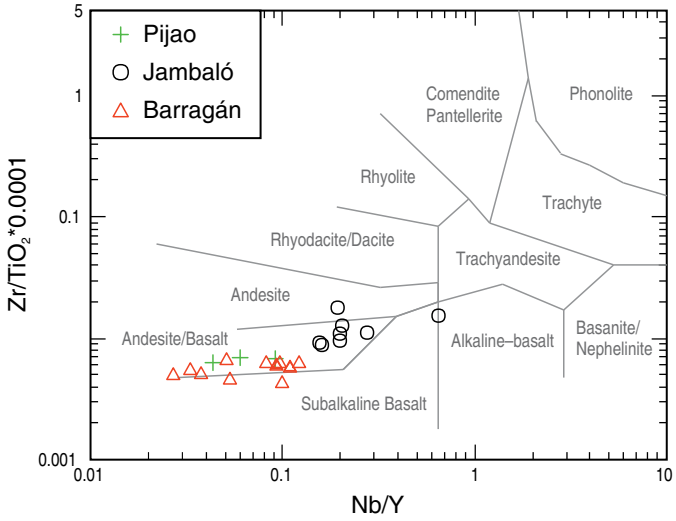

Figure 6. Classification of basic rocks based on the Nb/Y versus Zr/TiO_2 diagram, after Winchester & Floyd (1977).

grew over plume–modified oceanic crust (Bustamante, 2008). Thus, the Early Cretaceous metamorphic event may be linked to the subduction of the Farallón Plate, whereas the Late Cretaceous metamorphism is linked to the Caribbean Plate.

4.2. Tectonic Implications and Possible Correlations

The Early Cretaceous high–pressure metamorphic event recorded in the Central Cordillera (Figure 10; Barragán and Pijao rocks) may represent an event of subduction–accretion that occurred before the collision of the Caribbean Plate with the western margin of South America (Avellaneda et al., 2017; Bustamante et al., 2012). Until the high–pressure metamorphic event occurred, between 128 to 120 Ma according to the data presented above, the western margin of the northern Andes was characterized by an oblique convergence with the Farallón Plate which may have caused a transpressive margin and the ending of the arc–related magmatism that dominated between the Early Jurassic and Early Cretaceous (ca. 200 to 130 Ma sensu Bustamante et al., 2016). These tectonic scenarios differ from those proposed by García–Ramírez et al. (2017), who suggest the slab roll–back process during the same time interval as the western margin of the northern Andes, caused by the eclogitization of the subduction slab and, hence, an increase in its density. The slab roll–back model was previously proposed to explain the magmatic evolution of the northern Andes from the Jurassic until Early Cretaceous (Cochrane et al., 2014; Leal–Mejía, 2011; Spikings et al., 2015). However, this mechanism involves the progressive increase of back–arc extension, triggering the exhumation of high–pressure rocks and even ultra–high–pressure rocks (Brun & Faccenna, 2008).

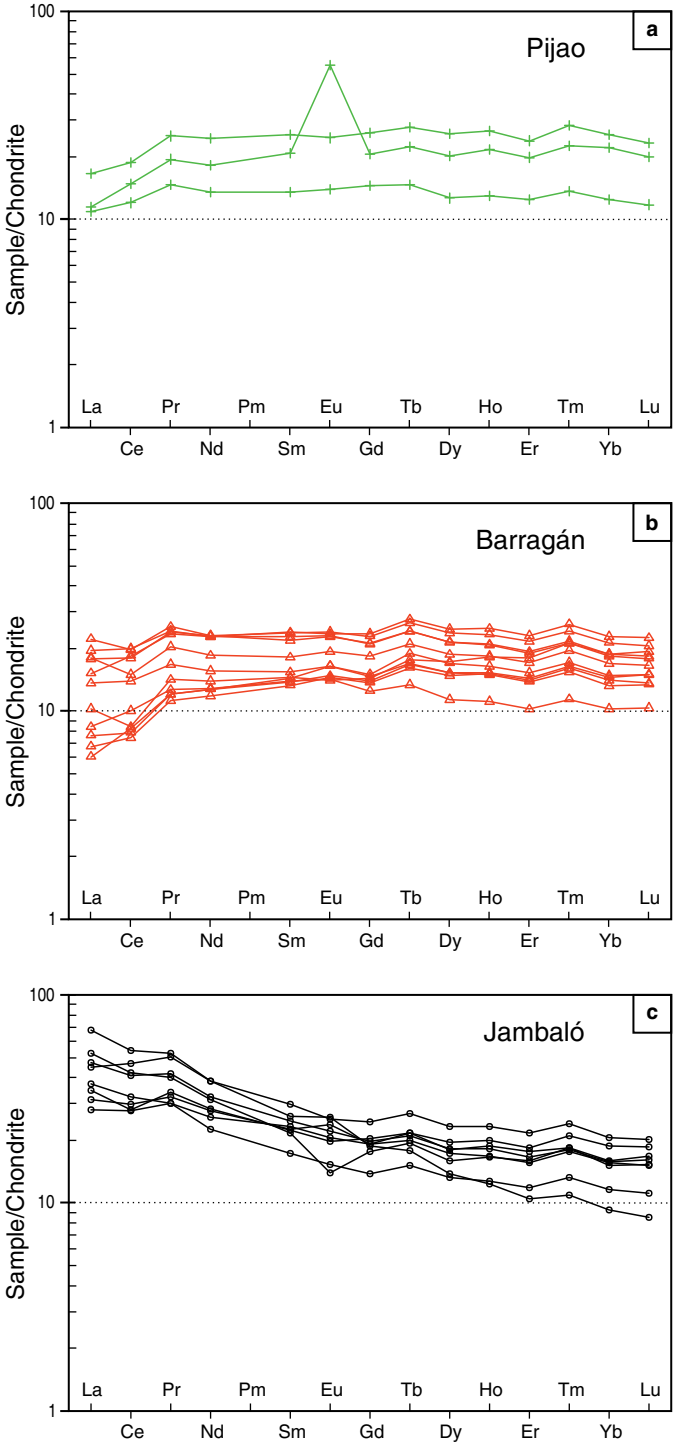

Figure 7. Chondrite–normalized REE patterns of the high–pressure metamorphic rocks. Diagram after Nakamura et al. (1974). **(a)** Pijao. **(b)** Barragán. **(c)** Jambaló.

Spikings et al. (2015) suggest that the Lower Cretaceous high–pressure metamorphic sequence (including the Jambaló blueschists) originated as a MORB and metamorphosed within the same subduction zone, followed by its exhumation between 120 and 112 Ma. Additionally, they report that the

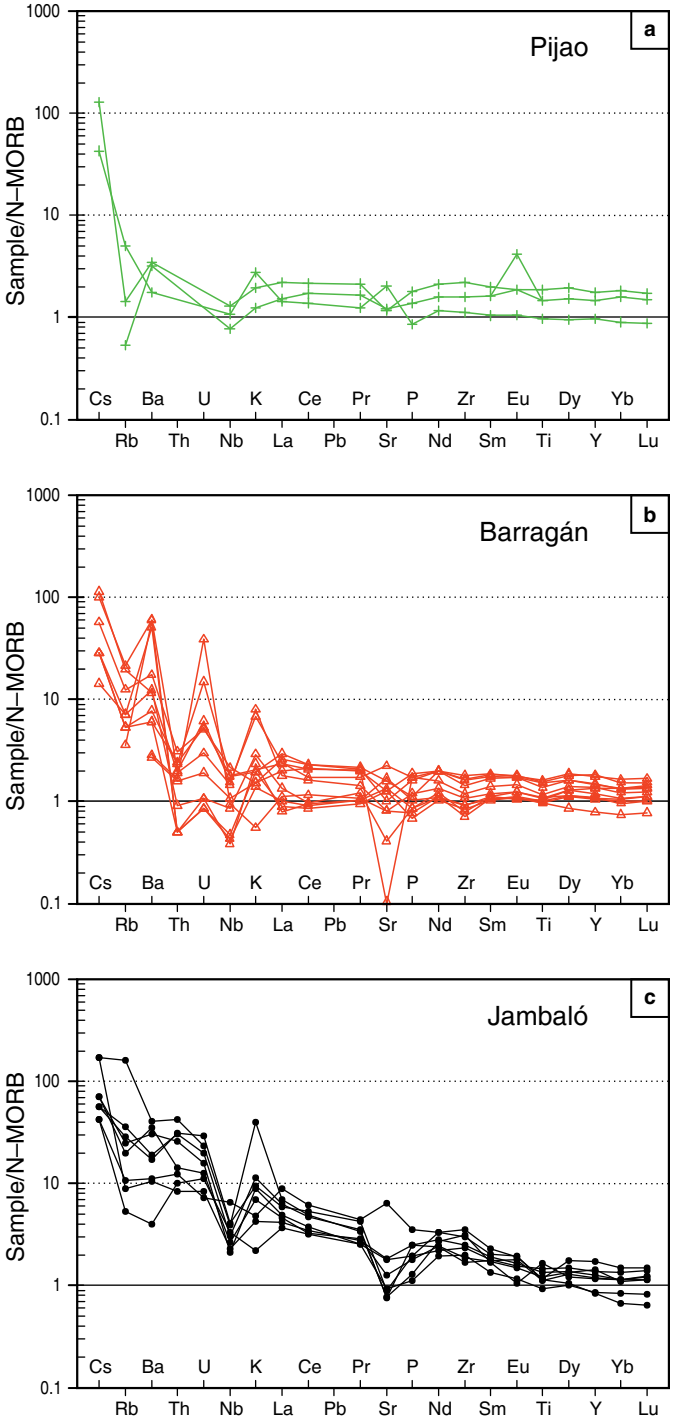

Figure 8. Multi–element plot normalized to primitive mantle after Sun & McDonough (1989). **(a)** Pijao. **(b)** Barragán. **(c)** Jambaló.

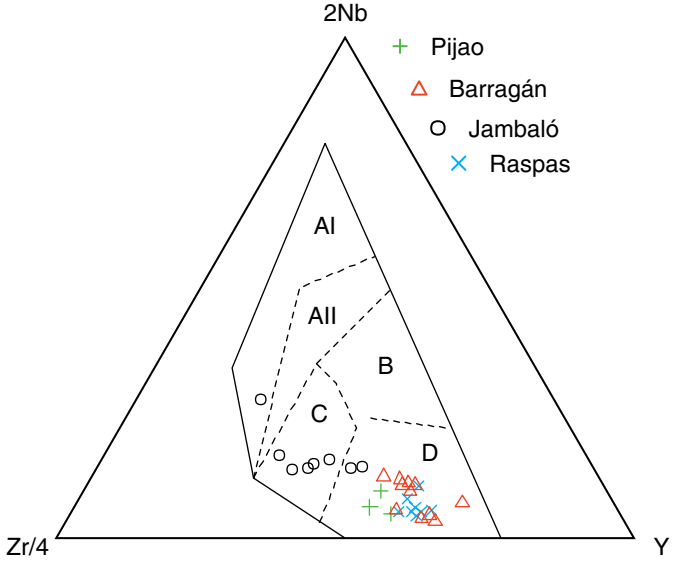

Figure 9. Zr/4–2Nb–Y diagram for classifying tholeiitic basalts from Meschede (1986).

high–pressure rocks of the Raspas Metamorphic Complex in Ecuador may be correlated with those of the Central Cordillera of Colombia, due to their similar tectonic position, lithological similarities, and degree of metamorphism. However, the Ar–Ar ages obtained in the Jambaló rocks (Bustamante et al., 2011) are discarded in that model as the geochemical constraints are, in fact, not based on the high–pressure rocks, but in associated garnet–amphibolites grouped in the Arquía Complex (Maya & González, 1995).

A second subduction zone, active during the Early Cretaceous, was the location of the high–pressure metamorphism of the Jambaló rocks (Figure 10). The basaltic rocks comprising their protolith may have formed in an intra–oceanic arc originated over a plume modified lithosphere, according to the results of Bustamante (2008). This intra–oceanic arc further collided with the continental margin of NW South America which contributed to an increase in its thickness as recorded in the Eocene high Sr/Y arc–related magmas distributed along the Central Cordillera (Bustamante et al., 2017b). This may be the only record of Caribbean–related high–pressure metamorphism in the northern Andes.

The blueschists and eclogites of the Raspas Metamorphic Complex in the Eastern Cordillera of Ecuador have MORB and seamount–like protoliths. These rocks reached their metamorphic peak conditions at ca. 130 Ma (John et al., 2010). Their geochemical trends and the age of metamorphism recorded within the Barragán high–pressure rocks, when compared with the Raspas Metamorphic Complex (Figure 9), allowed Spikings et al. (2015) to propose that these high–pressure belts shared the same geological history. Although such a comparison may be valid based on the abovementioned similarities, caution should be taken when evaluating this high–pressure metamorphic belt since the pressure–temperature–time (P–T–t) paths of its constituents have never been compared. It is clear that the Jambaló schists should not be considered as a continuation of the same high–pressure belt

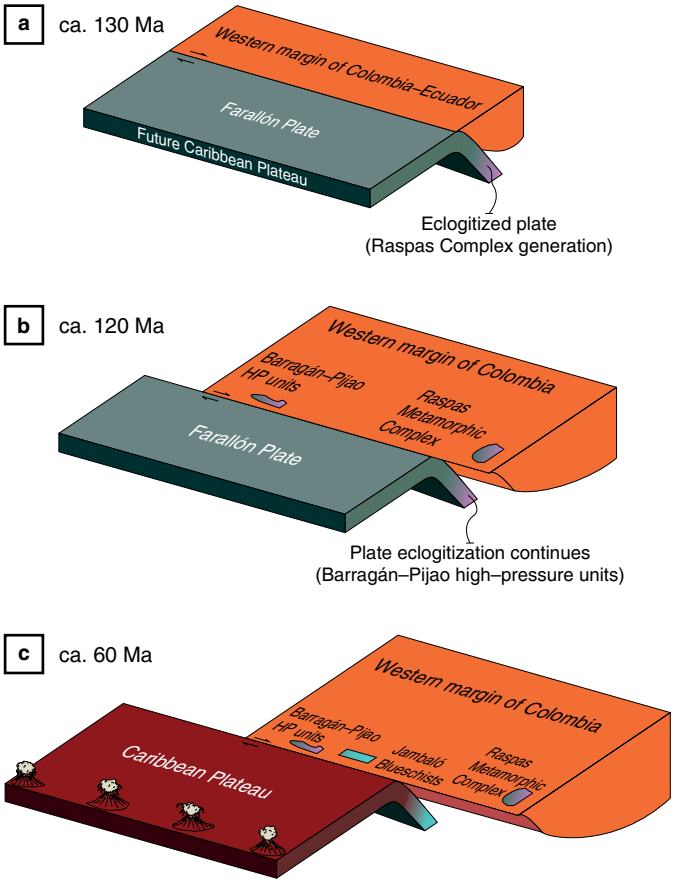

Figure 10. Cartoons (not to scale) of the proposed model for the generation of high–pressure metamorphic rocks at the northern Andes (including Raspas Metamorphic Complex) at three instances: ca. 130 Ma, ca. 120 Ma, and ca. 60 Ma. The figure suggests the relationships between oblique convergence and the exhumation of the high–pressure metamorphic units (HP units). **(a)** Farallón Plate subducts beneath South American Plate. Eclogitization of Farallón Plate results in Raspas Metamorphic Complex generation. **(b)** Farallón Plate eclogitization continues to form Barragán–Pijao high–pressure units. **(c)** Caribbean Plateau replaces Farallón Plate and begins its subduction process to form the Jambaló blueschists. In the portion shown, the eclogite facies is not reached. Oblique convergence continues.

as proposed by Spikings et al. (2015), according to the geochemical and age differences that these rocks present with the other high–pressure rock sequences (Bustamante, 2008). No other Lower Cretaceous – Paleogene blueschists are present in the northern Andes, and hence no similar rocks exist with which they can be compared.

5. Conclusions

High–pressure metamorphic rocks in Colombia, including blueschists and eclogites, are currently recognized at three localities: Pijao (eclogites), Barragán (blueschists and retrograded eclogites), and Jambaló (blueschists). The first two share the same N–MORB–like protolith, and an Early Cretaceous metamorphic age, whereas extensive geochemical data of the Jambaló blueschists is instead indicative of a protolith formed in a plume–influenced intra–oceanic arc, whose metamorphism occurred between the Late Cretaceous and Paleogene.

From these high–pressure lithologies in the Central Cordillera, it is postulated that two subduction events occurred during the Cretaceous. The first, characterized by episodes of subduction–accretion, would have provoked high–pressure metamorphism in an oblique subduction regime, forcing the slab roll–back process otherwise not plausible during this time. The second episode of subduction produced the Jambaló blueschists in an intra–oceanic arc, involving further collision with the continental margin and increasing its thickness, as recorded in the adakite–like magmatism of the Central Cordillera.

Possible correlations of the Pijao and Barragán rocks with similar rocks of the Raspas Metamorphic Complex in the Eastern Cordillera of Ecuador are possible as they are geochemically similar and contemporaneous. However, P–T–t paths are required to form these conclusions. Conversely, the Jambaló rocks have no similarities with Pijao and Barragán rocks, which impede their correlation.

Acknowledgments

We express our gratitude to the Servicio Geológico Colombiano for inviting us to contribute to this book. Interesting discussions with Agustín CARDONA (Escuela de Procesos y Energía, Universidad Nacional de Colombia) helped improve the style and conclusions of this work. The writers benefited from many discussions with Caetano JULIANI (Instituto de Geociências, Universidade de São Paulo, Brazil) and Antonio GARCÍA CASCO (Departamento de Mineralogía y Petrología, Universidad de Granada, Spain). Comments from Victor A. RAMOS and Franco URBANI helped improve the quality of this manuscript.

References

Agard, P., Yamato, P., Jolivet, L. & Burov, E. 2009. Exhumation of oceanic blueschists and eclogites in subduction zones: Timing and mechanisms. Earth–Science Reviews, 92(1–2): 53–79. https://doi.org/10.1016/j.earscirev.2008.11.002

Alcárcel, F.A. & Gómez, J., compilers. 2019. Mapa Geológico de Colombia 2019. Scale 1:2 000 000. Servicio Geológico Colombiano. Bogotá.

Aspden, J.A. & McCourt, W.J. 1986. Mesozoic oceanic terrane in the central Andes of Colombia. Geology, 14(5): 415–418. https://doi.org/10.1130/0091-7613(1986)14<415:MOTITC>2.0.CO;2

Aspden, J.A., Bonilla, W. & Duque, P. 1995. The El Oro Metamorphic Complex, Ecuador: Geology and economic mineral deposits.

British Geological Survey, Overseas Geology and Mineral Resources 67, 63 p. Nottingham, UK.

Avellaneda, D.S., Cardona, A. & Valencia, V. 2017. Yuxtaposición de escamas metamórficas contrastantes en las rocas del Grupo Bugalagrande y Complejo Rosario: Implicaciones en un régimen de subducción/colisión para el Cretácico Inferior. XVI Congreso Colombiano de Geología. Memoirs, p. 1805–1808. Santa Marta.

Blanco–Quintero, I.F., García–Casco, A., Toro, L.M., Moreno–Sánchez, M., Ruiz, E.C., Vinasco, C.J., Cardona, A., Lázaro, C. & Morata, D. 2014. Late Jurassic terrane collision in the northwestern margin of Gondwana (Cajamarca Complex, eastern flank of the Central Cordillera, Colombia). International Geology Review, 56(15): 1852–1872. https://doi.org/10.1080/00206814.2014.963710

Bosch, D., Gabriele, P., Lapierre, H., Malfere, J.L. & Jaillard, E. 2002. Geodynamic significance of the Raspas Metamorphic Complex (SW Ecuador): Geochemical and isotopic constraints. Tectonophysics, 345(1–4): 83–102. https://doi.org/10.1016/S0040-1951(01)00207-4

Botero, G. 1963. Contribución al conocimiento de la geología de la zona central de Antioquia. Universidad Nacional de Colombia, Anales de la Facultad de Minas, 57, 101 p. Medellín.

Bourgois, J., Toussaint, J.F., González, H., Azema, J., Calle, B., Desmet, A., Murcia, L.A., Acevedo, A.P., Parra, E. & Tournon, J. 1987. Geological history of the Cretaceous ophiolitic complexes of northwestern South America (Colombian Andes). Tectonophysics, 143(4): 307–327. https://doi.org/10.1016/0040-1951(87)90215-0

Brun, J.P. & Faccenna, C. 2008. Exhumation of high–pressure rocks driven by slab rollback. Earth and Planetary Science Letters, 272(1–2): 1–7. https://doi.org/10.1016/j.epsl.2008.02.038

Bustamante, A. 2008. Geotermobarometria, geoquímica, geocronologia e evolução tectônica das rochas da fácies xisto azul nas áreas de Jambaló (Cauca) e Barragán (Valle del Cauca), Colômbia. Doctoral thesis, Universidade de São Paulo, 242 p. São Paulo. https://doi.org/10.11606/T.44.2008.tde-22082008-155904

Bustamante, A., Juliani, C., Hall, C.M. & Essene, E.J. 2011. $^{40}Ar/^{39}Ar$ ages from blueschists of the Jambaló region, Central Cordillera of Colombia: Implications on the styles of accretion in the northern Andes. Geologica Acta, 9(3–4): 351–362. https://doi.org/10.1344/105.000001697

Bustamante, A., Juliani, C., Essene, E.J., Hall, C.M. & Hyppolito, T. 2012. Geochemical constraints on blueschist– and amphibolite–facies rocks of the Central Cordillera of Colombia: The Andean Barragán region. International Geology Review, 54(9): 1013–1030. https://doi.org/10.1080/00206814.2011.594226

Bustamante, C., Archanjo, C.J., Cardona, A. & Vervoort, J.D. 2016. Late Jurassic to Early Cretaceous plutonism in the Colombian Andes: A record of long–term arc maturity. Geological Society of America Bulletin, 128(11–12): 1762–1779. https://doi.org/10.1130/B31307.1

Bustamante, C., Archanjo, C.J., Cardona, A., Bustamante, A. & Valencia, V.A. 2017a. U–Pb ages and Hf isotopes in zircons from parautochthonous Mesozoic terranes in the western margin of Pangea: Implications for the terrane configurations in the northern Andes. The Journal of Geology, 125(5): 487–500. https://doi.org/10.1086/693014

Bustamante, C., Cardona, A., Archanjo, C.J., Bayona, G., Lara, M. & Valencia, V. 2017b. Geochemistry and isotopic signatures of Paleogene plutonic and detrital rocks of the northern Andes of Colombia: A record of post–collisional arc magmatism. Lithos, 277: 199–209. https://doi.org/10.1016/j.lithos.2016.11.025

Cardona, A., Montes, C., Ayala, C., Bustamante, C., Hoyos, N., Montenegro, O., Ojeda, C., Niño, H., Ramírez, V., Valencia, V., Rincón, D., Vervoort, J.D. & Zapata, S. 2012. From arc–continent collision to continuous convergence, clues from Paleogene conglomerates along the southern Caribbean–South America Plate boundary. Tectonophysics, 580: 58–87. https://doi.org/10.1016/j.tecto.2012.08.039

Clauer, N. & Chaudhuri, S. 1999. Isotopic dating of very low–grade metasedimentary and metavolcanic rocks: Techniques and methods. In: Frey, M. & Robinson, D. (editors), Low–grade metamorphism. Blackwell–Science, p. 202–226. https://doi.org/10.1002/9781444313345.ch7

Cochrane, R., Spikings, R., Gerdes, A., Winkler, W., Ulianov, A., Mora, A. & Chiaradia, M. 2014. Distinguishing between in–situ and accretionary growth of continents along active margins. Lithos, 202–203: 382–394. https://doi.org/10.1016/j.lithos.2014.05.031

Dallmeyer, R.D. & Takasu, A. 1992. $^{40}Ar/^{39}Ar$ ages of detrital muscovite and whole–rock slate/phyllite, Narragansett Basin, RI–MA, USA: Implications for rejuvenation during very low–grade metamorphism. Contributions to Mineralogy and Petrology, 110(4): 515–527. https://doi.org/10.1007/BF00344085

De Souza, H.A.F., Espinosa, A. & Delaloye, M. 1984. K–Ar ages of basic rocks in the Patía valley, southwest Colombia. Tectonophysics, 107(1–2): 135–145. https://doi.org/10.1016/0040-1951(84)90031-3

Ernst, W.G. 1988. Tectonic history of subduction zones inferred from retrograde blueschist P–T paths. Geology, 16(12): 1081–1084. https://doi.org/10.1130/0091-7613(1988)016<1081:THOSZI>2.3.CO;2

Feininger, T. 1980. Eclogite and related high–pressure regional metamorphic rocks from the Andes of Ecuador. Journal of Petrology, 21(1): 107–140. https://doi.org/10.1093/petrology/21.1.107

Feininger, T. 1982. Glaucophane schist in the Andes at Jambalo, Colombia. The Canadian Mineralogist, 20(1): 41–48.

García–Ramírez, C.A., Ríos–Reyes, C.A., Castellanos–Alarcón, O.M. & Mantilla–Figueroa, L.C. 2017. Petrology, geochemistry and

geochronology of the Arquía Complex´s metabasites at the Pijao–Génova sector, Central Cordillera, Colombian Andes. Boletín de Geología, 39(1): 105–126.

González, H. 1997. Metagabros y eclogitas asociadas en el área de Barragán, departamento del Valle, Colombia. Geología Colombiana, 22: 151–170.

John, T., Scherer, E.E., Schenk, V., Herms, P., Halama, R. & Garbe–Schönberg, D. 2010. Subducted seamounts in an eclogite–facies ophiolite sequence: The Andean Raspas Complex, SW Ecuador. Contributions to Mineralogy and Petrology, 159(2): 265–284. https://doi.org/10.1007/s00410-009-0427-0

Kerr, A.C., Marriner, G.F., Tarney, J., Nivia, Á., Saunders, A.D., Thirlwall, M.F. & Sinton, C.W. 1997. Cretaceous basaltic terranes in western Colombia: Elemental, chronological and Sr–Nd isotopic constraints on petrogenesis. Journal of Petrology, 38(6): 677–702. https://doi.org/10.1093/petrology/38.6.677

Leal–Mejía, H. 2011. Phanerozoic gold metallogeny in the Colombian Andes: A tectono–magmatic approach. Doctoral thesis, Universitat de Barcelona, 989 p. Barcelona.

Maruyama, S., Liou, J.G. & Terabayashi, M. 1996. Blueschists and eclogites of the world and their exhumation. International Geology Review, 38(6): 485–594. https://doi.org/10.1080/00206819709465347

Maya, M. & González, H. 1995. Unidades litodémicas en la cordillera Central de Colombia. Boletín Geológico, 35(2–3): 43–57.

McCourt, W.J. & Feininger, T. 1984. High pressure metamorphic rocks in the Central Cordillera of Colombia. British Geological Survey Reprint Series, 84(1): 28–35.

Meschede, M. 1986. A method of discriminating between different types of mid–ocean ridge basalts and continental tholeiites with the Nb–Zr–Y diagram. Chemical Geology, 56(3–4): 207–218. https://doi.org/10.1016/0009-2541(86)90004-5

Nakamura, N. 1974. Determination of REE, Ba, Fe, Mg, Na and K in carbonaceous and ordinary chondrites. Geochimica et Cosmochimica Acta, 38(5): 757–775. https://doi.org/10.1016/0016-7037(74)90149-5

Núñez, A. & Murillo, A. 1978. Esquistos de glaucofana en el municipio de Pijao, Quindío (Colombia). II Congreso Colombiano de Geología. Memoirs, II, p. 17. Bogotá.

Orrego, A., Cepeda, H. & Rodríguez, G. 1980a. Esquistos glaucofánicos en el área de Jambaló, Cauca (Colombia). Geología Norandina, (1): 5–10.

Orrego, A., Restrepo J.J., Toussaint, J.F. & Linares, E. 1980b. Datación de un esquisto sericítico de Jambaló, Cauca. Boletín de Ciencias de la Tierra, (5–6): 133–134.

Pindell, J.L. & Kennan, L. 2009. Tectonic evolution of the Gulf of Mexico, Caribbean and northern South America in the mantle reference frame: An update. In: James, K.H., Lorente, M.A. & Pindell J.L. (editors), The origin and evolution of the Caribbean Plate. Geological Society of London, Special Publication 328, p. 1–55. https://doi.org/10.1144/SP328.1

Ramos, V.A. 2009. Anatomy and global context of the Andes: Main geologic features and the Andean orogenic cycle. In: Kay, S.M., Ramos, V.A. & Dickinson, W.R. (editors), Backbone of the Americas: Shallow subduction, plateau uplift, and ridge and terrane collision. Geological Society of America, Memoirs 204, p. 31–65. https://doi.org/10.1130/2009.1204(02)

Restrepo, J.J. & Toussaint, J.F. 1988. Terranes and continental accretion in the Colombian Andes. Episodes, 11(3): 189–193.

Spikings, R., Cochrane, R., Villagómez, D., van der Lelij, R., Vallejo, C., Winkler, W. & Beate, B. 2015. The geological history of northwestern South America: From Pangaea to the early collision of the Caribbean Large Igneous Province (290–75 Ma). Gondwana Research, 27(1): 95–139. https://doi.org/10.1016/j.gr.2014.06.004

Sun, S.S. & McDonough, W.F. 1989. Chemical and isotopic systematics of oceanic basalts: Implications for mantle composition and processes. In: Saunders, A.D. & Norry, M.J. (editors), Magmatism in the ocean basins. Geological Society of London, Special Publication 42, p. 313–345. https://doi.org/10.1144/GSL.SP.1989.042.01.19

Villagómez, D. & Spikings, R. 2013. Thermochronology and tectonics of the Central and Western Cordilleras of Colombia: Early Cretaceous – Tertiary evolution of the northern Andes. Lithos, 160–161: 228–249. https://doi.org/10.1016/j.lithos.2012.12.008

Villagómez, D., Spikings, R., Magna, T., Kammer, A., Winkler, W. & Beltrán, A. 2011. Geochronology, geochemistry and tectonic evolution of the Western and Central Cordilleras of Colombia. Lithos, 125(3–4): 875–896. https://doi.org/10.1016/j.lithos.2011.05.003

Winchester, J.A. & Floyd, P.A. 1977. Geochemical discrimination of different magma series and their differentiation products using immobile elements. Chemical Geology, 20: 325–343. https://doi.org/10.1016/0009-2541(77)90057-2

Explanation of Acronyms, Abbreviations, and Symbols:

HREE	Heavy rare earth element
LREE	Light rare earth element
MREE	Middle rare earth element
N–MORB	Normal mid–ocean ridge basalt
REE	Rare earth element

Authors' Biographical Notes

Camilo BUSTAMANTE obtained his undergraduate degree in geology in 2007 (Universidad EAFIT) and PhD in mineralogy and petrology in 2016 (Universidade de São Paulo). He is currently a professor of igneous petrology at the Universidad EAFIT in Colombia. His main research area is the tectono–magmatic and metamorphic evolution of the northern Andes.

Andres BUSTAMANTE is a geologist (Universidad EAFIT) and PhD in mineralogy and petrology (Universidade de São Paulo). He is currently a professor of metamorphic petrology and geological mapping at Universidade Federal de Pernambuco, in the northeastern region of Brazil. His main research interests are focused on high–pressure metamorphic processes in South America.

Bogotá, Colombia
2020